タンパク質機能の１分子デザインとシステム構築

(研究課題番号　14002008)

平成 14 年度～平成 18 年度科学研究費補助金（特別推進研究）

研究成果報告書

平成 19 年 5 月

研究代表者　石渡　信一

(早稲田大学理工学術院・教授)

はしがき

本報告書は、平成１４年度（2002年4月）から１８年度（2007年3月）にわたる5年間で行った文部科学省特別推進研究「タンパク質機能の1分子デザインとシステム構築（課題番号14002008)」の研究成果をまとめたものである。まず未発表のものを含めて主要な研究成果についてまとめたのち、各研究担当者による報告を掲載した。これらの報告の中にはまだ論文として公表していないものも含まれるが、なるべく早い公表を期したい。

本研究には多くの大学院生たちが関与している。特に鈴木団（2005.3博士号取得：現、早大客員講師)、佐々木大輔（2006.3博士号取得：現、東京女子医大PD)、上村想太郎（2004.3博士号取得：Stanford大PDを経て現、東大助手)、下澤東吾（早大博士課程を経て早大助手、現、東北大助教)、島本勇太（早大博士課程を経て現、早大助手)、小口祐伴（早大 D3）らの寄与が大きい。我々のグループとしては、特別推進研究によって初めてPDを雇用する機会を得たと言っても良い。適任者を見いだすのに時間を要したことで3年目からの雇用となったが、Sergey V. Mikhailenko、Vadim Zeeb（モスクワからの訪問研究者)、大木高志、板橋岳志らのリードなくしてこれまでの研究の進展はなかった。

さらに、幾つかのグループと共同研究を行った。樋口秀男（東北大教授)、Enrique M. De La Cruz (Yale大准教授)、武藤悦子（理研研究員)、福田紀男（慈恵医大講師)、栗原敏（同教授)、安田賢二（東大総合文化研究科助教授、現、東京医科歯科大教授)、豊島陽子（東大総合文化研究科教授)、河合正隆（Iowa大教授)、Svetlana M. Strukova（Moscow大教授）の諸氏との研究は幸い論文としてまとめることができた。論文にはなっていないが、Tarun Kapoor（Rockefeller大准教授）研との研究は着実に進んでいる。また、Liou Ying-Ming氏（国立中興大教授）は本研究によって毎夏・冬数ヶ月滞在して研究を行ったが、最近では台湾で獲得した自己資金で来日して研究を継続している。このように、共同研究を国内にとどまらず海外へと広げることができたのは、ひとえに本研究課題のおかげである。

本研究期間の途中で船津高志が早稲田大学から東京大学薬学研究科教授として転出したが、その後も共同研究を継続するだけでなく、数ヶ月に一度、石渡研・船津研合同のシンポジウムを開催し、適宜会合を開くことを通じて研究成果に関する情報交換を行ってきた。さらに、それぞれの研究室の大学院生・スタッフたちは互いに懇意であることから、細々した情報交換も自由に行ってきたことを強調したい。

また、国立岡崎研究機構・統合バイオサイエンスセンターから2005年4月に早稲田大学物理学科に移った木下一彦氏とそのグループとは、それまで以上に緊密な研究交流を続けてきた。CREST研究の当初から、数ヶ月に一度、木下研、吉田賢右研（東工大）を中心にSKYセミナーを開催してきたが、一旦中断していたSKYセミナーを今では毎月早稲田大学で開催し、修士課程以上の大学院生やPDを中心に最新の未発表データを示して意見交換をしている。また20年以上に亘って、慈恵医大馬詰良樹研とは毎年一度の合宿ゼミを開いている。こうして、多くの研究室や研究仲間との交流をとおして、若手の成長をみることができた。記して関係各位に感謝したい。

平成19年5月

研究代表者　　石渡 信一

研究課題の目的及び意義（申請書から抜粋）

天然にデザインされたタンパク質の機能は、３次元的なアミノ酸配置として組み込まれており、そこに働く分子間力と熱揺らぎ（環境）の織りなすダイナミクスによって実現している。機能性タンパク質分子機械の仕掛け（機能発現のための設計原理である分子デザイン）を、１分子と分子集合体のレベルで明らかにしたい。我々は今、１分子イメージング・機能解析・操作のための独自の顕微技術を手にしており、タンパク質の機能発現に伴うnmの動き（構造変化、Brown運動）とサブpNの力（エネルギー）を時々刻々１分子レベルで記録・解析することができる。そこで、タンパク質機能が、物理的・化学的環境という制約の中で、どのようにデザインされているか（非生物を支配する物理・化学法則をどのように利用して生物固有の性質を生み出すか）を、タンパク質の“動きと力”を指標に時空間的に記録し解析する。この目的のために力学酵素（ミオシン、キネシンなどの分子モーター）、細胞骨格（アクチンフィラメント、微小管）やシャペロニン、心筋培養細胞などを取り上げる。動き（結合・解離）を１分子イメージングし、力を計測して機能素過程を解明する一方、力を加えて機能（酵素作用）を変調・制御する。さらに、生体ナノマシンを集積し、高次の生体機能を発現させる。天然の生体システムの構成要素を交換したり、生物固有の構造を選択的に解体・再構築することによって、生体構造の形成メカニズムと生体機能の分子メカニズムを明らかにし、それらを自在に制御するための手法を追究する。

研究成果の概要

研究代表者の石渡グループは、生体分子モーターを中心に、１分子からシステム（分子集合体、超分子構造、細胞）に亘る機能発現のメカニズムに着目し、新しい実験系や新しい実験法を開発しつつ当初の研究目的に沿って研究を継続した。

１．分子で機能する分子モーター（Myosin V,VIとキネシン）の１分子結合力計測と１分子運動測定

この研究課題のために、まず「１分子高速力学測定のための顕微鏡システム」を構築した。このシステムは、２ヶ所で捕捉可能な光ピンセットを搭載し、４分割フォトダイオードによるビーズの高速変位検出や、落射照明とエバネッセント照明の切り替えが可能なことから、１分子蛍光イメージングと力学測定同時可能という特徴がある。

キネシン・微小管系で成功を収めた１分子破断力計測（2003年に *Nature Struct. Biol.*と *Biophys.J.*に発表：上村想太郎の報告）を、Myosin V、VIとアクチンフィラメントの結合力計測に応用し、幾つかのヌクレオチド状態での結合破断力への負荷上昇速度、負荷方向依存性を明らかにした（Yale大学 De La Cruz研との共同研究）。この計測は、分子間の結合寿命に対する外部負荷の大きさと方向の依存性を明らかにするものであり、分子モーターの運動メカニズムにおける力と酵素活性との相関を直接的に明らかにするための有力なアプローチである（Myosin Vについては小口祐伴の報告、Myosin VIについてはS.V.Mikhailenkoの報告；論文投稿中）。Myosin・アクチン系の１分子計測は、キネシン・微小管系と比べて格段に難しく（主としてアクチンフィラメントが細く、柔らかいため）、測定法の確立までに半年以上を要したが、１年以上にわたる研究を通じて大変興味深い成果が得られた。さらにキネシンについては、大腸菌に発現させた単頭キネシンを研究室で精製することができるようになり、実験応用範囲を広げることが可能になった。

一方、アクチンフィラメント上でのMyosin Vの１分子歩行運動を高時空間分解能で顕微解析し、Myosin V分子モーターの36 nmステップが24 nmと12 nmのサブステップからなることを見出した。この研究ではDe La Cruz研（Yale大学）と協力し、BDM（筋弛緩剤）の作用が無機リン酸Piの解離を抑制する筋ミオシンIIの場合とは異なり、意外なことにADPの解離を抑制するものであることを明らかにしたことによって、サブステップとATP加水分解過程（特にADP解離）との対応関係が明らかになり、新しい歩行モデルを提出することができた（2004年に *Nature Struct. Mol. Biol.*に論文発表：上村想太郎の報告）。

2．アクチンフィラメント・微小管（アミノ酸置換体を含む）の構造と機能

1本のアクチンフィラメントの重合･脱重合ダイナミクスをエバネッセント照明法によって顕微直視し、トレッドミル機構の存在を証明した。さらに定常状態での長さ揺らぎがアクチン1分子の結合･解離の揺らぎでは説明できず、協同的な結合・解離（動的不安定性の現れかもしれない）を示唆した。この研究は石渡研と船津研との共同研究が実を結んだものであり、とくにエバネッセント照明法を組み上げる際にその力が発揮できた（2002年に *Nature Cell Biol.*に発表したが、Newsとして同号にLittlefield & Fowlerによる解説記事が掲載された：藤原郁子の報告)。

アミノ酸置換をした変異アクチンを用いた研究を展開する予定であったが、それを任意に調製できる環境を作るのに3年以上を要した。この点については、遺伝子組み換え技術をもつプロフェッショナルのPDを雇用することが出来なかったことが最大の原因であり､本研究課題における反省点である。一言その理由を述べれば、平成16年度の段階で、352番目のPheをArgに置換したアクチン分子を調製することができ、しかもMyosin VとMyosin IIの運動特性への影響を調べた結果、負荷を加えたときの運動速度などに変化が現れるなど、大変興味深い結果が得られたことから、十分な見通しが立ったと判断したことが大きい。しかしその後このアクチンを調製することができなくなったことで、一時的に変異アクチンを用いた研究が頓挫することとなった。というわけで、変異アクチンを用いた研究はやっと最近になって軌道に乗り始めたというのが実情である。

アミノ酸置換微小管（チューブリン）については、その調製が武藤研（理研）で実現したことから、とくにキネシンとの強結合部位を形成すると予測されていた部位についてアミノ酸置換したチューブリン変異体に対するキネシン分子の1分子結合破断力測定を行い、結合破断力とStall力（ATP存在下での最大発生力）との間に強い相関があることが見いだされた（2006年、*EMBO. J.*に論文発表：小口祐伴の報告)。

その一方で、正常なアクチンフィラメントや微小管の構造（柔らかさ）と機能（アクチン結合タンパク質との相互作用など）を1分子レベルで計測することができる実験系を開発してきた。そこで、本研究課題の一つの目標でもあった“バイオナノゲージ”の開発という課題に取り組んだ。その結果､アクチンフィラメントに結合した蛍光分子(アクチンのCys374にラベルしたRhodamine)の蛍光強度が、加えた負荷の大きさに応じて可逆的に変化するというバイオナノゲージにつながる研究成果を得た。一方、同じCys374へのラベルであってもBODIPYの場合には負荷依存的な蛍光強度の変化が非常に小さいこと、またコントロールとして計測したRhodamine-Phalloidinについても同様であることが見いだされた（論文作成中)。

3．A帯滑り運動系（Bio-nanomuscle）の開発と収縮運動特性

ミオシン(太い)フィラメントの束からなるA帯に、1本のアクチンフィラメントを滑り込ませ、そこに発生する力を計測するという“A帯滑り運動系（Bio-nanomuscle)”については、我々は10年間に亘って開発を続けてきたが、やっと実験系として確立することができた。この実験系は、筋収縮系の秩序構造を保った最小の収縮運動系といえる。この実験系では、一本のアクチンフィラメントと相互作用するミオシン分子（Cross-bridge）の数が10個程度であるために、結合するCross-bridgeの数が揺らぎ、発生力が大きく揺らぐが、平均の発生力は、ミオシンフィラメントとアクチンフィラメントの重なり部分の大きさに比例した。滑り運動機構の最も重要な性質を確認できたことになる。このような結果を中心に*Biophys. J.*の2005年7月号に論文を掲載、それに対してNew and NotableにJ. Molloyが紹介記事を書いた。そこでは、この実験系を、1分子系と筋収縮系をつなぐ全く新しい第三の実験系として評価している。その後、低ATP濃度におけるステップ状運動の解析や、SPOC（自励振動）条件での力発生、運動性を検討した（鈴木団の報告：未発表)。

4．SPOCの分子メカニズム

我々が1988年に報告したSPOC（SPontaneous Oscillatory Contraction）現象は、収縮と弛緩の中間の条件で発生する、筋収縮系の不安定状態であるが、これは骨格筋、心筋に共通する普遍的な現象であることが近年明らかになりつつある。しかし、その分子メカニズムは未だに解明されていない。そこで、SPOCの前駆状態であるADP収縮状態における筋原線維の発生力-サルコメア長関係や、外部力学刺激に対する不安定性を詳細に調べた。その結果、通常の収縮状態とは逆に、アクチ

ンフィラメントと相互作用するCross-bridgeの数が多い（少ない）ほど小さな（大きな）力が発生し、外部力学刺激に対して不安定（安定）であることなどが明らかになった。そして筋フィラメント格子構造に特有の性質として、フィラメント間隔（格子定数）が筋節に応じて変化することが、Cross-bridge数と収縮（不）安定性の関係にとって鍵となっていることが見いだされた（島本勇太らの報告：論文投稿中)。中間活性化状態で多数のCross-bridgeが働くときに初めて顕著になる非線形現象、分子間協調性（分子間シンクロ）がここにある。これまで隠されていた分子モーターシステムの特性が明らかになりつつあると言える。これらの実験的研究と並行して、SPOCモデルに関する理論的研究も進めている（大瀧昌子の報告)。

5．SPOCの生理的意義

SPOC現象は、骨格筋においては生理的な意義は少ないと考えられるが、振動（拍動）することが生理機能そのものである心筋の場合には生理的意義があるか否かを検討する価値がある。少なくともADP-SPOC（人為的な溶液条件で発生するが、心筋だけでなく骨格筋でも安定なSPOCが見られる）において、様々な動物（ラット、ウサギ、イヌ、ブタ、ウシ）から調製した心筋収縮系のSPOC周期とSPOC波伝播速度が、それぞれの動物の心拍と強く相関することから、SPOC特性が心拍に何らかの役割を演じていることが示唆された（2005年、*J. Muscle Res. Cell Motil.*に発表)。さらに、心筋にとって生理的条件の範囲内にあるCa-SPOC条件においても同様に、SPOC周期とSPOC波伝播速度が動物の心拍と強く相関することが見出された（2006年、*Biochem. Biophys. Res. Commun.*に発表：佐々木大輔の報告)。このことから我々は、SPOCが心拍を支える収縮系にとって本質的な特性であるという、全く新しい概念を提唱するに至った。

6．心筋培養細胞の拍動と、細胞機能研究へのミクロ温度計の応用

心筋培養細胞において、自動拍動におけるCa^{2+}濃度の振動と収縮振動とを、アクトミオシン相互作用抑制剤であるBTSによってある程度uncoupleさせることができた。その性質をもとに、Ca^{2+}濃度振動に及ぼす収縮振動の作用を解析しつつある。

一方、2004年に新しいミクロ温度計とミクロン領域での熱注入手法を開発したが（*J. Neurosci. Meth.*に発表)、これらを用いて1個のHeLa細胞（あるいは心筋細胞）におけるCa^{2+}放出にともなう熱発生の顕微イメージングを試みた。その結果、イオノマイシン添加によって誘起されるERへのCa^{2+}取り込みに伴って細胞温度が1℃上昇することを見いだした（2007年に*Biophys. J.*にLetterとして発表：鈴木団の報告)。これは細胞熱力学という新分野を開く端緒になる研究だと期待している。

一方、研究分担者の船津グループは、1分子機能解析のための新しい技術開発に取り組んだ。その研究成果を技術開発に焦点を絞ってまとめる。

1．エバネッセント場を用いた弱い生体分子間相互作用の1分子イメージング

生体分子の機能や相互作用機構を研究するうえで、1分子蛍光イメージング法は極めて有効である。既に、全反射によるエバネッセント場顕微鏡を用いて、生物分子モーターや受容体に関する1分子解析がなされ、重要な成果が得られている。この方法を用いて、シャペロニンGroELとGroESの結合・解離と、シャペロニンによる変性GFPの巻き戻しを1分子イメージングすることに成功した。その結果、シャペロニン反応が、変性タンパク質の落とし込みと巻き戻しの2つの律速過程で進行することを発見し大きな話題となった（2004年、*Mol. Cell*に論文発表)。

しかし、通常のエバネッセント照明法では溶液中の分子の濃度が50 nM以上になると、測定対象の分子の周囲に常に複数の分子が存在するため、1分子イメージングできないという問題があった。従って、従来の全反射照明法では結合定数が小さく、しかも結合速度定数の高いタンパク質間相互作用しか測定できなかった。これを解決するため、ナノ開口による1分子蛍光イメージング技術を考案し開発しつつある（特願2002-326217（特許公開2004-163122)「微小開口膜、及び生体分子間相互作用解析装置とその解析方法」)。この方法では、ガラスに金属を100 nm蒸着し、直径約100 nmの穴を開けてガラスを露出させ生体分子を固定する。ガラス側から励起光を入射すると約10 nmの極めて局在化したエバネッセント場が発生する。このエバネッセント場による励起領域は従来の

約千分の1なので、高濃度の生体分子を必要とする弱い生体分子間相互作用の1分子解析が可能となった。実際にGroEL-GroESの結合・解離反応を1分子イメージングし、その有効性を示した（上野太郎の報告）。

2．マイクロシステムによる生体分子の分離・回収と1分子機能解析

光学顕微鏡による1分子検出・操作技術と半導体微細加工技術を融合させ、チップ内で生体分子の機能評価を1分子レベルで行う技術を開発した。特に、チップ内で溶液交換を高速に行い生体分子のキネティクスを1分子解析することを可能にした。また、蛍光標識した生体分子をチップ内の微小流路に流して1分子ずつ分離・回収し、それと結合している未知の分子を同定する新たな生体分析化学技術を開発した（特願2002-319577（特許公開2004-152218）「マイクロシステム」、特願2003-40330（特許公開2004-249381）「マトリックス型可変マイクロ流路及びそのシステム」、特願2003-280503（特許公開 2005-042073）「樹脂製基板の接合方法及びこの接合方法を用いたソーティング装置」）。

3．アクチンフィラメント溶液における多量体分布の測定

顕微PCH（フォトンカウンティングヒストグラム）法を自作し、これをアクチンフィラメント溶液におけるアクチン分子の多量体分布の計測に応用した。その結果、大澤（文夫）らによって作られたアクチン重合の平衡論が予測する通り、アクチンフィラメントにはHelicalポリマーだけでなく、Helicalポリマーの前駆体としてLinearポリマーが存在することの実験的な証拠を初めて得た。これは石渡・船津グループによる共同研究の目に見えた成果の一つである（2007年に *Biophys. J.* に論文発表：寺田尚史の報告）。

4．生細胞中におけるRNAのプロセシングと輸送の1分子蛍光イメージング

新たにデザインした生体分子の機能評価は、最終的に生細胞中で行うべきである。生細胞中での1分子蛍光イメージングの技術開発を進めた。βアクチンのRNAはミオシンによって細胞質内を輸送されることが知られている。研究対象をRNAとして、スプライシング、核内と細胞質での運動と局在を調べた（山岸舞の報告）。

キーワード *Key Word*： 一分子生物物理学 *Single-molecule biophysics*、一分子生理学 *Single-molecule physiology*、ナノバイオロジー *Nano-biology*、一分子蛍光（偏光）イメージング *Single-molecule fluorescence (polarization) imaging*、光ピンセット *Optical tweezers*、光学顕微鏡, *Optical microscope*、ナノーピコ解析 *Nano-pico analysis*、分子モーター *Molecular motor*、力学酵素 *Mechano-enzyme*、アクチン *Actin*、トレッドミル機構 *Treadmill mechanism*、動的不安定性 *Dynamic instability*、アクチン結合タンパク質（ゲルゾリン、コフィリン、Arp2/3、トロポニン、トロポミオシン）*Actin-binding protein (gelsolin, cofilin, Arp2/3, troponin, tropomyosin)*、ミオシン(II, V, VI) *Myosin (II, V, VI)*、キネシン *Kinesin*、微小管 *Microtubule*、筋原線維 *Myofibril*、筋線維 *Muscle fiber*、筋収縮系の再構築 *Reconstitution of the contractile system of muscle*、自発的振動収縮 *SPOC (Spontaneous Oscillatory Contraction)*、心筋拍動 *Heart beat*、分子内・分子間協調（シンクロナイゼーション）*Intra- and inter-molecular synchronization*、化学ー力学共役（力と酵素活性の相関）*Mechano-chemical coupling*、シャペロニン *Shaperonin*、タンパク質の折りたたみ *Protein folding*、バイオナノゲージ *Bio-nanogauge*、自己組織化 *Self-organization*、生体分子ナノ機械（バイオナノマシン）*Bio-molecular nano-machine*（*Bio-nanomachine*）、A帯滑り運動系（ナノ筋収縮系）*A-band motility assay system*（*Bio-nanomuscle*）、ミクロ（ナノ）温度計 *micro(nano)-thermometer*、一細胞熱力学 Single-cell thermodynamics、細胞機能のイメージング *Imaging of cell function*、変異タンパク質（変異アクチン、変異チューブリン）*Mutant protein (mutant actin, mutant tubulin)*、タンパク質重合体の柔らかさ *Flexibility of protein polymers*

研　究　組　織

研究代表者

石渡　信一　　早稲田大学理工学術院・教授

研究分担者

船津　高志　　東京大学薬学研究科・教授
（2004年2月まで早稲田大学理工学術院･教授）

交付決定額（配分額）

（金額単位：千円）

	直接経費	間接経費	合　計
平成14年度	90,000	27,000	117,000
平成15年度	89,100	26,730	115,830
平成16年度	98,900	29,670	128,570
平成17年度	107,240	32,172	139,412
平成18年度	92,000	27,600	119,600
総　計	477,240	143,172	620,412

研 究 発 表

1． 学会誌等

1) Uemura, S., Kawaguchi, K., Yajima, J., Edamatsu, M., Toyoshima, Y. Y., Ishiwata, S. "Kinesin-microtubule binding depends on both nucleotide state and loading direction" *Proc. Natl. Acad. Sci. USA* **99**, 5977-5981 (2002).

2) Ali, M. Y., Uemura, S., Adachi, K., Itoh, H., Kinosita, K. Jr., Ishiwata, S. "Myosin V is a left-handed spiral motor on the right-handed actin helix" *Nature Struct. Biol.* **9**, 464-467 (2002).

3) Fujiwara, I., Suetsugu, S., Uemura, S., Takenawa, T., Ishiwata, S. "Visualization and force measurement of branching by Arp2/3 complex and N-WASP in actin filament" *Biochem. Biophys. Res. Commun.* **293** , 1550-1555 (2002).

4) Fujita, H., Sasaki, D., Fukuda, K. and Ishiwata, S. "Myosin of light chain 2 modulates MgADP-induced contraction in rabbit skeletal and bovine cardiac skinned muscle" *J. Physiol.* **542** , 221-229 (2002).

5) Fujiwara, I., Takahashi, S., Tadakuma, H., Funatsu, T., Ishiwata, S. "Direct observation of polymerization-depolymerization dynamics of single actin filaments" *Nature Cell Biol.* **4**, 666-673 (2002).

6) Kawaguchi, K., Uemura, S., Ishiwata, S. "Equilibrium and transition between single- and double-headed binding of kinesin as revealed by single-molecule mechanics" *Biophys. J.* **84**, 1103-1113 (2003).

7) Uemura, S., Ishiwata, S. " Loading direction regulates the affinity of ADP for kinesin " *Nature Struct. Biol.* **10**, 308-311 (2003).

8) Fujita, H., Lu, X., Suzuki, M., Ishiwata, S. and Kawai, M. "The effect of tropomyosin on isometric tension and the elementaty steps of the cross-bridge cycle" *J. Physiol. (Lond.)* **556**, 637-649 (2004).

9) Hattori, A., Moriguchi, H., Ishiwata, S. and Yasuda, K. "A 1480/1064 nm dual wavelength photo-thermal etching system for non-contact three-dimensional microstructure generation into agar microculture chip" *Sensors & Actuators B.* **100**, 458-462 (2004).

10) Zeeb, V., Suzuki, M. and Ishiwata, S. "A novel method of thermal activation and temperature measurement in the microscopic region around single living cells" *J. Neurosci. Meth.* **139**, 69-77 (2004).

11) Uemura, S., Higuchi, H.., Olivares, A. O., DeLaCruz, E. M. and Ishiwata, S. "Mechanochemical coupling of two substeps in a single myosin V motor" *Nature Struct. Mol. Biol.* **11**, 877-883 (2004).

12) Suzuki, M., Fujita, H. and Ishiwata, S. "A new muscle contractile system composed of a thick filament lattice and a single actin filament" *Biophys. J.* **89**, 321-328 (2005).

13) Sasaki, D., Fujita, H., Fukuda, N., Kurihara, S. and Ishiwata, S. "Auto-oscillations of skinned myocardium correlating with heartbeat" *J. Muscle Res. Cell Motil.* **26(2)**, 93-101 (2005).

14) Nara, I. and Ishiwata, S. "Processivity of kinesin motility is enhanced on increasing temprerature" *BIOPHYSICS* **2**, 13-21(2006).

15) Sasaki, D., Fukuda, N. and Ishiwata, S. "Myocardial sarcomeres spontaneously oscillate with the period of heartbeat under physiological conditions." *Biochem. Biophys. Res. Commun.* **343**, 1146-1152 (2006).

16) Kawai, M., Kido, T., Vogel, M., Fink, R.H.A. and Ishiwata, S. "Temperature change does not affect force between regulated actin filaments and HMM in single molecule experiments" *J. Physiol. (Lond.)* **574. 3**, 877-887 (2006).
17) Kawai, M. and Ishiwata, S. "Use of thin-filament reconstituted muscle fibres to probe the mechanism of force generation" *J. Muscle Res. Cell Motil.* **27**, 455-468 (2006).
18) Gorbacheva, L.R., Storozhevykh, T.P., Pinelis, V.G., Ishiwata, S. and Strukova, S.M. "Modulation of hippocampal neuron survival by thrombin and factor Xa" *Biochemistry* (Moscow) **71**, 1082-1089 (2006).
19) Uchimura, S., Oguchi, Y., Katsuki, M., Usui, T., Osada, H., Nikawa, J., Ishiwata, S. and Muto, E. "Identification of a strong binding site for kinesin on the microtubule using mutant analysis of tubulin" *EMBO J.* **25**, 5932-5941 (2006).
20) Terada, N., Shimozawa, T., Ishiwata, S. and Funatsu, T. "Size distribution of linear and helical polymers in actin solution analyzed by photon counting histogram" *Biophys. J.* **92**, 2162-2171 (2007).
21) Suzuki, M., Tseeb, V., Oyama, K. and Ishiwata, S. "Microscopic detection of thermogenesis in a single HeLa cell" *Biophys. J.* **92**, L46-L48 (2007).
22) Funatsu, T., T. Taniyama, T. Tajima, H. Tadakuma, and H. Namiki. "Rapid and Sensitive Detection Method of A Bacterium Using GFP Reporter Phage" *Microbiol. Immun.* **46**, 365-369 (2002).
23) Zhang,G., T. Tanii, T. Zako, T. Funatsu, and I. Ohdomari. 2004. "The immobilization of DNA on microstructured patterns fabricated by maskless lithography" Sensors and Actuators B. **97**, 243-248 (2004).
24) Zhang, G.-J., T. Tanii, T. Funatsu, and I. Ohdomari. "Patterning of DNA nanostructures on silicon surface by electron beam lithography of self-assembled monolayer" *Chem. Commun.* 786-787 (2004).
25) Ueno T., H. Taguchi, H. Tadakuma, M. Yoshida and T. Funatsu. "GroEL mediates protein folding with a two successive timer mechanism" *Molecular Cell*, **14**, 423-434 (2004).
26) Okochi, M., T. Nomura, T. Zako, R. Iizuka, H. Ueda, T. Funatsu, M. Leroux, and M. Yohda. "Kinetics and binding sites for interaction of prefoldin with group II chaperonin: contiguous non-native substrate and chaperonin binding sites in archaeal prefoldin" *J. Biol. Chem.* **279**, 31788-31795 (2004).
27) Zako T., T. Funatsu, and M. Yohda. "Kinetic analysis of interactions between archaeal prefoldin and chaperonin" *Recent Res. Develop. Biophys.* **3**, 475-483 (2004).
28) Zhang, G., H. Umezawa, H. Hata, T. Zako, T. Funatsu, I. Ohdomari, and H. Kawarada. "Micropatterning oligonucletides on single crystal diamond surface by photolithography" *Jpn. J. Appl. Phys.* **44**, L295-298 (2005).
29) Nonaka, S., M. Tsunoda, K. Imai, and T. Funatsu. "High-performance liquid chromatographic assay of N^G-monomethyl-L-arginine, N^G,N^G-dimethyl-L-arginine, and N^G,$N^{G'}$-dimethyl-L-arginine using 4-fluoro-7-nitro-2,1,3-benzoxadiazole as a fluorescent reagent" *J. Chromatogr. A*, **1066**, 41-45 (2005).
30) Hirano, Y., M. Tsunoda, T. Funatsu, and K. Imai. "Rapid assay for catechol-O-methyltransferase activity by high-performance liquid chromatography-fluorescence detection" *J. Chromatogr. B*, **819**, 41-46 (2005).
31) Tsukamoto Y., T. Santa, H. Saimaru, K. Imai, and T. Funatsu. "Synthesis of benzofurazan derivatization regents for carboxylic and acids and its application to analysis of fatty acids in rat plasma by high-performance liquid chromatography/electrospray ionization mass spectrometry" *Biomed. Chromatogy.* **20**, 358-364 (2005).

32) Tanii, T., T. Hosaka, T. Miyake, Y. Kanari, G.-J. Zhang, T. Funatsu, and I. Ohdomari. "Hybridization of deoxyribonucleic acid immobilization of green fluorescent protein on nanostructured porganosilane templates" *Jpn. J. App. Phys.* **44**, 5851-5855 (2005).

33) Zhang, G.-J., T. Tanii, T. Zako, T. Hosaka, T. Miyake, Y. Kanari, T. Funatsu, and I. Ohdomari. "Nanoscale patterning of protein using electron beam lithography of organosilane self-assembled monolayers" *Small,* **1**, 833-837 (2005).

34) Zako T., R. Iizuka, M. Okochi, T. Nomura, T. Ueno, H. Tadakuma1, M. Yohda and T. Funatsu. "Facilitated release of substrate protein from prefoldin by chaperonin" *FEBS Lett.* **579**, 3718-3724 (2005).

35) Tsunoda, M., S. Nonaka, T. Funatsu. "Determination of methylated arginines by column-switching high-performance liquid chromatography-fluorescence detection".*Analyst,* **130**, 1410-1413 (2005).

36) Terada, N., H. Tadakuma, Y. Ishihama, M. Yamagishi, T. Zako, and T. Funatsu. "Analysis of Nuclear Microenvironments by Translational Diffusion of GFP Using Fluorescence Correlation Spectroscopy" *Bioimages.* **13**, 1-10 (2005).

37) Tsukamoto Y, T. Santa, H. Yoshida, H. Miyano, T. Fukushima, K. Hirayama, K. Imai and T. Funatsu. "Synthesis of the isotope-labeled derivatization reagent for carboxylic acids, 7-(*N,N*-dimethylaminosulfonyl)-4-(aminoethyl)piperazino-2,1,3-benzoxadiazole (d_6) (DBD-PZ-NH_2 (D)), and its application to the quantification and the determination of relative amount of fatty acids in rat plasma samples by high-performance liquid chromatography/mass spectrometry" *Biomedical Chromatography.* **20**, 358-364 (2005).

38) Tsunoda, M., M. Nagayama, T. Funatsu, S. Hosoda, and K. Imai. "Catecholamine analysis with microcolumn LC-peroxyoxalate chemiluminescence reaction detection" *Clin. Chim. Acta.* **366**, 168-173 (2006).

39) Shirasaki, Y., J. Tanaka, H. Makazu, K. Tashiro, S. Shoji, S. Tsukita, and T. Funatsu. "On-chip cell sorting system using laser-induced heating of a thermo-reversible gelation polymer to control flow" *Anal. Chem.* **78**, 695-701 (2006).

40) Tokunaga, K., T. Shibuya, Y. Ishihama, H. Tadakuma, M. Ide, M. Yoshida, T. Funatsu, Y. Ohshima, and T. Tani. "Nucleocytoplasmic transport of fluorescent mRNA in living mammalian cells: Nuclear mRNA export is coupled to ongoing gene transcription" *Genes to Cells.* **11**, 305-317 (2006).

41) Zhang, G.J., K.S. Song, Y. Nakamura, T. Ueno, T. Funatsu, I. Ohdomari, H. Kawarada. "DNA micropatterning on polycrystalline diamond via one-step direct amination" *Langmuir,* **22**, 3728-3734 (2006).

42) Tsukamoto, Y., T. Santa, H. Yoshida, H. Miyano, T. Fukushima, K. Hirayama, K. Imai, and T. Funatsu. "A further study on the combined use of internal standard and isotope-labeled derivatization reagent for expansion of linear dynamic ranges in liquid chromatography-electrospray mass spectrometry" *Biomed. Chromatogr.* **20**, 1049-1055 (2006).

43) Tadakuma, H., Y. Ishihama, T. Shibuya, T. Tani, and T. Funatsu. "Imaging of single mRNA molecules moving within a living cell nucleus" *Biochem Biophys Res Commun.* **344**, 772-779 (2006).

44) Santa, T., C. Aoyama, T. Fukushima, K. Imai, and T. Funatsu. "Suppression of thiol exchange reaction in the determination of reduced-form thiols by high-performance liquid chromatography with fluorescence detection after derivatization with fluorogenic benzofurazan reagent, 7-fluoro-2,1,3-benzoxadiazole-4-sulfonate and 4-aminosulfonyl-7-fluoro-2,1,3- benzoxadiazole" *Biomed Chromatogr.* **20**, 656-661 (

45) Nonaka, S., M. Tsunoda, C. Aoyama, and T. Funatsu. "Determination of N^G,N^G-dimethyl-l-arginine in rat plasma and dimethylarginine dimethylaminohydrolase activity in rat kidney using a monolithic silica column" *J. Chromatogr. B.* **843**, 170-174 (2006).

46) Shiurba, R., T. Hirabayashi, M. Masuda, A. Kawamura, Y. Komoike, W. Klitz, K. Kinowaki, T. Funatsu, S. Kondo, S. Kiyokawa, T. Sugai, K. Kawamura, H. Namiki, and T. Higashinakagawa. "Cellular responses of the ciliate, *Tetrahymena thermophila*, to far infrared irradiation" *Photochem. Photobiol. Sci.* **5**, 799-807 (2006).

47) Zako, T., Y. Murase, R. Iizuka, T. Yoshida, T. Kanzaki, N. Ide, M. Maeda, T. Funatsu, and M. Yohda. "Localization of Prefoldin Interaction Sites in the Hyperthermophilic Group II Chaperonin and Correlations between Binding Rate and Protein Transfer Rate" *J. Mol. Biol.* **364**, 110-120 (2006).

48) Arakawa, T., Y. Shirasaki, T. Izumi, T. Aoki, H. Sugino, T. Funatsu, and S. Shoji. "High-speed particles and biomolecules sorting microsystem using thermosensitive hydrogel" *Meas. Sci. Techn.* **17**, 3141-3146 (2006).

49) Song K.S., G.J. Zhang, Y. Nakamura, K. Furukawa, T. Hiraki, J.H. Yang, T. Funatsu, I. Ohdomari and H. Kawarada. "Label-free DNA sensors using ultrasensitive diamond field-effect transistors in solution" *Phys Rev E Stat Nonlin Soft Matter Phys.* **74**, 041919 (2006).

50) Arakawa, T. Y. Shirasaki, T. Aoki, T. Funatsu, and S. Shoji. "Three-dimensional sheath flow sorting microsystem using thermosensitive hydrogel" *Sensors and Actuators A: Physical*, **135**, 99-105 (2007).

51) Yanagihara, N. H. Tadakuma, Y. Ishihama, K. Okabe, T. Funatsu. "Determination of potent antisense oligonucleotides in vitro by semi-empirical rules" *J. Biosci. Bioeng.* **103**, 270-277 (2007).

52) Shirasaki, Y., H. Sugino, M. Tatsuoka, J. Mizuno, S. Shoji, and T. Funatsu. "On-chip Cell Sorting System Using Thermoreversible Gelation Polymer" *IEEE J. Selected Topics in Quantum Electronics*, in press.

53) Hirano, Y., M. Tsunoda, T. Shimosawa, H. Matsui, T. Fujita, T. Funatsu, "Suppression of COMT activity through blunting α2-adrenoceptor can explain hypertension in Dahl Salt-Sensitive rats" *Hypertens. Res.*, in press.

2. 口頭発表

【国内会議】

1) 島本勇太、佐々木大輔、石渡信一「生体分子モーター系における分子シンクロナイゼーション」特定領域研究"分子シンクロ"全体会議（東京）2002. 6.

2) 石渡信一「バイオナノモーターの仕組みー１分子酵素力学ー」早大・東京女子医大連携大学院公開シンポジウム（東京）2002. 7. 13.

3) 石渡信一 「アクチン重合ダイナミクスと分子モーター酵素力学の１分子顕微解析」名古屋大学理学部分子生物セミナー（名古屋）2002. 10. 10.

4) 石渡信一「筋収縮のしくみ」第 15 回細胞生物学シンポジウム（東京）2002. 10. 19.

5) 上村想太郎、川口憲治、石渡信一「Single-molecular mechanochemical coupling in kinesin」分子モーターワークショップ（つくば）2002. 10. 21.

6) 石渡信一「分子モーターとアクチンフィラメントの１分子ダイナミクス」東大農学部セミナー（東京）2002. 10. 22.

7) 石渡信一「Bio-nanomuscle project: Contractile properties of single actin filaments in an

A-band motility assay system」 第4回藤原セミナー（箱根）2002. 10. 28-11. 1.

8) 鈴木団、佐々木大輔、石渡信一「カルシウム非感受性ゲルゾリン断片による細いフィラメントの状態検出」日本生物物理学会第40回年会（名古屋）2002. 11. 2-4.

9) 藤原郁子、佐々木大輔、石渡信一「トロポミオシン・トロポニン複合体を結合した単一アクチンフィラメント重合・脱重合過程の顕微解析」日本生物物理学会第40回年会（名古屋）2002. 11. 2-4.

10) 上村想太郎、樋口秀男、石渡信一「Myosin-Vは11nm+25nmでステップする」日本生物物理学会第40回年会（名古屋）2002. 11. 2-4.

11) 島本雄太、鈴木団、安田賢二、石渡信一「力学的刺激による筋収縮自励振動(SPOC)メカニズムの研究」日本生物物理学会第40回年会（名古屋）2002. 11. 2-4.

12) 阿部洋介、佐々木大輔、石渡信一「心筋SPOCにおけるConnectin/Titinの働き」日本生物物理学会第40回年会（名古屋）2002. 11. 2-4.

13) 青木匠、井手純一、S. Strukova、石渡信一「PARsを介したニワトリ胚心筋細胞と繊維芽細胞の活性化」日本生物物理学会第40回年会（名古屋）2002. 11. 2-4.

14) 奈良郁子、石渡信一「キネシンモーターにおけるProcessivityの温度依存性」日本生物物理学会第40回年会（名古屋）2002. 11. 2-4.

15) 若林英美、佐々木大輔、石渡信一「病変ラットにおける心拍とβミオシン重鎖発現との相関」日本生物物理学会第40回年会（名古屋）2002. 11. 2-4.

16) 石渡信一「バイオナノモーターの1分子計測」電気情報通信学会シンポジウム（東京）2002. 11. 27.

17) 石渡信一「バイオモーターにおける分子シンクロナイゼーション」高分子学会シンポジウム（仙台）2002. 11. 28.

18) 石渡信一「バイオモーターにおける分子シンクロナイゼーション」東北大学分子シンクロ・ミニシンポジウム（仙台）2002. 11. 28.

19) 島本勇太、鈴木団、安田賢二、石渡信一「筋収縮系にみる分子シンクロー外力によって誘起される収縮・弛緩転移ー」生体運動研究合同班会議（福岡）2003. 1. 9-11.

20) 石渡信一「はじめに：1分子モーター系を中心に」第80回日本生理学会（福岡）2003. 3. 23.-25.

21) 石渡信一「生物と物理の架け橋ー田中豊一が見たものー」物理学会春の分科会シンポジウム（仙台） 2003. 3. 28.

22) 新海典夫、上村想太郎、石渡信一「キネシン分子モーターの歩行モデル～状態間遷移確率に基づくシミュレーション～」第58回日本物理学会（仙台）2003. 3. 28-31.

23) 石渡信一「分子モーターとアクチン重合のダイナミクスー1分子からシステムへー」東京大学・分子細胞研究所（東京）2003. 7. 16.

24) 島本勇太、鈴木団、佐々木大輔、安田賢二、石渡信一「蛍光顕微解析による筋収縮系自動振動（SPOC）メカニズムの解明」第41回日本生物物理学会年会（新潟）2003. 9. 23-25.

25) 佐々木大輔、福田紀男、藤田英明、栗原敏、石渡信一「アクチンフィラメント再構成心筋における筋長効果」第41回日本生物物理学会年会（新潟）2003. 9. 23-25.

26) 石井俊男、鈴木団、石渡信一「アクチンフィラメント2価陽イオンパラクリスタルの顕微物性解析」第41回日本生物物理学会年会（新潟）2003. 9. 23-25.

27) 星野雄樹、三浦洋敬、石渡信一「Cys374ラベルによるアクチンフィラメントの機能阻害」第41回日本生物物理学会年会（新潟）2003. 9. 23-25.

28) 下澤東吾、石渡信一「蛍光性ATPアナログによるF-actinのイメージングとその機能解析」第41回日本生物物理学会年会（新潟）2003. 9. 23-25.

29) 前島永志、島本勇太、鈴木団、石渡信一「筋収縮系自励振動現象（SPOC）における外部力学刺激応答」第41回日本生物物理学会年会（新潟）2003. 9. 23-25.

30) 阿部洋介、佐々木大輔、石渡信一「心筋収縮系の自励振動現象」第41回日本生物物理学会年会（新潟）2003. 9. 23-25.

31) 若林英美、佐々木大輔、石渡信一「病変ラットにおける心拍数と心室筋収縮能との相関」第41回日本生物物理学会年会（新潟）2003. 9. 23-25.
32) 上村想太郎、樋口秀男、石渡信一「ATP結合とリン酸解離が引き起こすミオシンVのサブステップ解析」第41回日本生物物理学会年会（新潟）2003. 9. 23-25.
33) 久保田寛顕、上村想太郎、石渡信一「Subtilisin処理したアクチン線維上におけるミオシンV一分子運動」第41回日本生物物理学会年会（新潟）2003. 9. 23-25.
34) 河合正隆、木戸孝紀、鈴木団、石渡信一「再構成thin filament-HMM分子間の滑り力に対する温度の影響」第41回日本生物物理学会年会（新潟）2003. 9. 23-25.
35) 松縄恵理子、西村真紀、藤原郁子、石渡信一「HMM存在下でのアクチンフィラメント重合・脱重合ダイナミクスの一分子顕微解析」第41回日本生物物理学会年会(新潟)2003. 9. 23-25.
36) 青木匠、井手純一、S. Strukova、石渡信一「ニワトリ胚心筋細胞におけるPARsの機能発現」第41回日本生物物理学会年会（新潟）2003. 9. 23-25.
37) 石渡信一「生体分子モーターのダイナミクスー1分子からシステムへー」北海道大学理学部・高分子談話会（北海道）2003. 12. 18.
38) 石渡信一　「多元要素からなる自己組織系の物理～ホリスティック研究教育システム～」WTW3周年記念シンポジウム（早稲田大学）2003. 12. 20.
39) 石渡信一　「生体分子モーターシステムの物理」第1回21世紀COE自己組織系物理シンポジウム（西早稲田キャンパス）2004. 2. 27.
40) 石渡信一「分子モーターの生物物理　ーミクロからナノへー」物理生命システム科学科シンポジウム（日本大学文理学部・東京）2004. 5. 21.
41) 石渡信一「生体分子モーターのダイナミクスー1分子からシステムへー」横浜国立大学工学院・談話会（横浜）2004. 7. 2.
42) 石渡信一「分子モーターの生物物理ー1分子からシステムへー」青山学院大学理工学部コロキウム（東京）2004.11.25.
43) 石渡信一「Myosin Vの歩く仕組みー1分子計測で分かったことー」第27回日本分子生物学会年会（神戸）2004. 12. 11.（招待講演）
44) 三浦洋敬、小口祐伴、石渡信一「Dictyostelium Discoidiumによるmutant actinの精製と機能評価」第42回日本生物物理学会年会（京都）2004. 12. 13-15.
45) 下澤東吾、石渡信一「アクチンフィラメント分子内構造変化の蛍光イメージング」第42回日本生物物理学会年会（京都）2004. 12. 13-15.
46) 佐々木大輔、石渡信一「心筋SPOCと心拍との相関を規定する因子」第42回日本生物物理学会年会（京都）2004. 12. 13-15.
47) 島本勇太、鈴木団、安田賢二、石渡信一「筋収縮系自励振動（SPOC）における外力刺激応答のサルコメア長依存性」第42回日本生物物理学会年会（京都）2004. 12. 13-15.
48) 鈴木団、石渡信一「A帯滑り運動系と制御系タンパク質を用いた自励振動現象発生機構の解明」第42回日本生物物理学会年会（京都）2004. 12. 13-15.
49) 青山祥一朗、石渡信一「培養ラット心筋細胞のカルシウム振動に対するミオシンATPase抑制剤の作用」第42回日本生物物理学会年会（京都）2004. 12. 13-15.
50) 松縄恵理子、石渡信一「アクチンフィラメントの重合・脱重合ダイナミクスーHMMによる制御ー」第42回日本生物物理学会年会（京都）2004. 12. 13-15.
51) 久保田寛顕、石渡信一「Subtilisin処理アクチン線維上でのミオシンVプロセッシブ運動」第42回日本生物物理学会年会（京都）2004. 12. 13-15.
52) 小口祐伴、石渡信一「ミオシンV・アクチン間相互作用の1分子顕微解析」第42回日本生物物理学会年会（京都）2004. 12. 13-15.
53) Zeeb Vadim, 鈴木団、石渡信一「ミクロ熱励起・温度計測による新しい細胞機能解析法の開発」第42回日本生物物理学会年会（京都）2004. 12. 13-15.
54) 佐々木大輔、石渡信一「心筋SPOCと心拍数、及びミオシン運動活性との関係」2005年生体

運動研究合同班会議（大阪）2005. 1. 7-9.

55) 石渡信一「一分子破断力測定で分かったこと」2005 年生体運動研究合同班会議（大阪）2005. 1. 7-9.

56) 石渡信一「生体分子モーターの仕組み－1 分子機能とシステム構築－」群馬大学工学部セミナー（群馬）2005.7.21.

57) 石渡信一「分子モーター機能における分子内・分子間シンクロ」産総研セミナー（茨城）2005.10.21.

58) 鈴木団、Zeeb Vadim、石渡信一「ミクロ温度計を用いて HeLa 細胞の熱発生を検出する試み」第 43 回日本生物物理学会年会（札幌）2005.11.23-25.

59) 内村誠一、小口祐伴、仁川純一、石渡信一、武藤悦子「変異微小管を用いたキネシン結合部位の同定」第 43 回日本生物物理学会年会（札幌）2005.11.23-25.

60) 小口祐伴、Adrian O Olivares、Enrique M DeLa Cruz、石渡信一「ミオシン V 単頭結合状態の一分子顕微解析」第 43 回日本生物物理学会年会（札幌）2005.11.23-25.

61) 尾崎友治、下澤東吾、小口祐伴、石渡信一「微小管一本の力学特性の直接顕微計測」第 43 回日本生物物理学会年会（札幌）2005.11.23-25.

62) 井上智裕、久保田寛顕、石渡信一「ミオシン V 運動の温度依存性」第 43 回日本生物物理学会年会（札幌）2005.11.23-25.

63) 大森伸太郎、宇高潤、栗原敏、石渡信一「萎縮したラットひらめ筋における細いフィラメントの長さ制御機構の変化」第 43 回日本生物物理学会年会（札幌）2005.11.23-25.

64) 河野史明、島本勇太、石渡信一「SPOC に伴う筋原線維の形状変化：顕微画像解析」第 43 回日本生物物理学会年会（札幌）2005.11.23-25.

65) 大瀧昌子、石渡信一「筋収縮系のおける自励振動現象の数理モデル」第 43 回日本生物物理学会年会（札幌）2005.11.23-25.

66) 青山祥一朗、鈴木団、石渡信一「培養ラット心筋細胞の Ca2+振動に対するミオシン ATPase 抑制剤の作用」第 43 回日本生物物理学会年会（札幌）2005.11.23-25.

67) 秋山留美、小口祐伴、石渡信一「ATP 存在下におけるキネシン単頭結合内の状態変化」第 43 回日本生物物理学会年会（札幌）2005.11.23-25.

68) Mikhailenko Sergey、小口祐伴、Olivares Adrian、DeLa Cruz Enrique、石渡信一「Myosin VI-actin interaction: Dependence on loading direnction and nucleotide state of a motor」第 43 回日本生物物理学会年会（札幌）2005.11.23-25.

69) 久保圭、小口祐伴、久保田寛顕、芹澤加洋子、石渡信一「細胞性粘菌で発現した変異アクチンの機能評価」第 43 回日本生物物理学会年会（札幌）2005.11.23-25.

70) 大槻美里、秋山直生、島本勇太、石渡信一、国岡由紀、山田武範「BDM 存在下におけるアクチン－ミオシン相互作用の再検討」第 43 回日本生物物理学会年会（札幌）2005.11.23-25.

71) 島本勇太、鈴木団、石渡信一「分子モーター集合体における自律的状態制御－制御因子としてのミオシン ADP 複合体の役割－」第 43 回日本生物物理学会年会（札幌）2005.11.23-25.

72) 鈴木団、渡辺幸資、石渡信一「A 帯滑り運動系：低 ATP 濃度での単一アクチンフィラメントの動き」2006 年生体運動研究合同班会議（東大農学部キャンパス）2006.1.6-8.

73) 島本勇太、河野史明、鈴木団、石渡信一「Length-dependent activation by the ADP-bound myosin in skeletal myofibrils-Implications for the self-regulating mechanism of SPOC-」Fifth East Asia Biophysics Symposium & Forty-Fourth Annual Meeting of the Biophysical Society of Japan（Okinawa） Nov. 12-16, 2006.

74) 久保田寛顕、下澤東吾、久保圭、石渡信一「Functional analysis of M47A/E360H mutant actin expressed in Dictyostelium cells」Fifth East Asia Biophysics Symposium & Forty-Fourth Annual Meeting of the Biophysical Society of Japan（Okinawa） Nov. 12-16, 2006.

75) 渡辺幸資、鈴木団、石渡信一「Properties of "bio-nanomuscle" at various ATP concentrations analyzed with submillisecond resolution」Fifth East Asia Biophysics Symposium &

Forty-Fourth Annual Meeting of the Biophysical Society of Japan (Okinawa) Nov. 12-16, 2006.

76) 河野史明、島本勇太、石渡信一「Effect of lattice spacing on SPOC of skeletal myofibrils」Fifth East Asia Biophysics Symposium & Forty-Fourth Annual Meeting of the Biophysical Society of Japan (Okinawa) Nov. 12-16, 2006.

77) Sergey V. Mikhailenko, Yusuke Oguchi, Adrian O., Enrique M. De La Cruz, Shin'ichi Ishiwata "ADP affinity of myosin VI is modulated by load and depends on loading direction" Fifth East Asia Biophysics Symposium & Forty-Fourth Annual Meeting of the Biophysical Society of Japan (Okinawa) Nov. 12-16, 2006.

78) 尾崎友治、下澤東吾、大瀧昌子、石渡信一「Mechanical properties of a single microtubule measured by optical tweezers; The effect of kinesin binding」Fifth East Asia Biophysics Symposium & Forty-Fourth Annual Meeting of the Biophysical Society of Japan (Okinawa) Nov. 12-16, 2006.

79) Takeshi Itabashi, Yuta Shimamoto, Jedidiah Gaez, Jenny Z. Liu, Tarun M. Kapoor, Shin'ichi Ishiwata "Measurements of microtubule-dependent forces acting on mitotic spindle" Fifth East Asia Biophysics Symposium & Forty-Fourth Annual Meeting of the Biophysical Society of Japan (Okinawa) Nov. 12-16, 2006.

80) Yuta Abe, Takeshi Itabashi, Yuta Shimamoto, Shizuka Sato, Togo Shimozawa, Tarun M. Kapoor, Shin'ichi Ishiwata "Microviscoelasticity mapping of the environment around the mitotic spindle extracted from Xenopus egg" Fifth East Asia Biophysics Symposium & Forty-Fourth Annual Meeting of the Biophysical Society of Japan (Okinawa) Nov. 12-16, 2006.

81) Shouhei Tsukahara, Togo Shimozawa, Shin'ichi Ishiwata "Digitally controlled feedback system developed for the optical tweezers" Fifth East Asia Biophysics Symposium & Forty-Fourth Annual Meeting of the Biophysical Society of Japan (Okinawa) Nov. 12-16, 2006.

82) Togo Shimozawa, Shin'ichi Ishiwata "Modulation of the fouorescence intensity of a single actin filament by tensile force" Fifth East Asia Biophysics Symposium & Forty-Fourth Annual Meeting of the Biophysical Society of Japan (Okinawa) Nov. 12-16, 2006.

83) Chikanori Ohno, Togo Shimozawa, Naruki Sato, Shin'ichi Ishiwata "Direct observation of cofilin-actin interaction by fluorescence microscopy" Fifth East Asia Biophysics Symposium & Forty-Fourth Annual Meeting of the Biophysical Society of Japan (Okinawa) Nov. 12-16, 2006.

84) Vadim Tseeb, Madoka Suzuki, Shin'ichi Ishiwata "Detection of thermal response associated with intracellular calcium increase induced by ionomyocin in single HeLa cell" Fifth East Asia Biophysics Symposium & Forty-Fourth Annual Meeting of the Biophysical Society of Japan (Okinawa) Nov. 12-16, 2006.

85) Yusuke Oguchi, Sergey V. Mikhailenko, Adrian O. Olivares, Enrique M. De La Cruz, Shin'ichi Ishiwata "Loading direction controls the ADP affinity of myosin V" Fifth East Asia Biophysics Symposium & Forty-Fourth Annual Meeting of the Biophysical Society of Japan (Okinawa) Nov. 12-16, 2006.

86) Kayoko Serizawa, Shin'ichi Ishiwata "Characerization of actin SS-dimers obtained by oxidation" Fifth East Asia Biophysics Symposium & Forty-Fourth Annual Meeting of the Biophysical Society of Japan (Okinawa) Nov. 12-16, 2006.

87) Mutsuki Takeuchi, Shin'ichi Ishiwata "Effects of stretch and BTS on auto-oscillatory properties of contraction and Ca^{2+} concentration in cultured cardiac muscle" Fifth East Asia Biophysics Symposium & Forty-Fourth Annual Meeting 6of the Biophysical Society

of Japan（Okinawa） Nov. 12-16, 2006.

88) 島本勇太、河野史明、鈴木団、石渡信一「ADP 収縮にみられる筋節長依存的な力増強」筋生理の集い（慈恵医大）2006.12.9.

89) 石渡信一 「運動性タンパク質の 1 分子機能と多分子協調」第 2 回バイオナノ研究会（兵庫・城崎）2007.1.23-24.

90) Ishiwata, S., Shimamoto, Y., Suzuki, M., Itabashi, T. "Hierarchical organization of biomotile systems－from nano-muscle to sarcomere, myofibril, and mitotic spindle－" The Physiological Society of Japan 84th Annual Meeting (Osaka) 2007. 3.

91) Udaka, J., Terui, T., Ohmori, S., Ishiwata, S., Ohtaki, I., Fukuda, N., Kurihara, S. "Disuse-induced changes in length-dependence of activation in rat soleus muscle" The Physiological Society of Japan 84th Annual Meeting (Osaka) 2007. 3.

92) Udaka, J., Ohmori, S., Terui, T., Yamaguchi, M., Ishiwata, S., Ohtsuki, I., Fukuda, N., Kurihara, S. "Disuse-induced changes in Ca^{2+} sensitivity of force in rat soleus muscle" The Physiological Society of Japan 84th Annual Meeting (Osaka) 2007. 3.

93) 船津高志 2002.「１分子蛍光イメージングの現状と展望」 第 55 回日本細胞生物学会大会 細胞生物学会・発生生物学会合同大会横川電気株式会社ランチョンセミナー 2002. 5. 23. 神奈川県横浜市 パシフィコ横浜（招待講演）

94) 船津高志 2002.「１分子蛍光イメージング」 レーザー顕微鏡研究会第 28 回講演会 2002. 7. 5. 東京 富士写真フィルム株式会社 本社ホール（招待講演）

95) 船津高志 2002.「１分子蛍光イメージング法による生体分子機能解析」日本分光学会 医学生物学部会シンポジウム 2002『光ナノテクノロジー・生命科学への展開』2002. 9. 5. 幕張メッセ国際会議場（招待講演）

96) Yoshida, M., H.Taguchi, Y.Watanabe, F.Motojima, H.Tadakuma, T.Ueno, and T. Funatsu 2002. Rescue of unfolded or aggregated proteins by molecular chaperones 第 75 回日本生化学会大会 抄録集 2S15－1 (631pp) 2002. 10. 14-17. 国立京都国際会館、京都宝ヶ池プリンスホテル

97) 田口英樹、上野太郎、 多田隈尚史、 船津高志、 吉田賢右 2002. シャペロニンＧｒｏＥＬのＡＴＰ加水分解サイクル 第 75 回日本生化学会大会 抄録集 4ｐ－567(1057pp)2002. 10. 14-17. 京都府京都市 国立京都国際会館、京都宝ヶ池プリンスホテル

98) 船津高志 1 分子蛍光イメージング法による生体分子機能解析 第 11 回日本バイオイメージング学会学術集会 2002. 10. 30.（招待講演）

99) 座古保、飯塚怜、大河内美奈、上野太郎、養王田正文、船津高志 2002. 古細菌由来プレフォルディンと、基質タンパク質、シャペロニンとの相互作用について 日本生物物理学会第 40 回年会 2002 年 11 月 2 日 愛知県名古屋市 名古屋大学東山地区

100) 上野太郎、田口英樹、多田隈尚史、吉田賢右、船津高志 2002. GroEL の ATP 加水分解サイクルにおけるヌクレオチド状態 日本生物物理学会第 40 回年 2002. 11. 2. 愛知県名古屋市 名古屋大学東山地区

101) 細野和彦、上野太郎、田口英樹、元島史尋、座古保、吉田賢右、船津高志 2002. チロシンの蛍光郷土変化を指標とした GroEL の構造変化検出 日本生物物理学会第 40 回年会 2002. 11..2. 愛知県名古屋市 名古屋大学東山地区

102) 東條正、青木大輔、木脇圭一、シルヴィアイスカンダル、多田隈尚史、石渡信一、船津高志 2002. G タンパク質共益型受容体・FPR1 は GFP の有無に関わらず多量体形成する：蛍光一分子観察による解析 日本生物物理学会第 40 回年会 2002. 11. 3. 愛知県名古屋市 名古屋大学東山地区

103) 鞍馬秀輝、貴家康尋、多田隈尚史、永川豊広、船津高志、原田慶恵 2002. 蛍光標識β—actin mRNA の細胞内輸送と局在のイメージング 日本生物物理学会第 40 回年会 2002. 11. 4. 愛知県名古屋市 名古屋大学東山地区

104) 白崎善隆、真一弘士、田代浩一、池田晋吾、関口哲史、庄子習一、月田承一郎、船津高志 2002. 熱感受性ハイドロゲルを用いた生体分子ソーターの開発 日本生物物理学会第 40 回年会 2002. 11. 4. 愛知県名古屋市 名古屋大学東山地区

105) 刈間理介、東條正、灰野誠、船津高志、 2002. 松島綱治全反射レーザー顕微鏡（エバネッセント顕微鏡）による LPS の細胞膜における分子挙動の観察 第 32 回日本免疫学会総会・学術集会 2002. 12. 4-6. 東京新宿区 京王プラザホテル

106) 東條正、青木大輔、木脇圭一、シルヴィアイスカンダル、多田隈尚史、石渡信一、船津高志 2002. G蛋白質共役型受容体・ＦＰＲ１は GFP の有無に関わらず多量体形成する：蛍光一分子観察による解析 第 25 回日本分子生物学会年会 Annual Meeting of MBSJ in 2002 2002. 12. 11-14. 横浜市パシフィコ横浜

107) 船津高志 2003. 「1 分子蛍光イメージング法による生体分子機能解析第 227 回 CBI 学会研究講演会「タンパク質研究の最前線」」2003. 1. 20. 日本化学会 化学会館 7 F ホール（招待講演）

108) 船津高志 2003.「レーザー顕微鏡による生体分子イメージングと操作」レーザー学会学術講演会第 23 回年次大会 2003. 1. 30. アクトシティ浜松コングレスセンター（招待講演）

109) 船津高志 2003. 1 分子蛍光イメージング法による生体分子機能解析 International Symposium on Single-Molecule Bionalysis and Nano-biodevice 2003. 3. 11-12, 香川県高松市産総研四国センター講堂（招待講演）

110) 木脇圭一、東條正、シルビアイスカンダル、青木大輔、多田隈尚史、船津高志 2003. 多量体形成は走化性因子受容体に共通する特性である～1 分子蛍光イメージングによる研究～第 56 回日本細胞生物学会大会 2003. 5. 14-16, 滋賀県大津市ピアザ淡海滋賀県立県民交流センター

111) 座古保、飯塚怜、大河内美奈、上野太郎、養王田正文、船津高志 2003. 「蛍光顕微鏡を用いた古細菌由来プレフォルディンと、基質タンパク質、シャペロニンとの相互作用について」日本蛋白質科学会第 3 回年会 2003. 6. 23-25, 北海道札幌市札幌コンヴェンションセンター

112) 上野太郎、田口英樹、多田隈尚史、吉田賢右、船津高志 2003. 「FRET による GroEL 内部での基質タンパク質の運動解析」日本生物物理学会第 41 回年会 2003. 9. 23, 新潟県新潟市 朱鷺メッセ

113) 開田奈津来、座古保、船津高志 2003.「プロリン変異体を用いた GFP フォールディングの解析」日本生物物理学会第 41 回年会 2003. 9. 23, 新潟県新潟市 朱鷺メッセ

114) 細野和彦、上野太郎、座古保、田口英樹、吉田賢右、船津高志 2003. 「GroEL 変異体 AEX のキャラクタリゼーション」日本生物物理学会第 41 回年会 2003. 9. 23, 新潟県新潟市 朱鷺メッセ

115) 座古保、飯塚怜、大河内美奈、上野太郎、養王田正文、船津高志 2003.「蛍光顕微鏡を用いた、高熱菌由来プレフォルディンと基質タンパク質の相互作用解析」日本生物物理学会第 41 回年会 2003. 9. 23, 新潟県新潟市 朱鷺メッセ

116) Iskander Silvia、木脇圭一、青木大輔、東條正、多田隈尚史、船津高志 2003.「ケモカイン受容体 CXCR4 はリガンド非依存的に多量体を形成する」日本生物物理学会第 41 回年会 2003. 9. 23, 新潟県新潟市 朱鷺メッセ

117) 亀井保博、渡邉建二郎、船津高志、田口隆久、弓場俊輔 2003. 「遺伝子発現用赤外レーザ顕微鏡の開発」日本生物物理学会第 41 回年会 2003. 9. 23, 新潟県新潟市 朱鷺メッセ

118) 小玉優哉、白崎善隆、船津高志 2003.「高速溶液交換システムを備えた顕微観察法の開発」日本生物物理学会第 41 回年会 2003. 9. 23, 新潟県新潟市 朱鷺メッセ

119) 石浜陽、多田隈尚史、谷時雄、船津高志 2003.「多波長蛍光同時計測による mRNA スプライシング反応の可視化」日本生物物理学会第 41 回年会 2003. 9. 23, 新潟県新潟市 朱鷺メッセ

120) 白崎善隆、田中純一、関口哲史、庄子習一、月田承一朗、船津高志 2003.「昇温型温度感受性ハイドロゲルを用いた生体分子ソーターの開発」日本生物物理学会第 41 回年会 2003. 9. 23,

新潟県新潟市　朱鷺メッセ

121) 鞍馬秀輝、貴家康尋、多田隈尚史、永川豊広、船津高志、原慶恵　2003.「β-actin mRNAの細胞内輸送と局在のイメージング」　日本生物物理学会第41回年会 2003. 9. 23,　新潟県新潟市　朱鷺メッセ

122) 奥村政章、多田隈尚史、石浜陽、船津高志 2003.「量子ドットを用いたmRNA核外輸送の一分子蛍光リアルタイムイメージング」日本生物物理学会第41回年会 2003. 9. 23,　新潟県新潟市　朱鷺メッセ

123) 寺田尚史、奥村政章、河内康明、山口淳一、花木賢一、山本健二、船津高志 2003.「半導体ナノ粒子のブリンキングを制御する」日本生物物理学会第41回年会 2003. 9. 23,　新潟県新潟市　朱鷺メッセ

124) Funatsu, T. 2003. "Single Molecule Imaging of Biological Functions and Handling of Biomolecules in Micro Channels"(1分子蛍光イメージングによる生体分子機能解析と微小流路による生体分子ハンドリング)第2回 NSF-文部科学省合同シンポジウム US-Japan Symposium on Nanotechnology in Advanced Therapy and Diagnosis 2003. 10. 10-11, 横浜プリンスホテル (招待講演)

125) 白崎善隆、船津高志 2003. "A Novel Biomolecule Sorter Using Thermosensitve Hydrogel in Micro Flow System" 第2回 NSF-文部科学省合同シンポジウム US-Japan Symposium on Nanotechnology in Advanced Therapy and Diagnosis 2003. 10. 10-11, 横浜プリンスホテル

126) Sirasaki, Y.,and T. Funatsu 2003. "Biomolecule Sorting in Micro Flow System Using Thermal Gelation" Okinawa InternationalSymposium "New Horizons in Molecular Sciences and Systems: An Integrated Approach" October 16-18, 2003. Bankoku Shinryokan Nago City, Okinawa (沖縄国際シンポジウム"New Horizons in Molecular Sciences and Systems: An Integrated Approach" 2003. 10. 16-18, 沖縄県名護市 万国津梁館) ポスター発表

127) 亀井保博、渡邉建二郎、若松佑子、米田悦啓、船津高志、田口隆久、弓場 俊輔:赤外レーザによる遺伝子発現誘導—IR-Laser Evoked Gene Operation (LEGO) Systemの開発—、第25回日本分子生物学会年会(神戸)、2003. 12. 9-12.

128) 船津高志 2004.「単一分子計測とバイオフォトニクス」(Single molecule detection and Biophotonics) 第91回微小光学研究会 バイオフォトニクスと微小光学 2004. 3. 9,　キャンパスプラザ京都第3講義室

129) 谷井孝至、張 国軍、保坂 匠、三宅丈雄、座古保、船津高志、大泊巌 2004.「有機シラン単分子膜の電子線パターニングによる生体分子の高密度配列固定」 第51回春季応用物理学会 3. 28-31, 東京工科大学

130) 村山研、長尾朋和、鞍馬秀輝、長谷川明洋、船津高志、南谷晴之、新井孝夫、中山俊憲、鈴木和男「血管炎における活性化好中球のCD69分子」15回日本生体防御学会　7. 8-10,　長崎

131) 柳原直紀、多田隈尚史、石浜陽、船津高志 2004.　「アンチセンスoligoDNAの結合を指標としたGFPmRNAの2次構造解析」　第6回日本RNA学会年会　8. 4-6, 熊本テルサ

132) 野中聖子、角田誠、青山千顕、船津高志　2004.「ＨＰＬＣカラムスイッチングシステムを用いたＮＯＳ阻害物質の高感度定量法の開発」日本分析学会第53年会　9. 1-3,　千葉工業大学芝園キャンパス

133) 村上泰規、中野善和、宗光燮、梅沢仁、座古保、船津高志、本多光太郎、古川行夫、川原田洋 2004.「超分散ダイアモンド（UDD）を用いた生体分子固定とその評価」　第65回応用物理学会学術講演会　講演予稿集 pp.520　9. 1-4,　東北学院大学

134) 平野陽子、角田誠、下澤達雄、松井宏光、藤田敏郎、船津高志　2004.「Dahl 食塩感受性ラットにおけるCOMT活性の検討」　第27回日本高血圧学会総会　10. 7-9,　栃木県総合文化センター

135) 平野陽子、角田誠、下澤達雄、松井宏光、藤田敏郎、船津高

ットにおけるCOMT活性の検討」 第27回日本高血圧学会総会 10.7-9, 栃木県総合文化センター

136) 山岸舞、村山研、坂本明彦、新井孝夫、鈴木和男、船津高志 2004.「好中球に活性化にともなうCD69分子の細胞膜表面移行のイメージング」 第13回日本バイオイメージング学会学術集会 11.6-7, 京都府立医科大学 図書館ホール・基礎医学学舎講義室

137) 船津高志 2004.「1分子イメージングでタンパク質の機能を探る」 第25回日本レーザー医学会総会 11.11-12, 東京 ホテルオークラ（招待講演）

138) 船津高志 2004.「生体分子の1分子検出の研究動向」 未踏・ナノデバイステクノロジー第151回委員会第70回研究会 第4回「ナノバイオフージョン分科会」 11.24, 早稲田大学（招待講演）

139) 東條正、多田隈尚史、松島綱治、船津高志 「G 蛋白質共役型受容体は恒常的に多量体を形成する：蛍光一分子イメージングによる解析」第26回生体膜と薬物の相互作用シンポジウム 2004.11.25-26, 東京大学

140) 上野太郎、谷井孝至、島本直伸、三宅丈雄、大泊巌、庄子習一、船津高志 2004.「ナノ開口を用いた弱い生体分子間相互作用の1分子検出」 日本生物物理学会第42回年会 12.13-15, 京都 国立京都国際会館

141) 三浦貴宏、座古保、上野太郎，船津高志 2004.「シャペロニンGroELのC末端欠損変異体の機能解析」日本生物物理学会第42回年会 12.13-15, 京都 国立京都国際会館

142) 岡谷実季、山岸舞、船津高志 2004.「蛍光顕微鏡を用いたアクチンの折りたたみ機構の解析」日本生物物理学会第42回年会 12.13-15, 京都 国立京都国際会館

143) 柳原直紀、多田隈尚史、石浜陽、船津高志 2004.「アンチセンスoligoDNAの結合を指標としたGF-PmRNAの2次構造解析」日本生物物理学会第42回年会 12.13-15, 京都 国立京都国際会館

144) 寺田尚史、多田隈尚史、石浜陽、座古保、船津高志 2004.「蛍光相関分光法を用いた細胞内でのGFPの並進拡散運動の解析」 日本生物物理学会第42回年会 12.13-15, 京都 国立京都国際会館

145) 永川豊広、鞍馬秀輝、貴家康尋、原田慶恵、船津高志 2004.「β-actin mRNA と zipcode-binding protein 1 の結合・解離のキネティクス」 日本生物物理学会第42回年会 12.13-15, 京都 国立京都国際会館

146) 山岸舞、村山研、坂本明彦、新井孝夫、鈴木和男、船津高志 2004.「斜光照明蛍光顕微鏡による好中球のCD69分子の細胞膜表面移行のイメージング」日本生物物理学会第42回年会 12.13-15, 京都 国立京都国際会館

147) 石浜陽、多田隈尚史、谷時雄、船津高志 2004.「mRNAスプライシング反応の1分子蛍光顕微分光観察」日本生物物理学会第42回年会 12.13-15, 京都 国立京都国際会館

148) 杉野弘和、白崎善隆、和田恭雄、江面知彦、庄子習一、船津高志 2004.「温感性ハイドロゲルを用いたマイクロソーターの改良」日本生物物理学会第42回年会 12.13-15, 京都 国立京都国際会館

149) 白崎善隆、泉俊光、水野潤、庄子習一、和田恭雄、月田承一郎、船津高志 2004.「温感性ハイドロゲルを用いたマイクロソーターの開発」日本生物物理学会第42回年会 12.13-15, 京都 国立京都国際会館

152) 辰岡正康、下前智宏、渡部翔太、白崎善隆、水野潤、庄子習一、和田恭雄、船津高志 2004.「生体物質のマイクロチップ内ニ次元ハンドリングシステムの開発」日本生物物理学会第42回年回 12.13-15, 京都 国立京都国際会館

153) 船津高志 「単一分子計測とバイオフォトニクス」第146回 有機エレクトロニクス材料研究会 2005.1.18, 東京市ケ谷 自動車会館（招待講演）

154) Shoji, S. H. Sato, M. Kanai, M. Ishizaka, T. Arakawa, T. Funatsu 2005. Micro/nano flow systems for biological cell analysis. 3rd Sweden Japan Workshop on Nanobiotechnology,

2005.2.28-3.1 pp.16-17.

155) 船津高志 「１分子蛍光イメージング法による生体分子機能解析」 日本化学会 第85春季年会 2005. 3. 26, 神奈川県 神奈川大学横浜キャンパス （招待講演）

156) 船津高志 「１分子蛍光イメージング法による生体分子の機能と相互作用の解析」 第125年会 日本薬学会 2005. 3. 29-31, 東京有明・台場 （招待講演）

157) 角田誠、 長山雅俊、 細田磋一、 船津高志、 今井一洋 「HPLC-過シュウ酸エステル化学発光検出法を用いた高血圧患者運動時血中カテコールアミン動態解析」 第125年会 日本薬学会 2005. 3. 29-31, 東京有明・台場

158) 内野絵里香、角田誠、服部哲幸、早川和一、船津高志 「オンライン還元による高感度化を目指したニトロカテコールアミンの HPLC-化学発光検出法の開発」 第 125 年会 日本薬学会 2005. 3. 29-31, 東京有明・台場

159) 野中聖子、角田誠、青山千顕、船津高志 「HPLC-蛍光検出を用いた内因性 NOS 阻害物質の高感度定量法の開発」 第125年会 日本薬学会 2005. 3. 29-31, 東京有明・台場

160) 青山千顕、角田誠、船津高志 「HPLC-蛍光検出法による selenomethionine 定量法の開発」第125年会 日本薬学会 2005. 3. 29-31, 東京有明・台場

161) 平野陽子、角田誠、下澤達雄、松井宏光、藤田敏郎、船津高志 「Dahl ラットにおける COMT 活性と食塩感受性高血圧の関連性」 第125年会 日本薬学会 2005. 3. 29-31, 東京有明・台場

162) 船津高志 「生体分子のオンチップ分離・回収と１分子機能解析」 独立行政法人日本学術振興会ナノプローブテクノロジー第167委員会 第38回研究会 2005. 4. 19, 東京大学山上会館（招待講演）

163) 庄子習一、佐藤寛暢、叶井正樹、荒川貴博、船津高志「マイクロ／ナノ流体システムとその化学・バイオへの応用」 高分子学会 ポリマーフロンティア21、2005. 4. 22, 東京（招待講演）

164) 野中聖子、角田誠、船津高志「NBD-F を用いたメチルアルギニン類の HPLC-蛍光検出法の開発」第66回分析化学討論会 in 北見、北海道北見市、2005. 5. 14-15.

165) 角田誠、内野絵里香、早川和一、船津高志「HPLC-化学発光検出法を用いたカテコールアミン分析法の開発」 第 12 回クロマトグラフィーシンポジウム 福岡市九州大学病院地区 2005. 5. 19-20.

166) 平野陽子、角田誠、船津高志「HPLC-蛍光検出法を用いた迅速な COMT 活性測定法の開発と生体試料への応用」 第 12 回クロマトグラフィーシンポジウム 福岡市九州大学病院地区 2005. 5. 19-20.

167) 船津高志「１分子蛍光イメージング法による蛋白質間相互作用解析」 日本顕微鏡学会第 61 回学術講演会 つくば国際会議場 2005. 6. 1-3.（招待講演）

168) Watabe, S., M. Tatsuoka, T. Shimomae, Y. Shirasaki, J. Mizuno, T. Funatsu, and S. Shoji. "Multi particles and biomolecules sorting system using thermoreversible gelation controlled by DMD" TRANSDUCERS '05, 2005.6.6-9, Seoul (2005) pp.445.

169) Arakawa, T., Y. Sato, S. Shoji, T. Ueno, T. Funastu "Pinhole-free pyrex glass etching using HF-H_2SO_4 mixed acid and its applications for a PDMS microflow system" TRANSDUCERS '05, 2005.6.6-9, Seoul (2005) pp.1489.

170) 船津高志「1 分子蛍光イメージング法による生体分子機能解析」 Symposium on Atomic, Molecular, and Optical Sciences 2 （原子・分子・光科学（AMO）第2回討論会）、 理化学研究所、2005. 6. 18-19.（招待講演）

171) T. Funatsu "Analysis of Biomolecular Function and Interaction Using Single-Molecule Fluorescence Imaging" International Symposium on Soft-Nanotechnology 2005 (ISSN2005), Hokkaido University, 2005. 6. 20-21.（招待講演）

172) 船津高志 「１分子蛍光イメージング法による蛋白質間相互作用解析」 第62回 JBIRC セ

ミナー、臨海副都心センター、2005. 6. 23（招待講演）

173) 斉藤智、岸元愛子、上野太郎、船津高志、田口英樹 「全反射顕微鏡による酵母ブリオン線維の1分子イメージング」 第5回日本蛋白質科学会年会、福岡国際会議場、 2005. 6. 30-7. 2.

174) 船津高志 「1分子蛍光イメージング法による生体分子機能解析」バイオウィーク in Sapporo2005 シンポジウム―脂質機能研究・バイオセンサ研究の最先端― ホテルモントレエーデル札幌 2005. 7. 6.（招待講演）

175) S. Shoji, H. Sato, M. Kanai, M. Ishizuka, T. Arakawa, T. Funatsu, "Micro/Nano Flow Systems for Biological Cell Analysis", 19th Int. Symp. On Microscale Bioseparations; MSB Kobe, 2005.7.31-8.4, Kobe (2005) pp.54 （招待講演）

176) 船津高志 「1分子蛍光イメージング法による生体分子の機能と相互作用の解析」 第18回バイオメディカル分析科学シンポジウム グランシップ・静岡県コンベンションセンター 2005. 8. 5-7.（特別講演）

177) 角田誠、野中聖子、船津高志 「内因性 NOS 阻害物質の HPLC 高感度定量法の開発」 第18回バイオメディカル分析科学シンポジウム グランシップ・静岡県コンベンションセンター 2005. 8. 5-7.

178) 三浦貴宏、鈴木深保子、上野太郎、座古 保、船津高志 「シャペロニン GroEL の C 末端部位の機能解析」第18回バイオメディカル分析科学シンポジウム グランシップ・静岡県コンベンションセンター 2005. 8. 5-7.

179) 船津高志 「生体分子機能の1分子蛍光イメージング」 シンポジウム「バイオイメージングをナノとの融合によるブレークスルー」 化学工学会 第37回秋季大会 岡山大学 2005. 9. 16.（招待講演）

180) 野中聖子、角田誠、船津高志「モノリス型シリカカラムを用いた ADMA 測定法の開発及び DDAH 活性測定への応用」 日本分析化学会第54年会 名古屋大学東山キャンパス 2005. 9. 13-16.

181) 平野陽子、角田誠、船津高志「Dahl ラットにおける食塩感受成功血圧と COMT 活性の関連性」 第28回日本高血圧学会総会 旭川市民文化会館/旭川グランドホテル 2005. 9. 15-17.

182) Y. Ishihama, H. Tadakuma, T. Tani, and T. Funatsu "Single Molecule Imaging of mRNA Spicing" 4th International Symposium on Nucleic Acids Chemistry (32nd Symposium on Nucleic Acids Chemistry in Japan) 九州大学 2005. 9. 20-22.

183) K.Okabe, H. Ikeda, Y.Harada, and T. Funatsu "Development of Real time Imaging of Spacific Messenger RNA in a Living Cell Using Artificial Antisense nucleic Acids" 4th International Symposium on Nucleic Acids Chemistry(32nd Symposium on Nucleic Acids Chemistry in Japan) 九州大学 2005. 9. 20-22.

184) 角田誠、長山雅俊、細田磋一、今井一洋、船津高志 「ミクロカラムＬＣを用いたヒト運動時血中カテコールアミン類動態評価」第16回クロマトグラフィー科学会議 長良川国際会議場 2005. 11. 7-8.

185) 野中聖子、角田誠、船津高志「HPLC カラムスイッチングシステムを用いたメチルアルギニン類の高感度定量法の開発」 第 16 回クロマトグラフィー科学会議 長良川国際会議場 2005. 11. 7-8.

186) 平野陽子、角田誠、船津高志「HepG2 細胞における酸化ストレスの COMT 活性への影響」第16回クロマトグラフィー科学会議 長良川国際会議場 2005. 11. 7-8.

187) 船津高志 「タンパク質をどこまで観察できるか」ASMeW 医療計測ドメイン・WNTF 情報機能性材料部会共催シンポジウム「ナノ、バイオ技術の動向と融合」早稲田大学 2005. 11. 11.

188) 平野陽子、角田誠、下澤達雄、松井宏光、藤田敏郎、船津高志「食塩感受性高血圧と COMT の関連性」日本心血管内分泌代謝学会 東京コンファレンスセンター品川 2005. 11. 18-19.

189) 渡辺香織、角田誠、上野太郎、山岸舞、船津高志「局所1分子表面増強共鳴ラマン散乱法」日

本生物物理学会第43回年会　札幌コンベンションセンター　2005. 11. 23-25.

190) 山岸舞、貴家康尋、寺田佳代子、原田慶恵、船津高志「mRNAの細胞内ラベリングと運動解析」日本生物物理学会第43回年会　札幌コンベンションセンター　2005. 11. 23-25.

191) 岡部弘基、池田壽文、原田慶恵、船津高志「人口核酸を用いた生きた細胞内における特定のｍＲＮＡのリアルタイムイメージング」日本生物物理学会第43回年会　札幌コンベンションセンター　2005. 11. 23-25.

192) 岡谷実季、山岸舞、上野太郎、船津高志「完全無細胞翻訳系を用いたアクチンフィラメントの作成」日本生物物理学会第43回年会　札幌コンベンションセンター　2005. 11. 23-25.

193) 杉野弘和、白崎善隆、辰岡正康、筒井謙、水野潤、庄子習一、船津高志　「温感性ハイドロゲルを用いた多分岐マイクロソーターの開発」　日本生物物理学会第43回年会　札幌コンベンションセンター　2005. 11. 23-25.

194) 辰岡正康、渡部正太、白崎善隆、水野潤、庄子習一、船津高志「温感性高分子ゲルと赤外レーザーを用いた生体物質 2 次元ハンドリングシステムの開発」日本生物物理学会第 43 回年会　札幌コンベンションセンター　2005. 11. 23-25.

195) 坂本明彦、渡辺隆文、山岸舞、会沢洋一、加藤尚志、船津高志「ピューロマイシン類似体を用いたトロンボポエチンのＣ末端蛍光標識と 1 分子イメージングへの応用」日本生物物理学会第43回年会　札幌コンベンションセンター　2005. 11. 23-25.

196) 船津高志　「生体分子の機能と相互作用の１分子蛍光イメージング」第 4 回マイクロナノ・バイオデバイスの実用化を探る研究会・第 5 回マイクロマシンの応用を探る研究会　東京大学駒場キャンパスII　2005. 12. 9.（招待講演）

197) 青山千顕、角田誠、船津高志「オンライン酸化を用いた selenomethionine の HPLC－蛍光検出法の開発」第 126 年会日本薬学会　仙台国際センター、仙台市民会館、宮城県スポーツセンター、せんだいメディアテーク、仙台市繊細復興記念館、仙台エクセルホテル東急　2006. 3. 28-30.

198) 船津高志「生体分子機能の１分子蛍光イメージング」第83回日本生理学会大会　群馬県民会館・前橋商工会議所　2006. 3. 28-30.（招待講演）

199) 庄子習一，佐藤寛暢，叶井正樹，荒川貴博，船津高志，「マイクロ／ナノ流体システムとその化学・バイオへの応用」，高分子学会　ポリマーフロンティア 21，東京，2005.4.22 (2005) pp.1-4（招待講演）

200) 坂本明彦、船津高志 “In Vitro Translation of Thrombopoietin Labeled with Fluorescent Puromycin at the C-terminus” 第20回国際生化学・分子生物学会議兼第11回アジア・オセアニア生化学者・分子生物学者連合会議　京都市国立京都国際会館　2006. 6. 18-23.

201) K. Watanabe, M. Tsunoda, T. Ueno, M. Yamagishi, T. Funatsu “Single Molecule SERS Applied to Bio-Molecule” Tsukuba Satellite Symposium on Single Molecule and Tip-enhanced Raman Scattering, National Institute of Advanced Industrial Science and Technology (AIST)Tsukuba, Ibaragi Pre. 2006. 8. 17-19.

202) 高月壱、角田誠、青山千顕、白崎善隆、三田智文、船津高志「キャピラリーLCにおける新規蛍光顕微検出法の開発」　日本分析化学会第 55 年会　大阪大学豊中キャンパス　2006. 9. 20-22.

203) T. Funatsu “Analyses of Functions and Interactions of Protein Molecules by Single Molecular Imaging” The International Symposia for Bioimaging, Ikenobo Junior College, Kyoto, Japan, October 28-30, 2006 （招待講演）

204) T. Samesima, Y. Sato, T. Ueno, T. Arakawa, Y. Shirasaki, S. Shoji, T. Funatsu. “Development of a single molecule fluorescence microscope with rapid solution switching system using microfablication technique” Fifth East Asia Biophysics Symposium & Forty-forth Annual Meeting of the Biophysical Society of Japan. November 12-16, 2006, Okinawa Convention Center.

205) N. Terada, T. Shimozawa, S. Ishiwata, T. Funatsu. "Size distribution of actin oligomers in physiological actin solutions analyzed by photon counting histogram" Fifth East Asia Biophysics Symposium & Forty-forth Annual Meeting of the Biophysical Society of Japan. November 12-16, 2006, Okinawa Convention Center.

206) T. Ueno, T. Tanii, N. Shimamoto, T. Miyake, H. Sonobe, I. Odomari, T. Funatsu. "Single molecule imaging of chaperonin functions using zaro-mode waveguides" Fifth East Asia Biophysics Symposium & Forty-forth Annual Meeting of the Biophysical Society of Japan. November 12-16, 2006, Okinawa Convention Center.

207) H. Sugino, Y. Nara, Y. Shirasaki, T. Arakawa, S. Shoji, T. Funatsu. "Development of an on-chip biomolecule parallel sorter using thermoreversible gelation polymer" Fifth East Asia Biophysics Symposium & Forty-forth Annual Meeting of the Biophysical Society of Japan. November 12-16, 2006, Okinawa Convention Center.

208) Y. Shirasaki, T. Aoki, H. Sugino, T. Arakawa, S. Shoji, T. Funatsu. "Sorting biomolecules in a 3D sheath flow microchannel using thermoreversible gelation polymer" Fifth East Asia Biophysics Symposium & Forty-forth Annual Meeting of the Biophysical Society of Japan. November 12-16, 2006, Okinawa Convention Center.

209) Y. Ishihama, H. Tadakuma, T. Tani, T. Funatsu. "Dissociation of pre-mRNA from nuclear speckle domain is ATP dependent process" Fifth East Asia Biophysics Symposium & Forty-forth Annual Meeting of the Biophysical Society of Japan. November 12-16, 2006, Okinawa Convention Center.

210) K. Okabe, Y. Harada, T. Funatsu. "Real time imaging of specific messenger RNA in a living cell using artificial nucleic acids" Fifth East Asia Biophysics Symposium & Forty-forth Annual Meeting of the Biophysical Society of Japan. November 12-16, 2006, Okinawa Convention Center.

211) 船津高志「マイクロ・ナノデバイスを用いた生体分子の分離・回収と1分子機能解析」第6回 JST-SENTAN シンポジウム 2006. 11. 28, 品川プリンスホテル (招待講演)

212) 船津高志「1分子蛍光イメージング法による生体分子の機能と相互作用の解析」第14回 エレクトロニクス基礎研究所公開シンポジウム 原子・分子レベルの材料創製とキャラクタリゼーション 「先端計測分析技術の展望」 2007. 1. 16-17, 大阪電気通信大学 (招待講演)

213) 船津高志「生体分子機能の1分子イメージング」 SORT ジョイントシンポジウム(6) 超微量物質の同定／認識の化学 2007. 1. 30-31, コクヨホール (招待講演)

214) 三田智文、Al-Dirbashi OY, Rashed MS, 福島健、船津高志、今井一洋「ベンゾフラザン骨格を有する LC/MS/MS 用標識試薬の開発と応用」日本薬学会第 127 年会 2007. 3. 28-30, 富山

【国際会議】

1) Ishiwata, S.. "Mechanism of molecular motors: From single molecules to their assembly" Boston Biomedical Research Institute (Watertown), 2002. 6.

2) Ishiwata, S.. "Intra and Intemolecular synchronization observed in kinesin and myosin" Gordon Research Conferences (New London), 2002. 6.

3) Ishiwata, S. "Dynamics of protein motors – From single molecules to systems – " Summer School (Copenhagen), 2002. 8. 13.

4) Ide, J., Aoki, T., Strukova, S., Glusa, E., Ishiwata, S. "PAR 1 and PAR 2-mediated chick embryo cardiomyocytes and cardiofibroblasts stimulation" Jointo Meeting of the 16th International Congress of the International Society for Fibrinolysis and Proteolysis and the 17th International Fibrinogen Workshop of the International Fibrinogen Research Society(Germany), 2002. 9.

5) Ishiwata, S. "Single-molecular Physiology on Protein Motors" NEDO Symposium (Tokyo)

2002. 11. 19.

6) Ishiwata, S.. "The mechanism of motility of processive motors, myosin V and Kinesin" Winter Workshop on Single Molecule Biophysics, Aspen Center for Physics (USA), 2003. 1.
7) Ishiwata, S. "Dynamic properties of molecular motors – From single molecules to systems – " Vrije Univ. (Amsterdam), 2003. 1. 24.
8) Ishiwata, S. "Dynamic properties of molecular motors – From single molecules to systems – " Nanotech 2003 + Future (Tokyo), 2003. 2. 27.
9) Uemura, S., Higuchi, H., Ishiwata, S. "Substeps within each 36-nm step of single Myosin-V motors" Biophysical Society 47th Annual Meeting, San Antonio,Texas,USA 2003. 3. 1-5.
10) Fujita, H., Ishiwata, S., Tesi, C., Lombardi, V., Linari, M. "Mechanical properties of actin filament-reconstituted skinned rabbit myocardium without regulatory proteins" Biophysical Society 47th Annual Meeting, San Antonio,Texas,USA 2003. 3. 1-5.
11) Fujiwara, I., Sasaki, D., Ishiwata, S. "Microscopic analysis of polymerization and depolymerization dynamics of single actin filaments -Effects of regulatory proteins and Pi-" Biophysical Society 47th Annual Meeting, San Antonio,Texas,USA 2003. 3. 1-5.
12) Tojo, T., Aoki, D., Kinowaki, K., Iskandar, S., Tadakuma, H., Ishiwata, S., Funatsu, T. "Oligomerization of FPR1, a G-protein-coupled receptor, is independent of ligand binding in living cells; An analysis using single molecule imaging techniques" Biophysical Society 47th Annual Meeting, San Antonio,Texas,USA 2003. 3. 1-5.
13) Fujita, H., Lu, X., Suzuki, M., Ishiwata, S., Kawai, M. "Effect of Tropomyosin(Tim) on Active Tension and Elementary Steps of the Cross-bridge Cycle" Biophysical Society 47th Annual Meeting, San Antonio,Texas,USA 2003. 3. 1-5.
14) Suzuki, M. and Ishiwata, S. "Contraction and spontaneous oscillatory contraction of muscle studied in the A-band motility assay system" The Second International Symposium on Molecular Synchronization for Design of New Materials System (Yokohama), 2003. 7.
15) Shimamoto, Y., Suzuki, M., Sasaki, D., Yasuda, K. and Ishiwata, S. "Fluorescence microscopic analysis of inter-molecular synchronization observed in the assembly of molecular motors" The Second International Symposium on Molecular Synchronization for Design of New Materials System (Yokohama), 2003. 7.
16) Maejima, H., Shimamoto, Y., Suzuki, M., Ishiwata, S. "Response to mechanical stimuli in self-oscillatory contraction of the contractile system of muscle" The Second International Symposium on Molecular Synchronization for Design of New Materials System (Yokohama), 2003. 7.
17) Shimozawa, T. and Ishiwata, S. "Single-molecular imaging and functional analysis of F-actin by labeling with a fluorescent ATP analogue" The Second International Symposium on Molecular Synchronization for Design of New Materials System (Yokohama), 2003. 7.
18) Hattori, A., Moriguchi, H., Ishiwata, S. and Yasuda, K. "A 1480-nm/1064-nm dual wavelength photo-thermal etching system for non-contact three-dimensional microstructure generation into agar microculture chip" microTAS (USA), 2003. 10.
19) Ishiwata, S. "Dynamic properties of molecular motors –From single molecules to systems-" National Chung-Hsing University (Taichung), 2003. 11. 7.
20) Uemura, S. and Ishiwata, S. "The motile mechanism of kinesin revealed by unbinding force measurements" COE International Conference 2003 "Molecular Mechanism of Intracellular Transports: The Roles of Kinesin and Dynein Superfamily Proteins"

(Hakone), 2003. 11.

21) Ishiwata, S. "Microscopic Studies on Dynamic Properties of Protein Motors and Cytoskeleton" The 19th International Symposium in Conjunction with award of the International Prize for Biology, (Nara), 2003. 12. 2-4. (invited)

22) Ishiwata, S. "Dynamic properties of Actin Filaments and Molecular Motors Revealed by Optical Microscopy" Institute of Curie(France), 2004. 1. 22.

23) Suzuki, M., Ishiwata, S. "Spontaneous oscillatory movement of an actin filament in the A-band motility assay system with and without regulatory proteins" 48th Annual Meeting of the Biophysical Society, Baltimore(USA), 2004. 2. 14-18.

24) Shimamoto, Y., Maejima, H., Suzuki, M., Sasaki, D., Yasuda, K., Ishiwata, S. "Stability of the spontaneous oscillatory contraction(SPOC) in single myofibrils studied by mechanical response and fluorescence imaging" 48th Annual Meeting of the Biophysical Society, Baltimore(USA), 2004. 2. 14-18.

25) Sasaki, D., Fukuda, N., Fujita, H., Kurihara, S., Ishiwata, S. "Length dependence of activation in actin filament-reconstituted skinned bovine myocardium" 48th Annual Meeting of the Biophysical Society, Baltimore(USA), 2004. 2. 14-18.

26) Sasaki, N., Uemura, S., Ishiwata, S., Higuchi, H. "Kinetics of forward and backward steps by single myosin V molecules at low ATP concentration examined by photolysis of caged ATP" 48th Annual Meeting of the Biophysical Society, Baltimore(USA), 2004. 2. 14-18.

27) Uemura, S., Higuchi, H., Ishiwata, S. "12-and 24-nm substeps triggered by ATP binding and Pi release in the myosin-V motor" 48th Annual Meeting of the Biophysical Society, Baltimore(USA), 2004. 2. 14-18.

28) Ishiwata, S. "Molecular synchronization in actomyosin motor - From single molecules to muscle fibers via nanomuscle-" Muscle Symposium, (Tokyo), 2004. 3.7-10. (invited)

29) Ishiwata, S. "Microscopic Studies on Motor Proteins – From Single Molecules to Assemblies –" Rockefeller University (USA), 2004. 6. 2.

30) Ishiwata, S. "Single-molecular Dynamics of Actin Filaments and Molecular Motors" Boston Biomedical Research Institute (USA), 2004. 7. 16.

31) Ishiwata, S. "Auto-oscillations and molecular synchronization observed in protein motors" Gordon Research Conference on "Oscillation and Dynamic Instabilities in Chemical Systems" , Bates College, Lewiston Maine (USA), 2004. 7. 20. (invited)

32) Suzuki, M. and Ishiwata, S. "A-band motility assay with and with regulatory proteins" European Muscle Conference, Elba Island (Italy), 2004. 9. 21.

33) Ishiwata, S. "Synchronization of protein motors-From single-molecules to cells" Shanghai International Conference on Physiological Biophysics, Shanghai Convension Center (China), 2004. 11. 9-13.(invited)

34) Ishiwata, S. "Synchronization of protein motors—From single-molecules to systems—" ENS seminar, France, 2005. 1. 21.

35) Ishiwata, S. "Mechanochemistry of Kinesin Motility" 49th Annual Meeting of the Biophysical Society, Long Beach(USA), 2005. 2. 12-16.(invited)

36) Shimamoto, Y., Suzuki, M., Yasuda, K., Ishiwata, S. "Mechanical Instability of Sarcomeres ageinst Ramp Stretch in Spontaneous Oscillatory Contraction of Skeletal Myofibrils" 49th Annual Meeting of the Biophysical Society, Long Beach(USA), 2005. 2. 12-16.

37) Tseeb, V., Suzuki, M., Ishiwata, S. "Microheater and microthermometer for thermal activation and temperature measurement in the microscopic region around single living cells" 49th Annual Meeting of the Biophysical Society, Long Beach(USA), 2005. 2. 12-16.

38) Shimozawa, T., Ishiwata, S. "Fluorescence imaging of conformational changes in actin

filaments" 49th Annual Meeting of the Biophysical Society, Long Beach(USA), 2005. 2. 12-16.

39) Liou, Y-M., Watanabe, M., Ishiwata, S. "Studies with reconstitution of actin filaments into gelsolin-treated skinned smooth muscle strips of Taenia Caeci in Guinea Pigs" 49th Annual Meeting of the Biophysical Society, Long Beach(USA), 2005. 2. 12-16.

40) Ishiwata, S. "Molecular Synchronization in Acto-myosin II Motors" Gordon Research Conference, Colby-Sawyer College, New England(USA) 2005. 7.3-8.

41) Ishiwata, S. "Molecular synchronization in the assemblage of protein motors" GelSympo2005, Hokkaido University, Sapporo (Japan) Oct. 15-18. (invited)

42) Ishiwata, S. "Cooperative functions of actomyosin motors focusing on the auto-oscillation (SPOC)" National Institute of Physiological Sciences, Okazaki(Japan) Oct. 25-28, 2005.(invited)

43) Ishiwata, S. "Molecular motors and muscle fiber" APCTP-KU Joint Conference on Bio-complexity, Korea University, Seoul (Korea) Nov. 2-5, 2005. (invited)

44) Ishiwata, S. "Biophysics of molecular motors" 43rd Annual Meeting of the Biophysical Society of Japan, Sapporo (Japan) Nov. 23-25, 2005. (invited)

45) Ishiwata, S. "Holistic research and education center for physics of self-organization systems" 北京大学における早稲田デー, 北京大学 (中国) Dec. 5-7, 2005.

46) Itabashi, T., Harada, M., Shimamoto, Y., Gaetz, J., Liu, J. Z., Kapoor, T. M. and Ishiwata, S. "Examining the molecular and physical basis of forces that move chromosomes during cell division" 6th Human Frontier Science Program Awardees Annual Meeting, Institut Pasteur (Paris) July 3-5, 2006.

47) S. Ishiwata, "Single-molecular mechanochemistry of kinesin-microtubule interaction" Kinesin Symposium,Vrije University (Amsterdam) July 6, 2006. (invited)

48) S. Ishiwata, "SPOC analysis of cardiac muscle" British Heart Foundation Symposium, Imperial College London (London) July 10, 2006. (invited)

49) S. Ishiwata, "Dynamic properties of the contractile system of muscle as an auto-oscillator" International Symposium on Bio-nanosystems, Hotel Matsushima Taikanso (Miyagi) Sep. 1-3, 2006. (invited)

50) M. Suzuki, S. Ishiwata, "A-band motility assay with submillisecond time resolution" International Symposium on Bio-nanosystems, Hotel Matsushima Taikanso (Miyagi) Sep. 1-3, 2006.

51) M. Suzuki, V. Tseeb, K. Oyama, S. Ishiwata, "Microscopic Detection of Thermogenesis in a Single Hela Cell Associated with the Increase in Ca2+ Concentration Induced by Ionomycin" 51st Annual Meeting of the Biophysical Society, Baltimore (USA) March 3-7, 2007.

52) J. Udaka, T. Terui, S. Ohmori, I. Ohtsuki, S. Ishiwata, S. Kurihara, N. Fukuda, "Disuse-Induced Changes in Ca2+ Sensitivity of Force in Skeletal Muscle" 51st Annual Meeting of the Biophysical Society, Baltimore (USA) March 3-7, 2007.

53) J. Udaka, T. Terui, S. Ohmori, I. Ohtsuki, S. Ishiwata, S. Kurihara, N. Fukuda, "Disuse-Induced Changes in Length Dependence of Activation and Sarcomere Protein Expression in Skeletal Muscle" 51st Annual Meeting of the Biophysical Society, Baltimore (USA) March 3-7, 2007.

54) Y. Shimamoto, H. Kono, M. Suzuki, S. Ishiwata, "Length-Dependent Activation in Skeletal Myofibrils Induced by MgADP" 51st Annual Meeting of the Biophysical Society, Baltimore (USA) March 3-7, 2007.

55) M. Sodnomtseren, I. Ohtuski, S. Ishiwata, S. Kurihara, N. Fukuda, "Thin Filament-Based

Regulation of Sarcomere Length Dependence of Activation in Skinned Cardiac Muscle: Role of Troponin in the Frank-Starling Mechanism of the Heart" 51st Annual Meeting of the Biophysical Society, Baltimore (USA) March 3-7, 2007.

56) H. Kubota, T. Shimozawa, S. V. Mikhailenko, S. Ishiwata, "Functional Analysis of M47A/E360H Mutant Actin Expressed in Dictyostelium Cells" 51st Annual Meeting of the Biophysical Society, Baltimore (USA) March 3-7, 2007.

57) Y. Oguchi, S. V. Mikhailenko, T. Ohki, A. O. Olivares, E. M. De La Cruz, S. Ishiwata, "Load-Dependent Characteristics of the ADP Affinity of Myosin V" 51st Annual Meeting of the Biophysical Society, Baltimore (USA) March 3-7, 2007.

58) S. V. Mikhailenko, Y. Oguchi, T. Ohki, A. O. Olivares, E. M. De La Cruz, S. Ishiwata, "Mechanochemical Principles Controlling the Oppositely Directed Myosin Motors V and VI" 51st Annual Meeting of the Biophysical Society, Baltimore (USA) March 3-7, 2007.

60) L. R. Gorbacheva, T. P. Storozhevykh, V. G. Pinelis, S. Ishiwata, S. M. Strukova, "Thrombin, factor Xa and activated protein C can protect the rat cortical and hippocampal neurons from glutamate-induced death" Brain'07 and Brain PET'07, (Osaka) May 20-24, 2007.

61) Funatsu, T. 2002. "Single-molecule imaging of biological functions" Five International Biophysics Congress. In. Abstracts pp.55. 2002. 4. 27-5. 1. Buenos Aires, Argentina (招待講演)

62) S. Shoji, N. Honda, H. Sato, M. Kanai, M. Ishizuka, and T. Funatsu, 2003. "Micro Flow Devices /Systems and Biomolecules Handling in Micro Flow Channels" 1st Int. Meeting on Microsenseors & Microsystems, January 12-14, Tainan, pp.17-23.

63) Tojo, T., D. Aoki, K. Kinowaki, S. Iskandar, H. Tadakuma, S. Ishiwata, and T. Funatsu 2003. Oligomerization of FPR1, a G-protein-coupled receptor, is independent of ligand binding in living cells; An analysis using single molecule imaging techniques. Biophysical Society 47th Annual Meeting 2003. 3. 1-5. San Antonio, Texas, USA.

64) Tadakuma, H., T. Shibuya, Y. Ishihama, T. Tani, and T. Funatsu 2003. Imaging of Single mRNA Molecules Moving within a Nucleus of Living Cells Biophysical Society 47th Annual Meeting 2003. 3. 1-5. San Antonio, Texas, USA.

65) Ueno, T., H. Taguchi, H. Tadakuma, M. Yoshida, and T. Funatsu 2003. Nucleotide state in ATP hydrolysis cycle of GroEL Biophysical Society 47th Annual Meeting 2003. 3. 1-5. San Antonio, Texas, USA

66) Funatsu, T. 2003. 1 分子蛍光イメージング法による生体分子機能解析 International Symposium on Single-Molecule Bionalysis and Nano-biodevice 2003. 3. 11-12. 香川県高松市産総研四国センター講堂 (招待講演)

67) Funatsu, T. 2003. "Single Molecule Imaging of Biological Functions and Handling of Biomolecules in Micro Channels" (1分子蛍光イメージングによる生体分子機能解析と微小流路による生体分子ハンドリング) 第2回 NSF-文部科学省合同シンポジウム US-Japan Symposium on Nanotechnology in Advanced Therapy and Diagnosis 2003. 10. 10-11. 横浜プリンスホテル (招待講演)

68) Sirasaki, Y., Funatsu, T. 2003. "A Novel Biomolecule Sorter Using Thermosensitve Hydrogel in Micro Flow System" 第2回 NSF-文部科学省合同シンポジウム US-Japan Symposium on Nanotechnology in Advanced Therapy and Diagnosis 2003. 10. 10-11. 横浜プリンスホテル

69) Sirasaki, Y.,and T. Funatsu 2003. "Biomolecule Sorting in Micro Flow System Using Thermal Gelation" Okinawa InternationalSymposium "New Horizons in Molecular Sciences and Systems: An Integrated Approach" October 16-18, 2003. Bankoku

Shinryokan Nago City, Okinawa (沖縄国際シンポジウム "New Horizons in Molecular Sciences and Systems: An Integrated Approach" 2003. 10. 16-18. 沖縄県名護市 万国津梁館) ポスター発表

70) Hosono, K., T. Ueno, H. Taguchi, F. Motojima, T. Zako, M. Yoshida, and T. Funatsu 2003 "Conformational Change of GroEL studied by Tyrosine Fluorescence" The Fourth East Asian Biophysics Symposium (EABS) November 3-6, 2003. Grand Hotel, Taipei, Taiwan ポスター発表

71) Kinowaki, K., S. Iskandar, T. Tojo, D. Aoki, H. Tadakuma, and T. Funatsu 2003 "Single molecule imaging reveals oligomerization of chemoattractant receptors PI01" The Fourth East Asian Biophysics Symposium (EABS) November 3-6, 2003. Grand Hotel, Taipei, Taiwan ポスター発表

72) Shirasaki, Y., H. Makazu, K. Tashiro, S. Ikeda, T. Sekiguchi, S. Shoji, S. Tsukita, and T. Funatsu "A Novel Biomolecule Sorter Using Thermosensitve Hydrogel in Micro Flow System" The Fourth East Asian Biophysics Symposium (EABS) November 3-6, 2003. Grand Hotel, Taipei, Taiwan ポスター発表

73) Funatsu, T. 2004. "Single-Molecule Imaging of Biological Functions" The 53nd Annual convention of the Pharmaceutical Society of Korea Apri l 22-23, Chungnam National University, Taejon, Korea(韓国大田市) (招待講演)

74) Kohki Okabe, T.Santa, T. Funatsu, and K.Imai 2004. "Study on Fluorescence Properties of Benzofurazans for the Development of Hydrophilic Fluorescent Reagents" The XIth International Symposium on Luminescence Spectrometry-Detection Techniques in Biomedical and Environmental Analysis September 18-24, 中国北京市清華大学

75) Chiaki Aoyama, T.Santa, T. Funatsu, and K.Imai 2004. "A fully Automated Amino Acid Analyzer Using NBD-F as A Fluorescent Derivatization Reagent" The XIth International Symposium on Luminescence Spectrometry-Detection Techniques in Biomedical and Environmental Analysis September 18-24, 中国北京市清華大

76) Tanaka,J.-I., Y. Shirasaki, M. Tatsuoka, T. Funatsu, S. Watanabe, S. Shoji, T. Edura, J. Mizuno, K. Tsutsui, Y. Wada. 2004. "Specific flow control systems using IR laser indeced sol-gel tranfer of hydrogel" *2004 NSTI Nanotechnology Conference and Trade Show-NSTI Nanotech 2004* 1:296-299

77) Tatsuoka, M., T. Shimomae, Y. Shirasaki, J.Tanaka, J. Mizuno, T. Edura, K. Tsutusi, Y. Wada, S. Shoji, and T. Funatsu 2004. "2D Free Space Flow Control System using Termoreversible Gelation of Polymer by IR-Laser" μTAS 2004 Malmo Sweden、September 26-30, Malm・Ehibition and Convention Center (Proceedings, pp.252-254).

78) M. Tsunoda, T. Funatsu, and K. Imai 2004. "Investigation of Catechol-*O*-Methyltransferase Activitites in SHR" Global Conference on Cardiovascular Clinical Trials and Pharmaotherapy September 30-October 4 JW Marriott Hoterl Hong Kong.

79) S. Shoji, H. Sato, M. Kanai, I. Ishizuka, T. Arakawa, T. Funatsu, 2004. "Chemical and bio-applications of MEMS & Nanotechnology", 1st Int. Forum on Nano Science and Technology, Shanhai, 2004-12.

80) Hosono K., T. Ueno, H. Taguchi, F. Motojima, T. Zako, M. Yoshida, T. Funatsu. 2005. Conformational changes of GroEL studied by intrinsic tyrosine fluorescence. Biophysical Society 49th Annual Meeting 2005. 2. 12-16, Long Beach, CA, USA.

81) Zako T., T. Yoshida, Y. Murase, T Kanzaki, N. Ide, R. Iizuka, T. Funatsu, and M. Yohda. 2005. Interaction analysis between hyperthermophilic chaperonin and prefoldin using SPR sensor. Biophysical Society 49th Annual Meeting 2005. 2.12-16, Long Beach, CA,

USA.

82) T. Funatsu "Analysis of Biomolecular Function and Interaction Using Single-Molecule Fluorescence Imaging" International Symposium on Soft-Nanotechnology 2005(ISSN2005), Hokkaido University, 2005. 6. 20-21 (招待講演)

83) Tsunoda, M., S. Nonaka, T. Funatsu "Determination of Methylated Arginines by High-Performance Liquid Chromatography-Fluorescence Dtection" 29th International Symposium on Hifh performance Liquid Phase Setarations and Related Techniques Stockholm, Sweden 2005. 6. 26-30.

84) T. Funatsu "Single-molecule Imaging of Biological Functions" US-Japan Conference on Drug Development &Rational Drug Design、Los Angeles, USA 2005. 7. 31-8. 5 (招待講演)

85) T. Funatsu "Analysis of biomolecular Function and interaction Using Single-molecule Fluorescence Imaging" Symposium on Nanoscale, Processes and Devices. Hapuna Beach Prince Hotel, Hawaii 2005. 11. 2-4.

86) T. Ueno, T.Tanii, N.Shimamoto, T. Miyake, H. Sonobe, I. Odomari, T .Funatsu "Imaging of Single Bio-Molecules Using Fluorescence Microscopy with Nano-Scale Waveguides" 2005 Symposium on Nanoscale, Processes and Devices. Hapuna Beach Prince Hotel, Hawaii 2005. 11. 2-4.

87) K.Watanabe, M.Tsunoda, M.Yamagishi, T.Ueno, T.Funatsu "Surface enhanced resonance Raman scattering of proteins" Biophysical Society Annual Meeting2006, Salt Palace Convention Center, Salt Lake City, Utah, USA, February 18-22.

88) Y.Ishihama,,H.Tadakuma, T.Tani, T.Funatsu "Single Molecule Imaging of mRNA Splicing" Biophysical Society Annual Meeting 2006, Salt Palace Convention Center, Salt Lake City, Utah, USA, February 18-22.

89) K.Okabe, Y,Harada, T.Funatsu "Real Time Imaging of Specific Messenger RNA in a Living Cell Using Artifieical Nucleic Acids" Biophysical Society Annual Meeting 2006, Salt Palace Convention Center, Salt Lake City, Utah, USA, February 18-22.

90) Y.Shirasaki, S.Shoji, T.Funatsu "Rapid Flow Switching with Thermo-Reversible Hydrogel in Microfluidic System" Biophysical Society Annual Meeting 2006, Salt Palace Convention Center, Salt Lake City, Utah, USA, February 18-22.

91) S. Shoji, H. Sato, M. Kanai, M. Ishizuka, T. Arakawa, J. Mizuno, T. Funatsu, "Polymer MEMS and Micro/Nano Flow Systems for Bio/Chemical Applications", The 2nd International Symposium on Micro and Nano Technology; ISMNT-2, 2006.3.29-31, Hsinchu, Taiwan (2006) pp.9-11 (招待講演)

92) T. Funatsu "GroEL mediates protein folding with a two successive timer mechanism" 2006. Gordon Research Conference on Single Molecule Approaches to Biology, Colby-Sawyer college, New London, NH, USA, 18-23 June 2006.

93) T. Funatsu "Analyses of Function and Interactions of Protein Molecules by Single Fluorescent Molecular Imaging" International Conference on Optical MEMS and Their Applications, Big Sky Resort, Big Sky, Montana, USA, 21-25 August 2006. (招待講演)

94) T. Ueno, T. Tanii, N. Shimamoto, T. Miyake, H. Sonobe, I. Odomari, T. Funatsu "Single Molecule Imaging of Chaperonin Functions Using Zero-Mode Waveguides" 51st Annual Meeting of Biophysical Society, Baltimore, MD, USA, March 3-7, 2007

95) K.Okabe, Y.Harada and T.Funatsu, "Real Time Imaging of Specific Messenger RNA in a Living Cell Using Artificial Nucleic Acids", 51st Annual Meeting of Biophysical Society, Baltimore, MD, USA, March 3-7, 2007.

96) Y. Ishihama, H. Tadakuma, T. Tani, T. Funatsu. "The dynamics of pre-mRNAs at the

speckles in living cells revealed by iFRAP studies" 51st Annual Meeting of Biophysical Society. March 3-7, 2007, Baltimore, MD, USA.

3. 出版物

1) 川口憲治、上村想太郎、石渡信一 "キネシン分子モーターの仕組み"*生物物理* **42**, 156-161 (2002).
2) 石渡信一 "ゲルの臨界現象" ゲルと生命 東京大学出版会 pp.32, 総ページ 178 (2002).
3) 鈴木団、石渡信一 "7章生体システムを計測する 7-1.「分子からシステムまで" ナノテクノロジーハンドブック IV バイオ・化学へ使う」(ナノテクノロジーハンドブック編集委員会編) オーム社, pp. 115-119 総ページ 213 (2003).
4) Suzuki, M., Fujita, H. and Ishiwata, S. "Bio-nanomuscle project: Contractile properties of single actin filaments in an A-band motility assay system" In Molecular and cellular aspects of muscle contraction. (ed. by H. Sugi), Kluwer Acad./Plenum Press. pp. 103-110 (2003).
5) 寺崎一郎、石渡信一 "多元要素からなる自己組織系の物理" *大学の物理教育* (日本物理学会) **3**, 21-23 (2003).
6) 島本勇太、鈴木団、石渡信一 "分子モーター"「分子機能材料と素子開発」NTS, pp.574-580 総ページ 771 (2004).
7) Suzuki, M. and Ishiwata, S. "Contractile systems of muscles" In Reflexive polymers and hydrogels: Understandeing and designing fast-responsive polymeric systems. (ed. by N. Yui, R. Mrsny and K. Park), CRC Press LLC. pp.33-47 総ページ 452 (2004).
8) 石渡信一 "21 世紀 COE プログラムの展開" 塔 *早稲田大学理工学部・大学院報* **79**, 7 (2004).
9) 石渡信一 "生体分子モーターの物理" *InterLab* **68**, 75-78 (2004).
10) Ishiwata, S., Shimamoto, Y., Sasaki, D. and Suzuki, M. "Molecular synchronization in actomyosin motors from single molecule to muscle fiber via nanomuscle" Adv. Exp. Med. Biol. 565, 25-36 総ページ 431 (2005).
11) 石渡信一 "飛躍のとき" *生物物理* **45**, 1 (2005).
12) 上村想太郎、石渡信一 "生体分子モーターの一分子力学"*応用物理* **74**, No.2 196-201 (2005).
13) 石渡信一 "分子モーター" *パリティ* **20**, 22-24 (2005).
14) Ishiwata, S., Shimamoto, Y., Suzuki, M. and Sasaki, D. "Regulation of muscle contraction by Ca2+ and ADP: Focusing on the auto-oscillation (SPOC)" *Adv. Exp. Med. Biol.* **592**, 341-358 (2007).
15) 石渡信一 "生理学と生物物理:似ているところと似ていないところ"*日本生理学* **69**, 3 (2007).
16) 上野太郎、多田隈尚志、船津高志 "シャペロニン機能の 1 分子蛍光イメージング" センサマイクロマシーン準部門誌 123巻4号 pp.107-111 (2003).
17) 多田隈尚史 船津高志 2003 「5章 タンパク質を計測する 4 タンパク質の相互作用と機能」 ナノテクノロジーハンドブック (Ⅰ～Ⅳ) Ⅳ編バイオ・化学へ使う pp.94~99 総ページ 213 (オーム社：ナノテクノロジーハンドブック編修委員会編) 2」 "蛋白質を計測する 蛋白質の相互作用と機能" (2003).
18) 船津高志 「単一分子計測とバイオフォトニクス」 応用物理 第72巻 第6号 pp.727-730 (2003).
19) 多田隈尚史、船津高志、谷時雄 「ｍＲＮＡ核外輸送の可視化」蛋白質核酸酵素, 共立出版 vol.48 pp.421-429 (2003).
20) 船津高志 2 章「バイオのナノ構造」 ナノテクノロジー基礎シリーズ バイオナノテクノロジー (オーム社 堀池靖浩、片岡一則 編)pp.11-33 総ページ数 222 (2003).

21) 多田隈尚史、座古保、船津高志「蛍光分子イメージングを用いたナノ分子の検出と機能解析」ナノバイオテクノロジーの最前線(シーエムシー出版)6章 4節ナノバイオテクノロジー pp.371～379 総ページ数439(2003).
22) 上野太郎、多田隈尚史、船津高志 「1分子イメージングによるシャペロン研究」細胞における蛋白質の一生 (共立出版 小椋光、 遠藤斗志也、森正敬、吉田賢右 編) 49(7 Suppl): pp.855-856. 総ページ数1152(2004).
23) 船津高志 「1分子イメージングの考え方と実際」バイオイメージングがわかる (羊土社 高松哲郎 編) pp.34-42. 総ページ数 125(2005).
24) 船津高志、上野太郎 「エバネッセント場蛍光顕微鏡による生体分子の1分子機能解析」光学 34(10): 500-505(2005).
25) 船津高志 「1分子蛍光イメージング法による生体分子の機能と相互作用の解析」化学と生物 44(1): 34-38(2006).
26) 船津高志 「生体分子の1分子蛍光イメージング」 レーザー研究 (The Review of Laser Engineering) ,Vol.34,No.3 March 2006、pp.241-245(2006).
27) 船津高志 「1分子イメージングでタンパク質の機能を探る」日本レーザー医学会誌 Vol.26,No.4:327－332(2006).
28) 船津高志 「現場で役立つバイオイメージング 第1回 全反射蛍光顕微鏡による1分子イメージング(基礎編)」 バイオニクス 2006, 4月号、pp.76-83(2006).
29) 船津高志 「現場で役立つバイオイメージング 第2回 全反射蛍光顕微鏡による1分子イメージング(応用編)」 バイオニクス 2006, 5月号、pp.64-70(2006).
30) 船津高志、谷時雄 「mRNA 核内運動の1分子イメージング」 ファルマシア vol.42 No.8 803-806(2006).
31) 船津高志 「マイクロ・ナノデバイスを用いた生体分子の1分子計測と分離操作」 Drug Delivery System vol.21, No.6, pp. 608-613(2006).

研究成果による工業所有権の出願・取得状況

1) 特願 2002-319577「マイクロシステム」出願人：学校法人早稲田大学 発明者：船津高志、庄子習一、和田恭雄、筒井謙、水野潤、白崎善隆
2) 特願 2002-326217「微小開口膜、及び生体分子間相互作用解析装置とその解析方法」出願人：学校法人早稲田大学 発明者：船津高志、和田恭雄、筒井謙、水野潤
3) 特願 2003-40330「マトリックス型可変マイクロ流路及びそのシステム」出願人：学校法人早稲田大学 発明者：船津高志、庄子習一、白崎善隆
4) 特願 2003-173696「蛍光物質の蛍光強度を向上させる方法及び蛍光強度向上剤」 出願人：山本健二、山口由岐夫、積水化学工業株式会社 発明者：一谷基邦、山本健二、山口由岐夫、船津高志、花木賢一、白崎善隆
5) PCT/JP03/13902「マイクロシステム、並びに、微小開口膜、及び生体分子間相互作用解析装置とその解析方法」出願人：学校法人早稲田大学 発明者：船津高志、庄子習一、和田恭雄、筒井謙、水野潤、白崎善隆
6) 特願 2004-043806「温度測定法及び温度制御方法」出願人：独立行政法人産業技術総合研究所 発明者：弓場俊輔、船津高志
7) 特願 2005-219539「分子振動計測法、分子振動計測装置、試料調整用キット及び分子振動計測システム」出願人：国立大学法人東京大学 発明者：船津高志、角田誠、上野太郎、渡辺香織

研　究　成　果

1分子力学測定によって明らかとなった力と酵素活性の相関による新しいキネシン歩行モデル

上村　想太郎

＜研究の背景＞

キネシンは神経細胞において、神経伝達物質が入った小胞などの軸索輸送を担っているタンパク質である。キネシンは二量体からなり、N 末端側は ATPase 活性を有する 2 つの球状頭部（双頭構造）がある。キネシンはこの 2 つの頭部を微小管の最小単位であるチューブリンの分子間距離に相当する 8nm の間隔で交互に結合・解離を繰り返し、歩くように運動する「Hand-over-hand モデル」で運動していると考えられている。そこには、ATP の加水分解と共役した巧妙な仕組みが存在しているはずである。

一番の謎はキネシンがその相同頭部の結合・解離による歩行運動の際にどのように前頭と後頭を認識しているのかということである。正確な歩行運動を実現するためには前頭が解離する前に後頭が解離しなければ一方向に運動を維持することはできない。しかし 2 つの相同頭部がどのようにして“前”と“後”を認識しているのかを調べることができれば、歩行メカニズムの謎に大きく迫ることができる。そこで我々は、キネシン・微小管結合状態に対して光ピンセットによる分子間結合の破断力（結合を破断するのに必要な力）の測定を行うことで“前”と“後”を力で認識する新しい歩行モデルを考案し、歩行メカニズムの解明へ迫ることができた。

＜研究方法と結果＞

我々はキネシン微小管複合体に対して破断力測定を各 ADP 濃度で行った。1 分子キネシンを結合した直径 1μm のビーズを光捕捉し、ガラス基板上に固定した微小管上にビーズを近づける。微小管はあらかじめ、アミノ基を介してローダミン色素で標識されており、蛍光画像でその位置を確認することができる。しかも重合速度の異方性を利用することによって微小管を非対称的に蛍光ラベルし、重合端（＋端；キネシンの進行方向）と脱重合端（－端）とを識別する。ビーズの回転ブラウン運動によりキネシンと微小管は結合状態となった後、光ピンセットの捕捉中心を一定速度で微小管に沿って動かし続けることによってキネシン・微小管結合にほぼ一定の上昇速度で負荷を加えることができる。破断は熱揺らぎに依存する確率事象であるが，破断時に加わっていた負荷（破断力）を測定する。そしてさらに光捕捉中心を動かし続けることによって、キネシン・微小管の再結合による再破断を記録・計測することができる（図 1A）。ADP 存在下における典型的な生データを図 1BC に示した。ビーズの位置が捕捉中心からはずれるにつれて、徐々に外部負荷が加わるが、キネシンが微小管から解離するとビーズはすばやく捕捉中心に戻る。破断力はキネシンが解離した瞬間のビーズの輝度重心と捕捉中心との距離に光ピンセットのバネ定数（今回は 0.05pN/nm）を掛けて算出する。このように繰り返し測定によ

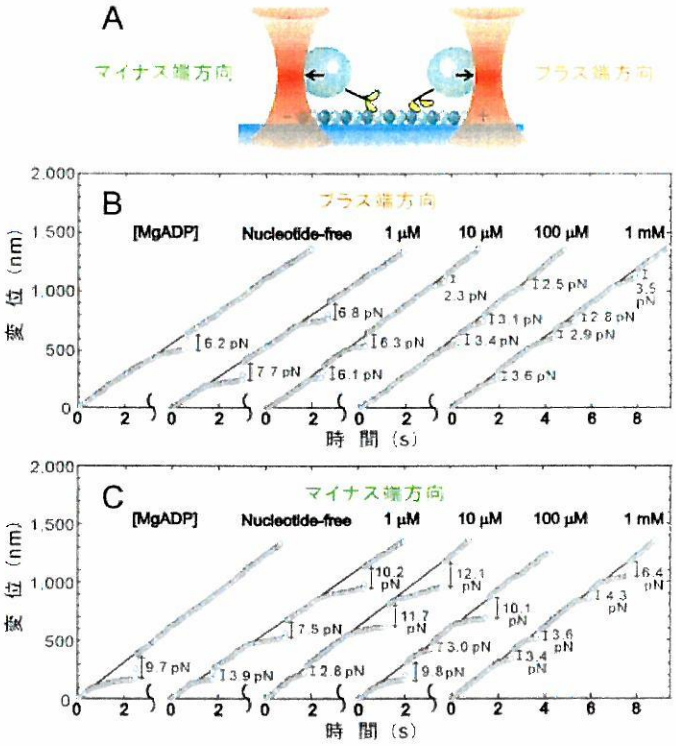

図 1　1 分子破断力測定　A,実験の模式図。光ピンセットの捕捉中心を微小管に沿って＋端方向及び－端方向へと一定の速度で動かし続ける。B,C,各 ADP 濃度におけるビーズ輝度重心の時間変化（＋端方向及び－端方向）。

って得た破断力分布は 1mMADP では＋端[－端]方向へ負荷を加えた場合、4[4]pN と弱結合となり、ヌクレオチドなしでは 7[9]pN と強結合だった。キネシンはこれらの ADP 濃度では単頭結合であることがすでに知られており、単頭結合内に弱結合と強結合の 2 状態が存在することがわかった。そこで ADP 濃度を徐々に上げて強結合と弱結合の割合を調べると，弱結合成分（4pN 付近のピーク）の割合が増加した。このことは，単頭内で強結合と弱結合とが平衡関係にあり、これが ADP の結合・解離と共役していることを示している。

そこで面白いことに、弱結合成分と強結合成分の割合がほぼ等しくなる ADP 濃度は、＋端方向への負荷の方が－端方向への負荷の場合よりも低かった。つまり、＋端方向に負荷が加わると ADP 結合が促進され、－端方向への負荷では ADP 結合が抑制されることを示している（図２）。この結果、分子モーターへのヌクレオチド結合の結合定数（平衡定数）が負荷の方向によって異なるという，力学過程と化学過程の直接的な共役が 1 分子レベルで明らかとなった。

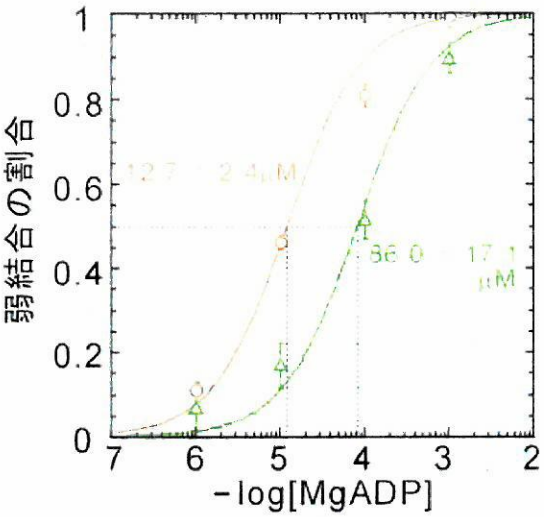

図２　各 ADP 濃度に対する弱結合の割合．○は負荷を微小管の＋端（F_+）方向，△は－端（F_-）方向に加えた場合．弱結合が 50% になる MgADP の濃度を図中に示した．

＜キネシンの内部負荷モデル＞

こうした力学－化学共役の性質はキネシンの運動にとって極めて重要な役割を果たしていると考えられる。前述のように双頭構造を持つキネシン型のモーターは一方向性を持って運動し続ける性質を持ち、各頭部を交互に微小管結合部位へと結合させることで運動する「歩く」分子モーターである。しかし，ホモダイマーであるキネシンは一体どのように前頭と後頭を区別しているのだろうか？一方向性運動を維持するためには各頭部を区別する巧妙な仕組みが存在しているに違いない。そこで＋端方向に負荷が加わると ADP 結合が促進され、－端方向への負荷では ADP 結合が抑制される結果を考慮し，図３のように双頭結合時の頭部間に内部負荷が生じると仮定する。実際にキネシンが微小管と結合していない状態では頭部間の距離は約 5nm であることが知られているため、微小管との双頭結合時には頭部間は約 3nm 分だけ伸びて結合しており、内部負荷が存在している状態であると考えられる。すると、負荷方向の違いにより後頭部が前頭部より ADP を結合しやすいことを意味し、後頭部が前頭部より微小管から解離しやすくなるので、双頭結合から次の一歩を踏み出しやすいという性質が生まれることになる。これは Hand-over-hand モデルにとって鍵となる性質であり、内部負荷による頭部への負荷方向の違いから前頭と後頭を区別していると考えることができる。こうした概念は歩行メカニズムの解明に大きく貢献しており、本研究成果は、Loading direction regulates the affinity of ADP for kinesin というタイトルで Nature Structural Biology 誌に掲載された。

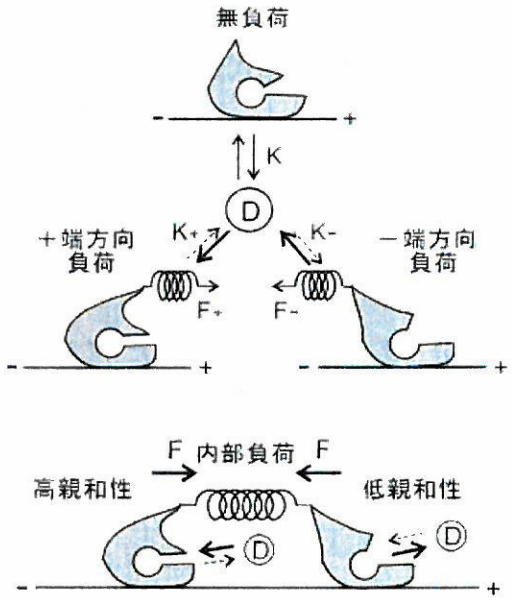

図３　負荷方向に依存する ADP 結合定数と双頭結合時に生じると期待される内部負荷の影響．負荷を微小管の＋端（F_+）あるいは－端（F_-）方向に加えたときの ADP の結合定数（K_+；＋端，K_-；－端）

ミオシンVに対するADP結合能の負荷方向依存性

小口 祐伴

概要

ミオシンVは、細胞中に張りめぐらされるアクチンフィラメント上を歩行運動するモータータンパク質である。ミオシンVの分子構造には足に相当しアクチンフィラメントと結合する部位が2つ存在し（図1左端）、その歩幅は36 nmである。また各足にはATP結合部位が存在し、各々の足とアクチンフィラメントとの結合・解離は各々に結合するヌクレオチドの状態依存的に制御されている。このような歩行運動は、各々の足が独立にアクチンフィラメントと結合・解離するのではなく、協調的に起こることで可能になる。すなわち、離れた2つの部位で起こるATPの加水分解反応が協調的に起こることが不可欠であると考えられているが、このような機構については未だに不明な点が多い。本研究は、ミオシンVの2本の足間には、各々をつなぎ合わせることで生じる“内部負荷”（前足には後足が前足を引っ張ることによって生じる後方負荷が、同様に後足にも前足による前方負荷）が存在することを仮定し、各々の足で起こるATPの加水分解反応がこの内部負荷によって制御されることで協調的な加水分解反応が生み出されることを推論し、実際にこのような機構の存在するか検討することを目的として行われた。特に、ATP加水分解産物であるADPのミオシンVに対する結合能とミオシンV分子に与えられる負荷の関係性に着目し、実際に顕微鏡下光ピンセット法を用いることによって、ミオシンV与える負荷方向依存的にADP結合能が変化することを明らかにした。

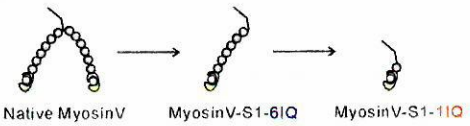

図1. ミオシンV分子模式図（native & construct）

天然に存在するミオシンV（左端）は2本の足に相当する部位を持ち、それぞれの部位でATP、アクチンフィラメントとの結合・解離が起こる。本研究では、1つの足の負荷依存的な振る舞いに着目する為に、遺伝子操作によって片足のミオシンVを作製し、1分子破断力測定を行なった。また、足の長さによる負荷依存的な振る舞いの違いを検討する為に2つの長さのコンストラクトを用いた。長い方を6IQ(中位)、短い方を1IQ（右端）と呼ぶ。

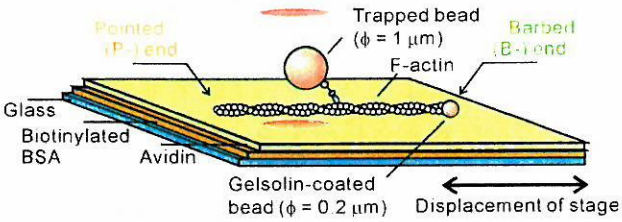

図2. ミオシンV・アクチン系における1分子破断力測定の模式図

アクチン結合B端キャップタンパク質ゲルゾリンを架橋した（直径0.2 μm）をアクチンフィラメントに結合させることで方向性を特定する。光ピンセット法により捕捉したミオシンビーズ（直径1 μm）をアクチンと相互作用させ、顕微鏡ステージを移動させることでミオシンV－アクチン結合部に徐々に負荷を与える。

実験系

本特別推進研究費により構築した1分子高速力学測定装置（昨年度までに報告済み）を用いて実験を行った。これまで我々は従来の装置（Nikon・TMD）を用いキネシン・微小管の破断力測定を行ってきたが、今回、1分子高速力学測定装置の高時間分解能な性質を活かし、より大きな負荷変

化率を与える実験が可能となった。これによりキネシン・微小管系で確立された1分子破断力測定をミオシンV・アクチン系に適用しただけではなく、より精度よく実験条件を制御することが可能になり、詳細な解析を行うことができた。

ミオシン V-S1-6IQ を用いた破断力測定

遺伝子操作によって作製した片足のミオシン V（ミオシン V-S1-6IQ）を anti-myc antibody を介して直径 1 μmビーズ表面に吸着し、光ピンセットで捕捉する。そして、光ピンセットの捕捉位置を変えずにアクチンを固定したガラス表面をステージごと一定速度で移動させることで、アクチン・ミオシン V 結合に負荷を徐々に加えていき、破断力を繰り返し測定した（図2）。また、アクチンフィラメント切断・B 端キャップタンパク質として知られるゲルゾリンを結合した直径 0.2 μmのポリスチレンビーズを作成し、ゲルゾリンを介することでアクチンフィラメントの B 端にビーズを結合させた。この B 端に結合したビーズによりアクチンフィラメントの方向性を特定し、負荷方向を B 端、P 端方向に分けて破断力の分布を測定した。その結果、rigor 状態（0 mM ADP 存在下；図3最下段）と ADP 結合状態（1 mM ADP 存在下；図3最上段）では平均破断力が異なることが明らかになった。また中間 ADP 濃度存在下においては、2つのピークを持つ破断力分布が得られた。これらの2つのピークは、中間 ADP 濃度において、ADP 結合状態、rigor 状態どちらの状態からも破断が起きていることを意味している。さらに各 ADP 濃度における rigor 状態と ADP 状態の存在比を近似した関数から算出したところ、これらは負荷方向によって異なり、各 ADP 濃度において、B 端方向より P 端方向に負荷を与えた方が ADP 状態の存在割合が高くなることが明らかになった（図4）。また、ADP 状態の存在割合は、ADP 濃度に対して次の式に従う。

$$\text{ADP 状態の存在割合} = \frac{[ADP]}{[ADP]+K_d} \qquad (1)$$

K_d ； みかけの ADP 解離定数

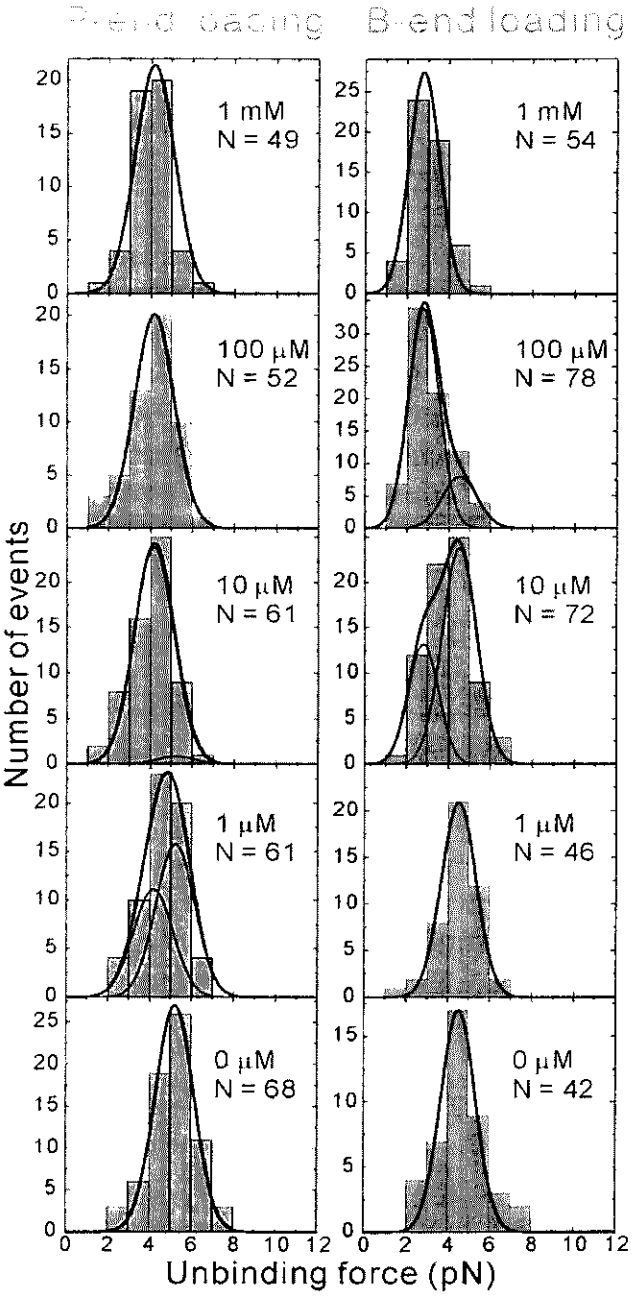

図3. ミオシンV-S1-6IQの破断力分布

この式（1）を、得られた各濃度に対する ADP 状態の存在割合に対してフィッテングしたところ、みかけの ADP 解離定数 K_d は各負荷方向においてそれぞれ、23 μM（B 端負荷）、1.2 μM（P 端負荷）となった。

ミオシン V-S1-1IQ を用いた破断力測定

ミオシン V-S1-1IQ（以後 1IQ と示す）は calmodulin を結合する IQ モチーフを 1 個しか持たない片足のミオシン V(Enrique DeLaCruz 研, Yale 大の協力による)であり、IQ モチーフを 6 個持つミオシン V-S1-6IQ（以後 6IQ と示す）に比べると足の短い遺伝子変異体とみなすことができる（図 1）。この足の短い 1IQ を用いて、6IQ と同様の破断力測定実験を行なったところ、6IQ 時に観測された負荷方向による ADP 結合能の差が小さくなることが明らかになった（図 5）。このことは、1IQ で欠如した部位が、負荷方向によって ADP 結合能を制御するために、重要な部位であることを示唆している。

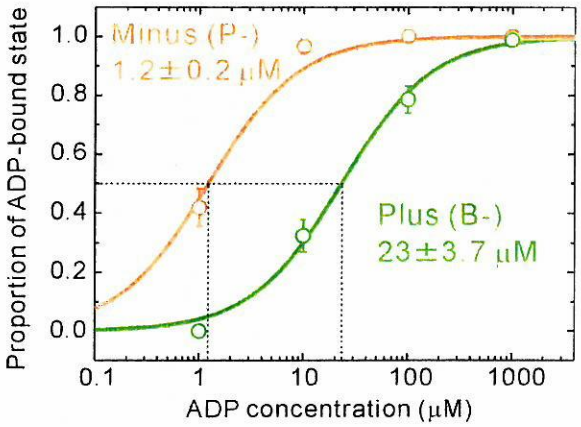

図 4. 各 ADP 濃度における ADP 状態の存在割合(ミオシン V-S1-6IQ における)
図 3 の破断力分布、各 ADP 濃度において近似する 2 つのガウス分布の面積比から、各 ADP 濃度における ADP 結合状態の存在割合を算出した(B 端方向負荷;緑色、P 端方向負荷;橙色)。

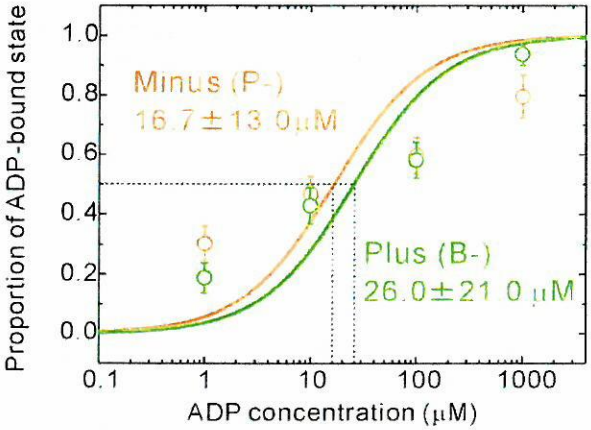

図 5. 各 ADP 濃度における ADP 状態の存在割合(ミオシン V-S1-1IQ における)
ミオシン V-S1-1IQ を用いて図 4.と同様の解析を行ったところ ADP 解離定数は、6IQ で観測されたほど負荷方向によって大き[所]

まとめと今後

特別推進研究費により新たに構築した 1 分子高速力学測定装置を用いて、ミオシン V・アクチン系における 1 分子破断力測定実験系を確立した。遺伝子組換え技術によって作成したアクチン結合部位を 1 つしか持たない片足のミオシン V を用いることにより、片足のミオシン V における力学ー化学共役変換に着目することができた。特に ATP 加水分解産物である ADP のミオシン V に対する結合能は負荷方向によって異なることを明らかにした。このことは native ミオシン V の前足と後足では ADP の結合能が異なり、前足に比べ後足からの ADP 解離が速く起こることで、より効率よく一方向歩行運動が可能となっていることを示唆する。また、これらのミオシン V（アクチン B 端方向歩行モーター）に関する結果とアクチンフィラメント上を逆向きに歩行するミオシン VI（アクチン P 端方向歩行モーター）の同様の実験結果を比較することで、歩行運動の方向性を生み出すメカニズムについて検討を深めていく予定である。

Study on the mechanism of myosin VI processivity by single-molecule mechanics

Sergey V. Mikhailenko

Myosins constitute a large group of the molecular motors, called myosin superfamily, which repetitively couple the successive steps of ATP binding, hydrolysis and product release to the generation of force and movement along actin filaments. The myosin superfamily currently includes eighteen classes; each class possesses subtle differences in structure, leading to the variations in the enzymatic properties in order to be perfectly fit for performing specific functions in living organisms.

Among all classes, myosin VI has been gathering particularly strong attention due to its several unique properties. First, myosin VI moves towards the pointed end of actin filament, which is opposite to all other characterized members of myosin superfamily. Second, single-molecule measurements have revealed that both single-headed and artificially dimerized myosin VI molecules record the displacements of actin filament much exceeding in size those predicted from the structure of the motor. The recently obtained crystal structure of its motor domain in the nucleotide-free state revealed the peculiarities of myosin VI structure responsible for the reverse of its movement, but has been unable to provide the decisive explanation for the large stepping of myosin VI. Therefore, the research on myosin VI still misses an important part of how it performs in living organisms. Considering the generality of mechanism of force production by myosins, it is highly plausible that this lacking part is applicable for other myosins as well and can therefore be an important component of the general theory of force production by the molecular motors. In particular, it remained unclear how the dimeric myosin molecules are able to move unidirectionally along an actin filament, taking multiple steps per single diffusional encounter. It has been hypothesized that the two heads communicate through the intramolecular strain, originating during the double-headed binding to actin, presumably in the rate-limiting ADP state. Such communication would result in the modulation of the biochemical processes in at least on of the heads, allowing for the unidirectional stepping. However, no direct experimental evidence has been provided.

In this project, we address the issue by directly measuring the ADP affinity of an individual single-headed myosin VI molecule under the external load, applied either in the direction of the myosin's motility or against it, mimicking the trailing or the leading head of the dimeric motor, respectively. To this end, we studied the mechanical properties of individual myosin VI-actin complexes in different nucleotide states, using our unique experimental apparatus for the unbinding force measurements. Its previous version has been successfully used in studies on single- and double-headed kinesins, which yielded the important information on the mechanism of the kinesin motility. This new, upgraded apparatus enables us to perform the measurements in a broader range of the experimental conditions with the higher temporal resolution and data reliability due to the improved mechanical, optical, and electronic parts.

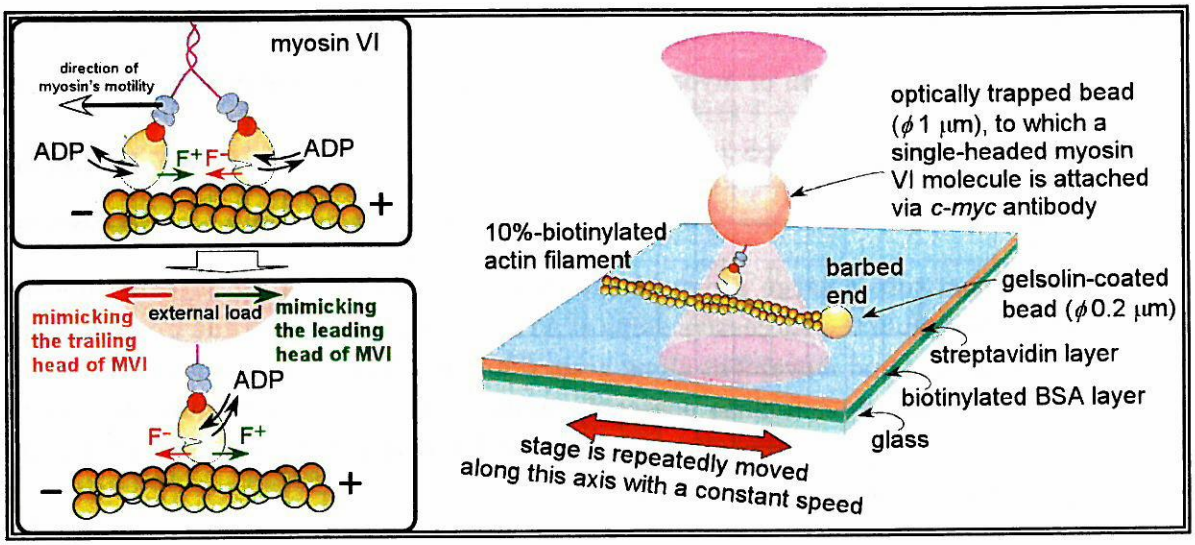

Fig. 1. Schematic representation of the experimental approach (left) and the experimental setup for the unbinding force measurements (right). Load is applied either towards the barbed end of an actin filament, mimicking the leading head, or in the opposite direction, mimicking the trailing head.

The brief description of the experimental method is as follows (Fig. 1). First, single molecules of myosin VI *myc*-tagged at the C-terminus are attached to a plastic bead (diameter 1 μm) via a *c-myc* antibody. The bead is then trapped by a laser beam (1064 nm) and brought close to a 10% biotinylated actin filament of known polarity, which has been firmly attached to the surface of a flow chamber. Next, the stage is displaced with a constant rate, using the electronically controlled piezo substage, thus exerting load on a myosin-actin bond, until at some load the bond breaks. The distribution of forces, at which the unbinding events occur, revealed strong dependence on the nucleotide state, such that the unbinding in the ADP state occurs under smaller load than in the absence of nucleotides. It allowed us to determine the proportion of the ADP state at the intermediate ADP concentrations, where the unbinding force distributions are bimodal, and thus to determine the ADP affinity under the directional load. The ADP affinity was lower under loads applied in the direction of motility, directly confirming the strain-induced modulation of the catalytic cycles in the two heads (Fig. 2).

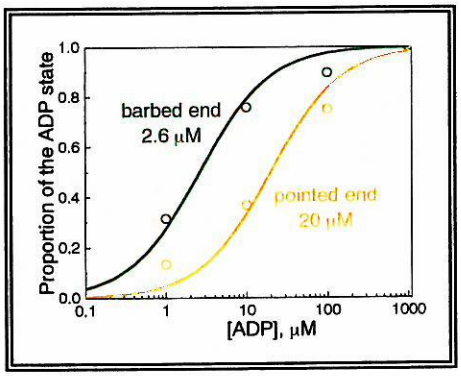

Fig. 2. ADP binds weaker under the pointed end directed loading, which mimics the trailing head.

Combined with our previous data on kinesin—microtubule interaction, the present results strongly suggest that the intramolecular strain that arises from double-headed binding of a motor to the lattice track is a major regulator of the mechanochemistry, which controls the unidirectional stepping of dimeric ATP-driven processive motors, regardless of whether the lattice is an actin filament or a microtubule.

キネシン微小管強結合部位の特定

小口 祐伴

概要

キネシンは細胞中の微小管上をATPの加水分解を伴いながら、たった一分子で数μmにわたって歩行することが出来るモータータンパク質である。キネシン分子内には微小管と相互作用する部位（モータードメイン）が2つ存在し、この2つの部位を交互に微小管と結合・解離させることで歩行運動を行うことができる。また、各々のモータードメインはモータードメインに結合するヌクレオチドの状態依存的に微小管との結合状態（強結合状態および弱結合状態）が制御されている。さらに近年では、他のグループによる極低温電子顕微鏡観察法などによって、各ヌクレオチド状態におけるモータードメインと微小管の3次元構造が明らかにされ、微小管を構成するβ-tubulinに存在するHelix 12は、キネシンと微小管の強結合状態（AMP-PNP結合状態）に密接に関係することが示唆されている。しかしながら、極低温電子顕微鏡観察法のような場合では、実際にキネシンが歩行できるような観察状態ではないため、どの相互作用部位がキネシン歩行運動にとって重要であるか特定することはできていない。本研究ではこれまで困難であったα, β-tubulin発現単離精製に成功することで、実際にキネシンが運動する条件下(*in vitro*)におけるtubulinのアミノ酸置換解析（武藤悦子研究室（理研）との共同研究）が可能になり、特にキネシンと微小管の強結合状態に重要であるアミノ酸を特定した。

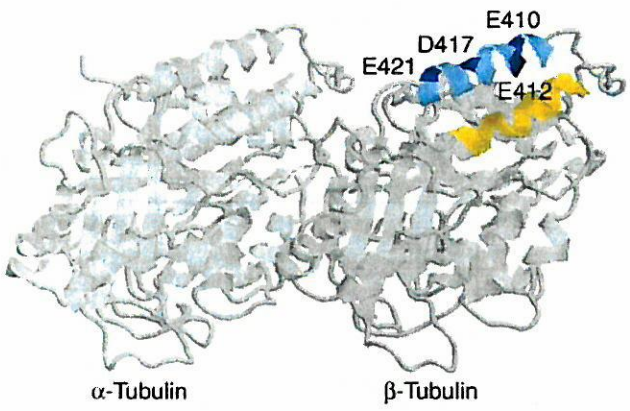

図1．チューブリンダイマーの立体構造
（プラス端は右方向）
ヌクレオチドフリーまたはAMP-PNP状態にあるキネシン微小管複合体では、β-tubulin内にあるHelix 11（オレンジ）、Helix 12（ブルー）とキネシンモータードメインが密接に関係していることが示唆されている。本研究では、これらの中にある負電荷をもつアミノ酸E410, E412, D417, E421をアラニンに置換し、*in vitro*においてキネシン微小管複合体の破断力測定とstall force（キネシン1分子最大発生力）測定を行なった。

単頭キネシンを用いた1分子破断力測定

単頭キネシンは微小管と相互作用するモータードメインを1つしか持たないキネシンである。この単頭キネシンと図1にあるようなアミノ酸を置換したβ-tubulinによって構成された微小管を用いて、1分子破断力測定（顕微鏡下光ピンセット法において）をおこなった。具体的には、1 mM AMP-PNP存在下（このときモータードメインと微小管は強結合状態にある）または、1 mM ADP存在下（モータードメインと微小管は弱結合状態）において、1つのキネシンモータードメインと微小管結合を破断させる力（破断力とよぶ）を測定した。すると、1 mM ADP存在下においてはキネシンの運動方向（微小管プラス端方向）、またはその逆方向（微小管マイナス端方向）に負荷を与えても、各変異体間で有意な差は認められなかった（図2A）。しかしながら、1 mM AMP-PNP存

在下においては、マイナス端方向に負荷を与えたときのみ、E410A, D417A, E421A では破断力の有意な減少が見られた(図２B;ただし E412 は有意な差が無かった)。これらの結果は、E410, D417, E421 がキネシンと微小管の強結合状態に重要なアミノ酸であることを示唆している。

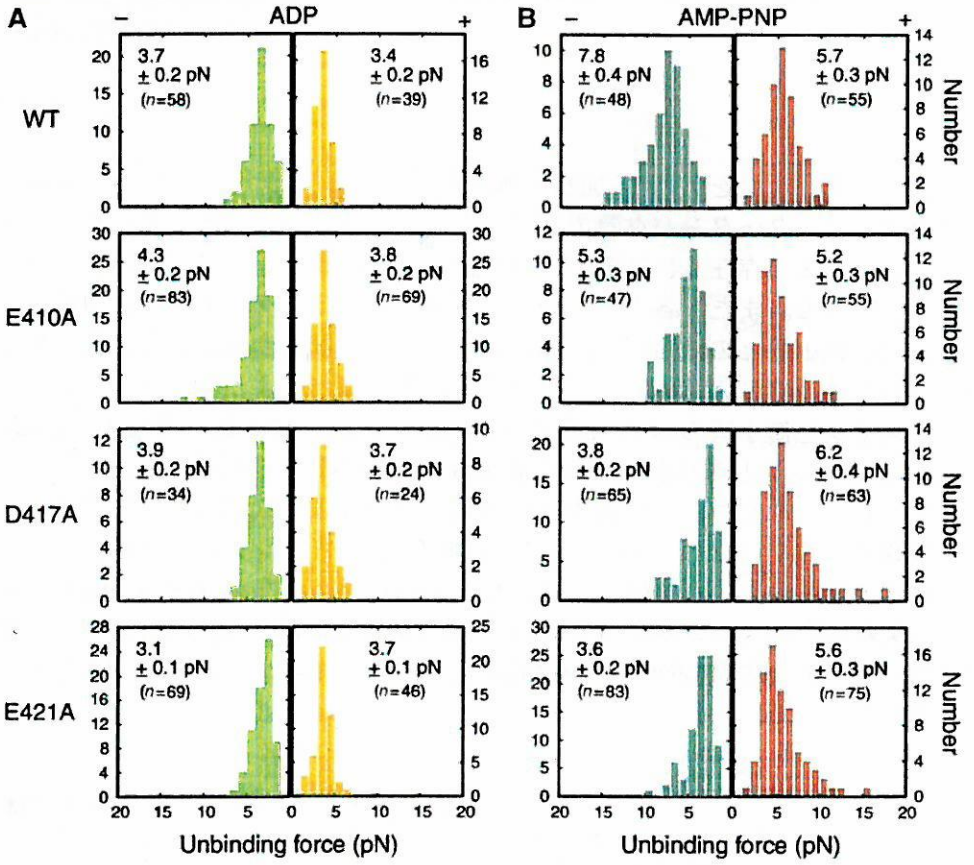

図２．破断力分布

キネシン１分子最大発生力（stall force）測定

顕微鏡下光ピンセット法を用いて、２つモーターードメインをもつネイティブキネシン 1 分子の、ATP 存在下における最大発生力（stall force）を測定した。すると、破断力測定(1 mM AMP-PNP 存在下)において WT と違いが見られた変異体（図２B）では、それに伴い stall force も減少することが明らかになった（図３左)。

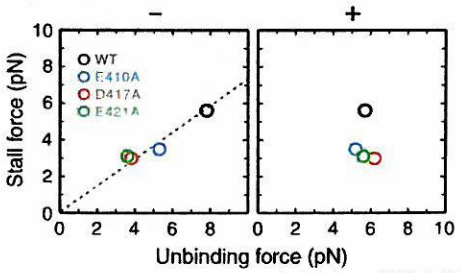

図３．Stall force と破断力の関係性

すなわち、stall force とマイナス端方向（stall force 測定時にキネシン分子に与えられる負荷の方向と同じ）における強結合状態破断力の間には相関性があり（図３)、キネシンの力発生には、キネシンと微小管の結合状態、特に強結合状態のマイナス端方向負荷に対する安定性が関与することが示唆された。

まとめと今後

遺伝子変異解析と *in vitro* 解析を融合することで、キネシン微小管強結合に重要な部位を特定できた。今後もこのような解析を行うことで他の相互作用に重要な部位を特定する予定である。

1分子高速力学測定によるプロセッシブ分子モーターミオシンVの機能解析と多機能顕微鏡システムの構築

上村 想太郎

【ミオシンVサブステップの高速運動解析】

ミオシンVはATPを加水分解しつつアクチンフィラメント上をプロセッシブに（長距離にわたって解離することなく）アクチンフィラメントのB端側へと運動するモータータンパク質である。現在までに、ミオシンVはアクチンフィラメントの右巻き長らせん半周期に相当する36nmステップを生じることが知られている。主として電子顕微鏡観察をもとに、ミオシンVの2つのモータードメインが交互に結合・解離を繰り返すことで36nmステップを生じると考えられているが、その詳しいメカニズムは分かっていない。そこで我々は従来までの時間分解能を上回るサンプリングレートでステップ運動を観測した。

<u>サブステップの検出</u>

その結果、36nm以下の連続サブステップを観測することができ（図1）、36nmステップが12nm＋24nmの2つのサブステップに分解されることがわかった。常に12nmステップの直後に24nmステップが生じることから、この順序でミオシンVの構造変化あるいはアクチンとの結合部位の変位があると考えられる。

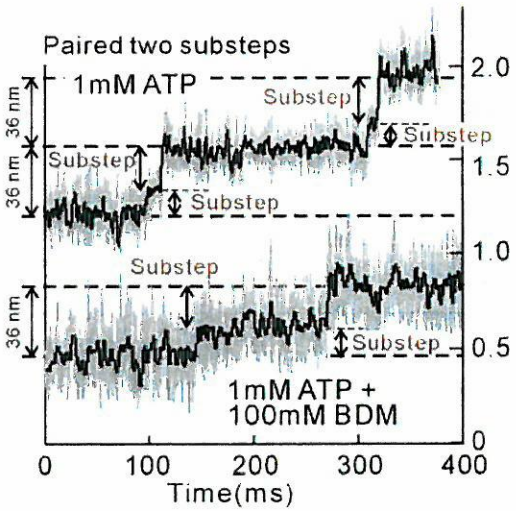

図1．ミオシンVの36nm以下の中間状態

<u>Dwell Time（滞在時間）解析による化学状態の特定</u>

こうした短い中間状態は筋弛緩剤として知られている（サブステップ）BDM(Butanedione manoxime)を加えると、その滞在時間を約7～8倍ほど伸ばすことがわかった。そこで化学（ヌクレオチド）状態を特定するために各状態でのDwell time解析をおこなった。12nmステップが生じた直後の中間状態のDwell timeのヒストグラムは1次反応を示す指数緩和型となり、ATP、ADP濃度依存性は見られなかった(図2a, b)。そこで当初は、＋BDMで滞在時間が伸びることと、筋収縮系においてBDMはリン酸解離を抑制していると言われていることから、リン酸の解離が次の24nmステップを引き起こすと考えられた。ところが、Yale大学のDe La Cruz研との協同研究の結果、驚くべきことにBDMはリン酸解離には影響せず、ADPの解離を抑制することが分った。

一方、24nmステップ後の主状態Dwell timeのヒストグラムは2次反応を示す山型分布となり(図2c,d)ATP濃度を低くするかADPを添加することにより滞在時間が伸びることから、ADP解離後ATPの結合により次の12nmステップを引き起こすと考えられた（図2）。

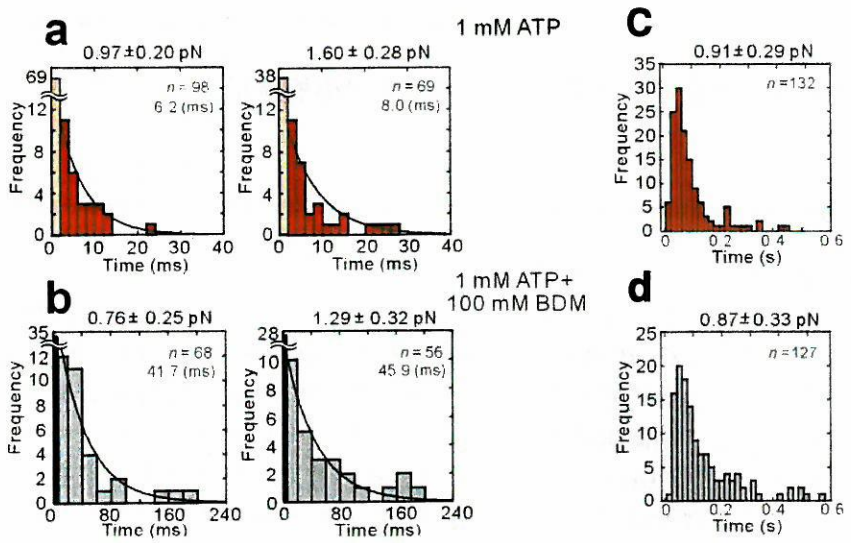

図２．各状態(1mM ATP for a,c, 1mM ATP+100mM BDM for b ,d)での Dwell time 分布。低負荷と高負荷の２つの負荷領域に分けて表示。　（左 a,b；中間状態、右 d,e；主状態）

運動モデルの構築

以上の結果をもとにミオシン V の歩行モデル（Hand-over-hand）を提案した（図３）。中間状態を見出し、さらにその化学（ヌクレオチド）状態を解析することにより、従来までの 36nm ステップのみの説明では困難であった詳細な歩行モデルを構築することが可能となった。

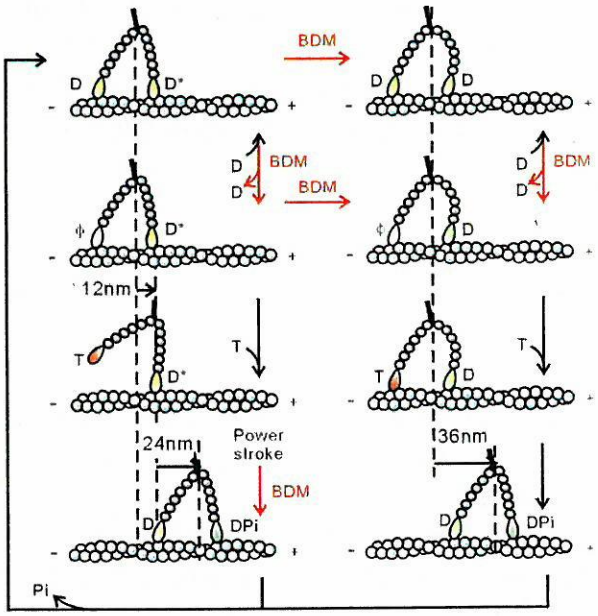

図３．ミオシン V 運動歩行モデル

（以上、東北大・樋口秀男研究室及び Yale 大・De La Cruz 研との共同実験）

【1 分子高速力学測定のための顕微鏡システムの構築】

我々の従来までの装置（Nikon・TMD）は、光ピンセット装置を組み込み、位相差像（ビーズ観察用）と蛍光像（蛍光色素観察用）を画面合成したものである。運動解析を行う際のビーズの変位はビデオフレームごとの輝度重心解析から求めることができる。ビデオ解析のため、ある程度の距離ビーズが移動してもビーズを追うことができるが、1 フレームは 1/30 秒のため、速い運動現象を追うことができないという欠点があった。

一方、速い現象を追うためにはビーズを四分割フォトダイオードへ投影すると時間分解能が飛躍的に伸びる。樋口秀男氏（東北大学・学際科学センター）の開発した赤色レーザーによる暗視野照明法（斜光照明による散乱光の集光）を用いた顕微鏡システムでは現在世界最高の時間分解能がある。四分割フォトダイオードに投影するビーズ像はなるべくバックノイズが少なく、光散乱強度の大きい方が時間・空間分解能が高くなる。そのため、できるだけ散乱光を集めるために高い N.A の

コンデンサレンズが必要（油浸）である。一方で直接光（一次の回折光）はバックノイズの原因となるのでコンデンサレンズの絞りを利用して調節する。ただし、ダイオードで観測できる範囲は狭く、運動経過を長距離に渡って観測することはできない。

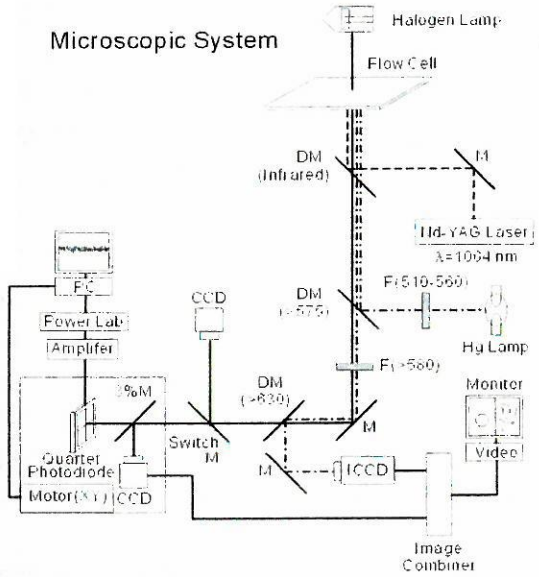

図４．顕微鏡システム（模式図）

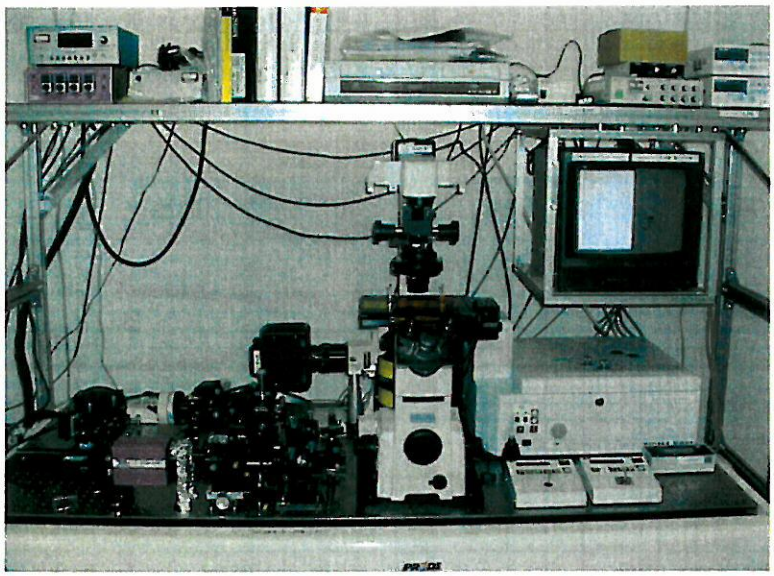

図５．顕微鏡システム
（全体写真）

そこで我々は、特別推進研究費によりこれら２つの顕微鏡システムの特徴を組み込んだハロゲン照明による四分割フォトダイオード顕微鏡システム（Nikon,TE-2000）を構築した（図４、５）。

本顕微鏡システムはシグマ光機（株）と共同で開発した。特徴は、1064nmYAG レーザーを用い、２ヶ所での光捕捉が可能な光ピンセットシステムを搭載し、蛍光像とハロゲン照明による四分割フォトダイオードによるビーズの高速変位検出の同時観測が可能な点である。さらに励起光源は水銀照明と緑色レーザー（波長；532nm）のどちらも使用可能であり、落射照明法と対物エバネッセント照明法を切り替えることも出来る。すなわち、1 分子蛍光イメージングと光ピンセットによる力学測定が可能である。また、細胞運動の観測を容易に可能にする微分干渉像も観測でき、細胞運動観測、１分子力学測定、そして１分子イメージングを同時に実現できる多機能顕微鏡システムである。

単一フィラメント顕微直視によるアクチン重合・脱重合ダイナミクスの研究

藤原 郁子

アクチンは、筋細胞に限らずあらゆる真核細胞に存在する普遍的なタンパク質であり、細胞骨格を構成する最も重要なタンパク質の一つである。従って、その重合・脱重合機構は、細胞のダイナミックな機能にとって本質的に重要な役目を担っている。細胞中においては、キャップタンパク質や切断タンパク質、枝化タンパク質、そして Ca^{2+}結合能をもつ様々な調節タンパク質系の働きによって、アクチンの重合・脱重合ダイナミクスは時間的・空間的に制御されている。従来、らせん構造を持つアクチンフィラメントの重合・脱重合ダイナミクスの研究は、溶液系を用いて行われてきた。その結果、重合過程は気・液凝縮過程に似て、核形成過程と成長過程からなることが明らかになった。本研究は、それを1分子レベルで観察し解析することで、アクチン重合・脱重合ダイナミクスの新しい側面を明らかにしようとしたものである。

直径7 nm のアクチンフィラメントを蛍光顕微鏡で可視化するために、アクチンの Cys374 に蛍光色素(tetramethyl-rhodamine-5-maleimide)を標識した。装置系として、ガラス面から約 150nm 程度しか励起光の届かないエバネッセント場照明法を用いた全反射蛍光顕微鏡装置を組み立てた。アクチンは臨界濃度以上で初めて重合するが、そのような高いタンパク質濃度では背景光が蛍光ノイズとなってしまい、従来の蛍光顕微鏡法ではフィラメントを直視することができない。この新しい照明法によって、フィラメント安定化因子ファロイジン（臨界濃度を殆どゼロにする）を添加しなくてもフィラメントの直視が可能となり、重合過程のみならず、脱重合過程をも捉えることが可能になった。

モノマーアクチンからフィラメントへの重合過程が、全反射蛍光顕微鏡装置を用いて実時間直視・解析した。30mM KCl, 2mM $MgCl_2$ 主体の塩溶液にモノマーアクチンを加えたところ、アクチンは単調に重合し、重合相を経て定常相に至った。顕微鏡下で観察を開始（塩添加後約6分）してから1分毎のアクチンフィラメントの長さ変化を約 30 分間観察した。アクチンの重合速度は、モノマーアクチン濃度が高くなるにつれて増加した。重合相において、アクチン濃度 0.3μM、0.5μM、0.7μM の平均の重合速度は、それぞれ 0.13±0.36μm/min、0.35±0.38μm/min、0.49±0.46μm/min であった。この値をもとに見積った重合速度定数は k^+=6.1/μM/s、脱重合速度定数は k^-=0.85/s、臨界濃度は Cc=0.14μM となり、溶液系の結果とよく一致した。特筆すべきことは、世界に先駆けて1本のアクチンフィラメント上でのトレッドミル過程を確認できたことである（図1参照）。トレッドミルとは、定常相で発生する現象である。定常相に達するとフィラメント全体(Total)では一定長を保っているが、B 端で重合し、P 端で脱重合するため、フィラメントは常に新しいアクチンに交換されるという現象である。これまでは、フィラメント安定化因子ファロイジンの影響によって脱重合過程を見ることが出来なかった。本研究では、10%ラベルという低い濃度で蛍光標識することにより、フィラメント上に出来る蛍光ムラを目印として利用し、目印からフィラメントの両端までの長さの変化を計測した。その結果、B 端では定常相においてもゆっくりと重合し続け(平均 0.069±0.037 μm/min)、P 端ではそれと見合う速度でゆっくりと脱重合(平均 −0.062±0.051 μm/min)していることが確認できた。さらに、アクチンフィラメントの長さは重合相においても定常相においても常に揺らいでいた。この長さ揺らぎが単なる計測誤差なのか、それ

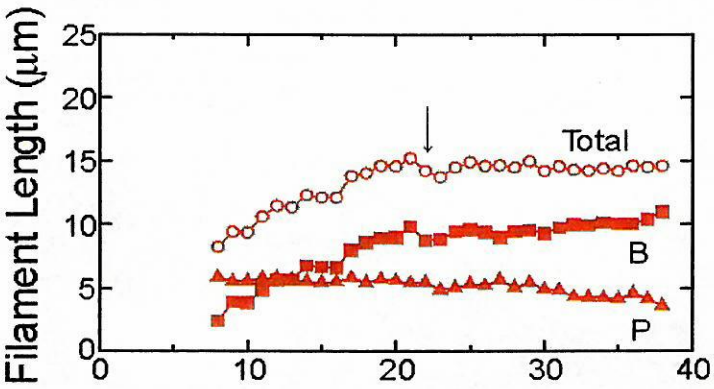

図1：塩添加（t=0）位のアクチンフィラメントの長さ変化の例

とも何らかのアクチン重合・脱重合ダイナミクスを表すものなのかを検討するため、計測の時間間隔τを変え、1分、2分、3分というそれぞれのτ（長さ変化の相関時間）におけるフィラメント長の変化を計測した。定常相におけるアクチンフィラメントの長さ変化の平均は、τに関わらずゼロだったが、長さ変化の大きさを示す長さ揺らぎ（S.D.）はτとともに増加した（図2参照）。言いかえれば、アクチンフィラメントの総量は変化しないが、1 本のフィラメントの長さは常に変化していることを示す。$(S.D.)^2$ をτに対してプロットしたところ、直線近似することができた。このことは、アクチンフィラメントの長さ揺らぎがランダムな拡散過程に従っていることを示している。こうして、近似直線の傾きからモノマーアクチン1個の重合速度定数・脱重合速度定数を見積もったところ、重合相から得られた値よりも約 40 倍程度大きかった。このことは、平均約6個のアクチンサブユニットが、まとまって重合・脱重合に関与しているとすると理解できる。以上より、定常相では、平均 6 個のアクチンサブユニットが重合・脱重合過程に関与してトレッドミルが生じていること、すなわち、微小管と比べて穏やかではあるが、動的不安定性が生じていることが明らかになった。

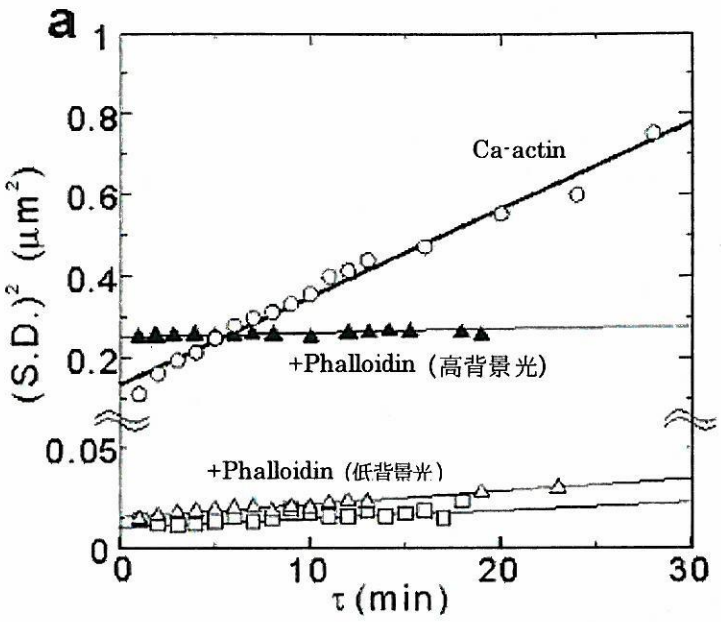

図2：定常相における長さゆらぎの時間相関。Ca-actin（○）。Phalloidin 添加によって長さ変化を抑制したもの。

A帯滑り運動系－Bio-nanomuscle－から見たクロスブリッジの動作特性と筋収縮機構

鈴木　団

＜背景と目的＞

除膜した骨格筋・心筋収縮モデルにおける自励振動現象が本研究室で発見されて以来、溶液条件の決定、張力計測などを通じて、そのメカニズム解明が試みられてきた。しかし実験系は筋線維・筋原線維を利用するものであり、筋原線維より下の階層においては検討されてこなかった。

本研究の目的は、ある溶液条件下の分子モーター集合体で起こる自励振動現象を通して、分子間協調の起こる分子メカニズムを解明することである。その方法として、我々が開発してきたA帯滑り運動系を利用した（図1）。

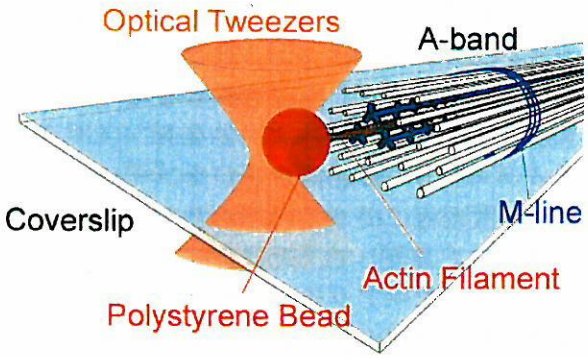

図1　A帯滑り運動系の模式図

筋収縮･制御機構の解明を目指して開発してきたこのA帯滑り運動系は、筋原線維から直接調製される分子モーター集合体（A帯）と、光ピンセット技術・蛍光観察技術から操作・計測される単一アクチンフィラメントにより構成される。これは、分子モーターがランダムに配置された *in vitro* 滑り運動系と、筋線維・筋原線維系との中間に位置づけられるものである。また、発生張力、収縮特性といった点で二つの系の間を取り持つ系であることが、これまでの実験結果から示されている。

＜研究方法＞

まず筋線維・筋原線維とで見られる自励振動現象の発生メカニズムを解明することを試みた。ここでは、筋収縮系の要素を一つ一つ再構成していく中で、各段階で張力振動がどのように発現するかを、台地状に加工したガラスを用いた *in vitro* 滑り運動系（図2）と、近年我々の開発したA帯滑り運動系（Bio-nanomuscle，図1, 3）を利用して調べた。

台地状加工ガラスを用いた *in vitro* 滑り運動系で調べたところ（図4A)、発生張力が不安定で一見振動しているようには見えるものの、周期的な振動ではなかった。また、筋収縮系で見られる自励振動現象特有のノコギリ波状の波形（ゆっくりした収縮と、素早い弛緩）も見られなかった。

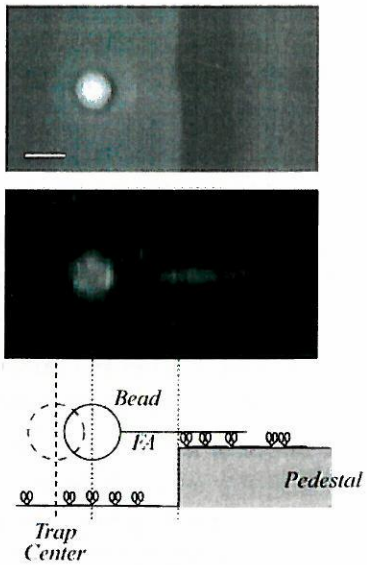

図2　台地状加工ガラスを用いた *in vitro* 滑り運動系。上から順に位相差像、蛍光像、模式図。

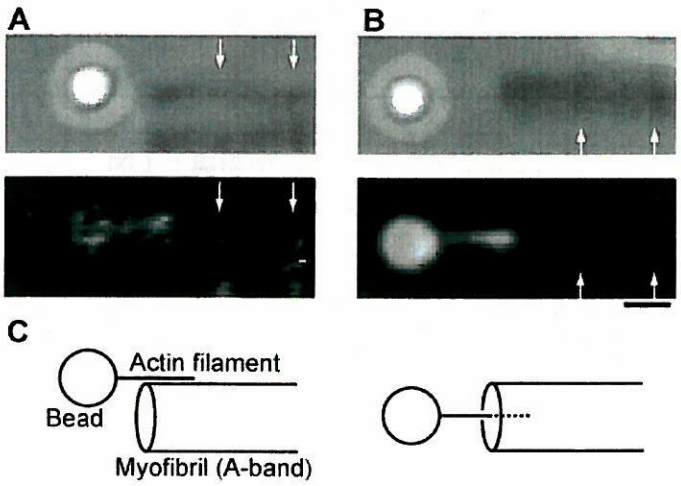

図3　A帯滑り運動系の位相差像(上)と蛍光像(下)。(A)アクチンフィラメントがA帯の表面と相互作用する場合。(B) アクチンフィラメントがA帯の端面と相互作用する場合。(C) ビーズ付きアクチンフィラメントとA帯との相対位置を表す模式図で、(A)及び(B)に対応。

さらにトロポニン・トロポミオシン複合体を加えて筋肉の細いフィラメントを再構成したときも、波形は同様であった(図4B)。次にA帯滑り運動系でアクチンフィラメントのみを用いたところ（図5 A, B)、ノコギリ波状の波形を持った張力振動が観察された。しかしその振動周期は一定ではなく、広くばらついていた。また、*in vitro*滑り運動系と同様にA帯滑り運動系でも、筋肉で存在する Ca2+感受性を回復させ発生張力を調べた（図5C)。すると、この再構成した細いフィラメントを用いたナノ筋収縮系で、筋線維・筋原線維で起こる自励振動現象に類似した振動が起こることが確かめられた。以上の研究の予備的な成果の一部は、2006 年に *Adv. Exp. Med. Biol.*誌へ発表した。

次に張力発生しているときのビーズの動きをより詳細に検討するため、これまでは秒速 30 フレームであったナノ筋収縮系に高速カメラを導入し、秒速 3000 フレームで画像を取得できるようにした。すると、時間分解能を上げても張力揺らぎの幅がほとんど変わらないことが分かった。また溶液中の ATP 濃度を下げ、力発生するミオシン分子の数を減らしたところ、１０μM までは張力揺らぎが観察されたものの、それ以下ではアクチンフィラメントがA帯に向かって連続的に引き込まれるようになった。さらに滞在しやすい点が周期的に存在することを示唆する結果を得た。それが何に由来するものなのかを明らかにすることが、今後の検討課題である。

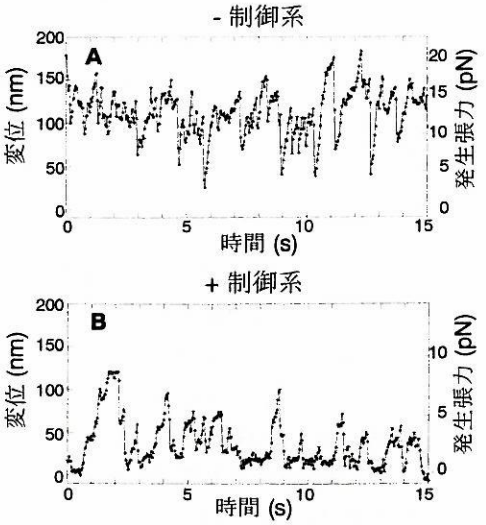

図 4 SPOC 条件における *in vitro* 滑り運動系での張力発生の様子。(A)アクチンフィラメントのみ。(B)制御系を再構成したアクチンフィラメント。

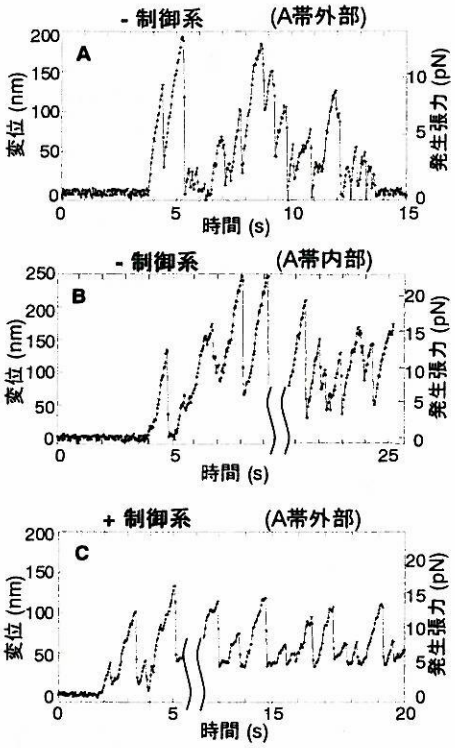

図 5 SPOC 条件における A 帯滑り運動系での張力発生。(A, B）アクチンフィラメントのみ。(C）制御系を再構成したアクチンフィラメント。

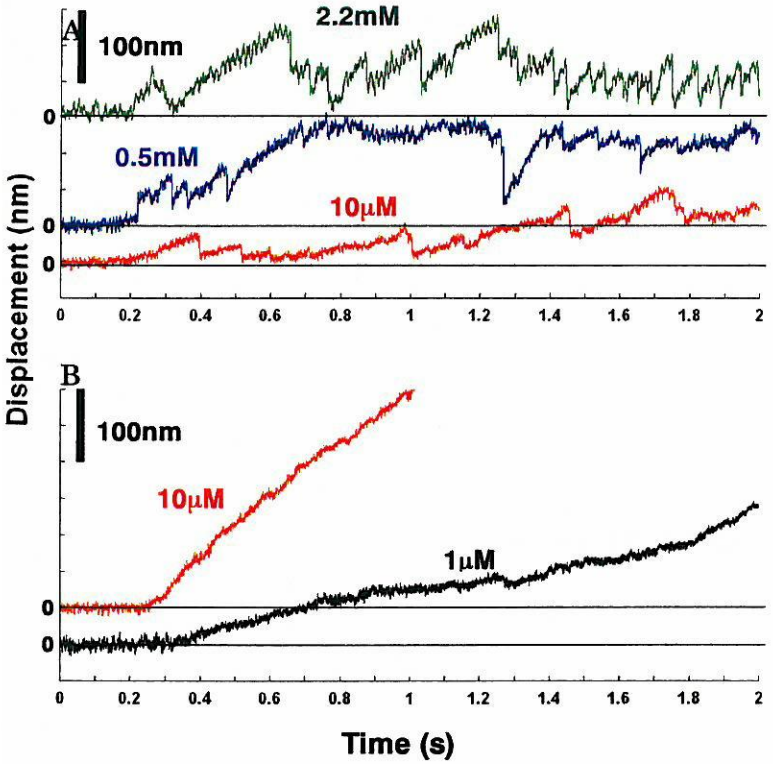

図 6　各 ATP 濃度におけるビーズの変位
（A）[ATP]＞10 μM（High [ATP]）のときのビーズ変位。緑線は ATP 濃度が 2.2 mM、光ピンセットのバネ定数が 0.07 pN/nm のとき。青線は 0.5 mM ATP、0.17 pN/nm のとき。赤線は 10 μM ATP、0.14 pN/nm のとき。　（B）[ATP]＜10 μM（Low [ATP]）のときのビーズ変位。赤線は 10 μM ATP、0.14 pN/nm のとき。黒線は 1 μM ATP、0.12 pN/nm のとき。

筋収縮系自励振動（SPOC）を発現する分子集合体メカニズムの解明

島本 勇太・前島 永志・河野 史明・河井 聖太郎

背景・目的

生体システムにおける高次機能は、一分子では確率的に機能するタンパク質分子機械が、集合体となり巧みに相互作用することによって生み出されている。確率的素子であるタンパク質分子によって構築されたシステムがうまく機能する背景には、何らかの情報を媒介した、分子間、ユニット間協調による自律的な状態制御のしくみが存在することが期待される。外部環境に柔軟に適応し、また自律的に状態制御する生体システムの仕組み、”生物らしさ”の物理的基盤を理解するためには、タンパク質一分子レベルでの計測、細胞レベルでの計測に加え、生体システムが、どのようにして単一分子の確率的な機能をまとめあげ、システムとしての機能を獲得するかという、生体システムの制御の分子基盤を明らかにすることが必要である。

そこで本研究では、分子機械集合体の典型である筋収縮システムを取り上げる。このシステムの生み出す動的秩序形成の顕著な表れである自励振動現象（SPOC：中間活性化条件で見られる自励振動現象、ゆっくりとした短縮とすばやい伸長を秒オーダーの周期で安定に繰り返す；図 1-1, 1-2）のしくみを解明することを通して、分子集合体の自律的な状態制御と、それによる動的秩序発現のしくみを解明することを目的とする。

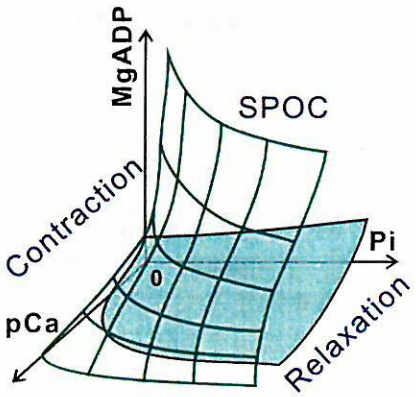

図 1-1 SPOC の状態相図　弛緩と収縮の中間条件下（ATP 存在下）において SPOC（自励振動）が発現する。

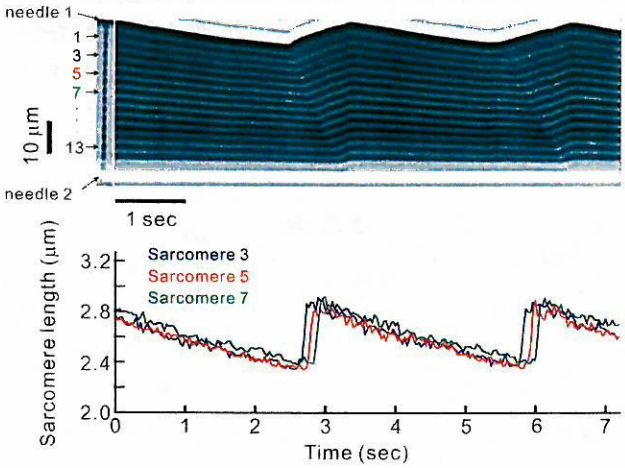

図 1-2 SPOC のカイモグラフ（上）と隣接する３つのサルコメア長波形(下)　ゆっくりとした短縮相と速い伸長相の安定な振動を繰り返す。また、伸長相は筋原線維の長軸方向へと伝播する。

１．中間活性化条件における力発生制御の基本原理を調べる

SPOC における自律的な力発生制御のしくみを明らかにするために、中間活性化条件において、筋収縮システムの最も基本的な性質の一つである「サルコメア長－発生力関係」を調べた。その結果、中間活性化条件における力発生は、サルコメア構造のナノメートルオーダーでの空間変調によって制御されていることがわかった。

【実験装置・方法】

筋原線維を用いた顕微力学計測装置を構築し、単一サルコメアレベルで詳細な力学計測を行った（図 2-1）。具体的には、位相差顕微鏡下で、一対のガラス微小針（直径 5-10 μm）によって筋原線

維（直径 1 μm, 長さ 20-50 μm）を保持し、針の屈曲変位から発生力を、位相差像からサルコメア長を計測した。

1．溶液交換系

2本の層流による溶液のスイッチングによって、高速（~30 msec）で溶液交換できる系を構築した。これにより、試料の劣化を抑え、同一試料での繰り返し計測を実現した（図 2-2)。また、力発生に伴うヌクレオチド結合・解離のキネティクスが追えるようになった。

2．発生力・サルコメア長計測系（図 2-3）

発生張力の計測は、4分割フォトダイオードを用いて、高時間分解能（~10 msec）で行った。一方、サルコメア長は、位相差像から各サルコメア長の時間変化を 2 %の精度で追った。

3．溶液条件

SPOC 条件(ATP, ADP, Pi 共存、Ca^{2+}非存在下)においては、サルコメアが異なる位相で自発的に振動しているために、各サルコメア長ごとの力発生の性質を定量化することが非常に困難である。そこで、ADP 収縮条件（1mM MgATP, 4-20mM MgADP, 2mM free Mg^{2+}, 4mM EGTA, 20mM MOPS (pH7.0), I.S. 180mM (KCl)）を用いて、力発生の性質を調べた。この条件は SPOC 条件から Pi を除去した条件であり、自発的な振動は起こりにくい。但し、ミオシン ADP 複合体による力発生の制御という点では SPOC と共通である。この SPOC と同じ活性化条件で、振動の各段階での力学的性質を詳細に計測した。

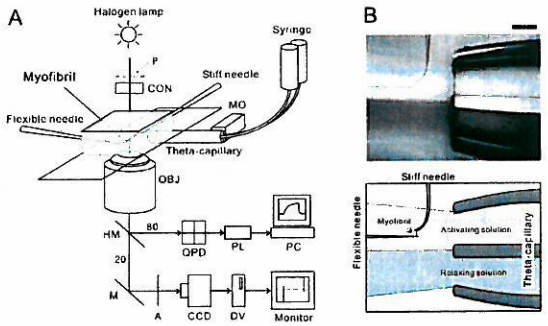

図 2-1　筋原線維の力学計測実験装置　位相差顕微鏡観察で単一サルコメア長を、分割フォトダイオードにより発生力をそれぞれ計測できる。また層流溶液交換系により、高速で収縮・弛緩の制御ができる。

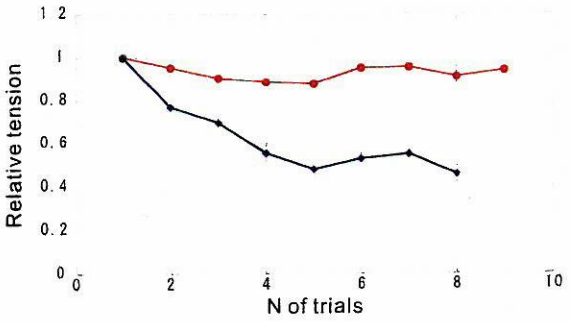

図 2-2　従来の液交換系（青）と層流による高速液交換系（赤）における繰り返し活性化時の発生力再現性。高速液交換により、同一試料での繰返し計測を実現した。

【結果と考察】

筋収縮システムの最大活性化条件においては、その発生力はサルコメア長に反比例、つまりアクチン・ミオシンフィラメントのオーバーラップ長に比例する。このことから、ミオシンは独立な力発生器であると考えられている。しかし、ADP 収縮の中間活性化条件においては、サルコメア長が長くなり、相互作用可能な分子モーター数が減少するほど大きな力発生が起こることがわかった（図 2-4)。これは Ca^{2+}による通常の収縮条件のものとは正反対の性質であり、中間活性化条件において、アクトミオシン分子モーター集合体が協同的に力発生の制御を行っていることを示すものである。さらに、高分子 dextran を用いた実験により、サルコメア構造のナノメートル程度の変調が、サルコメア活性に大きく寄与することがわかった（図 2-5)。以上の結果は、サルコメアの自律的な活性制御において、細いフィラメント上でのアロステリックな制御に加え、ミクロな構造体レベルでの空間変調が、システムの活性化状態を自律的に制御するための重要な因子であることを示唆するものである。

筋収縮系における自励振動現象の数理モデル

大瀧 昌子

[研究背景・目的]

サルコメアは、筋肉を構成している最小単位であるタンパク質の集合体である（図１）。そのサルコメアの集合体である筋原繊維は、Ca^{2+}濃度に依存して、収縮状態か弛緩状態かのいずれかの状態をとることが知られている。サルコメアに1μM以上のCa^{2+}が放出されると、アクチン（レールタンパク）とミオシン（分子モーター）が互いに滑り込み、サルコメアが直列に連結した筋原線維が収縮する。ところが、SPontaneous Oscillatory Contraction (SPOC)と呼ばれる、収縮と弛緩の２状態を行き来する、第３の状態が存在することが発見された（ S. Ishiwata and K.Yasuda, Phase Transitions **45**, 105-136 (1993)、石渡信一, 科学 **68**, 110-113 (1998))。SPOCは、サルコメアの長さが、Ca^{2+}濃度の変化なしに、収縮と弛緩を自発的に繰り返す自励振動現象である。骨格筋、心筋共に、ATPにADPとPiが共存すると、特にCa^{2+}非存在下においても、SPOCが発現することが知られている。Ca^{2+}濃度変化なくして、収縮と弛緩を繰り返すことは、通常の筋収縮機構では説明し難い。また、通常の筋収縮機構においても、分子モーター集団の協同的振舞いについては、未解明の部分が残されているのが現状である。そこで、本研究では、数理モデルの立場からSPOC現象のモデルを構築し、分子モーター集団の協同性についての解明を目指す。

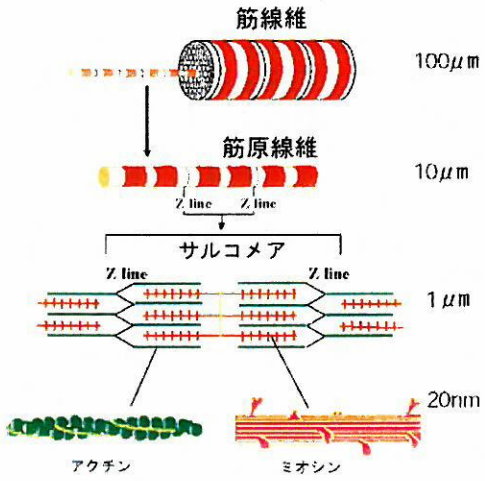

図1. 筋肉の階層構造。

[研究方法と結果]

筋フィラメントは、精緻な空間構造を保っているため、これらの空間構造に起因する何らかの協同性が、分子モーター間に存在することが期待される。そこでSPOC現象をモデル化するにあたって、サルコメア内のアクチンとミオシンの相互作用領域（重なり部分）の変化に着目した。ここでは、半分の大きさのサルコメアを考え、その模式図を図２に示す。図２において、緑の棒はアクチン、赤の棒の集まりはミオシンフィラメントを表す。アクチンは、バネ係数ωで、青で表されているZ線と繋がっている。このバネ要素は、注目しているサルコメアは、他のサルコメとZ線を通して接続し、全体として筋原線維という構造体をなしていることに由来する復元力を表している。図中のxは、アクチンとミオシンフィラメントが滑り込んだ長さを示している。x＋Lは相互作用領域の大きさを表す。但し、Lは定数であり、相互作用領域の最小の大きさを表す。つまり、相互作用領域はこれ以下にはならないことを仮定している。また、図２の黄色の領域で囲まれた式は、半サルコメアが従う運動方程式である。このときγは、分子摩擦に由来する摩擦係数を表す。モデルでは、ミオシン集団によってどのような力発生が行われ、振動が起こるのか、ということが問題である。そこで、一分子実験結果から類推

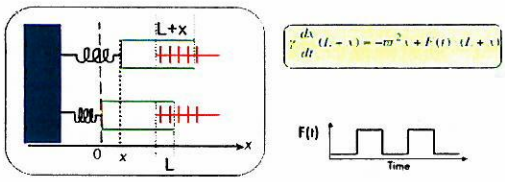

図2. 半サルコメアの模式図と運動方程式、力発生F(t)を矩形波で仮定。

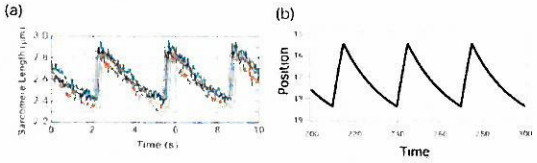

図3. (a)SPOCのノコギリ波型振動波形（実験）と(b)モデルの結果

し、ミオシン一分子による力発生はデルタ関数的である考え、何らかの協同性によりミオシンの力発生が連続的に起こるとし、半サルコメア内のミオシン集団が出す力の関数 F(t)は、矩形波的である仮定した。図３に、SPOC に現れるサルコメアの振動波形とモデルの結果を示す。図３に示したように、このモデルは、サルコメア長の速い伸長と遅い収縮から成る、SPOC の特徴であるノコギリ波型の振動波形を再現することに成功した。さらに、運動方程式に含まれている時間変化するミオシンとアクチンの相互作用領域が、ノコギリ波型の波形を出す事に大きく関与していることが結果を解析することによってわかった。

次に、これまで仮定していた、力発生の協同性を化学反応方程式から導きだすモデルを考えた（図４(a)）。モデルは、主要ないくつかの ATP 加水分解過程を考慮し、それらの化学反応式を書き下したもの（水色で囲まれた部分）と、半サルコメアの運動方程式（黄色で囲まれた部分）からなる。このモデルでは、先のモデルにおいて、最初から矩形波的関数であると仮定をしていた力発生関数 F(t)が、水色の反応方程式の結果から導きだされることになる。相互作用領域の時間変化を化学反応式、運動方程式の双方に考慮すると、図４(b)左に示されているように、ノコギリ波型の振動波形を得た。また、化学反応方程式において、相互作用領域の時間変化を考慮しないと、図４(b)右のように振動解を得ることはできないことがわかった。つまり、SPOC の振動を生み出すには、相互作用領域の時間変化が大事であることがわかった。

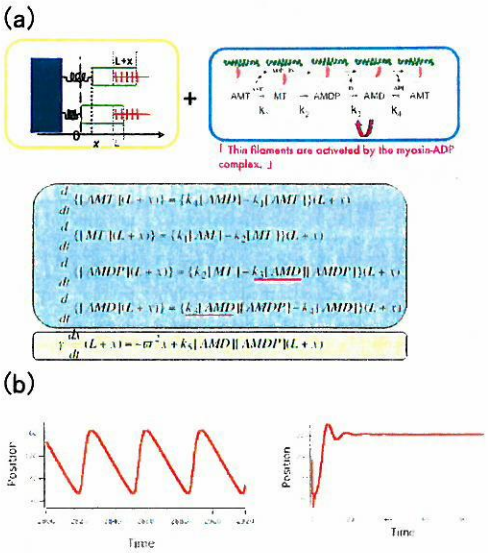

図4. (a)モデル式と(b)得られた振動波形(左：相互作用領域の時間変化を考慮した場合。 右：相互作用領域の時間変化を考慮しな

これら二つのモデルにより、時間変化する相互作用領域が作り出す協同性の結果として、SPOC が現れることが示唆することができた。SPOC の振動は、化学反応と運動の相互フィードバックが、相互作用領域が変動を通して、行われていることに起因しているといえる。特に、二つ目の反応方程式と運動方程式からなるモデルでは、外部の状態（このモデルでは相互作用領域の大きさで表される）によって励起される内部の状態（ミオシン集団が出す力）が、さらに外部の状態を変えていくことを繰り返すによって、振動という一つの安定した状態が生み出していることを示している。

[今後の展望]

提出したモデルで重要な点は、相互作用領域の時間変化を考慮した点である。また、今回のモデル化を通して、「時間変化する化学反応場による自己組織化」という新しいメカノケミカルカップリングモデルの概念を数理モデルの分野に導入できたといえる。しかしながら、まだ SPOC の全てが明らかになったわけではない。特に、分子モーター集団の協同性の具体的な描像には触れていないことや、SPOC の溶液条件と振動との関係を明らかにするミクロなメカニズムについてなど、まだモデルに取り込むべきことは多い。これら課題を念頭におきながら、さらなる SPOC のモデル化を試みたいと考えている。具体的には、サルコメアの格子間隔の変化が相互作用領域の変化とカップリングしていることを示す実験結果を受けて、“サルコメアの持つ空間構造”と“時間変化する化学反応場”の関係について明らかにしていくモデルの構築を行う予定である。サルコメアの格子間隔の変化は、具体的にミクロな分子モーターの力発生の確率に寄与していると考えられることから、より具体的な協同性にせまれる可能性があると思われる。また、「時間変化する化学反応場による自己組織化」を “形（空間構造）”と“反応場”とのカップリングによって生まれる、“機能”という概念に発展させ、生物をターゲットとした数理モデルの新しい研究分野も同時に提起していきたい。

心筋収縮系における自励振動現象　－心拍数との相関－

佐々木　大輔

（研究の背景と目的）

心臓における拍動のリズムは、洞房結節から伝わる規則的な活動電位によって制御されており、心筋は、この電気的シグナルに応じた細胞内 Ca^{2+}濃度の上がり下がりに追随して収縮、弛緩を繰り返す、ということはよく知られた事実である。一方、心筋の横紋構造を形成する筋節（サルコメア）は、中間活性化状態においては、定常的溶媒条件下でも自発的に収縮、伸展を繰り返す振動状態（SPOC）をとるが、この事実は一般にはほとんど認知されておらず、ましてやその生理的意義などまったく分かっていない。本研究においては、SPOC の振動特性と心拍との関係に焦点をあて、SPOC の生理的意義の解明を目的としている。SPOC が発生する条件は、一般的な収縮条件における Ca^{2+}濃度を調節することによって生じる Ca-SPOC と、Ca^{2+}非存在下において、ATP 及びその加水分解産物である ADP、Pi が共存することによって生じる ADP-SPOC の２種類に大別される。Ca-SPOC 条件は生理的であり、ADP-SPOC 条件は病理的であるとみなせるが、一定の ATP 濃度下で Ca^{2+}、ADP、Pi 濃度を変数とした３次元相図中に SPOC の発生する領域を表すと、両 SPOC 条件は、収縮及び弛緩領域に挟まれた１つの領域中に含まれる。我々は、心拍数の異なる様々な動物種（ラット、ウサギ、イヌ、ブタ、ウシ）から調製した除膜心筋線維試料を用い、(1) ADP-SPOC、及び (2) Ca-SPOC における筋節長振動特性と、各動物種の安静時心拍数との関係について調べた。

（1）ADP-SPOC と心拍数との相関

本研究は、東京慈恵会医科大学第２生理、福田紀男、栗原敏、及び東北大学先進医工学、藤田英明（平成 14 年 11 月まで早稲田大学学振特別研究員）との共同研究として行われ、先日原著論文として Sasaki, D. *et al.*, 2005. *J. Muscle Res. Cell Motil.* July 1, E. pub ahead of print に掲載された。

（実験方法）

実験には、51 %グリセリン溶液中にて保存したラット、ウサギ、イヌ、ブタ、ウシの左室乳頭筋を用いた。これらグリセリン処理筋の断片を、0 ℃以下に冷やした 51 %グリセリン溶液中で、実体顕微鏡とピンセットを用いて線維方向に沿って注意深く裂いていき、幅 100 μm 程度の細さの心筋線維試料を調製した。これらの試料を 1 %の TritonX-100 を含む硬直溶液に 20～30 分浸して除膜した。その後、蛍光色素 Alexa488 phalloidin（Molecular Probes, Inc）（0.33 μM）を含む弛緩溶液中に試料を浸し（3 hr）、心筋線維中の細いフィラメントを選択的に蛍光ラベルした。このようにして調製した除膜心筋線維試料を、ガラス底シャーレの底に長さ約 1mm になるように両面テープで両端を固定して、ADP-SPOC（41 mM KCl, 14.2 mM $MgCl_2$, 2.2 mM ATP, 16.4 mM ADP, 10mM Pi, 0.1 mM AP_5A, 10 mM MOPS (pH 7.0), 2.0 mM EGTA, 室温）を誘起し、共焦点蛍光顕微鏡を用いてその筋節長振動を観察・記録した（図 1-1）。こうして得られた共焦点蛍光画像から、各動物種の心筋線維における筋節長振動波形を詳細に解析した（図 1-2）。　また、各動物種の左心室からミオシンをそれぞれ精製し、これを用いて *in vitro* motility assay を行い、心筋ミオシンの運動活性を調べた。以上の実験結果をもとに、心筋 ADP-SPOC の筋節長振動特性、心筋ミオシンの運動活性、及び動物種の安静時心拍数との関係について明らかにした。

（結果と考察）

SPOC 状態の心筋線維内部における各筋節は、ゆっくりとした収縮相とすばやい伸長相からなる鋸歯状の波形をもって周期的に振動し、またこの伸長相は、隣接する筋節へ等速に伝播していく（SPOC 波；図 1-2）。これらの特徴は動物種の違いによらず SPOC に共通の性質であった。また、

SPOC における筋節長振動周期、及び SPOC 波の伝播速度は、共に各動物の安静時心拍数と強い相関を持つことが明らかとなった（図 1-3；各動物の安静時心拍数は、Biology Data Book, 1972-1974 より引用）。心筋収縮系にとっての固有振動に相当する SPOC の振動特性が、心拍、すなわち洞房結節からの電気的シグナルによって与えられる強制振動に対して相関を持つという本結果は、心臓の拍動過程において、心筋収縮系は単なる張力発生装置でしかないという従来の見解に一石を投じるものである。

また、この相関を分子レベルで規定する因子を明らかにするため、精製した心筋ミオシンを用いて *in vitro* motility assay を行ったところ、ミオシンの運動活性を表すアクチンの滑り速度も各動物の安静時心拍数と相関を持つことが明らかとなった。しかしながら、SPOC の筋節長振動における筋節収縮速度とアクチン滑り速度は比例関係にはなく、筋節収縮速度のアクチン滑り速度に対する比は、概して心拍の速い動物種ほど大きくなる傾向にあった。この結果は、筋節収縮速度がミオシンの運動活性に加え、その他の要素によって調節を受けていることを示している。

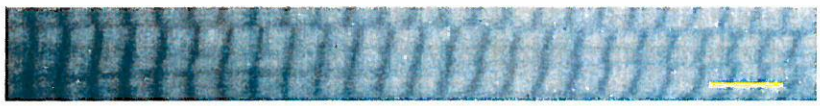

図 1-1　ブタ心筋線維の共焦点蛍光像（スケールバー：5 μm）

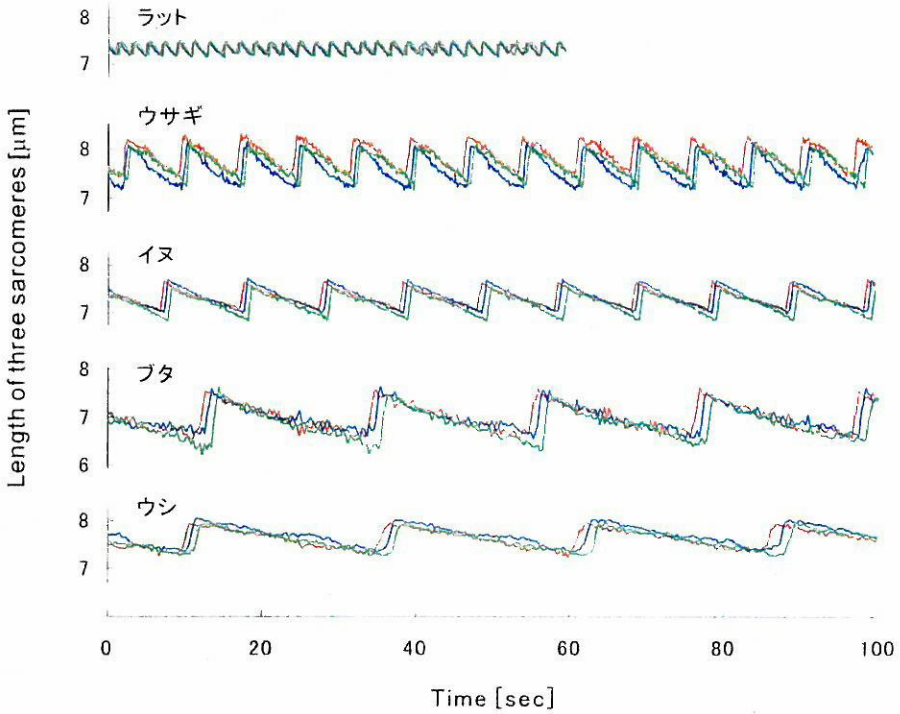

図 1-2　各動物種の心筋 SPOC における筋節長振動波形

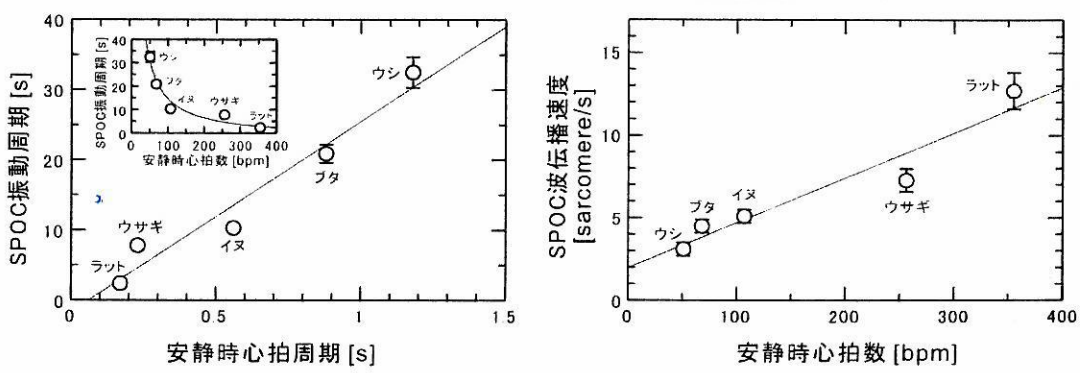

図 1-3　各動物種における安静時心拍と心筋 SPOC 振動特性との関係

(2) Ca-SPOC と心拍数との相関

ADP-SPOC と Ca-SPOC は同様の分子状態に起因するものと予測されるが、SPOC の生理的意義についての知見を得るためには、生理的収縮条件下において生じる Ca-SPOC について研究することが不可欠である。本研究では、各動物種（ラット、ウサギ、ブタ、ウシ）から調製した除膜心筋線維において Ca-SPOC が生じる Ca^{2+}濃度領域を明らかにし、またその筋節振動特性と安静時心拍数との関係について明らかにすることを目的としている。なお、本研究は現在進行中のものであり、具体的なデータはすべて未発表であるが、すでに主要な実験結果はまとまっており、現在 *PNAS* に投稿すべく原著論文を準備中である。本研究は、東京慈恵会医科大学第 2 生理、福田紀男との共同研究である。

（実験方法）

50 %グリセリン溶液中にて保存したラット、ウサギ、ブタ、ウシの除膜心筋切片を、0 ℃以下に冷やした 50 %グリセリン溶液中で、実体顕微鏡とピンセットを用いて線維方向に沿って注意深く裂いていき、幅 100～200 μm、長さ～2 mm の心筋線維試料を調製し、実験に用いた。試料の両端をマニピュレーターに接続された 2 本の針先に固定し、これを倒立顕微鏡上にセットした（図 2-1）。顕微鏡像を見つつ、筋節長が 2.3～2.4 μm になるようにマニピュレーターを調節した（図 2-2）。さまざまな pCa（$-\log[Ca^{2+}]$）に調節した収縮溶液を試料に流し込み、Ca-SPOC が生じるか否かを確認し、また Ca-SPOC が生じた場合はその筋節長振動周期を解析した。

（結果と考察）

実験に用いたすべての動物種の心筋線維試料において、生理的収縮条件を含むと考えられる幅広い pCa 範囲において Ca-SPOC が生じることが明らかになった。またその筋節長振動周期は、各動物種の安静時心拍の周期にほぼ対応するものであった。この結果は、心筋拍動における Ca-SPOC の関与を強く示唆する。心臓の拍動メカニズムにおける新たな概念を打ち立てるべく、引き続き研究を進めていきたい。

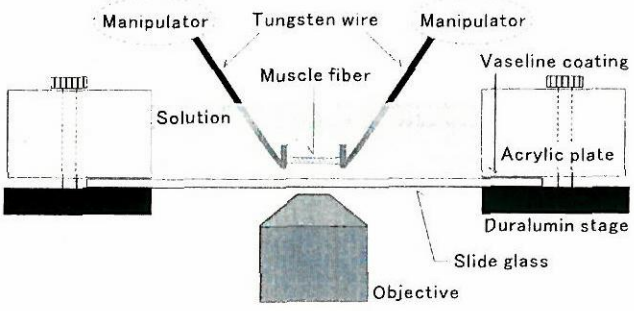

図 2-1　実験装置の模式図

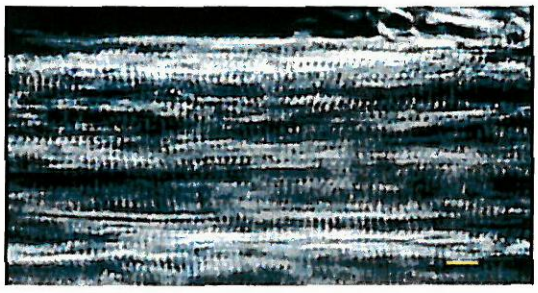

図 2-2　ブタ心筋線維の位相差顕微鏡像
（スケールバー：10 μm）

ミクロ熱励起・温度計測法による新しい細胞機能解析法の開発と応用

鈴木　団

＜研究の背景＞

生きた単一細胞の膜電位、細胞内 Ca^{2+}濃度といったパラメータは、ミリ秒オーダーで制御あるいは検出することができる。しかしながら、正確な制御や局所的な測定の難しい「温度」の場合は事情が異なる。通常、加熱・冷却や温度測定は、実験装置全体の温度を制御しつつ試料の近くに置いた「小さな」温度計で行われるため、どうしても時間・空間分解能には限界がある。

温度制御の場合には、例えば実験試料にランプやレーザーといった強力な光源からの照射光をパルス的に当てることで、急速な温度上昇を実現できる。しかし、暖められた試料の体積にもよるが、冷却速度はずっと遅い。この問題は、温度パルスを任意のμm 領域に制限しつつ、実験試料周辺、実験装置を温度一定にしておけば解決できる。急速な温度上昇と下降を局所的に起こすため、カバーガラスに固着した金属粉や金属薄膜に波長約 1μm の赤外レーザーを照射する方法が本研究室で開発された。この方法を用いると、温度パルスを単一細胞程度の局所的な範囲に限定して起こすことができる。

一方、温度を単一細胞と同程度の体積で測定することは簡単ではない。熱電対、NMR、FTIR、ラマン分光、放射分析法、焦電気膜、などといった方法はどれも温度検出に対して非常に感受性が高い。しかし、単一細胞の温度測定に用いるには技術的に様々な問題がある。そこで、温度感受性の蛍光色素を細胞内に流し込む方法が提案され、単一細胞における熱発生、局所的温度勾配の発生が報告されてきている。しかしこの魅力的な方法は、色素の環境変化（pH など）に対する感受性が高すぎるゆえに、正確な温度測定を行うには大きな問題があった。さらに細胞膜上で色素が不均一に分布してしまうことや退色が早いことは、温度と蛍光強度とのキャリブレーションを非常に困難にしていた。

＜研究目的＞

もし温度を局所パラメータとして扱えるようになれば、単一細胞レベルでの機能研究に新しい視点を与えることができる。例えばプロトンや Ca^{2+}濃度勾配の乱れに由来するような、生細胞内部での熱発生過程の存在が想定されているが、これまで充分な研究ができなかった。なぜなら単一細胞内部における化学反応プロセスの熱力学を *in vitro* 系で研究するとき、単一細胞レベルで言う「局所性」を備えることが、熱源・温度計の双方に求められるからである。そこで、本研究の目的を、ミクロ領域へ高速で繰り返し温度パルスを与え、かつ正確に温度測定できる手法を開発すること、そしてこの新手法を、細胞生物学に新次元を導入する手法として確立することとした。

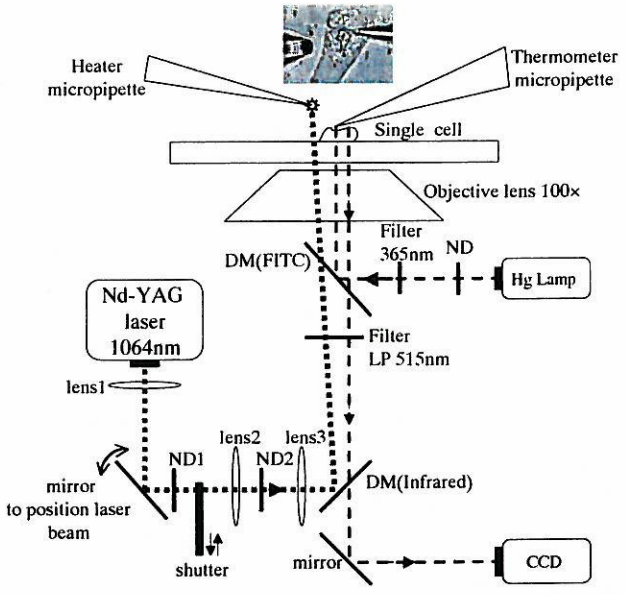

図 1　ミクロ領域温度パルス・温度センサーの装置図。

＜本研究の特色・独創的な点＞

マイクロメートルサイズの微小領域を対象に、顕微鏡下の任意の箇所で水温（室温）から水の沸点までに渡る広範な温度上昇と下降を行うことができる新しい技術を開発した（図 6）。温度上昇・下降の速さは約 10ms で、最高温度は任意に変えられる。さらに新規に開発したマイクロメートルの空間分解能を持つミクロ温度センサーを用いれば、蛍光色素の蛍光強度変化を利用して、0.1°C の

精度で局所的な温度変化を検出できる（図7)。温度変化による蛍光色素の蛍光強度変化は充分速く、時間分解能はビデオレート（毎秒30フレーム）を超える。

局所熱励起は、任意の領域へ移動できるように、マイクロマニピュレーターにより操作されるガラスマイクロピペット先端（直径 1〜2μm）に固着した金属微粒子に赤外レーザー（波長 1064nm）を照射して行う。赤外レーザー光は、レーザー通過領域に影響を与えずに金属微粒子のみが熱源となるよう、開口数の大きな対物レンズ（N.A.1.3〜1.4）を通して集光する。最高温度はレーザーの光路にNDフィルターを置いて入射レーザー光の強度を制御することで任意に変えられる（図1,2)。

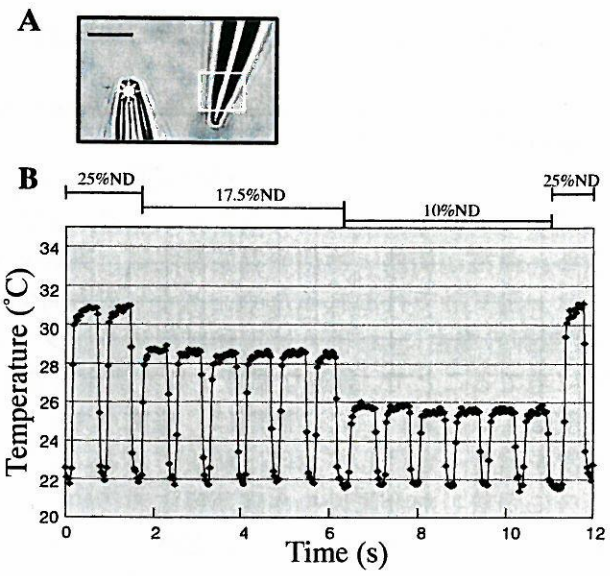

図2　温度パルスの幅は、NDフィルターにより変えられる。(A) 実験像。左は熱励起のためのマイクロピペットで、先端部に赤外レーザーを集光している。右はミクロ温度センサー。Europium-TTAが封じ込まれている。(B) 繰り返し温度パルスの例（1秒に30個のデータ)。NDフィルターにより最高温度を簡単に変えられる。特に温度下降速度の速いことに注目して欲しい。

ミクロ温度センサーには、水溶液から隔離された微小領域に閉じ込めた蛍光色素、Europium-TTAの蛍光強度変化を利用する。蛍光色素を外部環境から隔離することによって、色素が熱以外の環境変化に応答するという従来技術の欠点を克服した。これまでにマイクロピペット先端（直径 1〜2μm）に閉じ込めることに成功している。また色素濃度を高くすることで入射光強度を下げることができた。これにより色素の退色速度を遅くできるだけでなく、励起光による生体試料へのダメージを防ぐことができる。

この技術は、例えば標準的な電気生理学、蛍光イメージングの技術と互換性が良い。そのため、生きた単一細胞の局所熱刺激に対する応答性や、細胞内小器官からのイオンの流出に伴う局所温度変化を検出するなどといった、これまでにない全く新しい細胞生物学研究に、即座に応用可能である。

＜研究方法＞

Ca^{2+}担体のイオノマイシンをHeLa細胞に作用させると、細胞外から細胞質へのCa^{2+}の流入と細胞内小胞から細胞質へのCa^{2+}の流出により、細胞内Ca^{2+}濃度が上昇する。我々は単一HeLa細胞を対象にミクロ温度計を用いることで、この細胞内Ca^{2+}濃度の上昇から若干の遅れを持って、細胞が熱を発生することを見出した。この時間遅れは細胞外Ca^{2+}濃度と逆相関しており、さらにタプシガルギンを用いて細胞内小胞に存在するCa^{2+}-ATPaseの機能を阻害すると、イオノマイシンの作用により細胞内Ca^{2+}濃度は上昇するものの、温度の上昇が抑制された。以上の結果は、細胞内小胞のCa^{2+}-ATPaseの酵素活性が熱発生を導いたことを強く示唆している。

本研究が、単一細胞における熱発生の研究に新たな道を開いたと言える。

また本研究で用いたミクロ温度計は、脳スライスのような対象物を用いた実験において非常に有効に利用できる技術である。なぜなら本技術をこれら実験対象となる臓器へ応用すれば、その箇所の温度を、従来用いられている電気的、化学的、光学的手法から得られる生理的パラメータと同時に測定することができ、それらの相関を見ることが可能だからである。

本研究成果は、Microscopic Detection of Thermogenesis in a Single HeLa Cell.というタイトルで生物物理系専門誌であるBiophysical Journalに掲載された。

ナノ開口基板を用いたシャペロニン GroEL の 1 分子機能解析

上野太郎

【研究背景と目的】

シャペロニン GroEL はリング 2 つが背中合わせに結合したたる型構造をしており、リングの縁に変性タンパク質を結合した状態で、さらにふた型の GroES を結合して変性タンパク質を内部空洞に隔離し、他の変性タンパク質との凝集を防ぎながら折れたたみを進行させる。様々な生化学的実験により、GroEL の両側のリングには GroES が交互に結合して折れたたみを進行させるとされるが、電子顕微鏡では両側の縁に同時に結合する複合体（Football 型複合体）が観察されており、折れたたみ反応進行中にこの中間体が存在するか否かは定かではない（図 1）。本研究では、Football 型複合体の有無とその出現のタイミングの決定を行うことで、GroEL の両側のリング間に負の協同性が生まれるメカニズムを明らかにし、GroEL がどのように変性タンパク質の折れたたみを介助しているかを解明する。

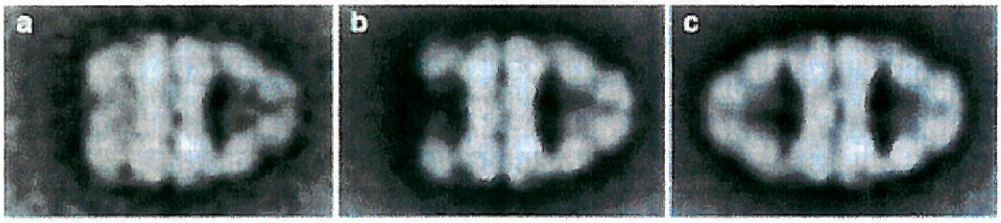

図 1. GroEL-GroES 複合体の電子顕微鏡写真（Beissinger, M. et al., *J. Mol. Biol.* 1999）
a)変性タンパク質-GroEL-GroES 複合体 b)GroEL-GroES 複合体 c)GroES-GroEL-GroES 複合体

GroEL が変性タンパク質や GroES と相互作用している環境下でリアルタイムに Football 型複合体を計測するには、1 分子の GroEL に対する GroES の結合解離を観察する必要がある。1 分子蛍光イメージング法はこの目的に最適であり、すでに 10 nM GroES 存在下でガラス基板上に固定した GroEL との結合解離反応を検出している（Taguchi et al., Nat. Biotechnol., 2001）。しかし、GroES は細胞内で約 5μM で存在しているため、50 nM 以下の蛍光色素存在下でしか測定できない従来の 1 分子蛍光イメージング法では Football 型複合体の有無を決定できない。

これを解決するため、ナノ開口による 1 分子蛍光イメージング技術を開発した。この方法では、ガラスに金属を蒸着した基板の金属部分に直径約 100 nm の穴を開け、ガラス側から励起光を入射して約 10 nm の極めて局在化したエバネッセント場を発生させる（図 2）。このエバネッセント場による励起領域は全反射を利用した従来法の約 1000 分の 1 なので、1000 倍高濃度の生体分子が存在しても 1 分子蛍光イメージングが可能である。すなわち、5 μM GroES 存在下で、GroEL との結合解離反応を 1 分子イメージングすることができると期待される。

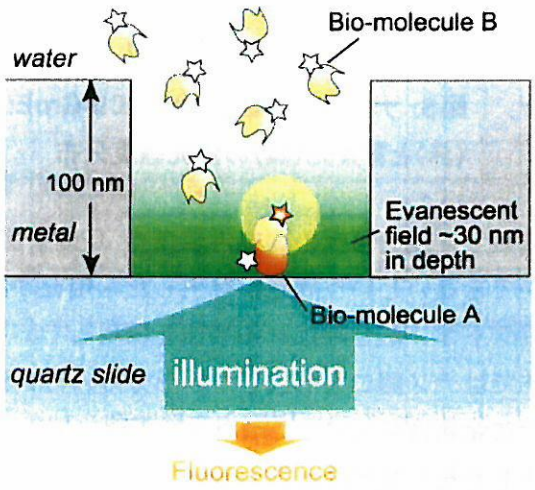

図 2. ナノ開口基板上での 1 分子イメージング

【ナノ開口基板の作製】

石英製のカバーガラスにタングステンを蒸着させ、電子線リソグラフィー及びエッチングにより直径約 100 nm の穴を配列させた（図 3)。この部分に蛍光色素 IC5 で標識したタンパク質（IC5-GroEL）を物理吸着させて蛍光顕微鏡で観察したところ、ナノ開口の位置に輝点が観察され、蛍光強度が段階的に減少した（図 4)。これは量子退色と呼ばれ、単一の蛍光色素の構造が壊れて無蛍光になる瞬間を捉えたものである。以上から、本基板を用いて 1 分子蛍光イメージングを行うことが可能であることが確かめられた。さらに、1μM の蛍光色素を含む溶液で基板を満たした状態でも量子退色が観察され、従来法に比べ少なくとも 20 倍高濃度の蛍光色素存在下で 1 分子イメージングが可能になった。

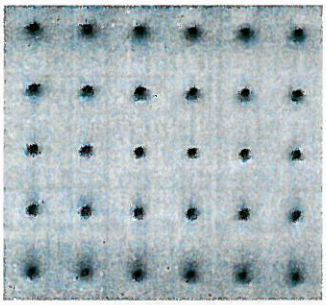

図3. 直径100 nmの穴を1μmおきに配列させたナノ開口基板のSEM画像

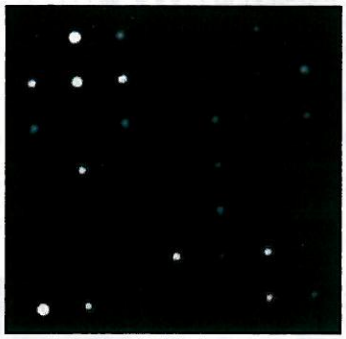

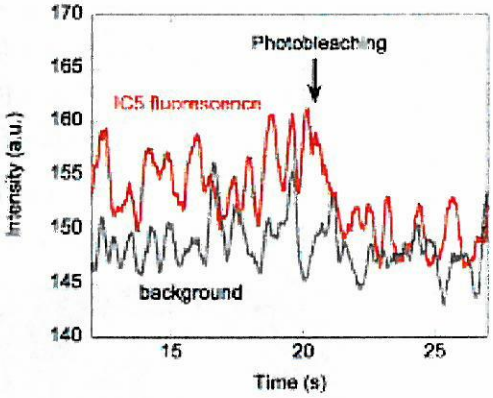

図 4. IC5-GroEL の蛍光像（左）と量子退色（右）

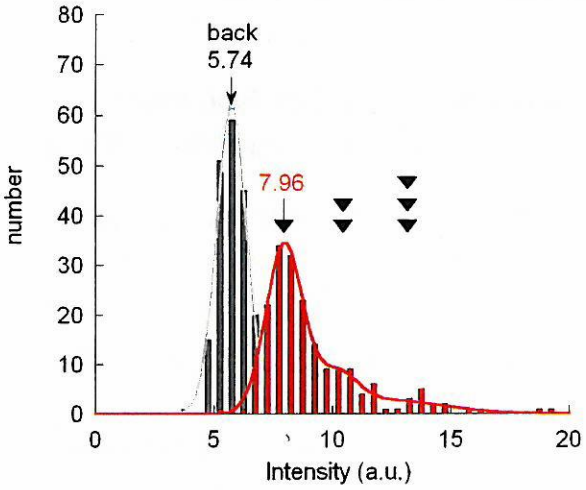

図5. ナノ開口に固定されたIC5-GroEL（赤)と背景光(黒)の蛍光強度分布

続いて、冷却 CCD カメラを用いて各輝点の蛍光強度を解析し、強度分布を作成した（図 5)。輝点の存在しない背景領域の強度分布は、ガウシアン分布でフィッティングされた。一方、輝点の分布は右側に肩を持つ山型となり、3 つのガウシアン分布の和でフィッティングされた。以上は、それぞれのナノ開口に対して蛍光色素 IC5 が量子的に分布していることを示している。

ところがその後、エッチング過程で取りきれなかったタングステンがナノ開口の底部に残り、複数のナノ開口基板の間で再現良く 1 分子蛍光を観察することができないという問題が発生した。現在は作製方法を変更し、リフトオフ法と呼ばれる手法を採用している（図 6)。この手法ではナノ開口を形成したい部分のみにレジストを残し、その上に金属薄膜（アルミニウム）を蒸着するため、レジストを除去した後に金属の残渣が残りにくいという利点がある。リフトオフ法を用いることにより、比較的再現の良い蛍光像の取得が可能になった。

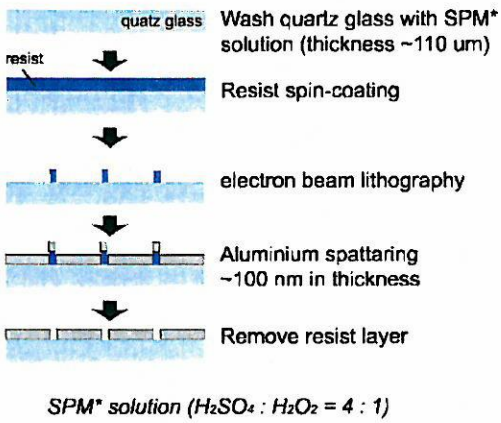

図 6. リフトオフ法によるナノ開口形成

【GroEL-GroESの結合解離の1分子蛍光イメージング】

GroELをナノ開口基板上に固定し、Cy3またはCy5で標識したGroESとの結合解離反応を1分子観察した。具体的には、biotin化BSA、streptavidinを介してIC5-GroELをナノ開口底部に固定した後、500 nM Cy3-GroES、500 nM Cy5-GroES、2mM ATP、変性タンパク質を含む溶液で満たし、蛍光顕微鏡で観察した（図7）。その結果、IC5-GroELが固定されたナノ開口の位置に、Cy3-GroESが何度も結合・解離する様子が観察され（図8）、Cy3-GroESとCy5-GroESが入れ替わりながらGroELと相互作用していることを示唆するデータが得られた。しかし、低頻度ながらもCy3-GroESとCy5-GroESが同時に結合している状態も見られており、さらに詳細な情報を得るためには、GroELを構成する2つのリングのどちら側にGroESが結合しているのかを区別する必要がある。

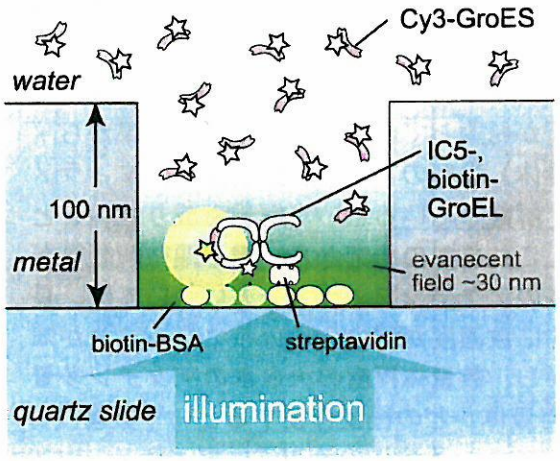

図7. ナノ開口基板を用いたGroELとGroESの結合解離反応の観察方法

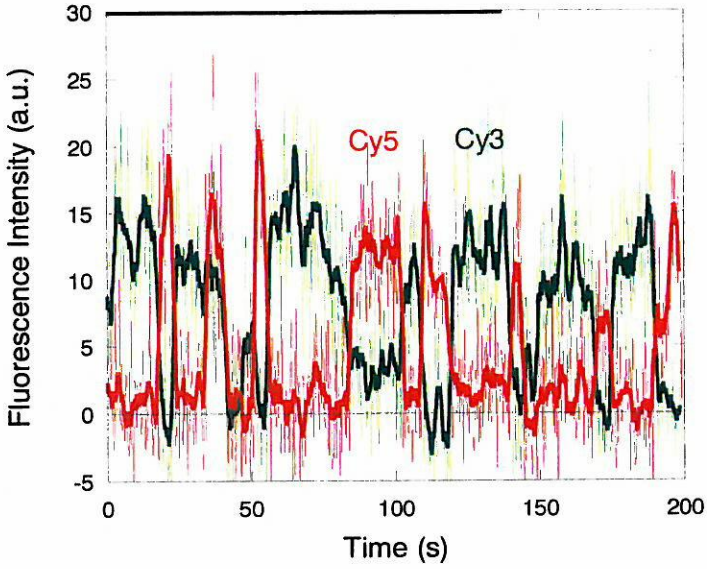

図8. GroES結合に伴うCy3,Cy5の蛍光強度変化

この問題を解決するため、現在2つの手法を試みている。1つ目は蛍光共鳴エネルギー移動（FRET）を利用する方法で、GroELの片側のリングのみにアクセプターを結合させ、ドナーを結合させたGroESとのFRETを指標に、どちら側のリングにGroESが結合したかを判別する。2つ目は、GroEL-GroES複合体の長軸方向の長さが約20nmであるのを利用し、fluorescence imaging with one nanometer accuracy (FIONA) と呼ばれる位置決定法を用いて2つのリングを区別する方法である。

【まとめ】

- ナノ開口を持つ石英ガラス基板を作製した
- 蛍光標識したタンパク質（IC5-GroEL）を固定し、量子退色を観察した
- ナノ開口内へのタンパク質の固定方法を確立した
- ナノ開口基板でGroEL-GroESの結合・解離反応を1分子イメージングできた

【謝辞】 ナノ開口基板は、早稲田大大学院理工学研究科の谷井孝至、島本直伸、三宅丈雄、大泊巌氏に作製していただいた。記して感謝します。

【今後】 本研究により、1μM GroES存在下でもGroELとの結合解離反応を観察することができるようになった。今後、Football型複合体の形成メカニズムの解明が期待される。一方、高濃度の蛍光色素存在下で相互作用を1分子観察できることから、結合速度定数が低いタンパク質間相互作用の1分子蛍光イメージングも可能である。

フォトンカウンティングヒストグラム法を用いたアクチン多量体の数濃度分布の解析

寺田 尚史

【研究の背景と目的】

細胞内には細胞骨格と呼ばれるフィラメント(繊維)状のタンパク質が網目構造を形成して存在しており、細胞内輸送・細胞の形の形成・細胞運動等に関与している。細胞骨格のフィラメントは、その構成単位であるタンパク質分子(単量体)が重合したタンパク質複合体(多量体)として形成されることが多い。代表的な細胞骨格タンパク質であるアクチンは、重合・脱重合をしてフィラメントの長さを調節することで筋肉構造を形成したり、細胞運動を引き起こしたりする。

精製単離したアクチンでも、試験管内の溶液中で重合させることが出来る。精製したアクチンを塩濃度の高い重合溶液に入れると、タンパク質濃度に依存してフィラメントを形成する。この際、臨界濃度と呼ばれるタンパク質濃度を超えた分のアクチンがフィラメントを形成する。二重らせんのフィラメントと重合していないアクチンとは共存して平衡状態にあり（図 1)、フィラメントの端ではアクチンが絶えず重合・脱重合をしている。近年、アクチンフィラメント 1 本を光学顕微鏡下で観察できる技術が発達してきたが、その観察結果から平均 6 個単位（6 量体）程度のアクチン集合体が、フィラメントの端で結合・解離しているという解釈も成り立つことが分かってきた。これまでの研究から、電子顕微鏡観察ができる程度の長さのアクチンフィラメントについては、長いほど指数関数的に数濃度が減少する分布になることが知られている。しかし、数量体程度の大きさのアクチン多量体については、何量体がどの程度存在するという数濃度分布がこれまで明らかでなかった。数量体~10 量体程度のアクチン多量体の分布は、フィラメントの端で何量体が結合・解離しているのかという重合機構の基本特性とも関連する重要な問題である。

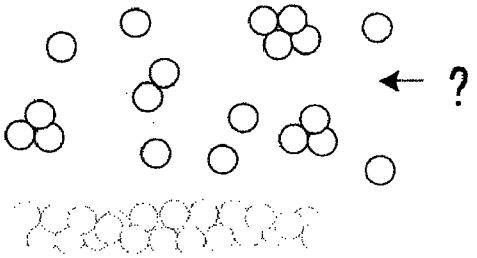

図 1　アクチンの多量体

本研究では、フォトンカウンティングヒストグラム法(PCH)を用いて、溶液中におけるアクチン多量体の数濃度分布を明らかにすることを目的とした。

【実験方法・結果】

アクチンの多量体の分布を調べるのに PCH を用いた。PCH では共焦点光学系を使用し、微小領域を横切る分子から発せられる光子数（図 2）のヒストグラム（図 3）を取得する。このヒストグラムにフィッティングを行うことで領域内平均粒子数と粒子の明るさの 2 種類のデータを取得する。重合溶液中では粒子の明るさが多量体数に比例すると仮定して解析を行い、多量体数を算出した。

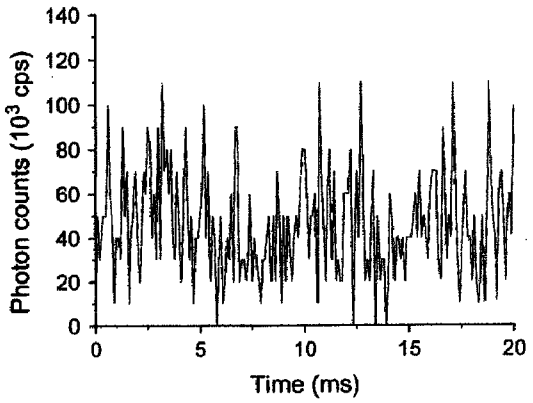

図 2　共焦点領域を横切るアクチンからの蛍光

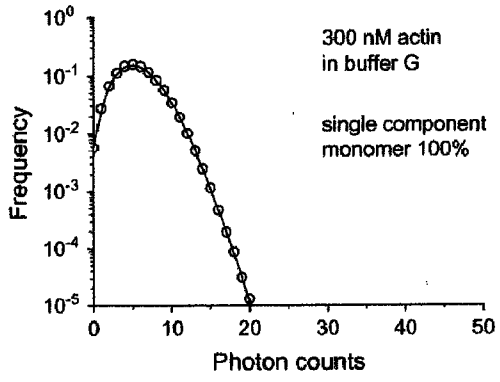

図 3　蛍光のヒストグラム

粒子の明るさが多量体数に比例すると仮定するためには、単量体の状態とフィラメントの状態で

明るさの変わらない色素でアクチンを染色する必要がある。我々はこの条件を満たす色素として Bodipy FL を使用した。この色素で染色したアクチンの 500-510nm の蛍光は、重合しても蛍光強度があまり変わらなかったので（図 4)、この波長領域の蛍光を取得する光学系を構築した。Bodipy FL アクチンが重合に影響を与えるかどうかを確認するために、Bodipy FL アクチンと無染色アクチンの濃度を変え、重合すると蛍光強度が増加する色素(Pyrene)で染色したアクチンを一定量混ぜて重合させた（図 5)。この際には全体のアクチン濃度は一定に保った。Bodipy FL で染色したアクチンの濃度は重合に大きく影響しなかった。また、重合時に色素間の距離が近くなることが蛍光強度に影響しないことを確認した。

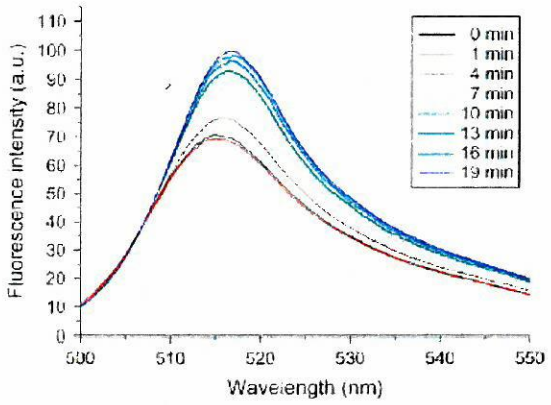

図 4　重合時の蛍光スペクトル変化

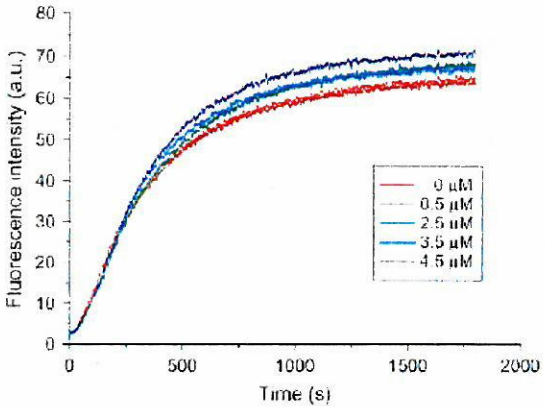

図 5　Bodipy FL アクチン濃度と重合特性

Bodipy FL アクチンを使用して、まず分散溶液(buffer G)中の単量体の明るさを求めた(図 6A)。次に重合溶液（buffer F）中でのアクチンの明るさの分布を求めたところ（図 6B)、単量体の明るさの 1-3 倍の位置にピークが出た。2 量体・3 量体が形成され、単量体の 2 倍・3 倍の明るさになっていると考えられる。

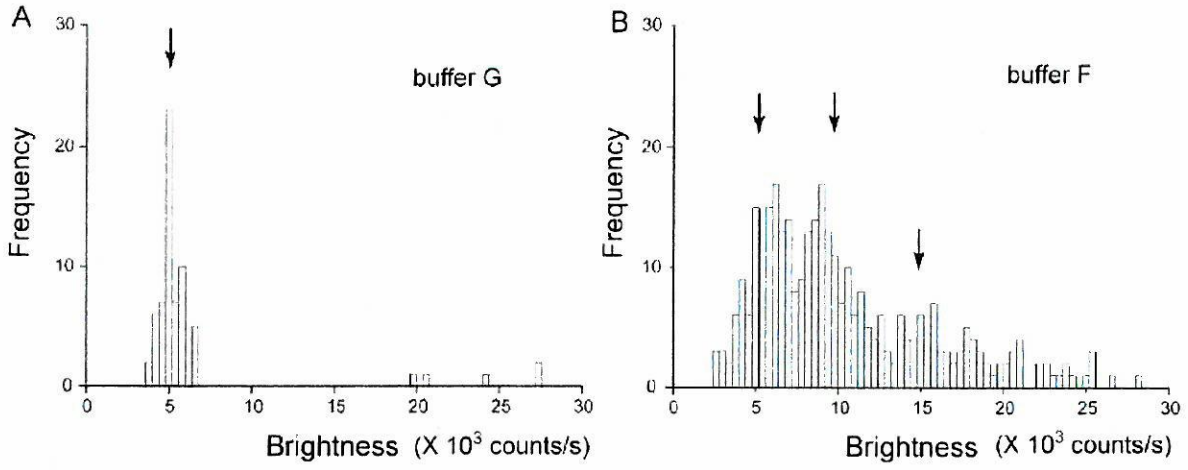

図 6　溶液中のアクチンの明るさの分布

単量体の i 倍の明るさの粒子を i 量体とみなして重合溶液中での数濃度分布を求めた（図 7)。その結果、分散溶液中では 99.5%以上のアクチンが単量体として存在するが、重合溶液中では 1-5 量体のアクチンが主に存在していることが明らかにされた。これにより、アクチンフィラメント端での重合・脱重合は 1-5 量体により起こっていることが示唆された。また、多量体の分布は 1-5 量体と 6-100 量体の 2 つの指数分布に分かれることが分かった。

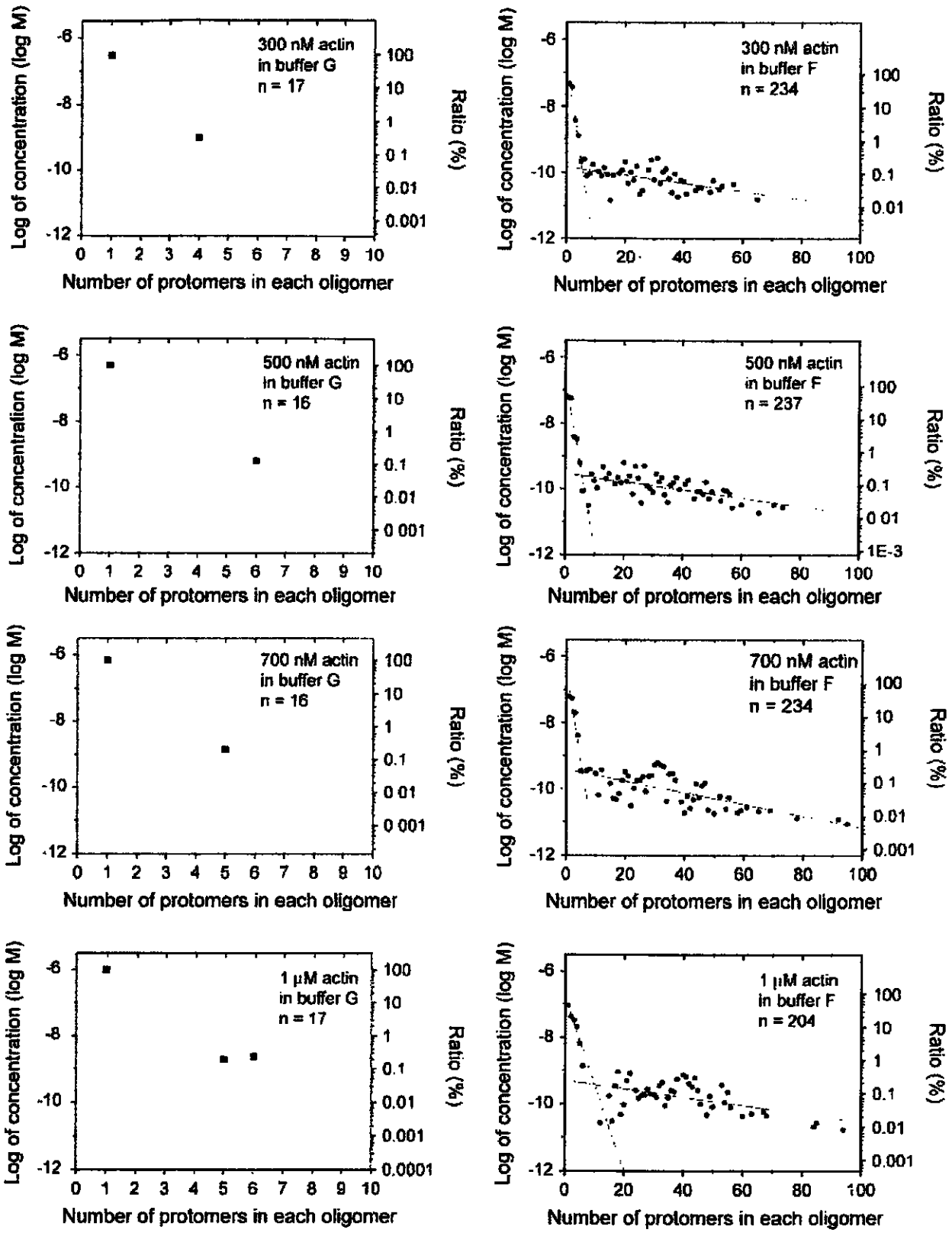

図7　アクチン多量体の数濃度分布

左が分散溶液（buffer G）中で右が重合溶液（buffer F）中。Protomer は多量体(oligomer)中の単量体であり、横軸は多量体数を示している。分散溶液中では 99.5%以上が単量体として存在している。重合溶液中の分布は 1-5 量体と 6-100 量体の 2 つの分布（それぞれ直線が引いてある）に分かれている。

この結果を大沢らのアクチン重合の理論に基づいて解析した。このモデルではアクチンの状態としてモノマー、直線状重合体、らせん状重合体の3種類の状態を考える（図8）。電子顕微鏡などでの観察から、アクチンフィラメントは二重らせん構造で、長いほど指数関数的に数濃度が減少することが知られている。そこで、ともに指数分布を示している（図7）10-100量体をらせん状重合体、1-5量体を直線状重合体と仮定して解析を行った。その結果、直線状重合体とモノマーとの間の平衡定数 K_l が$(5.2 \pm 1.1)\times 10^6$ /M と求まった。モデルによれば、らせん状3量体は、直線状3量体と比べてねじれる分だけ余分な自由エネルギーが必要となり、直線状3量体に対するらせん状3量体の割合 γ が小さいと考えられている。事実、γ の値を実験結果から求めると$(3.6 \pm 2.3)\times 10^{-2}$と小さかった。また、らせん状重合体に結合するモノマーは、らせん構造の端に存在する2個のアクチン分子に結合することになるため、直線状重合体より結合しやすくなると考えられている。解析の結果、らせん状重合体とモノマーとの間の平衡定数 K_h は$(1.6 \pm 0.5)\times 10^7$ /M（この逆数である60 nMが、アクチン重合の臨界濃度に対応する）と求められ、直線状重合体の場合と比べて3倍程度結合しやすくなっていることが示された。これらの結果から、直線状3量体（重合核）がらせん状3量体になるときの余分な自由エネルギーは2.0 kcal/molと計算された。ここでは重合核を3量体と仮定して解析したが、直線状かららせん状重合体への転移は5-7量体で起こることが分かった（図9）。

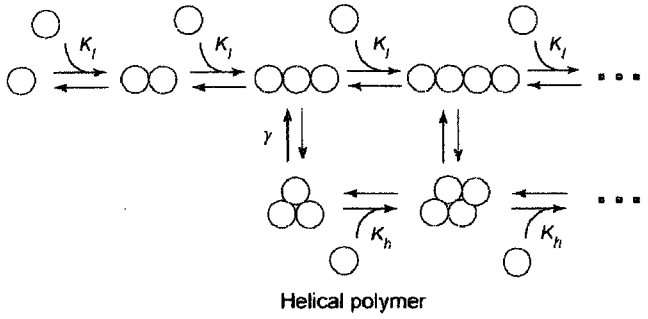

図8　大沢らのモデル

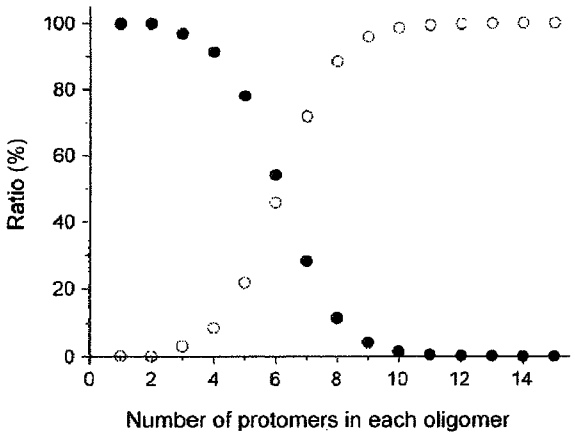

図9　直線状とらせん状重合体の比率
解析の結果得られた値を元に計算した。

mRNAの細胞内ラベリングと運動解析

山岸　舞

【研究の背景と目的】

mRNAは核内でDNAから転写され、修飾を受けた後、核外輸送されてリボソームへと運ばれる。一部のmRNAでは細胞質内での局在化がみられ、mRNAの機能制御のひとつと捉えられている。しかし、局在化の必然性が具体的に示された例は少ない。mRNAを可視化し、細胞質内局在化のメカニズムを明らかにすることで、局在化mRNAの機能をより明確にすることが期待される。生きた細胞内でのmRNAの動きを可視化する方法として、*in vitro*で蛍光ラベルしたmRNAを細胞内にインジェクションし、その蛍光輝点の動きを解析する実験が行われてきた。この方法は外因性のmRNAを用いるため、転写と並行しておこるmRNAのプロセシングの効果などを無視することになる。一方、細胞内で転写されたmRNAを*in situ*で蛍光ラベルし解析する方法として、特定RNA配列を認識し結合するタンパク質を利用する方法がある。たとえば、ファージのコートタンパク質であるMS2、スプライシング因子のひとつであるU1Aタンパク質を利用して酵母のASH1 mRNAの局在を可視化した報告がある（Bertrand, E. *et al.* (1998) *Mol. Cell.*, 2, 437-445、Irie, K. *et al.* (2002) *EMBO J.*, 21, 1158-1167）。また、MS2を利用する方法は哺乳類細胞での実験に応用されている（Fusco, D. *et al.* (2003) *Curr. Biol.*, 13, 161-167）。本研究では、MS2を利用する方法を細胞骨格タンパク質であるβactinのmRNAの可視化に適用した。βactinのmRNAはニワトリ胚由来線維芽細胞（CEF）内において細胞辺縁のleading edgeと呼ばれる部分に局在化することが知られている。mRNAの運動解析を行うことにより、leading edgeに局在化するメカニズムの考察を試みた。

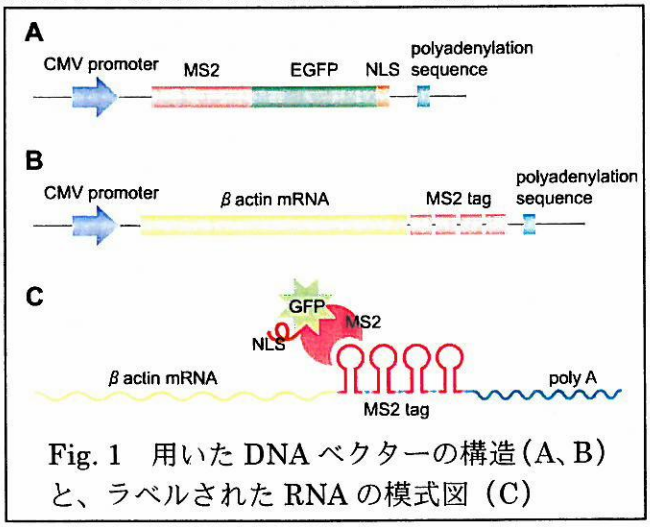

Fig. 1　用いたDNAベクターの構造（A、B）と、ラベルされたRNAの模式図（C）

【実験方法・結果】

EGFP融合MS2をコードするDNAベクター（Fig. 1A）と、βactin配列の下流にMS2認識配列（MS2 tag）を組み込んだDNAベクター（Fig. 1B）を同時に細胞内で発現させると、転写されたβactin mRNAの下流にMS2-EGFPが結合し、その結果βactin mRNAがEGFPラベルされる（Fig. 1C）。

βactin mRNAの核外輸送やleading edgeへの局在には、3'UTRに存在するzipcodeと呼ばれる配列（54 nt）が関与している（Kislauskis, E. *et al.* (1994) *J. Cell. Biol.*, 127, 441-451）とされ、zipcode配列に結合するタンパク質ZBP1が間接的にアクチンフィラメントに結合し、mRNAを能動輸送していると解釈されている。そのため3'UTRの有無はmRNAの運動に影響を及ぼすと考えられる。そこでβactin mRNAのほぼ全長（5'UTR 18 bp＋ORF 1,128 bp＋3'UTR 525 bp）と3'UTRを除いたもの（5'UTR 18 bp＋ORF 1,128 bp）をCEF内でMS2-EGFPラベルし、比較を試みた。全長mRNAは既報どおりleading edgeに局在化した（Fig. 2A）。3'UTRを除いたものは核外輸送や局在化に不全があるという予測に反し、細胞質においてmRNAの輝点が観察され、

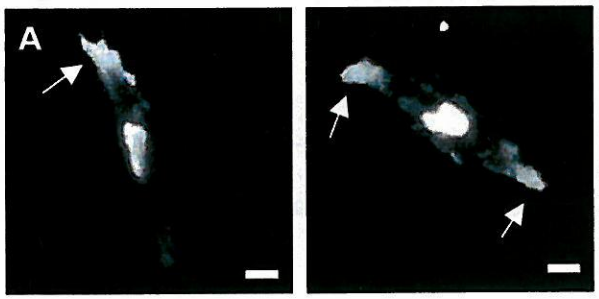

Fig. 2　MS2-GFPラベルされたmRNAの細胞内分布。矢印は局在化したmRNA（A）βactin mRNA全長（B）3'UTRを除いたβactin mRNA

全長 mRNA と同様の局在を示した（Fig. 2B）。実際、zipcode 配列が局在化に関与することを示した報告（Kislauskis *et al.*）においても、zipcode を欠いた mRNA がある程度は局在化を起こすというデータが示されている。このことは、3'UTR（zipcode を含む）は核外輸送や細胞質内の局在化に必須ではないことを示唆している。同様に、配列内に zipcode を含まないため CEF 内では leading edge への局在が見られないとされている α actin mRNA を用いても leading edge に局在することがわかり、mRNA を局在化させるための新たなメカニズムを想定する必要が生じた。そこで、まず局在化 mRNA の動態を 2 秒毎のタイムラプスで観察した。Leading edge に局在化した mRNA が一方向性に新しい leading edge へとリクルートされる様子が確認できた。古い leading edge から新しい leading edge への移動は細胞の縁を伝い、集団として移動していた。また、leading edge への局在は、仮足の突出と同期していた。能動輸送に想定される、細胞骨格のレールの沿った動きのようなものは観察されず、細胞の縁が主な通り道になっているようだった。およそ 8 ms の時間分解能で mRNA の一分子追跡を行い、個々の分子の運動解析を行ったところ、局在化している mRNA は自由拡散をしていた（Fig.3）。局在化していない部分（核周辺の暗い部分）の mRNA はおよそ 300 nm 四方の範囲内での拡散運動であり、細胞骨格の網目構造内の制限された運動をしているか、他の構造体にトラップされていることが考えられるのに対し、局在化部位にあたる leading edge は運動障壁が非常に少ないことが示唆された。自由に拡散運動している分子が一箇所に留められる、つまり局在化している理由として、細胞骨格が形成する網目構造の、細胞内部位による密度差が与えているのではないかと考えた。また、mRNA が集団で移動することから、媒質、つまりサイトゾル自体の流動が mRNA の輸送の主体なのではないかと考えた。この仮説が正しいとすれば、細胞骨格の密度差が運動に影響するような巨大分子は mRNA のような局在化をおこすことが想定される。そこで、分子量 2,000 kDa の FITC 標識デキストランを CEF にインジェクションしてみた。インジェクション後 25 min で leading edge に局在する様子が観察された。また、この細胞のリアルタイム観察により、インジェクションした場所でゆっくりと拡散運動をしていた FITC デキストランの塊が、leading edge 周辺で急速にほぐれて流されていく様子が観察できた。このことにより、サイトゾルの流動により制限された領域を緩やかに移動していた巨大分子が、leading edge 内で障壁の少ない自由拡散へと移行したことが示された。この結論は、mRNA の局在化自体が mRNA の機能制御のひとつであるという従来の認識に疑問を投げかけるものである。

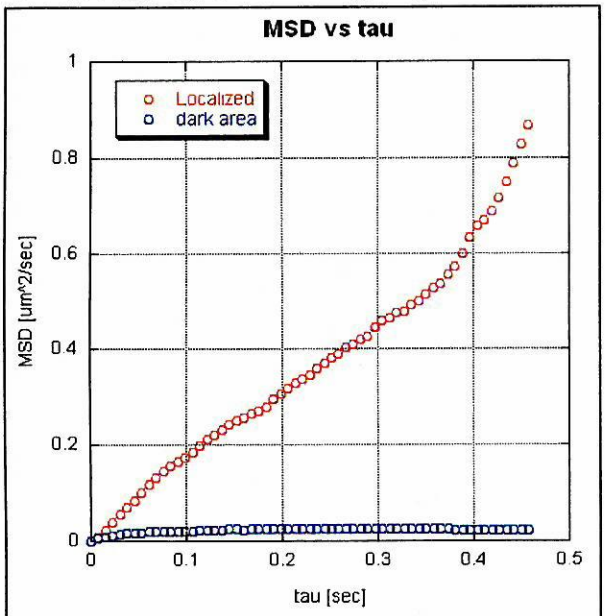

Fig. 3　mRNA の一分子追跡による運動解析　平均二乗変位を時間間隔に対してプロットしたもの。局在化部位の mRNA（赤）は時間間隔に対し一次の直線、ないしやや二次曲線のグラフが描けるのに対し、非局在化部分の mRNA（青）は変位の上限がある制限された運動を示すグラフとなる。

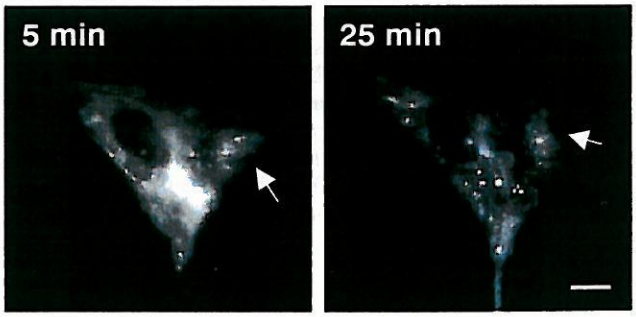

Fig. 4　2,000 kDa の FITC-デキストランをインジェクションした CEF（A）インジェクション後 5 分、（B）インジェクション後 25 分。5 分後でもすでに兆候はあるが、leading edge への局在が見られる。

Kinesin–microtubule binding depends on both nucleotide state and loading direction

Sotaro Uemura*, Kenji Kawaguchi*, Junichiro Yajima†, Masaki Edamatsu†, Yoko Yano Toyoshima†, and Shin'ichi Ishiwata*‡§¶

*Department of Physics, School of Science and Engineering, and ‡Advanced Research Institute for Science and Engineering, Waseda University, 3-4-1 Okubo, Shinjuku-ku, Tokyo 169-8555, Japan; †Graduate School of Arts and Sciences, University of Tokyo, 3-8-1 Komaba, Meguro-ku, Tokyo 153-8902, Japan; and §Core Research for Evolutional Science and Technology, Genetic Programming Team 13, Nogawa 907, Miyamae-ku, Kawasaki 216-0001, Japan

Edited by James A. Spudich, Stanford University School of Medicine, Stanford, CA, and approved February 26, 2002 (received for review October 22, 2001)

Kinesin is a motor protein that transports organelles along a microtubule toward its plus end by using the energy of ATP hydrolysis. To clarify the nucleotide-dependent binding mode, we measured the unbinding force for one-headed kinesin heterodimers in addition to conventional two-headed kinesin homodimers under several nucleotide states. We found that both a weak and a strong binding state exist in each head of kinesin corresponding to a small and a large unbinding force, respectively; that is, weak for the ADP state and strong for the nucleotide-free and adenosine 5′-[β,γ-imido]triphosphate states. Model analysis showed that (*i*) the two binding modes in each head could be explained by a difference in the binding energy and (*ii*) the directional instability of binding, i.e., dependence of unbinding force on loading direction, could be explained by a difference in the characteristic distance for the kinesin–microtubule interaction during plus- and minus-end-directed loading. Both these factors must play an important role in the molecular mechanism of kinesin motility.

Kinesin is a processive molecular motor that is essential for the transport of vesicles and organelles along a microtubule in various cells. Kinesin's processive movement has been explained by a mechanism that involves alternating between single- and double-headed bindings to a microtubule (1–5). Adjacent tubulin dimers of 8-nm length form consecutive binding sites (6), such that kinesin takes hundreds of 8-nm steps down a microtubule (7–10). Our recent single-molecule analysis of unbinding force (11) showed that conventional two-headed kinesin is involved in single-headed binding, both in the absence of nucleotides (nucleotide-free state) and in the coexistence of ADP and adenosine 5′-[β,γ-imido]triphosphate (AMP-PNP) (ATP analogue), and double-headed binding in the presence of AMP-PNP (AMP-PNP state), which is consistent with the putative mechanism of kinesin motility.

In the present study, we have measured the unbinding force of a single kinesin·microtubule complex under an optical microscope equipped with optical tweezers as was reported (11). To clarify the binding mode, we used one-headed kinesin heterodimers (12) in addition to conventional two-headed kinesin homodimers. Conventional two-headed homodimers or one-headed heterodimers of kinesin molecules were attached to a polystyrene bead such that single kinesin binds to a single bead, and each bead was manipulated with optical tweezers on a microtubule that was adsorbed onto a coverslip (1, 9). An external load was imposed on the attached kinesin molecule by moving the bead toward the plus or the minus end of the microtubule. Here, we found that the two binding states exist in each head of kinesin depending on the nucleotide state. Also, we found that the dependence of the unbinding force on loading direction (where the unbinding force is smaller for the plus-end loading than for the minus-end loading) was independent of nucleotide states.

We have analyzed the results for a weak and a strong binding of each head according to a simple model, where the detachment of the kinesin–microtubule complex is assumed to occur according to the load (F)-dependent lifetime (τ) expressed by $\tau(F) = \tau(0)\exp(-Fd/k_BT)$. $\tau(0)$, the lifetime in the absence of external load, is 1 s for the ADP state and 150 s for the AMP-PNP and nucleotide-free states; d is the characteristic distance, k_B, the Boltzmann constant, and T, the absolute temperature.

Materials and Methods

Proteins. Conventional two-headed kinesin homodimers and tubulin were prepared from bovine (9) and porcine (13) brains, respectively. One-headed kinesin heterodimers were engineered and purified as described (12). This construct includes the neck, rod, and tail domains but lacks one head domain. Polarity-marked microtubules labeled with tetramethyl-rhodamine succinimidyl ester (Molecular Probes) were prepared according to Hyman (14) except that *N*-ethylmaleimide-treated tubulin was not used; thus, polymerization at the minus end was not inhibited (compare figure 2A in ref. 11).

Unbinding Force Measurement. Kinesin-coated beads were prepared according to the established procedure (9) except for fluorescent polystyrene beads (1.0 μm in diameter, carboxylate-modified latex; yellow-green, Molecular Probes). The average number of functional kinesin molecules on a bead was estimated by statistical methods (1, 9). The polarity-marked fluorescent microtubules in an assay buffer (2 mM $MgCl_2$/80 mM Pipes, pH 6.8/1 mM EGTA) were introduced into a flow cell and incubated for 2 min to allow binding to the glass surface. The solvent was exchanged three times with an assay buffer containing 0.7 mg/ml filtered casein to coat the glass surface with casein. The flow cell was then filled with an assay buffer containing the kinesin-coated beads, filtered casein, and an oxygen-scavenging enzyme system. The final solvent condition was ≈0.1 pM kinesin-coated beads/2 mM $MgCl_2$/80 mM Pipes, pH 6.8/1 mM EGTA/0.7 mg/ml filtered casein/10 μM Taxol/10 mM DTT/4.5 mg/ml glucose/0.22 mg/ml glucose oxidase/0.036 mg/ml catalase/1 unit/ml apyrase (nucleotide-free state) or 1 mM AMP-PNP (AMP-PNP state) or 1 mM ADP containing 1 unit/ml hexokinase (ADP state). We were able to measure the unbinding force repeatedly on the same beads and hence, presumably, the same kinesin molecules. The proportion of beads that underwent the binding and unbinding cycle was about 40% of those examined. Among them the proportion for which unbinding did not occur even at the largest external load (about 20 pN) was less than 5%. The remaining beads (about 60%) did not bind even after three trials of unbinding experiments.

This paper was submitted directly (Track II) to the PNAS office.

Abbreviation: AMP-PNP, adenosine 5′-[β,γ-imido]triphosphate.

¶To whom reprint requests should be addressed. E-mail: ishiwata@mn.waseda.ac.jp.

The publication costs of this article were defrayed in part by page charge payment. This article must therefore be hereby marked "*advertisement*" in accordance with 18 U.S.C. §1734 solely to indicate this fact.

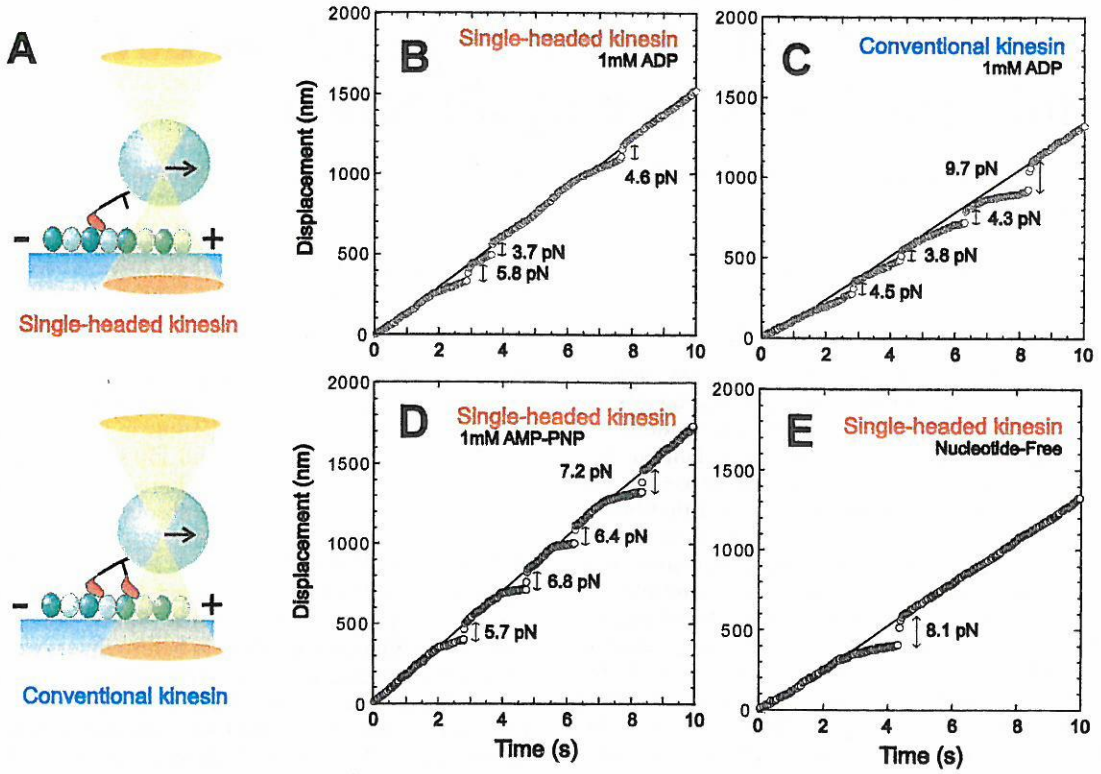

Fig. 1. Measurement of unbinding force. (*A*) Schematic illustration showing the method of application of external load to one-headed or two-headed kinesin-coated bead by using optical tweezers. The relative size of the bead to kinesin is reduced to about 1/10 of the actual scale. In this illustration, the load is applied toward the plus-end of a microtubule. (*B* and *C*) Examples in the ADP state showing the time course of movement of the trap center (thin lines) and the bead (circles) on which one-headed (*B*) or conventional two-headed (*C*) kinesin was attached. The trap center was moved at a constant rate toward the plus-end of a microtubule. The unbinding force was estimated from the abrupt displacement of the bead. (*D* and *E*) Examples showing the behavior of the bead in the AMP-PNP state (*D*) or in the nucleotide-free state (*E*). In all examples, the load was applied toward the plus end.

Model Analysis. For the model analysis, in which equilibrium between attached and detached states of one-headed kinesin is assumed to exist, the time dependence of the proportion of attached kinesin, $N(t)$, was calculated by using Mathematica for Windows. Here, the value of $N(t)$, was obtained by solving the kinetic equation $dN(t)/dt = -N(t)/\tau(F)$. The load (F) dependence of the lifetime (τ) of the attached state of kinesin was expressed as $\tau(F) = \tau(0)\exp(-Fd/k_BT)$, where T is the absolute temperature (300 K), k_B is the Boltzmann constant, and d is a characteristic distance. This relationship was obtained for the F-actin-HMM rigor complex (15). In the present study, F was linearly increased at a constant rate, α, such that $F = \alpha t$. Accordingly, $\tau(F)$ became a function of t as expressed by $\tau(t) = \tau(0)\exp(-d\alpha t/k_BT)$, such that we obtained $N(t) = \exp[k_BT(1 - \exp(d\alpha t/k_BT))/\tau(0)\alpha d]$ as a solution for the differential equation above. The unbinding force distribution, $P(F)\Delta F$ as a function of F or $P(t)\Delta t$ as a function of t, was thus obtained by $(dN(t)/dt)\Delta t$.

Apparatus. Microscopy system equipped with optical tweezers as described (16); the stiffness of the optical trap was estimated to be 0.050 pN/nm. Because the spatial resolution of our system is estimated to be a few nanometers at this stiffness of optical trap, the resolution of the force measurements made is considered to be ±0.2 pN.

Results and Discussion

A polystyrene bead, to which either a single one- or two-headed kinesin molecule was attached, was trapped with optical tweezers and placed in contact with a microtubule for 20–30 s (Fig. 1*A*). Then, the unbinding force was measured by pulling the kinesin-coated bead along the microtubule at constant velocity. Typical data are shown in Fig. 1 *B–E*, where thin lines and circles, respectively, show the time course of the trap center and the bead center. As the bead began to deviate from the trap center, an external load was gradually applied to the kinesin–microtubule complex. When kinesin was detached from the microtubule, the bead quickly returned to the trap center. The unbinding force was estimated by multiplying the magnitude of the abrupt displacement of the bead at the moment of detachment by the stiffness of the optical tweezers (0.050 pN/nm). Considering that the length of kinesin is 60 nm and the radius of the bead is 500 nm (for this geometry, see ref. 1), the angle between the tail of kinesin and the microtubule is estimated to be about 60° for plus-end loading, whereas about 120° for minus-end loading when the external load is imposed (11).

Regardless of whether kinesin was one- or two-headed, binding and unbinding events occurred repeatedly when the bead was kept moving along a microtubule in both the ADP state (Fig. 1 *B* and *C*) and the AMP-PNP state (Fig. 1*D*). In the nucleotide-free state (Fig. 1*E*), however, unbinding occurred only once and subsequent binding and unbinding events were not repeated as described (11), suggesting a low binding-rate constant. The external load could be applied not only toward the plus end but also toward the minus end of a microtubule.

The unbinding force distributions thus obtained in the presence of 1 mM ADP or 1 mM AMP-PNP, and in the absence of nucleotides are summarized in Fig. 2. We found that the main difference between the behavior of one-headed and two-headed kinesin molecules was that the distribution is bimodal for two-headed kinesin in the AMP-PNP state (compare Fig. 2 *A* and *B*). This result strongly supports the conclusion (11) that the smaller and larger values for the unbinding force represent

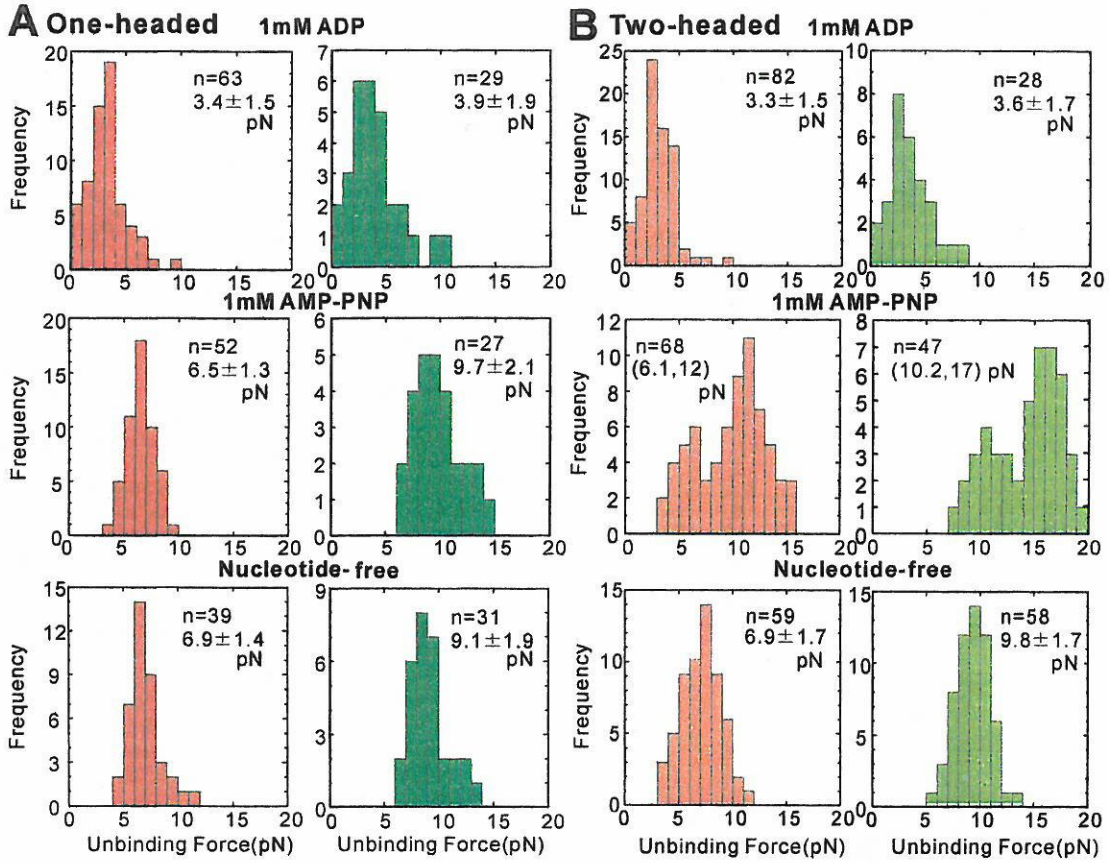

Fig. 2. Unbinding-force distribution for (*A*) one-headed kinesin and (*B*) conventional two-headed kinesin. External load was applied at a constant rate (5.0 ± 1.68 pN/s, n = 583) at several nucleotide states toward either the plus-end (red for *A* and orange for *B*) or the minus-end (dark green for *A* and light green for *B*) of the microtubule. The average unbinding force (pN) with SD is shown in each panel except in the presence of AMP-PNP (*B*), where only the average unbinding force of each peak is shown in the parentheses. The boundary between two peaks was determined by the junction of two Gaussian distributions that simulated two peaks.

single- and double-headed binding, respectively. We confirmed that the average unbinding force for minus-end loading was about 45% greater than that for plus-end loading in both the nucleotide-free and AMP-PNP states (11), both for one- and two-headed kinesin molecules.

An important finding in the present study is that the average unbinding force measured in the ADP state was smaller than both that in the nucleotide-free state and that for single-headed binding in the AMP-PNP state (Fig. 2). For plus-end loading, the values of the unbinding force were 3.3–3.4 pN for the ADP state, but 6.1–6.9 pN for the latter two states. On the other hand, for minus-end loading, the corresponding values obtained were 3.6–3.9 pN and 9.1–10 pN, respectively. Here, it should be noted that the dependence of the unbinding force distribution on loading direction in the ADP state was not as significant as in the latter two states. Moreover, we could not find any difference between the unbinding force distributions of one-headed and two-headed kinesin molecules, which implies that conventional two-headed kinesin binds single-headedly in the ADP state. The tail of the unbinding force distribution observed at higher than 5 pN (top row in Fig. 2 *A* and *B*) may be attributed to those heads that were nucleotide-free at the time of unbinding.

We have analyzed the results above according to a simple scheme illustrated in Fig. 3*A*. Here, the parameters to be determined are $\tau(0)$, the average lifetime of the kinesin–microtubule complex in the absence of external load, and d, a characteristic distance of kinesin-microtubule interaction. The most important result of this analysis is that, if the d value is assumed to be common to all of the nucleotide states, the small unbinding force in the ADP state could be explained by a short lifetime of the complex (i.e., large unbinding rate constant), $\tau(0)$ of 1 s, and the large unbinding force in the nucleotide-free and AMP-PNP states by a longer lifetime (i.e., smaller unbinding rate constant), $\tau(0)$ of 150 s, both of which are consistent with experimentally determined values (17). The loading-direction dependence of the unbinding force distribution, that is, the directional instability of binding, was attributable to the difference in the value of d, being 4.0 and 3.0 nm, respectively, for plus- and minus-end loading, regardless of the nucleotide state (Fig. 3). This implies that the effective load needed to induce unbinding is smaller for plus-end loading, which may be due to the asymmetrical geometry of the peptide chain through which the external load is applied.

Given that $\tau(0)$ is related to the binding energy, the result above suggests that two types of microtubule-binding sites exist in each head of kinesin. Amino acid sequence analysis also suggests that at least two binding regions exist in each head of kinesin, located at loop 12, and loop 7 or 8 (18–20). Furthermore, cryo-electron microscopy (21, 22) shows that the angle of the attached head against the microtubule in the ADP state is different from those in the nucleotide-free and AMP-PNP states. Recent polarization measurements of fluorophores rigidly attached to the kinesin heads have shown broad orientational distribution in the ADP state (23, 24), which suggests weak binding to the microtubule. The present results describing single molecular mechanics together with model analysis support this

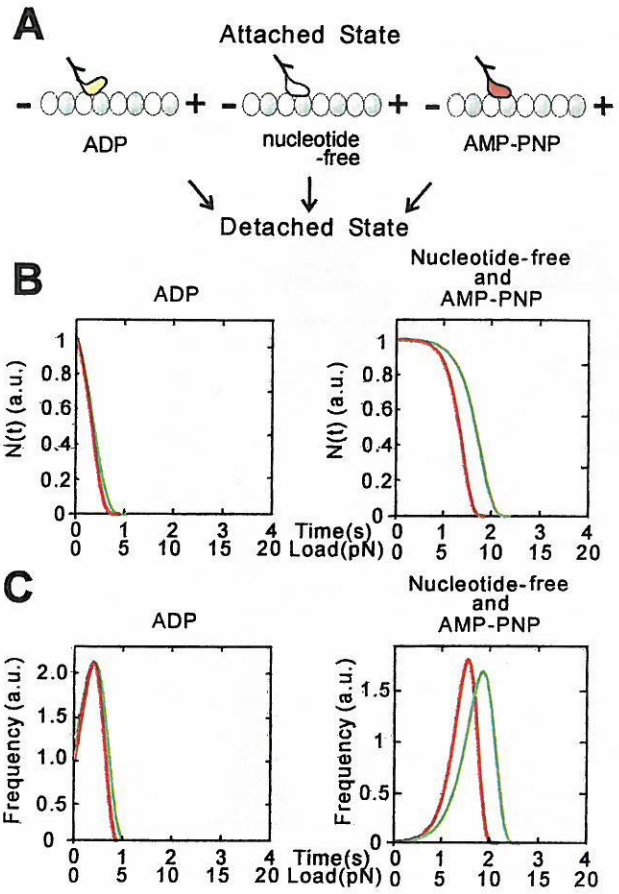

Fig. 3. Model analysis of unbinding-force distribution for one-headed kinesin in three nucleotide states. (*A*) Schematic illustration of two binding modes, i.e., weak binding in the ADP state and strong binding in the nucleotide-free and AMP-PNP states. (*B* and *C*) Total number of binding (*B*) and the frequency of unbinding events (*C*) depending on the loading time (*s*) and the unbinding force (pN) for plus-end (red) and minus-end (green) loading in the presence of ADP (*Left*) and in the absence of nucleotide or in the presence of AMP-PNP (*Right*). The loading rate α was assumed to be 5 pN/s (see *Materials and Methods*). In *B*, N(0), the proportion of attached kinesin at time 0, is defined as 1. In *C*, the frequency of unbinding events was obtained by differentiating N(*t*) in *B* with respect to *t* (see text). The value of *d* was chosen as 4.0 and 3.0 nm, respectively, for plus-end (red) and minus-end (green) loading regardless of nucleotide state. The value of $\tau(0)$ at the ADP state was defined as 1 s while that at the nucleotide-free and AMP-PNP states was chosen as 150 s.

result, and indicate that weak binding in the ADP state and strong binding in the nucleotide-free and AMP-PNP states can be attributed to a small and large binding energy, respectively.

Taking into account the present results, a mechanistic model of kinesin motility proposed to date (2–7, 11) is summarized as illustrated in Fig. 4. Although ⟨T,D⟩ and ⟨D,O⟩ states in Fig. 4 *C* and *E*, respectively, have not been identified by the present method, we assume that these states exist as intermediates in the

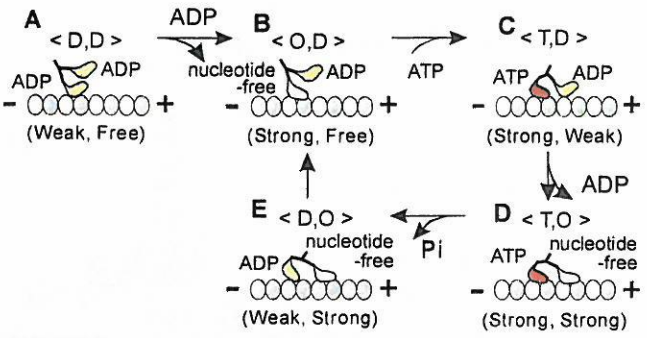

Fig. 4. Summary of the present results in relation to the walking model of kinesin motility. Upon weak attachment of one of two ADP-bound heads of kinesin to the microtubule (*A*, ⟨D,D⟩ state), the bound ADP immediately detaches, resulting in nucleotide-free strong binding of the attached head (*B*, ⟨O,D⟩ state). Due to the binding of ATP to the attached head, zippering of the neck linker of the ATP-bound head is expected to occur so that the free ADP-bound head tends to move forward, resulting in weak binding (*C*, ⟨T,D⟩ state). The bound ADP immediately detaches, so that the leading head assumes the strong binding state similar to that of the trailing head (*D*, ⟨T,O⟩ state). This double-headed binding state is the most stable in a single cycle of the present walking model. This ⟨T,O⟩ state is the only state in which double-headed binding was demonstrated by the present unbinding force measurements. ATP on the trailing head is then hydrolyzed into ADP and inorganic phosphate (Pi), so that the ADP-Pi-bound trailing head or the ADP-bound trailing head after Pi release becomes unstable (*E*, ⟨D,O⟩ state), resulting in its immediate detachment from the microtubule. As a result, the molecule takes an 8-nm step forward (the size of a tubulin heterodimer) that accompanies ATP hydrolysis. Note that the existence of states ⟨T,D⟩ and ⟨D,O⟩ have not yet been confirmed by the present method, but are assumed to exist as intermediates.

ATPase cycle. The present results suggest that the leading and the trailing ADP-bound heads in these states are in a weak-binding state.

Furthermore, it is inferred that the probability of detachment of the trailing head during double-headed binding is higher than that of the leading head by $\exp[F'(4.0–3.0\ \text{nm})/k_BT]$, where F' is the internal stress between the two attached heads. Here, if F' is assumed to be 4 pN, the unbinding force we obtained, at room temperature, the trailing head will detach more readily by a factor of about 3. Thus, such a difference in stability of the attachment of the leading and trailing heads to the microtubule caused by mechanical properties (vectorial stress and strain imposed on motor domain) coupled with enzymatic properties (binding of ATP and its hydrolytic products), can be seen to be essential to the mechanism of directional motility of processive molecular motors.

We thank Mr. Mark Chee of Duke University and Mr. Charles V. Sindelar of University of California, San Francisco, for critical reading of the manuscript and colleagues at Waseda University and Japan Science and Technology Corporation (CREST) for encouragement and support. This research was partly supported by Grants-in-Aid for Scientific Research, for Scientific Research on Priority Areas, and for the Bio-venture Project from the Ministry of Education, Culture, Sports, Science and Technology of Japan, and by Grants-in-Aid from CREST and the Mitsubishi Foundation.

1. Svoboda, K. & Block, S. M. (1994) *Cell* **77,** 773–784.
2. Hackney, D. D. (1994) *Proc. Natl. Acad. Sci. USA* **91,** 6865–6869.
3. Cross, R. A. (1995) *J. Muscle Res. Cell Motil.* **16,** 91–94.
4. Rice, S., Lin, A. W., Safer, D., Hart, C. L., Naber, N., Carragher, B. O., Cain, S. M., Pechatnikova, E., Wilson-Kubalek, E. M., Whittaker, M., *et al.* (1999) *Nature (London)* **402,** 778–784.
5. Vale, R. D. & Milligan, R. A. (2000) *Science* **288,** 88–95.
6. Lockhart, A., Crevel, I. M. & Cross, R. A. (1995) *J. Mol. Biol.* **249,** 763–771.
7. Howard, J. (1996) *Annu. Rev. Physiol.* **58,** 703–729.
8. Vale, R. D., Funatsu, T., Pierce, D. W., Romberg, L., Harada, Y. & Yanagida, T. (1996) *Nature (London)* **380,** 451–453.
9. Kojima, H., Muto, E., Higuchi, H. & Yanagida, T. (1997) *Biophys. J.* **73,** 2012–2022.
10. Svoboda, K., Schmidt, C. F., Schnapp, B. J. & Block, S. M. (1993) *Nature (London)* **365,** 721–727.
11. Kawaguchi, K. & Ishiwata, S. (2001) *Science* **291,** 667–669.
12. Hancock, W. O. & Howard, J. (1998) *J. Cell Biol.* **140,** 1395–1405.
13. Weingarten, M. D., Lockwood, A. H., Hwo, S. Y. & Kirschner, M. W. (1975) *Proc. Natl. Acad. Sci. USA* **72,** 1858–1862.

14. Hyman, A. A. (1991) *J. Cell Sci.* **s14,** 125–127.
15. Nishizaka, T., Seo, R., Tadakuma, H., Kinosita, K., Jr., & Ishiwata, S. (2000) *Biophys. J.* **79,** 962–974.
16. Nishizaka, T., Miyata, H., Yoshikawa, H., Ishiwata, S. & Kinosita, K., Jr. (1995) *Nature (London)* **377,** 251–254.
17. Hancock, W. O. & Howard, J. (1999) *Proc. Natl. Acad. Sci. USA* **96,** 13147–13152.
18. Woehlke, G., Ruby, A. K., Hart, C. L., Ly, B., Hom-Booher, N. & Vale, R. D. (1997) *Cell* **90,** 207–216.
19. Alonso, M. C., van Damme, J., Vandekerckhove, J. & Cross, R. (1998) *EMBO J.* **17,** 945–951.
20. Kikkawa, M., Okada, Y. & Hirokawa, N. (2000) *Cell* **100,** 241–252.
21. Hirose, K., Lockhart. A., Cross, R. A. & Amos, L. A. (1995) *Nature (London)* **376,** 277–279.
22. Kikkawa, M., Sablin, E. P., Okada, Y., Yajima, H., Fletterick, R. J. & Hirokawa, N. (2001) *Nature (London)* **411,** 439–445.
23. Quinlan, M. E., Forkey, J. N. & Goldman, Y. E. (2001) *Nat. Struct. Biol.* **8,** 478–480.
24. Sosa, H., Peterman, E. J., Moerner, W. E. & Goldstein, L. S. (2001) *Nat. Struct. Biol.* **8,** 540–544.

Myosin V is a left-handed spiral motor on the right-handed actin helix

M. Yusuf Ali[1–3], Sotaro Uemura[4], Kengo Adachi[1,2], Hiroyasu Itoh[2,5], Kazuhiko Kinosita Jr[1–3] and Shin'ichi Ishiwata[2,4]

[1]*Center for Integrative Bioscience, Okazaki National Research Institutes, Higashiyama 5-1, Myodaiji, Okazaki 444-8585, Japan.* [2]*CREST (Core Research for Evolutional Science and Technology), 'Genetic Programming' Team 13, Nogawa 907, Miyamae-ku, Kawasaki 216-0001, Japan.* [3]*Department of Physics, Faculty of Science and Technology, Keio University, Hiyoshi 3-14-1, Kohoku-ku, Yokohama 223-8522, Japan.* [4]*Department of Physics, School of Science and Engineering, Waseda University, Okubo 3-4-1, Shinjuku-ku, Tokyo 169-8555, Japan.* [5]*Tsukuba Research Laboratory, Hamamatsu Photonics KK, Tokodai, Tsukuba 300-2635, Japan.*

Published online: 13 May 2002, DOI: 10.1038/nsb803

Myosin V is a two-headed, actin-based molecular motor implicated in organelle transport. Previously, a single myosin V molecule has been shown to move processively along an actin filament in discrete ~36 nm steps. However, 36 nm is the helical repeat length of actin, and the geometry of the previous experiments may have forced the heads to bind to, or halt at, sites on one side of actin that are separated by 36 nm. To observe unconstrained motion, we suspended an actin filament in solution and attached a single myosin V molecule carrying a bead duplex. The duplex moved as a left-handed spiral around the filament, disregarding the right-handed actin helix. Our results indicate a stepwise walking mechanism in which myosin V positions and orients the unbound head such that the head will land at the 11th or 13th actin subunit on the opposing strand of the actin double helix.

Class V myosin has two globular motor domains that interact with an actin filament to generate force upon ATP hydrolysis; the motor supports a wide variety of cellular movements[1–5]. Myosin V consists of two identical heavy chains, each composed of an N-terminal motor domain ('head'), six IQ motifs that bind light chains ('neck'), a coiled coil tail domain and a globular cargo-binding domain[1]. A single myosin V molecule moves along an actin filament for many catalytic cycles without dissociating from the filament[6–8]. Steps of ~36 nm have been identified in this processive movement[6,7,9], and the two heads of myosin V have been shown to bind to actin ~36 nm apart[10], suggesting that myosin V 'walks' on actin with 36 nm strides by alternate binding of the two heads.

Whether myosin V really walks and, if so, how its step size is determined are fundamental issues relating to the motor mechanism. The step size measurements above were made either with myosin V fixed on a surface[6,9] or actin filaments lying on a surface[7,10] such that myosin V could approach an actin filament only from one side. Myosin V had to move straight on actin; thus, the motor may well have been forced to step on blue actin subunits (Fig. 1*a*), which are 36 nm apart. Here we allow myosin V to freely rotate around an actin filament and monitor how or whether the motor walks. If myosin V walks but its natural step size is slightly longer or shorter than 36 nm, unconstrained motion should be a right- or left-handed, long-pitch spiral.

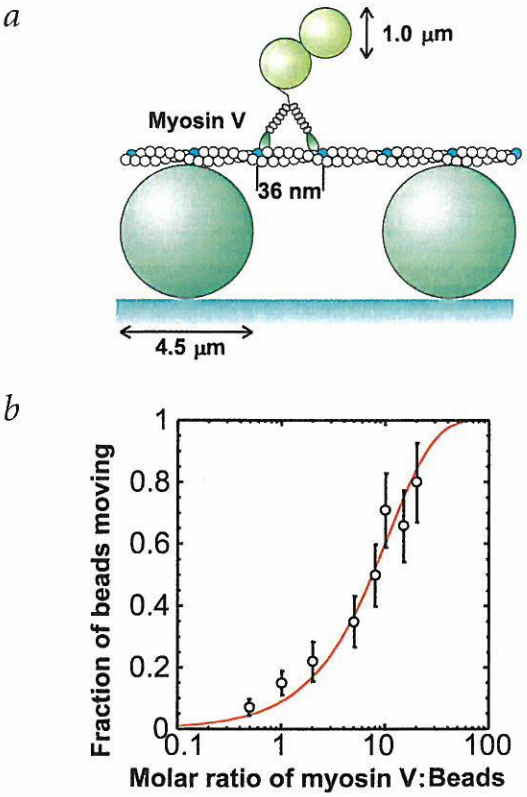

Fig. 1 Experimental design. ***a***, Motility assay system (not to scale). The heads of myosin V are green; the necks, gray. Every 13th actin subunit is blue. ***b***, Fraction of beads that moved more than ~0.5 μm along an actin filament (see Methods). Error bars indicate $\pm n^{1/2} N^{-1}$, where n is the number of beads that moved and N (50 or 100) is the number of trials. Line shows the theoretical probability that a bead carries one or more active motors, $1 - \exp(-\lambda c)$, where c is the molar ratio of myosin V to beads and λ (0.092) is the fit parameter[30].

Alternatively, steps may be so short that myosin V sequentially interacts with neighboring actin subunits in one of the two helical strands (crossing onto the other strand would require extremely 'bowlegged' necks). In this case, myosin V would undergo extensive right-handed rotation, as does RNA polymerase around DNA[11]. A single head might glide over many actin subunits in a strand during one ATPase cycle[12]. Such gliding is not necessarily inconsistent with the observed ~36 nm steps, because gliding would be forced to stop at ~36 nm when rotation around the actin filament is prohibited. Direct observation of rotation will distinguish between these cases.

Myosin V rotates as a left-handed screw

To allow myosin V to freely rotate around an actin filament, we suspended an actin filament between two large (4.5 μm) beads immobilized on a glass surface[13] (Fig. 1*a*); a similar system has been reported[14]. Using optical tweezers, we positioned a duplex of smaller (1 μm) beads that were pre-incubated with myosin V at the molar ratio of 1:1 onto the midpoint of the filament. When the laser trap was turned off, the duplex started to move along and, at the same time, rotate around the actin filament. Results from experiments in which single 1 μm beads prepared at various myosin:bead ratios were allowed to move along an actin filament (Fig. 1*b*) indicate that a single myosin V molecule is most likely responsible for this motion. The fraction of moving beads as a function of myosin:bead ratio fit well to a

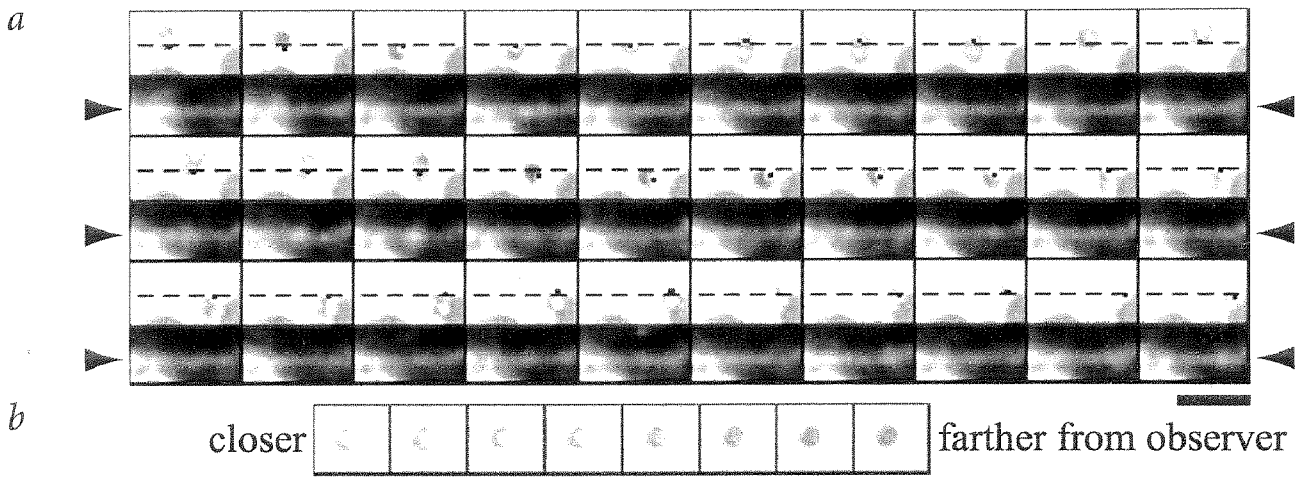

Fig. 2 Spiral motion of myosin V around an actin filament at 400 μM ATP. ***a***, Sequential images at 1 s intervals. Upper and lower panels show bright-field and corresponding fluorescence images, respectively. The bar corresponds to 5 μm. Dashed lines are the position of the actin filament deduced from lower panels (arrow heads); dots, center of the beads that are judged to be on actin. Note that the actin filament remained straight. ***b***, Images of a 1 μm bead at decreasing heights (left to right at ~0.2 μm intervals) from the glass surface. Because our images represent views from above the sample[27], white beads in (*a*) and (*b*) are closer to the observer, whereas the black beads are farther away.

Poisson distribution (solid line); this fit indicates that >95% of moving beads were driven by only one myosin V molecule. These single beads also rotated around the actin filament, but precise analysis was far easier with the bead duplex.

Myosin V-decorated bead duplexes were allowed to move along an actin filament at 400 μM ATP, where the linear velocity of the motor was maximal. Sequential video images of such a system reveal that the bead duplex rotates around the actin filament (Fig. 2*a*; movies at *http://k2.ims.ac.jp*). In these images, a bead that appears white is closer to the observer, whereas a black one is farther from the observer (Fig. 2*b*). Thus, the duplex moved as a left-handed screw, making two revolutions while traveling over ~4.4 μm. Such complete rotations were observed at all ATP concentrations examined, and all complete rotations were left-handed. This is in contrast to myosin II, which rotates as a right-handed screw[15]. Not all bead duplexes bound to an actin filament showed clear rotation (Table 1), the primary reasons being either that they did not move long enough or the filament was <2 μm from the surface. There were 10 instances where, with no apparent reason, the duplex moved for >1 μm without appreciable rotation (Fig. 3*c*; Table 1). Presumably, the filament height was ~2 μm or some debris was attached to the duplex and impeded rotation. Indeed, we occasionally observed beads carrying relatively large debris, including short actin filaments, in the fluorescence image. Smaller debris would have been unnoticed. That myosin V can move without rotation is consistent with the previous observations of stepping on actin lying on a surface.

Table 1 Summary of bead duplex experiments at 1:1 myosin V:bead

Total number of bead duplexes tested at 1–1,000 μM ATP	1,040
Duplexes bound to actin	229
Active duplexes[1]	156 (100%)
Moved only for <1 μm	57 (37%)[2]
Moved for >1 μm and made >0.5 revolution	43 (28%)
Moved for >1 μm without rotation[3]	46 (29%)
Moved for >1 μm without rotation[4]	10 (6%)

[1]Defined as having moved along actin for >0.5 μm.
[2]Actin filaments were not long enough in 22 cases.
[3]The filament height was <2 μm.
[4]Reason for no rotation is unknown.

Unconstrained step size is 34.8 nm

From the time courses of rotation and displacement along actin for individual bead duplexes (Fig. 3*a–c*), we determined the relation between rotation and displacement for all duplexes that made >~1 revolution (solid lines in Fig. 3*d*). All of these curves (Fig. 3*d*) are within a narrow zone, showing that the rotation and displacement are well correlated, except for the presumably impeded cases (Fig. 3*c*, dotted lines in Fig. 3*d*). Myosin V travels a distance of 2.2 ± 0.3 μm per one left-handed revolution (mean ± s.d. for linear fits to 22 solid curves in Fig. 3*d*), which is constant over ATP concentrations from 1 μM to 1 mM, where the linear velocity of the motor changes from 5 to 320 nm s^{-1}.

The left-handed rotation of single myosin V molecules indicates a step size slightly smaller than the actin helical repeat of 36 nm (Fig. 4). Steps shorter than 18 nm, including the case of sliding along one helical strand[12], would result in right-handed rotation. Because the difference between the helical repeat of actin and the step size of myosin V motor (blue/cyan *versus* red in Fig. 4) must add up to one full turn of actin helix (72 nm) over the travel distance of 2.2 μm, the average step size is given by 36 nm × (2,200 nm − 72 nm) / (2,200 nm) = 34.8 nm. This number derived from the actin repeat is rather precise (±0.1 nm) and is insensitive to the uncertainty in the 2,200 nm value. On average, myosin V rotates 6° (360° × 34.8 nm / 2,200 nm) per step left around the actin filament.

Step size is constant

The step size of 34.8 nm above is the one at no load. Hydrodynamic friction against the bead duplex is given by $2 \times 6\pi\eta a v$, where η (0.001 N m^{-2} s) is the viscosity of water; a (0.5 μm), the bead radius; and v (<320 nm s^{-1}), the bead velocity. Thus, the frictional load is at most 0.006 pN, far less than the maximal pulling force, 3 pN, produced by a single myosin V molecule[6]. The frictional torque against rotation is given by[16]: $(2 \times 8\pi\eta a^3 + 6\pi\eta a^3 + 6\pi\eta a r^2)\omega$, where r is the distance between

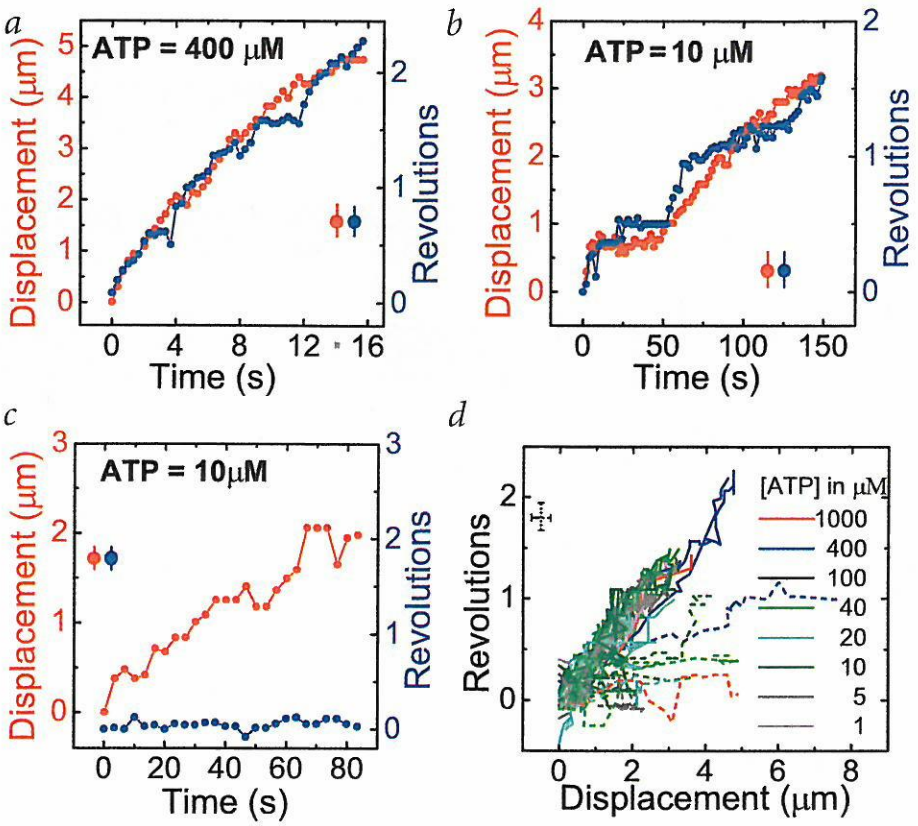

Fig. 3 Correlations between displacement and rotation. ***a,b***, Typical time courses. Error bars are likely uncertainties in human judgment (see Methods). ***c***, A case of linear motion. ***d***, Relationship between sliding distance and rotation. ATP concentrations are distinguished by color and indicated in μM. Dashed lines represent linear motion or irregular rotation.

the center of the outer bead and actin filament, and ω is the angular velocity. A duplex with r = 1.2 μm was found to rotate at ω = 0.9 radian s^{-1}, giving the highest torque of 20 pN nm, and several other duplexes showed the torque at >10 pN nm. These values are apparently quite high, comparable to the 40 pN nm of torque produced by the rotary molecular motor F_1ATPase[17]. In one step, however, myosin V rotates only 6° = 0.1 radian; thus, the work done for rotation is at most 2 pN nm (20 pN nm × 0.1 radian), only half the thermal energy. The frictional torque is completely negligible at low ATP concentrations.

The step size of myosin V is ~35 nm under a variety of conditions. Duplexes prepared at 10^4 myosin V molecules per bead also made one left-handed rotation per 2.5 ± 0.5 μm at 40 μM ATP (n = 8). This is a loaded condition, because a stepping myosin V molecule has to work against others that are simultaneously bound to actin. Consistent with this, a step size of 35 nm has recently been reported[9] under a load of 1 pN. Load independence of the step size may imply that myosin V does not readily fluctuate toward right or left when it stands on one foot ('head'). To determine if myosin V tends to interact with intervening actin subunits during the long strides, we examined bead motions at increasing ionic strengths, which would result in diminished actin–myosin interaction[18]. The average distances traveled at 50, 100, 200 and 300 mM KCl were 2.1, 2.1, 1.5 and 1.1 μm (n = 8, 23, 7 and 7), respectively, indicating reduction in processivity as expected. Rotations, however, were all left-handed and one revolution per 2.3 ± 0.5 μm at all ionic strengths. Myosin V seems to stride over intervening actin subunits.

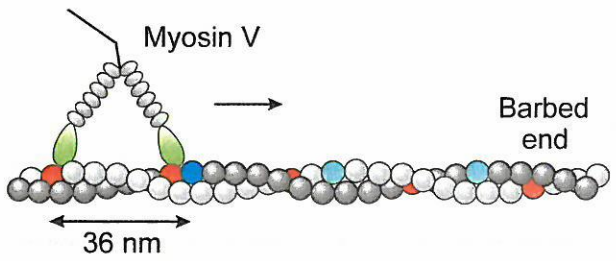

Fig. 4 Interpretation of the left-handed rotation. Stepping on every 11th actin subunit (red) would result in left-handed spiral movement, whereas linear movement is expected on the 13th subunits (blue/cyan). The estimated step size of 34.8 nm is between the 11th and 13th subunits.

Discussion

Spiral motion of a single motor molecule around a helical track should reveal how the motor successively interacts with the repeating units composing the track. To our knowledge, myosin V is the first example of a processive motor spiraling with a pitch incommensurate to the helical pitch of the track; kinesin[19] and RNA polymerase[11] precisely follow their respective helical track. The deduced step size of 34.8 nm for myosin V is much larger than the intersubunit distance of 5.5 nm in one strand of the actin filament, indicating that myosin V walks with long strides; sliding along one strand of actin helix[12] is unlikely.

There are 13 actin subunits per 36 nm, counting both strands. Our results indicate that, during unconstrained walking, myosin V aims at the 11th (red, Fig. 4) or 13th (blue) actin subunit on the opposing strand (binding to the 12th subunit on the opposite side of the filament would be sterically hindered). This almost straight walking is not a trivial task, because, unlike a human, the two feet ('heads') of myosin V are identical and related by basic two-fold symmetry. Landing on the 13th subunit would require 180° twist of the neck from its symmetry-related orientation. Although the twist would imply extensive flexibility in the neck (and/or head), a proper posture of the bound head and neck is to aim at a correct target among identical actin subunits in the double helix. Recent reports[20,21] suggest that ~25 nm of the step size of ~35 nm is accounted for by the swing of the bound neck and the rest by diffusion of the unbound head. The swing, then, must be a delicate combination of bending and twisting that ensures diffusional landing on, mostly, the 11th or 13th subunit, irrespective of load.

The natural way of walking is one in which the two heads move forward alternately[22]. Alternate binding of two identical heads should result in 180° rotation of the entire molecule

around its symmetry axis every time the motor steps[22], but kinesin failed to show this[23]. We examined whether our bead duplex would rotate around the point of attachment to actin at low concentrations of ATP (500 nM–1 μM), but, similar to kinesin, we have seen no convincing evidence of 180° rotation. This is apparently inconsistent with simple walking, although oblique attachment of myosin V to the bead surface may have impeded the rotation of the bead duplex. Simple walking has also been challenged by recent findings: myosin VI[9,24] and mutated myosin V[12], both short necked, made large steps apparently incompatible with the head and neck sizes. Conformational changes, or melting, in the head/neck region would be required to allow a long stride, as in kinesin[25]. Whether, or in which direction, these short-necked myosins rotate remains to be seen.

Methods

Sample preparation. Myosin V was purified from chick brain[26]. Rabbit skeletal actin was biotinylated and stained with phalloidin-tetramethylrhodamine essentially as described[27] but without crosslinking; the molar ratio of actin to biotin-PE-maleimide was 1:2. Polystyrene beads (1 μm, F-8814, Molecular Probes) were incubated for 30 min in buffer A (10 mM imidazole, pH 7.6, 100 mM KCl, 4 mM $MgCl_2$, 1 mM EGTA and 5 mM dithiothreitol (DTT)) containing 10 mg ml^{-1} BSA and centrifuged for 15 min at 18,000× *g*. Of the beads, ~10% formed duplexes. The beads were coated with myosin V as described[7]. To assess the coating efficiency (Fig. 1*b*), a single bead was selected and held in an optical trap[28] near an actin filament suspended in buffer A containing 1 mM ATP (see below). Then, the filament was moved across the bead in various directions by moving the microscope stage until the bead attached to the filament. If attachment did not occur within ~1 min, the bead was repositioned and the manipulation was repeated several times. After attachment, the trap was turned off to allow movement of the bead along actin. The fraction of beads that were bound but did not move >~0.5 μm was <~0.1 (0.03 at the myosin/bead ratio, c, of 0.5 and 0.09 at c = 1). The motility assay below was done on duplex beads prepared at c = 1, unless stated otherwise.

Motility assay. Carboxylated polystyrene beads (4.5 μm; Polyscience) were amino-derivatized and biotinylated[29]. The beads were incubated with 10 mg ml^{-1} streptavidin, washed and infused in a flow chamber. After 10 min, 5 mg ml^{-1} BSA was infused and incubated for 1 min. Biotinylated and labeled actin filaments were infused and allowed to bind to the 4.5 μm beads to form actin bridges. Then, 0.25–1 pM of beads decorated with myosin V in buffer A containing ATP, 6 mg ml^{-1} glucose, 0.2 mg ml^{-1} glucose oxidase, 0.02 mg ml^{-1} catalase and 0.2% β-mercaptoethanol were infused into the flow cell. To minimize Brownian motion, only tightly suspended actin filaments were used. If such a filament was not found, we moved the 4.5 μm beads with the optical tweezers to form a tight actin bridge. Torsional Brownian motion of actin is <±50° for a 10 μm filament[13]. Finally, we positioned a bead duplex onto an actin filament using the optical tweezers, moved the filament until it bound the duplex and turned off the optical trap to let the duplex move along the actin filament. If unsuccessful, this maneuver was repeated 10–30×. The microscope system has been described[28]; bright-field images showing bead movement and fluorescence images showing actin filaments were simultaneously recorded with video cameras. Positions and orientations of bead duplexes were analyzed by eye to the precision of ±0.5 μm and ±0.25 revolutions. For the orientation, video images were compared with pairs of overlapping circles representing views of two spheres at known angles. Because of drift in the microscope focus, there were rare occasions where distinction between the two beads became difficult; large deviations from linear relationship in Fig. 3*d*, seen in some curves, may be due to human error. Observations were made at 23 °C.

Acknowledgments

We thank R. Yasuda, H. Noji, T. Nishizaka, Y. Harada and T. Nishinaka for discussion; L.B. Roksana, K. Kawashima, K. Yogo, R. Shimo, J. Yamaguchi and H. Kubota for sample preparation; M. Shio for microscope setup and H. Umezawa for laboratory management. M.Y.A. was a research fellow of the Japan Society for the Promotion of Science. This work was supported in part by Grants-in-Aid from the Ministry of Education, Culture, Sports, Science, and Technology of Japan.

Competing interests statement

The authors declare that they have no competing financial interests.

Correspondence should be addressed to K.K. *email: kazuhiko@ims.ac.jp*

Received 7 March, 2002; accepted 16 April, 2002.

1. Cheney, R.E. *et al. Cell* **75**, 13–23 (1993).
2. Mermall, V., Post, P.L. & Mooseker, M.S. *Science* **279**, 527–533 (1998).
3. Rogers, S.L. & Gelfand, V.I. *Curr. Biol.* **8**, 161–164 (1998).
4. Tabb, J.S., Molyneaux, B.J., Cohen, D.L., Kuznetsov, S.A. & Langford, G.M. *J. Cell Sci.* **111**, 3221–3234 (1998).
5. Hodge, T. & Cope, M.J. *J. Cell Sci.* **113**, 3353–3354 (2000).
6. Mehta, A.D. *et al. Nature* **400**, 590–593 (1999).
7. Rief, M. *et al. Proc. Natl. Acad. Sci. USA* **97**, 9482–9486 (2000).
8. Sakamoto, T., Amitani, I., Yokota, E. & Ando, T. *Biochem. Biophys. Res. Commun.* **272**, 586–590 (2000).
9. Rock, R.S. *et al. Proc. Natl. Acad. Sci. USA* **98**, 13655–13659 (2001).
10. Walker, M.L. *et al. Nature* **405**, 804–807 (2000).
11. Harada, Y. *et al. Nature* **409**, 113–115 (2001).
12. Tanaka, H. *et al. Nature* **415**, 192–195 (2002).
13. Yasuda, R., Miyata, H. & Kinosita, K. Jr *J. Mol. Biol.* **263**, 227–236 (1996).
14. Yamada, T. *et al. Biophys. J.* **80**, 80a (2001).
15. Nishizaka, T., Yagi, T., Tanaka, Y. & Ishiwata, S. *Nature* **361**, 269–271 (1993).
16. Suzuki, N., Miyata, H., Ishiwata, S. & Kinosita, K. Jr *Biophys. J.* **70**, 401–408 (1996).
17. Yasuda, R., Noji, H., Kinosita, K. Jr & Yoshida, M. *Cell* **93**, 1117–1124 (1998).
18. Homsher, E., Wang, F. & Sellers, J.R. *Am. J. Physiol.* **262**, 714–723 (1992).
19. Gelles, J., Schnapp, B.J. & Sheetz, M.P. *Nature* **331**, 450–453 (1988).
20. Moore J.R., Krementsova, E.B., Trybus, K.M. & Warshaw, D.M. *J. Cell Biol.* **155**, 625–635 (2001).
21. Veigel, C., Wang, F., Bartoo, M.L., Sellers, J.R. & Molloy, J.E. *Nature Cell Biol.* **4**, 59–65 (2002).
22. Howard, J. *Annu. Rev. Physiol.* **58**, 703–729 (1996).
23. Hua, W., Chung, J. & Gelles, J. *Science* **295**, 844–848 (2002).
24. Nishikawa, S. *et al. Biochem. Biophys. Res. Commun.* **290**, 311–317 (2002).
25. Rice, S. *et al. Nature* **402**, 778–784 (1999).
26. Cheney, R.E. *Methods Enzymol.* **298**, 3–18 (1998).
27. Noji, H., Yasuda, R., Yoshida, M. & Kinosita, K. Jr *Nature* **386**, 299–302 (1997).
28. Miyata, H. *et al. Biophys. J.* **68**, 286s–290s (1995).
29. Harada, Y. *et al. Biophys. J.* **76**, 709–715 (1999).
30. Block, S.M., Goldstein, L.S. & Schnapp, B.J. *Nature* **348**, 348–352 (1990).

ACADEMIC PRESS

Biochemical and Biophysical Research Communications 293 (2002) 1550–1555

BBRC

www.academicpress.com

Visualization and force measurement of branching by Arp2/3 complex and N-WASP in actin filament

Ikuko Fujiwara,[a] Shiro Suetsugu,[b] Sotaro Uemura,[a] Tadaomi Takenawa,[b] and Shin'ichi Ishiwata[a,c]

[a] *Department of Physics, School of Science and Engineering, Waseda University, 3-4-1 Okubo, Shinjuku, Tokyo 169-8555, Japan*
[b] *Department of Biochemistry, Institute of Medical Science, University of Tokyo, Tokyo, Japan and CREST, Japan Science and Technology Corporation (JST), 4-6-1 Shirokanedai, Minato, Tokyo 108-8639, Japan*
[c] *Advanced Research Institute for Science and Engineering, Waseda University, 3-4-1 Okubo, Shinjuku, Tokyo 169-8555, Japan*

Received 22 April 2002

Abstract

To determine whether the Arp2/3 complex activated by N-WASP (VCA) branches actin filaments at the side (side branching), or at the barbed (B-)end (end branching) of the mother filaments, we have directly observed the branching process of actin filaments and examined single-molecule unbinding under optical microscope. We found that side branching was predominant, though not exclusive. At the initial stage of polymerization, the branching at the B-end occurred and subsequently the side branching started to occur. In either type of branching, the mother and daughter filaments elongated at nearly the same rate (growing type). Independently of the stage of polymerization, branching due to the direct coupling of filaments with an acute angle to the mother filaments (a coupling type) occurred. Phalloidin suppressed the growing type of branching but not the coupling type, implying that actin monomers are required for the former but not the latter. We found, by single molecule measurements using optical tweezers, that the Arp2/3 complex attaches to the side of actin filaments and the N-WASP appears to detach from the actin–Arp2/3 complex at 6–7 pN.

Keywords: Arp2/3 complex; VCA; N-WASP; Optical tweezers; Branching of actin filaments; Polymerization of actin; Total internal reflection fluorescence microscopy

Polymerization–depolymerization dynamics of actin filaments is a key process for many cellular events. The dynamics of the filaments is spatially and temporarily regulated by various kinds of functions of regulatory proteins such as capping, severing, and branching, together with control through the binding of Ca^{2+} and phosphorylation and so on. Among the regulatory proteins, the Arp2/3 complex and a WASP (Wiskott–Aldrich syndrome protein) family have recently been recognized as important for regulating polymerization of actin and creating fast-growing B-ends and for generating a branched actin filament network at the leading edge of moving cells [1–5].

All WASP family proteins have VCA (verprolin-homology, cofilin-homology, and acidic or C-terminal region of WASP family proteins) domain, a minimum region for the activation of Arp2/3 complex [6–9], which results in the formation of branched and mesh-like actin filaments [10]. Not only the electron microscopic structure [11] of Arp2/3 complex in the actin filament but also its crystal structure [12] have recently been determined, so that the mechanism of branching is going to be clarified on a molecular level. But, a controversy exists on the mechanism of branching of actin filaments, especially, on the branching from the side or the end of the mother actin filaments [13–16]. Although total internal reflection fluorescence microscopy [17] for imaging fluorescent single actin filaments has recently revealed a side branching that preferably occurs near the B-end [18–20], a more detailed analysis under different conditions is required to clarify the branching mechanism.

We examined how branching of actin filaments occurs during polymerization in the presence of Arp2/3

* Corresponding author. Fax: +81-3-5286-3437.
E-mail address: ishiwata@mn.waseda.ac.jp (S. Ishiwata).

0006-291X/02/$ - see front matter
PII: S0006-291X(02)00421-7

complex and VCA. As time proceeds after the addition of salts, not only the polymerization of individual actin filaments but also the branching of the filaments becomes observable. We could distinguish the branching from simple overlapping of two filaments by observing translational and bending Brownian movement of filaments.

Materials and methods

Preparation of proteins. Pure actin was prepared from rabbit muscle [21] except that tropomyosin–troponin complex was removed before preparing acetone powder according to Ebashi with slight modifications [22]. Bovine Arp2/3 complex was prepared according to a published protocol [23]. GST-fusion VCA was purified as described previously [7]. Fluorescent-dye labeling (100%) of Cys 374 of actin was done by tetramethylrhodamine-5-maleimide (TMR-5-MA, Molecular Probes) dissolved in dimethylformamide (a final concentration, less than 0.1%; Aldrich) in 0.1 M KCl, 1 mM $MgCl_2$, 0.2 mM ATP, and 10 mM imidazole buffer, pH 7.0. The free fluorescent-dye was removed by ultracentrifugation of the labeled F-actin solution and then by column chromatography (Sephadex G-25) of labeled G-actin solution.

Observation of polymerization and branching. Actin (42 kDa, 500 nM, of which 10 % was labeled with TMR-5-MA) in the presence of Arp2/3 complex (220 kDa, 70 nM) and GST-fusion VCA (39 kDa, 600 nM) was started to be polymerized in a test tube at time zero by addition of a polymerization buffer, i.e., 50 mM KCl, 1 mM $MgCl_2$, 4 mM ATP, 1 mM EGTA, 10 mM imidazole buffer, pH 7.0, 100 mM dithiothreitol, 20 μg/ml catalase, 100 μg/ml glucose oxidase, 3 mg/ml glucose, and 0.3 (w/v)% methylcellulose at room temperature (27 °C). Immediately after the addition of salt, the solution was put on a glass cover and the four sides of a cover slip were sealed with enamel, and then the microscopic observation was started. To image the filaments

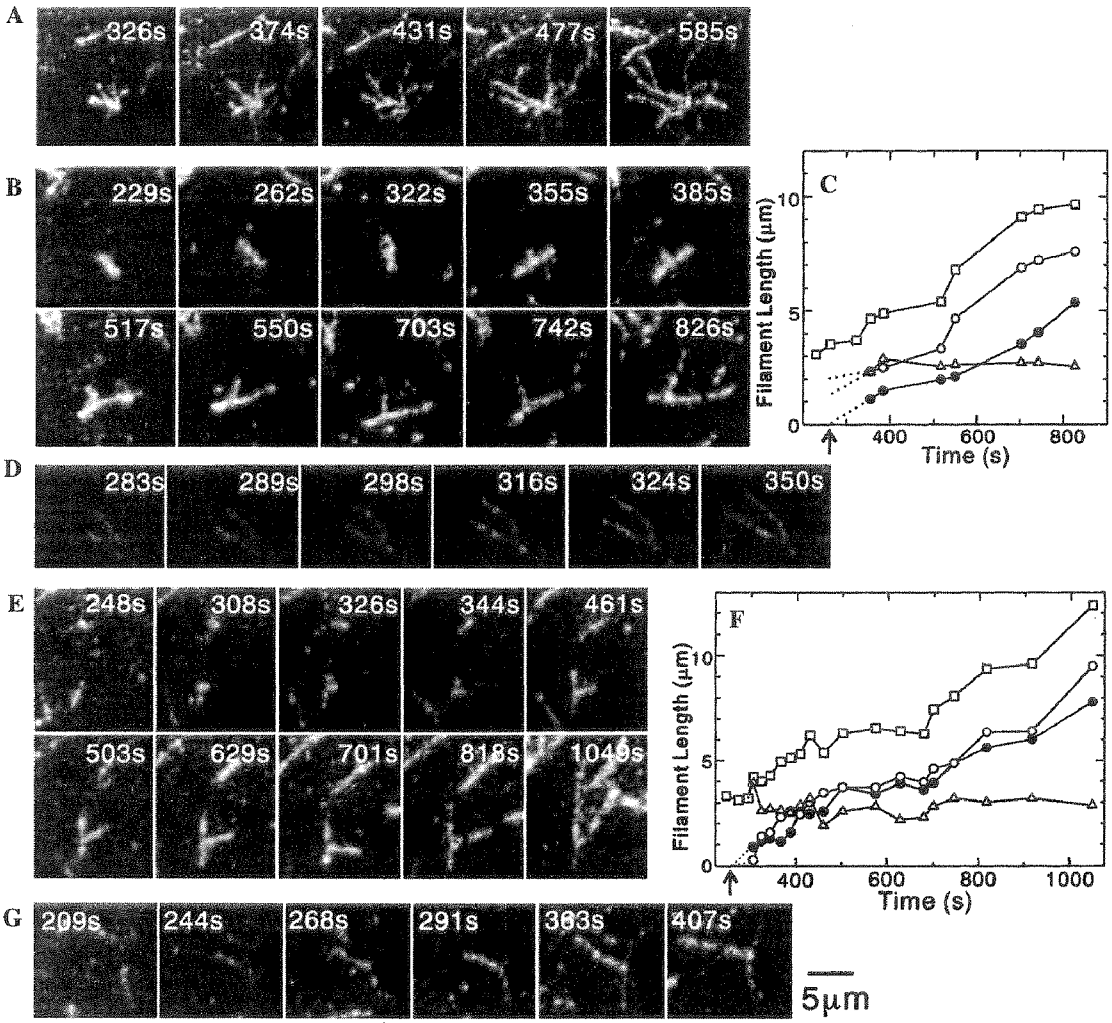

Fig. 1. Typical patterns of fluorescence image showing branching and polymerization of actin filaments observed in the presence of Arp2/3 complex and VCA and in the absence of phalloidin. (A) Formation of a dendritic network of actin filaments (movies are available at http://www.phys.waseda.ac.jp/bio/ishiwata/movies.html). (B) A growing type of side branching (movie). (C) Time course of the polymerization of the mother and daughter filaments in B. Here, open squares show total length, open circles the length between the B-end and the branching point, and open triangles the length between the P-end and the branching point of the mother filament. Closed circles show the length of the daughter filament. (D) A coupling type of side branching (movie). (E) A growing type of B-end branching (movie). (F) Time course of the polymerization of the mother and daughter filaments in E (symbols, the same as in C). (G) A coupling type of B-end branching (movie). The time (s) indicates that after the addition of salts. Scale bar, 5 μm.

in a high contrast, we added methylcellulose, which considerably suppressed the lateral Brownian movement of the filaments and partly the longitudinal movement. Note that the Brownian movement was too vigorous to obtain a clear fluorescence image of the filaments when the concentration of methylcellulose was less than 0.3%. When the effect of phalloidin was examined, the TMR-5-MA(10%)-labeled actin was first polymerized in the presence of phalloidin. The imaging of branching was begun just after the addition of the Arp2/3 complex and VCA to the actin filaments at room temperature (27 °C).

Microscopic analysis. Fluorescent dye-labeled single actin filaments were visualized by total internal reflection fluorescence microscopy (IX70, Olympus) with a green laser (#4301-050, μGreen) [17], which illuminates only ~150 nm in depth above the cover slip. Fluorescence images were collected using a SIT camera (C2400, Hamamatsu Photonics) equipped with an image intensifier (VS4-1815, Video Scope) and recorded on a Hi-8 video (EVO9650, Sony). To obtain the fluorescence image of high contrast for individual actin filaments, eight consecutive images taken at a video rate (for 0.27 s) were superimposed by using Scion image software (Scion Image). The spatial resolution was estimated to be 0.5 μm.

Microscopic measurement of unbinding force. To observe unbinding of an actin filament from the Arp2/3 complex with VCA by imposing external load, various concentrations (from 33 to 800 nM) of biotinylated VCA were attached to the cover slip. The cover slip was coated with avidin attached to the biotinylated BSA, which was adsorbed to the glass surface beforehand. The solution containing rhodamine phalloidin-labeled actin (6.6 nM) filaments and the Arp2/3 complex (12 nM), which was mixed just before the experiments, was infused into the cell. The bead (1 μm in diam)-tailed actin filaments (gelsolin, a B-end capping protein, was covalently fixed to the bead surface) were prepared according to the method previously described [24]. The bead was manipulated with optical tweezers of which trap stiffness was set to be 0.10 pN/nm. The loading rate used for measuring the unbinding force was 50.5 ± 17.3 pN/s (Ave. ± SD, $n = 61$). The position of the bead was determined from the centroid of a phase-contrast image of the bead using a frame memory computer (DIPS-C2000; Hamamatsu Photonics). The unbinding force (resolution, ±0.2 pN) was estimated from the displacement of the bead from the trap center [25–27].

Results and discussion

Direct observation of several types of branching

The first example is a dendritic network grown from the nuclei composed of actin filaments (Fig. 1A). Among several types of branching, the most noticeable was growing of daughter filaments from the side of mother filaments (a growing type of side branching; Fig. 1B). In this example, the polymerization rates at the B-ends of the mother and daughter filaments were, respectively, 9.7×10^6 and 10.4×10^6 M/s, being nearly the same to each other; while that at the slow-growing pointed (P-)end of the mother filament was -0.28×10^6 M/s (Fig. 1C), both of which were consistent with the values obtained in solution [28]. Also, a direct coupling of daughter filaments with an acute angle to the side of the mother filament was observed (a coupling type of side branching; Fig. 1D). After the coupling occurred, the polymerization continued from both B-ends of the mother and daughter filaments at nearly the same rates.

Fig. 1E is an example attributed to a growing type of end branching (B-end branching unless otherwise stated; elongation of the two filaments from the same point, i.e., the B-end within the spatial resolution of optical microscope, was confirmed by rewinding the videotape). Both the mother and the daughter filaments polymerized at nearly the same rates, i.e., 9.0×10^6 and 7.5×10^6 M/s, respectively, whereas the polymerization rate at the P-end of the mother filament was -0.36×10^6 M/s (Fig. 1F). Thus, depolymerization occurred at the P-end of the mother filaments under the

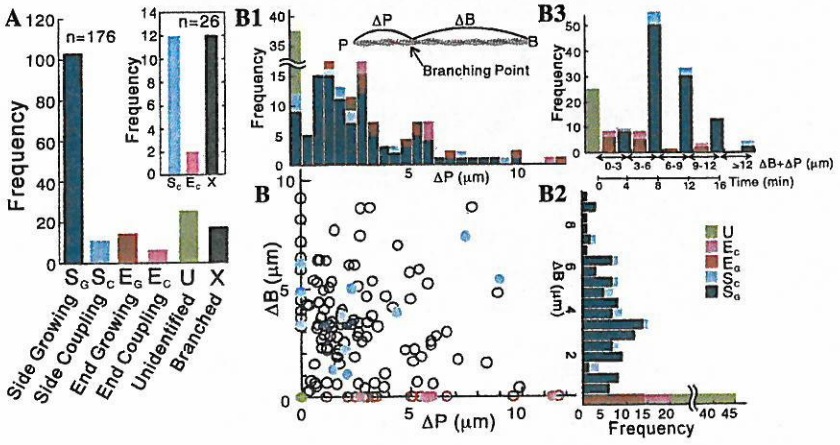

Fig. 2. Frequency of several types of branching. (A) Histogram showing the frequency of several types of branching in the presence of Arp2/3 complex and VCA and in the absence or the presence of phalloidin (inset). S_G, S_C, E_G, E_C, U, and X, respectively, growing type of side branching; coupling type of side branching; growing type of end branching; coupling type of end branching; *unidentified* (the type of branching could not be identified because the mother filaments were too short); and *already branched* at the beginning of observation. (B) Two-dimensional map showing the distribution of the distance of the branching point from the B-end (ΔB, ordinate) and the P-end (ΔP, abscissa) of mother filaments. (B1, B2, and B3) Frequency of several types of branching against ΔP (B1), ΔB (B2), and $\Delta B + \Delta P$ (total length of mother filaments; B3). The time on the abscissa of B3 was estimated from the average rate of polymerization (about 0.7 μm/min, Fig. 1C and F). The frequency of the B-end branching ($\Delta B = 0$) in B2 and that of the P-end branching ($\Delta P = 0$) in B1 are shown outside the abscissa and the ordinate of B, respectively.

given condition. Fig. 1G is an example showing direct coupling of the filament to the B-end of the mother filament. Also, we noticed that the frequency of head-to-tail annealing of filaments became about twice higher than that in the control, suggesting that the Arp2/3 complex activated by VCA increases the affinity of head-to-tail binding of filaments.

Analysis of branching mechanism

First, we classified the branching into several types. As summarized in Fig. 2A, excluding the data already branched at the beginning of the observation, about 72% was classified as side branching, 12% as end branching, and the remaining 16% as *unidentified* because the length of the mother filaments was too short.

Then, we examined how actin monomers are involved in these branching processes, so that the effect of phalloidin was examined. (On the polymerization process of pure actin in the presence of phalloidin, see [29].) As the inset of Fig. 2A shows, the growing type disappeared but the coupling type was still observed. Thus, we conclude that actin monomers are involved in the growing type of branching but not responsible for the direct coupling of daughter filaments.

Next, we quantitatively analyzed the data of the branching. The 2-D map in Fig. 2B shows the distance between either the B-end (ΔB on the ordinate) or the P-end (ΔP on the abscissa) of the mother filament and the branching point at the beginning of branching. From this 2-D map, we could extract the essential features of the branching, that is,

(1) at which part of the mother filaments the branching tends to occur. We made a projection of the frequency distribution to the ΔP and ΔB axes at every 0.5 μm interval (the limit of spatial resolution) as shown in Figs. 2B1 and B2, respectively. Fig. 2B1 shows that the frequency of side branching is higher at the P-end region of mother filaments. Moreover, note that the frequency of side branching is higher at the upper left portion of the line of $\Delta B = \Delta P$ in the 2-D map (Fig. 2B). This reflects a bias of side branching toward the P-end, which is in contrast to the previous observation that the side branching tended to occur at the B-end region [18]. We interpret this result as indicating that the binding of Arp2/3 complex to the side of actin filaments occurs as soon as the mother filaments began to polymerize, but the elongation of daughter filaments is delayed such that the polymerization of mother filaments proceeds. This apparent contradiction may be attributable to the difference in the experimental conditions between the two groups; the main difference is whether one is observing the polymerization process in solution without using nuclei in the presence of all the components (this study) or using pre-existing filaments fixed to the glass surface [18]. On the other hand, Fig. 2B2 shows that the frequency of branching at the B-end exceeds the average frequency of the side branching, suggesting that B-end branching occurs. The end branching may occur immediately after the binding of the Arp2/3 complex to the B-end of mother filaments. In this respect, it is interesting that the frequency of branching on short mother filaments (classified as *unidentified*) was high.

(2) The projection of the 2-D map along the total length of mother filaments ($=\Delta B + \Delta P$) (Fig. 2B3) shows what the most probable length of mother filaments for each type of branching is, in other words, *when* each type of branching occurs (note that the total length divided by the average polymerization rate represents the time after the beginning of polymerization). Fig. 2B3 shows that the B-end branching occurred at an early stage of polymerization and subsequently the side branching started to occur. Again, this is consistent with the above interpretation that the elongation of daughter filaments on the side branching is delayed.

Force measurement of branching

Next, we observed the binding of actin filaments to the Arp2/3 complex activated by VCA and measured its unbinding by imposing an external load (Fig. 3A). A fluorescence micrograph (Fig. 3B) shows how an actin filament was attached to and detached from the glass surface on which VCA and activated Arp2/3 complex are expected to be attached, demonstrating that the Arp2/3 complex and VCA certainly associate with the side of actin filaments. A possibility that the Arp2/3 complex is incorporated as a protomer into the mother filaments is excluded because the filaments were stabilized by phalloidin and gelsolin.

Fig. 3C shows the time course of the displacement of the bead from the trap center during the movement of the cover slip, so that each peak represents an unbinding event. Because VCA is firmly attached to the glass surface through the avidin–biotin bond, it is likely that detachment occurs at the interface between Arp2/3 complex and VCA. The fact that the filament once detached could reattach to the glass surface at the same point on the filament suggests that the Arp2/3 complex is remained attached to the side of actin filaments. We estimate that the unbinding force, of which distribution has a peak at 6–7 pN (Fig. 3D), is weaker than that for the actin-S1 rigor bonds [27], taking into account the high loading rate, 50 pN/s, used in the present study. From the relationship between the unbinding force and the binding lifetime [27] and the value of the unbinding force obtained here, we estimate that the binding lifetime in the absence of external load is shorter than 100 s, which is the one for the actin-S1 rigor bonds. On the other hand, the lifetime of the branch was longer than 10 min (data not shown), so that the lifetime of the binding of Arp2/3

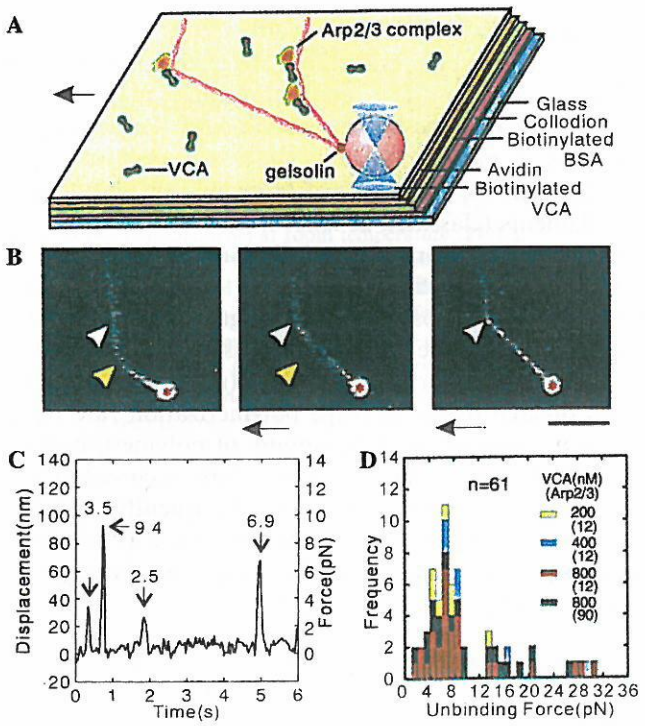

Fig. 3. Measurement of unbinding between a single actin filament and the Arp2/3 complex with VCA. (A) Schematic illustration showing how to measure the unbinding force by manipulating the bead, on which the B-end of an actin filament was attached, with optical tweezers. The external load was imposed by moving the cover slip toward the left at a constant rate (ca. 50 pN/s) as shown by a black arrow (also see arrows in B). (B) Fluorescence micrographs showing the unbinding of an actin filament from the VCA, which was attached to the glass surface through the biotin–avidin bond. Two arrowheads show the position where the VCA and the Arp2/3 complex must be located. The red asterisk shows the position of the trap center that was fixed. The VCA indicated by a yellow arrowhead was detached first, whereas the filament remained attached through the VCA indicated by a white arrowhead. The cover slip was manually moved toward the right when we tried the rebinding. After searching for the rebinding point, an external load was imposed again by moving the cover slip toward the left. Scale bar, 5 μm. (C) An example of raw data showing the time course of the displacement of the bead. The number at each peak indicates the unbinding force, which was obtained by multiplying the displacement of the bead and the trap stiffness (0.10 pN/nm) together. (D) Histogram showing the unbinding force distribution under various combinations of the concentrations of VCA and Arp2/3 complex. We found that the attachment of actin filaments to the glass surface was observed only at the VCA concentrations higher than about 200 nM. As the VCA concentration was increased, the linear density of the attachment points along the actin filament increased. We confirmed that the biotinylated BSA did not detach from the collodion-coated glass surface under the conditions examined here.

complex and an actin filament is expected to be an order of magnitude longer than that characteristic of the binding examined here.

A model of branching

Finally, we propose a model of branching mechanism based on the above analysis. As illustrated in Fig. 4,

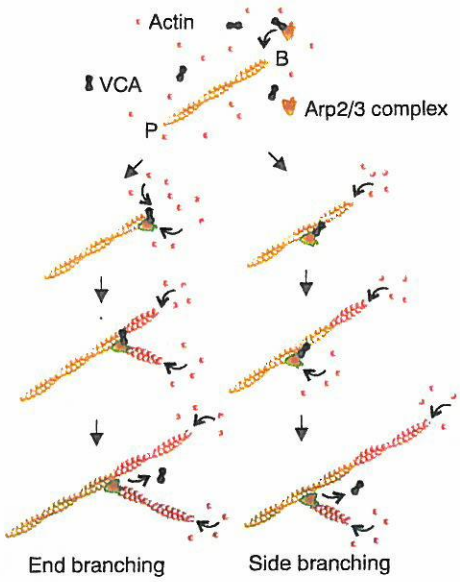

Fig. 4. Schematic illustration showing the two types of branching mechanism. The end branching (left column) and the side branching (right column), due to the binding of the Arp2/3 complex and VCA, respectively, to the B-end and to the side of the actin filament, are illustrated as proposed according to the present results.

accompanying the polymerization of actin, the Arp2/3 complex activated by VCA attaches to the actin filaments, so that the branching at the B-end of the mother filaments occurs at the same time and at the same polymerization rate on the mother and daughter filaments. The Arp2/3 complex also attaches to the side of the actin filaments (as evidenced by the unbinding force measurements), so that the daughter filament starts to polymerize but a little *behind* the B-end branching (Fig. 2B3). Even in the side branching, once the polymerization starts, the rate becomes the same (Fig. 1C). Note that, as far as the frequency is concerned, the side branching is definitely major, probably because the number of Arp2/3 complex attached to the side of actin filaments is much larger than that at the B-end. In addition to the growing type of branching, the coupling type of branching occurs regardless of the timing (Fig. 2B3). Hence, at least under the present experimental conditions, both the end branching and the side branching of growing type and coupling type occur with different timings and different frequencies. The temporal and spatial regulation of such differing types of branching takes place in various situations in vivo via several kinds of regulatory proteins in addition to the Arp2/3 complex and the WASP family proteins. The regulatory mechanism of branching will be clarified in greater detail by applying the technique of single filament imaging and manipulation as presented here to various combinations of regulatory proteins under various conditions.

Acknowledgments

We thank Drs. H. Tadakuma and T. Funatsu of Waseda University for technical assistance and discussion, and Dr. W. Rozycki of Waseda University for reading the manuscript. This research was partly supported by Grants-in-Aid for Scientific Research, for Scientific Research on Priority Areas, and for Bio-venture Project from the Ministry of Education, Culture, Sports, Science, and Technology of Japan, and by Grants-in-Aid from the Japan Science and Technology Corporation (CREST) and the Mitsubishi Foundation. We also thank colleagues at Waseda University and CREST for their encouragement and support.

References

[1] T.D. Pollard, L. Blanchoin, R.D. Mullins, Molecular mechanisms controlling actin filament dynamics in nonmuscle cells, Annu. Rev. Biophys. Biomol. Struct. 29 (2000) 545–576.
[2] D. Pantaloni, C. Le-Clainche, M.-F. Carlier, Mechanism of actin-based motility, Science 292 (2001) 1502–1506.
[3] J. Condeelis, How is actin polymerization nucleated in vivo? Trends Cell Biol. 11 (2001) 288–293.
[4] T. Takenawa, H. Miki, WASP and WAVE family proteins: key molecules for rapid rearrangement of cortical actin filaments and cell movement, J. Cell Sci. 114 (2001) 1801–1809.
[5] T.M. Svitkina, G.G. Borisy, Arp2/3 complex and actin depolymerizing factor/cofilin in dendritic organization and treadmilling of actin filament array in lamellipodia, J. Cell Biol. 145 (1999) 1009–1026.
[6] L.M. Machesky, R.D. Mullins, H.N. Higgs, D.A. Kaiser, L. Blanchoin, R.C. May, M.E. Hall, T.D. Pollard, Scar, a WASP-related protein, activates nucleation of actin filaments by the Arp2/3 complex, Proc. Natl. Acad. Sci. USA 96 (1999) 3739–3744.
[7] H. Miki, K. Miura, T. Takenawa, N-WASP, a novel actin-depolymerizing protein, regulates the cortical cytoskeletal rearrangement in a PIP2-dependent manner downstream of tyrosine kinases, EMBO J. 15 (1996) 5326–5335.
[8] H. Miki, T. Sasaki, Y. Takai, T. Takenawa, Induction of filopodium formation by WASP-related actin-depolymerizing protein N-WASP, Nature 391 (1998) 93–96.
[9] S. Suetsugu, H. Miki, H. Yamaguchi, T. Obinata, T. Takenawa, Enhancement of branching efficiency by the actin filament-binding activity of N-WASP/WAVE2, J. Cell Sci. 114 (2001) 4533–4542.
[10] H. Miki, T. Takenawa, Direct binding of the verprolin-homology domain in N-WASP to actin is essential for cytoskeletal reorganization, Biochem. Biophys. Res. Commun. 243 (1998) 73–78.
[11] N. Volkmann, K.J. Amann, S. Stoilova-McPhie, C. Egile, D.C. Winter, L. Hazelwood, J.E. Heuser, R. Li, T.D. Pollard, D. Hanein, Structure of Arp2/3 complex in its activated state and in actin filament branch junctions, Science 293 (2001) 2456–2459.
[12] R.C. Robinson, K. Turbedsky, D.A. Kaiser, J.B. Marchand, H.N. Higgs, S. Choe, T.D. Pollard, Crystal structure of Arp2/3 complex, Science 294 (2001) 1679–1684.
[13] K.J. Amann, T.D. Pollard, The Arp2/3 complex nucleates actin filament branches from the sides of pre-existing filaments, Nat. Cell Biol. 3 (2001) 306–310.
[14] L. Blanchoin, K.J. Amann, H.N. Higgs, J.B. Marchand, D.A. Kaiser, T.D. Pollard, Direct observation of dendritic actin filament networks nucleated by Arp2/3 complex and WASP/Scar proteins, Nature 404 (2000) 1007–1011.
[15] D. Pantaloni, R. Boujemaa, D. Didry, P. Gounon, M.-F. Carlier, The Arp2/3 complex branches filament barbed ends: functional antagonism with capping proteins, Nat. Cell Biol. 2 (2000) 385–391.
[16] R. Boujemaa-Paterski, E. Gouin, G. Hansen, S. Samarin, C. Le-Clainche, D. Didry, P. Dehoux, P. Cossart, C. Kocks, M.F. Carlier, D. Pantaloni, Listeria protein ActA mimics WASP family proteins: it activates filament barbed end branching by Arp2/3 complex, Biochemistry 40 (2001) 11390–11404.
[17] T. Funatsu, Y. Harada, M. Tokunaga, K. Saito, T. Yanagida, Imaging of single fluorescent molecules and individual ATP turnovers by single myosin molecules in aqueous solution, Nature 374 (1995) 555–559.
[18] J.K. Amann, T.D. Pollard, Direct real-time observation of actin filament branching mediated by Arp2/3 complex using total internal reflection fluorescence microscopy, Proc. Natl. Acad. Sci. USA 98 (2001) 15009–15013.
[19] J.A. Cooper, M.A. Wear, A.M. Weaver, Arp2/3 complex: advances on the inner workings of a molecular machine, Cell 107 (2001) 703–705.
[20] I. Ichetovkin, W. Grant, J. Condeelis, Cofilin produces newly polymerized actin filaments that are preferred for dendritic nucleation by the Arp2/3 complex, Curr. Biol. 12 (2002) 79–84.
[21] J.A. Spudich, S. Watt, The regulation of rabbit skeletal muscle contraction. I. Biochemical studies of the interaction of the tropomyosin–troponin complex with actin and the proteolytic fragments of myosin, J. Biol. Chem. 246 (1971) 4866–4871.
[22] H. Kondo, S. Ishiwata, Uni-directional growth of F-actin, J. Biochem. 79 (1976) 159–171.
[23] H. Yamaguchi, H. Miki, S. Suetsugu, L. Ma, M.W. Kirschner, T. Takenawa, Two tandem verprolin homology domains are necessary for a strong activation of Arp2/3 complex-induced actin polymerization and induction of microspike formation by N-WASP, Proc. Natl. Acad. Sci. USA 97 (2000) 12631–12636.
[24] N. Suzuki, H. Miyata, S. Ishiwata, K. Kinosita Jr., Preparation of bead-tailed actin filaments: estimation of the torque produced by the sliding force in an in vitro motility assay, Biophys. J. 70 (1996) 401–408.
[25] H. Miyata, H. Yoshikawa, H. Hakozaki, N. Suzuki, T. Furuno, A. Ikegami, K. Kinosita Jr., T. Nishizaka, S. Ishiwata, Mechanical measurements of single actomyosin motor force, Biophys. J. 68 (1995) 286s–290s.
[26] T. Nishizaka, H. Miyata, H. Yoshikawa, S. Ishiwata, K. Kinosita Jr., Unbinding force of a single motor molecule of muscle measured using optical tweezers, Nature 377 (1995) 251–254.
[27] T. Nishizaka, R. Seo, H. Tadakuma, K. Kinosita Jr., S. Ishiwata, Characterization of single actomyosin rigor bonds: load dependence of lifetime and mechanical properties, Biophys. J. 79 (2000) 962–974.
[28] T.D. Pollard, J.A. Cooper, Actin and actin-binding proteins. A critical evaluation of mechanisms and functions., Annu. Rev. Biochem. 55 (1986) 987–1035.
[29] S. Ishiwata, J. Tadashige, I. Masui, T. Nishizaka, K. Kinosita Jr., Microscopic analysis of polymerization and fragmentation of individual actin filaments, in: C.G. dos Remedios, D.D. Thomas (Eds.), Molecular Interactions of Actin, Springer, Heidelberg, 2001, pp. 79–94.

Journal of Physiology (2002), **542.1**, *pp.* 221–229
DOI: 10.1113/jphysiol.2002.017111
www.jphysiol.org

Myosin light chain 2 modulates MgADP-induced contraction in rabbit skeletal and bovine cardiac skinned muscle

Hideaki Fujita *, Daisuke Sasaki *, Kenji Fukuda * and Shin'ichi Ishiwata *†

**Department of Physics, School of Science and Engineering and †Advanced Research Institute for Science and Engineering, Waseda University, 3-4-1 Okubo, Shinjuku-ku, Tokyo 169-8555, Japan*

Skinned skeletal and cardiac muscle fibres can be activated by MgADP in the presence of MgATP without Ca^{2+}; the isometric tension is developed in a sigmoidal manner with the addition of MgADP under relaxing conditions. The critical concentrations of MgADP for this MgADP-induced contraction are about 7.5 and 2.6 mM for skeletal and cardiac muscle fibres, respectively. To investigate whether muscle regulatory proteins, myosin light chain 2 (LC_2) and troponin C (TnC), play a part in the MgADP-induced contraction, these proteins were partly extracted by treatment with *trans*-1,2-cyclohexanediamine-*N,N,N′,N′*-tetraacetic acid (CDTA), a chelater of divalent cations, and the MgADP–tension relationship was examined in rabbit psoas and bovine cardiac skinned fibres. We found that the sigmoidal MgADP–tension relationship became hyperbolic after a partial extraction of LC_2 (about 30 %) and TnC (about 70 %). Reconstitution with LC_2 restored the sigmoidal MgADP–tension relationship of control fibres almost fully in both skeletal and cardiac fibres, whereas reconstitution with TnC alone had no effect. Furthermore, cardiac fibres reconstituted with skeletal LC_2 exhibited an MgADP–tension relationship intermediate between skeletal and cardiac fibres. The partial extraction of LC_2 and TnC resulted in a reduction of the inhibitory effect of inorganic phosphate (P_i) on the MgADP-activated tension. Reconstitution with LC_2 restored the original P_i–tension relationship, whereas reconstitution with TnC had no effect. In other words, extraction of LC_2 apparently increased the affinity of myosin for MgADP but decreased the affinity for P_i. These results demonstrate that LC_2 modulates MgADP-induced activation of actomyosin interaction.

(Received 16 January 2002; accepted after revision 16 April 2002)
Corresponding author S. Ishiwata, Department of Physics, School of Science and Engineering, Waseda University, 3-4-1 Okubo, Shinjuku-ku, Tokyo 169-8555, Japan. Email: ishiwata@mn.waseda.jp

Muscle contraction is initiated by a release of Ca^{2+} from an inner membrane storage site (Ebashi & Endo, 1968), but the molecular mechanism of the Ca^{2+} regulation differs among muscle types. It is generally accepted that, in vertebrate striated muscle cells, the regulatory switch is located on the thin filament (Ebashi & Endo, 1968). Ca^{2+} binds to troponin (strictly speaking, the Ca^{2+}-binding subunit of troponin, TnC), which in turn removes the inhibition of tropomyosin and enables actomyosin interaction. In vertebrate smooth muscle cells, the regulatory switch is located on the myosin molecule. Phosphorylation of myosin regulatory light chain by Ca^{2+}- and calmodulin-dependent myosin light chain kinase initiates the contraction (cf. Kendrick-Jones & Scholey, 1981; Kamm & Stull, 1985). The role of myosin regulatory light chain (LC_2) in vertebrate striated muscle is still elusive, although recent studies have suggested the possible roles of LC_2 in regulation of muscle contraction. A partial extraction of LC_2 did not affect maximum Ca^{2+}-activated tension and stiffness, whereas at submaximum Ca^{2+} activation, the partial extraction increased tension, stiffness and rate of tension development in skinned skeletal muscle fibres (Hofmann *et al.* 1990; VanBuren *et al.* 1994; Patel *et al.* 1996).

Although the thin filament in striated muscle is activated by Ca^{2+}, formation of strong-binding cross-bridges is also known to activate the thin filament (Bremel & Weber, 1972; Greene & Eisenberg, 1980; McKillop & Geeves, 1993; Swartz *et al.* 1996) and enhance actomyosin interaction. Rigor cross-bridges formed by the reduction of MgATP concentration can 'turn on' the thin filament in a cooperative manner, allowing neighbouring MgATP-bound cross-bridges to interact with actin and produce tension (Kawai & Brandt, 1976). Lowering the MgATP concentration increases maximum Ca^{2+}-activated tension and increases Ca^{2+} sensitivity in crayfish muscle fibres (Brandt *et al.* 1972), skeletal muscle fibres (Godt, 1974) and cardiac muscle fibres (Fabiato & Fabiato, 1975; Best *et al.* 1977). Similarly, exogenously added MgADP activates the thin filament in the absence of Ca^{2+}, and increases maximum Ca^{2+}-activated tension and Ca^{2+} sensitivity both in skeletal (Hoar *et al.* 1987; Shimizu *et al.* 1992) and cardiac muscle fibres (Fukuda *et al.* 1996, 1998).

In the present study, we have investigated the effect of partial extraction of LC_2 on isometric tension induced by MgADP in the absence of Ca^{2+} (MgADP-activated tension) to further clarify the regulatory roles of LC_2. After the partial extraction of LC_2, the sigmoidal relationship between the MgADP concentration and tension (MgADP–tension relationship) became hyperbolic with a concomitant increase in the apparent affinity of MgADP for cross-bridges. This effect was reversed by reconstitution with LC_2. In addition, the inhibitory effect of P_i on the MgADP-activated tension was reduced by the partial extraction of LC_2 and recovered by reconstitution with LC_2. These results indicate that, in striated muscles, LC_2 modulates the MgADP-induced activation mechanism by cross-bridges.

METHODS

Solutions

The solutions used were as follows (mM): rigor solution, 170 KCl, 1.0 $MgCl_2$, 1.0 EGTA and 10 3-(*N*-morpholino) propanesulphonic acid (Mops) (pH adjusted to 7.0 with HCl); relaxing solution, 117 KCl, 5.0 $MgCl_2$, 4.0 ATP, 1.0 EGTA, 10 Mops (pH adjusted to 7.0 with HCl), 20 2,3-butanedione 2-monoxime (BDM); ADP assay solutions, 34–120 KCl (ionic strength 150 mM), 4.3–20 $MgCl_2$ (2.0 mM free Mg^{2+}), 2.2 ATP (2.0 mM MgATP), 0–22.8 ADP (0–15 mM MgADP), 2.0 EGTA, 10 Mops (pH adjusted to 7.0 with HCl) and 50 μM P^1,P^5-di(adenosine-5′)pentaphosphate (AP_5A); P_i assay solutions, 18–58 KCl (ionic strength 150 mM), 14.2 $MgCl_2$ (2.0 mM free Mg^{2+}), 2.2 ATP (2.0 mM MgATP), 16.4 ADP (10 mM MgADP), 0–10 P_i, 2.0 EGTA, 10 Mops (pH adjusted to 7.0 with HCl) and 50 μM AP_5A; Ca^{2+}-activating solutions, 117 KCl, 4.3 $MgCl_2$, 2.2 ATP, 2.0 EGTA, 20 Mops (pH adjusted to 7.0 with HCl) and 1.9 $CaCl_2$ (pCa 4.7) or 0.77 $CaCl_2$ (pCa 6.5). ATP (disodium salt), ADP (potassium salt) and AP_5A were purchased from Boehringer Ingelheim (Ingelheim, Germany); EGTA and Mops were from Dojindo Laboratories (Kumamoto, Japan). All chemicals were of reagent grade. The concentrations of free Mg^{2+}, free Ca^{2+}, MgATP, MgADP, P_i and other ionic species were calculated by a computer program using published stability constant values (Horiuti, 1986).

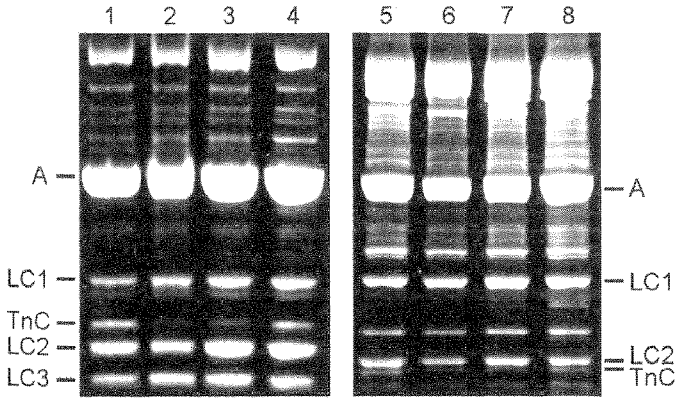

Figure 1. SDS-PAGE of muscle fibres before and after CDTA treatment and after reconstitution with LC_2 and TnC

Lanes 1–4, skeletal fibres; lanes 5–8, cardiac fibres; lanes 1 and 5, control; lanes 2 and 6, after CDTA treatment; lanes 3 and 7, after reconstitution with LC_2; lanes 4 and 8, after reconstitution with TnC and LC_2. LC_2 and TnC used for lanes 3 and 4 were prepared from skeletal muscle and LC_2 and TnC used for lanes 7 and 8 were prepared from cardiac muscle. Abbreviations: A, actin; LC1, LC2 and LC3, myosin light chains 1, 2 and 3, respectively; TnC, troponin C.

Muscle fibres and proteins

Skeletal muscle fibres were prepared from rabbit psoas muscle according to the Guidelines for the Care and Use of Laboratory Animals in the Human Science Department of Waseda University. Cardiac muscle fibres were prepared from a straight portion of bovine left ventricular papillary muscle obtained from a local abattoir (Fukuda *et al.* 1996). Muscle bundles (for skeletal muscle, approximately 7 cm in length and 3 mm in diameter; for cardiac muscle, approximately 5 cm in length and 5 mm in diameter) were excised and both ends were tied to a glass rod and the muscle was incubated in glycerol solution (rigor) composed of 50 % (v/v) glycerol, 0.5 mM $NaHCO_3$, 5.0 mM EGTA (pH adjusted to 7.0 with HCl) and 2.0 mM leupeptin at 0 °C, overnight. Fibres were then stored in fresh glycerol solution at −20 °C. Glycerinated fibres were used between 2 and 8 weeks after preparation. TnC was prepared from rabbit white skeletal muscle (sTnC) and from bovine cardiac muscle (cTnC) according to the method of Ebashi (1974) and column purified using DEAE Sephadex A-25 (Pharmacia, Stockholm, Sweden). LC_2 was prepared from rabbit white skeletal muscle (sLC_2) and from bovine cardiac muscle (cLC_2) according to the method of Weeds & Lowey (1971) and free 5,5′-dithiobis-(2-nitrobenzoic) acid (DTNB) was removed using DEAE Sephadex G-25 (Pharmacia).

Tension measurement

For tension measurement (cf. Fujita & Ishiwata, 1999), a glycerinated thin bundle (~1 mm in length, ⩽ 100 μm in diameter) was removed with a pair of forceps under a stereomicroscope just before the experiment. To prepare a thin bundle, dissection was carried out in glycerol solution at about −10 °C (Fukuda *et al.* 1996). Both ends of the muscle fibres were fixed to thin tungsten wires with enamel and one of the wires was attached to a tension transducer (AE-801, SensoNor a.s., Holten, Norway). The muscle was then immersed in the rigor solution containing 1 % (v/v) Triton X-100 for 20 min to remove the residual internal membrane system. Triton X-100 was washed out with rigor solution before experiments. Sarcomere length was set at 2.6–2.7 μm for skeletal and 2.0–2.1 μm for cardiac fibres. For tension measurement, fibres were immersed in relaxing solution and then active tension was measured by immersing the fibres in an activating solution. Measurements were recorded with a pen recorder (VP-6533A, National, Osaka, Japan). The tension measurement was carried out in a chamber made from a silicon-coated aluminum block (10 cm × 10 cm × 1 cm) with several small holes (5 mm in diameter) filled with approximately 0.4 ml each of the experimental solutions (Horiuti, 1986).

SDS-PAGE

Fibres were collected and dissolved in lysis solution (7.5 % SDS, 10 % (v/v) glycerol, 1.0 mM dithiothreitol (DTT) and 10 mM Tris-HCl (pH 6.8) and heated for 3 min at 90 °C. SDS-PAGE was carried out according to the method of Laemmli (1970) with 5–20 % gradient running gel. Proteins were fluorescently stained with SYPRO Ruby Protein gel stain (Molecular Probes Inc., Eugene, OR, USA), which is more sensitive than Coomassie Brilliant Blue R. The gel pattern was analysed by using a densitometre (model AE-6920-V, ATTO Inc., Tokyo, Japan) after the linearity of staining against the amount of proteins was confirmed.

Extraction and reconstitution of LC_2 and TnC

To extract LC_2 and TnC, fibres were immersed in a solution composed of 5.0 mM *trans*-1,2-cyclohexanediamine-*N,N,N′,N′*-tetraacetic acid (CDTA), 40 mM Tris-HCl (pH 8.4), 0.6 mM NaN_3 and 0.1 mM DTT for 90 min for skeletal and for 120 min for cardiac fibres at 25 °C. CDTA was washed out for 10 min in the solution composed of 90 mM KCl, 10 mM Mops (pH 7.0), 1.0 mM NaN_3 and 0.1 mM DTT. To reconstitute LC_2 and/or TnC, fibres were immersed in relaxing solution containing 1.2 mg ml^{-1} LC_2 and/or 1.5 mg ml^{-1} TnC for 60 min at 25 °C. Figure 1 shows SDS-PAGE analysis of fibres before and after the CDTA treatment and after the reconstitution with LC_2 and TnC. The LC_2 content was determined from the $LC_2/(LC_1 + LC_3)$ ratio for skeletal fibres and the $LC_2:LC_1$ ratio for cardiac fibres. The TnC content was determined from the TnC : actin ratio. After the CDTA treatment, approximately 30 % of LC_2 and 70 % of TnC were removed from the fibres, based on the densitometric trace of the gel stained with the fluorescent dye. Similarly, the densitometric trace showed that almost 100 % of LC_2 and TnC were recovered after the reconstitution. Our LC_2 preparation contained a small amount of TnC. Because of this, some TnC may have been reconstituted when LC_2 was added. Contamination was not detected in our TnC preparation.

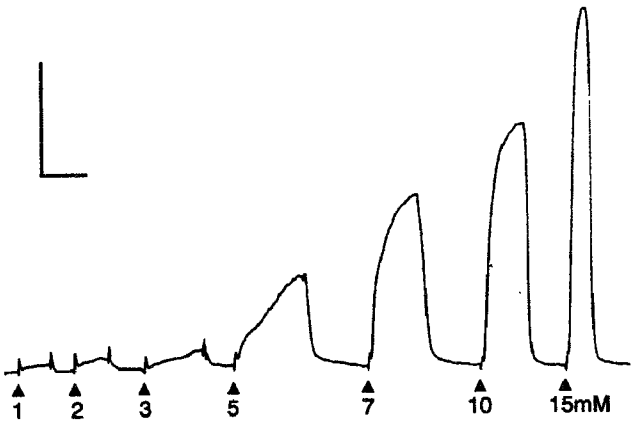

Figure 2. Recordings of isometric tension at various MgADP concentrations in control skeletal muscle fibres

Arrowheads indicate the exchange of solutions. The MgADP concentrations of activating solutions are indicated below the arrowheads. The fibre was relaxed after each activation by immersion in relaxing solution. Spikes are artefacts due to solution exchange. Tension was measured at 25 °C. Vertical and horizontal bars, 5×10^{-5} N and 2 min, respectively.

RESULTS

Effect of LC_2 and TnC on MgADP-induced contraction in skeletal fibres

Figure 2 shows a pen trace of MgADP-activated isometric tension developed by skeletal muscle fibres in the absence of Ca^{2+}. With increasing MgADP concentration, fibres generated increased tension in a sigmoidal manner, which is in good agreement with previous results in skeletal (Shimizu *et al.* 1992) and cardiac muscle fibres (Fukuda *et al.* 1996).

Figure 3 shows pen traces of isometric tension at various MgADP concentrations (indicated) or in pCa solutions (pCa 6.5 or 4.7) after treatment with CDTA (Fig. 3*A*), after reconstitution with sTnC (Fig. 3*B*) and then after reconstitution with sLC_2 (Fig. 3*C*). These records were made sequentially from the same muscle fibre. To avoid the deterioration of fibres due to rigor tension development upon the exchange of relaxing solution with rigor solution of low ionic strength for CDTA treatment (see Methods), control experiments were performed using different fibres. The MgADP-activated tension at 15 mM did not differ significantly after reconstitution with sLC_2. Active tension at pCa 6.5 and 4.7 in the absence of MgADP was also measured to compare the results with earlier studies (Hofmann *et al.* 1990). The maximum Ca^{2+}-activated tension at pCa 4.7 did not change, whereas tension at pCa 6.5, which was developed after the removal of LC_2, disappeared again upon reconstitution with sLC_2.

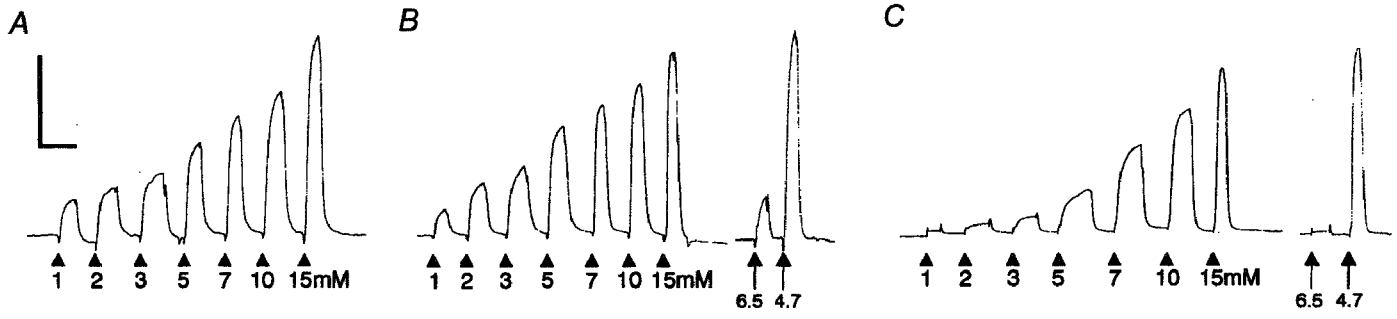

Figure 3. Recordings of isometric tension at various MgADP concentrations in skeletal muscle fibres

Recordings were made after treatment with CDTA (*A*), after reconstitution with sTnC (*B*) and after reconstitution with sLC_2 (*C*). All tension records were taken from the same fibre sequentially. Arrows and arrowheads indicate the exchange of solutions. The MgADP concentrations of activating solutions are indicated below the arrowheads. The pCa values of Ca^{2+}-activating solution are indicated below the arrows. The fibre was relaxed after each activation by immersion in relaxing solution. Spikes are artefacts due to solution exchange. Tension was measured at 25 °C. Vertical and horizontal bars, 5×10^{-5} N and 2 min, respectively.

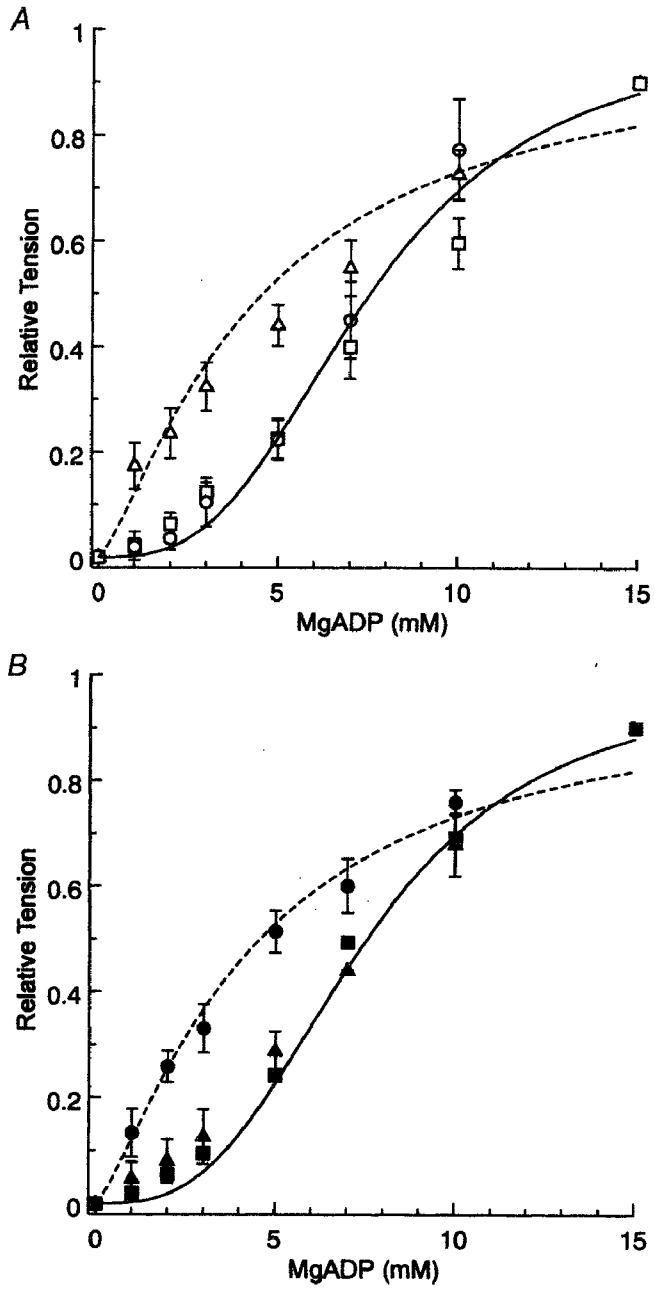

Figure 4. Effect of MgADP on the isometric tension in skeletal muscle fibres

Fibres were treated with CDTA for 90 min before reconstitution except for control fibres. Control (○), after CDTA treatment for 90 min (△), reconstituted with sLC_2 (□), reconstituted with sTnC (●), reconstituted with sTnC and then with sLC_2 (▲), and reconstituted with sLC_2 and then with sTnC (■). Lines in *A* are fitted for control (continuous line) and CDTA-treated fibres (dashed line) by the Hill equation (cf. Fukuda & Ishiwata, 1999) using the values in Table 1. To fit the data, we assumed that tension at 15 mM MgADP was 90 % of the saturated tension value. The same lines as in *A* were drawn in *B* for comparison. Reconstitution with LC_2 or TnC was achieved by immersing the CDTA-treated fibres in solution containing 1.2 mg ml^{-1} LC_2 or 1.5 mg ml^{-1} TnC for 60 min at 25 °C. Tension was measured in ADP assay solution at 25 °C and normalized to that obtained at 15 mM MgADP (the relative value was assumed to be 0.9) for each fibre tested. Data points and vertical bars show mean and S.D. calculated from 5 experiments using different preparations.

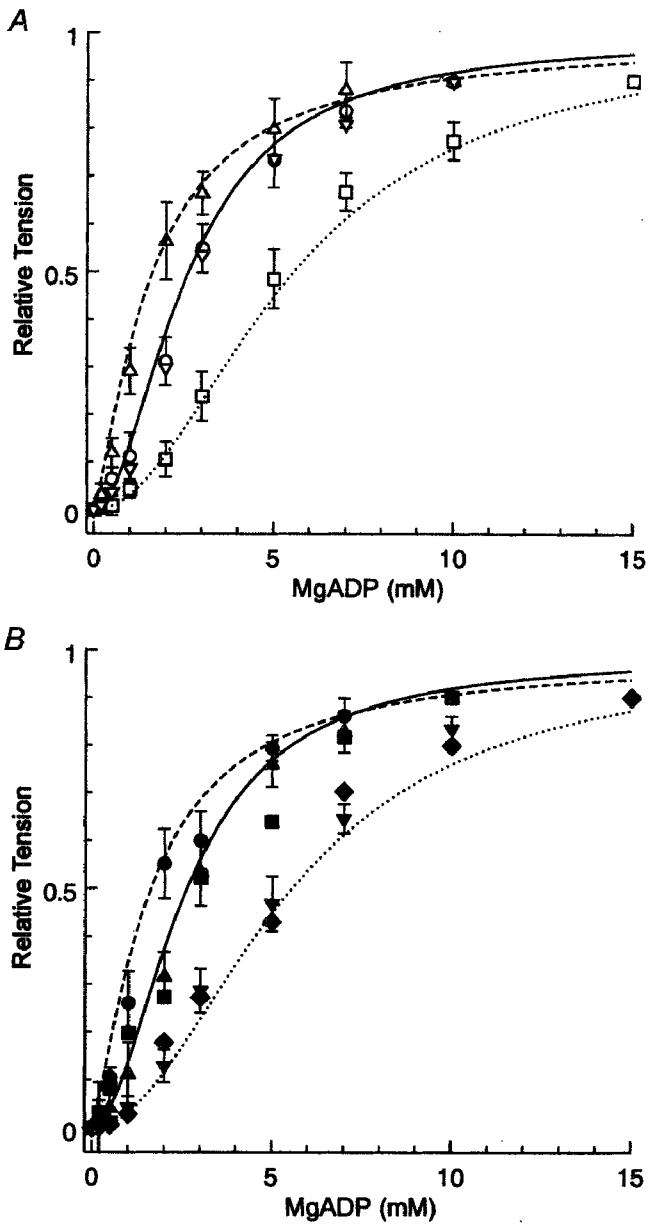

Figure 5. Effect of MgADP on isometric tension in cardiac muscle fibres

Fibres were treated with CDTA for 120 min before reconstitution except for control fibres. Control (○), after CDTA treatment for 120 min(△), reconstituted with cLC_2 (▽), reconstituted with sLC_2 (□), reconstituted with cTnC (●), reconstituted with cTnC and then with cLC_2 (▲), reconstituted with cLC_2 and then with cTnC(■), reconstituted with cTnC and then with sLC_2 (▼), and reconstituted with sLC_2 and then with cTnC (◆). Lines in *A* are fitted for control (continuous line), CDTA-treated (dashed line), and sLC_2-reconstituted fibres (dotted line) by the Hill equation using the values in Table 1. Other methods are the same as in Fig. 4, except that tension was normalised to that obtained at 10 mM MgADP, of which the relative value was assumed to be 0.9 for each fibre tested. For fibres reconstituted with sLC_2, tension was nomalised to that obtained at 15 mM MgADP (the relative value was assumed to be 0.9). Data points and vertical bars show mean and S.D. calculated from 3–5 experiments using different preparations.

Figure 4*A* summarises the MgADP–tension relationship of skeletal muscle fibres before and after treatment with CDTA and after LC_2 reconstitution. Control fibres generated active tension in a sigmoidal manner on increasing the MgADP concentration (Fig. 4*A*, ○). In contrast, tension developed in a hyperbolic manner (Fig. 4*A*, △) in the CDTA-treated fibres. After reconstitution with sLC_2, the MgADP–tension relationship became sigmoidal, which was not different from that of control fibres (Fig. 4*A*, □).

Since CDTA treatment partly extracts TnC (Fig. 1) as well as LC_2, the effect of TnC reconstitution on the MgADP-activated tension was also examined. The CDTA-treated fibres reconstituted with sTnC showed a hyperbolic MgADP–tension relationship (Fig. 4*B*, ●), which was not different from that of CDTA-treated fibres. Only when sLC_2 was added to the sTnC-reconstituted fibres could the MgADP–tension relationship of control fibres be restored (Fig. 4*B*, ▲). The order of reconstitution did not affect the result (Fig. 4*B*, ■), indicating that TnC has little effect on the modulation of MgADP-induced tension.

Effect of LC_2 and TnC on MgADP-induced contraction in cardiac fibres

The effect of LC_2 extraction and reconstitution on the MgADP–tension relationship was also examined in cardiac fibres. With the addition of MgADP, cardiac fibres developed isometric tension in a sigmoidal manner similar to skeletal fibres, but the critical MgADP concentration ($MgADP_{50}$) was much lower (Fig. 5*A*, ○) and the Hill coefficient (n_H) was smaller (Table 1), consistent with a previous report (Fukuda *et al.* 1998). With extraction of LC_2 and TnC, the MgADP–tension relationship became hyperbolic (Fig. 5*A*, △), and reconstitution with cLC_2 restored the sigmoidal MgADP–tension relationship (Fig. 5*A*, ▽; cf. Table 1). These results are qualitatively the same as those of skeletal fibres. Interestingly, when the CDTA-treated cardiac fibres were reconstituted with sLC_2, the MgADP–tension relationship also became sigmoidal, but $MgADP_{50}$ became larger than that of cardiac control fibres (Fig. 5*A*, □) and assumed a value intermediate between skeletal and cardiac control fibres (Table 1).

The effect of TnC on the MgADP–tension relationship was also examined in cardiac fibres (Fig. 5*B*). Reconstitution with cTnC in the CDTA-treated cardiac fibres did not change the hyperbolic MgADP–tension relationship (Fig. 5*B*, ●). When cLC_2 was added to the cTnC-reconstituted fibres, the MgADP–tension relationship became sigmoidal (Fig. 5*B*, ▲). The MgADP–tension relationship of cLC_2-reconstituted fibres remained unchanged on addition of cTnC (Fig. 5*B*, ■). Similar results were obtained for fibres reconstituted with sLC_2 either before (Fig. 5*B*, ◆) or after the cTnC reconstitution (Fig. 5*B*, ▼). These fibres exhibited an $MgADP_{50}$ value intermediate between those of control skeletal and cardiac fibres. These results indicate that TnC does not modulate the MgADP–tension relationship either in cardiac or skeletal fibres.

Table 1. Values of n_H and $MgADP_{50}$ for various types of muscle model

	n_H	$MgADP_{50}$
Skeletal		
Control	3.0	7.5
CDTA treated	1.3	4.5
+ Skeletal LC_2	2.5	7.9
Cardiac		
Control	1.9	2.6
CDTA treated	1.3	1.6
+ Cardiac LC_2	2.1	2.8
+ Skeletal LC_2	2.0	5.5

Values were obtained from Figs 4 and 5 by fitting the averaged points to the Hill equation by the method of least squares.

Effect of LC_2 and TnC on inhibitory role of P_i in MgADP-induced contraction

In the following experiments, we examined the effect of P_i on MgADP-activated tension before and after partial extraction of LC_2 and TnC. Figure 6*A* summarises the effect of P_i on control (○), CDTA-treated (△) and sLC_2-reconstituted (□) skeletal fibres in the presence of 10 mM MgADP. In control fibres, the MgADP-activated tension decreased markedly with the addition of P_i and reached a plateau at approximately 20 % at 7 mM P_i. In contrast, in the CDTA-treated fibres, the extent of tension reduction was less and reached a plateau at approximately 40 % at 7 mM P_i. On reconstitution with sLC_2, this P_i–tension relationship regained its original shape. The effect of sTnC reconstitution on the P_i–tension relationship is summarised in Fig. 6*B*. Reconstitution with sTnC had no effect on the P_i–tension relationship in CDTA-treated (▲) and sLC_2-reconstituted fibres (■). Only when sLC_2 was added to the TnC-reconstituted fibres (●) did the P_i–tension relationship resume the shape of that of control fibres.

Figure 7*A* summarises the effect of P_i in cardiac fibres. In control fibres, tension inhibition by P_i was much smaller than that in skeletal fibres, reaching a plateau at approximately 65 % at 10 mM P_i (○), consistent with previous results (Fukuda *et al.* 1998; Fukuda & Ishiwata, 1999). On treatment with CDTA, the extent of reduction in tension became even less, reaching a plateau at approximately 75 % at 10 mM P_i (△). The original P_i–tension relationship recovered on reconstitution with cLC_2 (▽). sLC_2-reconstituted fibres also showed a P_i–tension relationship resembling that of control cardiac fibres (□). As summarised in Fig. 7*B*, the reconstitution of cTnC did not change the P_i–tension relationship significantly in CDTA-treated fibres (▲) and also in cLC_2-

and sLC_2-reconstituted fibres (■ and ◆, respectively). Addition of either cLC_2 or sLC_2 to the cTnC-reconstituted fibres (● and ▼, respectively) produced P_i–tension relationships similar to that of control cardiac fibres. In contrast to the higher effectiveness of sLC_2 in the MgADP–tension relationship (Fig. 5), the effectiveness of sLC_2 in the inhibitory role of P_i in the MgADP-activated tension was indistinguishable from that of cLC_2 (Fig. 7).

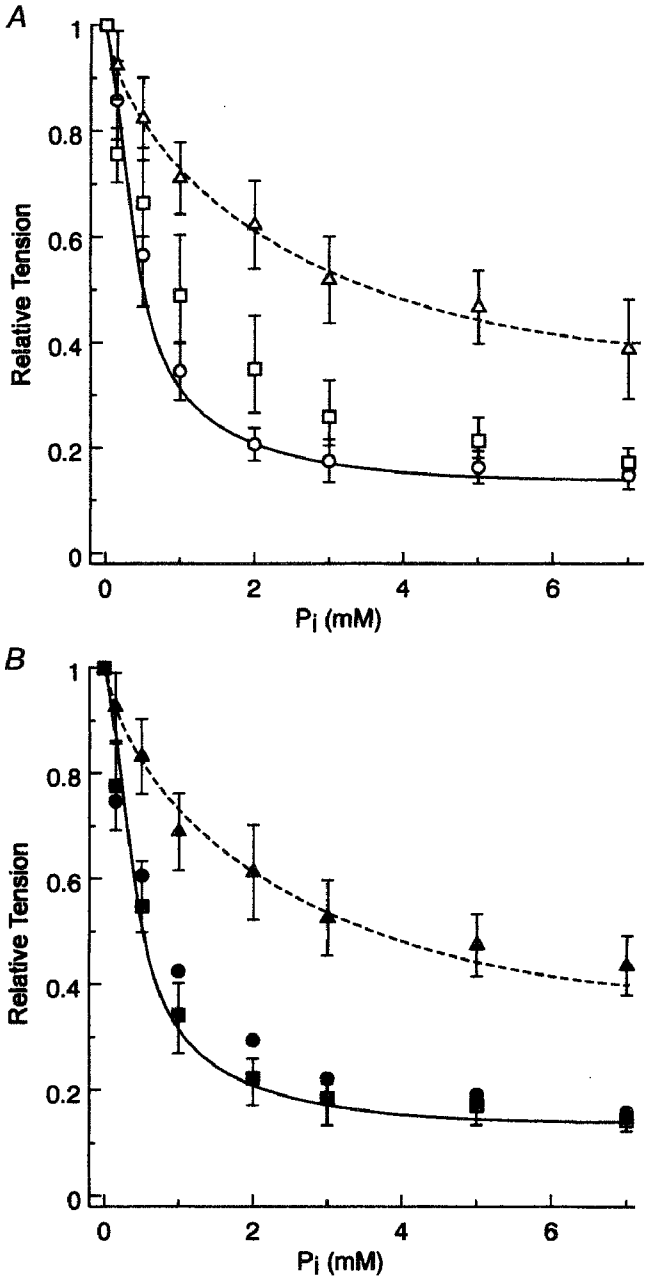

Figure 6. Effect of P_i on (10 mM) MgADP-induced isometric tension in skeletal muscle fibres

Fibres were treated with CDTA for 90 min before reconstitution except for control fibres. Control (○), after CDTA treatment for 90 min (△), reconstituted with sLC_2 (□), reconstituted with sTnC (▲), reconstituted with sTnC and then with sLC_2 (●), and reconstituted with sLC_2 and then with sTnC (■). Lines in *A* are fitted by eye. The same lines were drawn in *B* for comparison. Reconstitution with LC_2 or TnC was achieved by immersing the CDTA-treated fibres in solution containing 1.2 mg ml^{-1} LC_2 or 1.5 mg ml^{-1} TnC for 60 min at 25 °C, respectively. Tension was measured in P_i assay solutions at 25 °C and normalized to that obtained at 0 mM P_i for each fibre tested. Data points and vertical bars show mean and S.D. calculated from 5 experiments using different preparations.

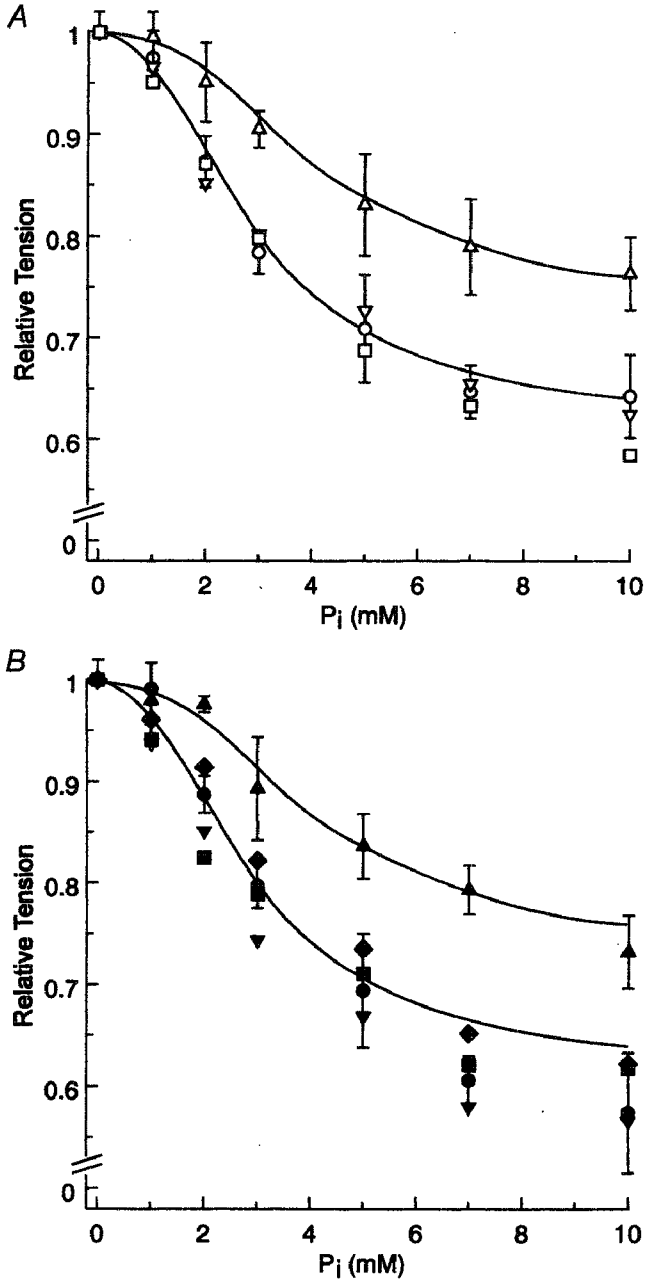

Figure 7. Effect of P_i on (10 mM) MgADP-induced isometric tension in cardiac muscle fibres

Fibres were treated with CDTA for 120 min before reconstitution except for control fibres. Control (○), after CDTA-treatment for 120 min (△), reconstituted with cLC_2 (▽), reconstituted with sLC_2 (□), reconstituted with cTnC (▲), reconstituted with cTnC and then with cLC_2 (●), reconstituted with cLC_2 and then with cTnC (■), reconstituted with cTnC and then with sLC_2 (▼), and reconstituted with sLC_2 and then with cTnC (◆). Lines in *A* are fitted by eye. The same lines were drawn in *B* for comparison. Other methods are the same as in Fig. 6. Data points and vertical bars show mean and S.D. calculated from 3–5 experiments using different preparations.

DISCUSSION

Extraction of LC_2 and TnC by treatment with CDTA

As demonstrated from the analysis of SDS-PAGE (Fig. 1), treatment with CDTA removed approximately 30 % of LC_2 and 70 % of TnC from skeletal and cardiac muscle fibres. These proteins were fully reconstituted into the fibres by immersing the CDTA-treated fibres in relaxing solution containing purified LC_2 and TnC. After reconstitution with TnC, active tension at 15 mM MgADP (without Ca^{2+}) was ~85 % of the maximum Ca^{2+}-activated tension (P_0), which was in good agreement with previous results that the fibres fully activated by MgADP (without Ca^{2+}) produced ~90 % of P_0 (Shimizu *et al.* 1992). This shows that TnC was fully reconstituted into the fibres.

To further confirm the removal and reconstitution of LC_2, tension at submaximal Ca^{2+} activation (pCa 6.5) was compared to that at maximal Ca^{2+} activation (pCa 4.7). It has been reported that Ca^{2+} sensitivity was increased by the removal of LC_2 in skeletal muscle fibres (Hofmann *et al.* 1990). In skeletal muscle fibres, active tension does not develop at pCa 6.5 (data not shown) at pH 7.0. When LC_2 was partly removed (TnC-reconstituted fibres), active tension at pCa 6.5 was 14 % P_0. This result is consistent with a previous report that LC_2-extracted fibres increased Ca^{2+} sensitivity and generated 16 % of P_0 at pCa 6.5 (Hofmann *et al.* 1990). Active tension at pCa 6.5 after the reconstitution with LC_2 was only < 1 % of P_0, confirming the reconstitution of LC_2 into the fibre.

The active tension at 15 mM MgADP (without Ca^{2+}) was reduced by approximately 5 % after reconstitution with TnC and by 20 % after reconstitution with LC_2 (Fig. 3). Because active tension tends to decrease after large tension development, we conclude that the removal and reconstitution of TnC and LC_2 did not affect the MgADP-activated tension. This is in agreement with previous results that removal of LC_2 did not affect the maximal Ca^{2+}-activated tension (Hofmann *et al.* 1990), and thus did not affect the force-generating ability of cross-bridges.

In this study, we used CDTA as a chelater of divalent cations, which resulted in a dissociation of LC_2 from myosin. This procedure extracted only 30 % of LC_2. If the removal of LC_2 occurs at random, 30 % reduction in LC_2 means that 42 % (= 2 × 0.3 × 0.7) of myosin lost one LC_2, 9 % (= 0.3 × 0.3) of myosin lost 2 LC_2 molecules, but 49 % (= 0.7 × 0.7) of myosin was still intact. However, a previous study suggested that the second LC_2 is more difficult to extract than the first LC_2 in a procedure using EDTA (Kendrick-Jones *et al.* 1976). Thus, if such a cooperative removal of LC_2 also occurs with our CDTA treatment, approximately 60 % of myosin could have lost one of the two LC_2 molecules.

The extent of LC_2 removal could be enhanced by treatment with DTNB and EDTA, a procedure that was reported to be capable of complete LC_2 removal (Szczesna *et al.* 1996). We did not use this procedure because oxidized SH-groups produced by the DTNB treatment may remain oxidized even after DTT treatment. Even though this is the case, complete removal of LC_2 using DTNB and EDTA would be worth investigating to enhance our present results.

Effect of LC_2 on MgADP activation

Removal of LC_2 shifted the critical MgADP concentration ($MgADP_{50}$) towards a lower value, by 3.0 and 1.0 mM in skeletal (Fig. 4) and cardiac fibres (Fig. 5), respectively. This change in $MgADP_{50}$ can be interpreted to mean that myosin molecules without LC_2 have higher binding affinity to the thin filament in muscle fibres (Hofmann *et al.* 1990). This result is consistent with that reported in solution (Wagner, 1984). Because LC_2 is located at the head–rod junction of the myosin molecule, which is distal to MgADP or actin-binding site (Rayment *et al.* 1993), the increase in affinity for the thin filament is attributable to allosteric regulation of the ADP- and actin-binding sites of the myosin head through structural change in the head–rod junction. The difference between skeletal and cardiac muscle fibres in the MgADP–tension relationship is attributable to the difference in the LC_2 isoforms, since addition of skeletal LC_2 to the LC_2-extracted cardiac fibres shifted the $MgADP_{50}$ towards that of skeletal fibres (Fig. 5 and Table 1). It is notable that extraction of only 30 % of LC_2 was sufficient to transform the qualitative change in the MgADP–tension relationship from sigmoidal to hyperbolic. Such a large effect on MgADP activation by a relatively small change in the protein composition suggests that the allosteric effect of LC_2 is highly cooperative.

Effect of LC_2 on deactivating effect of P_i in MgADP-activated fibres

It is known that MgADP-activated fibres are deactivated by P_i in skeletal (Shimizu *et al.* 1992) and cardiac fibres (Fukuda *et al.* 1996), but the extent of deactivation is larger in skeletal than in cardiac fibres. With partial extraction of LC_2, inhibition of tension by P_i decreased significantly both in skeletal and cardiac fibres (Figs 6 and 7). The CDTA-treated cardiac fibres reconstituted with sLC_2 showed the P_i–tension relationship of control cardiac fibres rather than skeletal fibres (Fig. 7). This observation is in contrast to the other observation that sLC_2 altered the MgADP-binding affinity of cardiac fibres towards the skeletal type (Fig. 5). The reason why sLC_2 did not modify the P_i effects in cardiac fibres may be attributable to the fact that the proportion of LC_2 exchanged was not large enough to overcome the high affinity for MgADP of cardiac myosin containing a cLC_2 isoform. In the presence of 10 mM MgADP, the effect of MgADP may be saturated, such that the apparent affinity of P_i was maintained.

An alternative and interesting explanation for the above contrasting observation is to assume the following hypotheses, in which the cooperativity of two heads of the

myosin molecule is considered (cf. Tokiwa & Morales, 1971; Chaen *et al.* 1986). (1) Both heads should bind MgADP to turn on the thin filament, which is in the inhibitory state in the absence of Ca^{2+} (Fig. 8, top) and, conversely, (2) both MgADP heads should bind exogenous P_i to lose the ability to turn on the thin filament (Fig. 8, bottom). The high $MgADP_{50}$ value of the MgADP–tension relationship observed in the sLC_2-reconstituted cardiac fibres (Fig. 5) is consistent with hypothesis (1), because the myosin molecule containing sLC_2 cannot turn on the thin filament until the sLC_2-bound head, having a lower affinity to MgADP, binds MgADP. The contrasting result that the substitution of sLC_2 in cardiac fibres was not sufficient to produce inhibition of the MgADP-activated tension by P_i (Fig. 7), can be explained by hypothesis (2), such that tension does not decrease until the cLC_2-bound head binds P_i because this head has a lower affinity for P_i. Hypothesis (2) also explains the sigmoidal relationship between the P_i concentration and the MgADP-activated tension shown in Fig. 7. Note that the sigmoidal feature was not evident in skeletal fibres (Fig. 6), probably because the MgADP concentration (10 mM) was not high enough to saturate the myosin heads with MgADP. In fact, the sigmoidal feature has been observed even in skeletal fibres when the concentration of MgADP was high, e.g. 15 mM (see Fig. 7 of Shimizu *et al.* 1992).

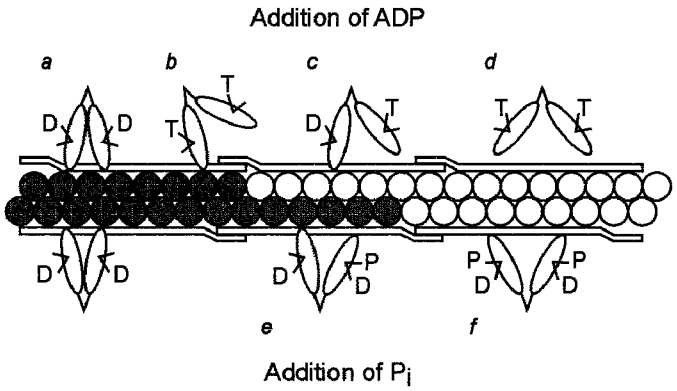

Figure 8. A schematic illustration showing the activation mechanism by MgADP-bound cross-bridges (top) and deactivation mechanism by P_i (bottom)

Actin protomers shown by open circles are in the off-state, whereas those shown by shaded circles are in the on-state. Thin filament is assumed to be cooperatively activated over a certain distance when cross-bridges of which both heads bind MgADP are formed (*a*), so that neighbouring MgATP-bound cross-bridges can interact with actin and produce force (*b*). Both cross-bridges with only one head binding MgADP (*c*) and those without MgADP but with MgATP (*d*) cannot activate the thin filament, so that MgATP-bound cross-bridges cannot produce force in this region. The activated region of the thin filament is still activated when one head binds P_i when the other head binds MgADP (*e*) and deactivated only when both heads bind P_i (*f*). Rigor heads are practically absent. Abbreviations: D, MgADP; T, MgATP; and P, P_i.

There is a possibility that two-headed myosin is not necessary for the ADP activation to occur. For example, it is known that exogenously added *N*-ethylmaleimide-treated myosin subfragment 1 (NEM-S1) is sufficient to activate muscle fibres (Swartz & Moss, 1992). Thus, the binding of two independent ADP-bound myosin heads to the regulatory unit may be enough to activate the thin filament, although the cooperativity may be different.

Physiological significance

In summary, the ability of LC_2 to modulate MgADP-induced contraction as presented here, together with abilities to decrease the Ca^{2+} sensitivity of tension development (Hofmann *et al.* 1990) and to increase the rate of tension development at submaximal Ca^{2+} activation (Metzger & Moss, 1992; Patel *et al.* 1996), enables us to conclude that LC_2 plays substantial roles in the modulation of muscle contraction.

In skeletal muscle in normal physiological conditions, the MgADP concentration may not reach such high levels that ADP activation becomes significant because of the ATP-regenerating system. However, in myocardium, the accumulation of submillimolar concentrations of ADP that occurs in ischaemia may cause abnormal tension development, because cardiac muscle has a higher affinity for MgADP (compare Figs 4 and 5). In this respect, the regulatory role of LC_2 in lowering the affinity for ADP may be important, especially in myocardium.

REFERENCES

BEST, P. M., DONALDSON, S. K. & KERRICK, W. G. L. (1977). Tension in mechanically disrupted mammalian cardiac cells: effects of magnesium adenosine triphosphate. *Journal of Physiology* **265**, 1–17.

BRANDT, P. W., REUBEN, J. P. & GRUNDFEST, H. (1972). Regulation of tension in the skinned crayfish muscle fiber. *Journal of General Physiology* **59**, 305–317.

BREMEL, R. D. & WEBER, A. (1972). Cooperation within actin filament in vertebrate skeletal muscle. *Nature New Biology* **238**, 97–101.

CHAEN, S., SHIMADA, M. & SUGI, H. (1986). Evidence for cooperative interactions of myosin heads with thin filament in the force generation of vertebrate skeletal muscle fibers. *Journal of Biological Chemistry* **261**, 13 632–13 636.

EBASHI, S. (1974). Energy, regulation and biosynthesis in molecular biology. In *Lipman Symposium*, ed. RICHTER, D., pp.165–178. Walter du Gruyter, Berlin, Germany.

EBASHI, S. & ENDO, M. (1968). Calcium ions and muscle contraction. *Progress in Biophysics and Molecular Biology* **18**, 123–183.

FABIATO, A. & FABIATO, F. (1975). Effect of magnesium on contractile activation of skinned cardiac cells. *Journal of Physiology* **249**, 497–517.

FUJITA, H. & ISHIWATA, S. (1999). Tropomyosin modulates pH dependence of isometric tension. *Biophysical Journal* **77**, 1540–1546.

FUKUDA, N., FUJITA, H., FUJITA, T. & ISHIWATA, S. (1996). Spontaneous tension oscillation in skinned bovine cardiac muscle. *Pflügers Archiv* **433**, 1–8.

FUKUDA, N., FUJITA, H., FUJITA, T. & ISHIWATA, S. (1998). Regulatory roles of MgADP and calcium in tension development of skinned cardiac muscle. *Journal of Muscle Research and Cell Motility* **19**, 909–921.

FUKUDA, N. & ISHIWATA, S. (1999). Effects of pH on spontaneous tension oscillation in skinned bovine cardiac muscle. *Pflügers Archiv* **438**, 125–132.

GODT, R. E. (1974). Calcium-activated tension of skinned muscle fibers of the frog. *Journal of General Physiology* **63**, 722–739.

GREENE, L. E. & EISENBERG, E. (1980). Cooperative binding of myosin subfragment-1 to the actin-troponin-tropomyosin complex. *Proceedings of the National Academy of Sciences of the USA* **77**, 2616–2620.

HOAR, P. E., MAHONEY, C. W. & KERRICK, W. G. L. (1987). MgADP increases maximum tension and Ca^{2+} sensitivity in skinned rabbit soleus fibers. *Pflügers Archiv* **410**, 30–36.

HOFMANN, P. A., METZGER, J. M., GREASER, M. L. & MOSS, R. L. (1990). Effects of partial extraction of light chain 2 on the Ca^{2+} sensitivities of isometric tension, stiffness, and velocity of shortening in skinned skeletal muscle fibers. *Journal of General Physiology* **95**, 477–498.

HORIUTI, K. (1986). Some properties of the contractile system and sarcoplasmic reticulum of skinned slow fibers from *Xenopus* muscle. *Journal of Physiology* **373**, 1–23.

KAMM, K. E. & STULL, J. T. (1985). The function of myosin and myosin light chain kinase phosphorylation in smooth muscle. *Annual Review of Pharmacology and Toxicology* **25**, 593–620.

KAWAI, M. & BRANDT, P. W. (1976). Two rigor states in skinned crayfish single muscle fibers. *Journal of General Physiology* **68**, 267–280.

KENDRICK-JONES, J. & SCHOLEY, J. M. (1981). Myosin-linked regulatory systems. *Journal of Muscle Research and Cell Motility* **2**, 347–371.

KENDRICK-JONES, J., SZENTKIRALYI, E. M. & SZENT-GYÖRGYI, A. G. (1976). Regulatory light chains in myosins. *Journal of Molecular Biology* **104**, 747–775.

LAEMMLI, U. K. (1970). Cleavage of structural proteins during the assembly of the head of bacteriophage T4. *Nature* **227**, 680–685.

MCKILLOP, D. F. A. & GEEVES, M. A. (1993). Regulation of the interaction between actin and myosin subfragment 1: evidence for three states of the thin filament. *Biophysical Journal* **65**, 693–701.

METZGER, J. M. & MOSS, R. L. (1992). Myosin light chain 2 modulated calcium-sensitive cross-bridge transitions in vertebrate skeletal muscle. *Biophysical Journal* **63**, 460–468.

PATEL, J. R., DIFFEE, G. M. & MOSS, R. L. (1996). Myosin regulatory light chain modulates the Ca^{2+} dependence of the kinetics of tension development in skeletal muscle fibers. *Biophysical Journal* **70**, 2333–2340.

RAYMENT, I., RYPNIEWSKI, W. R., SCHMIDT-BASE, K., SMITH, R., TOMCHICK, D. R., BENNING, M. M., WINKELMANN, D. A., WESENBERG, G. & HOLDEN, H. M. (1993). Three-dimensional structure of myosin subfragment-1: a molecular motor. *Science* **261**, 50–58.

SHIMIZU, H., FUJITA, T. & ISHIWATA, S. (1992). Regulation of tension development by MgADP and Pi without Ca^{2+}. Role in spontaneous oscillation of skeletal muscle. *Biophysical Journal* **61**, 1087–1098.

SWARTZ, K. R. & MOSS, R. L. (1992). Influence of a strong-binding myosin analogue on calcium-sensitive mechanical properties of skinned skeletal muscle fibers. *Journal of Biological Chemistry* **267**, 20 497–20 506.

SWARTZ, K. R., MOSS, R. L. & GREASER, M. L. (1996). Calcium alone does not fully activate the thin filament for S1 binding to rigor myofibrils. *Biophysical Journal* **71**, 1891–1904.

SZCZESNA, D., ZHAO, J. & POTTER, J. D. (1996). The regulatory light chains of myosin modulate cross-bridge cycling in skeletal muscle. *Journal of Biological Chemistry* **271**, 5246–5250.

TOKIWA, K. & MORALES, M. F. (1971). Independent and cooperative reactions of myosin heads with F-actin in the presence of adenosine triphosphate. *Biochemistry* **10**, 1722–1727.

VANBUREN, P., WALLER, G. S., HARRIS, D. E., TRYBUS, K. M., WARSHAW, D. M. & LOWEY, S. (1994). The essential light chain is required for full force production by skeletal muscle myosin. *Proceedings of the National Academy of Sciences of the USA* **91**, 12 403–12 407.

WAGNER, P. D. (1984). Effect of skeletal muscle myosin light chain 2 on the Ca-sensitive interaction of myosin and heavy meromyosin with regulated actin. *Biochemistry* **23**, 5950–5956.

WEEDS, A. G. & LOWEY, S. (1971). Substructure of myosin molecule. II. The light chains of myosin. *Journal of Molecular Biology* **61**, 701–725.

Acknowledgements

We thank Professor M. Kawai of the University of Iowa for his critical reading of the manuscript. This research was partly supported by Grants-in-Aid for Scientific Research, for Scientific Research on Priority Areas and for the High-tech Research Center Project from the Ministry of Education, Culture, Sports, Science and Technology of Japan. H. Fujita is the recipient of a Research Fellowship from the Japan Society for the Promotion of Science for Young Scientists.

生物物理 42 (4), 156-161 (2002)

解説

キネシン分子モーターの仕組み

早稲田大学理工学部物理学科　川口憲治, 上村想太郎, 石渡信一

Kinesin motors are mechano-enzymes that hydrolyze ATP to generate force and directional movement along a microtubule. Nucleotide-dependent conformational changes of the head and neck region of kinesin have been shown by cryoelectron microscopy and spectroscopic techniques. Single molecule analysis supports key predictions of the hand-over-hand model for motility of dimeric conventional kinesin, whereas the discovery of a processive one-headed kinesin strongly supports the biased Brownian ratchet model. In this short review, we summarize the present status of research on the mechanism of kinesin motility.

kinesin / microtubule / unbinding force measurements / hand-over-hand model / biased Brownian ratchet model

1. はじめに

キネシンは, ダイニンに続く微小管系の第2のモータータンパク質として約15年前にイカの神経軸索で見出された[1]. 細胞内で小胞や細胞内小器官の輸送を行い, 順行性（神経体からシナプス末端へ向かう）の軸索流や, 細胞分裂時の中心体の分離と紡錘体の形成にも重要な役割を担っている. ゲノム解析の結果, キネシンは10種のサブファミリーに分類され（キネシン様タンパク質, KRP), ヒトやマウスでは45種類が同定されている. 最初にイカから精製された天然のキネシン（従来型キネシン, conventional kinesinとよぶ）は一般に神経軸索にあって小胞輸送を担い, 340個のアミノ酸からなる相同な2つの球状頭部をもつ（図1). キネシン分子モーターは, この2つの頭部が微小管との結合・解離を交互に繰り返しつつ微小管のプラス端（重合端）側に向かって“歩く”リニアモーターであるといわれている. そこにはATP加水分解と共役した巧妙な仕組みが存在する.

キネシンの特徴は, たった1分子でも微小管から解離することなく長距離（1 μm程度）かつ長時間（1秒程度）にわたって運動を持続するというプロセッシブ性（逐次前進性）にある. このことと, 分子量が小さく安定なことから, キネシンはミオシンやダイニンに比べて研究しやすく, 最近の研究の進展には目覚しいものがある. 原子間力顕微鏡（AFM）や光ピンセットによる1分子操作・計測, 電子顕微鏡構造解析や光学顕微鏡による1分子イメージングなどの生物物理学的手法, それに加えて, 特定のアミノ酸を置換した変異体を調製できる遺伝子工学的手法を用いた多くの研究成果が報告されている. ここでは, これまでに明らかになった実験事実とキネシンの歩く仕組みを中心に解説し, 我々の研究成果を交えてまとめるとともに, 未解明な部分や今後解明すべき興味ある問題について述べる.

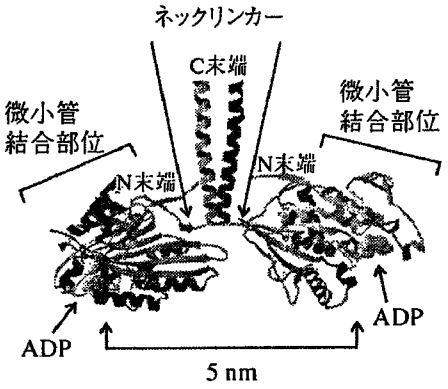

図1　従来型キネシンの立体構造[12]
ホモダイマーのN末端側にある2つの頭部は, それぞれ同じ微小管結合部位とATP/ADP結合部位をもつ. 両方の頭部にADPを結合している状態では頭部の間隔は約5 nmである.

Molecular Mechanism of Kinesin Motor

Kenji KAWAGUCHI, Sotaro UEMURA and Shin'ichi ISHIWATA
Department of Physics, School of Science & Engineering, Waseda University

2. キネシンの歩行メカニズム

2.1 Hand-over-hand モデル

研究初期の重要な生化学上の発見は，キネシンに結合したADPの解離を微小管との結合が促進するというものであった．精製したキネシンはその両方の頭部にADPを結合している．ADPの結合はキネシンの構造を安定化し，解離速度は非常に遅い（キネシンはヌクレオチドがないと変性しやすいが，微小管に結合すると安定化する）．ところがそこに微小管を加えると，結合していたADPの半分が解離した．さらにATPを加えると，もう半分のADPが解離した．この結果の解釈は，一方の頭部が微小管に結合するとADPを解離し，その頭部にATPが結合することによってもう一方のADP結合頭部が微小管に結合できるようになり，ADPの解離が起こるというものである．このことから，微小管に結合した頭部にATPが結合すると，キネシンは次の一歩を踏み出すための構造変化を起こす，という描像が生まれた[2),3)]．

双頭構造をもつ従来型キネシンはプロセッシブであり，微小管から解離するまでに8 nmステップを1秒間に100回以上繰り返す[4)]．8 nmはα,βサブユニットから成るチューブリンヘテロダイマー（微小管の構成単位）のサイズに対応する．また，従来型キネシンはタイトカップリング型モーターであり，8 nmステップは1回のATP加水分解を伴う．では，ATPaseサイクルのどの段階でステップを生じるのだろうか？　ATP結合時か，それとも加水分解した後か？　あるいは前頭部が結合する瞬間にステップが生じるのだろうか？　ATP結合に伴ってネックリンカーと呼ばれる部分が構造変化を起こすことがわかっているが（2～4節で詳述），これにはエネルギー変化がほとんど伴わないといわれている．したがって，少なくともATP結合時ではないと推測される．モーターのステップとATPaseサイクルの各段階との対応づけは確定していない．最近西山ら[5)]によって8 nmステップが2つの4 nmステップからなっていることが示されたこともあり，この問題は今後キネシンの歩行メカニズムを解明する上での鍵である．

キネシンのプロセッシブ性を説明するために以前から提案されているのが，hand-over-handモデルである[6)-8)]．図2-1に，現在知られているこのモデルの大筋を示した．

(A) ADP結合状態で精製されたキネシンの一方の頭部は，微小管に結合すると直ちにADPを解離してヌクレオチドなし状態で結合する．もう一方の頭部はADPを結合したまま解離状態にある．

(B) 微小管と結合している頭部にATPが結合するとその頭部内のネックリンカードメインが構造変化を起こしてプラス端方向に固定される（結合頭部の2重矢印）．

(C) その結果，解離頭部は前方に移動し，微小管の結合部位に結合できるようになり，ADPを放出してヌクレオチドなし状態で結合する．つまり，この瞬間に双頭結合になる．

(D) 後頭部に結合したATPは加水分解され，リン酸が放出されるとネックリンカードメインはまたもとの状態に戻り，後頭部は微小管から解離する（リン酸が放出される前に解離するのか，放出後に解離するのかは不明）[7)]．

このように，キネシンでは，ATP/ADPの結合部位にある硬いらせん構造をとったリン酸感受性ループと，ATPが結合すると固定されるネックリンカードメインとの間にアロステリック制御が働くとされる．

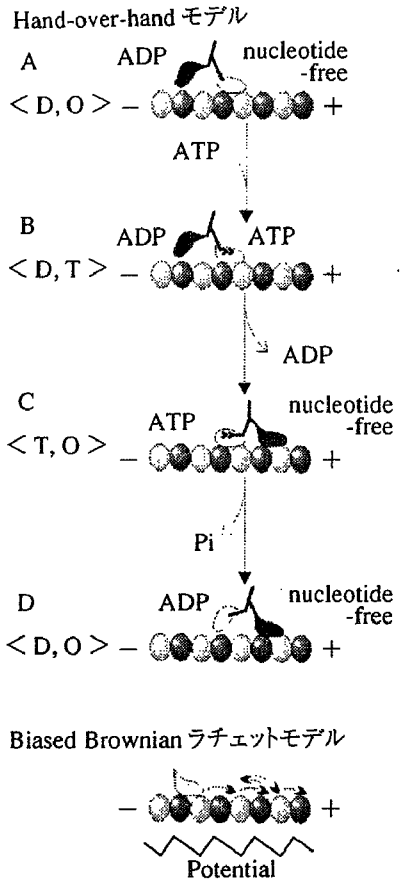

図2　1. さまざまな実験結果にもとづいて提案されている，hand-over-hand モデル
キネシンがそれぞれのヌクレオチド状態で構造変化を起こし，単頭，双頭結合を繰り返す．O：ヌクレオチドなし（nucleotide-free），D, T, Piはそれぞれ ADP, ATP, 無機リン酸を表している．
2. Biased Brownian ラチェットモデルの概念図
単頭キネシンと微小管との相互作用ポテンシャルとしてノコギリ歯状のものを仮定．ATP加水分解とブラウン運動を巧みに利用しつつ一方向に進む様子を表す．

2.2 キネシンのプロセッシブ性とメカノケミカルサイクル

分子モーターがプロセッシブであるためには高いduty ratio（1回のATP加水分解サイクルに占める結合時間の割合）が必須であるという考え方がある（図3）．双頭構造をもつ分子モーターがプロセッシブであるためには，それぞれの頭部のduty ratioは少なくとも0.5以上でなければならない．0.5以下だと双頭ともに解離してしまう瞬間が生じると考えるのである．一方，筋肉を構成する非プロセッシブなミオシンIIでは，duty ratioは0.01～0.1であり，したがってアクチンフィラメントに滑り運動を引き起こすためには10～100個の頭部が必要だというわけである（注：ミオシンIIのduty ratioについては異論がある）[8]．

2.3 破断力測定による結合様式の決定

キネシンのヌクレオチド結合部位はヌクレチドなし状態と，ATP, ADP・Pi, ADP結合の，少なくとも4つのヌクレオチド状態をとるはずである．この4つのヌクレオチド状態と，強結合・弱結合状態，および解離状態を区別したキネシンのメカノケミカルサイクルに関するモデルが上記のhand-over-handモデルであり，これを立証するためにはキネシンの2つの頭部がどのヌクレオチド状態で単頭結合なのか，あるいは双頭結合なのか，またこの2状態間の転移はいつどのように行われるのかを決定する必要がある．双頭キネシン・微小管複合体のクライオ電子顕微鏡による画像解析は決定的でなく，ヌクレオチドなし状態とAMP-PNP（非分解性のATPアナログ）存在下の両方で単頭結合が優位に観察されるという報告[9]と双頭結合が優位であるという報告[10]の両方がある．しかし，これらの結果は，微小管（チューブリン）よりもモル比で過剰なキネシン分子を加えた条件下で得られたものであり，隣接して結合することによってキネシン（あるいはチューブリン）の構造が歪んでいる可能性が指摘されている[10]．

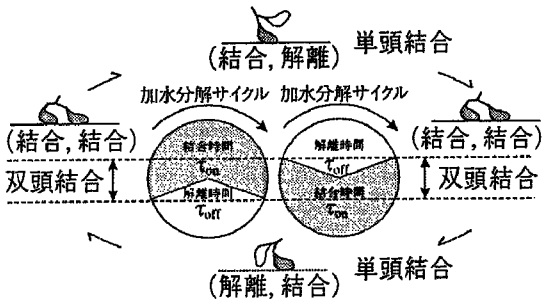

図3　プロセッシブモーター
双頭構造をもつ分子モーターがプロセッシブに運動するためには，各頭部のduty ratio（結合時間の割合）は少なくとも0.5以上であることが必要．この図は，ATP加水分解サイクルにおける2つの頭部の結合・解離のサイクルの位相が互いに180度ずれているという点で，頭部間の協調性を示している．

我々は最近，微小管に結合している1分子のキネシンの力学特性をそれぞれのヌクレオチド状態で調べ，単頭結合か双頭結合か，あるいは単頭結合であっても強結合か弱結合かの結合様式に関する直接的な証拠を得た[11),12)]．1分子の従来型キネシンが吸着したポリスチレンビーズを光ピンセットで捕捉・操作し，微小管に結合させた上で，微小管に平行にプラス端，あるいはマイナス端方向に負荷を加える．この結果の破断曲線や，破断直前の変位－負荷関係を解析することによって，キネシン・微小管複合体1分子結合の破断力と複合体の弾性率を求めた（図4）．AMP-PNP存在下（<T, O>に対応）での破断力と弾性率は，ともに，ヌクレオチドなし状態（実験条件からみて<D, O>に対応）あるいはAMP-PNPとADPとの共存状態（<D, T>に対応）で得られた値の2倍となった．この結果は，AMP-PNP存在下ではキネシンは双頭結合であり，あとの2状態では単頭結合であるということを強く示唆している．

また，破断力の大きさは，ヌクレオチド状態によらずプラス端よりもマイナス端方向に負荷をかけたときのほうが約1.4倍大きかった．このように，キネシン・微小管結合は負荷を加えることで不安定化し，しかもそれが負荷の向きに関して非対称になっている．そこで，双頭結合状態では双頭ブリッジを通じての内部応力が存在すると仮定すると，プラス端側に負荷を受ける後ろの結合頭部が比較的不安定で，解離しやすい傾向にあると推測できる．

2.4 ネックリンカーの構造変化の検出

キネシンと微小管の結合状態を捉えたクライオ電子顕微鏡解析もキネシン頭部の動きについて有力なヒントを与えた[9]．ヌクレオチドなし状態で結合頭部のマイナス端側に位置していた解離頭部が，AMP-PNPを加えると結合頭部のプラス端側へと移動しており，結合頭部のネックリンカーと呼ばれる部分が大きく構造変化しているように見えた．この結果は，ネックリンカーのC末端部を金コロイドでラベルしたキネシンモノマーにAMP-PNPが結合すると，期待通りに金コロイドの位置が頭部内を移動したことで最近確かめられた[13]．それによると，微小管に結合した頭部のネックリンカーは，ヌクレオチドなし状態，あるいはADP結合状態では動きやすい状態にあるが，ATPが結合すると微小管のプラス端方向に向かって振れ，結合頭部の表面に固定される．この動きを利用して解離頭部は前方のチューブリン分子の結合部位に近づき，結合できるようになると考え

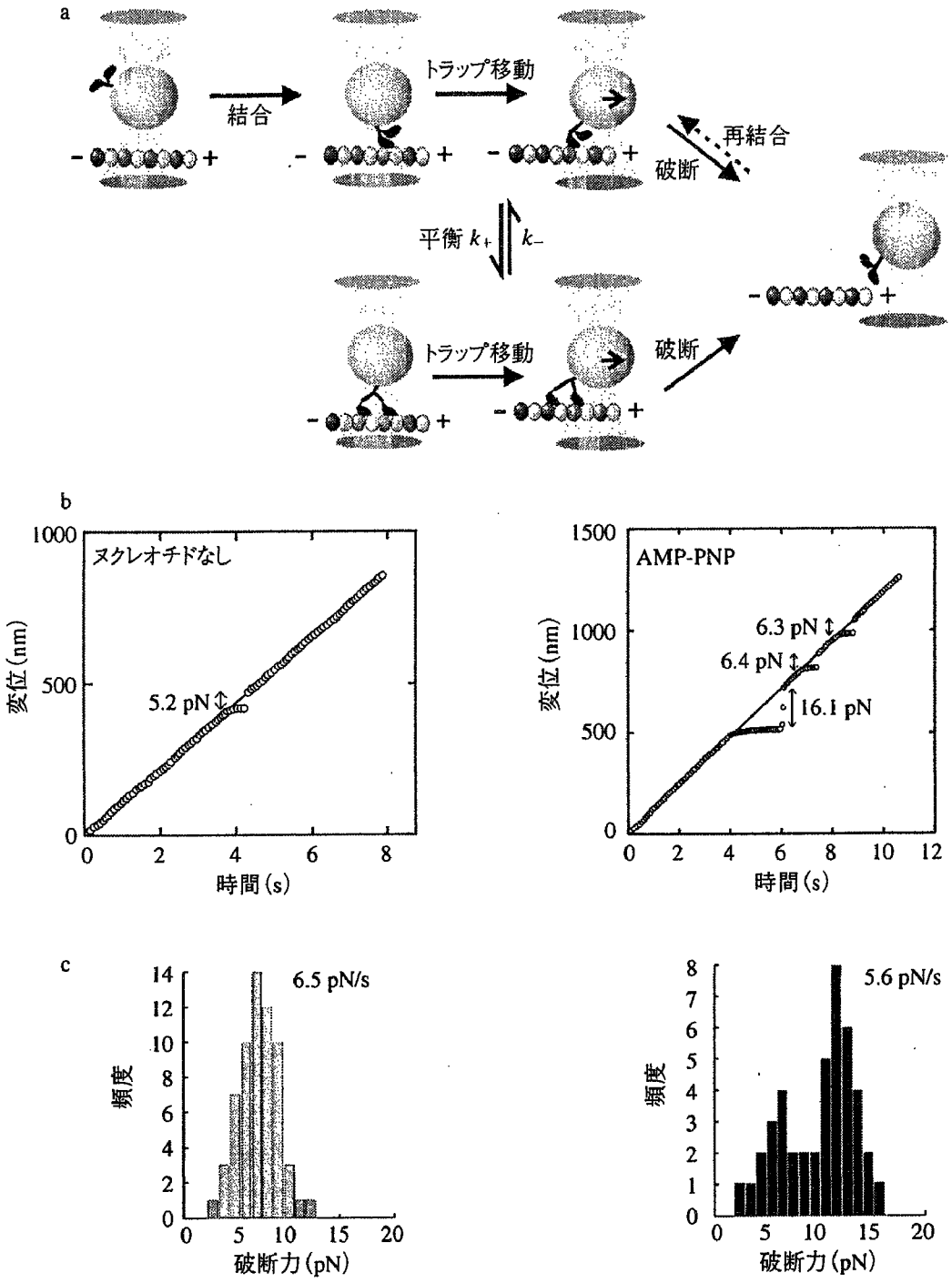

図4 光ピンセット法による1分子キネシンの運動・力学測定
(a) キネシン1分子を吸着した直径1 μmのビーズを，ローダミンで蛍光標識した微小管上へと光ピンセットを用いて移動し，相互作用させる．さらに捕捉中心を移動することによって，キネシン・微小管結合に負荷を加えると，結合が破断する．この測定は繰り返し行うことができる．(b) 光ピンセットの捕捉中心（実線）とビーズ中心（丸印）の距離から，キネシンに加わる負荷を計算することができ，破断の際の負荷（破断力）の大きさから結合状態（強・弱，単頭・双頭）を特定することができる．また弾性率を見積もることもできる[10]．特にAMP-PNP状態では，一度破断が起こった後も，微小管に沿って捕捉中心を動かし続けると，再結合・再破断が繰り返し起こる（図a参照）．(c) ヌクレオチドなし状態（左）と，AMP-PNP状態（右）での破断力分布（数字は負荷上昇速度）．

る. このように, せいぜい5 nmしか離れていない2つの頭部[14]がどのようにして8 nmのステップを踏めるのかという前々からの疑問が, ネックリンカーの構造変化で説明できるようになった.

それでは単に双頭構造であればプロセッシブになるかというと, そうではない. キネシン様モータータンパク質であるncdは双頭構造をもつにもかかわらず非プロセッシブであり, 連続して2回ステップすることさえできないからである[15]. 従来型キネシンが高いプロセッシブ性をもつ秘密は, 少なくとも一方の頭部が常に微小管に結合しつづけていることにある. すなわち, 単にduty ratioが0.5以上であるというだけでなく, 結合している頭部はもう一方の頭部が次の結合部位に結合するまでは離れない, という特別な仕組み (双頭間の協調性) が存在することになる.

2.5 Biased Brownian ラチェットモデル

hand-over-handモデルがキネシン分子自身の構造変化を中心に提案されたモデルであるのに対し, ブラウン運動 (熱揺らぎ) や相互作用ポテンシャルの非対称性が中心的な役割を果たしていると主張するのが, biased Brownianラチェットモデルである[16)-18)]. このモデルでは, キネシンと微小管の分子間相互作用ポテンシャルはノコギリ歯状になっていて, 熱揺らぎによってポテンシャルの山を越えるか, ATPの加水分解に伴ってポテンシャルが変形するかによってキネシンが一方向に移動できるようになると考える (図2-2). 最近, このモデルを支持するような実験データが, 単頭キネシン様モータータンパク質のKIF1Aで報告されている[19]. 単頭のKIF1Aが解離せずに平均1 μmも微小管のプラス端方向に移動するのである.

どのような仕組みで, 単頭KIF1Aは微小管から解離することなく一方向に移動できるのだろうか? 微小管と結合しているKIF1Aの触媒部位の構造を, ADP状態とAMP-PNP状態とで電子顕微鏡解析し, X線結晶解析で得られた構造をあてはめて解析すると, ADP状態の触媒部位の長軸 (頭部は楕円形をしている) はAMP-PNP状態のそれよりも20度ほど時計回りに傾いていた. つまり, AMP-PNP状態のほうが, KIF1Aの触媒部位が微小管のプラス端方向, つまり歩行する方向に向いているとみることができる[20]. その上, KIF1Aはキネシンと同様の微小管結合部位とリシンに富むループ (K-ループ) をもっていて, このループがチューブリンのグルタミン酸に富むC末端部と結合する. つまりKIF1Aは単頭内部に2つのチューブリン結合部位をもっていて, これを利用して解離することなく運動できることがわかってきた[20]. 事実, このループを削除したり変異させたりするとプロセッシブ性が減少した. さらに, 従来型キネシンの単頭部分 (そのままでは非プロセッシブ) のK-ループをリシン6個分だけのばすと, KIF1Aと同様にプロセッシブにすることができた.

KIF1Aの歩行運動は, その速度が大きく変動するという点でキネシンと異なる. さらに興味深いことに, KIF1Aの移動ステップは, ATPの加水分解と1:1に対応しなかった. 無負荷のときでさえ, 1ステップの間に数個のATPが分解した. これらのことは, KIF1Aの移動運動に, 微小管に沿った拡散 (ブラウン) 運動が大きな役割を演じていることを示唆する. この点が, 1ステップと1個のATP分解とが対応する (タイトカップリング) 従来型キネシンと大きく異なる. ところで最近喜多村らによって, ミオシンIIの単頭酵素断片 (S1) が1個のATP分解に対して5.5 nmのステップを1~5回行うこと (ルースカップリング) を示す結果が得られた[21]. したがって, ミオシンの運動は確率的な分子機構によることが示唆されている. つまり, 分子モーターは自らの構造変化だけでなくブラウン運動を巧みに利用して方向性運動を生み出しているというのがこのモデルの本質である.

3. キネシンの運動方向性の決定

キネシンは微小管のプラス端方向に歩行運動するが, 同じキネシンファミリーでもncdやKer3, それに細胞質ダイニンはマイナス端方向に運動する. 特にキネシンとncdではモーターコア (モータードメインのうちネックリンカーに相当する部位は含まない) のアミノ酸配列や立体構造がほとんど同じであるにもかかわらず運動の方向性が異なる. 事実, キネシンのモーターコアをncdのモーターコアと置換しても運動方向はプラス端方向であり, 逆の組み合わせにしても, マイナス端方向へのncdの運動性は変わらなかった.

両者が構造の上で大きく異なる点は, 二量体を形成するcoiled coil部分とモーターコアをつなぐドメイン (キネシンの場合はネックリンカーを含む) である. そのため, そのドメインの遺伝子改変による運動性の変化が研究され, ncdのモーターコアをキネシンのモーターコアに置換した上で, さらにcoiled coilをつなぐLoop L0のGly347とAsn348を削除した変異体がプラス端へと運動方向を変えることが示されている[22]. また, Endowと樋口により, ncdの同じドメインにある340番目のAspをLysに変えた変異体は, プラス端とマイナス端のどちらにも従来型ncdと同じ速さで運動することが見出された[15]. ちなみに, キネシンのモーターコアはN末端側にありncdではC末端側にあるが, この違いは

方向性に関与していないとされている.

このように, 運動方向性の研究も, この1, 2年で急速に進んでいる. ミオシンファミリーでも, 従来型のミオシンIIやミオシンVがアクチンのB端（重合端）側へそれぞれ滑り運動と歩行運動するのに対し, 最近発見されたミオシンVIは逆方向のP端側へと歩行運動する. 運動方向性のメカニズムについても, 立体構造による空間配置や負荷の影響など, 今後多角的な研究が期待される.

4. おわりに

この数年の間に, 分子モーターが1分子レベルでどのように働き, 力を発生するかの具体的な描像が得られるようになった. モーターコアのヌクレオチド結合部位で始まる小さな構造変化が歩行運動へと増幅されていく. 生化学, クライオ電子顕微鏡, 1分子計測の結果はすべて, 微小管に結合したキネシン頭部にATPが結合することによって構造変化が生じることを示している. この構造変化によって, 解離しているほうの頭部が微小管に結合できるようになり, そのことが後方の結合頭部に対して微小管のプラス端方向への内部負荷を生み出す.

では, 内部負荷がどのようなメカニズムで, 方向性運動を引き起こす分子内協調性を生み出すのだろうか? 最近, 一定負荷を加えるとキネシンのATPase活性が下がるという報告がある[23]. また我々も, 外部負荷がヌクレオチド結合性（酵素活性）を変化させるという証拠を得ている（上村, 石渡；未発表）. このような性質こそ, 化学力学酵素としての分子モーターの本質をつくものであろう. 内部負荷による分子内協調性のメカニズムを明らかにするための鍵もここにある.

今後はさらに高時空間分解能で構造変化を捉える研究が盛んになるだろう. 安藤らによって開発された高速AFMによるミオシンVのリアルタイム1分子挙動観測なども注目される[24]. キネシン歩行運動における構造変化の役割をさらに明確にするためには, 各ヌクレオチド結合状態での結晶構造解析が必要になる. そしてまた, ステップ中の頭部の動きを直接観察することができれば, もっと詳細にキネシンの歩行運動メカニズム, つまりそこにおける化学・力学共役の内容を理解することができるだろう. その一方で, 上で述べたように, 必ずしもタンパク質の構造変化を必要としないBiased Brownianラチェットモデルのほうが正しいようにみえる現象がある. ラチェットモデルを肯定的にしろ否定的にしろ実証するためには, どのような実験を組めば良いだろうか. これこそ実験家にとって大きなチャレンジである.

草稿の段階で有益な助言を頂いた広瀬恵子さん（産総研・ジーンディスカバリーセンター）に感謝します.

文 献

1) Vale, R. D., Reese, T. S. and Sheetz, M. P. (1985) *Cell* **42**, 39-50.
2) Hackney, D. D. (1988) *Proc. Natl. Acad. Sci. USA* **85**, 6314-6318.
3) Hackney, D. D. (1994) *Proc. Natl. Acad. Sci. USA* **91**, 6865-6869.
4) Svoboda, K., Schmidt, C. F., Schnapp, B. J. and Block, S. M. (1993) *Nature* **365**, 721-727.
5) Nishiyama, M., Muto, E., Inoue, Y., Yanagida, T. and Higuchi, H. (2001) *Nature Cell Biol.* **3**, 425-428.
6) Vale, R. D. and Milligan, R. A. (2000) *Science* **288**, 88-95.
7) Schief, W. R. and Howard, J. (2001) *Curr. Opin. Cell Biol.* **13**, 19-28.
8) Howard, J. (2001) Mechanics of motor proteins and the cytoskeleton. Sinauer Associates, Inc.
9) Hirose, K., Lowe, L., Alonso, M., Cross, R. A. and Amos, L. A. (1999) *Mol. Biol. Cell* **10**, 2063-2074.
10) Hoenger, A. *et al.* (2000) *J. Mol. Biol.* **297**, 1087-1103.
11) Kawaguchi, K. and Ishiwata, S. (2001) *Science* **291**, 667-669.
12) Uemura, S. *et al.* (2002) *Proc. Natl. Acad. Sci. USA* **99**, 5977-5981.
13) Rice, S. *et al.* (1999) *Nature* **402**, 778-784.
14) Kozielski, F. *et al.* (1997) *Cell* **91**, 985-994.
15) Endow, S. A. and Higuchi, H. (2000) *Nature* **406**, 913-916.
16) Vale, R. D. and Oosawa, F. (1990) *Adv. Biophys.* **26**, 97-134.
17) Astumian, R. D. (1997) *Sci. Am.* **285**, 56-64.
18) 徳永万喜洋 (1997) ナノピコスペースのイメージング－生物分子モーターのメカニズムを見る－ (柳田敏雄, 石渡信一編), 吉岡書店.
19) Okada, Y. and Hirokawa, N. (1999) *Science* **283**, 1152-1157.
20) Kikkawa, M. *et al.* (2001) *Nature* **411**, 439-445.
21) 喜多村和郎, 岩根敦子, 徳永万喜洋 (2000) 生物物理 **40**, 89-93.
22) Wade, R. H. and Kozielski, F. (2000) *Nature Struc. Biol.* **7**, 456-460.
23) Schnitzer, M. J., Visscher, K. and Block, S. M. (2000) *Nature Cell Biol.* **2**, 718-723.
24) Ando, T. *et al.* (2001) *Proc. Natl. Acad. Sci. USA* **98**, 12468-12472.

nature cell biology

Vol 4 No 9
September 2002
http://www.nature.com/naturecellbiology

Growing with TSC proteins

Actin treadmilling

Restricting telomerase access

Microscopic analysis of polymerization dynamics with individual actin filaments

Ikuko Fujiwara*, Shin Takahashi*, Hisashi Tadakuma*, Takashi Funatsu* and Shin'ichi Ishiwata*†‡

*Department of Physics, School of Science and Engineering, and †Advanced Research Institute for Science and Engineering, Waseda University, 3-4-1 Okubo, Shinjuku-ku, Tokyo 169-8555, Japan
‡e-mail: ishiwata@waseda.jp

Published online: 19 August 2002; DOI:10.1038/ncb841

The polymerization–depolymerization dynamics of actin is a key process in a variety of cellular functions. Many spectroscopic studies have been performed in solution, but studies on single actin filaments have just begun. Here, we show that the time course of polymerization of individual filaments consists of a polymerization phase and a subsequent steady-state phase. During the steady-state phase, a treadmilling process of elongation at the barbed end and shortening at the pointed end occurs, in which both components of the process proceed at approximately the same rate. The time correlation of length fluctuation of the filaments in the steady-state phase showed that the polymerization–depolymerization dynamics follow a diffusion (stochastic) process, which cannot be explained by simple association and dissociation of monomers at both ends of the filaments.

To date, there have been many physico-chemical studies of actin polymerization, all of which have been performed in solution. These studies have demonstrated that the polymerization of actin consists of nucleation and growth followed by a steady-state phase, where fragmentation and annealing of filaments may also occur. The average kinetics and thermodynamics of the overall process, and essential elements of these processes, have been experimentally clarified and theoretically formulated[1,2]. Electron microscopy showed that in common with microtubules, actin filaments have a structural polarity, such that the kinetics of polymerization and depolymerization at the two ends of the filaments are different[2–6]. The end of the filaments at which the polymerization rate is higher is called the 'barbed end'. The other end is referred to as the 'pointed end'.

After steady-state polymerization is attained, a treadmilling process is thought to occur[7]. Filament assembly occurs at the barbed end of filaments, whereas depolymerization occurs at the pointed end. This process ensures that the filament maintains a constant average length. The treadmilling process has been examined experimentally in solution[7,8].

When the rate of polymerization is greater than the rate of ATP hydrolysis, ATP-bound actin molecules should cap the ends of the filaments[8]. Depending on whether each end of the actin filaments is capped by ATP-bound actin (ATP cap) or ADP-bound actin (ADP cap), the dynamics of the filaments are predicted to be different, resulting in so-called 'dynamic instability' under appropriate conditions[8,9]. However, in contrast to microtubules[10,11], such a dynamic instability has not yet been demonstrated experimentally with actin filaments. Thus, the examination of whether such a dynamic process occurs with actin is still a challenging problem.

In the 1980s, it became possible to visualize single actin filaments under the fluorescence microscope through labelling with rhodamine–phalloidin (Rh–Ph)[12] or by directly labelling actin with a fluorescent dye, fluorescein isothiocyanate (FITC), and stabilizing the filament with phalloidin[13]. Phalloidin is added to suppress the depolymerization of actin filaments so that they can be imaged at extremely low actin concentrations. This technique is very useful for stable and clear visualization of filaments under a conventional fluorescence microscope, without disturbance of background fluorescence[14,15]. Using this technique, we have previously examined the polymerization process of single actin filaments[16].

In the present study, we have used actin directly labelled with a fluorescent dye. This overcomes the disadvantage of using phalloidin, which suppresses depolymerization. In addition, we have used total internal reflection fluorescence microscopy, which enabled us to study not only the polymerization process, but also the depolymerization process of individual actin filaments under standard polymerization conditions. This technique was recently applied to a study on the polymerization process of single actin filaments in the presence of the Arp2/3 complex[17,18]. Here, not only do we demonstrate the treadmilling process on single actin filaments, but we also extend previous studies by identifying new aspects of the polymerization–depolymerization dynamics of actin.

Results

Direct observation of the polymerization process of single actin filaments. Figure 1 shows direct observation of the actin(Ca) polymerization process, which was induced by the addition of polymerization buffer (potassium chloride and magnesium chloride). Although all the filaments examined were still short at 6 min after the addition of salts (Fig. 1a), most had elongated by more than 10 μm and the total number of filaments had increased after a further 34 min (Fig. 1b). It is clear that most of the filaments grew gradually with time (Fig. 1c–q). Transverse Brownian movement of actin filaments was suppressed by addition of methylcellulose, although longitudinal Brownian movement was not. It seems that there are two types of filament: those that elongated significantly (Fig. 1, white arrows) and those that did not (Fig. 1, arrowheads).

For the initial 30 min of observation, approximately 12% of the filaments showed no elongation (0.7 μM G-actin(Ca); $n = 212$). This may be attributed to adhesion of (or interference with) the filament ends to the glass surface and/or entanglement with methylcellulose, as the proportion of actin filaments that did not elongate detectably was not as high in our previous experiments with Rh–Ph[16], in which methylcellulose was not included.

Next, we examined the time course of change in the total length of individual actin filaments after the addition of salts at 0.3 μM (Fig. 2a), 0.5 μM (Fig. 2b) and 0.7 μM (Fig. 2c) actin. It is clear that the polymerization process of each filament consists of a polymerization phase and a subsequent steady-state phase (Fig. 2c). These two phases were not easily distinguishable at lower actin concentrations.

Table 1 **Polymerization and depolymerization rate constants.**

Conditions		k^+ (M^{-1} s^{-1})	k^- (s^{-1})	C_0 (μM)
		× 10^7		
Steady-state phase*	Ca	18	25	—
	Mg	45	29	—
Polymerization phase†	Ca	0.61	0.85	0.14
	Mg	1.0	0.64	0.064
Solution + 0.5%	Ca	0.75	0.94	0.13
methylcellulose‡	Mg	1.2	0.80	0.067
Solution§	Ca	0.50	0.57	0.11
	Mg	0.95	0.90	0.095

Conditions: 30 mM potassium chloride, 2 mM magnesium chloride, 4 mM ATP, 20 mM MOPS at pH 7.0, 10 mM DTT, with*†‡ or without§ 0.5% (w/v) methylcellulose.

*Estimated from the analysis of length fluctuation in the steady-state phase in single-molecule analysis.

†Estimated from the average length change in the polymerization phase in single-molecule analysis.

‡,§Obtained from the initial rate of increase in the fluorescence intensity in solution in the presence‡ or absence§ of methylcellulose.

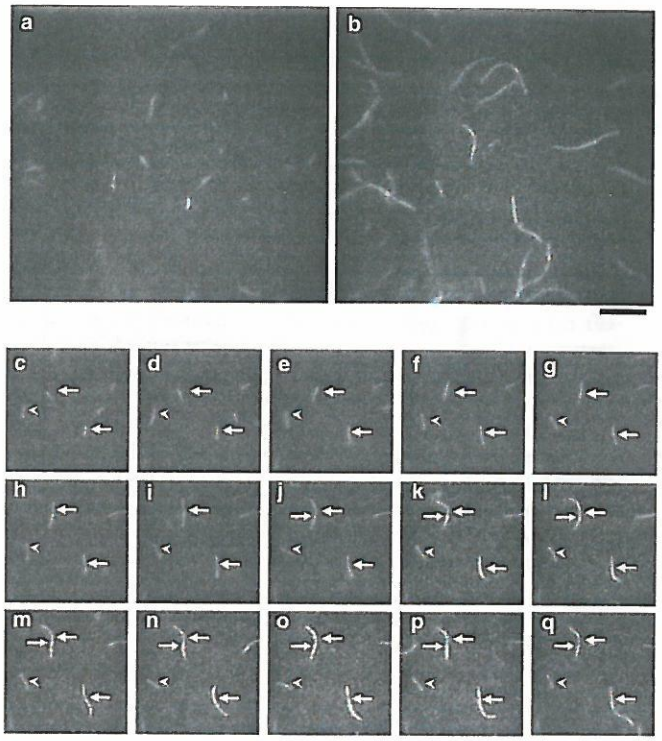

Figure 1 **Fluorescence micrographs of actin(Ca) polymerization. a,b,** Fluorescence micrographs taken 6 min (**a**) and 34 min (**b**) after the addition of salts (movies are available at http://www.phys.waseda.ac.jp/bio/ishiwata/movies.html). **c–q,** Fluorescence micrographs of the central regions in **a** and **b**, in which several filaments were visualized without interference by overlapping filaments. Micrographs were taken every 2 min, between 6 min (**c**) and 34 min (**q**) after the addition of salts. White arrows indicate the filaments for which polymerization could be observed, whereas an arrowhead indicates a filament which did not seem to polymerize. Yellow arrows indicate an example of a fluorescent blob on the actin filament, which was used as a fiducial marker to measure the length change at each end of the filament. Actin concentration, 0.7 μM. Scale bar represents 10 μm.

It is notable, especially in Fig. 2c, that the time at which the steady-state phase began varied between filaments. In both phases, all the actin filaments displayed small fluctuations in length. We did not observe any filaments that only underwent depolymerization or displayed any dynamic instability[10,11], as previously observed for microtubules. Occasionally, a large change in length, as a result of head-to-tail annealing of two filaments[4] (longer than a few microns), was observed. However, these data were not used for the analysis described below, as we focused on the polymerization–depolymerization dynamics at both ends of the filaments. We did not observe spontaneous fragmentation of actin filaments, as observed in the presence of gelsolin[16].

Generally, a fluorescence image of an actin filament (that is, an intensity profile along the filament) is not uniform. Indeed, we detected fluorescent blobs at fixed positions on the filaments (Fig. 1, yellow arrows). Using a blob as a fiducial marker, we measured the length of the filament portions on each side of the fluorescent marker (Fig. 2d). These measurements show that after the steady-state phase was attained, the filament continued growing at one end, whereas it began to shorten correspondingly at the other end. We assign the former as the barbed end and the latter as the pointed end, on the basis of the known difference in critical concentration for the two ends of the filament. This result demonstrates that the treadmilling process can occur on an individual actin filament. Among the data at 0.7 μM actin(Ca), we found seven examples that had a bright marker sufficient for quantitative analysis of the polymerization process at each end of the filament. At the steady-state phase, the polymerization rate averaged over these seven cases was +0.069 ± 0.037 μm min^{-1} (± standard deviation, S.D.) at the fast-growing end (barbed end), −0.062 ± 0.051 μm min^{-1} at the slow-growing end (pointed end) and 0.006 ± 0.062 μm min^{-1} for the total length of the filaments. This confirms that on average, the growing rate at the barbed end was compensated by the shortening rate at the pointed end. However, the growing and the shortening rates did not necessarily coincide with each other in each filament, at least within the time range we examined (8–30 min).

As a control, the time course of length change in a single actin filament at steady state in the presence of phalloidin was determined (Fig. 2e). Phalloidin was added to a final concentration of 150 nM, which is equal to the actin concentration and higher than the dissociation constant of phalloidin to actin (17 nM)[19].

Estimation of the polymerization rate of actin(Ca) during the polymerization phase. To determine the relationship between the polymerization rate and actin concentration, we analysed the change in length of actin filaments for 6 min after commencing microscopic observation. This represents the polymerization rate of actin during the initial polymerization phase (Fig. 2). We failed to record the earliest initial phase of polymerization; however, the polymerization rate estimated from our measurements is reliable, as linear extrapolation of our data passes through the origin (zero length at time zero).

The change in length was measured at 1-min intervals for the initial 6-min observation period (Fig. 2). The data is presented as a histogram, showing the distribution of the change in length at three different concentrations of actin (Fig. 3a–c). Thus, the polymerization rate obtained from the average distribution and the S.D. from the width of the distribution are estimated as 0.13 ± 0.30 μm min^{-1}, 0.35 ± 0.38 μm min^{-1} and 0.49 ± 0.46 μm min^{-1} at 0.3, 0.5 and 0.7 μM actin, respectively. The relationship between the polymerization rate and the actin concentration is summarized in Fig. 3d. On the basis that an actin filament of 1 μm in length consists of 400 monomers, polymerization and depolymerization rate constants were estimated to be 6.1 × 10^6 M^{-1} s^{-1} and 0.85 s^{-1}, respectively. The critical concentration for polymerization was determined as 0.14 μM (see Table 1).

Analysis of length fluctuation of actin(Ca). The total length of

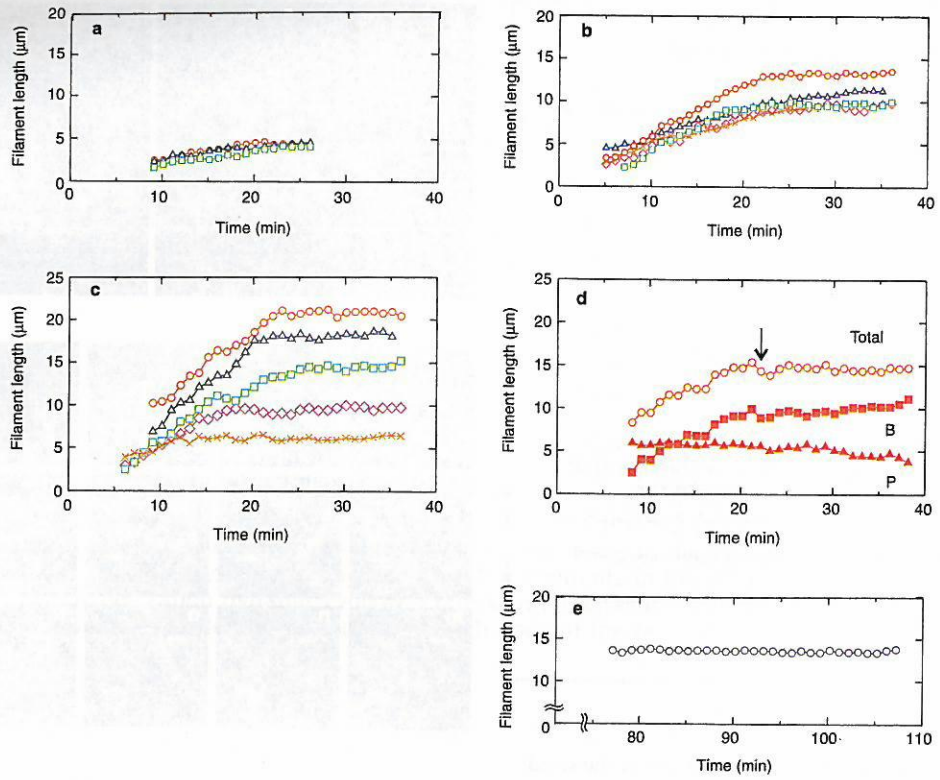

Figure 2 **Time course of actin(Ca) polymerization at various actin concentrations. a–c**, Examples showing the time course of polymerization of single actin(Ca) filaments at 0.3 μM (**a**), 0.5 μM (**b**) and 0.7 μM (**c**) actin. **d**, An example showing the time course of polymerization of a single actin(Ca) filament (actin, 0.7 μM), in which the barbed end and pointed end could be distinguished. An arrow indicates the start of the steady-state phase. Total, total length of the actin filament; B, length between the barbed end and the fluorescent marker; P, length between the pointed end and the fluorescent marker. **e**, A control time course experiment showing the length fluctuation of actin(Ca) filaments stabilized with phalloidin. To maintain the same conditions that were used for the above experiments without phallotoxin, the proportion of TMR-labelled actin was adjusted to 10% of total. Additionally, G-actin(Ca) was added to a final concentration of 140 nM, a critical concentration for polymerization (see Table 1), to match the background fluorescence noise of samples without phallotoxin (see Discussion). Here, the filament length was measured between 77 and 107 min after the observation cell was prepared. Actin and phalloidin were used at 0.15 μM.

each actin filament fluctuated continuously with time (Fig. 2). Fluctuations not only occurred during the polymerization phase (where the length of the filaments increased steadily), but also during the steady-state phase (where the average length of the filaments was almost constant). To examine whether this fluctuation in length could also provide information on the dynamics of polymerization–depolymerization, we analysed the relationship between time and the fluctuation of length. The change in length during various time intervals, termed the correlation time, τ, was measured in the steady-state phase (Fig. 4a). If the fluctuations in length are caused solely by random error in the measurements, then they should be independent of τ.

To confirm the above hypothesis, we examined the effect of phallotoxin, which is expected to suppress the length change caused by depolymerization. In fact, the addition of phalloidin significantly reduced the fluctuation in length (Fig. 2e). Furthermore, as expected, the width of the distribution of length fluctuation seemed to be almost independent of τ (Fig. 4b). This suggests that the width of the distribution obtained for the phallotoxin-labelled actin filaments may represent the degree of error in the length measurements.

By contrast, the width of the distribution of length fluctuation obtained for actin filaments without phallotoxin increased coordinately with τ, whereas the average of the distribution was almost zero, implying that the steady-state phase had been attained (Fig. 4c).

Polymerization dynamics of actin(Mg). The same polymerization properties described above for actin(Ca) have also been shown for actin(Mg)[20]. In contrast to actin(Ca), the resolution of length measurements was lower because of the lower contrast of the fluorescence image. This is probably attributable to a large background fluorescence originating from a large number of short filaments, because nucleation occurs more easily with actin(Mg).

Fluorescence images of polymerized filaments taken 7 and 35 min after the addition of salts showed that the filament density seems to be higher than that of actin(Ca), even if the actin concentration was less than half (compare Fig. 5a with Fig. 1). Furthermore, the polymerization rate constant was 1.0×10^7 $M^{-1}s^{-1}$, approximately twice that of actin(Ca), and the depolymerization rate constant was 0.6 s^{-1} (Fig. 5b). The critical concentration was 0.064 μM (see Table 1).

Next, we analysed the length fluctuation of actin(Mg) filaments once the steady-state phase had been achieved (Fig. 5c). As observed in Fig 5c,d, the degree of length fluctuation of actin(Mg) was larger than that of actin(Ca) (note that the width (S.D.) of the distribution in Fig. 5d is greater than that in Fig. 4c).

Polymerization dynamics of single actin filaments follow a diffusion process. We examined the polymerization and depolymerization dynamics of single actin filaments by analysing the distribution of the length fluctuation during the steady-state phase (Figs 4c,5d). If the fluctuation in length is a result of errors in measurement, it must be independent of τ. However, if it originates from the stochastic process of actin polymerization and depolymerization at both ends of the filaments, the square of the distribution width (S.D.) must be proportional to τ (see ref. 21, chapter 4) and its analysis will provide information on the polymerization–depolymerization dynamics, as described below. To examine this mechanism, we obtained a relationship between $(S.D.)^2$ and τ, as shown in Fig. 6. As a control, we

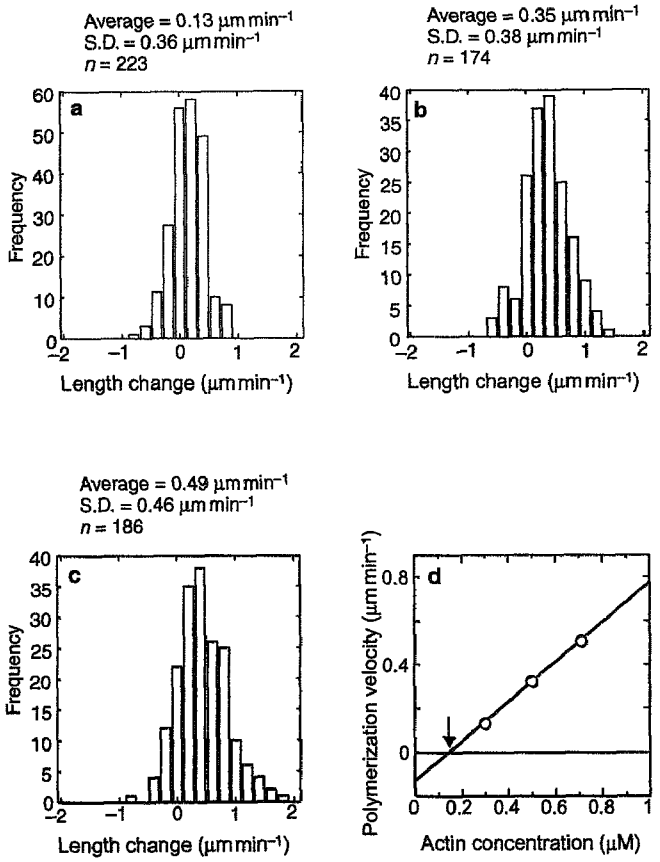

Figure 3 **The effects of G-actin(Ca) concentration on filament growth during polymerization.** The rate of change in length for actin filaments in the polymerization phase is shown for 0.3 μM (**a**), 0.5 μM (**b**) and 0.7 μM (**c**) G-actin(Ca). Data were collected for 6 min after the time at which the length measurement could be initiated (see Fig. 2a–c). The histograms show not only the magnitude of the length fluctuation during polymerization (from the S.D. of the histogram), but also the average polymerization rate (from the centre of the histogram). The average polymerization velocity, the width of the histogram and the total number of measurements (*n*) are shown. **d**, The relationship between the average polymerization rate and actin concentration. The arrow indicates the critical actin concentration for polymerization. The slope indicates the polymerization rate and the intercept of this line with the *y* axis indicates an apparent depolymerization rate.

obtained the same relationship for the phallotoxin-labelled actin filaments under different levels of background fluorescence noise (Fig. 6a).

The line describing the relationship between $(S.D.)^2$ and τ did not pass through the origin, but intersected with the *y* axis for both kinds of actin (Ca or Mg). Thus, the relationship between $(S.D.)^2$ and τ could be expressed as $(S.D.)^2 = (S.D._0)^2 + \alpha\tau$, where α is a constant. We considered that the constant term, $(S.D._0)^2$, is attributable to a measurement error caused by the spatial resolution, which depends on the contrast of the fluorescence image of actin filaments.

It is understandable that the $S.D._0$ value of phallotoxin-labelled actin filaments was smaller (Figs 4b,6a) if we consider that the contrast of the fluorescence image was much higher. To ensure the validity of this explanation, we examined the length fluctuation of phallotoxin-labelled actin filaments at different levels of background fluorescence noise by adding 10%-labelled (Fig. 6a, open triangles and squares) or 50%-labelled (Fig. 6a, closed triangles) G-actin(Ca). We confirmed that the value of $S.D._0$ increased as the contrast of filament fluorescence image decreased (through an increase in the background fluorescence noise). Thus, we conclude that the reason why the value of $S.D._0$ for actin(Mg) (Fig. 6b) was larger than that for actin(Ca) (Fig. 6a) is that the contrast of fluorescence image of actin(Mg) filaments was worse than that of actin(Ca).

Discussion

Treadmilling of actin filaments was first introduced as a theory by Wegner[7] in 1976. Since then, the process has been studied extensively, although only in solutions containing many actin filaments. Here, we have shown through direct examination that the treadmilling process also occurs at the level of individual actin filaments. We observed that continuous elongation at the barbed end and shortening at the pointed end occurred on individual actin filaments during the steady-state phase (Fig. 2d). We also demonstrated that dynamic instability, as observed in microtubules[10,11], does not occur, at least in pure actin filaments.

Here, we formulate the theoretical basis for the linear relationship between $(S.D.)^2$ and τ obtained by analysis of the length fluctuation (Fig. 6)[21]. Assuming that the length fluctuation of actin filaments is caused by the stochastic process of association and dissociation of actin, the existence probability of actin filaments of length x, at time t, $P(x,t)$, $(0 \le P(x,t) \le 1)$, is determined by the following differential equation,

$$\frac{\partial P(x,t)}{\partial t} = \{k^-P(x+a) - k^+CP(x)\} + \{k^+CP(x-a) - k^-P(x)\} \quad (1)$$

where k^+ and k^- are a polymerization and a depolymerization rate constant, respectively, C is the concentration of the polymerization unit (in the simplest case, actin monomers) coexisting with the filaments, and a is an effective length of polymerization and depolymerization unit (in the simplest case, a represents an effective length of an actin subunit in the filament, that is, 2.7 nm). When we distinguish the barbed end and the pointed end, $k^+ = k_B^+ + k_P^+$ and $k^- = k_B^- + k_P^-$, where $k_{B(P)}^+$ and $k_{B(P)}^-$ are the polymerization and depolymerization rates at the B(P)-end, respectively. Also, note that the present model does not explicitly take into account the heterogeneous state of actin subunits in the filaments coupled with ATP hydrolysis (see below).

Equation 1 is reduced to equation 2 (see below), which is the equivalent of a diffusion equation. Here, we expand the $P(x+a)$ and $P(x-a)$ terms in equation 1 with the Taylor series at x, assuming $a << x$ and remain the first three terms up to those containing a^2.

$$\frac{\partial P(x,t)}{\partial t} = \frac{1}{2}a^2\frac{\partial^2 P(x,t)}{\partial x^2}(k^+C + k^-) - a^2\frac{\partial P(x,t)}{\partial x}(k^+C - k^-) \quad (2)$$

The first term and the second term in the right side of the equation are attributed to diffusion and net polymerization (flow term), respectively. The proportionality coefficient in the first term corresponds to the diffusion coefficient D, which appears in the diffusion equation, as

$$D = \frac{1}{2}a^2(k^+C + k^-) \quad (3)$$

Note that C in the steady-state phase must be C_0, that is, the critical concentration for polymerization of actin when the polymerization unit is an actin monomer.

The fact that $(S.D.)^2$ was proportional to τ (Fig. 6) demonstrates that the polymerization–depolymerization dynamics at both ends

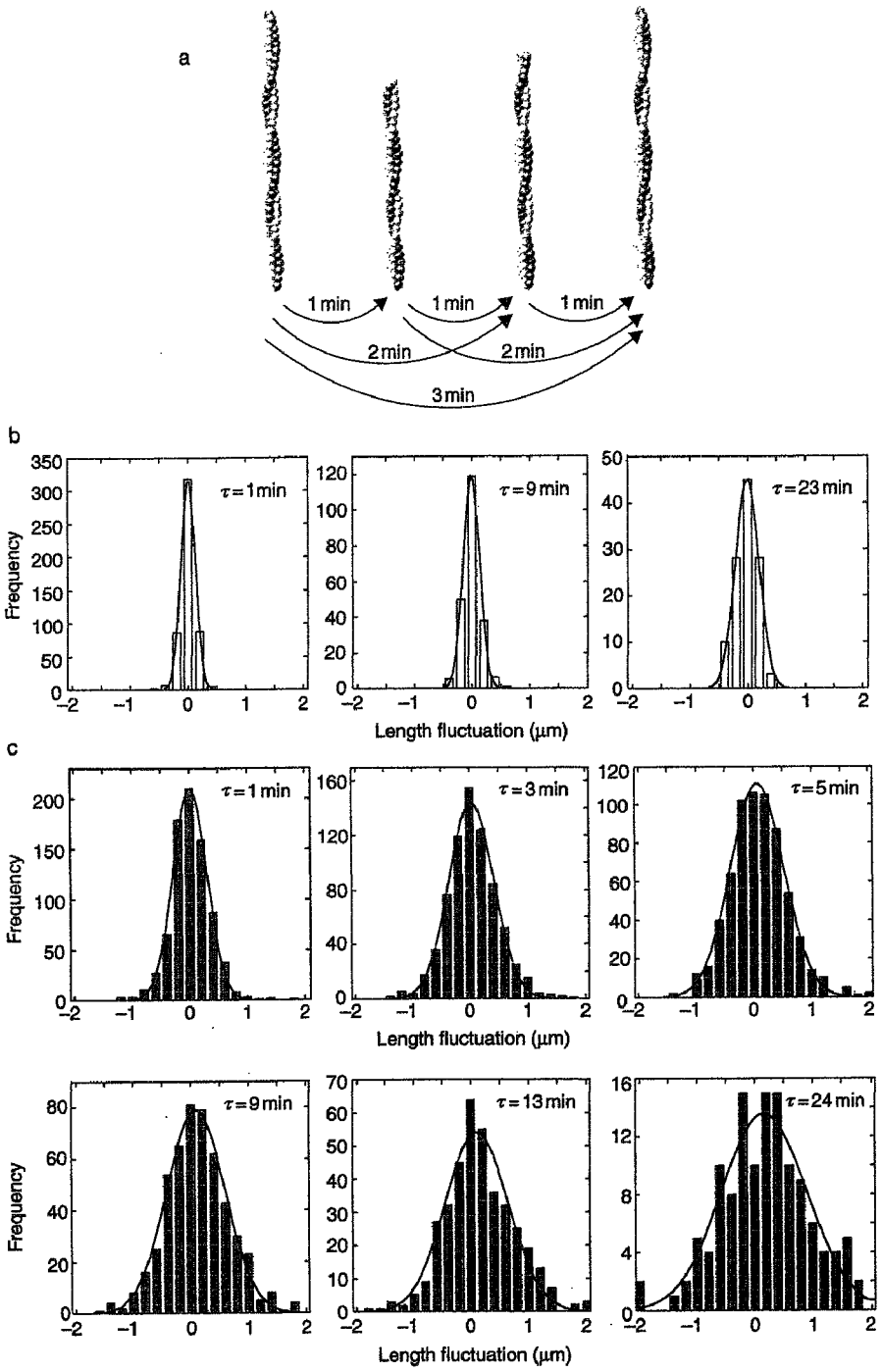

Figure 4 **Frequency of actin(Ca) filament length fluctuation in a steady-state phase. a**, A schematic illustration of how to measure the frequency of length fluctuation. The change in the length of filaments was measured at intervals of τ min, as indicated. **b,c**, Histograms showing the frequency of length fluctuations at various values of τ in the presence (**b**) or absence (**c**) of phalloidin (0.15 μM). Note that the average polymerization velocity was almost zero, independent of the value of τ, implying that a steady-state phase had been attained. Actin was used at 0.15 μM (**b**) or 0.7 μM (**c**).

of actin filaments obey the diffusion (stochastic) process, such that $(\text{S.D.})^2 = 2D\tau = a^2(k^+C_0 + k^-)\tau$. This is because we have confirmed that the steady-state phase has been attained, so that the flow term in the right side of equation 2 can be neglected ($k^+C = k^-$ at $C = C_0$). Thus, we can estimate the kinetic constants for polymerization and depolymerization during the steady-state phase from the slope of the relationship shown in Fig. 6. The slight positive slope of the $(\text{S.D.})^2$ versus τ relationship observed in the phallotoxin-labelled filaments (Fig. 6a) is attributable to a gradual lowering of the fluorescence contrast of the image through photo-bleaching. Thus, the large slope observed in the absence of phallotoxin may include this effect, but it is negligible.

To obtain the polymerization and depolymerization rate constants during the steady-state phase, the values of C_0 obtained above, 0.14 μM for actin(Ca) and 0.064 μM for actin(Mg) (Figs 3d,5b) were used. Assuming that the value of a is 2.7 nm, the values of k^+ and k^- have been estimated as $1.8 \times 10^8\ \text{M}^{-1}\text{s}^{-1}$ and $25\ \text{s}^{-1}$ for actin(Ca) (Fig. 6a) and $4.5 \times 10^8\ \text{M}^{-1}\text{s}^{-1}$ and $29\ \text{s}^{-1}$ for actin(Mg) (Fig. 6b), respectively. Unexpectedly, the values were 30–45 times larger than those obtained from the polymerization phase. The results of our analysis are summarized in Table 1 and a possible reason for such a discrepancy is discussed below.

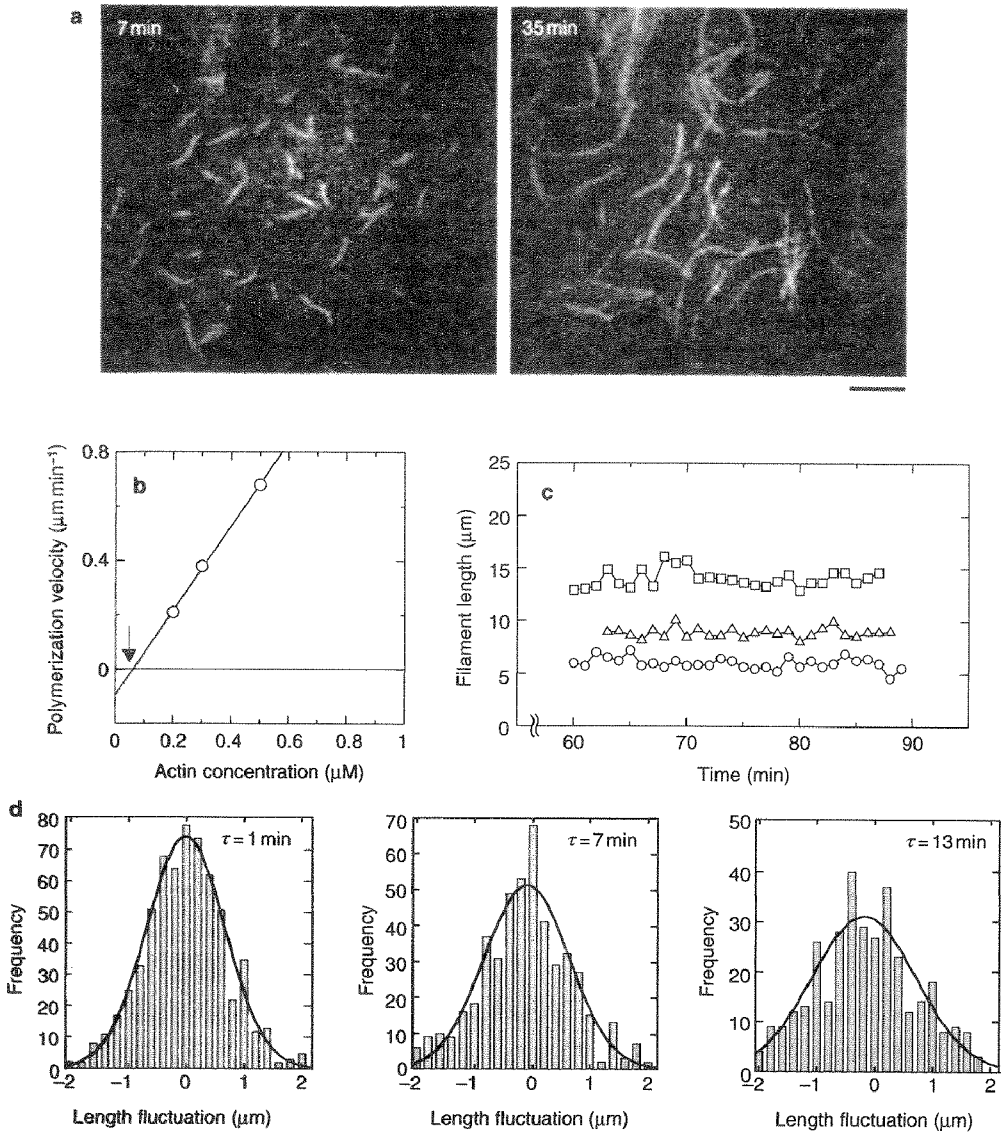

Figure 5 **Analysis of the polymerization dynamics of actin(Mg).** **a**, Fluorescence micrographs show polymerized filaments 7 min and 35 min after the addition of salts. Scale bar represents 10 μm. **b**, The relationship between average polymerization velocity and actin concentration. The arrow indicates the critical actin concentration for polymerization (see Fig. 3d). The slope of the linear approximation line shows the polymerization rate and the intercept of this line with the *y* axis indicates an apparent depolymerization rate. **c**, Three examples showing the length fluctuation observed at steady state. Actin was used at 0.3 μM in **a** and **c**. **d**, Histograms showing the frequency of length change at several values of τ.

In conclusion, we will summarize the polymerization and depolymerization rates and the critical concentration for polymerization obtained through different methods. As shown in Table 1, the kinetic constants were consistent, except for those estimated from the analysis of the length fluctuation at steady state on the basis of the diffusion process. The latter was approximately 40 times larger than the others. Also, note that the critical concentration for actin(Ca) obtained in the present study was smaller than that for actin(Ca) in which polymerization was induced by calcium[6]. This is probably because in our experiments, calcium attached to actin(Ca) monomers can exchange with free magnesium after the addition of salts (potassium chloride and magnesium chloride), so that actin(Ca) may have partly been transformed into actin(Mg).

There are several possible reasons for the apparent discrepancy between the kinetic constants described above: first, the kinetic constants obtained in the steady-state phase may be intrinsically different from those obtained in the initial phase of polymerization. As previously reported[9], the ratio of ADP-type to ATP-type actin at both ends of the filaments is larger in the steady-state phase than in the initial phase of polymerization. It is known that the depolymerization velocity of ADP-actin is an order of magnitude higher than that of ATP-actin, at least at the barbed end[6]. Second, the annealing of actin fragments may be responsible, as for the large polymerization rate that must be balanced by the depolymerization rate in the steady-state phase. As previously reported, the annealing rate constant is comparable to the polymerization rate (10^7 $M^{-1}s^{-1}$, ref. 22; for qualitative data, see ref. 4). This suggests that a polymerization unit may not be a monomer alone, but an average of monomers, oligomers and fragments. In addition, the size of the depolymerization unit may be different from that of the polymerization unit described above. Third, the size of a polymerization–depolymerization unit, *a*, may not necessarily indicate a size of a monomer, an oligomer and a fragment of actin, as described above. Rather, it may represent an effective size of a unit involved in cooperative (consecutive) polymerization and depolymerization, implying that each cycle of polymerization and depolymerization is

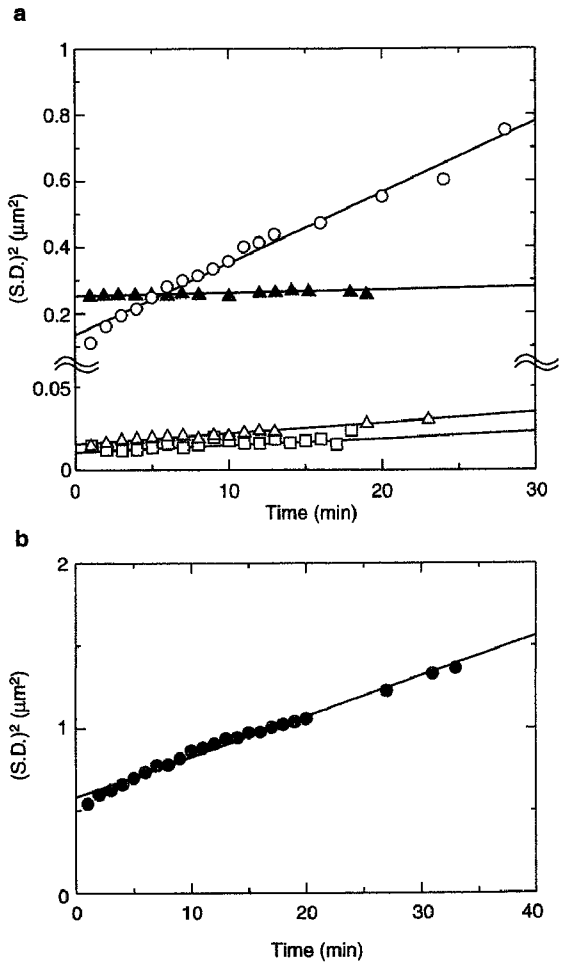

Figure 6 **Square of the width of the length fluctuation histogram versus correlation time.** This relationship was obtained at steady state (Figs 4,5). **a**, Actin (Ca). Circles represent 0.7 μM actin(Ca) without phallotoxin (see Fig. 4c), where $(S.D.)^2 = 0.022\tau + 0.14$. Open and closed triangles represent 0.15 μM phalloidin–actin(Ca), where $(S.D.)^2 = 0.00065\tau + 0.016$ for open triangles (see Fig. 4b) and $(S.D.)^2 = 0.00071\tau + 0.25$ for closed triangles. After actin filaments were stabilized with phalloidin, 0.14 μM G-actin(Ca), of which 10% (open triangles) or 50% (closed triangles) was TMR-labelled, was added to produce a fluorescence background noise. Open squares represent 0.15 μM phallacidin–actin(Ca), where $(S.D.)^2 = 0.00041\tau + 0.015$. As above, 0.14 μM G-actin(Ca), of which 10% was TMR-labelled, was added. **b**, 0.3 μM actin(Mg) without phallotoxin (see Fig. 5d), where $(S.D.)^2 = 0.025\tau + 0.58$.

dependent on the previous one (a non-Markov process). In fact, the treadmilling (cooperative) process occurs through the coupling of polymerization with ATP hydrolysis on actin, which may be equivalent to dynamic instability for actin. Whatever the mechanism, one plausible way to account for the large (40×) rate constants is through a difference in the effective size of *a*. If *a* is approximately six times larger than that of actin monomers, using equation 3, a^2 becomes 36 times larger, which is a close approximation of the 40× values. To clarify the polymerization–depolymerization dynamics at each end of the filaments, we need more detailed analysis of length change, with higher spatio-temporal resolution after distinguishing the barbed end and the pointed end.

Significantly, the usual methods used to monitor the average process of polymerization and depolymerization may miss the annealing process discussed above. For example, the fluorescence intensity of pyrene is very sensitive to the polymerization and depolymerization of monomers, but insensitive to the annealing of fragments. This may explain why, on the basis of analysis of incorporation of pyrene-labelled actin into the filaments in the steady-state phase, Brenner and Korn[23] obtained the kinetic constants consistent with those obtained from the polymerization phase, but did not find a discrepancy similar to that found in this study.

Thus, the single-filament analysis of actin polymerization has not only demonstrated the treadmilling process on single actin filaments, but has also identified a new aspect of polymerization–depolymerization dynamics by making it possible to analyse fluctuations in length at steady state. The present results indicate that the polymerization–depolymerization dynamics of pure actin filaments are not as 'dynamic' as those of microtubules. However, because actin is a central component of the cytoskeleton, a wide variety of actin-specific dynamic processes exist. It will be important to investigate the effects of various actin-binding proteins on the polymerization phase and the length fluctuations of actin filaments at steady state. We infer that the dynamic properties of polymerization and depolymerization of pure filaments may allow actin to perform different dynamic functions in different cell types, through interactions with cell-specific regulatory proteins. □

Methods

Preparation of actin

G-actin(Ca) was prepared from rabbit muscle according to Spudich and Watt[24], except that the tropomyosin–troponin complex was removed before preparing acetone powder, as previously desctibed[4]. G-actin(Ca) was solubilized in 2 mM Tris-HCl at pH 8.0, 0.1 mM calcium chloride, 0.1 mM ATP (Boehringer Ingelheim, Ingelheim, Germany) and 2 mM sodium azide. The concentration of actin was determined from ultraviolet absorption (UV 2000, Shimadzu, Japan) with $A^{1\%}_{290} = 6.3\ cm^{-1}$.

Labelling of actin with fluorescent dye was performed by incubating 1.7 mg ml^{-1} F-actin in a solution containing 0.1 M potassium chloride, 0.2 mM magnesium chloride, 0.1 mM ATP, 10 mM MOPS at pH 7.0 and 100 μM tetramethylrhodamine-5-maleimide (TMR-5-MA; Molecular Probes, Eugene, OR) dissolved in dimethylformamide (DMF; Sigma, St Louis, MO) for 2 h at room temperature. TMR-5-MA (20 mM) dissolved in DMF was slowly added to the F-actin solution with continuous stirring. TMR-labelled F-actin was centrifuged at 411,000*g* for 45 min at 8 °C. The pellet was then dissolved in and dialysed against 20 mM PIPES at pH 6.8, 0.1 mM ATP and 0.1 mM calcium chloride overnight at 2 °C. After centrifugation at 411,000*g* for 20 min at 2 °C, the fluorescent dye was removed from the G-actin solution by Sephadex G-25 column chromatograpy. The concentration of TMR was estimated from the molar extinction coefficient at 550 nm, 96,900 $M^{-1}cm^{-1}$ (Molecular Probes). The concentration of labelled G-actin(Ca) was determined by subtracting $0.208 \times A_{550}$ from the A_{290} value. The molar ratio of the label to actin was estimated to be >96%. TMR-labelled G-actin(Mg) was prepared by incubating labelled G-actin(Ca) in 0.2 mM EGTA (Dojindo, Kumamoto, Japan), 0.1 mM ATP, 20 mM PIPES at pH 6.8 and 0.1 mM magnesium chloride for 60 min at 0 °C[25] before centrifugation at 350,000*g* for 1 h at 2 °C. The supernatant was used as labelled G-actin(Mg). Pyrenyl–actin was prepared as previously described[26].

Experimental conditions

For microscopic examination, the *in vitro* polymerization of actin was initiated by addition of polymerization buffer (final concentrations: 30 mM potassium chloride, 2 mM magnesium chloride, 4 mM ATP, 20 mM MOPS at pH 7.0, 10 mM dithiothreitol (DTT) and 0.5% (w/v) methylcellulose) at 27 °C. This solution was then immediately transferred to a glass coverslip before microscopic examination. The proportion of TMR-labelled actin was maintained at 10%. It has been confirmed that at this labelling ratio, the polymerization rate and critical concentration in solution are unchanged[18]. For examination in solution, polymerization of actin(Ca or Mg) containing 10% pyrenyl–actin was initiated in a cuvette by adding the polymerization buffer, with or without methylcellulose. Fluorescence intensity was measured at 27 °C in a fluorescence spectrophotometer (F-4500, Hitachi, Tokyo, Japan). We confirmed that methylcellulose does not affect the average polymerization properties of actin in solution (Table 1). When the effect of phallotoxin was examined, the phallotoxin (phalloidin or phallacidin; Sigma) was added after the polymerization of actin(Ca) (10% TMR-labelled) was complete. The length of phallotoxin-labelled actin filaments was measured after a 1:10 dilution of the solution against the polymerization buffer containing 0.14 μM G-actin(Ca) (the critical concentration for polymerization), of which either 10% or 50% was labelled with TMR as background fluorescence noise. Here, we examined not only phalloidin, but also phallacidin, because the stabilizing properties of phallacidin for actin filaments seemed to be stronger than those of phalloidin (see ref. 16).

Optical system

Fluorescently labelled single actin filaments were visualized by total internal reflection fluorescence microscopy[27] (IX70, Olympus, Tokyo, Japan), which illuminates to a depth of only ~150nm below the coverslip. Samples were illuminated with a green laser (μ-Green model 4301-050; Uniphase, San Jose, CA). After 100 video frames (duration 3 s) were superimposed by using a digital image processing system (DIPS, Hamamatsu Photonics, Hamamatsu, Japan), the length of actin filaments was measured. The distance between adjacent pixels was 0.128 μm, to which the spatial resolution was limited.

RECEIVED 25 FEBRUARY 2002; REVISED 15 JUNE 2002; ACCEPTED 17 JULY 2002;
PUBLISHED 19 AUGUST 2002.

1. Oosawa, F. & Kasai, M. Theory of linear and helical aggregations of macromolecules. *J. Mol. Biol.* 4, 12–15 (1962).
2. Oosawa, F. & Asakura, S. *Thermodynamics of the Polymerization of Proteins* (Academic Press, New York, 1975).
3. Woodrum, D. T., Rich, S. A. & Pollard, T. D. Evidence for biased bidirectional polymerization of actin filaments using heavy meromyosin prepared by an improved method. *J. Cell Biol.* 67, 231–237 (1975).
4. Kondo, H. & Ishiwata, S. Uni-directional growth of F-actin. *J. Biochem.* 79, 159–171 (1976).
5. Hayashi, T. & Ip, W. Polymerization polarity of actin. *J. Mechanochem. Cell Motil.* 3, 163–169 (1976).
6. Pollard, T. D. & Cooper, J. A. Actin and actin-binding proteins. A critical evaluation of mechanism and functions. *Annu. Rev. Biochem.* 55, 987–1035 (1986).
7. Wegner, A. Head to tail polymerization of actin. *J. Mol. Biol.* 108, 139–150 (1976).
8. Korn, E. D., Carlier, M.-F. & Pantaloni, D. Actin polymerization and ATP hydrolysis. *Science* 238, 638–644 (1987).
9. Carlier, M.-F. Role of nucleotide hydrolysis in the dynamics of actin filaments and microtubules. *Int. Rev. Cytol.* 115, 139–170 (1989).
10. Mitchison, T. & Kirschner, M. Dynamic instability of microtubule growth. *Nature* 312, 237–242 (1984).
11. Horio, T. & Hotani, H. Visualization of the dynamic instability of individual microtubles by dark-field microscopy. *Nature* 321, 605–607 (1986).
12. Yanagida, T., Nakase, M., Nishiyama, K. & Oosawa, F. Direct observation of motion of single actin filaments in the presence of myosin. *Nature* 307, 58–60 (1984).
13. Honda, H., Nagashima, H. & Asakura, S. Directional movement of F-actin *in vitro*. *J. Mol. Biol.* 191, 131–133 (1986).
14. Harada, Y., Sakurada, K., Aoki, T., Thomas, D. D. & Yanagida, T. Mechanochemical coupling in actomyosin energy transduction studied by *in vitro* movement assay. *J. Mol. Biol.* 216, 49–68 (1991).
15. Huang, Z. J., Haugland, R. P., You, W. M. & Haugland, R. P. Phallotoxin and actin binding assay by fluorescence enhancement. *Anal. Biochem.* 200, 199–204 (1992).
16. Ishiwata, S., Tadashige, J., Masui, I., Nishizaka, T. & Kinosita, K. Jr in *Molecular Interactions of Actin* (eds dos Remedios, C. G. & Thomas, D. D.) 79–94 (Springer-Verlag, Heidelberg, 2001).
17. Amann, K. J. & Pollard, T. D. Direct real-time observation of actin filament branching mediated by Arp2/3 complex using total internal reflection fluorescence microscopy. *Proc. Natl Acad. Sci. USA* 98, 15009–15013 (2001).
18. Fujiwara, I., Suetsugu, S., Uemura, S., Takenawa, T. & Ishiwata, S. Visualization and force measurement of branching by Arp2/3 complex and N-WASP in actin filament. *Biochem. Biophys. Res. Comm.* 293, 1550–1555 (2002).
19. De La Cruz, E. M. & Pollard, T. D. Kinetics and thermodynamics of phalloidin binding to actin filaments from three divergent species. *Biochemistry* 35, 14054–14061 (1994).
20. Estes, J. E., Selden, L. A., Kinosian, H. J. & Gershman, L. C. Tightly-bound divalent cation of actin. *J. Muscle Res. Cell Motil.* 13, 272–284 (1992).
21. Howard, J. *Mechanics of Motor Proteins and the Cytoskeleton* (Sinauer Associates, Inc., Massachusetts, 2001).
22. Murphy, D. B., Gray, R. O., Grasser, W. A. & Pollard, T. D. Direct demonstration of actin filament annealing *in vitro*. *J. Cell Biol.* 106, 1947–1954 (1988).
23. Brenner, S. L. & Korn, E. D. On the mechanism of actin monomer–polymer subunit exchange at steady state. *J. Biol. Chem.* 258, 5013–5020 (1983).
24. Spudich, J. A. & Watt, S. The regulation of rabbit skeletal muscle contraction. I. Biochemical studies of the interaction of the tropomyosin–troponin complex with actin and the proteolytic fragments of myosin. *J. Biol. Chem.* 246, 4866–4871 (1971).
25. Yasuda, R., Miyata, H. & Kinosita, K. Jr. Direct measurement of the torsional rigidity of single actin filaments. *J. Mol. Biol.* 263, 227–236 (1996).
26. Kouyama, T. & Mihashi, K. Fluorimetry study of *N*-(1-pyrenyl) iodoacetamide-labelled F-actin. Local structural change of actin protomer both on polymerization and on binding of heavy meromyosin. *Eur. J. Biochem.* 114, 33–38 (1981).
27. Funatsu, T., Harada, Y., Tokunaga, M., Saito, K. & Yanagida, T. Imaging of single fluorescent molecules and individual ATP turnovers by single myosin molecules in aqueous solution. *Nature* 374, 555–559 (1995).

ACKNOWLEDGEMENTS

This research was partly supported by Grants-in-Aid for Scientific Research, Scientific Research on Priority Areas and Bio-venture Projects from the Ministry of Education, Culture, Sports, Science and Technology of Japan, and by Grants-in-Aid from the Japan Science and Technology Corporation (CREST) and the Mitsubishi Foundation. We thank W. Rozycki for reading the manuscript. We also thank colleagues at Waseda University and CREST for their encouragement and support. I.F. is a research fellow of the Japan Society for the Promotion of Science.

Correspondence and requests for material should be addressed to S.I.

COMPETING FINANCIAL INTERESTS

The authors declare that they have no competing financial interests.

Equilibrium and Transition between Single- and Double-Headed Binding of Kinesin as Revealed by Single-Molecule Mechanics

Kenji Kawaguchi,* Sotaro Uemura,* and Shin'ichi Ishiwata*†
*Department of Physics, School of Science and Engineering, †Advanced Research Institute for Science and Engineering, and Materials Research Laboratory for Bioscience and Photonics, Waseda University, 3-4-1 Okubo, Shinjuku-ku, Tokyo 169-8555, Japan

ABSTRACT Kinesin is a processive motor protein that "walks" on a microtubule toward its plus end. We reported previously that the distribution of unbinding force and elastic modulus for a single kinesin-microtubule complex was either unimodal or bimodal depending on the nucleotide states of the kinesin heads, hence showing that the kinesin may bind the microtubule either with one head or with both heads at once. Here, we found that the shape of the unbinding-force distribution depends both on the loading rate and on the manner of loading not only in the presence of AMP-PNP but also in the absence of nucleotides. Irrespective of the nucleotide state and the loading conditions examined here, the unbinding force obtained by loading directed toward the minus end of microtubule was 45% greater than that for plus end-directed loading. These results could be explained by a model in which equilibrium exists between single- and double-headed binding and the load (F) dependence of lifetime, $\tau(F)$, of each binding is expressed by $\tau(F) = \tau(0)\exp(-Fd/k_BT)$, where $\tau(0)$ is the lifetime without external load and d a characteristic distance, both of which depend on single- or double-headed binding, k_B, the Boltzmann constant and T, the absolute temperature. The model analysis showed that the forward and backward rates of transition from single- to double-headed binding are 2 and 0.2/s for the AMP-PNP state, and 70 and 7/s for the nucleotide-free state. Moreover, in the presence of AMP-PNP, we detected the moment of transition from single- to double-headed binding through an abrupt increase in the elastic modulus and estimated the transition rate to be ~1/s, which is consistent with the model analysis.

INTRODUCTION

Kinesin is a processive molecular motor that transports vesicles and organelles toward the plus end of a microtubule, i.e., from the central region to the periphery of various cells (Vale, 1999; Hirokawa, 1998). Upon binding to a microtubule, kinesin takes more than 100 consecutive steps before dissociating, with each step measuring 8 nm, a distance equal to the size of a single heterodimer subunit of the microtubule (Block et al., 1990; Svoboda et al., 1993; Howard, 1996; Vale et al., 1996). Each step taken is coupled to one cycle of ATP hydrolysis (Hua et al., 1997; Schnitzer and Block, 1997; Mandelkow and Johnson, 1998; Coy et al., 1999). The run length, a measure of processivity, estimated in a single molecular in vitro assay, is ~1 μm and depends on such experimental variables as ionic strength (Block et al., 1990; Vale et al., 1996) and temperature (Kawaguchi and Ishiwata, 2000; 2001b). Kinesin's high processivity has been explained by a model in which the two heads of kinesin alternate repeatedly between single-headed and double-headed binding to a microtubule, which allows for movement accompanied by ATP hydrolysis (Hackney, 1994; Cross, 1995; Rice et al., 1999; Vale and Milligan, 2000).

To investigate the binding mode of kinesin with microtubules at various nucleotide states, we measured the mechanical properties of a single kinesin-microtubule complex (Kawaguchi and Ishiwata, 2001a), including the unbinding force and the elastic modulus, by using optical tweezers (Nishizaka et al., 1995). Conventional two-headed kinesin molecules purified from bovine brain were attached to a polystyrene bead in a 1:1 molar ratio, and each bead was manipulated with optical tweezers on a microtubule that was adsorbed on to a coverslip (Svoboda and Block, 1994; Higuchi et al., 1997; Kojima et al., 1997). An external load was imposed on the attached kinesin molecule either by moving the bead toward the plus or minus end of the microtubule, or alternatively, moving the microscope stage on which the microtubule was mounted.

In the previous paper (Kawaguchi and Ishiwata, 2001a), we found that kinesin is involved primarily in single-headed binding in the absence of nucleotides (nucleotide-free state; strictly speaking, the absence of exogenous nucleotides) and in the coexistence of ADP and AMP-PNP, and double-headed binding in the presence of AMP-PNP (AMP-PNP state), which is consistent with the current model of kinesin motility. Here, we found that the average unbinding force and the apparent ratio between single- and double-headed binding in the unbinding-force distribution were dependent on the loading direction and the loading rate, respectively. Additionally, we could detect the moment of transition from single- to double-headed binding in the AMP-PNP state through an abrupt increase in the elastic modulus during loading, and estimated that the transition rate from the single- to double-headed binding was ~1/s. We have shown that all the data could be explained by a model in which equilibrium exists between single- and double-headed binding (the transition rate between the two binding states is assumed) and detachment from the microtubule occurs during either single- or double-headed binding. We conclude that the

Submitted July 15, 2002, and accepted for publication October 23, 2002.

Address reprint requests to Dr. Shin'ichi Ishiwata, Department of Physics, School of Science and Engineering, Waseda University, 3-4-1 Okubo, Shinjuku-ku, Tokyo 169-8555, Japan. Tel.: +81-3-5286-3437; Fax: +81-3-5286-3437; E-mail: ishiwata@waseda.jp.

0006-3495/03/02/1103/11 $2.00

double-headed binding state is predominant under equilibrium in the absence of external load not only in the AMP-PNP state, but also in the nucleotide-free state.

Double-headed binding was not detected in the nucleotide-free state in the previous study (Kawaguchi and Ishiwata, 2001a) due to the fact that the loading rate used was significantly lower than the rate constant for the transition between single- and double-headed binding in the nucleotide-free state, which was an order-of-magnitude larger than that in the AMP-PNP state. In general, the lower the loading rate, the higher the probability of unbinding at single-headed binding.

MATERIALS AND METHODS

Proteins

Kinesin and tubulin were prepared from bovine (Kojima et al., 1997) and porcine (Hyman, 1991) brains, respectively. Polarity-marked microtubules labeled with tetramethylrhodamine succinimidyl ester (Molecular Probes, Eugene, OR) were prepared according to Hyman (1991) except that the tubulin used was not N-ethylmaleimide(NEM)-treated, hence polymerization also occurred at the minus end (compare to Fig. 2 *A* in Kawaguchi and Ishiwata, 2001a).

Bead assay

Kinesin-coated beads were prepared according to the established procedure (Kojima et al., 1997) except that yellow-green fluorescent latex beads were used (1.0 μm in diameter, carboxylate-modified; Molecular Probes). Kinesin molecules were mixed with the beads at a molar ratio of 1:1. The average number of functional kinesin molecules per bead was estimated to be 1 by statistical methods (Svoboda and Block, 1994). Polarity-marked fluorescent microtubules in an assay buffer (2 mM $MgCl_2$, 80 mM PIPES-KOH, pH 6.8, and 1 mM EGTA) were introduced into a flow cell and incubated for 2 min to allow for binding to the glass surface. The solvent was exchanged with an assay buffer containing 0.7 mg/ml filtered casein to coat the glass surface with casein. The flow cell was then filled with an assay buffer containing the kinesin-coated beads, filtered casein, and an enzymatic oxygen-scavenging system, and sealed with enamel (nail polish). The final solvent condition was ~0.1 pM kinesin-coated beads, 2 mM $MgCl_2$, 80 mM PIPES-KOH, pH 6.8, 1 mM EGTA, 0.7 mg/ml filtered casein, 1 U/ml apyrase (nucleotide-free state), or 1 mM AMP-PNP (AMP-PNP state), 10 μM taxol, 10 mM dithiothreitol (DTT), 4.5 mg/ml glucose, 0.22 mg/ml glucose oxidase, and 0.036 mg/ml catalase. As nucleotide-free kinesin is reportedly unstable in the absence of microtubule (Crevel et al., 1996), apyrase (a scavenger of ATP and ADP) was added just before each measurement. We were able to measure the unbinding force repeatedly on the same bead, and confirmed that there was no significant difference in either the unbinding force distribution or binding properties regardless of the presence or absence of apyrase. It is therefore unlikely that kinesin denatured during measurement in the absence of nucleotides. However, it should be noted that we found that kinesin eventually failed to attach to the microtubules after ~30 min from the addition of apyrase, suggesting that kinesin was denatured due to prolonged incubation with apyrase. Hence the data acquisition was always completed within ~10 min after the addition of apyrase. We confirmed that kinesin molecules moved toward the plus end of the polarity-marked microtubules in the presence of ATP. When the external load was imposed, either the trap center or the glass cover (only at the highest loading rate in Fig. 2 *b*) was moved at a constant rate. The proportion of beads that underwent the binding-unbinding cycle was ~40% of the total examined, whereas the proportion in which unbinding did not occur even at the largest external load imposed by optical tweezers (~20 pN) was less than 5%. The remaining beads (~60%) failed to bind even after three trials of steps *1–2* in Fig. 1. All experiments were performed at 25 ± 1°C.

Apparatus

The microscopy system employed was equipped with optical tweezers as previously described (Nishizaka et al., 1995; 2000) and already applied for studies of the mechanics of the kinesin-microtubule interaction (Kawaguchi and Ishiwata, 2000; 2001a). Stiffness of the optical trap was estimated to be 0.087 pN/nm based on two kinds of techniques as previously described (Nishizaka et al., 1995).

Model analysis

For the model analysis, in which equilibrium is assumed to exist between attached and detached states, and also between single- and double-headed binding states of kinesin, we calculated the time dependence of the proportion of attached kinesin molecules, $N(t)$, using *Mathematica* for *Windows*.

RESULTS

Measuring the unbinding force of a kinesin-microtubule complex

As shown schematically in Fig. 1, the bead in the medium was first trapped by optical tweezers, *1*, and placed in contact with a microtubule for 20–30 s (from *1* to *2*), which is considered sufficient time for realizing the binding equilibrium between kinesin molecule and a microtubule in the absence of loading, *2*. The trap center was then moved at a constant rate toward either the plus or minus end of the microtubule (from *2* to *3*). After the bead was moved following the trap center for some distance, regardless of the loading rates and solvent conditions, the load began to be imposed on the kinesin-microtubule complex from the point

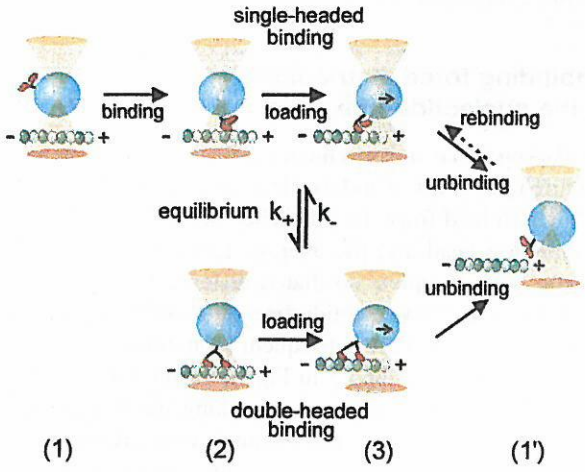

FIGURE 1 Schematic illustration showing the binding states of kinesin with a microtubule and measurement procedures. We assume that equilibrium exists between single- and double-headed binding with the rate constants k_+ and k_- (for more details, see text).

where the bead started to deviate from the trap center (*3*; loading direction shown by small arrows at the bead).

Upon imposition of the external load, unbinding between kinesin and the microtubule occurred from *3* to *1′* (termed "initial unbinding"). This cycle (from *1* to *1′*) could be repeated several times for the same bead on the same microtubule. When the trap center was kept moving along the microtubule after the initial unbinding (from *3* to *1′*), rebinding (from *1′* to *3*) and subsequent unbinding (from *3* to *1′*) sometimes occurred (termed "subsequent unbinding"). As reported previously (Kawaguchi and Ishiwata, 2001a), we were able to repeat the unbinding force measurements on the same microtubule several times for the same bead, presumably for the same kinesin molecule.

With a single molecule forming the attachment between the bead and the microtubule, it is possible for the bead to move some distance relative to the microtubule without deviating from the trap center, mainly because of rotational movement of the bead within the trap. This rotational movement does not register on the position detector. As observed in Figs. 2 *a* and 3 *a*, for the first part of the movement of the bead, the kinesin may be attached to the microtubule but this does not show in the displacement until the bead-kinesin-microtubule link tautens. Based on the size and geometry of the kinesin-tethered bead (Svoboda and Block, 1994; radius of bead, 0.5 μm; length of kinesin, 60 nm), the largest displacement required before the external load is imposed for the initial unbinding event is ~600 nm. In fact, this average displacement was as large as 300 nm (compare with Kawaguchi and Ishiwata, 2001a). Thus, unbinding data for beads that were displaced further than 600 nm before imposition of the external load began for the initial unbinding event were regarded as subsequent unbinding data but not initial unbinding data (~10% of measured beads for the AMP-PNP state; not observed for the nucleotide-free state).

Unbinding force distribution in the nucleotide-free state

Unbinding force measurements were performed at various loading rates (Figs. 2 and 3). Here, note that the loading rate was determined from the difference between the velocity of the moving bead and the average rate of extension of the protein-bead complex, so that it differed for every experiment. First, in the nucleotide-free state, unbinding occurred once (Fig. 2 *a*), but the subsequent rebinding and unbinding process (between *1′* and *3* in Fig. 1) could not be observed when the bead was kept moving along the microtubule at a velocity of between 20 and 130 nm/s, even after moving for several seconds. Inasmuch as the unbinding force measurements could be repeated several times for the same beads (Kawaguchi and Ishiwata, 2001a), this was probably not due to the denaturation of kinesin but rather to a small (re)binding rate constant in the nucleotide-free condition. A

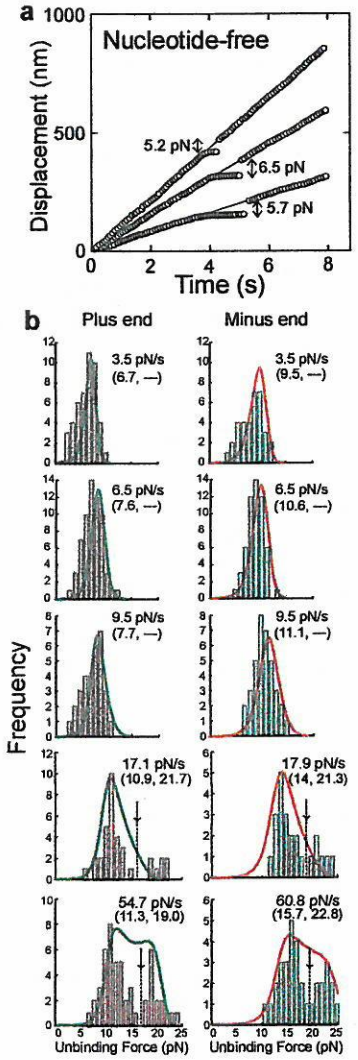

FIGURE 2 Loading rate dependence of unbinding force distribution in the nucleotide-free state. Unbinding force was measured by loading toward either the plus end (*a* and *left column* in *b*) or the minus end (*right column* in *b*). (*a*), Examples showing the time course of movement of the trap center (*thin lines*) and a bead (*circles*) at various moving velocities (110, 75, and 40 nm/s from *top* to *bottom*). (*b*), Histograms showing unbinding force distribution at various loading rates (*pN/s*) for the plus end (*pink*) or minus end (*light green*) loading. At the loading rate higher than 50 pN/s, the glass cover was moved instead of the trap center, so that the position of the trap center was fixed. Note that the loading rate was determined either simply from the moving velocity of the bead (only at the highest loading rate) or from the difference between the moving velocity of the bead and the average extension velocity (see the *insert* of Fig. 4 *a*) of the kinesin-microtubule-bead complex, so that the loading rate was different at every measurement even if the moving velocity of the bead is the same. (*Dotted lines with arrow*), The boundary between *S*- and *L*-components, were determined by eye. Average unbinding force (*pN*) for the *S*- and *L*-components is shown in parentheses. On simulation curves for unbinding-force distribution (*green curves* for the plus-end loading, and *red curves* for the minus-end loading), see the model analysis in Discussion and Fig. 6.

where the bead started to deviate from the trap center (*3*; loading direction shown by small arrows at the bead).

Upon imposition of the external load, unbinding between kinesin and the microtubule occurred from *3* to *1′* (termed "initial unbinding"). This cycle (from *1* to *1′*) could be repeated several times for the same bead on the same microtubule. When the trap center was kept moving along the microtubule after the initial unbinding (from *3* to *1′*), rebinding (from *1′* to *3*) and subsequent unbinding (from *3* to *1′*) sometimes occurred (termed "subsequent unbinding"). As reported previously (Kawaguchi and Ishiwata, 2001a), we were able to repeat the unbinding force measurements on the same microtubule several times for the same bead, presumably for the same kinesin molecule.

With a single molecule forming the attachment between the bead and the microtubule, it is possible for the bead to move some distance relative to the microtubule without deviating from the trap center, mainly because of rotational movement of the bead within the trap. This rotational movement does not register on the position detector. As observed in Figs. 2 *a* and 3 *a*, for the first part of the movement of the bead, the kinesin may be attached to the microtubule but this does not show in the displacement until the bead-kinesin-microtubule link tautens. Based on the size and geometry of the kinesin-tethered bead (Svoboda and Block, 1994; radius of bead, 0.5 μm; length of kinesin, 60 nm), the largest displacement required before the external load is imposed for the initial unbinding event is ~600 nm. In fact, this average displacement was as large as 300 nm (compare with Kawaguchi and Ishiwata, 2001a). Thus, unbinding data for beads that were displaced further than 600 nm before imposition of the external load began for the initial unbinding event were regarded as subsequent unbinding data but not initial unbinding data (~10% of measured beads for the AMP-PNP state; not observed for the nucleotide-free state).

Unbinding force distribution in the nucleotide-free state

Unbinding force measurements were performed at various loading rates (Figs. 2 and 3). Here, note that the loading rate was determined from the difference between the velocity of the moving bead and the average rate of extension of the protein-bead complex, so that it differed for every experiment. First, in the nucleotide-free state, unbinding occurred once (Fig. 2 *a*), but the subsequent rebinding and unbinding process (between *1′* and *3* in Fig. 1) could not be observed when the bead was kept moving along the microtubule at a velocity of between 20 and 130 nm/s, even after moving for several seconds. Inasmuch as the unbinding force measurements could be repeated several times for the same beads (Kawaguchi and Ishiwata, 2001a), this was probably not due to the denaturation of kinesin but rather to a small (re)binding rate constant in the nucleotide-free condition. A

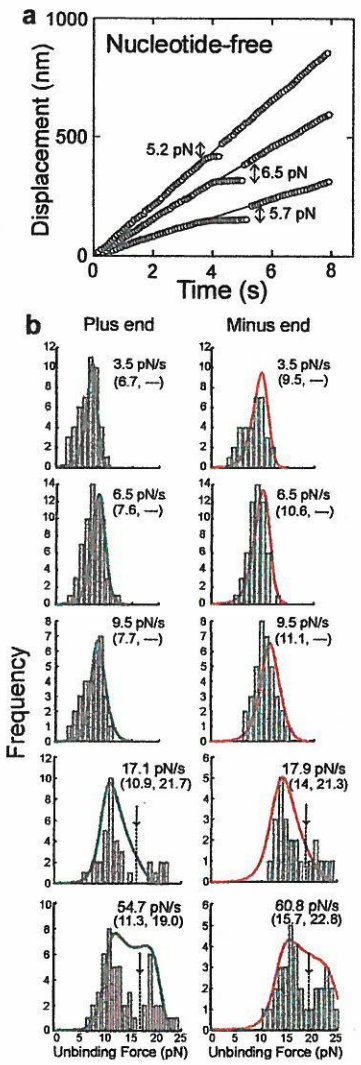

FIGURE 2 Loading rate dependence of unbinding force distribution in the nucleotide-free state. Unbinding force was measured by loading toward either the plus end (*a* and *left column* in *b*) or the minus end (*right column* in *b*). (*a*), Examples showing the time course of movement of the trap center (*thin lines*) and a bead (*circles*) at various moving velocities (110, 75, and 40 nm/s from *top* to *bottom*). (*b*), Histograms showing unbinding force distribution at various loading rates (*pN/s*) for the plus end (*pink*) or minus end (*light green*) loading. At the loading rate higher than 50 pN/s, the glass cover was moved instead of the trap center, so that the position of the trap center was fixed. Note that the loading rate was determined either simply from the moving velocity of the bead (only at the highest loading rate) or from the difference between the moving velocity of the bead and the average extension velocity (see the *insert* of Fig. 4 *a*) of the kinesin-microtubule-bead complex, so that the loading rate was different at every measurement even if the moving velocity of the bead is the same. (*Dotted lines with arrow*), The boundary between *S*- and *L*-components, were determined by eye. Average unbinding force (*pN*) for the *S*- and *L*-components is shown in parentheses. On simulation curves for unbinding-force distribution (*green curves* for the plus-end loading, and *red curves* for the minus-end loading), see the model analysis in Discussion and Fig. 6.

different tendency (right-most columns of Fig. 3, *b* and *c*). As the loading rate was increased, the proportion of the *L*-component increased once, and then eventually disappeared. This characteristic is clearly seen in Fig. 3 *d*: at the highest loading rate, the initial unbinding contained only the *L*-component, whereas subsequent unbinding contained only the *S*-component. At loading rates less than ~6 pN/s, however, the unbinding-force distributions obtained under the two different procedures became indistinguishable. It should also be noted that in the subsequent unbinding (irrespective of the loading direction), the average unbinding force of *S*-component, which increased by 10–40% on increasing the loading rate from 2.4 to 9.8 pN/s, decreased by 20–30% when the loading rate was increased still further, from 9.8 to 18.2 pN/s. These characteristics have been explained by a model as described below in the Discussion. The simulation curves are overlaid in Fig. 3, *b* and *c*, with those that deviated significantly from (qualitatively different from) the data indicated by dashed curves (for more details, see Discussion).

Elastic modulus of a kinesin-microtubule complex

We estimated the elastic modulus of kinesin molecules and examined its relation to the unbinding force. Fig. 4 *a* shows an example of the force-extension relation for plus-end loading in the nucleotide-free state. Unlike that for complexes of F-actin and heavy meromyosin (Fig. 2 *b* of Nishizaka et al., 1995), ~40% of data showed a linear relationship as shown in Fig. 4 *a*, and the remaining 60% of data were scattered to some extent, but all the data could be simulated by a straight line by the least squares fit. Thus, the elastic modulus could be estimated from the slope of the line to be 0.35 ± 0.14 ($n = 46$), 0.34 ± 0.18 ($n = 62$), and 0.40 ± 0.18 ($n = 31$) pN/nm, respectively, at 3.5, 6.5, and 9.5 pN/s, which appears to be independent of loading rate (Fig. 4 *b*). The elastic modulus obtained for minus-end loading was 0.38 ± 0.15 ($n = 34$), 0.41 ± 0.17 ($n = 56$), and 0.37 ± 0.19 ($n = 36$) pN/nm, respectively, at 3.5, 6.5, and 9.5 pN/s. Thus, the elastic modulus was independent not only of the loading rates within the range we examined but also the loading direction.

In contrast to the nucleotide-free state, the force-extension relation in the AMP-PNP state showed a complex characteristic. The force-extension relation depended on whether the unbinding event was the initial or the subsequent one. That is, the relation for the initial unbinding was always linear irrespective of the *S*-component (data not shown) or the *L*-component (see Fig. 5 *a*), and the elastic modulus of the *S*-component was nearly equal to that in the nucleotide-free state (see Fig. 4 *a*). That is, the elastic modulus of the *S*- and the *L*-component was, respectively, 0.36 ± 0.15 ($n = 23$) and 0.77 ± 0.29 ($n = 30$) pN/nm for the plus-end loading, and 0.33 ± 0.18 ($n = 19$) and 0.81 ± 0.21 ($n = 21$) pN/nm for the minus-end loading at the loading rate of 1.8 pN/s. Just as in the nucleotide-free state, the elastic modulus was independent of the loading rate examined and the loading direction.

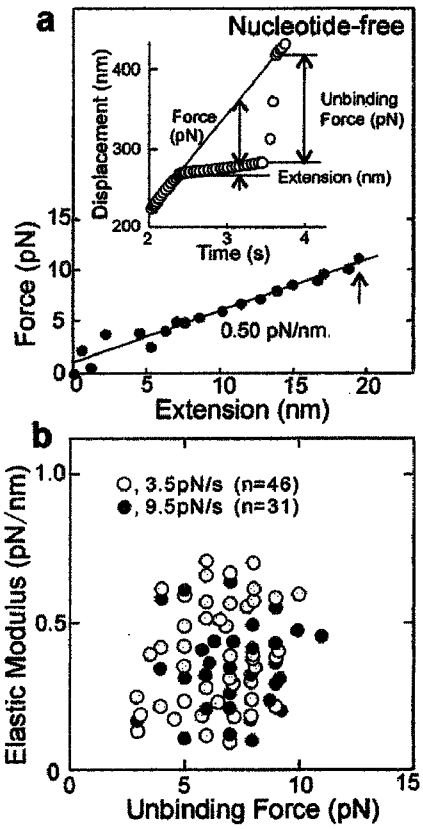

FIGURE 4 Relation between the elastic modulus and unbinding force for the *S*-component of kinesin molecules measured by the plus-end loading in the nucleotide-free state. (*a*), The force-extension relation was obtained from the time course of bead displacement (*insert*; Kawaguchi and Ishiwata, 2001a; Nishizaka et al., 1995) at the loading rate of ~9 pN/s (see the legend of Fig. 2). Strictly speaking, the force means the force component parallel to the glass surface, and the extension means the displacement of the bead in parallel to the glass surface (see Discussion). An arrow shows the moment at which unbinding occurred. The elastic modulus was estimated from the slope of the thin line (this datum is included in *b*). (*b*), Relation between the elastic modulus and unbinding force at different loading rates, 3.5 pN/s (*gray circles*) and 9.5 pN/s (*black circles*), shown in the left column of Fig. 2 *b*. The elastic modulus (Mean ± SD, unit in pN/nm) is 0.35 ± 0.14 ($n = 46$) for 3.5 pN/s and 0.40 ± 0.18 ($n = 31$) for 9.5 pN/s.

On the other hand, the force-extension relation for the subsequent unbinding was linear (composed of single phase) for all the data for the *S*-component (not shown). The elastic modulus obtained from this relation was 0.39 ± 0.17 ($n = 14$) pN/nm for the plus-end loading and 0.42 ± 0.11 ($n = 25$) pN/nm for the minus-end loading at a loading rate of 5.6 pN/s. As for the *L*-component, ~25% of the force-extension relation was broken once in the middle (composed of double phase as shown in Fig. 5 *a*) and half of the remaining 75% appeared to be linear, whereas the other was not clearly identified as the data points were somewhat scattered. They could, however, be simulated by a straight line. The elastic

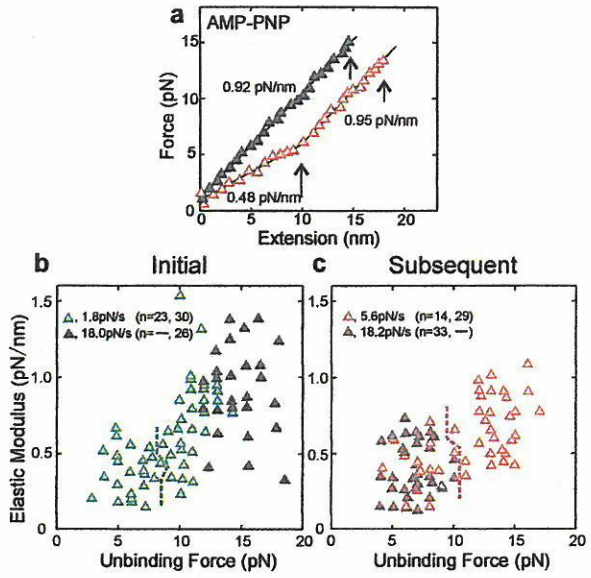

FIGURE 5 Relation between the elastic modulus and unbinding force of kinesin molecules measured by the plus-end loading in the AMP-PNP state. (*a*), Examples showing the force-extension relation obtained from the time course of bead displacement (see Fig. 4 *a*) for the initial unbinding (*dark green*) and the subsequent unbinding (*pink*). Short arrows show the moment at which the detachment of kinesin occurred. A long arrow shows the moment at which the transition occurred from a smaller to a larger slope. Data shown by dark green and pink were included in one of the data shown in *b* and *c*, respectively. (*b*) and (*c*), Relation between the elastic modulus and unbinding force for the initial unbinding measurements (*b*, compare with *left column* of Fig. 3 *b*) at 1.8 pN/s (*light green*) and 18.0 pN/s (*dark green*), and for the subsequent unbinding measurements (*c*, compare with *right column* of Fig. 3 *b*) at 5.6 pN/s (*pink*) and 18.2 pN/s (*red*). When the force-extension relation was once broken at the middle, both initial and final slopes were plotted in *c*. The two regions separated by a dashed line correspond to the *S*- and *L*-components determined in Fig. 3 *b*. The elastic modulus (Mean ± SD, unit in pN/nm; *S*- and *L*-components, respectively) is (0.36 ± 0.15 ($n = 23$), 0.77 ± 0.29 ($n = 30$)) at 1.8 pN/s and (−, 0.86 ± 0.28 ($n = 26$)) at 18.0 pN/s for the initial unbinding, and (0.39 ± 0.17 ($n = 14$), 0.67 ± 0.21 ($n = 29$)) at 5.6 pN/s and (0.38 ± 0.19 ($n = 33$), −) at 18.2 pN/s for the subsequent unbinding.

modulus obtained from the data categorized to the latter type, either linear or scattered, was 0.71 ± 0.15 ($n = 8$) and 0.65 ± 0.12 ($n = 11$) pN/nm for the plus-end loading and 0.68 ± 0.15 ($n = 9$) and 0.62 ± 0.18 ($n = 25$) pN/nm for the minus-end loading at the loading rate of 5.6 pN/s.

As for data showing the double phase, the second slope (0.95 pN/nm in the example shown in Fig. 5 *a*) coincided with the slope of the *L*-component (0.92 pN/nm in the example shown in Fig. 5 *a*) in the initial unbinding (see Fig. 5 *b*). The first slope of the double phase (0.48 pN/nm in the example shown in Fig. 5 *a*) coincided with the slope of the *S*-component (Fig. 5, *b* and *c*). The average values of the elastic modulus for the first and the second slope of the double phase were 0.33 ± 0.14 and 0.69 ± 0.10 ($n = 10$) pN/nm, respectively, for plus-end loading and 0.31 ± 0.12 and 0.64 ± 0.15 ($n = 6$) pN/nm for minus-end loading at a loading rate of 5.6 pN/s. Again, the elastic modulus appears to be independent of the loading rate we examined and the loading direction (data not shown).

Finally, we determined the time at which the transition occurred from the first slope to the second slope in the force-extension relation that showed a double-phase in the subsequent unbinding. Although the shape of distribution could not be determined due to the lack of data ($n = 30$), the transition time was distributed from zero to 1.6 s and the average time was determined to be ~1 s, irrespective of the loading rate and the loading direction: that is, 1.11 ± 0.23 s ($n = 20$) for plus-end loading and 1.18 ± 0.17 s ($n = 10$) for minus-end loading.

DISCUSSION

Single- and double-headed binding of kinesin

The findings that the unbinding force and elastic modulus were classified into two groups with values differing by a factor of nearly 2 are attributable to single- (Figs. 2 *b* and 4 *b*) and double-headed binding (Fig. 3, *b* and *c*, Fig. 5, *b* and *c*; and Kawaguchi and Ishiwata, 2001a). Direct evidence for this explanation was recently obtained by using a one-headed construct of kinesin heterodimer. The unbinding-force distribution was unimodal and the average unbinding force coincided with that of *S*-component for the conventional two-headed kinesin homodimer used here (Uemura et al., 2002).

The above situation is analogous to that examined using AFM that showed the unbinding force for a pair of streptavidin-biotin complexes to be twice as large as that for a single complex (Wong et al., 1998). Our finding that the average unbinding force increased with increasing a loading rate (Fig. 2 *b* and Fig. 3, *b* and *c*) is consistent with AFM measurement for streptavidin-biotin complexes (Merkel et al., 1999), suggesting that this property is common to protein-protein interactions. This property has also been explained by the present model analysis.

Binding mode of kinesin in the AMP-PNP state and in the nucleotide-free state

As can be seen from Fig. 3, the fact that the *L*-component was predominant at 18 pN/s, the highest loading rate for the initial unbinding (the *bottom* of the *left column* in Fig. 3, *b* and *c*), implies that double-headed binding is predominant at equilibrium in the absence of external load in the AMP-PNP state. If the loading rate used to cause unbinding is significantly larger than the rate constants of the single-to-double-headed binding equilibrium, the unbinding-force distribution is expected to reflect the distribution at the binding equilibrium. This interpretation has been confirmed by the model analysis described below (Fig. 6).

Furthermore, in the nucleotide-free state, the *L*-component appeared to increase with the loading rate (Fig. 2 *b*). It

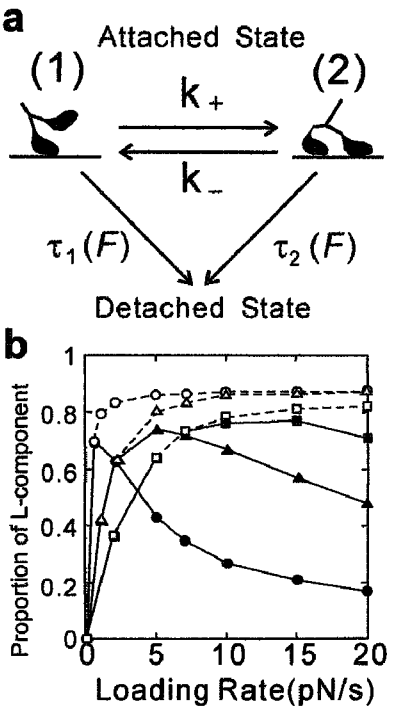

FIGURE 6 Scheme to explain the dependence on loading rate and loading direction of the average unbinding force and the unbinding-force distribution. (*a*), A model where equilibrium is assumed to exist between single-headed (*1*) and double-headed (*2*) binding with the rate constants, k_+ and k_-, between the two binding states. The lifetime, the inverse of the detachment rate, of each binding state is expressed as $\tau_i(F) = \tau_i(0)\exp(-F \times d_i/k_BT)$ (i = 1, 2), where d_i is a characteristic distance, k_B Boltzmann constant and T the absolute temperature (compare with Nishizaka et al., 2000). In this model calculation, the value of $\tau(0)$ was determined according to experimentally derived values (Hancock and Howard, 1999), so that the adjustable parameters were d, k_+ , and k_-. (*b*), According to the above model, we tried to determine the most appropriate values of rate constants to reproduce the data shown in Fig. 3 *d*, i.e., the loading-rate dependence of the proportion of the *L*-component for the initial and subsequent unbinding in the presence of AMP-PNP. Here, we show the results of model simulation for plus-end loading in the AMP-PNP state where the kinetic constants, k_+ and k_-, were changed keeping the equilibrium constant, i.e., the ratio k_+/k_-, as 10 considering that the values of $\tau_1(0)$ and $\tau_2(0)$ were, respectively, chosen as 150 and 2000 s, so that the ratio of $\tau_1(0)$ and $\tau_2(0)$ was ~1:10. *Open* and *solid symbols*, respectively, show the initial and the subsequent unbinding, in which we assumed that the values of k_+ and k_- did not depend on the initial or the subsequent unbinding. The values of k_+ and k_- (1/s) chosen were, respectively, 0.5 and 0.05 (*circles*); 2 and 0.2 (*triangles*); and 5 and 0.5 (*squares*).

should, however, be noted that the transition of the unbinding-force distribution from the *S*-component to the *L*-component occurred at a much higher loading rate (above 50 pN/s), than the few pN/s in the AMP-PNP state. The model described below has also explained these properties (Fig. 6).

It can be inferred that the *S*-component was, on the other hand, predominant at the highest loading rate, for the subsequent unbinding in the AMP-PNP state (the *bottom* of the *right column* in Fig. 3, *b* and *c*) is due to the unbinding of the attached head during single-headed binding before the attachment of the second head of the kinesin molecule, inasmuch as the loading rate was too high for the transition from single- to double-headed binding to occur. This inference could also be confirmed according to the same model as described below. It must be stressed that the only difference between the initial and the subsequent unbinding in the model analysis was in the initial conditions. The proportion of single- and double-headed bindings was 1:10 for the former and 1:0 for the latter, implying that the results obtained by two different methods could be explained by the same mechanism.

In the AMP-PNP state, at loading rates lower than ~5.6 pN/s, corresponding to a rate constant of 0.8 /s (= (5.6 pN/s)/(7 pN)), the proportion of double-headed binding for the initial and subsequent unbinding coincided as shown in Fig. 3 *d*. This is probably because, at such low loading rates, the binding equilibrium is attained throughout loading, thus the unbinding-force distribution becomes independent of the initial conditions. Fig. 3 also shows that the proportion of double-headed binding decreased markedly on further lowering of the loading rate, which is reasonable as the probability of unbinding during single-headed binding is higher at a lower loading rate.

The data summarized in Fig. 3 *d* are expected to contain information on the rate constants, k_+ and k_-, for transition between single- and double-headed bindings (compare to Fig. 1). As for the subsequent unbinding in the AMP-PNP state, k_+ can be estimated as 1/s (= (7.0 pN/s)/(7 pN)) by assuming that the unattached second head binds during the period in which the first head is still attached, and considering that the average unbinding force for single-headed binding is 7 pN and the proportion of double-headed binding becomes 50% at the loading rate 7.0 pN/s (see *arrow* in Fig. 3 *d*). This consideration had been more directly detected as a change in the elastic modulus during loading (Fig. 5 *a*). The time over which the transition occurred was estimated as ~1 s, which is consistent with the above estimation for k_+.

It is intriguing that the loading-rate dependence of unbinding force distribution, determined primarily by k_+ in our scheme, was independent of loading direction. This property seems to be in contrast with that of the active state in the presence of ATP, where kinesin's walking velocity is increased by the plus-end loading (Coppin et al., 1997) or the loading perpendicular to the microtubule (Gittes et al., 1996), so that k_+ is expected to depend on the loading direction. Thus, the above property may be intrinsic to the equilibrium state attained in the absence of nucleotides and in the presence of AMP-PNP.

It should be noted that the average unbinding force dropped significantly at the highest loading rate during subsequent unbinding (*right-most columns* in Fig. 3, *b* and *c*). The scheme described below could not explain this result (see the large deviation, especially on the peak position, from that of the distribution obtained by the model analysis). This may be explained by taking into account the presence of two binding sites, weak and strong, within each head (Woehlke

et al., 1997; Hirose et al., 1995; Crevel et al., 1996; Uemura et al., 2002), meaning that in the subsequent unbinding, the weak single-headed binding may occur first, so that at the highest loading rate, the single-headed binding may detach before the attached head undergoes the transition from weak to strong binding. This proposal does not contradict the fact that the elastic modulus remained unchanged despite the decrease in the average unbinding force (Fig. 5 *c*) because the most compliant part may not exist near the binding site. This should be confirmed experimentally in the future by using one-headed kinesin instead of conventional two-headed kinesin (Uemura et al., 2002).

Model analysis

We have done a model analysis as shown in Fig. 6 to explain the above results, particularly *1*) the loading-rate dependence of the average unbinding force and the unbinding force distribution, not only in the absence of nucleotides (Fig. 2 *b*) but also for both the initial and the subsequent unbinding in the presence of AMP-PNP (Fig. 3, *b* and *c*), and *2*) the dependence on the loading direction of unbinding force obtained under all the conditions examined.

First, we analyzed the dependence on time (t) and external load (F) of the proportion of the attached state of kinesin, $N(t, F)$, according to the scheme illustrated in Fig. 6 *a*. In the case of the one-headed kinesin heterodimer previously examined (Uemura et al., 2002), the unbinding is assumed to occur through a single step (only *state 1* is present in Fig. 6 *a*). In the present study, $N(t, F)$ is a function of only t because F is expressed as $F = \alpha t$, where α is a constant loading rate. Thus, $N(t)$ is expressed as $N(t) = N(0)\exp(-t/\tau(F))$, where $N(0)$ is the proportion of the attached state at time zero and $\tau(F)$ is a binding lifetime dependent on F, such that τ is also a function of only t in the present study. Here, we assume that, according to the results for an actin-myosin (HMM and S1) rigor complex (Nishizaka et al., 2000), $\tau(F) = \tau(0)\exp(-Fd/k_BT) = \tau(0)\exp(-\alpha d/k_BT)t = \tau(t)$, where $\tau(0)$ is a lifetime in the absence of external load, 150 s (Hancock and Howard, 1999; Uemura et al., 2002), d a characteristic distance, k_B the Boltzmann constant and T the absolute temperature. This model could simulate not only the increase in the average unbinding force with increasing loading rate but also predicts the unbinding force to be greater by 45% for minus-end loading compared with plus-end loading by assuming the d value for the plus-end loading (d_+) as 4.0 nm and that for minus-end loading (d_-) as 3.0 nm (compare with Uemura et al., 2002).

Conversely, when conventional two-headed kinesin homodimer was used, the results were not so simple. To explain the present results (Figs. 3 and 5; see also Fig. 2 in Kawaguchi and Ishiwata, 2001a), we assume that equilibrium exists between single- and double-headed binding as illustrated in Fig. 6 *a*. We also assume that the detachment of kinesin from a microtubule occurs during both single- and double-headed binding with different $\tau(0)$ values and characteristic distances (in contrast to the model by Strunz et al., 2000). Thus, $N_1(t)$ and $N_2(t)$, respectively the proportion of single-headed and double-headed binding, obey the following differential equations:

$$\frac{dN_1(t)}{dt} = k_-N_2(t) - \left\{k_+ + \frac{1}{\tau_1(t)}\right\}N_1(t) \quad (1)$$

$$\frac{dN_2(t)}{dt} = k_+N_1(t) - \left\{k_- + \frac{1}{\tau_2(t)}\right\}N_2(t) \quad (2)$$

where the relation $N_1 + N_2 = 1$ is always maintained. After the above differential equations (Eqs. 1 and 2) are solved, the unbinding force distribution, $P(F(t))$, can be obtained by the following derivative (Eq. 3):

$$P(F(t)) = \frac{d(N_1(t) + N_2(t))}{dt} = \frac{N_1(t)}{\tau_1(t)} + \frac{N_2(t)}{\tau_2(t)} \quad (3)$$

Here, the histogram of the unbinding force distribution can be obtained by $P(t)dt$ (or $P(F)dF$), i.e., the probability for the unbinding to occur between t and $t + dt$ (or between F and $F + dF$).

We assume the direct detachment from double-headed binding because the unbinding force distribution becomes very broad without this assumption (compare with Strunz et al., 2000). It is inferred that the load imposed on the attached head is instantaneously doubled upon detachment of one of two attached heads, so that for a kinesin molecule engaged in double-headed binding to a microtubule, the detachment of the remaining attached head occurs immediately after one head detaches, which is equivalent to the *simultaneous* detachment of both heads from the microtubule. In practice, we have never observed a moment at which a single-headed binding appeared to occur immediately after the double-headed unbinding occurred (see a record of the time course of the bead displacement shown in Figs. 2 *a*, 3 *a*, and 4 *a*). To detect the transient state of single-headed binding, higher time resolution may be needed.

In the model analysis, to reproduce the loading-direction and the loading-rate dependence of the unbinding force, the values of $\tau_1(0)$ and $\tau_2(0)$ were chosen as 150 s and 2000 s, respectively, and the values of d_1 and d_2 were 4.0 and 3.0 nm, respectively, for the plus-end loading (+), and 3.0 and 2.5 nm, respectively, for the minus-end loading (−; see Table 1; compare with Uemura et al., 2002). The lifetime of double-headed binding state, $\tau_2(0)$, shown in the model (*state 2* in Fig. 6 *a*) was determined to be 2000 s so as to make the *average* lifetime of the two-headed kinesin-microtubule complex equal to the 1000 s experimentally determined in the absence of external load (Hancock and Howard, 1999), where $\tau_1(0)$ was fixed as 150 s. The average lifetime, 1000 s, did not depend on the absolute values of k_+ and k_- as far as the ratio of k_+ and k_- was kept constant, 10. As the ratio of $\tau_1(0)$ and $\tau_2(0)$ was chosen as ~1:10, $N_1(0)$

TABLE 1 Parameters used for model analysis

		AMP-PNP		Nucleotide-free
		initial	subsequent	initial
$\tau_1(0)$, $\tau_2(0)$	[s]	150, 2000	150, 2000	150, 2000
$d_{+(1)}$, $d_{+(2)}$	[nm]	4.0, 3.0	4.0, 3.0	4.0, 3.0
$d_{-(1)}$, $d_{-(2)}$		3.0, 2.5	3.0, 2.5	3.0, 2.5
$N_1(0)$, $N_2(0)$		1/11, 10/11	1, 0	1/11, 10/11
k_+, k_-	[1/s]		2.0, 0.2	2.0, 0.2 70, 7

and $N_2(0)$ were, respectively, chosen as 1/11 and 10/11 (i.e., $k_+/k_- = 10$) for the initial unbinding event. Here, the initial unbinding is assumed to occur after the binding equilibrium is attained. On the other hand, $N_1(0)$ and $N_2(0)$ for the subsequent unbinding event were chosen as 1 and 0, respectively, because it is assumed that the subsequent unbinding event always starts from single-headed binding. As a result of computer analysis (an example is shown in Fig. 6 *b*), the values of k_+ and k_- were chosen as 2.0 and 0.2/s, respectively, for the AMP-PNP state and 70 and 7/s, respectively, for the nucleotide-free state for the best fit of simulation (keeping the ratio 10).

Thus, the above model analysis was able to simulate the essential features of the unbinding force distribution (see *solid curves* in Fig. 2 *b*, and Fig. 3, *b* and *c*) when a set of parameters indicated with triangles in Fig. 6 *b* was chosen. However, this simple model could not simulate the abrupt decrease in N_2 at higher than 5 pN/s for the subsequent unbinding (compare Fig. 6 *b* with Fig. 3 *d*, and also see *dashed curves* in Fig. 3, *b* and *c*). This large deviation observed in the subsequent unbinding at higher loading rates could be improved upon by considering the large dependence of k_+ and/or k_- on the loading rate. For example, as shown in Fig. 6 *b*, if the rate constants, 2 and 0.2/s at 5 pN/s is lowered to 0.5 and 0.05/s at 7.5 pN/s, the large loading-rate dependence observed in Fig. 3 *d* can be simulated. The loading-rate dependence of the rate constants may suggest that the visco-elastic properties of kinesin-microtubule complex could play a role in the forced unbinding.

We did not need to take into account the load (and loading-rate) dependence of the rate constants, k_+ and k_- for the initial unbinding. However, this does not necessarily mean that the rate constants are insensitive to external load during the initial unbinding but that the introduction of load-dependent rate constants did not improve the simulation as far as the present model is concerned. Also, note that the unbinding-force distribution in the nucleotide-free state was obtained only for the initial unbinding, in which the shape of distribution was almost independent of whether or not the load dependence of the rate constants was taken into account or not.

Thus, the time and load dependence of the number (or the proportion when normalized) of the kinesin-microtubule binding for the initial and the subsequent unbinding have been simulated. The parameters finally determined as the best to simulate the data are summarized in Table 1. The unbinding force distribution thus obtained reproduced the characteristics of experimental results (as shown by *solid curves* in Fig. 2 *b* for the nucleotide-free state and Fig. 3, *b–d* for the AMP-PNP state). It should be stressed that the initial and subsequent unbinding in the model analysis differed solely in the initial conditions (see the legend of Fig. 6); it was not necessary to change the values of other parameters.

The major difference observed in the initial unbinding between the nucleotide-free state and the AMP-PNP state was that the loading rate at which the transition between unimodal and bimodal distributions occurs was larger for the nucleotide-free state (larger than 50 pN/s, see Fig. 2 *b*) than for the AMP-PNP state (smaller than 2 pN/s, see Fig. 3, *b–d*). In the present model, this difference was attributable to the difference in the rate constants between single- and double-headed binding: that is, the model predicts that the rate constants for the former, 70 and 7/s, are an order-of-magnitude larger than those for the latter, 2 and 0.2/s (Table 1).

Asymmetry of mechanical properties, loading direction, and its physiological implication

A simple explanation for the dependence of the unbinding force on loading direction (Figs. 2 and 3) is that the load imposed toward the minus end is effectively smaller than that toward the plus end. This is conceivable if the part of neck linker of kinesin, through which the external load is imposed, is connected to the head part facing to the minus end of kinesin, being asymmetric against the binding interface (Rice et al., 1999). This will cause the asymmetrical geometry of the point of action of external load. Hence, the external load is imposed on the kinesin-microtubule binding interface asymmetrically (see the illustration of kinesin molecule in Fig. 1; see Rice et al., 1999, and Hoenger et al., 2000).

In our model analysis, the asymmetry of the unbinding force was attributed to the difference in the characteristic distance, d, which is larger for plus-end loading than for minus-end loading. This implies that the effective load required to induce the unbinding is smaller for plus-end loading, which is consistent with the above interpretation.

The smaller unbinding force for plus-end loading seems to indicate that it is favorable for kinesin to walk toward the plus end of a microtubule. Upon double-headed binding, the two heads are bridged. If the leading head pulls the trailing head and vice versa, the binding of the trailing head will thus become unstable compared with that of the leading head even if both heads are in the same nucleotide state (compare with Uemura et al., 2002). Moreover, if this destabilization of the binding of the trailing head due to forward pulling is coupled to the attachment or detachment of nucleotides, that is, if such a synchronization occurs within a molecule through mechano-chemical coupling, directional movement

of kinesin molecules on microtubule will be possible through the repetition of alternating single- and double-headed binding.

Relation between lifetime and unbinding force for kinesin-microtubule complex

The lifetime of kinesin-microtubule complex, which is related to the binding energy, has been measured in the absence of external load to be ~1000 s in both the nucleotide-free and AMP-PNP states for two-headed kinesin and ~100 s for one-headed kinesin (Hancock and Howard, 1999). The present experiments showed that the average lifetime of the attached state decreased to ~1 s at 10 pN. Assuming that the relation between the binding lifetime (τ) and the external load (F) is expressed as $\tau(F) = \tau(0)\exp(-Fd/k_BT)$ as in the case of the rigor bond of acto-heavy meromyosin complexes (Nishizaka et al., 1995; 2000), the present model analysis showed that the d value most appropriate for simulating the data was 3.0–4.0 nm for the plus-end loading and 2.5–3.0 nm for the minus-end loading. Our preliminary experiments on the load dependence of the binding lifetime in the presence of AMP-PNP supported this estimate (Seo and Ishiwata, unpublished results). This value is an order-of-magnitude larger than that for the average protein-protein interaction (compare with Nishizaka et al., 2000). Thus, we propose that such a large characteristic distance may be inherent to motor proteins.

Extension of a kinesin-microtubule complex

The extension of kinesin molecules, at which unbinding occurred, can be estimated from the ratio of the unbinding force and the elastic modulus as ~18 nm for the plus-end loading (or 21 nm for the minus-end loading) regardless of conditions. However, this estimate is only an apparent one. Taking into account the fact that the radius of bead is 0.5 μm and that the length of kinesin is 60 ± 20 nm (Svoboda and Block, 1994), the extension of kinesin corresponding to the 18 (or 21) nm displacement of bead is estimated to be 8.3 ± 1 (9.7 ± 1) nm, which is ~18 (or 21) nm × cos(θ), where θ (1.1 ± 0.1 rad) is the angle between the long axis of kinesin and the glass surface (Kawaguchi and Ishiwata, 2001a). However, the extension of 8.3 (or 9.7) nm may still be too large for the small protein molecules such as kinesin. Such a large extension may be attributable not only to the extension and partial unfolding, e.g., forced unzippering of neck linker region (Rice et al., 1999) of each head of kinesin, but also to that of the binding region of the tubulin heterodimer.

In conclusion, the present study has demonstrated that single molecule measurements of the unbinding force and the elastic modulus can determine the manner and kinetics of kinesin binding to a microtubule under various nucleotide-binding states.

We thank Dr. K. Kinosita, Jr. of Okazaki National Research Institute and Dr. T. Nishizaka of Kansai Advanced Research Center for continuous collaboration. We are grateful to Drs. Y. Y. Toyoshima and T. Yagi of The University of Tokyo for their suggestions on the preparation of kinesin and tubulin, and to Dr. H. Higuchi of Tohoku University for the kinesin bead assay protocol. We also thank Mr. Mark Chee of Duke University for his critical reading of the manuscript.

This research was partly supported by Grants-in-Aid for Specially Promoted Research, for Scientific Research on Priority Areas, and for the Bio-venture Project from the Ministry of Education, Sports, Culture, Science and Technology of Japan; and by the Mitsubishi Foundation.

REFERENCES

Block, S. M., L. S. B. Goldstein, and B. J. Schnapp. 1990. Bead movement by single kinesin molecules studied with optical tweezers. *Nature*. 348:348–352.

Coppin, C. M., D. W. Pierce, L. Hsu, and R. D. Vale. 1997. The load dependence of kinesin's mechanical cycle. *Proc. Natl. Acad. Sci. USA*. 94:8539–8544.

Coy, D. L., M. Wagenbach, and J. Howard. 1999. Kinesin takes one 8-nm step for each ATP that it hydrolyzes. *J. Biol. Chem.* 276:3667–3671.

Crevel, I. M., A. Lockhart, and R. A. Cross. 1996. Weak and strong states of kinesin and NCD. *J. Mol. Biol.* 257:66–76.

Cross, R. A. 1995. On the hand over hand footsteps of kinesin heads. *J. Muscle Res. Cell Motil.* 16:91–94.

Gittes, F., E. Meyhöfer, S. Baek, and J. Howard. 1996. Directional loading of the kinesin motor molecule as it buckles a microtubule. *Biophys. J.* 70:418–429.

Hackney, D. D. 1994. Evidence for alternating head catalysis by kinesin during microtubule-stimulated ATP hydrolysis. *Proc. Natl. Acad. Sci. USA*. 91:6865–6869.

Hancock, W. O., and J. Howard. 1999. Kinesin's processivity results from mechanical and chemical coordination between the ATP hydrolysis cycles of the two motor domains. *Proc. Natl. Acad. Sci. USA*. 96: 13147–13152.

Higuchi, H., E. Muto, Y. Inoue, and T. Yanagida. 1997. Kinetics of force generation by single kinesin molecules activated by laser photolysis of caged ATP. *Proc. Natl. Acad. Sci. USA*. 94:4395–4400.

Hirokawa, N. 1998. Kinesin and dynein superfamily proteins and mechanism of organelle transport. *Science*. 279:519–526.

Hirose, K., A. Lockhart, R. A. Cross, and L. A. Amos. 1995. Nucleotide-dependent angular change in kinesin motor domain bound to tubulin. *Nature*. 376:277–279.

Hoenger, A., M. Thormahlen, R. Diaz-Avalos, M. Doerhoefer, K. N. Goldie, J. Muller, and E. Mandelkow. 2000. A new look at the microtubule binding patterns of dimeric kinesins. *J. Mol. Biol.* 297: 1087–1103.

Howard, J. 1996. The movement of kinesin along microtubules. *Annu. Rev. Physiol.* 58:703–729.

Hua, W., E. C. Young, M. L. Fleming, and J. Gelles. 1997. Coupling of kinesin steps to ATP hydrolysis. *Nature*. 388:390–393.

Hyman, A. A. 1991. Preparation of marked microtubules for the assay of the polarity of microtubule-based motors by fluorescence. *J. Cell Sci.* 14:125–127.

Kawaguchi, K., and S. Ishiwata. 2000. Temperature dependence of force, velocity and processivity of single kinesin molecules. *Biochem. Biophys. Res. Commun.* 272:895–899.

Kawaguchi, K., and S. Ishiwata. 2001a. Nucleotide-dependent single- to double-headed binding of kinesin. *Science*. 291:667–669.

Kawaguchi, K., and S. Ishiwata. 2001b. Thermal activation of single kinesin molecules with temperature pulse microscopy. *Cell Motil. Cytoskeleton*. 49:41–47.

Kojima, H., E. Muto, H. Higuchi, and T. Yanagida. 1997. Mechanics of single kinesin molecules measurement by optical trapping nanometry. *Biophys. J.* 73:2012–2022.

Mandelkow, E., and K. A. Johnson. 1998. The structural and mechanochemical cycle of kinesin. *TIBS.* 23:429–433.

Merkel, R., P. Nassoy, A. Leung, K. Ritchie, and E. Evans. 1999. Energy landscapes of receptor-ligand explored with dynamic force spectroscopy. *Nature.* 397:50–53.

Nishizaka, T., T. Miyata, H. Yoshikawa, S. Ishiwata, and K. Kinosita, Jr. 1995. Unbinding force of a single motor molecule of muscle measured using optical tweezers. *Nature.* 377:251–254.

Nishizaka, T., R. Seo, H. Tadakuma, K. Kinosita, Jr., and S. Ishiwata. 2000. Characterization of single actomyosin rigor bonds—load-dependence of lifetime and mechanical properties. *Biophys. J.* 79:962–974.

Rice, S., A. W. Lin, D. Safer, C. L. Hart, N. Naber, B. O. Carragher, S. M. Cain, E. Pechatnikova, E. M. Wilson-Kubalek, M. Whittaker, E. Pate, R. Cooke, E. W. Taylor, R. A. Milligan, and R. D. Vale. 1999. A structural change in the kinesin motor protein that drives motility. *Nature.* 402:778–784.

Schnitzer, M. J., and S. M. Block. 1997. Kinesin hydrolyses one ATP per 8-nm step. *Nature.* 388:386–390.

Strunz, T., K. Oroszlan, I. Schumakovitch, H.-J. Güntherodt, and M. Hegner. 2000. Model energy landscapes and the force-induced dissociation of ligand-receptor bonds. *Biophys. J.* 79:1206–1212.

Svoboda, K., C. F. Schmidt, B. J. Schnapp, and S. M. Block. 1993. Direct observation of kinesin stepping by optical trapping interferometry. *Nature.* 365:721–727.

Svoboda, K., and S. M. Block. 1994. Force and velocity measured for single kinesin molecules. *Cell.* 77:773–784.

Uemura, S., K. Kawaguchi, J. Yajima, M. Edamatsu, Y. Y. Toyoshima, and S. Ishiwata. 2002. Kinesin-microtubule binding is dependent on both nucleotide state and loading direction. *Proc. Natl. Acad. Sci. USA.* 99: 5977–5981.

Vale, R. D., T. Funatsu, D. W. Pierce, L. Romberg, Y. Harada, and T. Yanagida. 1996. Direct observation of single kinesin molecules moving along microtubules. *Nature.* 380:451–453.

Vale, R. D. 1999. Guidebook to the Cytoskeletal and Motor Proteins, 2nd ed. T. E. Kreis, editor. Oxford University Press, Oxford, England. 398–402.

Vale, R. D., and R. A. Milligan. 2000. The way things move: looking under the hood of molecular motor proteins. *Science.* 288: 88–95.

Woehlke, G., A. K. Ruby, C. L. Hart, B. Ly, N. Hom-Booher, and R. D. Vale. 1997. Microtubule interaction site of the kinesin motor. *Cell.* 90: 207–216.

Wong, S. S., E. Joselevich, A. T. Woolley, C. L. Cheung, and C. M. Lieber. 1998. Covalently functionalized nanotubes as nanometer-sized probes in chemistry and biology. *Nature.* 394:52–55.

Loading direction regulates the affinity of ADP for kinesin

Sotaro Uemura[1] and Shin'ichi Ishiwata[1,2]

Published online 17 March 2003; doi:10.1038/nsb911

Kinesin is an ATP-driven molecular motor that moves processively along a microtubule. Processivity has been explained as a mechanism that involves alternating single- and double-headed binding of kinesin to microtubules coupled to the ATPase cycle of the motor. The internal load imposed between the two bound heads has been proposed to be a key factor regulating the ATPase cycle in each head. Here we show that external load imposed along the direction of motility on a single kinesin molecule enhances the binding affinity of ADP for kinesin, whereas an external load imposed against the direction of motility decreases it. This coupling between loading direction and enzymatic activity is in accord with the idea that the internal load plays a key role in the unidirectional and cooperative movement of processive motors.

Kinesin, which was initially purified from squid neural tissue[1], bovine brain[2] and sea urchin eggs[3], is a motor protein widely distributed in eukaryotic cells[4]. Kinesin is a processive motor that 'walks' along a microtubule toward its plus end and is essential for the transport of vesicles and organelles[5–7]. Upon binding to a microtubule, kinesin takes >100 consecutive steps before dissociation. Each 8 nm step is coupled to one cycle of ATP hydrolysis, indicating a tight coupling between enzymatic reaction and mechanical event. The high processivity of kinesin has been explained by a model in which the two heads of kinesin alternate iteratively between single-headed and double-headed binding to a microtubule[8–12].

How can kinesin molecules convert chemical energy to mechanical work, and how do two heads communicate with each other to realize a coordinated processive movement along a microtubule[8–12]? This communication has been proposed to be mediated by the internal load that is imposed on kinesin when both of its heads are bound to the microtubule. It is assumed that, in this configuration, the leading head and the trailing head experience a load backward and forward, respectively, through the connection between the two heads[13–17]. However, there is as yet no direct experimental evidence supporting this hypothesis.

Recently, we measured the unbinding force of single kinesin–microtubule complexes in nucleotide-free, ADP-bound and AMP-PNP (adenosine 5′-[β,γ-imido] triphosphate, an ATP analog)–bound conditions to determine how kinesin binds to the microtubule in these states: with single-headed or double-headed binding and with weak or strong binding[10,11]. We were

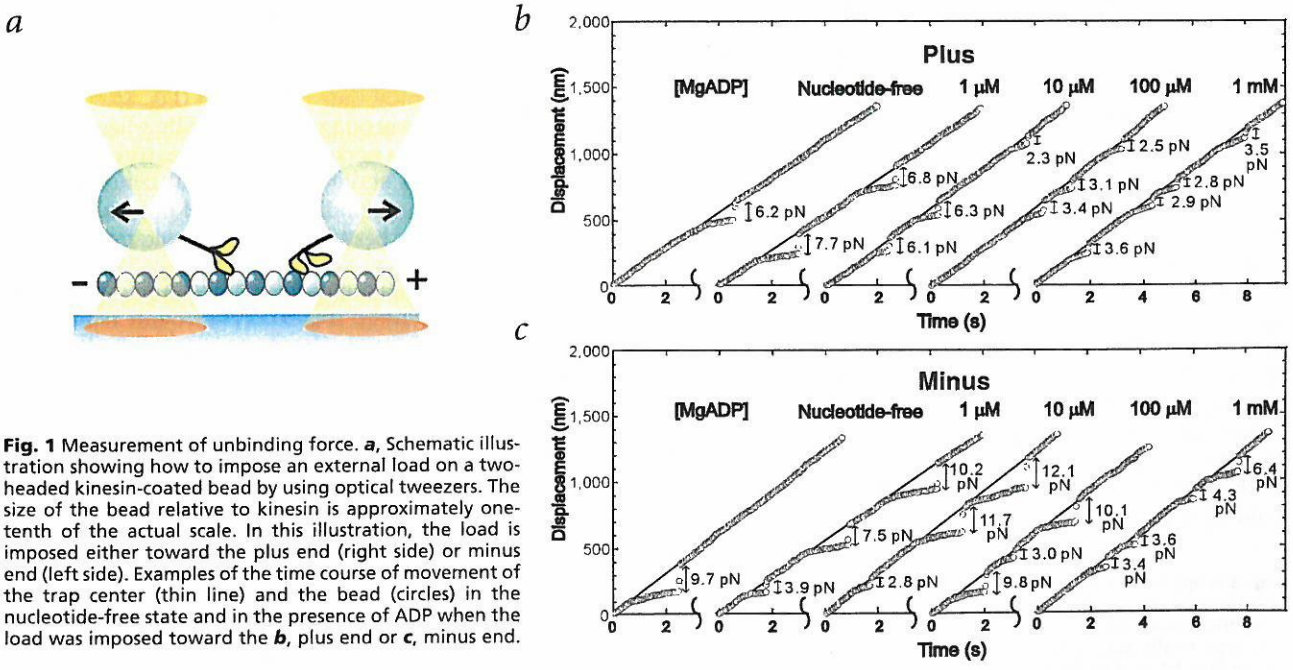

Fig. 1 Measurement of unbinding force. ***a***, Schematic illustration showing how to impose an external load on a two-headed kinesin-coated bead by using optical tweezers. The size of the bead relative to kinesin is approximately one-tenth of the actual scale. In this illustration, the load is imposed either toward the plus end (right side) or minus end (left side). Examples of the time course of movement of the trap center (thin line) and the bead (circles) in the nucleotide-free state and in the presence of ADP when the load was imposed toward the ***b***, plus end or ***c***, minus end.

[1]Department of Physics, School of Science and Engineering, and [2]Advanced Research Institute for Science and Engineering, Waseda University, 3-4-1 Okubo, Shinjuku-ku, Tokyo 169-8555, Japan.

Correspondence should be addressed to S.I. *e-mail: ishiwata@waseda.jp*

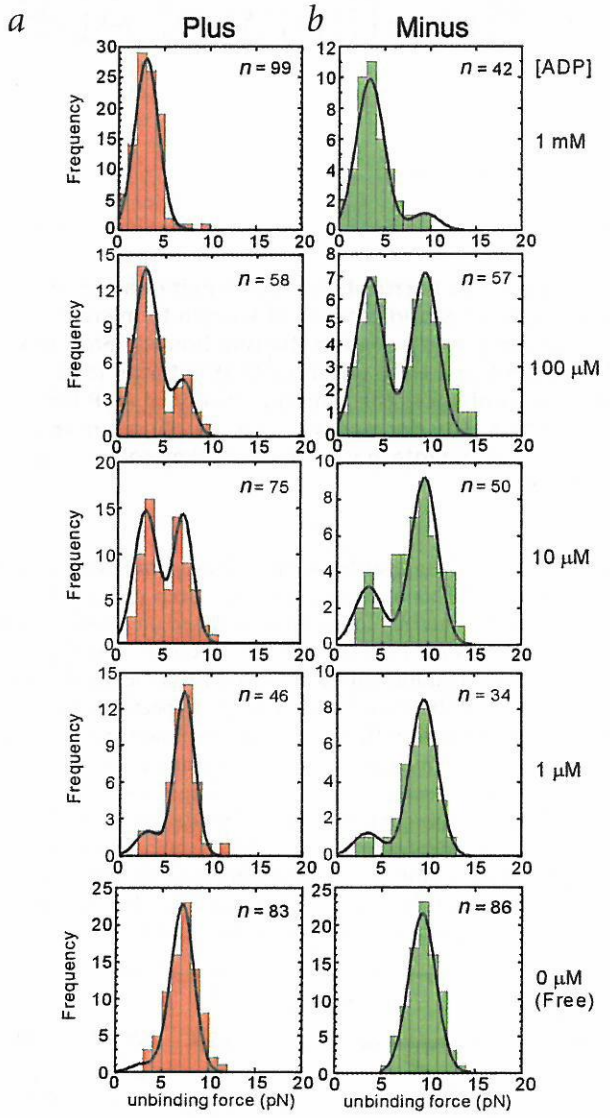

Fig. 2 Unbinding force distributions at various ADP concentrations. The ADP concentrations are shown on the right side of each distribution. ***a***, Plus-end loading is shown in orange, and ***b***, minus-end loading is shown in green. The solid curves are results of globally fitting the histograms to two Gaussian distributions for the plus-end and minus-end loading separately[24].

able to distinguish between single-headed and double-headed binding by analyzing the shape of the unbinding force distribution as unimodal and bimodal, respectively. Furthermore, we were able to distinguish between weak and strong binding on the basis of the peak value of the unbinding force distribution. We observed that double-headed, strong binding is predominant in the AMP-PNP–binding state, whereas single-headed, strong binding is predominant in the presence of AMP-PNP plus ADP[11]. In contrast, in the ADP binding state, single-headed binding is predominant and the binding is weak[10]. In the nucleotide-free state, the binding is strong but single-headed binding is predominant when unbinding is observed at a low loading rate[10–12]. In this study, we monitored the effects of loading direction on the affinity of ADP for kinesin.

Unbinding force at various ADP concentrations

We have examined the effect of imposing a load on the equilibrium between the weak binding state (realized predominantly in the presence of ADP) and the strong binding state (realized predominantly in the absence of nucleotide). To accomplish this, we measured the unbinding force at various ADP concentrations (1,000, 100, 10, 1 and 0 μM) for either the plus- or minus-end loading at a low loading rate (5.5 ± 0.14 pN s^{-1}, mean ± s.e.m., n = 630) using a previous reported method[10–12]. Here, a narrow distribution of the estimated loading rate (the rate of increase in the imposed load) exists because it was determined from the difference between the velocity of the bead moving along a microtubule (kept constant in the experiments) and the average extension of the protein–bead complex (differed for each measurement). The loading rate in the current study is slower than the rates of ADP binding and dissociation, as well as the rate of interconversion between single-headed and double-headed binding. Under this condition, the microtubule-bound kinesin is expected to sample predominantly the weak, single-headed binding state (ADP bound)[10] and strong, single-headed binding state (nucleotide free)[10–12] throughout the course of the experiments.

A kinesin-coated bead was first trapped by optical tweezers and placed in contact with a microtubule for 20–30 s to allow the kinesin–microtubule binding to reach equilibrium. Then, the unbinding force was measured by pulling the bead toward the plus end or the minus end of the microtubule at a constant velocity (Fig. 1*a*). Typical time course data (Fig. 1*b*,*c*) indicate that the unbinding events occurred repeatedly when the bead was kept moving along a microtubule. This was true not only at 1 mM ADP but also at intermediate ADP concentrations. In contrast, rebinding/unbinding events did not occur during the movement of the bead in the nucleotide-free state[10–12] (Fig. 1*b*,*c*).

We determined the unbinding force distributions obtained at various ADP concentrations (Fig. 2). As previously reported, in

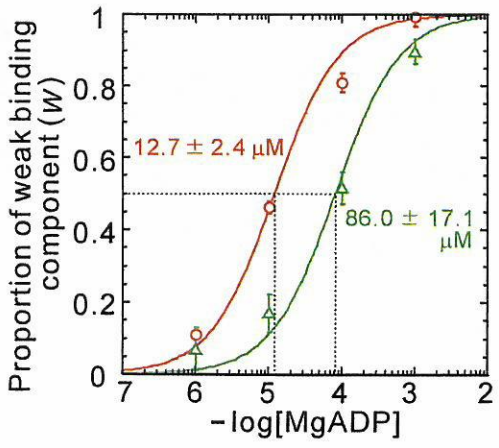

Fig. 3 Proportion of weak binding component, W, at various ADP concentrations. The proportion of weak binding component was estimated from the ratio of the area (peak × width) of the left peak of Gaussian distribution to the total area (sum of two Gaussian distributions) of the unbinding force distribution obtained by the global fit as shown in Fig. 2. Orange circles and green triangles show the data for plus-end and minus-end loading respectively. Data were fit to a hyperbola (orange and green lines), $W = [ADP] / (K + [ADP])$, in which the dissociation constant K was determined as 12.7 ± 2.4 μM for plus-end loading (K_+) and 86.0 ± 17.1 μM for minus-end loading (K_-). Error bars were obtained from the global fit.

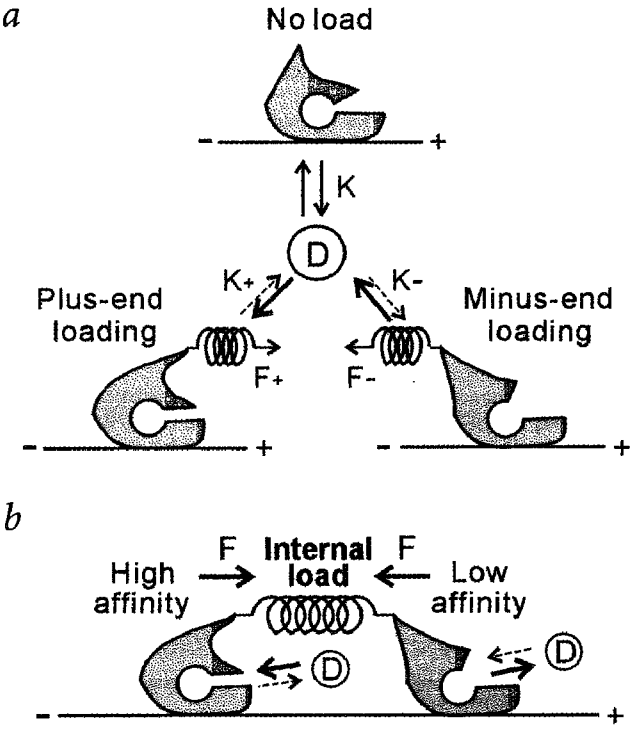

Fig. 4 Schematic illustrations showing equilibrium of ADP (D) binding to a complex of kinesin (nucleotide-binding pocket is shown) and microtubule (thin line, where both the plus and the minus ends are shown). ***a***, The effect of imposing a load toward the plus end (F_+) or the minus end (F_-) of a microtubule on the binding equilibrium. The dissociation constants of ADP in a kinesin-microtubule complex in the absence of load (K), under plus-end loading, K_+, and under minus-end loading, K_-, are also shown. ***b***, A possible role of an internal load within a two-headed kinesin molecule on the binding equilibrium. In (*b*), such a situation is illustrated that the internal load, which may be produced by extension of the link between the two heads upon binding to a microtubule, increases the binding affinity of ADP for the trailing head (left side) and decreases that for the leading head (right side). Here, we assume that the internal load imposed between the two heads is equivalent to the plus-end loading for the trailing head and the minus-end loading for the leading head.

1 mM ADP, binding of kinesin to microtubule was weak, with an average unbinding force of ~3 pN (ref. 10). Here we demonstrate that, at various ADP concentrations, only the proportion of the weak and strong binding components differed, maintaining constant values of the unbinding force. Specifically, the proportion of the weak-binding component increases as the ADP concentration increases, irrespective of the loading direction (Fig. 2). The ADP concentration at which the weak and strong binding components become equal appears to be lower for the plus-end loading (~10 μM ADP, Fig. 2*a*) than for minus-end loading (~100 μM ADP, Fig. 2*b*).

Affinity for ADP depends on loading direction

Next, we quantify the correlation between the relative proportion of the weak binding component and the ADP concentration. This correlation could be fit by a hyperbola, in which an apparent dissociation constant of ADP in the kinesin–microtubule complex was determined. There is a seven-fold difference in the affinity of kinesin for ADP: 12.7 ± 2.4 μM for plus-end loading and 86.0 ± 17.1 μM for minus-end loading (Fig. 3). This result indicates that the ADP binding is regulated by the direction of loading.

We summarized the results obtained above in a schematic illustration (Fig. 4*a*). The dissociation constant of ADP in the kinesin–microtubule complex in solution (K, in the absence of external load) has been reported to be ~50 μM[18,19], which is between the values of K_+ and K_- obtained here (Fig. 3). Thus, the dissociation constant of ADP seems to be decreased by plus-end loading and increased by minus-end loading. This result presents direct evidence for the regulation of the ATPase cycle by an imposed load and demonstrates that the effect of load is directionally dependent. The coupling between enzymatic activity and force is the essence of a mechano-enzyme. It is interesting to note that the intracellular concentration of free ADP in a rat brain was reported to be 54–128 μM[20], which falls within the range between K_+ and K_- obtained here, suggesting that the regulation of binding affinity of ADP by loading may occur *in vivo*.

Internal load and processivity

Thus far, several published reports suggest that the ATPase cycle of molecular motors depends on the external load[21–24]. Hancock and Howard[13] first suggested the positive role of internal load based on the comparison of the processivity and the ATPase activity of two-headed conventional kinesin homodimers with those of one-headed heterodimers. Thus, the mechanism of processivity of both kinesin[13–17] and myosin V[23,25,26] is usually explained by assuming an internal load imposed between the two heads. With double-headed binding, the leading and trailing heads of kinesin are pulled toward the minus and plus ends of a microtubule, respectively, such that the binding affinity of ADP becomes lower for the leading head and higher for the trailing head (Fig. 4*b*). The conformation of the nucleotide-binding site is predicted to be asymmetrically distorted by the internal load. This property is in agreement with the hand-over-hand model, which assumes that the dissociation of ADP occurs more easily at the leading head than at the trailing head. Taking into account that the binding lifetime of an attached head becomes ~150× longer upon dissociation of ADP and the internal load is assumed to be 4 pN (ref. 10), the average lifetime of the attached state of leading head is estimated to be an order of magnitude longer than that of the trailing head. Thus, the internal load is a possible key factor for the processivity of kinesin motility. Direct evidence of the existence of internal load is the next challenging target in the biophysical research of molecular motors.

Methods

Proteins. Conventional two-headed kinesin homodimer and tubulin were prepared from bovine[27] and porcine brains[28], respectively. Both brain tissues were purchased from a local slaughterhouse. Polarity-marked microtubules labeled with tetramethyl-rhodamine succinimidyl ester (Molecular Probes) were prepared according to Hyman[29], except that *N*-ethylmaleimide–treated tubulin was not used so that polymerization at the minus end was not inhibited. We found that ~50% of the microtubules thus prepared were correctly marked (as shown in Fig. 2A of ref. 11), whereas almost all the others were block copolymers — that is, the plural nuclei strongly labeled with rhodamine existed in the same microtubules. These microtubules were not used for our experiments.

Unbinding force measurement. Kinesin-coated beads (1.0 μm in diameter, carboxylate-modified latex, Molecular Probes) were prepared according to the established procedure[27] with slight modifications. Kinesin molecules were mixed with the beads at a molar ratio of 2:1. The polarity-marked fluorescent microtubules in assay buffer (2 mM $MgCl_2$, 80 mM PIPES-KOH, pH 6.8, and 1 mM EGTA) were introduced into a flow cell and incubated for 2 min to allow binding to the glass surface. The solvent was exchanged three times with an assay buffer containing 0.7 mg ml^{-1} filtered casein to coat the glass surface with casein. The flow cell was then filled with an

assay buffer containing the kinesin-coated beads, filtered casein and an oxygen-scavenging enzyme system. The final solvent condition was ~0.1 pM kinesin-coated beads, 2 mM $MgCl_2$, 80 mM PIPES-KOH, pH 6.8, 1 mM EGTA, 0.7 mg ml^{-1} filtered casein, 10 μM taxol, 10 mM dithiothreitol, 4.5 mg ml^{-1} glucose, 0.22 mg ml^{-1} glucose oxidase, 0.036 mg ml^{-1} catalase and 1 U ml^{-1} apyrase (nucleotide-free state) or 1 mM ADP containing 1 U ml^{-1} hexokinase (ADP state). We were able to repeat the unbinding force measurements on the same microtubules several times on the same beads, presumably for the same kinesin molecules, by using optical tweezers for manipulation[10–12]. We confirmed that there was no significant difference in either the unbinding force distribution or binding properties regardless of the presence or absence of apyrase. Therefore, the denaturing of kinesin during measurement in the absence of nucleotides is unlikely. The average number of functional kinesin molecules on a bead was estimated to be one by statistical methods (considering the geometry of the kinesin on the bead, we estimate that only single kinesin molecules interacted with a microtubule in almost all the measurements)[5,27]. Global fits of unbinding force distribution to two Gaussian distributions were achieved by nonlinear optimization using SigmaPlot 8.0 (Windows)[24]. The microscopy system equipped with optical tweezers was as described[30]; the stiffness of the optical trap was estimated to be 0.05 pN nm^{-1} (ref. 30). All experiments were performed at 25 ± 1 °C.

Acknowledgments

We thank S.S. Rosenfeld and M. Chee for critical reading of the manuscript. We also thank D.D. Hackney and K. Kinosita Jr. for valuable discussion. This research was partly supported by Grants-in-Aid for Specially Promoted Research and for the Bio-venture Project from the Ministry of Education, Sports, Culture, Science and Technology of Japan. S.U. is a recipient of predoctoral fellowship of the Japan Society for the Promotion of Science.

Competing interests statement

The authors declare that they have no competing financial interests.

Received 6 November, 2002; accepted 10 February, 2003.

1. Vale, R.D., Reese, T.S. & Sheetz, M.P. Identification of a novel force-generating protein, kinesin, involved in microtubule-based motility. *Cell* **42**, 39–50 (1985).
2. Brady, S.T. A novel brain ATPase with properties expected for the fast axonal transport motor. *Nature* **317**, 73–75 (1985).
3. Scholey, J.M., Porter, M.E., Grissom, P.M. & McIntosh, J.R. Identification of kinesin in sea urchin eggs and evidence for its localization in the mitotic spindle. *Nature* **318**, 483–486 (1985).
4. Hirokawa, N. Kinesin and dynein superfamily proteins and the mechanism of organelle transport. *Science* **279**, 519–526 (1998).
5. Svoboda, K. & Block, S.M. Force and velocity measured for single kinesin molecules. *Cell* **77**, 773–784 (1994).
6. Hackney, D.D. Evidence for alternating head catalysis by kinesin during microtubule-stimulated ATP hydrolysis. *Proc. Natl. Acad. Sci. USA* **91**, 6865–6869 (1994).
7. Rice, S. *et al.* A structural change in the kinesin motor protein that drives motility. *Nature* **402**, 778–784 (1999).
8. Vale, R.D. & Milligan, R.A. The way things move: looking under the hood of molecular motor proteins. *Science* **288**, 88–95 (2000).
9. Mandelkow, E. & Johnson, K.A. The structural and mechanochemical cycle of kinesin. *Trends Biochem. Sci.* **23**, 429–433 (1998).
10. Uemura, S. *et al.* Kinesin-microtubule binding depends on both nucleotide state and loading direction. *Proc. Natl. Acad. Sci. USA* **99**, 5977–5981 (2002).
11. Kawaguchi, K. & Ishiwata, S. Nucleotide-dependent single- to double-headed binding of kinesin. *Science* **291**, 667–669 (2001).
12. Kawaguchi, K., Uemura, S. & Ishiwata, S. Equilibrium and transition between single- and double-headed binding of kinesin as revealed by single-molecule mechanics. *Biophys. J.* **84**, 1103–1113 (2003).
13. Hancock, W.O. & Howard, J. Kinesin's processivity results from mechanical and chemical coordination between the ATP hydrolysis cycles of the two motor domains. *Proc. Natl. Acad. Sci. USA* **96**, 13147–13152 (1999).
14. Derenyi, I. & Vicsek, T. The kinesin walk: a dynamic model with elastically coupled head. *Proc. Natl. Acad. Sci. USA* **93**, 6775–6779 (1996).
15. Cross, R.A. *et al.* The conformational cycle of kinesin. *Philos. Trans. R. Soc. Lond. B Biol. Sci.* **355**, 459–464 (2000).
16. Crevel, I., Carter, N., Schliwa, M. & Cross, R. Coupled chemical and mechanical reaction steps in a processive *Neurospora* kinesin. *EMBO J.* **18**, 5863–5872 (1999).
17. Xing, J. *et al.* Kinesin has three nucleotide-dependent conformations. Implications for strain-dependent release. *J. Biol. Chem.* **275**, 35413–35423 (2000).
18. Ma, Y.Z. & Taylor, E.W. Kinetic mechanism of a monomeric kinesin construct. *J. Biol. Chem.* **272**, 717–723 (1997).
19. Ma, Y.Z. & Taylor, E.W. Interacting head mechanism of microtubule-kinesin ATPase. *J. Biol. Chem.* **272**, 724–730 (1997).
20. Askenasy, N. & Koretsky, A.P. Transgenic livers expressing mitochondrial and cytosolic CK: mitochondrial CK modulates free ADP levels. *Am. J. Physiol. Cell Physiol.* **282**, C338–346 (2002).
21. Visscher, K., Schnitzer, M.J & Block, S.M. Single kinesin molecules studied with a molecular force clamp. *Nature* **400**, 184–189 (1999).
22. Nishiyama, M., Higuchi, H. & Yanagida, T. Chemomechanical coupling of the forward and backward steps of single kinesin molecules. *Nat. Cell Biol.* **4**, 790–797 (2002).
23. Rief, M. *et al.* Myosin-V stepping kinetics: a molecular model for processivity. *Proc. Natl. Acad. Sci. USA* **97**, 9482–9486 (2000).
24. Schnitzer, M.J., Visscher, K. & Block, S.M. Force production by single kinesin motors. *Nat. Cell Biol.* **2**, 718–723 (2000).
25. Veigel, C., Wang, F., Bartoo, M.C., Sellers, J.R. & Molloy, J.E. The gated gait of the processive molecular motor, myosin V. *Nat. Cell Biol.* **4**, 59–65 (2002).
26. Spudich, J.A. & Rock, R.S. A crossbridge too far. *Nat. Cell Biol.* **4**, E8–E10 (2002).
27. Kojima, H., Muto, E., Higuchi, H. & Yanagida, T. Mechanics of single kinesin molecules measured by optical trapping nanometry. *Biophys. J.* **73**, 2012–2022 (1997).
28. Weingarten, M.D., Lockwood, A.H., Hwo, S.Y. & Kirschner, M.W. A protein factor essential for microtubule assembly. *Proc. Natl. Acad. Sci. USA* **72**, 1858–1862 (1975).
29. Hyman, A.A. Preparation of marked microtubules for the assay of the polarity of microtubule-based motors by fluorescence. *J. Cell Sci.* **s14**, 125–127 (1991).
30. Nishizaka, T., Miyata, H., Yoshikawa, H., Ishiwata, S. & Kinosita, K. Jr. Unbinding force of a single motor molecule of muscle measured using optical tweezers. *Nature* **377**, 251–254 (1995).

7章 生体システムを計測する

7・1 分子からシステムまで

ここではナノメートル計測の対象となる生体システムの例として，筋収縮系を取り上げる[1]．筋収縮系は，筋肉を構成するアクチン，ミオシンといった主要な生体運動タンパク質レベル（特に，運動性酵素であるミオシンは，“分子モータ”と呼ばれる）から，筋細胞あるいは心臓という組織レベルまで，階層構造をなしている．図7・1に模式的に示したように，10 nmオーダの分子モータ・筋フィラメントレベルに始まり，ミオシン分子の重合体である太いフィラメントと，アクチン分子の重合体である細いフィラメントが格子構造をなす，太さ約1 μm，長さ2～3 μmの筋節（横紋筋という周期構造体を形成する最小構造単位，サルコメアとも呼ぶ），筋節が直列に接続した筋原線維（横紋筋として力発生を担う最小機能単位），そして筋原線維が束状につながり，いわゆる横紋構造をなす筋線維（筋細胞）に至る．筋線維は神経などと連携して組織（臓器）を構成する．ナノバイオといわれる分野の中でも，我々のように，生体機能を担っているタンパク質分子装置（分子機械）の仕組みに注目する研究は，このような生体構造の各階層ごとに，特定の分子機械が機能する仕組みを一分子レベルで捉えようとする．特定の分子に注目し，その動き，状態，構造を，その分子に結合した蛍光分子が発する情報をよりどころにして解析しようとする．ここでは，筋収縮系の階層構造を一分子レベルから，分子集合体レベルを経て筋収縮系までたどり，生体システム計測におけるナノテク応用研究の現状の一断面と，その将来性について述べる．

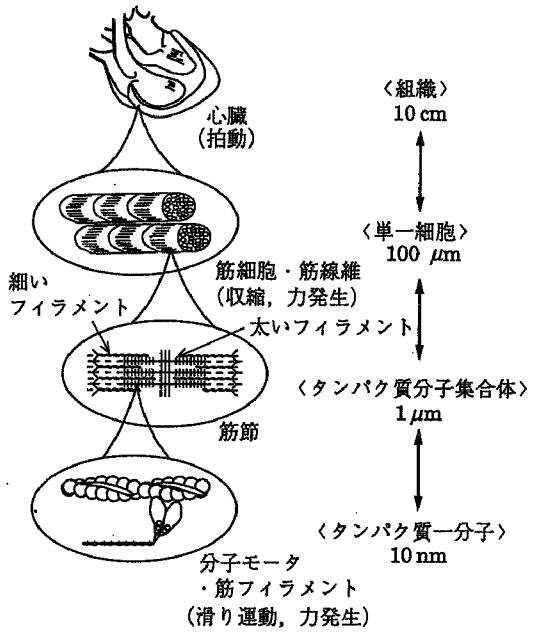

図7・1　筋収縮系の階層構造

[1] タンパク質一分子を測る

ミオシン分子モータの一分子計測については6・1節にも詳しく述べられている．ここではそこで触れられていない点について述べる．

分子モータはエネルギー源であるアデノシン三リン酸（ATP）を加水分解しつつ相手方のタンパク質フィラメントと結合・解離を繰り返し，フィラメントに沿って“滑り運動”をする．これまで多くの研究室で，滑り運動に必要な力の計測が行われてきた．一方我々は，ミオシン分子とアクチンフィラメントとの結合力（正確には結合破断力）を一分子レベルで計測してきた．ガラス表面に固定したS1分子およびHMM分子（myosin subfragment-1およびheavy meromyosin：ミオシン分子を酵素処理して得られる水溶性の部分．ATP加水分解機能やアクチン結合機能といったミオシン分子の生理機能は保持されている．S1は酵素部位とアクチン結合部位を一つもち，HMMは二つもつ）と1本のアクチンフィラメントとの結合を，光ピンセットを使ってむりやり引き離すことで，分

子間の結合破断力を測ることができる[2)3)]．この一分子計測のために，アクチンフィラメントのB端（アクチンフィラメントの構造には方向性があり，滑り運動する先端部をP端，後端をB端と呼ぶ）に直径1 μmのポリスチレンビーズを結合し，そのビーズを光ピンセットで捕捉して操作・計測する．ビーズをアクチンフィラメントのB端に結合するために，B端に選択的に結合するタンパク質ゲルゾリンを，あらかじめビーズ表面に固定しておく．このビーズとアクチンフィラメント（あらかじめファロイジンと呼ばれるキノコ毒に蛍光色素を結合した蛍光性ファロイジンを結合することによって，フィラメント構造を安定化したうえで，フィラメントを蛍光性にしておく．そうすることによって，蛍光顕微鏡下で1本のフィラメントを安定にイメージングすることができる）を溶液中で混合すると，ある頻度でB端にビーズを結合したアクチンフィラメントを調製することができる．

こうして調製したビーズを光ピンセットで捕捉し，捕捉中心を移動することによってフィラメントとミオシン分子との間に負荷を加えることができる．そこで破断力分布のヒストグラムをつくってみると，S1は一つの山，HMMは二つの山からなっていた．山のピークは平均の破断力を表しているが，S1の場合は約7 pN，HMMの場合は約7 pNと約15 pNで，前者は単頭結合，後者は双頭結合に対応することがわかった．

次に，アクチンとミオシンの硬直結合（ATP非存在下の結合）の結合寿命（平均約1 000 s）に対する負荷の影響を調べた．その結果，結合寿命τの負荷（F）依存性として，$\tau(F) = \tau(0) \times \exp(-Fd/(k_BT))$という実験式を得た．ここで，$\tau(0)$は無負荷での結合寿命（1 000 s），$d$は分子間相互作用を特徴づける特性距離，$k_B$はボルツマン定数，$T$は絶対温度である．タンパク質間の結合は，外から無理に力を加えなくても，ある時間待つと自然に“破断”する．ということは，結合破断力はその分子間結合に固有の量ではない，ということである．結合破断力は負荷上昇速度に大きく依存する量である．ゆっくりと負荷を上げていくと，いくらでも小さな力で破断が生じる．逆に，急激に負荷を上昇すると破断力はいくらでも大きくなる．我々が見積もった，アクチン・ミオシン硬直結合の破断力は，あくまでも負荷上昇速度が光ピンセットの捕捉力と捕捉中心の移動速度（10 pN/s前後）という，限られた条件のもとで得られた値である．光ピンセットのダイナミックレンジは狭い．その点原子間力顕微鏡（AFM）は非常に広い範囲にわたって負荷上昇速度を変えることができる．事実，6桁という広い範囲にわたる負荷上昇速度でアビジン・ビオチン結合の破断が計測され，我々が得た実験式と同じ形式のものが得られている[4)]．

タンパク質の機能は温度に大きく依存する．我々は微小領域の温度を短時間に数十度上げ下げすることのできる簡便な手法を開発した[5)]．直径0.1～1.0 μmのアルミニウムなどの金属粒子がかたまってできた数 μmほどの金属塊を，波長1 μmの赤外レーザで照射し，直径約10～20 μmの範囲で10 ms以内に1～2 ℃/μmの温度勾配をつくることができる．いったん60 ℃以上まで上がった温度が，レーザ光を遮断することで10 ms以内にもとの温度に下がる．そのため，高温にさらされると変性してしまうタンパク質（ミオシンやキネシンといった分子モータ）であっても，十分短い時間スケール（1 s以下）では変性せず，それまで測定不可能であった高温において，滑り運動速度や発生張力などの分子モータの機能が活性化されることがわかった．

[2] タンパク質フィラメントを測る

筋肉を構成する主要なタンパク質であるアクチンとミオシンは，筋肉中では重合してフィラメントを形成し，秩序だった格子構造の中で機能している．それぞれのフィラメントには，構造タンパク質や調節タンパク質が結合し，機能

の効率化に寄与し，機能の調節を司っている．ここでは，直径数nm，長さ数μmのアクチンフィラメント1本の物性計測，重合・脱重合ダイナミクスの直視，滑り運動に伴う回転運動の直視について述べる．

(a) アクチンフィラメントの物性（硬さ，ねじれ）計測　ガラスを熱して引き伸ばしてつくった2本の微小ガラス針に，蛍光顕微鏡下で，蛍光性ファロイジンをラベルした1本のアクチンフィラメントの両端を結合する．一方の針の変位をピエゾ素子によりサブnmサイズでコントロールしながら，同時に針のたわみを四分割フォトダイオードでナノメートル計測するという手法である．アクチン結合タンパク質を加えることで筋肉中のフィラメント（細いフィラメント）に近いものを顕微鏡下で再構築することもできる．この方法により，細いフィラメントの粘弾性が計測され，粘性はmsの時間幅内では無視できるほど小さく，収縮中での筋線維のコンプライアンス（弾性率の逆数）の約50％は細いフィラメントに起因することが示唆された[6]．

太いほうのガラス微小針をアクチンフィラメントが付着した後に回転することによって，アクチンフィラメントを長軸の周りにねじることができる．その結果，回転の向きによらず，ねじれを生じたフィラメントはより弱い力（90°ねじれると約半分になる）で引きちぎられることがわかった[7]．アクチンフィラメントのねじれの硬さを測ることもできる．フィラメントの一端をガラス面に固定し，他端に直径2μmのポリスチレンビーズを結合して，そのビーズを光ピンセットでz軸方向に引っ張ることによって，ビーズの表面に吸着した直径0.01μmの小さな蛍光ビーズの動きを観察する．この小ビーズの動きはフィラメントの長軸周りの回転運動を反映しているので，その動きやすさからフィラメントのねじれの硬さを見積もることができる[7]．一方，ガラス面に固定した直径0.88μmの二つのビーズにまたがるように結合したアクチンフィラメントの真中付近に，ビーズが2個くっついたダブルビーズを付着し，明視野像でダブルビーズの回転を観察する．この方法により，単一アクチンフィラメントのねじれの硬さを直接計測することができた[8]．この二つの方法で得られたねじれの硬さは互いに似た値であった．

(b) アクチンフィラメントの重合・脱重合の直視　蛍光ラベルしたアクチンフィラメント一本一本を詳細に観察することによって，重合・脱重合に伴う長さ変化を直接計測することもできる[9)10)]．数十分という長時間にわたって同じフィラメントを観察し続けるための工夫が必要だが，①ガラス表面にフィラメントの一部を固定する方法[9]，②高分子メチルセルロースを加えることでフィラメントの横方向のブラウン運動を抑える方法[10]，このいずれかの方法が用いられた．こうして，フィラメントの両端において，蛍光ラベルアクチンが次々と結合解離を繰り返す様が見えてきた（空間分解能は0.2μm程度）．溶液中の遊離アクチン分子の濃度が高いので，通常の蛍光照明法では背景の蛍光が強すぎて1本のフィラメントを鮮明にイメージングすることができない．そのため，エバネッセント波を用いた全反射蛍光観察法（TIRFM：Total Internal Reflection Fluorescence Microscopy）を用いた．その結果，単一アクチンフィラメントの長さ揺らぎを定常状態において直接計測することができた．しかも，定常状態ではB端で重合しP端で脱重合することによってフィラメントの長さがほぼ一定に保たれる，“トレッドミル機構”が一分子レベルで存在することを証明することができた[10]．

(c) 滑り運動中のアクチンフィラメントの回転運動　さらに，ガラス表面に固定されたミオシン分子モータ上を滑り運動する“*in vitro* 滑り運動系”を用いて，アクチンフィラメントの回転運動を観察したり[11]，回転の速度を計測する[12]こともできる．まず，滑り運動するアクチンフィラメントの先端部をガラス表面に固

定し，後端部分がミオシン分子と相互作用して滑り運動するような人工系を工夫したところ，フィラメントが左巻きの超らせんを形成することが観察された．このことから，ミオシン分子の滑り運動力成分には，右ねじトルク成分が含まれていることが示された[11]．

次に，アクチンフィラメントの回転運動を直接観察するために，蛍光偏光の一分子イメージングが行われた[12]．5-イオドアセトアミドテトラメチルローダミンという蛍光色素をラベルしたアクチンがごく少量混ざったアクチンフィラメントをファロイジンで安定化させる．アクチン分子に結合したこの色素はアクチンフィラメントの長軸に対して約45°の角度に偏光している．そこで，互いに垂直な偏光フィルタを通してこのフィラメントの横偏光画像と縦偏光画像を別々にイメージングする．もし滑り運動に伴ってフィラメントが長軸周りの回転運動をしているのであれば，蛍光色素の横偏光画像と縦偏光画像とが交互に現れるはずである．実際この現象が捉えられ，アクチンフィラメントがHMM上を滑り運動するときには，1 μm進むごとに1回転することが明らかになった．

[3] 筋収縮系内での一分子計測と今後の展望

筋線維を構成するある特定のタンパク質（ポリペプチド）だけを選択的に除去することや，除去した後で精製タンパク質（ポリペプチド）を加えることによって再構築することが可能である．筋収縮系では，① トロポニンCやミオシン軽鎖[13]といった小さなタンパク質（ポリペプチド）の解離と再構成については，溶液条件を生体内のものから極端に変えることで，タンパク質間の結合力を弱めて解離させる方法や，② アクチンフィラメントにおけるゲルゾリンのように，特定のフィラメントの脱重合因子を解体のための分子道具として用いる方法がある[14]．こうして，特定のタンパク質を取り除いた後でアミノ酸置換や，化学修飾した同じタンパク質を加えると，① の場合には，生理的な溶液条件のもとでのタンパク質のもつ自己集合能によって，そのタンパク質が本来結合すべき場所に再結合することや，② の場合には，アクチン重合の特徴（核形成，成長など）をうまく利用することによって，再構成が実現されている．このような手法を用いれば，分子集合体のみならず，細胞レベルのシステムであっても，その中での一分子の振舞いを観察・計測することができる．

最後に，筋収縮系において一分子レベルと細胞レベルとの間に位置する，分子集合体レベルの実験系について簡単に述べたい．筋節は，A帯と呼ばれる太いフィラメントの束と，その一端をZ線に結合した細いフィラメント（アクチンフィラメント＋制御タンパク質）の束が，互いに入り組んだ格子構造体である．筋節にゲルゾリンを作用して細いフィラメントを選択的に解体除去すると，A帯がむき出しになる．そこに上で述べた，ビーズを後端に結合した1本のアクチンフィラメントの先端部を光ピンセットの操作によって近づけると，アクチンフィラメントはA帯に引き込まれる．この実験系こそ，筋フィラメントの格子構造を保持した最小の筋収縮構造であり，我々はこれをnanomuscleと呼んでいる．ミオシン分子モータが分散した*in vitro*滑り運動系は，分子の向きがランダムであること，二次元に展開されていること，そのために生理的なイオン環境下での実験ができないことなどの点で，生体系とは多くの点でかけ離れている．Nanomuscleは多分子系の特徴を保持しつつしかも一分子計測ができるという点で，今後の研究の発展が期待される実験系である[15]．

ここで述べた手法は，どれも筋収縮システムを構築する手法の一つである．このような「システムの再構築」を発展させることで，再構成システム中での一分子計測が可能となるだろう．筋肉研究は筋線維，筋原線維を使った研究から始まり階層構造を下ってタンパク質一分子を個々に操作し計測するところまできたが，次は各階層を結びつける作業が必要であり，その

ための準備が整いつつある．

7-2 二次元システム・生体膜

1972年に提案されたSingerとNicolsonの生体膜についての「流動モザイクモデル」の特徴は，脂質二分子膜中に浮かぶ貫通形膜タンパク質がモザイク様に混在していること，しかも膜は，流動性のある二次元液体のような構造をもち，膜中の分子は膜内を熱拡散運動をしているということであった．その後の研究で細胞膜はのっぺらぼうで一様な分布をとっているのではなく，細胞膜の重要な機能の多くは膜中のある決まったドメインごとに役割が分担されていることが明らかとなってきた．例えば，細胞間接着のためのカドヘリン集合ドメイン，細胞・基質間接着のための接着斑ドメイン，受容体の細胞内への取込みのためのクラスリン被覆ピットなどの膜ドメインが知られている．しかしながら，個々の構造の形成機構を超えて，ドメインを形成させる駆動力は何か，ドメインは安定で一定の構造を取り続けるのか，あるいは形成消滅を繰り返しているのか，その場合どのくらいの寿命をもつのかなど膜ドメインの組織化機構の共通な，基本的なルールはどうなっているのかはほとんど不明であった．最近，これらに関する研究が進展しはじめた．これはnmレベルで起こる事象を調べる方法の進展に負うところが大きい．特に一分子レベルで運動や分布・反応を調べる方法によって細胞膜中のドメイン構造の動的性質が明らかになりはじめた．生化学的手法や多分子の測定ではわからなかったnmオーダレベルでの膜構造の詳細が明らかとなった．

[1] 一分子法での細胞膜構成成分の運動の追跡

個々の分子を観察することにより，多分子の観察では平均化されてわからないような全体の中のほんの一部の分子の変化を見つけたり，その変化した瞬間をとらえることが可能となる．一分子法には主に一粒子追跡法（SPT：Single Particle Tracking）と一蛍光分子ビデオイメージング（SFVI：Single Fluorophore Video Imaging）がある（図7·2）．SPTでは，細胞膜上の膜タンパク質や脂質分子を抗体のFab断片で被覆した直径40 nmの金粒子で標識し，ビデオエンハンス顕微鏡を用いてその運動を観察する[1)2)]．SPTでの観察の利点は一つの粒子を数十分にわたり観察可能なこと，空間精度が数nmと高いこと，時間分解能を25 μs/フレームにまで上げて観察できることなどである．また，レーザを用いてプローブを捕捉し（光ピンセット），引っ張ることもできる[3)]．しかしながら，SPTでの一分子運動を観察するのは実験条件設定が難しい．なぜなら，金粒子に結合したタンパク質のほとんどは変性するので，結合活性をもつプローブをつくることが難しく，また，特定分子を認識するプローブができたとしても，立体障害やクロスリンクの問題を解決する必要がある．一方，SFVIはレーザの全反射照明によるエバネッセント照明を利用して背景光をできる限り少なくして蛍光一分子を可視化する方法である．細胞中の目的の分子を蛍光で標識したり，さらに最近では蛍光を発するタンパク質である緑色蛍光タンパク質（GFP：Green Fluorescence Protein）の生細胞中での一分子観察が可能となり[4)]，生細胞中でのSFVIが非常に身近になった．SFVIの場合，クロスリンクの心配はなく，さまざまな細胞膜中のタンパク質を比較的容易に確実に一分子を

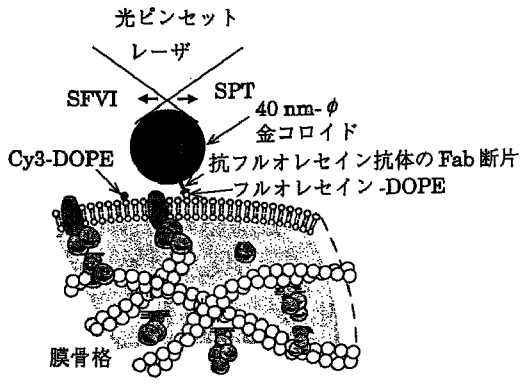

図7·2 細胞膜上の膜分子の運動を追跡するための一分子法

引用・参考文献

7・1節

1) 石渡信一 編：生体分子モーターの仕組み－シリーズ・ニューバイオフィジックス４－，共立出版 (1997)
2) T. Nishizaka, H. Miyata, H. Yoshikawa, S. Ishiwata and K. Kinosita, Jr. : Unbinding force of a single motor molecule of muscle measured using optical tweezers, Nature, Vol. 377, No. 251-254 (1995)
3) T. Nishizaka, R. Seo, H. Tadakuma, K. Kinosita, Jr. and S. Ishiwata : Characterization of single actomyosin rigor bonds : Load dependence of lifetime and mechanical properties, Biophys. J., Vol. 79, pp. 962-974 (2000)
4) R. Merkel, P. Nassoy, A. Leung, K. Ritchie and E. Evans : Energy landscapes of receptor-ligand bonds explored with dynamic force spectroscopy, Nature, Vol. 397, pp. 50-53 (1999)
5) H. Kato, T. Nishizaka, T. Iga, K. Kinosita, Jr. and S. Ishiwata : Imaging of thermal activation of actomyosin motors, Proc. Natl. Acad. Sci. USA, Vol. 96, pp. 9602-9606 (1999)
6) H. Kojima, A. Ishijima and T. Yanagida : Direct measurement of stiffness of single actin filaments with and without tropomyosin by *in vitro* nanomanipulation, Proc. Natl. Acad. Sci. USA, Vol. 91, pp. 12962-12966 (1994)
7) Y. Tsuda, H. Yasutake, A. Ishijima and T. Yanagida : Torsional rigidity of single actin filaments and actin-actin bond breaking force under torsion measured directly by *in vitro* micromanipulation, Proc. Natl. Acad. Sci. USA, Vol. 93, pp. 12937-12942 (1996)
8) R. Yasuda, H. Miyata and K. Kinosita Jr. : Direct measurement of the torsional rigidity of single actin filaments, J. Mol. Biol., Vol. 263, pp. 227-236 (1996)
9) S. Ishiwata, J. Tadashige, I. Masui, T. Nishizaka and K. Kinosita, Jr. : Microscopic analysis of polymerization and fragmentation of individual actin filaments, Molecular Interactions of Actin : Actin Structure and Actin-binding Proteins, C.G. dos Remedios and D.D. Thomas, eds., pp. 79-94, Springer Verlag, Heidelberg (2001)
10) I. Fujiwara, S. Takahashi, H. Tadakuma, T. Funatsu and S. Ishiwata : Microscopic analysis of polymerization dynamics with individual actin filaments, Nature Cell Biol., Vol. 4, pp. 666-673 (2002)
11) T. Nishizaka, T. Yagi, Y. Tanaka and S. Ishiwata : Right-handed rotation of ac actin filament in an in vitro motile system, Nature, Vol. 361, pp. 269-271 (1993)
12) I. Sase, H. Miyata, S. Ishiwata and K. Kinosita, Jr. : Axial rotation of sliding actin filaments revealed by single-fluorophore imaging, Proc. Natl. Acad. Sci. USA, Vol. 94, pp. 5646-5650 (1997)
13) S.C. Hopkins, C. Sabido-David, U.A. van der Heide, R.E. Ferguson, B.D. Brandmeier, R.E. Dale, J. Kendrick-Jones, J.E. Corrie, D.R. Trentham, M. Irving and Y.E. Goldman : Orientation changes of the myosin light chain domain during filament sliding in active and rigor muscle, J. Mol. Biol., Vol. 318, pp. 1275-1291 (2002)
14) H. Fujita, K. Yasuda, S. Niitsu, T. Funatsu and S. Ishiwata : Structural and functional reconstitution of thin filaments in the contractile apparatus of cardiac muscle, Biophys. J., Vol. 71, pp. 2307-2318 (1996)
15) M. Suzuki, H. Fujita and S. Ishiwata : New aspects of muscle contraction from the A-band motility assay system, Biophys. J., Vol. 82, p. 362a, Abstract (2002)

7・2節

1) A. Kusumi and Y. Sako : Cell surface organization by the membrane skeleton, Curr. Opin. Cell Biol., Vol. 8, pp. 566-574 (1996)
2) M. J. Saxton and K. Jacobson : Single-particle tracking : Applications to membrane dynamics, Annu. Rev. Biophys. Biomol. Struct., Vol. 26, pp. 373-399 (1997)
3) M. Edidin, S. C. Kuo and M. P. Sheetz : Lateral movements of membrane glycoproteins restricted by dynamic cytoplasmic barriers, Science, Vol. 254, pp. 1379-1382 (1991)
4) R. Iino, I. Koyama and A. Kusumi : Single molecule imaging of green fluorescent proteins in living cells : E-cadherin forms oligomers on the free cell surface, Biophys. J., Vol. 80, pp. 2667-2677 (2001)
5) T. Fujiwara, K. Ritchie, H. Murakoshi and A. Kusumi : Phospholipids undergo hop diffusion in compartmentalized cell membrane, J. Cell Biol., Vol. 157, pp. 1071-1081 (2002)
6) K. Simons and E. Ikonen : Functional rafts in cell membrane, Nature, Vol. 387, pp. 569-572 (1997)
7) K. Suzuki, F. Sanematsu, T. Fujiwara, M. Edidin and A. Kusumi : Rapid, continual formation/dispersion of raft-like domains in the resting cell membrane, Mol. Biol. Cell., Vol. 12, p. 470a (2001)
8) K. Suzuki, F. Sanematsu, T. Fujiwara, M. Edidin and A. Kusumi : Stimulation-induced formation of temporal but stabilized rafts, Biophys. J., Vol. 82, p. 348a (2002)

7・3節

1) Y. Sako, S. Minoguchi and T. Yanagida : Single molecule imaging of EGFR signal transduction on the living cell surface, Nature Cell Biol., Vol. 2, pp. 168-172 (2000)
2) 多田隈尚史：ビデオレート共焦点顕微鏡による１分子蛍光イメージング，生物物理，Vol. 241, pp. 137-139 (2002)
3) G. J. Schütz, K. Gerald, V. Ph. Pastuchenko and H. Schindler : Properties of lipid microdomains in a muscle cell membrane visualized by single molecule microscopy, EMBO J., Vol. 19, pp. 892-

BIO-NANOMUSCLE PROJECT: CONTRACTILE PROPERTIES OF SINGLE ACTIN FILAMENTS IN AN A-BAND MOTILITY ASSAY SYSTEM

Madoka Suzuki, Hideaki Fujita, and Shin'ichi Ishiwata*

1. ABSTRACT

We have developed a new microscopic technique to measure the force generated on a single actin filament (FA) in the A-band in which the intact lattice structure composed of myosin thick filaments is maintained; we call this newly developed system "*Bio-nanomuscle* (or an A-band motility assay system)". The A-bands were prepared by selective removal of thin filaments from rabbit skeletal glycerinated myofibrils under optical microscope with the use of gelsolin (a severing and barbed (B)-end capping protein of FA) that was prepared from bovine serum. A polystyrene bead of 1 μm in diameter attached to the B-end of FA (through a gelsolin molecule attached to the surface of the bead) was trapped and manipulated with optical tweezers. The displacement of the bead up to 200 nm (corresponding to the force of ~ 40 pN) was determined by phase-contrast image analysis. At the initial stage of this study, the overlapping length of an FA with the A-band was determined from the fluorescence image of FA labeled with rhodamine-phalloidin (Rh-Ph) and the phase-contrast image, but we later improved the method of determination by moving the sample stage stepwise using the piezo actuator. The average force per overlap was subsequently estimated and the histogram was fitted with two Gaussian distributions. Each peak is supposed to correspond to the force developed by FA interacting outside or inside the A-band, and the peak value of the latter was estimated to be 140 pN/μm. From this value, the average force developed per each cross-bridge (CB; a two-headed myosin molecule) was determined to be 1.3 pN.

* Department of Physics, School of Science and Engineering, Waseda University, 3-4-1 Okubo, Shinjuku-ku, Tokyo 169-8555, Japan
ishiwata@mn.waseda.ac.jp

Molecular and Cellular Aspects of Muscle Contraction
Edited by H. Sugi, Kluwer Academic/Plenum Publishers, 2003

2. INTRODUCTION

The contractile system of muscle is composed of two kinds of myofilaments: a thick filament mainly composed of myosin and a thin filament composed of actin and associated regulatory proteins, including tropomyosin and troponin. These two kinds of filaments are hexagonally packed, and slide past one another when muscle contracts[1, 2]. Muscle fibers[3, 4] or myofibrils[5-7] have been an appropriate preparation for studying the properties of the interaction between FA and myosin, and they have shown many insights into the mechanism and physiological roles of both cardiac and skeletal muscle contraction. Over the last decade, an *in vitro* motility assay has been widely used for studying the sliding movement and force generation on a single FA to explain the molecular mechanism of muscle contraction. However, these studies have been performed only at low ionic strength (usually lower than 50 mM) because myosin molecules easily detach from FA at higher ionic strength (even at a physiological one). Furthermore, myosin molecules adhere to the glass surface two-dimensionally in random fashion, and some of the molecules are denatured.

Our aim is to establish a new experimental system that bridges the gap between the muscle contractile system and the *in vitro* motility assay system. We expect that the bio-nanomuscle (A-band motility assay) system reported here may reveal new aspects of the mechanism of muscle contraction and its regulation.

3. MATERIALS AND METHODS

3.1. Myofibrils and Proteins

Myofibrils were prepared by homogenizing rabbit psoas muscle fibers glycerinated in 50% (v/v) glycerol containing 0.5 mM $NaHCO_3$, 5 mM EGTA, and 1 mM leupeptin for more than 3 weeks at –20 °C as described previously[8]. Glycerol in the suspension of myofibrils was removed by centrifugation at 3000 × g in a rigor solution (60 mM KCl, 5 mM $MgCl_2$, 10 mM 3-(N-morpholino)propanesulfonic acid (MOPS) (pH 7.0) and 1 mM EGTA) at 4 °C.

Actin was prepared from rabbit skeletal white muscle according to a standard procedure[9]. Bovine plasma gelsolin was prepared according to the method of Kurokawa et al.[10]; during this preparation, the incubation time of gelsolin in Ca^{2+}-free buffer was kept as short as possible as the severing activity was lowered by incubation in the Ca^{2+}-free buffer.

3.2. Preparation of an A-band Motility Assay System from the Myofibrils on the Coverslip

About 100 µl of the suspension of myofibrils in the rigor solution was placed on one side of the coverslip and the rigor solution was exchanged with a gelsolin solution A (60 mM KCl, 4 mM $MgCl_2$, 20 mM MOPS (pH7.0), 2 mM EGTA, 1.9 mM $CaCl_2$, 1.5 mM NaN_3, 2 mM leupeptin and 0.3 mg/ml gelsolin) with a pipette, taking care not to suck up

myofibrils (gelsolin treatment A). After a 30-min gelsolin treatment, the gelsolin soluion A was exchanged to gelsolin solution B (gelsolin solution A plus 20 mM BDM and 1 mM ATP) with a pipette (gelsolin treatment B). After a 20-min gelsolin treatment B, the myofibrils were washed first with relaxing solution (120 mM KCl, 4 mM $MgCl_2$, 20 mM MOPS (pH7.0), 4 mM EGTA, 4 mM ATP and 10 mM dithiothreitol (DTT)), then with the rigor solution containing 10mM DTT. The suspension of myofibrils after gelsolin treatment A and B was then moved to the opposite side of the coverslip using a pipette, where gelsolin was not present on the glass surface. Myofibrils without thin filaments were treated with 2 volumes of the rigor solution containing 10 mM DTT and 0.5% (v/v) TritonX-100 and washed several times with the rigor solution containing 10 mM DTT to remove TritonX-100. All procedures were carried out at 0 °C.

After the flow cell was washed with an assay buffer (AB) (100 mM KCl, 2 mM Mg^{2+}, 2 mM MgATP, 25 mM Imidazole-HCl (pH7.4), 1 mM EGTA, 0.5 mg/ml bovine serum albumin, 10 mM DTT, 4.5 mg/ml D(+)-Glucose, 50 units/ml Glucose Oxidase, 50 units/ml Catalase, 15 mM Creatine Phosphate and 150 units/ml Creatine Phosphokinase), bead-tailed FAs in AB-buffer were applied and both edges of the flow cell were sealed with non-fluorescent nail polish. Bead-tailed FAs were prepared as previously reported[11, 12]. A-bands shorter than 1.6 μm in length or that had ends which looked dark in a phase-contrast image were not used for our assays as they were considered to have contracted or partly dissociated during gelsolin treatment. All the experiments were done at 27-29 °C.

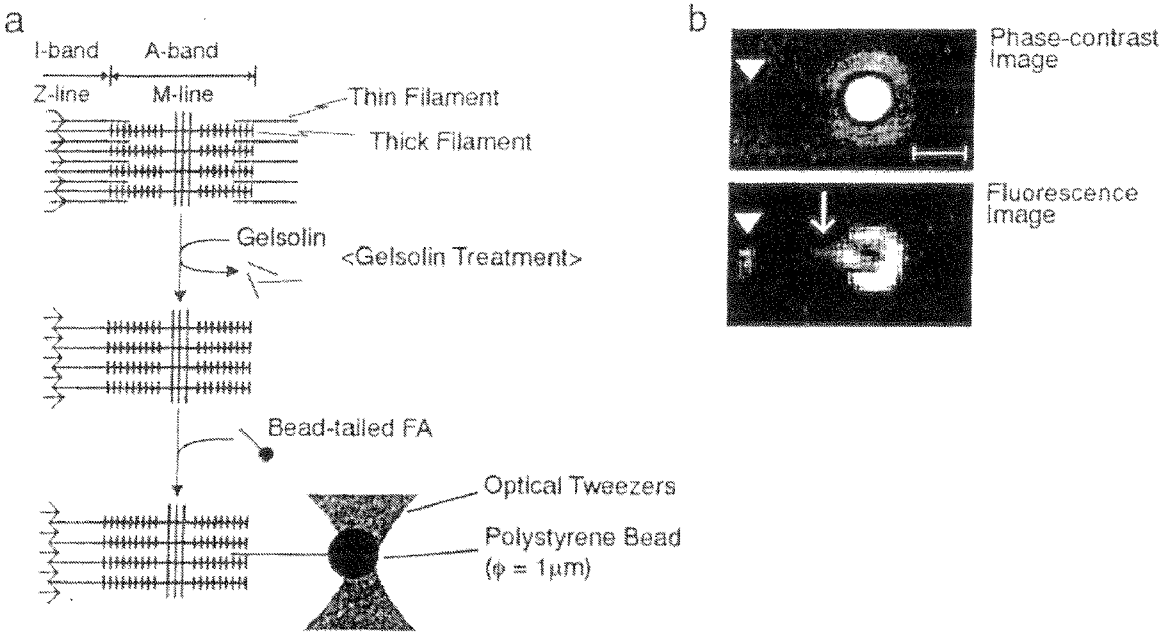

Figure1. a, Schematic diagram illustrating the experimental procedure for preparing the A-band motility assay system in a myofibril. b, Phase-contrast image and fluorescence image during tension generation. Both images were integrated for one second (30 frames) while FA (indicated by an arrow) was interacting with the A-band. Arrowheads indicate the Z-line. Scale bar, 1 μm.

4. RESULTS AND DISCUSSION

Figure 1 illustrates the experimental procedure for preparing A-band motility assay system from skeletal myofibrils. Myofibrils were treated with gelsolin, and the thin filaments were selectively removed from the filament lattice. Since myofibrils are usually cut at the I-band by homogenization, some of them had no Z-lines at their ends, although the others did. The Z-lines in myofibrils were observed in phase-contrast microscope and even in fluorescence microscope after the bead-tailed FAs were applied because the Z-lines remaining were easily labeled with free Rh-Ph, and thus were rendered fluorescent. When the bead-tailed FA was attached to the Z-line remaining at the end of the A-band, the FA was stuck to the Z-line strongly without generating tension, so that it could not be detached by pulling with optical tweezers. There were some myofibrils that did not have the Z-lines at their ends but instead had dark ends of high density that were distinguishable in a phase-contrast image. It was difficult for FA to attach to the ends of these A-bands. We consider this dense edge is attributable to connectin/titin not being removed successfully by homogenization. Some of the A-bands were shorter than 1.6 μm and the both ends looked dense under the phase-contrast microscope. Also, some of the A-bands were spreading thin. All such "unfavorable" myofibrils were not used for the following motility assay.

The bead-tailed FA was kept near the A-band until the FA began to interact with it. Before the FA began to interact with the A-band, the bead stayed at the trap center and showed rotational Brownian motion. As soon as the FA was attached to the edge of the A-band, tension was generated continuously some of the time, and transiently at other times. At the beginning of this study, the length of an overlap of FA with the A-band was determined by comparing the fluorescence image of FA with phase-contrast images of the bead and the edge of the A-band. As it was often difficult, however, to determine the position of the edge of the A-band (even when the edge can be identified, the resolution is low), we altered the method as follows: after the steady tension was obtained, that is, after the tension generated by CBs in the A-band and the load imposed by the optical tweezers were balanced, the sample stage was moved stepwise by moving a piezo actuator. The tension and the load were balanced again at a new position of higher or lower level of tension depending on the direction of the movement of the sample stage. The degree of the change in overlap was calculated from the displacement of the sample stage and that of the bead due to the movement of the stage (Fig. 2). The difference in tension before and after the movement of the stage was calculated from the displacement of the bead and the stiffness of the optical tweezers (0.12 pN/nm in Fig. 2). Tension per unit length overlap (pN/μm) thus estimated from the microscopic image analysis and from the displacement of the stage was summarized as a histogram in Fig. 3.

The histogram in Fig. 3 was fitted by two Gaussian distributions with peaks at 74 pN/μm and 140 pN/μm. We assume that these two values correspond to two situations for FA, that is, FA interacting outside or inside the A-band, respectively. It is thought that the FA interacting outside the A-band could interact with a smaller number of thick filaments than those inside the A-band because the former is thought to interact with the thick filaments two dimensionally arranged, whereas the latter is considered to be located at the trigonal position of the native thick filament lattice three dimensionally arranged. Thus, higher tension is expected to be generated inside the A-band than outside.

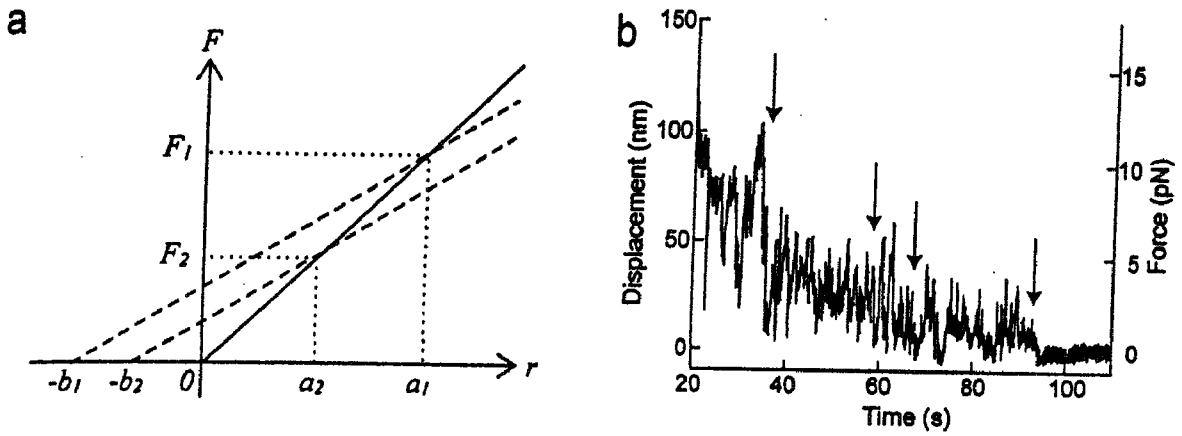

Figure 2. Method for estimating the force generated per unit length of overlap by stepwise moving the sample stage. a, Relationship between the load applied by the optical tweezers (solid line) and the force generated by the A-band (broken line) vs. displacement from the trap center (at the origin of the abscissa), r. At first, the two forces are balanced at $F = F_1 = k \cdot a_1$, where k is the stiffness of the optical tweezers and a_1 the average position of the bead. When the sample stage, or the A-band, is moved away from the trap center by $\Delta b = -b_2 - (-b_1) = b_1 - b_2$, the bead position must be shifted from a_1 to a_2 and the generated tension is decreased from F_1 to $F_2 = k \cdot a_2$. Therefore, the change of the overlap between the thick filaments and the FA, Δr, is $(a_1 - a_2) + \Delta b$. Thus, the tension generated per unit length of overlap can be calculated as $\Delta F/\Delta r = (F_1 - F_2) / \Delta r = k (a_1 - a_2) / \Delta r$. All the variables could be determined from the experiments. b, Time course of the displacement of the trapped bead interacting with the A-band. The stage was moved away from the trap center four times at the instances indicated by arrows. When FA was pulled out from the A-band, the bead went back to the trap center at the time shown by the fourth arrow.

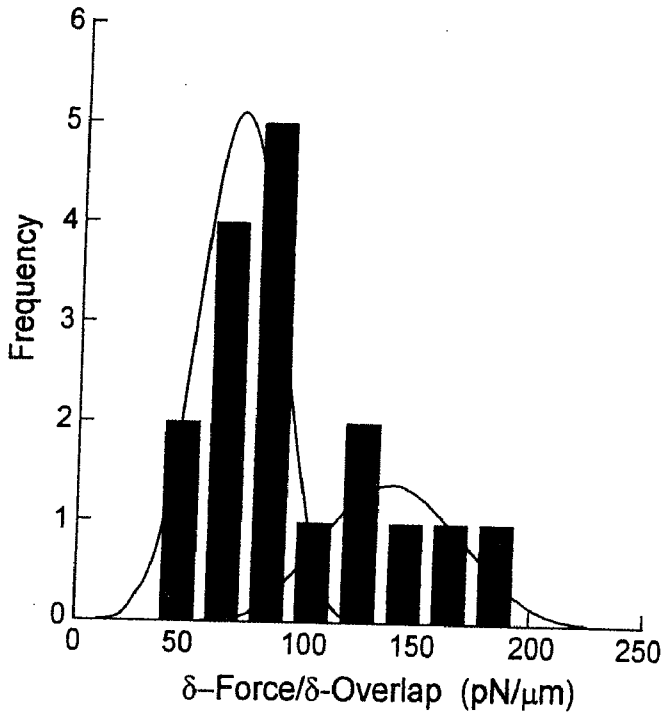

Figure 3. Histogram showing the tension generated on single FA per overlap (normalized to 1 μm) between FA and the A-band. The histogram was fitted by two Gaussian distributions, for which peak values were determined to be 74 and 140 pN/μm, respectively.

Next, we calculated the number of CBs (= myosin molecules) that can interact with a single FA inside the A-band. Since each myosin thick filament (1.6 μm long) consists of 300 myosin molecules, there are 150 CBs in half a sarcomere. As a single FA is surrounded by three thick filaments being located at the corner of the triangular lattice, one sixth (60°/360°) of the three thick filaments have a chance to interact with each FA. Consequently, we estimate that 150×3/6=75 CBs are available to each FA per half a sarcomere, in which the effective length of half an A-band is estimated to be 0.7 μm after the removal of the central bare zone of 0.2 μm. According to this estimation and the average value of the second peak in Fig. 3, we estimate that the average force over the ATPase cycle generated by each CB inside the A-band is 1.3 pN. If we remember that the number of CBs estimated by the way described above is the maximum number of CBs that can interact with each FA, it is safe to say that single CBs can generate a force of more than 1.3 pN.

In our motility assay system, the force is measured on the plane almost parallel to the glass surface, which is different from our previous *in vitro* motility assay system where the bead-tailed FA is positioned upward from the surface by optical tweezers[12-14]. The present system can also control the orientation of myosin molecules. They are arranged parallel to the long axis of a myofibril, so that this is considered to be the most suitable for the generation of force[15]. Ishijima et al.[16] estimated the force generated by myosin molecules oriented in single synthetic myosin rod cofilaments by the noise analysis of the generated force to be 2.1 ± 0.4 pN. The difference between these two values could be explained by the difference in the solvent conditions, especially different ionic strength (higher ionic strength in our experiments). The interaction between myosin and FA is generally weakened when the ionic strength increases. The *in vitro* motility assay has been limited to low ionic strength like 25 mM KCl because myosin molecules easily detach from FA at higher ionic strength unless FAs are suppressed by viscous polymer networks like methylcellulose added to the assay buffer. In our system, on the other hand, a FA is surrounded by the thick filaments and keeps the interaction even under higher ionic strength, e.g., higher than 100 mM KCl. It is also interesting that some FAs with large overlap kept interacting and generating force continuously even outside the A-band under the same conditions, whereas a large part of FAs only generated force transiently. This indicates that the number of myosin molecules interacting could be enough to generate weak but steady force even at 100 mM KCl. The array of thick filaments in our system that cannot be achieved in an *in vitro* assay made this phenomenon possible.

The value of the average force generated by each CB obtained in the present study was a little smaller than what has been obtained from the muscle contractile system. This may be due to us using only pure FAs and not reconstituted thin filaments. The association of regulatory proteins such as tropomyosin and troponin may elevate the tension[17]. In the present study, we examined tension generation under auxotonic condition instead of isometric or isotonic condition. The next step of our bio-nanomuscle project would be to measure tension generated under such physiological conditions. It will also be very interesting to examine the effects of the regulatory proteins under the well defined conditions. Using this approach, we aim to bridge the gap between the experimental systems and conditions mentioned above, and elucidate the mechanism of molecular motors in a protein assembly.

5. ACKNOWLEDGMENTS

We are grateful to Mark Chee of Duke University for his critical reading of the manuscript. This work was partly supported by Grants-in-Aid for Specially Promoted Research and for the Bio-venture Project from the Ministry of Education, Sports, Culture, Science and Technology of Japan.

6. REFERENCES

1. Huxley, A.F. & Niedergerke, R. *Nature* **173**, 971-973 (1954)
2. Huxley, H.E. & Hanson, J. *Nature* **173**, 973-976 (1954)
3. Goldman, Y.E. & Brenner, B. *Annu. Rev. Physiol.* **49**, 629-636 (1987)
4. Cooke, R. *CRC Rev. Biochem.* **21**, 53-118 (1986)
5. Anazawa T., Yasuda, K. & Ishiwata, S. *Biophys. J.* **61**, 1099-1108 (1992)
6. Yasuda, K., Shindo, Y. & Ishiwata, S. *Biophys. J.* **70**, 1823-1829 (1996)
7. Friedman, A.L. & Goldman, Y.E. *Biophys. J.* **71**, 2774-2785 (1996)
8. Ishiwata, S. & Funatsu, T. *J. Cell Biol.* **100**, 282-291 (1985)
9. Kondo, H. & Ishiwata, S. *J. Biochem.* **79**, 159-171 (1976)
10. Kurokawa, H., Fujii, W., Ohmi, K., Sakurai, T. & Nonomura, Y. *Biochem. Biophys. Res. Commun.* **168**, 451-457 (1990)
11. Suzuki, N., Miyata, H., Ishiwata, S. & Kinosita, K. Jr. *Biophys. J.* **70**, 401-408 (1996)
12. Nishizaka, T., Seo, R., Tadakuma, H., Kinosita, K. Jr. & Ishiwata, S. *Biophys. J.* **79**, 962-974 (2000)
13. Miyata, H., Hakozaki, H., Yoshikawa, H., Suzuki, N., Kinosita, K. Jr., Nishizaka, T. & Ishiwata, S. *J. Biochem.* **115**, 644-647 (1994)
14. Nishizaka, T., Miyata, H., Yoshikawa, H., Ishiwata, S. & Kinosita, K. Jr. *Nature* **377**, 251-254 (1995)
15. Tanaka, H., Ishijima, A., Honda, M., Saito, K. & Yanagida, T. *Biophys. J.* **75**, 1886-1894 (1998)
16. Ishijima, A., Kojima, H., Higuchi, H., Harada, Y., Funatsu, T. & Yanagida, T. *Biophys. J.* **70**, 383-400 (1996)
17. Fujita, H., Sasaki, D., Ishiwata, S. & Kawai, M. *Biophys. J.* **82**, 915-928 (2002)

DISCUSSION

Gonzalez-Serratos: As the number of cross-bridges attached to actin depends on the free Ca^{2+} concentration in muscle, what is the free Ca^{2+} concentration at which all the cross-bridges are attached to actin?

Ishiwata: We have not yet studied the effect of Ca^{2+} because we first focused on the tension generation in the nanomuscle system using pure actin filaments. It would be a next subject in our nanomuscle project.

Ranatunga: I just wondered as to what happens to the titin filaments in the A-band? Titin may interact with actin.

Ishiwata: We do not know about whether or not and how connectin/titin linkages remain at the edge of the A-band. Because the Z-band is removed, it is probably folded at the ends of thick filaments. It appears that the folded connectin/titin does not disturb the tension generation.

Sugi: The motion of an actin filament should be helicoidal when actin filament is made to interact with myosin at the outer edge of the myofibril. How do you think about this?

Ishiwata: The actin filament motion can be helicoidal to some extent even if an actin filament is made to interact inside the A-band.

Sugi: Yes, but the helicoidal motion should be most pronounced at the outer surface of the A-band.

Ishiwata: Well, if the helicoidal motion of an actin filament occurs, I believe that it is due to the torque produced by cross-bridges, so that the helicoidal (rotational) motion of an actin filament must occur equally in both regions.

Huxley: How did you estimate the tension per cross-bridge?

Ishiwata: Assuming that the number of myosin molecules (=cross-bridges) in each thick filament is 300, and that the actin filament is located within the triangular lattice of thick filaments, we estimate that 75 cross-bridges (c.b.) are available for interacting with the actin filament of 0.7μm long, so that the density of cross-bridges along the actin filament is 75c.b./700nm=0.1c.b./nm. Thus, the average tension generated by each cross-bridge is estimated to be (0.2pN/nm)/ (0.1c.b./nm)=2pN/c.b.

4 分子モーター

1．はじめに

生物は10万種類ものタンパク質を持ち，それぞれが限られた空間内で限られた時間に，様々な生体機能を発現している。ここで，「エネルギーを使いながら並進あるいは回転運動をするタンパク質」のことを分子モーターと呼ぶ。筋収縮をつかさどるミオシン分子モーター(図1)や，細胞内物質輸送を担うキネシン分子モーターはその代表であり，細菌の鞭毛の回転を担う分子装置も典型的な分子モーター系である。さらに，細胞小器官ミトコンドリア膜に存在して膜内外のpH差を基にATPを合成し，また逆にATP加水分解によってプロトン輸送を行うF_0F_1ATP合成酵素や，さらにはDNAポリメラーゼ(DNAを複製する酵素)やRNAポリメラーゼ(DNAの遺伝情報をRNAに写し取る働きをする酵素)なども，分子モーターと呼べる。

筋収縮運動や細胞運動などの生体運動は，階層構造の最下層に位置するタンパク質分子モーターによって担われている。モーター部分の大きさは，

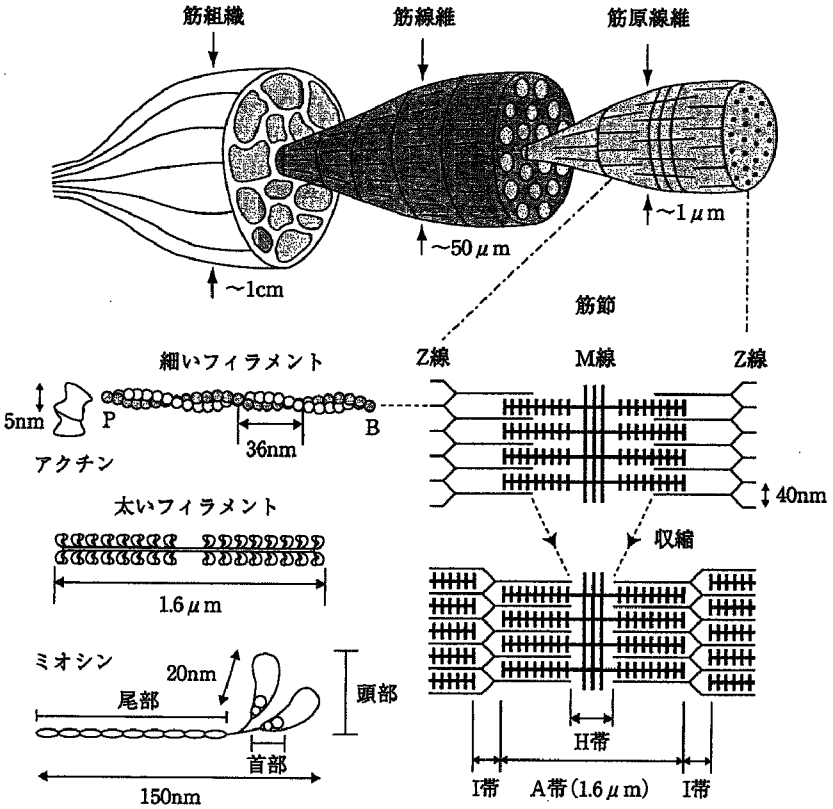

図 1　横紋筋の階層構造

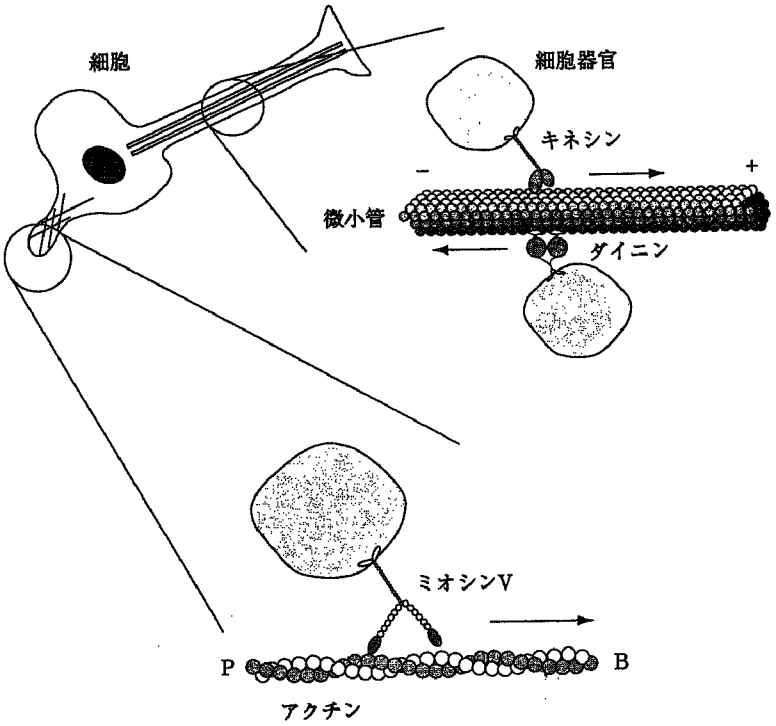

図 2　非筋細胞の物質輸送を担う分子モーター

10 nm (ナノメートル=10^{-9}m) オーダである。このタンパク質は通常 ATP 加水分解酵素であり，ATP の結合・加水分解・解離に伴って構造変化が生じ，外部に仕事をすることができる。タンパク質への ATP や ADP などのヌクレオチドの結合は，ヌクレオチドのブラウン運動による確率的な衝突によって起こり，さらに加水分解や解離も確率的に起きる。このため，分子モーターは確率的に作動するナノマシンである。

この小さな分子モーターの働く世界は，物理的には粘性力とブラウン運動の支配する世界である。タンパク質分子モーターは非常に小さく軽いので，慣性力は無視できる。一方，相対的に溶媒から受ける粘性力は大きい。このため，力が働いていないときの分子モーターの並進・回転運動は非常に早く減衰する。溶媒中での μm〜nm サイズの物体の運動は，質量よりもサイズや形状に関係する物理量が実効的となる。また，タンパク質分子機械は常に溶媒分子のランダムな衝突にさらされ，その結果ブラウン運動が引き起こされる。このような環境下で，分子モーターは高効率なアクチュエータとして生体運動機能を実現している。このことから，分子モーターの働きは，マクロな人工的機械と本質的に異なる世界で実現され，そのしくみも異なることが期待される。

2．分子モーターのしくみ

真核細胞は，生物が生まれてから細胞周期を繰り返して死ぬまでに様々な運動をするが，それらの細胞運動の基盤を担っているのが細胞骨格と呼ばれるアクチンフィラメントと微小管の 2 種類のタンパク質フィラメントである(図 2 参照)。アクチンフィラメントに沿ってモータータンパク質ミオシンが移動することで生まれる運動には，筋収縮，細胞質分裂，白血球やアメーバなどの細胞移動運動，植物細胞の原形質流動などがある。一方，細胞内顆粒の輸送，精子の鞭毛運動，細胞分裂における有糸分裂などは，微小管の上をモータータンパク質であるダイニンやキネシンが移動することによって生まれる。さらに冒頭で述べたように，分子モーターと一口にいってもその種類は多岐にわたる。ここではアクチン系モータータンパク質であるミオシンと，微小管系モータータンパク質

であるキネシンについて話を進めよう。

2.1 アクチン・ミオシン系

アクチンフィラメントに沿って動くモータータンパク質であるミオシンは，1930年代に筋肉から抽出され最初に発見されたモータータンパク質である。その後非筋細胞で様々なミオシンが単離精製されただけでなく，最近では主に遺伝子解析によって次々と見つかっており，現在までに140種類以上のミオシンが，系統発生学的に18のグループに分類されている[1]。ミオシンには，ATP加水分解能とアクチン結合能とを持つ頭部と呼ばれる部分がある。ミオシンタンパク質ファミリーはこの頭部のアミノ酸配列の相同性を基に同定されている。ミオシンファミリーには，単頭のものと双頭のものとがある。尾部はミオシンの種類によってアミノ酸配列，構造，大きさが大きく異なる。またその機能も，重合体形成であったり，ミオシン結合タンパク質との結合であったり，膜小胞との結合であったりと様々であり，各ミオシンの様々な生体機能は尾部の持つこのような多様性によって決まっているといえる。

2.1.1 筋肉ミオシン（ミオシンII）

ミオシン・アクチン間の相互作用について得られている知識の大部分は，骨格筋（手や足のように運動神経の支配で随意に動かすことができる筋肉。両端は腱を介して骨格に付着する）の研究によるものである。骨格筋に存在するミオシンは収縮装置の約50%を占めており，ミオシンタンパク質ファミリーのなかでミオシンII（以下で単にミオシンと呼ぶときはミオシンIIを指す）に分類されている。筋肉中では，ミオシンもアクチンも重合して，それぞれ太いフィラメントと細いフィラメントを形成している。長い棒状に伸びているミオシン尾部は主に静電力によって分子同士を会合させて二極性のフィラメントを形成する役割を担っている。フィラメントから突き出たミオシン頭部はアクチンフィラメントと相互作用してATPを分解しつつ構造変化を行い，力発生する。筋収縮は，こうして2種のフィラメントがその全長を変えずに互いに「滑り運動」するという「滑り機構」によって説明されている（図1参照）。

滑り運動で発生する張力の1分子計測はこの10年来いくつかの研究室で行われてきた[2~4]。一方我々は，ミオシン分子頭部とアクチンフィラメントとの結合破断力を1分子レベルで測定した。ガラス表面上に固定したミオシン分子（正確にはミオシン分子を酵素処理して得られる断片で，活性部位を二つ保持したHMM分子と一つのみのS1分子，それぞれ双頭構造，単頭構造を持つ）と単一アクチンフィラメントとの結合を無理やり引き離すことで，分子間の結合破断力を図ることができる〔図3(a)参照〕。この1分子計測のために，近赤外のレーザ光を開口数の大きな対物レンズで集光し，媒質よりも大きな屈折率を持つ物体を捕捉する光ピンセット法を用いた。アクチンフィラメントの構造には極性があり，滑り運動するときの進行方向前端をP端，後端をB端と呼ぶ。このB端にアクチンフィラメント切断・キャップタンパク質であるゲルゾリンを介して結合した直径1 μmのポリスチレンビーズを光捕捉することによってアクチンフィラメントを操作し，ナノメートル(nm)精度の変位計測とピコニュートン(pN)オーダの力計測を行う。光ピンセットの捕捉中心を移動することで，ミオシン頭部と，そこに結合したアクチンフィラメントとの間に負荷を加えることができる。ビーズには，ビーズと光捕捉中心(焦点近傍)からの距離に比例した，捕捉中心方向へ向かう復元力が働く。負荷を加えていけばいつかアクチン・ミオシン間の結合は破断する。こうして一定の割合で負荷を上昇していくことによって得られた破断力の分布のヒストグラムから，硬直結合（ATP非存在下での結合）の平均破断力が単頭結合で約7 pN，双頭結合で約15 pNと見積もられた（ただし，ここでの負荷上昇速度は12 pN/s)。しかしここで注意すべきは，アクチン・ミオシン間の結合は負荷を加えなくても自然に解離するということである（その解離過程は熱揺らぎによる確率過程であることは硬直結合一つひとつの解離過程を観測することで示される)。

そこで，アクチン・ミオシン硬直結合の結合寿

(a) アクチン・ミオシンII

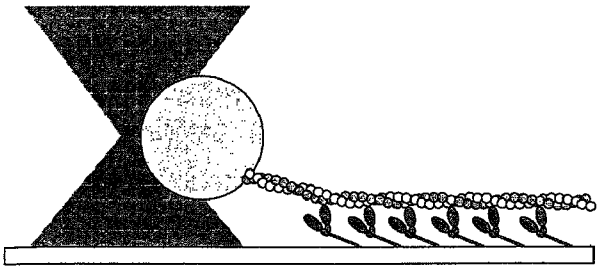

(b) アクチン・ミオシンV

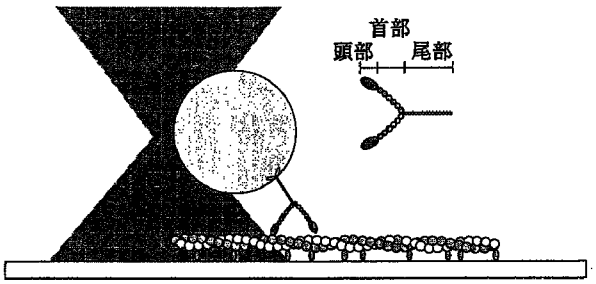

(c) 微小管・キネシン

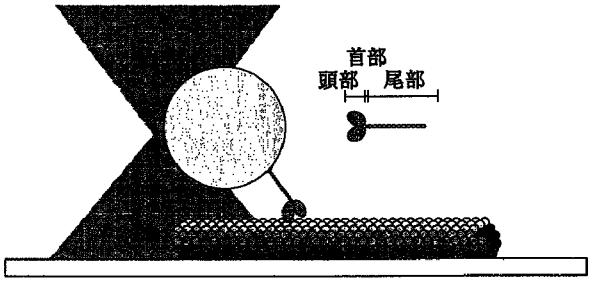

(a)ガラス基板上に吸着したミオシンII分子に，アクチンフィラメントを相互作用させる。アクチンフィラメントのB端にキャップタンパク質ゲルゾリンを結合し，それを表面に吸着した直径約1 μm のプラスチックビーズを，集光したレーザ光で光捕捉する
(b), (c)1分子で機能するミオシンVやキネシンの尾部はプラスチックビーズの表面に吸着しやすいので，図のような1分子計測が可能。この場合にはそれぞれアクチンフィラメントと微小管をガラス基盤上に固定する

図 3　光ピンセット法による分子モーターの1分子運動機能の顕微計測法の模式図

命に対する負荷の影響を調べたところ，平均の結合寿命（τ）の負荷（F）依存性として，$\tau(F)=\tau(0)\,exp(-Fd/k_BT)$ という実験式が得られた。ここで $\tau(0)$ は無負荷での平均の結合寿命（HMMは約1,000秒，S1は約100秒），d は分子間相互作用を特徴づける特性距離（HMMは1.4 nm，S1は2.4 nm），k_Bはボルツマン定数，T は絶対温度である[5,6]。この分子間結合寿命の負荷依存性の形（結合ポテンシャルの深さを $F\cdot d$ だけ押し上げる）は，分子モーターに限らずほかのタンパク質間結合においても原子間力顕微鏡（AFM）法を用いて得られている[7]。しかし，分子モーターの特徴は，相互作用の特性距離 d の値が大きいことである。結合寿命が負荷の大きさに依存するということは，上で述べた結合破断力は負荷上昇速度に依存することを意味する。結合は自然に破断するので，じわりじわりと負荷を加えていけば，得られる破断力はいくらでも小さくなる。逆に負荷上昇速度が大きいほど，破断力は大きくなる。注意すべきは，この破断力は平均値に関するものであって，一つひとつの結合破断力はあくまで確率的に変動する。

以上のようにミオシンIIとアクチンフィラメント間の分子間結合の性質が，徐々に1分子レベルで明らかになりつつある。とくに注目すべきは，ATPが存在する滑り運動条件下で，ミオシンIIはATPaseサイクルのほとんどの時間，アクチンフィラメントから解離しているということである。すなわち，ミオシン1分子ではアクチンフィラメントに持続的な“滑り運動”を引き起こすことはできない。この点が，後述するミオシンVやキネシン分子モーターと異なる。ミオシンIIは多分子が集まることで初めて機能する多分子モーターである。筋収縮のような集団運動を効率よく生み出すうえで最適の性質を備えているものと考えられる。

次にここで注目したいことは，アクチンフィラメントが，力発生や滑り運動機能に果たす役割である。ミオシンは単独では方向性を持つ運動を行えない。相互作用するアクチンフィラメントがあってこそミオシン分子のATP加水分解能は活性化されるし，結合して力を発生することができる。

筋収縮滑り機構では筋フィラメントが長さを変えないことになっている。しかし筋フィラメントは剛体ではなく，粘弾性体である。実際，アクチンフィラメントの曲げの硬さは同じ形状の鉄と比べると1桁か2桁小さい。この値は30年以上も前に，溶液中で熱揺らぎするフィラメントによって

散乱されるレーザ光の周波数変化を計測し解析することによって見積もられた。準弾性光散乱法あるいは動的光散乱法と呼ばれるこの方法により，アクチンフィラメントはミオシンの結合によって，ATP非存在下だけでなくATP存在（収縮条件）下でも柔らかくなることが分かった[8]。さらに，精製したアクチンフィラメントに制御系タンパク質（トロポミオシン，トロポニン）を添加することによって再構成した細いフィラメントでは，1 μM（pCa＝6）程度のCa^{2+}濃度に依存して硬さが変わることも見いだされた。この再構成筋フィラメントの硬さは，Ca^{2+}存在下（pCa＜6の収縮条件）でミオシンと相互作用するときに最も柔らかく，Ca^{2+}非存在下（pCa＞6の弛緩条件）ではミオシン分子がないのと同じく最も硬かった[9]。

その後，蛍光色素で標識した1本のアクチンフィラメントを蛍光顕微鏡の下で観察し，曲げのブラウン運動を解析することによって，アクチンフィラメントの硬さが見積もられた。曲げのブラウン運動の緩和時間が長いほど，フィラメントはより柔らかいことになる。この方法で見積もられたアクチンフィラメントと，再構成した細いフィラメントの硬さは共に，光散乱法で得られていた値とほぼ一致した[10]。以上の結果は，フィラメントの硬さ・柔らかさが筋収縮の単なる制御機構のみならず，筋収縮機構そのものにも関与していることを示唆するものである。アクチンフィラメントは単なるレールであるか否かは，こうして長年にわたって未解決の課題となっている。

2.1.2　非筋細胞ミオシン（ミオシンV）

次にミオシンVについて述べる。ミオシンVは非筋細胞内にあって，1分子で小胞輸送を担う分子モーターである（図2参照）。ミオシンファミリーに属し，相互作用する“レール”はアクチンフィラメントである。ミオシンVもほかの多くの分子モーターと同様双頭構造を持つ。

前述した光ピンセット法により，ミオシンVを結合したビーズを捕捉し，その動きを計測することで〔図3(b)〕，ミオシンVは平均35～37 nm，すなわちアクチンフィラメントの二重らせん構造の半ピッチに相当する大きさのステップを踏みながら歩行運動することが分かった[11]。ミオシンIIとの決定的な違いは，1分子で何十歩も連続してステップを踏んで前進できるというプロセッシブ性（逐次前進性）を備えているという点である。ミオシンIIは1歩を踏むこともまれである。また，ミオシンIIと比べて首の部分が長い。

ステップサイズが首の長さに依存するかしないかの検証は，歩くしくみを解く鍵を与えるはずである。そこで遺伝子工学を用いて首の長さ（すなわち双頭間の長さ）を変えたミオシンVのステップサイズが比較された。ところが，首の長さによってステップサイズが変化するという結果[12]と，首の長さに依存せず同じ大きさのステップを踏むという[13]，全く異なる結果が報告されている。また，ミオシンVより首の短い天然ミオシンVIのステップサイズを計測したところ，約30 nmであり，二つの頭部の間隔を最大に広げたときの双頭間距離よりも大きなステップサイズが得られた[14]。したがってこの方法では，歩くしくみについて決定的な結論が得られなかった。

ごく最近，ミオシンVの軽鎖を構成する六つのカルモジュリン残基の一つを蛍光色素でラベルし，ミオシンVの運動に伴う蛍光色素1個の位置変化が1.5 nmの高空間分解能で計測された。双頭構造のうち片側の首の部分にだけ目印が付いたミオシンVを観察した結果，蛍光色素のステップは，74 nmに平均のピークを持つステップ，52 nmと23 nmを交互に繰り返すステップ，42 nmと33 nmを交互に繰り返すステップの三つが観測された。アクチンフィラメントに沿った，ミオシンVの重心から蛍光色素が結合している位置までの距離xによって，37（ミオシンVの歩幅）＋2x，37－2xの交互のステップが観測されたことになる。この結果は，ミオシンVがHand-over-hand機構（頭部を交互に動かして歩く機構）で動作することを示す有力な証拠である[15]。

2.2　キネシン・微小管系

キネシンはミオシンVと同様プロセッシブモーターであり，1分子でレールフィラメント上を解

離することなく前進することができる。キネシンは，球状のチューブリン分子（直径4 nm）が筒状に重合した微小管と呼ばれるレールフィラメント（直径約25 nm）と相互作用して一方向に動く。キネシンは，微小管上を8 nmステップを踏んで運動し，解離するまでに連続して平均100歩ほどステップすることができる。顕微解析〔図3(c)〕の結果は，キネシン分子を吸着したビーズの変位が常に8 nmの決まったステップ状であることを示した。これにより，キネシンは常に8 nm，つまりチューブリン分子二つ分と同じ大きさの決まったステップを踏むことが明らかになった[16]。

キネシンの各頭部がATPaseサイクルを行うときに，そのヌクレオチド状態の違いによって微小管との親和性が変化する。それぞれの頭部が微小管に結合している時間（duty ratio）は，1回のATPaseサイクルの80%以上といわれており，二つの頭部が同時に微小管から外れる確率はミオシンIIに比べると圧倒的に小さい。したがって，長い間1分子で結合し続けることができることは容易に理解できる。しかし，どのようなしくみで二つの頭部が交互に前進することができるかという，プロセッシブ性の本質はこれだけでは分からない。プロセッシブモーターは，非プロセッシブモーター同様，同じ構造を持つポリペプチドの二量体である（単量体でもプロセッシブにゆっくりと運動するモーターKIF1Aも見つかっている[17]）。同じ性質を持った二つの頭部が完全に独立かつランダムに作動するならば，長距離にわたる一方向性の運動は不可能であろう。しかし実際には一方向に交互に足を出して（頭部を動かして）長距離にわたって運動することができる。

プロセッシブモーターが巧みにステップを踏むしくみとして，分子内部負荷によるATPaseサイクルの自律的制御が考えられている。キネシンを結合したビーズを光ピンセット法によって操作し，様々なヌクレオチド状態で微小管のプラス端（進行）方向とマイナス端（進行方向と逆）方向に負荷を加え，破断力が計測された[18,19]。その結果，進行方向に負荷が加わるとADPが結合しやすく，逆方向に負荷が加わるとADPが解離しやすいことが分かった[20]。すなわち，分子モーターに対するヌクレオチドの親和性が，負荷方向依存性を持つことを意味する。この結果は，歩行時，二つの頭部がレールフィラメントに同時に結合した双頭結合時に分子モーターに内部負荷が発生すれば，内部負荷のベクトル性によって，自律的に双頭間で位置情報をやりとりし，確率的運動を制御しうることを示唆している。つまり，双頭で微小管に結合したとき，結合部位の構造的制約によってキネシン内部に非対称なひずみが生じる。前頭が後ろに，後頭が前に引っ張られれば，それによって生じる非対称なひずみによって，まず後頭が解離しやすくなり，さらにそれぞれの頭部に対するヌクレオチドの結合解離・加水分解の確率が制御され，交互に足を踏み出す（頭を突き出す）ことができるのではないか。この内部負荷による歩行タイミングの制御が，分子モーターが等価な二つの頭部を協調的に動かすしくみとして有力視されている。

分子モーターに対する負荷依存的なヌクレオチドの親和性は，ミオシンIIの集合体である筋収縮レベルでも報告されている[21]。タンパク質分子モーターは，化学エネルギーを力学エネルギーに変換するだけの素子ではなく，分子内部に力学センサ機構を備えており，これによって自律的な運動制御を実現しているようである。

3．おわりに

以上，アクチン・ミオシン系，キネシン・微小管系に関する我々のグループの研究成果を中心に，分子モーターの動作機構の一面を述べた。分子モーターの動作原理については世界的に多くの研究が進められている。とくにF_0F_1ATPaseや鞭毛モーターといった回転モーターについての研究は，わが国で先駆的研究が行われている。最近になって，改めてレールフィラメントが分子モーターの動作に積極的にかかわっている可能性が指摘されるようになり，アクチンフィラメントや微小管の構造変化に注目する研究も進められるようになった。

分子モーターの動作機構については，構造解析（X線結晶解析，NMR，ESRなど），遺伝子工学，1分子計測などの技術を用いて様々な特質が明らかにされてきている。しかし，エネルギー変換の分子機構については本質的なところはいまだ不明である。ナノレベルの世界でアクチュエータを実現しようとするとき，その素子は常に熱揺らぎにさらされることになる。素子が常にノイズにさらされるために，出力が完全に正確な素子を作ることは不可能であろう。このような高ノイズ条件下で利用可能な素子を作るには，いかに熱揺らぎを制御し，またいかに利用するかがキーポイントとなる。生体分子モーターは，ナノメートルサイズの構造の中にこの機能を内蔵しているのである。生体内で働く分子モーターがどのような自律的しくみで化学的エネルギーを力学的エネルギーに変換しているのか，これを解明することがナノスケールでの人工分子モーターを開発するための近道であるかもしれない。

【引用・参考文献】

1) http://www.mrc-lmb.cam.ac.uk/myosin/
2) J. T. Finer, R. M. Simmons and J. A. Spudich：*Nature* **368**, 113-119 (1994).
3) H. Miyata, H. Yoshikawa, H. Hakozaki, N. Suzuki, T. Furuno, A. Ikegami, K. Kinosita Jr. and S. Ishiwata：*Biophys. J.* **68**, 286 S-289 S (1995).
4) A. Ishijima, H. Kojima, T. Funatsu, M. Tokunaga, H. Higuchi, H. Tanaka and T. Yanagida：*Cell* **92**, 161-171 (1998).
5) T. Nishizaka, H. Miyata, H. Yoshikawa, S. Ishiwata and K. Kinosita Jr.：*Nature* **377**, 251-254 (1995).
6) T. Nishizaka, R. Seo, H. Tadakuma, K. Kinosita Jr. and S. Ishiwata：*Biophys. J.* **79**, 962-974 (2000).
7) R. Merkel, P. Nassoy, A. Leung, K. Ritchie and E. Evans：*Nature* **397**, 50-53 (1999).
8) F. Oosawa, S. Fujime, S. Ishiwata and K. Mihashi：*Cold Spring Harb. Symp. Quant. Biol.* **37**, 277-286 (1973).
9) S. Ishiwata and S. Fujime：*J. Mol. Biol.* **68**, 511-522 (1972).
10) T. Yanagida, M. Nakase, K. Nishiyama and F. Oosawa：*Nature* **307**, 58-60 (1984).
11) M. Rief, R. S. Rock, A. D. Mehta, M. S. Mooseker, R. E. Cheney and J. A. Spudich：*Proc. Natl. Acad. Sci. USA.* **97**, 9482-9486 (2000).
12) T. J. Purcell, C. Morris, J. A. Spudich and H. L. Sweeney：*Proc. Natl. Acad. Sci. USA.* **99**, 14159-14164 (2002).
13) H. Tanaka, K. Homma, A. H. Iwane, E. Katayama, R. Ikebe, J. Saito, T. Yanagida and M. Ikebe：*Nature* **415**, 192-195 (2002).
14) R. S. Rock, S. E. Rice, A. L. Wells, T. J. Purcell, J. A. Spudich and H. L. Sweeney：*Proc. Natl. Acad. Sci. USA.* **98**, 13655-13659 (2001).
15) A. Yildiz, J. N. Forkey, S. A. McKinney, T. Ha, Y. E. Goldman and P. R. Selvin：*Science* **300**, 2061-2065 (2003).
16) K. Svoboda, C. F. Schmidt, B. J. Schnapp and S. M. Block：*Nature* **365**, 721-727 (1993).
17) Y. Okada, H. Higuchi and N. Hirokawa：*Nature* **424**, 574-577 (2003).
18) K. Kawaguchi and S. Ishiwata：*Science* **291**, 667-669 (2001).
19) K. Kawaguchi, S. Uemura and S. Ishiwata：*Biophys J.* **84** (2 Pt 1), 1103-1113 (2003).
20) S. Uemura, K. Kawaguchi, J. Yajima, M. Edamatsu, Y. Y. Toyoshima and S. Ishiwata：*Proc. Natl. Acad. Sci. USA.* **99**, 5977-5981 (2002).
21) J. A. Dantzig, M. G. Hibberd, D. R. Trentham and Y. E. Goldman：*J. Physiol.* **432**, 639-680 (1991).

<島本　勇太／鈴木　団／石渡　信一>

3 Contractile Systems of Muscles

Madoka Suzuki and Shin'ichi Ishiwata

CONTENTS

INTRODUCTION

The voluntary movements of the human body required for walking, running, eating, and talking are made possible by the organized movement of the muscle–skeleton (or muscle–connective tissue) system. The active component of this system is the *skeletal muscle,* both ends of which adhere to bone or elastic tissue through tendons. The states of contraction or relaxation of voluntary muscles are regulated in an all-or-nothing fashion by electric signals transmitted from neurons.

The contractile system of skeletal muscle constitutes a hierarchy from a single-molecule (protein) to a tissue (Figure 3.1). The contractile system is a highly ordered structure that supports physiological functions. The structures in the system range in size from 10 nm to about 1 cm. The former requires an electron microscope or scanning probe microscope such as an atomic force microscope (AFM) for us to observe, and the latter can be observed with our eyes and touched with our hands. Macroscopic muscle contraction results from the accumulated efforts of microscopic or nanoscopic assemblies of several kinds of muscle proteins such as a complex of

0-8493-1487-9/04/$0.00+$1.50

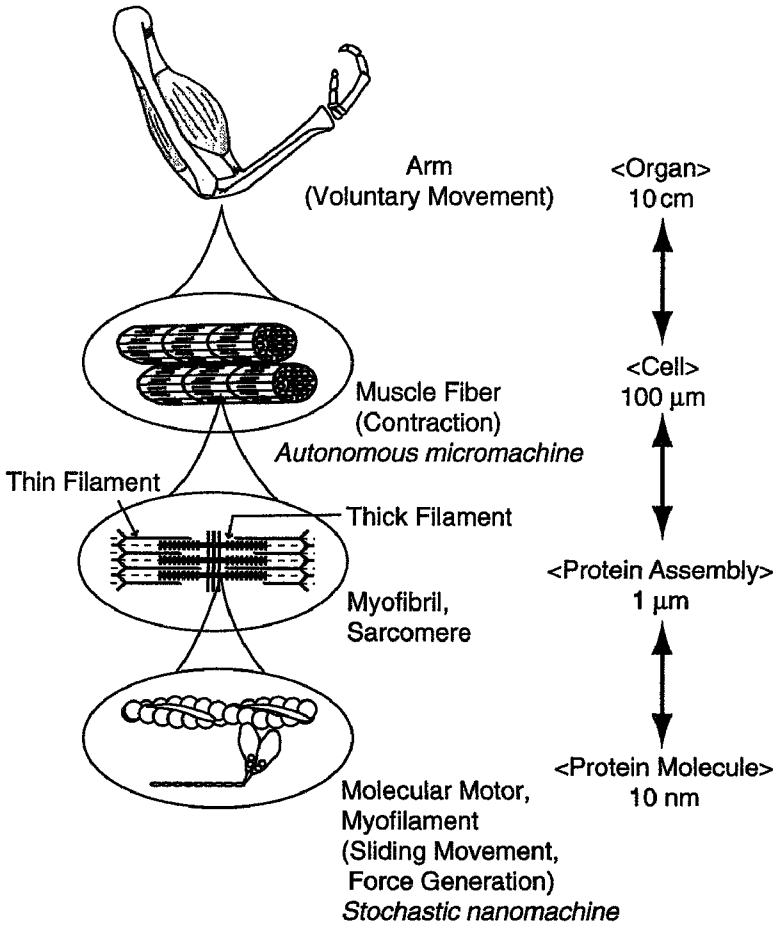

FIGURE 3.1 Hierarchy of muscle contractile system. The system ranging from a single molecular level on a nanometer scale to a tissue level on a centimeter scale constitutes a hierarchical structure. The hierarchy illustrated is common to all kinds of striated muscles, i.e., both skeletal and heart muscles.

actin and myosin (a mechano-enzyme), tropomyosin and troponin (regulatory proteins), and connectin/titin (an elastic protein).We stress here the one-to-one correspondence between the motile organs created by nature and the motile machines made by human beings. As shown in Figure 3.2, although necessary and sufficient conditions for constructing a motile system are common to both natural and artificial systems, the principles required to produce a motile system (software) and the materials to construct the framework (hardware) are very different. It is now possible to produce an artificial machine as small as a micrometer or even a few hundred nanometers so that the sizes are within the same order. However, the principle that generates force and movement in muscle is chemomechanical transduction. Force and movement in man-made micro- and nano-sized machines usually proceed via electromechanical transduction.

The working principles of artificial machines are fully clarified; for example, an automobile moves based on physical principles such as thermodynamics and mechanics. However, we do not yet fully understand the physical principles of mechanochemical energy transduction that operate in the molecular motors of muscles.

Automobile (Artificial Machine)	MECHANISM	Muscle (Natural Machine)
Computer and electric system	**-Control System-**	Nerve signal to the membrane
Spark ignition	**-Trigger-**	Ca^{2+} release from inner membrane system
Cylinder, Piston	**-Engine-**	Actin, Myosin (Mechano enzyme)
<Thermodynamics>		*<Mechanochemical coupling>*
Strokes of a piston	**-Work Production-**	Conformational change
Combustion of the mixture of gasoline and air	**-Energy Conversion-**	Hydrolysis of ATP
Power transmission	**-Amplifying System-**	Sarcomere repeat, Elastic component
Wheel rotation	**-Movement as a Whole-**	Contraction (Shortening)
<Rigid connection>		*<Flexible connection, Feedback>*

FIGURE 3.2 Necessary and sufficient conditions for constructing a motile system. Comparison of motile systems created by nature (muscle) and human beings (automobile). Necessary and sufficient conditions for constructing a motile system are common to natural and artificial systems, so that the systems have one-to-one correspondence. However, at least two significant differences exist: the principle of motility (force generation) and the materials.

Muscles require proteins; artificial machines require metals or chemical compounds. Every protein is a complex system composed of heterogeneous elements and possesses a flexibility (self-regulatory feedback mechanism) that can respond quickly to changes of environment. However, the methods of response and regulation of a man-made machine must be artificially designed and programmed beforehand.

In this chapter, we describe the structure and function of the muscle contractile system as a typical example of a biological fast responsive movement system that has a hierarchical structure. We also focus on the stochastic properties of molecular motors, i.e., nanoscopic systems composed of myosin and actin (also called stochastic bionanomachines). We would like to stress that flexibility is the essence of the structures and functions of constituent proteins — something very distinct from the characteristics of artificial machines.

MUSCLE CONTRACTILE SYSTEM

The structural and functional unit of the skeletal muscle is the *muscle fiber* (Figure 3.3). A muscle fiber is a long (e.g., 1 m in a giraffe) and thin (10 to 100 μm in diameter), cylindrical, multinucleus cell created by fusion. The fiber is surrounded by a cell membrane to which a nerve end is attached. The muscle fibers are assembled parallel to each other and form a bundle that is organized into muscle tissue.[1]

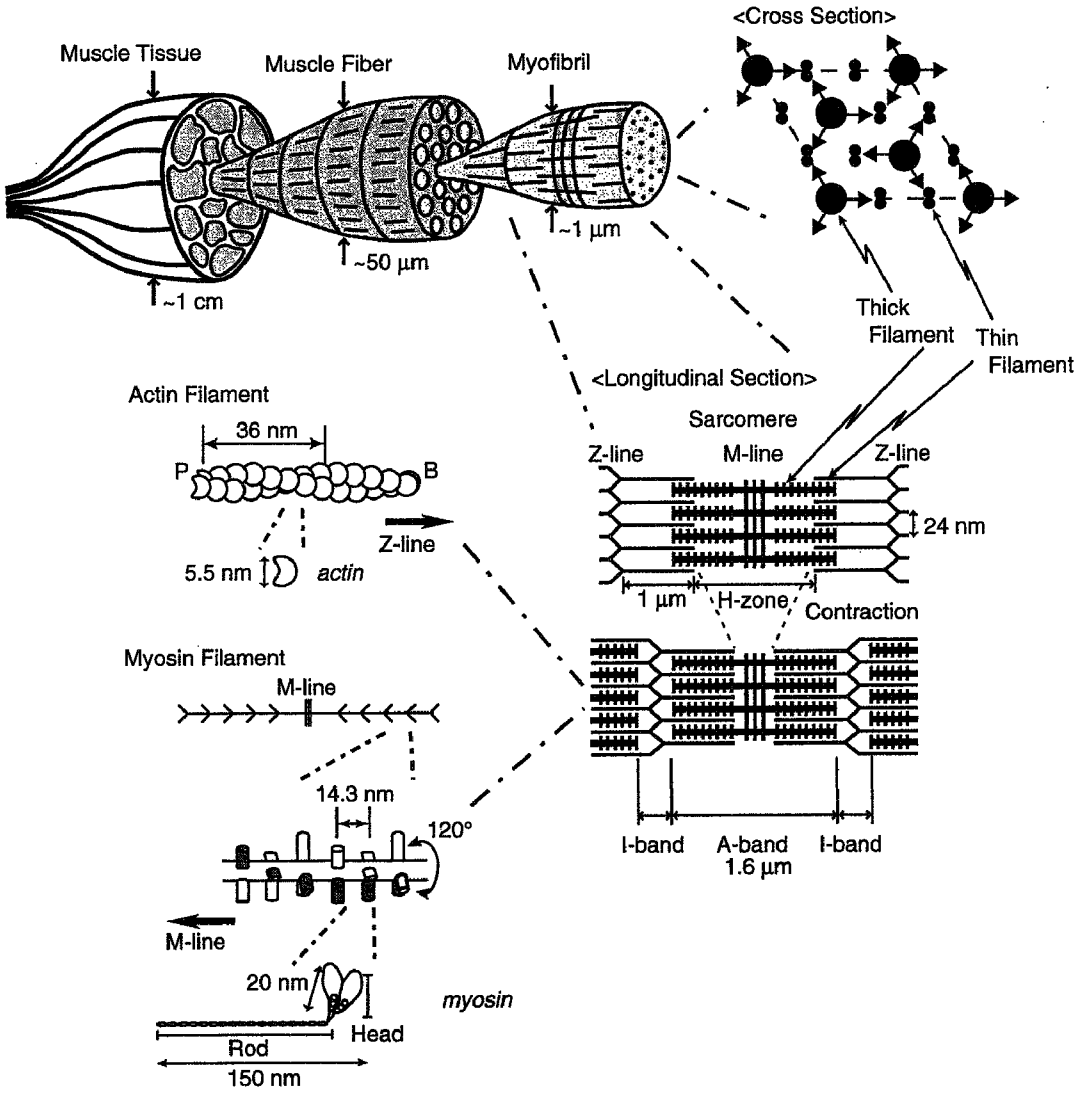

FIGURE 3.3 Muscle contractile system. The minimum structural and functional unit of the system is a sarcomere constructed from a lattice structure composed of thin and thick filaments that are, respectively, polar and bipolar helical polymers. Myosin is a long molecule having two head domains that bind to an actin filament to form a cross-bridge and hydrolyze ATP. Another domain called a rod is composed of a coiled–coil structure. The neck domain connects the head and rod domains. Actin is a horse hoof-shaped small molecule that polymerizes into a helical polymer; the end that attaches to the Z-line is called the B-end, and the other is the free P-end.

A muscle fiber is a parallel assembly of many *myofibril*s that constitute a contractile apparatus about 1 μm in diameter. Because myofibril has a striation pattern and neighboring myofibrils are assembled in phase, muscle fibers also have striation patterns. Striation patterns are common to skeletal and cardiac muscles, in contrast to smooth muscles that do not have such ordered periodical structures. Striation of myofibrils is attributable to the periodic alignment of the A-band, a structure about 1.6 μm long, and the I-band, a structure of variable width. The thick line crossing the center of each I-band is called the Z-line or Z-disk. A structural

unit of the striation pattern is divided by the Z-lines and is called a sarcomere; it is usually 2 to 3 μm long.

The A-band consists of thick filaments, the centers of which are bundled at the M-line. The I-band is composed of a parallel array of thin filaments about 8 nm thick and 1 μm long. The thin filaments extend from the Z-line toward the center of the A-band and partially overlap the thick filaments in the A-band. The central region of the A-band in which the thin filaments are absent is called the H-zone. The two kinds of myofilaments construct a lattice structure. For example, in mammalian skeletal muscle, these filaments are hexagonally packed in a way that a single thin filament is surrounded by three thick filaments located at the corner of the triangular lattice (see Figure 3.3, top right).

Myosin and actin molecules are the main components of the thick and thin filaments, respectively. The thick filament is a bipolar polymer composed of about 300 myosin molecules; and their structures are symmetrical against the centers at which M-proteins are attached to form M-line structures. The thin filament is a polar helical polymer composed of actin molecules. The free ends of the thin filaments are called the P-ends to which capping proteins named tropomodulins attach.[2] The other (B) end attaches to the Z-line so that the thin filament lattice is fixed at the Z-line to form the I-Z-I brush, the structure of which is symmetrical against the Z-line. Myosin and actin molecules account for about 70% of the muscle proteins constituting the contractile apparatus.

MOLECULAR MECHANISMS OF MUSCLE CONTRACTIONS

Sliding Filament Mechanism

The contraction of a myofibril can be explained by the *sliding-filament* mechanism.[3–5] The head part of a myosin molecule protruding from the surface of the thick filament forms a *cross-bridge* by interacting with the thin filament. The essence of the sliding-filament mechanism is that the cross-bridge changes its conformation accompanied by the hydrolysis of adenosine triphosphate (ATP) to generate force. The thick and thin filaments slide past each other while maintaining the total length of each filament (that is, the elasticity of the myofilaments is not taken into account in the sliding-filament mechanism).

The fact that the lengths of the thick and thin filaments remain constant during sliding and while generating force was first demonstrated by optical[3] and electron[4] microscopy. The length of the A-band was unchanged, whereas the widths of both the I-band and the H-zone changed in parallel. This demonstration was done under static conditions, that is, after relaxing a myofibril for optical microscopy and chemical fixation of the muscle preparation for electron microscopy under various sarcomere lengths. Thus, the length of the myofilament during shortening or generating force was not examined. The possibility that the repetition of local extension and shortening of myofilaments plays an important part in force generation has not been eliminated.

In practice, myofilaments are elastic, not rigid, bodies. For example, the flexural rigidity of actin filaments was estimated to be one to two orders of magnitude smaller

than that of steel of the same size. This estimation was first demonstrated more than 30 years ago by S. Fujime, who measured and analyzed the frequency shifts of laser light scattered from filaments that fluctuated thermally in solution.[6] This technique (called quasielastic scattering of laser light or dynamic light scattering) revealed that the flexibility of actin filaments increased upon the binding of myosin in the absence of ATP (rigor condition)[7] and also in the presence of ATP (contraction condition).[8,9] The flexibility of the thin filaments reconstituted from purified actin and the regulatory proteins (tropomyosin and troponin) changed, depending on the concentration of free Ca^{2+} around micromolar levels (corresponding to a pCa value of 6). The filament became flexible when the pCa value was below about 6, which led to the binding of Ca^{2+} to troponin and accordingly the activation of the contractile system.[10] When the reconstituted thin filaments interacted with myosin molecules, the effect of Ca^{2+} on flexibility was remarkable.[8,9] The flexibility of reconstituted thin filaments interacting with myosin was largest (most flexible) in the presence of Ca^{2+} (pCa < ca. 6 corresponding to the contraction condition), but smallest (most rigid) in the absence of Ca^{2+} (pCa > ca. 6 corresponding to the relaxation condition) as if myosin molecules were absent. These effects of Ca^{2+} were reversible, suggesting that the flexibility of thin filaments may be involved in the regulatory mechanism and also in the contraction mechanism.

Since the imaging of single actin filaments became possible under fluorescence microscopy by labeling the filaments with a fluorescent dye,[11] the elastic modulus (inverse of the flexibility) of actin filaments could be measured by analyzing the bending Brownian motion (the longer the relaxation time of bending Brownian motion, the more flexible the filament). The flexural rigidity of actin filaments and reconstituted thin filaments thus obtained was consistent with that estimated using dynamic laser light scattering, about 10^{-17} dyn cm^2.[7,10–13]

The sliding-filament mechanism has been established,[5,14] but the detailed mechanism of contraction, the dynamic feature of myosin motors and actin, has yet to be clarified. There is a consensus that the elastic modulus of muscle fiber during contraction is attributable to both the cross-bridges and the thin filaments.[15] Low angle x-ray diffraction of muscle fibers has shown that the thin filaments extend by an order of 0.1% during force generation.[16,17] However, whether the flexibility of the thin filaments is directly involved in the mechanism of contraction (force generation) is still an open question.

The contractile system does not work solely by the actin–myosin motor system; contractile properties depend on several factors such as the elastic components organizing the contractile system and the geometry of the lattice structure of myofilaments. An elastic framework is needed to stabilize the lattice structures of myofilaments during force generation and transmit the generated force effectively to the ends of myofibrils (compare Figure 3.3). For example, both ends of the thick filaments are connected to the Z-line through an elastic protein called connectin/titin in each sarcomere. Connectin/titin is the largest protein in nature, with a molecular weight of about 3×10^6. When the sarcomere is stretched by about 30% of its resting length (or longer than about 3 μm), an extension of the connectin/titin molecules develops tension. This implies that the elastic force developed by this extension plays a role in maintaining the thick filament at the center of each sarcomere. The passive tension

developed under relaxing conditions is called resting tension, and is attributable to the connectin/titin extension. Moreover, experimental evidence shows that cross-bridges are activated in response to muscle stretch, implying that connectin/titin-based passive tension modulates cross-bridge activity.[18,19] This property is considered significant in the Frank–Starling law (development of active tension in response to muscle stretch), which is known to be an essential element of the systolic function of the heart.

Cross-Bridge Mechanism

During the sliding of myofilaments and the generation of force, or even during force generation without sliding (isometric contraction: the total length of the fiber is adjusted to be constant during tension development), the repeated attachment and detachment of cross-bridges is accompanied by the hydrolysis of ATP. Huxley and Simmons studied the cross-bridge dynamics of single muscle fibers in relation to the molecular mechanism of force generation. The transient response of muscle fibers was analyzed by applying small stepwise changes of length during contraction. When muscle fiber under isometric contraction was suddenly shortened or stretched within 1 ms, tension was instantaneously dropped or elevated, and then recovered to the initial tension level. The degree of tension drop was proportional to the extent of shortening. The isometric tension diminished transiently when the extent of shortening per half a sarcomere became only about 4 nm; one possible interpretation is that the compliant parts of cross-bridges and/or the thin filaments were stretched by about 4 nm. The extension of the compliant part is the origin of the generated force.

Huxley and Simmons constructed a theoretical model of cross-bridge rotation (the lever-arm model)[20] that explains their results.[5] Their lever-arm model was recently supported by the measurement of the polarization of a fluorophore fixed to the neck region of myosin in muscle fibers that may monitor the orientation of cross-bridges.[21] Although the lever-arm mechanism seems established, it is possible that molecular motors may have other properties. To elucidate the essence of the molecular motor, we need to fully understand the cooperative behaviors of cross-bridges (described below) and the role of the dynamic properties of thin filaments (discussed above in relation to the flexibility changes of thin filaments).

Synchronization of Cross-Bridges

Under normal physiological solvent conditions, the state of the contractile system of muscle is regulated by concentrations of free Ca^{2+}. Contraction or relaxation will occur, depending on whether the pCa value is below or above about 6, respectively. When the conditions are set to be intermediate between those of contraction and relaxation, a third state known as spontaneous oscillatory contraction (SPOC) appears. Intermediate conditions are realized at a pCa value slightly above 6 (Ca-SPOC) for cardiac muscle or in coexistence with ATP, adenosine diphosphate (ADP), and inorganic phosphate (Pi) without Ca^{2+} (ADP-SPOC) for cardiac and skeletal muscle.

An example of ADP-SPOC observed in a single skeletal myofibril with both ends fixed at a pair of glass microneedles is shown in Figure 3.4. One of the two

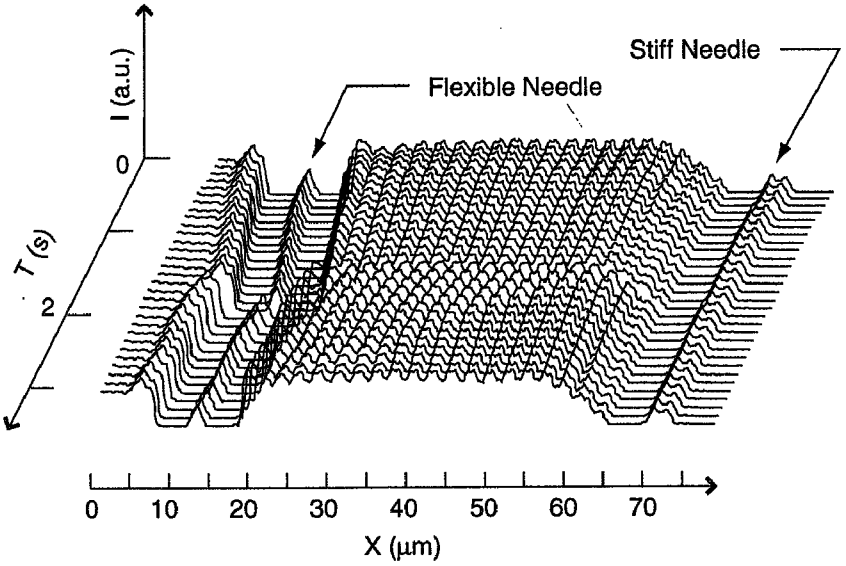

FIGURE 3.4 Time course of the image profile of a myofibril showing spontaneous oscillatory contraction (SPOC). The T, X, and I axes, respectively, represent the time course of the SPOC (every 0.1 s), the position along the myofibril, and the brightness of the phase-contrast image. Each end of the myofibril was fixed to a pair of glass microneedles. The glass microneedle on the left side is flexible so that the developed tension is represented by its deflection. The needle on the right side is rigid so that the myofibril can be quickly stretched or released by a stepwise move of this needle. Solvent conditions are 120 mM KCl, 4 mM $MgCl_2$, 0.2 mM ATP, 4 mM ADP, 4 mM Pi, 20 mM MOPS (pH 7.0), and 4 mM EGTA. Temperature = 25°C. (From Shimamoto, Y., M.S. thesis, Waseda University, Tokyo, 2003. With permission.)

microneedles is flexible so that its deflection can monitor tension generation. Under SPOC conditions, tension spontaneously oscillates and the length of each sarcomere oscillates in a sawtooth waveform consisting of rapid lengthening and slow shortening phases within 1 to 6 s, depending on solvent conditions. Further, the lengthening phase is propagated to adjacent sarcomeres one by one, creating a traveling wave along a myofibril (SPOC wave).

The necessary conditions for the sliding mechanism described do not hold during SPOC. That is, sarcomeres of longer lengths (smaller numbers of interacting cross-bridges) and those of shorter lengths (larger numbers of interacting cross-bridges) coexist in the same myofibril under the same external load, implying that the forces generated by different numbers of cross-bridges in every sarcomere must be balanced against each other. The SPOC phenomena strongly suggest that cross-bridges gain the ability to self-regulate their states through intermolecular interaction, that is, they gain intermolecular synchronization by assembling in an organized structure.

A-Band Motility Assay System

We have recently developed a new motility system that locates in the hierarchical structure between the muscle contractile system and the *in vitro* motility assay system as shown in Figure 3.1. This system we designated the *A-band motility assay system* (or *bionanomuscle*) is prepared by selective removal of the thin filaments from a

myofibril using gelsolin (an actin-binding protein that severs an actin filament and caps its B-end) as a molecular tool.[22] This system consists of exposed A-bands in which the thick filaments are supposed to maintain the filament lattice as in the intact myofibrils. By applying a single actin filament with the B-end attached to a polystyrene bead through gelsolin adhered to the surface of the bead and by trapping the bead with optical tweezers, the displacement of the bead from the trap center and the force generated on the actin filament can be measured.

It should be stressed again that one characteristic of the A-band motility assay system is that the ordered structure of thick filament lattice is kept native and other components that are expected to contribute to the contractile properties in the fibers such as connectin/titin have been removed. Thus, the physiological functions of these missing components can be investigated.

The time course showing the sliding movement of an actin filament in the A-band motility assay system revealed a considerable force fluctuation both in the rising phase of force generation and even in the steady phase in which the force generated by cross-bridges and the load applied by the optical tweezers are balanced (Figure 3.5). It was estimated that 20 to 30 cross-bridges (myosin molecules) interacted with the actin filament in this example. The result implies that the tension generated on each thin filament fluctuates at random even when working in the ordered structure of a myofilament lattice. This is attributable to the fact that the period of the force-generating state for each cross-bridge is very short (on the order of 1 ms) and the

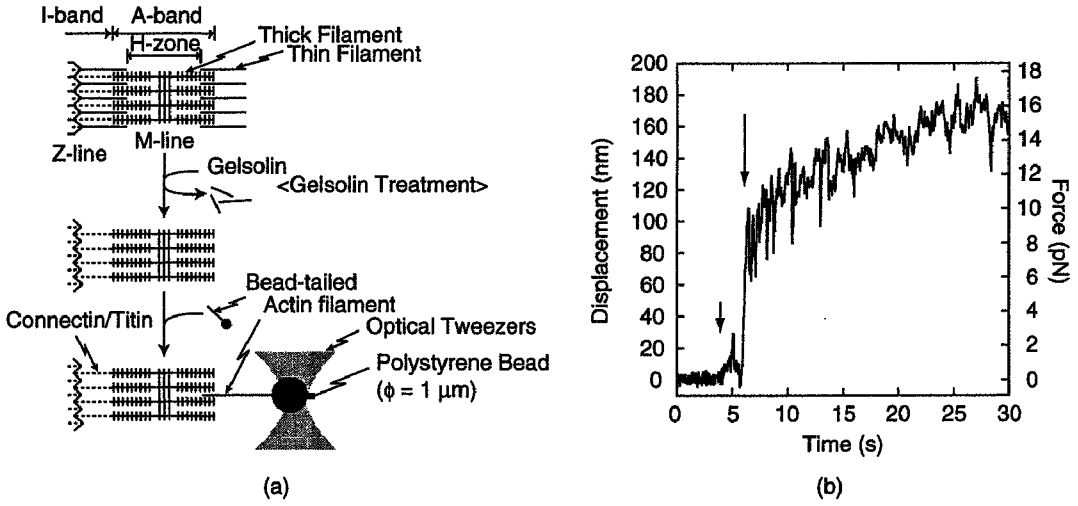

FIGURE 3.5 (a) A-band motility assay system. An exposed A-band is obtained by selective removal of thin filaments from a myofibril using gelsolin, an actin-binding protein that severs the actin filament. A single actin filament attached to a polystyrene bead 1 μm in diameter is brought into contact with the edge of the A-band by optical tweezers. (b) Time course of the displacement of the trapped bead interacting with the A-band. When the actin filament began to interact with the A-band, the filament was pulled into the A-band and the bead was pulled away from the trap center (ordinate = 0) at the distance indicated by a short arrow. The bead, once pulled back to the trap center, was pulled away again (long arrow) accompanied by a large force fluctuation of a few pN. The force fluctuation continued even at the steady phase where the force generated on the actin filament and the load applied by the optical tweezers were balanced (about 22 s).

proportion of the period of the force-generating state occupying one cycle of ATP hydrolysis (i.e., duty ratio) is small (less than 0.1). The chemical reaction occurs stochastically for each cross-bridge. The stochastic properties of force generation of molecular motors are shown in an *in vitro* motility assay as described below. However, in living muscle, where more than 10^5 cross-bridges work at the same time in parallel within a single myofibril, the fluctuation of tension is smoothed so that a steady force is developed.

We confirmed that the average tension level is proportional to the average length of overlap between the thin and thick filaments. These results suggest that, at least under normal contracting conditions, tension develops in proportion to the number of interacting cross-bridges, so myosin II molecular motors in skeletal muscles function as independent force generators.[14] Under certain conditions intermediate between contraction and relaxation, SPOC phenomena appear; cooperative force generation is expected to exist where cross-bridges are not independent of each other.

NANOSCOPIC SYSTEM OF MOTILITY

Single Molecular Mechanics of Molecular Motors

Progress in microscopic techniques has meant that it is now possible to manipulate single protein molecules and detect movements and the force generation of single molecular motors on the order of nanometers and piconewtons, respectively. Structural changes in the myosin of muscle (myosin II) occurring during interaction with actin can be examined via microscopic technique: Finer et al.[23] and Miyata et al.[24] showed that stepwise movements of about 10 nm were occasionally observable at low ATP concentrations, probably accompanying ATP hydrolysis. At physiological ATP concentrations, myosin II is easily detached from actin, so that it is difficult to examine the elementary processes of single myosin II motors under physiological conditions.[23,25]

Veigel et al. measured the mechanical transitions made by a single myosin head (nonmuscle compound called myosin I that may correspond to each head or subfragment-1 (S1) of myosin II) while it was attached to actin.[26] They found that the working stroke of myosin I was divided into two distinct steps: 6 nm followed by 5.5 nm. The initial movement after the attachment of the myosin head to the actin took fewer than 10 ms. They could not detect two separate steps for skeletal muscle myosin S1, because the second step that might have occurred was too small or too fast to be observed. However, they found that the tension rose in 5 ms and fell within 1 ms; and concluded that the S1 working stroke occurs within 5 ms of the binding of myosin to actin.

In a different type of experiment, Kitamura et al. showed that myosin S1 moved along an actin filament with approximately 5.3-nm steps.[27] They suggested that this result supports the idea that the movement of molecular motors occurs without large conformational changes within the motors, but is attributable to the change of the interaction potential or rather to the structural changes of actin. While the former mechanism has much data supporting it, more data will be needed to provide a similar level of support for the latter mechanism.

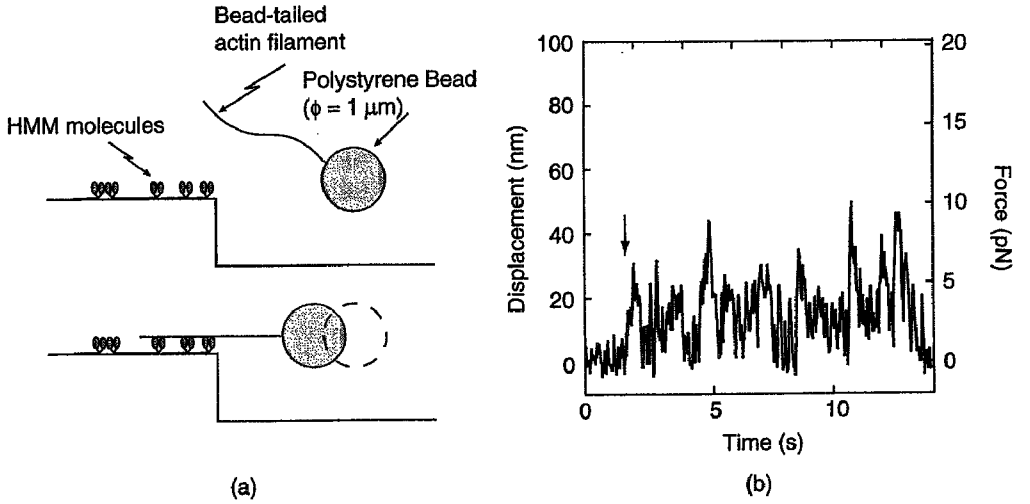

FIGURE 3.6 Tension measurements in an *in vitro* motility assay. (a) Schematic illustration of the *in vitro* motility assay system on a chemically-etched coverslip. HMM molecules adhere to the glass surface. A single actin filament attached to a polystyrene bead 1 μm in diameter is brought into contact with HMMs on the pedestal by optical tweezers. (b) Time course of the displacement of the trapped bead interacting with the HMMs. When the actin filament began to interact with the HMMs, the filament was pulled so that the bead was pulled away from the trap center (ordinate = 0) (indicated by arrow).

Comparison of Tension Measurement in *In Vitro* Motility Assay and A-Band Motility Assay

The microscopic measurement of tension development in an *in vitro* motility assay was first achieved by Kishino and Yanagida.[28] Using the same technique shown in Figure 3.6a, we measured the tension developed on a single actin filament by chymotryptic fragments of myosin (HMM) molecules adhered to a glass surface. As shown in Figure 3.6b, the developed tension fluctuated similarly to that obtained in the A-band motility assay (Figure 3.5b). The observation of such a large fluctuation in both systems is due to the small number of motors working on a single actin filament. These results demonstrate that the function of the molecular motor is stochastic at a single molecular level.

A substantial difference between the two systems is that the *in vitro* assay system is two-dimensional, whereas the A-band assay system is three-dimensional, so that actin filaments easily dissociate from the motor molecules under physiological ionic strength. The average tension per cross-bridge obtained at the lower ionic strength in the *in vitro* assay was less than half of that obtained at physiological ionic strength in the A-band motility assay. The smaller tension development in the *in vitro* assay was attributable to the two-dimensional arrangement of HMM molecules and also to the random orientation of the molecules. Further, in the A-band motility system, we found that stepwise movement (tension development) of an actin filament corresponded to the periodic arrangement of the cross-bridges within the thick filaments. Thus, we expect that the A-band motility assay system can bridge the gap between the regularly arranged organized structures of myofibrils and a randomly oriented single molecular system.

Temperature-Pulse Microscopy (TPM) in *In Vitro* Motility Assay: Response to Thermal Activation

A motor protein is a mechano-enzyme in that it responds to both mechanical perturbation and thermal activation. The way temperature affects the properties of muscle contraction has been studied. The rate of ATP hydrolysis is very sensitive to the temperature and increases about five times with a temperature increase from 22 to 30°C. The sliding velocity of actin filaments examined in an *in vitro* motility assay showed exactly the same temperature dependency, implying that the sliding movement is tightly coupled with the rate of ATP hydrolysis. On the other hand, the force in muscle fiber rose by a factor of two to three between 5 and 20°C, but only by a factor of about one or 1.5 between 20 and 40°C.

A protein is a biological machine that is too sensitive to bear a higher temperature than that for which it was originally designed, so it is highly desirable to restore the initial temperature as soon as measurements are finished in temperature-jump experiments to prevent thermal deterioration of biological samples and confirm the absence of deterioration. In a temperature-pulse microscopy (TPM) technique we devised, temperature (higher than 60°C at the peak) was elevated spatially (in a region of approximately 10 μm in diameter) and temporally (within about 10 ms) by illuminating a lump of metal particles using an infrared laser. A concentric temperature gradient was created around the lump of metal particles.[29] The speed of temperature elevation may be sufficiently high in TPM to make a square-wave temperature pulse with rise and fall times of less than 10 ms as the heat rapidly diffused into the surrounding medium (a coverslip and water) when the laser beam was cut. As temperature was monitored through the fluorescence intensity of the temperature-sensitive rhodamine phalloidin labeled to actin filaments in the sample chamber, temperature on a single actin filament could be imaged even when it was sliding. This TPM technique was applied to the thermal activation of the sliding movement and tension development of actomyosin motors in an *in vitro* motility assay.

At first we observed a reversible acceleration of the sliding movement by repetitive application of relatively long temperature pulses (0.5 to several seconds) and found that the sliding velocities reversibly reached two steady-state values within 1/30 s between 2 and 20 μm/s when the temperature jumped up and down between 18 and 40°C. Next, we examined how sliding movements responded to very short temperature pulses with durations of 1/16 to 1/128 s. When a laser pulse of 1/16 s was applied, an abrupt displacement of the actin filament occurred, which corresponded to a sliding velocity of about 26 μm/s. The average temperature during this illumination was estimated to be 45°C and the maximum temperature exceeded 60°C. When the duration of the temperature pulse was shortened, the degree of abrupt displacement correspondingly decreased, suggesting that steady-state sliding at the high temperature had been achieved at the shortest duration of 1/128 s.

As demonstrated by TPM, motor activity reversibly and quickly responded to thermal stimulus without being denatured, even when the temperature was raised above physiological level (up to double) if the duration was sufficiently short.

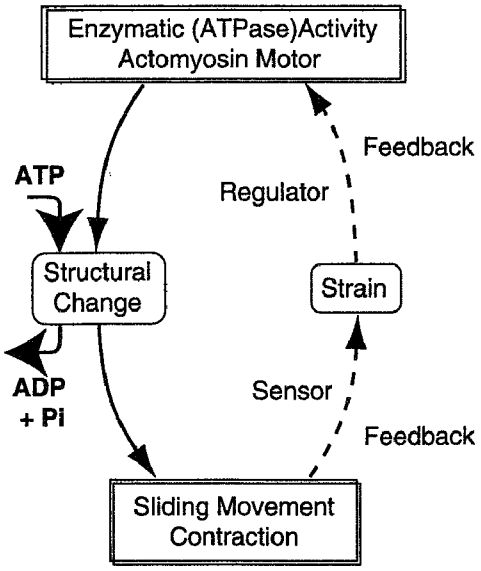

FIGURE 3.7 Spatiotemporal synchronization characteristic of a mechano-enzyme. A feedback loop is present between the enzymatic activity and the mechanical output in an assembly of nonprocessive motors.

CONCLUDING REMARKS

Molecular motors are mechano-enzymes that perform mechanical work using chemical energy produced by hydrolysis of ATP. Molecular motors in muscles work only in assemblies in which feedback loops are present.[30] As shown in Figure 3.7, structural changes of molecular motors occur accompanied by ATP hydrolysis and tension is generated, which results in force generation and sliding movement of the myofilament (shown by solid arrows).

Contraction in one part of a muscle produces strains on other motors located nearby (shown by dashed arrows), resulting in modulation of the enzymatic activity of the assembly of motors. Thus, this spatiotemporal synchronization within a protein assembly is characteristic of the mechano-enzymes, i.e., molecular motors of muscles. In essence, molecular motors of muscles might have been designed in nature as motors that respond quickly only to electric signals and mechanical stimuli from outside when working in assemblies. The next challenge in muscle research is to clarify the physical and chemical principles (corresponding to the physical principles or thermodynamics of a man-made machine) that govern force generation and synchronization of molecules.

REFERENCES

1. Engel, A.G. and Franzini-Armstrong, C., *Myology*, 2nd ed., McGraw Hill, New York, 1994.
2. Littlefield, R., Almenar-Queralt, A., and Fowler, V.M., Actin dynamics at pointed ends regulates thin filament length in striated muscle, *Nature Cell Biol.*, 3, 544–551, 2001.

3. Huxley, A.F. and Niedergerke, R., Interference microscopy of living muscle fibres, *Nature*, 173, 971–973, 1954.
4. Huxley, H.E. and Hanson, J., Changes in the cross-striations of muscle during contraction and stretch and their structural interpretation, *Nature*, 173, 973–976, 1954.
5. Huxley, A.F. and Simmons, R.M., Proposed mechanism of force generation in striated muscle, *Nature*, 233, 533–538, 1971.
6. Fujime, S., Quasi-elastic light scattering from solutions of macromolecules. II. Doppler broadening of light scattered from solutions of semi-flexible polymers, F-actin, *J. Phys. Soc. Jpn.*, 29, 751–759, 1970.
7. Fujime, S. and Ishiwata, S., Dynamic study of F-actin by quasielastic scattering of laser light, *J. Mol. Biol.*, 62, 251–265, 1971.
8. Oosawa, F., Fujime, S., Ishiwata, S., and Mihashi, K., Dynamic property of F-actin and thin filament, *Cold Spring Harb. Symp. Quant. Biol.*, 37, 277–286, 1973.
9. Ishiwata, S., Study on Muscle and Muscle Proteins: Principal Dynamic Properties of Actin Filament Studied by Quasielastic Scattering of Laser Light, Ph.D. thesis, Nagoya University, Japan, 1975.
10. Ishiwata, S. and Fujime, S., Effect of calcium ions on the flexibility of reconstituted thin filaments of muscle studied by quasielastic scattering of laser light, *J. Mol. Biol.*, 68, 511–522, 1972.
11. Yanagida, T., Nakase, M., Nishiyama, K., and Oosawa, F., Direct observation of motion of single F-actin filaments in the presence of myosin, *Nature*, 307, 58–60, 1984.
12. Fujime, S., Quasi-elastic scattering of laser light: a new tool for the dynamic study of biological macromolecules, *Adv. Biophys.*, 3, 1–43, 1972.
13. Isambert, H., Venier, P., Maggs, A.C., Fattoum, A., Kassab, R., Pantaloni, D., and Carlier, M.F., Flexibility of actin filaments derived from thermal fluctuations, *J. Biol. Chem.*, 19, 11437–11444, 1995.
14. Huxley, A.F., Muscle structure and theories of contraction, *Progr. Biophys. Biophys. Chem.*, 7, 255–318, 1957.
15. Higuchi, H., Yanagida, T., and Goldman, Y.E., Compliance of thin filaments in skinned fibers of rabbit skeletal muscle, *Biophys. J.*, 69, 1000–1010, 1995.
16. Huxley, H.E., Stewart, A., Sosa, H., and Irving, T.C., X-ray diffraction measurements of the extensibility of actin and myosin filaments in contracting muscle, *Biophys. J.*, 67, 2411–2421, 1994.
17. Wakabayashi, K., Sugimoto, Y., Tanak, Y., Ueno, Y., Takezawa, Y., and Amemiya, Y., X-ray diffraction evidence for the extensibility of actin and myosin filaments during muscle contraction, *Biophys. J.*, 67, 2422–2435, 1994.
18. Fukuda, N., Sasaki, D., Ishiwata, S., and Kurihara, S., Length dependence of tension generation in rat skinned cardiac muscle: role of titin in the Frank–Starling mechanism of the heart, *Circulation*, 104, 1639–1645, 2001.
19. Granzier, H. and Irving, T.C., Passive tension in cardiac muscle: contribution of collagen, titin, microtubules, and intermediate filaments, *Biophys. J.*, 68, 1027–1044, 1995.
20. Huxley, H.E., The mechanism of muscular contraction, *Science*, 164, 1356–1365, 1969.
21. Corrie, J.E.T., Brandmeier, B.D., Ferguson, R.E., Trentham, D.R., Kendrick-Jones, J., Hopkins, S.C., Van der Heide, U.A., Goldman, Y.E., Sabido-David, C., Dale, R.E., Criddle, S., and Irving, M., Dynamic measurement of myosin light-chain-domain tilt and twist in muscle contraction, *Nature*, 400, 425–430, 1999.

22. Suzuki, M., Fujita, H., and Ishiwata, S., New aspects of muscle contraction from the A-band motility assay system, *Biophys. J.*, 82, 362a, 2002 (Abstr.).
23. Finer, J.T., Simmons, R.M., and Spudich, J.A., Single myosin molecule mechanics: piconewton forces and nanometre steps, *Nature*, 368, 113–119, 1994.
24. Miyata, H., Hakozaki, H., Yoshikawa, H., Suzuki, N., Kinosita, K., Jr., Nishizaka, T., and Ishiwata, S., Stepwise motion of an actin filament over a small number of heavy meromyosin molecules is revealed in an *in vitro* motility assay, *J. Biochem. (Tokyo)*, 115, 644–647, 1994.
25. Miyata, H., Yoshikawa, H., Hakozaki, H., Suzuki, N., Furuno, T., Ikegami, A., Kinosita, K., Jr., Nishizaka, T., and Ishiwata, S., Mechanical measurements of single actomyosin motor force, *Biophys. J.*, 68, 286S–289S, 1995.
26. Veigel, C., Coluccio, L.M., Jontes, J.D., Sparrow, J.C., Milligan, R.A., and Molloy, J.E., The motor protein myosin-I produces its working stroke in two steps, *Nature*, 398, 530–533, 1999.
27. Kitamura, K., Tokunaga, M., Iwane, A.H., and Yanagida, T., A single myosin head moves along an actin filament with regular steps of 5.3 nanometres, *Nature*, 397, 129–134, 1999.
28. Kishino, A. and Yanagida, T., Force measurements by micromanipulation of a single actin filament by glass needles, *Nature*, 334, 74–76, 1988.
29. Kato, H., Nishizaka, T., Iga, T., Kinosita, K., Jr., and Ishiwata, S., Imaging of thermal activation of actomyosin motors, *Proc. Natl. Acad. Sci. USA*, 96, 9602–9606, 1999.
30. Shimamoto, Y., Microscopic Analysis of Inter-molecular Synchronization Observed in the Assembly of Molecular Motors, M.S. thesis, Waseda University, Tokyo, Japan, 2003.

J Physiol 556.2 (2004) pp 637–649

The effect of tropomyosin on force and elementary steps of the cross-bridge cycle in reconstituted bovine myocardium

Hideaki Fujita[1,2], Xiaoying Lu[1], Madoka Suzuki[2], Shin'ichi Ishiwata[2,3] and Masataka Kawai[1]

[1]*Department of Anatomy and Cell Biology, The University of Iowa, Iowa City, Iowa 52242, USA*
[2]*Department of Physics, School of Science and Engineering, and* [3]*Advanced Research Institute for Science and Engineering, Waseda University, 3-4-1 Okubo, Shinjuku-ku, Tokyo 169-8555, Japan*

The role of tropomyosin (Tm) in the elementary steps of the cross-bridge cycle in bovine myocardium was investigated. The thin filament was selectively removed using gelsolin (thin filament severing protein), and the actin filament was reconstituted from G-actin. Tm was further reconstituted without troponin (Tn), and the kinetic constants of the elementary steps of the cross-bridge cycle were deduced using sinusoidal analysis at pCa $\leq$ 4.66, pH 7.00, and 25°C. The association constant of MgATP to cross-bridges (K_1) after reconstitution of Tm was 20.7 $\pm$ 2.3 mM^{-1}, which was about 2 $\times$ the control (untreated) myocardium (9.1 $\pm$ 1.3 mM^{-1}). Following reconstitution of Tm, the equilibrium constant of the cross-bridge detachment step (K_2), the phosphate (P_i) association constant (K_5) and the equilibrium constant of the force-generation step (K_4), which significantly changed in the actin filament-reconstituted myocardium, recovered to those of the control myocardium. Active tension after reconstitution of Tm was 0.69 $\times$ the control myocardium, a value between the control (1.00 $\times$) and the actin filament-reconstituted myocardium (0.59 $\times$). Tm-reconstituted myocardium was further reconstituted with Tn, and the effect of MgATP on the rate constants (K_1, K_2) was studied. Following reconstitution with Tn, the myocardium regained the Ca^{2+} sensitivity and the active tension became 0.83 $\times$ the control myocardium. In addition, K_1 recovered to the value of the control myocardium with Tn reconstitution. These results indicate that both Tm and Tn enhance the force generated by each cross-bridge, and that Tm is primarily responsible for the change in the kinetic constants of the elementary steps of the cross-bridge cycle.

(Resubmitted 17 December 2003; accepted after revision 20 January 2004; first published online 23 January 2004)
Corresponding author M. Kawai: Department of Anatomy and Cell Biology, College of Medicine, The University of Iowa, Iowa City, IA 52242, USA. Email: masataka-kawai@uiowa.edu

It has been known for some time that force generation in muscle is accomplished by a cyclic interaction between the myosin molecule, the main component of the thick filament, and the actin molecule, the main component of the thin filament. Myosin and actin convert the chemical energy stored in ATP to mechanical work, resulting in a sliding motion between the thick and thin filaments (Huxley & Niedergerke, 1954; Huxley & Hanson, 1954). In skeletal and cardiac muscles, the Ca^{2+}-dependent regulatory switch, the tropomyosin (Tm)–troponin (Tn) system, is located on the thin filament (Ebashi & Endo, 1968). Tm is a filamentous dimeric protein which spans seven actin monomers along the thin filament with one Tn complex attached to the Tm dimer. In the steric blocking mechanism, Tm blocks the myosin binding site on the actin filament when Ca^{2+} is absent, resulting in an inhibition of the actomyosin interaction (Haselgrove, 1973; Huxley, 1973). The binding of Ca^{2+} to Tn removes this inhibition by azimuthal movement of Tm, allowing myosin to interact freely with actin (Lehman *et al.* 1994, 1995).

Although the steric blocking mechanism is supported by many lines of evidence, the regulation of actomyosin interaction by a simple movement of Tm from a blocked position to an open position cannot explain some of the biochemical observations (McKillop & Geeves, 1993; Tobacman & Butters, 2000). While it has been shown in regulated actin that the ATP hydrolysis rate is inhibited by 96% in the absence of Ca^{2+}, the association constant of myosin subfragment 1 (S1) to actin is almost unchanged regardless of the presence of Ca^{2+} (Chalovich *et al.*

DOI: 10.1113/jphysiol.2003.059956

1981; Chalovich & Eisenberg, 1982). Covalently cross-linked acto-S1 still possesses Ca^{2+} regulation of the ATP hydrolysis rate when Tm and Tn are present (King & Greene, 1985). These findings indicate that the Tm–Tn system does not act just as a shield between actin and myosin, but serves a more complex role that alters actomyosin interaction and concomitant cross-bridge kinetics. Furthermore, a partial extraction of TnC is known to alter the kinetics of the cross-bridge cycle by promoting ATP binding and the rate of cross-bridge detachment and suppressing the rate of force generation (Zhao *et al.* 1996). Actomyosin ATPase activity is known to increase when Tm is added (Bremel *et al.* 1972; Murray *et al.* 1980). These observations also indicate that the Tm–Tn system modulates muscle contraction via a more complex mechanism.

Recently, we have demonstrated, using the thin filament-reconstitution method, that the Tm–Tn system alters the kinetic constants of the elementary steps of the cross-bridge cycle and increases the force supported by each cross-bridge in bovine myocardium (Fujita *et al.* 2002). In our experiments, the thin filament in bovine myocardium was selectively removed by plasma protein gelsolin, and the actin filament was reconstituted by adding purified G-actin in a polymerizing condition (Fujita *et al.* 1996). The actin filament-reconstituted myocardium generates active tension in a Ca^{2+}-insensitive manner because of the lack of regulatory proteins. This tension was about 2/3 of the control myocardium. The thin filament with full Ca^{2+} sensitivity can be reconstituted by adding native tropomyosin (nTm: a complex of Tm and Tn) to the actin filament-reconstituted myocardium. This reconstitution resulted in a larger tension similar to that of control myocardium (Fujita *et al.* 2002). Because in our previous studies, the regulatory system was reconstituted as nTm, it remained to be seen whether the effect was caused by Tm, Tn, or both. In this study, we reconstituted Tm and Tn sequentially after reconstitution of the actin filament. We found that Tm is primarily responsible for the change in the kinetic constants that we observed using nTm (except for the MgATP association constant), and that both Tm and Tn contribute to an increase of force supported by each cross-bridge.

Methods

Solutions

The relaxing solution (Rx) contained (mM): 6 EGTA, 2.2 MgATP, 5 ATP, 8 P_i, 41 NaProp (Prop = propionate), 75 KProp, 10 Mops (3-(*N*-morpholino) propane sulphonic acid), and 40 BDM (2,3-butanedione 2-monoxime). The rigor solution (Rg) contained 8 P_i, 55 NaProp, 122 KProp, and 10 Mops. Experimental solutions are indicated by *m*Sn*n*P, where *m* represents the millimolar concentration of $MgATP^{2-}$, and *n* represents the millimolar concentration of phosphate (P_i). The 5S0P solution contained (mM): 6 CaEGTA, 5.83 MgATP, 1.36 ATP, 15 phosphocreatine (CP), 1 NaProp, 92 KProp, 10 NaN_3, and 10 Mops. The 5S32P solution contained (mM): 6 CaEGTA, 5.7 MgATP, 1.36 ATP, 15 CP, 32 P_i, 1 NaProp, 17 KProp, 10 NaN_3, and 10 Mops. The 0S8P solution contained (mM): 6 CaEGTA, 0.85 $MgProp_2$, 15 CP, 8 P_i, 15 NaProp, 88 KProp, 10 NaN_3, and 10 Mops. The 5S8P solution contained (mM): 6 CaEGTA, 5.8 MgATP, 1.36 ATP, 15 CP, 8 P_i, 1 NaProp, 73 KProp, 10 NaN_3, and 10 Mops. The –Ca solution (5S8P solution without Ca) contained (mM): 6 EGTA, 5.9 MgATP, 1.25 ATP, 15 CP, 8 P_i, 1 NaProp, 73 KProp, 10 NaN_3, and 10 Mops. The 5S8P solution is also called the standard activating solution. The pCa of all activating solutions was ≤ 4.66, pH was adjusted to 7.00 by KOH, the Mg^{2+} concentration was 0.5 mM, the total sodium concentration was 55 mM, ionic strength was adjusted to 200 mM by NaProp and KProp, and all activating solutions contained 320 units ml^{-1} (=0.64 mg ml^{-1}) creatine kinase (CK). All solution components were added from neutral stock solutions: EGTA as K_2H_2EGTA, CaEGTA as $K_2CaEGTA$, P_i as $K_{1.5}H_{1.5}PO_4$, MgATP as Na_2MgATP, ATP as $Na_2K_{1.7}H_{0.3}ATP$, and CP as Na_2CP. Multiple equilibria were assumed, and individual concentrations of multivalent ionic species were calculated using our computer program with the following apparent association constants at pH 7.0 (log values): CaEGTA, 6.28; MgEGTA, 1.61; CaATP, 3.70; MgATP, 4.00; CaCP, 1.15; MgCP, 1.30. The experiments were performed at 25°C.

Na_2CP, Na_2H_2ATP, Mops and H_4EGTA were purchased from Sigma Chemical Co. (St Louis, MO, USA); $CaCO_3$, MgO, NaOH, KOH, KH_2PO_4, K_2HPO_4, NaN_3 and propionic acid were purchased from Fisher Scientific Co. (Itasca, IL, USA); creatine kinase was purchased from Boehringer Mannheim (Indianapolis, IN, USA).

Muscle fibres and proteins

Bovine hearts were obtained from a slaughterhouse within 15 min of death, and immediately cooled with ice. The muscle bundles (~2 mm in diameter, ~10 mm in length) were excised from a straight portion of the ventricular papillary muscles and incubated in the sodium-skinning solution (mM): 2 DTT (dithiothreitol), 30 BDM, 10 EGTA, 5 ATP, 2 MgATP, 122 NaProp and 10 Mops (pH 7.0) for 3 h at 0°C. The sodium-skinning solution was used to

minimize contraction. For further skinning, the solution was replaced with potassium-skinning solution containing (mM): 2 DTT, 30 BDM, 10 EGTA, 5 ATP, 2 MgATP, 122 KProp and 10 Mops (pH 7.0), and stored overnight at 0°C. BDM and EGTA were used to minimize force generation. The solution was further replaced with one containing 50% (v/v) glycerol and (mM): 2 DTT, 30 BDM, 10 EGTA, 5 ATP, 2 MgATP, 122 KProp and 10 Mops (pH 7.0) and stored at 0°C. The solution was replaced once again the next morning, and the muscle bundles were stored at a low temperature (−20°C).

G-actin was extracted and purified from acetone powder (Kondo & Ishiwata, 1976) of rabbit white skeletal muscles as described by Spudich & Watt (1971). G-actin was stored at 0°C and used within 2 weeks of extraction. Tm and Tn were prepared from bovine cardiac muscle as described by Ebashi *et al.* (1968) and purified using DEAE Sephadex A-25 (Pharmacia, Sweden). Tm was further purified as described by Yamaguchi *et al.* (1974). Bovine plasma gelsolin was prepared as described by Kurokawa *et al.* (1990).

Selective removal and reconstitution of actin filament were performed as reported by Fujita *et al.* (1996, 2002). Tm and Tn were reconstituted as reported by Fujita & Ishiwata, (1999).

Experimental procedure and deduction of kinetic constants

A strip of myocardium (90–160 μm in width and 2 mm in length) was dissected from a skinned muscle bundle. One end of the myocardium was connected to a tension transducer via a stainless steel wire (210 μm in diameter), and the other end was connected to a length driver via another stainless steel wire. Nail polish was used to glue the ends of myocardium to the wires. The myocardium was stretched until a small passive tension was observed, when the length (L_0) of the myocardium was determined. The width was measured under a dissecting microscope (20 ×) and the cross-sectional area was estimated assuming a circular cross-section. At this stage, the myocardium was chemically skinned further in the relaxing solution containing 1% (v/v) Triton X-100 for 20 min.

Two muscle models (Tm-reconstituted and Tm–Tn-reconstituted myocardium) were maximally activated in the presence of saturating Ca^{2+} in a bath in which the temperature was controlled at 25°C. A 0.25% L_0 peak-to-peak sinusoidal waveform at 18 discrete frequencies between 0.13 and 100 Hz was digitally synthesized in a 386 CPU PC (Industrial Computer Source, San Diego, CA, USA) that controlled the length driver via a 14-bit DAC. Tension and length signals were simultaneously sampled by two 16-bit A/D converters and complex modulus data $Y(f)$ were calculated as the ratio of the force change to the length change in the frequency domain. The complex modulus data observed during relaxation was subtracted. The complex modulus data were resolved into two exponential processes (B and C) by fitting the data to eqn (1) by minimizing the sum of modulus squares (Kawai & Brandt, 1980; Wannenburg *et al.* 2000):

$$Y(f) = H - \underset{\text{Process B}}{B/(1 + b/fi)} + \underset{\text{Process C}}{C/(1 + c/fi)} \quad (1)$$

where $i = \sqrt{-1}$. Uppercase letters B and C represent their respective magnitudes (amplitudes) and lower case letters b and c represent the characteristic frequencies of the respective processes. $2\pi b$ and $2\pi c$ are the apparent rate constants of the respective processes. Process B corresponds to phase 3, process C corresponds to phase 2, and $Y(\infty)$ corresponds to phase 1 of tension transients of step analysis (Huxley & Simmons, 1971). In relaxed and rigor muscle fibres, these exponential processes were absent, indicating that these processes are signatures of cycling cross-bridges. $Y(\infty)$ is referred to 'stiffness' in this paper. The complex modulus data were corrected by those of the rigor condition.

The results were analysed based on scheme 1, where A = actin, M = myosin, S = MgATP, D = MgADP, and

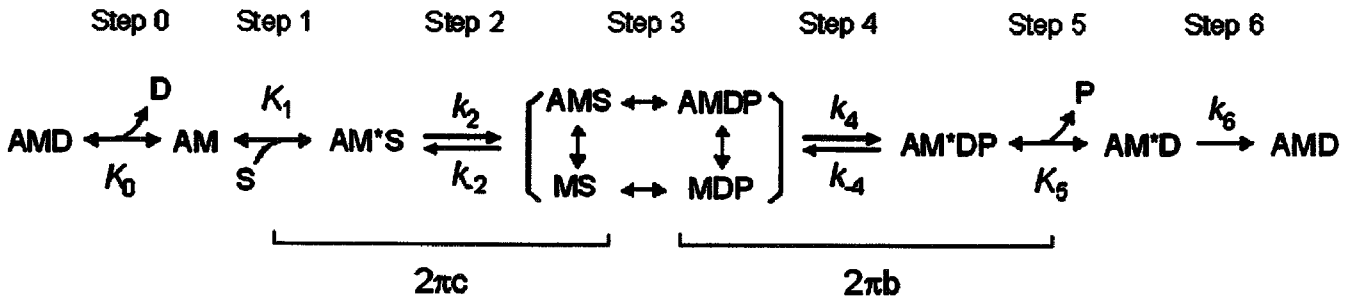

Scheme 1.
Elementary steps of the cross-bridge cycle

P = P_i = phosphate. The kinetic constants of elementary step 1 and 2 of the cross-bridge cycle were determined by fitting the MgATP dependence of $2\pi c$ to eqn (2) by minimizing the sum of squares (Kawai & Halvorson, 1989).

$$2\pi c = k_2K_1S/(1 + K_1S) + k_{-2} \quad (2)$$

The kinetic constants of elementary steps 4 and 5 of the cross-bridge cycle were determined by fitting the P_i dependence of $2\pi b$ to eqn (3) by minimizing the sum of squares (Kawai & Halvorson, 1991).

$$2\pi b = \sigma k_4 + k_{-4}K_5P/(1 + K_5P) \quad (3)$$

where

$$\sigma = K_2K_1S/\{1 + (1 + K_2)K_1S\} \quad (4)$$

In these equations, S and P indicate their respective concentrations: S = [MgATP] and P = [P_i]. K_1 and K_2 obtained from the MgATP study and $S = 5$ mM were used for calculation of σ in eqn (4). Details of the sinusoidal analysis technique have been published (Kawai & Brandt, 1980).

SDS-gel electrophoresis

Approximately 10 muscle fibres, each similar in size to those for mechanical measurements, were placed in the corner (500 μl) of a small, tilted petri dish and followed through the extraction and reconstitution protocol. Five petri dishes (50 fibres) corresponding to 5 different kinds of treatment were used. They were then solubilized and electrophoresed at 20 mA for about 90 min at 22°C using acrylamide gradient (8–16%) ready gels (Tris-HCl, 15 wells, Cat. No. 161-1223, Bio-Rad), as described by Laemmli (1970). Gels were stained with Coomassie Brilliant Blue R250.

Confocal fluorescence microscopy

Tetramethyl rhodamine-5-iodoacetamide (Rh-IA) and fluorescein phalloidin (Fl-Ph) were purchased from Molecular Probes (Eugene, OR, USA). Rh-IA-labelled Tm was prepared according to the method of Ishii & Lehrer (1990). The thin filament was first removed by treatment with gelsolin for 80 min, and then the actin filament was reconstituted for a total of 28 min (7 min × 4). Then, the myocardium was incubated in relaxing solution containing Rh-IA-labelled Tm for 12 h. Next, the myocardium was fixed with relaxing solution containing 1% formaldehyde for 30 min and stained with 6.6 μM Fl-Ph in relaxing solution for 5 h. For observation, the myocardium was mounted on a cover slip and washed with relaxing solution containing 4.5 mg ml^{-1} glucose, 0.22 mg ml^{-1} glucose oxidase, 0.036 mg ml^{-1} catalase, and 10 mM DTT. This preparation was observed under a laser scanning confocal microscope equipped with 25 mW Ar laser at 488 nm (Fluoview-IX/AR; Olympus Co., Tokyo). No crossover between the fluorescence images of rhodamine (> 610 nm) and fluorescein (510–540 nm) was detected.

Results

Removal and reconstitution of the thin filament

Figure 1 shows SDS-PAGE of myocardium at each step of reconstitution. In control myocardium (lane 1), thick filament proteins, myosin heavy chain and myosin light chains 1 and 2, can be seen. Also seen are thin filament proteins, actin, TnT, Tm and TnI. TnC could not be stained with the method we used. In gelsolin-treated myocardium (lane 2), the amount of thin filament proteins decreased significantly, but the amount of MLC1 and MLC2 remained about the same. In actin filament-reconstituted myocardium (lane 3), the amount of actin increased significantly. In Tm-reconstituted myocardium (lane 4), the amount of Tm increased significantly. In Tm–Tn-reconstituted myocardium (lane 5), the amount

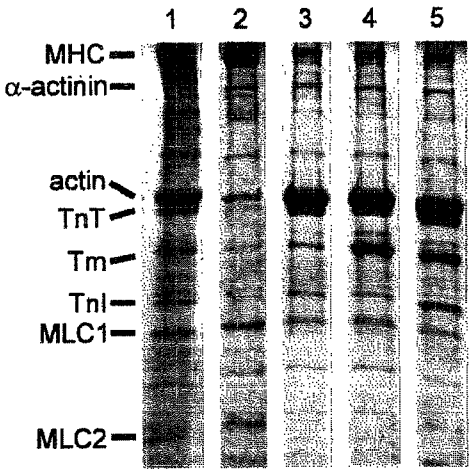

Figure 1. SDS-PAGE of myocardium at each step of reconstitution

Lane 1, control myocardium; lane 2, gelsolin-treated myocardium; lane 3, actin filament-reconstituted myocardium; lane 4, Tm-reconstituted myocardium; lane 5, Tm–Tn-reconstituted myocardium. The Tm-reconstituted myocardium (lane 4) was first treated with gelsolin, then actin filament was reconstituted before Tm was reconstituted. The Tm–Tn-reconstituted myocardium (lane 5) was first treated with gelsolin, then actin filament was reconstituted, followed by sequential reconstitution of Tm and Tn. In lane 2, gelsolin is visible just below the α-actinin band. Lane 1 is from one gel, and lanes 2–5 are from another gel with a different order. Abbreviations: MHC, myosin heavy chain; Tm, tropomyosin; TnT, troponin T; TnI, troponin I; MLC1, myosin light chain 1; MLC2, myosin light chain 2.

of TnT and TnI increased significantly, hence all thin filament proteins were observed here. In lane 2, some residual actin (~20% of lane 1) can be seen, although a similarly treated preparation did not develop tension (Fig. 3*B*). This residual actin is presumably located within and/or near to the Z-line, but does not overlap with the thick filament. This amount of actin is essential for a successful reconstitution of the actin filament (Fujita *et al.* 2002).

Figure 2 shows confocal fluorescent microscope images of myocardium reconstituted with Rh-IA-labelled Tm and stained with Fl-Ph. The distribution of Fl fluorescence (green), indicating the actin filament, shows a repetitive pattern of bright and dark bands (Fig. 2*A*). The centre of the bright band corresponds to the Z-line. The distribution of Rh fluorescence (red), indicating Tm, similarly shows a repetitive pattern (Fig. 2*B*), and the banding pattern appears to be identical to that of the actin filament. To demonstrate colocalization of Tm and the actin filament, both images were superimposed in Fig. 2*C*, which shows that Tm was homogeneously incorporated onto the actin filament.

Figure 3*A–E* shows slow pen traces of isometric tension at each step of the thin filament extraction and reconstitution. The myocardium was initially activated with the 5S8P solution and the standard active tension was measured at 25°C (Fig. 3*A*). Then the myocardium was treated with gelsolin for 100 min (Fig. 3*B*, Ge) at 2°C in the solution that contained (mM): 117 KCl, 4.25 $MgCl_2$ (2.2 mM free Mg^{2+}), 2.2 ATP (2.0 $MgATP^{2-}$), 2.0 EGTA, 20 Mops (pH 7.0), 2 $CaCl_2$, 40 BDM, and 0.3 mg ml^{-1} gelsolin. BDM was used to suppress tension development during the gelsolin treatment, because Ca^{2+} is a cofactor for this protein and needed for the extraction. After the gelsolin treatment, active tension did not develop in the standard activating solution (Fig. 3*B*), demonstrating a removal of the thin filament.

The myocardium was then immersed in the actin-polymerizing solution containing (mM): 80 KI, 4 $MgCl_2$, 4 ATP, 4 EGTA, 40 BDM, 20 KP_i (pH 7.0), and 1.0 mg ml^{-1} G-actin at 2°C to reconstitute the actin filament (Fig. 3*C*, Ac). The actin-polymerizing solution was replaced every 7 min to avoid spontaneous nucleation in the muscle chamber. Similarly, KI instead of KCl was used to deter the nucleation (Funatsu *et al.* 1994). Actin polymerization was performed for a total of 28 min (=7 min × 4). Subsequently, the myocardium was tested with the –Ca solution (5S8P solution without Ca^{2+}), and then with the Ca^{2+} solution (5S8P) at 25°C (Fig. 3*C*). Because of the lack of regulatory proteins, this myocardium developed the same tension regardless of the presence of Ca^{2+}. Active tension after reconstitution of actin filament was 59 ± 2% (± S.E.M., $n = 17$) of the control myocardium when tested by the standard activating solution (5S8P) that had 8 mM P_i. Relaxation was achieved by including 40 mM BDM in the relaxing solution.

To reconstitute Tm, actin filament-reconstituted myocardium was immersed in the relaxing solution containing 1.2 mg ml^{-1} Tm for 12 h at 2°C (Fig. 3*D*, Tm). Tm-reconstituted myocardium developed active tension regardless of the presence of Ca^{2+} (Fig. 3*D*). At 25°C, this tension was generally greater than that of actin filament-reconstituted myocardium: active tension after Tm reconstitution was 69 ± 6% ($n = 17$) of control myocardium, an increase of 10% (=69%-59%) over the actin filament-reconstituted myocardium.

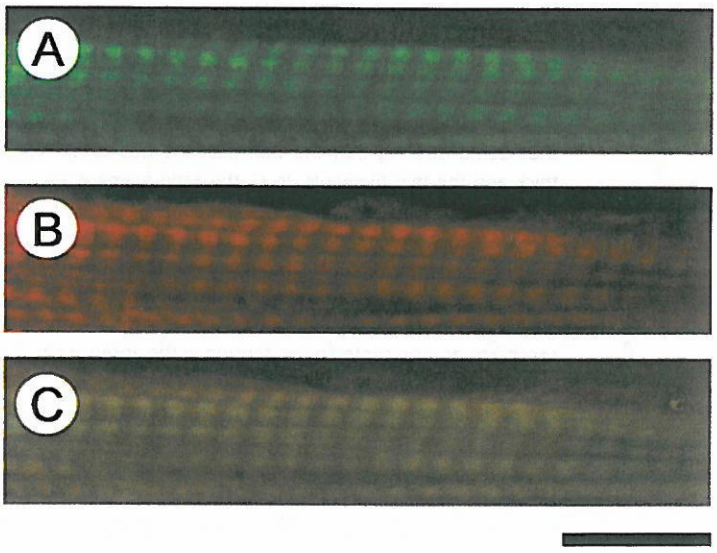

Figure 2. Confocal fluorescence micrographs of bovine myocardium reconstituted with Rh-IA-labelled Tm and labelled with Fl-Ph
The thin filament was first removed by gelsolin, and sequentially reconstituted with actin, followed by Rh-IA-labelled Tm. The preparation was then treated with Fl-conjugated phalloidin to label the actin filament. *A*, Fl fluorescence showing the distribution of the actin filament; *B*, Rh fluorescence showing the distribution of Tm; *C*, colocalization of the actin filament and Tm. Calibration bar, 10 μm.

The myocardium was further reconstituted with Tn by immersing it in the relaxing solution containing 1.0 mg ml^{-1} Tn at 2°C (Fig. 3*E*, Tn). As shown in this figure, 3 h reconstitution with Tn was not adequate, because ~1/3 of Ca^{2+}-insensitive tension developed, and an additional 2 h was needed to fully restore the Ca^{2+} sensitivity; the Tm–Tn-reconstituted myocardium did not develop active tension when Ca^{2+} was absent, but it did develop active tension when Ca^{2+} was present (Fig. 3*E*). This observation indicates that Tm and Tn were fully reconstituted. With the reconstitution of Tn, active tension increased to 83 ± 9% ($n = 7$) of control myocardium, an increase of 14% (=83% – 69%) over the Tm-reconstituted myocardium.

Effect of MgATP on the exponential process C

Figure 3*F–I* shows isometric tension of another myocardium as the thin filament was extracted and reconstituted. In this series of experiments, the reconstitution was only through Tm, and the MgATP and the P_i studies were performed. The purpose of these experiments was to investigate whether the larger force observed in the presence of Tm than in its absence is related to a larger force per cross-bridge or to a larger number of force-generating cross-bridges. The effect of MgATP on exponential process *C* on Tm-reconstituted and Tm–Tn-reconstituted myocardium was studied in the

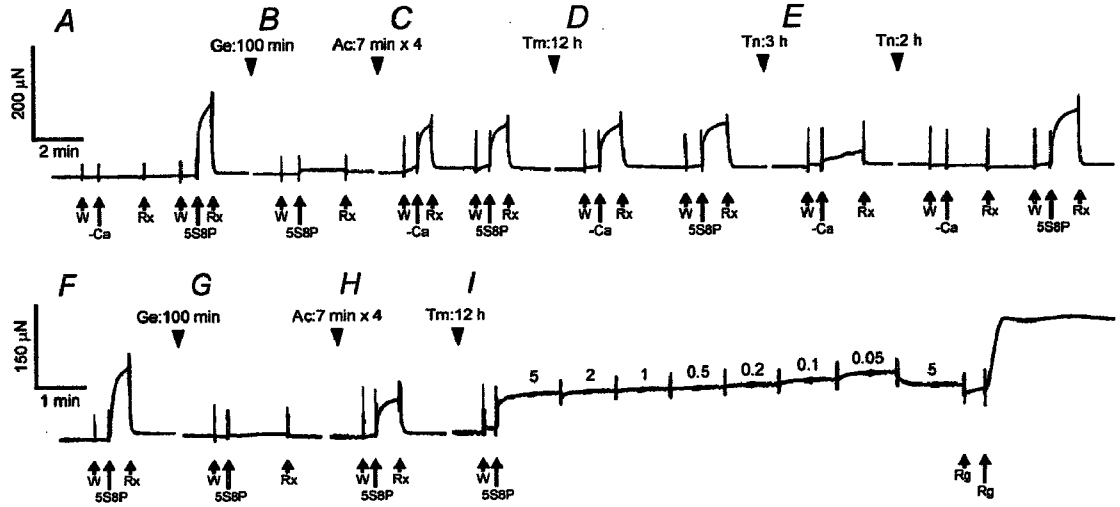

Figure 3. Slow pen traces of isometric tension at each step of reconstitution
A–E, a slow pen trace of isometric tension at each step of removal and reconstitution of the thin filament in one myocardium. In *A*, a control (untreated) myocardium was first tested with a solution without Ca^{2+} (–Ca) to demonstrate that active tension did not develop without Ca^{2+}. Then the myocardium was treated with the standard activating solution (5S8P, pCa 4.66) at 25°C. Before activation, the myocardium was immersed in the same 5S8P solution at 0°C (labelled W) to wash out BDM, which was present in the Rx solution. The myocardium did not develop active tension in W because of the low temperature. In *B*, the myocardium was treated by gelsolin (Ge) for 100 min, and then immersed in the 5S8P solution at 25°C with the result that no tension developed, thus demonstrating that the thin filament was sufficiently removed so that there is no overlap between the thick and the thin filaments. In *C*, the actin filament was reconstituted for 28 min over four sessions (Ac), then the myocardium was immersed in the solution without Ca^{2+} (–Ca) followed by the solution with Ca^{2+} (5S8P) at 25°C. Both treatments resulted in the same active tension development, demonstrating the absence of the regulatory system. In *D*, Tm was reconstituted for 12 h (Tm). Once again, the active tension developed irrespective of Ca^{2+}. In *E*, reconstitution with Tn was first performed for 3 h; this turned out to be insufficient, as can be seen by the Ca^{2+}-insensitive tension. An additional reconstitution for 2 h was necessary to fully restore the Ca^{2+} sensitivity, as represented by no tension in the absence of Ca^{2+}, and tension levels close to the original tension (*A*) in the presence of Ca^{2+}. *F–I*, another myocardium was similarly treated as in *A–D*, resulting in reconstitution of the actin filament with Tm. In this myocardium, the complex modulus data were collected at 7 different MgATP concentrations (0.05–5 mM), as indicated in *I*. The standard activation at 5 mM MgATP (5S8P) was repeated to detect any decrease in active tension; the preparation was discarded if more than 20% of tension was lost. This activation was followed by an induction of the rigor state with the Rg solution. In all experiments, relaxation was obtained in the solution containing 40 mM BDM (Rx) at 0°C. All activations including rigor (Rg) were performed at 25°C.

range of 0.05–5 mM in the presence of 8 mM P_i under the maximal Ca^{2+}-activating condition (pCa $\leq$ 4.66) and as shown in Fig. 3*I*. This study characterizes the elementary steps of the MgATP binding step 1 and subsequent cross-bridge detachment step 2 in Scheme 1. Figure 4*A* shows the Nyquist plot of the complex modulus $Y(f)$ in the Tm-reconstituted myocardium activated at three different MgATP concentrations (0.1 mM, 0.5 mM, 5 mM). These plots and the MgATP effect are similar to other myocardial systems reported earlier (Kawai *et al.* 1993; Zhao & Kawai, 1996; Wannenburg *et al.* 2000; Fujita *et al.* 2002).

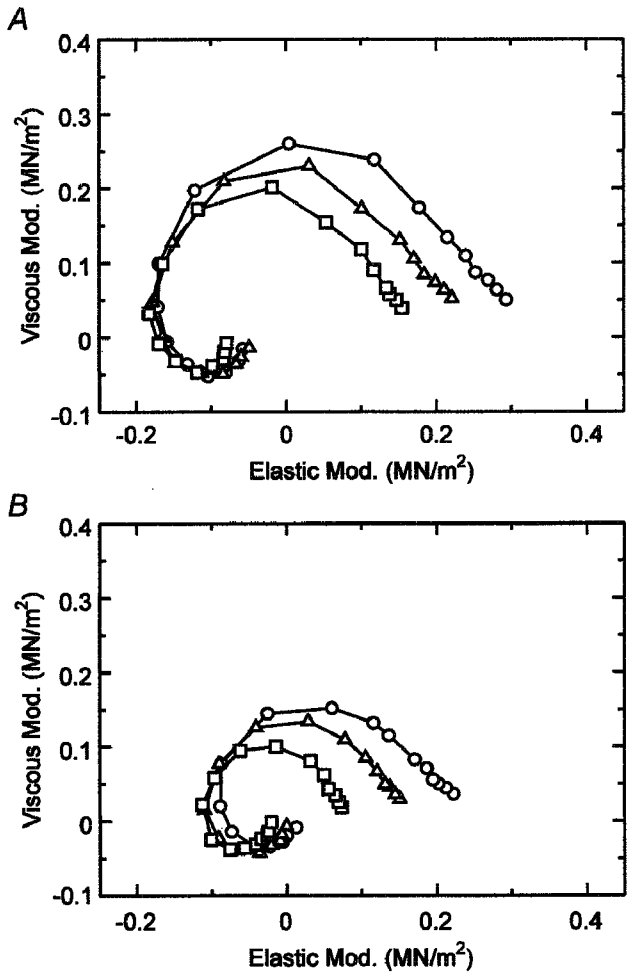

Figure 4. Nyquist plots of the complex modulus of Tm-reconstituted myocardium

A, the effect of MgATP on the complex modulus $Y(f)$ in Tm-reconstituted myocardium (average of 9 data). ○, 0.1 mM MgATP; △, 0.5 mM MgATP; □, 5 mM MgATP. The phosphate concentration was fixed at 8 mM. *B*, the effect of P_i on the complex modulus $Y(f)$ in Tm-reconstituted myocardium (average of 11 data). ○, 2 mM P_i; △, 8 mM P_i; □, 32 mM P_i. The MgATP concentration was fixed at 5 mM. Peak-to-peak amplitude was 0.25% L_0. Data are shown in the Nyquist plot, which is a plot of elastic modulus in the abscissa *versus* viscous modulus in the ordinate. Frequencies used are (clockwise): 0.13, 0.25, 0.35, 0.5, 0.7, 1, 1.4, 2, 3.1, 5, 7.5, 11, 17, 25, 35, 50, 70 and 100 Hz.

The MgATP dependence on $2\pi c$ of Tm-reconstituted (○), and Tm–Tn-reconstituted (●) myocardium is shown in Fig. 5 with S.E.M. error bars. The kinetic constants of elementary steps 1 and 2 of the cross-bridge cycle were determined by fitting the MgATP dependence of $2\pi c$ to eqn (2), and the results are summarized in Table 1. In Tm-reconstituted myocardium, the association constant of MgATP to cross-bridges (K_1) was 20.7 ± 2.3 mM^{-1} (± S.E.M., $n = 9$). This value is about twice of that of control bovine myocardium (9.1 mM^{-1}) reported previously (Fujita *et al.* 2002). The forward rate constant of cross-bridge detachment step 2 (k_2) was 25.7 ± 2.7 s^{-1}, the backward rate constant (k_{-2}) was 13.8 ± 1.8 s^{-1}, and the equilibrium constant K_2 ($= k_2/k_{-2}$) was 2.3 ± 0.5. These values are almost the same as those of control bovine myocardium reported previously ($k_2 = 26.6$, $k_{-2} = 12.1$, and $K_2 = 2.6$; Fujita *et al.* 2002). In Tm–Tn-reconstituted myocardium, K_1 decreased significantly to 13.3 ± 1.9 mM^{-1} ($n = 7$), which is comparable to the control myocardium. The k_2, k_{-2}, and K_2 values did not change significantly by the reconstitution of Tn.

Effects of P_i on the exponential process *B*

To determine the kinetic constants associated with elementary steps 4 and 5 of Scheme 1, we studied the effect of P_i in the range of 0–32 mM on exponential process *B* in Tm-reconstituted myocardium. The study

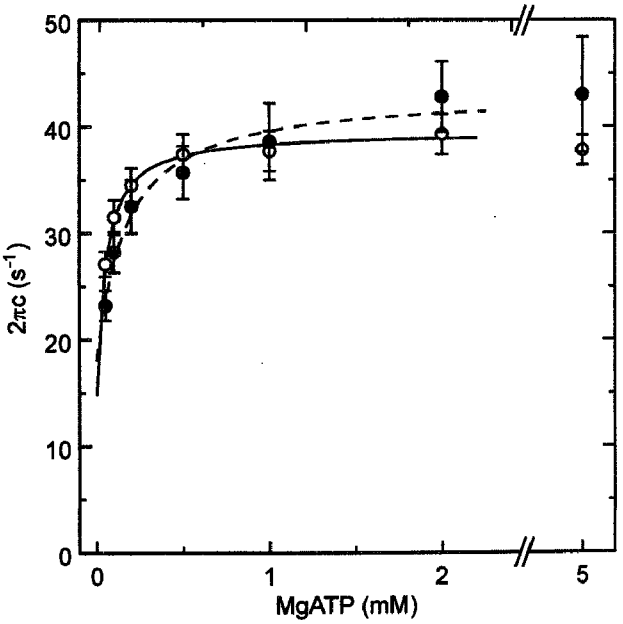

Figure 5. The rate constant $2\pi c$ is plotted as a function of the MgATP concentration in Tm- and Tm-Tn-reconstituted myocardium

○, Tm-reconstituted myocardium ($n = 9$); ●, Tm-Tn-reconstituted myocardium ($n = 7$). Error bars represent S.E.M. Continuous curves are based on eqn (2) with best fit parameters.

Table 1. The kinetic constants of Tm-reconstituted and Tm-Tn-reconstituted bovine myocardium

Kinetic constants	Units	Tm-reconstituted	Tm–Tn-reconstituted
K_1	mM^{-1}	20.7 ± 2.3 (9)	13.3 ± 1.9 (7)
k_2	s^{-1}	25.7 ± 2.7 (9)	27.6 ± 3.6 (7)
k_{-2}	s^{-1}	13.8 ± 1.8 (9)	12.4 ± 1.6 (7)
K_2	—	2.32 ± 0.48 (9)	2.70 ± 0.61 (7)
k_4	s^{-1}	6.80 ± 0.60 (11)	—
k_{-4}	s^{-1}	13.5 ± 1.70 (11)	—
K_4	—	0.57 ± 0.08 (11)	—
K_5	mM^{-1}	0.13 ± 0.05 (11)	—

Values are means ± S.E.M. The number of observations is shown in parentheses.

was carried out in the presence of the saturating MgATP concentration (5 mM) under maximal Ca^{2+}-activating conditions (pCa 4.66). Figure 4*B* shows the Nyquist plot of the complex modulus $Y(f)$ in the Tm-reconstituted myocardium activated at three different P_i concentrations (2 mM, 8 mM, 32 mM). The complex modulus data were fitted to eqn (1) to obtain the apparent rate constant $2\pi b$. $2\pi b$ data were then plotted against P_i concentration (Fig. 6) and fitted to eqn (3) (Kawai & Halvorson, 1991) to deduce the kinetic constants of elementary steps 4 and 5. The results are summarized in Table 1. In the Tm-reconstituted myocardium, the rate constant of the force generation step (k_4) was 6.8 ± 0.6 s^{-1} (n = 11) and its reversal step (k_{-4}) was 13.5 ± 1.7 s^{-1}. Its equilibrium constant K_4 (= k_4/k_{-4}) was 0.57 ± 0.08, and the P_i association constant (K_5) was 0.13 ± 0.05 mM^{-1}. These values are qualitatively the same compared to the control myocardium reported earlier (k_4 = 7.1, k_{-4} = 12.6, K_4 = 0.59, and K_5 = 0.14; Fujita *et al.* 2002).

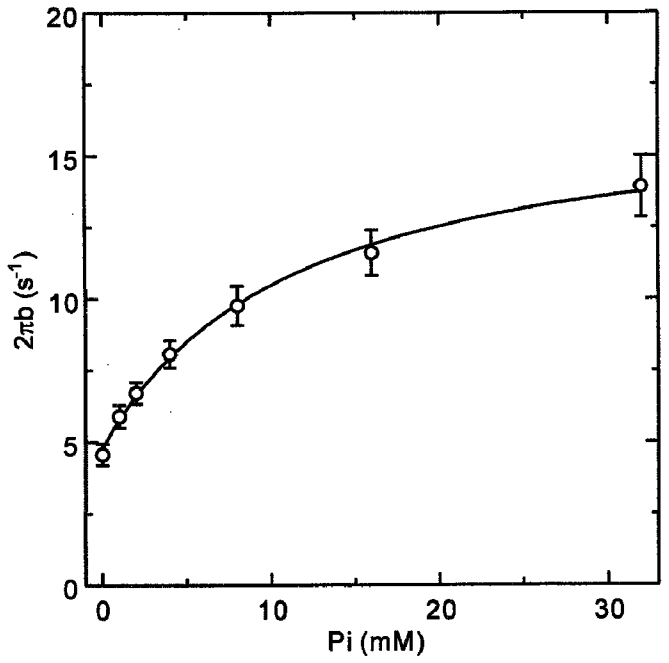

Figure 6. The rate constant $2\pi b$ is plotted as a function of the P_i concentration in Tm-reconstituted myocardium
Error bars represent S.E.M. (n = 11). A continuous curve is based on eqn (3) with best fit parameters.

Isometric tension and stiffness

Figure 7 shows isometric tension, stiffness, and the tension/stiffness ratio plotted against MgATP concentration in the Tm-reconstituted myocardium. These results are based on the same experiments as shown in Fig. 5. Both isometric tension and stiffness decreased whereas the ratio increased by the increase in the MgATP concentration. This result is in agreement with previous results in myocardium (Kawai *et al.* 1993; Fujita *et al.* 2002) as well as in skeletal muscle fibres (Kawai & Zhao, 1993). Figure 8 shows isometric tension, stiffness, and the tension/stiffness ratio plotted against the P_i concentration for the same experiments as shown in Fig. 6 in Tm-reconstituted myocardium. Both isometric tension and stiffness decreased with the increase in the P_i concentration, which is in agreement with previous results in myocardium (Nosek *et al.* 1990; Kawai *et al.* 1993; Fujita *et al.* 2002) as well as in skeletal muscle fibres (Dantzig *et al.* 1992; Kawai & Zhao, 1993).

In the presence of 8 mM P_i (standard activating condition with 5S8P), isometric tension in the control myocardium was 15.4 ± 1.1 kN m^{-2} (n = 17). In the absence of added P_i (5S0P), isometric tension in the control myocardium was 27.6 ± 3.2 kN m^{-2} (n = 11). Isometric tension after reconstitution of the actin filament decreased to 61 ± 5% (n = 11) of the control myocardium when tested with the 5S0P solution. After reconstitution of Tm, the active tension increased to 69 ± 7% (n = 11) of the control myocardium with the 5S0P solution.

Cross-bridge distribution

Cross-bridge distribution at the standard activation condition (5S8P) of Tm-reconstituted myocardium was calculated based on eqn (18) of Kawai & Halvorson (1991)

using the equilibrium constants in Table 1, and shown in Fig. 9. The probability of cross-bridges in the AM state was 0.16% and not significantly populated. This is because K_1 is large and a saturating concentration of MgATP was used. The probability of force-generating states AM*DP and AM*D was about 22% each, and the probability of the AM*S state was about 17%. Cross-bridges were mostly populated in the 'Det' state, which was about 39%. The Det state is a combination of detached states (MS and

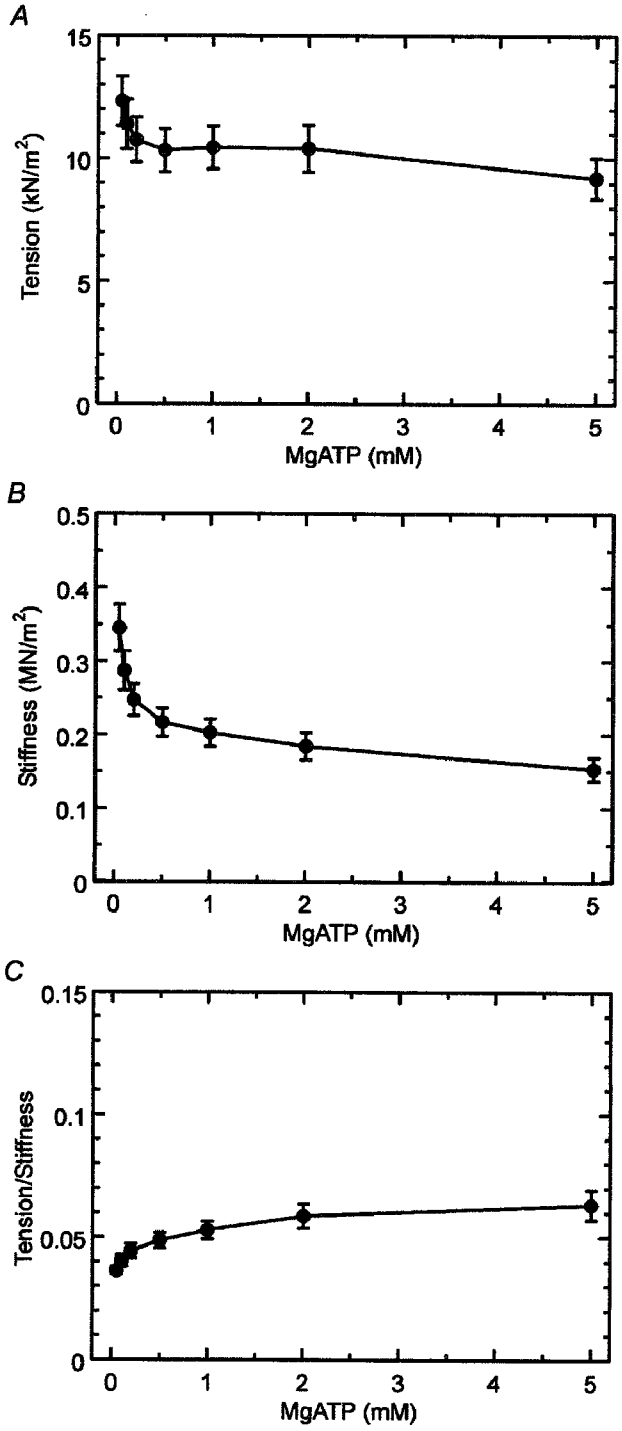

Figure 7. Isometric tension (*A*), stiffness (*B*), and the ratio (tension/stiffness) (*C*) are plotted against MgATP concentration in Tm-reconstituted myocardium
Error bars represent S.E.M. ($n = 9$). Experiments were performed in the presence of 8 mM P_i.

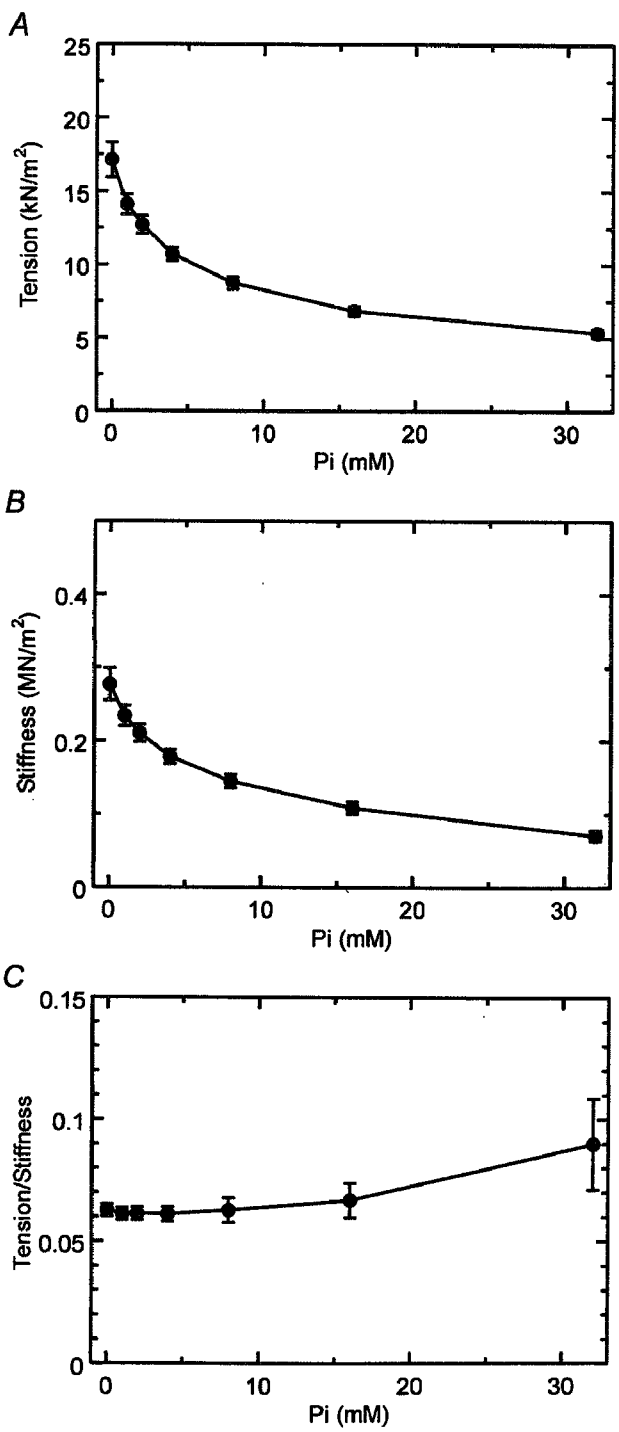

Figure 8. Isometric tension (*A*), stiffness (*B*), and the ratio (tension/stiffness) (*C*) are plotted against the P_i concentration in Tm-reconstituted myocardium
Error bars represent S.E.M. ($n = 11$). Experiments were performed in the presence of 5 mM MgATP.

MDP) and weakly attached states (AMS and AMDP) (see Scheme 1). These states cannot be distinguished with our analysis, which depends on strongly attached states. This cross-bridge distribution was not significantly different from the control bovine myocardium or the nTm-reconstituted myocardium reported previously (cf. Fig. 6 of Fujita *et al.* 2002).

Discussion

Reconstitution of Tm and Tn

We have succeeded in selectively removing the thin filament from bovine myocardium, and sequentially reconstituting the myocardium with actin, Tm, and then with Tn. The degree of reconstitution was quantified by SDS-PAGE (Fig. 1), confocal images (Fig. 2), and isometric tension (Fig. 3). The SDS-PAGE demonstrates removal of the thin filament (Fig. 1, lane 2), reconstitution of the actin filament (lane 3), reconstitution of Tm (lane 4), and reconstitution of Tn (lane 5). In lane 5, TnT and TnI can be identified. As expected, the confocal images demonstrate that actin (Fig. 2*A*) and Tm (Fig. 2*B*) can be seen colocalized (Fig. 2*C*), indicating that Tm was incorporated into the actin filament homogeneously. The functional reconstitution was assessed by isometric tension (Fig. 3). Both actin filament-reconstituted myocardium and Tm-reconstituted myocardium developed tension irrespective of the presence of Ca^{2+} (Figs 3*C* and *D*). These results demonstrate that the Ca^{2+} regulatory system was absent in these preparations as expected. In Tm–Tn-reconstituted myocardium, the Ca^{2+} sensitivity returned: the myocardium developed tension when Ca^{2+} was added to the activating solution, and the myocardium relaxed when Ca^{2+} was removed from the solution (Fig. 3*E*). These results imply that the Ca^{2+} regulatory system was restored by the Tm and Tn reconstitution. Thus, we conclude that the reconstitution of the thin filament-extracted myocardium with actin, Tm and Tn was both structurally and functionally complete.

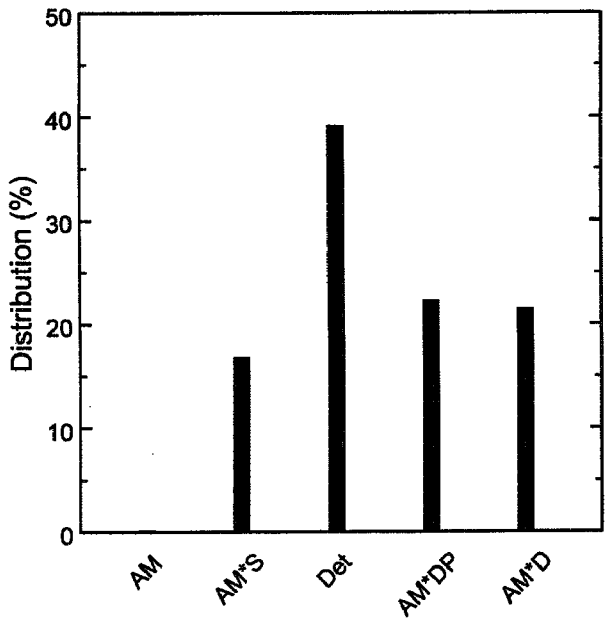

Figure 9. Calculated cross-bridge distribution in Tm-reconstituted myocardium
Calculated cross-bridge distribution based on the equilibrium constants shown in Table 1 and under standard activating conditions (5S8P). Det, detached state, which is a combination of weakly attached states (AMS and AMDP) and truly detached states (MS and MDP). Other abbreviations are the same as those in Scheme 1.

Tension augmentation by reconstitution of Tm

Our previous study (Fujita *et al.* 2002) was focused on the effect of native tropomyosin (nTm), which is a complex of Tm and Tn. We noticed enhancement of active tension by 40% (relative to initial control tension) with nTm, from which we concluded that the enhancement was based on an increase in the force supported by each cross-bridge. This conclusion was also supported by our observation that the number of force-generating cross-bridges decreased by about 20% with the nTm reconstitution (Fujita *et al.* 2002). However, at that time we were not able to tell whether this enhancement was based on Tm, Tn or both. To determine which one of these proteins enhances isometric tension, we reconstituted Tm and Tn sequentially in this report. We found that Tm in the absence of Tn enhanced isometric tension by about 10%. This result demonstrates that Tm partially contributes to the enhancement of isometric tension. Previous studies using *in vitro* motility assays on actin and heavy meromyosin (HMM) demonstrated a similar contribution of Tm to force (VanBuren *et al.* 1999; Bing *et al.* 2000). This coincidence of results from two very different methods is remarkable, because fibre experiments are typically carried out at or near physiological ionic strength (~200 mM), whereas *in vitro* motility assays are typically carried out at low ionic strength (50–70 mM). It has been known for some time that the mechanisms of force generation depend on ionic interaction (Sutoh, 1993) as well as hydrophobic interaction (Zhao & Kawai, 1994). The ionic interaction is diminished by an increase in the ionic strength, whereas the hydrophobic interaction is unchanged by ionic strength.

Tension augmentation by reconstitution of Tn

We then added Tn to the Tm-reconstituted myocardium. We found that the isometric tension increased further by 14% when Tn was added to the Tm-reconstituted myocardium in the presence of Ca^{2+}. This fact implies that Tn has a further activating role in the actomyosin interaction. This activating role must be mediated by Tm, actin, or both. Such an enhancement of tension by Tn and Ca^{2+} was observed previously in single molecule experiments on tension and gliding speed (Gordon *et al.* 1998; Bing *et al.* 2000; Homsher *et al.* 2000) using *in vitro* motility assays. The combined recovery of isometric tension was 24%, which is consistent with our earlier results (Fujita *et al.* 2002) using nTm to reconstitute the regulatory system.

The effect of Tm on the elementary steps of the cross-bridge cycle

We studied the cross-bridge kinetics of Tm-reconstituted myocardium by sinusoidal analysis, and found that most kinetic constants of the elementary steps resumed those of the control myocardium as soon as Tm was reconstituted. An exception was K_1 (MgATP binding constant) which was about 2 × the control myocardium. These results contrast with our previous study of actin-filament-reconstituted myocardium, in which K_2, K_4 and K_5 became 0.23×, 4.4× and 2.8× of the control myocardium, respectivley (Fujita *et al.* 2002); there was little change in K_1. Thus, it can be concluded that Tm enhances ATP binding, but otherwise Tm reconstitution recovers the equilibrium constants to the control level. The distribution of cross-bridge states is not very different between Tm-reconstituted (Fig. 9), nTm-reconstituted, and control myocardium (Fig. 6 of Fujita *et al.* 2002). These facts imply that Tm partially modifies actin configuration so as to enhance stereospecific and hydrophobic interaction between actin and myosin molecules. This modification increases the force generated by each cross-bridge. A similar line of evidence was presented by using Δ23Tm, a Tm mutant (Lu *et al.* 2003). A model that accounts for the regulatory proteins–actin interaction was proposed by Tobacman & Butters (2000).

The effect of Tn on the elementary steps of the cross-bridge cycle

We found that the kinetic constants simulated those of the control myocardium as soon as Tn was reconstituted and Ca^{2+} was included in the activating saline. This fact implies that the reconstitution was functionally complete. What is important is that isometric tension increased further to 1.2 × with the Tn reconstitution. The kinetic constants of Tm-reconstituted myocardium and Tm–Tn-reconstituted myocardium were almost the same, except that K_1 decreased following the Tn reconstitution (see above). This decrease, however, does not seriously affect the overall distribution of cross-bridges among the six states; hence the number of force-generating cross-bridges is approximately the same before and after the Tn reconstitution (cf. Fig. 9 and Fig. 6 of Fujita *et al.* 2002). The reason for the tension increase must therefore be based on an increase in cross-bridge force, i.e. each cross-bridge must generate a larger force as Tn is reconstituted. The fact that the addition of Tn enhanced isometric tension by 14% over the Tm-reconstituted myocardium implies that the tension on each cross-bridge increased by ~14%.

It may be interesting to discuss why K_1 was altered at each step of reconstitution. This observation is consistent with the idea that Tm and Tn affect the microenvironment of the nucleotide-binding site on myosin. This effect must be mediated through chain reactions that include Tm, actin, actomyosin interface and the myosin head. How could this be possible? One possibility is that isometric tension itself can mediate such chain reactions: we have known from previous studies that K_1 becomes larger with smaller tensions in rabbit psoas fibres (Zhao *et al.* 1996). Furthermore, our earlier studies have shown that different muscle types have different K_1 values when the amino acid sequence of the nucleotide-binding site is nearly identical (Wang & Kawai, 2001). This difference may depend on the charge distribution of loop 1 of MHC: if it is more positive, the $MgATP^{2-}$ molecule may bind more strongly. It is likely that the positively charged loop 1 readily attracts the negatively charged MgATP molecule. Therefore, the possibility arises that the charge distribution and the position of loop 1 may contribute to the ATP binding affinity (Kelley *et al.* 1993; Rovner *et al.* 1997; Sweeney *et al.* 1998; Wang & Kawai, 2001). In fact, it is known that loop 1 comes close to the nucleotide-binding pocket (Rayment *et al.* 1993); hence loop 1 could serve as a local ATP carrier. This loop exists between the N-terminus 25K and 50K domains of the myosin head, and its position may change depending on the state of the thin filament and/or tension imposed on the myosin head. An interesting hypothesis is that the position of the loop 1 is altered by each step of reconstitution of Tm and Tn on the actin filament, so as to change the binding affinity of the $MgATP^{2-}$ molecule.

References

Bing W, Knott A & Marston SB (2000). A simple method for measuring the relative force exerted by myosin on actin filaments in the in vitro motility assay: evidence that tropomyosin and troponin increase force in single thin filaments. *Biochem J* **350**, 693–699.

Bremel RD, Murray JM & Weber A (1972). Manifestations of cooperative behavior in the regulated actin filament during actin-activated ATP hydrolysis in the presence of calcium. *Cold Spring Hbr Symp Quant Biol* **37**, 267–275.

Chalovich JM, Chock PB & Eisenberg E (1981). Mechanism of action of troponin·tropomyosin. Inhibition of actomyosin ATPase activity without inhibition of myosin binding to actin. *J Biol Chem* **256**, 575–578.

Chalovich JM & Eisenberg E (1982). Inhibition of actomyosin ATPase activity by troponin-tropomyosin without blocking the binding of myosin to actin. *J Biol Chem* **257**, 2432–2437.

Dantzig JA, Goldman YE, Millar NC, Lacktis J & Homsher E (1992). Reversal of the cross-bridge force-generating transition by photogeneration of phosphate in rabbit psoas muscle fibres. *J Physiol* **451**, 247–278.

Ebashi S & Endo M (1968). Calcium ions and muscle contraction. *Prog Biophys Mol Biol* **18**, 123–183.

Ebashi S, Kodama A & Ebashi F (1968). Troponin. I. Preparation and physiological function. *J Biochem (Tokyo)* **64**, 465–477.

Fujita H & Ishiwata S (1999). Tropomyosin modulates pH dependence of isometric tension. *Biophys J* **77**, 1540–1546.

Fujita H, Sasaki D, Ishiwata S & Kawai M (2002). Elementary steps of the cross-bridge cycle in bovine myocardium with and without regulatory proteins. *Biophys J* **82**, 915–928.

Fujita H, Yasuda K, Niitsu S, Funatsu T & Ishiwata S (1996). Structural and functional reconstitution of thin filaments in the contractile apparatus of cardiac muscle. *Biophys J* **71**, 2307–2318.

Funatsu T, Anazawa T & Ishiwata S (1994). Structural and functional reconstitution of thin filaments in skeletal muscle. *J Muscle Res Cell Motil* **15**, 158–171.

Gordon AM, Chen Y, Liang B, Lamadrid M, Luo Z & Chase PB (1998). Skeletal muscle regulatory proteins enhance F-actin in vitro motility. *Adv Exp Med Biol* **453**, 187–196.

Haselgrove JC (1973). X-ray evidence for a conformational change in the actin-containing filaments of vertebrate striated muscle. *Cold Spg Hbr Symp Quant Biol* **37**, 341–352.

Homsher E, Lee DM, Morris C, Pavlov D & Tobacman LS (2000). Regulation of force and unloaded sliding speed in single thin filaments: effects of regulatory proteins and calcium. *J Physiol* **524**, 233–243.

Huxley AF & Niedergerke R (1954). Interference microscopy of living muscle fibres. *Nature* **173**, 971–973.

Huxley AF & Simmons RM (1971). Proposal mechanisms of force generation in striated muscle. *Nature* **233**, 533–538.

Huxley HE (1973). Structural changes in the actin- and myosin-containing filaments during contraction. *Cold Spg Hbr Symp Quant Biol* **37**, 361–376.

Huxley HE & Hanson J (1954). Changes in the cross-striations of muscle during contraction and stretch and their structural interpretation. *Nature* **173**, 973–976.

Ishii Y & Lehrer SS (1990). Excimer fluorescence of pyrenyliodoacetamide-labeled tropomyosin: a probe of the state of tropomyosin in reconstituted muscle thin filaments. *Biochem* **29**, 1160–1166.

Kawai M & Brandt PW (1980). Sinusoidal analysis: a high resolution method for correlating biochemical reactions with physiological processes in activated skeletal muscle of rabbit, frog and crayfish. *J Muscle Res Cell Mot* **1**, 279–303.

Kawai M & Halvorson HR (1989). Role of MgATP and MgADP in the cross-bridge kinetics in chemically skinned rabbit psoas fibers. Study of a fast exponential process (C). *Biophys J* **55**, 595–603.

Kawai M & Halvorson HR (1991). Two step mechanism of phosphate release and the mechanism of force generation in chemically skinned fibers of rabbit psoas muscle. *Biophys J* **59**, 329–342.

Kawai M, Saeki Y & Zhao Y (1993). Crossbridge scheme and the kinetic constants of elementary steps deduced from chemically skinned papillary and trabecular muscles of ferret. *Circ Res* **73**, 35–50.

Kawai M & Zhao Y (1993). Cross-bridge scheme and force per cross-bridge state in skinned rabbit psoas muscle fibers. *Biophys J* **5**, 638–651.

Kelley CA & Takahashi M., Yu JH & Adelstein RS (1993). An insert of seven amino acids confers functional differences between smooth muscle myosins from the intestines and vasculature. *J Biol Chem* **268**, 12848–12884.

King RT & Greene LE (1985). Regulation of the adenosinetriphosphatase activity of cross-linked actin-myosin subfragment 1 by troponin-tropomyosin. *Biochem* **24**, 7009–7014.

Kondo H & Ishiwata S (1976). Uni-directional growth of F-actin. *J Biochem (Tokyo)* **79**, 159–171.

Kurokawa H, Fujii W, Ohmi K, Sakurai T & Nonomura Y (1990). Simple and rapid purification of brevin. *Biochem Biophys Res Commu* **168**, 451–457.

Laemmli UK (1970). Cleavage of structural proteins during the assembly of the head of bacteriophage T4. *Nature* **227**, 680–685.

Lehman W, Craig R & Vibert P (1994). Ca^{2+}-induced tropomyosin movement in Limulus thin filaments revealed by three-dimensional reconstitution. *Nature* **368**, 65–67.

Lehman W, Vibert P, Uman P & Craig R (1995). Steric-blocking by tropomyosin visualized in relaxed vertebrate muscle thin filaments. *J Mol Biol* **251**, 191–196.

Lu X, Tobacman LS & Kawai M (2003). Effects of tropomyosin internal deletion Δ23Tm on isometric tension and the cross-bridge kinetics in bovine myocardium. *J Physiol* **553**, 457–471.

McKillop DF & Geeves MA (1993). Regulation of the interaction between actin and myosin subfragment 1: evidence for three states of the thin filament. *Biophys J* **65**, 693–701.

Murray JM, Knox MK, Trueblood CE & Weber A (1980). Do tropomyosin and myosin compete for actin sites in the presence of calcium? *FEBS Lett* **114**, 169–173.

Nosek TM, Leal-Cardoso JH, Mclaughlin M & Godt RE (1990). Inhibitory influence of phosphate and arsenate on contraction of skinned skeletal and cardiac muscle. *Am J Physiol* **259**, C933–C939.

Rayment I, Rypniewski WR, Schmidt-Bäse K, Smith R, Tomchick DR, Benning MM, Winkelmann DA, Wesenberg G & Holden HM (1993*a*). Three-dimensional structure of myosin subfragment-1: a molecular motor. *Science* **261**, 50–58.

Rovner AS, Freyzon Y & Trybus KM (1997). An insert in the motor domain determines the functional properties of expressed smooth muscle myosin isoforms. *J Muscle Res Cell Mot* **18**, 103–110.

Spudich JA & Watt S (1971). The regulation of rabbit skeletal muscle contraction. I. Biochemical studies of the interaction of the tropomyosin-troponin complex with actin and the proteolytic fragments of myosin. *J Biol Chem* **246**, 4866–4871.

Sutoh K (1993). Identification of actin surface interacting with myosin during the actin-myosin sliding. *Adv Exp Med Bio* **332**, 241–245.

Sweeney HL, Rosenfeld SS, Brown F, Faust L, Smith J, Xin J, Stein LA & Sellers JR (1998). Kinetic tuning of myosin via a flexible loop adjacent to the nucleotide binding pocket. *J Biol Chem* **273**, 6262–6270.

Tobacman LS & Butters CA (2000). A new model of cooperative myosin-thin filament binding. *J Biol Chem* **275**, 27587–27593.

VanBuren P, Palmiter KA & Warshaw DM (1999). Tropomyosin directly modulates actomyosin mechanical performance at the level of a single actin filament. *Proc Natl Acad Sci U S A* **96**, 12488–12493.

Wang G & Kawai M (2001). Effect of temperature on elementary steps of the cross-bridge cycle in rabbit soleus slow-twitch muscle fibres. *J Physiol (Lond) 531* **1**, 219–234.

Wannenburg T, Heijne GH, Geerdink JH, Van den Dool HW, Janssen PML & de Tombe PP (2000). Cross-bridge kinetics in rat myocardium: Effect of sarcomere length and calcium activation. *Am J Physiol* **279**, H779–H790.

Yamaguchi M, Greaser ML & Cassens RG (1974). Interactions of troponin subunits with different forms of tropomyosin. *J Ultrastruct Res* **48**, 33–58.

Zhao Y & Kawai M (1994). Kinetic and thermodynamic studies of the cross-bridge cycle in rabbit psoas muscle fibers. *Biophys J* **67**, 1655–1668.

Zhao Y & Kawai M (1996). Inotropic agent EMD-53998 weakens nucleotide and phosphate binding to cross bridges in porcine myocardium. *Am J Physiol* **271**, H1394–H1406.

Zhao Y, Swamy PMG, Humphries KA & Kawai M (1996). The effect of partial extraction of troponin C on the elementary steps of the cross-bridge cycle in rabbit psoas fibers. *Biophys J* **71**, 2759–2773.

Acknowledgements

The authors would like to thank to Dr Lary Tobacman for his gift of tropomyosin and troponin at the final stage of this work, and to Miss Mary Bryant for her excellent technical assistance. This work was supported in part by grants from NSF IBN 98-14441 and NIH HL70041 to M.K. This research was also supported in part by Grants-in-Aid for Specially Promoted Research, for the Bioventure Project, and for the 21st century COE program (Physics of Self-organization Systems) at Waseda University from the Ministry of Education, Sports, Culture, Science and Technology of Japan to S.I. Any opinions, findings, and conclusions or the contents of this work are solely the responsibility of the authors and do not necessarily reflect the views of the National Science Foundation. Similarly, the contents of this work are solely the responsibility of the authors and do not necessarily represent the official view of National Institute of Health.

Available online at www.sciencedirect.com
SCIENCE DIRECT®
Sensors and Actuators B 100 (2004) 455–462
SENSORS AND ACTUATORS B CHEMICAL
www.elsevier.com/locate/snb

A 1480/1064 nm dual wavelength photo-thermal etching system for non-contact three-dimensional microstructure generation into agar microculture chip

Akihiro Hattori[a,b], Hiroyuki Moriguchi[b], Shin'ichi Ishiwata[c], Kenji Yasuda[b,*]

[a] *System Products Division, Sigma Koki Co. Ltd., 17-2 Shimo-takahagi-shinden, Hidaka, Saitama 350-1297, Japan*
[b] *Department of Life Sciences, Graduate School of Arts and Sciences, The University of Tokyo, 3-8-1 Komaba, Meguro, Tokyo 153-8902, Japan*
[c] *Department of Physics, School of Science and Engineering, and Advanced Research Institute for Science and Engineering, Waseda University, 3-4-1 Okubo, Shinjuku, Tokyo 169-8555, Japan*

Received 30 December 2002; received in revised form 17 November 2003; accepted 24 November 2003

Available online 24 April 2004

Abstract

We have developed a new type of non-contact three-dimensional photo-thermal etching method for agar microculture chips exploiting the characteristics of two different wavelengths of infrared laser beams. We used two different wavelengths of infrared (1480 and 1064 nm) focused laser beam as a heat source to melt and remove a portion of 200 μm high agar gel layer on the 5 nm thick chromium-coated glass slide. As the 1480 nm infrared beam is absorbed by water, the agar gel on the light pathway is heated and melted. On the other hand, as the 1064 nm infrared beam is not absorbed by water and agar, the melting of the agar occurred just near the chromium thin layer that absorbs 1064 nm infrared light. Using this non-contact etching, we can easily make microstructures in agar-layer using infrared laser beam only within a few minutes; i.e. cell-culture holes are melted by 100 mW, 1480 nm laser and tunnels by 100 μm/s, 40 mW, 1064 nm laser, respectively. The size of holes and tunnels were also controlled by choosing the irradiation power and time of infrared lasers. Those results indicate that we can make and use microstructures for biological use without any expensive microfablication facilities nor a series of complicated procedure and time.

Keywords: Dual wavelength photo-thermal etching; Agar microchamber; 1480/1064 nm infrared focused beam; Flexible change of structure

1. Introduction

Single-cell based cell assay becomes more and more important for drug screening and studies about genetic/epigenetic information in cells. In the field of genome studies, novel sequencing analysis methods like the multi capillary electrophoresis have led to dramatic progress. In contrast, effective approaches to studying cell-based epigenetic information are still being sought. One of the main interests of epigenetic studies is how the information is controlled and recorded. It is especially important to gain understanding of the effect of the number of cell groups and the topology of cell–cell interactions, which we call 'community effect'. For this purpose, a silicon wafer and a glass slide with holes and metal decorations using the latest micromachine technologies have been created and tested [1–4]. We have also developed an on-chip single-cell based cell cultivation systems for studying epigenetic information in cells by using a microchamber array and optical tweezers [5–7]. Although these conventional microfabrication techniques provide structures with fine spatial resolution, it is still hard to change their shape during cell cultivation, which is usually unpredictable and is only defined during cultivation.

Creating small tunnels to connect two chambers without cells passing through them is essential in cell cultivation studies of cell–cell interactions such as the community effect. Thus a variety of materials and several well-known methods, including bonding, sacrificial layer techniques, and lamination have been used to create tunnel-shaped microstructures between two microchambers [8–10]. However, making these microstructures on a chip requires a number of steps, and it is impossible to fabricate them during cell cultivation; that is, we need to make all the structures on the chip before we use it. Thus we have developed a new single-cell cultivation method and a system using agar microstructures, based on 1064 nm photo-thermal etching

* Corresponding author. Tel.: +81-3-5454-6479; fax: +81-3-5454-6479.
E-mail address: cyasuda@mail.ecc.u-tokyo.ac.jp (K. Yasuda).

0925-4005/$ – see front matter © 2004 Elsevier B.V. All rights reserved.
doi:10.1016/j.snb.2003.11.041

[11,12]. Using this method, though we can change the structure of the microchambers' connection by making new tunnels using 1064 nm photo-thermal etching during cultivation, we still have to make microchambers by use of the cast molding before cultivation starts.

In this paper, we have therefore proposed the improved photo-thermal etching method called '1480/1064 nm dual wavelength photo-thermal etching'. In this method, we exploit the characteristics of two different wavelengths of infrared laser beams, i.e., we used 1480 nm infrared beam to melt all the agar gel on the light pathway, and used the 1064 nm infrared beam for melting of the agar just near the chromium thin layer. This system gives us possible to create and use microstructures even when we do not have facilities for making micro casts like SU-8 microstructures. In other word, using this system, we can create desired shape of microstructures into the agar layer on the chip within 10–20 min in their cultivation room, not in the clean room. We believe it is innovative thing for popularization of on-chip technologies to cell biologists.

2. Apparatus design and experimental methods

2.1. A 1480/106 nm dual wavelength photo-thermal etching system

Fig. 1 shows the schematic drawing of the 1480/1064 nm dual wavelength photo-thermal etching system. The system we have developed is basically the same as the one we previously reported [12], except for the addition of 1480 nm laser and the flexible-slide focusing lenses to control the focal points of infrared lasers. The system consists of the following two parts: a phase-contrast microscope (IX-70; with a phase-contrast objective lens, 40×, Olympus, Tokyo, Japan) with an automated *X–Y* stage (BIOS-201T, Sigma Koki, Hidaka, Saitama, Japan), and the dual wavelength focused laser irradiation module with a 1064 nm Nd:YAG laser (maximum 1 W; Forte-1064, Laser Quantum, Emery Court, Vale Road, Stockport, Cheshire, UK) and a 1480 nm Raman fiber laser (maximum 1 W; PYL-1-10480-M, IPG Photonics, Oxford, MA, USA). For phase-contrast microscopy and μm scale photo-thermal etching, three different wavelengths (visible light for observation and 1480/1064 nm infrared lasers for spot heating) were used simultaneously to observe the positions of agar chip surface and to melt a portion of the agar in the heated area. Phase-contrast image was acquired by using a charge-coupled device (CCD) camera (CS230, Olympus). The dichroic mirrors and lenses in the system were chosen suitable for those three different wavelengths. The flexible-slide focusing lenses were added in the way of infrared laser beam to control the focal positions of the lasers for correcting their different focal lengths, which depend on their wavelengths.

2.2. Principle of 1480/1064 nm dual wavelength photo-thermal etching

In this system, we used a new type of non-contact three-dimensional photo-thermal etching method for agar-microetching exploiting the characteristics of two different wavelengths of infrared laser beams (1480 and 1064 nm). As the 1480 nm infrared beam has the absorbance to water and agar gel, the agar gel on the light pathway was heated and melted all. On the other hand, as the 1064 nm infrared beam does not have the absorbance to water and agar, the melting of the agar occurred just near the chromium thin layer, which absorbs 1064 nm infrared laser beam.

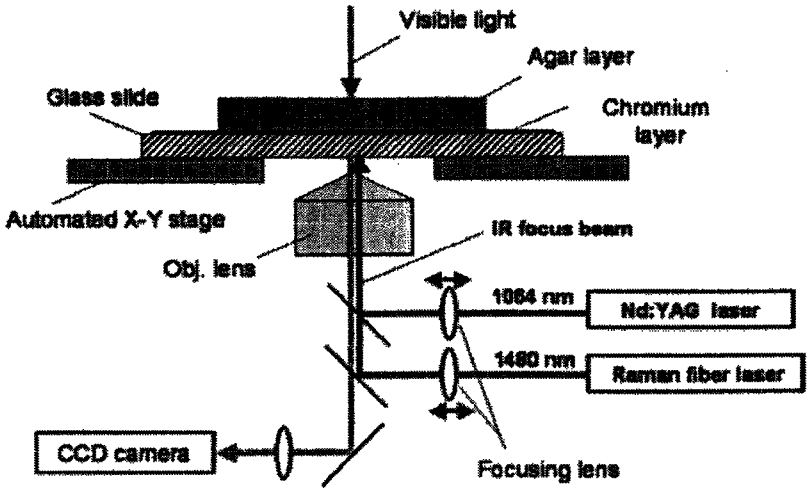

Fig. 1. A schematic illustration of the 1064/1480 nm dual wavelength photo-thermal etching system. For phase-contrast/fluorescence microscopy and photo-thermal etching, three different wavelengths (visible light for observation and 1064/1480 nm infrared lasers for spot heating) were used simultaneously to observe the positions of agar chip surface and to melt a portion of the agar in the heated area. The agar chip is the chip for cell cultivation covered with 200 μm thick low melting point agar on the 5 nm chromium-coated 0.2 mm thick glass slide. The positions of focal points of lasers are flexibly controlled by the automated *X–Y* stage and focal lenses.

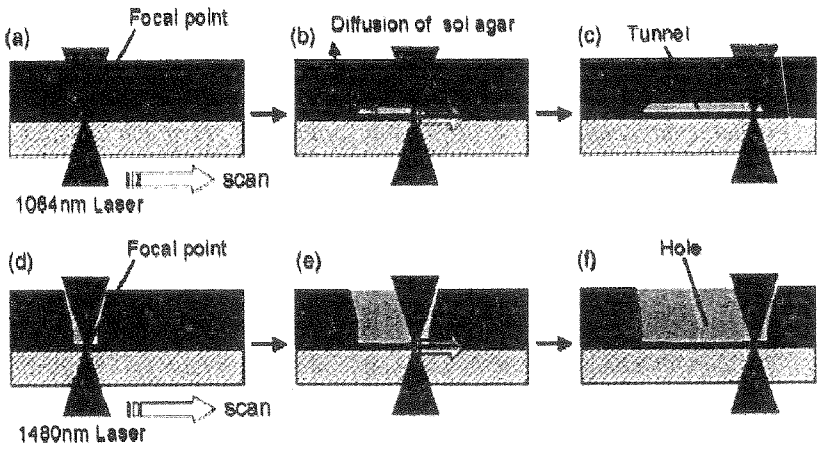

Fig. 2. A schematic drawing illustrating photo-thermal etching. First, a 1064 nm infrared laser beam was focused on the chromium layer on the glass slide (a); next, the focused beam was moved parallel to the chip surface and a portion of agar at the spot-heated point melted and diffused into water through agar mesh (b); finally, after the heated spot had been moved, a tunnel was created at the bottom of the agar layer (c). On the other hand, a 1480 nm infrared laser beam was focused on the agar glass slide (d); next, the focused beam was moved parallel to the chip surface and a portion of agar in the light pathway melted and diffused into water (e); finally, after the heated spot had been moved, a hole was created on the glass slide (f).

Using this non-contact etching, we could easily make microstructures like holes and tunnels only within a few minutes. As shown in Fig. 2, the melting of agar by laser occurred as follows: when a 1064 nm infrared laser beam was focused on the chromium layer on the glass slide, the agar at the focal point near the chromium layer started to melt (a); next, when the focused beam was moved parallel to the chip surface, a portion of agar at the spot-heated point melted and diffused into water through agar mesh (b); finally, after the heated spot had been moved, a tunnel was created at the bottom of the agar layer (c). On the other hand, when a 1480 nm infrared laser beam was focused on the agar glass slide, the agar on the light pathway started to melt (d); next, when the focused beam was moved parallel to the chip surface, a portion of agar in the light pathway melted and diffused into water (e); finally, after the heated spot had been moved, a hole was created on the glass slide (f).

2.3. Agar microchambers and photo-thermal etching

The agar chip is a microcultivation chip for cells covered with 200 μm thick low-melting-point agar on the 5 nm chromium-coated 0.2 mm thick glass slide. Although, in our previous report [12], we made a series of 50 μm square holes molded by using a 50 μm thick cube array cast of thick photoresist, SU-8, microstructure, in this report we made holes using non-contact photo-thermal etching using 1480 nm focused laser of the system, which we have described above.

The following process was used for the agar chip creation. First, a 200 μm thick agar layer was made on the 5 nm chromium-coated glass slide with spreading sol state 2% (w/v) agar (ISC BioExpress, GenePure LowMelt: melting temperature 65 °C). Next, agar-decorated chip was placed in a refrigerator at 4 °C until it was hardened into gel. The microstructures were next fabricated using the dual-wavelength non-contact photo-thermal etching in the system described

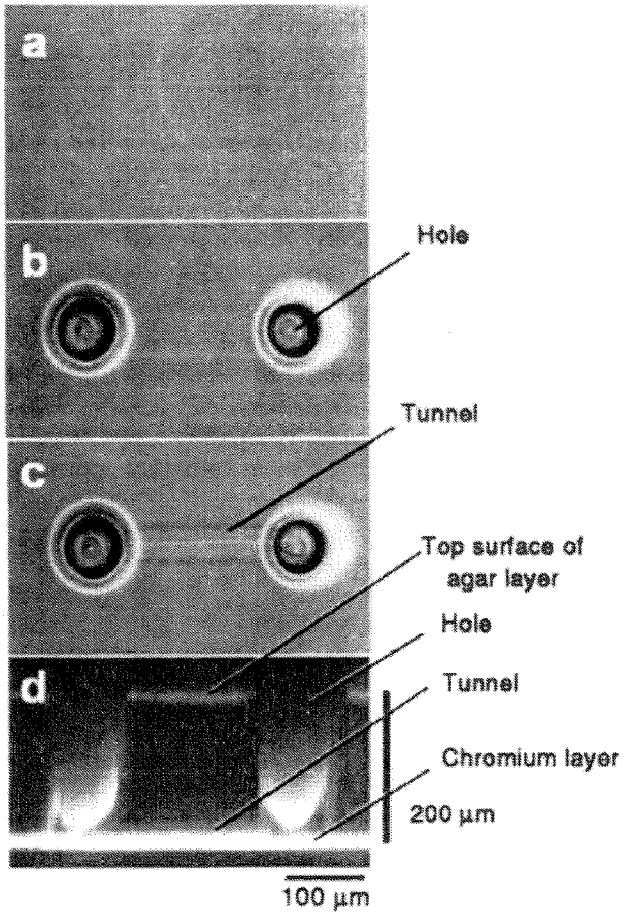

Fig. 3. One example of microstructure created in an agar chip. (a) Micrograph of agar chip before infrared laser irradiation. (b) Two holes created in the chip with 100 mW, 1480 nm infrared focused beam irradiation. (c) Two holes connected by a tunnel with 40 mW, 1064 nm infrared focused beam.

above. After the position of the heating spot is checked by optical microscope, 1480/1064 nm laser was irradiated on the chip. Then the melting was confirmed by the microscope and the heating was continued until the size of sport reached to the desired one, or the heating position was shifted to make a desired shape.

3. Experimental results and discussion

3.1. Photo-thermal etching

As explained above, photo-thermal etching is an area-specific melting of agar microchambers by spot heating using a focused laser beam and a thin layer made of a light-absorbing material such as chromium. Although agar does not absorb light with a 1064 nm wavelength, it does with a 1480 nm wavelength. Thus we could melt a portion of agar on the thin chromium layer at a spot-heated by the 1064 nm laser beam and could also melt whole agar on the light pathway by the 1480 nm laser beam. One example of the process of creating microstructure in an agar chip is shown in Fig. 3: first, we focused a 1480 nm infrared laser beam on the agar chip to create two holes having 50–100 μm in diameter and 200 μm deep (b). Next, we focused a 1064 nm infrared laser beam on the chromium layer of the chip at the position of one of the holes, and moved it in the direction to the other hole. Finally, a portion of the bottom of the agar layer melted, so that a tunnel was created and two adjacent holes were connected (Figs. 3(c) and (d)). As shown in Fig. 3(d), the cross-sectional view of microstructure was checked by the confocal microscopy (Fluoview FV300, Olympus) and found that the holes, created by 100 mW, 1480 nm focused laser, were successfully opened and the tunnel, created by 40 mW, 1064 nm focused laser, was also opened just on the chromium layer in the 200 μm thick agar layer.

3.2. The dependence on the1480 nm irradiated-laser power of hole width

In the previous report [12], we reported that the melting of agar in the chip by 1064 nm infrared laser in detail. When the power was weaker than 3 mW, etching did not occur (Fig. 10 in [12]). When the power was stronger than 50 mW, etching was also difficult because of the bubble generation caused by boiling of water. When the irradiated-laser power was between 3 and 50 mW, the channel width could be controlled linearly, and it ranged from 2 to 50 μm. The channel width could be estimated as:

$$W\ (\mu\text{m}) = 0.96I\ (\text{mW}), \quad (1)$$

where W is the width of the channel, and I the laser power. The above linear relationship indicates that the photo-thermal etching occurs only as a result of direct heating by a spot of light of an area where the balance between heating and cooling was higher than that of the melting point. In contrast to the width data, the height of the tunnel was not proportional to the laser power and seemed to have a limit of 20 μm (Fig. 10(c) in [12]). Thus the cross-sectional shape of tunnel changed from a circle to an ellipse according to the laser power increased.

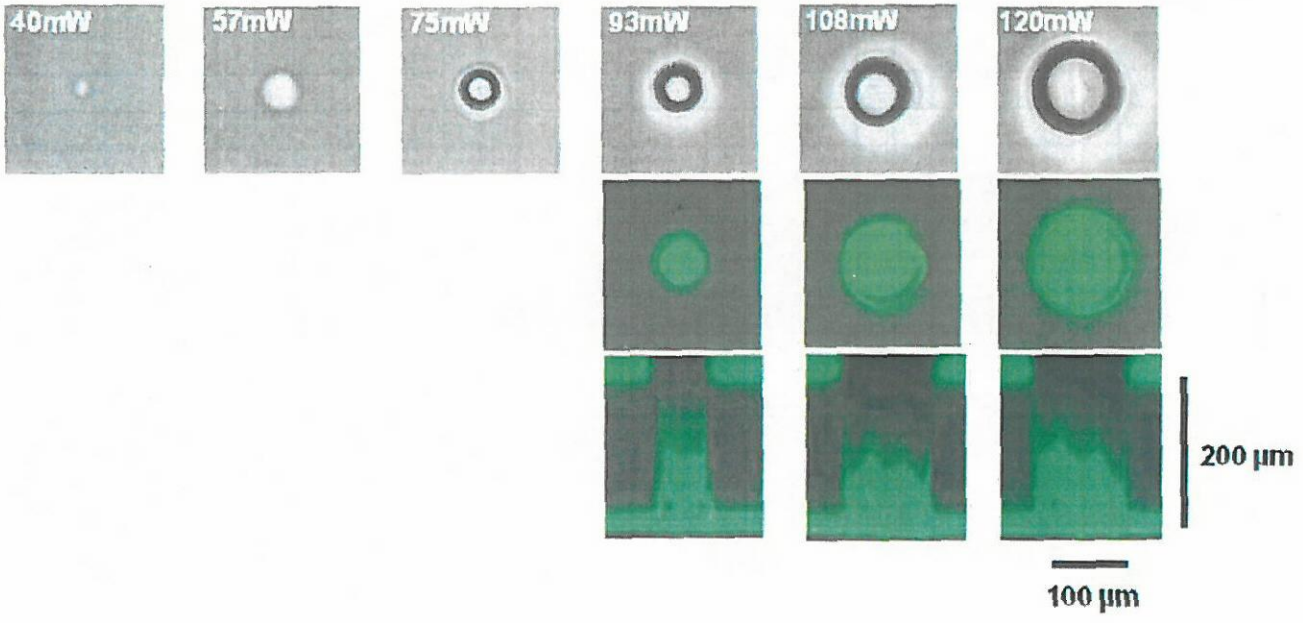

Fig. 4. The dependence of the width of thermally etched holes on the power of the 30 s irradiated 1480 nm laser. Upper micrographs show the phase-contrast images of holes from 40 to 120 mW; middle is the same images using confocal microscopy; lower micrographs show the heights of the photo-thermally etched holes.

In contrast to the 1064 nm infrared focused laser, the 1480 nm infrared laser can melt the agar in light pathway all. Fig. 4 shows the dependence of the width of photo-thermally etched holes on the power of the 30 s irradiated 1480 nm laser. Upper and middle micrographs in Fig. 4 show the phase-contrast and confocal top-view images of holes with laser power from 40 to 120 mW, and the lower micrographs show the cross-sectional views of the photo-thermally etched holes, respectively. In this example, the irradiation time of laser was 30 s, each. Although the holes could be observed by the phase-contrast microscopy, we could not observe them by the confocal images at less than 93 mW. This is because 30 s irradiation at 1480 nm was not enough to open the holes at the top surface, which is essential to introduce fluorescent dye into the holes for confocal imaging. Fig. 5 shows the dependence of the hole width on the laser power measured by the optical micrographs (see Fig. 4). The results indicated that the power dependency of the hole width in 1480 nm laser showed the linear relationship as was the case for 1064 nm laser:

$$W\ (\mu\text{m}) = I - 20\ (\text{mW}) \quad (2)$$

3.3. The time-dependency of melting spot size

Fig. 6 shows the micrographs showing the spot created by photo-thermal etching with 120 mW, 1480 nm infrared laser. Fig. 7 summarizes the time course of the change in the size of the melting spot. As shown in the graph, the melting spot sizes became larger linearly according to the time progress, which is the contrast to the 1064 nm laser, which becomes to the equilibrium size within 20 s after laser irradiation started. It should be noted that we should strictly control the irradiation time for fabrication the desired shape in agar chip.

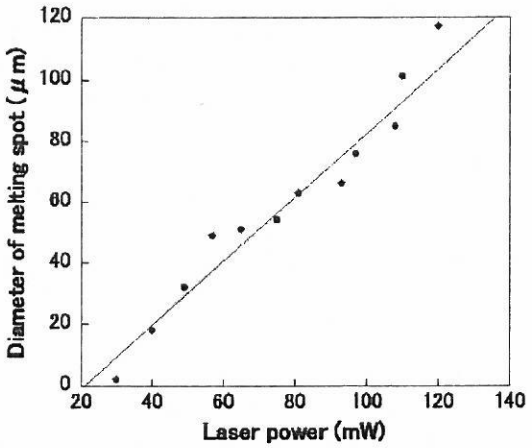

Fig. 5. The dependence of the hole width on the laser power.

3.4. Three-dimensional structure of the agar-microchamber chip

We examined the three-dimensional structure of the agar microchambers and tunnels by using a confocal microscopy system. The vacant space in agar layer in the chip was col-

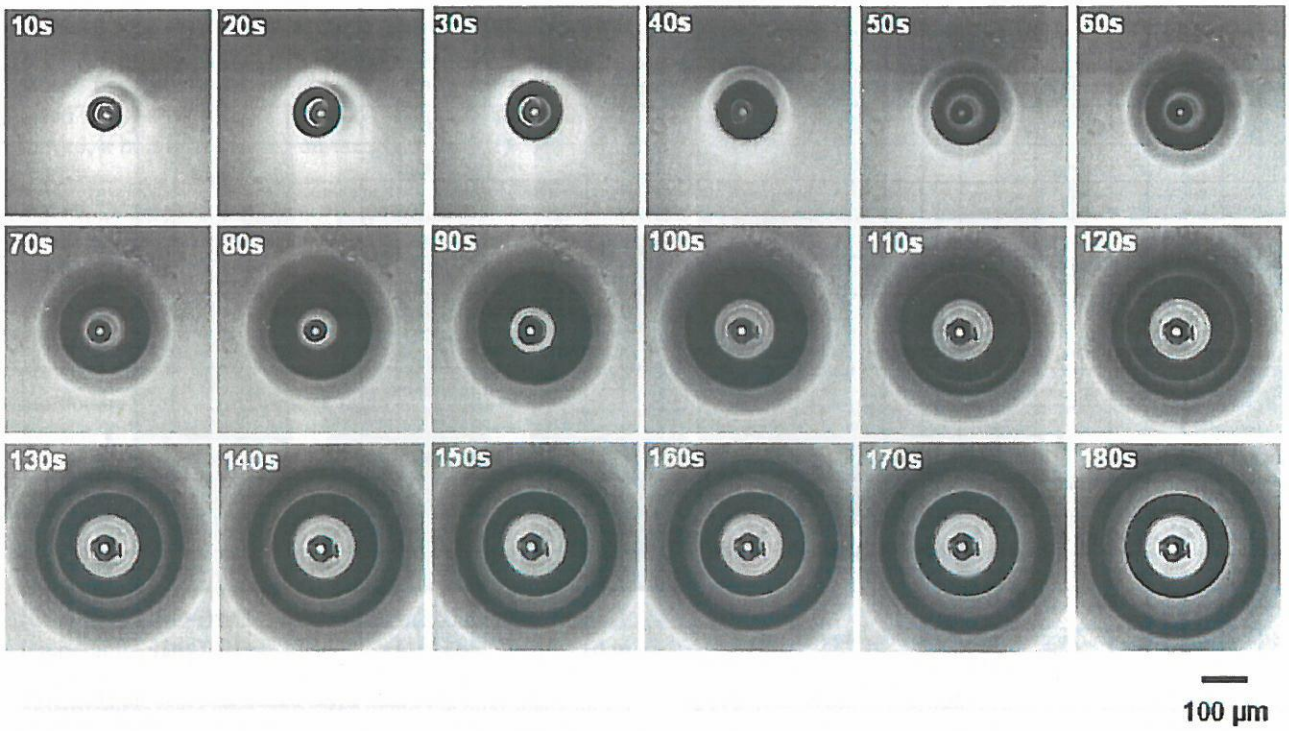

Fig. 6. Time course of the change in melting spot size created by photo-thermal etching with 120 mW, 1480 nm infrared laser.

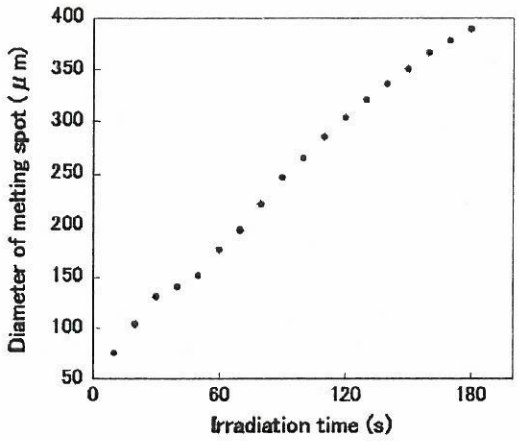

Fig. 7. Time course of the change in melting spot size.

ored by filling the microchambers with a fluorescence dye solution as shown in Figs. 3 and 4. Left micrographs in Fig. 8 are the top-view of the agar microchambers connected by small channels. The cross-sectional views are shown in right of Fig. 8, in which we can easily see a narrow tunnel connecting cylindrical holes in a thick agar layer just on the chromium layer. These cross-sectional micrographs prove that we can successfully create the cell cultivation holes and narrow tunnels in the agar layer by the dual wavelength photo-thermal etching.

3.5. Controlling the direction of synaptic connection of hippocampal cells using photo-thermal etching method

After creating the agar microstructures into the agar substrate, we cultured hippocampal cells in the chip. We first made an agar microchambers with 1480 nm photo-thermal etching, and made tunnels between adjacent chambers, one end of which was connected to chambers but the other side was not connected, with 1064 nm photo-thermal etching (Fig. 9(a)). After axons were elongated enough into the tunnels, we next melted a portion of agar substrate at the closed ends of the tunnels to connect two adjacent microchambers (see black arrows in Fig. 9(b)). A day after connecting the

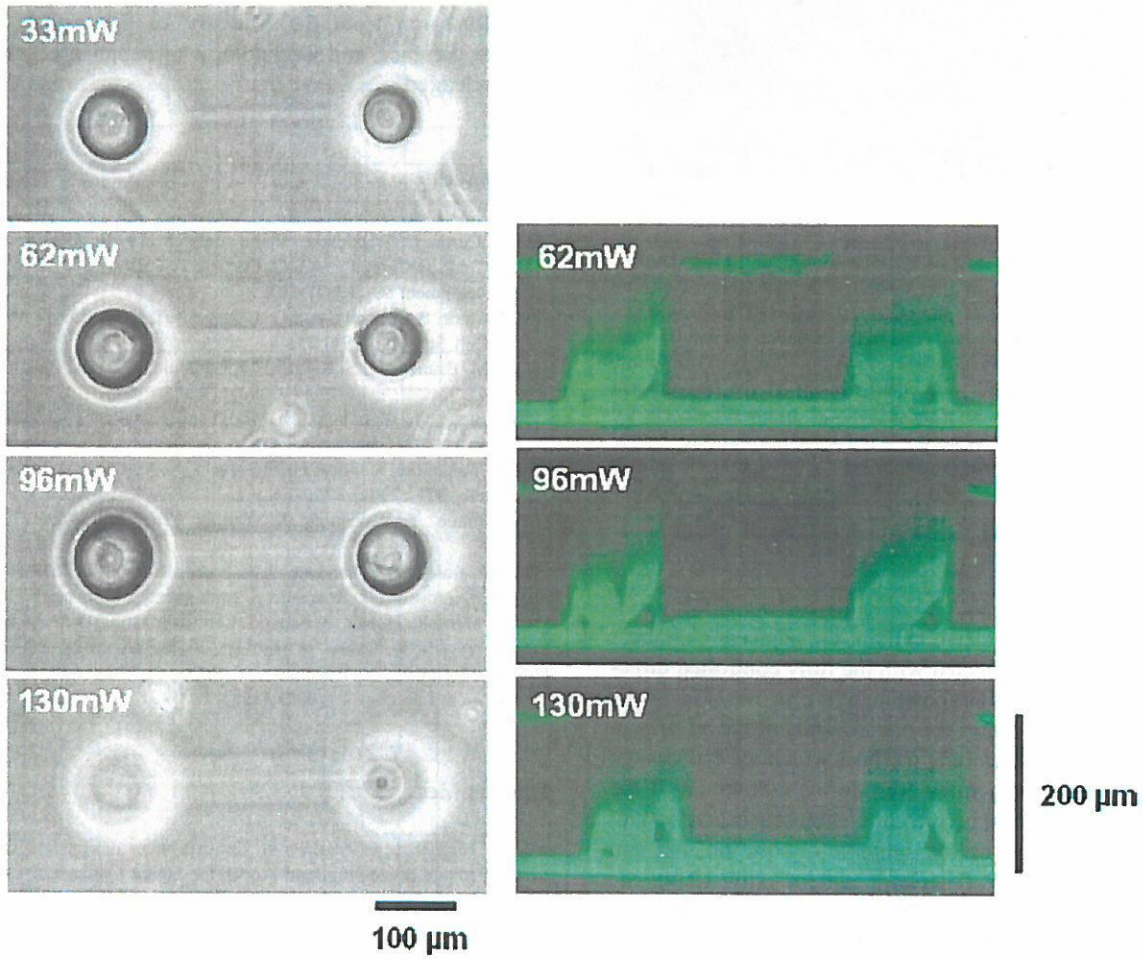

Fig. 8. Phase-contrast micrographs and their confocal cross-sectional micrographs of the agar-microchamber array with holes created by 1480 nm laser and tunnels by 1064 nm photo-thermal etching. The irradiated 1064 nm laser powers are as shown in figures, and the tracing speed of 1064 nm spot was 100 μm/s.

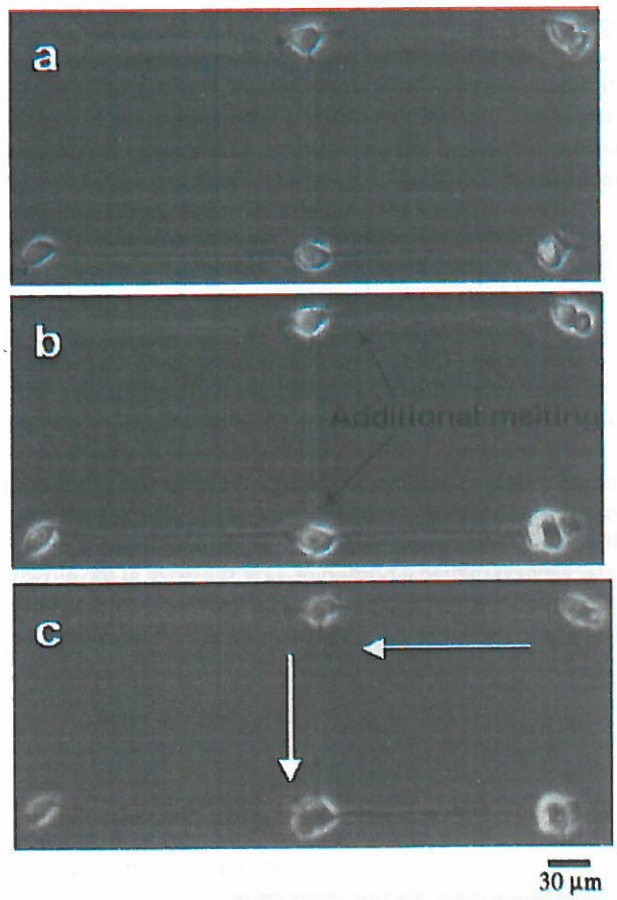

Fig. 9. Controlling the direction of synaptic connection of hippocampal cells with stepwise melting of agar tunnels with photo-thermal etching method. The micrographs show phase-contrast images of the growth and network formation of hippocampal cells in the chamber: (a) and (b) were obtained after 2 days of cultivation, and (c) was after 3 days of cultivation, respectively. (a) The tunnels were connected one of the two adjacent microchambers and axons were elongated enough within the tunnels; (b) tunnels were connected the adjacent microchabmers with photo-thermal etching (see black arrows); (c) the axons were connected to the cells in the neighbouring agar microchambers. White arrows indicate the direction of synaptic connection.

two adjacent chambers, two cells in the adjacent chambers were successfully connected with the fully controlled direction of axon directions as shown in white arrows (Fig. 9(c)).

The above result shows the one example of the advantage of our photo-thermal etching method, which we can change the shape of microstructures even during cultivation. If the tunnels were connected before cultivation started, we cannot control the direction of the synaptic connection, but can control the geometry of network pattern only. Using the method described above, we can easily control the direction of axon elongation. The method for fully controlling the direction of the synaptic connection has the potential to make the more strictly designed artificial neural network pattern on the chip.

4. Conclusion

We developed a 1480/1064 nm dual wavelength photo-thermal etching system that can be used in combination with photo-thermal etching to flexibly change the shape of agar microchambers simply and quickly without microfablication facilities. It also enables creating tunnels in a thick agar layer with a thin light-absorbing layer at the bottom. This system must be valuable for the biological researchers, who do not have microfablication facilities in the clean room, because they can make whole microstructures on the agar chip only with this improved system without any special facilities for microfabrication. Thus this system can potentially be used for the next stage of single-cell cultivation and measurement in laboratories of biological/medical fields.

Acknowledgements

Financial support, in part by the Japan Science and Technology Corporation, and by Grants-in-Aids for Science Research from the Ministry of Education, Sports, Culture, Science and Technology of Japan are gratefully acknowledged.

References

[1] A. Curtis, C. Wilkinson, Biomaterials 18 (1997) 1573.
[2] P. Clark, P. Connolly, A.S.G. Curtis, J.A.T. Dow, C.D.W. Wilkinson, Development 99 (1987) 439.
[3] P. Clark, P. Connolly, A.S.G. Curtis, J.A.T. Dow, C.D.W. Wilkinson, J. Cell Sci. 99 (1991) 73.
[4] D.M. Brunette, G.S. Kenner, T.R.L. Gould, J. Dental Res. 62 (1983) 1045.
[5] I. Inoue, Y. Wakamoto, H. Moriguchi, K. Okano, K. Yasuda, Lab Chip 1 (2001) 50.
[6] Y. Wakamoto, I. Inoue, H. Moriguchi, K. Yasuda, Fresenius J. Anal. Chem. 371 (2001) 276.
[7] I. Inoue, Y. Wakamoto, K. Yasuda, Proc. Jpn. Acad. 77 (2001) 145.
[8] N.F. Raley, J.C. Davidson, J.W. Balch, Proc. SPIE 2639 (1995) 40.
[9] M. Stjernstrom, J. Roeraade, J. Micromech. Microeng. 8 (1998) 33.
[10] S. Metz, R. Holzer, P. Renaud, Lab Chip 1 (2001) 29.
[11] K. Yasuda, K. Okano, S. Ishiwata, Biotechniques 28 (2000) 1006.
[12] H. Moriguchi, Y. Wakamoto, Y. Sugio, K. Takahashi, I. Inoue, K. Yasuda, Lab chip 2 (2002) 125.

Biographies

Akihiro Hattori is an engineer in optics system design and computer-assisted image processing, and works for Sigma Optics Co. Ltd. He is also studying the next-stage of microfablication technologies in Yasuda Lab.

Hiroyuki Moriguchi is one of the graduate students in Yasuda Lab. He studies single-cell based post-genome analysis using newly developed on-chip analysis system.

Shin'ichi Ishiwata is a professor in Waseda University and is also the President-elect of Biophysical Society of Japan. He studies biophysics of molecular motors, and structure and function of muscle.

Kenji Yasuda is an associate professor in The University of Tokyo. He was graduated from Ishiwata Lab and studies biophysics such as contractile mechanism of skeletal muscle using micromanipulation technique and cellomics studies using microfabrications and cells. He also studies the basic properties and applications of acoustic radiation force in μm scale fields.

ELSEVIER

Journal of Neuroscience Methods 139 (2004) 69–77

JOURNAL OF NEUROSCIENCE METHODS

www.elsevier.com/locate/jneumeth

A novel method of thermal activation and temperature measurement in the microscopic region around single living cells

Vadim Zeeb[a,b,1], Madoka Suzuki[a,1], Shin'ichi Ishiwata[a,c,*]

[a] *Department of Physics, School of Science and Engineering, Waseda University, 3-4-1 Okubo, Shinjuku-ku, Tokyo 169-8555, Japan*
[b] *Institute of Theoretical and Experimental Biophysics, Russian Academy of Sciences, Moscow 142290, Russia*
[c] *Advanced Research Institute for Science and Engineering, Waseda University, 3-4-1 Okubo, Shinjuku-ku, Tokyo 169-8555, Japan*

Received 11 February 2004; received in revised form 13 April 2004; accepted 16 April 2004

Abstract

We present a simple approach to bring fast and reversible temperature steps of a wide range of amplitudes from the temperature of the experimental chamber up to the boiling point of water in a desired position, with rise and fall times of around 10 ms in a microvolume of μm in size, such as in a single cell. For this purpose, we applied a technique for illuminating a metal aggregate (1–2 μm in diameter) placed at the tip of a glass micropipette with a focused infrared (1064 nm) laser beam under an optical microscope. Stable temperature gradients were created around the metal aggregate using an appropriate neutral density filter set for the laser output. To monitor the local temperature, we devised a new microthermometer composed of the tip of a micropipette filled with thermosensitive fluorescent dye Europium-TTA possessing steep temperature-dependent phosphorescence upon 365 nm excitation. The μm size of the tip of this pipette was able to measure the local temperature with 0.1 °C precision and μm spatial resolution. This new approach is compatible with standard electrophysiological and imaging techniques.

Keywords: Europium-TTA; Fluorescence imaging; Infrared laser; Microheater; Micropipette; Microthermometer; Optical microscope

1. Introduction

Local temperature as a macroscopic thermodynamic parameter can be assigned to a volume comparable to the size of a single cell, as long as this microscopic volume contains a macroscopic number of molecules. The transmembrane voltage, internal free calcium concentration and many other single cell parameters are subject to fast manipulations and detection on a millisecond time scale within the single living cell. This is not usually the case for the temperature, which is difficult to control reliably and measure locally. Heating, cooling and temperature monitoring are normally attributed to the whole of the experimental chamber with a "small" thermocouple near the preparation. This limits the temporal and spatial resolutions.

An aqueous solution in a small experimental chamber can be heated by the induction of a rapid temperature jump using a pulse of illumination from powerful light sources, a lamp (Parker, 1989) or a laser (Ward et al., 2000). However, the recovery to the initial temperature is then relatively slow, depending on the heated volume. This problem can be solved by the generation of temperature steps restricted to the desired parts of the preparation of μm in size, while keeping the whole of the experimental chamber and the rest of the preparation in an isothermal condition. A fast increase and decrease in the local temperature can be realized by illuminating metal particles or a metal thin layer with an infrared (IR) laser light of wavelength of about 1 μm (Kato et al., 1999; Kawaguchi and Ishiwata, 2001). In this case, the temperature steps could be confined to only the volume of the single cell. Thus, this method could be an attractive tool for modulating, or even initiating, spatially-localized and pharmacologically-isolated cellular responses. This approach can minimize the interference of the multiple cumulative temperature-dependent effects on the process under study, and in addition, prevents irreversible damage to the

* Corresponding author. Tel.: +81-3-5286-3437; fax: +81-3-5286-3437.
E-mail address: ishiwata@waseda.jp (S. Ishiwata).
[1] These authors contributed equally to this work.

0165-0270/$ – see front matter © 2004 Elsevier B.V. All rights reserved.
doi:10.1016/j.jneumeth.2004.04.010

preparation resulting from the execution of a wide range of temperature steps.

Temperature inevitably shifts the equilibrium in chemical reactions, and affects any kind of flow driven by electrochemical gradients (Kondepudi and Prigogine, 1998). This is crucially important for ion channel functioning (Benndorf, 1993; Matteson and Armstrong, 1982; Quartararo and Barry, 1988; Tseeb et al., 1991), synaptic transmission (David and Barrett, 2000; Hardingham and Larkman, 1998) and secretion (Bittner and Holz, 1992; Dinkelacker et al., 2000; Gil et al., 2001).

Intracellular Ca^{2+} homeostasis relies on the thermodynamic limitations of ATP-dependent Ca^{2+} pumping against chemical or electrochemical gradients (Alonso and Hecht, 1990; Reis et al., 2002; Shannon and Bers, 1997) and had been found to be highly temperature-sensitive in a variety of cell types: myocytes (Landeira-Fernandez et al., 2004; Shiels et al., 2002; Tian et al., 1998), neurons (Reichling and Levine, 1997), and spermatogenic cells (Herrera et al., 2001). This list can be expanded if temperature control and measurements in a small volume of μm in size become available. However, this is not an easy task because of several practical and, in particular, theoretical reasons arising from the definition of temperature as a thermodynamic parameter of the whole of the macroscopic system in a state of equilibrium (Landau and Lifshitz, 1964). Thus, it is necessary to comment on the use of the temperature in small volumes such as a single living cell or its compartments in non-equilibrium situations.

A description of temperature gradients inevitably implies an absence of equilibrium in the system under study, and requires a special local equilibrium assumption. A simplified meaning of this approach of non-equilibrium thermodynamics (Kondepudi and Prigogine, 1998) is as follows: when a macroscopic system is shifted from its state of equilibrium, for example, by means of heating from one side, then the relaxation time to equilibrium is on the order of L^2/D (L is the linear size of the system ($L = V^{1/3}$, V is the volume), D the thermal diffusion coefficient). Thus, a small system will relax to equilibrium much faster than a large one. This allows us to define local equilibrium thermodynamic parameters in each small elementary volume δV constituting a large system of volume V. Each δV reaches its own local equilibrium very fast in comparison with the whole of the large system V. Thus, the definition of the size of an elementary δV (which should itself contain a macroscopic amount of molecules, see further) reflects the physical limit of the time resolution of the description of the temperature gradients, which cannot be better than the time of local relaxation. For example, if we have a space resolution of $\delta V = \mu m^3$, the time resolution cannot be better than 10^{-5} s, where the thermal diffusion coefficient of water, D, is assumed to be 1.43×10^{-7} m^2/s ($=k/\rho/C$ in Appendix A; Weast et al., 1986).

The size limitation for δV reflects the fact that spontaneous fluctuations in thermodynamic parameters depend on the number of molecules constituting the thermodynamic system (Kondepudi and Prigogine, 1998). Thermodynamics itself had initially been introduced to explain processes in large technical devices, for example, engines powered by heat. That is why the lower limits for the size of the thermodynamic system had not been frequently emphasized. Textbooks normally mention that a thermodynamic system must contain a large number of molecules, comparable with Avogadro's number (Landau and Lifshitz, 1964). Due partially to this indirect, size-related reason, temperature is not widely recognized as a local parameter in cell physiology, leading to an almost complete absence of studies of temperature gradients at the single cell level, even when the presence of many powerful intracellular heat-generating processes have been well documented (de Meis, 2003; Lowell and Spiegelman, 2000; Palou et al., 1998; Tullis et al., 1991). In practice, except for the case of nerves (Abbott et al., 1958; Hill, 1926; Howarth et al., 1968) and several recent works (Chapman et al., 1995; Zohar et al., 1998), most of the data related to heat generation and temperature monitoring had been found in "large" thermodynamic systems: organisms, isolated organs and large populations of cells.

Meanwhile, simple estimations show that a thermodynamic approach can be easily applied to small, even submicrometer-sized systems, as long as this system contains a macroscopic amount of molecules sufficient to neglect the spontaneous fluctuations in the thermodynamic parameters. For example, 1 μm^3 of water contains around $N = 30 \times 10^9$ molecules, and the corresponding spontaneous relative fluctuations in the thermodynamic parameters will be on the order of $N^{-1/2}$. This is still too small to be taken into account. Therefore, theoretically, you can freely manipulate all intensive and extensive macroscopic thermodynamic parameters for a system of μm and even submicrometer sizes containing dense matter such as liquids or solids (Kondepudi and Prigogine, 1998).

In practice, the measurement of temperature in small volumes such as single living cells is not easy to perform. Thermocouples, NMR, FTIR, Raman spectroscopy, radiometric techniques, pyroelectric films and so on are all extremely sensitive methods of temperature detection, but not suitable for single cell measurements due to various technical reasons (Chapman et al., 1995). Then, the loading of some temperature-sensitive fluorescent probes to a single cell was proposed as the solution to the problem. Zohar et al. (1998) showed heat production and local temperature gradient generation by m1-muscarinic ligand–receptor interactions in a single Chinese hamster ovary cell. But this attractive approach suffers from a high environmental (e.g., pH) sensitivity of the probes, which makes accurate temperature detection quite problematic. In addition, the non-homogeneous distribution of the dye on the membrane and intensive photobleaching (Zohar et al., 1998) make calibration especially difficult. Such difficulties were also present for temperature measurements through changes in the fluorescence intensity

of the dyes directly labeled to the actin filaments (Kato et al., 1999) or microtubules (Kawaguchi and Ishiwata, 2001). To avoid these problems, we used a closed-tip patch pipette filled with the fluorescent dye Europium-TTA (Eu-TTA) dissolved in 100% DMSO. Eu-TTA, excited at 365 nm, possesses an extremely temperature-sensitive emission near 615 nm (Bhaumik, 1964; Zohar et al., 1998), and initially had been used for temperature monitoring in integrated circuits (Kolodner and Tyson, 1982). In our experiments, local temperature monitoring with 0.1 °C resolution was performed with the μm-sized tip of a pipette filled with Eu-TTA/DMSO. Now, we can completely avoid the above problems arising from the loading of this dye into the cell, including the calibration, essential for accurate measurements of temperature. Temperature is thus the only parameter under registration, because the tip of the pipette, which is in tight contact with the cell membrane, constitutes a closed system (energy transfer is possible, substance transfer is not).

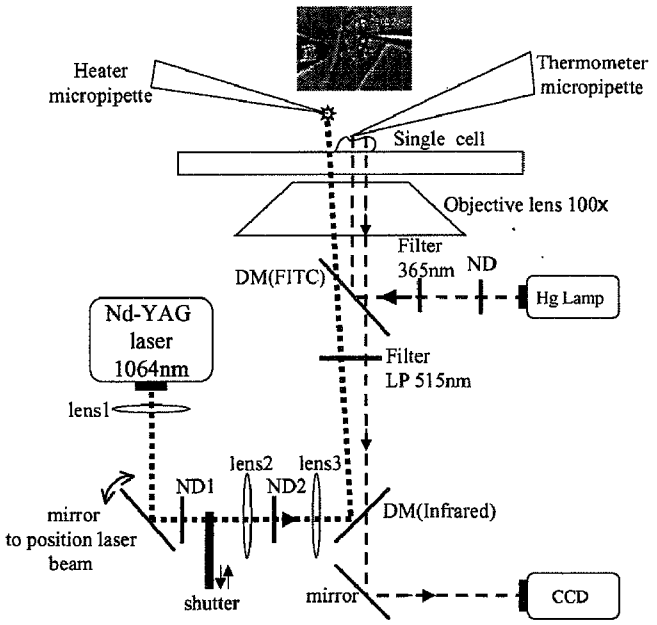

Fig. 1. Experimental setup for implementing local and fast temperature control and measurements in a microscopic volume. The dotted lines and the broken lines represent the IR laser and fluorescence imaging optical paths, respectively. The IR laser beam from an Nd-YAG laser expanded by lens1 was reflected by a movable mirror, passed through ND filters (ND1 and ND2) and lenses (lens2 and lens3), and was focused by an objective lens 100× onto the heater micropipette. Excitation light of 365 nm from an Hg lamp for Eu-TTA is obtained through filter 365 nm, reflected by a dichroic mirror DM(FITC) and focused onto the thermometer micropipette. Emission light of near 615 nm from Eu-TTA was collected by an objective lens and introduced to a CCD camera CCD through a filter LP 515 nm.

2. Materials and methods

For some of our experiments, we used a camera and an excitation/monochromator-acquisition system from T.I.L.L. Photonics, Germany, configured with an FITC dichroic mirror and a 515 nm filter in the emission pathway; a 75 W Xenon lamp as an excitation source in the monochrometer, a Peltier-cooled SensiCam camera (640 × 480 pixels) connected to a 12 bit A/D converter, a 100× objective and T.I.L.L. image analysis procedures with an IGOR programming environment (Wavemetrics, USA). This configuration was used to obtain a spectrum of excitation of Eu-TTA (0.05 mM Europium-TTA in 100% DMSO in the pipette; see Fig. 2), and for testing the temperature sensitivity of the micropipette filled with 0.05 mM Eu-TTA in 100% DMSO (see Fig. 3).

The rest of the experiments presented in Figs. 4–6, have been done with 50 mM Eu-TTA dissolved in 100% DMSO in the pipette, which allowed us to overcome photobleaching using much lower intensities of excitation, and a CCD camera: a CCD-300, DAGE-MTI of MC Inc. (Michigan City, IN, USA) with a similar excitation–emission optical configuration: 365 excitation/FITC dichroic/515LP emission combined with an infrared laser Nd-YAG (1064 nm): T10-V-106C, 2.5 W, Spectra-Physics Lasers Inc. (Mountain View, CA, USA), as shown in Fig. 1.

Images were acquired at 33 Hz and recorded using a digital tape recorder: DSR-11, Sony (Tokyo, Japan). The data was then stored and analyzed in a personal computer, Apple Japan (Tokyo, Japan) through a frame grabber LG3, Scion Corporation (Frederick, MD, USA).

The optical system was constructed with an inverted microscope IX70, Olympus (Tokyo, Japan) equipped with an objective PlanApo100×/1.40/oil, mounted onto the table: RS4000, Newport (Irvine, CA, USA), equipped with a High Performance Laminar Flow Isolator I-2000 Series (cf. Nishizaka et al., 1995).

Both the heater and thermometer micropipettes were fabricated using glass tubes: 1.2 mm in diameter, Drummond Sci. Co. (Broomall, PA, USA). Pulling was performed using a pipette puller: PB-7, Narishige (Tokyo, Japan), and polishing (closing the tip of the pipette) was performed with a micro Forge: MF-900, Narishige.

We performed a calibration of the temperature responses obtained from the emission intensity readout from the region of interest at around 3–5 μm^2 at the very tip of the microthermometer pipette filled with Eu-TTA using a thermocouple: 0.5 mm in diameter (0.1 °C resolution): SN-170, Nekken Co. Ltd. (Tokyo, Japan). The thermocouple was placed 3 mm away from the tip of the microthermometer pipette (see Section 3 for details).

To position the laser beam, a movable mirror with dc servomotors was used: Opt-Mike-E, Sigma Koki (Saitama, Japan). The microthermometer pipette filled with Eu-TTA and the heater micropipette with the aluminum aggregate in the tip were placed at the desired position using two sets of remote-controlled water-filled hydraulic micromanipulators: WR-90, Narishige.

2.1. Reagents

Eu-TTA, europium(III) thenoyltrifluoroacetonate trihydrate, was purchased from Acros Organics (Pittsburgh, PA, USA). DMSO was purchased from Sigma–Aldrich (St. Louis, MO, USA). Aluminum powder of 0.1 μm in diameter was purchased from Nilako (Tokyo, Japan). Fluorescent microspheres: FluoSpheres carboxylate-modified microspheres, 1.0 μm, red-orange fluorescent (565/580) F-8822, were purchased from Molecular Probes Inc. (Eugene, OR, USA).

3. Results

3.1. Preparation of the microthermometer pipette

The micropipettes were fabricated using two-stage pulling. The final diameter of the tip was around 1–2 μm. The tip of the pipette was closed by means of a gentle mechanical touch with a high-temperature polishing filament of the micro Forge. These closed-tip pipettes were then filled with 1 μl of 0.05 or 50 mM Eu-TTA dissolved in 100% DMSO. The air remaining at the tip could be removed by shaking the micropipette. The other end of the dye solution was not sealed but exposed to the air. The microthermometer pipette thus prepared could be used repeatedly. The temperature calibration of the microthermometer was performed immediately after optical recording by applying hot water (45 °C) to the chamber followed by a stepwise recording of the emission intensity from the same region of interest in the tip of the micropipette (with 2 °C steps) until natural cooling brought the temperature of the chamber to 22–24 °C. The calibration curves relating temperature and emission intensity with 50 mM Eu-TTA were well approximated by linear relationships. The only problem was the small change in the baseline sometimes observed upon temperature steps, as shown in Fig. 4. This was attributable to a drift in the position of the pipette, probably due to thermally-driven glass expansion. This problem could be eliminated by fabricating the obtuse pipette with the same diameter as the tip (1–2 μm), and by minimizing the length of the pipette in contact with the water.

3.2. Principle of temperature measurement

The principle of optical temperature registration is presented in Figs. 2 and 3. The spectrum of the excitation of the Eu-TTA, which was performed in the 320–420 nm range with 5 nm steps and collected using a 515 nm long pass filter, demonstrates a strong temperature dependence of the emission intensity (Fig. 2). A temperature wave of the desired amplitude of around 1 °C was delivered to the experimental chamber (2.5 ml) by the rapid (around 2 s) insertion of the small part of the silicon tube of a continuously-running perfusion (3 ml/min) into hot water which was placed in front of the chamber. This temperature wave was measured by a thermocouple in the chamber (Fig. 2A). The thermocouple was placed 3 mm away from the tip of a pipette filled with 0.05 mM Eu-TTA/DMSO. Simultaneous execution of the protocol of the emission intensity registration (100 ms exposure, 3 Hz) was performed for a 5 μm^2 region of interest at the very tip of this Eu-TTA microthermometer pipette (Fig. 3E). The emission intensity was affected by

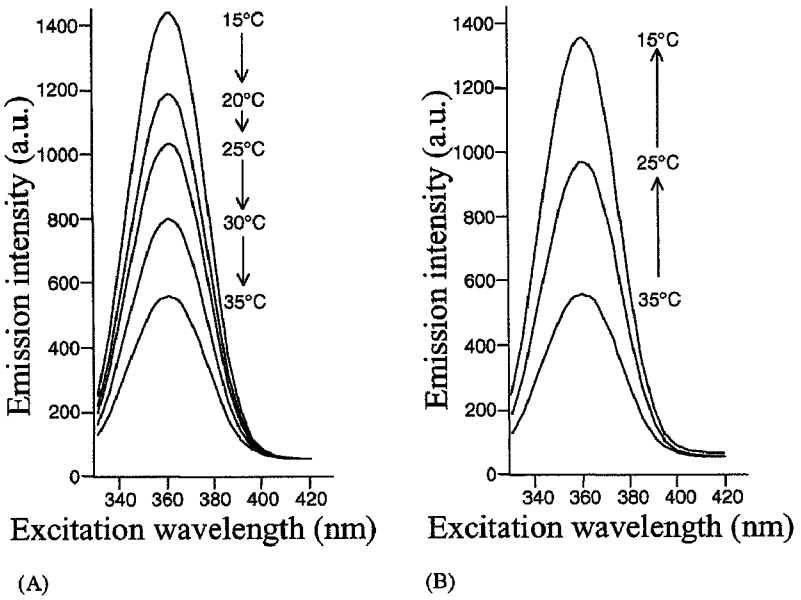

Fig. 2. Excitation spectrum from a glass micropipette filled with 0.05 mM Eu-TTA dissolved in 100% DMSO. The protocol of excitation (from 320 to 420 nm with a step size of 5 nm and a 100 ms exposure time) was constructed using T.I.L.L. programming facilities. The emission was collected, using a 515 nm filter, from the region of interest in the very tip of the micropipette, as shown in Fig. 3E. (A) Heating (from 15 to 35 °C with 5 °C steps). (B) Cooling (from 35 to 15 °C with 10 °C steps).

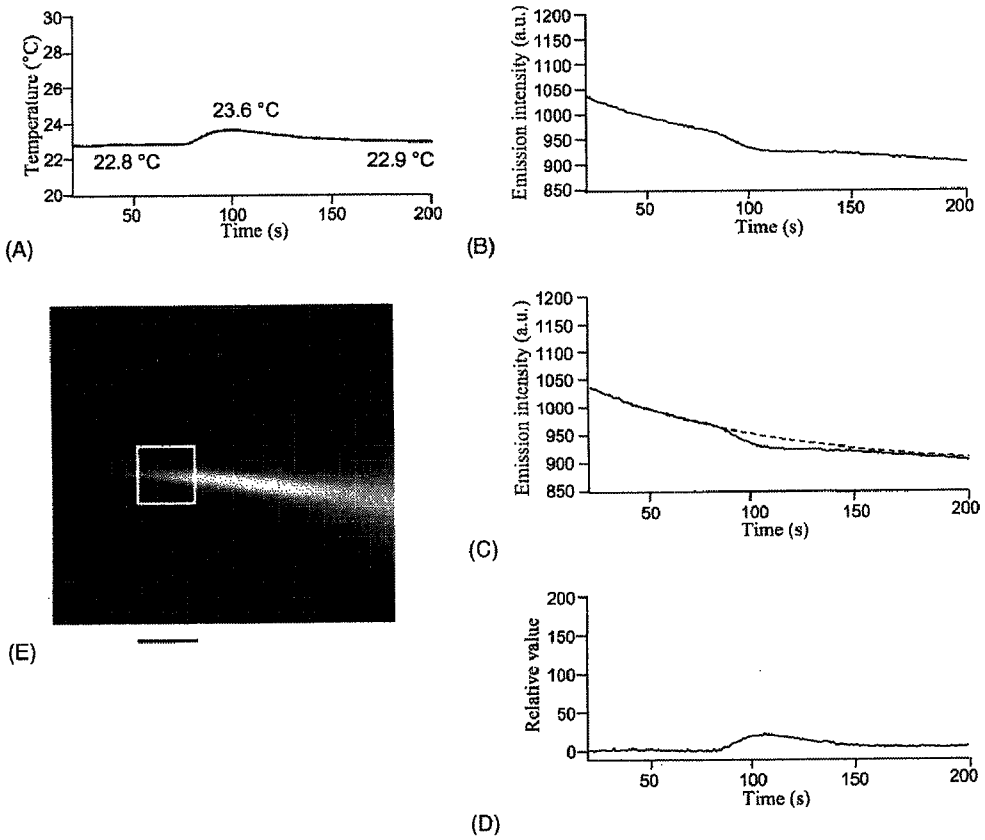

Fig. 3. Principle of temperature measurement using the readout of the emission intensity (365 nm excitation/LP 515 nm emission) from the tip of the micropipette filled with 0.05 mM Eu-TTA/100% DMSO. (A) Test temperature wave, which was delivered by circulating hot water through a silicon tube connected to the experimental chamber for a few seconds. The temperature of water in the chamber was measured by a thermocouple placed 3 mm away from the tip of the pipette filled with Eu-TTA/DMSO. (B) The same temperature wave as (A), but measured from the emission intensity at the very tip of the pipette (5 μm^2 region of interest). (C) A single exponential decay of emission intensity due to photobleaching at a constant temperature. This is shown by the dashed line, which is an exponential fit of the emission intensity at 22.8 °C (that was before the delivery of the temperature wave), and which has been superimposed on the response shown in (B). (D) Temperature wave measured by a micropipette filled with Eu-TTA/DMSO. The temperature-dependent change in the emission intensity of Eu-TTA was calculated by means of a subtraction of the raw emission intensity (B) from the single exponential fit obtained in (C). (E) The emission intensity of Eu-TTA/DMSO in the pipette had been measured in the region surrounded by the square. Scale bar: 5 μm.

both thermobleaching and photobleaching. The time course of photobleaching could be expressed by a single exponential, so that it was taken into account by subtraction from the recorded optical signal (before the appearance of the temperature wave) (Fig. 3C). To reduce the photobleaching effect, we then used a higher concentration of the Eu-TTA in the pipette up to 50 mM, and a smaller intensity of excitation (Figs. 4–6).

3.3. Preparation of the microheater

The micropipettes of the same size as for the microthermometer (tip of 1–2 μm in diameter) were used. The sharp tip of the pipette had been inserted for 3 s into the suspension of the aluminum particles (size 0.1 μm; 50 mg/ml) in water. Then, within 10–15 s the natural evaporation of the water from the pipette resulted in the appearance of an aluminum microaggregate in the very tip of the pipette. This microaggregate had been firmly fixed by bringing it appropriately close to the high-temperature polishing filament of the micro Forge as is the usual procedure for preparing a patch clamp pipette. The heater micropipette thus prepared could be used as a heat source by illuminating it with a focused laser beam.

3.4. Centering the laser beam

To position the IR laser beam at a desired point, the trapping effect of the beam on the fluorescent microspheres had been used (Ashkin and Dziedzic, 1987). The precise positioning of the reflecting mirror using an Opt-Mike-E controller allowed us to move the focus of the laser beam onto the desired point confined to the position of the metal microaggregate within the μm accuracy because the radius of the focused laser beam was about 0.8 μm (Nishizaka et al., 1995). The simple shutter (pendulum) had been introduced in the path of the laser beam in front of the entrance to the microscope to produce a stepwise illumination of the metal microaggregate. The relaxation time for the temperature field stabilization near the metal aggregate was around

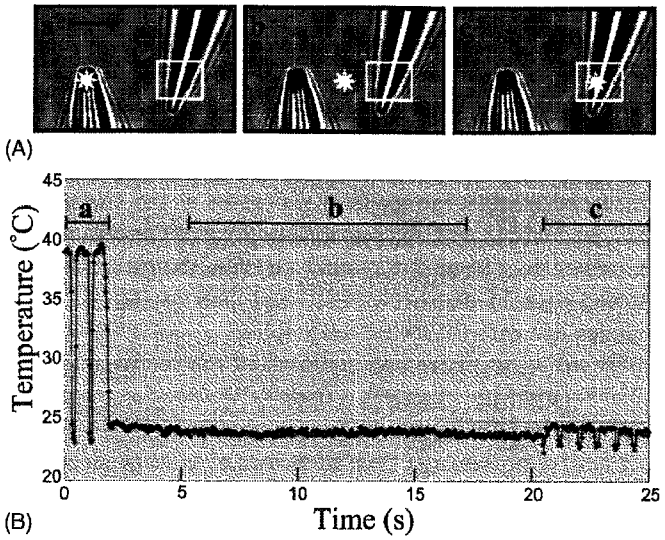

Fig. 4. Temperature change depending on the position of the focus of the IR laser beam (17.5% ND was used). (A) Experimental configuration. The left and right micropipettes are the heater and thermometer, respectively. The position of the focus was moved from the heater to the thermometer pipette (a → b → c). An asterisk shows the position of the focus of the IR laser beam. The square region is where the emission intensity of 50 mM Eu-TTA/100% DMSO in the pipette had been measured. Scale bar: 5 μm. (B) Temperature change induced by the IR laser illumination. The laser was illuminated during the periods shown by thin lines at the positions a, b and c, as indicated by the asterisks in (A).

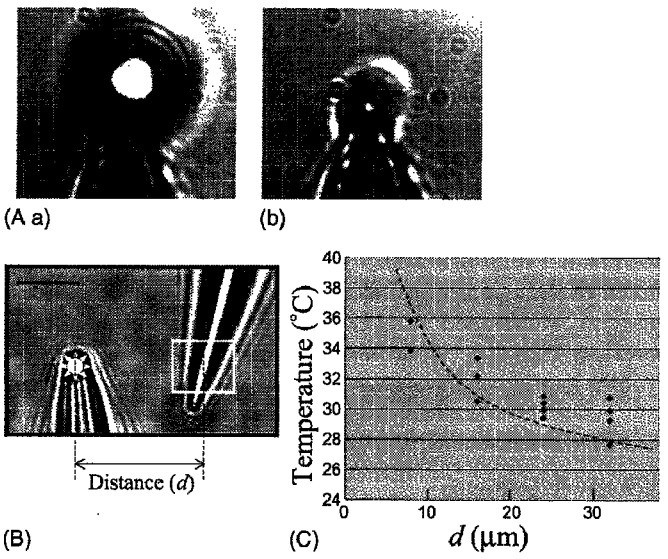

Fig. 5. Powerful heat production at the heater micropipette due to the focused strong IR laser beam (A) and the temperature gradient in the vicinity of the heater micropipette (B and C). (A) Laser transmission was 100% (a) and 25% (b). (B) Experimental configuration. The left and right micropipettes are the heater and thermometer, respectively. An asterisk shows the position of the focus of the IR laser beam. A square shows the region of interest where an emission intensity of 50 mM Eu-TTA/100% DMSO in the pipette was measured. The distance between the heater and the thermometer is indicated by d. Scale bar: 5 μm. (C) Temperature gradient created in the vicinity of the heater micropipette. Temperature was plotted against d. The dashed line is represented by $T = \text{constant}/d + T_0$ (25 °C). The room temperature was kept at T_0, 25 °C, by an air conditioner.

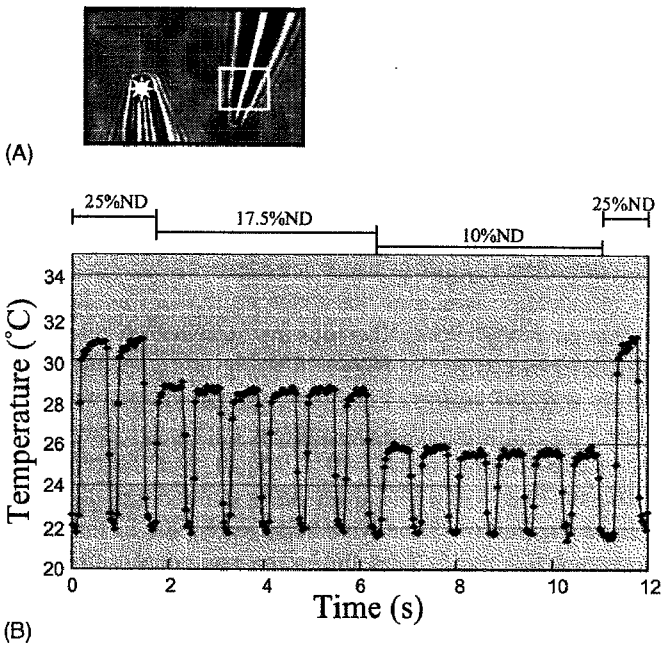

Fig. 6. Control of the amplitude of temperature steps using different ND filter sets. (A) Experimental configuration (the same as in Fig. 5B). Scale bar: 5 μm. (B) Temperature change induced by the IR laser beam. Time durations in which different ND filters were used are indicated at the top by thin lines.

10 ms (Kato et al., 1999). In the present experiments, the relaxation time was found to be approximately 50 ms, which is due to the limited speed of the laser beam cutoff by this specific pendulum (shutter).

3.5. Microscopic thermal activation and temperature measurements

The usual characterization of a living cell at isothermal conditions with respect to its neighboring surroundings is based on the assumption that artificial or endogenous heat generation processes are not sufficiently powerful to create detectable temperature gradients in the aqueous intracellular compartments. In fact, water has a very low thermal conductivity, $k = 0.597$ W/m/K (Weast et al., 1986), close to the range of thermoinsulators. This favors creating stable steep temperature gradients near the heat source immersed in the water solution (see Appendix A). In practice, previous work revealed steep artificial temperature gradients as large as 2 °C/μm near metal particles of submicrometer size in the water solution heated by an IR laser of about 1 μm in wavelength (Kato et al., 1999), and also near the thin aluminum layer (10 μm in diameter) circularly evaporated on a coverslip (Kawaguchi and Ishiwata, 2001). The relaxation time to realize a stable concentric temperature gradient was about 10 ms after the onset of laser illumination.

Thus, we used the technique of local heating by fixing the metal microaggregate into the tip of the patch clamp pipette and in its precise positioning to the desired microvolume subscribed for temperature control (Fig. 1). Another

closed-tip patch pipette was filled with Eu-TTA (in DMSO) to detect the local temperature. The temperature readout was performed by monitoring the emission fluorescence intensity from the tip of this pipette placed directly into the heated microvolume. At the power of the IR laser used, detectable temperature gradients did not occur in water without direct focusing of the beam at the metal microaggregate (Fig. 4). The insertion of the microaggregate into the focus of the laser beam in water produced visible boiling in the immediate vicinity of the metal, so that it was damped by intensive (e.g., 25% ND) filtering to lower the power of the laser beam (Fig. 5). Higher filtering (17.5% ND) completely avoided boiling. The stable gradient of the temperature near the illuminated aluminum microaggregates was very steep—approximately 10 °C/15 μm over the range of 5–20 μm (Figs. 4 and 5). Lower stable temperature distributions in the microvolume were achieved by the insertion of additional ND filters. This offers the unique possibility of creating temperature steps of the desired amplitudes (up to tenths of degrees) with rise and fall times of around 10 ms in the small μm-sized volumes (Fig. 6). One of the attractions of this method is the simplicity of the equipment in use. In general, except for the IR laser path, the experimental setup consists of hydraulic manipulators and patch clamp pipettes, together with a digital imaging system configured for fluo-3 (FITC dichroic mirror, 515LP filter) and the use of a 365 nm cutoff filter for the Eu-TTA excitation.

4. Discussion

One of the advantages of the method presented here is the small volume of the pipette, by which we can thermally activate and simultaneously measure the temperature within the same size comparable to that of the single cell. As both the heater and the thermometer pipettes are controlled by manipulators, it is possible to activate a certain position thermally and to measure the temperature field distribution.

Contrary to other attempts at taking temperature measurements engaging a direct loading of the dye into the cell (Zohar et al., 1998) or the labeling to proteins (Kato et al., 1999; Kawaguchi and Ishiwata, 2001), the emission intensity of the dye in the present method is the only variable in the temperature because the dye, confined to the micropipette, constitutes a closed system, preventing a direct contact of the dye with the environment. Besides, a pipette glass has a higher heat conductivity coefficient and a smaller heat capacity than water (Weast et al., 1986), so that it should be sufficiently "transparent" for temperature change detections.

This configuration completely avoids typical artifacts, which relate to the non-homogeneous distribution and environmental sensitivity of the fluorescent dye introduced into the cell, incorporated onto the membrane or labeled to proteins. The small but detectable mechanical shift in the pipette due to the thermal expansion of the glass was the only artifact under consideration. This was probably the cause of the small baseline shift observed in Figs. 4 and 6.

The method of fast and reversible temperature step delivery in the micro volume and the precise local temperature monitoring can be a useful tool in many experimental situations related to the study of the "in vivo" thermodynamics of endogenous intracellular processes at the single cell level. In contrast with the practical notions of temperature as a slowly changing and non-local variable, the present study showed that, in microvolumes, local and fast temperature changes can easily become reversible.

According to linear non-equilibrium thermodynamics (a linear relationship connects a thermodynamic force and the corresponding flow), a temperature gradient, in addition to heat flow, can induce a flow of matter as well as electrical current (Kondepudi and Prigogine, 1998). Thus, local temperature jumps, in principle, can be transformed into local transmembrane ionic currents or other flows at the single cell level.

Obviously, many interesting questions can be asked in studies on the single cell level if temperature is available as a local cellular parameter. The relative simplicity of artificial temperature gradient induction in microvolumes raises other related questions concerning the possible presence of detectable endogenous temperature variations in living cells, accompanying many potentially powerful heat generation processes, especially those related to proton and calcium gradient disruptions.

Water is not such a perfect heat conductor. We experience this from the contact with our skin in hot or cold showers, especially when compared with the feeling experienced in contact with air. In the absence of flow (mass transfer), the ability of water to dampen temperature gradients is restricted by Fourier's law of heat transfer by conduction (see Appendix A). This raises many questions related to local thermodynamics in aqueous, yet crowded intracellular compartments (Verkman, 2002).

All of these questions necessarily involve heat translocation into a restricted number of the cellular and subcellular physical variables, subjected to the fast, local and precise control and measurement of temperatures in living cells.

Acknowledgements

V.Z. acknowledges Dr. Tobias Moser and Mr. Andreas Brandt for allowing the use of the T.I.L.L. imaging system for obtaining Figs. 2 and 3. We also thank Dr. Paul Black of Waseda University for reading an early version of the manuscript. This research was partly supported by Grants-in-Aid for Specially Promoted Research, for the 21st Century COE Program at Waseda University, and for the Bio-venture Project from the Ministry of Education, Sports, Culture, Science and Technology of Japan to S.I. This research was also partly supported by Grants-in-Aid for Special Research Projects 2002A-867 of Waseda University and

for the New Technology Development Project from the Ministry of Education, Sports, Culture, Science and Technology of Japan to M.S.

Appendix A

For simplicity, we consider the one-dimensional situation where the heat source is connected through the thermoconductive material of length L to an isothermal space, which is kept at a constant temperature T_0 (Fig. 7). If the heat source is producing a constant heat flow J (this is one of the boundary conditions. Another boundary condition is that the temperature of the space at the distance L from the heat source is kept constant). This flow initiates the increase in temperature in the neighboring areas of the medium until the system achieves a stationary temperature distribution $T(x)$ with a uniform heat flow along the length L (Fig. 7). The stationary situation means that there is no further accumulation of heat in the medium, and all the heat produced by the source dissipates into the isothermal space. This stabilization is a consequence of Fourier's law.

For the simplest case (Kondepudi and Prigogine, 1998):

(1) $\rho C\,\partial T/\partial t = -\partial J/\partial x$, where C is the heat capacity of the medium, ρ the density of water and t the time.
(2) $J = -k(\partial T/\partial x)$, where k is the thermal conductivity of the medium.

Then, the diffusion equation is obtained, i.e., $\rho C\,\partial T/\partial t = k\,\partial^2 T/\partial x^2$. In the stationary situation, $\partial T/\partial t = 0$ and $\partial^2 T/\partial x^2 = 0$, so that T is a linear function of x. Because J is constant in the stationary situation (1), the stationary temperature gradient $(\partial T/\partial x) = -J/k$ is obtained (2).

The temperature gradient attained at a constant heat flow, J, is inversely proportional to the thermal conductivity, k.

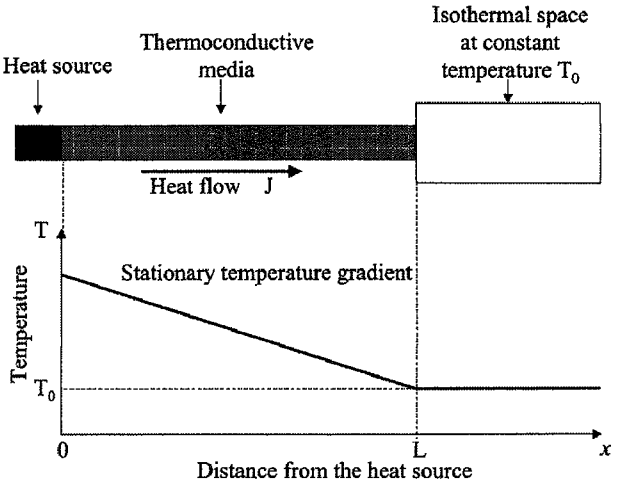

Fig. 7. Illustration showing a linear temperature gradient realized at a stationary state between the heat source and the isothermal space through a thermoconductive medium. A constant heat flow, J, is transmitted from the heat source to the isothermal space, of which the temperature is kept at a constant T_0.

This means that the same heat source will produce a larger temperature gradient in the medium when the value of k is lower. When the thermoconductive medium is water, the value of k is 0.597 W/m/K, which is in fact close to the range of thermoinsulators (Weast et al., 1986). The large heat capacity C of water only prolongs the relaxation time required to reach the final steep stationary temperature gradient, since the thermal diffusion coefficient is equal to $k/\rho/C$. Thus, it is possible to artificially create steep temperature gradients near a small heat source in water solutions.

For the three-dimensional situation, the stable temperature field distribution in water obtained by a highly focused laser beam was described in detail in Liu et al. (1995).

References

Abbott BC, Hill AV, Howarth JV. The positive and negative heat production associated with a nerve impulse. Proc R Soc Lond B Biol Sci 1958;148:149–87.

Alonso GL, Hecht JP. Thermodynamics of Ca^{2+} transport through sarcoplasmic reticulum membranes during the transient-state of simulated reactions. J Theor Biol 1990;147:161–76.

Ashkin A, Dziedzic JM. Optical trapping and manipulation of viruses and bacteria. Science 1987;235:1517–20.

Benndorf K. Multiple levels of native cardiac Na^+ channels at elevated temperature measured with high-bandwidth/low-noise patch clamp. Pflugers Arch 1993;422:506–15.

Bhaumik ML. Quenching and temperature dependence of fluorescence in rare earth chelates. J Chem Phys 1964;40:3711–5.

Bittner MA, Holz RW. A temperature-sensitive step in exocytosis. J Biol Chem 1992;267:16226–9.

Chapman CF, Liu Y, Sonek GJ, Tromberg BJ. The use of exogenous fluorescent probes for temperature measurements in single living cells. Photochem Photobiol 1995;62:416–25.

David G, Barrett EF. Stimulation-evoked increases in cytosolic $[Ca^{2+}]$ in mouse motor nerve terminals are limited by mitochondrial uptake and are temperature-dependent. J Neurosci 2000;20:7290–6.

de Meis L. Brown adipose tissue Ca^{2+}-ATPase: uncoupled ATP hydrolysis and thermogenic activity. J Biol Chem 2003;278:41856–61.

Dinkelacker V, Voets T, Neher E, Moser T. The readily releasable pool of vesicles in chromaffin cells is replenished in a temperature-dependent manner and transiently overfills at 37 °C. J Neurosci 2000;20:8377–83.

Gil A, Viniegra S, Gutierrez LM. Temperature and PMA affect different phases of exocytosis in bovine chromaffin cells. Eur J Neurosci 2001;13:1380–6.

Hardingham NR, Larkman AU. Rapid report: the reliability of excitatory synaptic transmission in slices of rat visual cortex in vitro is temperature dependent. J Physiol (Lond) 1998;507:249–56.

Herrera E, Salas K, Lagos N, Benos DJ, Reyes JG. Temperature dependence of intracellular Ca^{2+} homeostasis in rat meiotic and postmeiotic spermatogenic cells. Reproduction 2001;122:545–51.

Hill AV. The heat production of nerve. J Pharmacol 1926;29:161–5.

Howarth JV, Keynes RD, Ritchie JM. The origin of the initial heat associated with a single impulse in mammalian non myelinated nerve fibres. J Physiol (Lond) 1968;194:745–93.

Kato H, Nishizaka T, Iga T, Kinosita Jr K, Ishiwata S. Imaging of thermal activation of actomyosin motors. Proc Natl Acad Sci USA 1999;96:9602–6.

Kawaguchi K, Ishiwata S. Thermal activation of single kinesin molecules with temperature pulse microscopy. Cell Motil Cytoskeleton 2001;49:41–7.

Kolodner P, Tyson A. Microscopic fluorescent imaging of surface temperature profiles with 0.01 °C resolution. Appl Phys Lett 1982;40: 782–4.

Kondepudi D, Prigogine I. Modern thermodynamics. 1st ed. West Sussex, UK: Wiley; 1998. p. 333–50, 385–406.

Landau LD, Lifshitz EM. Statistical physics. Course of theoretical physics, vol. 5. Moscow: Nauka Press; 1964. p. 13–9.

Landeira-Fernandez AM, Morrissette JM, Blank JM, Block BA. Temperature dependence of the Ca^{2+}-ATPase (SERCA2) in the ventricles of tuna and mackerel. Am J Physiol Regul Integr Comp Physiol 2004;286:398–404.

Liu Y, Cheng DK, Sonek GJ, Berns MW, Chapman CF, Tromberg BJ. Evidence for localized cell heating induced by infrared optical tweezers. Biophys J 1995;68:2137–44.

Lowell BB, Spiegelman BM. Towards a molecular understanding of adaptive thermogenesis. Nature 2000;404:652–60.

Matteson DR, Armstrong CM. Evidence for a population of sleepy sodium channels in squid axon at low temperature. Gen Physiol 1982;79:739–58.

Nishizaka T, Miyata H, Yoshikawa H, Ishiwata S, Kinosita Jr K. Unbinding force of a single motor molecule of muscle measured using optical tweezers. Nature 1995;377:251–4.

Palou A, Pico C, Bonet ML, Oliver P. The uncoupling protein, thermogenin. Int J Biochem Cell Biol 1998;30:7–11.

Parker I. Ionic and charge-displacement currents evoked by temperature jumps in *Xenopus* oocytes. Proc R Soc Lond B Biol Sci 1989;237:379–87.

Quartararo N, Barry PH. Ion permeation through single ACh-activated channels in denervated adult toad sartorius skeletal muscle fibres: effect of temperature. Pflugers Arch 1988;411:101–12.

Reichling DB, Levine JD. Heat transduction in rat sensory neurons by calcium-dependent activation of a cation channel. Proc Natl Acad Sci USA 1997;94:7006–11.

Reis M, Farage M, de Meis L. Thermogenesis and energy expenditure: control of heat production by the Ca^{2+}-ATPase of fast and slow muscle. Mol Membr Biol 2002;19:301–10.

Shannon TR, Bers DM. Assessment of intra-SR free [Ca^{2+}] and buffering in rat heart. Biophys J 1997;73:1524–31.

Shiels HA, Vornanen M, Farrell AP. Effects of temperature on intracellular Ca^{2+} in trout atrial myocytes. J Exp Biol 2002;205:3641–50.

Tian R, Halow JM, Meyer M, Dillmann WH, Figueredo VM, Ingwall JS, et al. Thermodynamic limitation for Ca^{2+} handling contributes to decreased contractile reserve in rat hearts. Am J Physiol 1998;275:H2064–71.

Tseeb VE, Geletiuk VI, Kazachenko VN. Temperature dependence of the conductivity of individual potential-dependent K^+-channels in mollusk neurons. Biofizika 1991;36:810–21.

Tullis A, Block BA, Sidell BD. Activities of key metabolic enzymes in the heater organs of scombroid fishes. Exp Biol 1991;161:383–403.

Verkman AS. Solute and macromolecule diffusion in cellular aqueous compartments. Trends Biochem Sci 2002;27:27–33.

Ward GD, Watson IA, Stewart-Tull DE, Wardlaw AC, Wang RK, Nutley MA, et al. Bactericidal action of high-power Nd:YAG laser light on *Escherichia coli* in saline suspension. J Appl Microbiol 2000;89:517–25.

Weast RC, Astle MJ, Beyer WH, editors. Handbook of chemistry and physics. 67th ed. Boca Raton, FL: CRC Press; 1986.

Zohar O, Ikeda M, Shinagawa H, Inoue H, Nakamura H, Elbaum D, et al. Thermal imaging of receptor-activated heat production in single cells. Biophys J 1998;74:82–9.

nature
structural &
molecular biology

Mechanochemical coupling of two substeps in a single myosin V motor

Sotaro Uemura[1], Hideo Higuchi[2,3], Adrian O Olivares[4], Enrique M De La Cruz[4] & Shin'ichi Ishiwata[1,5]

Myosin V is a double-headed processive molecular motor that moves along an actin filament by taking 36-nm steps. Using optical trapping nanometry with high spatiotemporal resolution, we discovered that there are two possible pathways for the 36-nm steps, one with 12- and 24-nm substeps, in this order, and the other without substeps. Based on the analyses of effects of ATP, ADP and 2,3-butanedione 2-monoxime (a reagent shown here to slow ADP release from actomyosin V) on the dwell time and the occurrence frequency of the main and the intermediate states, we propose that the 12-nm substep occurs after ATP binding to the bound trailing head and the 24-nm substep results from a mechanical step following the isomerization of an actomyosin-ADP state on the bound leading head. When the isomerization precedes the 12-nm substep, the 36-nm step occurs without substeps.

Myosin V belongs to the myosin superfamily of actin-based molecular motors and is involved in the intracellular transport of organelles[1–4]. Myosin V consists of two identical heavy chains, each composed of an N-terminal motor domain ('head'), a domain comprising six IQ motifs that bind light chains ('neck'), a coiled coil dimerization domain and a globular cargo-binding tail domain[1,3]. Myosin V is a processive motor that 'walks' along an actin filament toward the barbed end over a long distance without dissociating from the filament[5,6]. Electron microscopy of actomyosin V in the presence of low ATP concentrations shows both motor domains of myosin V bound to the actin filament at sites spaced 36 nm apart, which corresponds to the half pitch of the filament long-pitch helix[7]. Experiments using optical tweezers identified processive 36-nm steps of a bead, on which single myosin V molecules were adsorbed[6,8]. Moreover, it was shown that myosin V walks as a left-handed spiral motor along an actin filament, because the average step size is slightly shorter than the half pitch of the long-pitch actin helix[9].

The hand-over-hand walking model has received strong support from two recent experiments that (i) observed the orientation of the neck domain of myosin V by monitoring the polarization of a single fluorophore covalently attached to a light chain[10] and (ii) measured the stepwise displacement of a single fluorophore labeled at one of six light chains of myosin V[11].

Solution kinetic studies demonstrate that ADP release occurs at ~15 s^{-1} and limits the myosin V ATPase cycle[12]. Microscopic analysis of myosin V stepping under various nucleotide conditions is consistent with rate-limiting ADP release[13]. The next key target is to determine how the mechanical and biochemical cycles are coupled to each other at the single-molecule level.

Here, we focused on mechanical events and detected substeps that occur within each regular 36-nm step with high temporal resolution. Each regular 36-nm step is composed of two consecutive substeps, one generating a 12-nm substep and the other a 24-nm substep. To investigate how these substeps and the states attained after the steps are coupled to the ATPase cycle of myosin V, we examined the effects of ATP and ADP concentrations, and 2,3-butanedione 2-monoxime (BDM)[14]. We also examined the force dependence of the occurrence frequency of each step and substep, and the dwell time of each state.

RESULTS

Movement of myosin V along an actin filament

A single myosin V–coated bead was trapped with optical tweezers and brought into contact with a fluorescently labeled biotinylated actin filament, which was immobilized on an avidin-coated glass surface through biotinylated BSA (**Fig. 1a**). A focused red light (685 nm) laser was used to diagonally illuminate the bead, and its dark-field image was projected onto a quadrant photodiode. The bead displacement was determined by measuring the differential output of the quadrant photodiode with nanometer accuracy and a 10-kHz sampling rate[15]. The use of a 200-nm-diameter bead here instead of a 1-μm bead was essential to obtain a high spatiotemporal resolution.

An example of the time course of bead displacement along an actin filament (**Fig. 1b**) shows three consecutive runs of a single myosin V molecule along an actin filament at a saturating ATP concentration (1 mM). As the bead began to deviate from the trap center, a positive external load was applied to the myosin V–actin complex (toward the pointed end of an actin filament). Myosin V detached from actin at a stall force of ~3 pN. After detachment, the bead quickly returned to the

[1]Department of Physics, School of Science and Engineering, Waseda University, 3-4-1 Okubo, Shinjuku-ku, Tokyo 169-8555, Japan. [2]Department of Metallurgy, Graduate School of Engineering, [3]Center of Interdisciplinary Research, Tohoku University, Sendai, 980-8579, Japan. [4]Department of Molecular Biophysics and Biochemistry, Yale University, New Haven, Connecticut 06520, USA. [5]Advanced Research Institute for Science and Engineering, Waseda University, 3-4-1 Okubo, Shinjuku-ku, Tokyo 169-8555, Japan. Correspondence should be addressed to S.I. (ishiwata@waseda.jp).

Published online 1 August 2004; doi:10.1038/nsmb806

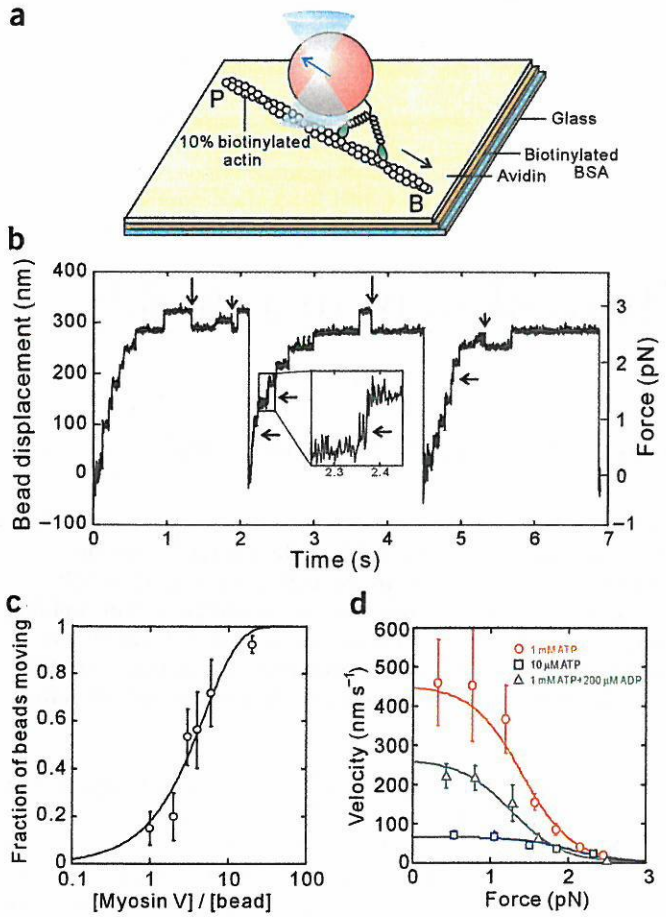

Figure 1 Stepwise movement of single myosin V motor under various external loads. (**a**) Schematic illustration showing how the movement of a myosin V–coated bead is measured. To allow the interaction of myosin V with an actin filament, the bead trapped with optical tweezers was moved onto a single actin filament attached to the glass surface through BSA using the biotin-avidin interaction. The position of the trap center was then fixed. The black and blue arrows, respectively, show the directions for the myosin V movement and the applied external load. (**b**) An example showing the displacement of the bead, where the consecutive 36-nm stepwise movements are clearly seen. A backward 36-nm step is shown by a large vertical arrow. A backward step for the substep is shown by a vertical small arrow. An intermediate state (shown by horizontal arrows) after a short step (substep) is sometimes observable; the 36-nm step in the middle trace is enlarged in an inset. The force was calculated from the displacement of the bead from the trap center times trap stiffness (0.009 pN nm^{-1} in **b**; right axis). (**c**) Relation between proportion of beads that moved along an actin filament and a mixing molar ratio of myosin V to beads. The proportion of moved beads (avg. ± s.d.) was obtained by examining three trials for each bead (20 different beads) at each point. A solid curve was obtained by fitting with $1 - e^{-\lambda c}$, where c is the mixing molar ratio of myosin V to beads, and λ (0.197) is the fitting parameter[9,17,18]. (**d**) Force-velocity relationship obtained under different conditions (n = 8–24 at each point, total = 405). The relationship shown by solid curves was obtained as described in the Methods section.

trap center and immediately began to deviate from the trap center again as a result of the processive motility of myosin V along actin.

We observed regular forward steps of ~36 nm, approximately equal to the half pitch of the actin filament helix. Nearly half of the 36-nm steps contained an 'intermediate state', indicated by horizontal arrows in **Fig. 1b** (compare inset). At higher forces ≥2 pN, backward 36-nm steps (see large vertical arrows in **Fig. 1b**) and backward steps from the intermediate state (see small vertical arrows in **Fig. 1b**) were identified[8,16].

To confirm that a single molecule is sufficient to generate the movement observed, we examined the fraction of beads that bind and move processively along an actin filament at various mixing ratios of myosin V and bead. We confirmed by statistical analysis that single myosin V molecules were sufficient to move the beads (**Fig. 1c**)[17,18].

The force-velocity relationships in the presence of 1 mM ATP (± ADP) were sigmoidal, showing a steep decrease in the velocity at higher than ~1 pN (**Fig. 1d**). In comparison, the relationship in the presence of 10 μM ATP showed a small force dependence. ADP release is rate limiting in the presence of 1 mM ATP[12], whereas ATP binding becomes rate limiting at low ATP concentrations[12]. The present results suggest that ADP release is more load dependent than ATP binding. It should be noted that the stall force, 2.5–3 pN, does not depend on the nucleotide conditions (**Fig. 1d**).

Measurement of substeps within each 36-nm step

The time course of bead movement examined on an expanded time scale with 0.1-ms time intervals clearly shows the existence of substeps within the regular 36-nm step (**Fig. 2**). We identified the presence of

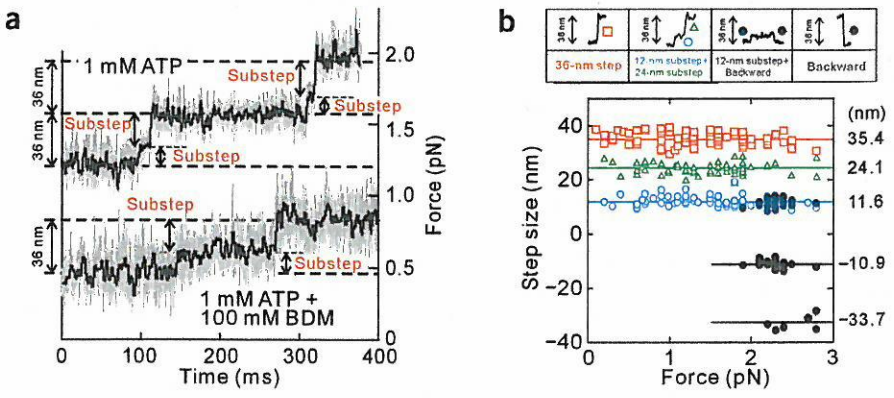

Figure 2 The time course of myosin V movement at a 10-kHz sampling rate and force dependence of the occurrence of various steps. (**a**) Consecutive two substeps at 1 mM ATP shown in the upper trace and at 1 mM ATP + 100 mM BDM shown in the lower trace. We determined whether or not substeps were present by obtaining the histogram of the bead positions at 0.1-ms time intervals (gray lines). Black lines were obtained by the smoothing of 21 successive points. (**b**) Force dependence of step size in the presence of 1 mM ATP. The size of the steps was estimated as described in Methods. The first 12-nm substep, blue circle; the second 24-nm substep, green triangle; the 36-nm step in which substeps could not be identified, red square; the 12-nm substep that was followed by a backward step, dark blue circle; the backward steps, black circles. We could not determine the occurrence of the 24-nm backward step. The figures along the right ordinate are the average step size estimated independent of force as shown by a straight line parallel to the abscissa.

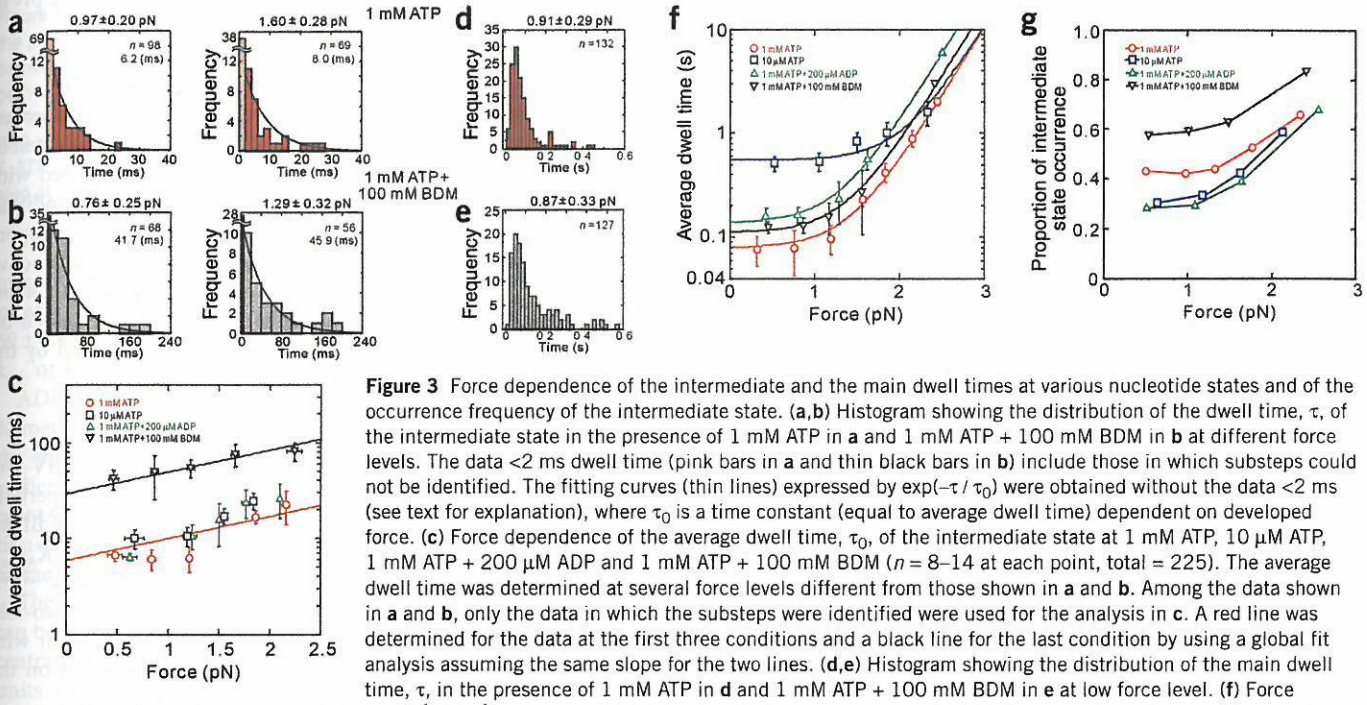

Figure 3 Force dependence of the intermediate and the main dwell times at various nucleotide states and of the occurrence frequency of the intermediate state. (**a**,**b**) Histogram showing the distribution of the dwell time, τ, of the intermediate state in the presence of 1 mM ATP in **a** and 1 mM ATP + 100 mM BDM in **b** at different force levels. The data <2 ms dwell time (pink bars in **a** and thin black bars in **b**) include those in which substeps could not be identified. The fitting curves (thin lines) expressed by $\exp(-\tau / \tau_0)$ were obtained without the data <2 ms (see text for explanation), where τ_0 is a time constant (equal to average dwell time) dependent on developed force. (**c**) Force dependence of the average dwell time, τ_0, of the intermediate state at 1 mM ATP, 10 μM ATP, 1 mM ATP + 200 μM ADP and 1 mM ATP + 100 mM BDM (n = 8–14 at each point, total = 225). The average dwell time was determined at several force levels different from those shown in **a** and **b**. Among the data shown in **a** and **b**, only the data in which the substeps were identified were used for the analysis in **c**. A red line was determined for the data at the first three conditions and a black line for the last condition by using a global fit analysis assuming the same slope for the two lines. (**d**,**e**) Histogram showing the distribution of the main dwell time, τ, in the presence of 1 mM ATP in **d** and 1 mM ATP + 100 mM BDM in **e** at low force level. (**f**) Force dependence of the average dwell time, τ_0 ($= k_1^{-1} + k_2^{-1}$) of the main state at 1 mM ATP, 10 μM ATP, 1 mM ATP + 200 μM ADP and 1 mM ATP + 100 mM BDM (n = 18–32 at each point, total = 562). The average dwell time was determined at several force levels different from those shown in **d** and **e**. All the data shown in **d** and **e** were used for the analysis in **f**. The force dependence of τ_0 for each condition was expressed by $\tau_D \exp(Fd_D / k_B T) + \tau_C$, where τ_C is the time constant representing the dwell time independent of force. The values obtained are summarized in **Table 1**. (**g**) The occurrence frequency of the intermediate state at several force levels for each nucleotide condition. Not only the 36-nm steps with substeps but also those without substeps are included in the first column shown by pink and thin black bars in **a** and **b**. Thus, the occurrence frequency of the 36-nm main steps without substeps was estimated by subtracting that obtained by extrapolating the exponential function of the dwell time distribution for the intermediate state.

the intermediate state by making a histogram of the bead position before and after each 36-nm step. We refer to each 36-nm step, in which substeps could not be identified, as a 'main step'. The state populated after the main step or subsequent to the intermediate state is termed a 'main state'. The intermediate state had a lifetime of a few milliseconds at low forces in the presence of 1 mM ATP (an upper trace in **Fig. 2a**) and tens of milliseconds in the presence of 100 mM BDM (lower trace in **Fig. 2a**). The main state had a longer lifetime (several tens of milliseconds) than the intermediate state in all the conditions tested. The substeps occurred at random and did not correlate with the occurrence of the 36-nm main steps.

The step size was determined directly from the time course of stepwise movements of the myosin V–coated bead. A step size distribution had peaks at 11.6 nm (12-nm substep), 24.1 nm (24-nm substep) and 35.4 nm (36-nm step in which substeps could not be identified), and included backward steps at 12 nm and 36 nm (**Fig. 2b**). The step size of either the two substeps or for the single main step depended little on the force level (**Fig. 2b**), although a possibility that the step size depends on the force level cannot be excluded because we did not take account of the attenuation factor to estimate the step size (see Methods). On the other hand, approaching the stall force, the occurrence frequency of 24-nm and 36-nm steps decreased and that of backward steps increased.

Characterization of the intermediate state

Histograms showing the distribution of intermediate state dwell times under several nucleotide and force conditions fit single exponentials regardless of the nucleotide conditions (**Fig. 3a,b**), indicating that this dwell time is coupled with a single chemical reaction. The decay time estimated by exponential fitting became longer as force (balanced to external load) increased. It should be noted here that the occurrence frequency <2 ms dwell time (shown by pink bars in **Fig. 3a** and thin black bars in **Fig. 3b**) largely exceeded that estimated from the exponential fitting of the dwell time, strongly suggesting that there is a pathway for the 36-nm main step without the intermediate state. In the Discussion, we attempt to construct a walking model that can explain this postulate.

The intermediate dwell time did not depend on the concentrations of ATP and ADP (**Fig. 3c**), suggesting that the intermediate state is not coupled with nucleotide binding or release. On the other hand, BDM markedly prolonged the intermediate dwell time (**Figs. 2a** and **3b**).

The force dependence of the average dwell time of the intermediate state is expressed by the single exponential function of the force, $\tau_i \exp(Fd_i / k_B T)$, where τ_i is the average dwell time in the absence of force (F), d_i the characteristic distance (a parameter having the dimension of length that characterizes the bond instability against applied load), k_B the Boltzmann constant and T the absolute temperature (**Fig. 3c**). We determined the values of τ_i and d_i by global fitting of all the data[19,20], assuming that τ_i is only prolonged by the addition of BDM and d_i is common to all the conditions examined (see **Table 1**).

Characterization of the main state

In contrast to the intermediate dwell time (**Fig. 3a–c**), the histogram of the main dwell time (**Fig. 3d,e**) shows a peak. The main dwell time can be expressed by the sum of two exponential functions as shown previously[8], indicating that the main dwell time is coupled with two consecutive chemical reactions.

Table 1 Parameters obtained by dwell time analysis

	$\tau_{Total} = \tau_D \exp(Fd_D / k_BT) + \tau_C + \tau_i \exp(Fd_i / k_BT)$			
Nucleotide states	τ_{Total} ($F = 0$)	τ_D (ms), d_D (nm)	τ_C (ms)	τ_i(ms), d_i (nm)
1 mM ATP	86.7 ± 13.0	1.1 ± 0.3, 12.5 ± 0.4	79.7 ± 11.5	5.9 ± 1.2, 2.2 ± 0.2
1 mM ATP + 100 mM BDM	141.2 ± 16.2	1.7 ± 0.4, 12.5 ± 0.4	110.6 ± 9.2	28.9 ± 6.6, 2.2 ± 0.2
1 mM ATP + 200 μM ADP	145.5 ± 20.2	2.8 ± 0.3, 12.5 ± 0.4	136.8 ± 18.7	5.9 ± 1.2, 2.2 ± 0.2
10 μM ATP	553.5 ± 50.1	1.1 ± 0.3, 12.5 ± 0.4	546.5 ± 48.6	5.9 ± 1.2, 2.2 ± 0.2

The main dwell time was fit to the sum of a force-dependent exponential and a constant, whereas the intermediate dwell time was fit to a force-dependent single exponential. The values of parameters τ_D, d_D, τ_C, τ_i and d_i were determined by global fit with nonlinear optimization[19,20] using SigmaPlot 8.0. For the global fit analysis, we assumed that the values of d_D and d_i are common to the main and intermediate states, respectively, and τ_D and τ_i for some nucleotide states.

Either lowering the ATP concentration or adding ADP caused an increase in the average dwell time, τ_0 ($\tau_0 = k_1^{-1} + k_2^{-1}$) (**Fig. 3f**). This indicates that ATP binding and ADP release shorten the dwell time of the main state[8]. We also confirmed that the average dwell time increases with force (**Fig. 3f**). We observed that 100 mM BDM prolonged this dwell time at every force level.

The force (F) dependence of the average main dwell time is expressed by $\tau_D \exp(Fd_D / k_BT) + \tau_C$, where the values of τ_D, d_D and τ_C were determined by global fitting of all the data[19,20], assuming that d_D is common to all the conditions examined, τ_D is longer in the presence of either ADP or BDM, and τ_C is different at every condition. We conclude that τ_D is attributable to ADP release in the absence of load, because the value of τ_D is determined independent of the ATP concentration but prolonged by ADP and BDM (see **Table 1**). τ_C is a constant term, which increased on lowering the ATP concentration and adding ADP (see **Table 1**). Also, it is to be noted that the large value of d_D (12.5 nm) indicates that ADP release largely depends on the force level. (Note that this factor becomes predominant at the force level higher than ~1 pN in 1 mM ATP or ~2 pN in 10 μM ATP, as observed in **Fig. 3f**.)

Frequency of the intermediate state

The occurrence frequency of the intermediate state within the 36-nm main step is greatest in the presence of BDM and is increased with force irrespective of the nucleotide condition (**Fig. 3g**). In the absence of BDM, the proportion merged at a high force level irrespective of the nucleotide conditions, whereas at a low force level the proportion was decreased on lowering the ATP concentration and by the addition of ADP.

Effects of BDM on the ATPase kinetics of myosin V

Actin filaments activate the steady-state ATPase activity of MV-1IQ (**Fig. 4a**). The solid line in **Fig. 4a** is the best fit to a hyperbola (rate = (V_{max} × [actin] / (K_{ATPase} + [actin])). In the absence of BDM, the maximum turnover rate, V_{max}, was 13.7 ± 0.9 s^{-1} and the K_{ATPase} was 3.5 ± 0.6 μM, in agreement with earlier determinations[12,21,22]. BDM (100 mM) reduces the V_{max} and K_{ATPase} approximately two-fold to 6.9 ± 0.2 s^{-1} and 2.3 ± 0.2 μM, respectively. In agreement with an earlier study[23], ~10 mM BDM has no appreciable effect on the maximal steady-state cycling of MV-1IQ.

Actin filaments accelerate the rate of transient P_i release from MV-1IQ-ADP-P_i (**Fig. 4b**). Time courses of P_i release follow single exponentials (**Fig. 4b** inset) because myosin V is limited to a single ATP turnover by including excess ADP in the actin filament solution (see Methods). In the absence of BDM, the maximum rate of P_i release from MV-1IQ-ADP-P_i (k_{+4}' following nomenclature of ref. 24) was 60 ± 9 s^{-1} and the actin concentration at the half-maximum rate (K_9^{-1}, ref. 24) was 7.3 ± 0.6 μM. The rate of myosin V-ADP-P_i binding

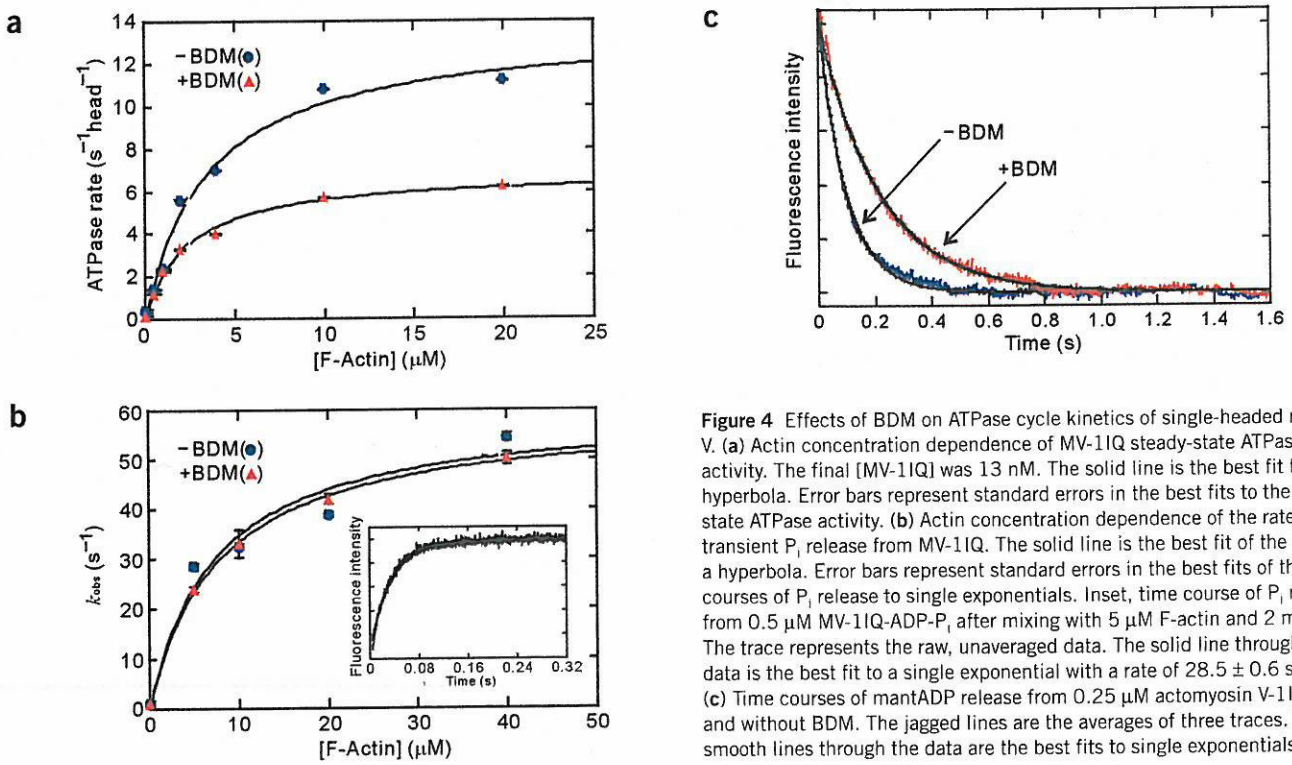

Figure 4 Effects of BDM on ATPase cycle kinetics of single-headed myosin V. (**a**) Actin concentration dependence of MV-1IQ steady-state ATPase activity. The final [MV-1IQ] was 13 nM. The solid line is the best fit to a hyperbola. Error bars represent standard errors in the best fits to the steady-state ATPase activity. (**b**) Actin concentration dependence of the rate of transient P_i release from MV-1IQ. The solid line is the best fit of the data to a hyperbola. Error bars represent standard errors in the best fits of the time courses of P_i release to single exponentials. Inset, time course of P_i release from 0.5 μM MV-1IQ-ADP-P_i after mixing with 5 μM F-actin and 2 mM ADP. The trace represents the raw, unaveraged data. The solid line through the data is the best fit to a single exponential with a rate of 28.5 ± 0.6 s^{-1}. (**c**) Time courses of mantADP release from 0.25 μM actomyosin V-1IQ with and without BDM. The jagged lines are the averages of three traces. The smooth lines through the data are the best fits to single exponentials.

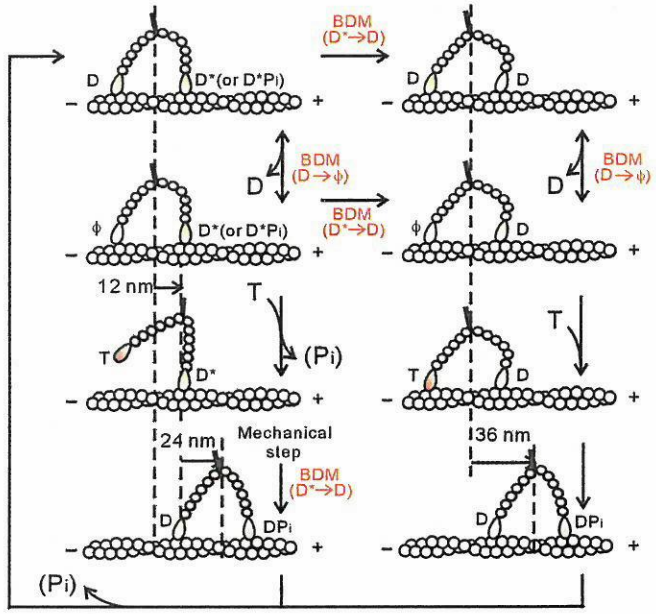

Figure 5 Hand-over-hand model coupled with nucleotide states explaining the present results. We propose that there are two possible pathways: pathway 1 in which 12-nm and 24-nm substeps occur (left column), and pathway 2 in which only the 36-nm main step occurs (right column). BDM is assumed to stabilize both the AMD complex (D) and the AM*D complex (D*), so that the transition rates indicated by red arrows are slowed down. T, ATP; D, ADP; P_i, inorganic phosphate; ϕ, no nucleotides; (P_i), a possible step at which P_i release occurs. For more details, see the text.

to actin filaments (K_9k_{+4}') was ~8 μM^{-1} s^{-1}, comparable to earlier measurements[12]. In the presence of 100 mM BDM, k_{+4}' was 59 ± 1.4 s^{-1} and K_9^{-1} was 7.7 ± 0.6 μM. BDM (100 mM) does not affect k_{+4}' or K_9^{-1} (**Fig. 4b**).

ADP release limits steady-state cycling of myosin V[12,21]. The rate of *N*-methylanthraniloyl-ADP (mantADP) release from actoMV-1IQ in the absence of BDM (**Fig. 4c**) was 10.2 ± 0.1 s^{-1}, in agreement with earlier determinations[12,21,22]. BDM (100 mM) slowed the rate of mantADP release approximately two-fold to 4.6 ± 0.1 s^{-1}. The reduction in ADP release accounts for the slower turnover rate in the presence of 100 mM BDM.

The K_{ATPase} of a myosin with rate-limiting ADP release ($k_{+5}' = V_{max}$) can be related to the maximum rate of P_i release (k_{+4}'), the actin concentration needed to reach half of the maximum P_i release rate (K_9, in units of M^{-1}), and the equilibrium constant for ATP hydrolysis (K_3)(ref. 21): $K_{ATPase} = k_{+5}'(K_9/k_{+4}')$ ($\{1 + K_3\}/K_3$). The two-fold reduction of ADP release (k_{+5}') by 100 mM BDM accounts for the two-fold reduction in V_{max} and K_{ATPase}, suggesting that BDM does not greatly affect the equilibrium constant for ATP hydrolysis (K_3), even though it was not measured directly. This result is in contrast to the case of muscle myosin II, where BDM stabilizes the actomyosin ADP-P_i state and accordingly suppresses P_i release[25]. Finally, we confirmed that the velocity of bead movement in the absence of external load decreased as the concentrations of BDM increased in the presence of 1 mM ATP. The BDM concentration dependence of the average bead velocity showed that the velocity decreases to nearly half with the addition of 100 mM BDM (data not shown). These results are consistent with those of the steady-state ATPase (**Fig. 4a**).

DISCUSSION

We propose here a hand-over-hand walking model of myosin V by taking into account all the experimental data described here together with those reported elsewhere[7,26,27].

First, considering that BDM reduces the rate of ADP release from actomyosin V (**Fig. 4c**) and largely prolongs the intermediate state (**Fig. 3a–c**), it is possible that the main species of the intermediate state is the actomyosin V–ADP complex and that the 24-nm substeps occur accompanied by the ADP release. However, this contradicts the observation that exogenous ADP does not affect the dwell time of the intermediate state. To resolve this apparent contradiction, we assume that isomerization exists in the actomyosin V (AM)–ADP complex, that is, AM*ADP (D*) and AMADP (D). It has already been proposed on the basis of a kinetic study using mant-nucleotides[13] that two states exist in the AM-ADP complex. Furthermore, it is well known that such an isomerization exists in the contraction mechanism of the muscle actomyosin II system[28]. Here, D is a complex produced by the binding of ADP to AM, whereas D* is produced after the hydrolysis of ATP on the AM-ATP complex[28,29]. We assume that D* is the major component of the intermediate state, implying that BDM stabilizes the D* state.

The intermediate state is terminated by the 24-nm substep, so that a straightforward deduction from such consideration is that the 24-nm substep occurs by the mechanical step mainly following the transition from D* to D (a part of the 24-nm substep may be attributable to the binding of detached head (T or DP_i) to actin after Brownian motion). It is notable that one set of researchers[30] showed that, in a single-headed myosin V, there exist two stable binding modes with different angles of the neck region in the ADP-bound state. Also, another group[31] recently showed that a one-headed myosin V produces a 25-nm working stroke.

The occurrence frequency of the 36-nm main step, in which the intermediate state could not be identified, was substantially larger than that predicted from the frequency extrapolated from the exponential fitting of the distribution of the dwell time of the intermediate states (**Fig. 3a,b**). This is understandable if we assume that there are two kinetic pathways for the 36-nm steps with (pathway 1) and without (pathway 2) passing through the intermediate state.

On the main state, the dwell time is largely prolonged on lowering the ATP concentration, and by adding ADP or 100 mM BDM (**Fig. 3d–f**), implying that it is shortened by the attachment of ATP and the detachment of ADP. The simplest assumption deduced from these results is that the main state is terminated; that is, the 12-nm substep occurs upon the ATP binding to a bound trailing head of myosin V from which ADP has been released. This assumption is similar to that predicted by Kolomeisky and Fisher[32] and also consistent with several models previously proposed for myosin V[7,22,24,26,27] and for myosin VI[24]. This is also consistent with the effect of BDM that slows the ADP release (**Fig. 4c**) and the overall ATPase activity as shown by the decrease in the velocity of myosin V movement (data not shown). That is, BDM stabilizes not only the D* state but also the D state.

Thus, we propose the hand-over-hand model as illustrated in **Fig. 5**, which incorporates the previous models[7,26,27] and which can explain, at least qualitatively, all the data presented here. First, the model can account for the existence of two kinds of steps: the 36-nm step composed of the sequential 12-nm and 24-nm substeps (pathway 1), and the 36-nm main step without substeps (pathway 2). The occurrence frequency of these two pathways depends on the conditions as discussed later. According to this model, the intermediate state is in a single-headed binding, whereas the main state is in a double-headed binding. This may be experimentally confirmed by the measurements of the stiffness of the protein-bead complex. In this respect, it is notable

that Veigel *et al.*[31] reported that the low stiffness intervals, which may imply the single-headed binding, exist during the main steps.

Second, the 12-nm substep is assumed to occur upon the binding of ATP to the bound trailing head. Although we do not know whether the bound leading head is D* or D*P_i at this stage (the upper left in **Fig. 5**), we infer that the 12-nm step may be attributable to the conformational change of the leading head due to the transition from DP_i to D* (or D*P_i).

Third, if the transition rate from D* to D decreases on increasing the force level, not only the dwell time of the intermediate state but also that of the main state are prolonged. Besides, we can understand that the higher the force level, the higher the occurrence frequency of the intermediate state irrespective of the nucleotide conditions (**Fig. 3g**), because the transition probability of the process shown by the horizontal arrows in **Fig. 5** (from the pathway 1 to the pathway 2) is suppressed irrespective of the nucleotide conditions.

Fourth, because we assumed that BDM stabilizes not only the D* state but also the D state, both the intermediate state and the main state are stabilized, so that the dwell times of both states are expected to be prolonged. This assumption can also explain a large degree of extension of the dwell time, τ_i, of the intermediate state, because it is tightly coupled to the lifetime of the D* state, whereas the degree of extension of the dwell time of the main state was less because several other states must be involved in the main state.

Fifth, at low ATP concentrations, the attachment of ATP to the bound trailing head is slowed down, so that the probability increases that the transition from D* to D occurs at the bound leading head before ATP binds to the trailing head. This results in the increase in the occurrence frequency of the pathway 2. In the pathway 2, it is expected that the internal strain is largest within the D-D complex, because the leading head is considered to take the orientation similar to that realized after the 24-nm mechanical step. Thus, the D-D (also ϕ-D) complex may have a telemark shape as observed by electron microscopy[7]. It is to be stressed that the two pathways are not independent of each other, but the pathway 1 (or 2) is chosen when the transition from D* to D occurs after (or before) the 12-nm substep; that is, the model in **Fig. 5** proposes that the timing of the 12-nm substep and the isomerization (the transition from D* to D) determines the pathways.

Finally, if the binding affinity of ADP for the bound trailing head is lower than that for the bound leading head because of the mechanochemical coupling due to the internal strain, ADP tends to detach from the bound trailing head, which results in the binding of ATP to the trailing head. Such an asymmetrical binding affinity of ADP may be prerequisite for the directional movement of myosin V toward the barbed end of an actin filament, although this must be experimentally confirmed. We infer that the loading-direction dependency of binding affinity of ADP assumed for myosin V is the reverse of that for kinesin as recently reported by us[20]. Also, another study[33] showed that the binding of ATP to the bound leading head is prerequisite for the directional movement of kinesin toward the plus-end of a microtubule. The correspondence between internal strain and nucleotide affinity in mechanochemical coupling for myosin V may be different from that for kinesin.

METHODS

Protein and assays used for optical trapping measurements. Myosin V was purified from chick brains[34]. Actin purified from rabbit skeletal muscle was biotinylated by 10% and, after polymerization, the filaments were labeled with rhodamine phalloidin (Molecular Probes)[35]. About 1 nM of fluorescent polystyrene beads (200 nm in diameter, yellow-green; Molecular Probes) were incubated for 20 min in an assay buffer (10 mM imidazole-HCl, pH 7.2, 75 mM KCl, 2.5 mM $MgCl_2$, 2 mM DTT and 0.1 mM EGTA) containing 10 mg ml^{-1} BSA. Myosin V (650 kDa) molecules were mixed with the beads at a molar ratio of 3:1 in assay buffer containing 300 mM KCl instead of 75 mM KCl as had been used in the previous studies. The average number of functional myosin V molecules on a bead was estimated by statistical analyses to be one (considering the geometry of the myosin V on the bead, we estimate that only single myosin V molecules interacted with an actin filament in almost all the measurements[17,20]). Assay buffer containing biotinylated BSA at 3 mg ml^{-1} was introduced into a flow cell and incubated for 2 min to coat the glass surface with biotinylated BSA. After rinsing with two volumes of assay buffer, 2 mg ml^{-1} streptavidin in assay buffer was flowed into the cell and incubated for 2 min. After rinsing with assay buffer, a solution of actin filaments, of which 10% was biotinylated and labeled with rhodamine-phalloidin, was flowed into the cell to allow binding of the filaments to the glass surface through avidin-bound biotinylated BSA. The flow cell was then filled with assay solution containing the myosin V–coated beads, filtered BSA and an oxygen-scavenging enzyme system[9]. The final solvent condition was approximately 0.1 pM myosin V–coated beads, 10 mM imidazole-HCl, pH 7.2, 75 mM KCl, 2.5 mM $MgCl_2$, 2 mM DTT, 0.1 mM EGTA, 3.6 mg ml^{-1} glucose, 0.08 mg ml^{-1} glucose oxidase, 0.01 mg ml^{-1} catalase, 0.95% (v/v) β-mercaptoethanol and nucleotides (1 mM ATP, 10 μM ATP, 1 mM ATP + 200 μM ADP or 1 mM ATP + 100 mM BDM). We were able to observe repeatedly the stepwise movements of myosin V–coated beads along the same actin filaments on the same beads, presumably for the same myosin V molecules, by using optical tweezers to manipulate the beads. All experiments on microscopy were done at 24 ± 1 °C.

We found that the percentage of biotinylation of actin is important for the processive movement of myosin V. In other words, myosin V could move processively on 1% and 10% biotinylated actin filaments, whereas it could not on 100% biotinylated ones, suggesting that the manner in which actin filaments bind to the glass surface is crucial. It should be noted that myosin V is reported to be a left-handed spiral motor[9], so that the revolution of a myosin V–coated bead around the actin filament could be sterically hindered. However, this possibility could be ignored, because the maximum distance of bead displacement was less than ~0.3 μm (**Fig. 1b**), such that it was much shorter than the distance, 2 μm, for one revolution[9].

The velocity of myosin V under no external load was obtained from the time course of bead movement along an actin filament in the absence of optical trap. The bead position was determined by the center of the fluorescence intensity distribution of the bead every video frame.

Proteins and reagents used for biochemical experiments. Actin was purified from rabbit skeletal muscle and gel filtered over Sephacryl S-300HR (ref. 12). The motor domain of myosin V containing the first IQ motif (MV-1IQ) and the essential light chain, LC-1sa, were co-expressed in Sf9 insect cells and purified by FLAG affinity chromatography[12]. The fluorescently labeled mutant of the phosphate-binding protein (MDCC-PBP; clone provided by M.R. Webb, National Institute for Medical Research, London) was expressed, purified and labeled as described[36]. ATP and ADP were purchased from Roche Molecular Biochemicals. mantADP was synthesized as described[37] or purchased from Molecular Probes with identical results. A molar equivalent of $MgCl_2$ was added to nucleotides immediately before use. BDM was purchased from Sigma (lot 092K1722) and prepared as a 250 mM stock solution in KMg50-MOPS (10 mM MOPS, pH 7.0, 50 mM KCl, 1 mM $MgCl_2$, 1 mM EGTA and 1 mM DTT) immediately before use[21].

Instrumentation and calibration. The myosin V–coated bead was trapped with an optical tweezers—that is, a focused infrared laser beam (λ = 1,064 nm, 2 W; Spectra Physics)—and illuminated diagonally by a focused red laser beam (λ = 685 nm, 20 mW; Phototechnica) through an objective lens (fluor ×100/1.3 oil; Nikon). The light scattered by the bead was gathered by an objective lens with an aperture (NA = 0.5, ×100 oil; Olympus) and projected onto a quadrant photodiode sensor (S4349; Hamamatsu Photonics) coupled to a differential amplifier (20-kHz roll-off frequency; OP711, Sentec). The fluorescently labeled beads and actin labeled with rhodamine-phalloidin were excited by a green laser (λ = 532 nm, 50 mW; Peace Engineering), and the fluorescence images were captured by a silicon-intensified target camera (C-2740; Hamamatsu Photonics) and displayed on a video monitor. The bead positions were

recorded on a computer equipped with a laboratory interface board (MacLab; AD Instruments)[15] at a sampling rate of 10 kHz through a digital low-pass filter at 10 kHz. The bead displacement was calibrated by moving the photodiode[15]. The trap stiffness of the optical tweezers was calibrated for every bead from the standard deviation of the position fluctuation of the trapped bead (0.009–0.011 pN nm^{-1}). The step size was obtained directly from individual stepwise movements of the bead at a sampling time of 0.1 ms and estimated as the difference between the average bead positions determined for 5 ms each interval just before and after the steps. We did not take into account the attenuation factor, which is a function of the stiffness of optical trap and the stiffness of the protein-bead complex[15,17], because the trap stiffness we used is considered to be much smaller than that of the protein-bead complex. The average velocity of bead movement (v) was estimated by dividing the average step size (36 nm) by the average total dwell time (τ_{Total} in units of ms) at each external load, which is balanced to the force (F) generated by myosin V. Force-velocity relationships were described by the following function: $v = 36 \text{ nm} / \tau_{Total} = 36/\{\tau_D \exp(Fd_D / k_BT) + \tau_C + \tau_i \exp(Fd_i / k_BT)\}$ (nm ms^{-1}), where τ_D, d_D, τ_C, τ_i, d_i, k_B and T are described in the text.

Steady-state and transient kinetic experiments. All kinetic experiments were done at 25 ± 0.1 °C in KMg50-MOPS with an SX.18MV-R stopped-flow apparatus (Applied Photophysics). Fitting was done with Pro-K software provided with the instrument. Steady-state ATPase activity of MV-1IQ was measured using the ATP-regenerating, NADH-coupled assay as described[21]. BDM had minimal effects on the assay components as determined by direct mixing with MgADP.

Transient P_i release of MV-1IQ was measured using MDCC-PBP (λ_{ex} = 430 nm, 455 nm emission filter) with the instrument in sequential mixing mode as described[24]. Briefly, 2 μM MV-1IQ (treated with 0.01 U ml^{-1} potato grade VII apyrase to remove residual ADP and ATP, ± 200 mM BDM) was mixed with 300 μM MgATP (± 200 mM BDM) and aged for 40–60 ms to allow for nucleotide binding and hydrolysis to occur, then mixed with an equal volume of a range of actin filament concentrations. As first described for myosin VI[24], myosin V was limited to a single ATP turnover by including 2 mM MgADP with the actin. ADP competes with ATP for binding to myosin V after the first turnover and inhibits subsequent steady-state cycling. Therefore, time courses follow single exponentials (see Fig. 4b inset) rather than exponentials followed by a linear steady-state component, permitting more accurate fitting of the P_i release time courses. This method of measuring P_i release can be used for all high-duty-ratio myosins with rapid rates of ADP binding and high ADP affinities.

ADP release was measured with a fluorescent nucleotide mantADP[12]. The fluorescence of mantADP (λ_{ex} = 366 nm, 400-nm emission filter) was monitored after an equilibrated mixture of 0.5 μM actomyosin V-1IQ (± 200 mM BDM) and 20 μM mantADP was mixed with an equal volume of 2 mM MgADP.

ACKNOWLEDGMENTS

We thank M.R. Webb for the phosphate-binding protein clone and suggestions on purification and labeling, and H.L. Sweeney for providing the myosin V heavy and light chain viruses. We are grateful to N. Sasaki, M.Y. Ali, K. Kinosita, Jr. and E.M. Ostap for encouragement and stimulating discussions. This research was partly supported by Grants-in-Aid for Specially Promoted Research, for the Bio-venture Project and for The 21st Century COE Program (Physics of Self-Organization Systems) at Waseda Univ. from the Ministry of Education, Sports, Culture, Science and Technology of Japan (to S.I.) and supported by a Scientist Development Grant from the American Heart Association and a grant from the US National Science Foundation (to E.M.D.L.C.). S.U. is a postdoctoral fellow of the Japan Society for the Promotion of Science. A.O.O. is supported by a Cellular & Molecular Biology graduate training grant (Yale University).

COMPETING INTERESTS STATEMENT

The authors declare that they have no competing financial interests.

Received 31 March; accepted 18 June 2004
Published online at http://www.nature.com/nsmb/

1 Cheney, R.E. *et al.* Brain myosin V is a two-headed unconventional myosin with motor activity. *Cell* **75**, 13–23 (1993).
2. Miller, K.E. & Sheetz, M.P. Characterization of myosin V binding to brain vesicles. *J. Biol. Chem.* **275**, 2598–2606 (2000).
3. Vale, R.D. The molecular motor toolbox for intracellular transport. *Cell* **112**, 467–480 (2003).
4. Reck-Peterson, S., Provance, D.W., Mooseker, M.S. & Mercer, J.A. Review: class V myosins. *Biochim. Biophys. Acta* **1496**, 36–51 (2000).
5. Sakamoto, T., Amitani, I., Yokota, E. & Ando, T. Direct observation of processive movement by individual myosin V molecules. *Biochem. Biophys. Res. Commun.* **272**, 586–590 (2000).
6. Mehta, A.D. *et al.* Myosin V is a processive actin-based motor. *Nature* **400**, 590–593 (1999).
7. Walker, M. *et al.* Two-headed bindings of a processive myosin to F-actin. *Nature* **405**, 804–807 (2000).
8. Rief, M. *et al.* Myosin V stepping kinetics: a molecular model for processivity. *Proc. Natl. Acad. Sci. USA* **97**, 9482–9486 (2002).
9. Ali, M.Y. *et al.* Myosin V is a left-handed spiral motor on the right-handed actin helix. *Nat. Struct. Biol.* **9**, 464–467 (2002).
10. Forkey, J.N., Quinlan, M.E., Shaw, M.A., Corrie, J.E. & Goldman, Y.E. Three-dimensional structural dynamics of myosin V by single-molecule fluorescence polarization. *Nature* **422**, 399–404 (2003).
11. Yildiz, A. *et al.* Myosin V walks hand-over-hand: single fluorophore imaging with 1.5-nm localization. *Science* **300**, 2061–2065 (2003).
12. De La Cruz, E.M., Wells, A.L., Rosenfeld, S.S., Ostap, E.M. & Sweeney, H.L. The kinetic mechanism of myosin V. *Proc. Natl. Acad. Sci. USA* **96**, 13726–13731 (1999).
13. Trybus, K.M., Krementsova, E. & Freyzon, Y. Kinetic characterization of a monomeric unconventional myosin V construct. *J. Biol. Chem.* **274**, 27448–27456 (1999).
14. Higuchi, H. & Takemori, S. Butanedione monoxime suppresses contraction and ATPase activity of rabbit skeletal muscle. *J. Biochem.* **105**, 638–643 (1989).
15. Nishiyama, M., Higuchi, H. & Yanagida, T. Chemomechanical coupling of the forward and backward steps of single kinesin molecules. *Nat. Cell Biol.* **4**, 790–797 (2002).
16. Moore, J.R., Krementsova, E.B., Trybus, K.M. & Warshaw, D.M. Myosin V exhibits a high duty cycle and large unitary displacement. *J. Cell Biol.* **155**, 625–635 (2001).
17. Kojima, H., Muto, E., Higuchi, H. & Yanagida, T. Mechanics of single kinesin molecules measured by optical trapping nanometry. *Biophys. J.* **73**, 2012–2022 (1997).
18. Svoboda, K., Schmidt, C.F., Schnapp, B.J. & Block, S.M. Direct observation of kinesin stepping by optical trapping interferometry. *Nature* **365**, 721–727 (1993).
19. Schnitzer, M.J., Visscher, K. & Block, S.M. Force production by single kinesin motors. *Nat. Cell Biol.* **2**, 718–723 (2000).
20. Uemura, S. & Ishiwata, S. Loading direction regulates the affinity of ADP for kinesin. *Nat. Struct. Biol.* **10**, 308–311 (2003).
21. De La Cruz, E.M., Sweeney, H.L. & Ostap, E.M. ADP inhibition of myosin V ATPase activity. *Biophys. J.* **79**, 1524–1529 (2000).
22. De La Cruz, E.M., Wells, A.L., Sweeney, H.L. & Ostap, E.M. Actin and light chain isoform dependence of myosin V kinetics. *Biochemistry* **39**, 14196–14202 (2000).
23. Ostap, E.M. 2,3-Butanedione monoxime (BDM) as a myosin inhibitor. *J. Muscle Res. Cell Motil.* **23**, 305–308 (2002).
24. De La Cruz, E.M., Ostap, E.M. & Sweeney, H.L. Kinetic mechanism and regulation of myosin VI. *J. Biol. Chem.* **276**, 32373–32381 (2001).
25. Herrmann, C., Wray, J., Travers, F. & Barman, T. Effect of 2,3-butanedione monoxime on myosin and myofibrillar ATPases. An example of an uncompetitive inhibitor. *Biochemistry* **31**, 12227–12232 (1992).
26. Spudich, J.A. & Rock, R.S. A crossbridge too far. *Nat. Cell Biol.* **4**, E8–E10 (2002).
27. Vale, R.D. Myosin V motor proteins: marching stepwise towards a mechanism. *J. Cell Biol.* **163**, 445–450 (2003).
28. Goldman, Y.E. and Brenner, B. Special topic: molecular mechanism of muscle contraction. *Annu. Rev. Physiol.* **49**, 629–636 (1987).
29. Dantzig, J.A., Hibberd, M.G., Trentham, D.R. & Goldman, Y.E. Cross-bridge kinetics in the presence of MgADP investigated by photolysis of caged ATP in rabbit psoas muscle fibres. *J. Physiol.* **432**, 639–680 (1991).
30. Burgess, S. *et al.* The prepower stroke conformation of myosin V. *J. Cell Biol.* **159**, 983–991 (2002).
31. Veigel, C., Wang, F., Bartoo, M.L., Sellers, J.R. & Molloy, J.E. The gated gait of the processive molecular motor myosin V. *Nat. Cell Biol.* **4**, 59–65 (2002).
32. Kolomeisky, A.B. & Fisher, M.E. A simple model describes the processivity of Myosin V. *Biophys. J.* **84**, 1642–1650 (2003).
33. Rosenfeld, S.S., Fordyce, P.M., Jefferson, G.M., King, P.H. & Block, S.M. Stepping and stretching. How kinesin uses internal strain to walk processively. *J. Biol. Chem.* **278**, 18550–18556 (2003).
34. Cheney, R.E. Purification and assay of myosin V. *Methods Enzymol.* **293**, 3–18 (1998).
35. Yanagida, T., Nakase, M., Nishiyama, K. & Oosawa, F. Direct observation of motion of single F-actin filaments in the presence of myosin. *Nature* **307**, 58–60 (1984).
36. Brune, M. *et al.* Mechanism of inorganic phosphate interaction with phosphate binding protein from *Escherichia coli*. *Biochemistry* **37**, 10370–10380 (1998).
37. Hiratsuka, T. New ribose-modified fluorescent analogs of adenine and guanine nucleotides available as substrates for various enzymes. *Biochim. Biophys. Acta* **742**, 496–508 (1983).

MOLECULAR SYNCHRONIZATION IN ACTOMYOSIN MOTORS - FROM SINGLE MOLECULE TO MUSCLE FIBER VIA NANOMUSCLE

Shin'ichi Ishiwata*#, Yuta Shimamoto*, Daisuke Sasaki* and Madoka Suzuki*

1. INTRODUCTION

What mysteries exist in the sliding filament mechanism? No one doubts that the thick (myosin) and thin (actin) filaments "slide" along side each other during the shortening of muscles. In the sliding filament mechanism, it is widely considered that the head part of myosin molecules interacts with actin to form a cross-bridge and its conformational change occurs in association with ATP hydrolysis: that is, the cross-bridge works as a lever arm. Here, it is assumed that a conformational change in actin is not required, implying that the actin filaments are a rigid body, so that a thin (actin) filament is sometimes called a "track" for molecular motors. Myosin molecules of muscle (Myosin II) are considered to be typical molecular motors. Thus, in the sliding filament mechanism, the cross-bridge is considered to work as an independent force generator; in other words, the force developed in each track is the sum of the forces developed by each cross-bridge.

What are the questions that remain to be answered in the sliding filament mechanism? We would like to raise the following questions to be answered in the future: 1) Are cross-bridges an independent force generator under all conditions, not only under the conditions of full activation but also under intermediate conditions? 2) Is the

*Department of Physics, School of Science and Engineering, and #Advanced Research Institute for Science and Engineering, Waseda University, 3-4-1 Okubo, Shinjuku-ku, Tokyo 169-8555, Japan

track really a rigid body (only a basis of the movement of molecular motors)?

The contractile system of striated muscle, i.e., skeletal and cardiac, consists of a hierarchy, i.e., from the single molecular level to a myofilament and a sarcomere composed of an assembly of actin and myosin molecules and several accessory proteins, and to a myofibril and a muscle fiber. An in vitro motility assay system demonstrated that single actin filaments can slide on myosin molecules randomly adhered to the two-dimensional glass surface, and tension can be developed on a single filament level, implying that the organized structure of myofilament lattice is not indispensable to the tension development.

Now, we raise the following question from a different point of view: Are all of the contractile properties of fibers (myofibrils) solely attributable to the characteristics of single molecular systems? In practice, the spontaneous oscillatory contraction of sarcomeres (length oscillation of the saw-tooth waveform of each sarcomere and the traveling wave of the lengthening phase to the adjacent sarcomeres) observed in single myofibrils under the conditions intermediate between relaxation and contraction (named SPOC) seems to be characteristic of the organized contractile system. We consider that myosin-II motors, which function as a stochastic molecular machine on a single molecular level, are synchronized not only with the external mechanical impulse but also with the force generated by other motors when assembled into a sarcomere and a myofibril (a series connection of sarcomeres). This may be a typical example showing that molecular motors do not necessarily function as independent force generators but *inter-molecular synchronization* is essential for the higher-ordered function in the organized system.

We examined whether the SPOC phenomenon occurs in the "nanomuscle" system that we have recently developed (as reported in the last Symposium supported by the Fujihara Foundation of Science; Suzuki et al., 2003): this newly devised motile system is composed of a single A-band and a single actin filament of which the B-end is trapped with optical tweezers through an attached plastic bead. The preliminary results showed that, under some intermediate condition for activation, an actin filament moved in a saw-tooth waveform composed of a slow shortening phase and a rapid yielding phase, but a periodic oscillation like that of a sarcomere oscillation in SPOC was not observed. This suggests that regulatory proteins and/or higher-ordered structure are necessary for regular SPOC to occur. It is to be noted that the series connection of sarcomeres is indispensable for the SPOC wave to occur. The elastic framework present in the sarcomere and/or between sarcomeres may partly be involved in such a collective mode of motion.

Molecular motors are classified into processive and non-processive motors. The processive motor works as a single molecule and can walk along the track, e.g., myosin V along an actin filament and kinesin along a microtubule. On the other hand, the non-processive motor cannot walk alone but can function only as an assembly. A typical example of this kind of motor is a muscle motor, i.e., myosin II. We discuss that, in processive motors such as kinesin and myosin V, the *intra-molecular synchronization* between the two bound heads is essential for the processivity. That is, the asymmetry (the distinction between the leading and the trailing heads) occurs through the internal force that exists between the heads bound to the track, such that the binding affinity of nucleotides becomes different for the two bound heads, which brings about the dissociation of the trailing head, and directional walking becomes possible.

Now, we focus on the "inter- and intra-molecular synchronization" occurring in the

function of molecular motors at various levels of hierarchy.

2. MATERIALS AND METHODS

2.1. Proteins.

Actin and myosin II were prepared from rabbit skeletal white muscle according to a standard procedure (Kondo and Ishiwata, 1976). F-actin (FA) was labeled with rhodamine-phalloidin (Rh-Ph) and the bead-tailed FA, i.e., FA with the barbed (B-) end attached to a polystyrene bead (1 _m in diam.) through gelsolin, was prepared as previously reported (Suzuki et al., 1996; Nishizaka et al., 2000). Myosin V was prepared from chick brain (Ali et al., 2002); gelsolin from bovine plasma (Funatsu et al., 1990; Nishizaka et al., 1995 & 2000), and kinesin and tubulin from bovine and porcine brains, respectively (Kawaguchi and Ishiwata, 2001; Uemura et al., 2002; Kawaguchi et al., 2003).

2.2. Myofibrils and Muscle Fibers.

Myofibrils were prepared by homogenizing rabbit psoas glycerinated muscle fibers as described previously (Ishiwata et al., 1993; Yasuda et al., 1996). Glycerinated muscle fibers (a single fiber for skeletal muscle and a small bundle of cardiac muscle) were prepared by incubating in glycerol (50%) solution and then treating with Triton X-100. "Nanomuscle" was prepared by the treatment of myofibril with gelsolin (Suzuki et al., 2003; Suzuki and Ishiwata, 2004). All experiments were performed at room temperature.

2.3. Optical Microscopy.

The microscopy system and the method used for carrying out the image analysis were basically the same as those reported previously (Nishizaka et al., 2000). The fluorescence images of an F-actin and a bead were visualized using an ICCD camera (ICCD-350F; Video Scope International, Washington D.C.). A Nd:YAG laser (T10-V-106C; 2.5 W, Spectra-Physics Lasers, Inc., Mountain View, CA) was used as the optical tweezers.

3. RESULTS AND DICUSSION

The contractile system of muscle constructs the hierarchical structure, as schematically illustrated in Fig. 1: that is, from a single molecular system composed of a single myosin molecule and a single actin filament, to a protein assemblage such as thick and thin filaments, and to the sarcomere composed of the myofilament lattice structure and the myofibrils composed of a series connection of sarcomeres. Each hierarchy has contractile properties characteristic of its own. That is, each myosin motor functions as a stochastic nano-machine. Besides, myosin II is a "non-processive" motor that does not walk along the thin filament by itself. This is in contrast with a "processive" motor such as myosin V walking along an actin filament towards its B-end and kinesin walking along a microtubule towards its plus-end. Thus, we call myosin II a running (jumping)

motor (Kinosita et al., 1998). Myosin II motors exhibit a physiological function only when they are assembled into the thick filaments. In the case of striated muscle,

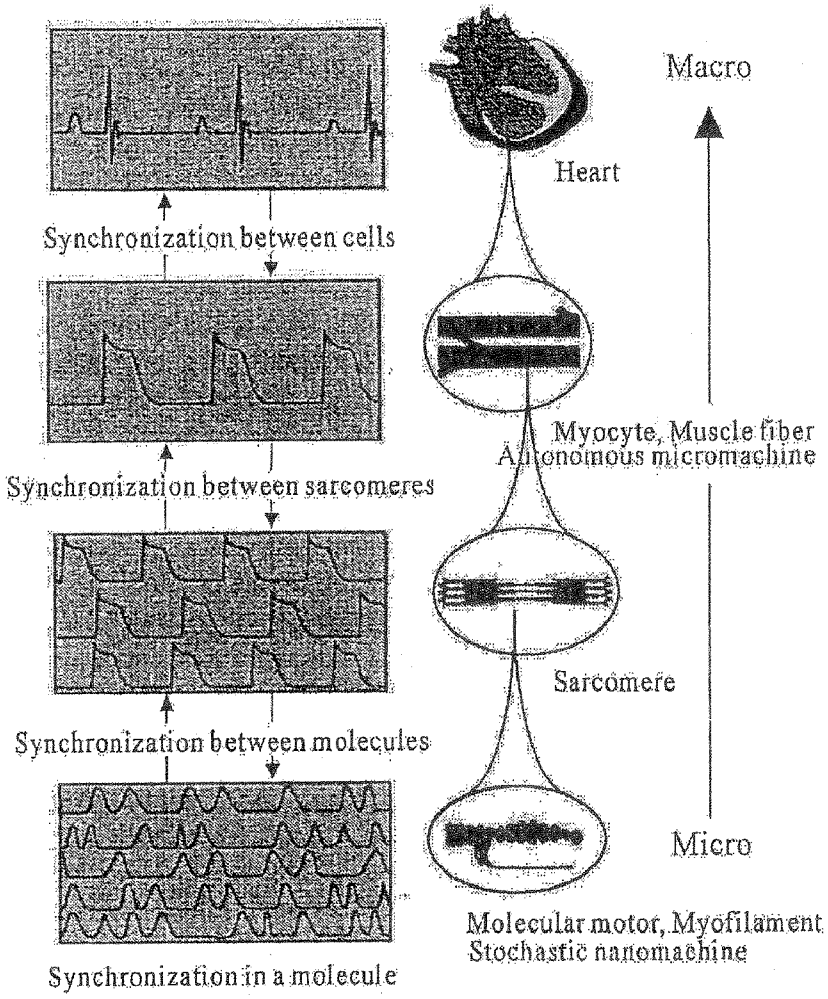

Figure 1. A schematic illustration showing the hierarchical structure of the contractile system of cardiac muscle. Molecular motors in striated muscle, i.e., myosin II, function as stochastic nano-machines. Myosin II molecules cannot work alone but can exhibit a physiological function only as an assembly, where intermolecular synchronization plays an essential role.

the thick filaments need to be incorporated further into a sarcomere and a myofibril that is composed of a series of connections of sarcomeres and then a muscle fiber that is composed of a parallel connection of myofibrils. The contractile properties are organized stepwise as the system is elevated to the upper level of hierarchy, organized from a random distribution to an ordered assembly.

We have demonstrated that myosin V is a left-handed spiral motor, which walks along an actin filament step by step with a step size of approximately 36 nm, a little shorter than a half pitch of a right-handed long helix of actin filaments (Ali et al., 2002). The walking mechanism is called the hand-over-hand mechanism. The processive motor can walk directionally in spite of the fact that the two heads of each molecular motor are identical. It is to be noted, however, that the directionality is created by the asymmetrical structure of actin filaments and microtubules, in which protomers (i.e.,

actin or tubulin molecules) are oriented in one direction and form a helical polymer. Thus, the two identical heads of molecular motors are attached to the track with the same orientation. Here, there still remains a question: how the motors can step uni-directionally. If the rate of detachment of one head were identical to the other, the probability of a step forward would be equal to that of a step backward. Therefore, what is the mechanism leading to the directional movement for the processive motors?

In this respect, many data have been accumulated suggesting that the internal load imposed between the two bound heads, which creates an asymmetrical distortion of the bound heads, may play a key role in determining the directionality of the stepping movement.

We found recently that the apparent binding affinity of ADP to kinesin depends on the loading direction (Uemura and Ishiwata, 2003). There is a way to distinguish the binding mode of protein motors with the "track" filaments. That is, we can determine whether there is a strong binding or a weak binding, and single-headed binding or double-headed binding, through measurements of the unbinding force under each nucleotide condition, i.e., nucleotide-free (strong-binding), ADP-bound (weak-binding) and AMP-PNP-bound (strong-binding) states (Kawaguchi and Ishiwata, 2001; Uemura et al., 2002; Kawaguchi et al., 2003). We confirmed that, on adding ADP stepwise to the nucleotide-free kinesin-microtubule complex, the proportion of the weak-binding state increased according to the simple hyperbolic relationship with the MgADP concentrations (Uemura and Ishiwata, 2003). Interestingly, we found that the apparent binding affinity of ADP depends on the loading direction: the MgADP concentration at which the proportion of the weak-binding state becomes equal to that of the strong-binding state was about 90 μM for backward loading, whereas it was about 10 μM for forward loading, indicating that ADP has a tendency to bind to the kinesin head in which the load is applied in the forward direction. This implies that, if we assume that an internal load exists between the two bound heads, the ADP prefers to bind to the trailing head, so that the probability of detachment of the trailing head increases. This can produce the directionality of the movement for the processive motors.

Now, let us move on to a discussion of the *in vitro* motility assay system for the acto-myosin II complex (Kinosita et al., 1991; Kato et al., 1999). First, we show that the cross-bridges produce the torque on actin filaments. When the front part of the actin filaments is fixed to a glass surface in an in vitro assay system, the myosin II molecules that adhered to the glass surface push the rear part of the filament, so that the middle part of the filament is buckled. Because the left-handed super-coil was always formed after the buckling, we concluded that the rear part of the filament slides like a right-handed screw, implying that the myosin II motors produce the right-handed torque (Nishizaka et al., 1993; Sase et al., 1997).

In in vitro motility assay systems, some curious phenomena have been observed. For example, a ring of actin filaments is formed because the pointed end of FA is sometimes linked to the barbed end during circular motion (Tanaka et al., 1992). The phalloidin, a stabilizer for the actin-actin bond, functions as glue. Even a twisted-ring for which the structure is analogous to a super-coil of DNA is formed when both ends of the twisted filament are linked. Besides, the filament sliding occurs even in such rings accompanied by the twisting motion. Thus, it is to be stressed that the in vitro motility assay system is artificial in some respects because the sliding of the actin filaments occurs on the 2D substrate like a glass surface on which myosin II molecules are randomly adhered.

To bridge the gap between the in vitro motility assay system and the fiber system, we have been trying to develop a new experimental system named "bio-nanomuscle" (Suzuki et al., 2003; Suzuki and Ishiwata, 2004). The bio-nanomuscle is composed of a single A-band and a bead-tailed actin filament that is trapped with optical tweezers. The single A-band was prepared by the treatment of a myofibril with gelsolin, an actin filament severing protein, to selectively remove the thin filaments. The bead-tailed actin filament trapped with optical tweezers was approached to the edge of the A-band. As soon as the free end of the actin filament touched the end plane or the outer surface of the A-band, the filament began to be pulled into the thick filament lattice and showed a large fluctuation in tension development that is balanced by the trapping force of the optical tweezers. We confirmed that the time average of the developed tension is proportional to the degree of overlap between the thick and the actin filaments. We also found that the average force developed per unit length of an actin filament is smaller when the interaction occurs outside the A-band than when the interaction occurs inside. This result is attributable to the difference in the number of thick filaments interacting with a single FA between the inside and the outside of the A-band.

Finally, let us describe the auto-oscillatory properties characteristic of each single myofibril, i.e., the phenomenon named SPOC (Spontaneous Oscillatory Contraction; Okamura and Ishiwata, 1988; Ishiwata and Yasuda, 1993). Under the solvent conditions intermediate between relaxation and contraction, the contractile system shows SPOC: The length of each sarcomere spontaneously oscillates with a saw-tooth waveform composed of a quick stretching phase and a slow shortening phase, and this oscillation (the stretching phase) propagates to the adjacent sarcomeres (more strictly speaking, to the adjacent half sarcomeres) as a traveling wave. When the myofibrils are bundled, several traveling waves appear here and there within the same bundle of myofibrils. It appears that there is a particular sarcomere (a "trigger" sarcomere), at which the SPOC wave is born, and the SPOC wave travels from the trigger sarcomere in both directions. Once the SPOC wave is born, the same pattern of SPOC wave continues for a while. But, the sarcomere from which the SPOC wave appears to begin is not necessarily fixed in the myofibril. The trigger sarcomere is exchangeable for others if the SPOC is once reset by washing with the relaxing solution, implying that the trigger sarcomere is not a particular damaged one but is interchangeable.

We have several results indicating that the elastic properties of connectin/titin (Fukuda et al., 2001) are *not* the major components required for the SPOC to occur. Firstly, the SPOC occurs even at short sarcomere lengths (shorter than 2.4 μm) where the resting tension is not developed (the connectin/titin is considered to be slacked). Secondly, when the sarcomere was stretched to longer than 2.4 μm and up to 2.8-2.9 μm, the SPOC period was slightly elongated but the major feature of the SPOC did not change. Only when the sarcomere length was elongated longer than about 3.0 μm did the SPOC stop, suggesting that the passive tension due to the elongation of the connectin/titin becomes comparable to or overcomes the active tension developed by cross-bridges.

Even when the total length of myofibrils is maintained constant (isometric condition), the length of every sarcomere oscillates but is forced to be out of phase (not synchronized) with each other. When the total length of a myofibril is long (the myofibril is composed of many, several tens of sarcomeres), the SPOC wave occurs here and there (locally) under the condition that the total length of the myofibril is maintained

constant (for movies, see the following homepage of our laboratory: http://www.phys.waseda.ac.jp/bio/ishiwata). The movie shows that the sarcomere oscillation occurs without a change in the length of the A-band; only the lengths of both the I-band and the H-zone change. One can visualize the filament sliding repeatedly on the same single myofibril during SPOC.

We can measure the tension oscillation developed under the SPOC conditions not only for the muscle fibers but also for the single myofibrils. The difficulty in examining the SPOC in muscle fibers is that the tension oscillation tends to occur only transiently, although the sarcomere length oscillation continues within the fiber. This is probably because the SPOC solvent condition is not maintained uniformly within a fiber, so that the sarcomere oscillation tends to become out of phase. On the other hand, in myofibrils, the SPOC (both oscillations in the sarcomere length and the tension) continues for a while, even for an hour, if the SPOC solution is continuously flowed. So, using the microscopic technique of holding both ends of a myofibril with a pair of glass micro-needles, we can study the dynamics of SPOC under various conditions (Anazawa et al., 1992; Yasuda et al., 1996). This situation is schematically illustrated in Fig. 2.

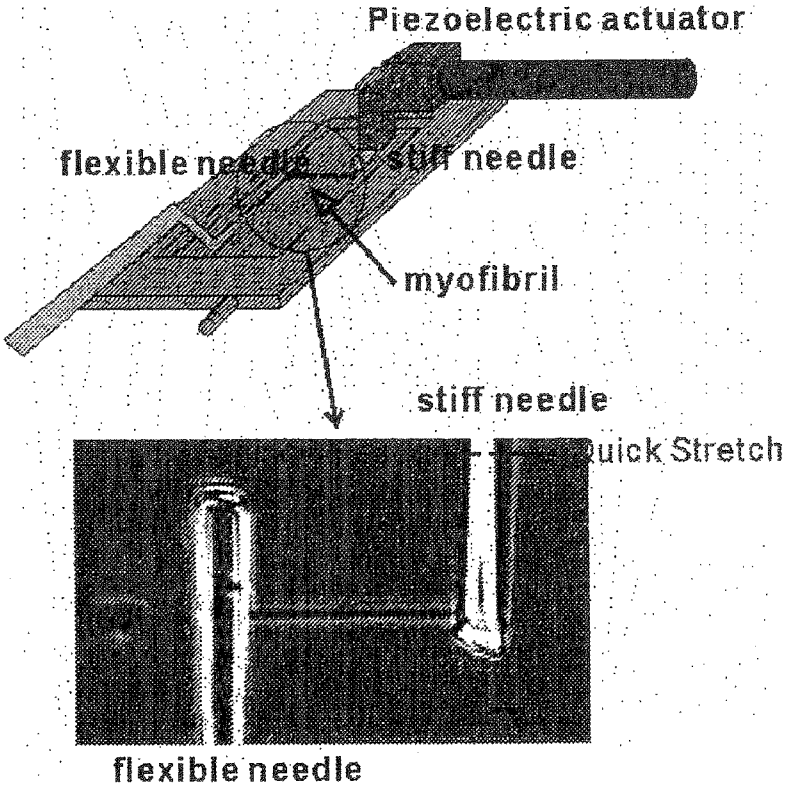

Figure 2. A schematic illustration of how to measure the tension development of myofibrils under optical microscopy. The total length of an oscillating myofibril is measured from the distance between the two glass micro-needles. The developed tension can be estimated from the deflection of a flexible needle from its equilibrium position. Video movies showing the SPOC of a myofibril are available from our homepage (http://www.phys.waseda.ac.jp/bio/ishiwata).

When one end of the myofibrils is fixed to a flexible micro-needle, both the tension and the sarcomere lengths oscillate under SPOC conditions (this boundary condition is named an "auxotonic" condition). When the myofibrils are composed of about 20-30 sarcomeres, it is easy to observe the SPOC wave traveling from one end to the other of the myofibril (*metachronal* SPOC). We found that the metachronal SPOC wave traveling over the whole length of the myofibril is easily to be induced upon stretching the myofibril to some extent under the condition that the average sarcomere length is less than about 3 μm.

Under an isotonic condition, which is achieved using a feedback control of the position of the rigid needle to keep the position of the flexible needle fixed (tension is maintained constant), we found that the traveling velocity of the SPOC wave tended to become very fast, such that the oscillation of every sarcomere tended to be synchronized to each other (the oscillation tends to be in phase, i.e., *synchronous* SPOC; Yasuda et al., 1996). This was the first evidence showing that the SPOC pattern can be mechanically controlled, implying that mechano-chemical coupling should exist in the molecular mechanism of SPOC.

What happens when the external mechanical impulse (by stepwise stretching or shortening of the myofibrils) is suddenly applied during the SPOC? We found that quick yielding occurs on all of the oscillating sarcomeres in response to the external mechanical impulse if the magnitude and the rate of the impulse are over some critical values.

The interesting finding is that a strong instability against the external mechanical impulse exists for the ADP contraction that is induced by the activation with the addition of ADP under relaxation conditions (Shimizu et al., 1992). Under ADP-contraction conditions, both slow shortening of the sarcomeres (about one tenth of the shortening velocity under usual activation conditions) and slow tension development (up to 70-80% of active isometric tension) occur, but no oscillations occur. Under ADP-contraction conditions, we can demonstrate that the yielding of every sarcomere occurs instantaneously upon the application of a mechanical impulse, so that the whole length of the myofibril is quickly elongated and then slowly shortens up to the original length where the isometric tension is balanced with the external load. If the mechanical impulse is applied repetitively, the myofibril can respond to each impulse, meaning that the oscillation of the myofibril is controlled by the external mechanical oscillation (Shimamoto et al., 2004 & manuscript in preparation).

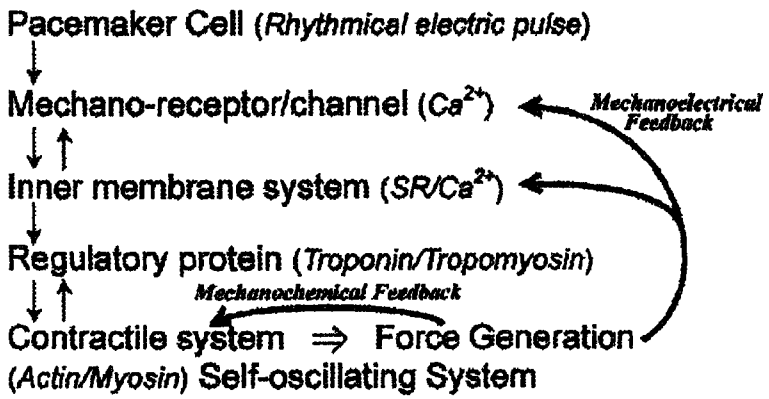

Figure 3. Hypothesis on the feedback regulation and molecular synchronization in cardiac muscle.

SPOC also occurs in the contractile system of cardiac muscle (Fabiato and Fabiato, 1978; Linke et al., 1993; Fukuda et al., 1996). It is interesting to note that SPOC more readily occurs in cardiac muscle than in skeletal muscle. That is, the state diagram showing the regions in which contraction, relaxation or SPOC occur was constructed for various concentrations of MgADP, Pi, free Ca^{2+} (pCa) and pH at several fixed concentrations of MgATP (Ishiwata and Yasuda, 1993; Ishiwata et al., 1993 & 1998; Fukuda and Ishiwata, 1999). This state diagram clearly showed that the SPOC region for cardiac muscle is much larger than that for skeletal muscle.

It is widely known that the free Ca^{2+} concentration in cardiac cells does not increase up to a fully activated level; that is, the activation is at most in the intermediate level, which just suits the condition for Ca-SPOC (the SPOC that occurs at a pCa of around 6 in the presence of MgATP: Fabiato and Fabiato, 1978; Linke et al., 1993; Fukuda et al., 1996). We should stress here that the contractile system of muscle itself is a self-oscillating system, which can respond to external forces. The state, contraction or relaxation, of the contractile system of muscle is controlled by the level of free Ca^{2+} concentration that is regulated by electric impulses (Ebashi and Endo, 1968), implying that the contractile system follows only the external signal. However, it is interesting to speculate that the flexible control of a heart beat due to an electric pulse (originally produced by pacemaker cells) is possible because the contractile system intrinsically possesses auto-oscillatory properties that can adapt to environmental changes. This situation is schematically illustrated in Fig. 3, in which we assume that not only the "mechano-electrical feedback" but also the "mechano-chemical feedback" plays a role in the regulation of the heart beat mechanism.

In summary, the contractile system of striated (skeletal and cardiac) muscle exhibits properties characteristic of each level of hierarchy, i.e., single-molecular level, myofibril and muscle fiber and so on. We have described several properties observed at each level of hierarchy, focusing on the synchronization that occurs in between the two heads within a single motor protein (intra-molecular synchronization) and in between myosin II motors within each sarcomere (inter-molecular synchronization) and in between

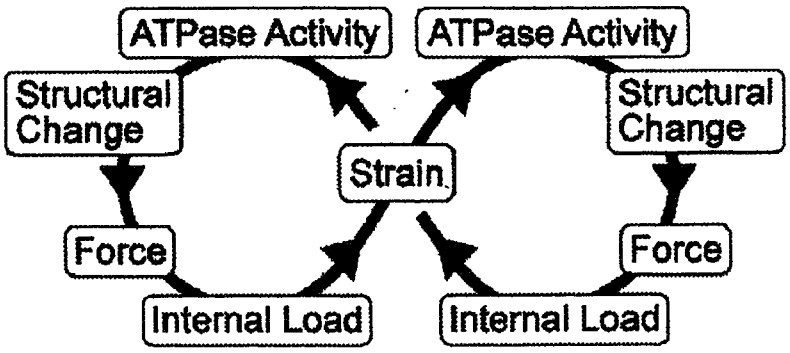

Figure 4. A feedback loop that exists in the intra- and inter-molecular synchronization of the mechano-chemical coupling mechanism of molecular motors.

sarcomeres within each myofibril. The feedback loop that exists in the coupling between the enzymatic activity and the mechanical event seems to be essential for the molecular mechanism of biological motors (Fig. 4).

This research was partly supported by Grants-in-Aid for Specially Promoted Research, for the Bio-venture Project and for The 21st Century COE Program (Physics of Self-organization Systems) at Waseda University from the Ministry of Education, Sports, Culture, Science and Technology of Japan.

4. REFERENCES

Ali, Y. M., Uemura, S., Adachi, K., Itoh, H., Kinosita, Jr., K., and Ishiwata, S., 2002, Myosin V is a left-handed spiral motor on the right-handed actin helix, *Nature Struct. Biol.* **9**: 464-467.

Anazawa, T., Yasuda, K., and Ishiwata, S., 1992, Spontaneous oscillation of tension and sarcomere length in skeletal myofibrils. Microscopic measurement and analysis, *Biophys. J.* **61**: 1099-1108.

Ebashi, S., and Endo, M., 1968, Calcium ions and muscle contraction, *Prog. Biophys. Mol. Biol.* **18**: 123-183.

Fabiato, A., and Fabiato, F., 1978, Myofilament-generated tension oscillations during partial calcium activation and activation dependence of the sarcomere length-tension relation of skinned cardiac cells, *J. Gen. Physiol.* **72**: 667-699.

Fukuda, N., Fujita, H., Fujita, T., and Ishiwata, S., 1996, Spontaneous tension oscillation in skinned bovine cardiac muscle, *Pflugers Arch.* **433**: 1-8.

Fukuda, N., and Ishiwata, S., 1999, Effects of pH on spontaneous tension oscillation in skinned bovine cardiac muscle, *Pflugers Arch.* **438**: 125-132.

Fukuda, N., Sasaki, D., Ishiwata, S., and Kurihara, S., 2001, Length dependence of tension generation in rat skinned cardiac muscle. Role of titin in the Frank-Starling mechanism of the heart, *Circulation.* **104**: 1639-1645.

Funatsu, T., Higuchi, H., and Ishiwata, S., 1990, Elastic filaments in skeletal muscle revealed by selective removal of thin filaments with plasma gelsolin, *J. Cell Biol.* **110**: 53-62.

Ishiwata, S., Anazawa, T., Fujita, T., Fukuda, N., Shimizu, H., and Yasuda, K., 1993, Spontaneous tension oscillation (SPOC) of muscle fibers and myofibrils. Minimum requirements for SPOC, *In* Mechanism of myofilament sliding in muscle contraction. (ed. by H. Sugi & G. H. Pollack) pp. 545-556. (Plenum Press)

Ishiwata, S., Funatsu, T., and Fujita, H. 1998, Contractile properties of thin (actin) filament-reconstituted muscle fibers, *In* Mechanism of work production and work absorption in muscle. (ed. by H. Sugi & G. H. Pollack) pp. 319-329. (Plenum Press)

Ishiwata, S., and Yasuda, K., 1993, Mechano-chemical coupling in spontaneous oscillatory contraction of muscle, *Phase Transitions.* **45**: 105-136.

Kato, H., Nishizaka, T., Iga, T., Kinosita, Jr., K., and Ishiwata, S., 1999, Imaging of thermal activation of actomyosin motors, *Proc. Natl. Acad. Sci. U.S.A.* **96**: 9602-9606.

Kawaguchi, K., and Ishiwata, S., 2001, Nucleotide-dependent single- to double-headed binding of kinesin *Science*, **291**: 667-669.

Kawaguchi, K., Uemura, S., and Ishiwata, S., 2003, Equilibrium and transition mechanics between single- and double-headed binding of kinesin revealed by single-molecule mechanics, *Biophys. J.* **84**: 1103-1113.

Kinosita, Jr., K., Yasuda, R., Noji, H., Ishiwata, S., and Yoshida, M., 1998, F1-ATPase: A rotary motor made of a single molecule, *Cell.* **93**: 21-24.

Kinosita, Jr., K., Itoh, H., Ishiwata, S., Hirano, K., Nishizaka, T., and Hayakawa, T., 1991, Dual-view microscopy with a single camera: Real-time imaging of molecular orientations and calcium, *J. Cell Biol.* **115**: 67-73.

Kondo, H., and Ishiwata, S., 1976, Uni-directional growth of F-actin, *J. Biochem.* **79**: 159-171.

Linke, W.A., Bartoo, M. L., and Pollack, G. H., 1993, Spontaneous sarcomere oscillations at intermediate activation levels in single isolated cardiac myofibrils, *Circ. Res.* **73**: 724-734.

Nishizaka, T., Yagi, T., Tanaka, Y., and Ishiwata, S., 1993, Right-handed rotation of an actin filament in an in vitro motile system, *Nature.* **361**: 269-271.

Nishizaka, T., Miyata, H., Yoshikawa, H., Ishiwata, S., and Kinosita, Jr., K., 1995, Mechanical properties of a single protein motor of muscle studied by optical tweezers, *Nature* **377**: 251-254.

Nishizaka, T., Seo, R., Tadakuma, H., Kinosita, Jr., K., and Ishiwata, S., 2000, Characterization of single

actomyosin rigor bonds: Load dependence of lifetime and mechanical properties, *Biophys. J.* 79: 962-974.
Okamura, N., and Ishiwata, S., 1988, Spontaneous oscillatory contraction of sarcomeres in skeletal myofibrils, *J. Muscle Res. Cell Motil.* 9: 111-119.
Sase, I., Miyata, H., Ishiwata, S., and Kinosita, Jr., K., 1997, Axial rotation of sliding actin filaments revealed by single-fluorophore Imaging, *Proc. Natl. Acad. Sci. U.S.A.* 94: 5646-5650.
Shimamoto, Y., Maejima, H., Suzuki, M., Sasaki, D., Yasuda, K., and Ishiwata, S., 2004, Stability of the spontaneous oscillatory contraction (SPOC) in single myofibrils studied by mechanical response and fluorescence imaging, *Biophys. J.* 86: 564a (Abstract).
Shimizu, H., Fujita, T., and Ishiwata, S., 1992, Regulation of tension development by MgADP and Pi without Ca^{2+}. Role in spontaneous tension oscillation of skeletal muscle, *Biophys. J.* 61: 1087-1096.
Suzuki, M., Fujita, H., and Ishiwata, S., 2003, Bio-nanomuscle project: Contractile properties of single actin filaments in an A-band motility assay system, *In* Molecular and cellular aspects of muscle contraction. (ed. by H. Sugi), Kluwer Acad./Plenum Press. pp. 103-110.
Suzuki, M., and Ishiwata, S., 2004, Contractile systems of muscles, *In* Reflexive polymers and hydrogels: Understanding and designing fast-responsive polymeric systems. (ed. by N. Yui, R. Mrsny and K. Park), CRC Press LLC. pp. 33-48.
Suzuki, N., Miyata, H., Ishiwata, S., and Kinosita, Jr., K., 1996, Preparation of bead-tailed actin filaments: Estimation of the torque produced by the sliding force in an in vitro motility assay, *Biophys. J.* 70: 401-408.
Tanaka, Y., Ishijima, A., and Ishiwata, S., 1992, Super helix formation of actin filaments in an in vitro motile system, *Biochim. Biophys. Acta.* 1159: 94-98.
Uemura, S., and Ishiwata, S., 2003, Loading direction regulates the affinity of ADP for kinesin, *Nature Struct. Biol.* 10: 308-311.
Uemura, S., Kawaguchi, K., Yajima, J., Edamatsu, M., Toyoshima, Y. Y., and Ishiwata, S., 2002, Kinesin-microtubule binding depends on both nucleotide state and loading direction, *Proc. Natl. Acad. Sci. U.S.A.* 99: 5977-5981.
Yasuda, K., Shindo, Y., and Ishiwata, S., 1996, Synchronous behavior of spontaneous oscillations of sarcomeres in skeletal myofibrils under isotonic conditions, *Biophys. J.* 70: 1823-1829.

DISCUSSION

Pollack: You suggested that the SPOC may be related to pacemaking. Are you suggesting that the oscillations you observe are associated with corresponding electrical oscillations?

Ishiwata: I think that the SPOC is not coupled with electrical oscillations, but originates from the contractile system. I have an idea that the role of pacemaker cells is to trigger the auto-oscillatory properties inherent to the contractile system.

Gonzalez-Serratos: Dr Inesi and I published a paper showing, in permeabilized isolated heart cells, the same type of traveling waves that you presented. At that time, we proposed that this traveling contraction waves were caused by Ca^{2+} uptake and release by the sarcoplasmic reticulum, resulting in a Ca^{2+} gradient. In your preparation, there is no sarcoplasmic reticulum and you attributed the traveling wave only to contractile protein interaction. How would you reconcile both results and propositions.

Ishiwata: To examine the SPOC, we are using detergent-treated myofibrils and muscle fibers, so that Ca^{2+} uptake and release by the SR do not take place. We speculate that the mechanochemical coupling (force-dependent modulation of enzymatic activity) propagates to adjacent sarcomeres. Unfortunately, it is at present difficult to prove the validity of this speculation.

Cecchi: 1) Is it possible from the effect of BDM on the dwell time to estimate the effect on force? 2) Can you estimate the actin filament compliance with your nanomuscle model?

Ishiwata: 1) It is possible to examine the effect of BDM on force development of myosin V. We found that the size of substeps was maintained constant in the presence of BDM under various loads, suggesting that BDM does not affect the amount of force development. BDM only prolongs the dwell time.
2) We have not yet examined it.

生体分子モーターの一分子力学

上村 想太郎* ・ 石渡 信一

光学顕微鏡技術の進歩によって，生体分子1個の挙動を生きたまま実時間で観察し，nmオーダーの動きやpNオーダーの力を計測できるようになった．特にこの手法は，生体運動を担う分子モーターのメカニズム解明に応用されて大きな成果をあげている．ここでは，光ピンセットを用いたミオシン(アクチン)，キネシン(微小管)分子モーター研究の一断面を紹介する．

Keywords : biomolecular motors, optical tweezers, single-molecular mechanics, kinesin, microtubule, actin, myosin II, myosin V, optical microscopy, single-molecular biophysics

1. まえがき

生体分子モーターはさまざまな細胞運動を担っているたんぱく質である．一般に，ATP（アデノシン三リン酸）を加水分解することによって得られる化学エネルギーを力学エネルギーに変換する分子ナノマシンである．近年，顕微鏡技術の発展により，分子モーター1個のナノメートル（nm）の動きとピコニュートン（pN）の発生力を実時間で観測できるまでになった．その代表的な技術に一分子蛍光イメージング法や光ピンセットによる一分子操作・力計測法がある．筆者らは特に光ピンセット法を用い，1分子で機能することができる「キネシン」や「ミオシンV」と呼ばれる分子モーターの一分子力学計測を行うことによって，分子メカニズムの解明を目指している．ここでは最近のわれわれの研究成果を中心に，分子モーター研究の一断面を述べる．

真核細胞の内部は細胞骨格と呼ばれる繊維状の構造物が無数に張りめぐらされている．細胞骨格はアクチン分子の重合体であるアクチンフィラメント，チューブリンの重合体である微小管，それに中間径フィラメントの，3種類の繊維状重合体の総称である．1分子で機能する生体分子モーターは，アクチンフィラメント，あるいは微小管と相互作用しつつ，それに沿ってミトコンドリア，ゴルジ体，リソソームといった細胞内小器官を運ぶ．こうした細胞内輸送は，たんぱく質合成，細胞分裂，細胞運動，細胞内情報伝達など，あらゆる生命活動と密接にかかわっている[1]．

一方，筋収縮を担うミオシンIIや，べん毛の波打ち運動を担うダイニンは長年にわたって研究されているが，これらの分子モーターは1分子では正常に機能せず，多数の分子が集合することによって初めて協調的な運動機能を発揮する．筋収縮やべん毛の波打ち運動は分子モーター集団の協同性を必要としている．そのために，分子レベルでの実験的研究はいまだに難しい．生体分子モーターの研究は，筋収縮系やべん毛，原形質流動といった運動システムを対象に半世紀以上にもわたって行われてきたが，そのメカニズムを真に分子レベルで解明することの困難さはいまだに変わらない．

2. 一分子力学計測

ところが近年，1分子で機能する分子モーター「キネシン」や「ミオシンV」などが次々と発見・同定され，1分子イメージングと1分子操作が可能になったことや，遺伝子操作技術の発展とあいまって，分子モーター機能とメカニズムの研究はめざましい発展を遂げることとなった．さらに，X線結晶構造解析によってたんぱく質の立体構造が明らかになったこと，結晶化できない複合たんぱく質も，相互作用している瞬間像が電子顕微鏡によって得られることなども研究の進展に大きく寄与している．しかし何といってもその最大の要因は，光ピンセット法や画像解析法などの光学（蛍光）顕微鏡法の進歩にある．

光ピンセット法とは，大きな開口数（N.A.）の対物レンズを用いてレーザー光を集光することで，直径がサブμmから数μmの粒子をその焦点付近に捕そくし，自由自在に操作する技術である．微粒子には捕そく中心からの変位に比例した復元力が働くことから，顕微画像解析法を用いて微粒子の変位をnm精度で計測すると，微粒子に加わる力をpN精度で測定できる．具体的には，1個の分子モーターを微粒子(通常はポリスチレンビーズ)に結合し，分子モーターの動きや発生力を，ビーズの動きを通して計測する．微粒子を捕そくすることで，間接的だが，分子モーターの

早稲田大学理工学部物理学科 〒169-8555 東京都新宿区大久保3-4-1. e-mail : ishiwata@waseda.jp
* 現在，スタンフォード大学物理学科
分類番号 9.4, 9.1
Single-molecular mechanics of biomolecular motors. Sotaro UEMURA* and Shin'ichi ISHIWATA. Department of Physics, School of Science and Engineering, Waseda University (3-4-1 Okubo, Shinjuku-ku, Tokyo 169-8555)
* Department of Physics, Stanford University

変位を精度よく計測することができる．微粒子を使うもう一つの利点は，分子のブラウン運動（熱運動）を抑えることにある．光ピンセット法で用いるレーザー光の波長は通常近赤外光である（YAG レーザーによる 1064 nm など）．その理由として，蛍光標識観察の邪魔になる可視領域を避けること，生体物質にダメージを与える紫外領域から遠いこと，かといって，数 μm の赤外領域になると水分子による吸収があり温度上昇があるのでこれを避けること，などがあげられる．

われわれは 1 分子単独で機能する生体分子モーターのうち，その素過程が活発に研究されている「キネシン」と「ミオシン V」を取りあげた．これら 2 種類の分子モーターの共通点はプロセッシブ性にある．プロセッシブ性は逐次前進性と訳されるが，結合する基質フィラメントの上を，数 μm ほど解離せずに同じ方向に運動し続けることを意味する．この性質のおかげで長時間の細胞内輸送が可能となる．しかも連続的な力発生が可能であることから，運動の素過程の研究にうってつけの分子モーターである．さらに，たんぱく質として安定で扱いやすいという点も実験家にはうれしい．

3. キネシン・微小管結合

「キネシン」は 1985 年に R. Vale らによってダイニンに続く微小管系の第 2 のモーターたんぱく質としてイカの神経軸索で見いだされた[2]．キネシンの細胞内での主な役割は細胞内小器官の輸送や，細胞分裂時の中心体の分離と紡錘体形成などである．ゲノム解析の結果，キネシンは 10 種類のサブファミリーに分類され，ヒトやマウスでは 45 種類が同定されている．もっぱら実験に用いられている天然キネシンは神経軸索にあって小胞輸送を担い，340 個のアミノ酸からなる相同な二つの球状頭部（双頭構造）をもつ．

最初に光ピンセットをキネシン研究に応用したのは Block らである[3]．彼らは世界で初めて 1 分子キネシンが連続してステップ状に運動することを見いだし，各ステップの大きさが，負荷の大きさによらず，微小管の最小単位であるチューブリン分子の 8 nm 間隔に相当することを発見した[3]．これを説明する最も簡単なモデルは，キネシンの二つの頭部が 8 nm 間隔のチューブリン分子と交互に結合・解離を繰り返し，歩くように運動する「Hand-over-hand モデル」である．そこでは，ATP の加水分解と共役した巧妙な仕組みが存在しているはずである．

われわれは歩行メカニズムを解明するため，光ピンセットによる分子間結合の破断力（結合を破断するのに必要な力）の測定を，ATP 加水分解過程と対応させうるいくつかのヌクレオチド状態で行った．そこでわれわれは，ATP 存在下でキネシンが能動的に運動している状態ではなく，NF（ヌクレオチドなし），ADP（アデノシン二リン酸）存在下，AMPPNP（加水分解しない ATP アナログ）存在下という，結合・解離の平衡状態が得られる 3 状態に着目した．そこで，さまざまな負荷上昇速度のもとで破断力分布を得れば，結合ポテンシャルの外力依存性を知ることができる（一般に負荷上昇速度が大きいほど破断力は大きい）．

たんぱく質間の結合は，熱エネルギー（k_BT）程度の弱い分子間相互作用（ファンデルワールス力，水素結合，クーロン力，疎水結合など）の組み合わせによって形成されている．つまり，ほとんどの分子間結合では，熱エネルギーの揺らぎによって結合ポテンシャルの安定点からポテンシャル障壁を乗り越えることができる．すなわち，分子結合の解離は熱揺らぎに依存する確率事象である．よって無負荷時の結合持続時間（結合寿命）の分布は指数関数的に減少すると考えられる．そこで，外力を加えるとポテンシャル障壁が低くなり解離する確率が上昇し，平均の結合寿命が短くなる．この性質を利用して，どれくらいの外力で解離（破断）させることができるかを調べることで，ポテンシャル障壁の高さを見積もることができる．われわれは，各ヌクレオチド状態にある結合複合体に外力を加え，得られた破断力の大きさと分布をもとに結合様式を特定した[4,5]．

結合状態を特定するために，天然双頭キネシンだけでなく遺伝子的に改変した単頭キネシンも用いた．1 分子キネシンを結合した直径 1 μm のビーズを光捕そくし，ガラス基板上に固定した微小管上にビーズを近づける．微小管はあらかじめ，アミノ基を介してローダミン色素で標識されており，蛍光画像でその位置を確認することができる．しかも重合速度の異方向性を利用することによって微小管を非対称的に蛍光ラベルし，重合端（＋端）と脱重合端（－端）とを識別する．キネシンは微小管の＋端方向に動く分子モーターである．各ヌクレオチド状態で，キネシン吸着ビーズを微小管上で約 30 秒間保持する．その間に，ビーズは回転ブラウン運動をし，キネシンと微小管とは結合・解離の平衡状態に達する．その後，光ピンセットの捕そく中心を一定速度で微小管に沿って動かし続けることによってキネシン・微小管結合にほぼ一定の上昇速度で負荷を加えることができる．破断は確率的に生じるが，破断時に加わっていた負荷（破断力）を測定する．そしてさらに光捕そく中心を動かし続けることによって，キネシン・微小管の再結合による再破断を記録・計測することができる（**図 1**）[5]．典型的な生データを図 1（**b**），（**c**）に示した．ビーズの位置が捕そく中心からはずれるにつれて，徐々に外部負荷が加わるが，キネシンが微小管から解離するとビーズはすばやく捕そく中心に戻る．破断力はキネシンが解離した瞬間のビーズの輝度重心と捕そく中心との距離に光ピンセットのバネ定数（例えば 0.05 pN/nm）を掛けて算出する．このように繰り返し測定によって得た破断力分布は，1 mM AMP-PNP では，＋端（－端）方向へ負荷を加えた場合，双頭キネシンは 6 (10) pN と 12 (17) pN に二つのピークをもった．一方，単頭キネシンの場合は平均 6 (10) pN のピークが一つだった．そしてヌクレオチドなしと 1 mM ADP では双頭キネシン，単頭キネシンともそれぞれ，6 (10) pN，3 (4) pN に一つのピークをもつ分布となった．この

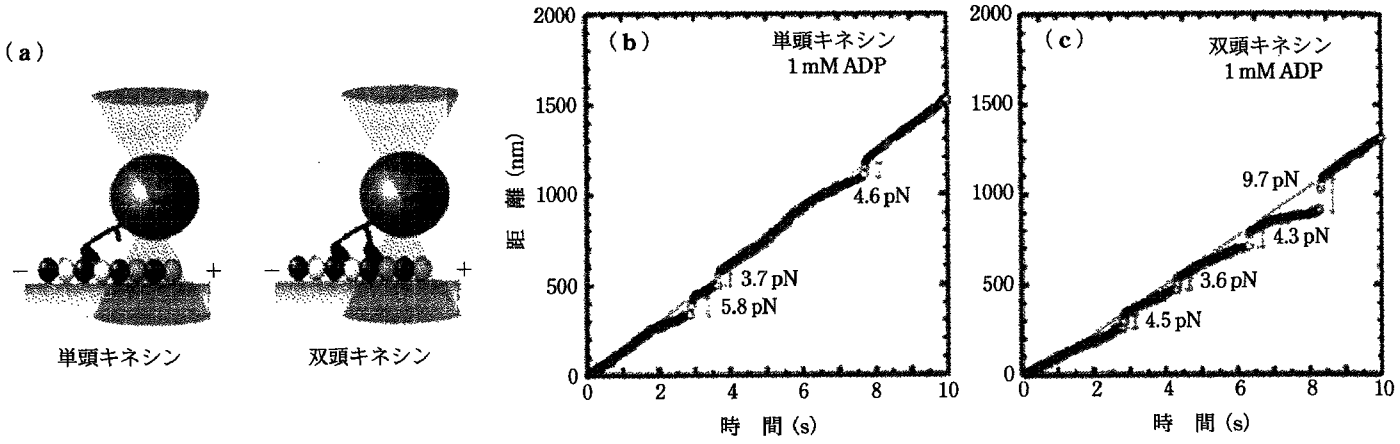

図1 破断力の1分子測定．(**a**)ビーズに結合した単頭キネシン(左)あるいは双頭キネシン(右)と微小管との結合に，微小管の＋端方向に向けて(矢印)負荷を加えた様子．一定速度で光ピンセット捕捉中心を移動させたとき(細線)のビーズ輝度重心の変位(丸印)の時間経過．＋1 mM ADP での単頭キネシン(**b**)と双頭キネシン(**c**)の結合の様子．結合が破断する際の捕捉中心(細線)とビーズ中心(丸印)の距離(両矢印)に，ピンセットのバネ定数 0.05 pN/nm を掛けることによって破断力を見積もることができる(Uemura *et al.*, 2002[5] を改変)．

結果は，1 mM AMP-PNP では単頭結合と双頭結合の2状態，ヌクレオチドなしでは単頭強結合状態，そして1 mM ADP では単頭弱結合状態にあることを示しており，ATP 加水分解過程でキネシンがこれらの結合状態をへめぐっていることが示唆される(**図2**：実はヌクレオチドなし[Nucleotide-free]の場合も，1けた高い負荷上昇速度で破断力を計測すると，破断力分布が二つのピークからなることがわかった．その解釈は，双頭キネシンの場合には，ヌクレオチド状態によらず単頭結合と双頭結合の2状態をとるが，2状態間を行き来する速度が，AMP-PNP 存在下と比べてヌクレオチドなし条件の方が1けた大きいということである[6])．

一端方向負荷の場合の破断力は，＋端方向負荷のそれよりもおよそ45%大きかった．これは結合ポテンシャルが非対称であることを示しており，一端方向への負荷に対しては解離しにくい結合をしていることを意味する．この結果を説明するために速度論から破断力分布のシミュレーションを行い，単頭強結合と単頭弱結合の破断力分布が再現されることを確認した[5,6]．単頭キネシンについてのモデル計算には，結合と解離の2状態を考える（双頭キネシンの場

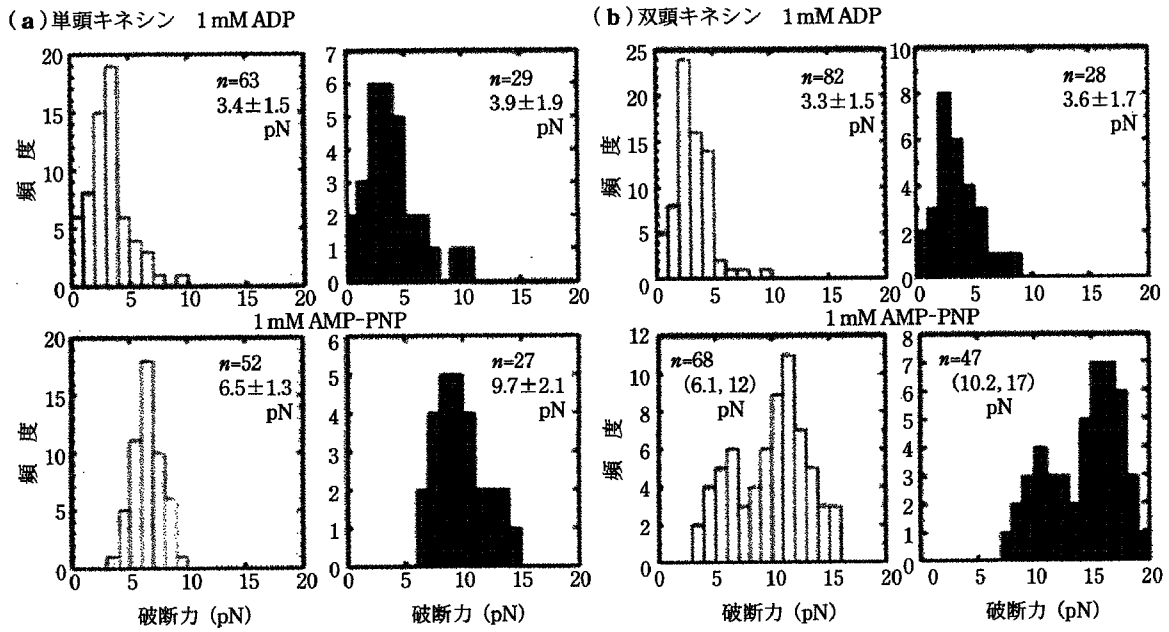

図2 各ヌクレオチド条件における破断力分布．単頭キネシン(**a**)と双頭キネシン(**b**)．各状態においてそれぞれ＋端側負荷(白抜き)と－端側負荷(灰色)を示している．各分布の右上にはそれぞれデータ数(n)とピーク値が記載されている．負荷上昇速度は 5.0±1.7 pN/s(Uemura *et al.*, 2002[5] を改変)．

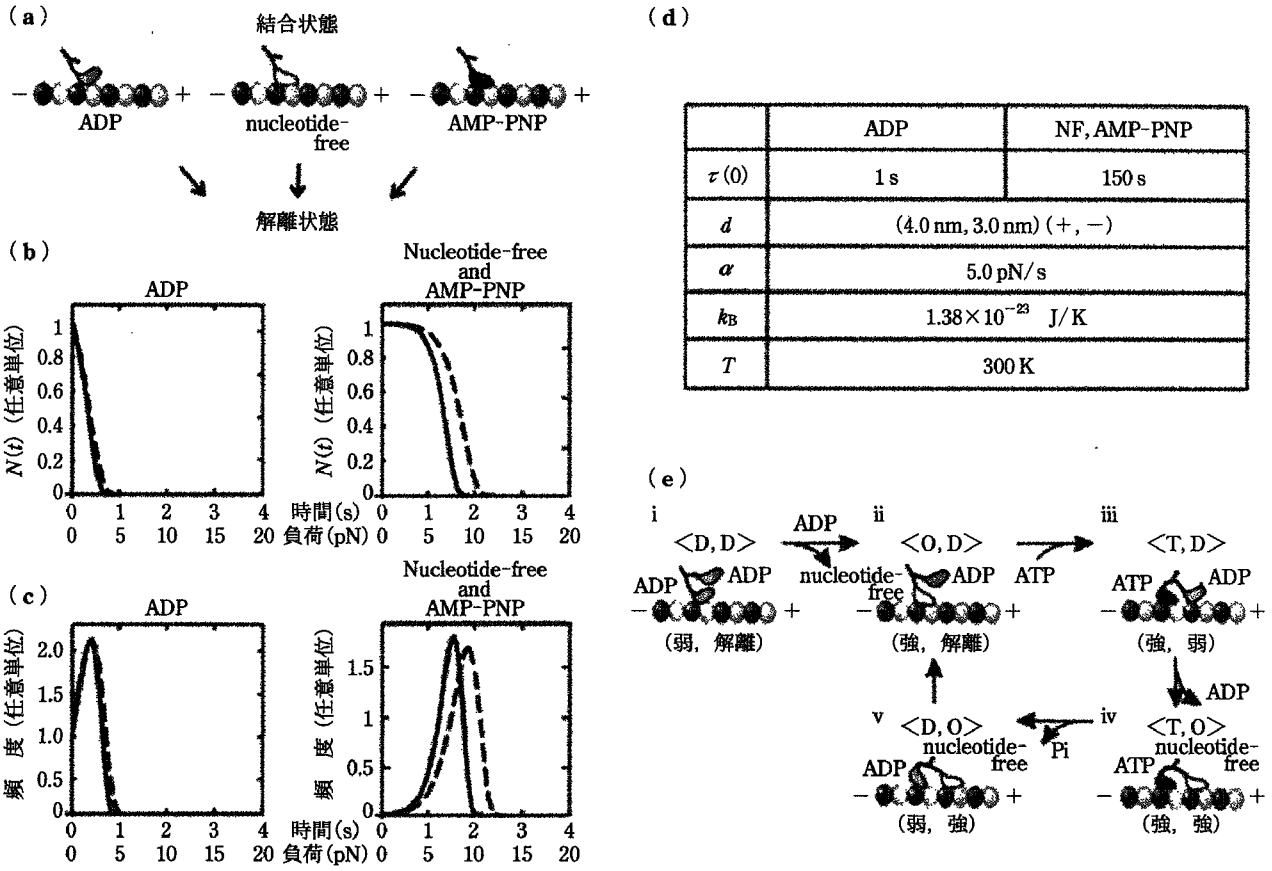

(d)

	ADP	NF, AMP-PNP
$\tau(0)$	1 s	150 s
d	(4.0 nm, 3.0 nm) (+, −)	
α	5.0 pN/s	
k_B	1.38×10^{-23} J/K	
T	300 K	

図3　モデル計算のためのスキームと，得られた破断力分布（**a**）～（**c**）．各パラメーターの値（右上表（**d**）：NF, Nucleotide-free）．結合数の時間変化 $N(t)$（**b**）と破断力分布 $P(t)$（**c**）はそれぞれ＋端側負荷（実線）と－端側負荷（破線）で示されている．これらの方向依存性は異なる相互作用距離 d（表参照）によって説明することができた．ここで，$N(t)$ と $P(t)$ の数値計算は Mathematica (Windows) ソフトを用いて行った．（**e**）ヌクレオチド状態と対応づけた Hand-over-hand モデル（Uemura *et al.*, 2002[5] を改変）．詳細は本文参照．

合のモデル計算には，単頭・双頭結合，解離の3状態を仮定：文献6参照）．ここで，結合寿命の負荷依存性を $\tau(F)=\tau(0)\exp(-Fd/k_BT)$ とした．$\tau(0)$ は無負荷時における結合寿命，F は外部負荷，d は分子間相互作用特性距離，k_B はボルツマン定数，そして T は絶対温度である．この関係式は，アクチンと筋肉ミオシン（ミオシンII）との間の結合（ヌクレオチドなし）に関して得られた実験式である[7]．そこで，負荷依存性をもつ解離速度定数を $k(F)=1/\tau(F)$ とすると，結合数（結合の割合）の時間変化 $N(t)$ として微分方程式

$$\frac{dN(t)}{dt}=-k(F)N(t)=-\frac{N(t)}{\tau(F)}$$

が成り立つ．破断力測定の際には，ほぼ一定の速度で負荷を加えるため，$F=\alpha t$（α：負荷上昇速度で一定値）として t の関数とし，微分方程式を解くことで $N(t)$ を求めることができる．破断力分布 $P(t)$ は結合数 $N(t)$ の時間的変化率 $P(t)=N(t)/dt$ として表すことができるため，$P(t)$ は $\tau(0)$，α，d，T の値で決まる．

Howard らの報告[8]をもとに，単頭弱結合状態（1 mM ADP）では $\tau(0)=1$ 秒，単頭強結合状態（ヌクレオチドなしおよび1 mM AMP-PNP）では $\tau(0)=150$ 秒とすると，破断力分布が最もよく再現された[5]．相互作用特性距離 d は，ヌクレオチド状態によらず＋端側破断の場合 4.0 nm，－端側破断の場合 3.0 nm と見積もられた．このことは，キネシン・微小管結合の安定性は負荷の方向に対して非対称だが，非対称の程度はヌクレオチドの種類や，ヌクレオチドの有無によらないことを意味する．ヌクレオチドの種類と有無に依存するのは無負荷での結合寿命 $\tau(0)$，すなわち，結合ポテンシャルの障壁の高さであった（**図3**）．

上で述べたように，ADP がキネシン・微小管複合体に結合すると単頭弱結合状態で破断し，ADP が解離してヌクレオチドなし状態になると単頭強結合状態で破断する．そこでわれわれは，ある一定の負荷上昇速度のもとで，さまざまな ADP 濃度での強結合と弱結合の割合を調べた．その結果，ADP 濃度を上げていくと，＋端破断，－端破断ともに，単頭弱結合成分（3 pN 付近のピーク）の割合が増加した．このことは，単頭内で強結合と弱結合とが平衡関係にあり，これが ADP の結合・解離と共役していることを示している[9]．

そこで面白いことに，弱結合成分と強結合成分の割合がほぼ等しくなる ADP 濃度は，＋端破断の方が－端破断の場合より低かった．つまり，＋端方向に負荷が加わると

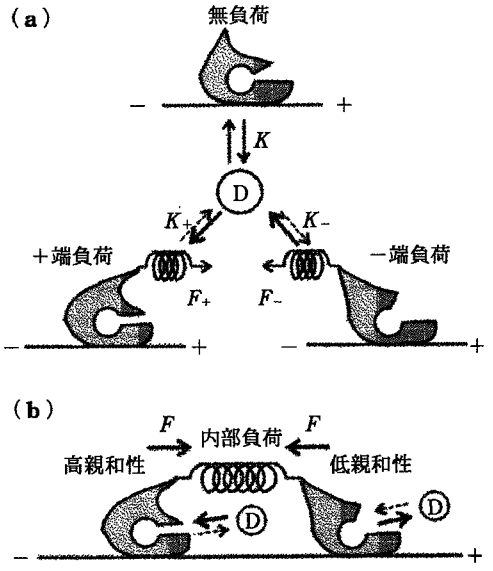

図4 負荷方向に依存するキネシン・微小管複合体(ヌクレオチドポケット)へのADPの結合平衡．負荷を微小管の＋端(F_+)あるいは－端(F_-)方向に加えたときのADPの結合定数(K_+；＋端，K_-；－端)(**a**)．双頭結合時に生じると期待される内部負荷の影響(**b**)．双頭結合の際にそのつなぎ部分に内部負荷が生じる(Uemura & Ishiwata, 2003[9] を改変)．

ADP結合が促進され，－端方向負荷ではADP結合が抑制されることを示している．この結果，分子モーターへのヌクレオチド結合の結合定数(平衡定数)が負荷の方向によって異なるという，力学過程と化学過程の直接的な共役が1分子レベルで明らかとなった[9]．さらにこの性質は，**図4**のように双頭結合時の頭部間に内部負荷が生じると仮定すると，後頭部が前頭部よりADPを結合しやすいことを意味する．すると，後頭部が前頭部より微小管から解離しやすくなるので，双頭状態から次の一歩を踏み出しやすいという性質が生まれることになる．これは，Hand-over-handモデル（**図3e**）にとって鍵となる性質である[9]．

4. ミオシンV・アクチン結合

最後に，キネシンと同様の運動機能をもつと考えられるミオシンVについての最近の研究成果を述べる．ミオシンVはアクチンフィラメントに沿って，そのらせん半周期に相当する36 nmの連続ステップを引き起こす[10]．しかしステップ運動は非常に早く，ステップの微細構造を詳細にとらえるのは容易ではない．そこで東北大・学際センター(現，先進医工学研究機構）の樋口秀男氏と共同で高時間・空間分解能の顕微鏡装置を用い，36 nmステップ以下の高速サブステップ計測をめざした[11]．装置の心臓部は，捕そくしたビーズに赤色レーザーを集光し，その散乱光を4分割の位置検出フォトダイオードに投影する部分である．時間分解能を向上させるために，粘性抵抗の小さい直径0.2 μmのビーズを使用した．

10 kHzのサンプリングレートで運動を観察した結果，36 nmステップは12 nmと24 nmに分離されることを見いだした[11]（**図5**）．これらのサブステップは長い寿命

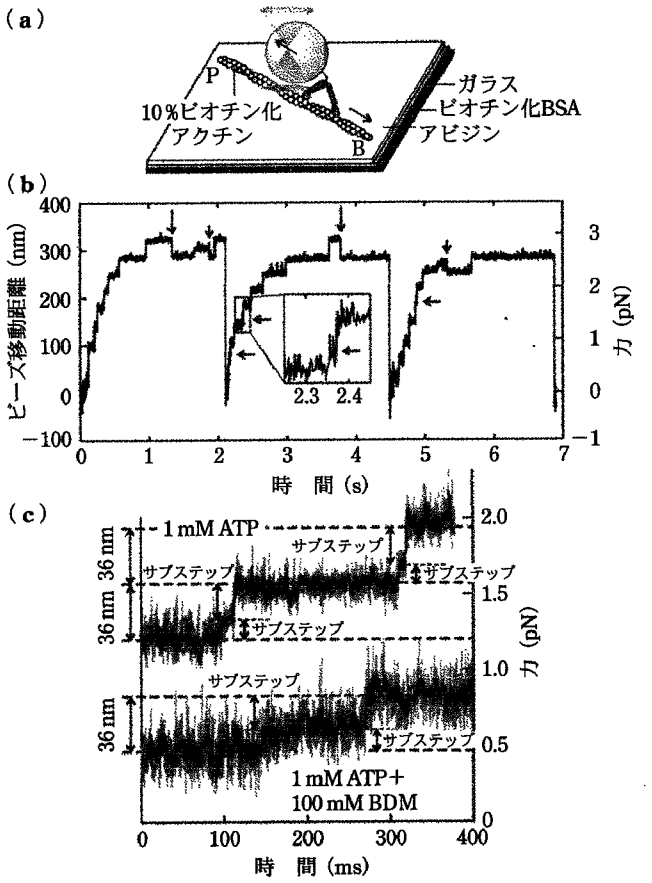

図5 ミオシンVの1分子運動解析．光ピンセットで捕捉したビーズに1分子のミオシンV分子が結合し，ガラス基板上に，アビジン・ビオチン結合を介して固定されたアクチンフィラメントと相互作用する(**a**)．ATP存在下では，ミオシンVがアクチンフィラメント上を36 nmの歩幅でステップ運動する((**b**)，36 nm間隔で点線が引かれている)が，高時間・空間分解能での計測をしたところ，36 nmステップは12 nmと24 nmのサブステップからなることがわかった((b)，横向きの矢印)．縦矢印はバックステップを示す(長い方は36 nm，短い方は12 nm)．時間軸を引き伸ばすと，12 nmサブステップの後の中間状態がよくわかる(**c**)．破線上の台地が主状態，破線と破線の間の台地が中間状態に対応．筋弛緩剤として知られるBDMを高濃度加えたところ，この中間状態の寿命が大きく引き伸ばされた(Uemura *et al.*, 2004[11] を改変)．

(Dwell Time) の主状態を経た後，12 nmステップ，そして続けて24 nmステップの順番で出現した．12 nmステップ後の中間状態の寿命は負荷の大きさに依存し，寿命の分布は1次反応(A → A* 型の1段階反応)を示す指数減衰型の曲線となった．さらに24 nmと36 nmステップ後に現れる主状態の寿命も負荷の大きさに依存し，その分布はすでに報告されているように一つのピークをもつ2次反応（A → A*→ A** 型の2段階反応)を示すものだった．また，中間状態の寿命はATPとADPの濃度には依存しなかった．ところが，ミオシンのATPase活性を抑制し，筋弛緩剤（力発生を抑制する試薬）として知られているBDM (2,3-butanedione monoxime) を加えるとADPの解離速度が抑制され，中間状態の寿命が7～8倍ほど長くなった．これらのことから，ミオシンVのATP加水分解サイクルの中でADPの解離過程が抑制されると中間状態の寿命が

延びることが判明した．さらに，ATP 濃度を低くしても中間状態の寿命は変化せず，主状態の寿命が延びることも判明した．これらの結果をもとに，12 nm サブステップは ATP 結合によって生じ，24 nm サブステップは ADP 結合状態における 2 状態間の遷移 (isomerization：M をミオシン V とすると，M*ADP から MADP への転移) によって引き起こされると結論し，新しいミオシン V の歩行モデルを構築することができた(詳細については文献 11 を参照)．

6. むすび

われわれは光ピンセット法を応用して，1 分子で機能する分子モーターの結合破断力や，発生力を測定して ATP 加水分解過程と運動過程の仕組みに迫ることができた．しかし，力が働いているときの分子内部の構造変化など，未解明の点は多い．真に分子レベルのメカニズムに迫るためには，1 分子の力学過程と構造変化，そして酵素としての化学反応過程を同時に測定する必要がある．さらにいえば，同時に計測して，力学過程と化学過程との時間的な関係が明らかになったとしても，それだけでは十分でない．原因と結果の因果関係がはっきりしなければいけない．そのうえで，ATP の加水分解という化学過程から，分子運動という力学過程に至るまでの道筋，構造変化の時間的な流れ，エネルギー変換の過程が分子内レベルで明らかにならなければ，「生体分子モーターの物理」が明らかになったとはいえないだろう．

文　献

1) B. Alberts *et al.*: *Molecular Biology of the Cell, 4th ed.* (Garland Sci., NY, 2002).
2) R. D. Vale, T. S. Reese and M. P. Sheetz: *Cell*. **42**, 39 (1985).
3) K. Svoboda, C. F. Schmidt, B. J. Schnapp and S. M. Block: *Nature*. **365**, 721 (1993).
4) K. Kawaguchi and S. Ishiwata: *Science* **291**, 667 (2001).
5) S. Uemura, K. Kawaguchi, J. Yajima, M. Edamatsu, Y. Y. Toyoshima and S. Ishiwata: *Proc. Natl. Acad. Sci. USA*. **99**, 5977 (2002).
6) K. Kawaguchi, S. Uemura and S. Ishiwata: *Biophys. J*. **84**, 1103 (2003).
7) T. Nishizaka, R. Seo, H. Tadakuma, K. Kinosita, Jr. and S. Ishiwata: *Biophys. J*. **79**, 962 (2000).
8) W. O. Hancock and J. Howard: *Proc. Natl. Acad. Sci. USA*. **96**, 13147 (1999).
9) S. Uemura and S. Ishiwata: *Nature Struct. Biol*. **10**, 308 (2003).
10) A. D. Mehta, R. S. Rock, M. Rief, J. A. Spudich, M. S. Mooseker and R. E. Cheney: *Nature*. **400**, 590 (1999).
11) S. Uemura, H. Higuchi, A. O. Olivares, E. M. De La Cruz and S. Ishiwata: *Nature Struct. & Mol. Biol*. **11**, 877 (2004).

(2004 年 11 月 24 日　受理)

上村　想太郎（うえむら　そうたろう）

日本学術振興会特別研究員．理学博士(早大)．現在米国 Stanford 大学 Steven Chu 博士(ノーベル物理学賞)のもとで研究．2005 年 4 月より日本学術振興会海外特別研究員．1 分子で機能する分子機械のメカニズムを 1 分子力測定により研究．

e-mail: sotaro_uemura@akane.waseda.jp
suemura1@stanford.edu

石渡　信一（いしわた　しんいち）

早稲田大学理工学部物理学科教授．2003 年度より，21 世紀 COE“自己組織系物理”(早大)拠点リーダー．04，05 年日本生物物理学会会長．さまざまな生体運動系を，1 分子レベルから分子集合体，細胞まで，階層性と機能に着目しつつ研究．

e-mail: Ishiwata@waseda.jp

A New Muscle Contractile System Composed of a Thick Filament Lattice and a Single Actin Filament

Madoka Suzuki,* Hideaki Fujita,† and Shin'ichi Ishiwata*‡§

*Department of Physics, School of Science and Engineering, Waseda University, Tokyo, Japan; †Tohoku University Biomedical Engineering Research Organization, Miyagi, Japan; and ‡Advanced Research Institute for Science and Engineering, and §Consolidated Research Institute for Advanced Science and Medical Care, Waseda University, Tokyo, Japan

ABSTRACT To bridge the gap between the contractile system in muscle and in vitro motility assay, we have devised an A-band motility assay system. A glycerinated skeletal myofibril was treated with gelsolin to selectively remove the thin filaments and expose a single A-band. A single bead-tailed actin filament trapped by optical tweezers was made to interact with the inside or the outer surface of the A-band, and the displacement of the bead-tailed filament was measured in a physiological ionic condition by phase-contrast and fluorescence microscopy. We observed large back-and-forth displacement of the filament accompanied by a large change in developed force. Despite this large tension fluctuation, we found that the average force was proportional to the overlap inside and outside the A-band up to ~150 nm and 300 nm from the end of the A-band, respectively. Consistent with the difference in the density of myosin molecules, the average force per unit length of the overlap inside the A-band (the time-averaged force/myosin head was ~1 pN) was approximately twice as large as that outside. Thus, we conclude that the A-band motility assay system described here is suitable for studying force generation on a single actin filament, and its sliding movement within a regular three-dimensional thick filament lattice.

INTRODUCTION

Mechanically (1,2) or chemically (3–5) skinned muscle fibers and myofibrils (6,7) have long been used in muscle physiology to study properties of the interaction between actin and myosin. Such muscle models have provided important information about the molecular mechanisms in both skeletal and cardiac muscle contraction. However, since the development of the in vitro motility assay (8,9) and single-molecule imaging (10,11) and manipulation (12,13) techniques, these new systems and techniques have been widely used to study sliding movement and force generation on a single actin filament and myosin molecules (14). Such studies are indispensable for direct measurements of force, working stroke, and the kinetics of each single molecular interaction (15–22). Although the sliding mechanism of muscle contraction appeared established from reports after the introduction of in vitro systems, some differences have since been found between muscle models and in vitro systems. For example, there are interesting phenomena observed only in muscle model systems, such as stretch activation and spontaneous oscillatory contraction (23). These phenomena are probably attributable to the characteristics of a high-ordered system. Myosin molecules in in vitro systems are usually adhered to glass or bead surfaces two-dimensionally in a random fashion, and there seem to be some myosin molecules with only one head available (17). Therefore, as an actin filament tends to detach from myosin heads, especially at physiological conditions characterized by higher ionic strength, experimental conditions must be limited to low ionic strength. These limitations could be critical for studying the mechanism of muscle contraction that occurs in an ordered array of myofilaments. In fact, it is reported that force generation largely depends on the orientation of myosin molecules (24) and ionic conditions.

Here, we present a new motility assay system in which a single actin filament is pulled into a thick-filament lattice. This system, which we call an A-band motility assay system or "bionanomuscle", is composed of a single actin filament and the A-band, where the lattice structure of myosin thick filaments is maintained. We hope to answer some long-standing questions in muscle physiology, such as whether the myosin molecule is an independent force generator irrespective of the conditions, or if there is cooperativity in force generation and its regulatory mechanisms.

In this study, we have succeeded in measuring the force and determining a length-force relationship for a single actin filament working in an organized structure, i.e., a thick-filament lattice. We observed large fluctuations in force development and the displacement of an actin filament around the mean values. This phenomenon is related to what Borejdo and Morales (25) intended to record to characterize individual cross-bridge functions in muscle fibers. Some results we obtained at the preliminary stage of this project, and which are not included here, have been published (26).

MATERIALS AND METHODS

Preparation of myofibrils and proteins

All procedures were performed according to the Regulations for Animal Experimentation at Waseda University. Male white rabbits (2.0–2.5 kg)

Submitted October 22, 2004, and accepted for publication January 14, 2005.

Address reprint requests to Shin'ichi Ishiwata, Dept. of Physics, School of Science and Engineering, Waseda University, 3-4-1 Okubo, Shinjuku-ku, Tokyo 169-8555, Japan. Tel.: 81-3-5286-3437; Fax.: 81-3-5286-3437; E-mail: ishiwata@waseda.jp.

0006-3495/05/07/321/08 $2.00

doi: 10.1529/biophysj.104.054957

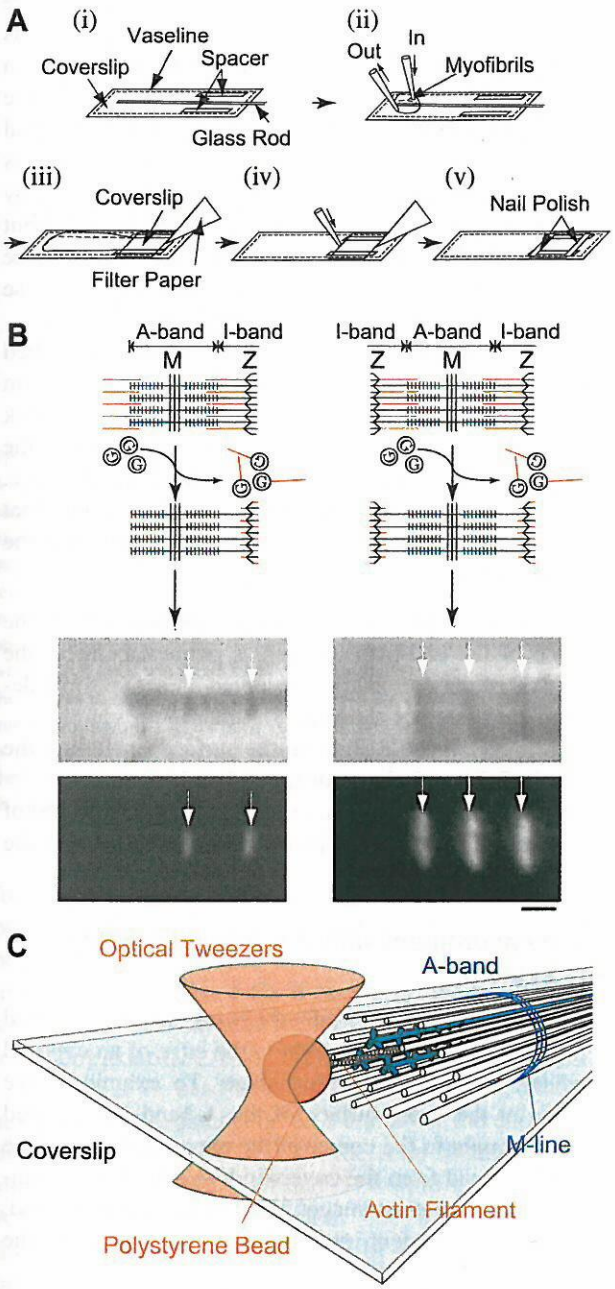

FIGURE 1 (*A*) Procedure for preparing the A-band motility assay system on a coverslip. A thin glass rod prepared by heating and stretching a glass micropipette was employed to exchange the solution smoothly without sucking up myofibrils (see text). (*B*) Schematic diagram illustrating the longitudinal section of the A-band motility assay system (*upper*) and snap shots (*lower*) obtained after the gelsolin treatment of myofibrils, to which a bead-tailed actin filament trapped with optical tweezers was approached from the left. (*Left*) A myofibril used for the experiments. (*Right*) A small bundle of myofibrils not used for the experiments. Myofibrils prepared from glycerinated rabbit psoas muscle fibers were exposed to gelsolin (*Gs in circles*), so that the thin filaments (*red line*) were selectively removed. Snap shots show phase-contrast (*top*) and fluorescence (*bottom*) images of a myofibril (*left*) and a small bundle of myofibrils (*right*) after the gelsolin treatment. Myofibrils were labeled with Rh-Ph after the gelsolin treatment to identify the position of the Z-lines. Every image was obtained by integrating for 1 s (30 frames). Arrows indicate the Z-lines. Scale bar, 1 μm. (*C*) Schematic three-dimensional illustration of the A-band motility assay system. A bead-tailed actin filament was brought into contact with the edge of the exposed A-band using optical tweezers.

were anesthetized with sodium pentobarbital (150 mg/kg). The body, in which psoas, back, and leg muscles were exposed, was incubated in crushed ice for 15 min. Myofibrils were prepared by homogenizing glycerinated rabbit psoas muscle fibers in rigor solution (60 mM KCl, 5 mM $MgCl_2$, 10 mM 3-(*N*-morpholino)propanesulfonic acid (MOPS), pH 7.0, and 1 mM EGTA). Glycerination was performed as described previously (27). G-actin was prepared from rabbit white skeletal muscle (28). Actin filaments were labeled with rhodamine-phalloidin (Rh-Ph, R-415; Molecular Probes, Eugene, OR). The bead-tailed actin filament, i.e., an actin filament with the barbed (B-) end attached to a 1-$\mu m\phi$, carboxylate-modified polystyrene bead (08226-15, Polysciences, Warrington, PA) through gelsolin, was prepared as previously reported (17,29). Bovine plasma gelsolin was prepared according to the method of Kurokawa et al. (30); during this preparation, the incubation time of gelsolin in Ca^{2+}-free buffer was shortened as much as possible because severing activity was lowered by incubation in the Ca^{2+}-free buffer. The concentrations of free Mg^{2+}, MgATP, MgADP, and other chemicals were calculated by computer, using the published values for stability constants (31).

Microscopy

The microscopy system and the method for image analysis were basically the same as those reported previously (17), with some modifications as follows: The phase-contrast image of the bead, acquired with a CCD camera (CCD-300, Dage-MTI, Michigan City, IN), was stored in a personal computer (Apple Japan, Tokyo, Japan) with a frame grabber LG3 (National Institutes of Health, Washington, DC). The bead position was determined from digitized camera frames having a 30/s sampling video rate. Fluorescence images of an actin filament and a bead were visualized using an ICCD camera (ICCD-350F, Video Scope International, Washington, DC). An Nd:YAG laser (T10-V-106C, 2.5 W, Spectra-Physics Lasers, Mountain View, CA) was used as the optical tweezers. The stiffness of the optical tweezers, 0.10–0.25 pN/nm, was determined as described previously (32). On the other hand, we estimated the spatial resolution of the data obtained at a time resolution of 1/30 s, because the movement of the bead was recorded at the video rate (see Nishizaka et al. (17)). Thus, the standard deviation of the fluctuation of the position of the bead trapped for 40 s by the optical tweezers with a stiffness of 0.12 pN/nm was 1.43 nm in the x direction and 1.46 nm in the y direction ($n = 9$). The SD of the fluctuation of the position of the bead attached to a glass surface for 40 s was 2.15 nm in the x direction and 1.71 nm in the y direction ($n = 9$).

Preparation of the A-band motility assay system

As schematically illustrated in Fig. 1, our A-band motility assay system was prepared by removing the thin filaments selectively from a single or a small bundle of myofibrils with gelsolin treatment on ice (33–35). First, an embankment was made with Vaseline along the edge of the coverslip to keep the solution from spilling. Spacers 75 μm thick, and a glass rod made by heating and stretching a 100-μl glass micropipette (2-000-100, Drummond Scientific, Broomall, PA) were placed as illustrated in Fig. 1 *A i*. We found that a glass rod was useful for carefully changing the solution without sucking up myofibrils, because it worked as an obstacle, preventing myofibrils from flowing.

Second, the suspension of myofibrils (100 μl) in a rigor solution was placed on one side of a coverslip (Fig. 1 *A ii*) and the rigor solution was slowly exchanged with a gelsolin solution A (60 mM KCl, 4 mM $MgCl_2$, 20 mM MOPS, pH 7.0, 2 mM EGTA, 1.9 mM $CaCl_2$ (pCa ~5), 1.5 mM NaN_3, 2 mM leupeptin, and 0.3 mg/ml gelsolin) using a pair of micropipettes

and taking care not to suck up myofibrils. After 30 min of gelsolin treatment, the gelsolin solution A was exchanged with the gelsolin solution B (gelsolin solution A plus 20 mM 2,3-butanedione 2-monoxime and 1 mM ATP) using a pair of micropipettes. After 20 min of treatment, the myofibrils were washed first with a relaxing solution (120 mM KCl, 4 mM $MgCl_2$, 20 mM MOPS, pH 7.0, 4 mM EGTA, 4 mM ATP, and 10 mM dithiothreitol (DTT)), and then with a rigor solution containing 10 mM DTT. Then, after the glass rod was removed, the whole area surrounded by the embankment of Vaseline was filled with the rigor solution containing DTT (Fig. 1 *A iii*). A flow cell was made by putting a smaller coverslip on spacers placed on the other side of the larger coverslip. The solution was then sucked by a piece of filter paper to move the A-band toward the flow cell, which resulted in the attachment of the A-band to the surface of a larger coverslip, where gelsolin was not present. In this step, it was essential to attach the A-band to the glass surface where gelsolin treatment had not been carried out. The bead-tailed actin filament tended to be cut when the experiments were performed at the place where the gelsolin treatment was done, probably because free gelsolin molecules attached to the glass surface could not be washed away. During this procedure, myofibrils aligned in the same orientation along the flow line. The A-band assay system thus prepared was treated with 0.5% (v/v) Triton X-100 in the rigor solution containing 10 mM DTT and then washed several times with the rigor solution containing 10 mM DTT to remove Triton X-100 (Fig. 1 *A iv*). This wash is important for thoroughly washing away contaminating gelsolin. All procedures were carried out on ice.

Finally, we mounted the flow cell on the stage of a microscope and attempted to find the A-band motility assay system appropriate for the following experiments. The Z-line of the exposed A-band at the end of a myofibril should be absent. If necessary, a fresh rigor solution with DTT was poured into the flow cell during the search as the solution in the flow cell was easily evaporated. After an appropriate A-band was selected, the flow cell was washed with an assay buffer (100 mM KCl, 4.2 mM $MgCl_2$ (free Mg^{2+} = 2 mM), 25 mM imidazole-HCl, pH 7.4, 1 mM EGTA, 2.2 mM ATP (MgATP = 2 mM), 0.5 mg/ml bovine serum albumin, 10 mM DTT, 4.5 mg/ml D(+)-glucose, 50 units/ml glucose oxidase, 50 units/ml catalase, 15 mM creatine phosphate and 150 units/ml creatine phosphokinase). Then, the bead-tailed actin filaments in the assay buffer were applied, and both edges of the flow cell were sealed with nonfluorescent nail polish (Fig. 1 *A v*). All the experiments were carried out at 27–29°C.

RESULTS

Development of the A-band motility assay system

The ends of the myofibrils have either exposed A-bands (the left column of Fig. 1 *B*) or Z-lines (the right column of Fig. 1 *B*) as myofibrils tend to be cut at the I-band during homogenization in the rigor solution. As shown in Fig. 1 *B*, the Z-line was observable as a black line in a phase-contrast image and a bright line in a fluorescent image. (Here, short actin filaments remaining at the Z-line were fully labeled with Rh-Ph after the gelsolin treatment. In most observations, the Z-line became weakly fluorescent by the binding of free Rh-Ph molecules in the actin solution (Fig. 2).) We could confirm that exposed A-bands maintained their original thickness (usually >1 μm) by referring to a phase-contrast image of a bead 1 μm in diameter attached to the glass surface. It is to be noted that some preparations were composed of a few myofibrils (see the micrograph in the right column of Fig. 1 *B*), so that these preparations were thicker than 2 μm. The A-band motility assay system we devised is schematically illustrated in Fig. 1 *C*.

In some gelsolin-treated myofibrils, the A-bands were shorter than 1.6 μm, probably because the thick filaments were partially depolymerized from the ends (36). Also, in some preparations both ends of the A-bands looked dense under the phase-contrast microscope. This dense material may be attributable to the folded ends of thick filaments and/or some materials that were not successfully removed by homogenization (33). Some of the A-bands looked faint under the phase-contrast microscope, probably because the thick-filament lattice was partially disorganized (37). These preparations were not used in the experiments.

Even in A-bands that have not looked like those described above, we were concerned that folded connectin/titin molecules might have been present at the end of the thick filaments, because such folded molecules could interrupt the entrance of actin filaments into the thick-filament lattice. However, we concluded from the following observations that there were no obstacles interacting with actin filaments at the edge of the A-band:

1. When a bead-tailed actin filament interacted with the surface of the end-plane, which is perpendicular to the long axis of the A-band, we observed an active force development (data not shown).
2. Actin filaments could slide on the surface (including the surface of the end-plane) of the A-band.
3. Actin filaments were pulled out smoothly from the end of the A-band in addition to their smooth entrance into the A-band.

Force measurement with the A-band motility assay system

A bead-tailed actin filament of ~1–3 μm long was trapped with optical tweezers and brought to the edge of an exposed A-band by moving the sample stage. To examine force generation at the outer surface of the A-band, the trapped bead was brought to the corner of the exposed A-band. The height of the bead from the coverslip was adjusted by comparing the phase-contrast images of the A-band and the bead, so that the actin filament interacted with the outside of the A-band (Fig. 2 *A*).

To examine the force generation inside the A-band, the trap center was set near the end plane of the A-band, such that the actin filament did not reach the A-band. The position of the trap center was carefully selected to be located at the center of the end-plane of the A-band not only laterally but also in depth. Here, we made sure that the bead did not attach to the glass surface. Then, with the use of a stepping motor on the sample stage, the A-band was moved in 25-nm steps toward the bead held in the trap center. Insofar as the actin filament did not interact with the A-band, the trapped bead freely rotated in the trap (a movie is available at http://www.phys.waseda.ac.jp/bio/ishiwata/movies/sfibj2004movie1.avi). If the interaction did not occur even when the actin filament was pointed at the A-band, the sample stage was moved

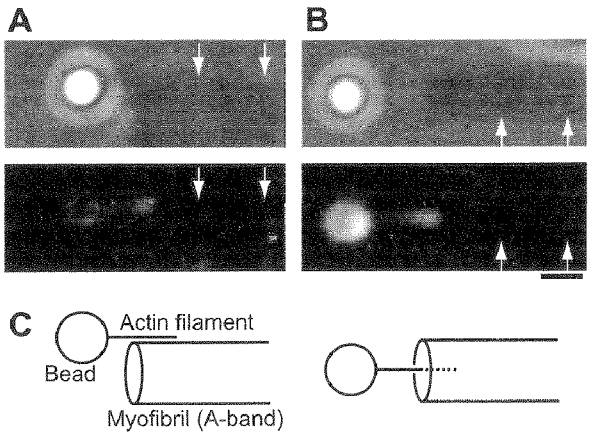

FIGURE 2 Phase-contrast (*top*) and fluorescence (*bottom*) images of the A-band motility assay system. (*A*) An actin filament made to interact with the outer surface of the A-band. (*B*) An actin filament interacting with the end-plane of the A-band (a movie is available at http://www.phys.waseda.ac.jp/bio/ishiwata/movies/sfibj2004movie1.avi). (*C*) Schematic illustrations representing the arrangement of the bead-tailed actin filament and the A-band in *A* and *B*, respectively. Unlike in Fig. 1 *B*, the Z-lines have become observable because of free Rh-Ph with bead-tailed actin filaments. Even when the Z-lines were less labeled, the brightness was enough to identify the Z-lines in fluorescence images (*bottom*). Every image was obtained by integrating for 1 s (30 frames). A part of an actin filament near the bead is photobleached, probably due to two-photon illumination (532 nm) by the laser light used for the optical tweezers. Arrows indicate the Z-lines. Scale bar, 1 μm.

further to bring the A-band closer to the bead. When the pointed end of the actin filament touched the A-band, a force began to be generated, so that the actin filament was pulled into the A-band (Fig. 1 *C*). If necessary, the position of the sample stage was adjusted to make the actin filament parallel to the long axis of the A-band and to the glass surface (Fig. 2 *B*).

As soon as the bead-tailed actin filament touched the outer surface of the A-band (Fig. 3, *A* and *B*) or the end-plane of the A-band (Fig. 3, *C* and *D*), the actin filament began to slide quickly (cf. Fig. 3, *A* and *D*) toward the center of the A-band, i.e., the M-line region. The sliding of the actin filament continued, accompanied by changes in the overlapping length and load (this is a so-called auxotonic condition). At the steady level, the force generated by myosin molecules in the A-band needs to balance the load applied by the optical tweezers. When an actin filament interacted with the outer surface of the A-band, a sudden detachment of the filament from the A-band sometimes occurred, so that the bead was returned to the trap center. Even after the force reached a steady state, fluctuations in the overlapping length and the force continued (usually as much as ± 30 nm and sometimes $\sim \pm 50$ nm for the displacement, and up to ± 10 pN for the force around the average position). It should be noted here that the extent of these fluctuations is much larger than a measurement error (cf. Materials and Methods).

Several seconds after a steady state was attained, either the laser power was suddenly changed (Fig. 4 *A*, method 1) or the sample stage was stepwise moved in parallel to the long axis of the A-band (Fig. 4 *B*, method 2). By repeating this procedure, we could successively obtain new steady levels. Examples of data from the former and latter methods are shown in Fig. 3, *A* and *C*, and *B* and *D*, respectively. These experiments were designed to determine the length-force relationship.

As expected from the mechanical constraints schematically shown in Fig. 4, the larger the stiffness of the optical tweezers, the smaller the amount of the displacement. Also, a steady level does not exist unless the stiffness of the optical tweezers is larger than the slope of the length-force relationship of the A-band. In practice, the bead often escaped from the optical trap and slid into the A-band when the stiffness of the optical tweezers was lowered.

Length-force relationship

Fig. 5, *A* and *C*, show relationships between the displacement of the bead and the change in the generated force due to the change in overlap of an actin filament and the A-band. The point, where the developed and trapping forces were on average balanced was plotted on the ordinate. The average forces then obtained after stepwise changing the stiffness of the optical tweezers (method 1) or moving the sample stage (method 2) were plotted to the right or the left depending on whether the actin filament slid into or was pulled out from the A-band, respectively. Because each set of data obtained in each experiment appeared to be linear, each set was simulated by a straight line. The data obtained by methods 1 and 2 were indistinguishable from each other. The intercept with the abscissa of the straight line indicates the initial length of the overlap of the actin filament with the A-band (cf. Fig. 4). Correspondingly, the intercept with the ordinate of the straight line shows the average force initially developed. From the average slope of the data shown in Fig. 5, *A* and *C*, we obtained the force per unit length of overlap when an actin filament interacts with the outer surface or the end plane, respectively, of the A-band (Table 1). The former was determined as 0.097 ± 0.032 pN/nm (mean $\pm$ SE. of the slopes, $n = 10$), and the latter as 0.16 ± 0.051 pN/nm (mean $\pm$ SE, $n = 13$). We confirmed that these two sets of data were significantly different from each other (significance, $0.01 < P < 0.05$, verified by Kolmogorov-Smirnov test, and $P < 0.01$, verified by Mann-Whitney U-test).

Then, each set of data was moved parallel to the abscissa until the straight line obtained by the least-squares method extrapolated the origin (Fig. 5, *B* and *D*, for *A* and *C*, respectively). These procedures converted the relationship between the change in overlap and the average force (Fig. 5, *A* and *C*) to the overlapping length of actin filament with the A-band versus the average force (Fig. 5, *B* and *D*). Fig. 5 *B*, obtained from Fig. 5 *A*, shows linear relationship, but the data in Fig. 5 *D* were broadly distributed.

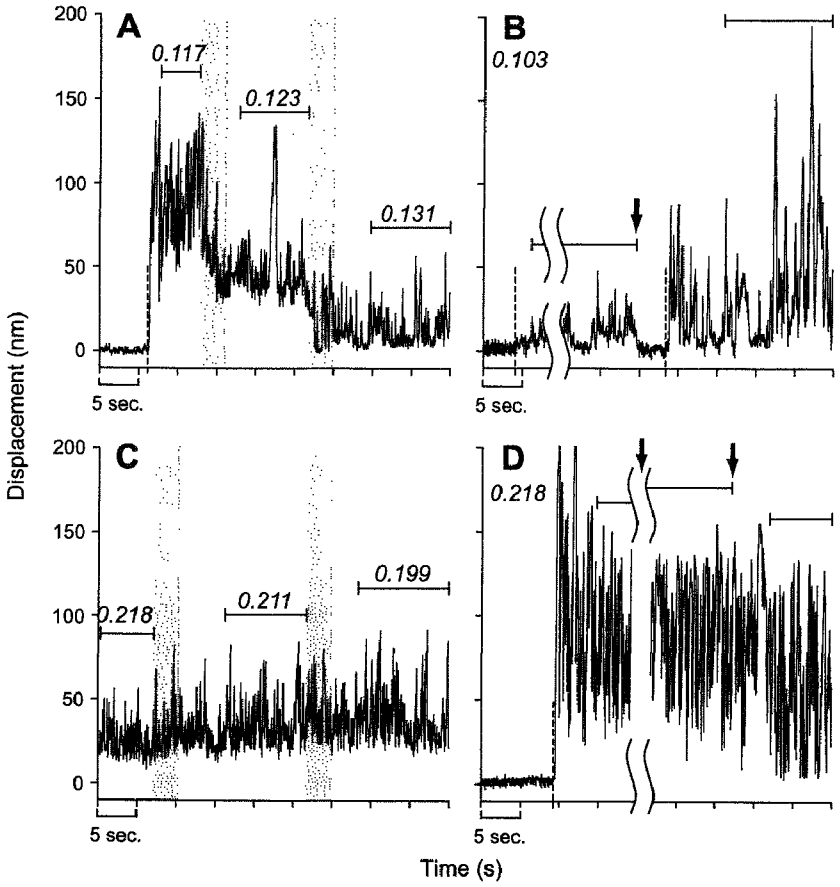

FIGURE 3 Time course of the displacement of a trapped bead in the A-band motility assay system. (*A* and *B*) An actin filament interacting with the outer surface of the A-band, corresponding to the situation shown in Fig. 2 *A*. (*C* and *D*) An actin filament interacted inside the A-band, corresponding to the situation shown in Fig. 2 *B*. At first, the bead stayed at the center of the trap (*A*, *B*, and *D*). The actin filament began to interact with the A-band at the moment shown by the broken lines. While the actin filament was interacting with the A-band, the laser power for the optical tweezers was changed to alter the stiffness of the optical tweezers (*A* and *C*), or the sample stage was moved stepwise (*B* and *D*). The average position of the bead was determined in the region indicated by solid horizontal lines. The italic figures indicate the stiffness of the optical tweezers (pN/nm). The gray rectangles in *A* and *C* show the period during which the laser power was changed. The arrows in *B* and *D* show the moment at which the sample stage was moved stepwise.

DISCUSSION

Average force generated by single myosin heads

In general, 95% of the data are included in the region surrounded by mean ± SE × 1.96. Therefore, 95% of the data of the slope shown in Fig. 5 *A* are included in the region surrounded by the dashed lines of 0.097 ± (0.032 × 1.96) pN/nm (Fig. 5 *B*). On the other hand, the data in Fig. 5 *D* appeared to be classified into two groups having different slopes. Because the smaller slope is nearly equal to that for Fig. 5 *B*, we tested whether a significant difference exists between the group having the smaller slope and the data in Fig. 5 *B*. Statistical analysis demonstrated no significant difference between the data in the region of 0.097 ± (0.032 × 1.96) pN/nm (the region surrounded by the *dashed lines*) in Fig. 5 *D* and those in Fig. 5 *B* ($P \sim 0.25$, verified by Mann-Whitney U-test). Thus, we conclude that the data classified into the group having the smaller slope in Fig. 5 *D* are attributable to the actin filaments interacting outside the A-band (or at an equivalent geometry; most probably the outer surface of the A-band located within a small bundle of myofibrils). Concerning the rest of the data, they were

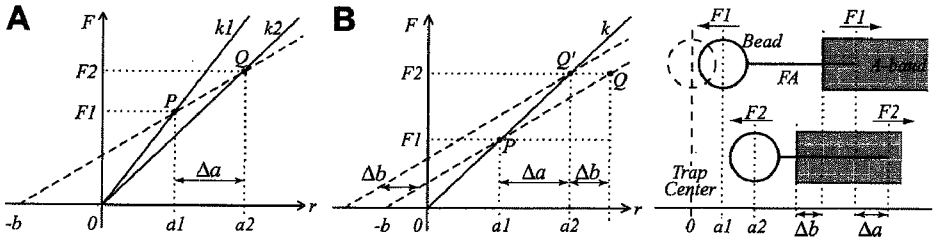

FIGURE 4 Methods to determine the balancing points by changing the stiffness of the optical tweezers (*A*, method 1), or moving the sample stage (*B*, method 2). Abscissa, displacement of the bead from the trap center ($r = 0$); ordinate, trapping force (*solid line*) or the force developed on an actin filament interacting with the A-band (*dashed line*); k, k_1, and k_2, stiffness of the optical tweezers; a_1 and a_2, displacement of the bead from the trap center, and $\Delta a = |a_1 - a_2|$; b, the initial length of the overlap between an actin filament and the A-band; Δb, displacement of the sample stage. (*A*) After the developed force (*dashed line*) and load (*solid line* k_1) are balanced at point $P(a_1, F_1)$, the stiffness of the optical tweezers is changed from k_1 to k_2, which results in a shift of the balancing point from P to $Q(a_2, F_2)$. The slope of the broken line, i.e., the force per unit length of overlap, is determined by $|F_2 - F_1|/\Delta a$. (*B, left*) At first, the developed force on the actin filament (*broken line* crossing the abscissa at $-b$) and the load applied by the optical tweezers (*solid line* k) are balanced at $P(a_1, F_1)$. When the sample stage is shifted toward the trap center by Δb, the balancing point moves to the point $Q'(a_2, F_2)$. Therefore, the slope of the broken line, i.e., the force per unit length of the overlap, passing through the points P and $Q(a_2 + \Delta b, F_2)$ is determined by $|F_1 - F_2|/(\Delta a + \Delta b)$. (*B, right*) Schematic illustration of this procedure.

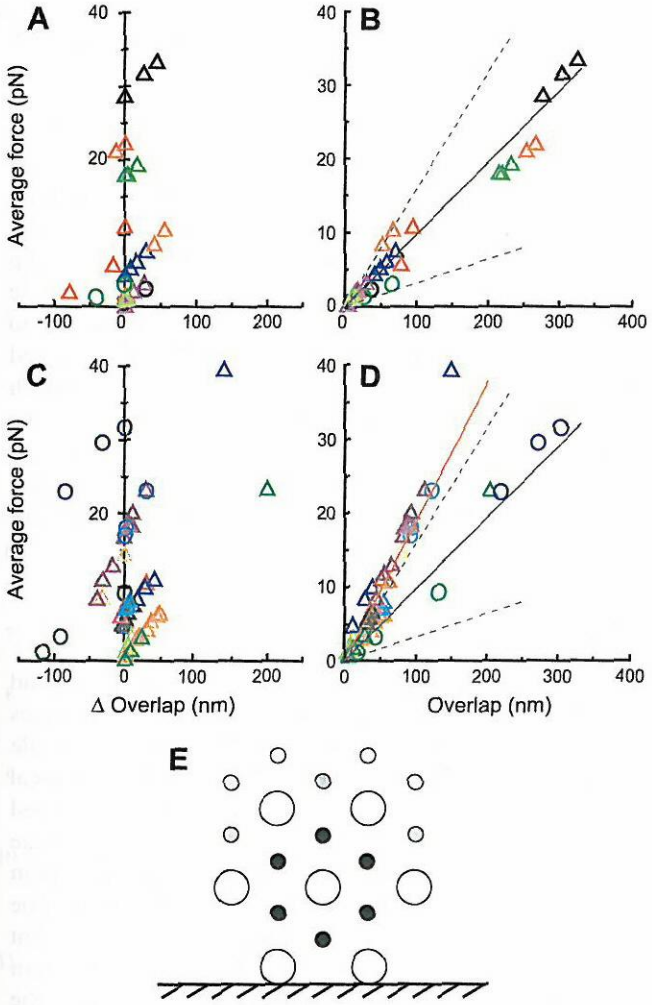

FIGURE 5 Length-force relationship in the A-band motility assay system. (*A* and *B*) Actin filaments interacted with the outer surface of the A-band (data were obtained from 10 different preparations). (*C* and *D*) Actin filaments interacted with the end plane of the A-band (data were obtained from 13 different preparations). (*A* and *C*) The change in overlap versus the average force. Each set of data points distinguished by color was obtained in one preparation by changing the stiffness of the optical tweezers (*triangles*) or by moving the sample stage (*circles*). The average force initially developed before the change in the stiffness or the movement of the stage is plotted on the ordinate. (*B* and *D*) Overlap versus the average force. Each data set in *A* and *C* was shifted in parallel to the abscissa, such that the approximate line determined for each data set by the least-squares method passed through the origin. (*B*) Length-force relationship obtained when an actin filament interacted with the outer surface of the A-band. The blue solid line, 0.097 pN/nm, indicates the mean of slopes. Two dashed lines, 0.097 ± (0.032 × 1.96) pN/nm, indicate the border of the 95% confidence interval of the population mean. (*D*) Length-force relationship obtained when an actin filament interacted with the end-plane of the A-band. A blue solid line and two dashed lines are identical to those in *B*. A red line indicates the mean of slopes for the data from outside the region surrounded by the two dashed lines. (*E*) Schematic illustration showing the geometry of the thick filaments (*open large circles*) and the actin filaments inside (*black circles*) and outside (*gray* and *open small circles*) the A-band.

TABLE 1 Summary of the mean force per unit length of overlap outside and inside the thick-filament lattice calculated from the slope for each set of data points in Fig. 5.

	Outside	Inside
	pN/nm	pN/nm
Outer surface of the A-band	0.097 ± 0.032 (10)	—
End-plane of the A-band	0.11 ± 0.028 (5)	0.19 ± .031 (8)

The values are given as mean ± SE with numbers of preparations, *n*, indicated in parentheses. Slopes were determined by the least-squares method. The data were obtained by the interaction of an actin filament with the outer surface or the end-plane of the A-band, which was determined by microscopic observation during the experiments according to the geometry of the actin filament and the A-band. The data obtained for the end-plane of the A-band were classified into two types, i.e., outside or inside the thick-filament lattice, according to the slope for the relationship of the average force versus overlap shown in Fig. 5 *D* (for more details, see the text).

significantly different from the data classified into the group having the smaller slope in Fig. 5, *B* and *D* ($P < 0.003$, verified by Mann-Whitney U-test). We therefore determined the force per unit length of the overlap from the values of the slopes as 0.19 ± 0.031 pN/nm (mean ± SE, $n = 8$). This is attributable to the force that is developed when the actin filament interacts at the center of the thick-filament triangular lattice (i.e., at the most stable position; see Fig. 5 *E*). The reason the force per unit length of overlap was smaller, ~1/2, outside than inside the A-band is probably that the number of thick filaments interacting with a single actin filament outside the A-band is 1/3–2/3 that inside (for the geometry of the thick-filament lattice, compare the *gray* and *open small circles* with the *filled circles* in Fig. 5 *E*).

The time average of the force generated by single myosin heads inside the A-band is estimated assuming that the actin filament is located at the most stable position in the thick-filament lattice. A thick filament (1.6 μm long) consists of 300 myosin molecules, implying that there are 150 myosin molecules (300 heads) in half a sarcomere. As a single actin filament is surrounded by three thick filaments (Fig. 5 *E*), we assumed that one-sixth (60°/360°) of the three thick filaments have a chance to interact with each actin filament. Consequently, we estimate that 300 × 3/6 = 150 myosin heads are available to each actin filament per half sarcomere. The effective length of the thick filament where myosin molecules are present in half a sarcomere is ~0.7 μm because myosin molecules are absent at the 0.2-μm-long central bare zone. Therefore, the average force per myosin head is estimated to be 0.19 pN/nm × 700 nm/150 = 0.9 pN. Note that 0.9 pN per myosin head corresponds to ~2×10^5 N/m^2, the force developed in muscle, if the calculation is done as described above. In the muscle model systems, the isometric tension has been estimated as 1.05–2.20 × 10^5 N/m^2 at an ionic strength of 200 mM (7), and the average force per myosin head as 1.6 pN at 90 mM KCl (38).

The usual in vitro motility assay using randomly oriented myosin molecules showed the average force per myosin head

of 0.42 pN at 25 mM KCl (39) and 0.2 pN at 35 mM KCl (14). On the other hand, the in vitro assay using a synthetic myosin rod cofilament with oriented myosin molecules gave a value of 2.1 pN at 25 mM KCl (38). However, these values can not be directly compared with those obtained in muscle, as the developed force largely depends on ionic strength. Also, there is a possibility that the fraction of attached myosins differs between the different assays and conditions. As an actin filament is surrounded by the thick filaments in the A-band motility assay system, sustained force generation and sliding movements were possible even under a higher ionic strength, 100 mM KCl (ionic strength ~140 mM). Our result demonstrates that the force equivalent to that in muscle can be developed on a reconstituted pure actin filament in the thick-filament lattice structure.

Linear relationship between force and overlap

Fig. 5, *B* and *D* , indicate that the relationship between the average force and the overlap of an actin filament with the A-band is consistent with the linear length-tension relationship observed in an intact muscle fiber under an isometric condition (40). We stress here that this linear relationship was obtained only for the time-averaged force-versus-overlap relationship. In practice, the tension largely fluctuated around the average force, indicating that the force instantaneously developed is much higher than the average. Such a nonlinear feature of tension (and length) fluctuation should be examined in future by data analysis with higher time resolution.

The linear relationship was retained irrespective of whether the interaction occurred outside (Fig. 5 *B*) or inside (Fig. 5 *D*) the A-band. These results imply that, at least on average, the total force can be described as the simple sum of the forces generated by each myosin molecule. However, because the trap force was not sufficiently large, this relationship could only be obtained at the end region of the A-band, i.e., less than half of a full overlap. We have not yet examined whether the linear relationship obtained here is extrapolated up to 700 nm (the edge of the pseudo-H-zone). Also, we need to examine whether no cooperativity exists among cross-bridges even after the regulatory proteins are reconstituted, or under the conditions intermediate between contraction and relaxation at which, for example, spontaneous oscillatory contraction occurs (23).

Force fluctuations

In the 1970s, Borejdo and Morales (25) tried to determine the rate constants for the elementary processes of each myosin molecule interacting with the thin filament by analyzing force fluctuation under the steady state in a muscle fiber. However, the amplitude of fluctuation was too small compared to the force level because of a large number of myosin molecules (>10 million) working in their system. Therefore, artifacts associated with the experimental procedure could not be absolutely excluded, as was mentioned by the authors. In contrast, here we observed large back-and-forth displacement of a single actin filament accompanied by a large change in developed force. This may be attributable to the number fluctuation of the force-generating cross-bridge because the number of available myosin heads is small, ~10. Our A-band motility assay system is suitable for such analysis, as the force fluctuations can be recorded with sufficient sensitivity on a single actin filament due to the small number of interacting myosin molecules. The next step for us is to improve time resolution, because the video rate was too slow to analyze the actual force fluctuations due to the elementary steps of each myosin molecule. We also need to achieve an isometric condition for this purpose, which when accomplished should make it possible to study the response against quick stretch and quick release, leading to a more detailed analysis of the mechanochemical coupling mechanism in muscle contraction in an ordered array of myosin molecules.

CONCLUSION

We have described a new motility assay system, the A-band motility assay. Its most important feature is that it makes possible study of the characteristics of the muscle contractile system at a single-actin filament level under physiological conditions. The force generation on a single reconstituted actin filament and its displacement can be measured in the minimum unit of striated muscle with an accuracy of within subpiconewtons and a few nanometers, respectively. The experiments can be performed at nearly physiological solvent conditions without the detachment of the actin filament from myosin molecules. Further, it will be possible to examine the roles of an actin filament with and without regulatory proteins in the mechanism of muscle contraction and regulation by using genetically engineered or chemically modified actin filaments and regulatory proteins. In this respect, our A-band motility assay system is complementary to the contractile system of muscle in which thin filaments are reconstituted (34,35).

SUPPLEMENTARY MATERIAL

An online supplement to this article can be found by visiting BJ Online at http://www.biophysj.org.

We thank Mr. T. Iga of Waseda University for his efforts at the initial stage of this research project.

This research was partly supported by Grants-in-Aid for Specially Promoted Research, from the 21st Century COE Program (Physics of Self-Organization Systems) at Waseda University, and from the Bio-venture Project from the Ministry of Education, Sports, Culture, Science and Technology of Japan to S.I., and by Grants-in-Aid for Special Research Projects from Waseda University (2002A-867 and 2004A-226), from the 21st Century COE program (Physics of Self-Organization Systems) at Waseda University, and from the New Technology Development Project of the Ministry of Education, Sports, Culture, Science and Technology of Japan to M.S.

REFERENCES

1. Natori, R. 1954. The role of myofibrils, sarcoplasm and sarcolemma. *Jikeikai Med. J.* 1:18–28.
2. Nakajima, Y., and M. Endo. 1973. Release of calcium induced by 'depolarisation' of the sarcoplasmic reticulum membrane. *Nat. New Biol.* 246:216–218.
3. Irving, M., G. Piazzesi, L. Lucii, Y.-B. Sun, J. J. Harford, I. M. Dobbie, M. A. Ferenczi, M. Reconditi, and V. Lombardi. 2000. Conformation of the myosin motor during force generation in skeletal muscle. *Nat. Struct. Biol.* 7:482–485.
4. Corrie, J. E. T., B. D. Brandmeier, R. E. Ferguson, D. R. Trentham, J. Kendrick-Jones, S. C. Hopkins, U. A. Van der Heide, Y. E. Goldman, C. Sabido-David, R. E. Dale, S. Criddle, and M. Irving. 1999. Dynamic measurement of myosin light-chain-domain tilt and twist in muscle contraction. *Nature.* 400:425–430.
5. Piazzesi, G., M. Reconditi, M. Linari, L. Lucil, Y.-B. Sun, T. Narayanan, P. Boesecke, V. Lombardi, and M. Irving. 2002. Mechanism of force generation by myosin heads in skeletal muscle. *Nature.* 415:659–662.
6. Anazawa, T., K. Yasuda, and S. Ishiwata. 1992. Spontaneous oscillation of tension and sarcomere length in skeletal myofibrils. *Biophys. J.* 61:1099–1108.
7. Friedman, A. L., and Y. E. Goldman. 1996. Mechanical characterization of skeletal muscle myofibrils. *Biophys. J.* 71:2774–2785.
8. Yanagida, T., M. Nakase, K. Nishiyama, and F. Oosawa. 1984. Direct observation of motion of single F-actin filaments in the presence of myosin. *Nature.* 307:58–60.
9. Kron, S. J., and J. A. Spudich. 1986. Fluorescent actin filaments move on myosin fixed to a glass surface. *Proc. Natl. Acad. Sci. USA.* 83: 6272–6276.
10. Funatsu, T., Y. Harada, M. Tokunaga, K. Saito, and T. Yanagida. 1995. Imaging of single fluorescent molecules and individual ATP turnovers by single myosin molecules in aqueous solution. *Nature.* 374:555–559.
11. Sase, I., H. Miyata, J. E. T. Corrie, J. S. Craik, and K. Kinosita, Jr. 1995. Real time imaging of single fluorophores on moving actin with an epifluorescence microscope. *Biophys. J.* 69:323–328.
12. Ashkin, A., J. M. Dziedzic, J. E. Bjorkholm, and S. Chu. 1986. Observation of a single-beam gradient force optical trap for dielectric particles. *Opt. Lett.* 11:288–290.
13. Ashkin, A., K. Schutze, J. M. Dziedzic, U. Euteneuer, and M. Schliwa. 1990. Force generation of organelle transport measured in vivo by an infrared laser trap. *Nature.* 348:346–348.
14. Kishino, A., and T. Yanagida. 1988. Force measurements by micromanipulation of a single actin filament by glass needles. *Nature.* 334: 74–76.
15. Ishijima, A., H. Kojima, T. Funatsu, M. Tokunaga, H. Higuchi, H. Tanaka, and T. Yanagida. 1998. Simultaneous observation of individual ATPase and mechanical events by a single myosin molecule during interaction with actin. *Cell.* 92:161–171.
16. Kitamura, K., M. Tokunaga, A. H. Iwane, and T. Yanagida. 1999. A single myosin head moves along an actin filament with regular steps of 5.3 nanometres. *Nature.* 397:129–134.
17. Nishizaka, T., R. Seo, H. Tadakuma, K. Kinosita, Jr., and S. Ishiwata. 2000. Characterization of single actomyosin rigor bonds: load dependence of lifetime and mechanical properties. *Biophys. J.* 79: 962–974.
18. Veigel, C., M. L. Bartoo, D. C. S. White, J. C. Sparrow, and J. E. Molloy. 1998. The stiffness of rabbit skeletal actomyosin cross-bridges determined with an optical tweezers transducer. *Biophys. J.* 75:1424–1438.
19. Molloy, J. E., J. E. Burns, J. Kendrick-Jones, R. T. Tregear, and D. C. S. White. 1995. Movement and force produced by a single myosin head. *Nature.* 378:209–212.
20. Mehta, A. D., J. T. Finer, and J. A. Spudich. 1997. Detection of single-molecule interactions using correlated thermal diffusion. *Proc. Natl. Acad. Sci. USA.* 94:7927–7931.
21. Finer, J. T., R. M. Simmons, and J. A. Spudich. 1994. Single myosin molecule mechanics: piconewton forces and nanometre steps. *Nature.* 368:113–119.
22. Miyata, H., H. Hakozaki, H. Yoshikawa, N. Suzuki, K. Kinosita, Jr., T. Nishizaka, and S. Ishiwata. 1994. Stepwise motion of an actin filament over a small number of heavy meromyosin molecules is revealed in an *in vitro* motility assay. *J. Biochem. (Tokyo).* 115:644–647.
23. Ishiwata, S., and K. Yasuda. 1993. Mechano-chemical coupling in spontaneous oscillatory contraction of muscle. *Phase Transit.* 45:105–136.
24. Tanaka, H., A. Ishijima, M. Honda, K. Saito, and T. Yanagida. 1998. Orientation dependence of displacements by a single one-headed myosin relative to the actin filament. *Biophys. J.* 75:1886–1894.
25. Borejdo, J., and M. F. Morales. 1977. Fluctuations in tension during contraction of single muscle fibers. *Biophys. J.* 20:315–334.
26. Suzuki, M., H. Fujita, and S. Ishiwata. 2003. Bio-nanomuscle project: contractile properties of single actin filaments in an A-band motility assay system. *In* Molecular and Cellular Aspects of Muscle Contraction. H. Sugi, editor. Kluwer Academic/Plenum Publishers, New York. 103–110.
27. Ishiwata, S., and T. Funatsu. 1985. Does actin bind to the ends of thin filaments in skeletal muscle? *J. Cell Biol.* 100:282–291.
28. Kondo, H., and S. Ishiwata. 1976. Uni-directional growth of F-actin. *J. Biochem. (Tokyo).* 79:159–171.
29. Suzuki, N., H. Miyata, S. Ishiwata, and K. Kinosita, Jr. 1996. Preparation of bead-tailed actin filaments: estimation of the torque produced by the sliding force in an in vitro motility assay. *Biophys. J.* 70:401–408.
30. Kurokawa, H., W. Fujii, K. Ohmi, T. Sakurai, and Y. Nonomura. 1990. Simple and rapid purification of brevin. *Biochem. Biophys. Res. Commun.* 168:451–457.
31. Horiuti, K. 1986. Some properties of the contractile system and sarcoplasmic reticulum of skinned slow fibres from Xenopus muscle. *J. Physiol. (Lond.).* 373:1–23.
32. Nishizaka, T., H. Miyata, H. Yoshikawa, S. Ishiwata, and K. Kinosita, Jr. 1995. Unbinding force of a single motor molecule of muscle measured using optical tweezers. *Nature.* 377:251–254.
33. Funatsu, T., H. Higuchi, and S. Ishiwata. 1990. Elastic filaments in skeletal muscle revealed by selective removal of thin filaments with plasma gelsolin. *J. Cell Biol.* 110:53–62.
34. Funatsu, T., T. Anazawa, and S. Ishiwata. 1994. Structural and functional reconstitution of thin filaments in skeletal muscle. *J. Muscle Res. Cell Motil.* 15:158–171.
35. Fujita, H., K. Yasuda, S. Niitsu, T. Funatsu, and S. Ishiwata. 1996. Structural and functional reconstitution of thin filaments in the contractile apparatus of cardiac muscle. *Biophys. J.* 71:2307–2318.
36. Ishiwata, S. 1981. Melting from both ends of an A-band in a myofibril. Observation with a phase-contrast microscope. *J. Biochem. (Tokyo).* 89:1647–1650.
37. Ishiwata, S., K. Muramatsu, and H. Higuchi. 1985. Disassembly from both ends of thick filaments in rabbit skeletal muscle fibers. An optical diffraction study. *Biophys. J.* 47:257–266.
38. Ishijima, A., H. Kojima, H. Higuchi, Y. Harada, T. Funatsu, and T. Yanagida. 1996. Multiple- and single-molecule analysis of the actomyosin motor by nanometer-piconewton manipulation with a microneedle: unitary steps and forces. *Biophys. J.* 70:383–400.
39. Ishijima, A., T. Doi, K. Sakurada, and T. Yanagida. 1991. Subpiconewton force fluctuations of actomyosin *in vitro*. *Nature.* 352:301–306.
40. Gordon, A. M., A. F. Huxley, and F. J. Julian. 1966. The variation in isometric tension with sarcomere length in vertebrate muscle fibres. *J. Physiol. (Lond.).* 184:170–192.

Journal of Muscle Research and Cell Motility (2005) 26:93–101
DOI 10.1007/s10974-005-0249-2

Auto-oscillations of skinned myocardium correlating with heartbeat

DAISUKE SASAKI[1], HIDEAKI FUJITA[2], NORIO FUKUDA[3], SATOSHI KURIHARA[3] and SHIN'ICHI ISHIWATA[4,5,*]

[1]*Integrative Bioscience and Biomedical Engineering, Graduate School of Science and Engineering, Waseda University, 3-4-1 Okubo, Shinjuku-ku, Tokyo 169-8555, Japan;* [2]*Tohoku University Biomedical Engineering Research Organization, 2-1 Seiryou-machi, Aobaku, Sendai, Miyagi 980-8575, Japan;* [3]*Department of Physiology (II), The Jikei University School of Medicine, 3-25-8 Nishishinbashi, Minato-ku, Tokyo 105-8461, Japan;* [4]*Department of Physics, School of Science and Engineering, Waseda University, 3-4-1 Okubo, Shinjuku-ku, Tokyo 169-8555, Japan;* [5]*Advanced Research Institute for Science and Engineering, Waseda University, 3-4-1 Okubo, Shinjuku-ku, Tokyo 169-8555, Japan*

Received 8 November 2004; accepted in revised form 6 January 2005

Abstract

Skinned myocardium (or myofibrils) exhibits auto-oscillations of sarcomere length and developed force called SPOC (SP*ontaneous* O*scillatory* C*ontraction*) under partial activation conditions. In SPOC, each sarcomere repeats the cycle of slow shortening and rapid lengthening, and the lengthening phase propagates sequentially to the adjacent sarcomeres in waves (SPOC wave). In this study, we analyzed the sarcomeric oscillation in SPOC in skinned myocardium of various animal species (rat, rabbit, dog, pig, and cow) with different heart rates. The period of oscillation, the sarcomere shortening velocity, and the velocity of SPOC wave, strongly correlated with the resting heart rate of the animal species. The shortening velocity in particular was proportional to the resting heart rate. We then examined the motile activity of each cardiac myosin by an *in vitro* motility assay. The sliding velocity of actin filaments, which is an index of the motile activity of myosin, also correlated with the resting heart rate but the relationship was not proportional. As a result, the ratio of sarcomere shortening velocity in SPOC to the sliding velocity of actin filaments was not constant but became higher with a higher heart rate. This suggests that the sarcomere shortening velocity in SPOC is modulated by some additional factors besides the motile activity of myosin, resulting in the proportional relationship between the shortening velocity of the sarcomere and the resting heart rate.

Introduction

In 1978, Fabiato and Fabiato reported that the bundles of cardiac myofibrils developed myofilament-generated tension oscillation during partial Ca^{2+} activation (Fabiato and Fabiato, 1978). About 10 years later, our laboratory found a similar type of oscillation in skeletal myofibrils in the presence of ATP, ADP and Pi, but in the absence of Ca^{2+} (Okamura and Ishiwata, 1988). We named these oscillation phenomena (SP*ontaneous* O*scillatory* C*ontraction* SPOC) and classified them as Ca-SPOC and ADP-SPOC (cf. Ishiwata and Yasuda, 1993). SPOC occurs under steady ionic conditions and is therefore distinct from chemical oscillations where the intracellular $[Ca^{2+}]$ oscillates. Therefore, SPOC can be considered as the third state of muscle, in addition to relaxation and contraction states. Previous studies have demonstrated that in both cases of Ca-SPOC and ADP-SPOC, each sarcomere repeats the cycle of slow shortening and rapid lengthening, composing a sawtooth waveform. The lengthening phase then propagates sequentially to the adjacent sarcomeres in waves (SPOC wave) (Ishiwata *et al.*, 1991; Anazawa *et al.*, 1992; Ishiwata and Yasuda, 1993; Linke *et al.*, 1993; Okamura and Ishiwata, 1988; Yasuda *et al.*, 1996). We constructed a state diagram using skinned bovine myocardium at varying concentrations of MgADP, Pi, and Ca^{2+}, with a fixed concentration of MgATP (Fukuda *et al.*, 1996), and at different pH values (Fukuda and Ishiwata, 1999). It was demonstrated that ADP-SPOC and Ca-SPOC regions were continuously connected and constituted a single SPOC region, which was sandwiched between contraction and relaxation regions. Although the solvent conditions of Ca-SPOC and ADP-SPOC are apparently different, the states of actomyosin cross-bridges in the myofilament lattice must be similar; weak binding cross-bridges (AM·ADP·Pi) and force-generating (strong binding) cross-bridges (AM·ADP) coexist over a certain threshold proportion (Ishiwata and Yasuda, 1993).

We speculate that the auto-oscillatory property of myofibrils may play an important role in myocardial beating in living heart. In this study, we analyzed the

* To whom correspondence should be addressed: Tel./fax: +81 3 5286 3437; E-mail: ishiwata@waseda.jp

sarcomeric oscillations in ADP-SPOC in skinned myocardium of several animal species (rat, rabbit, dog, pig, and cow) with different heart rates. We also examined the motile activity of cardiac myosin using an *in vitro* motility assay, where myosin was prepared from hearts from different animal species. As a result, we clarified the relationship among the properties of sarcomeric oscillations in SPOC, the motile activity of cardiac myosin, and the resting heart rate of each animal species.

Materials and methods

Preparation of skinned myocardium

Glycerinated myocardium from each animal species was prepared as described previously (Fukuda *et al.*, 1996; Fukuda and Ishiwata, 1999). Pig and cow hearts were obtained at a local slaughterhouse. Hearts from other animals (male Wistar rats, male JW rabbits, male beagle dogs) were isolated in our laboratory according to the Guidelines for Care and Use of Laboratory Animals by the School of Science and Engineering of Waseda University. Whole papillary muscles of rat (about 5 mm in length, 1 mm in width) and rabbit (about 8 mm in length, 3 mm in width), and papillary muscle bundles of dog, pig, and cow (20–50 mm in length, 3–5 mm in width) were dissected from the left ventricle. These muscles were stored overnight in a glycerol solution (51% v/v glycerol, 5 mM EGTA, 0.5 mM $NaHCO_3$, 2 mM leupeptin) at 4°C. On the next day, the glycerol solution was exchanged with a fresh glycerol solution once, and the muscles were stored at −20°C. They were used for experiments from 3 days to 5 weeks after dissection. Just before experiments, small muscle strips (about 100 μm in diameter, 1–2 mm in length) were dissected with forceps from these glycerinated muscles. To obtain a satisfactory preparation of small muscle strips, the dissection was carried out in a cooled glycerol solution of below 0°C (Fukuda et al., 1996; Fukuda and Ishiwata, 1999). Special care was taken to dissect the muscle preparation in the direction of the fiber axis and to avoid over-stretching of the preparation during dissection. The preparation was chemically skinned in rigor solution (10 mM MOPS-KOH, 1 mM EGTA, 5 mM $MgCl_2$, 120 mM KCl, pH 7.0) containing 1% v/v TritonX-100 for 20–30 min at 4°C and then washed with relaxing solution (3.8 mM ATP, 10 mM MOPS-KOH, 4 mM EGTA, 3.9 mM $MgCl_2$, 120 mM KCl, pH 7.0).

Analysis of sarcomeric oscillation

Thin (actin) filaments in the skinned myocardial preparation were fluorescently labeled by immersing the preparation in the relaxing solution containing 0.33 μM of Alexa488 phalloidin (Molecular Probes Inc., Eugene, OR) and 1 mM DTT for 2 h at 4°C. The preparation was washed with the relaxing solution, fixed at both ends on a glass bottom dish (code: 3910-035; ASAHI TECHNO GLASS Co., Chiba, Japan) with adhesive tapes and immersed in the relaxing solution. To generate SPOC, the relaxing solution was exchanged for SPOC solution (2.2 mM ATP (2 mM MgATP), 16.4 mM ADP (9.7 mM MgADP), 10 mM MOPS-KOH, 2 mM EGTA, 50 μM AP_5A, 14.2 mM $MgCl_2$ (1.8 mM Mg^{2+}), 10 mM Pi, 41 mM KCl (150 mM ionic strength), pH 7.0) containing 1mM DTT and an oxygen scavenging enzyme system composed of 4.5 mg/ml glucose, 50 units/ml glucose oxidase and 50 units/ml catalase. Confocal fluorescence images of sarcomeric oscillation were obtained with an inverted microscope (IX70; Olympus Co., Tokyo, Japan) equipped with a confocal scanning unit (CSU10; Yokogawa Electric Co., Tokyo, Japan), an Ar laser (GLG3100, 488 nm; Showa Optronics Co., Ltd., Tokyo, Japan), a CCD camera (CCD300-RC; DAGE-MTI Inc., Michigan City, IN), and recorded on videotape.

To check the effect of fluorescence labeling, a control experiment was performed on myocardial preparations that were not labeled with fluorescent phalloidin. The skinned myocardial preparation was fixed on a glass bottom dish (ASAHI TECHNO GLASS Co.) without labeling. Subsequently, it was immersed in the relaxing solution containing fluorescent beads (F-8812, 0.5 μm in diameter; Molecular Probes Inc.) for a few minutes, so that some of the beads were sparsely attached to the surface of the preparation. The solution was then exchanged for the SPOC solution and the movement of the bead along the fiber axis, due to sarcomere length (SL) oscillation, was observed by epi-illumination fluorescence microscopy (IX70; Olympus Co.), and recorded on videotape.

All experiments were carried out at 21–23°C. For image analysis, the video images were analyzed using NIH Image software (NIH, Bethesda, Maryland, USA).

Myosin preparation

Cardiac myosin was prepared from the left ventricle from hearts of different animal species. The fragments of left ventricular muscle were dissected and quickly frozen in liquid nitrogen, immediately after the heart excision. The muscles were preserved at −80°C overnight and used for the myosin preparation the next day. All procedures described below were performed at 4°C. About 3 g of frozen muscle was minced and immersed in 40 ml of Hasselbach–Schneider solution (0.3 M KCl, 0.15 M K_2HPO_4, 0.01 M $Na_4P_2O_7$, 1 mM $MgCl_2$, pH 6.8) (Hasselbach and Schneider, 1951) containing 5 mM DTT and protease inhibitors (0.01 mM leupeptin, 0.2 mM PMSF, 0.01 mM E-64) with gentle stirring for 20 min. The homogenate was centrifuged at 12,000 × *g* for 10 min to remove muscle residue. The supernatant was diluted with 800 ml of water containing 0.1 mM EDTA, 5 mM DTT, and the protease inhibitors, to precipitate myosin. After 2 h, the precipitate was collected by centrifugation at 12,000 × *g* for 10 min, and

carefully dissolved in 10 ml of buffer M (0.6 M KCl, 10 mM imidazole, 10 mM DTT, pH 6.8). The solution was centrifuged at 180,000 × *g* for 2 h to remove actomyosin. The upper half of the supernatant was collected and used for the experiment. Myosin concentration was measured by Bio-Rad Protein Assay using BSA as a standard (Bio-Rad, Hercules, CA). Typically, we obtained 5 ml of 0.6–0.9 mg/ml of myosin from 3 g of muscle. The concentration was adjusted to 0.5 mg/ml by adding buffer M. The myosin was used for the *in vitro* motility assay within the day.

In vitro motility assay

Actin was prepared from rabbit back and leg white muscle as previously described (Kondo and Ishiwata, 1976). Fluorescently labeled filamentous (F–) actin (0.1 mg/ml) was prepared in 6.6 μM Rhodamine phalloidin (Molecular Probes Inc.), 0.1 M KCl, 2 mM $MgCl_2$, 2 mM MOPS-KOH (pH 7.0), and 1.5 mM NaN_3, and stored at 4 °C in the dark until use. Just before the experiment, the F-actin was diluted to 0.25 μg/ml with buffer A (25 mM KCl, 25 mM imidazole, 4 mM $MgCl_2$, 1 mM EGTA, 10 mM DTT, pH 7.4). A flow cell with a volume of 20 μl was made from two coverslips (24 × 60 mm, 18 × 18 mm; MATSUNAMI GLASS IND., Ltd., Osaka, Japan) and double-sided tape. The glass surface of the flow cell was coated with casein by infusing 20 μl of the buffer M containing 1 mg/ml casein (Casein being preferable to BSA or nitrocellulose in these conditions). After 1 min, 20 μl of buffer M containing 0.5 mg/ml myosin was infused while the solution in the flow cell was absorbed with filter paper on the other side. Adsorption of myosin to the casein-coated glass surface was allowed for 1 min. Unbound myosin was washed out by perfusing 60 μl of buffer A. Next, 20 μl of the buffer A containing 0.25 μg/ml of Rhodamine phalloidin-labeled F-actin was infused. After 2 min, 60 μl of assay buffer (2 mM ATP and the oxygen scavenging enzyme system in buffer A) was perfused and the flow cell was sealed with nail polish. The flow cell was placed on an inverted microscope (IX70; Olympus Co.) equipped with an image intensifier (VS4-1845; Video Scope International, Ltd., Dulles, VA) and a SIT camera (C2400; Hamamatsu Photonics K. K., Shizuoka, Japan). The movement of actin filaments was observed by epi-illumination fluorescence microscopy and recorded on videotape. The experiment was carried out at 21–23°C. For image analysis, the video images were analyzed with NIH Image.

Results

Overall appearance of SPOC

The confocal fluorescence microscopy of SPOC showed that the muscle striation oscillated along the fiber axis due to the repetitive shortening and lengthening of each sarcomere. The shortening phase was longer than the lengthening phase. One striking feature of SPOC was that the lengthening phase was propagated to adjacent sarcomeres like a wave (SPOC wave; movies are available at http://www.phys.waseda.ac.jp/bio/movies.html). The SPOC wave spread through dozens of successive sarcomeres, and then disappeared by a collision with another wave or at an intercalated disc. Sometimes, the SPOC wave appeared to propagate through the intercalated disc. The bundle of laterally connected myofibrils oscillated almost in phase. These properties of SPOC were common to all animal species examined, and were consistent with previous observations on Ca-SPOCs of cardiac myofibril (Fabiato and Fabiato, 1978; Linke *et al.*, 1993) and ADP-SPOCs of skeletal myofibrils (Okamura and Ishiwata, 1988; Ishiwata *et al.*, 1991; Anazawa *et al.*, 1992; Ishiwata and Yasuda, 1993; Yasuda *et al.*, 1996).

Waveform of SL oscillation

Figure 1A shows the confocal fluorescence image of rat skinned myocardium in ADP-SPOC condition, in which actin filaments were labeled with Alexa488 phalloidin. Figure 1B shows the profile of vertically integrated fluorescence intensity of the region delineated by a rectangle in Figure 1A, which was smoothed by a moving average method. The center of the fluorescent I-Z-I brush, indicated by an arrow, represents the position of the Z-line. To determine the position of the Z-line, several points around the peak of the profile were fitted to a quadratic curve by a least squares method. The peak position of the fitted curve was calculated and the position of the Z-line was determined with high accuracy. Figure 1C shows the time course of the successive positions of the Z-lines numbered 1–10 as represented in Figure 1A. Each Z-line oscillated along the myofibril axis due to the SL oscillation. Figure 1D shows the time course of changes in the total lengths of three consecutive sarcomeres. The oscillatory waveform consisted of a slow shortening phase and a rapid lengthening phase that together formed a sawtooth waveform. The sequential displacements of the waveforms along the horizontal axis in the order of red, blue, and green indicated that the SPOC wave propagated in the direction from No. 1 toward No. 10. Figure 1E shows the SL oscillation of each sarcomere. The slope of the long dashed arrows indicates that the lengthening phase of one sarcomere was propagated to the next one at a constant velocity.

Relationship between SPOC and heartbeat

Figure 2 shows a typical oscillatory waveform of the total length of three consecutive sarcomeres in the myocardium of each animal species analyzed by the same method as in Figure 1D. It is apparent that the faster the heart rate of the animal species, the shorter the period of SPOC. On the other hand, the amplitude

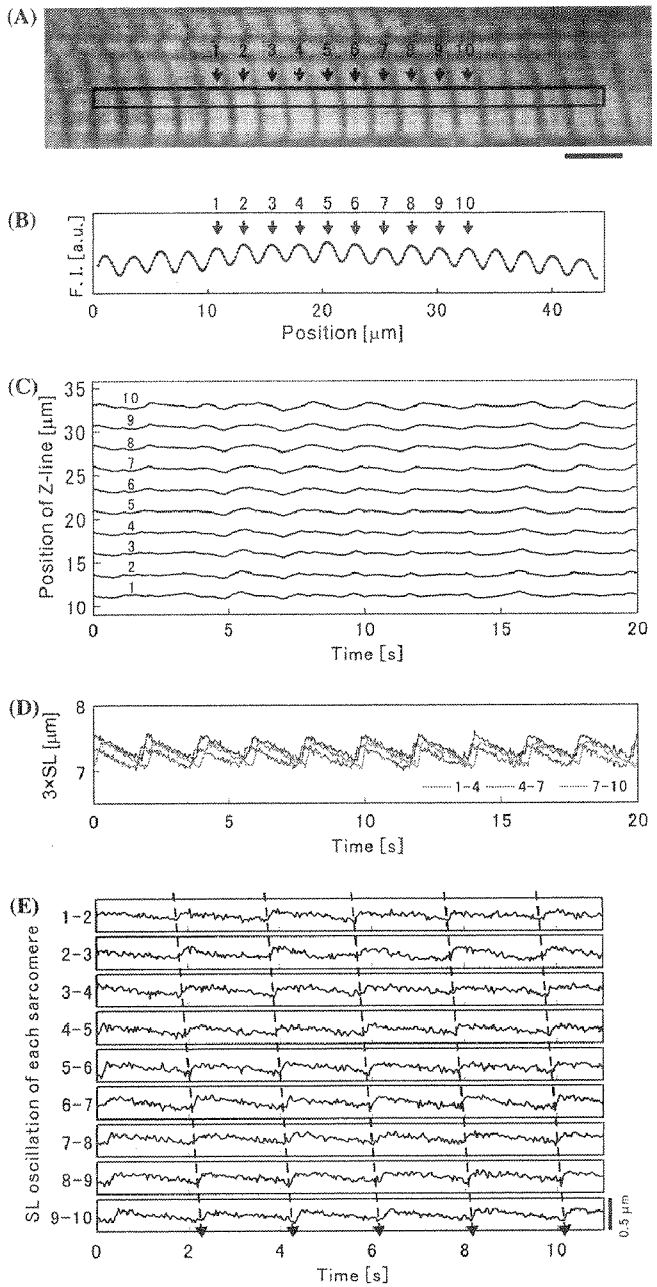

Fig. 1. Analysis of SPOC by confocal fluorescence microscopy. (A) Confocal fluorescence image of a rat myocardial preparation (movies are available at http://www.phys.waseda.ac.jp/bio/movies.html). Arrows indicate the positions of the Z-lines numbered 1–10. Scale bar, 5 μm. (B) Vertically integrated fluorescence intensity from the rectangular region in A, which was smoothed along the abscissa by the moving average method. The center of the fluorescence peaks numbered 1–10 corresponds to the positions of the Z-lines in A. (C) Time course of the position of the Z-line analyzed at the video rate of 30 frames/s. The numbers 1–10 correspond to those in A and B. The ordinate corresponds to the abscissa of B. (D) Time course of the total length of three consecutive sarcomeres, which is the distance between the Z-lines 1–4 (red), 4–7 (blue) and 7–10 (green), obtained from the data of C. (E) Time course of the length of nine successive sarcomeres, which is the distance between the adjacent Z-lines numbered 1–10, obtained from part of the data of C. Long dashed arrows represent the propagation of the lengthening phase (SPOC wave) in the direction from 1 to 10 of the Z-line.

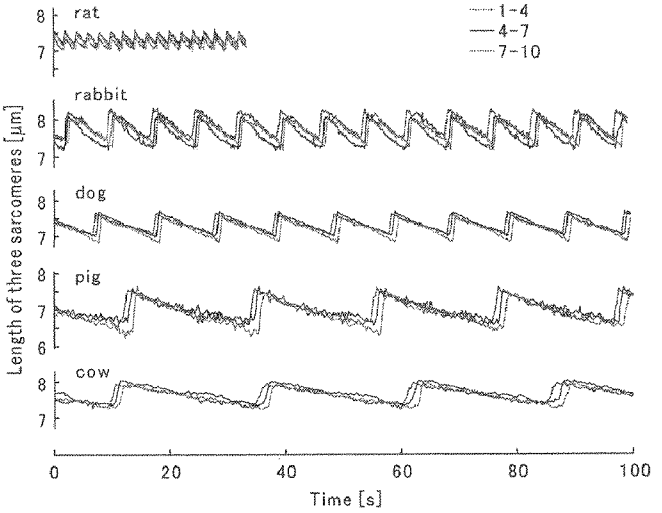

Fig. 2. Time course of the total length of three consecutive sarcomeres, obtained from skinned myocardium of each animal species in the SPOC state. The method of analysis is the same as in Figure 1D. The number at the upper right corner indicates the position of the Z-line as in Figure 1D.

of the SL oscillation is not so different across the animal species except for rat myocardium. We analyzed the period of SL oscillation, the amplitude of SL oscillation, the shortening velocity of the sarcomere in the shortening phase of SL oscillation, and the propagation velocity of SPOC wave for the myocardium of each animal species. Subsequently, we clarified the relationship between these parameters and the resting heart rate or the period of resting heartbeat of each animal species. The resting heart rate was quoted from *Biology Data Book* (Altman and Dittmer, 1974) in beats/min (bpm) unit; 355 for rat, 256 for rabbit, 107 for dog, 68 for pig, and 51 for cow. The period of resting heartbeat was derived from the resting heart rate, respectively; 0.17 s for rat, 0.23 s for rabbit, 0.56 s for dog, 0.88 s for pig, and 1.18 s for cow.

Figure 3A shows the relationship between the period of SPOC and the period of resting heartbeat. Values are represented as average ± SD. The period of SPOC was 2.4 ± 0.3 s ($n = 7$) in rat, 7.8 ± 1.3 s ($n = 10$) in rabbit, 10.3 ± 0.4 s ($n = 6$) in dog, 20.9 ± 2.8 s ($n = 5$) in pig, and 32.5 ± 5.5 s ($n = 6$) in cow. There was a good correlation between the two parameters with a correlation coefficient of 0.976. The solid line in the figure represents the regression line, while the dashed line represents the regression line crossing the origin. The close overlapping of these lines indicated that the relationship was almost proportional. Figure 3B shows the relationship between the peak-to-peak amplitude of SL oscillation and the resting heart rate. Values are represented as average ± SD. The peak-to-peak amplitude of SL oscillation was 0.15 ± 0.01 μm ($n = 7$) in rat, 0.29 ± 0.04 μm ($n = 10$) in rabbit, 0.21 ± 0.04 μm ($n = 6$) in dog, 0.27 ± 0.06 μm ($n = 5$) in pig, and 0.23 ± 0.03 μm ($n = 6$) in cow. They were similar, except for the rat myocardium, and an apparent correlative relationship was not found between the two parameters, although a weak-modest correlation existed (correlation coefficient, −0.406). Figure 3C shows the relationship between the shortening velocity of the

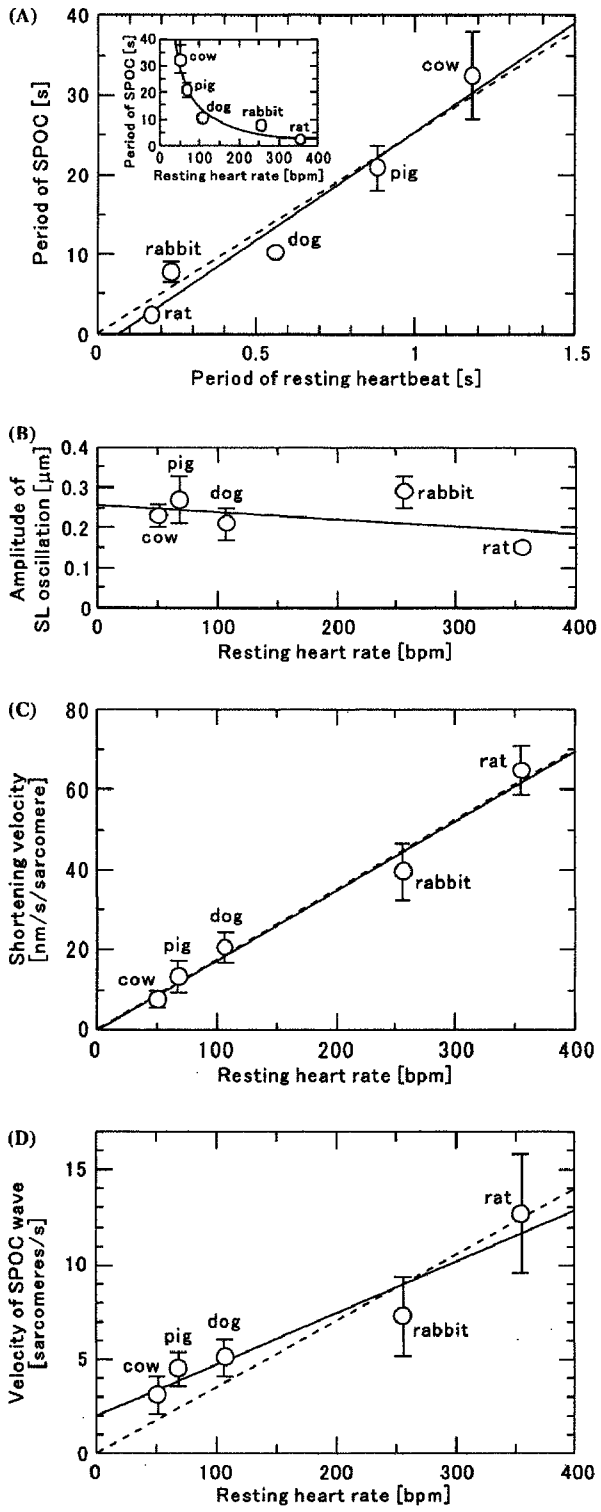

Fig. 3. Relationship between the properties of SPOC and the resting heart rate (or the period of resting heartbeat) of each animal species. The resting heart rate is quoted from *Biology Data Book* (Altman and Dittmer, 1974). (A) Relationship between the period of SPOC and the period of resting heartbeat. Inset shows the relationship between the period of SPOC and the resting heart rate. (B) Relationship between the peak-to-peak amplitude of SL oscillation and the resting heart rate. (C) Relationship between the shortening velocity of sarcomere in the shortening phase of SL oscillation and the resting heart rate. (D) Relationship between the propagation velocity of SPOC wave and the resting heart rate. The unit of the propagation velocity is represented by the number of propagated sarcomeres per second (sarcomeres/s). The solid line is the regression line. The dashed line is the regression line that crosses the origin, showing a proportional relationship. Vertical bars, SD of 5–10 data.

sarcomere in the shortening phase of SL oscillation and the resting heart rate. Values are represented as average ± SD. The shortening velocity of the sarcomere was 64.9 ± 6.0 nm/s ($n = 7$) in rat, 39.6 ± 7.0 nm/s ($n = 10$) in rabbit, 20.7 ± 3.8 nm/s ($n = 6$) in dog, 13.4 ± 4.0 nm/s ($n = 5$) in pig, and 7.7 ± 2.1 nm/s ($n = 6$) in cow. There was a good correlation (almost a proportional relationship) between the two parameters, with a correlation coefficient of 0.990. Figure 3D shows the relationship between the velocity of SPOC wave and the resting heart rate. Values are represented as average ± SD. The velocity (number of sarcomeres/s) was 12.7 ± 3.1 ($n = 7$) in rat, 7.3 ± 2.1 ($n = 10$) in rabbit, 5.1 ± 1.0 ($n = 6$) in dog, 4.5 ± 0.9 ($n = 5$) in pig, and 3.1 ± 1.0 ($n = 6$) in cow. There was a correlative relationship between the two parameters with a correlation coefficient of 0.960, although it deviated from a proportional relationship that is represented by a dashed line in Figure 3D. The faster the heart rate of the animal species, the faster the velocity of SPOC wave, as was the case with the period and shortening velocity of SL oscillation.

We also analyzed the period of SPOC using skinned myocardial preparations that were not labeled with fluorescent phalloidin (Figure 4A; a movie is available at http://www.phys.waseda.ac.jp/bio/movies.html). The period of SPOC was determined by FFT analysis of the oscillatory movement of the bead (Figure 4B) attached to the surface of the myocardium. The results were consistent with those obtained from fluorescently labeled skinned myocardium as shown in Figure 4C. Values are represented as average ± SD. The period was 3.0 ± 0.3 s ($n = 8$) in rat, 8.5 ± 1.7 s ($n = 24$) in rabbit, 11.1 ± 1.0 s ($n = 7$) in dog, 20.5 ± 4.9 s ($n = 16$) in pig, and 27.9 ± 8.3 s ($n = 13$) in cow (correlation coefficient, 0.982). After comparing Figure 3A and Figure 4C, we concluded that labeling of myocardial preparations with fluorescent phalloidin in this study had little effect on the oscillatory properties of SPOC.

Motile activity of cardiac myosin

We examined the motile activity of purified cardiac myosin by an *in vitro* motility assay. Myosin was prepared from the left ventricle of each animal's heart. SDS-PAGE patterns of purified cardiac myosin (Figure 5) showed that each myosin preparation was mainly composed of a heavy chain (MHC) and two light chains (LC1 & 2) with different molecular weights in the different animal species. Figure 6 shows the relationship between the sliding velocity of actin filaments and the resting heart rate of each animal species. Values are represented as average ± SD. The sliding velocity of actin filaments was 2.83 ± 0.48 μm/s ($n = 20$) in rat, 1.73 ± 0.22 μm/s ($n = 20$) in rabbit, 1.44 ± 0.14 μm/s ($n = 20$) in dog, 1.08 ± 0.15 μm/s ($n = 20$) in pig, and 0.93 ± 0.15 μm/s ($n = 20$) in cow. Some of these values were smaller than those previously reported (Sata *et al.*,

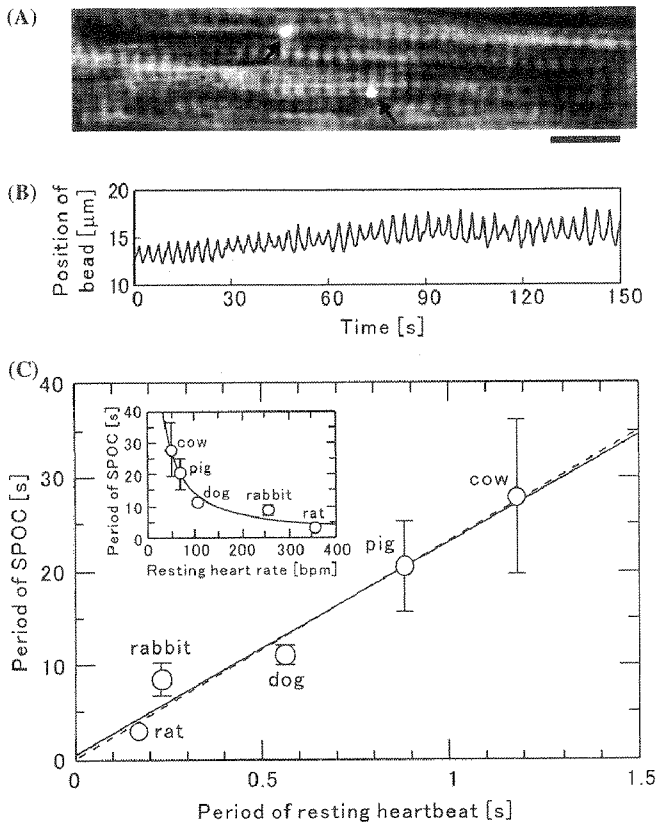

Fig. 4. (A) Superimposed image of a rat myocardial preparation by phase contrast and fluorescence microscopy (a movie is available at http://www.phys.waseda.ac.jp/bio/movies.html). The arrows indicate fluorescent beads attached to the surface of the preparation. Scale bar, 10 μm. (B) Time course of the translational movement of an attached bead in SPOC. (C) Relationship between the period of SPOC and the period of resting heartbeat. Inset shows the relationship between the period of SPOC and the resting heart rate. The solid line is the regression line. The dashed line is the regression line that crosses the origin, showing a proportional relationship. Vertical bars, SD of 7–24 data.

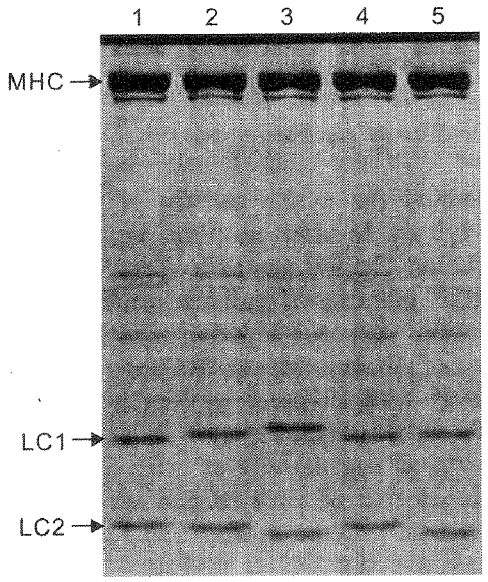

Fig. 5. SDS-PAGE pattern of cardiac myosin prepared from the left ventricle of each animal's heart. Lane 1, rat; lane 2, rabbit; lane 3, dog; lane 4, pig; lane 5, cow. MHC, myosin heavy chain; LC1 and LC2, myosin light chain 1 and 2, respectively.

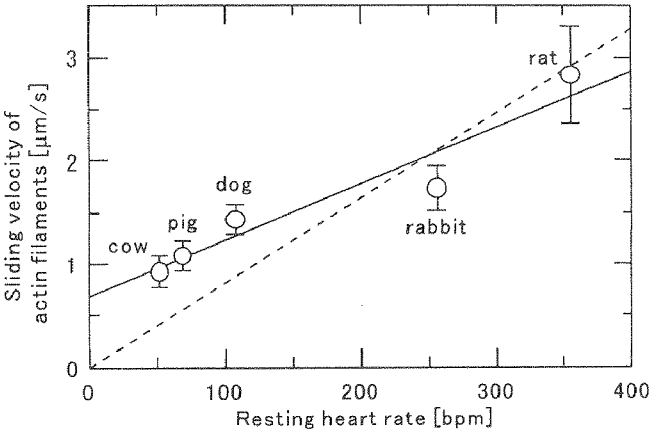

Fig. 6. Relationship between the sliding velocity of actin filaments and the resting heart rate. The solid line is the regression line. The dashed line is the regression line that crosses the origin, showing a proportional relationship. Vertical bars, SD of 20 data.

1993; VanBuren *et al.*, 1995; Svensson *et al.*, 1997), which may be attributable to the difference in the temperature at which the experiments were conducted. Although a good correlation existed between the sliding velocity of actin filaments and resting heart rate (correlation coefficient, 0.956), the relationship deviated from a proportional relationship shown by a dashed line (see Discussion).

Relationship between SPOC and motile activity of cardiac myosin

Figure 7A shows the relationship between the sliding velocity of actin filaments and the shortening velocity of the sarcomere in the shortening phase of SPOC. Although a good correlation existed between the two parameters (correlation coefficient, 0.987), the relationship deviated from a proportional relationship shown by a dashed line (see Discussion). Figure 7B shows the ratio of the shortening velocity of the sarcomere to the sliding velocity of actin filaments in each animal species. The ratio was higher in the animal species with higher resting heart rate on the whole. Figure 7C shows the relationship between the sliding velocity of actin filaments and the propagation velocity of SPOC wave. There was a good correlation between the two parameters (correlation coefficient, 0.993), and moreover, the relationship was nearly proportional.

Discussion

The sawtooth waveform of SL oscillation (Figures 1D, E and 2) implies that the period of SPOC is mainly determined by the shortening phase of the SL oscillation. Because the amplitude of SL oscillation is nearly constant, irrespective of animal species (Figure 3B), the proportional relationship between the period of SPOC and that of resting heartbeat (Figure 3A) corresponds to the proportional relationship between the shortening

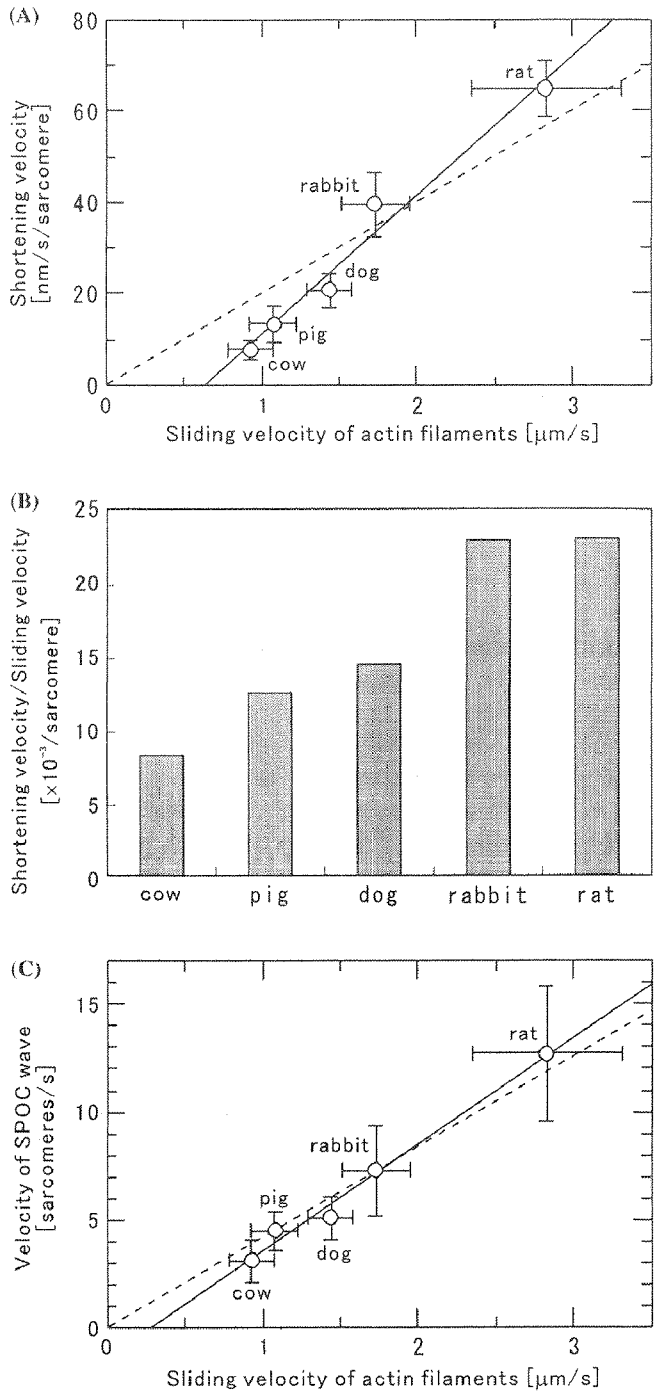

Fig. 7. (A) Relationship between the shortening velocity of the sarcomere in SPOC and the sliding velocity of actin filaments. (B) Ratio of the shortening velocity of the sarcomere to the sliding velocity of actin filaments in each animal species. (C) Relationship between the propagation velocity of SPOC wave and the sliding velocity of actin filaments. The solid line is the regression line. The dashed line is the regression line that crosses the origin, showing a proportional relationship. Vertical bars, SD of 5–10 data. Horizontal bars, SD of 20 data.

velocity of the sarcomere in the shortening phase and the resting heart rate of animal species (Figure 3C). Because it is well known that the shortening velocity of muscle under an activating condition correlates well with the actomyosin ATPase activity (Barany, 1967), we examined the motile activity of cardiac myosin by an *in vitro* motility assay, with myosin prepared from heart of different animal species. As shown in Figure 6, there was a correlative relationship between the sliding velocity of actin filaments and the resting heart rate, but it deviated from a proportional relationship. The difference in the sliding velocity in rabbit, dog, pig, and cow was moderate for the difference in the resting heart rate, while only the difference between rat and the others was relatively large. This does not correspond with the proportional relationship between the shortening velocity of the sarcomere in SPOC and the resting heart rate (Figure 3C). For example, the sliding velocity of actin filaments in rabbit was only 1.9 times higher than that of cow, whereas both the shortening velocity of sarcomere and the resting heart rate of rabbit were more than five times faster than those of cow.

The difference in the sliding velocity of actin filaments among the animal species can be partly explained by the difference in myosin isoforms in the ventricular muscles of these animal species. Mammalian heart expresses two isoforms of MHC, α-MHC and β-MHC, resulting in three different myosin isoforms, V1 (αα), V2 (αβ) and V3 (ββ). The actomyosin ATPase rate is fastest with V1 and slowest with V3 (Dillmann, 1984), and the sliding velocity of actin filaments in an *in vitro* motility assay is 2-3 times higher in V1 than that in V3 in rat (Sugiura *et al.*, 1996) and rabbit (VanBuren *et al.*, 1995). A previous study showed that V1 is predominant in the ventricles of animals with heart rates above 300 bpm (mouse and rat), whereas V3 is predominant in those with heart rates below 300 bpm (guinea pig, rabbit, dog, sheep, pig, and cow) (Hamilton and Ianuzzo, 1991). Therefore, the moderate differences in the sliding velocity of actin filaments among rabbit, dog, pig, and cow in our data (Figure 6) could be attributed to the species differences in V3 myosins. On the other hand, relatively large differences in the sliding velocity between rat and the other animal species could be attributed to the difference between V1 and V3 myosin in addition to the species difference. Moreover, the different LC 1 and 2 in animal species (Figure 5) may also contribute to the difference in the sliding velocity of actin filaments.

The shortening velocity of sarcomeres in SPOC well correlated with the sliding velocity of actin filaments as shown in Figure 7A. However, the relationship deviated from a proportional relationship which was shown by a dashed line in Figure 7A. To clarify this relationship in more detail, we obtained the ratio of the shortening velocity of the sarcomere to the sliding velocity of actin filaments in each animal species as shown in Figure 7B. The ratios in rat and rabbit were almost identical, indicating the proportional relationship between the shortening velocity of the sarcomere and the sliding velocity of actin filaments. This suggests that the difference in the shortening velocity between rat and rabbit is most likely due to the difference in the motile activity of myosin. However, there is an overall tendency for the ratio to be higher in the animal species with higher resting heart rate (Figure 7B). This suggests that the shortening velocity of the sarcomere is modulated by

additional factors besides the motile activity of myosin, resulting in higher shortening velocity in animal species with higher resting heart rate and/or lower shortening velocity in animal species with lower resting heart rate. Consequently, the proportional relationship between the shortening velocity of the sarcomere in the SPOC and the resting heart rate is achieved in all animal species examined (Figure 3C).

There are several proteins that modulate the sliding velocity of actin filaments or the shortening velocity of myofibrils, such as troponin (Tn), tropomyosin (Tm), and connectin/titin. It is known that the sliding velocity of actin filaments is enhanced by the reconstitution of Tn and Tm in an *in vitro* motility assay (cf. Homsher *et al.*, 2003). It is possible that Tn and Tm may differently affect the sliding velocity, depending on the animal species. Connectin/titin is a giant elastic protein connecting the end of the thick filament and the Z-line in a sarcomere (Wang, 1996; Maruyama, 1997). Connectin/titin-based passive tension in myocardium may accelerate the shortening velocity of the sarcomere in the early phase of contraction (Opitz *et al.*, 2003). It is possible that the contribution of connectin/titin to the shortening velocity may also depend on the species difference, because connectin/titin-based passive tension may be greater in the ventricle of animal species with a higher heart rate (Cazorla *et al.*, 2000). These possibilities remain to be examined in future study.

With respect to the propagation velocity of SPOC waves, there was also a correlation with the resting heart rate as shown in Figure 3D. Furthermore, the propagation velocity of SPOC wave was nearly proportional to the sliding velocity of actin filaments (Figure 7C). This result suggests that the kinetic properties of myosin may be relevant to the propagation velocity of the SPOC wave. Recently, a propagation phenomenon similar to the SPOC wave was reported in cardiac myofibrils (Stehle *et al.*, 2002). Because the propagation of the rapid lengthening phase of sarcomeres transiently occurred along a myofibril upon relaxation, the authors argued that this phenomenon may play a role in accelerating the relaxation of the myocardium. If both the propagation phenomenon and the SPOC wave are based on a common mechanism, the correlation between the propagation velocity of the SPOC wave and heart rate may be physiologically significant.

It should be noted here that there is a possibility that some of the properties discussed above may be attributed to the difference in the solvent conditions for SPOC and the *in vitro* motility assay. Because the SPOC solution was unsuitable for the *in vitro* motility assay due to its high ionic strength, we conducted the motility assay under standard assay conditions. In future studies it would be important to examine the effects of ADP and Pi on the sliding velocity of actin filaments on the different animal's cardiac myosin.

From a physiological viewpoint, the ionic condition of ADP-SPOC examined in this study is far from the physiological conditions of living cardiomyocyte, because there was a high concentration of ADP in the SPOC solution. However, SPOC does not necessarily require the high concentration of ADP, but requires the coexistence of weak binding cross-bridges (AM·ADP·Pi) and force generating cross-bridges (AM·ADP) over a certain threshold proportion (Ishiwata and Yasuda, 1993), which can also be achieved by partial Ca^{2+} activation (Ca-SPOC) under physiological ionic conditions (Fabiato and Fabiato, 1978; Linke *et al.*, 1993; Fukuda *et al.*, 1996; Fukuda and Ishiwata, 1999). For cardiac myofibrils, SPOC is an intrinsic oscillatory property, while the repeated contraction during the heartbeat is the forced oscillation that is externally compelled by electrical impulses from a sinoatrial node. Although further studies are required to clarify the physiological relevance of SPOC, our finding that the properties of SPOC correlate with the heartbeat suggests that the auto-oscillatory properties of cardiac myofibrils may play a part in the molecular mechanisms of myocardial beating.

Acknowledgements

We thank Dr. H. L. Granzier of Washington State University, Dr. R. Stehle of Universität zu Köln and Dr. M. Kawai of University of Iowa for their valuable discussions. This work was supported partly by Grants-in-Aid for Specially Promoted Research and for the Bio-venture Project, and by the 21st Century COE Program and "Establishment of Consolidated Research Institute for Advanced Science and Medical Care" from the Ministry of Education, Sports, Culture, Science and Technology of Japan to S. I. and by The Uehara Memorial Foundation to N.F and to S.K.

References

1. Altman PL and Dittmer DS (eds) (1974) Biology Data Book, 2nd edn. (vol. 3, pp. 1686–1693) Federation of American Societies for Experiental Biology, Bethesda, MD.
2. Anazawa T, Yasuda K and Ishiwata S (1992) Spontaneous oscillation of tension and sarcomere length in skeletal myofibrils. Microscopic measurement and analysis. *Biophys J* **61:** 1099–1108.
3. Barany M (1967) ATPase Activity of Myosin Correlated with Speed of Muscle Shortening. *J Gen Physiol* **50:** 197–218.
4. Cazorla O, Freiburg A, Helmes M, Centner T, McNabb M, Wu Y, Trombitas K, Labeit S and Granzier H (2000) Differential expression of cardiac titin isoforms and modulation of cellular stiffness. *Circ Res* **86:** 59–67.
5. Dillmann WH (1984) Hormonal influences on cardiac myosin ATPase activity and myosin isoenzyme distribution. *Mol Cell Endocrinol* **34:** 169–181.
6. Fabiato A and Fabiato F (1978) Myofilament-generated tension oscillations during partial calcium activation and activation dependence of the sarcomere length-tension relation of skinned cardiac cells. *J Gen Physiol* **72:** 667–699.
7. Fukuda N, Fujita H, Fujita T and Ishiwata S (1996) Spontaneous tension oscillation in skinned bovine cardiac muscle. *Pflügers Arch* **433:** 1–8.
8. Fukuda N and Ishiwata S (1999) Effects of pH on spontaneous tension oscillation in skinned bovine cardiac muscle. *Pflügers Arch* **438:** 125–132.

9. Hamilton N and Ianuzzo CD (1991) Contractile and calcium regulating capacities of myocardia of different sized mammals scale with resting heart rate. *Mol Cell Biochem* **106:** 133–141.
10. Hasselbach W and Schneider G (1951) L-Myosin and actin content of guinea-pig muscle. *Biochem Z* **321:** 462–475.
11. Homsher E, Nili M, Chen IY and Tobacman LS (2003) Regulatory proteins alter nucleotide binding to acto-myosin of sliding filaments in motility assays. *Biophys J* **85:** 1046–1052.
12. Ishiwata S, Okamura N, Shimizu H, Anazawa T and Yasuda K (1991) Spontaneous oscillatory contraction (SPOC) of sarcomeres in skeletal muscle. *Adv Biophys* **27:** 227–235.
13. Ishiwata S and Yasuda K (1993) Mechano-chemical coupling in spontaneous oscillatory contraction of muscle. *Phase Transitions* **45:** 105–136.
14. Kondo H and Ishiwata S (1976) Uni-directional growth of F-actin. *J Biochem (Tokyo)* **79:** 159–171.
15. Linke WA, Bartoo ML and Pollack GH (1993) Spontaneous sarcomeric oscillations at intermediate activation levels in single isolated cardiac myofibrils. *Circ Res* **73:** 724–734.
16. Maruyama K (1997) Connectin/titin, giant elastic protein of muscle. *FASEB J* **11:** 341–345.
17. Okamura N and Ishiwata S (1988) Spontaneous oscillatory contraction of sarcomeres in skeletal myofibrils. *J Muscle Res Cell Motil* **9:** 111–119.
18. Opitz CA, Kulke M, Leake MC, Neagoe C, Hinssen H, Hajjar RJ and Linke WA (2003) Damped elastic recoil of the titin spring in myofibrils of human myocardium. *Proc Natl Acad Sci U S A* **100:** 12688–12693.
19. Sata M, Sugiura S, Yamashita H, Momomura S and Serizawa T (1993) Dynamic interaction between cardiac myosin isoforms modifies velocity of actomyosin sliding *in vitro*. *Circ Res* **73:** 696–704.
20. Stehle R, Krüger M and Pfitzer G (2002) Force kinetics and individual sarcomere dynamics in cardiac myofibrils after rapid Ca^{2+} changes. *Biophys J* **83:** 2152–2161.
21. Sugiura S, Kobayakawa N, Momomura S, Chaen S, Omata M and Sugi H (1996) Different cardiac myosin isoforms exhibit equal force-generating ability in vitro. *Biochim Biophys Acta* **1273:** 73–76.
22. Svensson C, Morano I and Arner A (1997) In vitro motility assay of atrial and ventricular myosin from pig. *J Cell Biochem* **67:** 241–247.
23. VanBuren P, Harris DE, Alpert NR and Warshaw DM (1995) Cardiac V1 and V3 myosins differ in their hydrolytic and mechanical activities in vitro. *Circ Res* **77:** 439–444.
24. Wang K (1996) Titin/connectin and nebulin: giant protein rulers of muscle structure and function. *Adv Biophys* **33:** 123–134.
25. Yasuda K, Shindo Y and Ishiwata S (1996) Synchronous behavior of spontaneous oscillations of sarcomeres in skeletal myofibrils under isotonic conditions. *Biophys J* **70:** 1823–1829.

http://www.jstage.jst.go.jp/browse/biophysics

BIOPHYSICS

Vol. 2, pp. 13–21 (2006)
doi: 10.2142/biophysics.2.13

Processivity of kinesin motility is enhanced on increasing temperature

Ikuko Nara[1] and Shin'ichi Ishiwata[1,2]

[1]*Department of Physics, School of Science and Engineering, Waseda University, 3-4-1 Okubo, Shinjuku-ku, Tokyo169-8555, Japan*
[2]*Advanced Research Institute for Science and Engineering, Waseda University, 3-4-1 Okubo, Shinjuku-ku, Tokyo169-8555, Japan*

Received 12 November, 2005; Accepted 11 January, 2006

Kinesin is a motor protein that processively moves step by step along a microtubule. To investigate the effects of temperature on run length, i.e., processivity of kinesin motility, we performed a single-molecular bead assay at temperature range of 20–40°C. An increase in the walking velocity of kinesin corresponded to the Arrhenius activation enthalpy of 48 kJ/mol, being consistent with the previous reports. Here, we found that the run length increased, that is, the kinesin processivity enhanced with increasing temperature. Then, we estimated the probability of detachment of kinesin from a microtubule per one 8-nm stepping event, and found that it diminishes from 0.014 to 0.006/step with increasing temperature from 20 to 40°C. And we noticed that prolonged incubation at 30, 35 and 40°C significantly slowed down the walking velocity, but further increased the run length and duration. Those results are interpreted according to the effect of temperature on the rate constants of some key kinetic steps in the ATPase cycle.

Key words: TIRF, molecular motors, microtubule, hand-over-hand mechanism, run length

Conventional kinesin is a microtubule-based motor protein that transports vesicles and organelles within nerve cells. An important property of kinesin is processivity, that is, individual motor molecules can move continuously along a microtubule with hundreds of 8-nm steps[1,2] for about 1 μm without dissociating[3–5]. Processivity is attributable to the synchronization of attachment to and detachment from a microtubule of two heads of kinesin coupled with ATPase cycle[6]. Recent studies have focused on examining the coupling between each step of movement and the ATPase cycle[6–11]. Despite motility has been extensively studied from various aspects by single-molecule methods[11–13], the molecular mechanism of processivity has not yet been fully explored, although a consensus on the hand-over-hand model has been reached[2].

The interaction between kinesin and microtubule is regulated not only by the nucleotide state of kinesin, but also by solvent conditions and environment. For example, an increase in salt concentration (ionic strength) lowers the processivity[14,15]. An increase in temperature increases the walking velocity[16,18], although the maximum tension (stall force) is independent of temperature[16]. Here, to investigate the effect of temperature on the processivity, we performed a single-molecular bead assay at temperature range of 20–40°C. In the previous report[16], we briefly described qualitative results obtained at 15–35°C showing the enhancement of processivity at higher temperature.

Here, a single native kinesin molecule purified from bovine brain was attached to a polystyrene bead, and the bead movement on microtubules was examined with total internal reflection fluorescence microscope. We measured the distance over which kinesin molecules continue to move along a microtubule without detachment (*run length*), the period of time for each run (*duration*) and the average velocity obtained from the slope of the time course of bead displacement (*walking velocity*). The quantitative analysis of the results showed that the probability of detachment of kinesin from a microtubule decreases, implying the en-

Corresponding author: Shin'ichi Ishiwata, Department of Physics, School of Science and Engineering, Waseda University, 3-4-1 Okubo, Shinjuku-ku, Tokyo 169-8555, Japan. e-mail: ishiwata@waseda.jp

hancement of processivity, with increasing temperature. We also noticed that the processivity of kinesin is enhanced as the incubation time becomes longer, especially at higher temperatures.

Materials and methods

Proteins

Conventional kinesin was prepared from bovine brain according to the method of Kojima et al[19]. Tubulin was purified from porcine brain and labeled with tetramethylrhodamine succinimidyl ester (C-1171, Molecular Probes, USA) according to Hyman[20]. Fresh bovine and porcine brains were purchased from a local slaughterhouse. Microtubules were stabilized with 20 μM taxol.

Preparation of kinesin-bound beads

Kinesin-bound beads were prepared according to Kojima et al.[19] with slight modifications. We used fluorescent polystyrene beads (0.2 μm in diameter, carboxylate-modified, orange, F-8809; Molecular Probes). For the preparation of kinesin-bound beads, kinesin was mixed with beads at a 1 : 1 molar ratio, assuming the molecular weight of kinesin is 380 kDa. By using optical tweezers, we confirmed that even when mixed at a 1 : 5 (beads:kinesin) ratio, more than 90% of the beads that interact with a microtubule have single kinesin molecules bound[7,8,21-23].

Flow cell for beads assay

The fluorescent microtubules were introduced into a flow cell and incubated for 2 min to allow binding of the microtubule to glass surface. The cell was washed with a solution containing 0.8 mM $MgCl_2$, 64 mM PIPES (piperazine-1,4-bis(2-ethanesulfonic acid), pH 6.8), 0.8 mM EGTA, 1 mg/ml filtered casein and 20 μM taxol to remove unattached microtubules and left for 2 min to coat the glass surface with casein. The cell was then filled with an assay solution containing the kinesin-bound beads and an oxygen scavenging enzyme system [approximately 0.1 nM kinesin-bound beads, 1.4 mM $MgCl_2$, 56 mM PIPES (pH 6.8), 0.7 mM EGTA, 1.0 mg/ml filtered casein, 1 mM ATP, 40 μM taxol, 10 mM dithiothreitol (DTT), 4.5 mg/ml glucose, 50 units/ml glucose oxidase, 50 units/ml catalase] and sealed with enamel. The above procedure was performed at room temperature regardless of the temperature examined. All the chemicals were of reagent grade.

Microscope

Tetramethylrhodamine-labeled microtubules and kinesin-bound fluorescent beads were visualized by total internal reflection fluorescence microscopy (IX70, Olympus, Japan) with a green laser (μGreen #4301-050, Uniphase, USA), which illuminates only ~150 nm in depth above the coverslip[24]. Fluorescence images were collected using an SIT camera (C2400, Hamamatsu Photonics, Japan) equipped with an image intensifier (VS4-1815, Video Scope, USA) and recorded on a Digital Videocassette Recorder (DSR-20, Sony, Japan).

Temperature control

For experiments at 20 and 25°C, the room temperature was adjusted by an air conditioner. For experiments at 30, 35, and 40°C, the stage of the inverted microscope with a flow cell mounted on it was covered by a thermal insulation chamber (Olympus), and the temperature inside it was adjusted. The temperature was measured by a thermometer mounted on the microscope stage near the flow cell and kept within ±1°C of the required temperature.

Analysis of the processive movement of a kinesin-bound bead

The method of movement analysis employed in this article was different from the previous one[16], where a kinesin-bound bead had been manipulated and placed in contact with a microtubule by optical tweezers, which allowed to determining exactly the share of beads with bound kinesin molecules. Here we examined the kinesin-bound beads that spontaneously attached to and moved along a microtubule and then dissociated after a while (Supplementary Movies). As evident from the movies, the proportion of beads that interacted with a microtubule was small. It is still possible the beads with several kinesin molecules bound might have been included in our analysis. However, considering the bead-kinesin geometry, the probability of multiple kinesin molecules simultaneously interacting with a microtubule is sufficiently low under our experimental conditions.

Fluorescence images of moving beads were digitally recorded at a video rate (30 frames/s), and the center of the fluorescence intensity distribution of the bead image was determined using a custom-written software program supplied with the Halcon image processor (MVTec Software GmbH, Germany). From the analysis of a bead movement along a microtubule we obtained the three parameters characterizing kinesin motility at each temperature: the run length (distance travelled by a bead after attaching to and before detaching from a microtubule; in μm), the duration (time interval of the continuous movement of the bead along a microtubule; in seconds), and the velocity (the average slope of the time course of bead movement, which was determined by the least squares method; in μm/s). The recording of video started after incubating the flow cell at each temperature for 1 min, and continued for 10 min. Note that the flow cell was prepared at room temperature just before each experiment.

Results and Discussion

Effect of temperature on the time course of movement of a kinesin-bound bead along a microtubule

Figure 1 shows typical traces of movement of a kinesin-

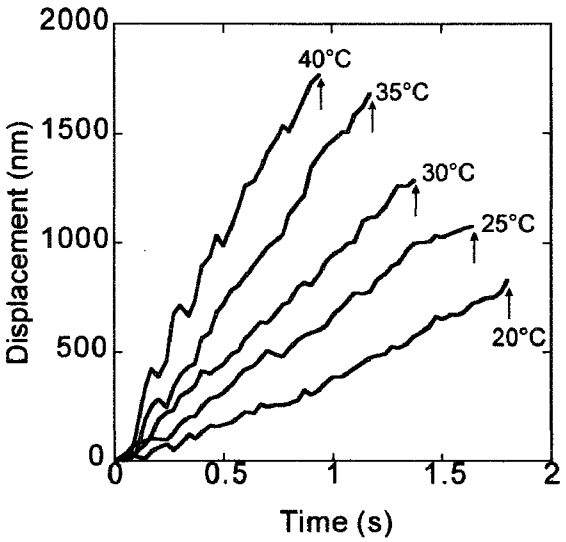

Figure 1 Typical traces showing the time course of bead movement along a microtubule at various temperatures (Supplementary Movies 1–5. Note that those movies do not necessarily correspond to the data shown here). These traces were taken between 1 and 6 min of the incubation at each temperature. Attachment of the bead to a microtubule occurred at the zero point. Arrows indicate the time at which the kinesin-bound bead detached from the microtubule, detected by the disappearance of the fluorescent image of the bead. Run length was defined as the ordinate of the detachment point. Duration is the period of time between attachment and detachment of the bead. Walking velocity was estimated from the average slope of the time course of the bead movement obtained by the least squares method.

bound bead at various temperatures we examined, i.e., 20, 25, 30, 35 and 40°C. We collected the data between 1 and 11 min after the beginning of incubation at each temperature. From these data, we obtained the values of run length, duration and velocity (parameters characterizing the processivity of molecular motors) of single kinesin molecules moving along a microtubule. Here, the run length is defined as the distance, which a bead travelled continuously before detachment. The duration is the period of time during which the bead continuously moved (the abscissa of the final position of raw data as shown in Fig. 1). The velocity was obtained from the average slope of the time course of bead displacement. As these data show, with increasing temperature both run length and velocity increased, whereas duration decreased. Note that only two parameters of these three are theoretically independent : the value of one parameter can be calculated from the others according to the relationship (run length) = (velocity) × (duration). However, this relationship is not exactly kept in practice, because the velocity is obtained as the average slope of the time course of bead movement, whereas both run length and duration are determined from the coordinates of the end point of the time course of the bead movement (see Fig. 1). In spite of the difference between the values obtained theoretically and experimentally, all the experimental data exhibit good agreement with the above relationship throughout the analysis. These results show therefore that the temperature dependence of the run length is weaker than that of the velocity, because the temperature dependence of duration is opposite.

Effect of temperature on run length

Figure 2 shows the distribution of run length at each temperature, which could be fitted by a single-exponential function, being consistent with the previous results[15,25]. As the temperature increased, the average run length became longer, and eventually increased more than twice from 0.6 μm to 1.3 μm with increasing temperature from 20 to 40°C. The results are summarized in Fig. 2F (points connected by a solid line). The fact that the run length increases at higher temperature was briefly mentioned in our previous paper[16]. Similar results were also reported for ncd and Eg5 molecular motors[4].

As we reported previously[8,16], the activity of kinesin motility appeared to change on lengthening the incubation time at higher temperatures. To quantitatively examine this for the data obtained at 30, 35 and 40°C, the data were divided into two groups, corresponding to the two periods, i.e., the one between 1 and 6 min and the other between 6 and 11 min after the beginning of incubation, because the two sets of data significantly differed at these temperatures; the average run length increased on lengthening the incubation time, although the shape of distribution remained the same. The results are shown by gray bars in Figs. 2C–E and right-half filled circles in Fig. 2F (points connected by a dashed line). For the data obtained at 20 and 25°C, the data is presented for both groups combined, because no difference was observed between them. This result suggests that the alteration of the motility of kinesin occurs during long incubation at the elevated temperature. We will discuss it in more detail below.

Effect of temperature on duration

The distribution of duration at each temperature was also fitted by a single exponential function (Fig. 3), implying that both the run length and duration vary stochastically, and the detachment of kinesin from a microtubule occurs at one kinetic step. As the temperature increased, the average value of duration decreased, by about a half, from 1.5 s at 20°C to 0.7 s at 40°C. Thus, the temperature dependence of duration is opposite to that of the run length.

Similarly, we analyzed the data for two different incubation periods. The results are summarized in Fig. 3F, showing that the elongation of the incubation time at higher temperatures prolonged the average duration. This tendency was similar to that of the run length. But note that with lengthening the incubation time, the temperature dependence of duration became weaker (Fig. 3), whereas it became stronger in case of the run length (Fig. 2F).

Effect of temperature on walking velocity

Next, we examined the effect of temperature on the

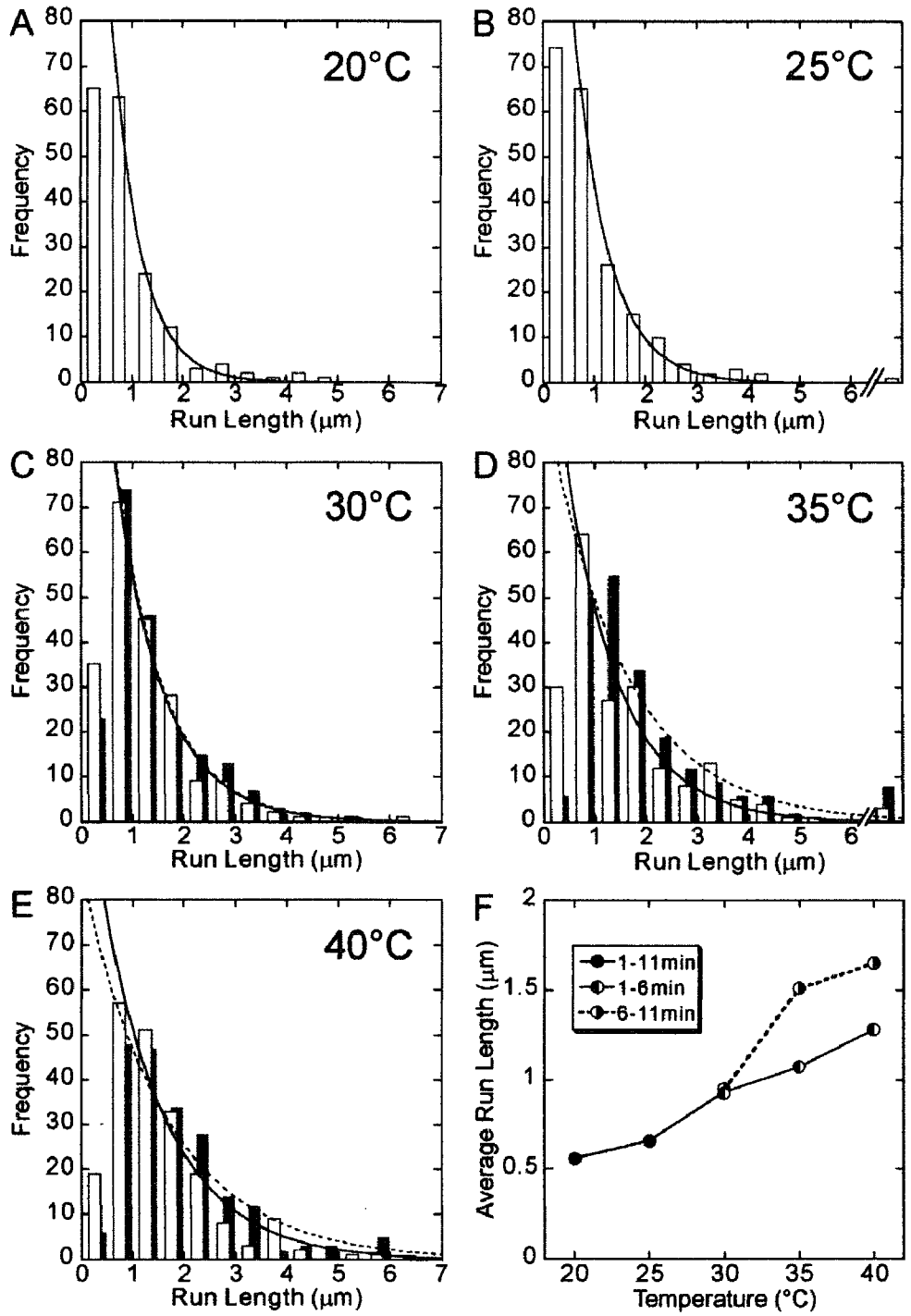

Figure 2 Temperature dependence of run length. The data at 20°C (A) and 25°C (B) were obtained between 1 and 11 min after the incubation at each temperature. On the other hand, for 30°C (C), 35°C (D) and 40°C (E), the data obtained between 1 and 6 min of incubation are shown by open bars, whereas those obtained between 6 and 11 min of incubation are shown by gray bars, because they showed a different set of values although the shape of the distribution was the same, i.e., approximated by a single exponential. Distribution of run lengths was fitted by an exponential function (a solid or a dashed curve). Here, the run lengths shorter than 0.5 μm were excluded from the analysis. The average run length, which was defined as the characteristic run length of the exponential function, obtained from each distribution shown here, was 0.56, 0.66, 0.93 (0.94), 1.07 (1.51) and 1.28 (1.65) μm at 20, 25, 30, 35 and 40°C, respectively (the values in the parentheses, the data for 6–11 min). In Fig. 2F, these values are shown by closed circles for 20 and 25°C and left-half filled circles for 30, 35 and 40°C connected by a solid line. Right-half filled circles (connected by a dashed line) show the average run length obtained from the data taken between 6 and 11 min of incubation at 30, 35 and 40°C.

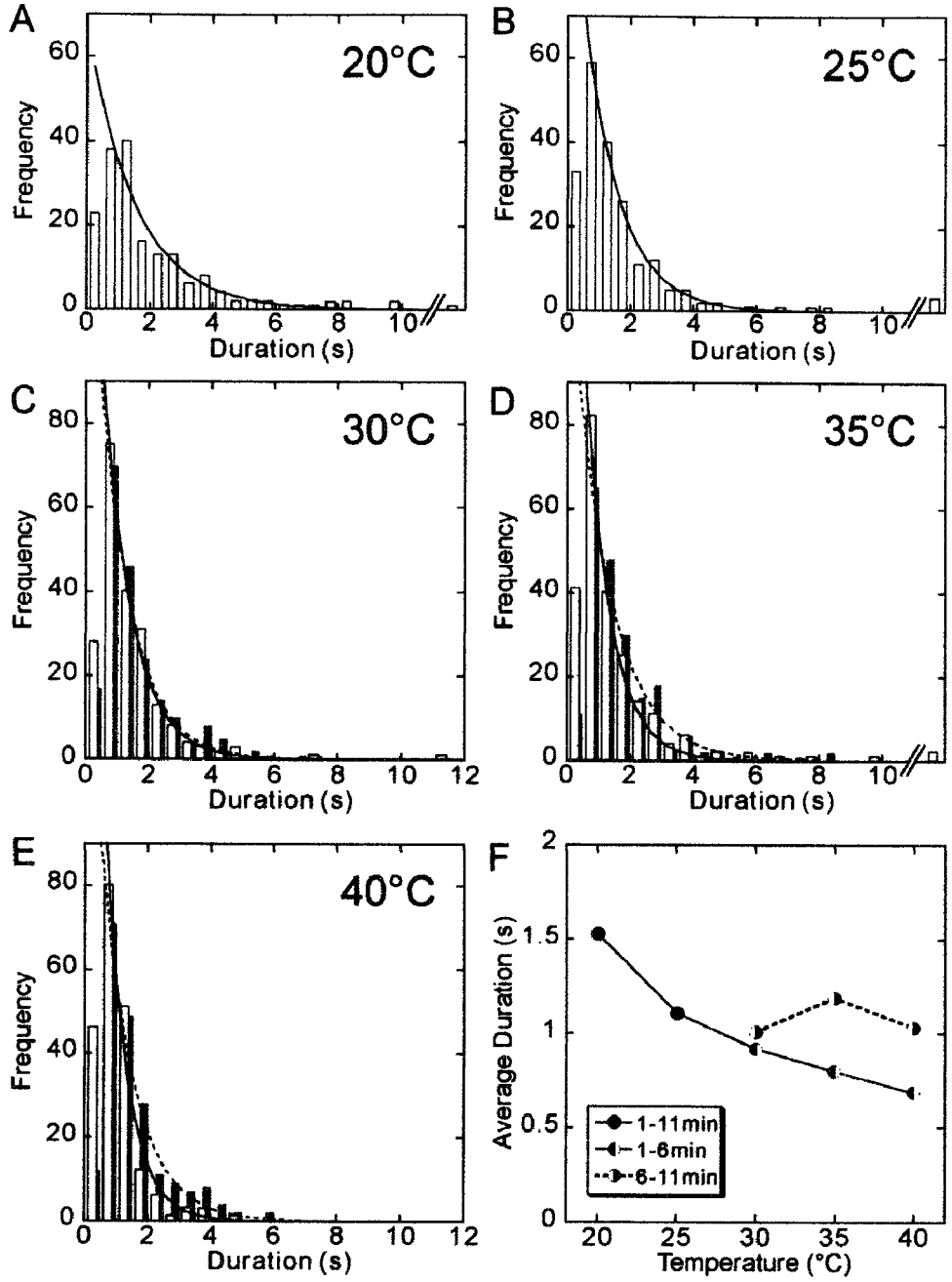

Figure 3 Temperature dependence of duration. The data at 20°C (A) and 25°C (B) were obtained between 1 and 11 min of incubation at each temperature. On the other hand, for 30°C (C), 35°C (D) and 40°C (E), the data obtained between 1 and 6 min of incubation are shown by open bars, whereas the data obtained between 6 and 11 min of incubation are shown by gray bars, because they showed a different set of values, although the shape of the distribution was the same, i.e., approximated by a single exponential. Every distribution of duration was fitted by an exponential function (a solid or a dashed curve). Only runs longer than 0.5 s were included in the analysis. The average duration, which was defined as the characteristic time of the exponential function, was 1.53, 1.11, 0.92 (1.01), 0.80 (1.19) and 0.69 (1.03) s, at 20, 25, 30, 35 and 40°C, respectively (the values in the parentheses, the data for 6–11 min). In Fig. 3F, these values are shown by closed circles for 20 and 25°C and left-half filled circles for 30, 35 and 40°C connected by a solid line. Right-half filled circles (connected by a dashed line) show the average duration obtained from the data taken between 6 and 11 min of incubation at 30, 35 and 40°C.

velocity of a kinesin molecule moving along a microtubule. As Fig. 4 shows, the distribution of velocity exhibited a sharp peak and could be simulated by a Gaussian because there is a positive correlation between the run length and duration. The average value of velocity, i.e., the peak value of the Gaussian distribution, increased with increasing temperature as previously reported[16,18].

The Arrhenius plot of the velocity obtained between 1 and 6 min of incubation was linear within the temperature range we examined (Fig. 5). The activation enthalpy was estimated to be 48 kJ/mol from the slope of the Arrhenius plot, being consistent with the previous data[16,17]. Here we

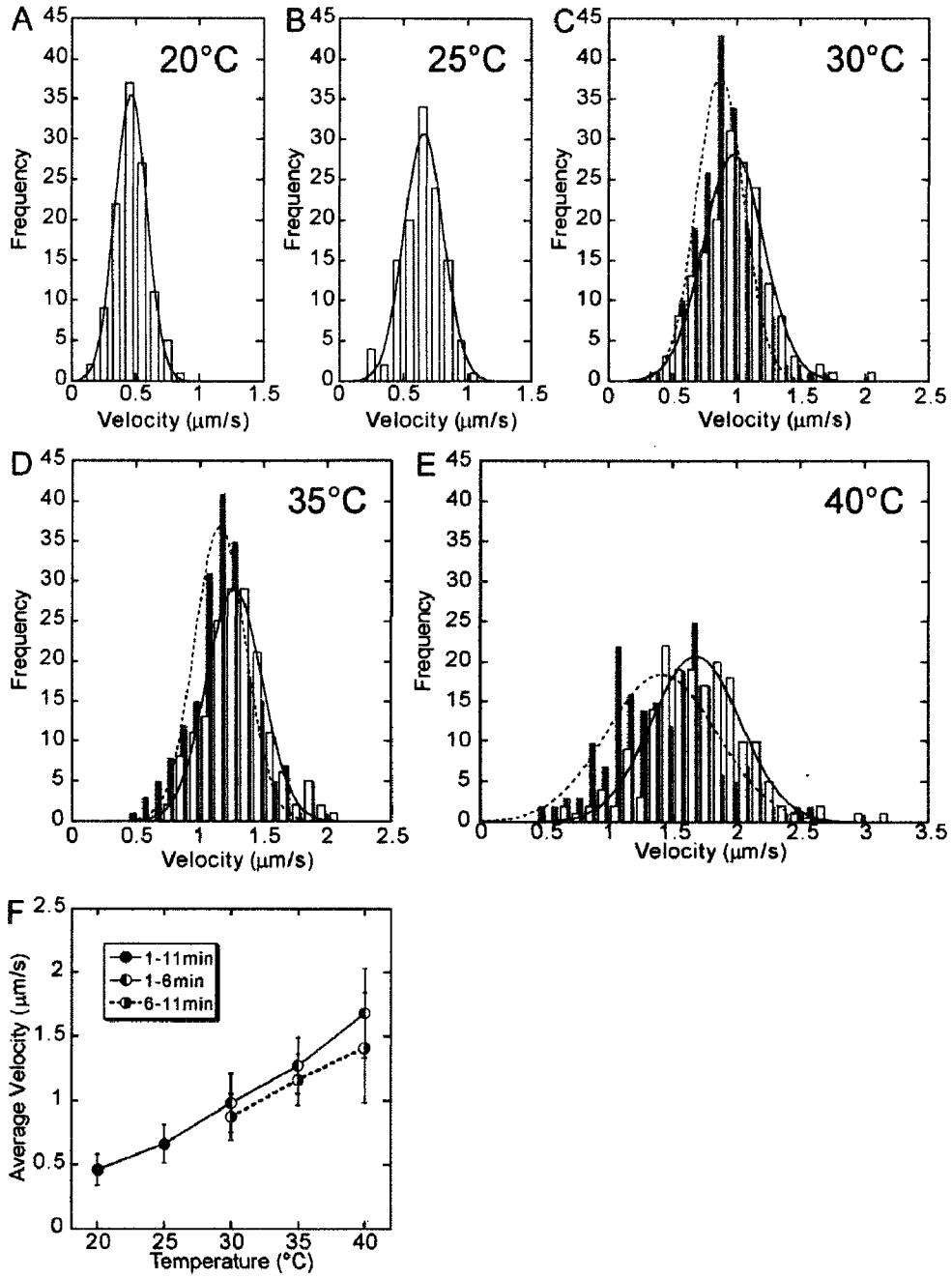

Figure 4 Temperature dependence of walking velocity. The data at 20°C (A) and 25°C (B) were obtained between 1 and 11 min of incubation at each temperature. On the other hand, for 30°C (C), 35°C (D) and 40°C (E), the data obtained between 1 and 6 min of incubation are shown by open bars, whereas the data obtained between 6 and 11 min after the incubation are shown by gray bars, because they showed a different set of values although the shape of the distribution was the same, i.e., approximated by a single Gaussian. The average walking velocity, which was defined as a peak of the Gaussian distribution, was 0.46, 0.66, 0.98 (0.87), 1.27 (1.16) and 1.68 (1.41) μm/s at 20, 25, 30, 35 and 40°C, respectively (the values in the parentheses, the data for 6–11 min). In Fig. 4F, these values are shown by closed circles for 20 and 25°C and left-half filled circles for 30, 35 and 40°C connected by a solid line. Right-half filled circles (connected by a dashed line) show the average velocity obtained from the data taken between 6 and 11 min of incubation at 30, 35 and 40°C.

found that, for the data obtained between 6 and 11 min of incubation, the linear relationship deviated from the straight line above around 30°C. These results imply that the protein functions are generally deteriorated by incubation at the elevated temperatures. The thermally deteriorated kinesin molecules may exhibit a slower rate of ATPase hydrolysis, and the walking velocity is therefore decreased. However, the detachment rate decreases to a larger extent, so that not only the duration but the run length as well is prolonged.

Effect of temperature on the probability of detachment during one cycle of stepping

Based on the above data, we estimated the probability, p, of detachment of kinesin from a microtubule during one

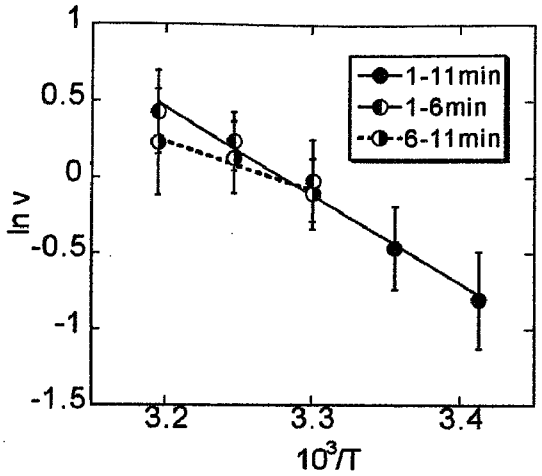

Figure 5 Arrhenius plot of walking velocity (v) vs. absolute temperature (*T*). The activation enthalpy was estimated as 48 kJ/mol and 27 kJ/mol from the slope of the solid line and the dashed lines, respectively. Symbols are the same as in Figs. 2–4.

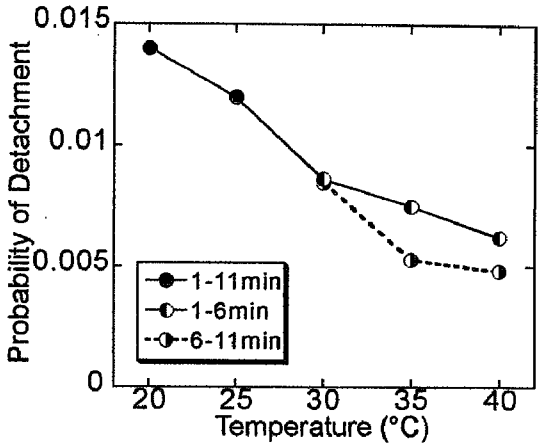

Figure 6 Temperature dependence of the probability of detachment per each 8 nm step. The probability of detachment was determined to be 0.0143, 0.0121, 0.0086 (0.0085), 0.0075 (0.0053) and 0.0062 (0.0048) at 20, 25, 30, 35 and 40°C, respectively (the values in the parentheses, the data for 6–11 min). Symbols are the same as in Figs. 2–5. For more details, see the text.

cycle of stepping. Now, we assume that the number of cycles (steps) in each processive movement, n, is determined by n = (run length)/(step size). Because the probability that a kinesin molecule detaches after the n-th step is equal to $(1-p)^{n-1}p$, the average number of steps, $\langle n \rangle$, is expressed as $\langle n \rangle = \Sigma_{n=1}^{\infty} n(1-p)^{n-1}p = 1/p$. Thus, the value of p can be determined from the inverse of $\langle n \rangle$, that is, the value of p is proportional to the inverse of the average run length. The results of this analysis show that the probability of detachment during one stepping cycle is around 0.01 and decreases with an increase in temperature, meaning that the processivity is enhanced at elevated temperatures (Fig. 6).

What is the cause for the larger processivity at higher temperature? If the two heads work independently from each other, a plausible cause would be that the duty ratio increases as temperature increases. Here, the duty ratio is defined as the share of strongly bound states during each cycle of stepping. Note that the strong binding occurs in the nucleotide-free and AMPPNP (an ATP analogue)-bound states, as demonstrated by a large unbinding force as compared to a small unbinding force in the ADP-bound state[7,17,22]. The duty ratio is expected to increase if the proportion of the lifetime of such strongly bound states during one ATPase cycle increases. If the hydrophobic interaction is involved in the strong binding, it is understandable that the duty ratio increases with increasing temperature. In practice, such endothermic properties of protein-protein interaction have been observed for the strong binding (a rigor bond) formed between actin and myosin II in the absence of ATP[26,27]. Whether the hydrophobic interaction is involved in the strongly bound state of the kinesin-microtubule complex should be examined in future.

The detachment of kinesin from a microtubule will probably occur when both heads are in a weakly bound (ADP-bound) state. So, if the duty ratio increases, the probability that both heads are in a weakly bound state decreases. This simple interpretation would be reasonable if the two heads of kinesin would have worked independently. However, this is not the case because, in practice, the two heads of kinesin must work cooperatively to ensure highly-efficient processive movement.

Thus, another possible and more plausible reason for the higher processivity at the elevated temperatures will be as follows. Let us consider the kinetic scheme of kinesin motility based on a simple hand-over-hand model as schematically shown in Fig. 7[8,11,23,25,28]. During processive run of 8 nm steps, kinesin successively adopts a single-headed strongly bound <O, D> state (A in Fig. 7), the <T, D> state at which the trailing head is strongly bound and the leading head is weakly bound or detached (B in Fig. 7), double-headed strongly bound <T, O> and <D·Pi, O> states (C and D in Fig. 7, respectively) and the <D, O> state at which the leading head is strongly bound and the trailing head is weakly bound (E in Fig. 7). In this scheme, the spontaneous detachment of kinesin is assumed to occur in the <D, D> state (D′ in Fig. 7), which is occasionally formed after passing through the <D·Pi, D> state (C′ in Fig. 7). It is to be noted that the D·Pi state may be a weakly bound state as well[11,25,29,30]. Because every step occurs stochastically, the detachment of kinesin is plausible even if the rate constants of the B→C and C′→D steps are much higher than those of the B→C′ and C′→D′ steps, respectively.

Now, based on this scheme, the interpretation of an increase in the processivity with increasing temperature is as follows. First, a kinetic constant at every kinetic step (especially, a rate-limiting step) becomes larger with increasing temperature, which results in an increase of the walking velocity (ATPase activity). However, the temperature dependence of the kinetic constants will be different for every step. Therefore, the most plausible interpretation is that the

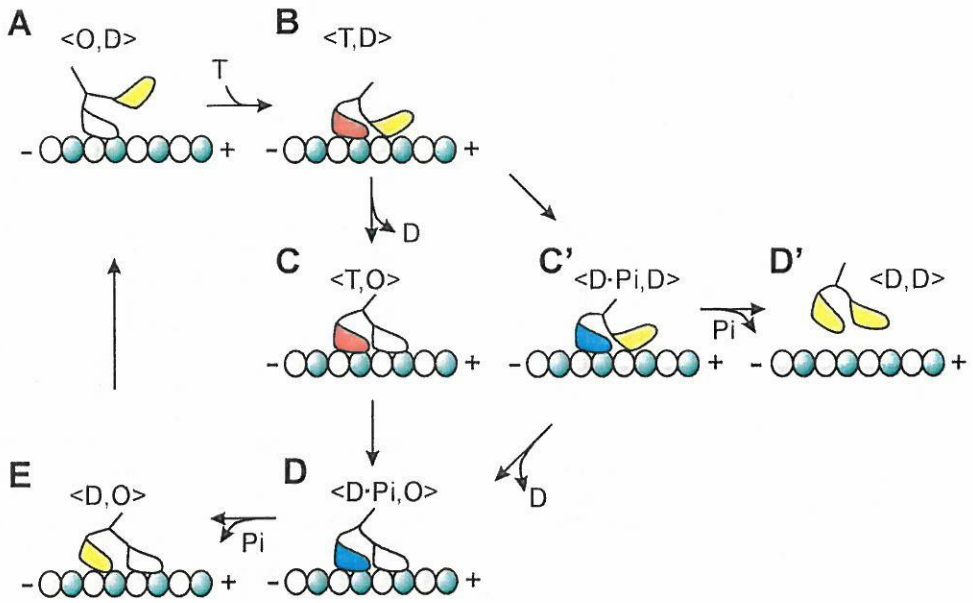

Figure 7 Simple kinetic pathway of the processive movement of kinesin. Each 8 nm step occurs stochastically and one ATP is hydrolysed in one cycle. T, D, Pi and O represent ATP, ADP, inorganic phosphate and nucleotide-free state, respectively. Here, we assume that there is a turning point, the <T, D> state (B), in which the pathway diverges; that is, one pathway proceeds to the next stepping event (from C to D, E, A and B), whereas the other proceeds to the state of detachment of kinesin from a microtubule (from C′ to D′). Dark- and light-green circles represent β- and α-subunits of tubulin, respectively. The plus and the minus ends of microtubule are represented by + and −, respectively. Manner of binding of each kinesin's head with α- and β-subunits of tubulin is not realistic and is only schematically drawn in all nucleotide states.

degree of an increase of the kinetic constant at the B→C step is higher than that of the B→C′ step. Besides, this may also be the case for the temperature dependence of the kinetic constants for the C′→D and C′→D′ transitions. From this consideration, it is interesting to infer that the rate of detachment of ADP from the bound leading head is accelerated much higher than the other transitions with increasing temperature (both B→C and C′→D steps).

Deterioration of motility at elevated temperatures

It has been reported that the melting transition of a part of the α-helix in the stalk region of kinesin occurs in a stepwise fashion at 25–30°C and 45–50°C[31]. Thus, there is a possibility that the deterioration observed here after 6–11 min incubation at 30–40°C may be attributable to a partial melting of the α-helix observed at 25–30°C. The denaturation of kinesin that forces a detachment from a microtubule may occur due to the melting transition of the α-helix at 45–50°C.

The interpretation of the effect of thermal deterioration, i.e., a decrease in the walking velocity and an increase in the processivity with longer incubation at elevated temperatures up to 40°C, based on the scheme shown in Fig. 7, is as follows. Due to the thermal deterioration, the kinetic constants decrease, resulting in a decrease in the walking velocity (ATPase activity). However, the rate of ADP release from the leading head (the B→C and C′→D steps) decreases to a smaller degree compared to the rates of the competing events in the trailing head (i.e., the B→C′ and C′→D′ transitions, respectively). Thus, all effects of temperature on the processivity and the walking velocity of kinesin observed in the present study are attributable explicitly to the temperature dependence of the kinetic constants, especially the rate of ADP release from the leading head in the hand-over-hand model shown in Fig. 7.

We previously reported that much longer incubation (20–30 min) at higher temperature (50°C) denatured kinesin that tends to detach from a microtubule in the presence of ATP[16]. This may be attributable to the melting of the α-helix observed at 45–50°C[31]. The partly deteriorated kinesin molecules obtained by incubation for 6–11 min at 30–40°C may be an intermediate between the native and the denatured ones. One possible intermediate state may be that either one of two heads of kinesin is thermally deteriorated. If it is the case, it would be interesting to examine how this thermally half-deteriorated kinesin walks along a microtubule as compared to the alternate stepwise motion of kinesin with heads genetically engineered[12,13].

We should mention here the possibility that our measurements may have been effected to some extent by the contribution of beads to which more than one kinesin molecules are bound and are able to interact with a microtubule at the same time (see Materials and Methods). Therefore, the enhancement of the processivity in the partially deteriorated state may be the property of a heterogeneous ensemble of more than one kinesin molecules (rather than the heterogeneity of the two heads of the same molecule as discussed above). This situation may be similar to that in the gliding

assay in which multiple kinesin molecules interact with a sliding microtubule.

Acknowledgements

We thank Drs. S. Uemura and I. Fujiwara of Waseda University for their technical assistance at the early stage of this research. We also thank Dr. S. V. Mikhailenko for his critical reading of the manuscript. This research was partly supported by Grants-in-Aid for Specially Promoted Research and for The 21st Century COE Program (Physics of Self-Organization Systems) at Waseda University from the Ministry of Education, Sports, Culture, Science and Technology of Japan (S. I.).

References

1. Svoboda, K., Schmidt, C. F., Schnapp, B. J. & Block, S. M. Direct observation of kinesin stepping by optical trapping interferometry. *Nature* **365**, 721–727 (1993).
2. Yildiz, A., Tomishige, M., Vale, R. D. & Selvin, P. R. Kinesin walks hand-over-hand. *Science* **303**, 676–678 (2004).
3. Block, S. M., Goldstein, L. S. & Schnapp, B. J. Bead movement by single kinesin molecules studied with optical tweezers. *Nature* **348**, 348–352 (1990).
4. Crevel, I. M., Lockhart, A. & Cross, R. A. Kinetic evidence for low chemical processivity in ncd and Eg5. *J. Mol. Biol.* **273**, 160–170 (1997).
5. Hancock, W. O. & Howard, J. Kinesin's processivity results from mechanical and chemical coordination between the ATP hydrolysis cycles of the two motor domains. *Proc. Natl. Acad. Sci. USA* **96**, 13147–13152 (1999).
6. Hackney, D. D. Evidence for alternating head catalysis by kinesin during microtubule-stimulated ATP hydrolysis. *Proc. Natl. Acad. Sci. USA* **91**, 6865–6869 (1994).
7. Kawaguchi, K., Uemura, S. & Ishiwata, S. Equilibrium and transition between single- and double-headed binding of kinesin as revealed by single-molecule mechanics. *Biophys. J.* **84**, 1103–1113 (2003).
8. Kawaguchi, K. & Ishiwata, S. Nucleotide-dependent single- to double-headed binding of kinesin. *Science* **291**, 667–669 (2001).
9. Rice, S., Lin, A. W., Safer, D., Hart, C. L., Naber, N., Carragher, B. O., Cain, S. M., Pechatnikova, E., Wilson-Kubalek, E. M., Whittaker, M., Pate, E., Cooke, R., Taylor, E. W., Milligan, R. A. & Vale, R. D. A structural change in the kinesin motor protein that drives motility. *Nature* **402**, 778–784 (1999).
10. Nishiyama, M., Higuchi, H. & Yanagida, T. Chemomechanical coupling of the forward and backward steps of single kinesin molecules. *Nat. Cell Biol.* **4**, 790–797 (2002).
11. Cross, R. A. The kinetic mechanism of kinesin. *Trends Biochem. Sci.* **29**, 301–309 (2004).
12. Kaseda, K., Higuchi, H. & Hirose, K. Alternate fast and slow stepping of a heterodimeric kinesin molecule. *Nat. Cell Biol.* **5**, 1079–1082 (2003).
13. Higuchi, H., Bronner, C. E., Park, H. W. & Endow, S. A. Rapid double 8-nm steps by a kinesin mutant. *EMBO J.* **23**, 2993–2999 (2004).
14. Gilbert, S. P., Webb, M. R., Brune, M. & Johnson, K. A. Pathway of processive ATP hydrolysis by kinesin. *Nature* **373**, 671–676 (1995).
15. Vale, R. D., Funatsu, T., Pierce, D. W., Romberg, L., Harada, Y. & Yanagida, T. Direct observation of single kinesin molecules moving along microtubules. *Nature* **380**, 451–453 (1996).
16. Kawaguchi, K. & Ishiwata, S. Temperature dependence of force, velocity, and processivity of single kinesin molecules. *Biochem. Biophys. Res. Commun.* **272**, 895–899 (2000).
17. Kawaguchi, K. & Ishiwata, S. Thermal activation of single kinesin molecules with temperature pulse microscopy. *Cell Motil. Cytoskeleton* **49**, 41–47 (2001).
18. Böhm, K. J., Stracke, R., Baum, M., Zieren, M. & Unger, E. Effect of temperature on kinesin-driven microtubule gliding and kinesin ATPase activity. *FEBS Lett.* **466**, 59–62 (2000).
19. Kojima, H., Muto, E., Higuchi, H. & Yanagida, T. Mechanics of single kinesin molecules measured by optical trapping nanometry. *Biophys. J.* **73**, 2012–2022 (1997).
20. Hyman, A. A. Preparation of marked microtubules for the assay of the polarity of microtubule-based motors by fluorescence. *J. Cell Sci. Suppl.* **14**, 125–127 (1991).
21. Svoboda, K. & Block, S. M. Force and velocity measured for single kinesin molecules. *Cell* **77**, 773–784 (1994).
22. Uemura, S., Kawaguchi, K., Yajima, J., Edamatsu, M., Toyoshima, Y. Y. & Ishiwata, S. Kinesin-microtubule binding depends on both nucleotide state and loading direction. *Proc. Natl. Acad. Sci. USA* **99**, 5977–5981 (2002).
23. Uemura, S. & Ishiwata, S. Loading direction regulates the affinity of ADP for kinesin. *Nat. Struct. Biol.* **10**, 308–311 (2003).
24. Fujiwara, I., Takahashi, S., Tadakuma, H., Funatsu, H. & Ishiwata, S. Microscopic analysis of polymerization dynamics with individual actin filaments. *Nature Cell Biol.* **4**, 666–673 (2002).
25. Yajima, J., Alonso, M. C., Cross, R. A. & Toyoshima, Y. Y. Direct long-term observation of kinesin processivity at low load. *Curr. Biol.* **12**, 301–306 (2002).
26. Highsmith, S. The effects of temperature and salts on myosin subfragment-1 and F-actin association. *Arch. Biochem. Biophys.* **180**, 404–408 (1977).
27. Ishiwata, S., Manuck, B. A., Seidel, J. C. & Gergely, J. Saturation transfer electron paramagnetic resonance study of the mobility of myosin heads in myofibrils under conditions of partial dissociation. *Biophys. J.* **49**, 821–828 (1986).
28. Vale, R. D. & Milligan, R. A. The way things move: Looking under the hood of molecular motor proteins. *Science* **288**, 88–95 (2000).
29. Crevel, I. M., Lockhart, A. & Cross, R. A. Weak and strong states of kinesin and ncd. *J. Mol. Biol.* **257**, 66–76 (1996).
30. Sosa, H., Peterman, E. J., Moerner, W. E. & Goldstein, L. S. ADP-induced rocking of the kinesin motor domain revealed by single-molecule fluorescence polarization microscopy. *Nat. Struct. Biol.* **8**, 540–544 (2001).
31. de Cuevas, M., Tao, T. & Goldstein, L. S. Evidence that the stalk of *Drosophila* kinesin heavy chain is an α-helical coiled coil. *J. Cell Biol.* **116**, 957–965 (1992).

Available online at www.sciencedirect.com
SCIENCE DIRECT
ELSEVIER
Biochemical and Biophysical Research Communications 343 (2006) 1146–1152
BBRC
www.elsevier.com/locate/ybbrc

Myocardial sarcomeres spontaneously oscillate with the period of heartbeat under physiological conditions

Daisuke Sasaki [a], Norio Fukuda [b], Shin'ichi Ishiwata [a,c,d,*]

[a] *Integrative Bioscience and Biomedical Engineering, Graduate School of Science and Engineering, Waseda University, 3-4-1 Okubo, Shinjuku-ku, Tokyo 169-8555, Japan*
[b] *Department of Physiology (II), The Jikei University School of Medicine, 3-25-8 Nishi-Shinbashi, Minato-ku, Tokyo 105-8461, Japan*
[c] *Department of Physics, School of Science and Engineering, Waseda University, 3-4-1 Okubo, Shinjuku-ku, Tokyo 169-8555, Japan*
[d] *Advanced Research Institute for Science and Engineering, Waseda University, 3-4-1 Okubo, Shinjuku-ku, Tokyo 169-8555, Japan*

Received 8 March 2006
Available online 24 March 2006

Abstract

During heartbeat, the repeated contractions of myocardium are induced by the oscillation of intracellular Ca^{2+} concentration. On the other hand, when intermediately activated at a certain Ca^{2+} concentration, cardiac myofibrils exhibit the spontaneous sarcomeric oscillation (Ca-SPOC) under steady ionic conditions. In the present study, we found that Ca-SPOC occurred over a wide range of Ca^{2+} concentrations, including physiological contractile conditions, in skinned myocardium prepared from various animal species (rat, rabbit, pig, and cow). The period of sarcomeric oscillation fell within the same range as the period of heartbeat of each animal species. On the basis of these results we propose that the intrinsic auto-oscillatory property of sarcomeres (myofibrils) significantly contributes to myocardial beating in vivo.

Keywords: SPOC; Cardiac muscle; Oscillation; Myocardium; Microscopy

Cardiac myofibrils and skinned myocardial preparations exhibit spontaneous oscillation of sarcomere length and active tension when intermediately activated by Ca^{2+} [1–5]. This oscillatory phenomenon is called Ca-SPOC (spontaneous oscillatory contraction) [6]. Ca-SPOC occurs under steady ionic conditions, without oscillation of Ca^{2+} concentration, indicating that the auto-oscillatory property is inherent in myofibrils. The oscillatory features of Ca-SPOC are different from those of the repeated contractions induced by sarcoplasmic reticulum (SR)-based oscillation of Ca^{2+} concentration [1]. In Ca-SPOC, each sarcomere repeats the cycle of slow shortening and rapid lengthening, forming a saw tooth waveform, and the lengthening phase propagates sequentially to the adjacent sarcomeres as waves (SPOC wave) [1–3]. We have previously reported that an apparently similar type of sarcomeric oscillation, called ADP-SPOC, occurs in the absence of Ca^{2+}, when ATP, ADP, and Pi coexist [4,5,7]. ADP-SPOC occurs not only in myocardium, but in skeletal muscle as well [6,8–12], while Ca-SPOC occurs only in myocardium [6]. Our recent study demonstrated that both the period of sarcomeric oscillations and the velocity of SPOC wave propagation in myocardial ADP-SPOC correlated well with the resting heart rate of various animal species [7]. To gain more insight into the physiological relevance of SPOC, in the present study we focused on Ca-SPOC, which occurs under physiological solvent conditions. We investigated its oscillatory properties in the myocardium of various animal species.

Materials and methods

Solutions. The composition of the solutions used in the experiments was calculated by using the computer program [13], kindly provided by

* Corresponding author. Fax: +81 3 5286 3437.
E-mail address: ishiwata@waseda.jp (S. Ishiwata).

0006-291X/$ - see front matter © 2006 Elsevier Inc. All rights reserved.
doi:10.1016/j.bbrc.2006.03.070

Dr. G.J.M. Stienen (VU University Medical Center, The Netherlands). Both the relaxing and the activating solutions included 5 mM MgATP, 1 mM Mg^{2+}, 10 mM EGTA, 40 mM BES, 1 mM DTT, 15 mM phosphocreatine, and 15 U/ml creatine phosphokinase (Type I; Sigma). The pCa values of the activating solution were adjusted to 6.5–4.5 by mixing EGTA and CaEGTA to the total concentration of EGTA 10 mM, while the relaxing solution did not include CaEGTA. The ionic strength was adjusted to 170 mM by potassium propionate and the pH was adjusted to 7.0 by KOH. It should be noted here that the activating solution included high concentrations of Ca^{2+} buffer (10 mM EGTA), at which the SR-based contractions reportedly do not occur [1,14].

Preparation of skinned myocardial fiber. Skinned myocardial fibers were prepared according to the method described previously [15]. Hearts of pig and cow were obtained at a local slaughterhouse, while hearts of rat (Wistar, male, 300 g) and rabbit (JW, male, 2.5 kg) were isolated in our laboratory according to "The Waseda University Guidelines for Care and Use of Laboratory Animals." Immediately after the isolation, the rat and rabbit hearts were washed by the backward perfusion of a Ca^{2+}-free Tyrode solution (140 mM NaCl, 5.4 mM KCl, 0.5 mM $MgCl_2$, 0.3 mM NaH_2PO_4, 5 mM Hepes, and 5.5 mM glucose, pH 7.4 adjusted by NaOH) from the aorta. From the left ventricle of these isolated hearts, the intact papillary muscles of rat (about 1 mm in width, 5 mm in length) and papillary muscle strips of rabbit, pig, and cow (about 2 mm in width, 5 mm in length) were dissected. These muscle strips were chemically skinned in the relaxing solution containing 1% (v/v) Triton X-100, 80 mM 2,3-butanedione 2-monoxime (BDM), and protease inhibitor cocktail (0.5 mM PMSF, 1 mM leupeptin, and 0.1 mM E-64) for 24 h at 4 °C, with one solution change. Muscles were then washed thoroughly with the relaxing solution containing 80 mM BDM and protease inhibitor cocktail at 4 °C, and incubated in the glycerol solution (the mixture of glycerol and the relaxing solution at a 1:1 volume ratio, containing 40 mM BDM and protease inhibitor cocktail) at 4 °C for 2 h, and stored at −20 °C. Rat myocardium was used within a week, while the others were used within two weeks. Just before the experiments, small myocardial fibers (100–200 μm in diameter, 1–2 mm in length) were dissected from the muscle strips described above. To obtain satisfactorily small myocardial fibers, the dissection was carried out in a glycerol solution cooled below 0 °C [4,7]. These fibers were then used for either tension measurements or microscopic observations.

Measurement of isometric tension. Isometric tension was measured according to the method described previously [4]. Both ends of the myocardial fiber prepared as described above were attached to the hooks of tension-measuring device equipped with a tension transducer (AE801; SensoNor, Horten, Norway) and washed with the relaxing solution. The sarcomere length (SL) was measured by laser diffraction (He-Ne, 20 mW; Showa Optronics, Tokyo, Japan) during relaxation and adjusted to either 2.0 or 2.3 μm by manipulating hooks. Ca^{2+}-activated isometric tension at various pCa values was measured at 22 ± 1 °C as voltaic signals, which were recorded by a computer equipped with an A/D converter (NR-250; KEYENCE, Osaka, Japan, or PowerLab; ADInstruments). We investigated the pCa–tension relationship at each SL and the SL dependence of fully Ca^{2+}-activated tension obtained at pCa 4.5, in the myocardium of various animal species.

Microscopic observation. For the observation of sarcomeric oscillation, the myocardial fiber, which was fixed at both ends to the hooks attached to manipulators, was mounted on the inverted microscope stage (IX70; Olympus) and washed with the relaxing solution. SL was measured by FFT analysis of the phase-contrast microscopic image during relaxation and adjusted to 2.3–2.4 μm by manipulating hooks. To investigate the pCa range in which Ca-SPOC occurs, the myocardial fiber was activated at various pCa values, and the occurrence of Ca-SPOC was examined. To measure the period of sarcomeric oscillation in Ca-SPOC, the myocardial fiber was immersed in the relaxing solution containing fluorescent beads (F-8822, 1 μm in diameter; Molecular Probes) for several minutes, so that a few beads attached to the fiber. The back-and-forth movement of the beads induced by the sarcomeric oscillation was observed by epi-illumination fluorescence microscopy, recorded on digital videotape, and analyzed by NIH Image software (NIH, Bethesda, MD). All the observations were carried out at 22 ± 1 °C, except for porcine myocardial fibers, in case of which the observations were also performed at 39 ± 1 °C (porcine body temperature) by covering the microscope stage with an acrylic box and heating the inside with a heater (IX-CBIB100; Olympus).

Results

pCa–tension relationship and tension oscillation

Fig. 1 shows the relationship between pCa and active tension at SLs 2.0 and 2.3 μm for the myocardium of all animal species examined. Each relationship was fitted by the Hill equation: $F = 10^{-n_H \cdot pCa}/(10^{-n_H \cdot pCa_{50}} + 10^{-n_H \cdot pCa})$, where F and n_H represent relative tension and the Hill coefficient, respectively, and pCa_{50} is the value of pCa at which half-maximal active tension is developed. The SL dependence of maximal active tension obtained at pCa 4.5 is also shown in Fig. 1. Stretching myocardial fiber from SL 2.0 μm to SL 2.3 μm augmented both Ca^{2+} sensitivity of tension and maximal active tension of myocardium in all animal species examined, which is consistent with the results of previous studies [16,17]. Table 1 summarizes the values of pCa_{50}, EC_{50} (= $10^{-pCa_{50}}$: free Ca^{2+} concentration at which half-maximal active tension is developed), the Hill coefficient (n_H), ΔEC_{50} (the difference in EC_{50} at SLs 2.0 and 2.3 μm), and T_{23}/T_{20} at pCa 4.5, where T_{20} and T_{23} represent the active tension at SLs 2.0 and 2.3 μm, respectively. These data reveal that the values of EC_{50} (or pCa_{50}) and n_H at both SLs, as well as ΔEC_{50}, differed between species. On the other hand, the magnitude of augmentation of maximal active tension

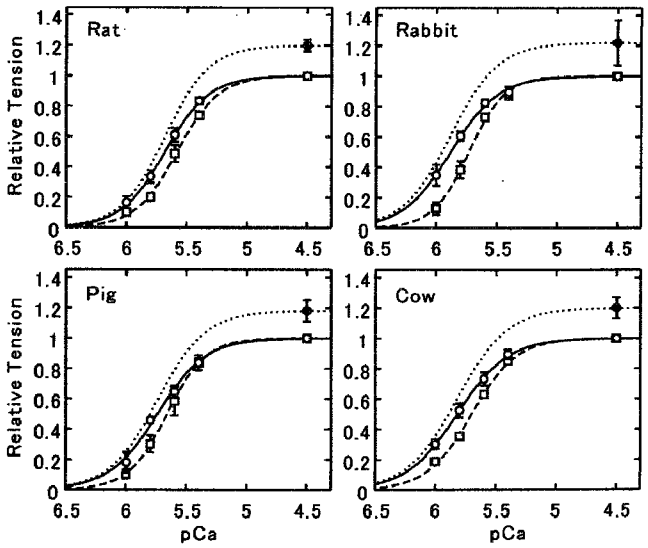

Fig. 1. Relationship between pCa and relative tension in the skinned myocardium of various animal species. Tension was measured at 22 ± 1 °C. Open squares and circles, relative tension at SLs 2.0 and 2.3 μm, respectively. Closed circles, relative maximal tension obtained at pCa 4.5 at SL 2.3 μm against that at SL 2.0 μm. Vertical bars, SD of five experiments. Dashed and solid curves are fitted by the Hill equation for relative tension at SLs 2.0 and 2.3 μm, respectively. Dotted curve was obtained according to the Hill equation for relative tension at SL 2.3 μm, passing through the relative maximal tension at SL 2.3 μm, pCa 4.5 (closed circles).

Table 1
Parameters of the Hill equation and SL-dependent maximal tension augmentation

		pCa_{50} (EC_{50})	n_H	ΔEC_{50} (μM)	T_{23}/T_{20} (pCa 4.5)
Rat	SL 2.0	5.58 (2.63 μM)	2.52	0.54	1.20 ± 0.04
	SL 2.3	5.68 (2.09 μM)	2.37		
Rabbit	SL 2.0	5.73 (1.86 μM)	2.95	0.54	1.22 ± 0.15
	SL 2.3	5.88 (1.32 μM)	2.21		
Pig	SL 2.0	5.66 (2.19 μM)	2.70	0.37	1.18 ± 0.07
	SL 2.3	5.74 (1.82 μM)	2.17		
Cow	SL 2.0	5.70 (2.00 μM)	2.36	0.49	1.20 ± 0.07
	SL 2.3	5.82 (1.51 μM)	2.08		

The values of T_{23}/T_{20} at pCa 4.5 are mean ± SD ($n = 5$).

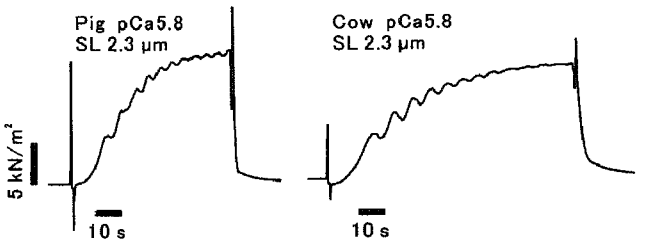

Fig. 2. Tension oscillation profiles of porcine and bovine myocardium at SL 2.3 μm and pCa 5.8. Spikes are the artifacts induced by solution change. Tension was measured at 22 ± 1 °C.

in response to stretch (T_{23}/T_{20}) was similar (ca. 1.2) for all animal species.

In some preparations of porcine and bovine myocardial fibers, tension oscillation was observed in a rising phase of tension development at pCa 6.0–5.4 at SL 2.3 μm as shown in Fig. 2, consistent with previous studies [4,5]. The tension oscillation was gradually damped and finally disappeared as the tension approached the steady level. The tension oscillation seemed to be detectable only when the myocardial fiber was of good quality, i.e., suffered almost no damage during preparation. Moreover, our previous studies indicated that in order to obtain the tension oscillation in bovine myocardial fiber reproducibly, it was better to use thinner myocardial fiber (<50 μm in width) [4,5]. Besides, prior to the activation, the myocardial fiber should be equilibrated in a pre-activating solution that includes low concentrations of EGTA (e.g., 0.4 mM) to allow for the rapid activation of myocardium. In such conditions, the tension rise was very quick and the tension oscillation was more apparent (see chart recordings in [4,5]). In the present study, however, the pre-activating solution was not used. The period of tension oscillation observed was ~5 s in porcine myocardium and ~7 s in bovine myocardium (Fig. 2). On the other hand, the tension oscillation was observed neither at SL 2.0 μm in both porcine and bovine myocardial fibers, nor in rat and rabbit myocardial fibers at both SLs.

Microscopic observation of Ca-SPOC

Sarcomeric oscillation of Ca-SPOC was directly observed by phase-contrast microscopy (Fig. 3). We found

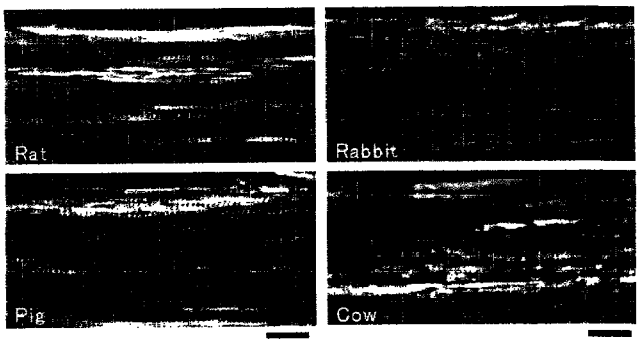

Fig. 3. Phase-contrast microscopic images of skinned myocardial fibers of various animal species. SL was adjusted to 2.3–2.4 μm. Scale bar, 20 μm.

that over a wide range of pCa, stable and periodic sarcomeric oscillations occurred reproducibly in the myocardium of all animal species (see online Movies 1–4, available in the supplementary material on website). The oscillation lasted for more than several tens of minutes. Table 2 summarizes the pCa range, in which Ca-SPOC occurred, and the range of corresponding relative active tension at SL 2.3 μm.

The most distinctive feature of Ca-SPOC was that the faster the heart rate of the animal species is, the shorter is the period of the sarcomeric oscillation. The amplitude of lateral movement of sarcomeres was much smaller in rat and rabbit myocardium than in porcine and bovine myocardium. The propagation of the lengthening phase of a sarcomere to the adjacent sarcomeres (SPOC wave) was apparent in porcine and bovine myocardium (see online Movies 3 and 4). On the other hand, SPOC wave was not apparent in rat and rabbit myocardium, because in rat myocardium the sarcomeric oscillation was very rapid (see online Movie 1), and in rabbit myocardium the striated pattern was not clear in Ca-SPOC state (see online Movie 2).

When Ca-SPOC occurred at relatively higher pCa values, where the lower tension is developed, almost all sarcomeres over the whole region of myocardial fiber exhibited oscillations. On the other hand, at relatively lower pCa values, where the higher tension is developed, the striated pattern of myocardium tended to become disordered, being separated into stretched regions and contracted regions. The sarcomeric oscillation stopped in the stretched regions, while it continued in the contracted regions. In fact, we confirmed in porcine myocardium that even in the myocardial fiber exhibiting sarcomeric oscillation over the entire region, the oscillation stopped when the myocardial fiber was stretched to SL ~2.8 μm by manipulating hooks (data not shown), being qualitatively consistent with the previous

Table 2
pCa range, in which Ca-SPOC occurs

	Ca-SPOC range	Range of relative tension (%)
Rat	pCa 5.75–4.5	41–100
Rabbit	pCa 6.2–4.5	16–100
Pig	pCa 6.1–5.4	14–85
Cow	pCa 6.2–5.6	14–74

observations [1,3]. On the other hand, when the hooks were gradually manipulated towards each other to relieve the stretch, the oscillation lasted until the fiber was slackened (when its SL dropped below 1.9 μm). In rat and rabbit myocardium, sarcomeric oscillations were locally observed even when fully activated at pCa 4.5, although the structural disorder was prominent.

Relationship between Ca-SPOC and heartbeat

To compare the period of sarcomeric oscillation among various animal species, we analyzed the period of sarcomeric oscillation at the standard Ca-SPOC condition, defined as pCa_{50} at SL 2.3 μm for each animal species, that is, 5.68 in rat, 5.88 in rabbit, 5.74 in pig, and 5.82 in cow (see Table 1). All observations were carried out at 22 ± 1 °C, except for the porcine myocardium, in which another series of experiments was carried out at 39 ± 1 °C (porcine body temperature) as well. The period was determined by the FFT analysis of the time course of the oscillatory movement of a bead attached to a myocardial fiber (Figs. 4A and B). Fig. 4C shows the relationship between the period of sarcomeric oscillation in the standard Ca-SPOC condition (the period of Ca-SPOC) and the period of the resting heartbeat. Here, the period of the resting heartbeat was derived by referring to *Biology Data Book* [18]; 0.17 s (355 bpm) for rat, 0.23 s (256 bpm) for rabbit, 0.88 s (68 bpm) for pig, and 1.18 s (51 bpm) for cow. There was a good correlation between the period of Ca-SPOC at 22 ± 1 °C and that of the resting heartbeat with the correlation coefficient of 0.94. It was also found that the period of Ca-SPOC in porcine myocardium became significantly shorter ($P < 0.01$ by Student's t test) as the temperature increased (Fig. 4C).

Dependence of Ca-SPOC on pCa

The relationship between the period of Ca-SPOC and pCa (or a relative tension at SL 2.3 μm corresponding to each pCa) was investigated in porcine myocardium and shown in Fig. 5. The relative tension was calculated from the Hill equation. The period of Ca-SPOC positively (negatively) correlated with pCa (relative tension) with the correlation coefficient of 0.87 (−0.87), although the dependence of the period on pCa was not as strong as to influence its dependence on the difference between species.

Waveform of SL oscillation

The waveform of the SL oscillation of Ca-SPOC in porcine myocardium at pCa 6.0 was analyzed by phase-contrast microscopy (Fig. 6A), according to the method described previously [7]. Fig. 6B shows the vertically averaged intensity profile of the region delineated by a rectangle in Fig. 6A. The inter-peak distance in the profile corresponds to SL. Fig. 6C shows the time course of the change in the total length of three consecutive sarcomeres (3 × SL),

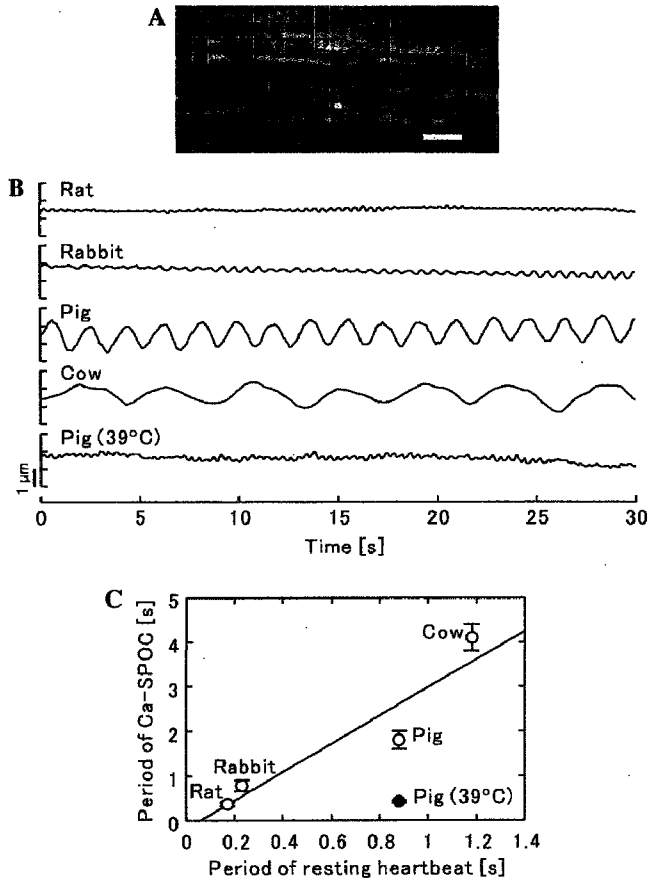

Fig. 4. Relationship between Ca-SPOC and heartbeat. (A) Superimposed image obtained by phase-contrast and epi-illumination fluorescence microscopy of a porcine myocardial fiber. The arrow shows the position of a fluorescent bead attached to the fiber. Scale bar, 10 μm. (B) Time course of the translational movement of an attached bead in Ca-SPOC. All the observations were carried out at 22 ± 1 °C except for porcine myocardium, in which the observations were carried out at 39 ± 1 °C as well. (C) Relationship between the period of Ca-SPOC and the period of resting heartbeat. Open and closed circles, the period of Ca-SPOC at 22 ± 1 and 39 ± 1 °C, respectively. Vertical bars, SD of five experiments. The solid line is the regression line for the period of Ca-SPOC at 22 ± 1 °C (correlation coefficient, 0.938).

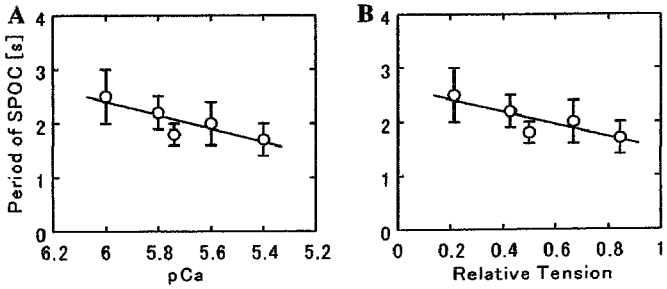

Fig. 5. Period of Ca-SPOC vs. pCa (relative tension) in porcine myocardium. The observations of Ca-SPOC were carried out at 22 ± 1 °C. (A) Relationship between the period of Ca-SPOC and pCa. (B) Relationship between the period of Ca-SPOC and the relative tension at SL 2.3 μm corresponding to each pCa (see Fig. 1). Vertical bars, SD of five experiments. The solid line is the regression line (correlation coefficient is 0.87 for A and −0.87 for B).

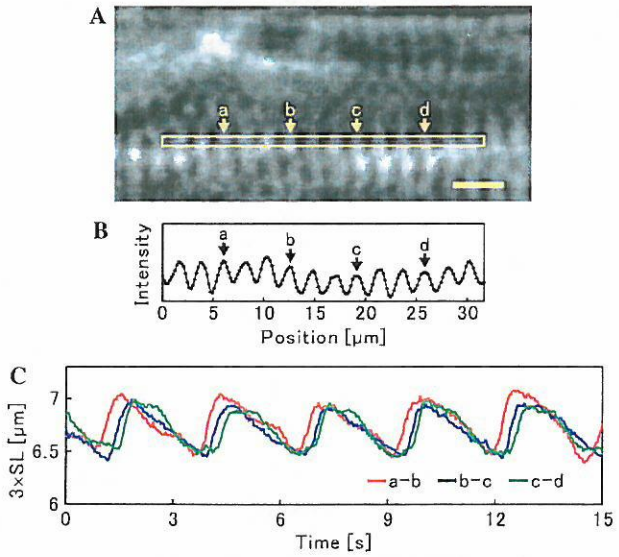

Fig. 6. Waveform of SL oscillation. (A) Phase-contrast microscopic image of a porcine myocardial fiber. Scale bar, 5 μm. (B) Vertically averaged intensity profile of the region delineated by a rectangle in (A). Arrows indicate the profile peaks, marked as "a," "b," "c," and "d." (C) Time course of the change in the total length of three consecutive sarcomeres (3 × SL), which is the pairwise distance between the profile peaks 'a' and 'b' (red), 'b' and 'c' (blue), and 'c' and 'd' (green). The observation was carried out at 22 ± 1 °C.

which is the pairwise distance between the profile peaks 'a' and 'b,' 'b' and 'c,' and 'c' and 'd,' indicated by the arrows in Figs. 6A and B. It was shown that the oscillatory waveform consisted of the slow shortening phase and the rapid lengthening phase, forming a saw tooth waveform. The sequential displacements of the waveforms along the horizontal axis in the order of red, blue, and green in Fig. 6C indicate that the lengthening phase propagated (SPOC wave) from left to right in the microscopic image. These features are consistent with the previous observations [3,7,8,10,12,19].

Effect of ryanodine and EGTA on Ca-SPOC

In order to confirm that Ca-SPOC is not induced by the SR-based oscillation of Ca^{2+} concentration, we first examined the effect of ryanodine on Ca-SPOC. We confirmed that the oscillatory properties of Ca-SPOC were unaffected by the addition of 0.1 mM ryanodine to the myocardium of all animal species (data not shown), consistent with the previous studies [2–4]. We also tested the effect of EGTA concentration on Ca-SPOC, varying the total EGTA concentration with the fixed pCa and ionic strength at the standard Ca-SPOC condition in porcine myocardium. The observations were carried out at 22 ± 1 °C. The period was 2.4 ± 0.4, 1.8 ± 0.2, and 2.3 ± 0.4 s (mean ± SD of five experiments) at 1, 10, and 20 mM EGTA, respectively. No apparent correlation between the period and the total EGTA concentration was observed (correlation coefficient, −0.18), indicating that Ca-SPOC is not induced by the oscillation of Ca^{2+} concentration.

Effect of dextran on Ca-SPOC

It is known that the skinned myocardial fibers are swollen, and, as a result, the distance between thick and thin filament (filament spacing) is larger compared with that of intact myocardium. Irving et al. [20] showed that the physiological filament spacing could be restored by the osmotic compression of skinned myocardial fibers with 5% (w/v) dextran. We examined whether Ca-SPOC occurs at the physiological filament spacing, by compressing porcine skinned myocardial fiber with 5% (w/v) dextran (400–500 kDa; Sigma). The observations were carried out at 22 ± 1 °C. The addition of dextran resulted in a compression of a fiber to 83 ± 3% (mean ± SD of five experiments) of its width in the absence of dextran. We confirmed that Ca-SPOC occurred in this compressed preparation as well, although the period of sarcomeric oscillation became 3.4 ± 0.7 s (mean ± SD of five experiments), which was significantly longer ($P < 0.01$ by Student's t test) than in the absence of dextran (1.8 ± 0.2 s).

Discussion

In the present study, we demonstrated that Ca-SPOC occurred over a wide range of pCa including physiological contractile conditions, in the myocardium of all animal species examined. Furthermore, the period of sarcomeric oscillation in Ca-SPOC fell within the same range as the period of heartbeat. Here, we discuss the possible mechanism and physiological relevance of Ca-SPOC.

Under the Ca-SPOC conditions, the sarcomeric oscillation was reproducibly observed in the myocardium of all animal species. However, the sarcomeric oscillation does not necessarily correspond to the tension oscillation because of the asynchronous properties of sarcomeric oscillations that counteract the oscillation of the entire myocardial fiber (i.e., tension oscillation). The tension oscillation can only be observed, when the sarcomeric oscillations are synchronous in a large region of a myocardial fiber. In fact, the tension oscillations were obtained in some preparations of porcine and bovine myocardial fibers at SL 2.3 μm (Fig. 2), but neither at SL 2.0 μm, nor in rat and rabbit myocardial fibers at both SLs 2.0 and 2.3 μm. This indicates that the sarcomeric oscillations are more synchronous, first, at longer SL, and second, in porcine and bovine myocardium rather than in rat and rabbit myocardium. Furthermore, the transient tension oscillation (Fig. 2; see also [4,5]) indicates that the sarcomeric oscillations are synchronous just after the activation upon the solution change and then gradually become asynchronous. This in turn suggests that the Ca^{2+} triggering may synchronize the sarcomeric oscillations, which results in the tension oscillation.

Fabiato and Fabiato argued that the augmentation of active tension in response to stretch of myocardium at intermediate Ca^{2+}-activation is important for the mechanism of the sarcomeric oscillation [1]. However, our present data showed that T_{23}/T_{20}, the index of SL-dependent

activation, increased with an increase in pCa above the upper limit of the pCa range, in which Ca-SPOC occurs, in the myocardium of all animal species (see Fig. 1 and Table 2). For example, in rat myocardium T_{23}/T_{20} was 1.86 at pCa 5.6, where Ca-SPOC occurred, while T_{23}/T_{20} was 2.66 at pCa 6.0, where Ca-SPOC did not occur. This result suggests that SL-dependent activation alone is not sufficient to account for the mechanism of Ca-SPOC. In the previous study, we concluded that the minimum prerequisite for SPOC (both Ca-SPOC and ADP-SPOC) is the coexistence of weakly bound cross-bridges and force generating (strongly bound) cross-bridges over certain threshold proportions [6]. As a further elaboration of this model, we consider that the ultimate basis of the sarcomeric oscillation is the inter-molecular synchronization between myosin heads in a sarcomere via the change in load on these cross-bridges.

We consider that the propagation of sarcomere lengthening (SPOC wave) and the sarcomeric auto-oscillation are based on different mechanisms. SPOC wave implies the existence of mechano-chemical signal transmission between adjacent half sarcomeres via Z-line and M-line [12]. Recently, another type of propagation of sarcomere lengthening, similar to SPOC wave, has been reported in a transient phase upon relaxation in cardiac and skeletal myofibrils [21–23]. The propagation occurred transiently when Ca^{2+}-activated myofibrils were relaxed by rapid removal of Ca^{2+}. Stehle et al. [21] suggested that the propagation might play a physiologically important role in accelerating the myocardial relaxation. It is likely that the propagation phenomenon and SPOC wave are based on a common molecular mechanism.

Our previous study showed that the period of sarcomeric oscillation in ADP-SPOC correlated well with that of the resting heartbeat of each animal species [7]. However, the period in ADP-SPOC was approximately 20 times longer than that of the resting heartbeat. The reason for the slow sarcomeric oscillation in ADP-SPOC is that exogenously added ADP increases the relative number of non-force-generating cross-bridges (actomyosin–ADP complexes), which act as a viscous drag in sarcomere shortening [24]. This effect, obviously, is absent in case of Ca-SPOC. Consequently, the period of Ca-SPOC at 22 ± 1 °C was only 2–4 times longer than that of the resting heart rate (Fig. 4C). Moreover, we demonstrated that the period of Ca-SPOC in porcine myocardium significantly diminished when the temperature increased to the body temperature (39 ± 1 °C; Fig. 4C). The period of Ca-SPOC at 39 ± 1 °C was approximately twice shorter than the period of the resting heartbeat in pig. Considering the broad distribution of the heart rates within the same animal species, it is reasonable to conclude that the period of Ca-SPOC fell within the same range as the period of the heartbeat.

Although the present results provide strong evidence for the physiological relevance of Ca-SPOC, the large-amplitude myocardial oscillation, such as that occurring in vivo (i.e., beating), does not occur because of the asynchronous property of sarcomeric oscillations. However, the transient tension oscillation that occurs immediately after the activation indicates that the changes in circumferential Ca^{2+} concentration have the ability to synchronize the sarcomeric auto-oscillations, resulting in the large-amplitude myocardial oscillation. This further implies that the sarcomeric auto-oscillation may be tunable by the oscillation of intracellular Ca^{2+} concentration. We propose that the intrinsic auto-oscillatory property of sarcomeres underlies the efficient beating of myocardium in vivo.

Acknowledgments

We thank Dr. S.V. Mikhailenko for his critical reading of the manuscript. This work was supported partly by Grants-in-Aid for Specially Promoted Research, the 21st Century COE Program and "Establishment of Consolidated Research Institute for Advanced Science and Medical Care" from the Ministry of Education, Sports, Culture, Science and Technology of Japan to S.I., and by The Descente and Ishimoto Memorial Foundation for the Promotion of Sports Science and The Jikei University Research Fund to N.F.

Appendix A. Supplementary data

Supplementary data associated with this article can be found, in the online version, at doi:10.1016/j.bbrc.2006.03.070.

References

[1] A. Fabiato, F. Fabiato, Myofilament-generated tension oscillations during partial calcium activation and activation dependence of the sarcomere length-tension relation of skinned cardiac cells, J. Gen. Physiol. 72 (1978) 667–699.
[2] N.K. Sweitzer, R.L. Moss, The effect of altered temperature on Ca^{2+}-sensitive force in permeabilized myocardium and skeletal muscle. Evidence for force dependence of thin filament activation, J. Gen. Physiol. 96 (1990) 1221–1245.
[3] W.A. Linke, M.L. Bartoo, G.H. Pollack, Spontaneous sarcomeric oscillations at intermediate activation levels in single isolated cardiac myofibrils, Circ. Res. 73 (1993) 724–734.
[4] N. Fukuda, H. Fujita, T. Fujita, S. Ishiwata, Spontaneous tension oscillation in skinned bovine cardiac muscle, Pflugers Arch. 433 (1996) 1–8.
[5] N. Fukuda, S. Ishiwata, Effects of pH on spontaneous tension oscillation in skinned bovine cardiac muscle, Pflugers Arch. 438 (1999) 125–132.
[6] S. Ishiwata, K. Yasuda, Mechano-chemical coupling in spontaneous oscillatory contraction of muscle, Phase Transitions 45 (1993) 105–136.
[7] D. Sasaki, H. Fujita, N. Fukuda, S. Kurihara, S. Ishiwata, Auto-oscillations of skinned myocardium correlating with heartbeat, J. Muscle Res. Cell Motil. 26 (2005) 93–101.
[8] N. Okamura, S. Ishiwata, Spontaneous oscillatory contraction of sarcomeres in skeletal myofibrils, J. Muscle Res. Cell Motil. 9 (1988) 111–119.
[9] S. Ishiwata, N. Okamura, H. Shimizu, T. Anazawa, K. Yasuda, Spontaneous oscillatory contraction (SPOC) of sarcomeres in skeletal muscle, Adv. Biophys. 27 (1991) 227–235.

[10] T. Anazawa, K. Yasuda, S. Ishiwata, Spontaneous oscillation of tension and sarcomere length in skeletal myofibrils. Microscopic measurement and analysis, Biophys. J. 61 (1992) 1099–1108.
[11] S. Ishiwata, T. Anazawa, T. Fujita, N. Fukuda, H. Shimizu, K. Yasuda, Spontaneous tension oscillation (SPOC) of muscle fibers and myofibrils minimum requirements for SPOC, Adv. Exp. Med. Biol. 332 (1993) 545–554.
[12] K. Yasuda, Y. Shindo, S. Ishiwata, Synchronous behavior of spontaneous oscillations of sarcomeres in skeletal myofibrils under isotonic conditions, Biophys. J. 70 (1996) 1823–1829.
[13] G.J. Stienen, J.L. Kiers, R. Bottinelli, C. Reggiani, Myofibrillar ATPase activity in skinned human skeletal muscle fibres: fibre type and temperature dependence, J. Physiol. (Lond.) 493 (1996) 299–307.
[14] A. Fabiato, F. Fabiato, Contractions induced by a calcium-triggered release of calcium from the sarcoplasmic reticulum of single skinned cardiac cells, J. Physiol. (Lond.) 249 (1975) 469–495.
[15] N. Fukuda, Y. Wu, G. Farman, T.C. Irving, H. Granzier, Titin isoform variance and length dependence of activation in skinned bovine cardiac muscle, J. Physiol. (Lond.) 553 (2003) 147–154.
[16] J.P. Konhilas, T.C. Irving, P.P. de Tombe, Frank-Starling law of the heart and the cellular mechanisms of length-dependent activation, Pflugers Arch. 445 (2002) 305–310.
[17] N. Fukuda, H. Granzier, Role of the giant elastic protein titin in the Frank-Starling mechanism of the heart, Curr. Vasc. Pharmacol. 2 (2004) 135–139.
[18] P.L. Altman, D.S. Dittmer, Biology Data Book, Federation of American Societies for Experimental Biology, Bethesda, 1974, pp. 1689–1693.
[19] A. Fabiato, F. Fabiato, Effects of magnesium on contractile activation of skinned cardiac cells, J. Physiol. (Lond.) 249 (1975) 497–517.
[20] T.C. Irving, J. Konhilas, D. Perry, R. Fischetti, P.P. Tombe, Myofilament lattice spacing as a function of sarcomere length in isolated rat myocardium, Am. J. Physiol. 279 (2000) H2568–H2573.
[21] R. Stehle, M. Krüger, G. Pfitzer, Force kinetics and individual sarcomere dynamics in cardiac myofibrils after rapid Ca^{2+} changes, Biophys. J. 83 (2002) 2152–2161.
[22] C. Tesi, N. Piroddi, F. Colomo, C. Poggesi, Relaxation kinetics following sudden Ca^{2+} reduction in single myofibrils from skeletal muscle, Biophys. J. 83 (2002) 2142–2151.
[23] C. Poggesi, C. Tesi, R. Stehle, Sarcomeric determinants of striated muscle relaxation kinetics, Pflugers Arch. 449 (2005) 505–517.
[24] J.A. Gorga, D.E. Fishbaugher, P. VanBuren, Activation of the calcium-regulated thin filament by myosin strong binding, Biophys. J. 85 (2003) 2484–2491.

Temperature change does not affect force between regulated actin filaments and heavy meromyosin in single-molecule experiments

Masataka Kawai[1], Takanori Kido[2], Martin Vogel[3], Rainer H. A. Fink[3] and Shin'ichi Ishiwata[2]

[1]*Department of Anatomy and Cell Biology, College of Medicine, University of Iowa, Iowa City, IA 52242, USA*
[2]*Department of Physics, School of Science and Engineering, Waseda University, Tokyo 169-8555, Japan*
[3]*Medical Biophysics Unit, Institute of Physiology and Pathophysiology, Ruprecht-Karls-Universität, Im Neuenheimer Feld 326, 69120 Heidelberg, Germany*

The temperature dependence of sliding velocity, force and the number of cross-bridges was studied on regulated actin filaments (reconstituted thin filaments) when they were placed on heavy meromyosin (HMM) attached to a glass surface. The regulated actin filaments were used because our previous study on muscle fibres demonstrated that the temperature effect was much reduced in the absence of regulatory proteins. A fluorescently labelled thin filament was attached to the gelsolin-coated surface of a polystyrene bead. The bead was trapped by optical tweezers, and HMM–thin filament interaction was performed at 20–35°C to study the temperature dependence of force at the single-molecule level. Our experiments showed that there was a small increase in force with temperature ($Q_{10} = 1.43$) and sliding velocity ($Q_{10} = 1.46$). The small increase in force was correlated with the small increase in the number of cross-bridges ($Q_{10} = 1.49$), and when force was divided by the number of cross-bridges, the result did not depend on the temperature ($Q_{10} = 1.03$). These results demonstrate that the force each cross-bridge generates is fixed and independent of temperature. Our additional experiments demonstrate that tropomyosin (Tm) in the presence of troponin (Tn) and Ca^{2+} enhances both force and velocity, and a truncated mutant, Δ23Tm, diminishes force and velocity. These results are consistent with the hypothesis that Tm in the presence of Tn and Ca^{2+} exerts a positive allosteric effect on actin to make actomyosin linkage more secure so that larger forces can be generated.

(Resubmitted 14 April 2006; accepted 16 May 2006; first published online 18 May 2006)
Corresponding author M. Kawai: Department of Anatomy and Cell Biology, University of Iowa, Iowa City, IA 52242, USA. Email: masataka-kawai@uiowa.edu

In striated muscles, it has been known for some time that an increase of temperature increases isometric tension at the maximal activating condition both in mammalian skeletal (Goldman *et al.* 1987; Bershitsky & Tsaturyan, 1992, 2002; Zhao & Kawai, 1994; Ranatunga, 1996; Coupland *et al.* 2001; Wang & Kawai, 2001) and cardiac muscle fibres (Ranatunga, 1999; Fujita & Kawai, 2002). The effect of temperature is largest in mammals, and it becomes progressively less in lower animals (Rall & Woledge, 1990). There are two leading hypotheses to explain the temperature effect. The first hypothesis states that an increase in the temperature results in an increase in the number of force-generating cross-bridges (Zhao & Kawai, 1994; Head *et al.* 1995; Coupland *et al.* 2001; Wang & Kawai, 2001; Kawai, 2003). The second hypothesis states that the tension generated by each cross-bridge is increased by an increase in the temperature (Goldman *et al.* 1987; Bershitsky & Tsaturyan, 1992, 2002; Linari *et al.* 2005).

To evaluate these hypotheses, a number of experiments have been performed by using skinned fibres and single molecules. Our skinned fibre experiments demonstrated that the step that generates force is endothermic, hence its equilibrium shifts significantly to the force-generating state at a higher temperature, thus supporting the first hypothesis (Zhao & Kawai, 1994; Wang & Kawai, 2001). It was also shown that this step accompanies a large entropy increase, which is based on burial of a large surface area consisting of hydrophobic amino acid residues (Murphy *et al.* 1996). Our experiment on single molecules using heavy meromyosin (HMM) and actin filaments demonstrated that force generated at the level of single molecules was independent of the temperature (Kawai *et al.* 2000), which is consistent with the first hypothesis.

However, our later experiments on reconstituted myocardium have demonstrated that, without regulatory proteins tropomyosin (Tm) and troponin complex (Tn),

DOI: 10.1113/jphysiol.2006.111708

Table 1. Composition of solutions

Solution	ATP (mM)	P_i (mM)	$CaCl_2$ (mM)	$MgCl_2$ (mM)	EGTA (mM)	KCl (mM)	DTT (mM)	Im-HCl (mM)	BSA (mg ml^{-1})	± GOC
Actin buffer	—	—	—	4	1	25	—	25	—	-
D_{HMM}	—	—	—	4	1	25	2	25	—	-
Relaxing	2	—	—	4	1	25	10	25	1	+
Activating (control)	2	—	1	4	1	23	10	25	1	+
Active + P_i	2	8	1	4	1	6	10	25	1	+
Rigor	—	—	—	4	1	28	10	25	1	+

D_{HMM}, diluting solution for HMM; DTT, dithiothreitol; Im-HCl, imidazole-HCl. GOC represents 4.5 mg ml^{-1} glucose, 0.216 mg ml^{-1} glucose oxidase and 0.036 mg ml^{-1} catalase to remove dissolved O_2 in order to minimize photobleaching of rhodamine (Harada *et al.* 1990). The pH of all solutions was adjusted to 7.40 by adding KOH or HCl.

the temperature effect on isometric tension is much reduced, indicating a possibility that the temperature effect is enhanced by regulatory proteins (Fujita & Kawai, 2002). Thus, it has become important to carry out a temperature study in the presence of Tm and Tn in single-molecule experiments, which is the main focus of this report. For this reason, we performed *in vitro* motility studies and measured force as the ambient temperature was changed in the range 20–35°C. Our results demonstrate that the single molecular force remains the same as temperature is changed, supporting the first hypothesis.

Methods

Experimental set-up

The experimental set-up used here was the same as that reported by Kawai *et al.* (2000) and mounted on a pneumatic isolation table (Herz Kogyo KK, Tokyo, Japan) as previously described (Miyata *et al.* 1994, 1995; Nishizaka *et al.* 1995*a*, 1995*b*, 2000; Nishizaka, 1996; Ishiwata, 1998). In brief, an inverted microscope (TMD-300, Nikon, Tokyo, Japan) was used for the central optical system. The light from an Nd-YLF laser (1053 nm, 1 W; Amoco Laser, Naperville, IL, USA) was led through the ×100 oil-immersion objective lens (n.a. = 1.3) and trapped a polystyrene bead in the flow cell to work as optical tweezers. The image of the flow cell and activities within were recorded by the CCD camera with the light originating from a halogen lamp filtered at 380–520 nm. Fluorescent light (> 590 nm) was led into the image intensifier (KS 1381, Video Scope, Washington, DC, USA) and recorded by another CCD camera (CCD-72, DAGE MTI, Michigan City, IN, USA). These were videotaped (Hi8 Video, Sony Corp, Tokyo, Japan) for later analysis.

Flow cell

Both surfaces of a large coverslip (24 × 60 mm; thickness, 0.12–0.17 mm) were coated with collodion dissolved in 3-methylbutyl acetate (1:20). A small coverslip (18 × 18 mm; thickness, 0.12–0.17 mm) was glued to the large coverslip with Vaseline and two spacers (thickness, 50 μm) along the two sides. The total volume of the flow cell was about 25 μl. From an open side, 25 μl of HMM solution (5 μg ml^{-1} for rigor; otherwise 30 μg ml^{-1} in D_{HMM}) was applied and left to settle for 60 s to allow the HMM molecules to be adsorbed onto the collodion-coated glass surface. Another 25 μl of HMM solution was applied from the other side and allowed to settle for 60 s. Subsequently, 25 μl of rhodamine-phalloidin-labelled regulated actin filaments in an experimental solution (Table 1) were applied twice from the same direction. Actin filaments were attached to polystyrene beads (see below), and then Tm and Tn were added to reconstitute the thin filaments. For this reconstitution, we did not need an annealing treatment (10 min at 45°C; longer time is needed if at lower temperatures), because the protein concentrations were low (Ishiwata, 1973). The two open sides were then sealed by Vaseline, and the flow cell was placed in the experimental apparatus.

Solutions

The compositions of solutions are listed in Table 1. After mixing solutions, doubly distilled water was depressurized for 10 min by aspirator to minimize dissolved O_2. ATP was added as $Na_2H_2ATP{\cdot}2H_2O$, P_i as $H_{1.5}Na_{1.5}PO_4$, EGTA as H_4EGTA and calcium as $CaCl_2$, and pH was adjusted to 7.40.

Polystyrene beads

Polystyrene beads (polybead carboxylate; catalogue number 08226; diameter, 1 μm) to which a carboxyl group (–COOH) was attached were purchased from Polysciences Inc. (Warrington, PA, USA). They were washed by Na-carbonate buffer (200 mM, pH 9.6), followed by Na-phosphate buffer (20 mM, pH 4.5). 1-ethyl-3-(3-dimethyl-aminopropyl)-carbodiimide (EDC) (208 mM) was then added to the beads in the phosphate buffer, and mixed gently for 2 h at room temperature. EDC reacts with the carboxyl group of the beads.

The beads were then washed by Na-borate buffer (200 mM, pH 8.4). Gelsolin (10 μg ml^{-1}), freshly prepared G-actin (10 μg ml^{-1}), TMR-(tetramethyl rhodamine)-BSA (17 μg ml^{-1}), BSA (303 μg ml^{-1}) and Na-borate (30 mM) were then added and gently mixed overnight at 2°C. This procedure results in a covalent bond between the carboxyl group of the beads and the amino group of gelsolin. G-Actin was bound to the gelsolin, presumably because of stereospecific (both ionic and hydrophobic) interactions: gelsolin is an actin-binding protein that caps the barbed end of actin filaments. TMR-BSA was attached to the beads to make them fluorescent. 2-Aminoethanol (20 mM) was added and mixed for 30 min at 2°C, and the beads were washed by the Na-borate buffer and stored in Na-phosphate buffer (200 mM, pH 7.4).

Proteins

G-Actin, HMM and a Tm–Tn complex were isolated from rabbit white skeletal muscles as previously described (Suzuki *et al.* 1996; Fujita *et al.* 1996). Rabbits were killed by decapitation after anaesthetizing with sodium pentobarbital (150 mg/kg) by IV injection; this method was approved by the Institutional Review Committee on Animal Experimentation at Waseda University. G-Actin (0.1 mg ml^{-1}) was polymerized to result in F-actin, rhodamine-conjugated phalloidin was bound to the F-actin, and then the F-actin (50 μg ml^{-1}) was attached to polystyrene beads (1.1 × 10^{10} particles ml^{-1}) via G-actin and gelsolin, which were previously attached to the beads as the nucleus (see above). Gelsolin was prepared from bovine serum by the method described by Kurokawa *et al.* (1990). The Tm–Tn complex was then added to the bead-tailed F-actin solution at a concentration of 1 mg ml^{-1} in a 500 μl test tube, and agitated for 30–60 min in a cold room on ice (0°C). This concentration is in excess of stoichiometric binding of Tm (about 12 μg ml^{-1}) and Tn (about 14 μg ml^{-1}) to F-actin (50 μg ml^{-1}).

Temperature control

The inverted microscope, including the stage and the flow cell, was enclosed by a Nikon-Plexiglass cover and the internal temperature was controlled by sending warm air from one side and by cooling with frozen antifreeze (1,2-ethanediole)–water mixture (1:1) on the other side. The temperature was measured by a thermister probe attached to the microscope stage at the flow cell and regulated within ± 0.5°C of the desired experimental temperature. The temperature in the cell was also estimated from thermal quenching of the fluorescence from rhodamine–maleimide conjugated to tubulin subunits of microtubule (Kawaguchi & Ishiwata, 2000, 2001) in a similar manner to that reported earlier (Kato *et al.* 1999).

Velocity measurement

A record consisting of 3 s (30 frames s^{-1}) was randomly selected from the video image, and the sliding velocity was calculated by using a computer program developed in Heidelberg for PC (Uttenweiler *et al.* 2000). This program uses a structure–tensor-based algorithm to identify a group of pixels moving together, follows its trajectory with time, and calculates the velocity of the pixel group.

Force measurement

To measure force, a bead to which a regulated actin filament was attached was caught by optical tweezers and placed several micrometres above the HMM-coated glass surface. The glass was moved horizontally to align the filament parallel to the surface. Then the bead was lowered close to the surface and filament–HMM interaction was initiated (Fig. 1 of Kawai *et al.* 2000). The displacement of the bead from the trap centre was measured from the video image. Force was calculated as Force = kP × displacement, where P is the power of the incident Nd-YLF laser beam at the level of the sample, which was measured by a power meter (Model LM-3, Coherent, Santa Clara, CA, USA) and ranged from 100 to 300 mW; k is the proportionality constant (k = 0.531 fN mW^{-1} nm^{-1}); and kP is the spring constant of the optical tweezers. The laser power could be attenuated to 30 or 50% by inserting a neutral density filter. The length of filaments was measured from the video image. Since force generated is proportional to the length of the filament (Kishino & Yanagida, 1988), the force value was divided by the length value to obtain force per unit length.

Results

Ca^{2+} regulation of the thin filament mobility

Regulated actin filaments (reconstituted thin filaments) were placed on the HMM-coated glass surface and first bathed in the EGTA relaxing solution in the presence of MgATP (2 mM). Then the mobility of the filaments was examined. There were no overall movements, demonstrating a good regulation by Tm and Tn. These filaments, however, exhibited a segmental motion, presumably caused by thermal bombardment of H_2O molecules on filaments, indicating that the actomyosin interaction is weak to nonexistent. When the regulated actin filaments were placed in the Ca^{2+} activating solution, they started sliding, demonstrating the presence of the Ca^{2+} activation mechanism. When the regulated actin filaments were placed in the rigor solution, there were no overall or segmental movements, demonstrating the strong interaction between the filaments and HMM molecules. In contrast, unregulated actin filaments moved regardless of the presence of Ca^{2+} as long as MgATP was present.

Effect of temperature on the sliding velocity

Regulated actin filaments were placed on the HMM-coated glass surface in the activating solution and then the sliding velocity was observed at four different temperatures (20, 25, 30 and 35°C). The experiments were carried out under unloaded conditions and in the presence of 2 mM ATP at pCa 4.74. For this series of experiments, the standard 30 μg ml^{-1} HMM was used to coat the glass surface. The velocity was measured as described in the Methods. The result is the number of pixel groups moving at a given velocity forming a velocity distribution, such as shown in Figs 1 and 2. Ten to twenty records from the same condition were analysed. We noticed that there were often two peaks in the distribution (Fig. 1). On visual inspection of the video images, it was apparent that the slower peak corresponds to the filaments with irregular movements that had an appearance of sticking to the glass surface. These presumably correspond to thin filaments interacting with partially denatured HMM molecules. Depending on the velocity distribution, a record is classified into three groups: (A) those with only fast-moving filaments; (B) those with both fast- and slow-moving filaments; and (C) those with only slow-moving filaments. The records were summated within each group, and plotted in Fig. 1. Because it is considered that the slow-moving group is based on denatured proteins with irregular movements, we have used only records with fast-moving filaments for subsequent analyses.

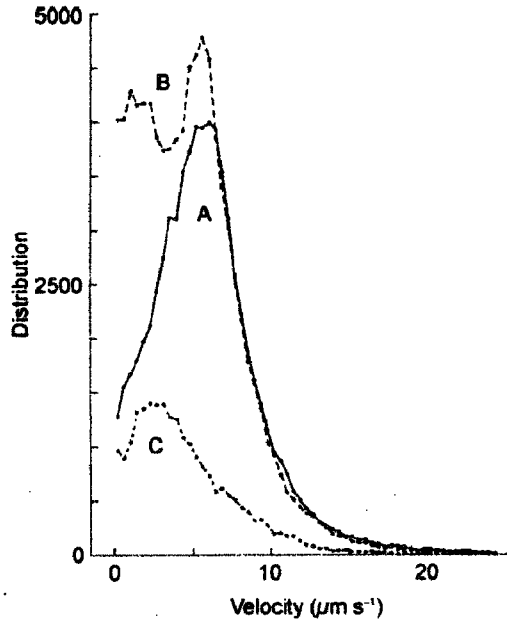

Figure 1. Distribution of the velocity at 25°C in the activating solution
Records, consisting of 3 s each of video image, were classified into three groups: (A) those with fast-moving thin filaments (11 records); (B) those with both fast- and slow-moving thin filaments (12 records); and (C) those with slow-moving thin filaments (6 records). The data in each group were then summated and plotted in this figure. The ordinate (distribution) represents the number of pixel groups moving at a given velocity. The velocity is sliced at the 0.417 μm s^{-1} (= 5/12) interval.

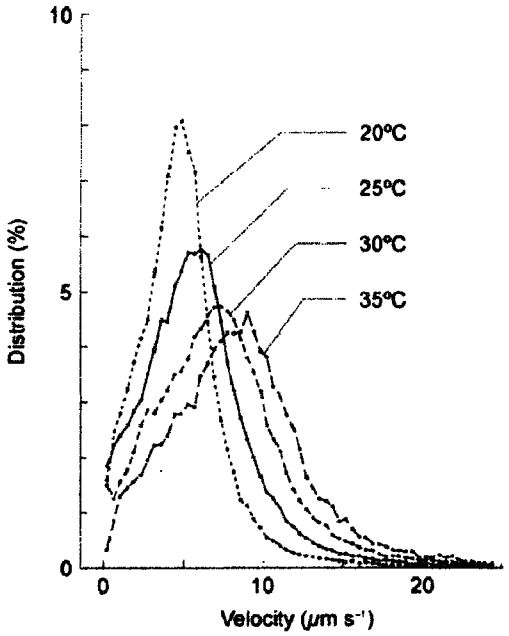

Figure 2. Distribution of the velocity of the fast-moving group at 4 different temperatures in the activating solution
The area under each curve is normalized to 100%. The number of records summated is: 11 (20°C), 11 (25°C), 13 (30°C) and 5 (35°C).

Figure 2 plots the velocity distribution at four different temperatures. An inspection of Fig. 2 reveals that the distribution is roughly Gaussian, peaks at ~6 μm s^{-1} (25°C) with a half-width of about 3 μm s^{-1}, but there is a long trailing tail at a larger velocity up to 25 μm s^{-1}, which may not be realistic. It turned out that this trailing tail was an artifact of the velocity calculation system, because a distribution of the velocity in the relaxing solution (absence of Ca^{2+}) or rigor solution (absence of MgATP) exhibited a similar trailing tail (data not shown). For this reason, only the velocity data within a half-width of the distribution were used to calculate the average velocity. The data were analysed for four different temperatures, and the results are plotted in Fig. 3 together with the standard deviation. This figure demonstrates that the velocity increased with an increase in the temperature. The temperature coefficient over a 10°C temperature range (Q_{10}) of the velocity was 1.46 ± 0.03 ($n = 3$) in the range 20°C to 35°C (where n is the number of data points).

Cross-bridge force at different temperatures during Ca^{2+} activation

Figure 4 represents a typical displacement of the bead position in the presence of Ca^{2+} and MgATP. Figure 5 represents averaged force plotted against the temperature

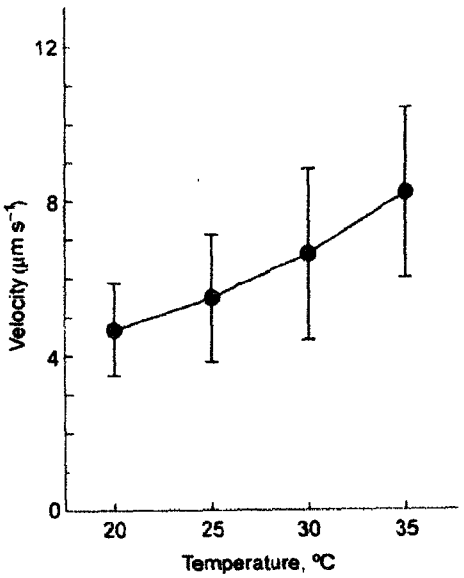

Figure 3. Sliding velocity plotted against the temperature for control conditions
The error bars represent ± S.D.

in the control activating solution (Table 1). As seen in Fig. 5, force was about the same at 20–25°C, but a gradual increase in force was observed as the temperature was raised from 25 to 35°C. From Fig. 5, the averaged Q_{10} was calculated to be 1.43 ± 0.19 ($n = 3$). This result is similar to that observed for unregulated actin filaments (Kawai *et al.* 2000).

The number of available cross-bridges

Because it is possible that the number of cross-bridges available for interaction with the regulated actin filament may vary at different temperatures, we decided to count the number of cross-bridges as described by Nishizaka *et al.* (2000). This experiment was carried out under rigor conditions in which no ATP was added (Table 1), since it is difficult to count the number of cross-bridges during Ca^{2+} activation. We reduced the concentration of HMM from 30 to 5 μg ml^{-1}, since counting becomes impractical when too many cross-bridges are interacting at the same time. It has been shown that the number of cross-bridges and the HMM concentration are proportionately related if the HMM concentration is less than 200 μg ml^{-1} (Nishizaka, 1996).

In Fig. 6*A*, a bead with a regulated actin filament that is interacting with HMM on the glass surface was caught by the optical tweezers. Care was taken to search for a linear filament, because subsequent data analysis is easier with a linear filament than a bent filament. If the bead was adsorbed onto the glass surface, it was first peeled off from the surface when possible. Then the bead was elevated at a constant speed (30–50 nm s^{-1}; Fig. 6*A*) and its horizontal position was monitored by phase-contrast microscope. Calculation of the bead position was carried out based on videotaped images. An example of the bead displacement is shown in Fig. 6*C*. As shown in this figure, the bead was displaced almost horizontally at a constant velocity as it was raised, and suddenly the bead was brought back to an earlier position. This is the time when a rigor cross-bridge breaks (Fig. 6*B*); hence, by counting the number of breaks, the number of available cross-bridges can be determined. The example of Fig. 6*C* has 10 break points, indicating 10 cross-bridges. If this number is divided by the length of the filament, then the cross-bridge density (equivalent to the available number of cross-bridges per unit length) on the filament can be obtained.

In Fig. 6*C*, we notice that there are pauses in the displacement trace at ~10 and ~15 s. These were the times when the filament was slack because the neighbouring HMM molecules were distant. It is also interesting to note

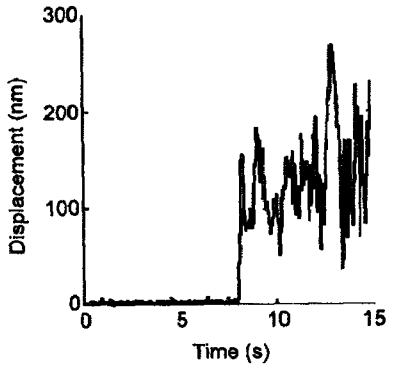

Figure 4. The time course of bead displacement to measure force on regulated actin filament
A filament-attached bead is placed within 1 μm above the HMM-coated surface, and filament–HMM interaction is initiated in the control activating solution. The displacement of the bead from the trap centre is traced against time at the rate of 30 frames per s^{-1}. Force is calculated as Force = kP × displacement, where kP is the spring constant of the optical trap (k = 0.531 fN mW^{-1} nm^{-1}), and P is the power of the incident laser beam at the level of the sample (150 mW).

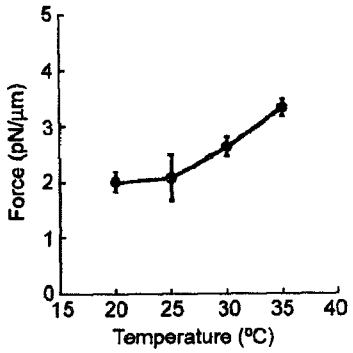

Figure 5. Force (in pN) per unit length (in μm) of regulated actin filament plotted against the temperature
The measurement was carried out in the presence of Ca^{2+} (pCa 4.74) and 2 mM MgATP. The error bars represent ± S.E.M. The number of observations is: 7 (20°C), 6 (25°C), 6 (30°C) and 5 (35°C).

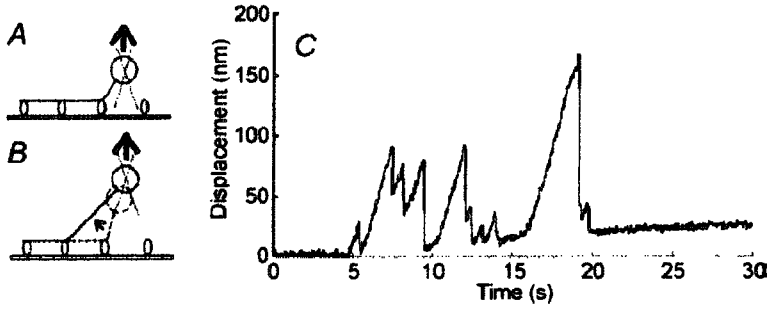

Figure 6. Experiment to break rigor cross-bridge
A and *B*, the method of breaking a rigor cross-bridge is depicted. A regulated actin filament is attached to a bead and makes a rigor interaction with HMM. *C*, the time course of the displacement of the horizontal position of the bead monitored by phase-contrast microscope. The bead was elevated at a constant speed in *A*, which displaced the bead from the trap centre. This is seen as a linear increase in the displacement in *C*. When a rigor cross-bridge breaks, the position of the bead returns to near starting point in *B*, which is seen as a vertical drop of the displacement in *C* (a break point). By counting the number of break points, the number of cross-bridges can be obtained. This number is divided by the length of the filament to obtain the number of cross-bridges per unit length. Ten break points can be counted from this trace. The length of this filament was 5.4 μm.

that the time of break and the break distance (horizontal drop of the displacement) are irregular. This fact implies that adjacent HMM molecules are not periodically spaced and/or consistently orientated. The main reason that the slope is nearly the same in all places ($\sim$40 nm s^{-1} in Fig. 6*C*) is that the angle formed by the glass surface and the HMM–bead vector did not vary much and the bead was elevated at a constant speed.

The number of cross-bridges is plotted in Fig. 7 as a function of the temperature. As seen in this figure, there is a small increase from 20 to 30°C and a significantly large increase from 30 to 35°C. These results demonstrate that the cross-bridge number increases as the temperature is increased with an average Q_{10} of 1.49 ± 0.31 ($n = 3$). This temperature dependence is similar to that in our earlier report (Kawai *et al.* 2000), which used a different method for counting the number of cross-bridges, in which $Q_{10} = 1.5 \pm 0.2$ ($n = 3$) was found. It is to be noted, however, that the present method detected roughly twice as many cross-bridges, presumably because of the differences in the HMM concentration and procedure used for preparing the flow cell.

Corrected cross-bridges force

Because the number of cross-bridges available for interaction with the regulated actin filament increased with the temperature (Fig. 7), the data of Fig. 5 were divided by the data of Fig. 7, and results are plotted in Fig. 8. The errors in Figs 5 and 7 were appropriately propagated and entered in Fig. 8 as described (Kawai *et al.* 2000). Figure 8 demonstrates that force per cross-bridge does not change much with the temperature in the range 20–35°C. From Fig. 8, the averaged Q_{10} was calculated to be 1.03 ± 0.25 ($n = 3$).

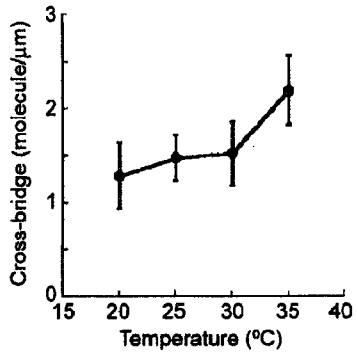

Figure 7. The number of cross-bridges per unit length (in μm) of regulated actin filament plotted against the temperature
The method of counting the number of cross-bridges is shown in Fig. 6. The error bars represent ± S.E.M.; n = 8 (20°C), 9 (25°C), 8 (30°C) and 10 (35°C).

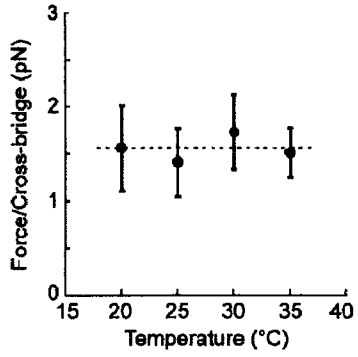

Figure 8. Corrected cross-bridge force plotted against temperature
The data were obtained by dividing the values of force (Fig. 5) by the number of cross-bridges (Fig. 7). The error bars are propagated from Figs 5 and 7 as described by Kawai *et al.* (2000).

Table 2. Force and velocity at 25°C

Condition	Force ± S.E.M. (*n*) (pN μm^{-1})	Velocity ± S.D. ($\mu m\ s^{-1}$)
Unregulated actin filament	1.89 ± 0.07 (9)	2.95 ± 1.11
Regulated actin filament	2.08 ± 0.48 (6)	5.49 ± 1.64
Regulated actin filament + 8 mM P_i	2.04 ± 0.08 (7)	5.87 ± 1.42
Actin filament with AS-Tm + Tn	2.68 ± 0.09 (6)	3.80 ± 1.44
Actin filament with AS-Δ23Tm + Tn	1.15 ± 0.04 (6)	1.98 ± 1.07

All measurements were carried out in the presence of Ca^{2+} (pCa 4.74) and 2 mM MgATP at 25°C.

Effect of P_i

In skinned fibres (or myofibrils), force is reduced as a low millimolar concentration of P_i is added to the activating solution (Cooke & Pate, 1985; Kawai, 1986; Fortune *et al.* 1991; Kawai & Halvorson, 1991; Dantzig *et al.* 1992; Tesi *et al.* 2002). For this reason, 8 mM P_i was added to the activating solution (by keeping ionic strength constant), and force and velocity were measured at 25°C (Table 2). Force was 2.08 pN μm^{-1} in the absence of added P_i, and 2.04 pN μm^{-1} in the presence of 8 mM P_i, indicating that there was no significant force attenuation as P_i was introduced to the activating solution. Similarly, there was no detectable difference in the velocity when 8 mM P_i was introduced to the activating solution. This result is consistent with our earlier results that used unregulated actin filaments (Kawai *et al.* 2000). The velocity result is consistent with the shortening velocity measurement on muscle fibres of Cooke & Pate (1985), but the force result is not consistent with that of muscle fibres (or myofibrils) reported by many investigators (Cooke & Pate, 1985; Kawai, 1986; Fortune *et al.* 1991; Kawai & Halvorson, 1991; Dantzig *et al.* 1992; Tesi *et al.* 2002).

Effect of regulatory proteins

For the next series of experiments, the force and velocity were compared in the absence and presence of a regulatory system at 25°C. As shown in Table 2, the velocity was 2.95 $\mu m\ s^{-1}$ in the absence and 5.49 $\mu m\ s^{-1}$ in the presence of the regulatory system. Thus, we conclude that the velocity was almost doubled by the regulatory system. The same table demonstrates that force was 1.89 pN μm^{-1} in the absence of the regulatory system and increased to 2.08 pN μm^{-1} in its presence. Thus, we conclude that force is enhanced by ~10% by the regulatory system.

To demonstrate that force and velocity are indeed influenced by the regulatory proteins, a truncated Tm mutant, AS-Δ23Tm (Hitchcock-DeGregori & Varnell, 1990), was used instead of normal Tm. AS-Δ23Tm lacks regions 2 and 3 out of 7 quasi-repeat regions that exist in normal Tm. Since AS-Δ23Tm is synthesized by *E. coli*, it lacks N-terminal acetylation that is normally present in mammalian Tm and which is necessary for its polymerization. To compensate for this effect, Ala-Ser- (AS-) was added at the N-terminus (Monteiro *et al.* 1994) and used as a control. We observed that the reconstituted thin filament with AS-Tm or AS-Δ23Tm was regulated by Ca^{2+} (see also Hitchcock-DeGregori & Varnell, 1990; Lu *et al.* 2003). Force developed with AS-Δ23Tm was 1.15 pN μm^{-1}, and only 43% of AS-Tm (2.68 pN μm^{-1}; Table 2). Sliding velocity of AS-Δ23Tm was 1.98 $\mu m\ s^{-1}$, and 52% of AS-Tm (3.80 $\mu m\ s^{-1}$; Table 2).

Discussion

The purpose of the present study was to determine whether the force generated between regulated actin filament and HMM at the single-molecule level remains the same when the temperature is increased. In our previous study, we showed in unregulated actin filaments that force per cross-bridge does not change with temperature (Kawai *et al.* 2000). However, in a more recent study using reconstituted skinned fibres, we found that an increase in isometric tension with temperature is much less when unregulated actin filaments are used instead of regulated actin filaments (Fujita & Kawai, 2002). Therefore, it is possible that the temperature effect is more enhanced in the *in vitro* motility study if the regulatory system (Tm and Tn) is present. For this series of experiments, we used actin filaments that were first attached to polystyrene beads; then both Tm and Tn were added. The interaction between regulated actin filaments and HMM was performed in the presence of Ca^{2+} and MgATP. It has been shown previously that Tm and the Tn complex stay bound to actin filaments up to about 40°C, although Tm without Tn dissociates at about 35°C (Ishiwata, 1978).

The velocity of the thin filament sliding on HMM was measured to compare the results with those measured previously. Our value (4.7–8.3 $\mu m\ s^{-1}$; Fig. 3) is similar to those observed by Honda & Asakura (1989) or by Homsher *et al.* (1992) in the same temperature range (20–35°C). These investigators used regulated actin filaments. Our velocity value is larger than those of Anson (1992) in rabbit fast-twitch muscles, and of Rossi *et al.* (2005) in rat type IIB muscles. This difference is likely to be related to the absence of regulatory proteins. The velocity nearly doubles with an addition of regulatory proteins (Table 2; see below).

As the temperature was elevated, we observed a moderate increase in force (Fig. 5; see also Kato *et al.* 1999). There are two possibilities to explain this finding: (1) the number of cross-bridges available for force generation increases with temperature; and (2) average force per cross-bridge increases with temperature. For this reason, we determined the number of cross-bridges in rigor conditions. This number increased in a similar manner to tension as the temperature was raised (Fig. 7). Therefore, we conclude that (1) is the case. There are several possibilities to account for the increase of the number of cross-bridges with temperature: (a) the Brownian motion of the HMM molecules may release more head domains from the glass surface at higher temperature without releasing the attached end; (b) the increased thermal motion of the thin filament could reach a larger number of HMM molecules, thereby forming the increased number of cross-bridges at higher temperature; and (c) the interaction between actin and myosin may be promoted at higher temperatures, because it is an endothermic reaction (Tonomura *et al.* 1962; Highsmith, 1977). However, whether this increase in the number of available cross-bridges is a physiological phenomenon is still an open question (Kato *et al.* 1999).

To calculate force per cross-bridge, we divided the force value in Fig. 5 by the number of cross-bridges (Fig. 7), and plotted the result in Fig. 8. This figure demonstrates that force per cross-bridge does not change with temperature when regulated actin filaments are used, and it averages 1.57 ± 0.07 pN ($n = 4$; Fig. 8, dashed line). This conclusion is consistent with our earlier results using unregulated actin filaments (Kawai *et al.* 2000). The force plotted in Fig. 8 is not the averaged unitary force. This is because the concentration of HMM used in Fig. 5 is $30\,\mu g\,ml^{-1}$, whereas that used in Fig. 7 is $5\,\mu g\,ml^{-1}$. Because the HMM concentration and the number of cross-bridges are proportional within this range (Nishizaka, 1996), the value in Fig. 8 must be divided by 6 (= 30/5) to obtain average unitary force, i.e. 0.26 pN can be deduced. If we assume that the duty ratio is about 0.1 (Howard, 1997), we can then conclude that the unitary force is about 2.6 pN. This value is within the range of those previously reported in single-molecule experiments (1–6 pN: Finer *et al.* 1994; Miyata *et al.* 1995; Molloy *et al.* 1995; Ishijima *et al.* 1996).

In muscle fibre studies, it has been reported that an increase in temperature resulted in increased isometric tension in maximally activated mammalian skeletal muscle fibres (Goldman *et al.* 1987; Bershitsky & Tsaturyan, 1992, 2002; Zhao & Kawai, 1994; Ranatunga, 1996; Coupland *et al.* 2001; Wang & Kawai, 2001) as well as in cardiac muscle fibres (Ranatunga, 1999; Fujita & Kawai, 2002). This process is called 'endothermic' because higher temperature favours larger force, which is consistent with the fact that heat is absorbed on force generation. There are two mechanisms proposed to account for this temperature effect. The first mechanism is a shift of equilibrium between the force-generating state(s) and the non-force-generating state(s) (Zhao & Kawai, 1994; Head *et al.* 1995; Coupland *et al.* 2001; Wang & Kawai, 2001). The second mechanism is an increase in the force per cross-bridge, but the number of force-generating cross-bridges does not change (Goldman *et al.* 1987; Kraft & Brenner, 1997; Bershitsky & Tsaturyan, 2002; Piazzesi *et al.* 2003; Linari *et al.* 2005). The first mechanism was proposed because the equilibrium constant of the force generation step increased with temperature (Zhao & Kawai, 1994; Wang & Kawai, 2001), and the tension–temperature plot can be predicted based on the equilibrium shift argument (Kawai, 2003). This mechanism is consistent with the hydrophobic interaction, the endothermic reaction, the positive standard entropy change and the negative heat capacity change, as observed in the muscle fibre system (Zhao & Kawai, 1994; Murphy *et al.* 1996; Wang & Kawai, 2001) and as reviewed by Kawai (2003). The second mechanism was proposed because stiffness did not change much with the temperature (Bershitsky *et al.*, 1997), or the change was less in stiffness than in tension. However, it has been found that series compliance plays a significant role in measured stiffness (Huxley *et al.* 1994; Kojima *et al.* 1994; Wakabayashi *et al.* 1994; Higuchi *et al.* 1995), and that the stiffness–temperature plot can be predicted based on a series compliance model in which ~50% of the compliance is placed in the series elements (Kawai, 2003). Most temperature studies (other than ours) were carried out in the absence of added P_i, a condition that increases the number of force-generating cross-bridges (Fortune *et al.* 1991; Kawai & Halvorson, 1991; Dantzig *et al.* 1992), thereby maximizing the stiffness in the overlap zone of the thick and the thin filaments. In this condition, a further increase in the number of force-generating cross-bridges with temperature may not be detected as a stiffness increase because of the series compliance. Our present result using the *in vitro* system is consistent with the first mechanism in the sense that the unitary force does not change with temperature.

The force and velocity are not modified much when 8 mM P_i is added in the activating solution in single molecules, and this result is the same whether the regulatory system is included (Table 2) or not (Kawai *et al.* 2000). These results using single molecules are very different from those using single fibres (or myofibrils), where addition of several millimolar P_i diminishes isometric force (Cooke & Pate, 1985; Kawai, 1986; Fortune *et al.* 1991; Kawai & Halvorson, 1991; Dantzig *et al.* 1992; Tesi *et al.* 2002). The cause of this discrepancy is not immediately apparent, but it is possible that the low ionic strength condition (~50 mM) used in the *in vitro* motility system makes a difference to the results; muscle

fibre experiments are typically carried out at around physiological ionic strength (180–200 mM). Because the electrostatic interaction is stronger at low ionic strength, it is possible that the negatively charged P_i ion may be trapped by positively charged amino acid residues of myosin before reaching the P_i-binding site. It is also possible that the presence of a large-scale co-operativity may modify the P_i-binding process.

When the regulatory system is added, both force and velocity increased (Table 2). These results are consistent with those of other investigators using single molecules (Gordon *et al.* 1998; VanBuren *et al.* 1999; Bing *et al.* 2000*a*,*b*; Homsher *et al.* 2000, 2003) and single fibres (Fujita *et al.* 2002, 2004; Fujita & Kawai, 2002). These results are in accord with the hypothesis that Tm and Tn apply a positive allosteric effect on the actomyosin interaction. This hypothesis is further supported by the experiment using a truncated mutant Tm. When AS-Δ23Tm is used, both force and velocity decrease to 43 and 52% of control values, respectively (Table 2). This observation demonstrates a presence of the negative allosteric effect of AS-Δ23Tm on the actomyosin interaction. These results are also consistent with those that measured ATP hydrolysis rate (Hitchcock-DeGregori & Varnell, 1990), *in vitro* motility assay (Landis *et al.* 1999), and reconstituted cardiac fibres (Lu *et al.* 2003), which compared the effect of native Tm, AS-Tm and AS-Δ23Tm.

The fact that the unitary force is independent of the temperature was also reported in the kinesin–microtubule system in the temperature range 15–35°C (Kawaguchi & Ishiwata, 2000). This fact may imply that the temperature insensitivity of the single molecular force is a fundamental property of a motor protein, and supports the hypothesis that force is associated with a particular molecular structure of the motor, which is consistent with the current knowledge of the mechanisms of force generation. In myosin, force is generated as a result of a swing of the lever arm (Dominguez *et al.* 1998; Geeves & Holmes, 1999; Holmes *et al.* 2004). Therefore, the force (ΔF) generated by a single molecule is:

$$\Delta F = \sigma \Delta L \quad (1)$$

where ΔL is the swing of the lever arm, which is known as the step size, and σ is the stiffness of series elements, including that of cross-bridges. The size of the lever arm is determined by the molecular structure of myosin, and it does not vary with temperature. The step size is determined by the length of the lever arm, hence the step size does not vary with temperature. σ is approximately independent of temperature because it is determined by the molecular structure of the myosin head and in-series elements to the head. Therefore, we can appreciate from eqn (1) that ΔF must be independent of the temperature. In conclusion, we have demonstrated that force per cross-bridge does not change with temperature in experiments using regulated actin filaments and HMM.

References

Anson M (1992). Temperature dependence and Arrhenius activation energy of F-actin velocity generated in vitro by skeletal myosin. *J Mol Biol* **224**, 1029–1038.

Bershitsky SY & Tsaturyan AK (1992). Tension responses to Joul temperature jump in skinned rabbit muscle fibres. *J Physiol* **447**, 425–448.

Bershitsky SY & Tsaturyan AK (2002). The elementary force generation process probed by temperature and length perturbations in muscle fibres from the rabbit. *J Physiol* **540**, 971–988.

Bershitsky SY, Tsaturyan AK, Bershitskaya ON, Mashanov GI, Brown P, Burns R & Ferenczi MA (1997). Muscle force is generated by myosin heads stereospecifically attached to actin. *Nature* **388**, 186–190.

Bing W, Knott A & Marston SB (2000*a*). A simple method for measuring the relative force exerted by myosin on actin filaments in the in vitro motility assay: evidence that tropomyosin and troponin increase force in single thin filaments. *Biochem J* **350**, 693–699.

Bing W, Knott A, Redwood C, Esposito G, Purcell I, Watkins H & Marston S (2000*b*). Effect of hypertrophic cardiomyopathy mutations in human cardiac muscle alpha-tropomyosin (Asp175Asn and Glu180Gly) on the regulatory properties of human cardiac troponin determined by in vitro motility assay. *J Mol Cell Cardiol* **32**, 1489–1498.

VanBuren P, Palmiter KA & Warshaw DM (1999). Tropomyosin directly modulates actomyosin mechanical performance at the level of a single actin filament. *Proc Natl Acad Sci USA* **96**, 12488–12493.

Cooke R & Pate E (1985). The effects of ADP and phosphate on the contraction of muscle fibers. *Biophys J* **48**, 789–798.

Coupland ME, Puchert E & Ranatunga KW (2001). Temperature dependence of active tension in mammalian (rabbit psoas) muscle fibres: effect of inorganic phosphate. *J Physiol* **536**, 879–891.

Dantzig J, Goldman Y, Millar NC, Lacktis J & Homsher E (1992). Reversal of the cross-bridge force-generation transition by the photogeneration of phosphate in rabbit psoas muscle fibers. *J Physiol* **451**, 247–278.

Dominguez R, Freyzon Y, Trybus KM & Cohen C (1998). Crystal structure of a vertebrate smooth muscle myosin motor domain and its complex with the essential light chain: visualization of the pre-power stroke state. *Cell* **94**, 559–571.

Finer JT, Simmons RM & Spudich JA (1994). Single myosin mechanics: piconewton forces and nanometre steps. *Nature* **368**, 113–119.

Fortune NS, Geeves MA & Ranatunga KW (1991). Tension responses to rapid pressure release in glycerinated rabbit muscle fibers. *Proc Natl Acad Sci USA* **88**, 7323–7327.

Fujita H & Kawai M (2002). Temperature effect on isometric tension is mediated by regulatory proteins tropomyosin and troponin in bovine myocardium. *J Physiol* **539**, 267–276.

Fujita H, Lu X, Suzuki M, Ishiwata S & Kawai M (2004). The effect of tropomyosin on force and elementary steps of the cross-bridge cycle in reconstituted bovine myocardium. *J Physiol* **556**, 637–649.

Fujita H, Sasaki D, Ishiwata S & Kawai M (2002). Elementary steps of the cross-bridge cycle in bovine myocardium with and without regulatory proteins. *Biophys J* **82**, 915–928.

Fujita H, Yasuda K, Niitsu S, Funatsu T & Ishiwata S (1996). Structural and functional reconstitution of thin filaments in the contractile apparatus of cardiac muscle. *Biophys J* **71**, 2307–2318.

Geeves MA & Holmes KC (1999). Structural mechanism of muscle contraction. *Annu Rev Biochem* **68**, 687–728.

Goldman YE, McCray JA & Ranatunga KW (1987). Transient tension changes initiated by laser temperature jumps in rabbit psoas muscle fibres. *J Physiol* **392**, 71–95.

Gordon AM, Chen Y, Liang B, LaMadrid M, Luo Z & Chase PB (1998). Skeletal muscle regulatory proteins enhance F-actin in vitro motility. *Adv Exp Med Biol* **453**, 187–196.

Harada Y, Sakurada K, Aoki T, Thomas DD & Yanagida T (1990). Mechanochemical coupling in actomyosin energy transduction studied by in vitro movement assay. *J Mol Biol* **216**, 49–68.

Head JG, Ritchie MD & Geeves MA (1995). Characterization of the equilibrium between blocked and closed states of muscle thin filaments. *Eur J Biochem* **227**, 694–699.

Highsmith S (1977). The effects of temperature and salts on myosin subfragment-1 and F-actin association. *Arch Biochem Biophys* **180**, 404–408.

Higuchi H, Yanagida T & Goldman YE (1995). Compliance of thin filaments in skinned fibers of rabbit skeletal muscle. *Biophys J* **69**, 1000–1010.

Hitchcock-DeGregori SE & Varnell TA (1990). Tm has discrete actin-binding sites with sevenfold and fourteenfold periodicities. *J Mol Biol* **214**, 885–896.

Holmes KC, Schröder RR, Sweeney HL & Houdusse A (2004). The structure of the rigor complex and its implications for the power stroke. *Philos Trans R Soc Lond B Biol Sci* **359**, 1819–1828.

Homsher E, Lee DM, Morris C, Pavlov D & Tobacman LS (2000). Regulation of force and unloaded sliding speed in single thin filaments: effects of regulatory proteins and calcium. *J Physiol* **524**, 233–243.

Homsher E, Nili M, Chen IY & Tobacman LS (2003). Regulatory proteins alter nucleotide binding to acto-myosin of sliding filaments in motility assays. *Biophys J* **85**, 1046–1052.

Homsher E, Wang F & Sellers JR (1992). Factors affecting movement of F-actin filaments propelled by skeletal muscle heavy meromyosin. *Am J Physiol* **262**, C714–C723.

Honda H & Asakura S (1989). Calcium-triggered movement of regulated actin in vitro. A fluorescence microscopy study. *J Mol Biol* **205**, 677–683.

Howard J (1997). Molecular motors: structural adaptations to cellular functions. *Nature* **389**, 561–567.

Huxley HE, Stewart A, Sosa H & Irving T (1994). X-ray diffraction measurements of the extensibility of actin and myosin filaments in contracting muscle. *Biophys J* **67**, 2411–2421.

Ishijima A, Kojima H, Higuchi H, Harada Y, Funatsu T & Yanagida T (1996). Multiple- and single-molecule analysis of the actomyosin motor by nanometer-piconewton manipulation with a microneedle: unitary steps and force. *Biophys J* **70**, 383–400.

Ishiwata S (1973). A study on the F-actin-tropomyosin-troponin complex. I. Gel-filament transformation. *Biochim Biophys Acta* **303**, 77–89.

Ishiwata S (1978). Studies on the F-actin.tropomyosin. troponin complex. III. Effects of troponin components and calcium ion on the binding affinity between tropomyosin and F-actin. *Biochim Biophys Acta* **534**, 350–357.

Ishiwata S (1998). The use of fluorescent probes. In *Current Methods in Muscle Physiology*, ed. Sugi H, pp. 199–222. Oxford University Press, Oxford.

Kato H, Nishizaka T, Iga T, Kinosita K Jr & Ishiwata S (1999). Imaging of thermal activation of actomyosin motors. *Proc Natl Acad Sci USA* **96**, 9602–9606.

Kawaguchi K & Ishiwata S (2000). Temperature dependence of force, velocity, and processivity of single kinesin molecules. *Biochem Biophys Res Commun* **272**, 895–899.

Kawaguchi K & Ishiwata S (2001). Thermal activation of single kinesin molecules with temperature pulse microscopy. *Cell Motil Cytoskeleton* **49**, 41–47.

Kawai M (1986). The role of orthophosphate in crossbridge kinetics in chemically skinned rabbit psoas fibres as detected with sinusoidal and step length alterations. *J Muscle Res Cell Motil* **7**, 421–434.

Kawai M (2003). What do we learn by studying the temperature effect on isometric tension and tension transients in mammalian striated muscle fibres? *J Muscle Res Cell Mot* **24**, 127–138.

Kawai M & Halvorson HR (1991). Two step mechanism of phosphate release and the mechanism of force generation in chemically skinned fibers of rabbit psoas muscle. *Biophys J* **59**, 329–342.

Kawai M, Kawaguchi K, Saito M & Ishiwata S (2000). Temperature change does not affect force between single actin filaments and HMM from rabbit muscles. *Biophys J* **78**, 3112–3119.

Kishino A & Yanagida T (1988). Force measurements by micromanipulation of a single actin filament by glass needles. *Nature* **334**, 74–76.

Kojima H, Ishijima A & Yanagida T (1994). Direct measurement of stiffness of single actin filaments with and without tropomyosin by in vitro nanomanipulation. *Proc Natl Acad Sci USA* **91**, 12962–12966.

Kraft T & Brenner B (1997). Force enhancement without changes in cross-bridge turnover kinetics: the effect of EMD 57033. *Biophys J* **72**, 272–282.

Kurokawa H, Fujii W, Ohmi K, Sakurai T & Nonomura Y (1990). Simple and rapid purification of brevin. *Biochem Biophys Res Commun* **168**, 451–457.

Landis C, Back N, Homsher E & Tobacman LS (1999). Effects of tropomyosin internal deletions on thin filament function. *J Biol Chem* **274**, 31279–31285.

Linari M, Brunello E, Reconditi M, Sun Y-B, Panine P, Narayanan T, Piazzesi G, Lombardi V & Irving M, (2005).The structural basis of the increase in isometric force production with temperature in frog skeletal muscle. *J Physiol* **567.2**, 459–469.

Lu X, Tobacman LS & Kawai M (2003). Effects of tropomyosin internal deletion Δ23Tm on isometric tension and the cross-bridge kinetics in bovine myocardium. *J Physiol* **553.2**, 457–471.

Miyata H, Hakozaki H, Yoshikawa H, Suzuki N, Kinosita K Jr, Nishizaka T & Ishiwata S (1994). Stepwise motion of an actin filament over small number of heavy meromyosin molecules is revealed in an in vitro motility assay. *J Biochem* **115**, 644–647.

Miyata H, Yoshikawa H, Hakozaki H, Suzuki N, Furuno T, Ikegami A, Kinosita K Jr, Nishizaka T & Ishiwata S (1995). Mechanical measurements of single actomyosin motor force. *Biophys J* **68**, 286S–290S.

Molloy JE, Burns JE, Kendrick-Jones J, Tregear RT & White DCS (1995). Movement and force produced by a single myosin head. *Nature* **378**, 209–212.

Monteiro PB, Lataro RC, Ferro JA & Reinach F de C (1994). Functional alpha-tropomyosin produced in Escherichia coli. A dipeptide extension can substitute the amino-terminal acetyl group. *J Biol Chem* **269**, 10461–10466.

Murphy KP, Zhao Y & Kawai M (1996). Molecular forces involved in force generation during skeletal muscle contraction. *J Exp Biol* **199**, 2565–2571.

Nishizaka T (1996). Microscopic analysis of function and mechanical properties of acto-myosin motor at single molecular level. PhD Thesis, Department of Physics, School of Science and Engineering, Waseda University, Tokyo, Japan. 160 pp.

Nishizaka T, Miyata H, Yoshikawa H, Ishiwata S & Kinosita K Jr (1995*a*). Unbinding force of a single motor molecule of muscle measured using optical tweezers. *Nature* **377**, 251–254.

Nishizaka T, Miyata H, Yoshikawa H, Ishiwata S & Kinosita K Jr (1995*b*). Mechanical properties of a single protein motor of muscle studied by optical tweezers. *Biophys J* **68**, 75S.

Nishizaka T, Seo R, Tadakuma H, Kinosita K Jr & Ishiwata S (2000). Characterization of single actomyosin rigor bonds: load dependence of lifetime and mechanical properties. *Biophys J* **79**, 962–974.

Piazzesi G, Reconditi M, Koubassova N, Decostre V, Linari M, Lucii L & Lombardi V (2003). Temperature dependence of the force-generating process in single fibres from frog skeletal muscle. *J Physiol* **549**, 93–106.

Rall JA & Woledge RC (1990). Influence of temperature on mechanics and energetics of muscle contraction. *Am J Physiol* **259**, R197–R203.

Ranatunga KW (1996). Endothermic force generation in fast and slow mammalian (rabbit) muscle fibers. *Biophys J* **71**, 1905–1913.

Ranatunga KW (1999). Endothermic force generation in skinned cardiac muscle from rat. *J Muscle Res Cell Motil* **20**, 489–496.

Rossi R, Maffei M, Bottinelli R & Canepari M (2005). Temperature dependence of speed of actin filaments propelled by slow and fast skeletal myosin isoforms. *J Appl Physiol* **99**, 2239–2245.

Suzuki N, Miyata H, Ishiwata S & Kinosita K Jr (1996). Preparation of bead-tailed actin filaments: estimation of the torque produced by the sliding force in an in vitro motility assay. *Biophys J* **70**, 401–408.

Tesi C, Colomo F, Piroddi N & Poggesi C (2002). Characterization of the cross-bridge force-generating step using inorganic phosphate and BDM in myofibrils from rabbit skeletal muscles. *J Physiol* **541**, 189–199.

Tonomura Y, Tokura S & Sekiya K (1962). Binding of myosin A to F-actin. *J Biol Chem* **237**, 1074–1081.

Uttenweiler D, Veigel C, Steubing R, Goetz C, Mann S, Haubecker H, Jaehne B & Fink RHA (2000). Motion determination in actin filament fluorescence images with a spatio-temporal orientation analysis method. *Biophys J* **78**, 2709–2715.

Wakabayashi K, Sugimoto Y, Tanaka H, Ueno Y, Takezawa Y & Amemiya Y (1994). X-ray diffraction evidence for the extensibility of actin and myosin filaments during muscle contraction. *Biophys J* **67**, 2422–2435.

Wang G & Kawai M (2001). Effect of temperature on elementary steps of the cross-bridge cycle in rabbit soleus slow-twitch muscle fibres. *J Physiol* **531**, 219–234.

Zhao Y & Kawai M (1994). Kinetic and thermodynamic studies of the cross-bridge cycle in rabbit psoas muscle fibers. *Biophys J* **67**, 1655–1668.

Acknowledgements

We would like to express our thanks to Dr Larry S. Tobacman for the gift of AS-Δ23Tm and AS Tm, to Dr Daisuke Sasaki for the gift of Tm and Tn, and to Dr Madoka Suzuki for technical help. This work was carried out during the tenure of a long-term fellowship to M.K. awarded by the Japan Society for Promotion of Science in the spring of 2003. This work was supported in part by an NIH grant HL70041 to M.K., and by an LFSP Baden-Württemberg grant to R.H.A.F. This research was also supported in part by Grants-in-Aid for Specially Promoted Research and for the 21st century COE program (Physics of Self-organization Systems) at Waseda University from the Ministry of Education, Sports, Culture, Science and Technology of Japan to S.I. The contents of this work are solely the responsibility of the authors and do not necessarily represent the official view of awarding organizations.

J Muscle Res Cell Motil (2006) 27:455–468
DOI 10.1007/s10974-006-9075-4

ORIGINAL PAPER

Use of thin filament reconstituted muscle fibres to probe the mechanism of force generation

Masataka Kawai · Shin'ichi Ishiwata

Received: 1 May 2006 / Accepted: 21 June 2006 / Published online: 15 August 2006

Abstract The technique of selective removal of the thin filament by gelsolin in bovine cardiac muscle fibres, and reconstitution of the thin filament from isolated proteins is reviewed, and papers that used reconstituted preparations are discussed. By comparing the results obtained in the absence/presence of regulatory proteins tropomyosin (Tm) and troponin (Tn), it is concluded that the role of Tm and Tn in force generation is not only to expose the binding site of actin to myosin, but also to modify actin for better stereospecific and hydrophobic interaction with myosin. This conclusion is further supported by experiments that used a truncated Tm mutant and the temperature study of reconstituted fibres. The conclusion is consistent with the hypothesis that there are three states in the thin filament: blocked state, closed state, and open state. Tm is the major player to produce these effects, with Tn playing the role of Ca^{2+} sensing and signal transmission mechanism. Experiments that changed the number of negative charges at the N-terminal finger of actin demonstrates that this part of actin is essential to promote the strong interaction between actin and myosin molecules, in addition to the well-known weak interaction that positions the myosin head at the active site of actin prior to force generation.

Keywords Actin · Regulatory proteins · Tropomyosin · Troponin · Myosin · Gelsolin · Cross-bridge kinetics · Sinusoidal analysis · BDM

M. Kawai (✉)
Department of Anatomy and Cell Biology, College of Medicine, The University of Iowa, Iowa City, IA 52242, USA
e-mail: masataka-kawai@uiowa.edu

Shin'ichi Ishiwata
Department of Physics, School of Science and Engineering, and Advanced Research Institute for Science and Engineering, Waseda University, Tokyo 169-8555, Japan

Thin filament reconstituted muscle fibre system

For the purpose of understanding the cross-bridge interaction with actin and the role of regulatory proteins in this interaction, we reconstituted the thin filament in cardiac muscle fibres. This method is schematically represented in Fig. 1. The thin filament is first removed by gelsolin (Fig. 1A to 1B), followed by sequential reconstitution with G-actin (Fig. 1C), and regulatory proteins, tropomyosin (Tm) and troponin (Tn) (Fig. 1D). Gelsolin is an actin and thin filament severing protein, hence its action is specific and it does not disrupt other sarcomeric structure. However, overtreatment with gelsolin would disrupt the Z-line structure, because actin is one of the main constituents in the Z-line. The thin filament reconstitution method was initially developed at Ishiwata's laboratory and the key properties of the reconstituted fibres, such as the recovery of isometric tension, the tension–pCa relationship, and the function of spontaneous oscillatory contraction, were examined on skeletal fibres (Funatsu et al. 1994), followed by cardiac fibres (Fujita et al. 1996; Fujita and Ishiwata 1998, 1999; for brief review see Ishiwata et al. 1998). In these works, it was demonstrated that bovine cardiac fibres were successful as the reconstituted system, in which actin, Tm and Tn can be

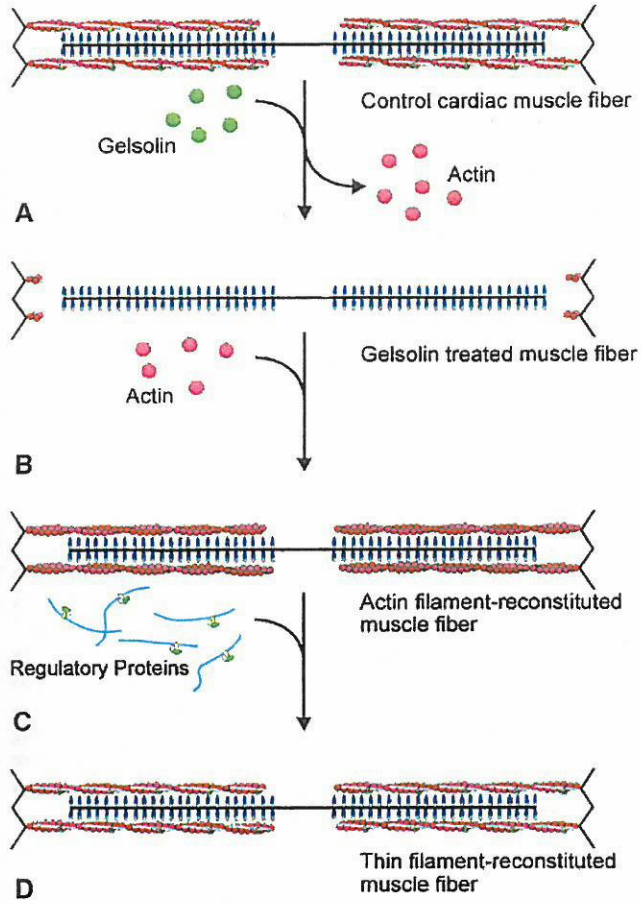

Fig. 1 Schematic diagram illustrating the removal and reconstitution protocol of the thin filament. The thin filament in cardiac muscle fibres (**A**) is removed by gelsolin, yielding thin filament-free fibres (**B**). (**C**) The actin filament is reconstituted by adding exogenous G-actin under the polymerizing condition. The thin filament is further reconstituted by adding nTm that contains both Tm and Tn (**D**). Dotted lines represent connectin (titin) that anchors the thick filament to the Z-line. Redrawn from *Biophysical Journal* (Fujita et al. 1996; Fujita and Ishiwata 1998)

replaced with those prepared from other muscles, for example, rabbit skeletal muscle proteins (Fujita et al. 1996; Fujita and Ishiwata 1999). The reconstitution method in cardiac fibres was successfully applied at Kawai's laboratory to study the role of regulatory proteins (Fujita et al. 2002, 2004; Fujita and Kawai 2002; Lu et al. 2003) and the role of N-terminal negative charges of actin (Lu et al. 2005) in cross-bridge kinetics.

Because the most of the work on thin filament reconstitution was performed on bovine cardiac fibres, we focus on this preparation in this review. From the bovine heart of 1–2 years of age, one can find ~80% of the time a nice trabecular muscle that is thin (2–4 mm) and slender (10–30 mm) with two ends suspended in the right ventricle but otherwise freely floating, from which long muscle bundles (about 0.5 mm in diameter, 10 mm in length) can be dissected. This is skinned for 7–14 days in the solution that contains (mM) 10 EGTA, 2 MgATP, 5 ATP, 122 KPropionate (Prop), 2 DTT, 30 BDM (2,3-butanedione 2-monoxime), and 10 MOPS (pH 7.0) at 2°C, and stored in the storage solution (50% glycerol is included in the skinning solution) at −20°C. Propionate has been used at Kawai's laboratory for muscle fibre studies for more than 20 years, however, it may not have been the best choice of anion (see Andrews et al. 1991). A fibre with the diameter of ~90 μm is dissected from a skinned bundle on the day of an experiment, and two ends of the preparation are respectively attached to a length driver and a tension transducer by nail polish. The fibre is then bathed at 2°C in the relaxing solution that contains (mM) 6 EGTA, 2.2 MgATP, 5 ATP, 8 phosphate (Pi), 41 NaProp, 75 KProp, 10 MOPS, and 200 ionic strength (pH 7.0). The pCa of this solution is >9 when contaminating Ca is considered (Reuben et al. 1971). The volume of the muscle chamber is 80 μl. A small volume is advantageous because the quantity of proteins used for reconstitution is usually limited. 90 μm is the optimal diameter of the preparation, which is important for good reproducibility of the results. The fibre is further skinned with 1% Triton-X100 in the relaxing solution for 20 min at 25°C. If a diffraction pattern is visible with He–Ne laser, the sarcomere length is adjusted to 2.0 μm. It is often difficult to obtain a good diffraction pattern in cardiac fibres, in which case the fibre is stretched slightly to remove the slack and to witness the sign of a tension rise. With this method the sarcomere length was shown to be in the range of 1.9–2.1 μm by confocal microscopy after staining with rhodamine-conjugated phalloidin (Fujita et al. 1996, 2002; Fujita and Ishiwata 1998, 1999). At this stage, the fibre length (L_0) is determined, which ranges 2–3 mm. The preparation is activated briefly for initial control tension at 25°C with the activating solution (5S0P) that contains (mM) 6 CaEGTA, 5.8 MgATP, 1.4 ATP, 15 creatine phosphate (CP), 1 NaProp, 92 KProp, 10 NaN_3, 10 MOPS, and 320 unit/ml creatine kinase (CK) (ionic strength 200 mM, pCa 4.66, pH 7.0), and relaxed immediately (Fig. 2A). The activation has to be brief or deterioration in the fibre may occur, which causes undesirable results in the subsequent reconstitution.

To perform reconstitution, the thin filament is first extracted in the solution that contains (mM) 2 CaEGTA, 2.2 ATP, 121 KCl, 4.25 $MgCl_2$, 2 leupeptin, 2 diisopropyl fluorophosphates (DFP), 40 BDM, 20 MOPS (pCa 4.66, pH 7.0) and ~0.3 mg/ml gelsolin at 2°C (Fig. 1A → B). Gelsolin has an apparent molecular

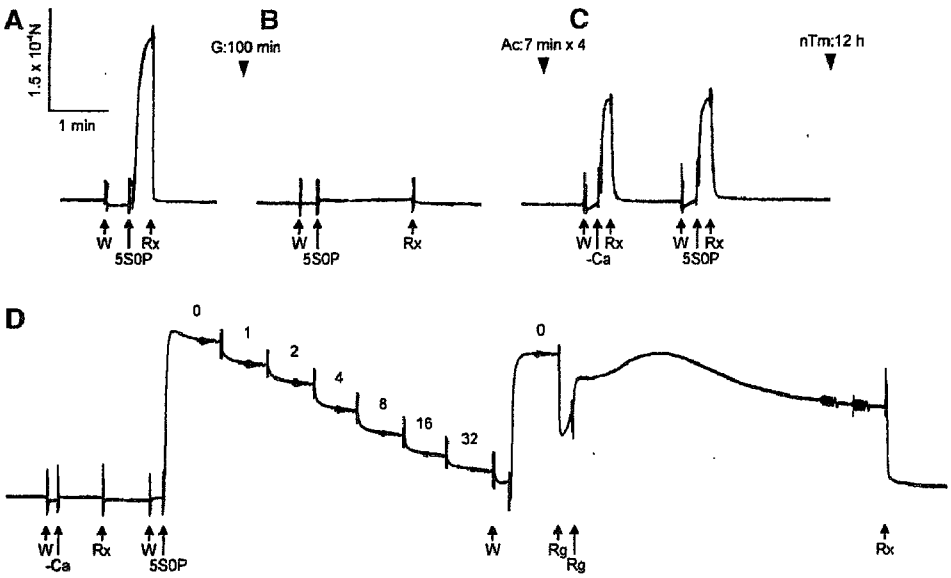

Fig. 2 A slow pen trace of isometric tension at each stage of removal and reconstitution of the thin filament. **A**, Control myocardium; **B**, after gelsolin treatment (G) for 100 min; **C**, after actin filament-reconstitution (Ac); and **D**, after thin filament-reconstitution (nTm). Control myocardium was first activated in the 5S0P solution (pCa 4.66) at 25°C (**A**) to test for isometric tension. After gelsolin treatment, myocardium was immersed in the 5S0P solution to confirm the removal of thin filament (**B**). After reconstitution of actin filament (Ac) in **C**, myocardium was immersed in the solution with Ca^{2+} (5S0P) and without Ca^{2+} (–Ca) at 25°C. The relaxation was attained in the solution containing 40 mM BDM (Rx). After reconstitution of regulatory proteins (nTm) in **D**, active tension did not develop without Ca^{2+} (–Ca), but it developed with Ca^{2+} (5S0P). In **D**, the complex modulus data were collected at seven different Pi concentrations (0–32 mM as indicated), and the initial activation at 0 mM Pi was repeated to detect any deterioration. All activations including rigor were performed at 25°C, and all records in this figure were taken from the same preparation. Reproduced from *Biophysical Journal* (Fujita et al. 2002) with permission

weight of ~86 kD, and it is purified from bovine plasma by the method developed by Kurokawa et al. (1990); its purity is checked by SDS-PAGE. To inhibit the trace amount of contaminating proteases, leupeptin and DFP are used so that other contractile structures are not destroyed. Ca^{2+} is a cofactor of gelsolin action, hence it is essential to include this ion in the extraction solution. Because Ca^{2+} activates the muscle fibre system, 40 mM BDM is added to prevent force generation (Blanchard et al. 1990; Herrmann et al. 1992; Zhao and Kawai 1994b). Generally, 60–120 min of extraction time is needed at 2°C, depending on the strength of gelsolin. The temperature can be raised if the extraction time exceeds 120 min. The degree of extraction is judged by a brief active tension at 25°C (Fig. 2B, 5S0P). If the tension is < 10% of the control tension, the extraction is stopped by washing out the gelsolin with the relaxing solution. It is important to know that overtreatment of fibres with gelsolin is not good for subsequent reconstitution, because a short segment of the thin filament remaining at the Z-line (Fig. 1B) is essential to nucleate the growth of the actin filament (Fujita et al. 1996).

The thin filament extracted fibre is then subjected to actin filament reconstitution (Fig. 1B → C) from G-actin under the polymerizing condition in the solution that contains (mM) 4 EGTA, 4 MgATP, 8 KCl, 80 KI, 40 BDM, 20 Pi (pH 7.0), and 1 mg/ml G-actin. A problem here is that F-actin may nucleate everywhere in the muscle chamber and form quickly. The F-actin formation outside the fibre can be seen as clouding of the solution which turns into a gel shortly. To delay this nucleation and to use actin fragments remaining at the Z-line as the polymerization seeds, 80 mM KI is used instead of KCl (Funatsu et al. 1994; Fujita et al. 1996) for the reconstitution solution, which is freshly made each time, and the duration of reconstitution is limited to 7 min each and performed at 0°C. Because actin elongation is not adequate with the short time interval (7 min), the reconstitution procedure is repeated. Four treatments will usually recover 50–70% of initial tension. If the tension recovery is less than this, the treatment may be repeated for 2–4 more times. The reconstitution is carried out in the presence of 40 mM BDM, because the reconstituted actin filament is spontaneously active owing to the lack of regulatory proteins. Therefore, the "active tension" is induced by deletion of BDM and by elevating the temperature to 25°C (Fig. 2C), and "relaxation" is induced by the solution that adds 40 mM BDM to the relaxing

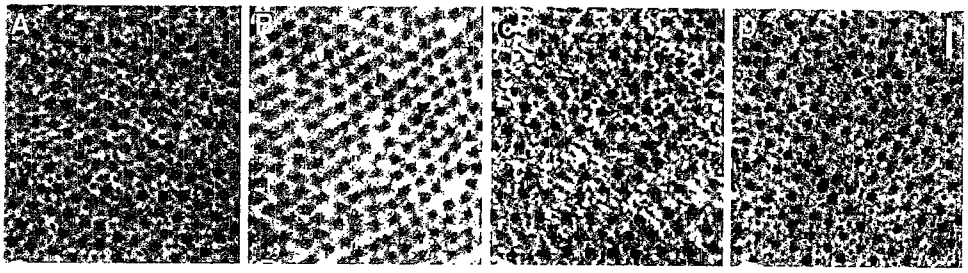

Fig. 3 Electron microscopic images of cross section of myocardium at each stage of extraction and reconstitution. (**A**) Control myocardium, (**B**) after gelsolin treatment, (**C**) after actin filament reconstitution, and (**D**) after the thin filament reconstitution with Tm and Tn. The scale bar is 100 nm. Reproduced from *Journal of Physiology* (Lu et al. 2003) with permission

solution and by lowering the temperature to 2°C. As it has been known for some time, active tension increases with temperature in mammalian muscles (Goldman et al. 1987; Ranatunga et al. 1987; Bershitsky and Tsaturyan 1992; Zhao and Kawai 1994a). Figure 2C demonstrates that the active tension is not sensitive to Ca^{2+}, as expected.

The actin filament reconstituted fibre is further reconstituted with regulatory proteins in the relaxing solution that contains both Tm and Tn (Fig. 1C → D). These regulatory proteins can be added together as native Tm (nTm) that contains both Tm and Tn in the stoichiometric amount (Fujita et al. 1996, 2002), or added sequentially (Fujita and Ishiwata 1999; Fujita et al. 2004). This reconstitution takes over night (12–15 h) at 2°C, because one Tm molecule binds 7 actin monomers, and neighbouring Tm molecules have to make the head-to-tail interaction. Any misaligned Tm molecules should be realigned by spontaneous unbinding/rebinding reaction that takes some time (Ishiwata 1973; Ishiwata and Kondo 1978). Once regulatory proteins are reconstituted, the fibre becomes fully Ca^{2+} sensitive; at this point the active tension is tested (Fig. 2D). This tension is 1.3–2× larger than tension with the actin filament alone (Fig. 2C), and close to the initial control tension (Fig. 2A). With repeated activations, tension increases somewhat further, presumably because the repeated activation cuts the actin/thin filament that may have grown in undesirable directions.

The extracted and/or reconstituted preparations are examined by electron microscopy (Fig. 3), confocal microscopy (Fig. 4), SDS-PAGE (Fig. 5), in addition to isometric tension (Fig. 2) and cross-bridge kinetics by using sinusoidal analysis technique (Figs. 6, 7). These results demonstrate that the extraction and reconstitution are satisfactory: the thin filament is extracted with gelsolin (Figs. 2B, 3B, 4B, 5B), the functional actin filament is formed (Figs. 2C, 3C, 4C, 5C, 6B), and the functional thin filament is formed (Figs. 2D, 3D, 5D, 6C).

Methods of studying cross-bridge kinetics

Once all components are reconstituted, the preparation is ready for mechanical analysis to test for its functions. Active isometric tension is the first parameter to be studied (Fig. 2D). In addition, there are several methods to study the cross-bridge kinetics in muscle fibres. Classically, force–velocity measurements were carried out, from which maximum force (P_0) and the maximum velocity of shortening (V_{max}) were studied (Huxley 1957; Edman 1979). More recently, the rate constant of force recovery (k_{tr}) is measured when the fibre is quickly shortened for a large distance (10–20% L_0) and restretched to the original length (Brenner and Eisenberg 1986; Metzger et al. 1989). The k_{tr} measurement has been also used to study the kinetics in single myofibrils (for review, see Poggesi et al. 2005). These methods require many cross-bridge cycles, hence the slowest step (rate limiting step) influences the measured parameters most significantly. These methods are comparable to the ATP hydrolysis rate measurement, because its rate is also limited by the slowest step in the cross-bridge cycle (Zhao and Kawai 1994a).

We implemented the sinusoidal analysis method (Kawai and Brandt 1980), which changes the muscle length in sinewaves of varying frequency (0.13–700 Hz); historically, this method was used by Pringle's group on insect flight muscles (Pringle 1967; White and Thorson 1974). The amplitude of the length change is small (0.125% L_0), which corresponds to 1.25 nm per half sarcomere when the sarcomere length is 2 μm. Because of the presence of series compliance in the thin filament and in other sarcomeric structures (Oosawa et al. 1972; Huxley et al. 1994; Wakabayashi et al.

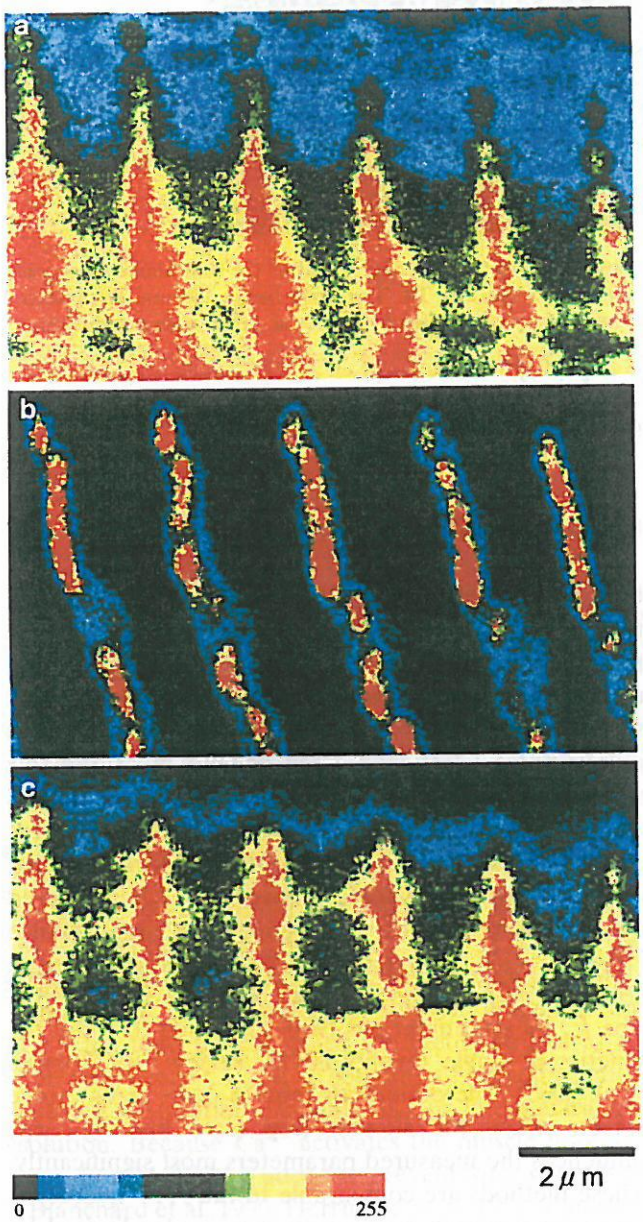

Fig. 4 Confocal fluorescence micrographs of cardiac fibres at each step of reconstitution showing the concentration of actin. (**A**) Control cardiac fibre, (**B**) after gelsolin treatment, (**C**) after reconstitution of the actin filament. The images have been pseudocolored using a linear scale (shown underneath) of fluorescence intensity of Rh-phalloidin that labelled actin. The highest intensity (red) corresponds to the Z-line. Calibration bar is 2 μm. Reproduced from *Biophysical Journal* (Fujita et al. 1996) with permission

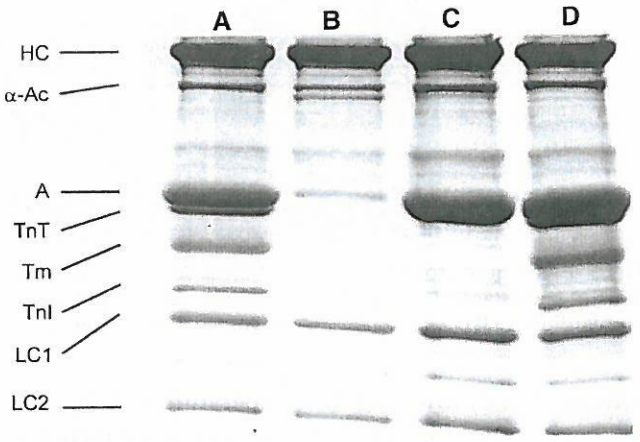

Fig. 5 SDS-PAGE of control (lane A), gelsolin-treated (lane B), actin filament-reconstituted (lane C), and thin filament-reconstituted (lane D) myocardium. Lane A corresponds to the myocardium in Fig. 2A, lane B to Fig. 2B, lane C to Fig. 2C, and lane D to Fig. 2D. HC = myosin heavy chain, α-Ac = α-actinin, A = actin, TnT = troponin T, Tm = tropomyosin, TnI = troponin I, LC1 = myosin light chain 1, LC2 = myosin light chain 2. The gelsolin band is visible just below α-actinin band in lane B. 8–16% gradient gel was used and stained by Coomassie brilliant blue R-250. Reproduced from *Biophysical Journal* (Fujita et al. 2002) with permission

1994; Higuchi et al. 1995), ~0.6 nm of the length change is applied at the cross-bridge level. This value is very much smaller than the step size (5.3 nm; Kitamura et al. 1999), hence there is a possibility that elementary steps of the cross-bridge cycle can be studied.

Theoretically, the sinusoidal analysis method is complementary to the more commonly used step analysis method (Huxley and Simmons 1971; Heinl et al. 1974; Abbott and Steiger 1977), which changes the length of muscle fibres in small steps. The above mentioned frequency range corresponds to 0.8–4400 s^{-1} in step analysis, because of the 2π factor that is multiplied to the frequency value for the frequency-to-time domain conversion. In rabbit psoas muscle fibres, the distortion of periodic force response to sinusoidal length change is small, and the total nonlinear power is <1%, linear power is >99%, hence the regression coefficient is >0.995 when the force time course is fitted to sinusoidal waveform (Kawai and Brandt 1980). In other words, the force response is almost perfectly linear in response to sinusoidal length changes under our experimental conditions. This is in contrast to step analysis, where the rate constant changes significantly with the step size as demonstrated by Huxley and Simmons (1971) on frog semitendinosus fibres, or Abbot and Steiger (1977) on rabbit psoas fibres.

Both sinusoidal and step analysis methods are a subset of perturbation analysis, that modifies an experimental condition, and follow the subsequent time course in tension. Other examples are temperature jump (Goldman et al. 1987; Bershitsky and Taturyan 1992), pressure release (Fortune et al. 1991), and a use of caged compounds which releases a specific ligand on photoflash (Goldman et al. 1984; Dantzig et al. 1992; Araujo and Walker 1996). The released

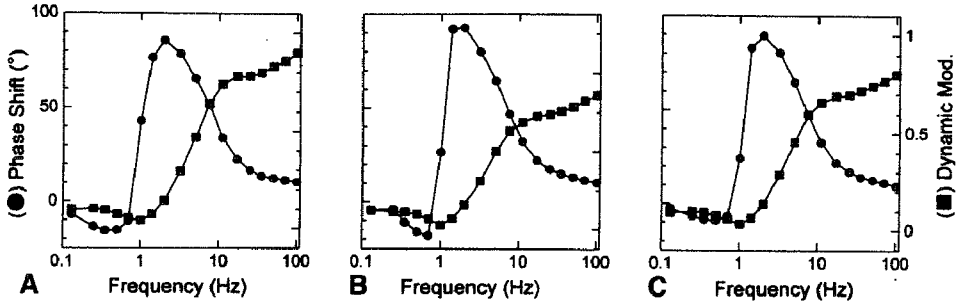

Fig. 6 **A**: Complex modulus Y(f) of the control bovine myocardium activated as in Fig. 2A. **B**: Complex modulus of actin filament-reconstituted myocardium activated as in Fig. 2C. **C**: Complex modulus of thin filament-reconstituted myocardium activated as in Fig. 2D. The complex modulus is shown in the dynamic modulus (= |Y(f)|, ■) and phase shift (= arg[Y(f)], ●) vs. frequency. The unit of the dynamic modulus is MPa. The 5S8P activating solution (mM: 6 CaEGTA, 5.8 MgATP, 1.36 ATP, 15 CP, 8 Pi, 1 NaProp, 73 KProp, 10 NaN_3, 10 MOPS, 200 ionic strength, 320 U/ml CK, pCa 4.66, pH 7.0) was used. Temperature of the experiment was 25°C

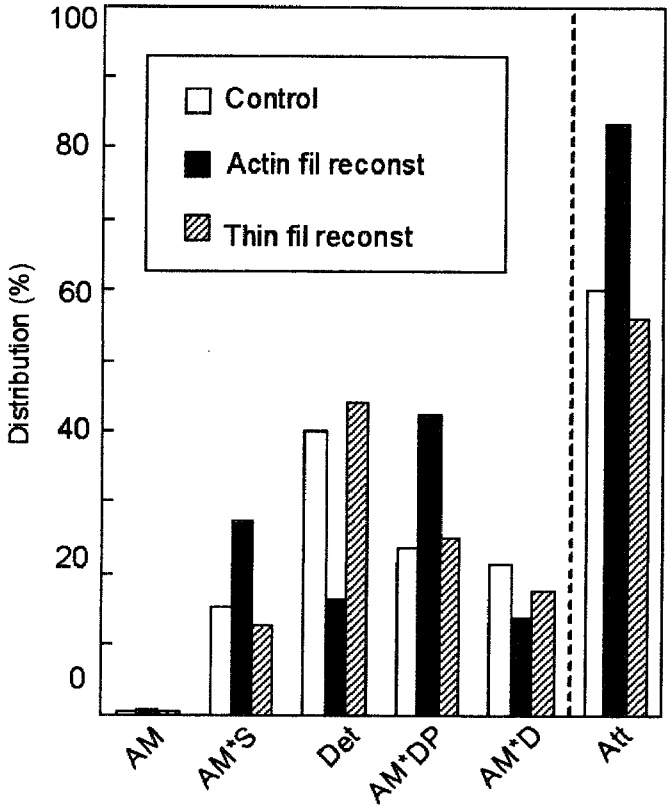

Fig. 7 Cross-bridge distribution in native cardiac fibres (*white bars*), actin filament-reconstituted fibres (*black bars*), and thin filament-reconstituted fibres (*hatched bars*) at 5 mM MgATP and 8 mM Pi (25°C). Calculation is based on the kinetic constants reported in Fujita et al. (2002) and Eq. 18 of Kawai and Halvorson (1991). Att = sum of all strongly attached states (AM, AM*S, AM*DP, AM*D). Det = sum of detached states (MS, MDP) and weakly attached states (AMS, AMDP). The distribution of AM is very small (<1%), because K_1[MgATP] ≫ 1. Because K_0 is not measured, the distribution of the AMD state is not entered here, but it is about the same or less than the distribution of the AM state. This is because [MgADP]≈0.01 mM in the presence of CP/CK, and K_0[MgADP] ≤ 1 in bovine myocardium (Lu et al. 2003). Redrawn from *Biophysical Journal* (Fujita et al. 2002)

ligand binds to a contractile protein to initiate a transient. All of these methods apply a quick change to an experimental condition, hence the speed of the change must be faster than the rate constants to be observed. The perturbation causes an instability in the cross-bridge cycle, which otherwise is at the steady-state, and results in a redistribution of cross-bridges among various states. The redistribution takes time, hence it can be observed as "tension transients", and analysed by a series of exponential functions to obtain the rate constants (called "apparent" or "observed" rate constants) in the exponential time course. For the same system (muscle fibres), the deduced rate constants are the same with any of the perturbation analysis methods employed. The purpose of this analysis is to construct a kinetic model of the cross-bridge cycle (Kawai 2003). There are several advantages in the sinusoidal analysis method including high resolution, covers a large frequency range, etc., but above all, it is worthwhile to point out that this method is simple to implement yet produces significant amounts of information. It is also a method that applies a minimal intervention to the fibres and no overall force change occurs, which is an advantage because no time is spent for stretching in-series compliance on a force increase, or no sarcomere dynamics (inhomogeneity or wave propagation) ensue that may occur with a force relaxation as observed in single myofibrils (Poggesi et al. 2005; Stehle et al. 2005). It is noteworthy that the sinusoidal analysis method is by far the least expensive method, hence the dollar amounts spent for each publication is minimal. In the last 28 years, Kawai's laboratory's peer reviewed publication cost on the average $60,000 per paper (direct cost), much of which (80%) was spent on personnel expenses.

To correlate the apparent rate constants with intrinsic rate constants of elementary steps of the cross-bridge cycle, it is necessary to study the MgATP effect, the MgADP effect and the phosphate (Pi) effect on the apparent rate constants (Kawai and Halvorson 1991). An example of the Pi study is shown in Fig. 2D, in which the numbers above the pen trace indicate the mM concentration of Pi added. From these studies, we succeeded in deducing a cross-bridge model with six states (Scheme 1 below) together with the rate constants (k_2, k_{-2}, k_4, k_{-4}) and the association constants (K_0, K_1, K_5) that characterize the elementary steps. These constants are as a whole called the "kinetic constants".

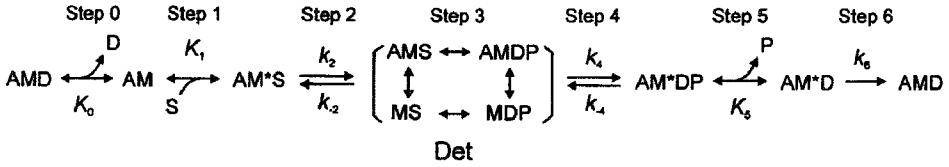

Scheme 1

In this scheme, S = MgATP, D = MgADP, P = phosphate, A = actin, and M = myosin. With the sinusoidal analysis method, we characterized the cross-bridge scheme in rabbit psoas fibres (Kawai and Halvorson 1991), soleus slow twitch fibres (Wang and Kawai 1997), ferret cardiac fibres (Kawai et al. 1993), porcine cardiac fibres (Zhao and Kawai 1996), bovine cardiac fibres (Fujita et al. 2002), and other fast twitch skeletal muscle fibres from the rabbit (Galler et al. 2005). The above Scheme 1 is consistent to those deduced from solution studies (Taylor 1979; Geeves et al. 1984) of isolated and reconstituted contractile proteins, except that in solution studies the strongly bound AM*DP state has not been identified, the Pi release step (step 5) is practically irreversible (Taylor 1979), and the ATP isomerization step (step 2) is irreversible ($k_{-2} = 0$) in the interaction of myosin subfragment 1 and MgATP (Bagshaw and Trentham 1974). The irreversibility (extremely large K) means that the free energy reduction is large because of the relationship: $\Delta G° = -RT \ln K$, which means that perhaps half of the ATP hydrolysis energy is dissipated at step 2 and another half at step 5 in the case of solution studies. In the muscle fibre system, step 5 is known to be reversible, presumably because the hydrolysis energy is retained in the myosin head as the potential energy (force development). For step 2, the data fit better to the reversible model in muscle fibres, and the cause of its difference with solution data may reside in the vast difference in the experimental materials and conditions. Steps 1–2 are consistent with those deduced by using caged ATP (Goldman et al. 1984), and steps 4–5 are consistent with those deduced by using caged Pi (Dantzig et al. 1992; Araujo and Walker 1996) or pressure-release (Fortune et al. 1991) on rabbit psoas fibres.

Experiments with reconstituted fibres

Figure 3A is an electron micrograph of the control fibre showing the cross section in which both thick and thin filaments can be seen in hexagonal lattice. Figure 3B is after gelsolin treatment, where the thin filament is lost and often left with empty space behind. Figure 3C is after actin filament reconstitution, and Fig. 3D is after Tm and Tn reconstitution. It is seen that the actin filament (Fig. 3C) and the thin filament (Fig. 3D) are formed and they occupy the proper strategic position for interaction with the thick filament. With confocal fluorescence microscopy (Fig. 4), the longitudinal periodic pattern of muscle fibres before (Fig. 4A) and after (Fig. 4B) the gelsolin treatment, and after the reconstitution of the actin filament (Fig. 4C) can be seen (Fujita et al. 1996). Figure 5A is an SDS-PAGE of the control fibres. In Fig. 5B, almost all the thin filament proteins (actin, Tm, TnT and TnI) are removed after gelsolin treatment, but thick filament proteins (MHC, MLC1 and MLC2) and a Z-line protein (α-actinin) are left behind. A small amount of actin observed in Fig. 5B can be attributed to actin fragments remaining at the Z-line together with α-actinin. In this gel, TnC is not visualized. In Fig. 5C, actin is seen to have come back after the actin filament reconstitution. In Fig. 5D, Tm, TnT and TnI are seen to have come back after reconstitution of regulatory proteins. In Fig. 5B, the thin band below α-actinin is gelsolin which remained in fibres.

In Fig. 2A, the control active tension can be seen. In Fig. 2B, there is hardly any active tension after gelsolin treatment for 100 min. When the actin filament is

reconstituted (Fig. 2C), tension develops irrespective of the presence of Ca^{2+}. This tension is only about 70% of the control tension (Fig. 2A). In Fig. 2D, it is seen that the Ca^{2+} sensitivity and full tension recover after overnight treatment with nTm. With our experiments (Fujita et al. 2002), tension recovery was 107 ± 4% (±SEM, N = 26) compared to initial control (Fig. 2A), and the degree of the recovery is controlled by the number of times of actin filament reconstitution (7 min interval). In some fibres, tension recovered up to 140% (Fujita et al. 1996; Ishiwata et al. 1998) presumably because, in cardiac fibres, the in situ length of the thin filament may not make a full overlap with the thick filament, and the extra length of reconstituted thin filament can generate additional force by interacting with myosin cross-bridges. At this stage, sinusoidal analysis is performed, which can be seen as small oscillations in the tension trace in Fig. 2D. Figure 6 compares amplitude and phase shift of control (in A), actin filament reconstituted (in B), and thin filament reconstituted (in C) preparations. The frequency profile is similar in all preparations, which indicates that there is no large change in cross-bridge kinetics. From each profile, two apparent rate constants ($2\pi b$ and $2\pi c$) can be extracted (Kawai and Brandt 1980; Wannenburg et al. 2000; Fujita et al. 2002). Our experiments demonstrate that reproducibility of $2\pi b$ is 98 ± 6%, and $2\pi c$ is 92 ± 4% after the thin filament reconstitution. These observations indicate that the thin filament reconstitution in cardiac fibres is at its near perfection in terms of the structure, proteins incorporated, tension generating ability, and the cross-bridge dynamics.

Effect of regulatory proteins on force per cross-bridge, and positive allosteric effect

As mentioned, tension in the absence of regulatory proteins (Fig. 2C) is only about 70% of control (Fig. 2A). Tension increases 1.5× when Tm and Tn are reconstituted (Fig. 2D) (Fujita et al. 2002). There are two possibilities to account for this increase: (1) an increase in the number of force generating cross-bridges, and (2) an increase in force/cross-bridge. For this reason, we performed sinusoidal analysis during maximal activation, changed MgATP, MgADP and Pi concentrations, and determined the kinetic constants of elementary steps based on the six state model (Scheme 1) for (a) control fibres, (b) actin filament reconstituted fibres, and (c) thin filament reconstituted fibres (Fujita et al. 2002). The kinetic constants of (a) and (c) agreed within an experimental error, which demonstrates a good functional reconstitution. When comparing (a) and (b), the rate constants of steps 2 and 4 differed by 2×, and their equilibrium constants differed as much as by 4×. The Pi association constant K_5 differed by 3×. Thus, there were substantial changes in the kinetic constants of the elementary steps with the addition of regulatory proteins. From these kinetic constants, we calculated the cross-bridge distribution at various intermediate states (Fig. 7). The results show that there is actually a decrease in the number of strongly bound cross-bridges (bars labelled Att in Fig. 7) by 27% when the regulatory proteins are added. In Scheme 1, strongly bound cross-bridges are identified as AM*DP, AM*D, AMD, AM and AM*S (Kawai and Zhao 1993). From these results, we concluded that the force/cross-bridge is increased by addition of the regulatory proteins by the factor of ~2 (Fujita et al. 2002). It is hypothesized that the reason for this increase is that the regulatory proteins in the presence of Ca^{2+} apply a positive allosteric effect on actin so that the actin–myosin interaction becomes stronger. In other words, Tm and Tn modify the actin–myosin interface for better stereospecific interaction so that the efficiency of the energy transduction mechanism in myosin is improved. Such a mechanism was proposed based on solution studies (Tobacman and Butters 2000). This mechanism is another view of the well known cooperative activation mechanism of the thin filament: Ca^{2+} binding to TnC shifts the equilibrium from the "blocked state" to the "closed state", and the cross-bridge binding shifts the equilibrium further to the "open state" (McKillop and Geeves 1993). In solution, it has been known that the cross-bridge binding to actin makes the Tm binding to actin stronger (Chalovich 1992). Thus, it is not surprising that Tm binding to the actin filament increased actin binding to myosin. The effect of regulatory proteins and the underlining mechanisms are generally consistent with studies that used single molecules (Gordon et al. 1998; VanBuren et al. 1999; Bing et al. 2000; Homsher et al. 2000; Kawai et al. 2006).

Negative allosteric effect

If the role of regulatory proteins is to apply an allosteric effect on the actin–myosin interaction, it may be possible to reverse the effect by using a Tm mutant. We used Δ23Tm (Hitchcock-DeGregori and An 1996; Landis et al. 1997) that lacks region 2 and 3 of 7 quasi repeat units of the Tm molecule (Hitchcock-DeGregori and Varnell 1990), and reconstituted together with normal Tn. Our result shows that the reconstituted fibre is Ca^{2+} sensitive, but active tension is only

40% of the control tension which is less than the tension generated by the actin filament without regulatory proteins (Lu et al. 2003). However, the number of strongly attached cross-bridges increased by 15%, indicating that tension/cross-bridge is decreased by the mutant Tm. This is an example of negative allosteric effect and supports the hypothesis that Δ23Tm diminishes the actin–myosin interaction or efficiency of transduction. Thus, we conclude that there is an allosteric signal sent from Tm to actin, which can be positive or negative depending on the character of the Tm molecule.

Tropomyosin or troponin?

The next question is whether this allosteric effect is caused by Tm or by both Tm and Tn. The overall effect is large because a change of up to 4× in the equilibrium constants was observed (Fujita et al. 2002). This question can be answered by reconstituting Tm and Tn sequentially. We carried out this experiment and compared the kinetic constants at each step of reconstitution. Our results show that active tension increased gradually, but all the kinetic constants, except for K_1, resumed the control value as soon as Tm was reconstituted without Tn (Fujita et al. 2004). K_1 resumed the control value when both Tm and Tn were reconstituted. These experiments demonstrate that Tm is the main player for the positive allosteric effect of the regulatory proteins on the actin–myosin interaction and subsequent energy transduction. This conclusion is further supported by the experiments showing that Tm but not Tn is responsible for the pH dependence of isometric tension (Fujita and Ishiwata 1999). From previous experiments we performed, we have known that K_1 is influenced by tension (Zhao et al. 1996), therefore by strain. That is, K_1 may change as a result of change in isometric tension. It was reported that the ATP binding step (K_1) may be influenced by loop 1 of myosin, because the charge distribution on the loop 1 and K_1 may be correlated (Wang and Kawai 2001); loop 1 comes close to the ATP binding site. It is possible that the position of loop 1 changes according to the strain on the myosin head, and this change in turn alters the ATP binding to the myosin head.

Temperature effect and hydrophobic interaction

There are two major categories of interaction between molecules. One is ionic and the other is hydrophobic. The initial interaction between actin and myosin is weak and thought to consist of the ionic interaction (Brenner et al. 1982). This interaction works over a long distance, helping the myosin head search for its binding site on actin. The interaction takes place between the N-terminal finger of actin, where four negative charges are found, and the loop 2 of myosin, where 5 positive charges are found. The subsequent interaction is strong and thought to consist of the hydrophobic interaction (Tonomura et al. 1962; Highsmith 1977; Rayment et al. 1993; Zhao and Kawai 1994a). This interaction is only possible when two molecules are close together and stereospecifically matched. The responsible site for actin is Leu^{140}, Tyr^{143}, Ile^{341}, Ile^{345}, Leu^{349} and Phe^{352} of a short helix-turn (140–149) and a long helix (337–351); the responsible site for myosin is (in chicken sequence) Pro^{529}, Met^{530}, Glu^{538}, Met^{541}, Phe^{542} and Pro^{543} of a helix-turn-helix (526–559) in the lower 50K domain (Holmes et al. 2004).

The hydrophobic interaction is endothermic ($\Delta H^\circ > 0$: absorbs heat), because a thin layer of structured water around the hydrophobic residues must be destroyed, a situation analogous to the melting of ice. Liberated water molecules go into the solution phase to gain thermal motion resulting in an increase in the entropy ($\Delta S^\circ > 0$). Because interacting proteins lose the thin layer of structured water, their combined heat capacity decreases ($\Delta C_P < 0$). $\Delta H^\circ > 0$ and $\Delta S^\circ > 0$ have been observed on actomyosin interaction in solution (Tonomura et al. 1962; Highsmith 1977) and in myofibrils (Ishiwata et al. 1986). $\Delta H^\circ > 0$, $\Delta S^\circ > 0$ and $\Delta C_P < 0$ have been observed in rabbit psoas fibres (Zhao and Kawai 1994a; Murphy et al. 1996) and soleus slow twitch fibres (Wang and Kawai 2001) on the step that generates force. This mechanism is consistent with the well known observation that isometric tension increases with an increase in the temperature both in mammalian skeletal (Goldman et al. 1987; Ranatunga et al. 1987; Zhao and Kawai 1994a; Coupland et al. 2001; Wang and Kawai 2001) and cardiac (Ranatunga 1999; Fujita and Kawai 2002) muscle fibres, and reviewed by Kawai (2003).

When the above two mechanisms are combined, then it follows that the tension increase with temperature is larger in the presence of regulatory proteins than in their absence. We performed this exact experiment, and obtained expected results. We found that the slope of the temperature–tension plot is much reduced in the absence of the regulatory proteins (Fujita and Kawai 2002). This experiment further supports the hypothesis that the regulatory proteins promote hydrophobic interaction between actin and

myosin beyond what is known currently (see above). That is, the crystal structure of the actin and myosin interaction may be incomplete unless regulatory proteins and Ca^{2+} are added.

Negative charges of actin's N-terminus

The N-terminal finger of actin is negatively charged across the phylogenic tree (Vandekerckhove and Weber 1978), and in muscles, this finger is known to make the weak (ionic) interaction with loop 2 of myosin (Sutoh 1982a, b; DasGupta and Reisler 1989; Furch et al. 1998); the loop 2 joins 50K and 20K domains and has 5 Lys residues. There is a line of evidence that the N-terminal finger activates S1 ATP hydrolysis rate in solution (Sutoh et al. 1991; Cook et al. 1993), which may suggest that the N-terminal finger also activates the strong (hydrophobic) interaction. For this reason, we used yeast (*Saccharomyces cerevisiae*) actin mutants (Cook et al. 1993) that vary in the number of N-terminal negative charges and asked a question whether the number of negative charges affects the strong interaction between actin and myosin molecules.

Yeast mutant actin molecules that vary N-terminal negative charges from 2 to 4 were raised and purified in Dr. Peter Rubenstein's laboratory at the University of Iowa, and used for actin filament reconstitution (Lu et al. 2005). We observed that active tension was 10% and minimal in 2Ac (2 N-terminal negative charges), 23% in 3Ac (3 N-terminal negative charges), and 44% in 4Ac (4 N-terminal negative charges) actins. The same pattern was observed in rigor stiffness, indicating that the actin–myosin interaction becomes stronger with a larger number of N-terminal negative charges. During activation, we characterized the elementary steps, and concluded that there is no large reapportionment of cross-bridges among the six states (Scheme 1), indicating that an increase in the N-terminal negative charge enhances tension generated by each cross-bridge (Lu et al. 2005). This result is consistent with the hypothesis that N-terminal negative charges affect strong interaction between actin and myosin molecules, presumably by changing the actomyosin interface (Cook et al. 1993; Joel et al. 2001). When rabbit skeletal actin (4 N-terminal negative charges) was used, tension increased further to 77%, indicating that there are still significant functional differences between yeast and rabbit actins, although they have 87% sequence identity. These experiments were carried out in the absence of regulatory proteins.

Capping of the pointed end

The reconstituted thin filament does not have tropomodulin, which is the pointed end cap of the thin filament (Fowler et al. 1993; Littlefield and Fowler 1998). The lack of tropomodulin may suggest that actin polymerization and depolymerization would occur, hence the actin/thin filament may be unstable (Ishiwata and Funatsu 1985). In fact, we demonstrated previously that the length of the thin filament in the I-Z-I brush (the structure composed of the Z-line and thin filaments on both sides) spontaneously decreased even in physiological ionic strength at the rate of about 0.05 μm/h (Funatsu et al. 1988). The I-Z-I brush was obtained from skeletal myofibrils (1–2 μm in diameter) in which the thick filament was removed by high salt solution, which also removes the P-end capping protein, now known as tropomodulin (Ishiwata and Funatsu 1985).

In actuality, however, the absence of the capping protein does not appear to affect the stability of actin/thin filament under our experimental conditions, judging from the fact that the length of thin filaments does not change during the reconstitution procedure with the regulatory proteins for 12–15 h (Fujita and Ishiwata 1999; Fujita et al. 2004). Its stability is further confirmed by experimental results which show that the isometric tension of reconstituted fibres does not decrease with repeated activations (Fujita et al. 2002). Thus, spontaneous actin/thin filament depolymerization at the P-end seems not to occur in our actin/thin filament reconstituted fibres, probably because of the presence of the thick filament which interacts weakly with the actin/thin filament during relaxation. It is also possible that G-actin at the critical concentration of polymerization may exist in the core of the filament lattice in muscle fibres, but not in myofibrils, because of their thickness difference. In fact, we have been finding that the reconstituted fibres are more stable than native fibres, and they can survive a larger number of repeated Ca^{2+} activations than native fibres. This unexpected finding could be explained if extra actin/thin filament is formed to stabilize the sarcomere structure but that it may not contribute to active force generation.

Reconstitution of the actin/thin filament in skeletal muscles

The thin filament extraction and reconstitution protocol works well for the cardiac preparations. The same method was tried with rabbit psoas fibres, but the tension reproduced was limited to 30% (Funatsu et al.

1994). Even this degree of recovery is remarkable, because such reconstituted fibres may offer numerous possibilities in testing hypotheses. It is possible that the presence of nebulin in skeletal muscle (Wang and Wright 1988) may hinder the formation of the actin filament. Nebulin wraps the thin filament in skeletal muscles, and it may be difficult to experimentally reproduce the correct actin–nebulin and actin–myosin interaction at the same time. Instead of nebulin, nebulette is present in cardiac preparations (Moncman and Wang 1995), but since its molecular weight is small (107 kD) and it is localized close to the Z-line, the interaction between nebulette and actin molecules may become normal with the actin/thin filament reconstitution. Connectin (titin) (Maruyama et al. 1976; Wang et al. 1979) does not appear to interfere with the actin/thin filament reconstitution, primarily because it wraps only around the thick filament in the A-band area, and it runs in parallel with the actin/thin filament in the I-band area, except at a region near the Z-line (Funatsu et al. 1990, 1993). Connectin is depicted as the thin line in Fig. 1. With an EM examination, cardiac muscles have a robust-appearing Z-line that is thicker than the Z-line of fast twitch skeletal muscles. It is probable that the thicker Z-line may be the reason for the higher stability against the gelsolin treatment (Fujita et al. 1996). In rabbit psoas fibres the structure of the Z-line appears to be disorganized by partial removal of the thin fragment, one of main constituents of the Z-line structure (Funatsu et al. 1994).

Future direction

The advantage of the thin filament reconstitution method is that any thin filament protein can be replaced with a mutant protein, force and force transients can be studied, and the kinetic constants that characterize the six state cross-bridge model can be deduced, hence the structure–function relationship can be established. We are currently studying the functional difference of α-Tm, β-Tm, and their phosphorylated form (Lu et al. 2006). In the future, any mutant protein of the thin filament origin that causes familial hypertrophic cardiomyopathy (Blanchard et al. 1999; Wolska and Wieczorek 2003) or dilative cardiomyopathy (Chang and Potter 2005) can be studied to elucidate the structure–function relationship of these diseases.

Acknowledgments We would like to thank Dr. Hideaki Fujita for drawing Fig. 1, and to Dr. Madoka Suzuki and Ms. Kristen Stanton for critical reading of the manuscript. This work was supported in part by an NIH grant HL70041 to MK, and by Grants-in-Aid for Specially Promoted Research and for the 21st Century COE program (Physics of Self-organization Systems), and by "Establishment of Consolidated Research Institute for Advanced Science and Medical Care" from the Ministry of Education, Sports, Culture, Science and Technology of Japan to SI. The contents of this work are solely the responsibility of the authors and do not necessarily represent the official view of awarding organizations.

References

Abbott RH, Steiger GJ (1977) Temperature and amplitude dependence of tension transients in glycerinated skeletal and insect fibrillar muscle. J Physiol (Lond) 266:13–42

Andrews MA, Maughan DW, Nosek TM, Godt RE (1991) Ion-specific and general ionic effects on contraction of skinned fast-twitch skeletal muscle from the rabbit. J Gen Physiol 98:1105–1125

Araujo A, Walker JW (1996) Phosphate release and force generation in cardiac myocytes investigated with caged phosphate and caged calcium. Biophys J 70:2316–2326

Bagshaw CR, Trentham DR (1974) The characterization of myosin-product complexes and of product-release steps during the magnesium ino-dependent adenosine triphosphatase reaction. Biochem J 141:331–349

Bershitsky SY, Tsaturyan AK (1992) Tension responses to joule temperature jump in skinned rabbit muscle fibres. J Physiol (Lond) 447:425–448

Bing W, Knott A, Marston SB (2000) A simple method for measuring the relative force exerted by myosin on actin filaments in the in vitro motility assay: evidence that tropomyosin and troponin increase force in single thin filaments. Biochem J 350:693–699

Blanchard E, Seidman C, Seidman JG, LeWinter M, Maughan D (1999) Altered crossbridge kinetics in the $\alpha MHC^{403/+}$ mouse model of familial hypertrophic cardiomyopathy. Circ Res 84:475–483

Blanchard EM, Smith GL, Allen DG, Alpert NR (1990) The effects of 2,3-butanedione monoxime on initial heat, tension, and aequorin light output of ferret papillary muscles. Pflugers Arch 416:219–221

Brenner B, Eisenberg E (1986) Rate of force generation in muscle: correlation with actomyosin ATPase activity in solution. Proc Natl Acad Sci USA 83:3542–3546

Brenner B, Schoenberg M, Chalovich JM, Greene LE, Eisenberg E (1982) Evidence for cross-bridge attachment in relaxed muscle at low ionic strength. Proc Natl Acad Sci USA 79:7288–7291

Chalovich JM (1992) Actin mediated regulation of muscle contraction. Pharmacol Ther 55:95–148

Chang AN, Potter JD (2005) Sarcomeric protein mutations in dilated cardiomyopathy. Heart Fail Rev 10:225–235

Cook RK, Root D, Miller C, Reisler E, Rubenstein PA (1993) Enhanced stimulation of myosin subfragment 1 ATPase activity by addition of negatively charged residues to the yeast actin NH2 terminus. J Biol Chem 268:2410–2415

Coupland ME, Puchert E, Ranatunga KW (2001) Temperature dependence of active tension in mammalian (rabbit psoas) muscle fibres: effect of inorganic phosphate. J Physiol (Lond) 536:879–891

Dantzig J, Goldman Y, Millar NC, Lacktis J, Homsher E (1992) Reversal of the cross-bridge force-generation transition by the photogeneration of phosphate in rabbit psoas muscle fibers. J Physiol (Lond) 451:247–278

DasGupta G, Reisler E (1989) Antibody against the amino terminus of alpha-actin inhibits actomyosin interactions in the presence of ATP. J Mol Biol 207:833–836

Edman KAP (1979) The velocity of unloaded shortening and its relation to sarcomere length and isometric force in vertebrate muscle fibres. J Physiol (Lond) 269:255–272

Fortune NS, Geeves MA, Ranatunga KW (1991) Tension responses to rapid pressure release in glycerinated rabbit muscle fibers. Proc Natl Acad Sci USA 88:7323–7327

Fowler VM, Sussmann MA, Miller PG, Flucher BE, Daniels MP (1993) Tropomodulin is associated with the free (pointed) ends of the thin filaments in rat skeletal muscle. J Cell Biol 120:411–420

Fujita H, Ishiwata S (1998) Spontaneous oscillatory contraction without regulatory proteins in actin filament-reconstituted fibers. Biophys J 75:1439–1445

Fujita H, Ishiwata S (1999) Tropomyosin modulates pH dependence of isometric tension. Biophys J 77:1540–1546

Fujita H, Kawai M (2002) Temperature effect on isometric tension is mediated by regulatory proteins tropomyosin and troponin in bovine myocardium. J Physiol (Lond) 539:267–276

Fujita H, Lu X, Suzuki M, Ishiwata S, Kawai M (2004) The effect of tropomyosin on force and elementary steps of the cross-bridge cycle in reconstituted bovine myocardium. J Physiol (Lond) 556:637–649

Fujita H, Sasaki D, Ishiwata S, Kawai M (2002) Elementary steps of the cross-bridge cycle in bovine myocardium with and without regulatory proteins. Biophys J 82:915–928

Fujita H, Yasuda K, Niitsu S, Funatsu T, Ishiwata S (1996) Structural and functional reconstitution of thin filaments in the contractile apparatus of cardiac muscle. Biophys J 71:2307–2318

Funatsu T, Anazawa T, Ishiwata S (1994) Structural and functional reconstitution of thin filaments in skeletal muscle. J Muscle Res Cell Motil 15:158–171

Funatsu T, Asami Y, Ishiwata S (1988) β-Actinin: a capping protein at the pointed end of thin filaments in skeletal muscle. J Biochem (Tokyo) 103:61–71

Funatsu T, Higuchi H, Ishiwata S (1990) Elastic filaments in skeletal muscle revealed by selective removal of thin filaments with plasma gelsolin. J Cell Biol 110:53–62

Funatsu T, Kono E, Higuchi H, Kimura S, Ishiwata S, Yoshioka T, Maruyama K, Tsukita S (1993) Elastic filaments in situ in cardiac muscle: deep-etch replica analysis in combination with selective removal of actin and myosin filaments. J Cell Biol 120:711–724

Furch M, Geeves MA, Manstein DJ (1998) Modulation of actin affinity and actomyosin adenosine triphosphatase by charge changes in the myosin motor domain. Biochemistry 37:6317–6326

Galler S, Wang BG, Kawai M (2005) Elementary steps of the cross-bridge cycle in fast-twitch fiber types from rabbit skeletal muscles. Biophys J 89:3248–3260

Geeves MA, Goody RS, Gutfreund H (1984) Kinetics of acto-S1 interaction as a guide to a model for the cross-bridge cycle. J Muscle Res Cell Motil 5:351–361

Goldman YE, Hibberd MG, Trentham DR (1984) Relaxation of rabbit psoas muscle fibres from rigor by photochemical generation of adenosine-5′-triphosphate. J Physiol (Lond) 354:577–604

Goldman YE, McCray JA, Ranatunga KW (1987) Transient tension changes initiated by laser temperature jumps in rabbit psoas muscle fibres. J Physiol (Lond) 392:71–95

Gordon AM, Chen Y, Liang B, LaMadrid M, Luo Z, Chase PB (1998) Skeletal muscle regulatory proteins enhance F-actin in vitro motility. Adv Exp Med Biol 453:187–196

Heinl P, Kuhn HJ, Rüegg JC (1974) Tension responses to quick length changes of glycerinated skeletal muscle fibres from the frog and tortoise. J Physiol (Lond) 237:243–258

Herrmann C, Wray J, Travers F, Barman T (1992) Effect of 2,3-butanedione monoxime on myosin and myofibrillar ATPases. An example of an uncompetitive inhibitor. Biochemistry 31:12227–12232

Highsmith S (1977) The effects of temperature and salts on myosin subfragment-1 and F-actin association. Arch Biochem Biophys 180:404–408

Higuchi H, Yanagida T, Goldman YE (1995) Compliance of thin filaments in skinned fibers of rabbit skeletal muscle. Biophys J 69:1000–1010

Hitchcock-DeGregori SE, An Y (1996) Integral repeats and a continuous coiled coil are required for binding of striated muscle tropomyosin to the regulated actin filament. J Biol Chem 16:3600–3603

Hitchcock-DeGregori SE, Varnell TA (1990) Tm has discrete actin-binding sites with sevenfold and fourteenfold periodicities. J Mol Biol 214:885–896

Holmes KC, Schroder RR, Sweeney HL, Houdusse A (2004) The structure of the rigor complex and its implications for the power stroke. Phil Trans Roy Soc Lond B Biol Sci 359:1819–1828

Homsher E, Lee DM, Morris C, Pavlov D, Tobacman LS (2000) Regulation of force and unloaded sliding speed in single thin filaments: effects of regulatory proteins and calcium. J Physiol (Lond) 524:233–243

Huxley AF (1957) Muscle structure and theories of contraction. Prog Biophys Chem 7:255–318

Huxley AF, Simmons RM (1971) Proposed mechanism of force generation in striated muscle. Nature 233:533–538

Huxley HE, Stewart A, Sosa H, Irving T (1994) X-ray diffraction measurements of the extensibility of actin and myosin filaments in contracting muscle. Biophys J 67:2411–2421

Ishiwata S (1973) A study on the F-actin, tropomyosin and troponin complex. I. Gel-filament transformation. Biochim Biophys Acta 303:77–89

Ishiwata S, Funatsu T (1985) Does actin bind to the ends of thin filaments in skeletal muscle?. J Cell Biol 100:282–291

Ishiwata S, Funatsu T, Fujita H (1998) Contractile properties of thin (actin) filament-reconstituted muscle fibers. Adv Exp Med Biol 453:319–329

Ishiwata S, Kondo H (1978) Studies on the F-actin–tropomyosin–troponin complex. II. Partial reconstitution of thin filament by F-actin, tropomyosin and tropomyosin binding component of troponin (TNT). Biochim Biophys Acta 534:341–349

Ishiwata S, Manuck BA, Seidel JC, Gergely J (1986) Saturation transfer electron paramagnetic resonance study of the mobility of myosin heads in myofibrils under conditions of partial dissociation. Biophys J 49:821–828

Joel PB, Trybus KM, Sweeney HL (2001) Two conserved lysines at the 50/20-kda junction of myosin are necessary for triggering actin activation. J Biol Chem 276:2998–3003

Kawai M (2003) What do we learn by studying the temperature effect on isometric tension and tension transients in mammalian striated muscle fibres?. J Muscle Res Cell Motil 24:127–138

Kawai M, Brandt PW (1980) Sinusoidal analysis: a high resolution method for correlating biochemical reactions with physiological processes in activated skeletal muscles of

rabbit, frog and crayfish. J Muscle Res Cell Motil 1:279–303
Kawai M, Halvorson HR (1991) Two step mechanism of phosphate release and the mechanism of force generation in chemically skinned fibers of rabbit psoas muscle. Biophys J 59:329–342
Kawai M, Kido T, Vogel M, Fink RH, Ishiwata S (2006) Temperature change does not affect force between regulated actin filaments and HMM in single molecule experiments. J Physiol (Lond) 574(pt 3):877–887
Kawai M, Saeki Y, Zhao Y (1993) Crossbridge scheme and the kinetic constants of elementary steps deduced from chemically skinned papillary and trabecular muscles of the ferret. Circ Res 73:35–50
Kawai M, Zhao Y (1993) Cross-bridge scheme and force per cross-bridge state in skinned rabbit psoas muscle fibers. Biophys J 65:638–651
Kitamura K, Tokunaga M, Iwane AH, Yanagida T (1999) A single myosin head moves along an actin filament with regular steps of 5.3 nanometres. Nature 397:129–134
Kurokawa H, Fujii W, Ohmi K, Sakurai T, Nonomura Y (1990) Simple and rapid purification of brevin. Biochem Biophys Res Commun 168:451–457
Landis CA, Bobkova A, Homsher E, Tobacman LS (1997) The active state of the thin filament is destabilized by an internal deletion in tropomyosin. J Biol Chem 272:14051–14056
Littlefield R, Fowler VM (1998) Defining actin filament length in striated muscle: rulers and caps or dynamic stability?. Annu Rev Cell Dev Biol 14:487–525
Lu X, Bryant MK, Bryan KE, Rubenstein PA, Kawai M (2005) Role of the N-terminal negative charges of actin in force generation and cross-bridge kinetics in reconstituted bovine cardiac muscle fibres. J Physiol (Lond) 564:65–82
Lu X, Heeley DH, Smillie LB, Kawai M (2006) Effects of tropomyosin (Tm) isoforms and phosphorylation on isometric tension and cross-bridge kinetics in bovine myocardium. Biophys J 90:120a (Abstr #558)
Lu X, Tobacman LS, Kawai M (2003) Effects of tropomyosin internal deletion Delta23Tm on isometric tension and the cross-bridge kinetics in bovine myocardium. J Physiol (Lond) 553.2:457–471
Maruyama K, Natori R, Nonomura Y (1976) New elastic protein from muscle. Nature 262:58–60
McKillop DFA, Geeves MA (1993) Regulation of the interaction between actin and myosin subfragment 1: evidence for three states of the thin filament. Biophys J 65:693–701
Metzger JM, Greaser ML, Moss RL (1989) Variations in cross-bridge attachment rate and tension with phosphorylation of myosin in mammalian skinned skeletal muscle fibers. Implications for twitch potentiation in intact muscle. J Gen Physiol 93:855–883
Moncman CL, Wang K (1995) Nebulette: a 107 kD nebulin-like protein in cardiac muscle. Cell Motil Cytoskeleton 32:205–225
Murphy KP, Zhao Y, Kawai M (1996) Molecular forces involved in force generation during skeletal muscle contraction. J Exp Biol 199:2565–2571
Oosawa F, Fujime S, Ishiwata S, Mihashi K (1972) Dynamic property of F-actin and thin filament. Cold Spr Harb Symp Quant Biol 37:277–285
Poggesi C, Tesi C, Stehle R (2005) Sarcomeric determinants of striated muscle relaxation kinetics. Pflugers Arch 449:505–517
Pringle JWS (1967) The contractile mechanism of insect fibrillar muscle. Prog Biophys Mol Biol 17:1–60
Ranatunga KW (1999) Endothermic force generation in skinned cardiac muscle from rat. J Muscle Res Cell Motil 20:489–496
Ranatunga KW, Sharpe B, Turnbull B (1987) Contraction of human skeletal muscle at different temperatures. J Physiol (Lond) 390:383–395
Rayment I, Holden HM, Whittaker M, Yohn CB, Lorenz M, Holmes KC, Milligan RA (1993) Structure of the actin–myosin complex and its implications for muscle contraction. Science 261:58–65
Reuben JP, Brandt PW, Berman M, Grundfest H (1971) Regulation of tension in the skinned crayfish muscle fiber. I. Contraction and relaxation in the absence of Ca (pCa is greater than 9). J Gen Physiol 57:385–407
Stehle R, Telley IA, Pfitzer G (2005) Transient kinetics in force and indivisual sarcomere lengths induced by phosphate. Biophys J 88:127a (Abstr #624)
Sutoh K (1982a) Identification of myosin-binding sites on the actin sequence. Biochemistry 21:3654–3661
Sutoh K (1982b) An actin-binding site on the 20K fragment of myosin subfragment 1. Biochemistry 21:4800–4804
Sutoh K, Ando M, Sutoh K, Toyoshima YY (1991) Site-directed mutations of Dictyostelium actin: disruption of a negative charge cluster at the N terminus. Proc Natl Acad Sci USA 88:7711–7714
Taylor EW (1979) Mechanism of actomyosin ATPase and the problem of muscle contraction. CRC Crit Rev Biochem 6:103–164
Tobacman LS, Butters CA (2000) A new model of cooperative myosin-thin filament binding. J Biol Chem 275:27587–27593
Tonomura Y, Tokura S, Sekiya K (1962) Binding of myosin A to F-actin. J Biol Chem 237:1074–1081
Van Buren P, Palmiter KA, Warshaw DM (1999) Tropomyosin directly modulates ctomyosin mechanical performance at the level of a single actin filament. Proc Natl Acad Sci USA 96:12488–12493
Vandekerckhove J, Weber K (1978) At least six different actins are expressed in a higher mammal: an analysis based on the amino acid sequence of the amino-terminal tryptic peptide. J Mol Biol 126:783–802
Wakabayashi K, Sugimoto Y, Tanaka H, Ueno Y, Takezawa Y, Amemiya Y (1994) X-ray diffraction evidence for the extensibility of actin and myosin filaments during muscle contraction. Biophys J 67:2422–2435
Wang G, Kawai M (1997) Force generation and phosphate release steps in skinned rabbit soleus slow-twitch muscle fibers. Biophys J 73:878–894
Wang G, Kawai M (2001) Effect of temperature on elementary steps of the cross-bridge cycle in rabbit soleus slow-twitch muscle fibres. J Physiol (Lond) 531:219–234
Wang K, McClure J, Tu A (1979) Titin: major myofibrillar components of striated muscle. Proc Natl Acad Sci USA 76:3698–3702
Wang K, Wright J (1988) Architecture of the sarcomere matrix of skeletal muscle: immunoelectron microscopic evidence that suggests a set of parallel inextensible nebulin filaments anchored at the Z line. J Cell Biol 107:2199–2212
Wannenburg T, Heijne GH, Geerdink JH, Van den Dool HW, Janssen PML, de Tombe PP (2000) Cross-bridge kinetics in rat myocardium: effect of sarcomere length and calcium activation. Am J Physiol 279:H779–H790
White DCS, Thorson J (1974) The kinetics of muscle contraction. Prog Biophys Mol Biol 27:173–255

Wolska BM, Wieczorek DF (2003) The role of tropomyosin in the regulation of myocardial contraction and relaxation. Pflugers Arch 446:1–8

Zhao Y, Kawai M (1994a) Kinetic and thermodynamic studies of the cross-bridge cycle in rabbit psoas muscle fibers. Biosphys J 67:1655–1668

Zhao Y, Kawai M (1994b) BDM affects nucleotide binding and force generation steps of the cross-bridge cycle in rabbit psoas muscle fibres. Am J Physiol (Cell Physiol 35) 266:C437–C447

Zhao Y, Kawai M (1996) Inotropic agent EMD-53998 weakens nucleotide and phosphate binding to cross bridges in porcine myocardium. Am J Physiol (Heart Circ Physiol 40) 271:H1394–H1406

Zhao Y, Swamy PMG, Humphries KA, Kawai M (1996) The effect of partial extraction of troponin C on the elementary steps of the cross-bridge cycle in rabbit psoas muscle fibers. Biophys J 71:2759–2773

ISSN 0006-2979, Biochemistry (Moscow), 2006, Vol. 71, No. 10, pp. 1082-1089. © Pleiades Publishing, Inc., 2006.
Original Russian Text © L. R. Gorbacheva, T. P. Storozhevykh, V. G. Pinelis, S. Ishiwata, S. M. Strukova, 2006, published in Biokhimiya, 2006, Vol. 71, No. 10, pp. 1338-1346.
Originally published in Biochemistry (Moscow) On-Line Papers in Press, as Manuscript BM06-117, September 10, 2006.

ACCELERATED PUBLICATION

Modulation of Hippocampal Neuron Survival by Thrombin and Factor Xa

L. R. Gorbacheva[1], T. P. Storozhevykh[2], V. G. Pinelis[2], S. Ishiwata[3], and S. M. Strukova[1]*

[1]*Department of Human and Animal Physiology, Biological Faculty, Lomonosov Moscow State University, 119899 Moscow, Russia; E-mail: strukova@mail.ru*
[2]*Scientific Center for Children's Health, Russian Academy of Medical Sciences, 119991 Moscow, Russia*
[3]*Department of Physics, Faculty of Science and Engineering, Advanced Research Institute for Science and Engineering, Waseda University, Tokyo, Japan*

Received April 28, 2006
Revision received June 8, 2006

Abstract—Effects of thrombin, factor Xa (FXa), and protease-activated receptor 1 and 2 agonist peptides (PAR1-AP and PAR2-AP) on survival and intracellular Ca^{2+} homeostasis in hippocampal neuron cultures treated with cytotoxic doses of glutamate were investigated. It is shown that at low concentrations (?10 nM) thrombin and FXa protect neurons from glutamate-induced excitotoxicity. Inactivation of the proteases blocked the neuroprotective effect. Using PAR1-AP, PAR2-AP, and PAR1 antagonist, we have demonstrated that the neuroprotective effect of thrombin is mediated through activation of PAR1, whereas the effect of FXa may involve novel subtype(s) of PARs. Unlike FXa, thrombin induced transient intracellular calcium signal in hippocampal neurons, which was mainly mediated via IP_3 receptors of the endoplasmic reticulum. Both of the serine proteases improved the recovery of neuronal Ca^{2+} homeostasis after glutamate treatment.

DOI: 10.1134/S000629790610004X

Key words: thrombin, factor Xa, glutamate toxicity, apoptosis, intracellular calcium, hippocampal neurons

Thrombin (EC 3.4.21.5), a highly specific protease from the trypsin family and a key protein in the blood coagulation system, is formed as a result of limited proteolysis of prothrombin by activated factor Xa at sites of tissue and vascular injury. Thrombin is involved in the regulation of many physiological and pathophysiological processes by interactions with protease-activated receptors (PAR1, PAR3, and PAR4) [1-3]. Thrombin activates positive and negative feedback reactions in hemostasis and fibrinolysis, participates in the regulation of vascular tonus, organism development, as well as in the processes of inflammation, tissue repair, atherogenesis, carcinogenesis, and neurodegenerative diseases (Alzheimer's disease and others) [2-6]. Thrombin multifunctionality is associated with the features of its tertiary structure and the presence of two subsites (besides the classical active site), so-called anion-binding exosites (ABE) (also called additional sites for substrate and receptor recognition) [6, 7]. Anion-binding exosite 2 (ABE2) enables thrombin binding to heparin and glycosaminoglycans [8]. ABE1, the recognition site for complementary domains of receptors (PAR1, thrombomodulin), specific substrates (fibrinogen), and inhibitors is responsible for high specificity of bond cleavage and selection of thrombin substrates, as well as thrombin regulatory functions during inflammation and tissue repair, which are always accompanied by activation of the coagulation system and thrombin accumulation at the site of injury of vessel and surrounding tissue [4, 7, 9, 10]. Contemporary data on the role of thrombin in traumatic and ischemic brain injury are controversial. Thrombin, whose effect is implicated through the seven transmembrane G-protein coupled protease-activated receptors (PAR), is considered both as a death factor and survival factor for neural cells [10-17]. It has been demonstrated that the introduction of thrombin in the caudate nucleus induces the development of inflamma-

Abbreviations: ABE1) anion-binding exosite 1; 2-APB) 2-aminoethoxydiphenyl borate; AraC) cytosine arabinoside; FXa) activated coagulation factor X; LDH) lactate dehydrogenase; PAR) protease-activated receptor; PAR1-AP) protease-activated receptor 1 agonist peptide; PMSF) phenylmethylsulfonyl fluoride.

* To whom correspondence should be addressed.

tion and edema, whereas low enzyme concentrations have a protective effect on central nervous system cells [13, 16]. Transient ischemic episodes in the nervous system result in development of resistance to subsequent severe brain ischemia, and thrombin is apparently involved in this phenomenon [16]. Functions of coagulation factor Xa (FXa), a serine protease that is able to activate PAR1 but predominantly activates PAR2 [3, 6], are poorly known beyond hemostasis and inflammation. Expression of prothrombin, FXa, and PAR mRNA was detected in brain regions most susceptible to ischemic damage, among those being cortex, striatum, hypothalamus, hippocampus, and cerebellum [13, 17-19]. Data on the role of PAR in regulation of cell survival are also contradictory. Neurodegenerative function of PAR2 has been reported [20]; however, cell death is diminished upon activation of these receptors in the course of neuroinflammation, injury, and ischemia [21-24]. A number of authors indicate increased brain damage upon activation of PAR1 under conditions of ischemia and hypoxia [24]. It is known that such damages of brain tissue as trauma, ischemia, and neurodegenerative diseases (Alzheimer's disease and others) are associated with hyperstimulation of glutamate receptors [25]. Massive Ca^{2+} influx into nerve cells through ionotropic glutamate receptor-associated channels disrupts the homeostasis of this intercellular messenger, which in turn results in initiation of a complex apoptotic cell death cascade [26, 27]. Therefore, the study of reactions triggered in nerve cells by serine proteases during glutamate toxicity is of special interest.

The aim of this work was to study the effect of thrombin and factor Xa on survival and calcium homeostasis of cultured rat hippocampal neuron cells during glutamate toxicity.

MATERIALS AND METHODS

Hippocampal neuron culture. Studies were performed using 9-14-day primary culture of neurons from hippocampus obtained from brain of 1-3-day-old Wistar rats. Cell suspension was obtained according to a previously described technique [28] and transferred onto a cover glass (one hippocampus in 200 μl per glass) covered with poly-D-lysine (10 mg/ml). The cells were allowed to sediment for 1 h at 37°C and 5% CO_2, then non-attached cells were removed and 1.5 ml of culture medium (neurobasal medium A containing 2% Supplement B-27 and 0.5 mM L-glutamine) was added. At day 3-4 cytosine arabinoside (AraC, 10^{-5} M) was added to suppress the growth of glial cells.

Determination of neuron death. Neuron death in culture was estimated 24 h after the cell exposure (for 15 min) to glutamate and other studied substances, which were added to cells upon replacement of culture medium with HEPES-saline buffer (HBSS). HBSS composition in mM was: NaCl, 145; KCl, 5; $CaCl_2$, 1.8; $MgCl_2$, 1.0; HEPES, 20; glucose, 5 (pH 7.4). Cell death was determined using two approaches, biochemical and morphological. The biochemical approach was based on the measurement of lactate dehydrogenase level (LDH) in the medium. The presence of cytoplasmic enzyme in the culture medium indicates the damage of cell membrane (necrosis). LDH activity was determined spectrophotometrically at 340 nm using an Anthos Lucy1 microplate reader (Anthos Labtec Instruments, Austria) and LDH-L reagent kit (Diagnostic Chemicals Limited, Canada). The percentage of neuron death was calculated as (LDH activity in cell medium/total LDH content) × 100, where total LDH content was determined after cell lysis by 0.2% Triton X-100 for 15 min at 37°C.

Morphological estimation of neuron death (apoptosis) included the study of nuclear fragmentation using a fluorescent DNA-tropic dye, Hoechst 33342 (absorption wavelength 360 nm, emission wavelength 460 nm), that is able to penetrate into living cells and bind to A-G pairs of damaged fragmented DNA [29]. Stained cells were investigated and visually counted using a fluorescence microscope Axiovert 200 (Zeiss, Germany); the amount of apoptotic cells was expressed as percentage.

Registration of intracellular calcium concentration $[Ca^{2+}]_i$. $[Ca^{2+}]_i$ was measured spectrophotometrically using fluorescent probes Fura-2/AM or Fura-2FF/AM with high or low affinity to Ca^{2+}, respectively. The fluorescence spectrum for these lipophilic probes is shifted to lower wavelength upon binding of the probe molecule to Ca^{2+}. *Prior to* the experiments the cells were loaded with the probe (5 μM) for 40 min in the culture medium, after which the cell culture was washed off with HBSS. A cell-coated glass was placed in a perfusion chamber (0.2 ml) assembled on the table of the Axiovert 200 microscope. Light of two different wavelengths (340 and 380 nm, alternating in 100-200 msec pulses) was used for excitation of fluorescence; emission was assayed at 505 ± 10 nm. A built-in video camera (Roper Scientific, USA) and computer software Metafluor 6.1 (Universal Imaging Corp., USA) allowed obtaining and processing a digital record of the experiment. In the experiments where Fura-2FF/AM was used, the change in $[Ca^{2+}]_i$ was estimated by the fluorescence ratio at 340 and 380 nm (F_{340}/F_{380}). In other experiments the absolute values of $[Ca^{2+}]_i$ were determined using calibration solutions according to [30]. In all experiments, the background fluorescence was subtracted from registered fluorescence emitted by neurons. All experiments were performed at room temperature (26°C).

Materials. Bovine thrombin, bovine FXa, fluorescent dye Hoechst 33342, NaCl, KCl, $CaCl_2$, $MgCl_2$, KH_2PO_4, HEPES, glucose, EGTA, 2-aminoethoxydiphenyl borate (2-APB), dantrolene, ionomycin, tetrodoxin, glutamate, NMDA, phenylmethylsulfonyl fluoride (PMSF), glutamax, AraC, Triton X-100, and poly-D-lysine were from Sigma (USA); Fura-2/AM and Fura-

2FF/AM from Molecular Probes (USA); synthetic PAR1 agonist peptide (PAR1-AP, TFLLRN) and PAR2 agonist peptide (PAR2-AP, SLIGRL) were from Biosyntan (Germany); PAR1 antagonist (Mpr(Cha)) (Mercaptopropionyl-F(Cha-Cha)RKPNDK-NH_2) was kindly provided by A. Kawabata; neurobasal medium A containing 2% Supplement B-27 (Gibco, USA) and L-glutamine (Gibco) was from Gibco; LDH-L reagent kit was from Diagnostic Chemicals Limited.

Statistical treatment of data was performed using Student's *t*-test for paired samples.

RESULTS

Effect of thrombin and FXa on the death of hippocampal neurons caused by glutamate toxicity. In the first set of experiments the death (by necrosis) of cultured rat hippocampal neurons was studied 24 h after exposure to 100 μM glutamate (for 15 min) or combined effect of glutamate, thrombin, and synthetic peptide – a PAR1 agonist (PAR1-AP) or PAR1 antagonist (Mpr(Cha)) using biochemical techniques (Fig. 1, a and b). Glutamate induced cell death in 34% of hippocampal neurons (Fig. 1a). Incubation of cell culture with thrombin at concentrations from 0.1 to 10 nM resulted in almost two-fold decrease in glutamate-induced neuron death (Fig. 1a). Thrombin at high concentration (100 nM) did not have a protective effect. Moreover, 100 nM thrombin caused cell death in 32% of neurons, which is comparable with glutamate-induced death (data not shown).

Experiments with specific PAR1 agonist peptide (TFLLRN) that selectively activates only PAR1 and with PAR1 antagonist peptide (Mpr(Cha)) indicate the involvement of PAR1 receptors in neuron activation by thrombin. According to our data, PAR1-AP (100 μM) protected neurons from the death from glutamate toxicity similarly to thrombin (Fig. 1b), whereas PAR1 antagonist peptide, Mpr(Cha) (100 μM), prevented the neuroprotective effect of thrombin (Fig. 1b).

In the second set of experiments, the death of rat hippocampal neurons was studied by morphological techniques using the apoptosis marker Hoechst 33342. Apoptotic neurons had condensed chromatin and fragmented nucleus (Fig. 2, a and b; see color insert). As seen from Fig. 2c, glutamate caused apoptosis after 24 h in 34% of neurons, thrombin (10 nM) decreased the number of apoptotic neurons to 17%, PAR1-AP (100 μM) imitated the neuroprotective effect of thrombin, and PAR1 antagonist peptide (100 μM) prevented the protective effect of thrombin. Therefore, the results of biochemical and morphological studies have confirmed our preliminary data on the involvement of PAR1 in the neuroprotective effect of thrombin [31].

In the next two sets of experiments the influence of a protease, FXa, on glutamate cytotoxicity was studied

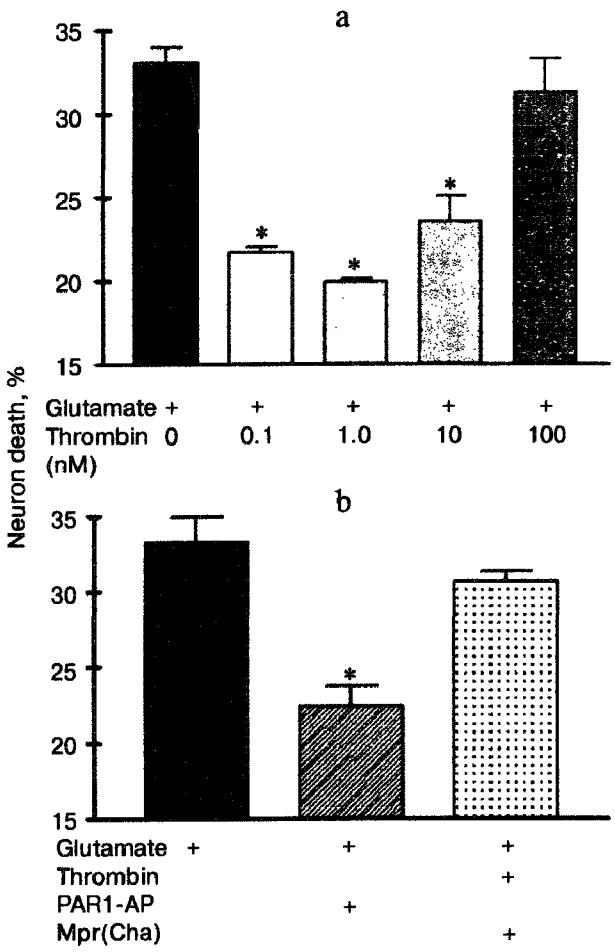

Fig. 1. Effect of thrombin, synthetic PAR1 agonist peptide (PAR1-AP), and PAR1 antagonist (Mpr(Cha)) on the death of hippocampal neurons induced by incubation of cell culture with 100 μM glutamate for 15 min. Cell death was estimated by the level of lactate dehydrogenase in cell cultures 24 h after application of glutamate. a) Effect of thrombin at concentrations from 0.1 to 100 nM on neuron death; b) effect of PAR1-AP (100 μM) and PAR1 antagonist Mpr(Cha) (100 μM) in combination with thrombin (10 nM) on death of neurons. * $p < 0.05$ compared to glutamate, here and further $n = 5$-7 independent experiments.

using the biochemical (Fig. 3) and morphological (Fig. 4, see color insert) approaches. It was found that FXa at the concentration of 1 and 10 nM decreased neuron death caused by a 15 min exposure to 100-μM glutamate down to 12 and 20%, respectively (Fig. 3a). The block of PAR1 receptors by Mpr(Cha) antagonist did not prevent the protective effect of FXa (Figs. 3b and 4c). Since the effect of FXa on cells is mediated predominantly by PAR2 [3], we used a synthetic PAR2 agonist peptide (PAR2-AP) (100 μM) for simulation of the FXa effect on neuron survival after glutamate toxicity. However, as seen from Figs. 3b and 4c, cell death after the incubation of neuron cultures with glutamate and PAR2-AP did not reliably differ from that caused by glutamate alone. The data obtained

by different techniques are in good agreement with each other and provide evidence that the PAR1 and PAR2 receptors are not involved in the neuroprotective effect of FXa. Apparently, the protective effect of FXa is realized through a yet unknown subtype of protease-activated receptors, in so far as the presence of proteolytic activity is absolutely necessary for displaying the effect of FXa. We have demonstrated that 10 nM FX, inactivated by PMSF, as well as PMSF-inactivated thrombin (10 nM), did not protect hippocampal neurons from death under conditions of glutamate cytotoxicity (30.5% neuron death vs. 34% resulting from the effect of glutamate alone). These results confirm the data obtained earlier regarding the protective effect of FXa during glutamate cytotoxicity [32].

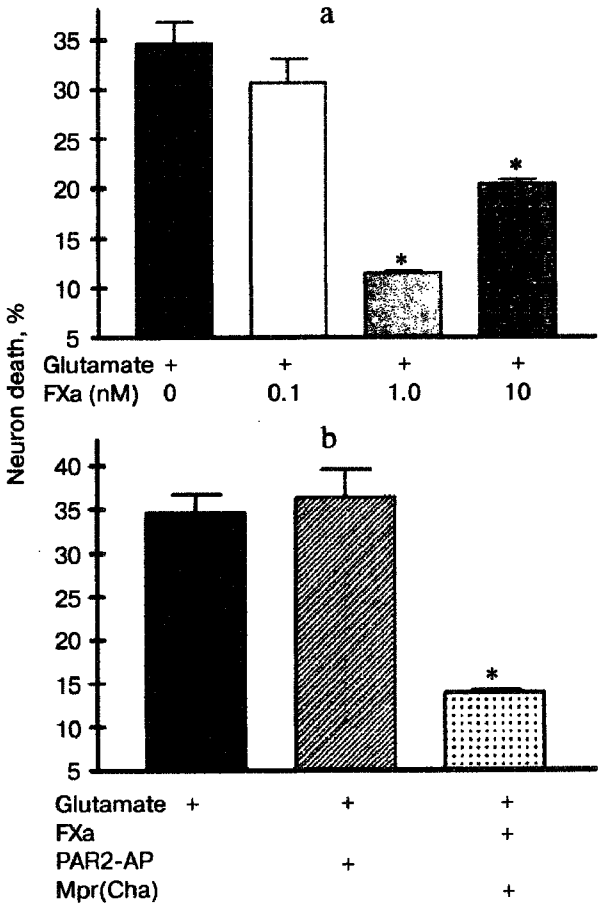

Fig. 3. Effect of factor Xa (FXa), PAR1 antagonist (Mpr(Cha)), and synthetic PAR2 agonist peptide (PAR2-AP) on the death of neurons caused by incubation of cell culture with 100 μM glutamate for 15 min. Cell death was estimated by the level of lactate dehydrogenase in cultures 24 h after application of glutamate. a) Effect of FXa at concentrations from 0.1 to 10 nM on neuron death; b) effect of PAR2-AP (100 μM) and PAR1 antagonist (Mpr(Cha)) (100 μM) in combination with 10 nM FXa on glutamate-induced death of neurons. * $p < 0.05$ compared to glutamate.

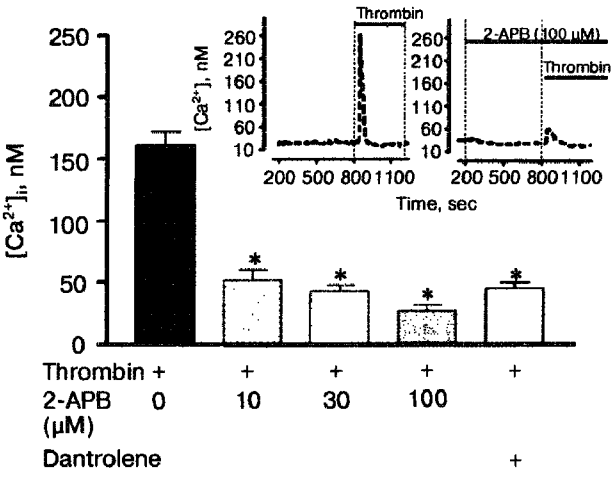

Fig. 5. Block of IP_3 receptors in neuron endoplasmic reticulum by 2-aminoethoxydiphenyl borate (2-APB) (10, 30, and 100 μM) or ryanodine receptors by dantrolene (30 μM) decreases the calcium signal induced by 10 nM thrombin. * $p < 0.05$ compared to glutamate. Insert at the top shows the original record of $[Ca^{2+}]_i$ change in hippocampal neuron in response to thrombin (left) and thrombin in combination with 2-APB (right). $[Ca^{2+}]_i$ was measured using the fluorescent probe Fura-2.

Effect of thrombin and FXa on $[Ca^{2+}]_i$ in hippocampal neurons. As seen from Fig. 5, activation of hippocampal neurons by 10 nM thrombin elicited a rapid, transient increase in $[Ca^{2+}]_i$, the concentration of which reached a maximum (150-200 nM) for 20-30 sec. Then, despite the presence of thrombin in the incubation medium, $[Ca^{2+}]_i$ reverted to the initial level. Not all hippocampal neurons responded to thrombin by changing $[Ca^{2+}]_i$; the number of responding neurons was on average 64% of the total number of studied neurons ($n = 36$).

Preliminary incubation of cells with 2-APB (10-100 μM), an IP_3 receptor blocker, decreased the calcium response in neurons by more than three-fold (Fig. 5). In such case, thrombin response in the presence of 2-APB was observed in 24% of cells. Incubation of cells with 30 μM dantrolene, an inhibitor of ryanodine receptors, did not change the number of cells responding to thrombin, but decreased the amplitude of calcium response by 3.1-fold. Contrary to thrombin, FXa did not induce the change in $[Ca^{2+}]_i$ at all concentrations studied (0.1-80 nM) (data not shown).

Next we studied the effect of thrombin and FXa on the change in $[Ca^{2+}]_i$ (by the ratio of F_{340}/F_{380}) in response to prolonged exposure (20 min) to 100 μM glutamate (Fig. 6). The ability of neurons to regenerate the basal level of $[Ca^{2+}]_i$ after the removal of glutamate from the solution has been analyzed (Fig. 6d). In these experiments low affinity probe Fura2-FF, which is sensitive only to substantial increase in $[Ca^{2+}]_i$ (more than 1 μM) was used for the registration of $[Ca^{2+}]_i$ signal. Glutamate caused a steady two-phase increase in $[Ca^{2+}]_i$ in neurons

(Fig. 6a). After removal of glutamate, $[Ca^{2+}]_i$ level in the vast majority of neurons did not revert to the original level (Fig. 6a). Incubation of cells with 10 nM thrombin did not have a significant effect on the increase in $[Ca^{2+}]_i$ caused by glutamate; however, it increased by more than two times the number of neurons in which the original level of $[Ca^{2+}]_i$ was recovered after removal of glutamate (Fig. 6, b and d). Similarly to thrombin, FXa facilitated rapid recovery of intracellular calcium homeostasis after prolonged exposure to glutamine (Fig. 6, c and d).

DISCUSSION

It is known that during focal cerebral ischemia the amount of the neurotransmitter glutamate, the toxic

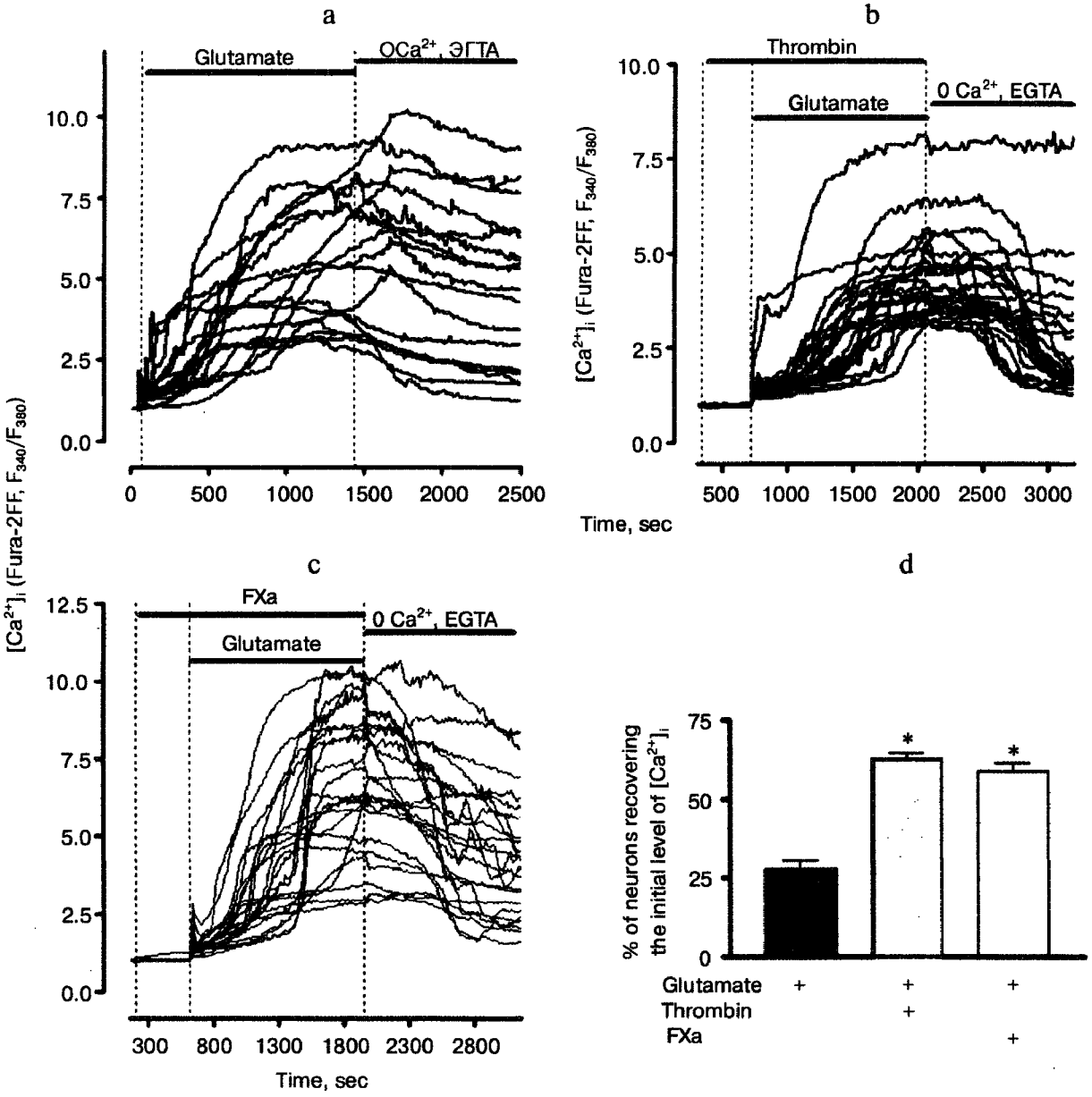

Fig. 6. Effect of thrombin and FXa on the change in $[Ca^{2+}]_i$ (by ratio of F_{340}/F_{380}) in hippocampal neurons upon prolonged exposure to 100 μM glutamate. Low affinity probe Fura-2FF was used. a) The original record of change in $[Ca^{2+}]_i$ in individual neurons before, during, and after the effect of glutamate. The cells were washed free of glutamate using calcium-deprived medium containing 100 μM EGTA; b) incubation of cell culture with 10 nM thrombin; c) incubation of cell culture with 10 nM FXa; d) effect of thrombin and FXa on the ability of neurons to recover the original level of $[Ca^{2+}]_i$ after the removal of glutamate. The number of cells (%) in which the F_{340}/F_{380} ratio 10 min after the washing free of glutamate was started did not exceed the original level by more than 25% is shown. * $p < 0.01$ compared to glutamate.

effect of which on neurons causes rapid, non-controlled increase in $[Ca^{2+}]_i$, is significantly increased in the intercellular space [33-35]. The disruption of $[Ca^{2+}]_i$ homeostasis triggers a cascade of intracellular reactions resulting in rapid or delayed cell death by apoptosis or necrosis [26, 27].

Primary neuron culture is a convenient experimental model for study of neurodestructive processes caused by glutamate, since the cytological and biochemical characteristics of cultured cells are similar to those observed in neurons *in situ* [36]. The glutamate concentration used in this work (100 μM) had a neurotoxic effect on hippocampal neurons, as indicated by the experiments for estimation of neuron cell death resulting from glutamate exposure (Figs. 1 and 2) as well by change in $[Ca^{2+}]_i$ (Fig. 6a). Hence, the selected model of glutamate cytotoxicity is comparable to endogenous pathological conditions of the injured brain.

In recent times, interest in the effect of serine proteases of the blood coagulation system beyond homeostasis has dramatically increased [3, 4, 6, 10]. However, the data on the effect of hemostasis proteases on neurons are contradictory and not abundant. We have attempted to characterize the role of thrombin, a key serine protease of hemostasis, and its precursor in the coagulation cascade, FXa, using the model of glutamate cytotoxicity in cultured rat hippocampal neurons.

The data indicate that at low concentrations (up to 10 nM) thrombin and FXa display a neuroprotective effect. At higher concentrations (100 nM), these proteases cause cell death. The minimal neuroprotective concentration of thrombin is 0.1 nM, and the corresponding FXa concentration is one order of magnitude higher, 1 nM (Fig. 3a). Different enzyme specificity to their substrates, PAR receptors, can be explained by a certain difference in the tertiary structure of these related enzymes. In the thrombin molecule there is a specific anion-binding exosite ABE1, which recognizes a complementary region in PAR1 exodomain, which in turn is similar to the negatively charged C-terminus of hirudin, a highly specific thrombin inhibitor [37]. Structural features of the enzymes are responsible for the difference between thrombin and FXa in the choice of their substrates and receptors. Our data on the protective effect of low thrombin concentrations confirm the results of a previous investigation [38], where the effect of thrombin on neurons was studied using hippocampal slices for modeling ischemia; however, they are not in agreement with other data [39] on the ability of thrombin to potentiate NMDA receptors in hippocampal neurons.

The effect of thrombin on cells is mediated by PAR1 as well as PAR4 [3, 4, 13, 40]. The use of agonist and antagonist showed that thrombin imparts a neuroprotective effect on hippocampal neurons through PAR1, since the PAR1 antagonist prevented the protective effect of thrombin, whereas the PAR1 agonist imitated its effect (Figs. 1b and 2c). Thus, thrombin exerts its neuroprotective effect in a narrow concentration range (0.1-10 nM) in conjunction with PAR1 receptors. It is probable that the destructive effect of thrombin simultaneously involves different types of receptors and in large amount.

There is evidence that FXa activates vascular endothelial cells through PAR1 and PAR2 receptors [41]. FXa induced calcium signal in fibroblasts through PAR1 receptors and stimulated cell proliferation and procollagen synthesis [42]. In our experiments, the preliminary incubation of cells with PAR2 agonist peptide did not protect the cells from glutamate-induced death, and with PAR1 antagonist it did not prevent the neuroprotective effect of FXa (Figs. 3b and 4c).

Therefore, according to our data, thrombin displays a protective effect on hippocampal neurons during glutamate toxicity by activation of PAR1. FXa exerts a protective effect through an unknown subtype of PAR, because the effect of FXa is not imitated by the PAR2 agonist and not blocked by PAR1 antagonist (Figs. 3 and 4).

Since glutamate at toxic concentrations causes irreversible increase in $[Ca^{2+}]_i$, it can be assumed that the reduction of neurotoxic glutamate effect on cells by thrombin is mediated by modulation of $[Ca^{2+}]_i$. There are sporadic data in literature concerning the change in $[Ca^{2+}]_i$ in rat hippocampal neurons caused by thrombin [43]. In the present work we have confirmed the data obtained by us earlier [31] that indicated that PAR1 agonist peptide imitates the thrombin-induced calcium signal in hippocampal cells, whereas the antagonist blocks it. It was demonstrated that PAR1 is involved in the calcium signal induced by thrombin in human brain astrocytes [44].

Increase in $[Ca^{2+}]_i$ in neurons may be associated both with mobilization of Ca^{2+} from intracellular stores and Ca^{2+} influx into cells. Earlier we have shown [31] that in calcium-free medium (100 μM EGTA), thrombin causes an increase in $[Ca^{2+}]_i$, but the amplitude of calcium signal is more than two times lower than in calcium-containing medium. After depleting the reticulum of neurons in calcium-free medium using cyclopiazonic acid (an inhibitor of reticulum Ca^{2+}-ATPase), the addition of thrombin did not result in increase in $[Ca^{2+}]_i$. These data indicate the role of intracellular reticulum in thrombin-induced calcium signal. Release of calcium from the reticulum can be realized by activation of two types of receptors, IP_3 and ryanodine. The use of corresponding blockers of the above receptors, 2-ABP and dantrolene, showed the predominant role of the IP_3 receptors in the calcium response to thrombin (Fig. 5). These results are in agreement with the data illustrating that the mechanism of PAR1-dependent calcium response in oligodendrocytes is also mediated by the IP_3 receptors of endoplasmic reticulum [45]. However, some authors mention that the reticulum IP_3 receptors are involved in the induction of death of granular cells in cerebellum [46].

Since the apoptotic effect of glutamate is based on the overloading of cells by calcium and disruption in the regulation of calcium homeostasis, we have studied the effect of thrombin on glutamate-induced increase in $[Ca^{2+}]_i$ in hippocampal neurons. It has been demonstrated that the incubation of cell culture with thrombin at the concentration of 10 nM or with FXa at the same concentration improves the recovery of calcium homeostasis in neurons after exposure to glutamate (Fig. 6). The mechanism of the effect is unknown; however, it can be assumed that through the activation of the intracellular factors serine proteases facilitate the calcium transport system (first of all, Ca^{2+}-ATPase of the plasma membrane), resulting in the enhancement of calcium efflux. It cannot be excluded that proteases might diminish the $[Ca^{2+}]_i$ signal induced by activation of glutamate receptors. Thus, we have previously found that preliminary incubation of cells with low concentrations of thrombin resulted in a decrease in intracellular calcium signal in hippocampal neurons upon application of NMDA, an agonist of NMDA subtype of glutamate receptor [31]. According to literature data [47], neuroprotection in hippocampal neurons can be achieved through decrease in ionic current mediated by NMDA receptors. At the same time, we have not found any change in $[Ca^{2+}]_i$ in hippocampal neurons induced by FXa. However, both thrombin and FXa decreased the number of hippocampal neurons in which the prolonged exposure to glutamate induced irreversible increase in $[Ca^{2+}]_i$ (Fig. 6). This matter requires further investigation.

As pointed out above, thrombin is able to activate PAR1 and PAR4 [17, 40]. However, the PAR4 molecule lacks the site complementary to anion-binding exosite 1 (ABE1) in thrombin, which is responsible for binding of highly specific substrates and receptors, and requires high thrombin concentrations for its activation [3]. This explains heterodirected effects of thrombin. Thus, effect of thrombin on microglia is realized mainly through PAR4, which is involved in brain inflammation processes associated with neurotrauma and neurodegeneration [16, 40]. Thrombin can release NO in rat microglial cell culture, and this being the case, PAR1 inhibitor does not block the above effect [48].

Both proapoptotic and antiapoptotic effects of thrombin are described in the literature. Upon intraventricular introduction, thrombin at high concentrations (25 and 100 nM, 0.25 μl/h, 28 days) caused apoptosis and decreased cognitive function in rats [49]. At concentrations higher than 25 nM, thrombin increased the sensitivity of cultured hippocampal neurons to glucose deprivation [44] and induced apoptosis in dopaminergic neurons [50]. In addition, thrombin protected astrocytes and hippocampal neurons from death caused by hypoglycemia and oxidative stress [38, 51-53].

In summary, though thrombin itself can induce death in a certain small population of hippocampal neurons, upon combined effect (at low concentration) with glutamate it is able to protect cells from glutamate-induced apoptosis and, moreover, a long time after the exposure to glutamate. The mechanism of neuroprotection is unknown. Activation of G-protein-coupled PAR1 receptors causes hydrolysis of phosphoinositides with formation of diacylglycerol, a well-known protein kinase C activator [3, 4, 6]. Perhaps the transduction of intracellular signal upon PAR1 activation occurs by the same pathway as for the activation of metabotropic glutamate receptors, which are also G-protein coupled. It has been shown that preliminary incubation of these receptors decreases the subsequent toxic effect of glutamate [54]. The increase in intracellular Ca^{2+} concentration induced by activation of PAR can influence a number of intracellular factors, both in nucleus and cytoplasm (transcription factors NF-κB, FosB/JunD, AP-1, and others) and trigger/suppress the expression of different genes including those proteins (Bax/Bad from Bcl family, AIF, MAP kinases, caspases) whose activity determines the progression of apoptosis during the toxic effect of glutamate [26, 55]. Investigation of mechanisms of interaction between glutamate and PAR receptors is a promising direction in the search for new approaches to treatment of cerebrovascular diseases.

This work was supported by the Russian Foundation for Basic Research grants (Nos. 05-04-49481 and 04-04-48513).

REFERENCES

1. Coughlin, S. R. (1999) *Proc. Natl. Acad. Sci. USA*, **96**, 11023-11027.
2. Coughlin, S. R. (2000) *Nature*, **407**, 258-264.
3. Ossovskaya, V. S., and Bunnett, N. W. (2004) *Physiol. Rev.*, **84**, 579-621.
4. Strukova, S. M. (2001) *Biochemistry (Moscow)*, **66**, 8-18.
5. Derian, C. K., Demiano, B. P., D'Andrea, M. R., and Andrade-Gordon, P. (2002) *Biochemistry (Moscow)*, **67**, 56-64.
6. Macfarlane, S. R., Seatter, M. J., Kanke, T., Hunter, G. D., and Plevin, R. (2001) *Pharmacol. Rev.*, **53**, 245-82.
7. Strukova, S. M., Serejskaya, A. A., and Osadchuk, T. V. (1989) *Uspekhi Sovrem. Biol.*, **107**, 41-54.
8. Sheehan, J. P., and Sadler, J. E. (1994) *Proc. Natl. Acad. Sci. USA*, **91**, 5518-5522.
9. Stubbs, M., and Bode, W. (1995) *Trends Biochem. Sci.*, **20**, 23-28.
10. Balezina, O. P., Gerasimenko, N. Yu., Dugina, T. N., and Strukova, S. M. (2004) *Uspekhi Fiziol. Nauk*, **35**, 37-49.
11. Suo, Z., Citron, B. A., and Festoff, B. W. (2004) *Curr. Drug Targets Inflamm. Allergy*, **3**, 105-114.
12. Striggow, F., Riek, M., Breder, J., Henrich-Noack, P., Reymann, K. G., and Reiser, G. (2000) *Proc. Natl. Acad. Sci. USA*, **97**, 2264-2269.
13. Striggow, F., Riek-Burchardt, M., and Reiser, G. (2001) *Eur. J. Neurosci.*, **14**, 595-608.

14. Yoshida, S., and Shiosaka, S. (1999) *Int. J. Mol. Med.*, **3**, 405-409.
15. Riek-Burchardt, M., Striggow, F., Henrich-Noack, P., Reiser, G., and Reymann, K. G. (2002) *Neurosci. Lett.*, **329**, 181-184.
16. Xi, G., Reiser, G., and Keep, R. F. (2003) *J. Neurochem.*, **84**, 3-9.
17. Wang, H., Ubl, J. J., and Reiser, G. (2002) *Glia*, **37**, 53-63.
18. Pompili, E., Nori, S. L., Geloso, M. C., Guadagni, E., Corvino, V., Michetti, F., and Fumagalli, L. (2004) *Brain Res. Mol. Brain Res.*, **122**, 93-98.
19. Rohatgi, T., Henrich-Noack, P., Sedehizade, F., Goertler, M., Wallesch, C. W., Reymann, K. G., and Reiser, G. (2004) *J. Neurosci. Res.*, **75**, 273-279.
20. Smith-Swintosky, V. L., Cheo-Isaacs, C. T., D'Andrea, M. R., Santulli, R. J., Darrow, A. L., and Andrade-Gordon, P. (1997) *J. Neurochem.*, **69**, 1890-1896.
21. Kawabata, A., Oono, Y., Yonezawa, D., Hiramatsu, K., Inoi, N., Sekiguchi, F., Honjo, M., Hirofuchi, M., Kanke, T., and Ishiwata, H. Br. (2005) *J. Pharmacol.*, **144**, 212-219.
22. Noorbakhsh, F., Vergnolle, N., McArthur, J. C., Silva, C., Vodjgani, M., Andrade-Gordon, P., Hollenberg, M. D., and Power, C. J. (2005) *Immunol.*, **174**, 7320-7329.
23. Jin, G., Hayashi, T., Kawagoe, J., Takizawa, T., Nagata, I., Syoji, M., and Abe, K. J. (2005) *Cerebr. Blood Flow Metab.*, **25**, 302-313.
24. Olson, E. E., Lyuboslavsky, P., Traynelis, S. F., and McKeon, R. J. (2004) *J. Cerebr. Blood Flow Metab.*, **24**, 964-971.
25. Hossain, M. A. (2005) *Epilepsy Behav.*, **7**, 204-213.
26. Orrenius, S., Zhivotovsky, B., and Nicotera, P. (2003) *Nat. Rev. Mol. Cell Biol.*, **4**, 552-565.
27. Dingledine, R., Borges, K., Bowie, D., and Traynelis, S. F. (1999) *Pharmacol. Rev.*, **51**, 7-60.
28. Khodorov, B. I., Storozhevykh, T. P., Surin, A. M., Sorokina, E. G., Yuryavichus, A. I., Borodin, A. V., Vinskaya, N. P., Khaspekov, L. G., and Pinelis, V. G. (2001) *Biol. Membr. (Moscow)*, **18**, 421-432.
29. Liu, X. Z., Xu, X. M., Hu, R., Du, C., Zhang, S. X., McDonald, J. W., Dong, H. X., Wu, Y. J., Fan, G. S., Jacquin, M. F., Hsu, C. Y., and Choi, D. W. (1997) *J. Neurosci.*, **17**, 5395-5406.
30. Kiedrowski, L., Brooker, G., and Costa, E. (1994) *Neuron*, **12**, 295-300.
31. Kiseleva, E. V., Storozhevykh, T. P., Pinelis, V. G., Gluza, E., and Strukova, S. M. (2004) *Byul. Eksp. Biol. Med.*, **137**, 519-523.
32. Strukova, S., Gorbacheva, L., Storozhevykh, T., Pinelis, V., and Smirnov, M. (2006) *J. Thromb. Haemost.*, **6**, 1409-1410.
33. Choi, D. W. (1992) *J. Neurobiol.*, **23**, 1261-1276.
34. Gusev, E. I., Skvortsova, V. I., and Raevsky, K. S. (1997) *Eur. J. Neurol.*, **4**, 78.
35. Danysz, W., and Parsons, C. (1998) *Pharmacol. Rev.*, **50**, 597-664.
36. Khaspekov, L. G. (1995) *Mechanisms and Factors of Neurodestructive Effect of Excitatory Amino Acids on Brain Neurons in vitro*: Author's abstract of Doctoral dissertation [in Russian], Moscow.
37. Gaussem, P., Picard, V., Chadeuf, G., Arnaud, E., and Aiach, M. (1995) *FEBS Lett.*, **365**, 219-222.
38. Henrich-Noack, P., Striggow, F., Reiser, G., and Reymann, K. G. (2005) *J. Neurosci. Res.*, **83**, 128-133.
39. Gingrich, M. B., Jung, C. E., Lyuboslavsky, P., and Traynelis, S. F. (2000) *J. Neurosci.*, **20**, 4582-4595.
40. Suo, Z., Wu, M., Citron, B. A., Gao, C., and Festoff, B. W. (2003) *J. Biol. Chem.*, **278**, 31177-31183.
41. McLean, K., Schirm, S., Johns, A., Morser, J., and Light, D. R. (2001) *Thromb. Res.*, **103**, 281-297.
42. Blanc-Brude, O. P., Archer, F., Leoni, P., Derian, C., Bolsover, S., Laurent, G. J., and Chambers, R. C. (2005) *Exp. Cell Res.*, **304**, 16-27.
43. Smith-Swintosky, V. L., Zimmer, S., Fento, J. W., II, and Mattson, M. P. (1995) *J. Neurosci.*, **15**, 5840-5850.
44. Junge, C. E., Lee, C. J., Hubbard, K. B., Zhang, Z., Olson, J. J., Hepler, L. R., Brat, D. J., and Traynelis, S. F. (2004) *Exp. Neurol.*, **188**, 94-103.
45. Wang, Y., Richter-Landsberg, C., and Reiser, G. (2004) *Neuroscience*, **126**, 69-82.
46. Limke, T. L., Bearss, J. J., and Atchison, W. D. (2004) *Toxicol. Sci.*, **80**, 60-68.
47. Blaabjerg, M., Baskys, A., Zimmer, J., and Vawter, M. P. (2003) *Mol. Brain Res.*, **117**, 196-205.
48. Ryu, J., Pyo, H., Jou, I., and Joe, E. J. (2000) *Biol. Chem.*, **275**, 29955-29959.
49. Mhatre, M., Nguyen, A., Kashani, S., Pham, T., Adesina, A., and Grammas, P. (2004) *Neurobiol. Aging*, **25**, 783-793.
50. Choi, S. H., Lee, da Y., Pyu, J. K., Kim, J., Joe, E. H., and Jin, B. K. (2003) *Neurobiol. Dis.*, **14**, 181-193.
51. Vaughan, P. J., Pike, C. J., Cotman, C. W., and Cunningham, D. D. (1995) *J. Neurosci.*, **15**, 5389-5401.
52. Chalmers, C. J., Balmanno, K., Hadfield, K., Ley, R., and Cook, S. J. (2003) *Biochem. J.*, **375**, 99-109.
53. Strukova, S. M., Kiseleva, E. V., Dugina, T. N., Gluza, E., Storozhevykh, T. P., and Pinelis, V. G. (2005) *Fiziol. Zh. im. I. M. Sechenova*, **91**, 53-60.
54. Sanchez-Perez, A., Llansola, M., Cauli, O., and Felipo, V. (2005) *Cerebellum*, **4**, 162-170.
55. Flynn, A. N., and Buret, A. G. (2001) *Apoptosis*, **9**, 729-737.

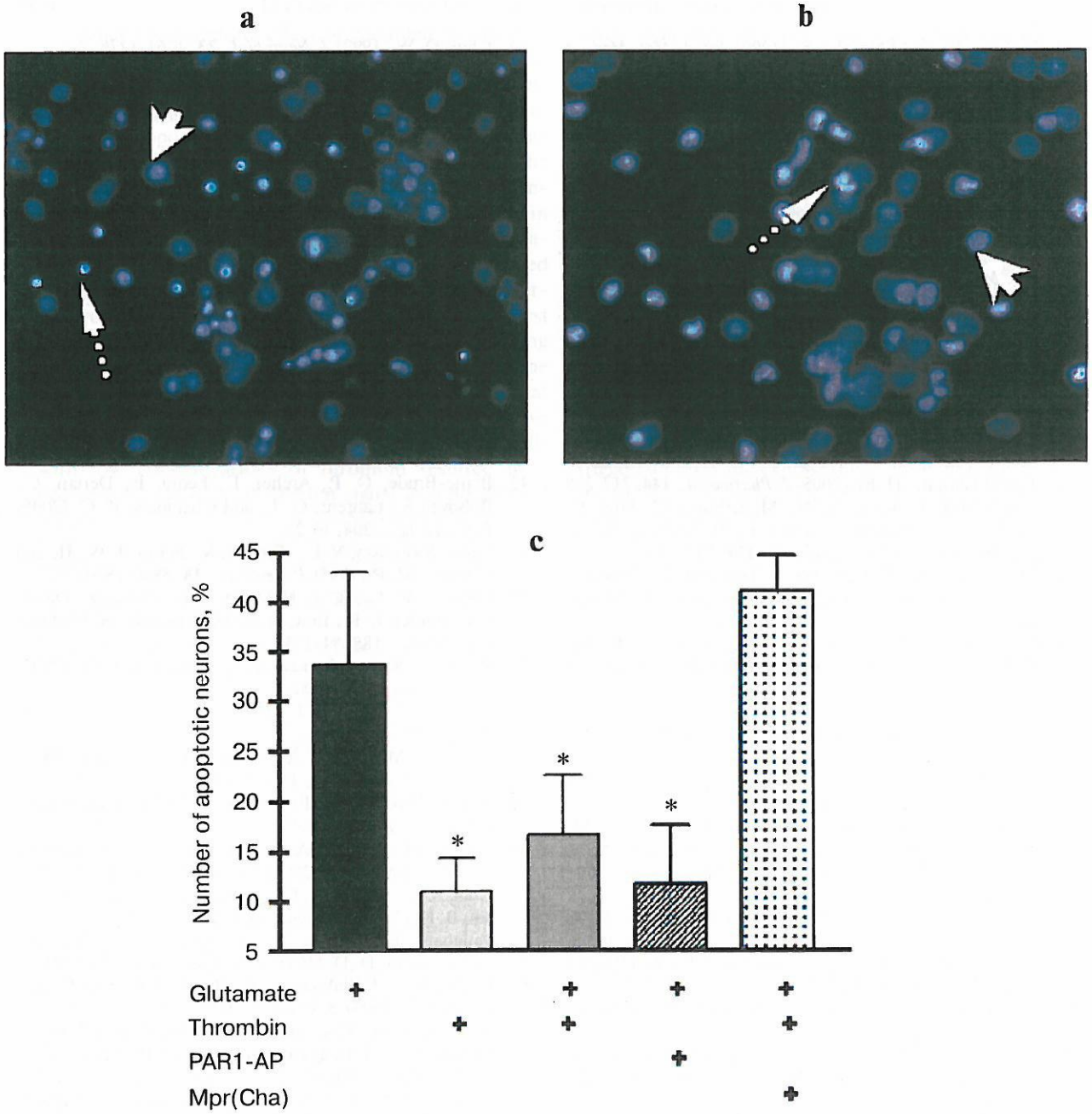

Fig. 2. (L. R. Gorbacheva et al.) Effect of thrombin on apoptosis of hippocampal neurons 24 h after the incubation of cell culture with 100 μM glutamate for 15 min. Results of cell count for living and apoptotic neurons stained with nuclear fluorescent dye Hoechst 33243. Solid arrow shows living cells and dashed arrow shows apoptotic cells. a) Cell fluorescence after the effect of glutamate; b) the same after the effect of glutamate in combination with 10 nM thrombin; c) effect of 10 nM thrombin, 100 μM PAR1 agonist (PAR1-AP), and 100 μM PAR1 antagonist (Mpr(Cha)) in combination with thrombin on glutamate-induced apoptosis. * $p < 0.05$ compared to glutamate.

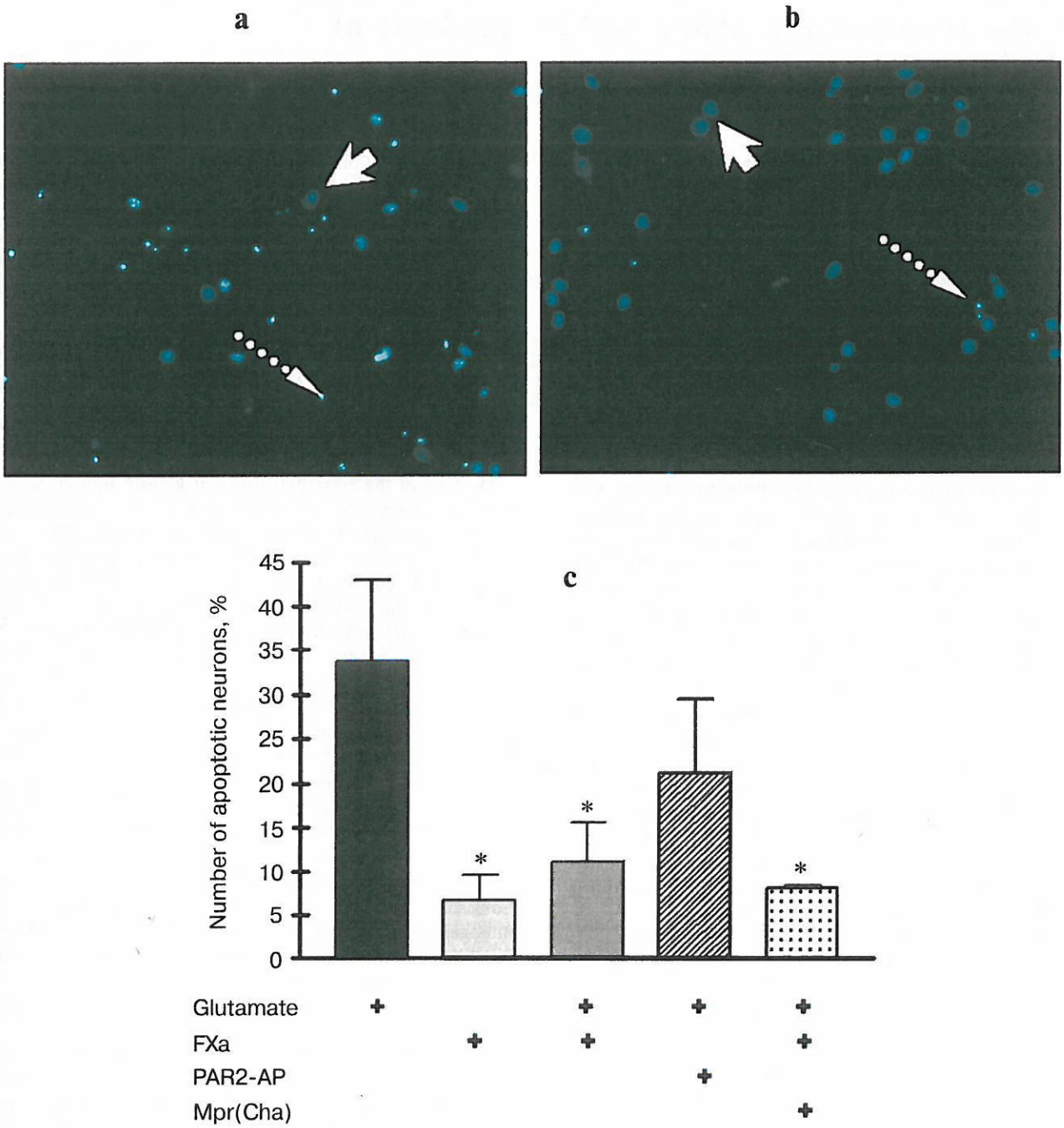

Fig. 4. (L. R. Gorbacheva et al.) Effect of FXa on apoptosis of hippocampal neurons 24 h after a 15 min incubation of cell culture with 100 μM glutamate. Results of cell count for living and apoptotic neurons stained with nuclear fluorescent dye Hoechst 33243. Solid arrow shows living cells and dashed arrow shows apoptotic cells. a) Cell fluorescence after the effect of glutamate; b) the same after the effect of glutamate in combination with 10 nM FXa; c) effect of 10 nM FXa, 100 μM PAR2 agonist (PAR2-AP), and 100 μM PAR1 antagonist (Mpr(Cha)) in combination with FXa on glutamate-induced apoptosis. * $p < 0.05$ compared to glutamate.

The EMBO Journal (2006) 25, 5932–5941 | © 2006 European Molecular Biology Organization | All Rights Reserved 0261-4189/06
www.embojournal.org

THE EMBO JOURNAL

Identification of a strong binding site for kinesin on the microtubule using mutant analysis of tubulin

Seiichi Uchimura[1,4,6], Yusuke Oguchi[2,6], Miho Katsuki[1,6,7], Takeo Usui[3,8], Hiroyuki Osada[3], Jun-ichi Nikawa[4], Shin'ichi Ishiwata[2,5] and Etsuko Muto[1,*]

[1]Brain Development Research Group, Brain Science Institute, RIKEN, Wako, Saitama, Japan, [2]Department of Physics, School of Science and Engineering, Waseda University, Tokyo, Japan, [3]Antibiotics Laboratory, Discovery Research Institute, RIKEN, Wako, Saitama, Japan, [4]Department of Bioscience and Bioinformatics, Faculty of Computer Science and Systems Engineering, Kyushu Institute of Technology, Fukuoka, Japan and [5]Advanced Research Institute for Science and Engineering, Waseda University, Tokyo, Japan

The kinesin-binding site on the microtubule has not been identified because of the technical difficulties involved in the mutant analyses of tubulin. Exploiting the budding yeast expression system, we succeeded in replacing the negatively charged residues in the α-helix 12 of β-tubulin with alanine and analyzed their effect on kinesin–microtubule interaction *in vitro*. The microtubule gliding assay showed that the affinity of the microtubules for kinesin was significantly reduced in E410A, D417A, and E421A, but not in E412A mutant. The unbinding force measurement revealed that in the former three mutants, the kinesin–microtubule interaction in the adenosine 5′-[β,γ-imido]triphosphate state (AMP-PNP state) became less stable when a load was imposed towards the microtubule minus end. In parallel with this decreased stability, the stall force of kinesin was reduced. Our results implicate residues E410, D417, and E421 as crucial for the kinesin–microtubule interaction in the strong binding state, thereby governing the size of kinesin stall force.

The EMBO Journal (2006) **25**, 5932–5941. doi:10.1038/sj.emboj.7601442; Published online 23 November 2006
Subject Categories: membranes & transport; structural biology
Keywords: kinesin; microtubule; mutant analysis; stall force; yeast

Introduction

Kinesin is a molecular motor involved in many cellular force-generating processes such as organelle transport and chromosome segregation (Vernos and Karsenti, 1996; Goldstein and Yang, 2000). Conventional kinesin contains two identical heavy chains and can move processively along a microtubule more than 1 μm in length without dissociation (Howard *et al*, 1989; Block *et al*, 1990). Processive movement of kinesin is explained by the hand-over-hand model, in which the motor maintains continuous contact with the microtubule as a result of alternating head catalysis of ATP (Hackney, 1994; Ma and Taylor, 1997). At each ATP hydrolysis cycle, kinesin makes an 8-nm step (equal to the size of tubulin dimer) towards the microtubule plus end (Hua *et al*, 1997; Schnitzer and Block, 1997), and this stepping motion is triggered by a conformational change in the ATP-bound head (Rice *et al*, 1999).

Docking of the crystal structure of kinesin into cryoelectron-microscopy maps of kinesin–microtubule complex indicated L8, L11, and α4/L12/α5 in the motor domain of kinesin as the structural key elements for microtubule binding in the presence of AMP-PNP, a non-hydrolyzable ATP analogue mimicking the ATP-bound state (Hirose *et al*, 1999; Hoenger *et al*, 2000; Kikkawa *et al*, 2000; Skiniotis *et al*, 2004). In this model, L8 may bind to α-helix 12 (H12) in β-tubulin, and L11 extends towards the H11–H12 loop in α-tubulin. α4/L12/α5 is also closely associated with H12 in β-tubulin and possibly with the C-terminus of β-tubulin, which is not defined in the crystal structure. The model indicates that kinesin–microtubule interaction might be mediated by electrostatic interactions. Some of the positively charged amino acids in these contact areas of kinesin potentially interact with the negatively charged surface of the microtubule, which is mainly composed of H12 in β-tubulin. Consistent with this assumption, using alanine-scanning mutagenesis of kinesin, several positively charged residues in L7/8, L11, and α4/L12/α5 have been identified as microtubule-interacting kinesin residues (Woehlke *et al*, 1997). However, the critical residues on tubulin have not been identified.

Proteolytic digestion of the C-terminal region of tubulin led to the reduced processivity of both single- and double-headed kinesin (Okada and Hirokawa, 2000; Thorn *et al*, 2000; Wang and Sheetz, 2000; Lakämper and Meyhöfer, 2005). The biochemical measurement of K_d of kinesin to both intact and protease-digested microtubule revealed that the negatively charged C-terminus of tubulin may be a binding partner for kinesin in the weak binding state (ADP state), but not in the strong binding state (AMP-PNP state) (Okada and Hirokawa, 2000; Skiniotis *et al*, 2004; Lakämper and Meyhöfer, 2005). A structural element other than the tubulin C-terminal region may serve as an interface that is specific for the strong binding state; the structural analyses have implicated H12 in β-tubulin as a potential candidate for this (Hirose *et al*, 1999; Hoenger *et al*, 2000; Kikkawa *et al*, 2000; Skiniotis *et al*, 2004). For elucidating the mechanism of kinesin motility, it is essential to identify the structural elements involved in each chemical state because the physi-

*Corresponding author. Brain Development Research Group, Brain Science Institute, RIKEN, Hirosawa 2-1, Wako, Saitama 351-0198, Japan. Tel.: +81 48 467 6959; Fax: +81 48 467 7145;
E-mail: emuto@brain.riken.jp
[6]These authors contributed equally to this work
[7]Present address: Molecular Motors Group, Marie Curie Research Institute, The Chart, Oxted, Surrey RH8 0TE, UK.
[8]Present address: Graduate School of Life and Environmental Sciences, University of Tsukuba, Tsukuba, Ibaraki, Japan

Received: 28 July 2006; accepted: 23 October 2006; published online: 23 November 2006

cochemical properties inherent to each chemical state might be critically dependent on the interface configuration and the surface force type that works between the interfaces (Israelachvili, 1992; Okada and Hirokawa, 2000; Skiniotis *et al*, 2004; Lakämper and Meyhöfer, 2005).

Our lack of knowledge about kinesin interface on tubulin is attributed to the technical difficulties involved in mutant analysis of tubulin. Tubulin is a heterodimer composed of α- and β-polypeptides, each requiring a distinct set of chaperons for proper folding. Apart from this complexity, multiple α- and β-tubulin genes are found in most eukaryotic cells, with each subunit undergoing different post-translational modifications (Luduena, 1998). Consequently, it has been difficult to express and purify isotypically pure tubulin in biochemically useful amounts.

Here, we have used the budding yeast *Saccharomyces cerevisiae* to conduct mutant analyses on microtubules. *S. cerevisiae* contains only two α-tubulin genes (*TUB1* and *TUB3*) and one β-tubulin gene (*TUB2*); since *TUB3* is non-essential, it provides a potential source of isotypically pure tubulin (Bode *et al*, 2003). Using *TUB3*-null cells, we succeeded in generating a set of charged-to-alanine point mutations in the sequence coding for H12 in β-tubulin. Each of these mutated tubulins was purified from the cell lysate, polymerized into microtubules, and the effect of mutation was examined in microtubule gliding assay on conventional two-headed kinesin. This showed that the affinity of microtubule for kinesin was reduced in E410A, D417A, and E421A mutants. The measurement of the unbinding force (Kawaguchi and Ishiwata, 2001; Uemura *et al*, 2002) revealed that in the former three mutants, the kinesin–microtubule interaction in AMP-PNP state became less stable for minus end loading, whereas their interaction in ADP state was unaffected by the mutations. These results indicate that the negatively charged amino-acid residues E410, D417, and E421 in β-tubulin are crucial for the strong binding of kinesin to the microtubule.

Hereafter, we have abbreviated the α-helix and β-sheet in the tubulin structures as 'H' and 'S,' corresponding to α and β, respectively, in the kinesin structure, according to the original paper on the structure of microtubule (Nogales *et al*, 1998).

Results

Construction, expression, and purification of H12 mutated microtubules

To prepare isotypically pure tubulin, we used *TUB3*-null yeast cells, having only a single α- and β-tubulin gene, *TUB1* and *TUB2*, respectively (see Supplementary Methods and Table SII). As the aim of this study was to examine the motility of kinesin along the mutated microtubules, it was necessary to obtain yeast microtubules that were stable at low concentrations required for *in vitro* motility assay (~10 μg/ml). Hence, Taxol-binding ability was introduced into a β-tubulin gene by site-directed mutagenesis at five amino acids (Gupta *et al*, 2003), and the gene *tub2-A19K-T23V-G26D-N227H-Y270F* thus obtained was referred to as $TUB2^{tax}$. The yeast strain expressing *TUB1* and $TUB2^{tax}$ was used as the wild-type in the following analyses.

To examine the function of β-tubulin H12 in kinesin motility, we generated a set of charged-to-alanine point mutations in the sequence coding for H12 in β-tubulin

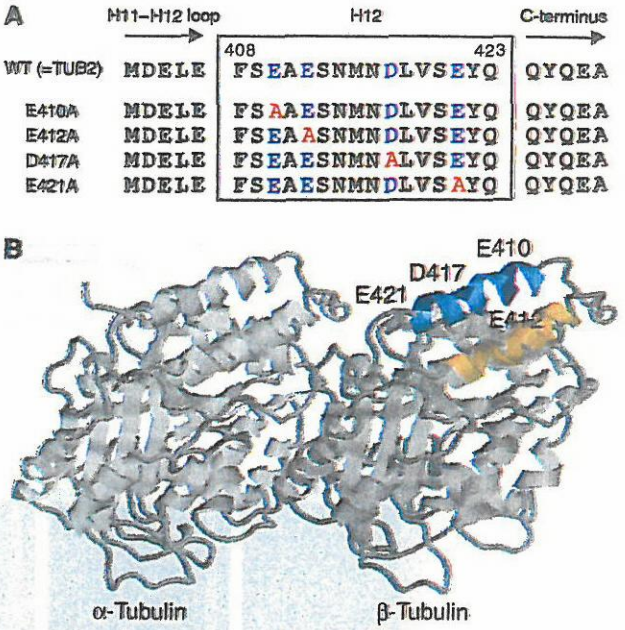

Figure 1 Design of the H12 mutants of β-tubulin in *Saccharomyces cerevisiae*. (**A**) Sequences of the H12 region are shown with negatively charged residues indicated by blue and the residues substituted by alanines are indicated by red. (**B**) A ribbon diagram of the tubulin dimer viewed from the side of the microtubule with its minus end to the left (Nogales *et al*, 1998). Image analysis of the kinesin–microtubule complex revealed that in both nucleotide free and AMP-PNP state, kinesin motor domain is associated in close proximity to H11 (orange), H12 (cyan), and the COOH terminus (undefined in crystal structure) of β-tubulin (Kikkawa *et al*, 2000; Hoenger *et al*, 2000). The acidic residues in H12 mutagenized to alanine are indicated in *blue*.

(Figure 1). Among these four mutants, E410A and D417A were haploid lethal. Therefore, we attempted to isolate these mutated tubulins by expressing two species of $tub2^{tax}$ genes in a strain, one of which, $tub2^{tax}$*-plusE* ($tub2^{tax\text{-}440}$*GDFGEEEEGEEEEGEEEEGEEEEA*), contains numerous negatively charged amino acids at the C-terminus and the other, $tub2^{tax}$*-E410A* or $tub2^{tax}$*-D417A*, which has point mutation in H12; the latter is under the control of the inducible galactose promoter (Burke *et al*, 1989). The haploid cells were first grown in YPD medium, expressing only $tub2^{tax}$*-plusE*. When the growth reached the late-log phase, the cells were transferred to YPG medium containing galactose for inducing the coexpression of $tub2^{tax}$*-E410A* (or $tub2^{tax}$*-D417A*). The cells were cultured for another 8 h in YPG medium, and then harvested for tubulin purification. The cell lysate contains two species of tubulin dimers, including either $Tub2^{tax}$p-plusE or $Tub2^{tax}$p-E410A (or $Tub2^{tax}$p-D417A) as β-tubulin subunit, but these two species can be separated using their charge differences during purification (see Supplementary Figure S1). For the other two mutants, E412A and E421A, tubulin could be readily purified from the cultured haploid cells as these cells containing only this mutated tubulin were viable under normal growth conditions (YPD medium).

To purify tubulin from the cell lysate, a couple of anion exchange column chromatographies were successively used (Davis *et al*, 1993), and the crude tubulin fraction eluted from the second column was further purified by polymerization

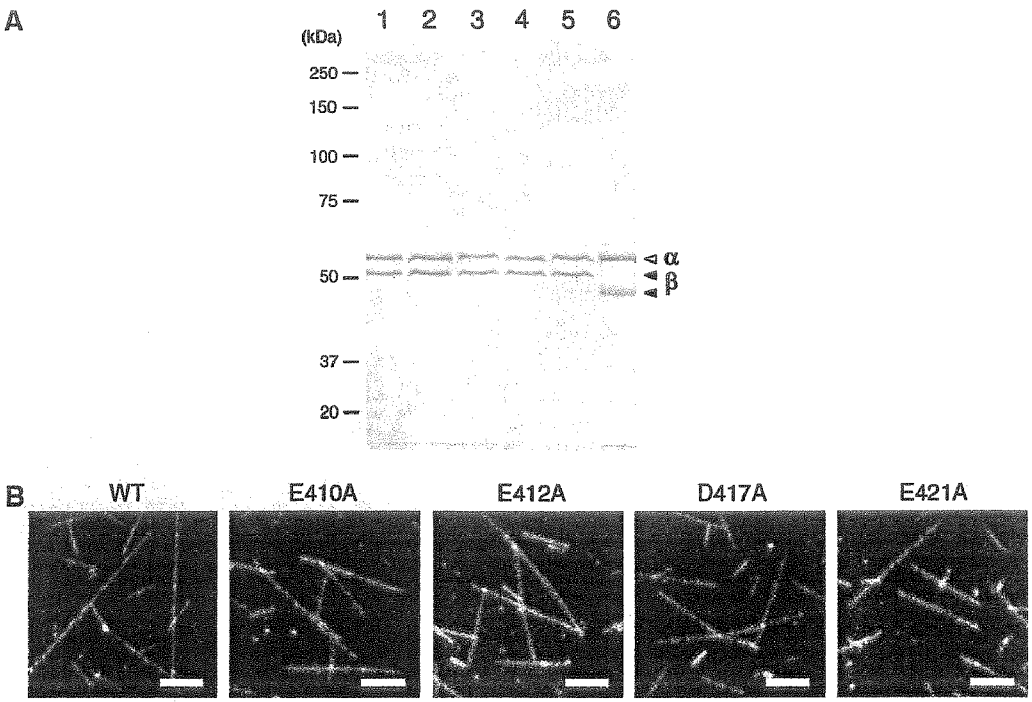

Figure 2 Purity of yeast tubulin and images of polymerized microtubules. (**A**) SDS–PAGE analysis of purified tubulin. Lane 1, yeast wild-type tubulin; lane 2, E410A; lane 3, E412A; lane 4, D417A; lane 5, E421A; and lane 6, porcine brain tubulin. In each lane, 1 μg of sample was loaded and stained by Coomassie blue. In SDS gel containing Sigma SDS (L-5750), α- and β-polypeptide of porcine brain tubulin were separated more as compared to these peptides purified from yeast cells (Best *et al*, 1981; Bode *et al*, 2003). (**B**) Dark-field images of the microtubules polymerized from yeast wild-type and mutated tubulins in the presence of 1 μM Taxol. Bar = 5 μm.

and depolymerization (see Supplementary Methods and Figure S2). This procedure generated approximately 30 μg of assembly-competent tubulin from 6L of culture with purity higher than 95% on SDS gel electrophoresis (Figure 2A). To examine if these mutated tubulins were post-translationally modified at their C-terminus (Luduena, 1998), both α- and β-polypeptides were analyzed by electrospray ionization/ion trap and quadrupole-TOF mass spectrometry. The MS and MS/MS data suggested that the isolated tubulin dimers predominantly contained α- and β-polypeptides lacking any post-translational modifications at the C-terminal region (Supplementary Figure S3).

When these isolated tubulins (0.5–1.0 mg/ml) were incubated at 30°C in the presence of 1 μM Taxol, all species of tubulins could polymerize into long filaments having length up to ~20 μm (Figure 2B).

In vitro motility assay

To examine the influence of the mutations on kinesin–microtubule interaction, these mutated microtubules were first tested in the microtubule gliding assay on the conventional two-headed kinesin. When the density of kinesin on the glass surfaces was $>1000\,\mu m^{-2}$, both wild-type and mutated microtubules showed smooth gliding movement at similar velocities (Table I). When the direction of the movement was examined using polarity marked microtubules (Tanaka-Takiguchi *et al*, 1998), the movement of kinesin was plus-end-directed in all cases. However, at kinesin density of $\sim100\,\mu m^{-2}$, the wild-type and the E412A microtubules showed smooth gliding movement, whereas the E410A, D417A, and E421A microtubules often rotated erratically about a roughly vertical axis, resulting in wobbly gliding motions. This indicates that the latter three mutants may have lower affinity for kinesin as compared to the wild-type.

Table I Velocity of microtubule movement in the gliding assay[a]

Construct	Velocity (μm/s)[b]	*n*
WT	0.75±0.08	120
E410A	0.78±0.06	120
E412A	0.76±0.06	103
D417A	0.73±0.08	123
E421A	0.74±0.10	102

[a]Gliding assay was performed at a kinesin density of $\sim2000/\mu m^2$.
[b]Mean±s.e.m.

To quantify the affinity of these mutated microtubules for kinesin, we measured the fraction of the microtubules that moved a distance greater than their own lengths, *f*, over a range of kinesin densities (Figure 3A and B; Howard *et al*, 1989). Here, to compare between each mutant and wild-type, the length of the microtubules was adjusted to approximately 3 μm in all strains (see Materials and methods). The result showed that in the wild-type, virtually all the microtubules moved more than their own length at kinesin density $>300\,\mu m^{-2}$, and the fraction of the microtubules that covered distances greater than their own length gradually decreased with the decrease in kinesin density. At kinesin density $<10\,\mu m^{-2}$, no microtubules covered distances greater than their own lengths. For continuous movement of a microtubule over distance greater than its own length, if a minimum number, *n*, of kinesin molecules are required to interact

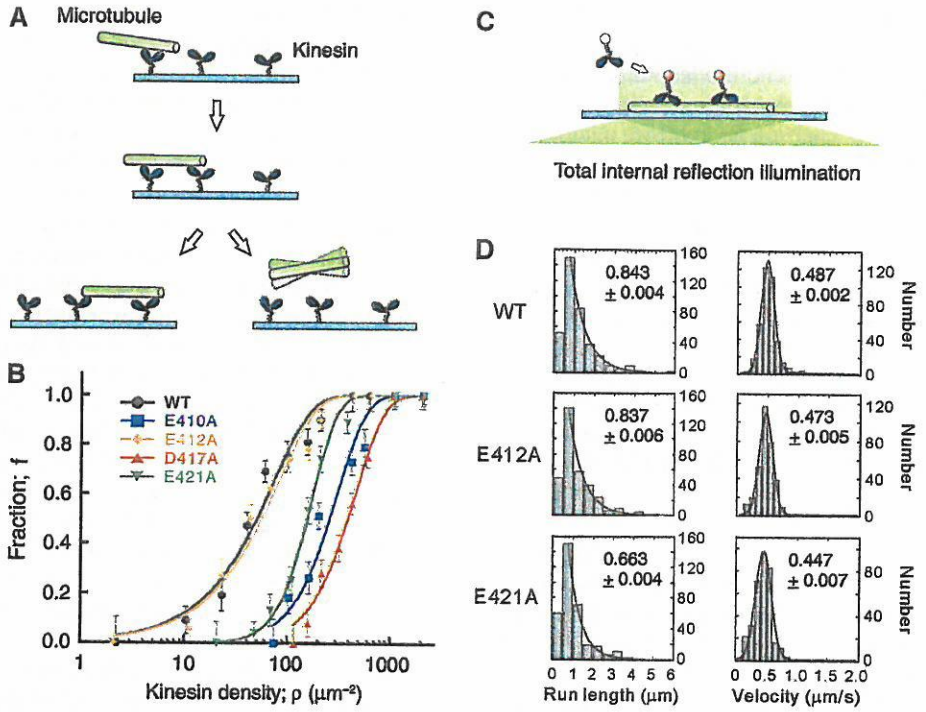

Figure 3 Motility assays using mutated microtubules. (**A**) In microtubule gliding assay, the fraction of microtubules that moved a distance greater than their own length (~3 μm), *f*, was measured, and (**B**) plotted as a function of kinesin density, ρ. Total number of microtubules counted for wild-type (black), E410A (blue), E412A (orange), D417A (red), and E421A (green) were 495, 328, 657, 496, and 388, respectively. Continuous curves are the plot of equation (1). Error bars represent the statistical counting errors, calculated according to Materials and methods. (**C**) In single molecule motility assay using TIRFM, the motility of HK560-Cy3 was examined, and (**D**) the distribution of the kinesin run length and the velocity was analyzed for both the wild-type and the mutated microtubules. HK560-Cy3 did not interact with the E410A and D417A microtubules. Total number of the events counted for wild-type, E412A, and E421A were 374, 329, and 333, respectively.The mean run length and the mean velocity, calculated according to Supplementary Methods, are shown in each panel with the errors of the curve fits.

with the microtubule, then the data points can be fit to the equation

$$f = 1 - \left(\sum_{i=1}^{n} (\rho/\rho_0)^i e^{-\rho/\rho_0}/i!\right)/(1 - e^{-\rho/\rho_0}) \qquad (1)$$

where ρ is the kinesin density (variable), ρ_0 is a fit parameter (Materials and methods; Howard *et al*, 1989; Hancock and Howard, 1998). The best fit was obtained with $n=1$ and $\rho_0 = 39.8\,\mu m^{-2}$ ($P=0.041$; χ^2 test), indicating that the wild-type microtubule can move processively along a single kinesin molecule randomly located on the glass surface. The result is similar to the previous observation on brain microtubules.

In contrast, whereas the data set for E412A showed a dependence on kinesin density similar to the wild-type ($n=1$, $\rho_0 = 43.6\,\mu m^{-2}$, $P=0.032$; χ^2 test), E410A, D417A, and E421A required significantly higher concentrations of kinesin to move a distance greater than their own lengths (Figure 3B). For the latter three mutants, the fraction curves were steeper and shifted to the right along the log density axis. When each of the data set was fit to the same equation, the best fit was obtained with $n=2$, $\rho_0 = 100.9\,\mu m^{-2}$ for E410A, $n=2$, $\rho_0 = 152.1\,\mu m^{-2}$ for D417A, and $n=3$, $\rho_0 = 42.9\,\mu m^{-2}$ for E421A, and the corresponding *P*-values were 0.047, 0.012, and 0.010, respectively (χ^2 test). These results indicate that alanine substitution at E410, D417, and E421 might have reduced the affinity of microtubules for kinesin either by lowering the efficiency of the initial interaction of the microtubules with kinesin molecules and/or by reducing the extent of microtubules processivity along the kinesin molecules.

ρ_0 for E410A and D417A was higher than that for the wild-type. This implies that at a given kinesin density, although the collision frequency was constant for all the species of microtubules, the initial interaction of the E410A/D417A microtubules with kinesin molecules might have occurred at a relatively low frequency as compared to the frequency observed with the wild-type microtubules. Contrastingly, ρ_0 for E421A was comparable to that of the wild-type, indicating that in E421A mutants, the initial interaction might have occurred at a frequency similar to that of the wild-type. The parameter ρ_0 may reflect the activation energy of the microtubule necessary for its initial interaction with kinesin on the glass surface (Fersht, 1984; Hackney, 1995).

Conversely, the parameter *n* is a measure of multivalency in the kinesin–microtubule interaction occurring at the microtubule's interface with the kinesin-coated surface. For E410A, D417A, and E421A mutants, *n* was >1. This result may indicate that either a simultaneous, collective action of multiple motor molecules is required for the stable gliding movement of mutated microtubules (Hancock and Howard, 1998; Shima *et al*, 2006) or that a run length of a single kinesin along the mutated microtubule is too short to support the gliding movement of microtubule over a distance greater than its own length.

To understand which the operative mechanism is, we conducted a single molecule motility assay (Figure 3C); the motility of fluorescently labeled two-headed kinesin HK560-Cy3 (0.29 nM) was examined along these mutated microtubules using total internal reflection fluorescence microscopy (TIRFM). The result showed that whereas kinesin moved processively along the wild-type and E412A microtubules, it scarcely interacted with the E410A and D417A microtubules (Figure 3D). For E421A, kinesin could move along the microtubule, but its processivity was reduced as compared to that of the wild-type. The mean run length of kinesin for the wild-type, E412A, and E421A microtubules was $0.843 \pm 0.004\,\mu m$, $0.837 \pm 0.006\,\mu m$, and $0.663 \pm 0.004\,\mu m$, respectively. These results are consistent with the values of ρ_0 and n derived from the fraction curves in Figure 3B. The estimated value of $n = 3$ for E421A was due to the reduced processivity of single kinesin.

It is reasonable that only the E410A, D417A, and E421A mutations affected the kinesin–microtubule interaction. Docking experiments of the crystal structure of kinesin into cryoelectron-microscopy maps of kinesin–microtubule complex revealed that H12 of β-tubulin is located on the surface of microtubules and aligned diagonally to the longitudinal axis of protofilament (Hoenger *et al*, 2000; Kikkawa *et al*, 2000). In its coiled structure, the residues E410, D417, and E421 are facing kinesin, whereas E412 is positioned on the opposite side, facing the microtubule core.

Unbinding force

To clarify the chemical state at which the binding affinity of the microtubules for kinesin was modulated in the mutants, we measured the force required to dissociate kinesin from these mutated microtubules (unbinding force) under two nucleotide conditions—in the presence of ADP and AMP-PNP (Kawaguchi and Ishiwata, 2001; Uemura *et al*, 2002).

One-headed kinesin heterodimers were used for the measurement because our previous work demonstrated that the two distinct binding modes (weak and strong), each inherent to the nucleotide condition, can be unambiguously characterized with the single-headed kinesin (Uemura *et al*, 2002). Using optical tweezers, a polystyrene bead attached with a single-headed kinesin (Kojima *et al*, 1997) was made to interact with a microtubule in the presence of either 1 mM ADP or 1 mM AMP-PNP. An external load was gradually applied to the kinesin–microtubule complex by moving the stage of the microscope towards the plus end or the minus end of the microtubule until the bead dissociated from it. The unbinding force was calculated by multiplying the magnitude of abrupt bead displacement during detachment with the stiffness of the optical tweezers.

The yeast wild-type microtubules showed properties similar to those observed previously for brain microtubules (Figure 4; Kawaguchi and Ishiwata, 2001; Uemura *et al*, 2002). Unbinding force in the AMP-PNP state was significantly higher than that in the ADP state, and in each nucleotide state, the unbinding force for the minus-end loading was

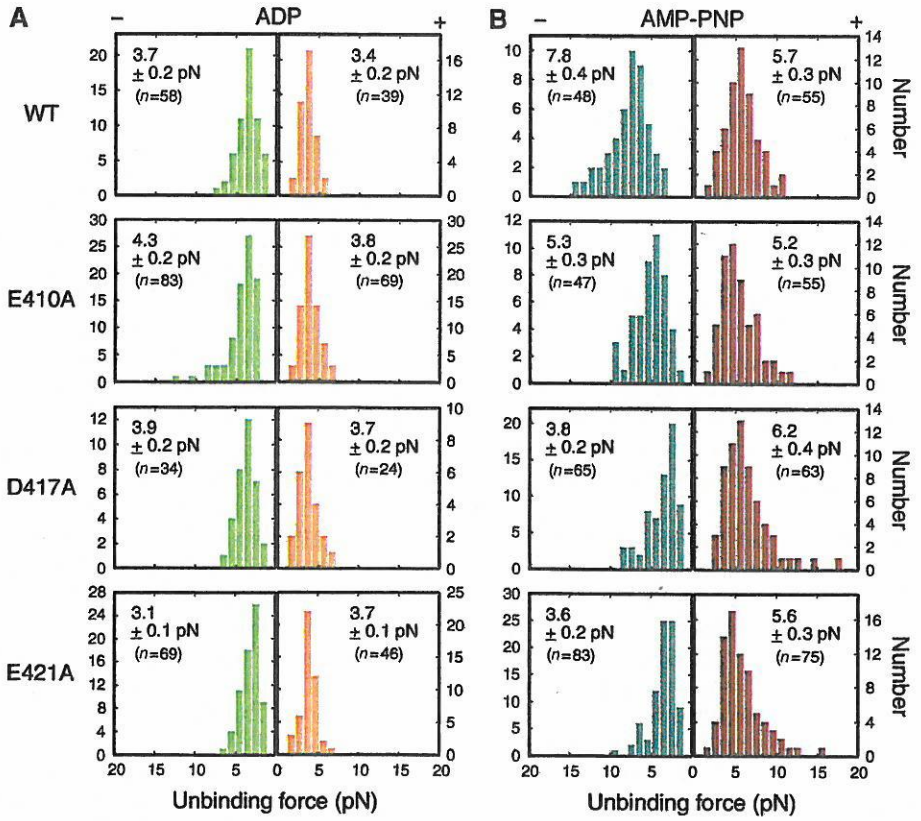

Figure 4 Unbinding force distribution of one-headed kinesin in (**A**) ADP and (**B**) AMP-PNP state. An external load was applied towards either the plus end (orange for (A) and red for (B)) or the minus end of the microtubule (light and dark green for (A) and (B), respectively). The stiffness of the trap was 0.038 pN/nm (ADP) and 0.076 pN/nm (AMP-PNP). The average unbinding force (pN) with s.e.m. is shown in each panel.

higher than that for the plus-end loading. The dependence on loading direction in the ADP state, however, was not as significant as in the AMP-PNP state.

Whereas the unbinding force in ADP state for mutated microtubules was almost similar to that measured for wild-type (Figure 4A), the unbinding force in AMP-PNP state was significantly altered by mutations (Figure 4B). In the presence of AMP-PNP, the unbinding force for minus-end loading was considerably reduced in all three mutants (7.8±0.4, 5.3±0.3, 3.8±0.2, and 3.6±0.2 pN for wild-type, E410A, D417A, and E421A, respectively; mean ±s.e.m.), yet the unbinding force for plus-end loading was scarcely affected (5.7±0.3, 5.2±0.3, 6.2±0.4, and 5.6±0.3 pN for wild-type, E410A, D417A, and E421A, respectively). Unexpectedly, the mutations rendered the kinesin–microtubule interaction less stable only for minus-end loading. In the presence of ADP, the unbinding force measured for mutants was fairly similar to that of the wild-type except in the case of E421A, where the asymmetry for loading direction was reversed.

The residues E410, D417, and E421 appeared to be crucial for the strong binding of kinesin to the microtubules, and this may underlie the reduced affinity of these mutated microtubules for kinesin during movement (Figure 3).

Stall force

Previous measurements of the mechanical properties of two-headed kinesin indicated that the kinesin stall force might be determined by (1) the binding affinity of the head to the microtubule in the strongly bound state and (2) the ATP-binding kinetics to the nucleotide-free head (Visscher *et al*, 1999; Nishiyama *et al*, 2002; Lakämper and Meyhöfer, 2005; Shao and Gao, 2006). Thus, the kinesin stall force exerted on the mutated microtubules with reduced affinity for kinesin in AMP-PNP state is expected to be smaller than that exerted on the wild-type microtubules. To examine this hypothesis, we next attempted to measure the stall force of conventional two-headed kinesin along these mutated microtubules.

When the displacements and forces caused by single kinesin molecules were measured in the presence of 1 mM ATP using optical tweezers (trap stiffness = 0.076 pN/nm), the stall force measured for E410A, D417A, and E421A was 3.5±0.1, 3.0±0.1, and 3.1±0.1 pN, respectively (mean± s.e.m.). These values were significantly lower than that measured for the wild-type (5.6±0.2 pN) (Figure 5A and B). Although we observed the processive movement of kinesin only for the wild-type, E412A, and E421A microtubules in the single molecule motility assay (Figure 3D), in the experiment using optical tweezers, a single-kinesin-bound bead is also observed to move along the E410A and

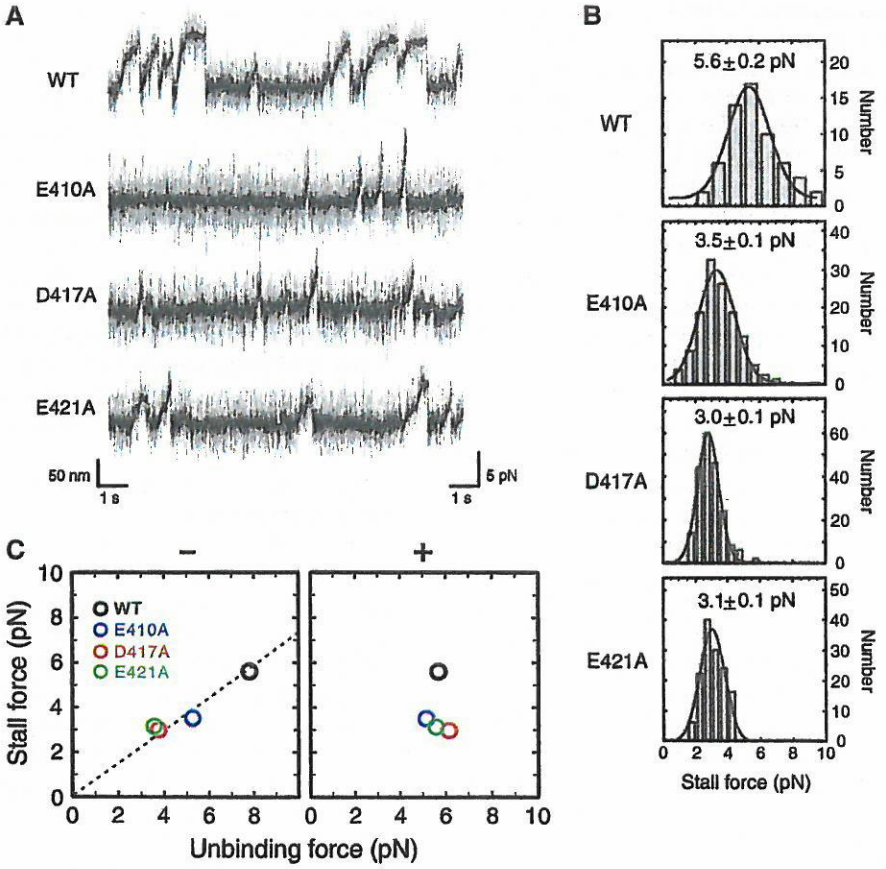

Figure 5 Stall force measurement. (**A**) Representative tracing of a trapped bead powered by a conventional two-headed kinesin along the wild-type, E410A, D417A, and E421A microtubules, measured at the trap stiffness of 0.076 pN/nm. Light shaded, unfiltered; solid, filtered at 100 Hz. (**B**) Distribution of the stall force for wild-type and mutated microtubules. The average stall force with s.e.m. is shown in each panel. Total number of events counted are (from top to bottom) 61, 104, 102, and 69, respectively. (**C**) The stall force plotted against the unbinding force for minus- (left) and plus-end loading (right). The stall force was linearly related to the unbinding force for minus-end loading (linear coefficient; 0.73).

D417A microtubules, probably because their initial interaction/successive interaction with the microtubule was enforced by the laser trap.

For wild-type and E421A mutant, the stall forces were independent of the trap stiffness, ranging from 0.019 to 0.076 pN/nm (Kojima *et al*, 1997). Contrastingly, for E410A and D417A microtubules, the stall force was almost constant down to the trap stiffness of 0.038 pN/nm. However, below this trap stiffness value, the stall force gradually declined with the decrease of the stiffness (data not shown), indicating that in these mutants, the duration of the kinesin–microtubule interaction might be limited not only by the limit in the maximum force but also by the limit in the run length (~200 nm).

When the stall force measured at the trap stiffness of 0.076 pN/nm was plotted against the unbinding force measured in the presence of AMP-PNP (Figure 5C), it became clear that the stall force is a linear function of the unbinding force for minus end loading. Our result clearly demonstrates that the size of the stall force depends on the force the head can bear against a load imposed towards the minus end in its strong binding state (Visscher *et al*, 1999; Nishiyama *et al*, 2002; Lakämper and Meyhöfer, 2005; Shao and Gao, 2006).

Discussion

Phenotype of yeast mutants and motility of the mutated microtubules in vitro

Utilizing yeast expression system, we have produced a set of charged-to-alanine mutations in β-tubulin H12, which has been implicated as a major constituent of kinesin interface in previous structural studies (Hirose *et al*, 1999; Hoenger *et al*, 2000; Kikkawa *et al*, 2000; Skiniotis *et al*, 2004). Among the four charged amino acids in H12, two amino-acid residues E410 and D417 appeared to be critical for the function of microtubules in living cells because substitution of these residues with alanine caused the yeast cells expressing only this mutated tubulin to become haploid lethal. It is unlikely that the lethality is due to the unsuccessful protein folding or global change in the tubulin structure because the mutated tubulins could polymerize into microtubules (Figure 2B). The most likely explanation for the observed lethality is that the alanine substitution of these charged residues might have deteriorated the intermolecular interaction of microtubules with various proteins (Al-Bassam *et al*, 2002; Mizuno *et al*, 2004), leading to the aberrant cellular transport and/or abnormal assembly of cellular architecture. All four acidic residues in H12 are highly conserved across the species (Little and Seehaus, 1988), indicating that the structure of H12 is refined through evolution to play a key role in the intermolecular interactions of microtubules.

Microtubule gliding assay using these mutated microtubules showed that the reduced charges in E410, D417, and E421 led to a decrease in their affinity for kinesin during movement, whereas the reduced charge in E412 had no influence (Figure 3B). Ineffectiveness of the mutation at residue E412 is consistent with the 3D model of kinesin–microtubule complex showing that E412 faces the microtubule core and is situated in a direction opposite the kinesin interface (Figure 1B; Hoenger *et al*, 2000; Kikkawa *et al*, 2000). Although the other three mutants showed reduced affinity for kinesin, the profile of their fraction curves indicates that the mechanism underlying the reduction of affinity might be different among the mutants; in E410A and D417A mutants, both initial interaction of kinesin with the microtubule and subsequent processive movement might have deteriorated, whereas in the E421A mutant, only the processivity might have been modulated by mutation. This interpretation was confirmed by the behavior of two-headed kinesin observed under TIRFM (Figure 3C and D). At the kinesin concentration of 0.29 nM, we could observe the processive movement of single kinesin molecules along the wild-type and E421A microtubules, whereas no interaction was observed for E410A and D417A microtubules. In the E421A mutant, the mean run length achieved by single kinesin was slightly reduced as compared to the wild-type.

It is possible that these differences between E410A/D417A and E421A mutants might explain the phenotypic differences between these two groups. The yeast cells of the former group were haploid lethal probably because the organelle vesicles with merely few motor proteins attached could not interact with the E410A/D417A microtubules, causing serious deterioration in organelle transport. As kinesin shares the same binding site on microtubules with the motors having opposite directionality (Lockhart *et al*, 1995; Mizuno *et al*, 2004), these mutations of microtubules might also disrupt the organelle transport directed towards the microtubule minus end. Conversely, the yeast E421A strain was viable because vesicles could still move along the E421A microtubules, although the efficiency of transport was lowered by the mutation.

The reduced stability of the kinesin–microtubule interaction in H12 mutants is consistent with the 3D model of the kinesin–microtubule complex showing that several positively charged amino acids in L8 and L12 of kinesin are located in close proximity to the negatively charged residues of H12 in β-tubulin (Hoenger *et al*, 2000; Kikkawa *et al*, 2000). Our result is also complementary to the result of the previous mutagenesis study on kinesin, demonstrating that the positively charged residues in L7/8, L11, and a4/L12/a5 of kinesin are crucial for kinesin–microtubule interaction during movement (Woehlke *et al*, 1997). These positively charged residues in kinesin L8 and L12 may electrostatically interact with the negatively charged residues of H12, playing a key role in the mechanism of motility.

Charge reduction in H12 decreased the stability of the strong binding state

Consistent with the reduced affinity measured in the motility assays, the measurement of the unbinding force has revealed that in these mutants, the stability of the kinesin–microtubule interaction in the AMP-PNP state was reduced for minus-end loading, but the stability in ADP state remained constant (Figure 4). This result contrasts with the previous observation that the removal of the negatively charged C-terminus of tubulin (E-hook) by protease treatment decreased the stability of the kinesin–microtubule interaction only in the ADP state, but not in the AMP-PNP state (Okada and Hirokawa, 2000; Skiniotis *et al*, 2004; Lakämper and Meyhöfer, 2005). E-hook and β-tubulin H12 apparently serve as an interface for kinesin specific for ADP and AMP-PNP state, respectively. These independent interfaces might be the structural basis for the physicochemical properties distinct for each chemical state. In the ADP state, mobility freedom of the motor has

to be ensured to a certain extent while it is loosely anchored to the microtubule surface (Okada and Hirokawa, 2000; Wang and Sheetz, 2000; Sosa *et al*, 2001; Skiniotis *et al*, 2004; Lakämper and Meyhöfer, 2005), whereas in the AMP-PNP state, the motor has to be tightly attached to the microtubule so that it can sustain load (Visscher *et al*, 1999; Kawaguchi and Ishiwata, 2001; Nishiyama *et al*, 2002; Uemura *et al*, 2002; Shao and Gao, 2006).

As suggested by the structural studies (Hoenger *et al*, 2000; Kikkawa *et al*, 2000) and the mutational analyses of kinesin (Woehlke *et al*, 1997), the binding site for kinesin in the strong binding state may not be confined in H12, but is rather spanned over an extensive area of tubulin. In this respect, it is noteworthy that the stability of the interaction in AMP-PNP state was modulated by mutations in H12 only for minus-end loading. For plus-end loading, some unidentified structure in tubulin, independent of β-tubulin H12, might be responsible for the stability of the interaction.

Although the structural elements that determine the shape of the binding potential for strong binding have not been fully identified, the measurement of the stall force demonstrated that the size of the stall force was linearly related to the unbinding force for minus-end loading, but it was independent of the unbinding force for plus-end loading (Figure 5C). As predicted from the analyses of the force–velocity relationship of single kinesin molecule (Visscher *et al*, 1999; Nishiyama *et al*, 2002; Carter and Cross, 2005; Lakämper and Meyhöfer, 2005; Shao and Gao, 2006), for two-headed kinesin to produce force, it might be crucial for the trailing head in the strong binding state to sustain against the load imposed towards the minus-end direction. Our result is the first direct demonstration that the stall force is directly related to the stability of the strong binding state.

Stability of the strong binding state is not directly related to kinesin processivity

Now, if we review the results obtained in two motility assays (Figure 3B and D) with the understanding that the affinity of the kinesin–microtubule interaction in the strong binding state was modulated in all three mutants (E410A, D417A, and E421A), we can have further insights into the mechanism of kinesin processivity. Despite the reduced affinity in the strong binding state, in the single molecule motility assay, processive movement of kinesin was reduced only slightly in the E421A mutant, whereas kinesin could scarcely interact with the E410A and D417A microtubules (Table II). In the latter two mutants, even when the initial interaction of kinesin with the microtubule was enforced using optical tweezers, kinesin showed only a poor processive movement, with its longest mean run length being ~200 nm (Figure 5). These results indicate that the stability of the strong binding state is not the only factor that determines the processivity of the two-headed kinesin.

Table II Summary of single molecule assay

	Motility assay		Mechanical measurement		
	Velocity (μm/s)	Run length (μm)	Stall force (pN)	Unbinding force (pN)[a]	
				(−)	(+)
WT	0.49	0.84	5.6	7.8	5.7
E410A	—[b]	—[b]	3.5	5.3	5.2
D417A	—[b]	—[b]	3.0	3.8	6.2
E421A	0.45	0.66	3.1	3.6	5.6

[a]Unbinding force obtained in AMP-PNP state in each minus- and plus-end loading direction.
[b]Data not available because single kinesin molecules did not spontaneously bind to these microtubules.

The differences between E410A/D417A and E421A mutants might depend on whether or not the leading head can readily attach to the microtubule before the trailing head dissociates from the microtubule. As proposed in the walking model of the kinesin movement, the processive movement of the two-headed kinesin might be a result of mechanical and chemical coordination between the two heads (Hackney, 1994; Ma and Taylor, 1997; Rice *et al*, 1999; Kawaguchi and Ishiwata, 2001; Uemura *et al*, 2002; Uemura and Ishiwata, 2003; Schief *et al*, 2004; Shao and Gao, 2006). If the ADP release from the leading head and the strong binding of this head to the microtubule occurs before the phosphate release from the trailing head and concomitant dissociation of the trailing head from the microtubule, kinesin might succeed to make a forward step. Such a coordination of the two heads might be somehow distracted in E410A/D417A mutants.

The 3D model of the kinesin–microtubule complex indicates that the basic residue in kinesin L8 faces the acidic residues E410 and D417 of β-tubulin, whereas some of the basic residues in kinesin L12 face the residue E421 of β-tubulin (Hoenger *et al*, 2000; Kikkawa *et al*, 2000; Skiniotis *et al*, 2004). Considering this structure, one can hypothesize that the interaction via kinesin L8 might be critical for the leading head to tightly bind the microtubule (Alonso *et al*, 1998; Klumpp *et al*, 2003; Ogawa *et al*, 2004). Currently, such an idea remains highly speculative, and to understand the exact mechanism, kinetical steps in the enzymatic cycle that are affected by each of the mutations should be addressed in future studies. Mutational analysis of tubulin developed in this study has opened a route for future studies to thoroughly identify the structural elements on kinesin interface in both strong and weak binding states, and to relate how each element is involved in the mechanochemical cycle of kinesin.

Materials and methods

Preparation of the H12 mutants

The plasmids and the yeast mutant strains were constructed as described in Supplementary Methods and are listed in Table SII.

Purification of yeast tubulin from mutants

Tubulin was purified from the yeast cell lysate via the successive use of ion exchange column chromatographies (DEAE-Sepharose and Mono-Q; Davis *et al*, 1993), followed by a cycle of tubulin polymerization and depolymerization. For details, see Supplementary Methods, Figures S1 and S2.

Microtubule gliding assay

We adapted a previously reported method (Howard *et al*, 1989) for our microtubule gliding assay, except that the standard buffer solution in the original assay was replaced by motility assay buffer (MA buffer) comprising 10 mM piperazine-*N*,*N*′-bis(2-ethanesulfonic acid) (PIPES), 5 mM K-acetate, 2 mM $MgSO_4$, 1 mM EGTA and 0.1 mM EDTA (pH 6.8) (see Supplementary Methods for detail). To maintain the ionic condition of the solution constant throughout the study, MA buffer was used in the microtubule gliding assay, single molecule motility assay, and unbinding force and stall force measurements.

In an experiment that measured the fraction of microtubules that moved for a distance greater than their own length (Figure 3A and B; Howard *et al*, 1989; Hancock and Howard, 1998), the mean lengths of the microtubules was adjusted to ~3 μm by controlling the concentration of tubulin and Taxol at the initial stage of polymerization. Based on the video images, microtubule lengths and distances that moved were measured using the public domain program, Image J. The data were collected at variable kinesin densities, and at each density, the fraction of microtubules that moved for a distance greater than their own length, f, was calculated. The data points were fit by equation (1), where ρ is the kinesin density (variable), ρ_0 is a fit parameter, and n is the number of kinesin molecules required for a microtubule to move for a distance greater than its own length. The error bars in the curves (Figure 3B) represent the statistical counting errors defined as follows, s.e.m. $= (f(1-f)/N)^{1/2}$, where $f \neq 0$ or 1; s.e.m. $= 1/N$ if $f = 0$ or 1. Although the lengths of the microtubules were adjusted to ~3 μm in both mutated and wild-type microtubules, their mean lengths were slightly different among the preparation of microtubules and among the populations of microtubules subjected to the analyses at each kinesin density. To compensate for this slight difference and to compare the ρ dependence of f between mutants, ρ in Figure 3B was corrected for each data point, assuming that the increase in the microtubules length is equivalent to the increase in the kinesin density in its effect, which increases the probability of the kinesin–microtubule encounter.

Single molecule motility assay

The protocol for single molecule motility assay originally designed for brain microtubules (Inoue *et al*, 2001) was modified for yeast microtubules. A flow chamber made of two coverslips (dimensions 9 mm × 9 mm × 80 μm) was first incubated with 6 μl of cytochrome *c* (C-2506, Sigma; 5 mg/ml in MA buffer) for 3 min, extensively washed with 50 μl of MA buffer, and loaded with 10 μl of yeast-microtubule solution (10 μg/ml in MA buffer containing 10 μM Taxol (Taxol without fluorescent label; T-7402, Sigma)). The coverslips were coated with cytochrome *c* to facilitate the adhesion of yeast microtubules, which had lower affinity for the glass surfaces than the brain microtubules, to the wall of chamber. The chamber was subsequently incubated with 15 μl of BSA (1 mg/ml in MA buffer) to block nonspecific binding of kinesin to the glass surface. Then, 15 μl of MA buffer containing 1 μM BODIPY-FL Taxol (P-7500, Molecular Probes) and an oxygen scavenger (Harada *et al*, 1990) was introduced into the chamber, and the microtubules were observed under TIRFM. After the position of a BODIPY-FL-labeled microtubule was recorded (Digital video recorder DR20; Sony), 15 μl of HK560-Cy3 solution (0.29 nM in MA buffer) containing 0.1 mg/ml casein, 1 mM ATP, 10 μM Taxol (Taxol without fluorescent label), and an oxygen scavenger was introduced into the chamber, and the interaction of HK560-Cy3 with the microtubule was recorded. For image analysis of kinesin movement and experimental setup of the TIRFM microscope, see Supplementary Methods.

Measurement of unbinding force and stall force

For measurement of the unbinding force, kinesin-coated beads were prepared as described previously (Kojima *et al*, 1997), except that the fluorescent polystyrene beads with a diameter of 1 μm (F-8823, Molecular Probes) were used. A flow chamber was first incubated with 15 μl of cytochrome *c* (5 mg/ml in MA buffer) for 5 min, and then washed with 50 μl of MA buffer. Subsequently, 10 μl of polarity-marked yeast microtubule solution including 10 μM Taxol (Taxol without fluorescent label) was infused into the chamber and microtubules were allowed to adsorb on the surface for 10 min. The chamber was then incubated with 15 μl of BSA (1 mg/ml in MA buffer) to block the nonspecific binding of kinesin-bound beads to the glass surface. Finally, 15 μl of kinesin-bound beads solution (25 fM of beads in MA buffer) containing an oxygen scavenger system (Harada *et al*, 1990), 1 μM BODIPY-564/570-Taxol (P-7501, Molecular Probes), 1 mM AMP-PNP and 1 U/ml apyrase (AMP-PNP state) or 1 mM ADP and 1 U/ml hexokinase (ADP-state) was introduced into the chamber.

The chamber was set under the fluorescence microscope (Nishizaka *et al*, 1995), and using optical tweezers, a single kinesin-bound bead was made to interact with a microtubule. An external load was applied to this bead–microtubule complex by moving the stage of the microscope at a constant speed (100 nm/s) by a piezoelectric transducer (P-611 NanoCube™, Physic Instrument, Germany). The stiffness of the optical trap was 0.038 and 0.076 pN/nm for the experiment in the presence of ADP and AMP-PNP, respectively. All experiments were carried out at 24 ± 1°C.

For the stall force measurement, the same protocol was used, except that the beads were coated with conventional two-headed kinesin and the force was measured in the presence of 1 mM ATP in a range of trap stiffness 0.019–0.076 pN/nm.

Supplementary data

Supplementary data are available at *The EMBO Journal* Online (http://www.embojournal.org).

Acknowledgements

We thank Dr RD Vale for the kind gift of the HK560cys kinesin construct, Dr K Kitamura for technical advice in establishing TIRFM, and Dr T Hashikawa for the assistance with electron microscopy. We are indebted to the Research Resources Centre in Brain Science Institute (RIKEN) for DNA sequencing and mass spectroscopy. This research was partly supported by the Grants-in-Aid for Specially Promoted Research and for the 21st Century COE Program (Physics of Self-Organization Systems) at Waseda University from the Ministry of Education, Sports, Culture, Science and Technology of Japan (SI).

References

Al-Bassam J, Ozer RS, Safer D, Halpain S, Milligan RA (2002) MAP2 and tau bind longitudinally along the outer ridges of microtubule protofilaments. *J Cell Biol* **157:** 1187–1196

Alonso MC, Damme J, Vandekerckhove J, Cross RA (1998) Proteolytic mapping of kinesin/ncd-microtubule interface: nucleotide dependent conformational changes in the loops L8 and L12. *EMBO J* **17:** 945–951

Best D, Warr PJ, Gull K (1981) Influence of the composition of commercial sodium dodecyl sulphate preparations on the separation of α- and β-tubulin during polyacrylamide gel electrophoresis. *Anal Biochem* **114:** 281–284

Block SM, Goldstein LSB, Schnapp BJ (1990) Bead movement by single kinesin molecules studied with optical tweezers. *Nature* **348:** 348–352

Bode CJ, Gupta ML, Suprenant KA, Himes RH (2003) The two alpha-tubulin isotypes in budding yeast have opposing effects on microtubule dynamics *in vitro*. *EMBO Rep* **4:** 94–99

Burke D, Gasdaska P, Hartwell L (1989) Dominant effects of tubulin overexpression in *Saccharomyces cerevisiae*. *Mol Cell Biol* **9:** 1049–1059

Carter NJ, Cross RA (2005) Mechanics of the kinesin step. *Nature* **435:** 308–312

Davis A, Sage CR, Wilson L, Farrell KW (1993) Purification and biochemical characterization of tubulin from the budding yeast *Saccharomyces cerevisiae*. *Biochemistry* **32:** 8823–8835

Fersht A (1984) Measurement and magnitude of enzymatic rate constants. In *Enzyme Structure and Mechanism*, pp 121–154. New York, USA: WH Freeman and Company Press

Goldstein LS, Yang Z (2000) Microtubule-based transport systems in neurons: the roles of kinesins and dyneins. *Annu Rev Neurosci* **23:** 39–71

Gupta Jr ML, Bode CJ, Georg GI, Himes RH (2003) Understanding tubulin–Taxol interactions: mutations that impart Taxol binding to yeast tubulin. *Proc Natl Acad Sci USA* **100:** 6394–6397

Hackney DD (1994) Evidence for alternating head catalysis by kinesin during microtubule-stimulated ATP hydrolysis. *Proc Natl Acad Sci USA* **91:** 6865–6869

Hackney DD (1995) Implications of diffusion-controlled limit for processivity of dimeric kinesin head domains. *Biophys J* **68:** 267s–270s

Hancock WO, Howard J (1998) Processivity of the motor protein kinesin requires two heads. *J Cell Biol* **140:** 1395–1405

Harada Y, Sakurada K, Aoki T, Thomas DD, Yanagida T (1990) Mechanochemical coupling in actomyosin energy transduction studied by *in vitro* movement assay. *J Mol Biol* **216:** 49–68

Hirose K, Löwe J, Alonso M, Cross RA, Amos LA (1999) 3D electron microscopy of the interaction of kinesin with tubulin. *Cell Struct Funct* **24:** 277–284

Hoenger A, Thormählen M, Diaz-Avalos R, Doerhoefer M, Goldie KM, Muller J, Mandelkow E (2000) A new look at the microtubule binding patterns of dimeric kinesins. *J Mol Biol* **297:** 1087–1103

Howard J, Hudspeth AJ, Vale RD (1989) Movement of microtubules by single kinesin molecules. *Nature* **342:** 154–158

Hua W, Young EC, Fleming ML, Gelles J (1997) Coupling of kinesin steps to ATP hydrolysis. *Nature* **388:** 390–393

Inoue Y, Hikikoshi-Iwane A, Miyai T, Muto E, Yanagida T (2001) Motility of single one-headed kinesin molecule along microtubules. *Biophys J* **81:** 2838–2850

Israelachvili JN (1992) *Intermolecular and Surface Forces*. San Diego, USA: Academic Press

Kawaguchi K, Ishiwata S (2001) Nucleotide-dependent single to double-headed binding of kinesin. *Science* **291:** 667–669

Kikkawa M, Okada Y, Hirokawa N (2000) 15 Å resolution model of the monomeric kinesin motor, KIF1A. *Cell* **100:** 241–252

Klumpp LM, Brendza KM, Rosenberg JM, Hoenger A, Gilbert SP (2003) Motor domain mutation traps kinesin as a microtubule rigor complex. *Biochemistry* **42:** 2595–2606

Kojima H, Muto E, Higuchi H, Yanagida T (1997) Mechanics of single kinesin molecules measured by optical trapping nanometry. *Biophys J* **73:** 2012–2022

Lakämper S, Meyhöfer E (2005) The E-hook of tubulin interacts with kinesin's head to increase processivity and speed. *Biophys J* **89:** 3223–3234

Little M, Seehaus T (1988) Comparative analysis of tubulin sequences. *Comp Biochem Physiol* **90B:** 655–670

Lockhart A, Crevel IM, Cross RA (1995) Kinesin and ncd bind through a single head to microtubules and compete for a shared MT binding site. *J Mol Biol* **249:** 763–771

Luduena RF (1998) Multiple forms of tubulin: different gene products and covalent modifications. *Int Rev Cytol* **178:** 207–275

Ma YZ, Taylor EW (1997) Interacting head mechanism of microtubule-kinesin ATPase. *J Biol Chem* **272:** 724–730

Mizuno N, Toba S, Edamatsu M, Watai-Nishii J, Hirokawa N, Toyoshima YY, Kikkawa M (2004) Dynein and kinesin share an overlapping microtubule-binding site. *EMBO J* **23:** 2459–2467

Nishiyama M, Higuchi H, Yanagida T (2002) Chemomechanical coupling of the forward and backward steps of single kinesin molecules. *Nat Cell Biol* **4:** 790–797

Nishizaka T, Miyata H, Yoshikawa H, Ishiwata S, Kinosita Jr K (1995) Unbinding force of a single motor molecule of muscle measured using optical tweezers. *Nature* **377:** 251–254

Nogales E, Wolf SG, Downing KH (1998) Structure of the alpha beta tubulin dimer by electron crystallography. *Nature* **391:** 199–203

Ogawa T, Nitta R, Okada Y, Hirokawa N (2004) A common mechanism for microtubule destabilizers—M type kinesins stabilize curling of the protofilament using the class-specific neck loops. *Cell* **116:** 591–602

Okada Y, Hirokawa N (2000) Mechanism of the single-headed processivity: diffusional anchoring between the K-loop of kinesin and the C terminus of tubulin. *Proc Natl Acad Sci USA* **97:** 640–645

Rice S, Lin AW, Safer D, Hart CL, Naber N, Carragher BO, Cain SM, Pechatnikova E, Wilson-Kubalek EM, Whittaker M, Pate E, Cooke R, Taylor EW, Milligan RA, Vale RD (1999) A structural change in the kinesin motor protein that drives motility. *Nature* **402:** 778–784

Schief WR, Clark RH, Crevenna AH, Howard J (2004) Inhibition of kinesin motility by ADP and phosphate supports a hand-over-hand mechanism. *Proc Natl Acad Sci USA* **101:** 1183–1188

Schnitzer MJ, Block SM (1997) Kinesin hydrolyses one ATP per 8-nm step. *Nature* **388:** 386–390

Shao Q, Gao YQ (2006) On the hand-over-hand mechanism of kinesin. *Proc Natl Acad Sci USA* **103:** 8072–8077

Shima T, Imamula K, Kon T, Ohkura R, Sutoh K (2006) Head-head coordination is required for the processive motion of cytoplasmic dynein, an AAA^+ molecular motor. *J Struct Biol* **156:** 182–189

Skiniotis G, Cochran JC, Muller J, Mandelkow E, Gilbert SP, Hoenger A (2004) Modulation of kinesin binding by the C-termini of tubulin. *EMBO J* **23:** 989–999

Sosa H, Peterman EJG, Moerner WE, Goldstein LSB (2001) ADP-induced rocking of the kinesin motor domain revealed by single-molecule fluorescence polarization microscopy. *Nat Struct Biol* **8:** 540–544

Tanaka-Takiguchi Y, Itoh TJ, Hotani H (1998) Visualization of the GDP-dependent switching in the growth polarity of microtubules. *J Mol Biol* **280:** 365–373

Thorn KS, Ubersax JA, Vale RD (2000) Engineering the processive run length of the kinesin motor. *J Cell Biol* **151:** 1093–1100

Uemura S, Ishiwata S (2003) Loading direction regulates the affinity of ADP for kinesin. *Nat Struct Biol* **10:** 308–311

Uemura S, Kawaguchi K, Yajima J, Edamatsu M, Toyoshima YY, Ishiwata S (2002) Kinesin–microtubule binding depends on both nucleotide state and loading direction. *Proc Natl Acad Sci USA* **99:** 5977–5981

Vernos I, Karsenti E (1996) Motors involved in spindle assembly and chromosome segregation. *Curr Opin Cell Biol* **8:** 4–9

Visscher K, Schnitzer MJ, Block SM (1999) Single kinesin molecules studied with a molecular force clamp. *Nature* **400:** 184–189

Wang Z, Sheetz MP (2000) The C-terminus of tubulin increases cytoplasmic dynein and kinesin processivity. *Biophys J* **78:** 1955–1964

Woehlke G, Ruby AK, Hart CL, Ly B, Hom-Booher N, Vale RD (1997) Microtubule interaction site of the kinesin motor. *Cell* **90:** 207–216

29

REGULATION OF MUSCLE CONTRACTION BY Ca^{2+} AND ADP: FOCUSING ON THE AUTO-OSCILLATION (SPOC)

Shin'ichi Ishiwata[1,2], Yuta Shimamoto[1], Madoka Suzuki[2] and Daisuke Sasaki[1]

29.1. ABSTRACT

A molecular motor in striated muscle, myosin II, is a non-processive motor that is unable to perform physiological functions as a single molecule and acts as an assembly of molecules. It is widely accepted that a myosin II motor is an independent force generator; the force generated at a steady state is usually considered to be a simple sum of those generated by each motor. This is the case at full activation (pCa <5 in the presence of MgATP); however, we found that the myosin II motors show cooperative functions, i.e., non-linear auto-oscillation, named SPOC (SPontaneous Oscillatory Contraction), when the activation level is intermediate between those of contraction and relaxation (that is, at the intermediate level of pCa, 5~6, for cardiac muscle, or at the coexistence of MgATP, MgADP and inorganic phosphate (Pi) at higher pCa (>7) for both skeletal and cardiac muscles). Here, we summarize the characteristics of SPOC phenomena, especially focusing on the physiological significance of SPOC in cardiac muscle. We propose a new concept that the auto-oscillatory property, which is inherent to the contractile system of cardiac muscle, underlies the molecular mechanism of heartbeat. Additionally, we briefly describe the dynamic properties of the thin filaments, i.e., the Ca^{2+}-dependent flexibility change of the thin filaments, which may be the basis for the SPOC phenomena. We also describe a newly developed experimental system named "bio-nanomuscle," in which tension is asserted on a single reconstituted thin filament by interacting with cross-bridges in the A-band composed of the thick filament lattice. This newly devised hybrid system is expected to fill the gap between the single-molecule level and the muscle system.

[1] Department of Physics, Faculty of Science and Engineering, Waseda University, 3-4-1 Okubo, Shinjuku-ku, Tokyo 169-8555, Japan, and [2]Consolidated Research Institute for Advanced Science and Medical Care, Waseda University, 513 Wasedatsurumaki-cho, Shinjuku-ku, Tokyo 162-0041, Japan
E-mail: Ishiwata@waseda.jp Tel/Fax: +81-3-5286-3437.

Regulatory Mechanisms of Striated Muscle Contraction
Edited by Ebashi and Ohtsuki, Springer, 2007

29.2. INTRODUCTION

In the early 1960s, Prof. S. Ebashi found that Ca^{2+} is a regulator of muscle contraction (Ebashi and Endo, 1968; Ebashi et al., 1969; Ebashi, 1972). This finding was the first demonstration of the universal role of Ca^{2+} as a regulator of various kinds of cellular functions. After a while, Prof. Ebashi and his associates (Ebashi et al., 1968) succeeded in isolating a protein named troponin (Tn) that specifically binds Ca^{2+} (troponin was the first protein identified as a Ca^{2+} receptor). It was demonstrated that the tropomyosin(Tm)-troponin(Tn) complex is located on the thin filament approximately every 40 nm along the axis of an actin filament (Ebashi and Endo, 1968; Ebashi et al., 1969; Ohtsuki et al., 1968, 1986). Since then, the most important research subjects on the regulation of muscle contraction have been focused on the Ca^{2+}-dependence of the state and the structure of the thin filaments.

In 1972, we reported that the flexibility of the reconstituted thin filaments (F-actin-Tm-Tn complexes) depends on the concentration of free Ca^{2+} ($pCa = -\log[Ca^{2+}]$), namely, the flexibility decreases upon detachment of Ca^{2+} from Tn (Ishiwata and Fujime, 1972). Our paper was the second reporting that the physico-chemical properties of the thin filaments change depending on the pCa value (following the work by Tonomura et al., 1969). In 1974, we proposed a model, in which the Ca^{2+}-induced changes in the flexibility of thin filaments play a role in the lattice effects on the tension development of striated muscle (Ishiwata and Oosawa, 1974). We would like to mention here that those old experiments and the model might still be of some significance in understanding the dynamic phenomena of *the contractile system of muscle* (being composed of an assembly of sarcomeres without membrane system such as sarcoplasmic reticulum (SR)).

About 20 years ago, we found that the sarcomere length of *skeletal* myofibrils auto-oscillate when the state of the contractile system is intermediate between contraction and relaxation (Okamura and Ishiwata, 1988). We named this auto-oscillatory phenomenon SPOC (Ishiwata and Yasuda, 1993). Particularly, SPOC that occurs at the coexistence of (Mg)ATP, (Mg)ADP and inorganic phosphate (Pi) in the absence of Ca^{2+} was named "ADP-SPOC." The dynamic properties of ADP-SPOC of skeletal muscle have been extensively examined under various conditions (Ishiwata et al., 1991, 1993; Shimizu et al., 1992; Ishiwata and Yasuda, 1993). *Cardiac* myofibrils (fibers) exhibit the auto-oscillation over a wider range of the intermediate activating conditions (Fukuda et al., 1996, 1998; Fujita and Ishiwata, 1998; Fukuda and Ishiwata, 1999). In particular, in cardiac muscle SPOC occurs at the intermediate Ca^{2+} concentrations, at which SPOC is not observed in skeletal muscle (Fabiato and Fabiato, 1978; Sweitzer and Moss, 1990; Linke et al., 1993; Fukuda et al., 1996; Fukuda and Ishiwata, 1999). We named this phenomenon "Ca-SPOC" (Ishiwata and Yasuda, 1993).

Though SPOC may not have direct relevance to physiological functions in skeletal muscle, we considered that it might be significant for the mechanism of heartbeat, because the auto-oscillation itself is the major physiological function of the contractile system of cardiac muscle. Indeed, we recently found that the period of ADP-SPOC observed in a contractile system of cardiac muscle (prepared from a ventricle of several animals, namely, rat, rabbit, dog, pig, and cow) has a linear relationship with the period of resting heartbeat of each animal (Sasaki et al., 2005). Moreover, we finally confirmed, after a long period of trial and error, that such a linear relationship exists in Ca-SPOC as well (Sasaki et al., 2006, and the poster presented at this Troponin Conference). Thus, we

propose here that the contractile system itself is an auto-oscillator that significantly contributes to the efficiency of the myocardial beating. We also discuss the molecular mechanism of SPOC based on the mechanical instability observed in myofibrils, and on the sliding behavior of an actin filament observed in the A-band motility assay, which we developed recently (Suzuki et al., 2005).

29.3. MATERIALS AND METHODS

29.3.1. Proteins and Fibers

The materials used in the present study spread over several levels of hierarchy in the striated muscle, that is, from a thin filament reconstituted by purified actin, Tm and Tn (or a native tropomyosin, i.e., a complex of Tm and Tn; Ebashi and Kodama, 1965), and an assembly of myofilaments (thick and thin filaments), to single myofibrils (Ishiwata and Funatsu, 1985; Anazawa et al., 1992) and muscle fibers (skeletal fibers, Ishiwata et al., 1985; Shimizu et al., 1992; cardiac fibers, Fukuda et al., 1996, 1998; Fujita and Ishiwata, 1998; Fukuda and Ishiwata, 1999; Sasaki et al., 2005, 2006). All the proteins were prepared from rabbit white skeletal muscle (Ishiwata, 1975).

29.3.2. Reconstitution of Thin Filaments

The thin filaments can be reconstituted *in vitro* by simply mixing an actin filament and a native Tm, or an actin filament, Tm and Tn in sequence. However, when the concentration of actin in the reconstituted thin filaments exceeds several μM, the solution undergoes gelation, exhibiting high viscoelasticity (thixotropy) due to the inter-filament interaction (Ebashi and Kodama, 1966; Ebashi and Endo, 1968). Ishiwata (1973) found that this thixotropic structure spontaneously disappears in temperature-dependent manner. The kinetics of this gel-sol transition are characterized by $\exp(-\Delta H^{\ddagger}/k_B T)$, where $\Delta H^{\ddagger}$ is the activation enthalpy, k_B is the Boltzmann constant and T is the absolute temperature; the value of $\Delta H^{\ddagger}$ depends on Ca^{2+} concentration (Ishiwata, 1973, 1978; Ishiwata and Kondo, 1978). We infer that the end-to-end interaction between Tm-Tn complexes bound to different actin filaments occurs due to protrusion of the end of the Tm-Tn complex from the side of an actin filament, namely, the deficiency of the binding sites on actin due to "the parking problem." The rearrangement of the Tm-Tn complexes to approach the most stable manner of binding along an actin filament occurs due to thermal agitation (an annealing effect), so that the kinetics of the irreversible transition from the gel structure to the dispersed filament structure obey the Arrhenius relation as described above. According to this finding, we devised a way to prepare the solution in which the reconstituted thin filaments are dispersed; that is, the standard protocol for the annealing treatment is to incubate the solution at 45°C for 10 min after mixing the proteins in the presence of several micromolar Ca^{2+} (Ishiwata and Fujime, 1972; Ishiwata, 1973).

29.3.3. A-band Motility Assay System

The A-band motility assay system (*Bio-nanomuscle* system) is composed of a single actin filament with a gelsolin-coated bead attached to its B-end (a bead-tailed actin

filament; Nishizaka et al., 1995; Suzuki et al., 1996), and an isolated A-band prepared by treating a single myofibril or a small bundle of myofibrils with gelsolin (Funatsu et al., 1990, 1993; Suzuki et al., 2005). The bead was trapped with the optical tweezers, and the tension developed on a single actin filament inside or at the outer surface of the A-band was estimated as the displacement of the bead from the trap center × the trap stiffness of the optical tweezers (Nishizaka et al., 1995, 2000). To prepare the reconstituted thin filaments, the Tm-Tn complex (prepared as native Tm) was mixed with very diluted solutions of F-actin, so that we need not to care about the entanglement of the filaments.

29.3.4. Myofibrils

Myofibrils were prepared by homogenizing the rabbit psoas (skeletal) glycerinated fibers according to the procedure described previously (Ishiwata and Funatsu, 1985). To measure the tension produced on a single myofibril, the two ends of the myofibril were fixed to a pair of glass micro-needles (one of which is flexible and the other is stiff) under an inverted optical (phase-contrast and fluorescence) microscope. The developed tension was measured by image analysis of the deflection of the flexible glass needle (Anazawa et al., 1992; Yasuda et al., 1996a).

29.3.5. Cardiac Muscle Fibers

Glycerinated cardiac muscle fibers were prepared from live hearts of rat, rabbit, dog, pig, and cow (Sasaki et al., 2005, 2006). The tension development was measured according to the standard technique (Fukuda et al., 1996). The striated pattern was observed under the phase contrast/confocal fluorescence microscope. To observe the oscillation pattern of each sarcomere under the SPOC conditions, the sarcomere length was estimated from the fluorescence image of muscle; here, the muscle was labeled with a fluorescent dye (rhodamine-phalloidin). Without chemical-fixative pretreatment, the thin filaments in cardiac muscle were labeled over the whole length with rhodamine-phalloidin, whereas in skeletal muscle only both ends of the thin filaments, i.e., the free (P-)ends and the Z-line region, were labeled (Yasuda et al., 1994). For the measurement of the period of oscillation, the back and forth movement of a plastic bead adhered to the surface of muscle fiber was recorded under a phase-contrast microscope.

29.4. RESULTS AND DISCUSSION

29.4.1. Characterization of Physical Properties of Thin Filaments

The thin (actin) filaments are usually considered to be a mere track for the molecular motors, namely myosins, to walk on it. In practice, there has been no explicit evidence demonstrating the direct coupling of the structural changes of the thin filaments with the function of molecular motors. However, a lot of experimental data indicates that the structure of the thin (actin) filaments changes as a result of the interaction with myosin II (cf. Oosawa et al., 1972). The bending flexibility of the reconstituted thin (or pure actin) filaments changes with the binding of myosin (HMM) (Fujime and Ishiwata, 1971; Ishiwata and Fujime, 1971, 1972). This has been demonstrated by the measurements of

the relaxation time of the bending Brownian motion in solution using quasielastic light scattering of laser beam (Fujime, 1970) and by direct observation of the bending Brownian motion of a single fluorescent actin filament in solution under a fluorescence microscope (Yanagida et al., 1985; Isambert et al., 1995). Namely, the bending relaxation time of an actin filament (FA) becomes shorter with the binding of Tm, implying that the FA-Tm complex is stiffer than the pure FA. When Tn is further complexed with the FA-Tm complex, the flexibility of the reconstituted thin filaments becomes sensitive to micromolar concentrations of Ca^{2+}. In the presence of higher concentrations of Ca^{2+}, the flexibility of the reconstituted thin filaments is similar to that of the FA-Tm complex, but it becomes least flexible with lowering the Ca^{2+} concentration. On the other hand, when HMM binds in the absence of ATP, FA becomes more flexible, exhibiting the maximum flexibility at a molar ratio of 6:1 (actin:HMM). When HMM binds to the reconstituted thin filament, the largest difference in the flexibility of the filament with and without Ca^{2+} is at the molar ratio of 2:1 (actin:HMM) (Ishiwata and Fujime, 1971; Ishiwata, 1975). These observations have been schematically depicted in Figure 29.1 (Fujime, 1972; Oosawa et al., 1972; Ishiwata, 1975).

In the traditional theory of muscle contraction (Huxley, 1957), the thin (actin) filaments are assumed to be a rigid body. But, in practice, it is not the case. The Young's modulus of the filament was estimated to be one to two orders magnitude smaller than that of steel from the quasi-elastic light scattering experiments (Fujime, 1970, 1972). This was later confirmed by microscopic analysis of the bending Brownian motion of single

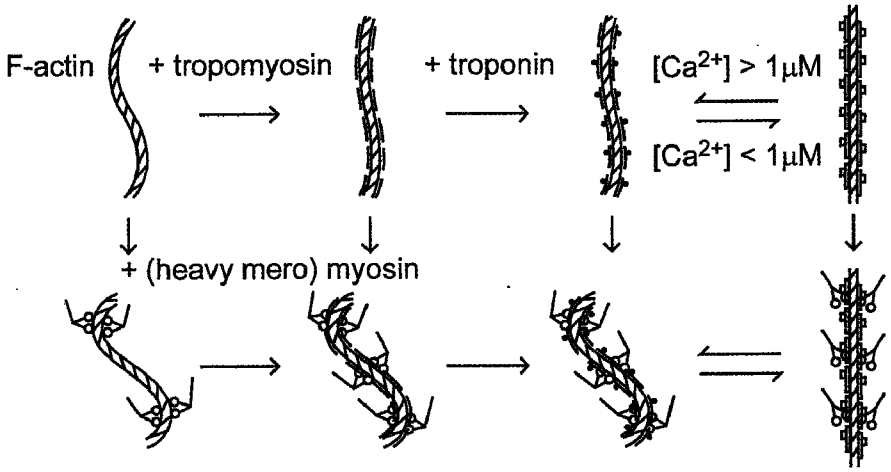

Figure 29.1. Schematic illustration showing the bending flexibility of an actin filament (FA) studied by quasi-elastic scattering of laser light (Oosawa et al., 1972; Ishiwata, 1975). The flexibility of FA (Fujime, 1970) decreased on the addition of Tm (tropomyosin) (Fujime and Ishiwata, 1971), and the flexibility of the FA-Tm complex remained nearly constant with the addition of Tn (troponin) in the presence of Ca^{2+} and decreased when Ca^{2+} was removed by the addition of EGTA (Ishiwata and Fujime, 1972). Additionally, the flexibility of FA increased on the addition of HMM in the absence of ATP (rigor condition) at an appropriate molar ratio (about 6:1) (Fujime and Ishiwata, 1971). The most flexible state of the FA-Tm complex was achieved by the addition of HMM in rigor condition at the molar ratio of about 2:1. In case of the reconstituted thin filament (an FA-Tm-Tn complex) in rigor, the transition between the most rigid and the most flexible states could be regulated by the concentration of Ca^{2+} in the presence of HMM at the molar ratio of about 2:1 (Ishiwata and Fujime, 1971; Ishiwata, 1975). Such a flexibility change was also observed in the presence of ATP (Oosawa et al., 1972; Ishiwata, 1975; Yanagida et al., 1985).

actin filaments (Yanagida et al., 1985; Isambert et al., 1995), and direct measurements of stiffness on muscle fiber (Higuchi et al., 1995) and a single actin filament (Kojima et al., 1994). Besides, the torsional rigidity of single actin filaments was directly measured on single actin filaments (Tsuda et al., 1996; Yasuda et al., 1996b). Thus, it was estimated that the 1 μm-long thin filament in the muscle fiber would elongate by a few nm under maximum tension. In practice, this estimation was experimentally demonstrated on skeletal muscle based on the analysis using a small-angle X-ray diffraction (Huxley et al., 1994; Wakabayashi et al., 1994). Besides, a lot of spectroscopic data showed the dynamic properties of actin filaments (on ESR, Thomas et al., 1975, 1979; on fluorescence data, cf. Ishiwata, 1998). It has also been established that the helical structure of actin filaments changes upon binding of regulatory proteins (cf. Egelman et al., 1982; McGough et al., 1997; Prochniewicz et al., 2005).

The structural changes of thin filaments that occur upon interaction with myosin and the regulatory proteins strongly suggest that the thin filaments are not a mere track (a rigid body) but may function as an active element in the molecular mechanism of tension development and its regulation (Prochniewicz-Nakayama et al., 1983). In fact, as described below, there are several phenomena in muscle, which cannot be explained simply by summing up independent force generators. In other words, there exists non-linearity in the mechanisms of tension generation and its regulation, where a long-range cooperativity along the thin filament is considered to play a role.

First, we would like to mention that tension does not necessarily depend linearly on the overlap between the thick and the thin filaments. As demonstrated by Gordon et al. (1966), tension is developed proportionally to the overlap, but this is the case only when the muscle is fully activated. In fact, Endo was the first to demonstrate that, when the muscle is activated partially at intermediate Ca^{2+} concentrations, the maximum tension is developed at a shorter overlap (longer SL), rather than at the maximum overlap (short SL) (Endo, 1972a,b; Stephenson and Wendt, 1984; cf. Figure 29.2b). This demonstrates that the tension is not necessarily proportional to the overlap between the thick and thin filaments; in other words, tension is not always proportional to the number of available cross-bridges.

The above results have been quantitatively explained according to the model shown in Figure 29.2, in which we assume that (1) the flexibility of the thin filaments increases with an increase in the concentration of free Ca^{2+}. In this model, the lateral position of actin, $P(q)$, is assumed to follow the Gaussian distribution, and the width of the Gaussian distribution, $(\langle q^2 \rangle)^{1/2}$, increases as the flexibility of the filament increases; (2) the interaction probability of myosin cross-bridges depends on the distance between the thick and the thin filaments, d, and the effective length of cross-bridges, a; (3) the volume of the filament lattice is constant irrespectively of the sarcomere length, and (4) the isometric tension is determined by (the length of overlap between the thick and the thin filaments) × (the interaction probability of cross-bridges, which is proportional to the hatched area in Figure 29.2a) (Ishiwata and Oosawa, 1974). The effective distance between the thick and the thin filaments decreases with increasing the flexibility of the thin filaments. In this model there are only two parameters, namely, $(\langle q^2 \rangle)^{1/2}$ and a (Figure 29.2a). With an increase in the sarcomere length, the distance between the thick and the thin filaments decreases due to the constant volume of the filament lattice. Because of this, the probability of cross-bridge formation increases, especially sharply at the intermediate level of activation, whereas the number of available myosin heads decreases only linearly. Thus,

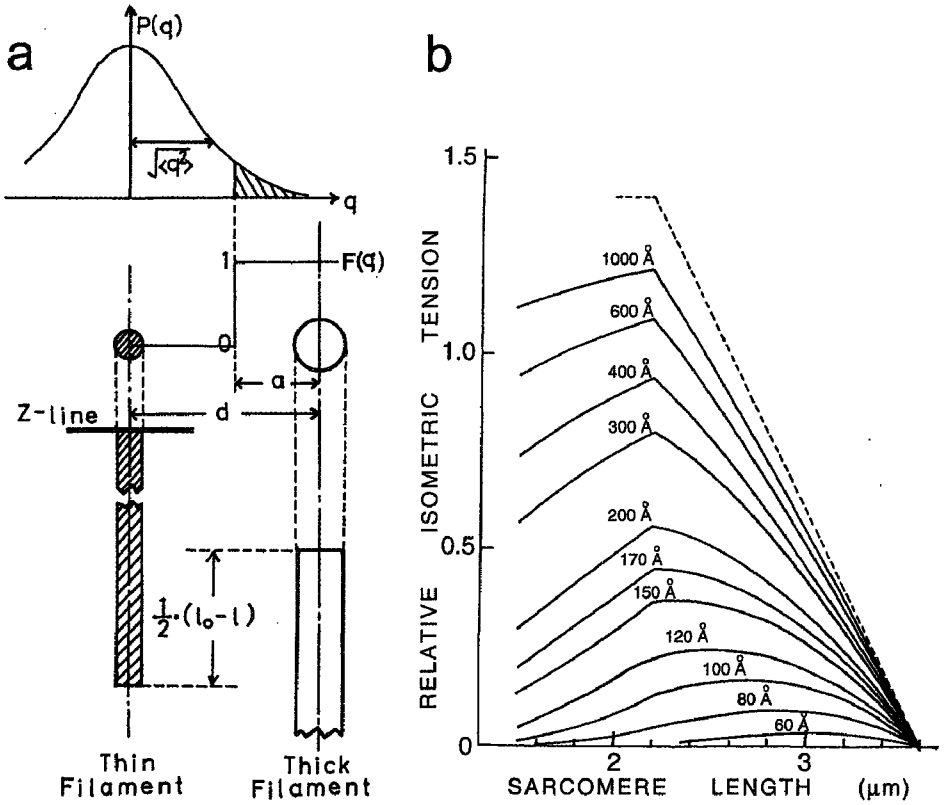

Figure 29.2. Model describing the length vs. tension relationship based on the flexibility change of the thin filaments. (a) Schematic diagram of the model. P(q), the Gaussian distribution showing the existence probability of actin against the lateral coordinate, q; $(\langle q^2 \rangle)^{1/2}$, the width of the Gaussian distribution that represents the bending flexibility of the thin filaments; F(q), the probability of cross-bridge formation; d, the distance between the thick and the thin filaments; a, the length of the region in which cross-bridges are formed (the effective length of cross-bridges) (cf. Kinosita et al., 1984; Ishiwata et al., 1987); l, sarcomere length; l_0, the sarcomere length, at which there is no overlap between the thick and the thin filaments, i.e., 3.6 μm in this model. We assume that the maximum overlap is realized at the sarcomere length of 2.2 μm. (b), Relative isometric tension vs. sarcomere length at various $(\langle q^2 \rangle)^{1/2}$ values as shown in this Figure. Here, the values of d and a were assumed to be 25 nm (at the sarcomere length of 2.5 μm) and 15 nm (independent of the sarcomere length), respectively. The length vs. tension relationship obtained at pCa of about 6 by Endo (1972a,b) approximately corresponds to 10 nm for the value of $(\langle q^2 \rangle)^{1/2}$. Taken from Ishiwata and Oosawa (1974).

at the intermediate level of activation, where the bending flexibility of the thin filaments is also intermediate, the developed tension becomes largest at a smaller overlap between the thick and the thin filaments. This mechanism may be relevant to the stretch activation, which is particularly profound in cardiac muscle, a property known as Frank-Starling law (Fukuda et al., 2001; Fuchs and Martyn, 2005).

29.4.2. A-band Motility Assay System (*Bio-nanomuscle*) with Reconstituted Thin Filaments

The A-band motility assay system is a newly devised hybrid experimental system that fills the gap between a single-molecular assay and a myofibril (Molloy, 2005; Suzuki et al., 2005). In this system, a single actin filament interacts with myosin cross-bridges that are regularly aligned in a thick filament lattice, i.e., an exposed A-band (cf.

Figure 29.3a). We found that the bead-tailed actin filament trapped with optical tweezers moved back and forth, probably due to the fluctuations in the number of interacting cross-bridges. In spite of these large tension fluctuations, the average force developed on a single actin filament was proportional to the overlap between the thick and the thin filaments, at least within ca. 300 nm from the end of the A-band. From this data, the average force developed by each head of myosin was estimated to be about 0.9 pN under a physiological ionic strength (Suzuki et al., 2005).

Here, we found that when the Tm-Tn complex was added to the above system, the Ca^{2+} sensitivity was recovered as shown in Figure 29.3. In the absence of Ca^{2+}, the reconstituted thin filament did not interact with the A-band (Figure 29.3b), whereas in the presence of Ca^{2+} the large tension development occurred (Figure 29.3c), as was the case for a pure actin filament (Suzuki et al., 2005). These data suggested that the average tension developed by each cross-bridge became larger compared with that in a pure actin filament. This result is consistent with that obtained in bovine cardiac muscle fiber, where

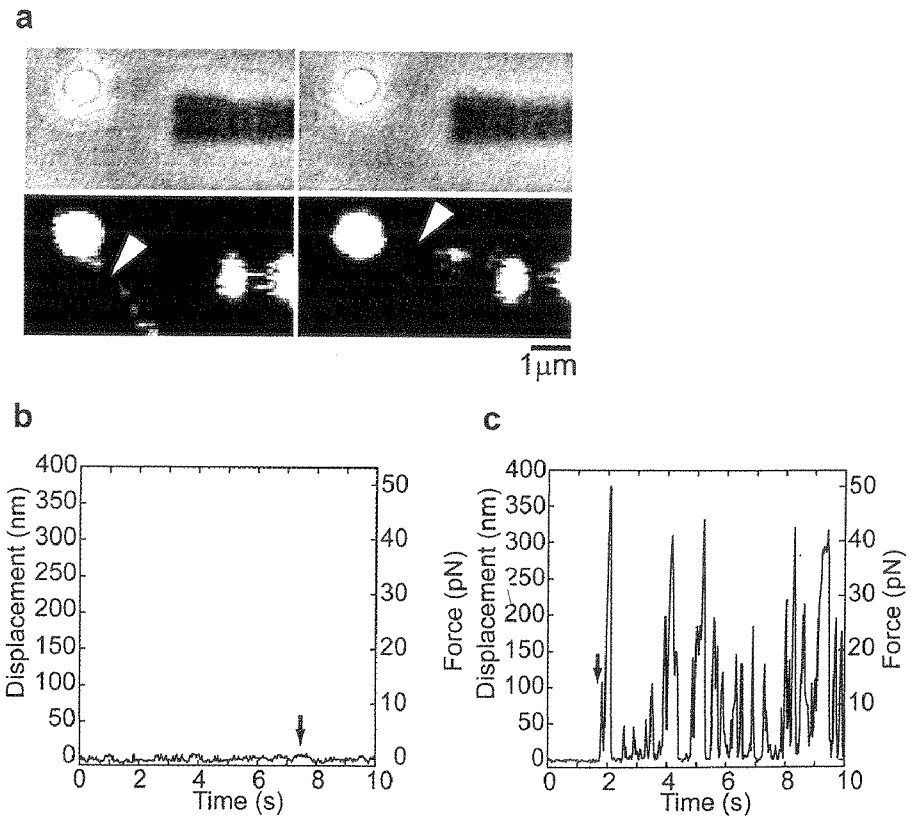

Figure 29.3. A-band motility assay system of muscle (*bio-nanomuscle*) with the reconstituted thin filament. (a) Phase-contrast (top) and fluorescence (bottom) images of the A-band motility assay system. The bead initially remained at the trap center, because the actin filament did not interact with the A-band (left). After the actin filament touched the outer surface of the A-band, the filament was drawn toward the A-band, as a result, the bead deviated from the trap center (right). Here, the arrowheads indicate the reconstituted thin filament bound to a polystyrene bead (1 μmϕ). (b, c) Time course of the bead movement in the absence (b) and the presence (c) of Ca^{2+}. Arrows indicate the moment at which the reconstituted thin filament touched the A-band (see Figure a, right). Solution conditions: 96 mM KCl, 25 mM Imidazole-HCl, pH 7.4, 4.2 mM $MgCl_2$, 2.2 mM ATP, 2 mM EGTA, – (b) or + (c) 2 mM $CaCl_2$, 10 mM DTT, 0.5 mg/ml BSA, 0.1 μM Tm-Tn complex, 4.5 mg/ml D(+)-glucose, 50 units/ml glucose oxidase, 50 units/ml catalase, 15 mM creatine phosphate and 150 units/ml creatine phosphokinase at 28°C.

the thin filaments were replaced with pure actin filaments (prepared from rabbit white muscle) using a technique of reconstitution of actin (thin) filaments after selective removal of the endogenous thin filaments with gelsolin treatment, and the effects of cardiac Tm-Tn complexes on the tension development were examined (Fujita et al., 1996, 2002; Kawai and Ishiwata, 2006, for cardiac muscle; Funatsu et al., 1994, for skeletal muscle).

Using the A-band motility assay system with the reconstituted thin filaments, we examined the ADP-SPOC conditions described below (Suzuki, M., unpublished). The results showed that the time course of the movement of the filament exhibited a saw-tooth waveform similar to that observed in SPOC of myofibrils (see Figure 29.4b), that is, after the filament had rather slowly been drawn inside the A-band, it was abruptly pulled out toward the trap center. However, in this case the saw-tooth waveform was less regular compared to that observed in SPOC. We expect that the detailed study under the SPOC conditions using a high-speed camera (1 ms temporal resolution), which is now underway, will contribute to clarifying the molecular mechanism of SPOC.

29.4.3. State of the Contractile System of Muscle

The previous studies showed that the contractile system of cardiac muscle spontaneously oscillates under the intermediate values of pCa; not only the tension, but the sarcomere lengths oscillate as well (Fabiato and Fabiato, 1978; Sweitzer and Moss, 1990; Linke et al., 1993; Fukuda et al., 1996).

The state exhibiting the auto-oscillation is considered to represent the third state, in addition to contraction and relaxation. The 3D-state diagram constructed against the concentrations of MgADP and Pi and the value of pCa at the fixed concentration of MgATP clearly shows that the SPOC region is located between the contraction and the relaxation regions (Figure 29.4a). The auto-oscillation that occurs in the SPOC region on the y-z plane in Figure 29.4a, the 2D space constructed against the concentrations of Mg-ADP and Pi in the absence of Ca, corresponds to ADP-SPOC, whereas the auto-oscillation that occurs on the x (pCa) axis represents Ca-SPOC.

The 3D state diagram is mostly similar in both skeletal and cardiac muscles. The main differences between skeletal and cardiac muscles are: 1) the SPOC region for cardiac muscle is broader than that for skeletal muscle, namely, the triple point on the z-axis, at which the transition from relaxation to contraction occurs, is lower in cardiac muscle, implying that the relative affinity for ADP compared to ATP is higher in cardiac muscle, and 2) the Ca-SPOC region clearly exists on the x-axis.

The molecular mechanism of SPOC has been primarily studied under the ADP-SPOC conditions using either a single skeletal myofibril or their small bundle. Under a phase-contrast microscope, two ends of the myofibril are twined to a pair of glass micro-needles, one of which is flexible and the other is rigid (Anazawa et al., 1992; Yasuda et al., 1996; see Figure 29.4b). The tension developed by the myofibril is determined from the deflection of the flexible needle (needle 1 in Figure 29.4b) and the mechanical impulse is applied by manipulating the rigid needle (needle 2 in Figure 29.4b). The interesting finding is that the ADP-bound cross-bridges function as an activator in the absence of Ca^{2+} (see the state change on the z-axis in the 3D state diagram shown in Figure 29.4a), which seems to be analogous to the rigor activation (Shimizu et al., 1992); in other words, the role of the ADP-bound cross-bridges is similar to that of rigor cross-bridges (Bremel and Weber, 1972).

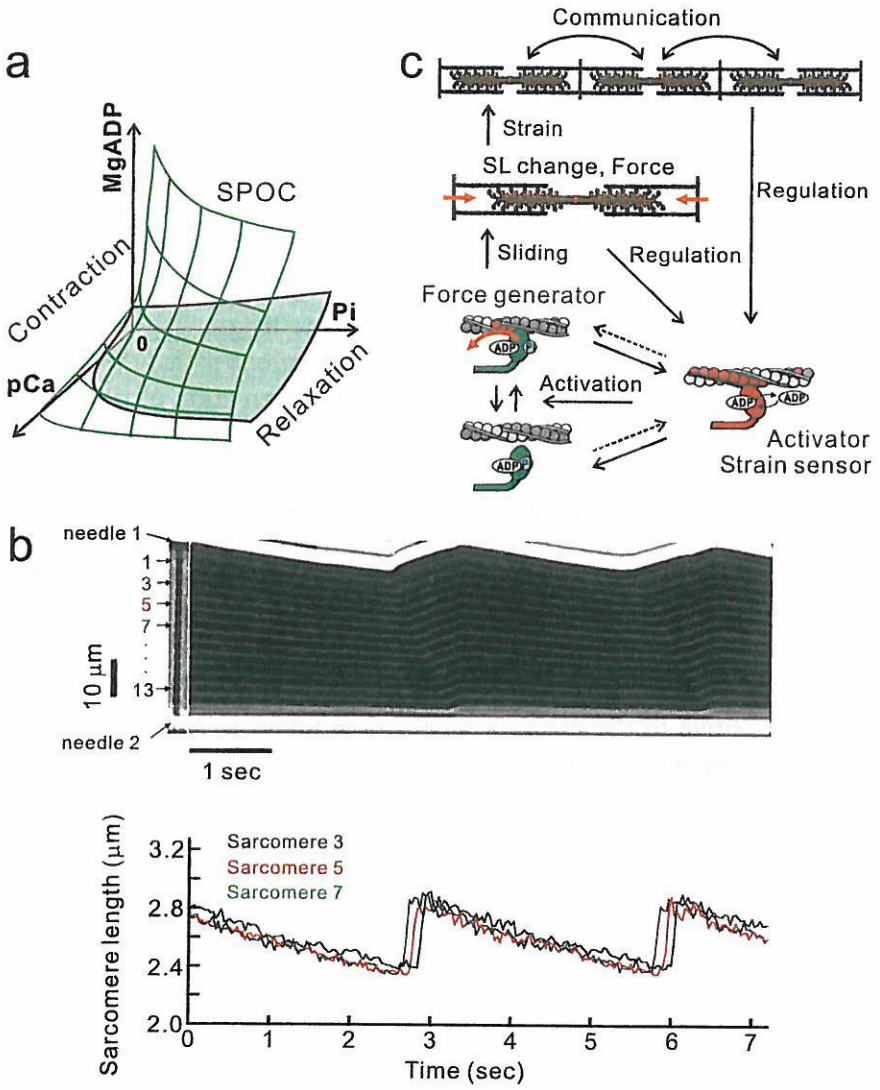

Figure 29.4. Schematic diagram showing the state of the contractile system of muscle. (a) 3D-state diagram showing the state of the contractile system of cardiac muscle against pCa (x-axis), the concentrations of Pi (y-axis) and MgADP (z-axis). The states are classified into three, i.e., contraction, relaxation and SPOC; in particular, we call the SPOC state on the y-z plane "ADP-SPOC" and the SPOC state along the x-axis "Ca-SPOC." (b) A typical pattern of ADP-SPOC as revealed by the auto-oscillation of sarcomere lengths in rabbit psoas myofibril. The kymograph was obtained by phase-contrast microscopy. Both ends of the myofibril were fixed to a pair of glass micro-needles; one is flexible (needle 1) and the other is stiff (needle 2). A propagation of the yielding phase of the sarcomere oscillation (SPOC wave) from the sarcomere #1 to #13 can be observed. (c) Schematic diagram showing the molecular aspects of feedback regulation in ADP-SPOC.

We have not fully clarified the molecular mechanism of SPOC yet, but, concerning the mechanism of length-dependent activation, we are now able to put forward the following hypothesis. 1) First, the activation at longer sarcomere lengths (in other words, inactivation at shorter sarcomere lengths) is expected to occur under the SPOC conditions. In fact, Endo (1972a,b) found that in skinned skeletal muscle fibers at the intermediate level of activation (pCa around 6) the higher tension is developed at longer sarcomere lengths. 2) Second, considering our model that can explain the essential

properties of the non-linear tension-length relationship at the intermediate level of activation (Ishiwata and Oosawa, 1974), we expect that the flexibility of the thin filaments, which depends on the binding of cross-bridges, may be important for the SPOC mechanism. In ADP-SPOC, the intermediate activation is realized due to the ADP-bound cross-bridges instead of binding of Ca^{2+} to Tn. If the flexibility of the thin filaments is increased by the ADP-bound cross-bridges, the positive feedback loop may occur as follows: as the sarcomere length changes, the occurrence probability of cross-bridge formation may change non-linearly due to the change in the distance between the thick and the thin filaments (cf. Figure 29.2a). Therefore, the cooperative activation (or deactivation) is expected to occur with an increase (or decrease) in the sarcomere length.

One apparent contradiction with the above considerations is that the flexibility of the reconstituted thin filaments does not increase upon the formation of rigor cross-bridges (the binding of HMM) in the absence of Ca^{2+} (see Figure 29.1). A possible explanation is that the flexibility of the thin filaments does increase at very low concentrations of ATP, where the so-called rigor activation occurs in the absence of Ca^{2+}, due to the coexistence of rigor and ATP-bound cross-bridges (practically, the ADP-Pi state of cross-bridges). Another possible reason is that, unlike the rigor cross-bridges, the ADP-bound cross-bridges do increase the flexibility of the filaments. Whether such inference is correct, must be examined in future.

Finally, it is to be noted that the activation state induced by the ADP-bound cross-bridges is very sensitive to the external mechanical impulse. Namely, the ADP-bound cross-bridges detach upon quick stretch of myofibril, so that the sarcomere is immediately relaxed. It results in the quick release of sarcomeres, which produces the saw-tooth waveform (Shimamoto et al., unpublished). It means that SPOC resonates with the external mechanical repetitive impulse; in other words, the SPOC period can be externally controlled within a certain region of frequencies. In addition, the state of each sarcomere under the SPOC conditions is influenced by the state of the contractile system surrounding the sarcomere. Such a situation is schematically summarized in Figure 29.4c. The ADP-bound cross-bridges are assumed to function as an activator that can activate the thin filaments even in the absence of Ca^{2+} and also function as a tension-sensitive regulator (Shimamoto et al., manuscript in preparation).

29.4.4. Physiological Significance of SPOC

It is interesting to examine whether SPOC has a physiological role in muscle function. To this end, we examined the properties of SPOC, namely, the SPOC period and the velocity of SPOC wave, in the demembranated cardiomyocytes prepared from several animals, i.e., rat, rabbit, dog, pig, and cow. As shown in Figure 29.5a, the sarcomere length oscillates with a saw-tooth waveform, which is common to all the species of muscles. To our surprise, we found that the period of SPOC has an excellent correlation (a linear relationship) with the period of resting heartbeat in each animal (Figure 29.5b–l), although the amplitude of sarcomere length oscillation varied only slightly between the species, implying that the higher the heartbeat is, the faster is the shortening velocity. On the other hand, the SPOC period exhibited nearly an inverse relation to the velocity of SPOC wave, implying that the latter has a linear relation to the heartbeat (Figure 29.5c). When the period of SPOC was measured at room temperature, e.g., 25°C, the period of ADP-SPOC was about 20 times slower than that of the heartbeat (Sasaki et al., 2005), but the period of Ca-SPOC was only

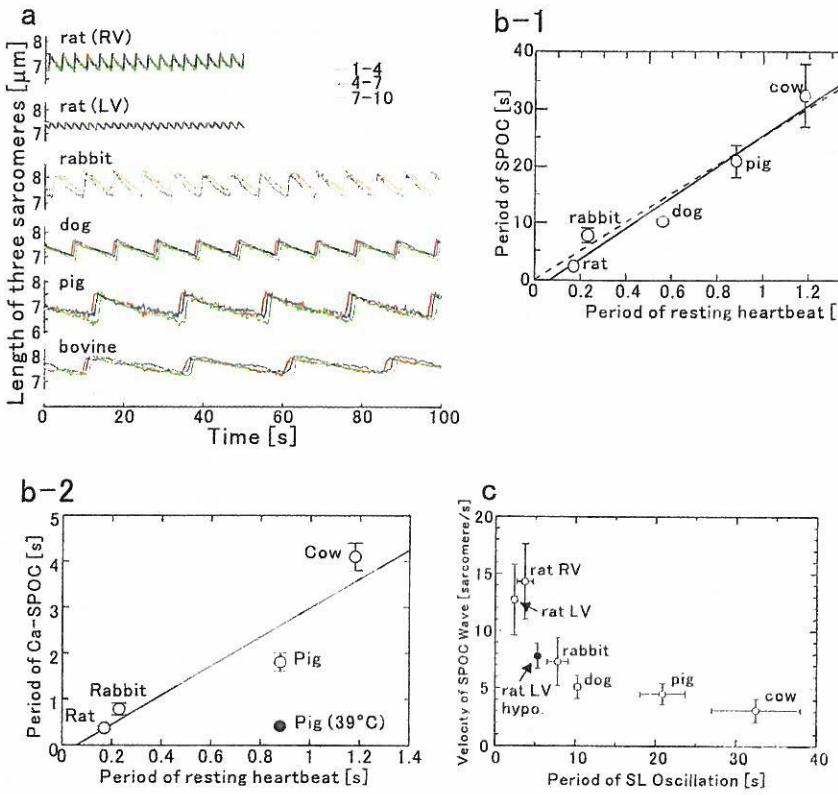

Figure 29.5. Characteristics of SPOC observed in the demembranated cardiomyocites. (a) A typical pattern of sarcomere length oscillation in ADP-SPOC observed in cardiac muscle fibers prepared from several animal species. (b) Relation between the period of SPOC (b-1, ADP-SPOC; b-2, Ca-SPOC) and the resting heartbeat of each animal. Modified from Sasaki et al. (2005) (b-1) and Sasaki et al. (2006) (b-2). (c) Relation between the period of SPOC and the velocity of SPOC wave under ADP-SPOC condition. The hypothyroid of rat (older than 10 weeks) were induced by drinking water containing 0.8 mg/ml propylthiouracil for more than 5 weeks.

three-fold slower than that of the heartbeat (Sasaki et al., 2006). Moreover, we found that the period of Ca-SPOC largely shortened with increasing temperature, and at the body temperature it fell exactly into the range of heartbeat (Figure 29.5b–2).

Though Ca-SPOC may play no significant role in skeletal muscle, there are good reasons to believe that Ca-SPOC may be an important factor for the mechanism of heartbeat: 1) Ca-SPOC occurs just within the physiological conditions of heartbeat. In particular, the level of Ca^{2+} concentration during heartbeat goes up and down in the region of the pCa values between <6 and >7, which exactly overlaps with the pCa region where Ca-SPOC occurs. 2) As described above, the period of SPOC (both ADP-SPOC and Ca-SPOC) has a linear relationship with the resting heartbeat of each animal. It means that the contractile machinery has been adapted to the physiological function of heartbeat in each animal. 3) The pattern of SPOC looks similar to that observed in the oscillation of sarcomeres during the heartbeat. 4) SPOC is synchronized with the external mechanical impulse, such as rapid stretch (Shimamoto et al., manuscript in preparation), and the mechanical boundary conditions, such as isotonic conditions (cf. Yasuda et al., 1996a); it is therefore plausible that these characteristics enable a long-range spatio-temporal

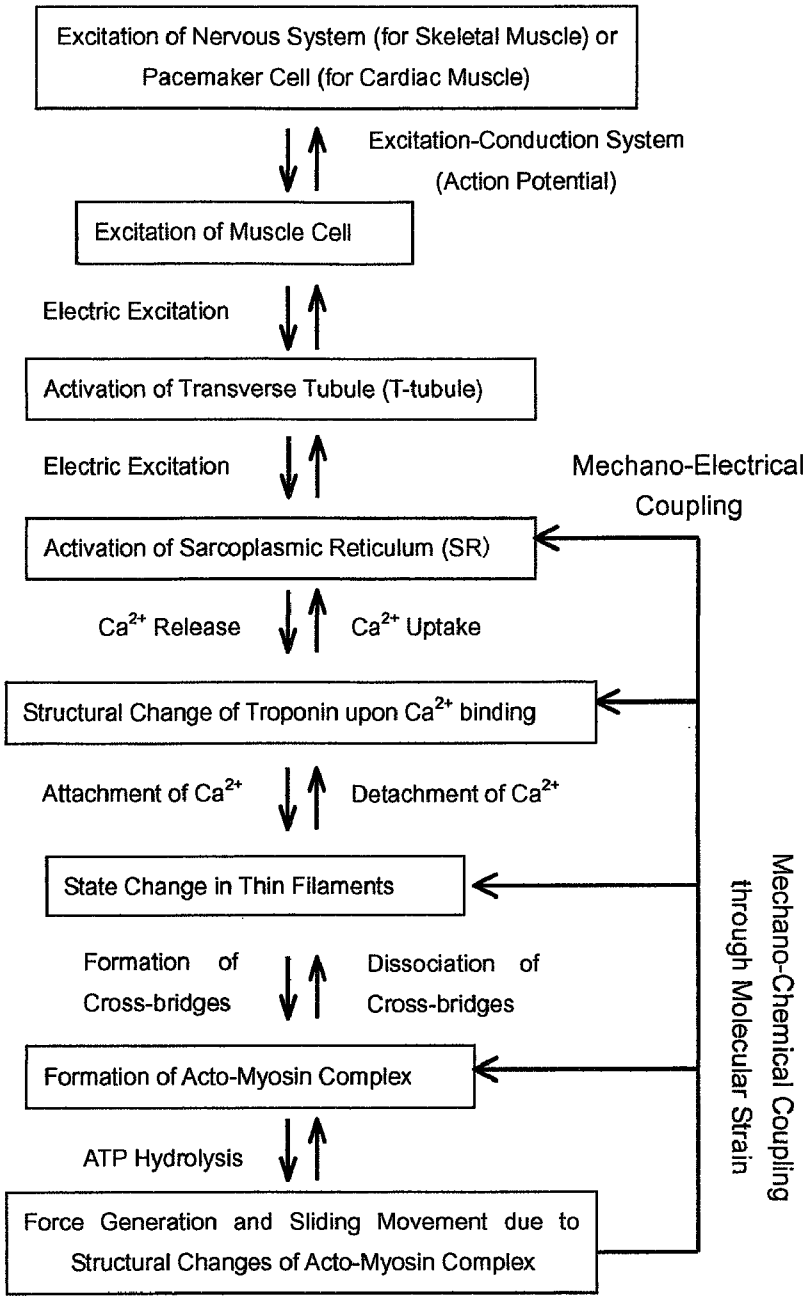

Figure 29.6. Hypothetical hierarchy in the regulation pathway in cardiac muscle. The rhythm of heartbeat is determined by the electrical impulse produced by pacemaker cells. In muscle cells, release and uptake of Ca^{2+} in SR are regulated by this electrical impulse. Ca^{2+} released in the cytoplasm binds to troponin, which turns the state of the thin filaments ON. In this sequential control mechanism, the contractile system is considered to be a force-producing machine that is regulated passively through the level of Ca^{2+}, i.e., pCa. The present study proposes that the contractile apparatus itself is an auto-oscillator that has an intrinsic oscillatory property with the period of oscillation characteristic of the heartbeat of each animal. This fact strongly suggests that in addition to the mechano-electrical feedback loops that may be relevant to the Ca^{2+} oscillation, there also exists a mechano-chemical feedback loop within the contractile apparatus. We hypothesize here that the ATPase enzymatic activities are modulated through the molecular strain that is induced by the force generation, which has already been hypothesized in the sliding theory of A. F. Huxley (1957); the direct experimental evidence has been obtained by studying the kinesin-microtubule interaction, where the ADP binding affinity of kinesin depended on the direction of the applied external force (Uemura and Ishiwata, 2003).

order of oscillation including the SPOC wave, so that it is expected that they are important for the macroscopic organization of the pumping function of the heart.

Next, a question arises: what is then the role of Ca^{2+} in the heartbeat, if the contractile apparatus is able to spontaneously oscillate without oscillation of Ca^{2+} concentration. It should be noted here that under steady SPOC conditions the metachronal oscillation wave in sarcomeres travels over several tens of sarcomeres in the fiber (SPOC wave). Therefore, various SPOC domains within the same fiber start to oscillate out of phase. An attractive idea that comes to mind here is that Ca^{2+} is necessary to ensure that the sarcomere oscillation occurs *in phase* over a large region of cardiac cell. In this sense, the real role of Ca^{2+} is to *synchronize* the oscillation of sarcomeres. This is an absolutely new concept on the mechanism of heartbeat: the contractile apparatus composed of actin, myosin, regulatory proteins and so on, is not a mere force generator that passively responds to Ca^{2+} as usually considered, but is actually a major player in the heartbeat. As summarized in Figure 29.6, there must exist several feedback loops in the mechanism of heartbeat; that is, the existence of feedback loops from the force generation to the SR function is now established. Additionally, the existence of Ca-SPOC strongly suggests that there must be a feedback loop within the force generation mechanism of the contractile apparatus. We thus propose that this oscillatory property, which is inherent to the contractile apparatus of the myocardium, is essential for the efficient functioning of the heart (Ishiwata et al., 2005; Sasaki et al., 2005, 2006).

29.5. CONCLUSION

In summary, we propose that the contractile apparatus is not a simple protein assembly, in which molecular motors independently generate tension; in fact, cooperativity exists not only between myosin motors, but within the thin filament as well. As a typical example supporting this idea, we focus on the auto-oscillation phenomena, especially on Ca-SPOC, which occurs within an intermediate range of Ca^{2+} concentrations under physiological conditions. The thin filament is usually considered to be a mere side player, or a mere track, on which the molecular motors produce tension. We are confident that SPOC is a key phenomenon for elucidating the mechanism of cooperativity operating in the assemblage composed of the cross-bridges and the thin filaments. Besides, we have proposed that the SPOC properties play an important role in the spatio-temporal organization of the heartbeat. It may be not easy to immediately accept this idea, however, we believe it is worth studying as a new concept that may open a new research field in muscle physiology.

29.6. ACKNOWLEDGMENT

We thank Dr. S. V. Mikhailenko for his critical reading of the manuscript. We also thank Ms. E. Wakabayashi for her excellent technical assistance on the SPOC experiments using diseased rats. This work was supported partly by Grants-in-Aid for Specially Promoted Research, the 21st Century COE Program and "Establishment of Consolidated Research Institute for Advanced Science and Medical Care" from the Ministry of Education, Sports, Culture, Science and Technology (MEXT) of Japan to S. I. and by

Grants-in-Aids for Young Investigator Research and Scientific Research in Priority Areas from the MEXT, Japan to M. S.

29.7. REFERENCES

Anazawa, T., Yasuda, K., and Ishiwata, S., 1992, Spontaneous oscillation of tension and sarcomere length in skeletal myofibrils. Microscopic measurement and analysis, *Biophys. J.* **61**:1099–1108.

Bremel, R. D., and Weber, A., 1972, Cooperative behavior within the functional unit of the actin filament in vertebrate skeletal muscle, *Nat. New Biol.* **238**:97–101.

Ebashi, S., 1972, Calcium ions and muscle contraction, *Nature* **240**:217–218.

Ebashi, S., and Endo, M., 1968, Calcium ions and muscle contraction, *Prog. Biophys. Mol. Biol.* **18**:123–183.

Ebashi, S., Endo, M., and Ohtsuki, I., 1969, Control of muscle contraction, *Quart. Rev. Biophys.* **2**:351–384.

Ebashi, S., and Kodama, A., 1965, A new protein factor promoting aggregation of tropomyosin, *J. Biochem.* **58**:107–108.

Ebashi, S., and Kodama, A., 1966, Interaction of troponin with F-actin in the presence of tropomyosin, *J. Biochem.* **59**:425–426.

Ebashi, S., Kodama, A., and Ebashi, F., 1968, Troponin. I. Preparation and physiological function, *J. Biochem.* **64**:465–477.

Egelman, E. H., Francis, N., and DeRosier, D. J., 1982, F-actin is a helix with a random variable twist, *Nature* **298**:131–135.

Endo, M., 1972a, Stretch-induced increase in activation of skinned muscle fibres by calcium, *Nat. New Biol.* **14**:211–213.

Endo, M., 1972b, Length dependence of activation of skinned muscle fibers by calcium, *Cold Spring Harb. Symp. Quant. Biol.* **37**:505–510.

Fabiato, A., and Fabiato, F., 1978, Myofilament-generated tension oscillations during partial calcium activation and activation dependence of the sarcomere length-tension relation of skinned cardiac cells, *J. Gen. Physiol.* **72**:667–699.

Fuchs, F., and Martyn, D. A. 2005. Length-dependent Ca^{2+} activation in cardiac muscle: some remaining questions, *J. Muscle Res. Cell Motil.* **26**:199–212.

Fujime, S., 1970, Quasi-elastic light scattering from solutions of macromolecules. II. Doppler broadening of light scattered from solutions of semi-flexible polymers, F-actin, *J. Phys. Soc. Jpn* **29**:751–759.

Fujime, S., 1972, Quasi-elastic scattering of laser light. A new tool for the dynamic study of biological macromolecules, *Adv. Biophys.* **3**:1–43.

Fujime, S., and Ishiwata, S., 1971, Dynamic study of F-actin by quasielastic scattering of laser light, *J. Mol. Biol.* **62**:251–265.

Fujita, H., and Ishiwata, S., 1998, Spontaneous oscillatory contraction without regulatory proteins in actin filament-reconstituted fibers, *Biophys. J.* **75**:1439–1445.

Fujita, H., Sasaki, D., Ishiwata, S., and Kawai, M., 2002, Elementary steps of the cross-bridge cycle in bovine myocardium with and without regulatory proteins, *Biophys. J.* **82**:915–928.

Fujita, H., Yasuda, K., Niitsu, S., Funatsu, T., and Ishiwata, S., 1996, Structural and functional reconstitution of thin filaments in the contractile apparatus of cardiac muscle, *Biophys. J.* **71**:2307–2318.

Fukuda, N., Fujita, H., Fujita, T., and Ishiwata, S., 1996, Spontaneous tension oscillation in skinned bovine cardiac muscle, *Pflügers Arch.* **433**:1–8.

Fukuda, N., Fujita, H., Fujita, T., and Ishiwata, S., 1998, Regulatory roles of MgADP and calcium in tension development of skinned cardiac muscle, *J. Muscle Res. Cell Motil.* **19**:909–921.

Fukuda, N., and Ishiwata, S., 1999, Effects of pH on spontaneous tension oscillation in skinned bovine cardiac muscle, *Pflugers Arch.* **438**:125–132.

Fukuda, N., Sasaki, D., Ishiwata, S., and Kurihara, S., 2001, Length dependence of tension generation in rat skinned cardiac muscle. Role of titin in the Frank-Starling mechanism of the heart, *Circulation* **104**:1639–1645.

Funatsu, T., Anazawa, T., and Ishiwata, S., 1994, Structural and functional reconstitution of thin filaments in skeletal muscle, *J. Muscle Res. Cell Motil.* **15**:158–171.

Funatsu, T., Higuchi, H., and Ishiwata, S., 1990, Elastic filaments in skeletal muscle revealed by selective removal of thin filaments with plasma gelsolin, *J. Cell Biol.* **110**:53–62.

Funatsu, T., Kono, E., Higuchi, H., Kimura, S., Ishiwata, S., Yoshioka, T., Maruyama, K., and Tsukita, S., 1993, Elastic filaments in situ in cardiac muscle: Deep-etch replica analysis in combination with selective removal of actin and myosin filaments, *J. Cell Biol.* **120**:711–724.

Gordon, A. M., Huxley, A. F., and Julian, F. J., 1966, The variation in isometric tension with sarcomere length in vertebrate muscle fibers, *J. Physiol.* **184**:170–192.

Higuchi, H., Yanagida, T., and Goldman, Y. E., 1995, Compliance of thin filaments in skinned fibers of rabbit skeletal muscle, *Biophys. J.* **69**:1000–1010.

Huxley, A. F., 1957, Muscle structure and theories of contraction, *Prog. Biophys. Biophys. Chem.* **7**:255–318.

Huxley, H. E., Stewart, A., Sosa, H., and Irving, T., 1994, X-ray diffraction measurements of the extensibility of actin and myosin filaments in contracting muscle, *Biophys. J.* **67**:2411–2421.

Isambert, H., Venier, P., Maggs, A. C., Fattoum, A., Kassab, R., Pantaloni, D., and Carlier, M. F., 1995, Flexibility of actin filaments derived from thermal fluctuations. Effect of bound nucleotide, phalloidin, and muscle regulatory proteins, *J. Biol. Chem.* **270**:11437–11444.

Ishiwata, S., 1973, A study on the F-actin, tropomyosin and troponin complex. I. Gel-filament transformation, *Biochim. Biophys. Acta* **303**:77–89.

Ishiwata, S., 1975, Doctoral Thesis, Nagoya University. "Study on muscle proteins – Principally, dynamic properties of actin filament studied by quasielastic scattering of laser light." pp. 229.

Ishiwata, S., 1978, Studies on the F-actin-tropomyosin-troponin complex. III. Effects of troponin components and calcium ion on the binding affinity between tropomyosin and F-actin, *Biochim. Biophys. Acta* **534**:350–357.

Ishiwata, S., 1998, Use of fluorescent probes, in: *Current Methods in Muscle Physiology-Advantages, Problems and Limitations-*, H. Sugi, ed., Oxford Univ. Press, Oxford, pp. 199–222.

Ishiwata, S., Anazawa, T., Fujita, T., Fukuda, N., Shimizu, H., and Yasuda, K., 1993, Spontaneous tension oscillation (SPOC) of muscle fibers and myofibrils. Minimum requirements for SPOC, *Adv. Exp. Med. Biol.* **332**:545–556.

Ishiwata, S., and Fujime, S., 1971, Effect of Ca^{2+} on dynamic properties of muscle proteins studied by quasi-elastic light scattering, *J. Phys. Soc. Jpn* **31**:1601.

Ishiwata, S., and Fujime, S., 1972, Effect of calcium ions on the flexibility of reconstituted thin filaments of muscle studied by quasielastic scattering of laser light, *J. Mol. Biol.* **68**:511–522.

Ishiwata, S., and Funatsu, T., 1985, Does actin bind to the ends of thin filaments in skeletal muscle? *J. Cell Biol.* **100**:282–291.

Ishiwata, S., Kinosita, Jr., K., Yoshimura, H., and Ikegami, A., 1987, Rotational motions of myosin heads in myofibril studied by phosphorescence anisotropy decay measurements, *J. Biol. Chem.* **262**: 8314–8317.

Ishiwata, S., and Kondo, H., 1978, Studies on the F-actin-tropomyosin-troponin complex. II. Partial reconstitution of thin filament by F-actin, tropomyosin and tropomyosin binding component of troponin (TNT), *Biochim. Biophys. Acta* **534**:341–349.

Ishiwata, S., Muramatsu, K., and Higuchi, H., 1985, Disassembly from both ends of thick filaments in rabbit skeletal muscle fibers. An optical diffraction study, *Biophys. J.* **47**:257–266.

Ishiwata, S., Okamura, N., Shimizu, H., Anazawa, T., and Yasuda, K., 1991, Spontaneous oscillatory contraction (SPOC) of sarcomeres in skeletal muscle, *Adv. Biophys.* **27**:227–235.

Ishiwata, S., and Oosawa, F., 1974, A regulatory mechanism of muscle contraction based on the flexibility change of the thin filament, *J. Mechanochem. Cell Motil.* **3**:9–17.

Ishiwata, S., Shimamoto, Y., Sasaki, D., and Suzuki, M., 2005, Molecular synchronization in actomyosin motors – From single molecules to muscle fibers via nanomuscle-, *Adv. Exp. Med. Biol.* **565**:25–36.

Ishiwata, S., and Yasuda, K., 1993, Mechano-chemical coupling in spontaneous oscillatory contraction of muscle, *Phase Transit.* **45**:105–136.

Kawai, M., and Ishiwata, S., 2006, Use of thin-filament reconstituted muscle fibres to probe the mechanism of force generation, *J. Muscle Res. Cell Motil.* 27:455–468.

Kinosita, K., Jr., Ishiwata, S., Yoshimura, H., Asai, H., and Ikegami, A., 1984, Submicrosecond and microsecond rotational motions of myosin head in solution and in myosin synthetic filaments as revealed by time-resolved optical anisotropy decay measurements, *Biochemistry* **23**:5963–5975.

Kojima, H., Ishijima, A., and Yanagida, T., 1994, Direct measurement of stiffness of single actin filaments with and without tropomyosin by in vitro nanomanipulation, *Proc. Natl. Acad. Sci. USA* **91**: 12962–12966.

Linke, W. A., Bartoo, M. L., and Pollack, G. H., 1993, Spontaneous sarcomeric oscillations at intermediate activation levels in single isolated cardiac myofibrils, *Circ. Res.* **73**:724–734.

McGough, A., Pope, B., Chiu, W., and Weeds, A., 1997, Cofilin changes the twist of F-actin: Implications for actin filament dynamics and cellular function, *J. Cell Biol.* **138**:771–781.

Molloy, J. E., 2005, Muscle contraction: actin filaments enter the fray, *Biophys. J.* **89**:1–2.

Nishizaka, T., Miyata, H., Yoshikawa, H., Ishiwata, S., and Kinosita, K., Jr., 1995, Unbinding force of a single motor molecule of muscle measured using optical tweezers, *Nature* **377**:251–254.

Nishizaka, T., Seo, R., Tadakuma, H., Kinosita, K., Jr., and Ishiwata, S., 2000, Characterization of single actomyosin rigor bonds – Load-dependence of lifetime and mechanical properties, *Biophys. J.* **79**: 962–974.

Ohtsuki, I., Maruyama, K., and Ebashi, S., 1986, Regulatory and cytoskeletal proteins of vertebrate skeletal muscle, *Adv. Protein Chem.* **38**:1–67.

Ohtsuki, I., Masaki, T., Nonomura, Y., and Ebashi, S., 1968, Periodic distribution of troponin along the thin filament, *J. Biochem.* **61**:817–819.

Okamura, N., and Ishiwata, S., 1988, Spontaneous oscillatory contraction of sarcomeres in skeletal myofibrils, *J. Muscle Res. Cell Motil.* **9**:111–119.

Oosawa, F., Fujime, S., Ishiwata, S., and Mihashi, K., 1972, Dynamic property of F-actin and thin filament, *Cold Spr. Harb. Symp. Quant. Biol.* **37**:277–285.

Prochniewicz, E., Janson, N., Thomas, D. D., and De La Cruz, E. M., 2005, Cofilin increases the torsional flexibility and dynamics of actin filaments, *J. Mol. Biol.* **353**:990–1000.

Prochniewicz-Nakayama, E., Yanagida, T., and Oosawa, F., 1983, Studies on conformation of F-actin in muscle fibers in the relaxed state, rigor, and during contraction using fluorescent phalloidin, *J. Cell Biol.* **97**: 1663–1667.

Sasaki, D., Fujita, H., Fukuda, N., Kurihara, S., and Ishiwata, S., 2005, Auto-oscillations of skinned myocardium correlating with heartbeat, *J. Muscle Res. Cell Motil.* **26**:93–101.

Sasaki, D., Fukuda, N., and Ishiwata, S., 2006, Myocardial sarcomeres spontaneously oscillate with the period of heartbeat under physiological conditions, *Biochem. Biophys. Res. Comm.* **343**:1146–1152.

Shimizu, H., Fujita, T., and Ishiwata, S., 1992, Regulation of tension development by MgADP and Pi without Ca^{2+}. Role in spontaneous tension oscillation of skeletal muscle, *Biophys. J.* **61**:1087–1096.

Stephenson, D. G., and Wendt, I. R., 1984, Length dependence of changes in sarcoplasmic calcium concentration and myofibrillar calcium sensitivity in striated muscle fibers, *J. Muscle Res. Cell Motil.* **5**: 243–272.

Suzuki, M., Fujita, H., and Ishiwata, S., 2005, A new muscle contractile system composed of a thick filament lattice and a single actin filament, *Biophys. J.* **89**:321–328.

Suzuki, N., Miyata, H., Ishiwata, S., and Kinosita, K., Jr., 1996, Preparation of bead-tailed actin filaments: Estimation of the torque produced by the sliding force in an in vitro motility assay, *Biophys. J.* **70**: 401–408.

Sweitzer, N. K., and Moss, R. L., 1990, The effect of altered temperature on Ca^{2+}-sensitive force in permeabilized myocardium and skeletal muscle. Evidence for force dependence of thin filament activation, *J. Gen. Physiol.* **96**:1221–1245.

Thomas, D. D., Seidel, J. C., and Gergely, J., 1979, Rotational dynamics of F-actin in submillisecond time range, *J. Mol. Biol.* **132**:257–273.

Thomas, D. D., Seidel, J. C., Hyde, J. S., and Gergely, J., 1975, Motion of subfragment-1 in myosin and its supramolecular complexes: saturation transfer electron paramagnetic resonance, *Proc. Natl. Acad. Sci. USA* **72**:1729–1733.

Tonomura, Y., Watanabe, S., and Morales, M. F., 1969, Conformational changes in the molecular control of muscle contraction, *Biochemistry* **8**:2171–2176.

Tsuda, Y., Yasutake, H., Ishijima, A., and Yanagida, T., 1996, Torsional rigidity of single actin filaments and actin-actin bond breaking force under torsion measured directly by in vitro micromanipulation, *Proc. Natl. Acad. Sci. USA* **93**:12937–12942.

Uemura, S., and Ishiwata, S., 2003, Loading direction regulates the affinity of ADP for kinesin, *Nat. Struct. Biol.* **10**:308–311.

Wakabayashi, K., Sugimoto, Y., Tanaka, H., Ueno, Y., Takezawa, Y., and Amemiya, Y., 1994, X-ray diffraction evidence for the extensibility of actin and myosin filaments during muscle contraction, *Biophys. J.* **67**: 2422–2435.

Yanagida, T., Nakase, M., Nishiyama, K., and Oosawa, F., 1985, Direct observation of motion of single F-actin filaments in the presence of myosin, *Nature* **307**:58–60.

Yasuda, K., Fujita, H., Fujiki, Y., and Ishiwata, S., 1994, Length regulation of thin filaments without nebulin, *Proc. Jap. Acad.* **70**, Ser. B.:151–156.

Yasuda, K., Shindo, Y., and Ishiwata, S., 1996a, Synchronous behavior of spontaneous oscillations of sarcomeres in skeletal myofibrils under isotonic conditions, *Biophys. J.* **70**:1823–1829.

Yasuda, R., Miyata, H., and Kinosita, K., Jr., 1996b, Direct measurement of the torsional rigidity of single actin filaments, *J. Mol. Biol.* **263**:227–236.

Size Distribution of Linear and Helical Polymers in Actin Solution Analyzed by Photon Counting Histogram

Naofumi Terada,* Togo Shimozawa,† Shin'ichi Ishiwata,*†‡ and Takashi Funatsu§¶

*Integrated Bioscience and Biomedical Engineering, Graduate School of Science and Engineering, †Department of Physics, Faculty of Science and Engineering, and ‡Advanced Research Institute for Science and Engineering, Waseda University, Shinjuku-ku, Tokyo, Japan; §Graduate School of Pharmaceutical Sciences, The University of Tokyo, Bunkyo-ku, Tokyo, Japan; and ¶Core Research for Evolutional Science and Technology, Japan Science and Technology Agency, Saitama, Japan

ABSTRACT Actin is a ubiquitous protein that is a major component of the cytoskeleton, playing an important role in muscle contraction and cell motility. At steady state, actin monomers and filaments (F-actin) coexist, and actin subunits continuously attach and detach at the filament ends. However, the size distribution of actin oligomers in F-actin solution has never been clarified. In this study, we investigated the size distribution of actin oligomers using photon-counting histograms. For this purpose, actin was labeled with a fluorescent dye, and the emitted photons were detected by confocal optics (the detection volume was of femtoliter (fL) order). Photon-counting histograms were analyzed to obtain the number distribution of actin oligomers in the detection area from their brightness, assuming that the brightness of an oligomer was proportional to the number of protomers. We found that the major populations at physiological ionic strength were 1–5mers. For data analysis, we successfully applied the theory of linear and helical aggregations of macromolecules. The model postulates three states of actin, i.e., monomers, linear polymers, and helical polymers. Here we obtained three parameters: the equilibrium constants for polymerization of linear polymers, $K_l = (5.2 \pm 1.1) \times 10^6\ M^{-1}$, and helical polymers, $K_h = (1.6 \pm 0.5) \times 10^7\ M^{-1}$; and the ratio of helical to linear trimers, $\gamma = (3.6 \pm 2.3) \times 10^{-2}$. The excess free energy of transforming a linear trimer to a helical trimer, which is assumed to be a nucleus for helical polymers, was calculated to be 2.0 kcal/mol. These analyses demonstrate that the oligomeric phase at steady state is predominantly composed of linear 1–5mers, and the transition from linear to helical polymers occurs on the level of 5–7mers.

INTRODUCTION

Actin is a ubiquitous protein, whose polymerization-depolymerization dynamics plays an important role in cell motility. At low-salt conditions, actin exists as monomers (G-actin), but polymerizes, forming filaments (F-actin), at physiological ionic conditions, if the concentration of actin monomers exceeds the critical concentration for polymerization (1). Actin polymerization starts after the polymerization nucleus is formed, and the polymerization rate depends on the total concentration of actin. Until now, actin polymerization has been studied by measuring viscosity (1), by static (2) and dynamic (3) light-scattering of the solution, by monitoring changes in fluorescence intensity of pyrenyl iodoacetamide-labeled actin (2), and so on. At steady state, actin monomers and filaments coexist, and monomers continue to attach and detach at the ends of filaments. Electron microscopy was used to study the distribution of the lengths of F-actin (4,5), to determine the asymmetrical growth rates at both ends of F-actin (6,7), and to observe direct coupling of short fragments of F-actin (7,8). Fluorescence microscopy observation of F-actin labeled with rhodamine-phalloidin allowed measurement of filament lengths and flexibility (9,10). Recently, polymerization dynamics of individual F-actin filaments was visualized by total internal reflection fluorescence microscopy (11–14), and large length fluctuations of the filaments provoked speculations that growth may proceed by oligomeric, in addition to monomeric, association-dissociation events (13). This inspired us to study the size distribution of actin oligomers at physiological ionic conditions.

The length distribution of F-actin polymerized in vitro was initially investigated by electron microscopy (4,5) and later by fluorescence microscopy (15). These studies reported the exponential distribution of F-actin particle lengths, supporting the theory of linear and helical aggregates (1,16). In this theory, the equilibrium between monomers and linear polymers, and between monomers and helical filaments, is postulated. Nucleation involves the association of three to four monomers into a stable nucleus from which a filament elongates by stochastic association of monomers to the ends of filaments. Filament elongation continues until the equilibrium phase, or steady state, is reached, where the rates of monomer association and dissociation are precisely balanced. In this phase, the stochastic exchange of monomers between filaments of different lengths leads to the redistribution of filament lengths, resulting in exponential distribution of lengths. To check the validity of this theory, the size distribution of small oligomers (1–10mers) has to be determined experimentally; however, it was impossible to do this by conventional methods.

To overcome this obstacle, we measured the size distribution of actin oligomers using the photon-counting histogram

Submitted October 5, 2006, and accepted for publication November 22, 2006.

Address reprint requests to Takashi Funatsu, Laboratory of Bio-Analytical Chemistry, Graduate School of Pharmaceutical Sciences, The University of Tokyo, 7-3-1, Hongo, Bunkyo-ku, Tokyo 113-0033, Japan. Tel.: 81-3-5841-4760; Fax: 81-3-5802-3339; E-mail: funatsu@mail.ecc.u-tokyo.ac.jp.

0006-3495/07/03/2162/10 $2.00

doi: 10.1529/biophysj.106.098871

(PCH) technique (17). This method enabled us to determine two parameters for each fluorescent species present, namely, the average number and brightness of the fluorescent particles in the observation volume, which in turn allowed us to distinguish between different species based on the difference in brightness. This method has been successfully applied to confirm protein oligomerization in living cells (18) and interactions between oligonucleotides and polycationic polymers (19). Recently, PCH analysis was extended to one-photon excitation for confocal spectroscopy (20–22). Here we use this PCH analysis to study the number distribution of actin oligomers. For this purpose, Cys-374 of actin was labeled with BODIPY FL-iodoacetamide, since labeling with this dye does not affect the polymerization-depolymerization dynamics of actin, as confirmed in the study described here. In addition, there exists a wavelength range in which the fluorescence intensity does not change upon polymerization, which is a requirement for PCH analysis. Photons emitted from the labeled actin were detected by confocal optics, and PCHs were analyzed to determine the size distribution of actin oligomers. Finally, the data were successfully analyzed by applying the theory of linear and helical aggregation of macromolecules (1,16).

MATERIALS AND METHODS

Preparation of fluorescent actin

G-actin was purified from acetone powder of rabbit skeletal muscle according to Spudich and Watt (23), except that the tropomyosin-troponin complex was removed before the preparation of the acetone powder, as previously described (7). G-actin was solubilized in 2 mM Tris-HCl (pH 8.0), 50 μM $CaCl_2$, 0.1 mM ATP, and 2 mM sodium azide. The concentration of unlabeled actin was determined from ultraviolet absorption (V-550, JASCO, Tokyo, Japan), assuming the molar extinction coefficient at 290 nm, 26,600 M^{-1} cm^{-1} (24). Labeling with fluorescent dye was performed by incubating 48 μM F-actin in a solution containing 0.1 M KCl, 2 mM $MgCl_2$, 1 mM ATP, 2 mM Tris-HCl (pH 8.0), and 200 μM *N*-((4,4-difluoro-5,7-dimethyl-4-bora-3a,4a-diaza-s-indacene-3-yl)methyl)iodoacetamide (BODIPY FL C_1-IA) (D6003, Molecular Probes, Eugene, OR) for 2 h at room temperature. BODIPY FL C_1-IA dissolved in dimethylformamide (20 mM) was slowly added to actin solution with continuous stirring. The reaction was terminated by adding 5 mM dithiothreitol (DTT), and BODIPY FL-labeled actin was centrifuged at 411,000 $\times$ *g* for 45 min at 8°C. The pellet was then dissolved in and dialyzed against a solution containing 20 mM MOPS (pH 7.0), 50 μM $CaCl_2$, 0.1 mM ATP, 1 mM DTT, and 1 mM sodium azide for 24 h at 2°C. After centrifugation at 411,000 $\times$ *g* for 20 min at 2°C, free fluorescent dye was removed from the G-actin solution by Sephadex G25 column chromatography. The concentration of BODIPY FL was estimated from the molar extinction coefficient at 505 nm, 49,000 M^{-1} cm^{-1}. The concentration of labeled actin was determined by subtracting 0.029 $\times$ A_{505} from the A_{290} value. The molar ratio of dye to actin in solution was 96–105% throughout the study. Pyrene iodoacetamide-labeled actin (P29, Molecular Probes) was prepared similarly, and the average labeling ratio was 105%.

Fluorescence spectroscopy of pyrene-actin and BODIPY FL-actin

To evaluate the effect of BODIPY FL labeling on polymerization of actin, pyrene-actin and BODIPY FL-actin of various mixing ratios were copolymerized, and the fluorescence intensity of pyrene was measured as follows (Fig. 1) 0.5 μM pyrene-actin and 0–4.5 μM BODIPY FL-actin were mixed with unlabeled actin so as to keep the total concentration of actin at 5 μM in buffer G (20 mM MOPS (pH 7.0), 50 μM $CaCl_2$, 1 mM ATP, and 1 mM DTT) containing 0.1 mg/ml BSA. To change actin-bound cations from Ca^{2+} to Mg^{2+}, 1/20 volume of mixed solution of 1 mM $MgCl_2$ and 4 mM EGTA was added to actin solution 5 min before the initiation of the polymerization at 27°C. Actin was polymerized by adding 1/20 volume of mixed solution of 1 M KCl and 40 mM $MgCl_2$. The time course of the fluorescence intensity of pyrene was measured at 27°C using a fluorescence spectrometer (F-4500, Hitachi, Tokyo, Japan) with excitation wavelength of 365 nm and emission wavelength of 408 nm.

Next, changes in the fluorescence spectra of BODIPY FL-actin upon polymerization were monitored as follows (Fig. 2). The polymerization of BODIPY FL-actin (5 μM) in buffer G was initiated by adding 1/20 volume of mixed solution of 2 M KCl and 40 mM $MgCl_2$, and fluorescence spectra were measured using the fluorescence spectrometer with excitation wavelength of 488 nm. The scan time of each spectrum was 3 s.

The dependence of the fluorescence intensity of BODIPY FL-actin on the labeling ratio was measured as follows (Fig. 3). BODIPY FL-actin was mixed with unlabeled actin in buffer G at various ratios such that the proportion of BODIPY FL-actin was 5–100% and the total concentration of actin was kept at 500 nM. Then actin was polymerized by adding 1/20 volume of mixed solution of 2 M KCl and 40 mM $MgCl_2$ and incubated overnight at room temperature. Fluorescence intensity was measured using the fluorescence spectrometer with excitation wavelength of 488 nm and emission wavelength of 507 nm.

Instrumentation and data analysis of PCH

The photon counting experiments were carried out using an inverted microscope with a 60× water immersion objective (UPlanApo, 60×w, NA 1.2, Olympus, Tokyo, Japan). Light from a solid-state laser (488 nm, Sapphire 488-20, Coherent, Tokyo, Japan) was reflected by a dichroic mirror (485DRLP, Omega Optical, Brattleboro, VT), and focused using the objective. The power of the laser was 13 μW at the focal plane. The fluorescence from the sample was collected by the objective, passed through the dichroic mirror, emission filters (D520/40m and S500/22m, Chroma

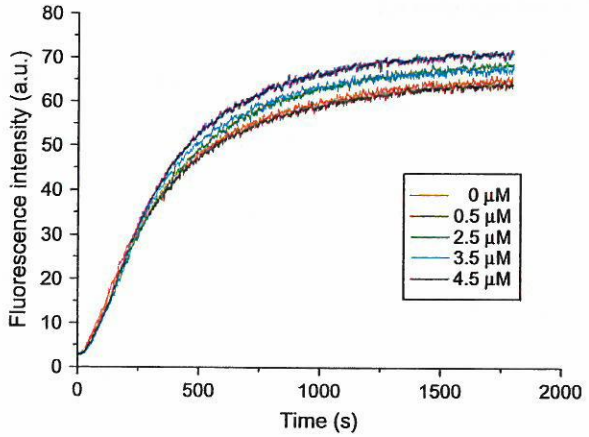

FIGURE 1 Time course of the fluorescence intensity of pyrene-actin copolymerized with various mixing ratios of BODIPY FL-actin. The concentration of pyrene-actin was 0.5 μM, and the concentrations of BODIPY FL-actin were varied from 0 to 4.5 μM. Total concentration was kept at 5 μM by adding unlabeled actin. Polymerization of actin was initiated by the addition of 50 mM KCl and 2 mM $MgCl_2$ to buffer G at 27°C. The polymerization rates were similar irrespective of the mixing ratios of BODIPY FL-actin, although the fluorescence intensity of pyrene was ~10% higher in 4.5 μM BODIPY FL-actin than in actin not labeled with BODIPY FL.

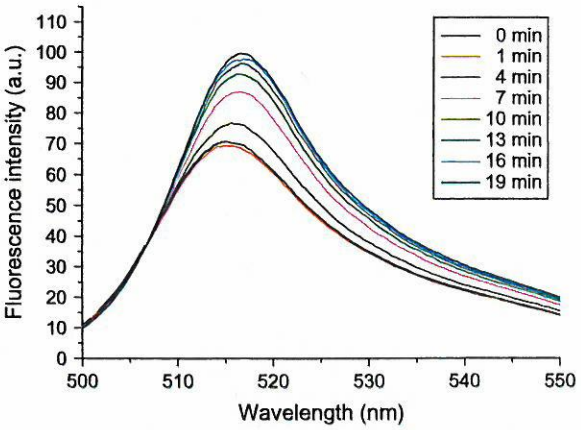

FIGURE 2 Time course of the fluorescence spectrum of BODIPY FL (~100% labeled)-actin after initiation of polymerization. Polymerization of BODIPY FL-actin was initiated by the addition of 0.1 M KCl and 2 mM $MgCl_2$ to buffer G at 27°C, and the fluorescence spectra of BODIPY FL were measured at each time point indicated in the graph. The spectrum at 0 min shows the spectrum in buffer G before the addition of KCl and $MgCl_2$.

Technology, Bellows Falls, VT), and a pinhole (diameter, 30 μm) located at the position conjugated to the focal plane. The transmission wavelength of the emission filters was from 502 to 512 nm. The fluorescence that passed through the pinhole was introduced into an optical fiber coupled to an avalanche photodiode (SPCM-AQR-14-PC, PerkinElmer, Wellesley, MA). The output of the avalanche photodiode was put into a counter (C8855, Hamamatsu Photonics, Hamamatsu City, Japan) with a gate time of 100 μs. A photon counting histogram was obtained from the data collected over a period of 100 s. Fitting of the data was performed according to the method of Chen et al. (17), using the correction for one-photon excitation (20). The correction parameter, F, for BODIPY FL was determined to be 0.70 ± 0.35 (mean ± SD, n = 16) (20,22). The program for the fitting was built with numerical routines according to Press and co-workers (25) by Visual C++ software (Microsoft, Redmond, WA).

PCH measurement

G-actin was diluted to 300 nM, 500 nM, 700 nM, and 1 μM with buffer G and incubated overnight at 0°C. F-actin was prepared by incubating actin at the above concentrations in buffer F (0.1 M KCl, 2 mM $MgCl_2$, 20 mM MOPS (pH 7.0), 50 μM $CaCl_2$, 1 mM ATP, and 1 mM DTT) overnight at room temperature. A 50-μl portion of each actin solution was placed on a coverslip, and the focal plane of the microscope was adjusted at 30 μm from the glass/solution interface. All PCH measurements were done at 23°C. PCHs of BODIPY FL-actin in buffer G were analyzed as follows.

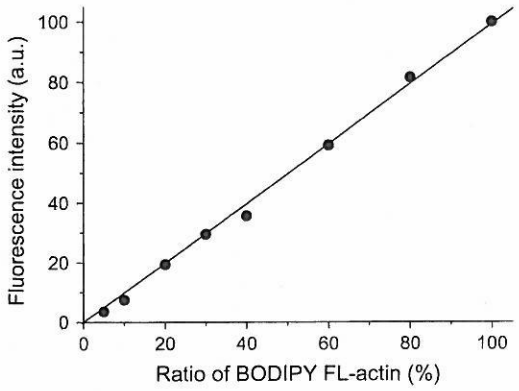

FIGURE 3 Fluorescence intensity versus a mixing ratio of BODIPY FL-actin. Actin containing various ratios of BODIPY FL-actin was polymerized in buffer F overnight at room temperature. Fluorescence intensity of F-actin solution was proportional to the labeling ratio of BODIPY FL-actin. The data were fit by a straight line.

The PCH for identical but independent particles is determined by two parameters, namely, N, the average number of molecules within the observation volume, and ε, the detected photon counts/molecule/sampling time. The probability of detecting k photoelectrons per sampling time is

$$\Pi(k;N,\varepsilon)=\sum_{M=0}^{\infty}p^{(M)}(k;V_0,\varepsilon)\frac{N^M e^{-N}}{M!}, \tag{1}$$

where V_0 is the reference volume. $p^{(M)}(k;V_0,\varepsilon)$ is the probability of detecting k photon counts from M fluorescent particles, defined as follows:

$$p^{(0)}(k;V_0,\varepsilon)=\begin{cases}1, & \text{for } k=0\\ 0, & \text{for } k\geq 1\end{cases} \tag{2}$$

$$p^{(1)}(k;V_0,\varepsilon)=\begin{cases}\dfrac{1}{(1+F)^2}\dfrac{1}{V_0}\dfrac{\pi\omega_0^2 z_0}{k!}\displaystyle\int_0^{\infty}\Gamma(k,\varepsilon e^{-2x^2})dx \\ \quad+\dfrac{\pi^{3/2}\omega_0^2 z_0}{V_0(1+F)^2}\dfrac{1}{2\sqrt{2}}\varepsilon, & \text{for } k=1\\ \dfrac{1}{(1+F)^2}\dfrac{1}{V_0}\dfrac{\pi\omega_0^2 z_0}{k!}\displaystyle\int_0^{\infty}\Gamma(k,\varepsilon e^{-2x^2})dx, & \text{for } k>1\end{cases} \tag{3}$$

where ω_0 is the beam waist and z_0 is the effective length of the confocal volume, Γ is the incomplete gamma function, and F is the correction parameter for one-photon excitation (21).

The M-particle PCH $p^{(M)}(k;V_0,\varepsilon)$was constructed by convolution of multiple single-particle PCHs $p^{(1)}(k;V_0,\varepsilon)$, as follows:

$$p^{(M)}(k;V_0,\varepsilon)=\underbrace{(p^{(1)}\otimes\cdots\otimes p^{(1)})}_{M\text{ times}}(k;V_0,\varepsilon). \tag{4}$$

If n different but independent particles (1, ..., n) are present, the PCH is obtained by convoluting the PCHs of individual species (17), as shown in Eq. (5):

$$\Pi(k;N_1,\cdots,N_n,\varepsilon_1,\cdots,\varepsilon_n)=\Pi(k;N_1,\varepsilon_1)\otimes\cdots\otimes\Pi(k;N_n,\varepsilon_n). \tag{5}$$

To fit the data, the histogram of the experimental data was calculated and then normalized to yield the experimental photon counting probability density $p(k)$. Since the probability of detecting k counts of photoelectrons for r times out of M trials (10^6 in our experiments) is given by the binominal distribution function, the expectation value is represented by $\langle r\rangle = Mp(k)$, and the standard deviation by $\sigma=[Mp(k)(1-p(k))]^{1/2}$. To obtain the best-fit parameters of N_i and ε_i ($1\leq i\leq n$), the theoretical density function was calculated for all the combinations of these parameters, and the combination of parameters N_i and ε_i that minimizes the following χ^2 function (17) was adopted as the best fit.

$$\chi^2=\frac{\displaystyle\sum_{k=k_{min}}^{k_{max}}\left(M\frac{p(k)-\Pi(k;N_1,\cdots,N_n,\varepsilon_1,\cdots,\varepsilon_n)}{\sigma}\right)^2}{k_{max}-k_{min}-2n}. \tag{6}$$

To analyze the number distribution of oligomers in buffer G, we assumed the number of species of actin oligomers, n, in buffer G to be distributed between 1 and 5 and fitted the data with the theoretical density functions $\Pi(k;N,\varepsilon)$, $\Pi(k;N_1,N_2,\varepsilon_1,\varepsilon_2)$, ···, $\Pi(k;N_1,\cdots N_5,\varepsilon_1,\cdots\varepsilon_5)$ by changing N_i

and ε_i as parameters. Then we determined n so as to minimize the χ^2 function (Eq. 6). Similar analyses were performed assuming that the number of species of actin oligomers in buffer F is distributed between 1 and 9.

We determined the number of protomers in each oligomer from the brightness, ε_i, assuming that the brightness of i-mers was i times that of the monomer. The number distribution of actin oligomers was obtained from N_i, the average number of oligomers within the observation volume. Finally, we calculated the proportion of the oligomers in total number concentration.

RESULTS

Polymerizability of BODIPY FL-actin

Labeling of Cys-374 with rhodamine-maleimide was reported to decrease the elongation rate of actin (11). To study the size distribution of F-actin by PCH, actin must be labeled with a fluorescent dye that does not affect the polymerization-depolymerization dynamics. We found that BODIPY FL iodoacetamide fulfilled this requirement. The polymerization of actin containing various ratios of BODIPY FL-labeled actin was initiated by the addition of 50 mM KCl and 2 mM $MgCl_2$. Pyrene-labeled actin (0.5 μM) was also included to monitor the polymerization process by changes in its fluorescence intensity (2). The total concentration of actin was kept at 5 μM, because the time course of polymerization depends on actin concentration. As shown in Fig. 1, though the fluorescence intensity of pyrene in the presence of 90% BODIPY FL-labeled actin was ~10% higher than that of unlabeled actin, the polymerization rates were similar irrespective of the mixing ratio of BODIPY FL-actin. These results indicate that the labeling of actin by BODIPY FL does not affect its polymerizability.

Fluorescence spectrum of BODIPY FL-actin before and after the polymerization

To obtain information about the size of actin oligomers by PCH, the fluorescence intensity of BODIPY FL must be constant irrespective of whether actin is monomeric or filamentous, because the number of protomers in each oligomer is determined by assuming that its brightness is proportional to the number of protomers. The changes in the fluorescence spectra during polymerization of 100% labeled BODIPY FL-actin are shown in Fig. 2. The wavelength of the peak was red-shifted and the peak intensity increased by ~50% upon polymerization. However, the fluorescence intensity of BODIPY FL-actin between 500 and 510 nm hardly changed upon polymerization. Therefore, we looked for commercially available optical filters that transmitted in this range, and found that the combination of bandpass filters D520/40m and S500/22m gave suitable transmission in the 502–512 nm range. The change in the fluorescence intensity upon polymerization of BODIPY FL-actin in this range was <11%.

Fluorescence intensity of BODIPY FL-actin was proportional to labeling ratio

When two fluorescent molecules come very close to each other, quenching of fluorescence sometimes occurs. There remains concern that Cys-374 residues of the adjacent actin protomers are close enough to quench each other. If this were the case, it would be impossible to determine the size distribution of oligomers using PCH. To exclude this possibility, we examined the dependence of the fluorescence intensity of BODIPY FL-actin on the labeling ratio. In principle, the lower the labeling ratio, the longer the average distance between fluorescent molecules, so that lowering the labeling ratio should reduce the effect of quenching. If there are quenching effects, the fluorescence intensity must be saturated at a higher labeling ratio rather than being proportional to the labeling ratio. As shown in Fig. 3, we found that the fluorescence intensity was proportional to the labeling ratio of BODIPY FL-actin up to 100%, indicating that no quenching of BODIPY FL occurred in the PCH experiments.

PCHs of BODIPY FL-actin

When a BODIPY-FL actin species passed through the confocal volume of femtoliter order, bursts of photons were observed. Fig. 4 shows the typical time courses of photon counts from BODIPY FL-actin in buffer G (Fig. 4 *A*) and in buffer F (Fig. 4 *B*). The number of photons was counted every 100 μs, and one million data points were collected.

Typical PCHs of BODIPY FL-actin in buffer G are shown in Fig. 5, *A–D*. Briefly, they were analyzed as follows (see Materials and Methods for details). The PCHs were normalized

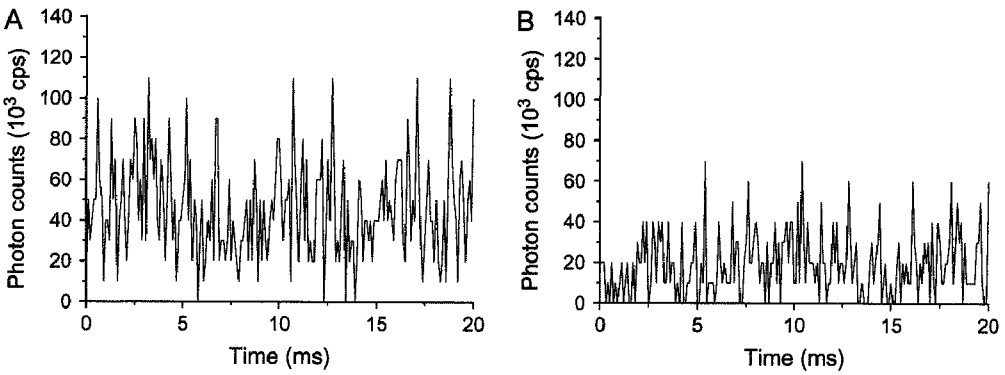

FIGURE 4 Time course of the fluorescence fluctuation profiles of 300 nM BODIPY FL-actin in buffer G (*A*) and buffer F (*B*) measured by the PCH setup.

to obtain the photon counting probability density, $p(k)$. We assumed that the number of species of actin oligomers, n, in buffer G was distributed between 1 and 5 and fitted the data with the theoretical density functions $\Pi(k; N, \varepsilon)$, $\Pi(k; N_1, N_2, \varepsilon_1, \varepsilon_2)$, $\cdots$, $\Pi(k; N_1, \cdots N_5, \varepsilon_1, \cdots \varepsilon_5)$ by changing N_i and ε_i as parameters. Then we determined n so as to minimize the χ^2 function (Eq. 6). Fig. 5 *E* shows the histogram of n obtained by 15 independent experiments at four different concentrations. The number of species of actin oligomers, n, was similar irrespective of the total actin concentration. About 90% of PCHs were fitted by the single component ($n = 1$) analysis and the remaining 10% were fitted by two components ($n = 2$). The reduced χ^2 function thus obtained was 1.1 ± 0.3 (mean $\pm$ SD). Next, we calculated the total number of protomers in each oligomer (see Fig. 7). The PCH analysis indicated that >99.5% of fluorescent actin in buffer G emitted photons at a similar rate ($(5.1 \pm 0.6) \times 10^3$ counts/s; mean $\pm$ SD, $n = 60$), suggesting that it was from monomeric BODIPY FL-actin. The content of oligomers (4–6mers) detected as the second component in Fig. 5 was <0.5%.

Next, we analyzed PCHs of BODIPY FL-actin in buffer F. Typical PCHs of BODIPY FL-actin in buffer F are shown in Fig. 6, *A–D*. We assumed that the number of species of actin oligomers, n, in buffer F was distributed from 1 to 9 and fitted the data as described above. Fig. 6 *E* shows the histogram of n obtained by 60 independent experiments at four different actin concentrations. The components larger than 100mers (~2%) were excluded from the analyses, because the length of such oligomers was greater than the width of the confocal volume. The components of less than one-half of the monomer brightness were also excluded from the analysis (the average brightness of such species was 1/7 of the monomer brightness). The number of species that minimized the χ^2 function was distributed between 2 and 8. The reduced χ^2 function thus obtained was 2.8 ± 2.0 (mean $\pm$ SD). Next, we calculated the total number of protomers in each oligomer assuming that the brightness of the monomer was 5.1×10^3 counts/s and that the brightness of an oligomer was proportional to the number of protomers. This assumption was justified by the observation that the major population in the

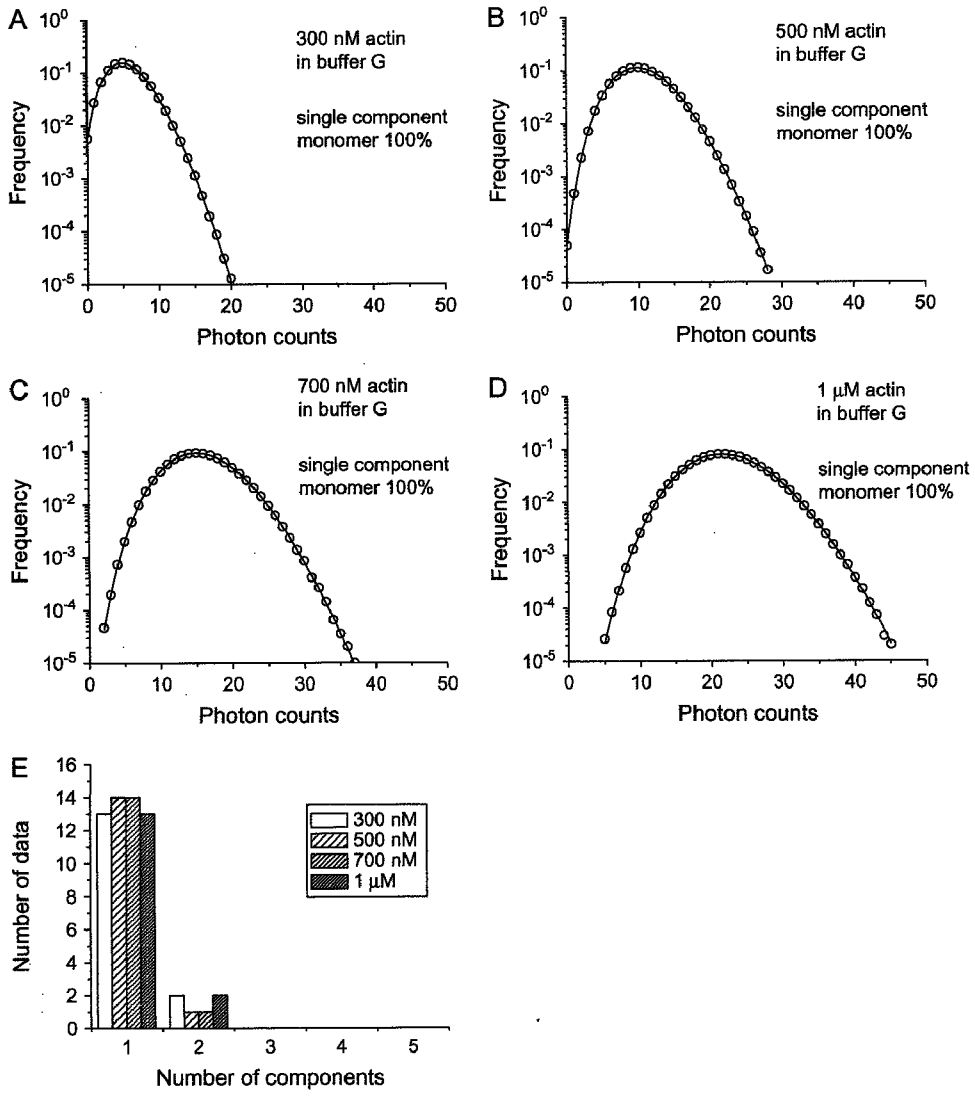

FIGURE 5 Examples of photon counting histograms of 300 nM (*A*), 500 nM (*B*), 700 nM (*C*), and 1 μM (*D*) BODIPY FL-actin in buffer G. The histograms are normalized to give the photon-counting probability density. The solid lines represent the best fit to the data. (*E*) The number of components required to fit the data. Most of the data could be fit assuming a single component (monomer). Panels *A–D* show the examples that could be fit by a single component, where the proportion of monomer was 100%.

brightness distribution of G-actin was at 5.1×10^3 counts/s and the histogram of brightness obtained by the PCH measurements in buffer F had peaks, or clusters, every 5×10^3 counts/s, namely, at $(5.6 \pm 1.2) \times 10^3$ counts/s, $(9.8 \pm 1.4) \times 10^3$ counts/s, and $(15.3 \pm 1.5) \times 10^3$ counts/s, corresponding to the brightness of a monomer, a dimer, and a trimer, respectively (see Supplementary Material).

Although the dimers, trimers, and oligomers were hardly detected in buffer G, they clearly existed in buffer F, as shown in Fig. 7. The major components of oligomers in buffer F were 1–5mers, and their total content was >94%. It should be noted that the distribution of oligomers could be classified into two populations having two different slopes for the relationship between the number concentration of i-mers and the value of i (Fig. 7). One class was 1–5mers and the other was 6–100mers. The two straight lines are crossed at around 6mer. The proportion of each oligomer larger than 6mer was <1%. The number concentrations of both populations were fitted by exponential functions with different parameters of A and B as follows:

$$c_i = A\exp(-Bi). \quad (7)$$

The obtained parameters of A and B are given in Table 1. The value of B is larger for 1–5mers than for 6–100mers, implying that the equilibrium constant of monomer and oligomer is lower for 1–5mers than for 6–100mers.

Based on the above analyses, we determined the number of actin monomers in both buffer G and buffer F in the confocal volume. As shown in Fig. 8, the number of actin monomers in buffer G linearly depends on actin concentration, whereas in buffer F it remains almost constant. It is to be noted, however, that the linear fit for the data in buffer G does not pass through the origin, which, at first glance, seems to indicate that the average number of monomers in the confocal volume was not exactly proportional to the total actin concentration. This result contradicts the observation that >99% of actin molecules were monomers in buffer G (Figs. 5 and 7). One plausible interpretation of this apparent discrepancy is that some part of actin molecules were adsorbed to the surface of a coverslip and the interface with

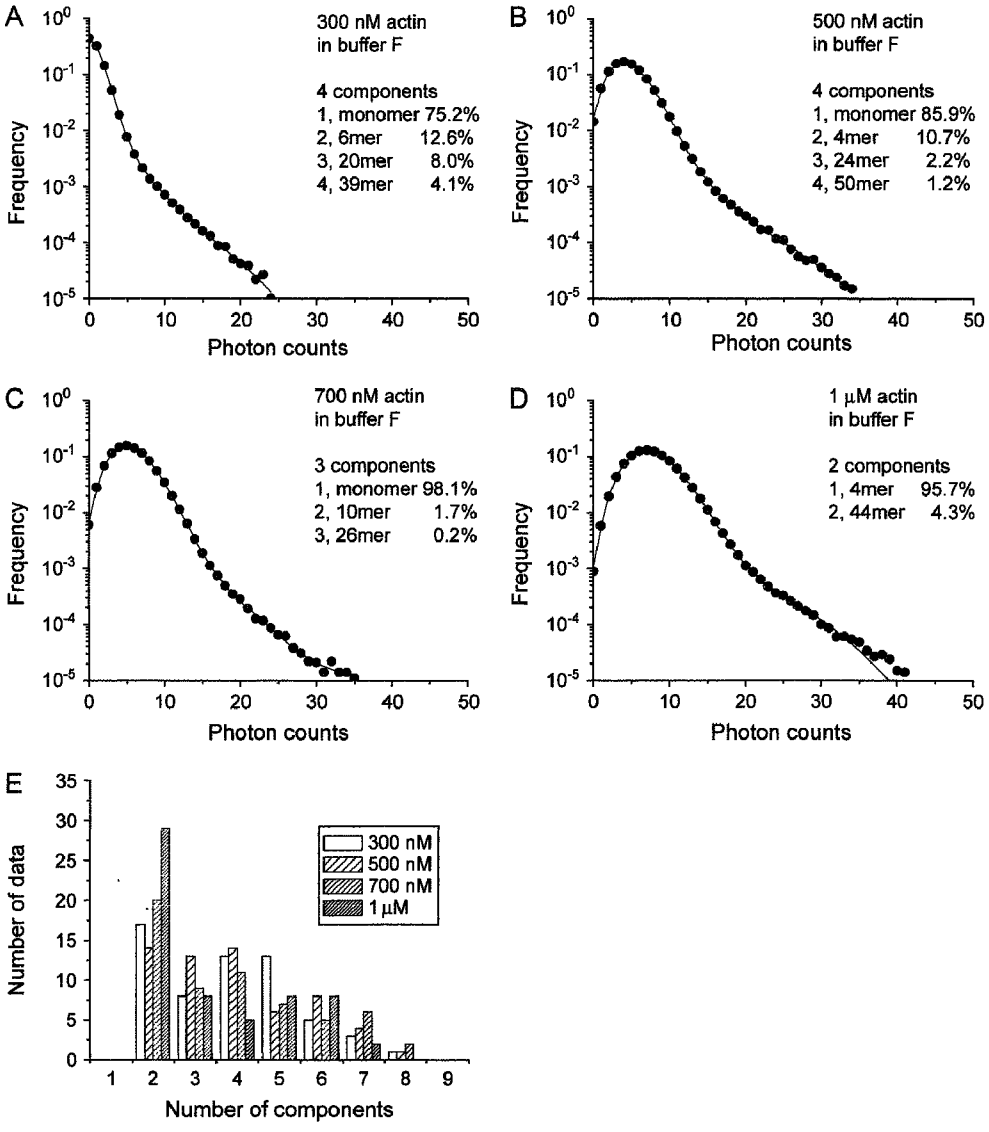

FIGURE 6 Examples of photon counting histograms of 300 nM (*A*), 500 nM (*B*), 700 nM (*C*), and 1 μM (D) BODIPY FL-actin in buffer F. The histograms are normalized to give the photon-counting probability density. The solid lines represent the best fit to the data. (*E*) The number of components required to fit the data was 2–8. Panels *A–D* show the examples that could be fit by three to four components. The proportions of the number concentration of each component are indicated in *A–D*.

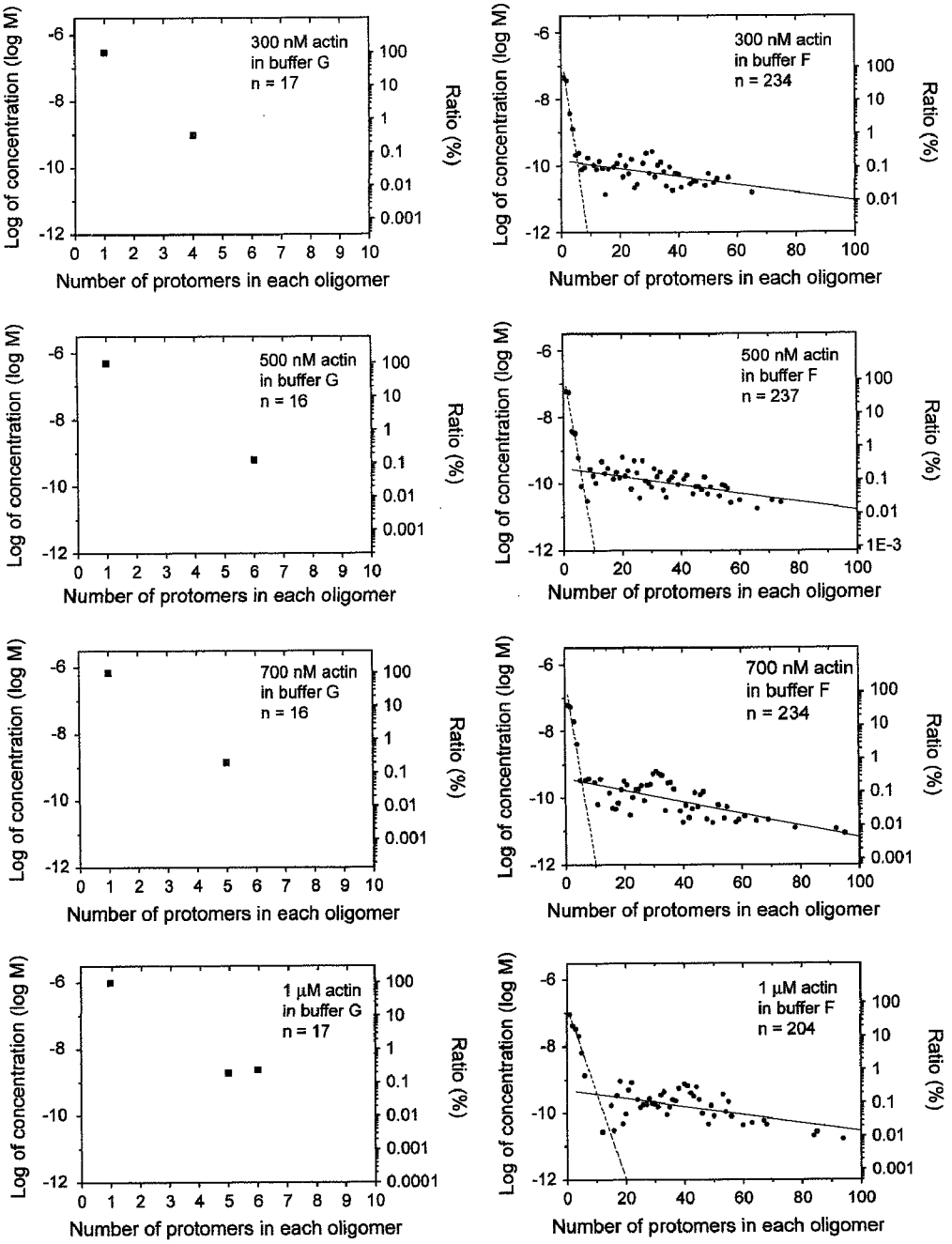

FIGURE 7 Logarithmic plot of the molar concentration of actin oligomers as a function of the number of protomers, i, in each oligomer. Most of the actin (>99%) in buffer G existed as monomers. The distribution of actin oligomers in buffer F had two distinct populations, 1–5mers and 6–100mers. The data for 1–5mers and 6–100mers were fit by dashed and solid lines, respectively.

air, so that the actual actin concentration was decreased by a fixed value proportional to the adsorption area. Based on this consideration, we set the cross-point of the linear fit with the abscissa as the true origin, implying that ~100 nM actin was adsorbed to the interface area of 50 μl of the actin solution used in the experiments. A rough estimation shows that the closely packed adsorption of actin molecules to the interface area is on the order of 10^{-11}–10^{-12} moles, which just corresponds to the loss of ~100 nM actin (= (10^{-11}–10^{-12} moles)/50 μl). On the other hand, the average number of monomers in the confocal volume in buffer F was 1.3 ± 0.4, irrespective of the total actin concentration. We consider that actin is adsorbed on the interface in buffer F in the same way, so that the newly determined origin is common for both conditions. Thus, the critical concentration for polymerization of actin in buffer F was determined to be 55 nM from the abscissa of the cross-point of the solid lines for buffer G and buffer F (Fig. 8).

DISCUSSION

PCH analysis to determine the size distribution of oligomers

So far, PCH analysis has been used to study the oligomerization of receptors in living cells (18). We have extended PCH analysis to probe much larger oligomers, i.e., actin polymers having an exponential length distribution at physiological

TABLE 1 Parameters for exponential fitting of the number concentration of *i*-mers

Conditions		A (M)*	B*
300 nM	1–5mers	3.0×10^{-7}	1.4
	>5mers	1.5×10^{-10}	2.8×10^{-2}
500 nM	1–5mers	2.8×10^{-7}	1.2
	>5mers	2.9×10^{-10}	2.9×10^{-2}
700 nM	1–5mers	4.9×10^{-7}	1.3
	>5mers	3.9×10^{-10}	4.1×10^{-2}
1 μM	1–5mers	1.7×10^{-7}	6.0×10^{-1}
	>5mers	4.9×10^{-10}	2.9×10^{-2}

*The number concentration of i-mers, c_i, is fitted as $c_i = A\exp(-Bi)$.

ionic strength (buffer F). The analyses of PCH data showed that the oligomeric phase in steady state is predominantly composed of linear 1–5mers (Fig. 7). Because the proportion of oligomers larger than 6mers was <1%, the accumulation of a large amount of data had to be performed to confirm the exponential distribution of the number concentrations of longer oligomers. The obtained result is consistent with those of previous EM studies (4,5). The only difference from earlier EM results (4) is that our data show an eight-times-faster decrease in the number population from 6 to 100mers, which may be attributable to the differences in experimental conditions, such as protein concentration and solvent composition.

As observed in Fig. 7, the distribution of oligomers in buffer F has two markedly distinct regions, corresponding to 1–5mers and 6–100mers (cf. Table 1). The equilibrium constants of the monomer binding estimated from the slopes indicate that the constant of binding to 1–5mers is smaller than the constant of binding to 6–100mers. The most plausible interpretation is that the former corresponds to the monomer binding to linear oligomers, K_l, whereas the latter corresponds to binding to helical oligomers, K_h (for detailed analysis, see below). The crossing point of the two lines in the panels on the right in Fig. 7 suggests that the transition from linear to helical oligomers occurs at 5–7mers.

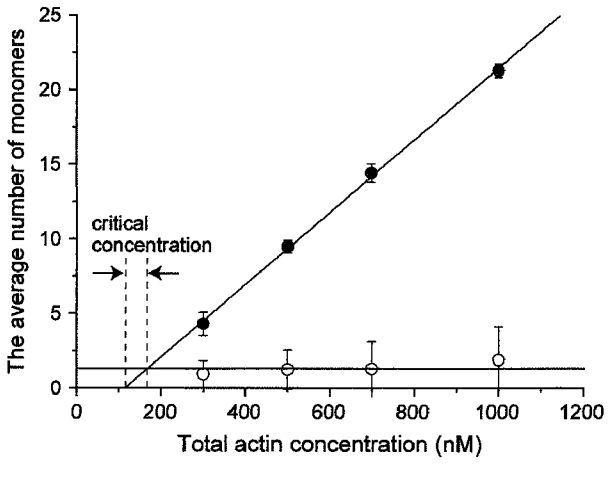

FIGURE 8 The average number of actin monomers within a confocal volume in buffer G (*solid circles*) and buffer F (*open circles*) as a function of total actin concentration. In buffer G, the number of monomers was proportional to the total actin concentration (*thin line*), but the fit did not pass through the origin. On the other hand, in buffer F, the number of monomers was almost constant. The critical concentration for polymerization was determined from the cross-point between the two lines (for details, see text). Error bars represent the standard deviation.

Analysis of PCH data by the theory of linear and helical aggregations of macromolecules

The PCH data obtained here were analyzed by the theory of Oosawa and Asakura, which postulates the equilibrium between monomers, linear polymers, and helical polymers, as shown in Fig. 9 *A* (1). The number concentrations of linear i-mers are denoted as c_{il}, which is given as follows:

$$c_{il} = K_l^{-1}(K_l c_1)^i, \tag{8}$$

where K_l is the equilibrium constant of monomer binding to a linear polymer, which is assumed to be independent of the degree of polymerization. The deformation of a linear polymer, leading to the creation of additional bonds, results in the formation of a helical polymer. Here we assume that the helical trimer is a nucleus for polymerization. Denoting the number concentration of helical i-mers as c_{ih},

$$c_{3h} = \gamma c_{3l} \tag{9}$$

and

$$c_{ih} = \gamma K_l^2 K_h^{-3}(K_h c_1)^i, \tag{10}$$

where γ is the concentration ratio of a helical to a linear trimer, and K_h is the equilibrium constant of monomer binding to the ends of the helical polymer. γ can be expressed by using the free energy ΔF necessary for the deformation of a linear trimer to produce a helical polymer as follows:

$$\gamma = \exp(-\Delta F/k_B T), \tag{11}$$

where k_B is the Boltzmann constant and T is absolute temperature.

The values of c_{ih} were obtained by logarithmic fitting of c_i in the panels on the right in Fig. 7 for $10 \le i < 100$ and extrapolating to $3 \le i < 10$. Accordingly, the values of c_{il} were obtained from $c_{il} = c_i$ (for $i = 1, 2$) and $c_{il} = c_i - c_{ih}$ (for $3 \le i < 10$). Then, the values of K_l, γ, and K_h were obtained from Eqs. 8–10, respectively. As a result, these three parameters were determined to be $K_l = (5.2 \pm 1.1) \times 10^6$ M^{-1}, $K_h = (1.6 \pm 0.5) \times 10^7$ M^{-1}, and $\gamma = (3.6 \pm 2.3) \times 10^{-2}$. A monomer attaches to two protomers at each end of a helical oligomer and to a single protomer in a linear oligomer, which results in the larger value of K_h compared to K_l. The critical concentration for polymerization was found to be $K_h^{-1} = 62$ nM, consistent with the value obtained from Fig. 8 (55 nM). The excess free energy of transforming a

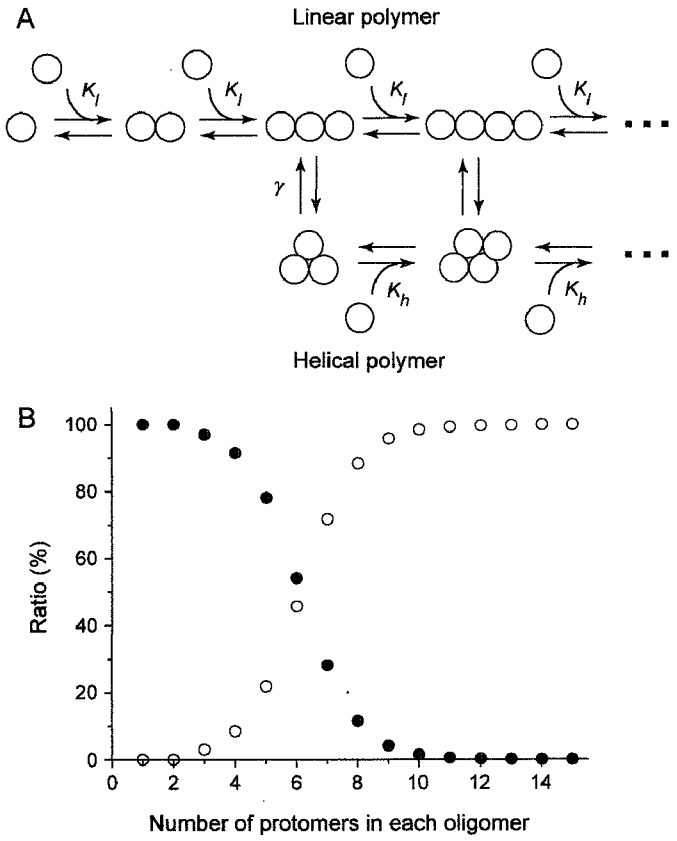

FIGURE 9 (*A*) Schematic diagram of the equilibrium of polymerization among monomers, linear polymers, and helical polymers used for the model analysis (for details, see Discussion). (*B*) Proportion of linear (*solid circles*) and helical (*open circles*) oligomers determined by Eqs. 8–10 and the data shown in Fig. 7. Here, the trimer was assumed to be the polymerization nucleus.

linear to a helical trimer, ΔF, was calculated to be 2.0 kcal/mol from Eq. 11.

Fig. 9 shows the existence ratio of linear and helical oligomers in 1–15mers determined from Eqs. 8–10 using the obtained values of the three parameters. These analyses suggest that 1), the oligomeric phase at steady state is predominantly composed of linear 1–5mers; 2), the transition from linear to helical oligomers occurs in 5–7mers (Fig. 9); and 3), most of the oligomers larger than 10mers are helical. In the analyses given above, we assumed that the helical trimer is a nucleus for polymerization. The analyses based on the assumption that the nucleus is the helical tetramer yielded a value of γ equal to $(1.3 \pm 1.1) \times 10^{-1}$ ($\Delta F = 1.2$ kcal/mol), whereas values of K_l and K_h remained unchanged, and the linear/helical existence ratio thus obtained was almost indistinguishable from that shown in Fig. 9 *B*. Therefore, from the present analyses, we cannot unambiguously deduce which oligomer serves as the polymerization nucleus. However, the trimer would be more probable due to the lower value of γ, which is the prerequisite for the condensation process of polymerization to helical assemblies such as actin filaments.

The most dominant species in the number distribution in F-actin solution is a monomer. Therefore, the most probable unit involved in polymerization events should be a monomer; however, the linear and helical oligomers identified in this study will also contribute to the polymerization dynamics of actin. In fact, our previous study indicated that the average size of a unit involved in the elementary process of polymerization-depolymerization dynamics is 5–6mers (13). Although structural studies on linear oligomers are necessary, future studies must also address the role of linear oligomers in polymerization dynamics.

CONCLUSIONS

The number distribution of actin oligomers in filamentous actin solution at physiological ionic conditions was determined using the PCH technique. The results confirm that the PCH is powerful enough to resolve the oligomeric state of fluorescently labeled actin. The experimental data were analyzed in terms of a theoretical model that assumes the equilibrium between monomers, linear and helical polymers of actin. This is the first report experimentally showing the existence of linear polymers in actin solution and indicating that the oligomeric phase at steady state is predominantly composed of linear 1–5mers. The transition from linear to helical polymers occurs on the level of 5–7mers.

We thank Dr. S. V. Mikhailenko for his critical reading of the manuscript.

This work was partly supported by Takeda Science Foundation and by Grants-in-Aid for Specially Promoted Research, Scientific Research (A), the 21st Century COE program, and "Establishment of Consolidated Research Institute for Advanced Science and Medical Care" from the Ministry of Education, Culture, Sports, Science and Technology (MEXT) of Japan.

REFERENCES

1. Oosawa, F., and S. Asakura. 1975. Thermodynamics of the polymerization of proteins. Academic Press, New York.
2. Kouyama, T., and K. Mihashi. 1981. Fluorimetry study of N-(1-pyrenyl)iodoacetamide-labelled F-actin. Local structural change of actin protomer both on polymerization and on binding of heavy meromyosin. *Eur. J. Biochem.* 114:33–38.
3. Masai, J., S. Ishiwata, and S. Fujime. 1986. Dynamic light-scattering study on polymerization process of muscle actin. *Biophys. Chem.* 25:253–269.
4. Kawamura, M., and K. Maruyama. 1970. Electron microscopic particle length of F-actin polymerized in vitro. *J. Biochem. (Tokyo).* 67:437–457.
5. Kawamura, M., and K. Maruyama. 1972. A further study of electron microscopic particle length of F-actin polymerized in vitro. *J. Biochem. (Tokyo).* 72:179–188.
6. Woodrum, D. T., S. A. Rich, and T. D. Pollard. 1975. Evidence for biased bidirectional polymerization of actin filaments using heavy meromyosin prepared by an improved method. *J. Cell Biol.* 67:231–237.
7. Kondo, H., and S. Ishiwata. 1976. Uni-directional growth of F-actin. *J. Biochem. (Tokyo).* 79:159–171.
8. Nakaoka, Y., and M. Kasai. 1969. Behaviour of sonicated actin polymers: adenosine triphosphate splitting and polymerization. *J. Mol. Biol.* 44:319–332.
9. Yanagida, T., M. Nakase, K. Nishiyama, and F. Oosawa. 1984. Direct observation of motion of single F-actin filaments in the presence of myosin. *Nature.* 307:58–60.

10. Honda, H., H. Nagashima, and S. Asakura. 1986. Directional movement of F-actin in vitro. *J. Mol. Biol.* 191:131–133.

11. Amann, K. J., and T. D. Pollard. 2001. Direct real-time observation of actin filament branching mediated by Arp2/3 complex using total internal reflection fluorescence microscopy. *Proc. Natl. Acad. Sci. USA.* 98:15009–15013.

12. Fujiwara, I., S. Suetsugu, S. Uemura, T. Takenawa, and S. Ishiwata. 2002. Visualization and force measurement of branching by Arp2/3 complex and N-WASP in actin filament. *Biochem. Biophys. Res. Commun.* 293:1550–1555.

13. Fujiwara, I., S. Takahashi, H. Tadakuma, T. Funatsu, and S. Ishiwata. 2002. Microscopic analysis of polymerization dynamics with individual actin filaments. *Nat. Cell Biol.* 4:666–673.

14. Kuhn, J. R., and T. D. Pollard. 2005. Real-time measurements of actin filament polymerization by total internal reflection fluorescence microscopy. *Biophys. J.* 88:1387–1402.

15. Burlacu, S., P. A. Janmey, and J. Borejdo. 1992. Distribution of actin filament lengths measured by fluorescence microscopy. *Am. J. Physiol.* 262:C569–C577.

16. Oosawa, F., and M. Kasai. 1962. A theory of linear and helical aggregations of macromolecules. *J. Mol. Biol.* 4:10–21.

17. Chen, Y., J. D. Muller, P. T. So, and E. Gratton. 1999. The photon counting histogram in fluorescence fluctuation spectroscopy. *Biophys. J.* 77:553–567.

18. Chen, Y., L. N. Wei, and J. D. Muller. 2003. Probing protein oligomerization in living cells with fluorescence fluctuation spectroscopy. *Proc. Natl. Acad. Sci. USA.* 100:15492–15497.

19. Van Rompaey, E., Y. Chen, J. D. Muller, E. Gratton, E. Van Craenenbroeck, Y. Engelborghs, S. De Smedt, and J. Demeester. 2001. Fluorescence fluctuation analysis for the study of interactions between oligonucleotides and polycationic polymers. *Biol. Chem.* 382:379–386.

20. Huang, B., T. D. Perroud, and R. N. Zare. 2004. Photon counting histogram: one-photon excitation. *ChemPhysChem.* 5:1523–1531.

21. Perroud, T. D., B. Huang, M. I. Wallace, and R. N. Zare. 2003. Photon counting histogram for one-photon excitation. *ChemPhysChem.* 4: 1121–1123.

22. Perroud, T. D., M. P. Bokoch, and R. N. Zare. 2005. Cytochrome *c* conformations resolved by the photon counting histogram: watching the alkaline transition with single-molecule sensitivity. *Proc. Natl. Acad. Sci. USA.* 102:17570–17575.

23. Spudich, J. A., and S. Watt. 1971. The regulation of rabbit skeletal muscle contraction. I. Biochemical studies of the interaction of the tropomyosin-troponin complex with actin and the proteolytic fragments of myosin. *J. Biol. Chem.* 246:4866–4871.

24. Houk, T. W., Jr., and K. Ue. 1974. The measurement of actin concentration in solution: a comparison of methods. *Anal. Biochem.* 62:66–74.

25. Press, W. H., S. A. Teukolsky, W. T. Vetterling, and B. P. Flannery. 1988. Numerical Recipes in C. Cambridge University Press, Cambridge, U.K.

Microscopic Detection of Thermogenesis in a Single HeLa Cell

Madoka Suzuki,* Vadim Tseeb,† Kotaro Oyama,† and Shin'ichi Ishiwata*†
*Consolidated Research Institute for Advanced Science and Medical Care, and †Department of Physics, Faculty of Science and Engineering, Waseda University, Tokyo, Japan

ABSTRACT We report here the technique for detection and measurement of the temperature changes in single cells using a recently devised microthermometer (a glass micropipette filled with the thermosensitive fluorescent dye Europium (III) thenoyltrifluoroacetonate trihydrate). We found that the heat production in a single HeLa cell occurred with some time delay after the ionomycin-induced Ca^{2+} influx from the extracellular space. The time delay inversely depended on extracellular [Ca^{2+}], and the increase in temperature was suppressed when Ca^{2+}-ATPases were blocked by thapsigargin. These observations strongly suggest that the enzymatic activity of Ca^{2+}-ATPases in endoplasmic reticulum leads to the heat production. This study has therefore paved the way for studying the thermogenesis at the single-cell level.

Received for publication 2 October 2006 and in final form 18 January 2007.

Madoka Suzuki and Vadim Tseeb contributed equally to this work.

Address reprint requests and inquiries to Shin'ichi Ishiwata, E-mail: ishiwata@waseda.jp.

In a long history of the physiological studies on thermogenesis, the thermodynamic parameters have mainly been examined for different parts of the body, tissues or organs, as a whole (1–4). Although several groups have succeeded in imaging the heat production in single cells by the direct incorporation of fluorescent dyes into each cell to detect temperature changes, these studies had obvious weak points: the fluorescence intensity was also sensitive to either the fluidity of the plasma membrane (5) or the pH value of solution (6). Thus, to overcome the technical problems in the study of thermogenesis in single cells, there was a need to devise a new tool to measure the local temperature in an aqueous solution, having high spatial resolution without interfering with any environmental parameters. For this purpose, we recently devised a microthermometer (7).

The directional flow of various kinds of ions in living cells driven by electrochemical potentials and energy-consuming pumping processes is hypothesized to result in the heat production (8,9). Steep temperature gradients in cells have recently attracted strong interest from cell biologists, especially concerning the effects of local intracellular thermogenesis on the rates of chemical reactions, the rate of the diffusion process (e.g., the transmitter-receptor mismatch in the brain (10)), the speed of exocytosis (11), and so on. One of the most interesting targets in this respect is the thermogenesis coupled with the changes in intracellular free Ca^{2+} concentration ($[Ca^{2+}]_{in}$), because up to 3% of the total energy production by a cell is estimated to be used even in the resting conditions, simply to maintain large [Ca^{2+}] gradients between the cytoplasm and the lumens of endoplasmic/sarcoplasmic reticulum, as well as against the extracellular space (12,13). Heat is produced by the initiation of calcium pumping because the sarco/endoplasmic reticulum Ca^{2+}-ATPase (SERCA) utilizes only a part of the energy of ATP hydrolysis to pump Ca^{2+}, whereas the rest is dissipated in the form of heat ranging from 10 to 30 kcal/mol hydrolyzed ATP (14).

Although the integrated thermogenesis in a large number of cells studied by microcalorimetry has been reported (15), the sensitivity of this method is not sufficient to measure heat production in single living cells. Therefore, to reveal how the cellular heat production correlates with $[Ca^{2+}]_{in}$ and other important cellular parameters, the measurements should be performed on the level of individual cells.

In this work we present a simple approach to measure the real-time thermogenesis in a single HeLa cell with simultaneously monitoring $[Ca^{2+}]_{in}$ regulated by ionomycin, which is a powerful ionophore making cellular and intracellular membranes highly permeable to Ca^{2+} (16). In all experiments, two microthermometers were used: one was gently pressing the cell to ensure good contact with the cell membrane, and the other, separated at least 20 μm from the cell, served as a reference thermometer (Figs. 1 and 2).

Ionomycin (20 μl of 0.2 mM solution) was added from one side of the dish (ϕ35 mm) containing 2 ml of the medium, to the final concentration 2 μM. The addition of this small volume did not result in the temperature change of the medium or the mechanical noise. The dish was kept still throughout the measurement. Although the HeLa cells survive in the presence of ionomycin better than other types of cells (16), we found that 10 min is the longest time the HeLa cells could survive in our conditions.

Next, we recorded three fluorescence signals: from Fluo-4 loaded into the cell to monitor $[Ca^{2+}]_{in}$, and from Europium (III) thenoyltrifluoroacetonate trihydrate (Eu-TTA) dissolved in DMSO, in two microthermometers, to monitor the

doi: 10.1529/biophysj.106.098673

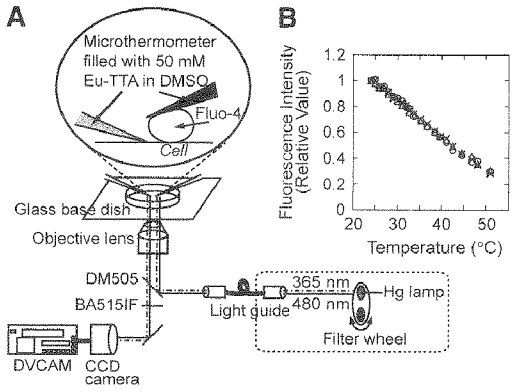

FIGURE 1 Schematic illustration of the setup (*A*) and the obtained temperature versus fluorescence intensity relationship (*B*). (*A*) See Supplementary Material for details. (*B*) Fluorescence intensity was measured in several regions of the microthermometer: the tip (*circles*), the central part (*triangles*), and the root (*crosses*).

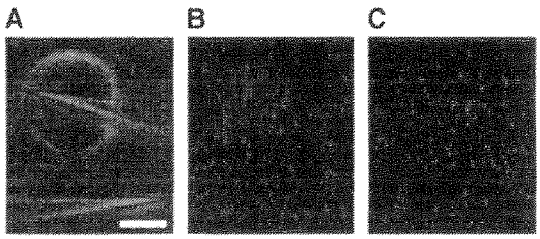

FIGURE 2 (*A*) Phase-contrast image of a cell and the two pipettes. (*Upper*) Measurement pipette. (*Lower*) Reference pipette. (*B* and *C*) Fluorescence images of Fluo-4 and Eu-TTA, respectively. Scale bar, 10 μm.

temperature. These two fluorescent dyes are compatible because their excitation spectra are well separated and the emission spectra are in the region of the wavelengths longer than 515 nm (cf. Fig. 1 and Supplementary Material). The temperature change was estimated with the use of the slope of the calibration curve, −0.0274/°C (Fig. 1 *B*), which indicates strong dependence of the Eu-TTA fluorescence on temperature compared with other dyes (e.g., −0.018/°C for the rhodamine fluorescence; (17)).

Fig. 3 shows the recordings of $[Ca^{2+}]_{in}$ made simultaneously with the thermogenesis detected in a single HeLa cell upon application of ionomycin, at two different extracellular $[Ca^{2+}]$, 5 mM (Fig. 3 *A*) and 1 mM (Fig. 3 *B*). As the filter wheel and the charge-coupled device camera were not synchronized, the signals from Fluo-4 and Eu-TTA were separated by subsequent analysis with the use of a self-written macro in Microsoft Excel. The recordings made over the long period of observation include photobleaching caused by excitation light. However, because the degree of photobleaching was small for 50 mM Eu-TTA (Fig. 3, *Aa* and *Ab*), it was well approximated by a single exponential and could therefore be removed from the raw traces.

When ionomycin reached the cell surface, the increment of $[Ca^{2+}]_{in}$ was observed (Fig. 3, *Ac* and *Ba*). As a result, the fluorescence intensity of Eu-TTA in a pipette contacting the cell decreased with some time delay (Fig. 3, *Ad* and *Bb*). No detectable change in the fluorescence intensity, however, occurred in the reference pipette (Fig. 3, *Ae* and *Bc*). The value of temperature change varied between the measurements

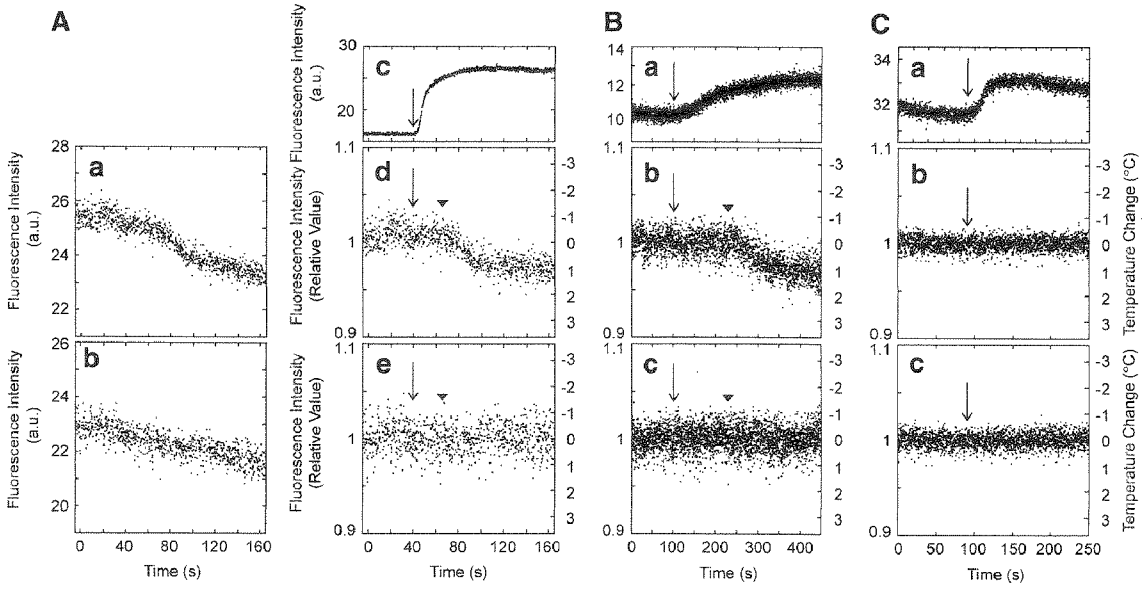

FIGURE 3 Time courses of the fluorescence intensity at different extracellular $[Ca^{2+}]$. Ionomycin was added to the petri dish at time 0 in the presence of 5 mM Ca^{2+} (*A*), 1 mM Ca^{2+} (*B*), and 2 mM Ca^{2+} with 2 μM thapsigargin after the pretreatment with 2 mM Ca^{2+} and 2 μM thapsigargin for 1 h (*C*). A part of the experiment in panel *A* is presented as Supplementary Movie 1. Each dot represents the average value in the region of interest at the tip of the pipette in a single video frame. (*Aa*, *Ad*, *Bb*, and *Cb*) The fluorescence intensity of Eu-TTA in the pipette contacting the cell. (*Ab*, *Ae*, *Bc*, and *Cc*) Fluorescence intensity of Eu-TTA in the reference pipette. (*Ac*, *Ba*, and *Ca*) The fluorescence intensity of Fluo-4. The arrows show the moment at which Fluo-4 signal increased, and the arrowheads indicate the moment at which the initiation of the positive thermogenesis was detected.

depending on the area of the contact between the pipette and the cell. The largest observed temperature increase was ~1°C.

The rate of the $[Ca^{2+}]_{in}$ increase was faster at higher extracellular $[Ca^{2+}]$ (Fig. 3, *Ac* and *Ba*), due to a larger gradient of $[Ca^{2+}]$ between the outside and the inside of the cell. The positive thermogenesis always followed the increase in $[Ca^{2+}]_{in}$ and, in addition, occurred earlier in the presence of 5 mM Ca^{2+} than with 1 mM (Fig. 3, *Ac*, *Ad*, *Ba*, and *Bb*). The values of the time delay (s, mean ± SE (N)) were 28 ± 5 (5) for 5 mM Ca^{2+} and 126 ± 12 (3) for 1 mM.

What is the heat source for the thermogenesis observed here? It is reasonable to consider that SERCA pumping up Ca^{2+} into endoplasmic reticulum (ER) is involved in the heat production (14). The dependence of the time delay on the extracellular $[Ca^{2+}]$ (Table 1) would then be understandable, because SERCA will have to start operating to keep constant $[Ca^{2+}]_{in}$ after $[Ca^{2+}]_{in}$ exceeds a threshold level due to the influx of extracellular Ca^{2+}. To confirm this consideration, we next examined the effect of thapsigargin, an inhibitor of SERCA for ER (18). In these experiments, cells were first incubated with 2 μM thapsigargin for 1 h in the presence of 2 mM Ca^{2+}, and then 2 μM ionomycin was applied together with 2 μM thapsigargin and 2 mM Ca^{2+}. As expected, we observed the influx of Ca^{2+} upon the application of ionomycin, but no temperature change was detected (Fig. 3 *C*).

In summary, we demonstrated that the coupling between the real-time thermogenesis and the SERCA's activity could be detected in single HeLa cells. We can therefore conclude that SERCA plays a key role in the cascade of cellular heat production. The next targets will be the quantitative determination of the temperature distribution inside the cell, the identification of the source(s) of the thermogenesis, and the elucidation of their physiological roles. The thermodynamic parameters for the cell, e.g., the thermal conductivity of the cytoplasm containing high concentrations of proteins, and of the inner structures with phospholipid bilayers, which must be different from the homogeneous medium, should also be clarified in future studies.

Finally, we stress that using a microthermometer is potentially a highly powerful technique for studying local thermogenesis in tissue experiments because it allows one to easily penetrate the tissue, such as a brain slice, with the simultaneous use of electronic, chemical, and optical setups to monitor other physiological parameters.

SUPPLEMENTARY MATERIAL

An online supplement to this article can be found by visiting BJ Online at http://www.biophysj.org.

ACKNOWLEDGMENTS

We thank Drs. S. V. Mikhailenko and B. C. Steel for their critical reading of the manuscript.

This work was partly supported by Grants-in-Aid for Specially Promoted Research and the 21st Century COE Program to S. I. and by Grants-in-Aid for Young Investigator Research and Scientific Research in Priority Areas to M. S. from the MEXT, Japan.

REFERENCES and FOOTNOTES

1. Jiang, J. Y., B. G. Lyeth, G. L. Clifton, L. W. Jenkins, R. J. Hamm, and R. L. Hayes. 1991. Relationship between body and brain temperature in traumatically brain-injured rodents. *J. Neurosurg.* 74:492–496.
2. Mellergard, P., and C. H. Nordstrom. 1990. Epidural temperature and possible intracerebral temperature gradients in man. *Br. J. Neurosurg.* 4:31–38.
3. Miyazawa, T., and K. A. Hossmann. 1992. Methodological requirements for accurate measurements of brain and body temperature during global forebrain ischemia of rat. *J. Cereb. Blood Flow Metab.* 12: 817–822.
4. Tanaka, H., H. Yoshimura, Y. Miyake, J. Imaizumi, K. Nagayama, and H. Shimizu. 1987. Information processing for the organization of chemotactic behavior of physarum polycephalum studied by microthermography. *Protoplasma.* 138:98–104.
5. Chapman, C. F., Y. Liu, G. J. Sonek, and B. J. Tromberg. 1995. The use of exogenous fluorescent probes for temperature measurements in single living cells. *Photochem. Photobiol.* 62:416–425.
6. Zohar, O., M. Ikeda, H. Shinagawa, H. Inoue, H. Nakamura, D. Elbaum, D. L. Alkon, and T. Yoshioka. 1998. Thermal imaging of receptor-activated heat production in single cells. *Biophys. J.* 74:82–89.
7. Zeeb, V., M. Suzuki, and S. Ishiwata. 2004. A novel method of thermal activation and temperature measurement in the microscopic region around single living cells. *J. Neurosci. Methods.* 139:69–77.
8. Chen, D. P., R. S. Eisenberg, J. W. Jerome, and C. W. Shu. 1995. Hydrodynamic model of temperature change in open ionic channels. *Biophys. J.* 69:2304–2322.
9. Kondepudi, D., and I. Prigogine. 1998. *In* Modern Thermodynamics. Wiley, West Sussex, UK. 333–350. Nonequilibrium thermodynamics.
10. Fuxe, K., A. Rivera, K. X. Jacobsen, M. Hoistad, G. Leo, T. L. Horvath, W. Staines, A. De la Calle, and L. F. Agnati. 2005. Dynamics of volume transmission in the brain. Focus on catecholamine and opioid peptide communication and the role of uncoupling protein 2. *J. Neural Transm.* 112:65–76.
11. Andrews, Z. B., S. Diano, and T. L. Horvath. 2005. Mitochondrial uncoupling proteins in the CNS: in support of function and survival. *Nat. Rev. Neurosci.* 6:829–840.
12. Alvarez, J., M. Montero, and J. Garcia-Sancho. 1999. Subcellular Ca^{2+} dynamics. *News Physiol. Sci.* 14:161–168.
13. Shannon, T. R., and D. M. Bers. 1997. Assessment of intra-SR free [Ca] and buffering in rat heart. *Biophys. J.* 73:1524–1531.
14. de Meis, L., A. P. Arruda, and D. P. Carvalho. 2005. Role of sarco/endoplasmic reticulum Ca^{2+}-ATPase in thermogenesis. *Biosci. Rep.* 25:181–190.
15. Engstrom, I., A. Waldenstrom, P. Nilsson-Ehle, and G. Ronquist. 1993. Dissipation of the calcium gradient in human erythrocytes results in increased heat production. *Clin. Chim. Acta.* 219:113–122.
16. Stege, G. J., P. K. Wierenga, H. H. Kampinga, and A. W. Konings. 1993. Hyperthermia, intracellular free calcium and calcium ionophores. *Int. J. Radiat. Biol.* 64:459–468.
17. Kato, H., T. Nishizaka, T. Iga, K. Kinosita Jr., and S. Ishiwata. 1999. Imaging of thermal activation of actomyosin motors. *Proc. Natl. Acad. Sci. USA.* 96:9602–9606.
18. Thastrup, O., P. J. Cullen, B. K. Drobak, M. R. Hanley, and A. P. Dawson. 1990. Thapsigargin, a tumor promoter, discharges intracellular Ca^{2+} stores by specific inhibition of the endoplasmic reticulum Ca^{2+}-ATPase. *Proc. Natl. Acad. Sci. USA.* 87:2466–2470.

Molecular Cell, Vol. 14, 423–434, May 21, 2004, Copyright ©2004 by Cell Press

GroEL Mediates Protein Folding with a Two Successive Timer Mechanism

Taro Ueno,[1,4] Hideki Taguchi,[2,3,4,5] Hisashi Tadakuma,[1] Masasuke Yoshida,[2,*] and Takashi Funatsu[1,*]
[1]Department of Physics
School of Science and Engineering
Waseda University
3-4-1 Okubo
Tokyo 169-8555
[2]Chemical Resources Laboratory
Tokyo Institute of Technology
4259 Nagatsuta
Yokohama 226-8503
[3]Precursory Research for Embryonic Science and Technology (PRESTO)
JST
Kawaguchi-shi, Saitama 332-0012
Japan

Summary

GroEL encapsulates nonnative substrate proteins in a central cavity capped by GroES, providing a safe folding cage. Conventional models assume that a single timer lasting ~8 s governs the ATP hydrolysis-driven GroEL chaperonin cycle. We examine single molecule imaging of GFP folding within the cavity, binding release dynamics of GroEL-GroES, ensemble measurements of GroEL/substrate FRET, and the initial kinetics of GroEL ATPase activity. We conclude that the cycle consists of two successive timers of ~3 s and ~5 s duration. During the first timer, GroEL is bound to ATP, substrate protein, and GroES. When the first timer ends, the substrate protein is released into the central cavity and folding begins. ATP hydrolysis and phosphate release immediately follow this transition. ADP, GroES, and substrate depart GroEL after the second timer is complete. This mechanism explains how GroES binding to a GroEL-substrate complex encapsulates the substrate rather than allowing it to escape into solution.

Introduction

In prokaryotes and eukaryotes, chaperonins facilitate folding of newly translated, newly translocated, or stress-damaged proteins in an ATP-dependent manner. The best-studied of these chaperonins is the *Escherichia coli* GroEL and its cochaperonin GroES (Bukau and Horwich, 1998; Sigler et al., 1998; Thirumalai and Lorimer, 2001; Hartl and Hayer-Hartl, 2002; Saibil and Ranson, 2002). GroEL comprises 14 identical 57 kDa subunits each containing a site for binding and hydrolysis of ATP (Braig et al., 1994; Boisvert et al., 1996). Seven GroEL subunits are arranged in a heptamer ring forming a central cavity, and two heptamer rings are stacked back to back (Braig et al., 1994). GroES is a dome-shaped, single heptamer ring of 10 kDa subunits (Hunt et al., 1996; Xu et al., 1997).

GroEL binds a wide range of nonnative proteins at the apical cavity rim (Viitanen et al., 1992; Horwich et al., 1993; Fenton et al., 1994; Ewalt et al., 1997; Houry et al., 1999), then subsequently binds ATP and GroES to the same (*cis*) GroEL ring (Xu et al., 1997), producing the *cis* ternary complex consisting of GroEL, nonnative protein, and GroES (Weissman et al., 1995; Mayhew et al., 1996). Since the residues of GroEL involved in GroES binding mostly overlap with those responsible for substrate protein binding (Fenton et al., 1994), it is presumed that, when GroES binds to GroEL, residues within GroES assume responsibility for binding from substrate protein. Then, instead of escaping into the bulk medium, nonnative protein is somehow guided into the cavity of the *cis* ring beneath GroES (the *cis* cavity) where it can initiate folding without risk of aggregation (Fenton et al., 1994; Xu et al., 1997; Chen and Sigler, 1999). As ATPs in the *cis* ring are hydrolyzed to ADP, the opposite side (*trans*) ring of GroEL becomes ready for binding nonnative proteins and ATP, which, in turn, induces the release of GroES, ADP, and substrate protein (whether folded or not) from the *cis* ring (Rye et al., 1997, 1999). Then the *trans* ring subsequently binds GroES, becoming a new *cis* ternary complex for the next chaperonin cycle (Rye et al., 1997, 1999). The functional GroEL cycle proceeds at maximum turnover rate, ~0.12 s^{-1}, when saturating amounts of GroES, ATP, and nonnative proteins are present (Burston et al., 1995; Rye et al., 1999). Under these optimum conditions, binding of these components to GroEL is very rapid, and, according to current model, the whole cycle of GroEL is actually governed by a single rate constant (0.12 s^{-1}) corresponding to the rate of ATP hydrolysis in the *cis* ring (the single timer model) (Weissman et al., 1996; Rye et al., 1997, 1999). Therefore, when the cycle is initiated by addition of ATP to the mixture of GroEL, substrate protein, and GroES, the folding-active *cis* ternary complex should form immediately and all subsequent events, including those of ATP hydrolysis reactions (cleavage of bound ATP, release of ADP and Pi) and decay of the *cis* ternary complex (release of GroES and substrate protein from GroEL), should take place apparently with a single rate constant, ~0.12 s^{-1}. As a result, the substrate protein can utilize almost the whole functional GroEL cycle of ~8 s [lifetime, 1/(0.12 s^{-1})] for productive folding.

However, single molecule imaging of dynamic binding release kinetics of GroES during steady-state functional GroEL cycle has revealed that release of GroES from GroEL occurs through two steps defined by rate constants, ~0.3 s^{-1} and ~0.2 s^{-1} (Taguchi et al., 2001). Typically, GroES binds very rapidly to GroEL, remains for ~3 s (lag period), and departs GroEL over ~5 s (Taguchi et al., 2001). Similar "two timer" kinetics of the

*Correspondence: myoshida@res.titech.ac.jp (M.Y.); funatsu@mol.f.u-tokyo.ac.jp (T.F.)
[4]These authors contributed equally to this work.
[5]Present address: Department of Integrated Biosciences, Graduate School of Frontier Sciences, The University of Tokyo, Kashiwa, Chiba 277-8562, Japan.

release of GroES from GroEL were observed by rapid scanning atomic force microscopy (Viani et al., 2000). These observations are in contrast to the prediction by the single timer model. This is not a trivial contradiction of kinetics because the appearance of another rate constant means the existence of a previously unnoticed intermediate in the functional GroEL cycle that would considerably improve our understanding on the GroEL mechanism. Indeed, a mutant GroEL that did not fit any of the intermediates in the single timer model has been reported (Kawata et al., 1999; Miyazaki et al., 2002).

Despite of a number of reports on GroEL kinetics, there is very little data which might distinguish the single timer model and the two timer model. Here, we report results on the kinetics of the functional GroEL cycle in the presence of ATP, GroES, and nonnative substrate proteins. For this purpose, we have developed a real-time, single molecule observation system for folding of green fluorescent protein (GFP) in the *cis* cavity and found that protein folding started after a lag period of ~3 s. Rearrangements of substrate protein in the *cis* cavity on this time scale were observed for GFP and malate dehydrogenase (MDH) by fluorescence resonance energy transfer (FRET). A second kinetic step necessitated the formation of new intermediates in the functional GroEL cycle, and initial pre-steady-state ATPase kinetics further clarified nucleotide states of these intermediates. This two timer mechanism may provide a possible explanation for the difficult problem of how GroEL can confine a substrate protein within the narrow *cis* cavity.

Results

Single Molecule Imaging Revealed that GFP Folding Was Arrested for the First ~3 s in the *cis* Ternary Complex

To analyze the events in a functional GroEL cycle, we need to monitor the recovery of the activity of the substrate protein in the *cis* cavity as a mark of completion of folding, with a time resolution of s, rather than min. Many studies on the time courses of GroEL(GroES)-mediated protein folding have been published, but few have reported such measurements. The substrate protein for this purpose should exhibit monomer activity that can be measured continuously while it is confined in the *cis* cavity. Since GFP exclusively satisfies these criteria, we developed a real-time, single molecule imaging system to observe folding of GFP in the *cis* cavity (Figure 1A). To immobilize and visualize GroEL, Asp490, which is located at the external surface of GroEL, was replaced by Cys (the mutant was termed EL490) and labeled with biotin-maleimide and IC5-maleimide at the same time. Labeled EL490, as well as unlabeled EL490, behaves like the wild-type GroEL as assessed by every analysis performed, including steady-state ATP hydrolysis and assisted folding of rhodanese and GFP as described previously (Taguchi et al., 2001). In addition, the second mutation D398A was introduced to EL490, termed EL398/490. Like a D398A mutant of GroEL, EL398/490 forms a *cis* ternary complex normally, but it hydrolyzes ATP very slowly, only 2% of wild-type (Rye et al., 1997). In the absence of ATP hydrolysis, EL398/490 keeps GFP in the *cis* cavity up to ~30 min where GFP can complete folding. GFP was denatured in 0.1 M HCl and diluted into a solution of neutral pH containing EL398/490 to form the EL398/490-GFP complex. The complex was infused into a flow cell and immobilized on the glass surface through biotin-streptavidin linker. The glass chamber was then filled with the solution containing GroES and caged ATP. First, the positions of EL398/490 molecules were determined by the fluorescence of IC5 using a total internal reflection fluorescence microscopy (TIRFM) (Figure 1B, "GroEL"). The functional GroEL cycle was triggered by generation of ATP from caged ATP (1 mM) on UV flash. About 40% of caged ATP was converted to ATP. As concentrations of generated ATP and GroES (1 μM) were saturating, their binding to GroEL should not limit the rate but should complete within 0.1 s, as calculated from the binding rate constants and concentrations (Taguchi et al., 2001). Following the photogeneration of ATP, fluorescent spots of the folded GFP appeared over time at the positions of EL398/490 (Figure 1B, "GFP"). Fluorescent spots of GFP that appeared at positions other than preassigned GroEL ones were ascribed to EL398/490 without the IC5 label. Folded GFP in the medium, if any, was not detected due to Brownian motion. All fluorescent spots were of the folded GFP within the *cis* ternary complex since no spots appeared in the absence of GroES.

A histogram of the waiting time for the appearance of GFP fluorescence showed a nonexponential distribution with a maximum at ~8 s (Figure 1C). The same data was replotted as the time course of the accumulated number of fluorescent GFP after UV flash (Figure 1C, inset) to compare with those of the following bulk phase experiments (Figure 2). The data shown in Figure 1C is well described by Equation 1 containing two transitions:

$$\text{denatured GFP}^* \xrightarrow[k]{} \text{denatured GFP} \xrightarrow[k']{} \text{native GFP} \quad (1)$$

A simulation of Equation 1 was plotted in Figure 1C with $k = 0.31\ s^{-1}$ and $k' = 0.034\ s^{-1}$ and, therefore, the lifetimes (the reciprocal of the rate constant) of "denatured GFP*" and "denatured GFP" were ~3 and ~33 s, respectively. This means that folding of GFP is arrested during the first ~3 s after GroES binds GroEL.

To avoid argument that these features are specific for the ATPase-deficient mutant, similar experiments were also performed using EL490. EL490 undergoes the normal functional GroEL cycle, and most GFP should be released into the bulk medium before folding is completed. Therefore, to keep maximum GFP in the *cis* cavity during the measuring time, we included apyrase in the reaction mixture to exhaust ATP within ~1 s after the UV flash so that the release of GroES from GroEL was suppressed by the lack of ATP for binding the *trans* ring (Rye et al., 1997, 1999). A histogram of the waiting time for the appearance of GFP fluorescence at the positions of EL490 after photogeneration of ATP showed a nonexponential distribution with a maximum at ~5 s (Figure 1D). The pattern of this histogram differed significantly from that of EL398/490. We measured the time course of the GroES release in the presence of apyrase using Cy3-GroES in a parallel experiment under the same conditions and calibrated the original data, taking into ac-

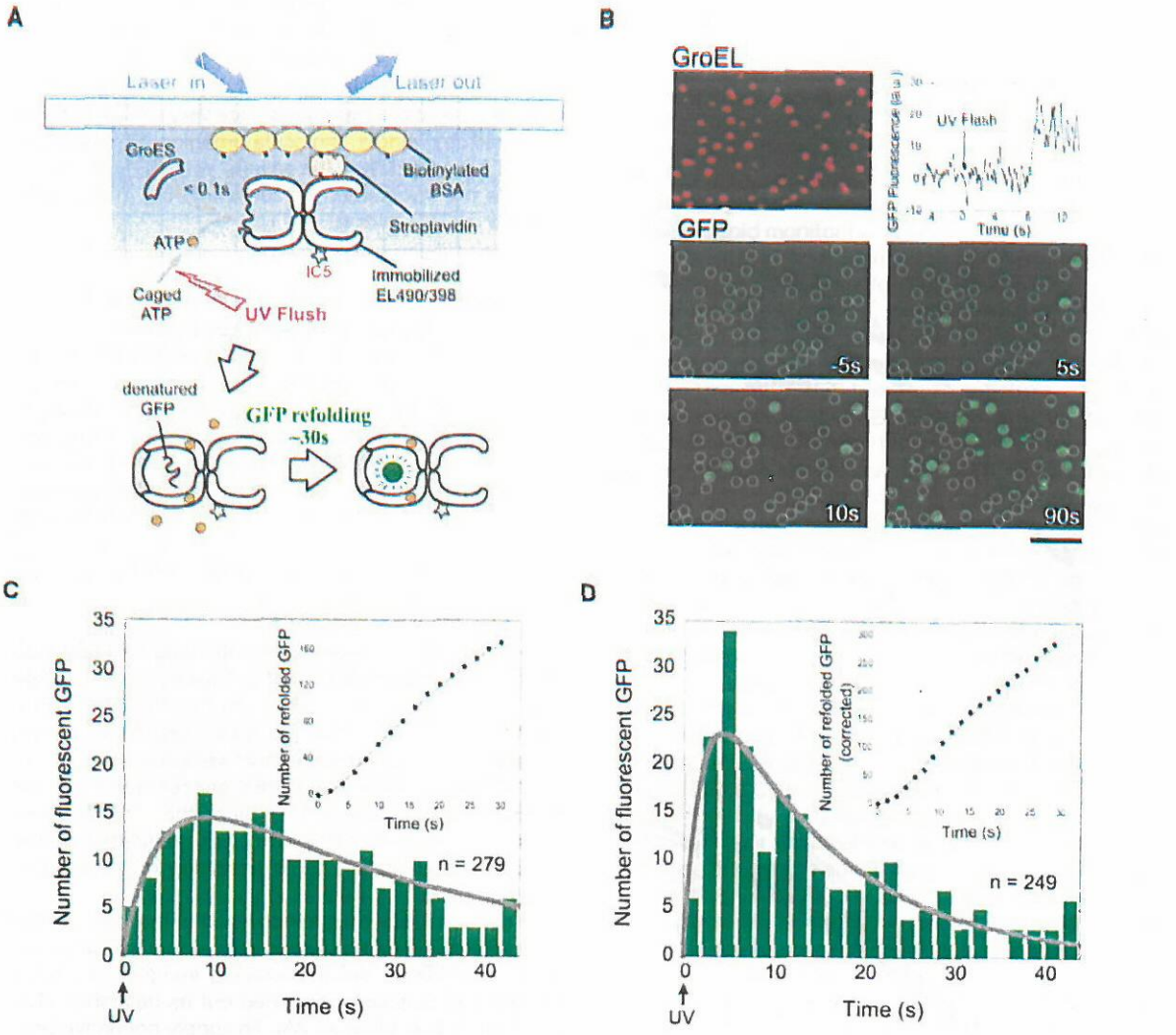

Figure 1. Imaging of Folding of Single Molecule GFP in the *cis* Cavity

(A) Schematic illustration of the experiment. The IC5-GroEL-denatured GFP complex was immobilized on the glass, and ATP was generated from caged ATP by a UV flash in the presence of a saturating amount of GroES. Appearance of GFP at the positions of GroEL was observed with TIRFM.

(B) Fluorescence images of GroEL molecules (GroEL) and GFP molecules (GFP), which folded within the *cis* cavity. ATP was generated at time 0 s. Positions of EL398/490 were indicated by circles colored yellow. Scale bar, 5 μm. (Inset) Time course of the fluorescence intensity of a GFP molecule at the position of GroEL (see Supplemental Movie S1 at http://www.molecule.org/cgi/content/full/14/4/423/DC1).

(C and D) Histograms of the time required for each GFP to gain native structure in (C) EL398/490 or (D) EL490, after the photogeneration of ATP. The solid line is the convolution of two exponentials, $Ck\,k'\,[\exp(-kt) - \exp(-k't)]/(k - k')$, fit to the data by least-squares fitting. This formula is derived from the two-step reaction of Equation 1. (Inset) Time course of the cumulative number of folded GFP molecules. Solid line is the integration of the above formula.

count the premature release of GFP. Including this correction, the histogram fit the two sequential transitions of Equation 1 with $k = 0.34\ s^{-1}$ and $k' = 0.029\ s^{-1}$ (gray line). The result again indicates that folding of denatured GFP in the *cis* ternary complex is arrested for ~3 s before it begins to regain the native conformation in the course of ~30 s. If the lag of ~3 s comes not from substrate release but from the kinetics of GFP refolding after release, the data in Figures 1 and 2 would be the remarkable evidence that the kinetics of protein refolding in the chaperonin cavity is completely different from those in free solution.

Bulk Phase Experiments Also Showed a ~3 s Lag of GFP Folding in the *cis* Ternary Complex

GFP folding was also monitored in bulk phase solution using a fluorometer (Figure 2A). Spontaneous folding, initiated by diluting acid-denatured GFP into a buffer of neutral pH, occurred with a single rate constant $0.032\ s^{-1}$. In this case, no lag was evident (Figure 2B). For GroEL-mediated GFP folding, acid-denatured GFP was diluted to a buffer containing GroEL and GroES to form the GroEL-GFP complex, and the functional GroEL cycle was initiated by addition of ATP. We tested three types of GroEL: EL490, EL398, and a single ring version

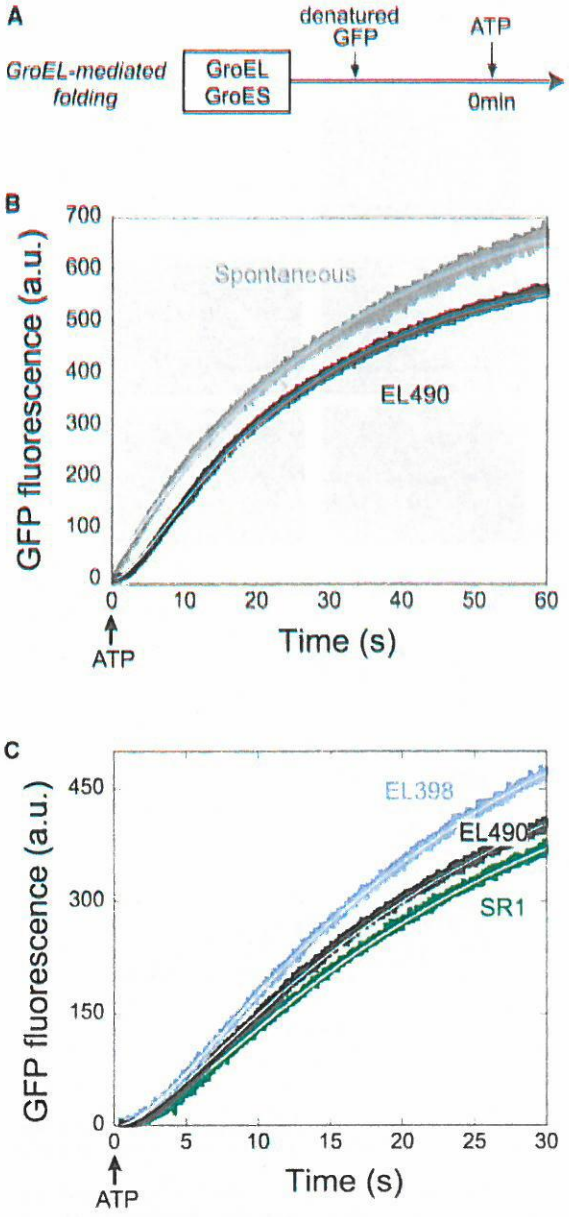

Figure 2. Bulk Phase Measurement of GFP Folding

(A) Diagram of experiments. GFP folding was initiated by adding ATP at 0 s to a buffer A containing GroES and the EL490-denatured GFP complex. Spontaneous folding of GFP was initiated by diluting acid-denatured GFP into buffer A.

(B) Spontaneous GFP folding and GFP folding in the presence of EL490. Spontaneous folding was fit by a single exponential. GFP folding in the presence of EL490 is fit to the data by the convolution of two exponentials.

(C) GFP folding in the presence of EL490, EL398, or SR1.

of GroEL (SR1) (Weissman et al., 1995). In the latter two cases, GFP was not released to the medium but remained in the *cis* cavity due to deficient ATPase (EL398) or lack of the signal from the *trans* ring (SR1). For every GroEL tested, folding of GFP started with an initial lag (Figures 2B and 2C). The time courses were well simulated by Equation 1, and rate constants of GFP folding mediated by EL490, EL398, and SR1 were obtained as k = 0.35, 0.35, and 0.30 s^{-1} and k' = 0.038, 0.040, and 0.037 s^{-1}, respectively. Simulated lines are shown by solid lines in Figure 2B. Thus, folding kinetics in the bulk phase experiments were very similar to those observed by single molecule imaging. A comment should be added that the results with SR1 appear to exclude the involvement of the *trans* ring in the initial kinetics of GFP folding.

Lags in GFP Folding and GroES Release Varied in the Same Way at Different Temperatures

We previously demonstrated single molecule imaging of binding-release dynamics of GroEL-GroES complex in the functional GroEL cycle (Taguchi et al., 2001). Analysis showed that, without added nonnative protein, release of GroES from GroEL occurred very slowly, but with added nonnative protein, GroES left GroEL in several seconds through two successive steps (Equation 2).

$$[\text{ES-EL}]^* \xrightarrow[k]{} [\text{ES-EL}] \xrightarrow[k']{} [\text{ES}] + [\text{EL}] \qquad (2)$$

Very similar rate constants were obtained for four kinds of nonnative substrate proteins. These were k = 0.26–0.34 s^{-1} and k' = 0.18–0.24 s^{-1}, that is, GroES remains bound to GroEL for ~3 s and then leaves GroEL in ~5 s, independent of species of nonnative protein. These values were not affected by GroES concentrations in the medium (Taguchi et al., 2001). Since the ~3 s lag coincided with that of GFP folding, we postulated that it probably reflected the same transition of the *cis* ternary complex.

To confirm this, we examined whether the lag in GroES release and GFP folding varied in the same way at different temperatures. Single molecule imaging of GroES binding and release was carried out as described (Taguchi et al., 2001) (Figure 3A). To supply nonnative protein during the observation period, pepsin, a permanently denatured protein at neutral pH (Aoki et al., 1997), was used as a substrate protein. Because GroES release kinetics are largely unaffected by the species of nonnative protein (Taguchi et al., 2001), we compared the kinetics of GroES release in the presence of pepsin to those of GFP folding. Binding and release of individual Cy3-ES molecules to IC5-EL490 were visualized by TIRFM at 18°C, 23°C, and 28°C. Histograms of the duration of bound state (on time) were simulated by Equation 2. The first rate constants (k) were 0.19, 0.33, and 0.44 s^{-1}, and the second rate constants (k') were 0.086, 0.14, and 0.21 s^{-1} at 18°C, 23°C, and 28°C, respectively (Figure 3B). The values increased in parallel with temperature. GFP folding was observed by single molecule imaging with ATPase-deficient EL398 and with EL490 under single turnover conditions by ATP quenching with apyrase. Bulk phase GFP folding also was measured. Plots of rate constants corresponding to the initial lags of GroES-release kinetics and those of GFP folding clearly showed that the values agreed fairly well at all three temperatures (Figure 3C). These results indicate that lag of GroES release and the lag of GFP folding reflects the same transition in the *cis* ternary complex.

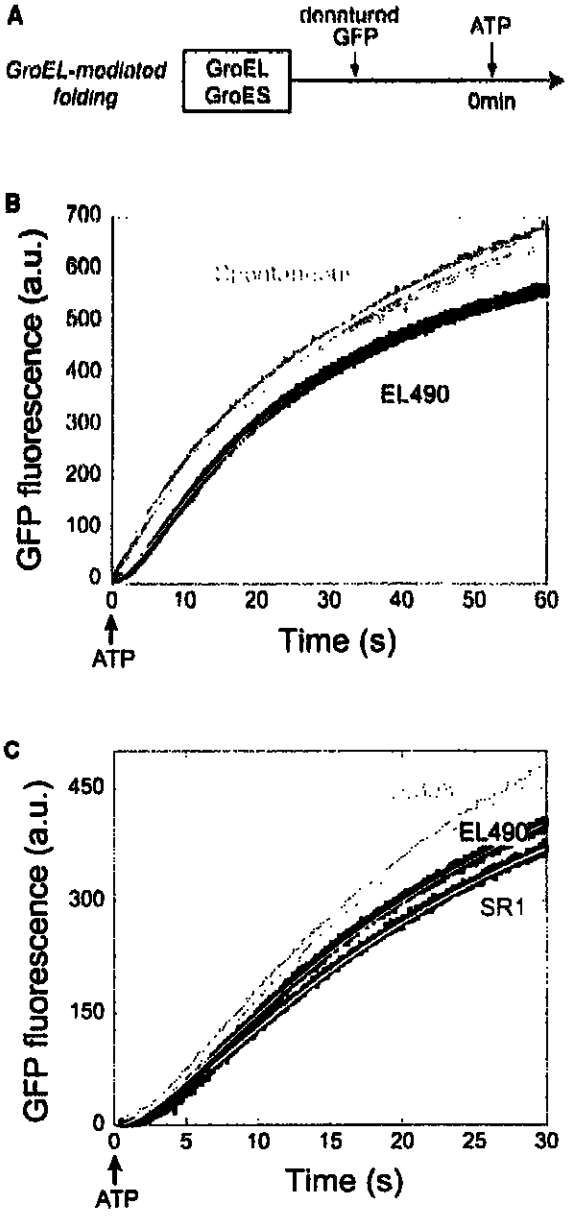

Figure 2. Bulk Phase Measurement of GFP Folding

(A) Diagram of experiments. GFP folding was initiated by adding ATP at 0 s to a buffer A containing GroES and the EL490-denatured GFP complex. Spontaneous folding of GFP was initiated by diluting acid-denatured GFP into buffer A.

(B) Spontaneous GFP folding and GFP folding in the presence of EL490. Spontaneous folding was fit by a single exponential. GFP folding in the presence of EL490 is fit to the data by the convolution of two exponentials.

(C) GFP folding in the presence of EL490, EL398, or SR1.

of GroEL (SR1) (Weissman et al., 1995). In the latter two cases, GFP was not released to the medium but remained in the *cis* cavity due to deficient ATPase (EL398) or lack of the signal from the *trans* ring (SR1). For every GroEL tested, folding of GFP started with an initial lag (Figures 2B and 2C). The time courses were well simulated by Equation 1, and rate constants of GFP folding mediated by EL490, EL398, and SR1 were obtained as k = 0.35, 0.35, and 0.30 s^{-1} and k' = 0.038, 0.040, and 0.037 s^{-1}, respectively. Simulated lines are shown by solid lines in Figure 2B. Thus, folding kinetics in the bulk phase experiments were very similar to those observed by single molecule imaging. A comment should be added that the results with SR1 appear to exclude the involvement of the *trans* ring in the initial kinetics of GFP folding.

Lags in GFP Folding and GroES Release Varied in the Same Way at Different Temperatures

We previously demonstrated single molecule imaging of binding-release dynamics of GroEL-GroES complex in the functional GroEL cycle (Taguchi et al., 2001). Analysis showed that, without added nonnative protein, release of GroES from GroEL occurred very slowly, but with added nonnative protein, GroES left GroEL in several seconds through two successive steps (Equation 2).

$$[ES\text{-}EL]^* \xrightarrow{k} [ES\text{-}EL] \xrightarrow{k'} [ES] + [EL] \qquad (2)$$

Very similar rate constants were obtained for four kinds of nonnative substrate proteins. These were k = 0.26–0.34 s^{-1} and k' = 0.18–0.24 s^{-1}, that is, GroES remains bound to GroEL for ~3 s and then leaves GroEL in ~5 s, independent of species of nonnative protein. These values were not affected by GroES concentrations in the medium (Taguchi et al., 2001). Since the ~3 s lag coincided with that of GFP folding, we postulated that it probably reflected the same transition of the *cis* ternary complex.

To confirm this, we examined whether the lag in GroES release and GFP folding varied in the same way at different temperatures. Single molecule imaging of GroES binding and release was carried out as described (Taguchi et al., 2001) (Figure 3A). To supply nonnative protein during the observation period, pepsin, a permanently denatured protein at neutral pH (Aoki et al., 1997), was used as a substrate protein. Because GroES release kinetics are largely unaffected by the species of nonnative protein (Taguchi et al., 2001), we compared the kinetics of GroES release in the presence of pepsin to those of GFP folding. Binding and release of individual Cy3-ES molecules to IC5-EL490 were visualized by TIRFM at 18°C, 23°C, and 28°C. Histograms of the duration of bound state (on time) were simulated by Equation 2. The first rate constants (k) were 0.19, 0.33, and 0.44 s^{-1}, and the second rate constants (k') were 0.086, 0.14, and 0.21 s^{-1} at 18°C, 23°C, and 28°C, respectively (Figure 3B). The values increased in parallel with temperature. GFP folding was observed by single molecule imaging with ATPase-deficient EL398 and with EL490 under single turnover conditions by ATP quenching with apyrase. Bulk phase GFP folding also was measured. Plots of rate constants corresponding to the initial lags of GroES-release kinetics and those of GFP folding clearly showed that the values agreed fairly well at all three temperatures (Figure 3C). These results indicate that lag of GroES release and the lag of GFP folding reflects the same transition in the *cis* ternary complex.

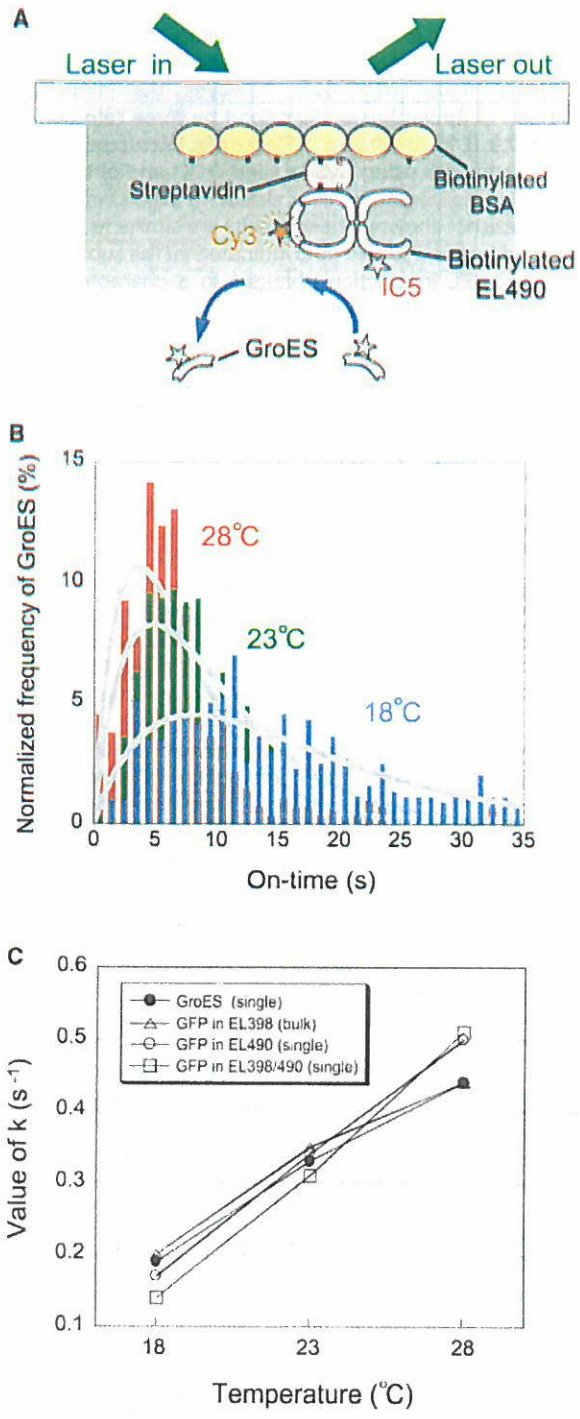

Figure 3. Temperature Dependency of the Lag Period of GFP Folding and that of GroES Release

(A) Schematic illustration of the single molecule imaging of the GroEL-GroES dynamics. Cy3-GroES was seen as a spot only when it bound to EL490 ("on time").

(B) Histograms of duration of GroES on time at different temperatures. The solid lines are the convolution of two exponentials fit to the data by least-squares fitting.

(C) The rate constants that determined the lag period in GroEL-GroES dynamics (*k* in Equation 2) and GFP folding (*k* in Equation 1) at three temperatures.

Bulk Phase Experiments Showed that FRET between Substrate Protein and GroEL Underwent Two Transitions after an Initial Rapid Change

As described above, GFP undergoes a ~3 s folding-arrested state in the initial *cis* ternary complex. To investigate whether this effect is specific for GFP or common to all substrate proteins, similar measurements for other substrate proteins should be performed. However, at present, rapid monitoring of the activity recovery of substrate protein in the *cis* ternary complex has been possible only for GFP, both for bulk phase experiment or single molecule imaging, due to technical difficulties. Instead of activity recovery, we performed ensemble measurement of the changes in fluorescence resonance energy transfer (FRET) between a substrate protein and the apical domain of GroEL (Figure 4A) as the transition of substrate protein from folding-arrested state to folding-competent state should accompany rearrangement of substrate protein in the *cis* ternary complex.

At first, the ensemble of FRET behavior of Cy3-labeled GFP was examined. The Cy3-GFP retained folding ability but recovered GFP fluorescence did not interfere with FRET measurement. A mutant GroEL, in which Glu315 at the apical domain was replaced with Cys (termed EL315) (Rye et al., 1999), was used for the specific labeling of an acceptor dye, IC5. EL315 and IC5-EL315 retained normal ATPase and chaperone activities of GroEL (data not shown). Cy3-GFP was denatured by 0.1 M HCl and diluted into a buffer containing IC5-EL315 to form a complex of Cy3-GFP and IC5-EL315. Then the fluorescence intensity of Cy3-GFP in the presence of EL315 with or without IC5 label was measured by a spectrometer to determine the efficiency of FRET. Upon formation of the complex Cy3-GFP and IC5-EL315, fluorescence intensity of the donor per acceptor decreased to 39% of that in the absence of acceptors, reflecting the close proximity of two dyes.

The GroEL cycle was initiated in the presence and absence of GroES by addition of ATP to the preformed Cy3-GFP-IC5-EL315 complex. In the absence of GroES, fluorescence intensity of the donor increased exponentially at a rate constant 0.13 s^{-1}, reflecting the simple release of Cy3-GFP from IC5-EL315. In the presence of GroES, by contrast, fluorescence intensity of the donor changed in three phases. An initial rapid increase transiently slowed, then increased again. The time course was simulated by assuming three rate constants, 2.1, 0.33, and 0.30 s^{-1} (Figure 4B). The first rate constant may represent a rapid transition that is included in the ~3 s lag. The second may represent the same transition that we observed as a lag in GFP folding. The third may correspond to the release of GFP into bulk solution.

Next, similar experiments were performed using MDH, a stringent substrate protein that folds efficiently only in the presence of GroEL, GroES, and ATP (Peralta et al., 1994; Chen et al., 2001). MDH was labeled with donor dye and Bodipy FL, and the labeled MDH (FL-MDH) retained the ability to fold within GroEL. FL-MDH was denatured in 6.4 M urea and diluted into the buffer containing IC5-EL315 to form a complex. Upon formation of the FL-MDH-IC5-EL315 complex, the fluorescence intensity of the donor per acceptor decreased to 51% of that in the absence of acceptors. The functional GroEL cycle was initiated by addition of ATP to the preformed

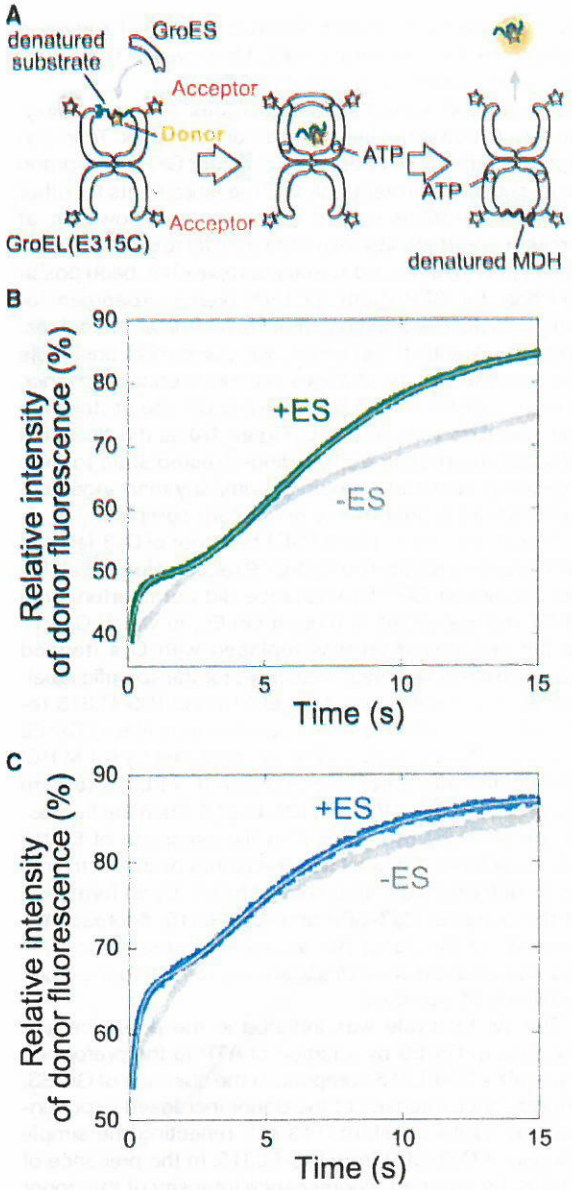

Figure 4. Bulk Phase Measurement of FRET between a Nonnative Protein and the Apical Domain of GroEL

(A) Schematic illustration of the FRET experiment. Denatured substrate protein with donor dye was trapped by EL315 with acceptor dyes. The functional GroEL cycle was initiated by addition of GroES, ATP, and excess nonlabeled denatured MDH to prevent rebinding of labeled denatured protein to EL315.

(B and C) Ensemble of the time course of the relative fluorescence intensity of (B) Cy3-GFP or (C) FL-MDH in the presence or absence of GroES. It was obtained from the ratio of the fluorescence of donor in the presence or absence of acceptor. The data were fit by assuming three-step reactions. Solid lines are the following functions. $D_4 + (D_1 - D_4)\exp(-k_1t) + (D_2 - D_4)k_1/(k_1 - k_2)[\exp(-k_2t) - \exp(-k_1t)] + (D_3 - D_4)k_1k_2/(k_1 - k_2)/(k_2 - k_3)/(k_1 - k_3)[(k_2 - k_3)\exp(-k_1t) - (k_1 - k_3)\exp(-k_2t) + (k_1 - k_2)\exp(-k_3t)]$. Parameters k_1, k_2, and k_3 are rate constants of a three-step reaction. D_1, D_2, D_3, and D_4 are percentages of donor fluorescence intensity.

FL-MDH-IC5-EL315 complex and GroES. The fluorescence intensity of the donor increased exponentially with a rate constant of 0.19 s^{-1} in the absence of GroES. In the presence of GroES, however, the intensity changed in three phases described by three rate constants, 2.9, 0.46, and 0.31 s^{-1} (Figure 4B). We also carried out experiments using Cy3-labeled MDH and obtained the three rate constants very similar to those with FL-MDH (data not shown). These results are similar to those obtained for the Cy3-GFP and indicate that the substrate protein-GroEL interaction changes in a characteristic manner, including a step that would be corresponding to the ~3 s lag observed in GFP folding kinetics.

Bulk Phase Experiments Showed that ATP Hydrolysis and Pi Release Are Described by the First Rate Constant and ADP Release by the Second Rate Constant

The results shown so far argue that the functional GroEL cycle proceeds with two major rate constants under optimum conditions. Since the whole cycle is driven by ATP hydrolysis, these two rate constants should correlate with the steps in ATPase cycle of GroEL. Although a number of studies on ATPase kinetics of GroEL and GroEL-GroES have been reported, all of these focused on ATPase activity in the absence of nonnative substrate protein (e.g., Todd et al., 1994; Cliff et al., 1999). Consequently, we performed ensemble measurements of the initial pre-steady-state time course of the ATPase cycle of GroEL in the presence of GroES and nonnative proteins. We employed three different assays (Figure 5A) to investigate each stage of the ATPase cycle. Hydrolytic cleavage of a β-γ bond of ATP was measured by total Pi generation with the malachite green method after the reaction was quenched by acid (Geladopoulos et al., 1991). This actually represents the progress of hydrolysis of GroEL-bound ATP. The release of Pi from GroEL was monitored by the Pi binding protein that captured free Pi in the medium and emitted enhanced fluorescence (Brune et al., 1994). Finally, release of ADP from GroEL was monitored by the appearance of free ADP in the medium by the oxidation of NADH with ATP regenerating auxiliary enzymes, pyruvate kinase, and lactate dehydrogenase (Pullman et al., 1960).

The results of total Pi generation are shown in Figure 5B. In the absence of GroES, Pi generation proceeded linearly with a single rate constant of 0.18 s^{-1} (gray line), but, in the presence of GroES, Pi generation started with an initial burst and reached a steady-state turnover (0.12 s^{-1}). The time course is consistent with Equation 3.

$$\begin{matrix}[\text{ES-EL-ATP}] & \xrightarrow{k} & [\text{ES-EL-ADP-Pi}] & \xrightarrow{k'} \\ [\text{ES}] + [\text{EL}] + [\text{ADP}] + [\text{Pi}] & & & \end{matrix} \quad (3)$$

The ATPase cycle has two steps with characteristic rate constants. ATP hydrolysis accompanies the first step. The solid line in Figure 5B is a simulated time course of the two rate constants, $k = 0.31\ s^{-1}$ and $k' = 0.16\ s^{-1}$.

Similar to total Pi generation, Pi release from GroEL showed an initial burst in the presence of GroES and denatured MDH (Figure 5C). The time course of Pi release was simulated by Equation 4.

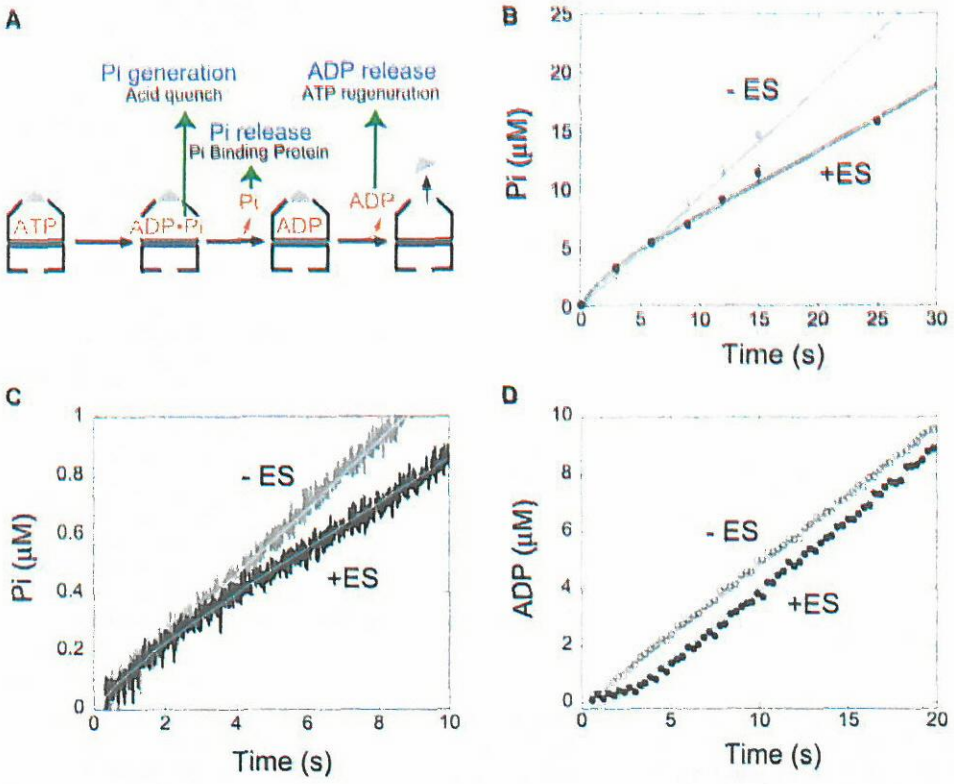

Figure 5. Bulk Phase Measurement of Initial ATPase Kinetics by GroEL in the Presence of Substrate Protein

(A) Schematic illustration of the three assays for ATP hydrolysis by GroEL: Pi generation, Pi release, and ADP release.

(B) Ensemble of the time course of ATP hydrolysis by GroEL in the presence (closed circles) or absence (open circles) of GroES.

(C) Ensemble of the time course of Pi release from GroEL in the presence (black line) or absence (gray line) of GroES.

(D) Ensemble of the time course of ADP release in the presence (black line) or absence (gray line) of GroES. The solid lines fit to the data obtained in the presence of GroES are functions $C_1k\,(k't - k/(k + k')\,\{\exp[-(k + k')t] - 1\})/(k + k')$ in (B) and (C), and $C_2 + k\,k'/(k + k')\,(t + \exp[-(k + k')t]/(k + k')$ in (D). These formulas are derived from the two-step reaction of Equations 3 and 4. The solid lines fit to the data obtained in the absence of GroES are linear functions of $C_3k\,t$.

$$[\text{ES-EL-ATP}] \xrightarrow[k]{} [\text{ES-EL-ADP}] + [\text{Pi}] \xrightarrow[k']{} [\text{ES}] + [\text{EL}] + [\text{ADP}] + [\text{Pi}] \quad (4)$$

There are two rate constants, $k = 0.33\ s^{-1}$ and $k' = 0.37\ s^{-1}$, and Pi release takes place during the first step defined by k. Using pepsin and reduced α lactalbumin as substrate proteins, we carried out similar experiments and obtained the values $k = 0.36, 0.26\ s^{-1}$ and $k' = 0.46, 0.20\ s^{-1}$, respectively. In the absence of GroES, on the other hand, no burst was observed and the ATPase cycle was defined by a single rate constant of $0.18\ s^{-1}$. The similarity of the k value for total Pi generation and that for Pi release suggests that Pi leaves GroEL immediately after Pi is generated by ATP hydrolysis on GroEL.

The time course of ADP release from GroEL in the presence of GroES and denatured MDH showed the initial lag and then reached the steady-state rate ($0.12\ s^{-1}$) (Figure 5D). The time course was consistent with Equation 4. Two rate constants were calculated as $k = 0.39\ s^{-1}$ and $k' = 0.23\ s^{-1}$, and ADP release occurred at the second transition defined by k'. Without GroES, ADP release proceeded linearly with time. Therefore, one product of ATP hydrolysis, ADP, stays bound for ~4 s after ATP hydrolysis until the next transition in the cycle completes while the other, Pi, leaves GroEL immediately after ATP hydrolysis.

Collectively, the data show that the ATPase cycle of GroEL proceeds with two major rate constants. The first ranges from 0.31 to $0.39\ s^{-1}$ and defines both ATP hydrolysis on GroEL and Pi release from GroEL. The second ranges from 0.16 to $0.37\ s^{-1}$ and governs the ADP release from GroEL. The values of the first rate constant are in close agreement with k values obtained from GFP folding and GroES release. This suggests that the same transition with this rate constant is responsible for the lags of GFP folding, GroES release, and ADP release and for the initial burst of ATP hydrolysis and Pi release. The second rate constants obtained from the ATPase cycle vary but are still in an acceptable range to suggest that they correspond to the rate constants k' obtained from other measurements.

Discussion

Two Timer Mechanism of the Functional GroEL Cycle

The single timer model of the functional GroEL cycle predicts that any events in the cycle after the *cis*-ATP

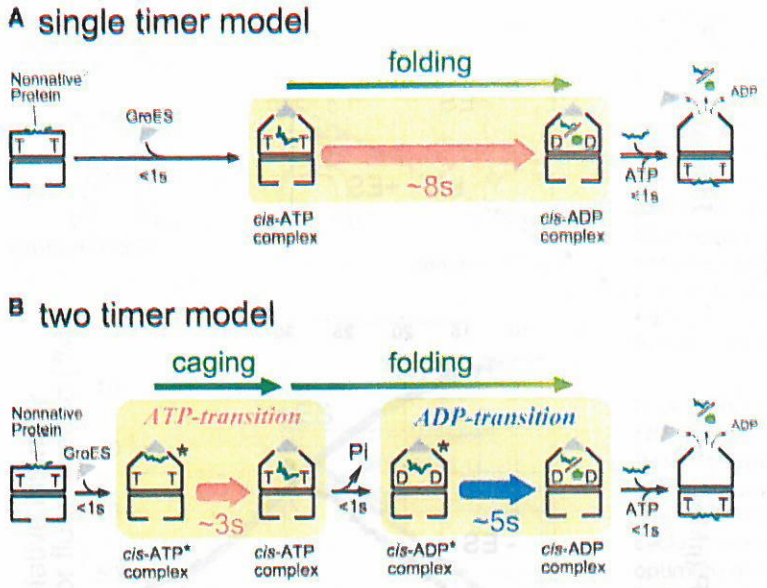

Figure 6. Single Timer Model and Two Timer Model of the Functional GroEL Cycle

(A) Single timer model of GroEL-GroES (Rye et al., 1999). In the presence of saturating amounts of ATP, GroES, and substrate proteins, only a single rate constant governs all events of the functional GroEL cycle, including ATP hydrolysis, release of Pi, ADP, GroES, and substrate protein from GroEL.

(B) Two timer model (this paper). In the presence of saturating amount of ATP, GroES, and substrate proteins, the functional GroEL cycle has two rate-limiting steps, which are represented by arrows colored red and blue. Binding of GroES (gray triangle) to the complex of GroEL-ATP-substrate protein produces the *cis*-ATP* complex in which substrate protein (green) is not fully released into the cavity. The first timer (lifetime, 3 s) is the "ATP transition" from the *cis*-ATP* complex to the *cis*-ATP complex, which results in full release of nonnative protein into the cavity where folding starts. ATP hydrolysis and Pi release of the *cis*-ATP complex occur rapidly to produce the *cis*-ADP* complex. The second timer (lifetime, 5 s) is the ADP transition from the *cis*-ADP* complex to the *cis*-ADP complex. The *cis*-ADP complex can accept ATP to the *trans* GroEL ring that induces rapid decay of the *cis* ternary complex (Rye et al., 1999). Encapsulation (caging) of the substrate protein occurs during ATP transition. Folding occurs in the *cis*-ATP complex and *cis*-ADP* complex.

complex should occur apparently with a single rate constant ~0.12 s^{-1} (lifetime, 8 s) (Figure 6A). This rate constant would correspond to the rate of ATP hydrolysis in the *cis* ring to produce the *cis*-ADP complex, the only rate-limiting step of the whole cycle (Weissman et al., 1996; Rye et al., 1997, 1999). However, all of the results in this report suggest that at least two rate-limiting steps exist in the cycle, and we propose here a model for the functional GroEL cycle, a successive two timer mechanism (Figure 6B). In this model, the GroEL-substrate protein complex binds ATP and GroES to generate the *cis*-ATP* complex in which, different from the *cis*-ATP complex in the single timer model, folding of substrate protein is arrested. The *cis*-ATP* complex is transformed to the *cis*-ATP complex with a rate constant ~0.3 s^{-1} (lifetime, 3 s). As soon as this transition takes place, three events immediately follow: the substrate protein becomes folding competent in the *cis* cavity, ATP is hydrolyzed, and Pi is released. The lifetime of the *cis*-ATP complex is very short, but folding continues in the next *cis*-ADP* complex. The *cis*-ADP* complex is further transformed to the *cis*-ADP complex with a rate constant ~0.2 s^{-1} (lifetime, 5 s). Similar to the *cis*-ADP complex in the single timer model, the *cis*-ADP complex in the two timer model can accept ATP and substrate protein to its *trans* ring, which immediately induces the decay of the *cis* ternary complex, that is, release of GroES, substrate protein, and ADP from the *cis* ring.

The ATP Transition Occurs without ATP Hydrolysis

The two timer mechanism assumes two critical transitions, from the *cis*-ATP* complex to the *cis*-ATP complex (ATP transition) and from the *cis*-ADP* complex to the *cis*-ADP complex (ADP transition) (Figure 6B). To define the ATP transition, it is important to note that an ATPase-deficient mutant EL398 (Figure 2C) or EL398/490 (Figure 1C) can mediate a single round *cis* folding of GFP with the same kinetics, ~3 s lag, as the EL490. This implies that nonnative GFP in the *cis*-ATP* complex reaches a folding-competent state prior to ATP hydrolysis. Therefore, the first rate-limiting step is not ATP hydrolysis. Rather, it is the conformational transition of the *cis*-ATP* complex that accompanies rearrangement of substrate protein from the folding-arrested state to the folding-competent state.

Rearrangement of Substrate Protein during the ATP Transition

The rearrangement of substrate protein in the complex during this transition was detected by FRET between substrate protein and GroEL (Figure 4). After a rapid increase that was not detected by other methods, the donor fluorescence increased with two transitions. The first likely reflects rearrangement of the substrate protein in the ATP transition and the second the decay of the *cis* ternary complex. The FRET time course of GFP and that of MDH are very similar. Likewise, the release kinetics of GroES in the functional GroEL cycle are not affected significantly by the species of substrate protein used: reduced α lactalbumin, an artificial nonstructured protein RP3-42, denatured pepsin, and denatured MDH (Taguchi et al., 2001). It appears that the timer is set only in the presence of substrate protein but ticks independent of the species of the bound substrate proteins. This was assumed in the single timer model, and it is also valid in the two timer model.

Horwich and his colleagues utilized fluorescence anisotropy of pyrene-labeled rhodanese and of intrinsic Trp of Rubisco to probe the rearrangement of substrate protein in the functional GroEL cycle initiated by addition of ATP and GroES to the GroEL-substrate protein complex (Weissman et al., 1996; Rye et al., 1997). For both substrates, two-phase transitions were observed, the first being a sharp drop in anisotropy (half time 1 s =

lifetime 1.4 s) reflecting the change of substrate protein from the restricted state to the flexible state (Weissman et al., 1996; Rye et al., 1997). The researchers assigned the flexible state to the folding-competent state in the *cis*-ATP complex but did not integrate the restricted state in their single timer model. However, we think that the most reasonable candidate for the restricted state might be the folding-arrested state in the *cis*-ATP* complex. The difference of lifetimes, ~1.5 s in their experiment and ~3 s in our model, is significant but acceptable when taking into account differing experimental conditions. Hydrogen exchange of substrate protein during functional GroEL cycle suggested a possible mechanical unfolding step before complete release of substrate protein into the *cis* cavity (Shtilerman et al., 1999). There is a possibility that this step might correspond to the *cis*-ATP* complex, but the short lifetime of this step (<1 s) makes this possibility rather unlikely. In addition, since another report using the same technique did not detect such an unfolding step (Chen et al., 2001), it is not clear that mechanical unfolding is a general step for various substrate proteins.

The Two Timer Mechanism Explains the Burst and Lag in the Initial Kinetics

Initial kinetics of ATP hydrolysis, GFP folding, and release kinetics of GroES in the cycle showed either lag or burst. We showed that upon initiation of the functional GroEL cycle by ATP addition, ATP hydrolysis in the *cis* ring, and release of Pi occurred as an initial burst with rate constant ~0.3 s^{-1} (Figures 5B and 5C). One might think from Figure 6B that there should be a lag rather than a burst for these events, because they occur after an event that has a lifetime of ~3 s. However, in general, if a rapid event follows a first slow event, these two events should be observed as if they occur simultaneously with the same rate constant, and a lag should not be observed in the rapid event. That happened in the case of ATP hydrolysis and Pi release, which occurred apparently at the same rate as that for ATP transition. Because the steady-state rate of ATP hydrolysis and Pi release (0.12 s^{-1}) is much slower than the initial rate (0.3 s^{-1}) due to the presence of the second rate-limiting step (0.2 s^{-1}), an initial burst should appear in the pre-steady-state kinetics. On the other hand, if a second slow event follows the first slow event, the second appears to occur after the lag period that corresponds to the time needed for the completion of the first slow event. This was the case for GFP folding, which showed a ~3 s lag. Following similar reasoning, decay of the *cis*-ADP complex (release of ADP, GroES, and substrate protein from GroEL) should be observed as if it occurs simultaneously with the ADP transition. Therefore, initial time courses of ADP release from GroEL showed a ~3 s lag when the cycle was initiated by addition of ATP.

The *cis*-ATP* Complex Ensures Efficient Caging of Substrate Protein

The essence of chaperonin function is encapsulation of nonnative protein into a narrow cage to facilitate folding in a protected environment (Weissman et al., 1995; Mayhew et al., 1996; Xu et al., 1997; Sakikawa et al., 1999). However, the mechanism of this efficient caging is only poorly understood. According to the single timer model, upon formation of the *cis*-ATP complex, GroES deprives the previously bound substrate protein of common binding sites on GroEL, and the substrate protein is released into the *cis* cavity. In a microscopic view, GroES can bind to GroEL only when nonnative substrate protein is released from GroEL to make the common binding sites available. It is unclear, however, how the release of substrate protein always results in encapsulation into the *cis* cavity rather than diffusing away to the bulk solution. The two timer model can offer rational explanation for the caging of the substrate protein. In the *cis*-ATP* complex, GroES is already bound but nonnative substrate protein remains in the folding-arrested state. This means that the polypeptide chain of the substrate protein should be interacting with the wall of the *cis* cavity. The ATP transition brings about a conformational change and the next intermediate, the *cis*-ATP complex, disfavors the interaction with substrate protein (Chaudhry et al., 2003). The substrate protein is thus set free to the *cis* cavity to start folding. Therefore the *cis*-ATP* complex plays a critical role in caging the substrate protein into the *cis* cavity.

The structural features of the *cis*-ATP* complex are as yet unknown. Intriguingly, the GroEL mutant C138W forms a folding-arrested *cis* ternary complex at 25°C, which can resume the cycle at 37°C (Kawata et al., 1999; Miyazaki et al., 2002). The arrested *cis* ternary complex of this mutant displays features of the *cis*-ATP* complex. It is noteworthy that substrate protein is located in a protease-inaccessible area in this complex. Amino acid residue C138 resides in the intermediate domain of GroEL and introduction of a bulky tryptophan at this position may restrict the hinge motion. One of candidates for the *cis*-ATP* complex could be such a complex in which a hinge of each GroEL subunit is partially "open."

Substrate Protein Is Free to Fold in the *cis*-ADP* Complex

It is well established that the substrate protein in the *cis*-ADP complex is released to the medium rapidly when ATP and nonnative substrate protein are present in the medium (Rye et al., 1999; Taguchi et al., 2001). Therefore, if the next intermediate after the *cis*-ATP complex is the *cis*-ADP complex, nonnative protein has little time to fold in the *cis* cavity. For this reason, a *cis*-ADP* complex, in which nonnative protein can fold, should be present before the *cis*-ADP complex. Our results show that the lifetime of the *cis*-ADP* complex, that is, the mean time given to nonnative protein to fold, is ~5 s. Because these two ADP complexes differ as to whether the *trans* ring can accept ATP or not, the ADP transition may bring about the conformational change mainly in the *trans* ring region. Cryo-electron micrography shows that the largest structural difference between the ATP-containing and ADP-containing GroEL-GroES complex is in the *trans* ring (Rye et al., 1999). This is reminiscent of the difference between *cis*-ADP* and *cis*-ADP complexes.

Both the ATP transition and the ADP transition do not accompany the change of chemical components of the complex. It seems that they are purely conformational

relaxation and that GroEL is at first raised to the "activated state" when it forms the *cis*-ATP* complex, and subsequent relaxation processes are coupled to exertion of the work. If this really is the case, the timers of GroEL are intrinsic ones built within the conformational dynamics.

Experimental Procedures

Proteins and Reagents

Bovine serum albumin, pepsin, glucose oxidase and catalase, "bacterial" purine nucleoside phosphorylase, phosphoenolpyruvate, and 7-methylguanosine were obtained from Sigma. Streptavidin and [2-(1-maleimidyl)ethyl]-7-(diethylamino)-coumarin-3-carboxamide (MDCC) were from Molecular Probes. Porcine heart malate dehydrogenase, rabbit muscle pyruvate kinase, and hog muscle lactate dehydrogenase were from Roche. The GroEL mutants (EL490, EL398, EL398/490, EL315) were produced by site-directed mutagenesis using the Kunkel method. GroEL mutants, GroES and GFP (S65T), were expressed in *Escherichia coli* and purified as described (Makino et al., 1997; Sakikawa et al., 1999; Motojima et al., 2000). GFP (S65T) was used throughout this work. Protein concentrations were determined by absorption spectroscopy using the following extinction coefficients at 280 nm: GroEL mutants 14-mer, 130480 $M^{-1}cm^{-1}$; GroES 7-mer, 8960 $M^{-1}cm^{-1}$; GFP (S65T) monomer, 18850 $M^{-1}cm^{-1}$. Protein concentration was expressed as oligomer (GroEL, 14-mer; SR1, 7-mer; GroES, 7-mer) throughout the study.

Microscopy

Total internal reflection fluorescence microscopy (TIRFM) was used for visualizing individual fluorescent molecules immobilized on the surface of a quartz slide. Single protein molecules labeled with Cy3 or IC5 were illuminated with a green solid-state laser (2.8 mW, 532 nm, μ-green model 4601, Uniphase, USA) or a He-Ne laser (1.0 mW, 632.8 nm, NEC, Japan), respectively. GFP molecules were illuminated with a blue solid-state laser (1.8 mW, 473 nm, HK-5511, Shimadzu Corporation, Japan) to visualize individual molecules. Images were taken by a SIT camera (C2400-08, Hamamatsu Photonics, Japan) coupled to an image intensifier (VS4-1845, Video Scope International, USA) and recorded on videotapes for subsequent analysis.

Imaging of GFP Folding

Folding of individual GFP molecules in GroEL was visualized by TIRFM. Both EL490 and EL398/490 were labeled with IC5-maleimide and biotin-$PEAC_5$-maleimide (Dojindo Laboratories, Japan) in buffer A (25 mM HEPES-KOH [pH 7.4], 100 mM KCl, 5 mM $MgCl_2$) as described previously (Taguchi et al., 2001). GFP (54 μM) was denatured for 2 min at 23°C in 0.1 M HCl and diluted to 2 μM with buffer A containing 400 nM EL490. After 5 min, EL490-denatured GFP complexes were infused into a flow cell and attached to the glass surface via streptavidin as described (Taguchi et al., 2001). Then the cell was filled with buffer A containing 1 μM GroES, 1 mM caged ATP, 25 units/ml apyrase, and an oxygen scavenger system (25 mM glucose, 2.5 μM glucose oxidase, 10 nM catalase, 10 mM dithiothreitol). The specimen was illuminated with a He-Ne laser to mark the position of EL490 and illuminated with a blue solid-state laser to visualize fluorescence of GFP. ATP was released by epifluorescence illumination of UV light for 250 ms with a 100 W mercury light source (U-MWU & IX-FLA, Olympus). Approximately 40% of caged ATP was split under the experimental condition, and ATP was hydrolyzed by apyrase in ~1 s. Appearance of the fluorescence of GFP at the position of EL490 after the photolysis of caged ATP was visualized by TIRFM. About 30% of the EL490 particles thus immobilized were active in folding of GFP.

Bulk Phase GFP Folding

In 1.2 ml of buffer A containing 5 mM dithiothreitol, 150 nM GroEL (EL490, EL398, or SR1), and 1.5 μM GroES at 23°C, 3 μl of acid-denatured GFP was diluted to a final concentration of 100 nM. After 15 min, 3 μl of ATP solution was added to a final concentration of 0.45 mM to start GroEL-GroES-assisted GFP folding. Fluorescence intensity of GFP was monitored continuously with a fluorometer (Ex 485 nm/Em 512 nm, F-4500, HITACHI). Dead time for the measurement was about 0.4 s.

Single Molecule Imaging of GroES-GroEL Dynamics

Single molecule imaging of GroEL-GroES dynamics was carried out using TIRFM as described (Taguchi et al., 2001). Experiments were performed at 18°C, 23°C, and 28°C.

Bulk Phase Measurements of FRET between GroEL and Substrate Protein

EL315 was labeled with IC5-maleimide. The molar ratio of IC5-label to the single ring of GroEL was 1.4. GFP was labeled with Cy3-NHS (Amersham-Pharmacia) at a molar ratio of 0.36. MDH was labeled with BodipyFL-SE (Molecular Probes) at a molar ratio of 0.25 per monomer. Cy3-GFP (8.3 μM) was denatured in 0.1 M HCl for 3 min and diluted to a final concentration of 50 nM with buffer A containing 100 nM IC5-EL315 and 5 mM DTT to make the complex of Cy3-GFP and IC5-EL315. After 5 min at 23°C, 3 μM GroES was added. The solution was loaded into a stopped-flow syringe, and buffer A containing 2 mM ATP, 5 mM DTT, and 1 μM denatured MDH was loaded into another syringe. Equal amounts of these solutions were mixed rapidly in a stopped-flow apparatus (RX 2000, Applied Photo Physics, UK) installed in a fluorometer (FP-6500, JASCO, Japan). The dead time for the measurement was about 0.07 s. To detect the fluorescence of Cy3 as a donor, the solution was excited at wavelength of 540 nm and the fluorescence from 565 to 575 nm was collected. A similar experiment was performed using EL315 without IC5 labeling. A time course of the relative intensity of Cy3 fluorescence was obtained from the ratio of Cy3-GFP fluorescence in the presence or absence of IC5-EL315 divided by the labeling ratio of IC5 per single ring of EL315. Förster distances between a Cy3-IC5 pair were expected to be ~4.9 nm (Wu and Brand, 1994). FRET between FL-MDH and IC-EL315 was measured as follows. FL-MDH (2 μM) was denatured in 6.4 M urea for more than 30 min at 23°C. Then it was diluted to the final concentration of 50 nM with buffer A containing 100 nM EL315, 5 mM DTT, and 3 μM GroES. Rapid mixing was performed as described for Cy3-GFP. The sample was excited at wavelength of 475 nm, and fluorescence from 507.5 to 512.5 nm was collected. Förster distances between a Bodipy FL-IC5 pair were expected to be ~4.7 nm.

Bulk Phase Measurements of Pre-Steady-State Kinetics of ATP Hydrolysis

The ATP hydrolysis reaction in the functional GroEL cycle was measured by three different assays at 23°C. Concentrations of the reaction components were varied to adjust the level suitable for each assay method.

Pi Generation

Generation of Pi from GroEL was measured using the malachite green assay (Geladopoulos et al., 1991). MDH (86 μM) denatured in 6 M urea was diluted to 3 μM into buffer A containing 1.5 μM GroEL and 5 mM DTT in the presence or absence of 4.5 μM GroES. After 5 min, 35 μl of the solution was injected into the same volume of buffer A containing 0.4 mM ATP that was vigorously stirred. The reactions were terminated by the addition of perchloric acid at the indicated times. The solution was centrifuged to remove protein precipitates. The supernatant was treated with a malachite green reagent, and the absorbance at 630 nm was measured.

Pi Release

Release of Pi from GroEL was measured using Pi binding protein (PBP) (Brune et al., 1994, 1998; Cliff et al., 1999). PBP labeled with MDCC, a coumarin derivative, was prepared as previously described (Brune et al., 1994, 1998). Binding of Pi to MDCC-labeled PBP (MDCC-PBP) increased the fluorescence emission at 466 nm when the complex was excited at 430 nm. By virtue of rapid binding of Pi to MDCC-PBP ($k_{on} = 1.36 \times 10^8\ M^{-1}\ s^{-1}$) and high affinity of PBP for Pi ($K_d = 0.1$ μM) (Brune et al., 1994, 1998), the increase in the Pi concentration in the solutions could be monitored as the increase of fluorescence emission in real time. To 1.2 ml of buffer A containing 0.07 μM GroEL, 10 μM MDCC-PBP in the presence or absence of 0.57 μM GroES, 12 μl of 60 μM MDH denatured in 6 M urea were added. After a 5 min incubation at 23°C, the solution was vigorously stirred and the reaction was initiated by injection of 1.5 μl ATP

solution, which contained 80 mM ATP, 800 μM 7-methylguanosine, and 0.1 unit/ml purine nucleoside phosphorylase. The latter two components were used to eliminate contaminating Pi. Changes in the fluorescence at 466 nm were monitored continuously with a fluorometer (F-4500, Hitachi).

ADP Release

Release of ADP from GroEL was measured spectrophotometrically with an ATP-regenerating system (Pullman et al., 1960; Kato et al., 1995). The assay mixture consisted of buffer A containing 0.2 mM NADH, 5 mM phosphoenolpyruvate, 100 μg/ml pyruvate kinase, 100 μg/ml lactate dehydrogenase, 2.5 mM DTT, and 1 mM ATP in the presence or absence of 1.4 μM GroES. MDH (47 μM) denatured in 6 M urea was diluted into the assay mixture to a final concentration of 1.0 μM. After 1 min, the reaction was initiated by injection of GroEL into the vigorously stirred solution. The decreases in the absorbance at 340 nm, due to oxidation of NADH, were monitored continuously with a spectrophotometer (V-550, Jasco, Japan).

Acknowledgments

We thank A. Horwich for critical discussion; M. Webb and T. Masaike for the use of the Pi binding protein assay; J. Suzuki and A. Koike for technical assistance; and R. Shiurba for comments on the manuscripts. This work was supported in part by Grants-in-Aid for Scientific Research on Priority Areas (to H.T. and M.Y.), Specially Promoted Research, COE research, the 21th Century COE program (to T.F.), and Scientific Research B (to H.T. and T.F.), from the Ministry of Education, Culture, Sports, Science, and Technology of Japan.

Received: October 2, 2003
Revised: March 29, 2004
Accepted: March 30, 2004
Published: May 20, 2004

References

Aoki, K., Taguchi, H., Shindo, Y., Yoshida, M., Ogasahara, K., Yutani, K., and Tanaka, N. (1997). Calorimetric observation of a GroEL-protein binding reaction with little contribution of hydrophobic interaction. J. Biol. Chem. *272*, 32158–32162.

Boisvert, D.C., Wang, J., Otwinowski, Z., Horwich, A.L., and Sigler, P.B. (1996). The 2.4 Å crystal structure of the bacterial chaperonin GroEL complexed with ATPgS. Nat. Struct. Biol. *3*, 170–177.

Braig, K., Otwinowski, Z., Hegde, R., Boisvert, D.C., Joachimiak, A., Horwich, A.L., and Sigler, P.B. (1994). The crystal structure of the bacterial chaperonin GroEL at 2.8 Å. Nature *371*, 578–586.

Brune, M., Hunter, J.L., Corrie, J.E., and Webb, M.R. (1994). Direct, real-time measurement of rapid inorganic phosphate release using a novel fluorescent probe and its application to actomyosin subfragment 1 ATPase. Biochemistry *33*, 8262–8271.

Brune, M., Hunter, J.L., Howell, S.A., Martin, S.R., Hazlett, T.L., Corrie, J.E., and Webb, M.R. (1998). Mechanism of inorganic phosphate interaction with phosphate binding protein from Escherichia coli. Biochemistry *37*, 10370–10380.

Bukau, B., and Horwich, A.L. (1998). The Hsp70 and Hsp60 chaperone machines. Cell *92*, 351–366.

Burston, S.G., Ranson, N.A., and Clarke, A.R. (1995). The origins and consequences of asymmetry in the chaperonin reaction cycle. J. Mol. Biol. *249*, 138–152.

Chaudhry, C., Farr, G.W., Todd, M.J., Rye, H.S., Brunger, A.T., Adams, P.D., Horwich, A.L., and Sigler, P.B. (2003). Role of the gamma-phosphate of ATP in triggering protein folding by GroEL-GroES: function, structure and energetics. EMBO J. *22*, 4877–4887.

Chen, L., and Sigler, P.B. (1999). The crystal structure of a GroEL/peptide complex: plasticity as a basis for substrate diversity. Cell *99*, 757–768.

Chen, J., Walter, S., Horwich, A.L., and Smith, D.L. (2001). Folding of malate dehydrogenase inside the GroEL-GroES cavity. Nat. Struct. Biol. *8*, 721–728.

Cliff, M.J., Kad, N.M., Hay, N., Lund, P.A., Webb, M.R., Burston, S.G., and Clarke, A.R. (1999). A kinetic analysis of the nucleotide-induced allosteric transitions of GroEL. J. Mol. Biol. *293*, 667–684.

Ewalt, K.L., Hendrick, J.P., Houry, W.A., and Hartl, F.U. (1997). In vivo observation of polypeptide flux through the bacterial chaperonin system. Cell *90*, 491–500.

Fenton, W.A., Kashi, Y., Furtak, K., and Horwich, A.L. (1994). Residues in chaperonin GroEL required for polypeptide binding and release. Nature *371*, 614–619.

Geladopoulos, T.P., Sotiroudis, T.G., and Evangelopoulos, A.E. (1991). A malachite green colorimetric assay for protein phosphatase activity. Anal. Biochem. *192*, 112–116.

Hartl, F.U., and Hayer-Hartl, M. (2002). Molecular chaperones in the cytosol: from nascent chain to folded protein. Science *295*, 1852–1858.

Horwich, A.L., Low, K.B., Fenton, W.A., Hirshfield, I.N., and Furtak, K. (1993). Folding in vivo of bacterial cytoplasmic proteins: role of GroEL. Cell *74*, 909–917.

Houry, W.A., Frishman, D., Eckerskorn, C., Lottspeich, F., and Hartl, F.U. (1999). Identification of in vivo substrates of the chaperonin GroEL. Nature *402*, 147–154.

Hunt, J.F., Weaver, A.J., Landry, S.J., Gierasch, L., and Deisenhofer, J. (1996). The crystal structure of the GroES co-chaperonin at 2.8 Å resolution. Nature *379*, 37–45.

Kato, Y., Sasayama, T., Muneyuki, E., and Yoshida, M. (1995). Analysis of time-dependent change of Escherichia coli F1-ATPase activity and its relationship with apparent negative cooperativity. Biochim. Biophys. Acta *1231*, 275–281.

Kawata, Y., Kawagoe, M., Hongo, K., Miyazaki, T., Higurashi, T., Mizobata, T., and Nagai, J. (1999). Functional communications between the apical and equatorial domains of GroEL through the intermediate domain. Biochemistry *38*, 15731–15740.

Makino, Y., Amada, K., Taguchi, H., and Yoshida, M. (1997). Chaperonin-mediated folding of green fluorescent protein. J. Biol. Chem. *272*, 12468–12474.

Mayhew, M., da Silva, A.C.R., Martin, J., Erdjument-Bromage, H., Tempst, P., and Hartl, F.U. (1996). Protein folding in the central cavity of the GroEL-GroES chaperonin complex. Nature *379*, 420–426.

Miyazaki, T., Yoshimi, T., Furutsu, Y., Hongo, K., Mizobata, T., Kanemori, M., and Kawata, Y. (2002). GroEL-substrate-GroES ternary complexes are an important transient intermediate of the chaperonin cycle. J. Biol. Chem. *277*, 50621–50628.

Motojima, F., Makio, T., Aoki, K., Makino, Y., Kuwajima, K., and Yoshida, M. (2000). Hydrophilic residues at the apical domain of GroEL contribute to GroES binding but attenuate polypeptide binding. Biochem. Biophys. Res. Commun. *267*, 842–849.

Peralta, D., Hartman, D.J., Hoogenraad, N.J., and Hoj, P.B. (1994). Generation of a stable folding intermediate which can be rescued by the chaperonins GroEL and GroES. FEBS Lett. *339*, 45–49.

Pullman, M.E., Penefsky, H.S., Datta, A., and Racker, E. (1960). Partial resolution of the enzymes catalyzing oxidative phosphorylation. J. Biol. Chem. *235*, 3322–3329.

Rye, H.S., Burston, S.G., Fenton, W.A., Beechem, J.M., Xu, Z., Sigler, P.B., and Horwich, A.L. (1997). Distinct actions of *cis* and *trans* ATP within the double ring of the chaperonin GroEL. Nature *388*, 792–798.

Rye, H.S., Roseman, A.M., Chen, S., Furtak, K., Fenton, W.A., Saibil, H.R., and Horwich, A.L. (1999). GroEL-GroES cycling: ATP and nonnative polypeptide direct alternation of folding-active rings. Cell *97*, 325–338.

Saibil, H.R., and Ranson, N.A. (2002). The chaperonin folding machine. Trends Biochem. Sci. *27*, 627–632.

Sakikawa, C., Taguchi, H., Makino, Y., and Yoshida, M. (1999). On the maximum size of proteins to stay and fold in the cavity of GroEL underneath GroES. J. Biol. Chem. *274*, 21251–21256.

Shtilerman, M., Lorimer, G.H., and Englander, S.W. (1999). Chaperonin function: folding by forced unfolding. Science *284*, 822–825.

Sigler, P.B., Xu, Z., Rye, H.S., Burston, S.G., Fenton, W.A., and Horwich, A.L. (1998). Structure and function in GroEL-mediated protein folding. Annu. Rev. Biochem. *67*, 581–608.

Taguchi, H., Ueno, T., Tadakuma, H., Yoshida, M., and Funatsu, T. (2001). Single-molecule observation of protein-protein interactions in the chaperonin system. Nat. Biotechnol. *19*, 861–865.

Thirumalai, D., and Lorimer, G.H. (2001). Chaperonin-mediated protein folding. Annu. Rev. Biophys. Biomol. Struct. *30*, 245–269.

Todd, M.J., Viitanen, P.V., and Lorimer, G.H. (1994). Dynamics of the chaperonin ATPase cycle: implications for facilitated protein folding. Science *265*, 659–666.

Viani, M.B., Pietrasanta, L.I., Thompson, J.B., Chand, A., Gebeshuber, I.C., Kindt, J.H., Richter, M., Hansma, H.G., and Hansma, P.K. (2000). Probing protein-protein interactions in real time. Nat. Struct. Biol. *7*, 644–647.

Viitanen, P.V., Gatenby, A.A., and Lorimer, G.H. (1992). Purified GroEL interacts with the non-native states of a multitude of E. coli proteins. Protein Sci. *1*, 361–369.

Weissman, J.S., Hohl, C.M., Kovalenko, O., Kashi, Y., Chen, S., Braig, K., Saibil, H.R., Fenton, W.A., and Horwich, A.L. (1995). Mechanism of GroEL action: productive release of polypeptide from a sequestered position under GroES. Cell *83*, 577–587.

Weissman, J.S., Rye, H.S., Fenton, W.A., Beechem, J.M., and Horwich, A.L. (1996). Characterization of the active intermediate of a GroEL-GroES-mediated protein folding reaction. Cell *84*, 481–490.

Wu, P.G., and Brand, L. (1994). Resonance energy transfer: methods and applications. Anal. Biochem. *218*, 1–13.

Xu, Z., Horwich, A.L., and Sigler, P.B. (1997). The crystal structure of the asymmetric GroEL-GroES-(ADP)7 chaperonin complex. Nature *388*, 741–750.

Available online at www.sciencedirect.com
SCIENCE DIRECT
ELSEVIER
Biochemical and Biophysical Research Communications 344 (2006) 772–779
BBRC
www.elsevier.com/locate/ybbrc

Imaging of single mRNA molecules moving within a living cell nucleus

Hisashi Tadakuma [a], Yo Ishihama [a], Toshiharu Shibuya [b], Tokio Tani [b], Takashi Funatsu [a,c,d,*]

[a] *Major in Integrative Bioscience and Biomedical Engineering, Graduate School of Science and Engineering, Waseda University, Shinjuku-ku, Tokyo 169-8555, Japan*
[b] *Department of Biological Science, Faculty of Science, Kumamoto University, 2-39-1, Kurokami, Kumamoto 860-8555, Japan*
[c] *Laboratory of Bio-Analytical Chemistry, Graduate School of Pharmaceutical Sciences, The University of Tokyo, Bunkyo-ku, Tokyo 113-0033, Japan*
[d] *Core Research for Evolutional Science and Technology, Japan Science and Technology Agency, Saitama 332-0012, Japan*

Received 25 March 2006
Available online 17 April 2006

Abstract

In eukaryotic cells, pre-mRNAs are transcribed in the nucleus, processed by 5′ capping, 3′-polyadenylation, and splicing, and exported to the cytoplasm for translation. To examine the nuclear mRNA transport mechanism, intron-deficient mRNAs of truncated β-globin and EGFP were synthesized, fluorescently labeled in vitro, and injected into the nucleus of living *Xenopus* A6 cells. The trajectories of single mRNA molecules in the nucleus were visualized using video-rate confocal microscopy. Approximately half the mRNAs moved by Brownian motion in the nucleoplasm, except the nucleoli, with an apparent diffusion coefficient of 0.2 $\mu m^2/s$, about 1/150 of that in water. The slow diffusion could not be explained by simple diffusion obeying the Stokes–Einstein equation, suggesting interactions of the mRNAs with nuclear components. The remaining mRNAs were stationary with an average residence time of about 30 s, comparable to the time required for mRNA diffusion from the site of synthesis to nuclear pores.

Keywords: Single molecule imaging; mRNA; Nucleus; Diffusion coefficient

In eukaryotic cells, most mRNAs are initially transcribed as pre-mRNAs, which undergo subsequent co- or post-transcriptional maturational processing including 5′ capping, removal of introns by splicing, and 3′-polyadenylation. After this processing, the mature mRNAs are exported to the cytoplasm through nuclear pores for translation. The processes of transcription, processing, and nuclear export are reported to be intimately related [1,2]. Thus, transport of mRNAs from the site of synthesis to nuclear pores is an essential process for gene expression.

A series of pieces of evidence that mRNAs move by Brownian motion through the interchromosomal space have accumulated over the past decade. Politz et al. reported that 2/3 of endogenous poly(A)$^+$ mRNAs labeled with fluorescent oligo(dT) diffused rapidly with diffusion coefficient comparable to that in water, and the other third moved very slowly as evaluated by fluorescent correlation spectroscopy and fluorescence recovery after photobleaching [3]. Poly(A)$^+$ mRNAs labeled with caged-fluorescein-conjugated oligo(dT) were spot-illuminated with ultraviolet rays to uncage the fluorophore, which allowed visualization of poly(A)$^+$ mRNA diffusion showing a diffusion coefficient of 0.6 $\mu m^2/s$ [4,5]. However, it is difficult to know the temporal stability of such hybrids in vivo. To overcome the above issue, Molenaar et al. used 2′*O*-methyl oligo(U) to improve the affinity for poly(A)$^+$ mRNA and observed similar, but slower, diffusion [6]. Since these experiments measured the ensemble average movements of mRNAs, it has been difficult to clarify the relationships among the dynamics of mRNA movement and nuclear substructures,

* Corresponding author. Fax: +81 3 5802 3339.
E-mail address: funatsu@mail.ecc.u-tokyo.ac.jp (T. Funatsu).

0006-291X/$ - see front matter © 2006 Elsevier Inc. All rights reserved.
doi:10.1016/j.bbrc.2006.03.202

or to analyze the spatial and temporal heterogeneity of the movement. Furthermore, it has been difficult to detect temporal active transport.

Single molecule imaging is a powerful tool for resolving such issues [7]. Single β-actin mRNA molecules in a fixed cell nucleus were first visualized using fluorescently labeled antisense oligonucleotides to reveal synchronous and cyclical transcription [8]. Fluorescently labeled U1 snRNP complex involved in splicing reactions was visualized in the nuclei of semi-intact cells [9]. U1 snRNP was diffusely distributed throughout the nucleus and concentrated in distinct nuclear substructures known as speckles. The diffusion coefficient of U1 snRNP was found to be 0.1–1 $\mu m^2/s$. Recently, single RNA molecules in the cytoplasm [10] and nucleus [11] were successfully visualized using fluorescent MS2, an RNA-binding protein. In these experiments, mRNAs containing the MS2 target sequence were visualized by binding of a fusion protein of yellow fluorescent protein (YFP) and MS2, designated YFP-MS2. Some mRNAs were observed to be moving by Brownian motion, while others were corralled in the nucleus except for the nucleolus. However, single-particle tracking (SPT) of nuclear mRNAs that remained in focus for more than 3 s was only performed at a time resolution of 330 ms. Furthermore, in order to distinguish YFP-MS2-tagged mRNA from free YFP-MS2, tandem MS2 target sequences with a combined length of about 1 kb, which are comparable to the mean length of the mature mRNA coding regions (1.3 kb), were required, and the possibility that such large sequence affects the movement of mRNAs in the nucleus cannot be ruled out.

In the present study, mRNAs of two different lengths and sequences, i.e., truncated β-globin mRNA of 405 nt and EGFP mRNA of 834 nt, were synthesized, fluorescently labeled in vitro, and injected into the nucleus of living *Xenopus* A6 cells. We used confocal microscopy to visualize the trajectories of single mRNA molecules. Furthermore, we imaged the movements of intronless mRNAs to avoid the effects of introns, which may complicate the movement of the mRNAs through interaction with the spliceosome.

Materials and methods

Cell cultures. The A6 cell line from *Xenopus* kidney was used for the experiments. The cells were cultured in a medium consisting of 50% L-15 medium without phenol red (21083-027; Gibco), 10% fetal calf serum, 40 U/ml penicillin, and 400 μg/ml streptomycin at 23 °C. The cells were subcultured in glass-bottomed culture dishes for 2 days before mRNA injection. For ATP-depletion experiments, the cells were incubated for 2 h in the culture medium containing 10 mM NaN_3 and 6 mM D-glucose [12].

Preparation of fluorescently labeled mRNAs. To prepare the truncated β-globin mRNA (405 nt) containing exons 1 and 2 but lacking intron 1 of the gene, pSP64-HβΔ6-IVS1,2 [13] was digested with *Hin*dIII and *Bam*HI, and subcloned between the *Hin*dIII and *Bam*HI sites of pSP64-poly(A) (Promega) [14]. To prepare the EGFP mRNA (834 nt), pEGFP-N1 (Clontech) was digested with *Not*I, followed by treatment with the Klenow Fragment (Takara). After digestion with *Pst*I, a fragment containing the EGFP gene was isolated and subcloned between the *Pst*I and *Sma*I sites of pSP64-poly(A). For in vitro transcription, the obtained pSP64-poly(A) plasmids, containing the individual genes as well as the SP6 promoter and a 30 nt poly(A) sequence, were digested with *Eco*RI and the linearized plasmids were transcribed using a RiboMAX kit (P2180; Promega). A cap analog, m^7GpppG (P1812; Promega), was incorporated into the 5′ end of the mRNAs during the transcription reaction according to the manufacturer's instructions. The mRNA molecules obtained were labeled with a Cy3 labeling kit (*Label* IT; Mirus), and unreacted dye was removed by gel filtration. The Cy3 and mRNA concentrations were calculated from their absorbances at 550 and 260 nm, respectively, using a spectrofluorometer (FP6500; Jasco). The fluorescence intensity/mRNA molecule increased as the labeling ratio became higher, until it reached a plateau at a labeling ratio of about 8 due to the quenching effect of the dyes. Therefore, mRNA molecules labeled with less than 8 dye molecules were used for single molecule imaging throughout this study.

Microinjection. Fluorescently labeled mRNA samples were dissolved at concentrations of 10–20 nM in RNase-free water (Mill-Q + Gengard; Millipore). Microinjection of mRNAs into A6 cells was performed using an injector (Transjector 5246+Micromanipulator 5171; Eppendorf) equipped with a microneedle (Femtotips II; Eppendorf). The injection duration was 0.4 s, and the injection and compensation pressures were 15–45 and 20 hPa, respectively. An approximate microinjection volume was 30 fL and hundreds of mRNAs were injected.

Confocal microscopy. An inverted microscope (IX-70; Olympus) equipped with a Nipkow disk-type confocal unit (CSU-10; Yokogawa Electric Co.) was used [15]. The Cy3 fluorophore was illuminated with a green solid-state laser (100 mW, 532 nm Compass 315M-100; Coherent). The laser beam illuminated an approximately 40 μm diameter region of the specimen using an oil-immersion objective (PlanApo 100×, NA = 1.4; Olympus). The laser power density at the specimen plane was 0.5–5 W/mm^2. Fluorescence images were taken using an ICCD video camera (ICCD-350F; Video Scope International) coupled to an image intensifier (VS4-1845; Video Scope International). The images were analyzed using a homemade program on a Halcon image processor (MVTec Software GmbH) or Scion Image (Scion Corporation).

Analysis of the mRNA fluorescence intensities. Cy3-labeled mRNA molecules (labeling ratio, 2.5 Cy3/mRNA) were attached to a glass coverslip coated with poly-L-lysine (P7890; Sigma), and the fluorescence intensities of the mRNAs were measured by integrating the signals from a circular region of interest (ROI) consisting of 140 image pixels and subtracting the background fluorescence. The fluorescence intensity of a single Cy3 molecule attached to the mRNA was obtained by quantized photobleaching [15]. In order to measure the fluorescence intensities of mRNAs in the nucleus, the confocal imaging plane of the microscope was set at 3 μm above the glass/solution interface, and the fluorescence intensities were measured as described above. Only fluorescence spots with fluorescence intensities greater than 3 SD of the background intensity were analyzed in order to exclude shot noise.

Analysis of the movement of mRNA molecules. Cy3-labeled mRNAs (labeling ratio, 8 Cy3/mRNA) were injected into cell nuclei and incubated for 5–60 min, before fluorescence images at 3 μm above the glass surface were captured by video for 10 s. All experiments were performed at 23 ± 1 °C. The position of the mRNA was determined using a homemade 2D Gaussian function fitting macro and the Halcon image library with a square ROI of 10 × 10 image pixels. The parameters of the 2D Gaussian function fitting were solved by a nonlinear χ^2-minimization routine [16]. To determine the apparent diffusion coefficient, D, of the mobile molecules, the mean square displacement (MSD) of mRNA molecules retained in the confocal cross-section (~0.7 μm) for less than 1 s was measured and D was determined according to the following equation:

$$4Ddt = \langle dx^2 + dy^2 \rangle, \quad (1)$$

where dt is the time interval and $\langle dx^2 + dy^2 \rangle$ is the MSD.

Molecules that stayed in the confocal cross-section (~0.7 μm) for more than 1 s and had an MSD for 1 s of less than 0.1 μm^2 were defined as stationary mRNAs. To determine the duration that the mRNAs remained stationary, fluorescence micrographs of mRNA molecules were taken every 15 s with an exposure time of 1 s, and the number of mRNAs that

remained stationary was counted. All observations were carried out at 5–20 min after the mRNA injection.

In order to carry out comparisons with the movements of mRNA in water, fluorescent mRNA (500 pM) was diluted in a solution containing 60% sucrose and fluorescence images at 3 μm above the glass surface were taken at 23 ± 1 °C and analyzed as described above. The diffusion coefficient of mRNA in water was deduced from that in sucrose solution assuming that the viscosities of water and the sucrose solution are 0.93 and 53.2 mPa·s, respectively.

Results

Single molecule imaging of mRNAs in living cell nuclei

Cy3-labeled mRNAs were synthesized in vitro and injected into the nuclei of A6 cells to visualize the movement and localization of mRNAs at the single molecule level. Upon microinjection of a Cy3-labeled mRNA, fluorescent spots appeared in the nucleus. Video analysis revealed that the mRNAs moved around the nucleoplasm, except for the nucleoli. In order to confirm that each fluorescent spot corresponded to a single mRNA, we measured the fluorescence intensity. First, the fluorescence intensity of single Cy3 molecules bound to mRNAs on the surface of a glass coverslip was measured as a reference. Specifically, β-globin mRNA was labeled with Cy3, attached to a glass surface coated with poly-L-lysine, and analyzed by quantized photobleaching (Fig. 1A) [15]. A histogram of the fluorescence intensity of the single Cy3 molecules determined by quantized photobleaching is shown in Fig. 1B. The mean value was normalized as 1 ± 0.3 ($n = 242$) and used as a standard value. Next, β-globin mRNA was injected into the nucleus and the fluorescence intensities of the molecules remained in a confocal image plane at 3 μm above the glass surface were measured. The mean fluorescence intensity was about 60% of that on the glass surface (data not shown), indicating that these spots corresponded to individual mRNAs. The decrease in fluorescence intensity may be ascribed to the fact that the mRNAs measured were not necessarily located at the center of the confocal image plane or to an aberration of the objective lens. Finally, to confirm that the microinjected mRNAs were free from degradation during the observation period, β-globin mRNAs (labeling efficiency, 8 Cy3/mRNA) were microinjected and the time-dependency of the fluorescent intensity was examined. The histograms of the mRNA fluorescence intensities after normalization by the mean intensity of Fig. 1B are shown in Fig. 1C. The shapes of these histograms were quite similar suggesting there was no extensive RNA degradation during the experiment.

SPT of mRNAs

In order to analyze the movement of the mRNAs more precisely, SPT of mRNAs was performed (Fig. 2). SPT of these mRNAs revealed two kinds of movement. In some instances, the mRNAs were highly mobile, whereas in other cases, the mRNAs were corralled within an area of 300 nm in diameter. Moreover, single mRNA molecules often made abrupt transitions between the stationary and mobile modes. For example, molecule No. 4 in Fig. 2F was corralled for an initial period of 1.5 s and then started moving (see also the inset in Fig. 2H).

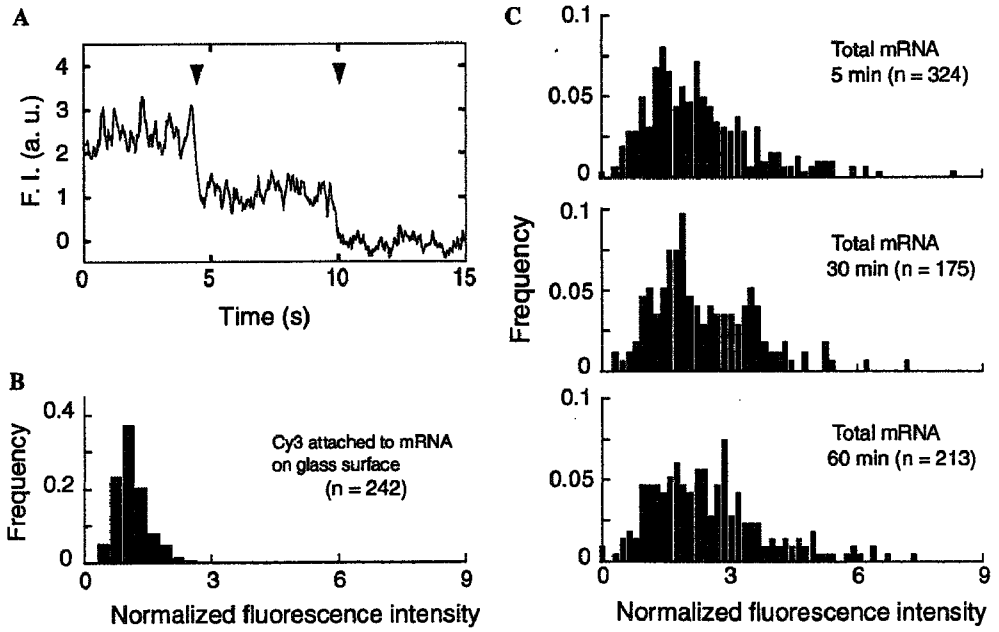

Fig. 1. Determination of the fluorescence intensities of β-globin mRNA molecules. (A) The time course of the fluorescence intensity of mRNA with two Cy3 molecules. Photobleaching occurred at the times indicated by the arrowheads. (B) Histogram of the fluorescence intensities of single Cy3 molecules attached to mRNAs determined by quantized photobleaching. The mean value was normalized as unity. (C) Histograms of the fluorescence intensities of Cy3-β-globin mRNA molecules measured at 5, 30, and 60 min after injection into the nucleus of A6 cells. The labeling ratio of Cy3 to β-globin mRNA was 8:1, and the fluorescence images were taken at 3 μm above the glass surface. The fluorescence intensity was normalized by the mean value in (B). See Materials and methods for details.

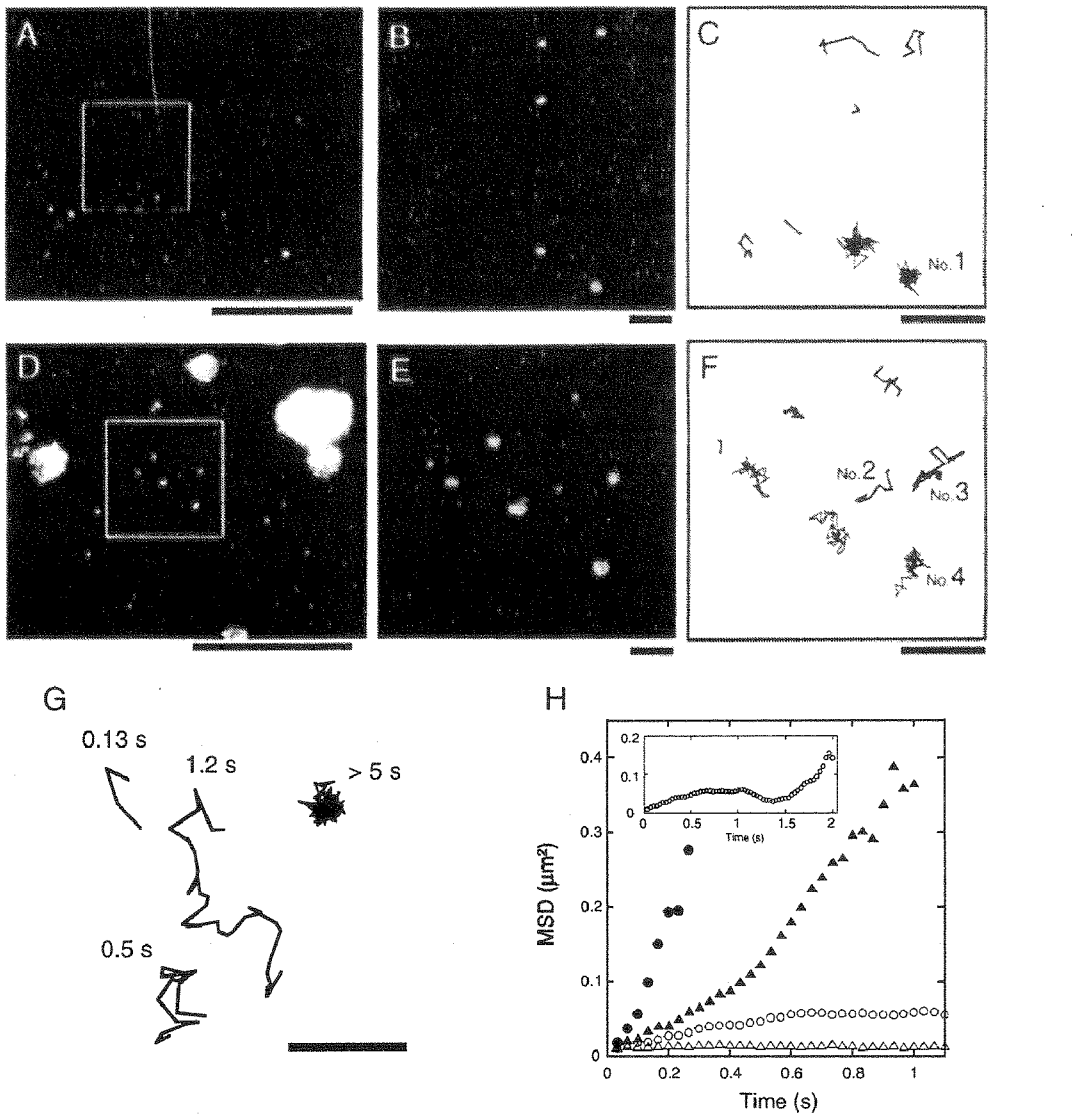

Fig. 2. Imaging of single mRNA molecules in nuclei and analysis of their trajectories. (A) Fluorescence micrograph of EGFP mRNA. The small fluorescent spots correspond to individual mRNA molecules. (B) High magnification view of the area indicated by the square in (A). (C) Trajectories of the mRNAs shown in (B). Note that the individual trajectories are placed so that their centers correspond to the positions of the mRNA molecules in (B), but shown at twice the magnification. (D–F) Similar to (A–C), except that the results for the β-globin mRNA are shown. The large fluorescent spots in D represent autofluorescence. (G) Other typical trajectories of β-globin mRNA molecules. The duration of each observation is shown above the trajectory. Scale bars in (A) and (D) are 10 μm, while the others are 1 μm. (H) Plot of the MSD versus time for molecules No. 1 (open triangles), No. 2 (closed circles), No. 3 (closed triangles), and No. 4 (open circles). The inset indicates the plot of No. 4 over a longer observation period.

Residence time of mRNAs in a confocal image plane

We measured the residence time of mRNAs in a confocal image plane for statistical analysis of the mobile and stationary mRNAs. We were only able to image molecules that stayed within a thin optical section ($dz = 0.7$ μm) using confocal microscopy [15]. The distributions of the mRNA residence times in the confocal image plane are shown in Fig. 3. The data were fitted with the sum of two exponential functions. The calculated durations and fractions of the fast and slow species were 0.18 s (94%) and 4.3 s (6%) for the β-globin mRNA (9 cells, $n = 453$), and 0.16 s (90%) and 3.6 s (10%) for the EGFP mRNA (7 cells, $n = 322$), respectively. It should be mentioned here that the fast species repeatedly passed through the confocal image plane while the stationary mRNA remained in the confocal plane. Thus, the ratio of the fast and slow mRNAs we measured did not show the real ratio of the two types. The slower time constants of about 6 s corresponded to those of photobleaching under the experimental conditions used.

Ratio of the numbers of mobile and stationary mRNA molecules

As shown in Fig. 3, the residence time of the mobile mRNAs in the confocal image plane was about 0.2 s, while that of the stationary mRNA was longer than the photobleaching time of 6 s. Thus, we defined practically that

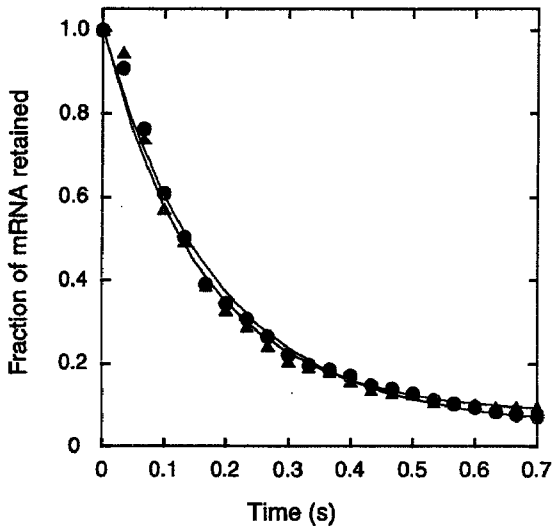

Fig. 3. Histogram of the residence time of mRNA in a confocal imaging plane. The closed circles and triangles represent β-globin (9 cells, $n = 453$) and EGFP (7 cells, $n = 322$) mRNAs, respectively. The solid lines indicate fitting of the curves with the sum of two exponential functions. The calculated durations and populations of the fast and slow species were 0.18 s (94%) and 4.3 s (6%) for β-globin, and 0.16 s (90%) and 3.6 s (10%) for EGFP, respectively.

mRNAs which stayed in the confocal image plane for more than 1 s and had an MSD for 1 s of less than 0.1 μm^2 were stationary, while the other mRNAs were mobile. The ratios of the number of mobile molecules to the total molecules were measured using β-globin mRNA, and found to be 0.45 ± 0.16 (mean ± S.D.; 6 cells, $n = 207$), 0.43 ± 0.12 (5 cells, $n = 176$), and 0.65 ± 0.07 (5 cells, $n = 282$) at 5, 30, and 60 min after the microinjection, respectively.

Analysis of the apparent diffusion coefficients of mobile mRNAs

Next, we statistically analyzed the movement of the mobile mRNA molecules. The MSD of the mobile mRNAs was plotted against time (Fig. 4A). The MSD increased linearly with time, indicating that the mRNA molecules were moving by Brownian motion. D was obtained using Eq. (1). The D values for the β-globin and EGFP mRNAs were 0.21 and 0.18 $\mu m^2/s$, respectively. To compare the D values in the nucleus with those in water, the β-globin and EGFP mRNAs were diluted in a solution containing 60% sucrose solution, since their Brownian motion in pure water was too rapid to be detected using a video camera. The diffusion coefficient of mRNA in water was deduced from that in sucrose solution. The D values in the nucleus were about 1/160 (β-globin) to 1/140 (EGFP) of the values in water (Fig. 4B).

To check whether or not the movement was an energy-dependent process, ATP was depleted by adding sodium azide and 2-deoxyglucose to the medium. Similar movements of β-globin mRNA with a D value of 0.51 $\mu m^2/s$ were still observed, indicating that the movement was Brownian motion (data not shown).

Residence time of stationary mRNA

Next, we measured the duration of the stationary state, since the SPT data suggested that the mRNA sometimes changed its state from the stationary to the mobile state (Fig. 2). To overcome the effect of photobleaching, we performed time-lapse imaging (Fig. 5). Fluorescence images were captured for 1 s by video at 15 s intervals using a low excitation laser power (photobleaching time was about 30 s). From the initial video image, the stationary mRNAs were determined and marked as shown in Fig. 5B. The relative number of remaining stationary mRNAs as a function of time is shown in Fig. 5C. The open circles and triangles indicate the β-globin (20 cells, $n = 141$) and EGFP (12 cells, $n = 81$) mRNAs, respectively, while the solid lines indicate exponential fitting of the data with a time constant of 24 s. The β-globin and EGFP mRNAs showed similar durations. Taking photobleaching into consideration, the

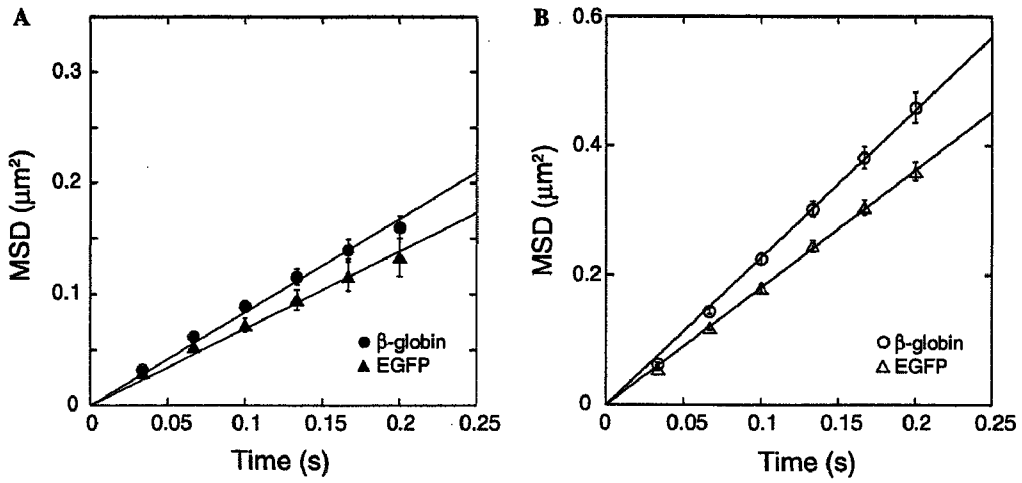

Fig. 4. MSD of mobile mRNA molecules as a function of time. The trajectories of mRNAs were captured using a video camera. (A) The closed circles and triangles indicate β-globin and EGFP mRNAs in the nuclei, respectively. (B) The open circles and triangles indicate β-globin and EGFP mRNAs in 60% sucrose solution, respectively. Error bars indicate standard errors of the mean.

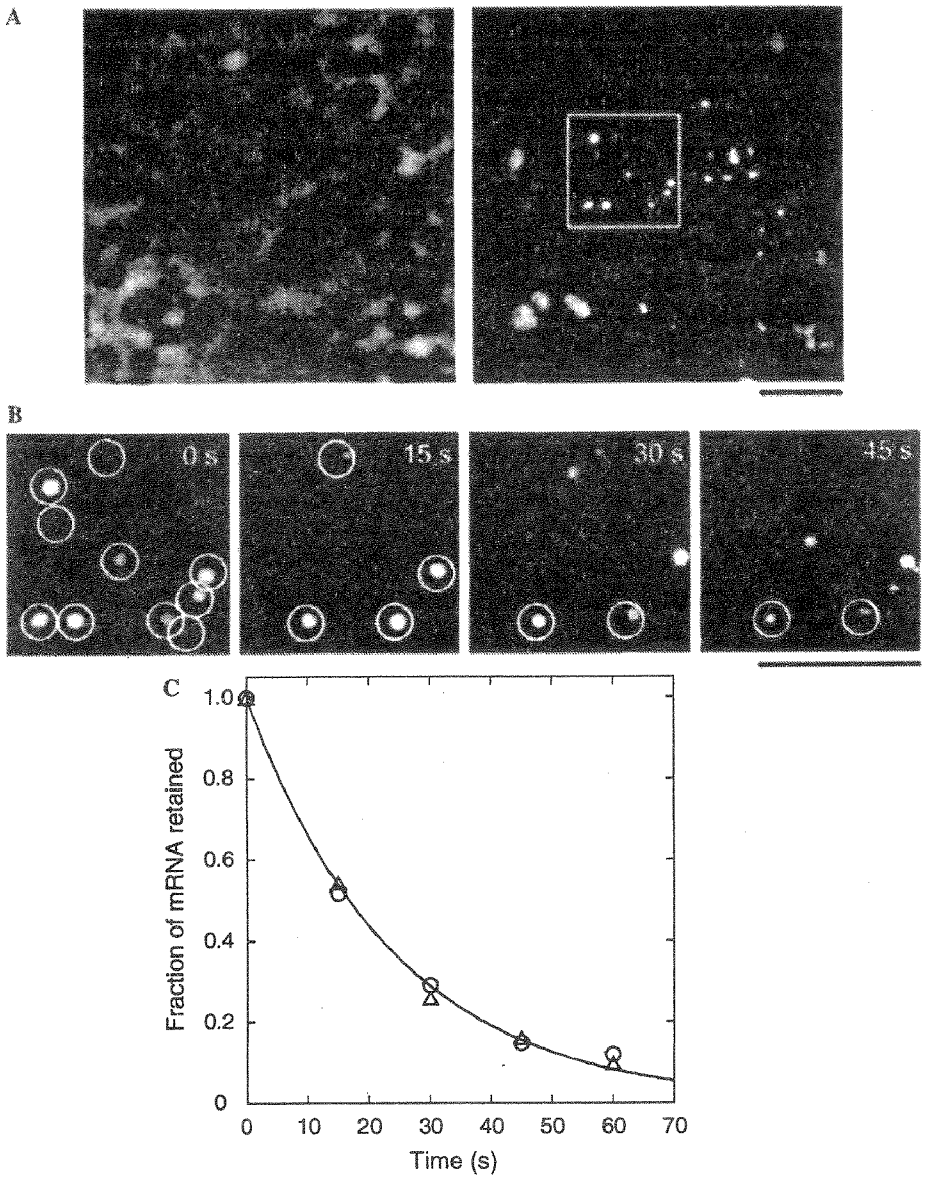

Fig. 5. Duration that the EGFP mRNAs remain stationary in the nucleus. (A) Typical phase contrast (left) and fluorescence (right) video micrographs of A6 cells. Scale bar, 5 μm. (B) Serial fluorescence video micrographs of the area indicated by the square in (A). Scale bar, 5 μm. To determine the duration that the mRNAs remain stationary, fluorescence micrographs of mRNA molecules were taken every 15 s. mRNA molecules that stayed in the confocal cross-section for more than 1 s and had an MSD for 1 s of less than 0.1 μm^2 are indicated by circles. Scale bar, 5 μm. (C) Fraction of mRNA molecules remaining in an optical section as a function of time. The open circles and triangles indicate β-globin (20 cells, $n = 141$) and EGFP (12 cells, $n = 81$) mRNAs, respectively. The solid line indicates exponential fitting of the data with a time constant of 24 s.

residence time of stationary mRNA was calculated to be about 30 s.

Discussion

In the present study, we visualized the movement of single mRNA molecules in living cell nuclei using fluorescence video microscopy. To visualize individual mRNAs, they were synthesized, labeled with Cy3 in vitro, and injected into the nucleus of living cells. We used an intron-deficient truncated β-globin mRNA, composed of exons 1 and 2, and an EGFP mRNA to analyze the movement without interference from the splicing reaction. The mRNAs became distributed in the nucleoplasm, except for the nucleolus, indicating that access of mRNA into the nucleolus was hindered. Fig. 1C suggested there was no extensive RNA degradation in the nucleus during the experiment. Some populations of mRNA were exported to the cytoplasm, since the fluorescence of EFG was detected 4 h after the injection of EGFP mRNAs without fluorescence labeling.

The trajectories of single mRNA molecules in the nucleus were visualized using video microscopy. About half the mRNAs were mobile, while the remaining mRNAs were stationary in a restricted region for about 24 s. Active transport of mRNA was not observed in the nucleus. These

results support the model that mRNA travels from the site of synthesis to nuclear pores by diffusion. D was about 0.2 $\mu m^2/s$, which was about 1/150 of that in water. This value is similar to those of U1 snRNP complex (165 nt RNA and U1 snRNP proteins; 1 $\mu m^2/s$) [9], 60S ribosomal subunits (0.3 $\mu m^2/s$) [17], and β-globin mRNA labeled with YFP-MS2 (2.8 k nt; 0.04 $\mu m^2/s$) [11]. These results are in contrast to behavior of EGFP in the nucleus, where the apparent diffusion coefficient of GFP is only 3–5-fold lower than that in water [18–20].

What is the origin of the slow diffusion of mRNA in the nucleus? According to the simple diffusion model, the diffusion coefficient follows the Stokes–Einstein equation:

$$D = kT/6\pi a\eta, \quad (2)$$

where k is the Boltzmann coefficient, T is the absolute temperature, a is the Stokes radius, and η is the viscosity of the solution. One candidate for the origin of the slow diffusion is a change in the viscosity. However, as mentioned above, the diffusion coefficient of GFP in the nucleus was about 1/3 of that in water. Furthermore, Seksek et al. reported that the diffusion coefficient of dextran in water with a molecular weight up to 500 kDa was about 1/3 of that in the nucleus [21]. Thus, the slow diffusion of mRNA cannot be explained by the viscosity of the nucleus. Another possible reason for the slow diffusion is a large Stokes radius, i.e., mRNA forms a large complex with RNA-binding proteins. The Stokes radius of β-globin mRNA is calculated to be 370 nm, assuming that $D = 0.2\ \mu m^2/s$ and $\eta = 3 \times 10^{-3}$ Pa·s, which is much longer than the straight chain length of β-globin (405 nt) mRNA. Taking these facts into consideration, we argue that the movement of mRNA in the nucleus is not the simple diffusion expressed by Eq. (2).

Another possible origin of the slow mRNA diffusion in the nucleus is the effects of macromolecular crowding. The diffusion coefficient of DNA in a two-dimensional array of spherical cavities interconnected by circular holes was reported to be two orders of magnitude smaller than that for free diffusion [22]. A mesh-like structure for the "nuclear matrix" has been reported, and mRNAs have been reported to move in interchromosomal channels [4]. The effect of molecular confinement is expected to reduce mRNA diffusion in the nucleus. Similarly, proteins involved in the diverse nuclear processes of living cells were reported to move throughout the entire nucleus with similar diffusion coefficients to that measured in the present study [23], and rapid association and dissociation with nuclear compartments have been proposed [24]. Although the mobile mRNA molecules did not show anomalous diffusion [25–27] under our experimental conditions, further studies with larger mRNAs are required to reveal the precise diffusion process in the nucleus.

About half the mRNAs were stationary, consistent with a previous report [11]. One possible reason of slower mobility is that mRNAs were partially corralled throughout the nonhomogeneous environment [11]. Another reason is that mRNAs were attached to some structure in the nucleus. We could not distinguish two cases since our microscopy could not measure the displacement shorter than 0.2 μm and the diffusion coefficient less than 0.003 $\mu m^2/s$. Our present paper is the first to measure the duration of about 30 s in the stationary state. This time period is comparable to the 30 s period required for mRNA to travel a distance of 5 μm (about the radius of the nucleus) by Brownian motion with a D of 0.2 $\mu m^2/s$. Thus, the stationary state will not substantially delay the diffusion time of mRNA to travel from the site of synthesis to the nuclear pores. As far as we measured, the duration of the stationary state was independent of the mRNA sequence and length over a factor of two. Further studies are required to reveal the origin of the stationary state.

Since the transcription, splicing, and nuclear export of eukaryotic mRNAs have been reported to be closely linked [1,2], we used intronless mRNAs to exclude the influence of the splicing reaction on the movement of the mRNA. Therefore, similar studies using mRNAs with introns should be performed in the future.

Acknowledgments

We thank Kaori Watanabe for critically reading the manuscript. This work was supported by the Uehara Memorial Foundation and by Grants-in-Aid for Specially Promoted Research, Scientific Research Priority Area (A) Nos. 14035249 and 15030238, and Scientific Research (B) No. 11480196, from the Ministry of Education, Culture, Sports, Science and Technology of Japan.

References

[1] T. Maniatis, R. Reed, An extensive network of coupling among gene expression machines, Nature 416 (2002) 499–506.
[2] G. Dreyfuss, V.N. Kim, N. Kataoka, Messenger-RNA-binding proteins and the messages they carry, Nat. Rev. Mol. Cell. Biol. 3 (2002) 195–205.
[3] J.C. Politz, E.S. Browne, D.E. Wolf, T. Pederson, Intranuclear diffusion and hybridization state of oligonucleotides measured by fluorescence correlation spectroscopy in living cells, Proc. Natl. Acad. Sci. USA 95 (1998) 6043–6048.
[4] J.C. Politz, R.A. Tuft, T. Pederson, R.H. Singer, Movement of nuclear poly(A) RNA throughout the interchromatin space in living cells, Curr. Biol. 9 (1999) 285–291.
[5] J.C. Politz, R.A. Tuft, K.V. Prasanth, N. Baudendistel, K.E. Fogarty, L.M. Lifshitz, J. Langowski, D.L. Spector, T. Pederson, Rapid, diffusional shuttling of poly(A) RNA between nuclear speckles and the nucleoplasm, Mol. Biol. Cell. 17 (2006) 1239–1249.
[6] C. Molenaar, A. Abdulle, A. Gena, H.J. Tanke, R.W. Dirks, Poly(A)$^+$ RNAs roam the cell nucleus and pass through speckle domains in transcriptionally active and inactive cells, J. Cell. Biol. 165 (2004) 191–202.
[7] Y. Sako, T. Yanagida, Single-molecule visualization in cell biology, Nat. Rev. Mol. Cell. Biol. Suppl. (2003) SS1–SS5.
[8] A.M. Femino, F.S. Fay, K. Fogarty, R.H. Singer, Visualization of single RNA transcripts in situ, Science 280 (1998) 585–590.
[9] T. Kues, A. Dickmanns, R. Luhrmann, R. Peters, U. Kubitscheck, High intranuclear mobility and dynamic clustering of the splicing factor U1 snRNP observed by single particle tracking, Proc. Natl. Acad. Sci. USA 98 (2001) 12021–12026.

[10] D. Fusco, N. Accornero, B. Lavoie, S.M. Shenoy, J.M. Blanchard, R.H. Singer, E. Bertrand, Single mRNA molecules demonstrate probabilistic movement in living mammalian cells, Curr. Biol. 13 (2003) 161–167.
[11] Y. Shav Tal, X. Darzacq, S.M. Shenoy, D. Fusco, S.M. Janicki, D.L. Spector, R.H. Singer, Dynamics of single mRNPs in nuclei of living cells, Science 304 (2004) 1797–1800.
[12] C. Dingwall, S.M. Dilworth, S.J. Black, S.E. Kearsey, L.S. Cox, R.A. Laskey, Nucleoplasmin cDNA sequence reveals polyglutamic acid tracts and a cluster of sequences homologous to putative nuclear localization signals, EMBO J. 6 (1987) 69–74.
[13] A.R. Krainer, T. Maniatis, B. Ruskin, M.R. Green, Normal and mutant human beta-globin pre-mRNAs are faithfully and efficiently spliced in vitro, Cell 36 (1984) 993–1005.
[14] K. Tokunaga, T. Shibuya, Y. Ishihama, H. Tadakuma, M. Ide, M. Yoshida, T. Funatsu, Y. Ohshima, T. Tani, Nucleocytoplasmic transport of fluorescent mRNA in living mammalian cells: nuclear mRNA export is coupled to ongoing gene transcription, Genes Cells 11 (2006) 305–317.
[15] H. Tadakuma, J. Yamaguchi, Y. Ishihama, T. Funatsu, Imaging of single fluorescent molecules using video-rate confocal microscopy, Biochem. Biophys. Res. Commun. 287 (2001) 323–327.
[16] W. Press, S.A. Teukolsky, W.V. Vetterling, B.P. Flannery, Numerical Recipes in C, Cambridge University Press, San Diego, 1992.
[17] J.C. Politz, R.A. Tuft, T. Pederson, Diffusion-based transport of nascent ribosomes in the nucleus, Mol. Biol. Cell 14 (2003) 4805–4812.
[18] Y. Chen, J.D. Muller, Q. Ruan, E. Gratton, Molecular brightness characterization of EGFP in vivo by fluorescence fluctuation spectroscopy, Biophys. J. 82 (2002) 133–144.
[19] M. Wachsmuth, W. Waldeck, J. Langowski, Anomalous diffusion of fluorescent probes inside living cell nuclei investigated by spatially-resolved fluorescence correlation spectroscopy, J. Mol. Biol. 298 (2000) 677–689.
[20] J. Beaudouin, F. Mora-Bermudez, T. Klee, N. Daigle, J. Ellenberg, Dissecting the contribution of diffusion and interactions to the mobility of nuclear proteins, Biophys. J. 90 (2006) 1878–1894.
[21] O. Seksek, J. Biwersi, A.S. Verkman, Translational diffusion of macromolecule-sized solutes in cytoplasm and nucleus, J. Cell. Biol. 138 (1997) 131–142.
[22] D. Nykypanchuk, H.H. Strey, D.A. Hoagland, Brownian motion of DNA confined within a two-dimensional array, Science 297 (2002) 987–990.
[23] R.D. Phair, T. Misteli, High mobility of proteins in the mammalian cell nucleus, Nature 404 (2000) 604–609.
[24] T. Misteli, Protein dynamics: implications for nuclear architecture and gene expression, Science 291 (2001) 843–847.
[25] M.J. Saxton, Anomalous diffusion due to obstacles: a Monte Carlo study, Biophys. J. 66 (1994) 394–401.
[26] M.J. Saxton, Single-particle tracking: effects of corrals, Biophys. J. 69 (1995) 389–398.
[27] M.J. Saxton, Anomalous diffusion due to binding: a Monte Carlo study, Biophys. J. 70 (1996) 1250–1262.

付録

37

CONTRACTILE PROPERTIES OF THIN (ACTIN) FILAMENT-RECONSTITUTED MUSCLE FIBERS

Shin'ichi Ishiwata,[1–4*] Takashi Funatsu,[1,3] and Hideaki Fujita[1]

[1]Department of Physics
School of Science and Engineering
[2]Advanced Research Institute for Science and Engineering
[3]Materials Research Laboratory for Bioscience and Photonics
Waseda University
Tokyo 169-8555
[4]Core Research for Evolutional Science and Technology (CREST)
"Genetic Programming" Team 13, Japan

ABSTRACT

Selective removal and reconstitution of the components of muscle fibers (fibrils) is a useful means of examining the molecular mechanism underlying the formation of the contractile apparatus. In addition, this approach is powerful for examining the structure-function relationship of a specific component of the contractile system. In previous studies, we have achieved the partial structural and functional reconstitution of thin filaments in the skeletal contractile apparatus and full reconstitution in the cardiac contractile apparatus. First, all thin filaments other than short fragments at the Z line were removed by treatment with plasma gelsolin, an actin filament-severing protein. Under these conditions, no active tension could be generated. By incorporating exogenous actin into these thin filament-free fibers, actin filaments were reconstituted by polymerization on the short actin fragments remaining at the Z line, and active tension, which was insensitive to Ca^{2+}, was restored. The active tension after the reconstitution of thin filaments reached as high as 30% of the original level in skeletal muscle, while it reached 140% in cardiac muscle. The augmentation of tension in cardiac muscle is mainly attributable to the elongation of reconstituted filaments, longer than the average length of thin filaments in an intact muscle. These results indicate that a muscle contractile apparatus with a high order structure and function

* Correspondence: S. Ishiwata, Department of Physics, School of Science and Engineering, Waseda University, 3-4-1 Okubo, Shinjuku-ku, Tokyo 169-8555, Japan. Tel: +81-3-5286-3437; Fax: +81-3-3200-2567; E-mail: ishiwata@mn.waseda.ac.jp

Mechanisms of Work Production and Work Absorption in Muscle,
edited by Sugi and Pollack. Plenum Press, New York, 1998.

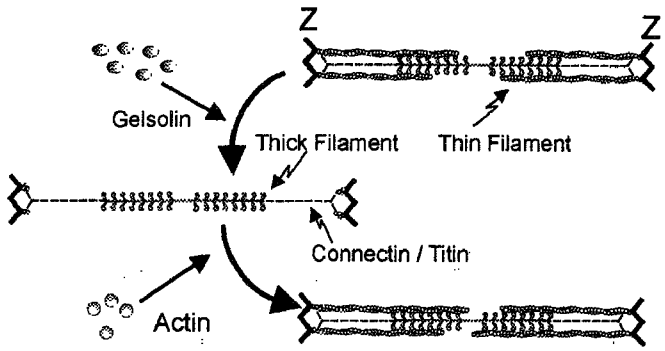

Figure 1. Schematic diagram illustrating the removal and reconstitution of thin filaments in a sarcomere of striated muscle. Both skeletal and cardiac muscles are classified into the category of striated muscle from the structural point of view, but there are several differences between them: (1) The length of thin filaments is precisely determined in skeletal muscle, but it has a broad distribution in cardiac muscle[22]. (2) Relating to (1), nebulin[23], which is assumed to be a ruler for regulating the length of thin filaments, is present in skeletal muscle, while absent in cardiac muscle, which instead contains nebulet, a small analogue of nebulin[24]. (3) The Z line structure in cardiac muscle appears to be more solid than that in skeletal muscle, because the former appears thicker than the latter under an electron microscope. Elastic filaments called connectin/titin are schematically shown by dotted lines[8,25,26].

can be constructed by the self-assembly of constituent proteins. Recently, we applied this reconstitution system to the study of the mechanism of spontaneous oscillatory contraction (SPOC) in thin (actin) filament-reconstituted cardiac muscle fibers. As a result, we found that SPOC occurs even in regulatory protein-free actin filament-reconstituted fibers (Fujita & Ishiwata, manuscript submitted), although the SPOC conditions were slightly different from the standard SPOC conditions. This result strongly suggests that spontaneous oscillation is intrinsic to actomyosin motors. We here summarize the contractile properties of the reconstitution system.

INTRODUCTION

The muscle contractile apparatus is composed of myofilaments called thick (myosin) and thin (actin) filaments and an elastic framework that maintain the crystalline lattice structure (Fig. 1). Muscle contraction occurs through mutual sliding between thick and thin filaments within the well-organized filamentous structure called the sarcomere. If one can find a method to remove either thick or thin filaments selectively and reconstitute them, studies not only on the formation mechanism of the myofilament structure but also on the molecular mechanism of muscle contraction and its regulation will be advanced. For example, the structural changes of actin molecules could be monitored by incorporating the fluorescent dye-labeled actin molecules into reconstituted actin (thin) filaments. Also, the reconstitution system would be useful for studying the molecular mechanism of regulation by tropomyosin-troponin complexes and other regulatory proteins. The mechanism of length regulation of thin (actin) filaments by protein rulers, capping proteins and so on could be studied in a structurally ordered contractile system.

Until recently, such an approach, i.e., studies based on the destruction and reconstitution strategy, have been exclusively performed for thick filaments. This is mainly because it is easy to remove thick filaments by increasing the ionic strength under relaxing conditions (fully relaxing conditions in the presence of MgATP or partially relaxing conditions in the presence of MgPPi[1]). However, full reconstitution of thick filaments has not

yet been achieved[2]. This is mainly because the nucleus formation is not necessarily a rate-limiting step for the polymerization process of myosin filaments, so that the exogenous myosin molecules were spontaneously polymerized outside the muscle fibers under all conditions we examined. Thus, although the central portion of thick filaments, which is expected to function as a nucleus, can be prepared after dissociation from both ends of thick filaments by mild treatment of fibers with high salt solution[1,3,4], exogenous myosin molecules were not polymerized onto the short bipolar filaments that remained at the central portion of the A band of fibers[5].

On the other hand, unlike thick filaments, it is difficult to remove thin filaments selectively by controlling ionic conditions. Recently, however, we succeeded in selectively removing thin filaments in skeletal[6,7] and cardiac[8] muscle. Then, we partly succeeded in reconstituting thin filaments by using thin filament-free skeletal muscle fibers and fibrils, and applying purified actin under appropriate conditions, but the maximum tension of the reconstituted fibers generated was less than 30% that of intact fibers[9]. As schematically illustrated in Fig. 1, structural and function reconstitution of thin filaments in the contractile apparatus could be achieved to nearly 100%, or even more (average recovery tension, 140%), by using a small segment of glycerinated muscle bundle extracted from a papillary muscle of bovine heart[10].

Here, we briefly summarize our work on the thin filament reconstitution system, focusing on a key point for the reconstitution, and the principal results obtained using this system.

MATERIALS AND METHODS

Muscle Fibers and Proteins

Glycerinated muscle fibers were prepared from bovine papillary muscle according to a procedure previously reported; that is, 2 to 5 weeks of incubation at –2020 in glycerol solution (50% glycerol, 1 mM $NaHCO_3$, 5 mM EGTA and 2 mM leupeptin). After dissecting a thin bundle (strip) of muscle fibers (30–50 m thick × 2 mm long) in cold glycerinated solution, the bundle was fixed to a tension transducer and selective removal and reconstitution of thin filaments were performed, and then the physiological properties were studied. The thinner the muscle bundle, the easier the reconstitution of actin filaments in the thin filament-free bundles, because the shorter the diffusion time for exogenous actin molecules to penetrate into the bundle, the better the degree of reconstitution.

Actin was prepared from rabbit white skeletal muscle and bovine cardiac muscle after preparing acetone powder according to a procedure previously reported[11]. Native tropomyosin, a complex of tropomyosin and troponin, was also prepared from both types of muscle. Gelsolin was prepared from bovine serum[10].

Methods to Examine the Structural and Functional Destruction and Reconstitution of Thin (Actin) Filaments in the Fibers

The internal structure of the sarcomeres in muscle fibers was examined by either thin-section electron microscopy or confocal fluorescence microscopy (LSM 410, Carl Zeiss, Tokyo or LSM GB200, Olympus, Tokyo), in fibers labeled with rhodamine-phalloidin which specifically attaches to actin filaments. The contractile ability of the fibers was examined by measuring the isometric tension at room temperature.

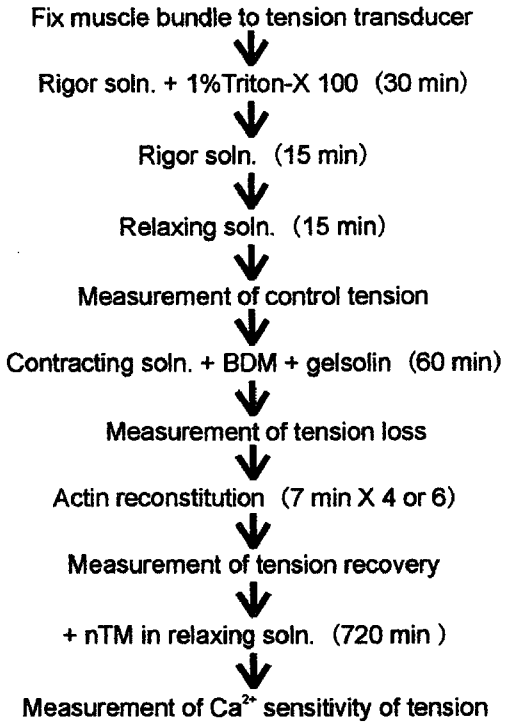

Figure 2. Experimental procedure for the removal and reconstitution of thin filaments in cardiac muscle. At each stage of selective removal and reconstitution of thin (actin) filaments, the isometric tension was measured to confirm whether the tension was lost or recovered. At the stage of actin reconstitution, fresh actin solution was exchanged either 4 times or 6 times, every 7 min, depending on the purpose of the experiments: the longer the time of exchange of solution, the longer the length of the reconstituted actin filaments, resulting in a larger recovery of tension (roughly speaking, the tension recovered to the original level by 4 times exchange and to a higher level by 6 times exchange[10].

Solutions

The solutions used were: rigor solution, 0.17 M KCl, 1 mM $MgCl_2$, 10 mM 3-(N-morpholino) propanesulfonic acid (MOPS) (pH 7.0) and 1 mM EGTA; relaxing solution, 117 mM KCl, 5 mM $MgCl_2$, 4 mM ATP, 10 mM MOPS (pH 7.0), 1 mM EGTA and 20 mM 2,3-butanedione 2-monoxime (BDM); contracting solution, 117 mM KCl, 4.25 mM $MgCl_2$, 2.2 mM ATP, 1.9 mM $CaCl_2$, 20 mM MOPS (pH 7.0) and 2 mM EGTA; standard SPOC solution, 41 mM KCl, 14.2 mM $MgCl_2$, 2.2 mM ATP, 16.4 mM ADP, 2 mM EGTA, 10 mM MOPS (pH 7.0), 10 mM inorganic phosphate (Pi) and 0.1 mM P^1,P^5-di(adenosine-5')pentaphosphate (AP_5A).

RESULTS AND DISCUSSION

The reconstitution of actin (thin) filaments in cardiac muscle bundles is not as difficult as one might imagine if the experimental protocol described in Fig. 2 is precisely followed. However, there are several key points for realizing the structural and functional reconstitution of actin filaments in thin filament-free fibers. The most important point is that the polymerization of actin must preferentially occur onto the short actin fragments remaining at the Z line. In other words, spontaneous polymerization that occurs outside the muscle bundle should be suppressed as much as possible, at least until exogenous actin

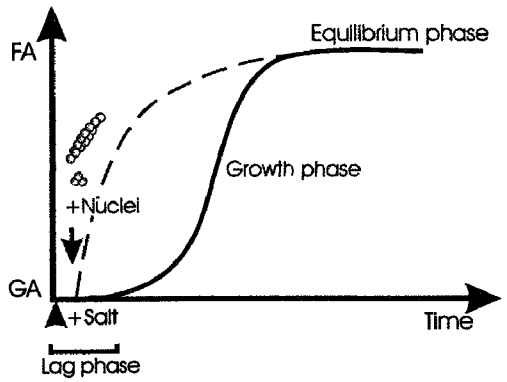

Figure 3. Schematic illustration showing the polymerization process of actin filaments with respect to the present reconstitution experiment. When nuclei of actin are exogenously added during the supersaturated phase of polymerization of actin, actin molecules preferentially polymerize onto the nuclei. This property plays a key role in the reconstitution of actin filaments in gelsolin-treated muscle fibers. That is, selective growth of actin onto the short actin fragments remaining at the Z line is realized by using this property.

molecules have penetrated into the myofilament lattice space by diffusion (this takes about 1 min in our preparation, which depends on the thickness of the fibers). As is well known, the polymerization process of actin consists of two processes; nucleation and growth. Nucleation is usually a rate-limiting step for the polymerization, such that the time course of polymerization of actin is as represented schematically in Fig. 3. During the initial lag phase, nucleation hardly occurs, but if nuclei are exogenously added during the lag phase, actin molecules immediately polymerize onto the added nuclei, resulting in the rapid growth of actin filaments as shown by the dashed line in Fig. 3. To fulfil the above requirements for reconstitution, we needed to determine a condition under which a long lag phase exists, such that the short fragments remaining at the Z line function as nuclei for polymerization of actin. By trial and error, we found that 80 mM KI instead of KCl is appropriate for obtaining a long-lasting lag phase. We confirmed that treatment of fibers with such a low concentration of KI did not affect the contractile properties of the fibers.

The polymerization rate at the B-end of actin filaments is a few to ten times higher than that at the P-end of actin filaments, depending on the conditions[11]. In any case, polymerization preferentially occurs at the B-end, so that the filament grows almost unidirectionally toward the B-end if both ends of the actin filaments are open, but if the B-end is closed, that is, blocked, for example, by binding of capping proteins, polymerization should occur selectively at the P-end. This was the case in our reconstitution system. In striated muscle, regardless of whether the length of thin filaments is precisely determined (skeletal muscle) or not (cardiac muscle), both the P-end and B-end are capped by capping proteins[12,13], i.e., tropomodulin[14] at the P-end and Cap Z[15] at the B-end. Here, the P-end capping proteins are removed accompanied by selective removal of thin filaments by gelsolin treatment, whereas the B-end structure is maintained intact because the short fragments, in which the B-end structure of thin filaments is included, are probably protected from the severing activity of gelsolin, especially in cardiac muscle in which the Z line structure is thick and appears to be solid. Thus, in the short fragments remaining at the Z line, the P-end is open, but the B-end is closed. Therefore, polymerization occurs in the correct direction, although it is relatively slow. Although we have not yet presented direct

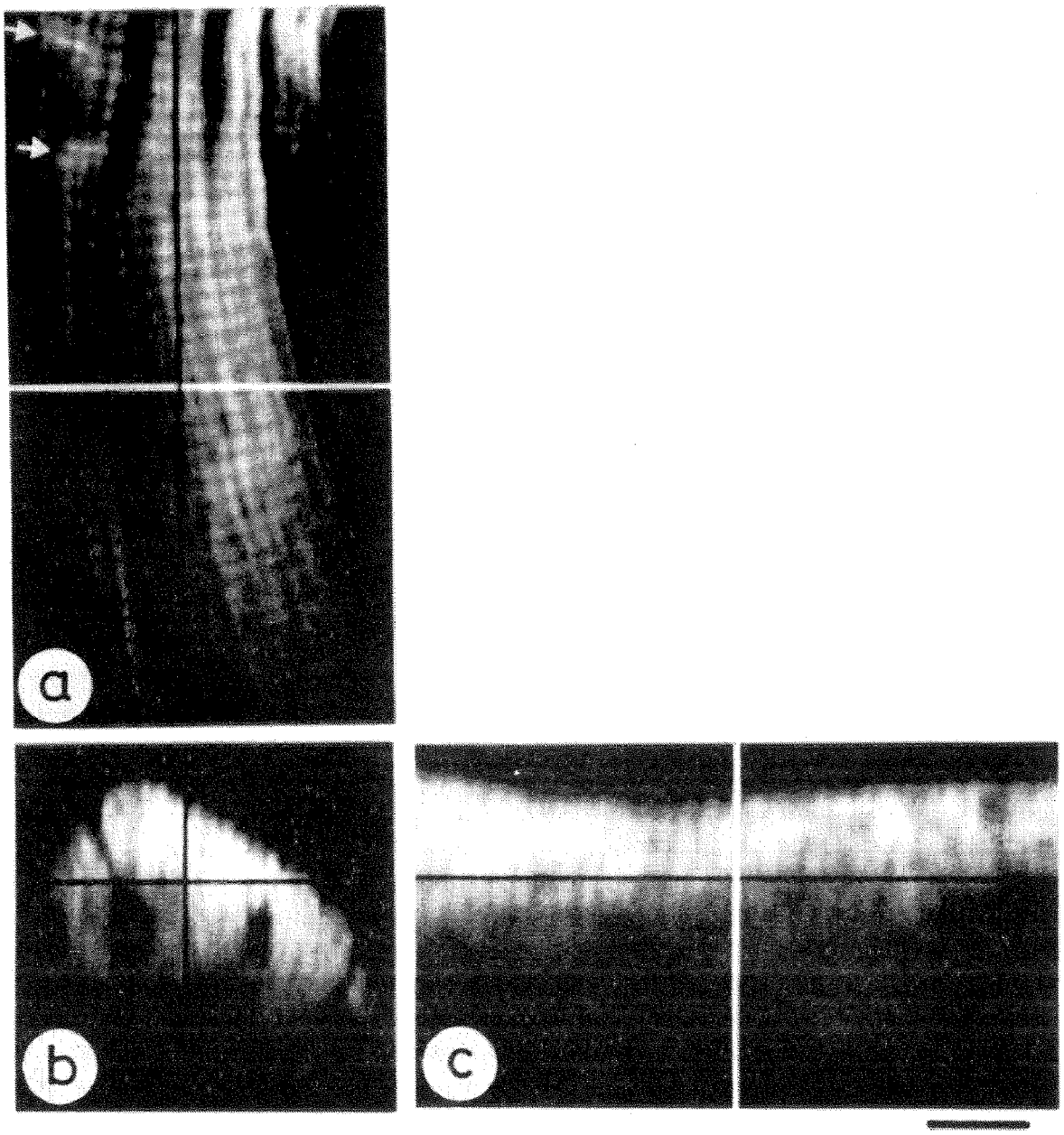

Figure 4. Confocal fluorescence micrographs of glycerinated cardiac muscle bundle. Both ends of a bundle were first fixed on a glass slide using cellophane adhesive tape, and then actin filaments were labeled with fluorescent rhodamine-phalloidin (7 μM) after chemical fixation with 3% formaldehyde for 30 min in rigor solution at room temperature. a, Real image of a longitudinal section of the bundle (arrows indicate intercalated disks); b, reconstituted image of a cross-section at the white line of Fig. a (horizontal and vertical black lines represent the sections of Figs. a and c, respectively); c, reconstituted image of a longitudinal section at the black line of Fig. a (black and white lines represent sections of Figs. a and b, respectively). Scale bar, 10 μm.

evidence for the above interpretation, the experimental results that the tension was fully recovered strongly supports this interpretation.

In addition, to realize the conditions for reconstitution, pure G-actin solution in which nuclei are absent should be carefully prepared. Also, the temperature of the polymerization solution should be kept low, at 2 a, at least. The low temperature is critical for realizing a long-lasting supersaturated phase.

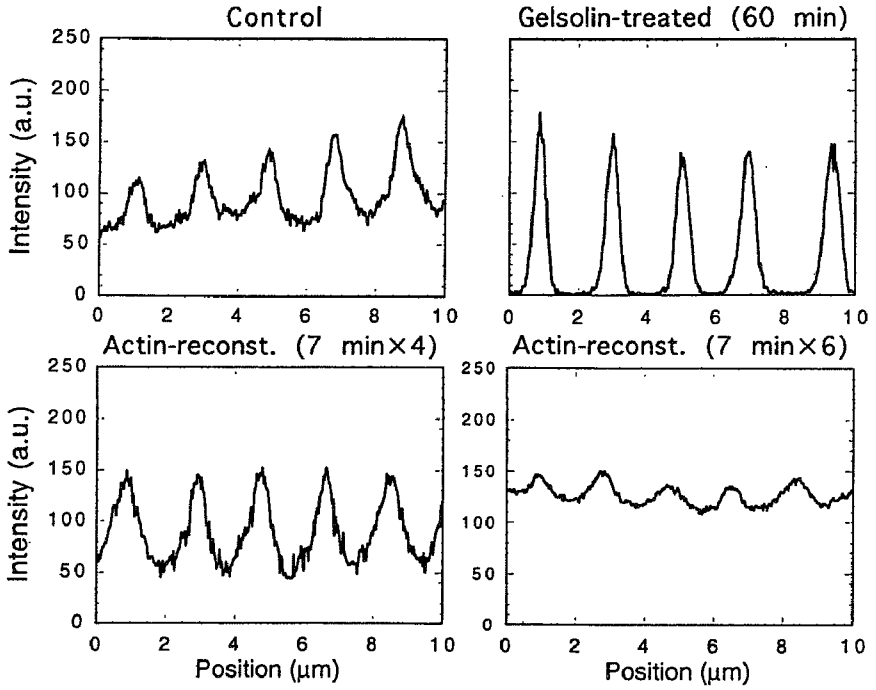

Figure 5. Intensity profile of fluorescence image of cardiac muscle bundle along the long axis of myofibrils. Micrographs were obtained for control, gelsolin-treated and actin filament-reconstituted fibers, under a confocal fluorescence microscope. Labeling and fixation procedure are the same as in Fig. 4, except the labeling and fixation were done after gelsolin treatment and reconstitution.

The degree of recovered tension did not depend on the source of the actin preparation; i.e., either rabbit skeletal or bovine cardiac muscle. Thus, the present reconstitution system is appropriate for examining the function of genetically engineered actin (and regulatory proteins) in the organized contractile system of muscle.

The reason why the structural and functional reconstitution was markedly better in cardiac muscle than in skeletal muscle is that the former's Z line structure was more resistant against the gelsolin treatment, so that the actin fragments almost fully remained at the Z line. This is probably because the Z line structure of cardiac muscle is thick; that is, there is a large overlap between thin filaments whose structural polarity is the reverse to each other. Besides, abundant accessory proteins (p-actinin etc.) may be associated with the Z line, so that the Z line structure is protected against the penetration and attachment of gelsolin (see structural model in ref. 16).

Figure 4 shows a typical sarcomeric structure and the periodic structure of myofibrils aligned along the long axis of a cardiac muscle bundle, indicating that the ordered structure of the contractile system is well preserved. The internal structure of the muscle bundle could be visualized by labeling thin filaments with fluorescent rhodamine-phalloidin and observing them under a confocal microscope. The brightest thick lines perpendicularly crossing the bundle (shown by arrows in Fig. 4a) correspond to intercalated disks, suggesting that the intercalated disks contain a high density of actin. As clearly seen in Fig. 4b, large spaces are present between muscle fibers; this is because abundant mitochondria present between fibers are removed by the detergent treatment after glycerination. We confirmed that such an ordered sarcomeric structure was not damaged even after the tension measurements.

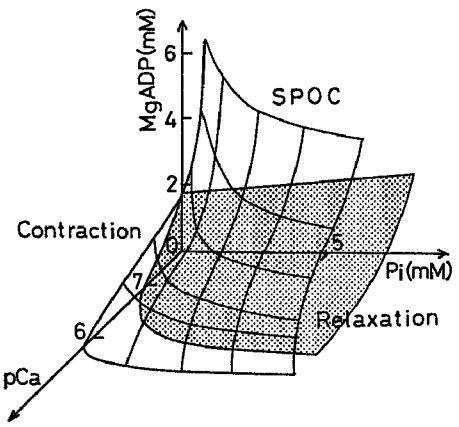

Figure 6. Three-dimensional state-diagram showing the state of the contractile apparatus of cardiac muscle under various concentrations of MgADP, Pi and free Ca^{2+}. The 3-D state-diagram was constructed by referring to the 2-D state-diagrams obtained on a pCa-Pi plane at various concentrations (0–10 mM) of MgADP in the presence of 2 mM MgATP[19]. The SPOC region is three-dimensionally sandwiched between the contraction region that is located in front of the meshed surface and the relaxation region that is located behind the dotted surface (this is a corrected and quantitative version of Fig. 3b of ref. 20). The state-diagram of skeletal muscle is the same as that of cardiac muscle except that the SPOC region on the pCa axis (Ca-SPOC region) is absent and the SPOC region on the MgADP-Pi plane (ADP-SPOC region) is shifted upward (toward higher MgADP concentrations).

The fluorescence intensity of the Z line was also high because of the large overlap of the B-end portion of thin filaments (Fig. 5). In cardiac muscle, the whole region of thin filaments was labeled with rhodamine-phalloidin[17]. This is in contrast to skeletal muscle in which rhodamine-phalloidin is attached to only both ends of thin filaments. This is probably because nebulin which associates side-by-side with the whole length of thin filaments blocks the binding sites of phalloidin; this nebulin is absent in cardiac muscle.

Here, we briefly describe the spontaneous oscillatory contraction (SPOC) of muscle fibers and fibrils. The physiological function of the cardiac contractile system is oscillatory contraction under the control of pacemaker cells. On the contrary, the physiological function of skeletal muscle is different from that of cardiac muscle in spite of the fact that the fine structure is the same as that of cardiac muscle; i.e., striated. That is, the muscle is either undergoing contraction (without oscillation) or relaxation, under the control of the nervous system. In fact, the physiological properties of the contractile system are different between them; cardiac muscle shows SPOC at micromolar concentrations of free Ca^{2+} (we call this Ca-SPOC), whereas skeletal muscle does not[18], but the skeletal muscle contractile system shows SPOC that is indistinguishable from Ca-SPOC under the coexistence of MgATP, MgADP and Pi in the absence of Ca^{2+} (we call this ADP-SPOC[18]). As summarized in Fig. 6, an ADP-SPOC region exists on the MgADP-Pi plane and a Ca-SPOC region exists on the pCa axis. These two SPOC regions are connected to each other, such that the SPOC region constitutes a single region which is sandwiched between contraction and relaxation regions[19–21].

As an application of the actin filament-reconstituted fibers, we examined whether the SPOC phenomena occur without the regulatory proteins, i.e., the tropomyosin-troponin complexes. A typical solvent condition for ADP-SPOC is coexistence of MgATP (sub-mM to a few mM) with MgADP (nearly equal concentration to (for cardiac) or a higher concentration of (for skeletal) that of MgATP) and Pi (higher than about 1 mM); Ca^{2+} is usually absent. Because of the absence of regulatory proteins, the reconstituted fibers develop tension even in the absence of Ca^{2+}. Therefore, the actin-reconstituted fibers

Table 1. SPOC conditions examined in the reconstitution system

	Standard SPOC[a]	+5 mM BDM[b]	+10 mM BDM[b]	+10 mM BDM[b] +Ca	+10 mM BDM[b] –Pi
Control	++	++	ND	++	–
Reconstituted	–	+	++	++	–

[a]Standard SPOC conditions: 41 mM KCl, 14.2 mM $MgCl_2$, 2.2 mM ATP, 16.4 mM ADP, 2 mM EGTA, 10 mM MOPS (pH 7.0), 10 mM Pi and 0.1 mM AP_5A at room temperature;
[b]+BDM (+Ca), BDM (and $CaCl_2$) was added to the standard SPOC solution; –Pi, Pi was omitted from the standard SPOC solution.
++: Large tension oscillation was observed; +: Small tension oscillation was observed; ND: Tension level was too low to detect tension oscillation; –: Tension oscillation was not observed.

developed tension without tension oscillation under typical ADP-SPOC conditions. Besides, Ca-SPOC did not occur because Ca^{2+} sensitivity was lost.

The essential point for SPOC to occur is that the condition must be intermediate between contraction and relaxation. We have proposed that such conditions as to generate intermediate tension are not sufficient for SPOC, and moreover, the proportions of force-generating species (e.g., AMADP) and non-force-generating species (e.g., AMADPPi) of actomyosin (AM) complex in (half-)sarcomeres must exceed certain threshold values[18]. By trial and error to find the chemical conditions that fulfil the above criteria, we could find SPOC conditions for the actin filament-reconstituted fibers (without regulatory proteins).

As summarized in Table 1, we found that SPOC occurred by making the fibers partially relax with the addition of BDM, a relaxing reagent, in the presence of MgATP, MgADP and Pi. Simple addition of BDM to the fibers in the presence of MgATP without MgADP and Pi did not induce SPOC even if the tension was decreased to the intermediate level; both MgADP and Pi were needed in coexistence with MgATP (Fujita & Ishiwata, manuscript submitted). Because of the absence of regulatory proteins, Ca^{2+} did not affect the SPOC conditions.

In the present study, we could demonstrate that SPOC occurs without regulatory proteins. Regulatory proteins are required for Ca-SPOC and may function to facilitate the occurrence of ADP-SPOC, but they are not indispensable. We conclude that auto-oscillatory properties are intrinsic to actomyosin motors. We anticipate that the auto-oscillation of tension (or sliding movement) of actomyosin motors can be realized in an *in vitro* motility assay system. SPOC may not occur in single molecular motors but occur in an assembly of motors. Besides, it would be interesting to examine whether or not alignment of motors is needed for SPOC to occur.

REFERENCES

1. Ishiwata, S. *J. Biochem.* **89**, 1647–1650 (1981).
2. Tawada, K., Yoshida, A. & Morita, K. *J. Biochem.* **80**, 121–127 (1976).
3. Ishiwata, S., Muramatsu, K. & Higuchi, H. *Biophys. J.* **47**, 257–266 (1985).
4. Ishiwata, S. & Okamura, N. *Biophys. J.* **56**, 1113–1120 (1989).
5. Ishiwata, S., Funatsu, T. & Asami, Y. Proc. 6th Taniguchi International Symposium on Biophysics (ed. S. Ishiwata) pp. 262–293, Taniguchi Foundation (1980).

6. Funatsu, T., Higuchi, H. & Ishiwata, S. *J. Cell Biol.* **110**, 53–62 (1990).
7. Yasuda, K., Anazawa, T. & Ishiwata, S. *Biophys. J.* **68**, 598–608 (1995)
8. Funatsu, T., Kono, E., Higuchi, H., Kimura, S., Ishiwata, S., Yoshioka, T., Maruyama, K. & Tsukita, S. *J. Cell Biol.* **120**, 711–724 (1993).
9. Funatsu, T., Anazawa, T. & Ishiwata, S. *J. Muscle Res. Cell Motil.* **15**, 158–171 (1994).
10. Fujita, H., Yasuda, K., Niitsu, S., Funatsu, T. & Ishiwata, S. *Biophys. J.* **71**, 2307–2318 (1996).
11. Kondo, H. & Ishiwata, S. *J. Biochem.* **79**, 159–171 (1976).
12. Ishiwata, S. & Funatsu, T. *J. Cell Biol.* **100**, 282–291 (1985).
13. Funatsu, T., Asami, Y. & Ishiwata, S. *J. Biochem.* **103**, 61–71 (1988).
14. Fowler, V.M. *J. Biol. Chem.* **262**, 12792–12800 (1987).
15. Casella, J.F., Craig, S.W., Maack, D.J. & Brown, A.E. *J. Cell Biol.* **105**, 371–379 (1987).
16. Yamaguchi, M., Izumimoto, M., Robson, R.M. & Stromer, M.H. *J. Mol. Biol.* **184**, 621–644 (1985).
17. Yasuda, K., Fujita, H., Fujiki, Y. & Ishiwata, S. *Proc. Jpn. Acad.* **70**, Ser. B., 151–156 (1994).
18. Ishiwata, S. & Yasuda, K. *Phase Transi.* **45**, 105–136 (1993).
19. Fukuda, N., Fujita, H., Fujita, T. & Ishiwata, S. *Pflug. Arch.* **433**, 1–8 (1996).
20. Ishiwata, S., Anazawa, T., Fujita, T., Fukuda, N., Shimizu, H. & Yasuda, K. in *Mechanism of Myofilament Sliding in Muscle Contraction* (eds. Sugi, H. & Pollack, G.H.) 545–556 (Plenum Press, New York, 1993).
21. Fukuda, N. Master's Degree, School of Science & Engineering, Waseda Univ. (1993).
22. Robinson, T.F. & Winegrad, S. *Nature* **267**, 74–75 (1977).
23. Wang, K. & Wright, J. *J. Cell Biol.* **107**, 2199–2212 (1988).
24. Moncman, C.L. & Wang, K. *Cell Motil. Cytoskeleton.* **32**, 205–225 (1995).
25. Maruyama, K., Yoshioka, T., Higuchi, H., Ohashi, K., Kimura, S. & Natori, R. *J. Cell Biol.* 101, 2167–2172 (1985).
26. Wang, K. in *Cell and Muscle Motility*. Vol. 6 (ed. Shay, J.W.) 315–369 (Plenum Publishing Co., New York, 1985).

DISCUSSION

Szent-Gyorgyi: Your system may be suitable to shed some light on the mechanism of filament length determination. I have two questions: Do the reconstituted filaments have a constant length? And, does filament length depend on sarcomere length?

Ishiwata: As you may know, the length of thin filaments in cardiac muscle is not well determined in contrast to that in skeletal muscle. The length distribution of reconstituted actin (thin) filaments in cardiac muscle was also broad. Besides, the average length was longer than that in the original. As for the second question, we could not change the sarcomere length over a wide range because it was difficult to stretch the cardiac fibers. The removal and reconstitution of thin filaments were done at sarcomere lengths of 2.0 ± 0.2 μm.

Rall: What is the reason why the recovered tension exceeded the original?

Ishiwata: The active tension of the reconstituted cardiac muscle fibers reached, on the average, about 140% of the original. This is partly explained by the elongation of reconstituted thin filaments. But, we can not explain why more than 200% augmentation of tension development was attained in some cases. Such a large tension augmentation can not be explained only by the elongation of reconstituted thin filaments longer than the original. So, we speculate that some tension suppressor that specifically attaches to the thin filaments is present in an intact muscle. We may have missed this factor during the removal of thin filaments. I am happy if we can get a chance to identify and isolate such a factor functioning in cardiac muscle.

Sugi: In my opinion, SPOC occurs due to the oscillation of the concentrations of chemical substances such as ADP and Pi in the myofilament lattice. So, I predict that if you flash such substances to myofibrils under a microscope, you would be able to initiate the SPOC and/or modify the SPOC.

Ishiwata: I abandoned the idea that SPOC is a chemical oscillation at the early stage of this study. That is because SPOC occurs very beatifully in a single myofibril of which diameter is only 1 μm so that the time for chemical substances to exchange is estimated to be an order of 1 ms, which is quite short compared with the period of SPOC which is about 1 s. So, I believe that the SPOC phenomena are attributable to the intrinsic properties of the contractile apparatus itself. Besides, I would like to stress that we could recently demonstrate that SPOC occurs even in the contractile system without regulatory proteins, suggesting that the auto-oscillation is characteristic of actomyosin motors themselves.